NASA TECHNICAL NOTE **NASA TN D-7940**

NASA TN D-7940

A FORMAL STRUCTURE FOR ADVANCED AUTOMATIC FLIGHT-CONTROL SYSTEMS

George Meyer and Luigi Cicolani

Ames Research Center
Moffett Field, Calif. 94035

NATIONAL AERONAUTICS AND SPACE ADMINISTRATION • WASHINGTON, D. C. • MAY 1975

1. Report No.	2. Government Accession No.	3. Recipient's Catalog No.
TN D-7940		

4. Title and Subtitle	5. Report Date
A FORMAL STRUCTURE FOR ADVANCED AUTOMATIC FLIGHT-CONTROL SYSTEMS	May 1975
	6. Performing Organization Code
7. Author(s) George Meyer and Luigi Cicolani	8. Performing Organization Report No. A-5710
9. Performing Organization Name and Address Ames Research Center Moffett Field, Calif., 94035	10. Work Unit No. 501-03-11
	11. Contract or Grant No.
12. Sponsoring Agency Name and Address National Aeronautics and Space Administration Washington, D. C. 20546	13. Type of Report and Period Covered Technical Note
	14. Sponsoring Agency Code

15. Supplementary Notes

16. Abstract

An effort is underway at Ames Research Center to develop techniques for the unified design of multimode, variable authority automatic flight-control systems for powered-lift STOL and VTOL aircraft. This report describes a structure for such systems which has been developed to deal with the strong nonlinearities inherent in this class of aircraft, to admit automatic coupling with advanced air traffic control requiring accurate execution of complex trajectories, and to admit a variety of active control tasks. The specific case being considered is the augmentor wing jet STOL research aircraft.

17. Key Words (Suggested by Author(s))	18. Distribution Statement
Handling qualities Flight controls Autopilot	Unclassified - unlimited STAR Category - 08

19. Security Classif. (of this report)	20. Security Classif. (of this page)	21. No. of Pages	22. Price*
Unclassified	Unclassified	39	$3.75

*For sale by the National Technical Information Service, Springfield, Virginia 22151

TABLE OF CONTENTS

SYMBOLS

A_{as} direction cosine matrix, actual attitude of the aircraft with respect to inertial space

A_{cs} direction cosine matrix, commanded attitude of the aircraft with respect to inertial space

A_{vs} direction cosine matrix, commanded velocity axes with respect to inertial space

b wing span

c wing chord

C_D drag coefficient

C_{Dc} commanded drag coefficient

C_J cold thrust coefficient

C_L lift coefficient

C_{Lc} commanded lift coefficient

C_{Ma} moment coefficient vector with respect to body axes

C_{Mac} commanded moment coefficient with respect to body axes

C_s total force vector coefficient

D drag

$E_i(\phi)$ elementary rotation about axis i through angle ϕ

f_s total aerodynamic and propulsive force in inertial coordinates

$f(x,u)$ right-hand side of system state equation

g acceleration of gravity

$g(\dot{x},x)$ trimmap

h_a body coordinates of total angular momentum

$h(e)$ right-hand side of transition dynamics

$K(\dot{x},x)$ feedback gain schedule

L lift

m	aircraft mass
M_a	body coordinates of aerodynamic and propulsive moment
Q	dynamic pressure
R_s	inertial coordinates of position vector
R_s^*	inertial coordinates of position vector commanded by air traffic control
R_{sc}	inertial coordinates of position given by command generator
S_w	wing area
t	time variable
δT	throttle
T_c	cold thrust
T_h	hot thrust
u	control vector
u_a	body coordinates of unit vector along relative velocity vector
u_s	inertial coordinates of unit vector along relative velocity vector
v	airspeed (true airspeed)
v_a	body coordinates of relative velocity vector
v_{am}	measured body coordinates of relative velocity vector
v_s	inertial coordinates of relative velocity vector
V_s	inertial coordinates of aircraft velocity vector
V_s^*	inertial coordinates of velocity commanded by air traffic control
V_{sc}	inertial coordinates of velocity commanded by command generator
$\dot{V}_s$	inertial coordinates of aircraft acceleration vector
$\dot{V}_s^*$	inertial coordinates of acceleration commanded by air traffic control
$\dot{V}_{sc}$	inertial coordinates of acceleration commanded by command generator
$\dot{V}_{sI}$	inertial coordinates of acceleration input to trimmap

$\dot{V}_{sm}$ inertial coordinates of acceleration modifications due to perturbation controller

w_s inertial coordinates of wind

$\hat{w}_s$ inertial coordinates of estimated wind

x system state

α angle of attack

β angle of sideslip

γ_v glide-slope angle of relative velocity vector

δ_{ec} elevator command

δ_F flap angle

δ_i column matrix with 1 in ith row and 0 in the other two rows

δ_{rc} rudder command

δ_T throttle command

δ_{wc} wheel command

η variables of unsteady aerodynamics

θ pitch angle

ν nozzle angle

ρ density of air

σ side-force angle

ϕ roll angle

ψ yaw angle

ω_a body coordinates of aircraft angular velocity

ω_n bandwidth

A FORMAL STRUCTURE FOR ADVANCED AUTOMATIC FLIGHT-CONTROL SYSTEMS

George Meyer and Luigi Cicolani

Ames Research Center

SUMMARY

An effort is underway at Ames Research Center to develop techniques for the unified design of multimode, variable authority automatic flight-control systems for powered-lift STOL and VTOL aircraft. This report describes a structure for such systems which has been developed to deal with the strong nonlinearities inherent in this class of aircraft, to admit automatic coupling with advanced air traffic control requiring accurate execution of complex trajectories, and to admit a variety of active control tasks. The specific case being considered is the augmentor wing jet STOL research aircraft.

INTRODUCTION

Government and industry are investing substantial resources in developing new aircraft configurations required to meet the needs of the nation in the 1980's and beyond. Present indications are that automatic flight-control systems will play a significant role in this development. The basis for such a forecast is a combination of three factors.

1. The mix of aircraft types such as VTOL, STOL, CTOL, and SST will require an advanced air traffic control (ATC) system. The accommodation of many aircraft covering a wide spectrum of speeds and maneuverability and at the same time satisfying stringent environmental constraints can be achieved only if the ATC has at its disposal a sufficiently large set of trajectories. Accurate execution of any one of a large set of complex trajectories will require a powerful automatic flight-control system that uses the maximum capability of each aircraft type.

2. Current work aimed at providing aircraft for short-haul transportation is developing the powered-lift technology. Among the concepts being considered are the augmentor wing, tilt rotor, lift fan, and externally blown flap. In all cases, the wide range of lift coefficient is achieved by inflight modifications of the aircraft configuration.

These modifications result in drastic changes in control characteristics of the aircraft; particularly in the high lift transition and landing configurations, the aircraft response to control inputs is very nonlinear. Moreover, the presence of powered- and direct-lift generators increases the total number of controls available to the pilot who must continually make decisions on control techniques. Accurate, unaided manual tracking of complex trajectories by manipulating a large set of interacting controls of an aircraft whose control characteristics are nonlinear and rapidly changing represents an unacceptably high pilot workload. Automatic flight control can reduce the pilot workload to an acceptable level by integrating control functions so as to generate desirable handling qualities without reducing the performance of the aircraft as an element of the advanced civil air transportation system. The advantages of automatic flight control are potentially even more substantial in military applications of STOL and VTOL aircraft. Both the advanced military STOL and the Sea Control Fighter VTOL must utilize to the fullest the maneuvering capability of the basic aircraft. The tracking of complex trajectories must be sufficiently accurate to properly execute a mission, and the pilot workload associated with flying must not adversely affect his ability to perform other tasks. Again, the maneuverability, accuracy, flexibility, and level of pilot workload can be improved with automatic flight control.

3. The rapidly advancing technology of sensors, actuators, and electronic components is approaching the point when servomechanisms with reliability comparable to that of a wing can be built and maintained economically. Consequently, the conventional direct mechanical systems composed of cables, push rods, bell cranks, and mixers that link the pilot to control surfaces can be replaced by fly-by-wire systems. Although fly-by-wire technology itself offers several advantages over the conventional mechanical control systems, the real goal lies in the application of active control technology (ACT) to future aircraft. The key idea of ACT is the integration of control with aerodynamics, structures, and propulsion early in the design cycle of the aircraft. Studies have shown that significant reductions in induced drag and structural weight, improvements in passenger comfort, and reduction of flight hazards can be achieved with ACT. These benefits are possible due to (a) a reduction in the sizes of stabilizing surfaces, with stability provided by dynamically controlling movable surfaces rather than statically with larged fixed surfaces as in the conventional designs; (b) reductions in structural strength requirements by applying maneuver load alleviation and gust load alleviation; (c) improvement of ride qualities by a ride quality control system; and (d) reduction in the occurrence of inadvertent flight hazard through automatic limitation of flight conditions. These and other ACT concepts are currently being developed. A total automatic flight-control system is required to integrate all these control functions with the autopilot.

Thus, indications are that automatic flight-control systems will play a significant role in the development of future aircraft. Of course, these systems were needed in the past, but the designer was severely limited by the characteristics of available transducers and, particularly, by the small inflight computational capacity. However, rapid advances have resulted in a large variety of accurate and reliable devices, while the capacity of digital flight computers has increased phenomenally and continues to increase. As a result, the designer is now limited primarily by the available methodology for the design of automatic flight-control systems.

The most severe limitation of the existing design techniques is their extreme reliance on linear perturbation models of the aircraft. So long as nonlinear effects are of minor significance, these techniques are quite adequate. But as nonlinearities become prominent because of either increased system accuracy requirements or the physics of force and moment generation in the powered-lift configurations, linear methods become less tractable. Many perturbation models are needed to cover the flight envelope adequately. Even the procedure for choosing reference trajectories about which to perturb is unclear at present, and controls corresponding to these trajectories that trim the aircraft cannot be generated easily or accurately by means of perturbation techniques. Logic must be provided in the flight computer for switching the perturbation control gains and reference controls as the aircraft leaves the domain of validity of one perturbation model and enters another. The result is a design that is complex in concept and implementation so that analyses of closed-loop sensitivity to modeling errors and subsystem failures are exceedingly difficult and not very convincing.

Design techniques are needed of sufficient generality to be applicable to a large set of aircraft types with nonlinear dynamics and multiple redundant controls. The techniques must admit an effective tradeoff between tracking accuracy requirements on the one hand and requirements imposed on the capacity of the flight computer and on the a priori knowledge of system dynamics on the other hand. The techniques must be nearly algorithmic to permit tradeoff studies early in the aircraft design cycle when many alternative aircraft configurations are being considered. Techniques are needed for integrating a variety of active control functions with an autopilot having a multitude of modes and for coupling the autopilot automatically with the air traffic control. Finally, these design techniques must result in designs sufficiently simple to admit an effective reliability analysis.

An effort is underway at Ames to develop the methodology for the design of advanced flight-control systems. This report describes the progress made in the first segment of this program, namely, the formulation of an overall logical structure for multimode, variable authority, automatic flight-control systems. The proposed structure consists of five major subsystems: (1) The force trimmap trims the aircraft to any admissible time-varying acceleration vector. One of the outputs of the force trimmap is the possibly time-varying trim attitude. (2) The attitude control system generates commands to the moment-generating control surfaces and thereby forces the aircraft attitude to follow the input from the force trimmap. (3) The wind estimator provides estimates of the aircraft velocity vector relative to the air mass which are needed in the force trimmap and attitude control system calculations. (4) The trajectory perturbation controller closes the loop around the inaccuracies of the force trimmap, attitude control system, and wind estimator. The result is a trajectory acceleration vector controller whose input-output relation between the commanded acceleration and actual aircraft acceleration is essentially an identity, provided the input is flyable and its bandwidth is suitably restricted. (5) The trajectory command generator transforms the inputs from the air traffic control or the pilot into trajectories whose acceleration is consistent with the limitations of the trajectory acceleration controller. The basis for the proposed structure as well as its feasibility, benefits, and limitations are discussed. The internal structure of the five major subsystems is presented in some detail to clarify the intent of each subsystem.

The augmentor wing jet STOL research aircraft is used as a specific example. It is emphasized, however, that the objective of this report is not to present a complete automatic flight-control system for a particular aircraft, but rather to propose an overall logical structure for such systems.

BASIC COMMANDS TO AUTOMATIC FLIGHT-CONTROL SYSTEM

The boundary of the system considered here is shown schematically in figure 1. In the following discussion, the automatic flight-control system is the complete control system of the aircraft. It consists of all sensors, actuators, and control logic. The set of sensors measures aircraft motion and includes devices that are onboard as well as ground-based systems such as the MLS (when available). The function of the control logic is to operate on the data from the sensors and commands from the (generalized) air traffic control (ATC) and thereby to generate commands to the actuators which, in turn, control the aircraft. The degree of automation of the control logic ranges from the fully automatic mode, in which the actuators are completely under the control of the flight computer, to the fully manual mode, in which the actuators are controlled exclusively by the pilot. Between these extremes, there is a spectrum of modes with specific functions such as handling quality control, ride quality control, gust load alleviation, maneuver load control, and a variety of autopilot modes such as autothrottle, altitude hold, heading capture, etc. Of course, combinations of such elementary modes may also be required. In addition, the control logic must be able to detect failures in various subsystems and switch (when necessary) to the next safest control strategy. The subject of this report is the design of such control logic. (The estimation problem associated with sensors and the design of fly-by-wire systems is not discussed.)

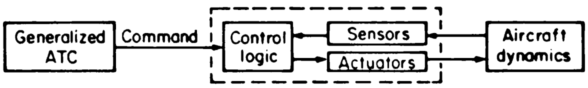

Figure 1.- Elements of automatic flight control system.

The basic input to the control logic is the trajectory to be followed by the aircraft. The trajectory may be commanded explicitly by the ATC or implicitly by the pilot. A simple case, conceptually, occurs when (based on wind estimates, the capabilities of the aircraft, and other considerations) ATC selects a flyable trajectory to be followed by the aircraft. Generally, the set of admissible trajectories consists of a sequence of continuous segments defined on relatively long (e.g., greater than 10 sec) intervals of time (ref. 1). Often the segments belong to a small set (e.g., lines and circles), in which case only the parameters and duration of the segments are transmitted to the aircraft and the commanded trajectory is reconstructed onboard. Otherwise, the coordinates of the trajectory are transmitted to the aircraft continuously. In either case, the segments are defined on intervals of time; hence, position, velocity, and acceleration vectors corresponding to the commanded trajectory are available to the control logic continuously. Moreover, since the motion of the aircraft in inertial space (a flat nonrotating earth is assumed throughout for simplicity) is of prime concern, inertial coordinates of these vectors are considered as fundamental. The situation is essentially the same whenever the aircraft is commanded to coincide with a moving target as, for example, a carrier landing or docking with another aircraft or a missile intercepting another object.

The pilot is an alternative source of commands. Of course, if he feeds the trajectory parameters into the autopilot either as a voice command from ATC or on his own initiative, he may be considered part of the ATC. However, many of the commonly used autopilot modes such as heading hold, altitude hold, autothrottle, glide-slope capture, control wheel steering, etc., generate the commanded trajectory only implicitly and often incompletely. Nevertheless, in most cases, an appropriate equivalent ATC trajectory can be constructed to represent the pilot command. The trajectory may contain a number of free parameters which the control logic can be instructed to ignore. Consequently, most commands concerning the motion of the aircraft center of mass may be considered, at least conceptually if not in actual mechanization, to be generated in a standard form by the generalized ATC.

In view of the preceding discussion, the following decision is made concerning the structure of the automatic flight-control system:

Decision 1: The basic command to the automatic flight-control system is a concatenation of continuous segments Γ_k^*, each of which is given by

$$\Gamma_k^* = \left\{ y^*(t) = \begin{pmatrix} R_s^*(t) \\ V_s^*(t) \\ \dot{V}_s^*(t) \end{pmatrix}, \quad t \in T_k^* \right\}, \qquad k = 1,2,\ldots \tag{1}$$

where the 9-tuple consists of inertial coordinates of commanded inertial position (R_s^*), velocity (V_s^*), and acceleration ($\dot{V}_s^*$) vectors.

The complete trajectory may have discontinuities across the boundaries of the intervals T_k. For example, all coordinates are discontinuous at $t = t_4$ in figure 2. The control logic must synthesize a transition trajectory consistent with the limitations imposed by dynamics. Another possibility is

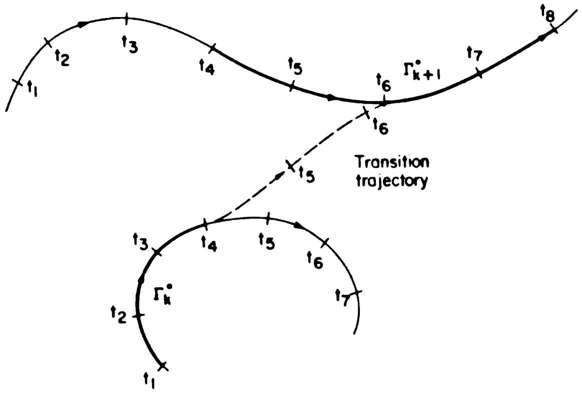

Figure 2.- A trajectory $\Gamma^* = \ldots \Gamma_k^* \, \Gamma_{k+1}^* \ldots$ with total discontinuity at $t = t_4$.

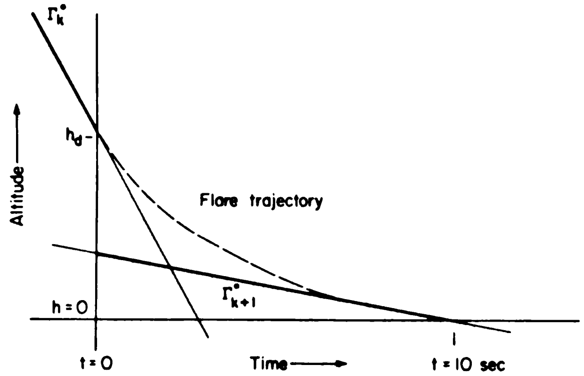

Figure 3.- ATC command, $\Gamma^* = \ldots \Gamma_{k+1}^*$, to land.

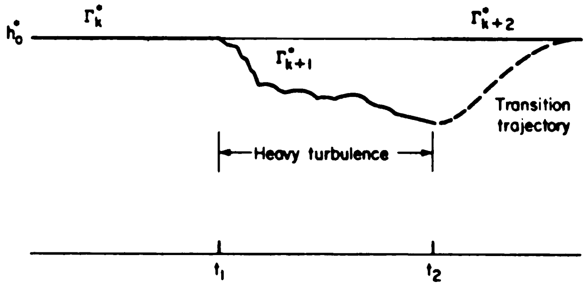

Figure 4.- Encounter with heavy turbulence.

illustrated in figure 3, which represents the vertical channel of the command to land. The segment Γ_k^* correspond to altitude variation while the aircraft is on the glide slope. The flare initiation altitude occurs at $t = 0$, at which time the segment Γ_{k+1}^* is commanded. Thus there is a discontinuity in both position and velocity at $t = 0$. Again, the control logic must synthesize an appropriate transition (flare) trajectory.

As already noted, some parameters of the commanded trajectory may be free. In particular, all nine coordinates need not be always tracked. For example, consider the three segments shown in figure 4. Segment Γ_k^* represents the command to track a four-dimensional trajectory with constant altitude h_o^*. At $t = t_1$, the aircraft encounters heavy turbulence. Depending on the severity of the turbulence relative to the limits imposed on aircraft dynamics, tracking may have to be relaxed from position, to velocity, or acceleration and, in the extreme case, only the attitude of the aircraft will be tracked while the ATC command is ignored completely. As a result, the aircraft is allowed to drift along some trajectory Γ_{k+1}^* away from the true ATC command. As turbulence subsides at $t = t_2$, four-dimensional tracking can be resumed. However, because of the errors accumulated in the interval (t_1, t_2), there will be, in general, a discontinuity in all coordinates of the command at $t = t_2$. The control logic must synthesize an appropriate transition trajectory to bring the aircraft back on Γ_{k+2}^*. The situation is essentially the same when the set of operating sensors changes with time or when the constraints imposed on the aircraft dynamics change perhaps because of failures in certain subsystems.

Based on the preceding discussion, the following decision is made concerning the formal structure of the control system.

Decision 2: The control logic contains a command generator that synthesizes trajectories

$$\Gamma = \left\{ y(t) = \begin{pmatrix} R_{sc}(t) \\ V_{sc}(t) \\ \dot{V}_{sc}(t) \end{pmatrix} , \forall t \right\}$$

which are flyable at all times by the aircraft with the available sensors and actuators and with existing constraints imposed on dynamics.

For example, the output of the command generator corresponding to the case in figure 3 is shown in figure 5. Note that there is no discontinuity in Γ at $t = 0$; while there is a discontinuity in Γ^* at the same instant. (The command generator is discussed further later in the report.)

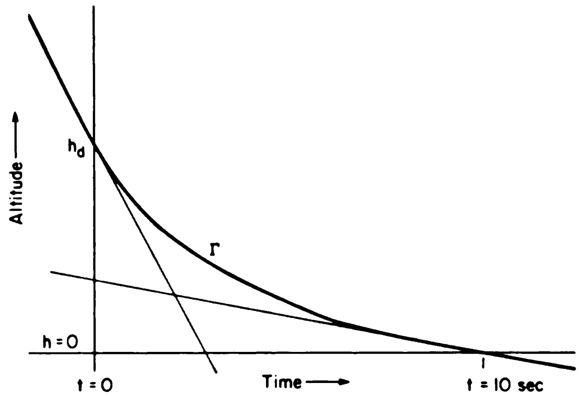

Figure 5.- Output of the command generator for a landing maneuver.

TRACKING ACCURACY

Clearly, one of the essential attributes of a control system is that it be as simple as possible, both in concept and in mechanization. The level of complexity, however, is determined ultimately by accuracy requirements. If the required accuracy is low, then many details of the aircraft equation of motion may be suppressed, and a simple model usually leads to a simple control law. As accuracy requirements are increased, a more detailed representation of aircraft dynamics becomes necessary. The model increases in complexity. The dimension of its state space increases as more dynamical elements are accounted for. New cross-coupling links appear. The number of parameters increases with finer representation of nonlinearities. All this increases the complexity of the control system. Moreover, the design methodology may have to be changed completely with an increase in accuracy requirement. As a result, tradeoff studies may become intractable. However, such studies are essential in the design of automatic flight-control systems advanced aircraft. Of particular interest is the tradeoff between the required capacity of the onboard computer and trajectory tracking accuracy. Hence, a single design methodology must be developed in which tracking accuracy is a variable.

The natural evolution of an AFCS for a new, possibly experimental, aircraft is by means of a sequence of refinements. For safety, initial flight tests are restricted to relatively simple maneuvers and to correspondingly simple modes of the control system with minimal authority and tracking accuracy. As flight data accumulate and good estimates of critical aircraft parameters become available, the set of maneuvers is expanded until, finally, it coincides with the designed flight envelope. Thus, the automatic flight-control system must be designed to allow a spectrum of tracking and modeling accuracies.

A spectrum of accuracy, rather than a single level, is also needed for normal aircraft operation. For example, in cruise, altitude tracking is obviously not as significant as during a landing maneuver and can be traded for, say, ride quality.

Therefore, the following decision is made concerning the structure of the control system.

Decision 3: The tracking accuracy enters the control logic as an independent variable, both during design as well as in normal operation.

The accuracy of a control system is ultimately limited by the accuracy of the navigation system. Hence the accuracy of the latter serves as an estimate of an upper bound on the former. The RAINPAL system (ref. 2) is one of the most accurate, flight-tested, navigation systems currently available. A comparison of RAINPAL errors with allowable errors for CTOL and SSV is given in table 1. In the remainder of this report, the RAINPAL errors are taken as the upper limit on the trajectory tracking requirements.

TABLE 1.- COMPARISON OF RAINPAL NAVIGATION ERRORS WITH ALLOWABLE ERRORS FOR CTOL AND SSV

Component	RAINPAL navigation error standard deviations	Navigation errors allowable for CTOL automatic landing systems	Navigation errors allowable for the SSV autoland system
X	0.9 ±0.6 m (3 ±2 ft)	132 m (433 ft)	43.2 m (139 ft)
Y	1.2 ±0.6 m (4 ±2 ft)	2.38 m (7.79 ft)	1.51 m (4.97 ft)
Z	0.9 ±0.6 m (3 ±2 ft)		2.46 m (8.08 ft)
$\dot{X}$	0.15 ±0.06 m/sec (0.5 ±0.2 ft/sec)		1.76 m/sec (5.77 ft/sec)
$\dot{Y}$	0.3 ±0.15 m/sec (1 ±0.5 ft/sec)		0.88 m/sec (2.89 ft/sec)
$\dot{Z}$	0.15 ±0.06 m/sec (0.5 ±0.2 ft/sec)		0.088 m/sec (0.289 ft/sec)

EQUATIONS OF MOTION

Let the inertial coordinates of the aircraft position and velocity with respect to the runway axes (flat, nonrotating earth is assumed throughout) be denoted by R_s and V_s, respectively. Then

$$\dot{R}_s = V_s \qquad (3)$$

where ($\dot{}$) denotes differentiation with respect to time t. Aerodynamic forces and moments depend on the velocity of the aircraft relative to the air mass. Let W_s denote the inertial coordinates of the wind velocity. Generally, W_s is a complicated function of position and time which may vary significantly over the dimensions of the aircraft. Let

$$W_s = w_s(R_s,t) + \delta w_s(R_s + r_s,t) \qquad (4)$$

where the first and second terms consist of wavelengths longer and shorter, respectively, than the aircraft dimensions, and r_s is position-referenced to the aircraft center of mass. The inertial coordinates v_s of the aircraft velocity relative to the air mass are defined in this report by

$$v_s = V_s - w_s \qquad (5)$$

where $w_s = w_s(R_s,t)$ is the average wind at the aircraft center of mass. Wind shear across the aircraft is ignored here. Polar coordinates of relative velocity are defined in a standard manner according to figure 6. Thus

$$v_s = vu_s \qquad (6)$$

and

$$u_s = E_3^T(\psi_v)E_2^T(\gamma_v)\delta_1 \qquad (7)$$

where $E_i(\phi)$ is an Euler rotation about axis i, $(\ )^T$ is the transpose of ( ), and δ_i is the column with 1 in the ith place and 0 in the other two. In the absence of wind, ψ_v is the aircraft heading angle and γ_v is the glide-slope angle.

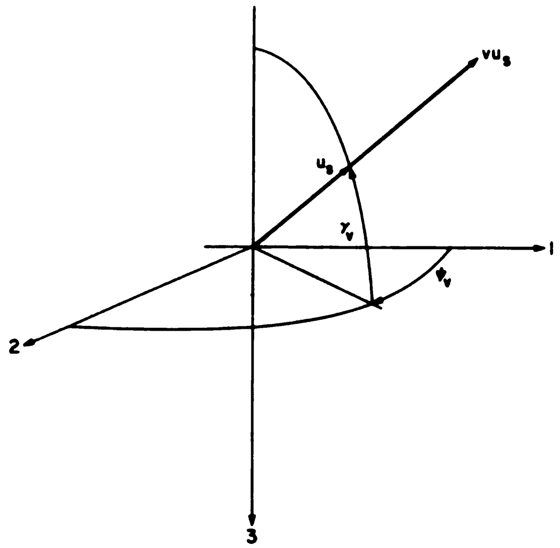

Figure 6.- Definition of airspeed, v, heading angle ψ_v and glide slope angle γ_v.

In the aircraft body axes, the relative velocity is given by

$$v_a = vu_a \qquad (8)$$

where

$$u_a = E_2(\alpha)E_3^T(\beta)\delta_1 \qquad (9)$$

Conversely,

$$\left.\begin{aligned}\alpha &= \tan^{-1}[u_a(3)/u_a(1)] \\ \beta &= \sin^{-1}[u_a(2)]\end{aligned}\right\} \qquad (1$$

where α and β are the angle of attack and sideslip angle as normally defined (ref. 3).

The attitude of the aircraft body axes with respect to the runway axes are defined by the direction cosine matrix A_{as}. If Euler angles are used in the 3-2-1 sequence, then

$$A_{as} = E_1(\phi)E_2(\theta)E_3(\psi) \qquad (1$$

The attitude can also be defined in terms of the angles associated with the direction of the relative velocity vector as

$$A_{as} = E_2(\alpha)E_3^T(\beta)E_1(\phi_v)E_2(\gamma_v)E_3(\psi_v) \qquad (1$$

where ϕ_v is the angle of roll about the relative velocity vector v_s. A block diagram representation of equation (12) is given in figure 7 for future reference. The term "heading" refers to the heading of the relative velocity vector.

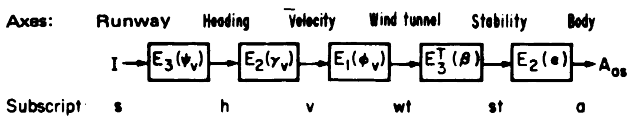

Figure 7.- Block diagram representation of equation (13).

Let the body coordinates of aircraft angular velocity with respect to the runway be denoted b ω_a. Then (see, e.g., ref. 4),

$$\dot{A}_{as} = S(\omega_a)A_{as} \qquad (13$$

where, for any column $x = (x_1, x_2, x_3)^T$,

$$S(x) = \begin{pmatrix} 0 & x_3 & -x_2 \\ -x_3 & 0 & x_1 \\ x_2 & -x_1 & 0 \end{pmatrix} \qquad (14$$

Equations (3) and (13) are the kinematic components of the aircraft equations of motion.

Let the inertial coordinates of total aerodynamic and propulsive force be denoted by f_s, and let m and g be the aircraft mass and acceleration of gravity, respectively. Then

$$\dot{V}_s = \frac{1}{m} f_s + g\delta_3 \tag{15}$$

The total aerodynamic and propulsive force is most directly expressed in terms of coordinates with respect to the wind-tunnel axes. Thus the total force along the relative velocity vector, henceforth to be called total drag,

$$D_{wt} = -QS_w C_D \delta_1 \tag{16}$$

where the dynamic pressure

$$Q = \frac{1}{2} \rho v^2 \tag{17}$$

for which ρ is the density of air, S_w is the wing area, and C_D is the total drag coefficient. The total force perpendicular to the relative velocity vector, henceforth to be called total lift,

$$L_{wt} = -QS_w C_L E_1^T(\sigma)\delta_3 \tag{18}$$

where C_L is the total lift coefficient and σ is defined in figure 8. Note that the present definition of the total lift coefficient includes the side force, and both total lift and drag coefficients include the effects of thrust. Generally,

$$\left.\begin{aligned} C_D &= C_D(\alpha,\beta,u;\eta) \\ C_L &= C_L(\alpha,\beta,u;\eta) \\ \sigma &= \sigma(\alpha,\beta,u;\eta) \end{aligned}\right\} \tag{19}$$

where u represents the available controls such as flaps, throttle, elevator, rudder, ailerons, etc., and η represents the dynamic variables such as $\dot{\alpha}$, $\dot{\beta}$, ω_a, etc., and other variables such as air temperature and density.

The inertial coordinates of the total aerodynamic and propulsive force are given by

$$f_s = QS_w C_s \tag{20}$$

where the total force vector coefficient is

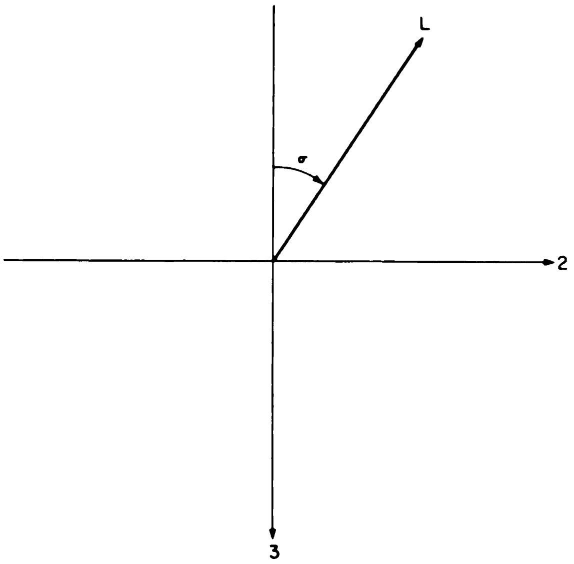

Figure 8.- Definition of lift vector used in report.

$$C_s = -A_{as}^T E_2(\alpha) E_3^T(\beta)[C_D \delta_1 + C_L E_1^T(\sigma)\delta_3] \tag{21}$$

The dynamic equation for rotation is given by

$$\dot{\omega}_a = J_a^{-1}[M_a + S(\omega_a)h_a] \tag{22}$$

where J_a is the aircraft moment of inertia in body axes, M_a is the total aerodynamic and propulsive moment, and h_a is the total aircraft angular momentum. When the angular momentum of spinning parts is negligible,

$$h_a = J_a \omega_a \tag{23}$$

The moment vector is defined in terms of the moment coefficients in the usual manner:

$$M_a = QS_w \begin{pmatrix} b & 0 & 0 \\ 0 & c & 0 \\ 0 & 0 & b \end{pmatrix} C_{Ma} \tag{24}$$

where b and c are the span and mean chord, respectively, of the wing. Generally,

$$C_{Ma} = C_m(\alpha, \beta, u; \eta) \tag{25}$$

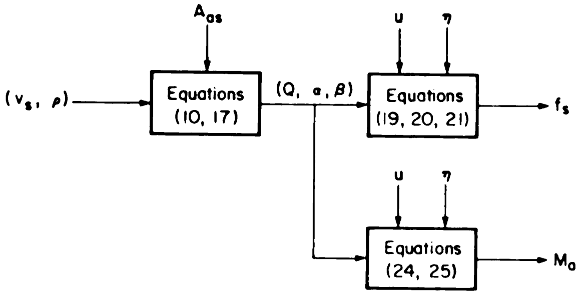

Figure 9.- Main information flow in force and moment generation.

The data represented by equations (19) and (25) are considered as the fundamental source of information concerning the total aerodynamic and propulsive force and moment. In the remainder of this report, these data are assumed to be given to various levels of accuracy. The information flow involved in force and moment generation is shown in figure 9.

Equations (3), (13), (15), and (22) are the fundamental components of the system state equation. Other effects such as the dynamics of actuators and sensors may be adjoined to these equations as the need arises to obtain the complete state equation modeling the aircraft.

A specific aircraft is described here to motivate and aid in the following discussion. Note that, although the discussion in the remainder of the report is directed toward this specific aircraft, the essential concepts are applicable to other types of aircraft.

The augmentor wing jet STOL research aircraft (AWJSRA) is a de Havilland C-8A "Buffalo" modified according to the general arrangement shown in figure 10. The wing area S_w is 80.36 m^2 (865 ft^2) and the maximum gross weight is 20,400 kg (45,000 lb). The aircraft is powered by two turbofan engines. The relatively cold flow from the front fans is ducted through the wing and fuselage to the augmented jet flap and blown ailerons. The arrangement of the augmentor flap is shown in figure 11. The entire flap unit pivots about the main hinge point. No provision is made in this installation to retract the upper flap units into the main wing contour. The Coanda surface serves to deflect the (cold) flow from the nozzle. The augmentor chokes at the trailing edges of the main flaps control the lift generated by the flaps. The two outboard flap chokes are used to control roll and all four chokes are used to spoil lift after landing.

The hot gas from the two turbofan engines flows through two pairs of nozzles that can be rotated in flight to provide vectoring of the hot thrust through a range of 98°. All nozzles are connected to move in unison in response to a single nozzle angle command. The geometry associated with the hot thrust is shown

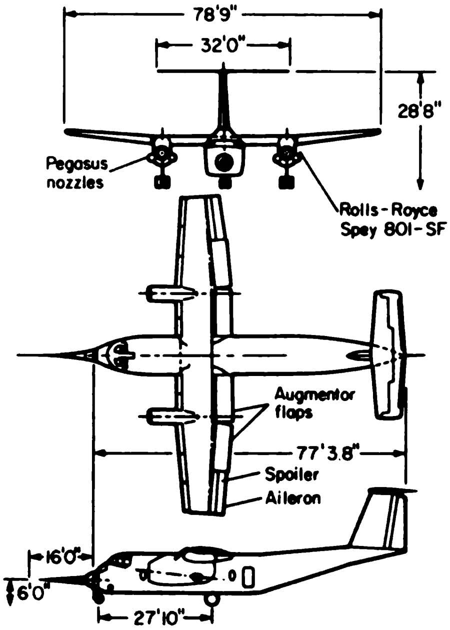

Figure 10.- General arrangement of the modified C-8A.

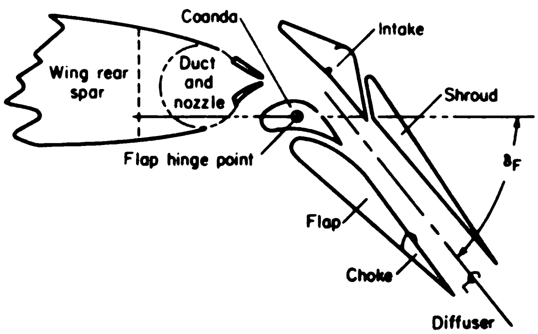

Figure 11.- Arrangement of the augmentor flap.

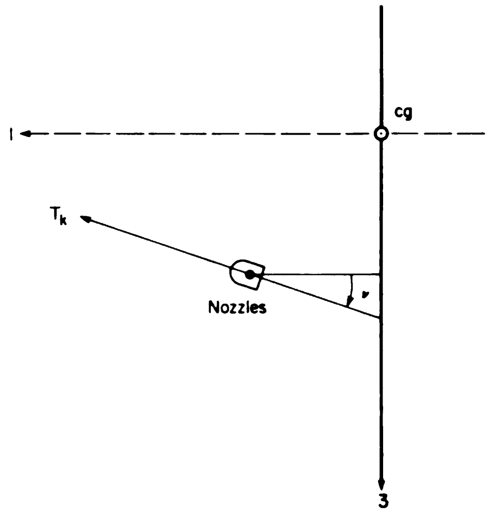

Figure 12.- Geometry of hot thrust in body coordinates.

in figure 12. Since the aircraft center of gravity is not on the axis of rotation of the nozzles, the hot thrust generates a moment that depends on the nozzle angle ν. The servos that control the nozzles are quite fast, being limited to 90°/sec. The hot and cold thrusts depend on the engine speed. The speed of both engines is controlled in unison by a single throttle command, δ_T. The associated servo system is relatively slow with a bandwidth of approximately 1 rad/sec. The cold flow has a pronounced effect on the wing-body polars of the aircraft as shown in figure 13, where the independent variables are flap angle δ_F, angle of attack α, and cold thrust coefficient $C_J = T_c/QS_w$.

Of particular significance for the design of automatic trajectory tracking systems is the large variation in the basic aerodynamic characteristics of the aircraft (evident in fig. 13). Certainly, there is quite a significant change between cruise configuration (flap = 4.5°) and landing configuration (flap = 65°). But present indications are that the nonlinearity is significant even over much smaller regions. For example,

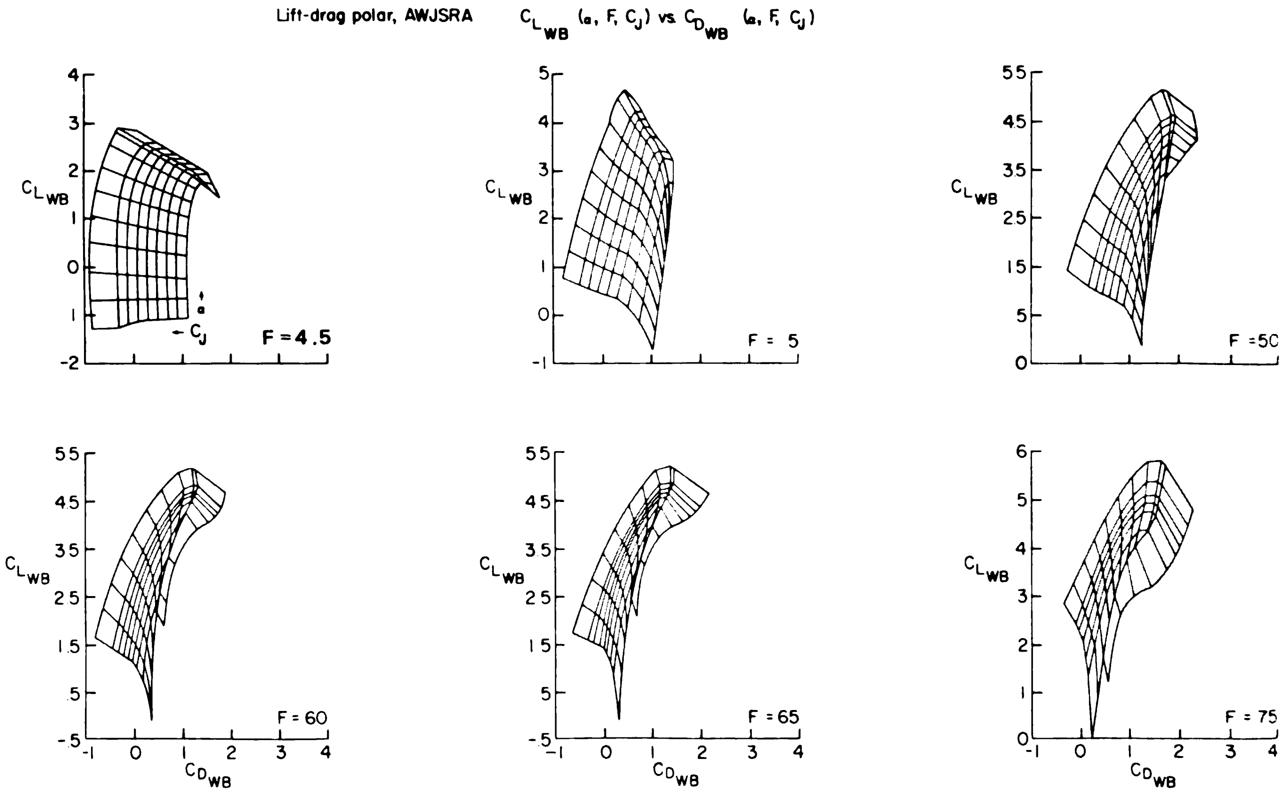

Figure 13.- Wing-body polars $(C_D, C_L)(\alpha, C_J, \delta_F)$.

figure 14 shows the total lift and drag coefficients, including the effects of the hot thrust for a constant flap, throttle, and airspeed which correspond to a typical landing configuration with angle of attack and nozzle angle as the independent variables.

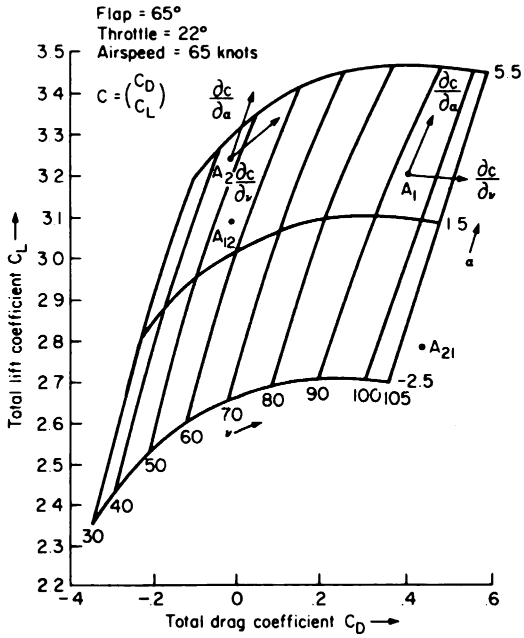

Figure 14.- Total force coefficient.

Point A_1 represents equilibrium flight at 65 knots along the -7.5° glide slope. Point A_2 represents level flight at the same speed. The derivatives of the total force vector coefficients are also shown at these two points. As the aircraft is maneuvered between A_1 and A_2, the change in these derivatives may adversely affect closed-loop stability. Of additional concern is the magnitude of steady-state error in altitude which will result if linearity is assumed in this region. Thus, for a maneuver that takes the aircraft from A_1 to A_2, the feedforward based on the linear model at A_1 will trim the aircraft to point A_{12} giving an error in the required lift coefficient, $\Delta C_L/C_L$ = 4.5 percent. This error will be absorbed by the altitude feedback, resulting in an error $h_e = 0.045g/\omega_n^2$, where g is the acceleration of gravity and ω_n is the bandwidth of the altitude loop. But, because of limitations imposed by the unsteady aerodynamics on this bandwidth, $\omega_n \le 0.5$ rad/sec at 65 knots; hence $h_e \ge 1.8$ m (5.8 ft). Similarly, a maneuver that takes the aircraft from level flight (point A_2) onto the -7.5° glide slope (point A_1) by means of the feedforward based on the linear model at A_2 will be trimmed to point A_{21}, resulting in a magnitude of altitude error $h_e \ge 4.9$ m (16 ft). Of course, this hang-off error can be removed by means of an integrator in the altitude error channel. Because of bandwidth limitation, such trim corrections will be too slow for many maneuvers. Consequently, when such errors cannot be tolerated, even the relatively small transition as between A_1 and A_2 must be considered nonlinear for the purposes of generating trim controls. So, as usual, the practical concept of linearity is intimately related to accuracy requirements.

The trim problem is further complicated by the presence of redundant controls. Thus, as shown in figure 14, the total lift and drag coefficients required for steady flight at 65 knots along the -7.5° glide slope (point A_1) can be achieved by the trim condition $(\alpha,\nu,\delta_T,\delta_F)$ = (2.5,92,22,65). However, the same coefficients can be achieved by other combinations of controls. This redundancy is shown in figure 15, where point A_1 corresponds to the particular solution A_1 in figure 14. The question (the redundant control problem) is which combination $(\alpha,\nu,\delta_T,\delta_F)$ to use in any given situation.

The preceding discussion of the characteristics of the AWJSRA implies that careful attention must be given to the problem of trimming the aircraft. Present indications are that other aircraft types that use powered lift and

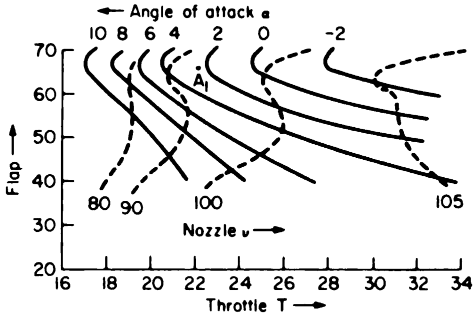

Figure 15.- Controls for one value of total force coefficient.

undergo rapid changes in configuration are similarly nonlinear and have redundant controls. Hence the following decision is made concerning the structure of the automatic flight-control system.

Decision 4: The control logic contains a section in which the control redundancy is resolved and trim controls are generated continuously. This section of the control logic is referred to as the trimmap.

The Trimmap

To solve the trim problem, one must, in effect, reverse some of the information flow shown in figure 9. Thus, given the relative velocity v_s and density ρ, and the commanded (trim) total force vector f_{sc} and moment vector M_{ac}, the problem is to find the required trim controls u_c. From equation (20), it follows that

$$C_{sc} = (QS_w)^{-1} f_{sc} \tag{26}$$

Since drag is defined as the force component along $-v_s$, and lift is defined as the total force perpendicular to v_s,

$$\left.\begin{aligned} C_{Dc} &= -u_s^T C_{sc} \\ C_{Lc} &= (C_{sc}^T C_{sc} - C_{Dc}^2)^{1/2} \end{aligned}\right\} \tag{27}$$

where u_s is defined by equation (6).

Two cases arise in the computation of the commanded side-force angle σ_c (see fig. 8), according to whether or not the commanded (trim) attitude of the aircraft A_{cs}^* is completely defined outside the trimmap.

If A_{cs}^* is completely defined, then the commanded angle of attack α_c and side-slip angle β_c are defined because the relative velocity vector v_s is not subject to control within trimmap; when in trim, $v_a = A_{cs}^* v_s$ and α and β are defined by equation (10). Consequently, the wind-tunnel coordinates (see fig. 7) of the total aerodynamic and propulsive force vector coefficient required for trim are given by

$$C_{wtc} = E_3(\beta_c) E_2^T(\alpha_c) A_{cs}^* C_{sc} \tag{28}$$

while equation (21) implies that

$$\sigma_c = \arctan[C_{wtc}(2),\ -C_{wtc}(3)] \tag{29}$$

so the problem is reduced to that of partially inverting the basic data of equations (19) and (25):

$$\left.\begin{aligned} C_D(\alpha,\beta,u;\eta) - C_{Dc} &= 0 \\ C_L(\alpha,\beta,u;\eta) - C_{Lc} &= 0 \\ \sigma(\alpha,\beta,u;\eta) - \sigma_c &= 0 \\ C_M(\alpha,\beta,u;\eta) - C_{Mac} &= 0 \end{aligned}\right\} \tag{30}$$

If A^*_{cs} is incompletely defined in that the trimmap is free to select the commanded angle of attack, then this angle and the controls must be chosen to satisfy equation (27) with constraints (30), which define the side-force angle σ_c. Then the commanded attitude can be defined according to equation (12), namely,

$$A^*_{cs} = E_2(\alpha_c)E_3^T(\beta_c)E_1(\phi_v)E_2(\gamma_v)E_3(\psi_v) \tag{31}$$

where

$$\phi_v = -\sigma_c + \arctan[C_{vc}(2),\ -C_{vc}(3)] \tag{32}$$

and (see fig. 7)

$$C_{vc} = E_2(\gamma_v)E_3(\psi_v)C_{sc} \tag{33}$$

The commanded attitude can also be defined without the explicit use of the angles (ϕ_v,γ_v,ψ_v) as follows. The unit vector u_s^p along the lift vector is given by

$$u_s^p = (C_{sc} + C_{Dc}u_s)/C_{Lc} \tag{34}$$

where C_{Dc} and C_{Lc} are defined by equation (27). Let the matrix U_{us} be the rotation defined by

$$U_{us} = [u_s,\ -S(u_s)u_s^p,\ -u_s^p] \tag{35}$$

where S is the vector cross-product operator defined by equation (12). The rotation U_{us} takes the axes that are initially aligned with the runway (inertial) axes into the attitude in which the relative velocity is along δ_1 and the lift vector is along $-\delta_3$. Hence the trim attitude is also given by

$$A_{cs}^{*} = E_2(\alpha_c)E_3^T(\beta_c)E_1(\sigma_c)U_{us} \tag{36}$$

The main flow of information in the automatic trim logic when the commanded attitude is incompletely defined is shown in figure 16. The primary inputs are the input translational acceleration $\dot{V}_{sI}$ and the input angular acceleration $\dot{\omega}_{aI}$. The output is the control, u, and the required trim attitude, A_{cs}^{*}. The solution of equations (30) (called the trimmap) is the core of the automatic trim logic. Within the trimmap, control redundancy is resolved and control strategy is modified in case of component failures. The trimmap provides a natural setting for monitoring the proximity of the aircraft to its performance limits and for protecting the aircraft from exceeding its design limits, that is envelope limiting. Furthermore, the primary purpose of the automatic trim logic is to provide a priori open-loop information to the overall automatic flight-control system and thereby relieve the perturbation controller whose feedback is intended to control the uncertainties of the process as well as relatively insignificant details that are known but ignored in the construction of the trimmap. Thus, it is also within trimmap that the major tradeoff between complexity and computer capacity on the one hand and accuracy of performance on the other takes place.

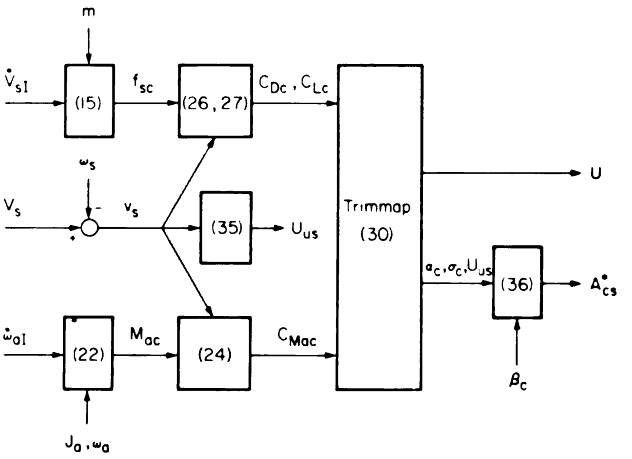

Figure 16.- Main information flow in automatic trim logic.

The perturbation controller is discussed in the next section. However, note that the relative velocity vector v_s is used in the trim logic. Since wind contributes significantly to the relative velocity, estimates of the wind must generally be computed. For this reason, the following decision regarding the structure of the automatic flight-control system is made.

Decision 5: The control logic includes a wind filter that estimates the inertial coordinates, w_s, of the wind vector. (The wind filter is discussed further later in the report.)

Perturbation Controller

The perturbation controller provides closed-loop, feedback control over details of the physical process not accounted for in the open-loop, feedforward, trim control either because they are not known a priori or because they have been purposely ignored to simplify the open-loop control. For the purposes of discussion, let the system state equation be

$$\dot{x} = f(x,u) \tag{37}$$

where x and u are the state and control, respectively, of appropriate dimension and, in addition, the control is restricted to a set U that may depend on the state. A trajectory $[x_o(t),\ t \in T]$ is flyable if, for all t in T, there is a control $u_o(t)$ such that

$$\dot{x}_o(t) = f[x_o(t),\ u_o(t)] \tag{38}$$

The trim problem (as discussed previously) is to find a control u_o that satisfies equation (38), given that the trim (nominal) trajectory x_o is flyable. The solution will be an inverse of the state equation (37), namely, a function (g,F), which we call the trimmap, so that for all $(\dot{x},x)$ in F,

$$f[x,g(\dot{x},x)] = \dot{x} \tag{39}$$

The corresponding trim control is given by

$$u_o = g(\dot{x}_o,x_o) \tag{40}$$

Usually, trim refers to cases with constant u_o. Here the concept is generalized to include open-loop controls that vary with time. As noted previously, when controls are redundant, the state equation (37) alone does not suffice to define the trimmap (g,F), and additional conditions must be introduced to resolve the redundancy.

The trim problem may be difficult to solve, but, evidently, its solution to the required accuracy is the essential first step in any design of automatic flight-control systems. The next step usually is to design feedback control systems based on perturbation models. Thus, given a flyable trajectory $(\dot{x}_o,x_o)$ trimmed by u_o according to equation (40), the linear model (41) is obtained for the perturbations $\delta x = x - x_o$ and $\delta u = u - u_o$:

$$\delta\dot{x} = \left(\frac{\partial f}{\partial x}\right)_o \delta x + \left(\frac{\partial f}{\partial u}\right)_o \delta u \tag{41}$$

where the partial derivatives are evaluated along the nominal trajectory. Then the application of the methods of linear control theory (ref. 5) yields the perturbation control law

$$\delta u = K_o \delta x \tag{42}$$

Since the coefficients in equation (41) depend on the nominal trajectory, the process must be repeated for a sufficiently large number N of nominal trajectories $(\dot{x}_o,x_o)$ in F until the flight envelope F is covered adequately. The result is a scheduled gain matrix $K(\dot{x}_o,x_o)$ and the complete control law is given by

$$u = g(\dot{x}_o,x_o) + K(\dot{x}_o,x_o)(x - x_o) \tag{43}$$

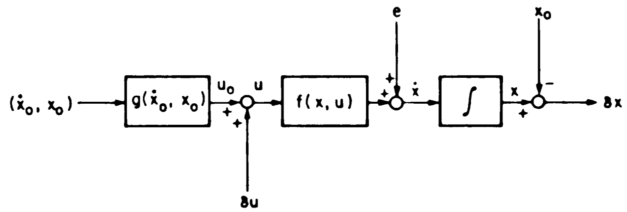

Figure 17.- Selected structure in conventional design.

The structure of the control system selected in the conventional perturbation controller design is shown in figure 17. The disturbance is represented by e.

The many advantages of the methods of quadratic optimization of linear systems are well publicized (ref. 5). Indeed, these methods are very powerful. But when the state equation (37) is highly nonlinear, the procedure for choosing the proper set $\{(\dot{x}_{oi},x_{oi})\}_N$ of nominal trajectories to adequately cover the flight envelope F with perturbation models so as to apply these methods to each of them is, at present, rather unclear. Then there is the problem of how to obtain envelope limiting. The perturbation control δu (see fig. 17) may, in response to a disturbance, force the aircraft outside its design limits even though the nominal control u_o is maintained by the trimmap well within these limits. If envelope limiting is achieved by limits δU on δu, then questions concerning the stability of the resulting nonlinear perturbation controller must be resolved for each of the N perturbation models. Since these limits on u are likely to depend on $(\dot{x}_o,x_o)$, $\delta U(\dot{x}_o,x_o)$ must be stored in the control logic in addition to the gain matrix $K(\dot{x}_o,x_o)$ and the trimmap $g(\dot{x}_o,x_o)$. If N discrete cases of these variables are stored, the dynamics of switching from one case to the next as the aircraft state moves through their domains of validity must be designed. For example, hysteresis may have to be introduced to prevent jitter when the aircraft is required to fly near the boundary separating these regions. Switching dynamics further increase the storage and computation requirements of the flight computer. Lastly, there is a plethora of problems associated with reliability. Typically, does the system remain stable when a column or row of the gain matrix K is lost? — which corresponds to the loss of a sensor or a control, respectively. Such questions concerning the structure of the feedback are, as yet, difficult within the framework of quadratic optimization. In this respect, the older classical design techniques based on sequential loop closures that result in a nesting (hierarchy) of subsystems with decreasing bandwidth are more effective for designing fail-safe systems.

Because of these considerations, the following decisions are made concerning the formal structure of the automatic flight-control system.

Decision 6: The feedback is closed through the automatic trim logic.

Decision 7: The structure of the control logic is hierarchical.

The information flow implied by decision 6 is shown in figure 18. The feedback is through perturbation $\delta\dot{x}_o$ in the trim condition $\dot{x}_o$. Suppose that, initially, $x = x_o$. In the absence of any modeling errors, the control

$$u = g(\dot{x}_o,x) \tag{44}$$

will maintain $x = x_o$. The tracking will be perfect even if, at some point in time, $\dot{x}_o$ is perturbed to $\dot{x}_o + \delta\dot{x}_o$, provided that $(\dot{x}_o + \delta\dot{x}_o, x)$ is in F. The corresponding control is

$$u = g(\dot{x}_o + \delta\dot{x}_o, x) \qquad (45)$$

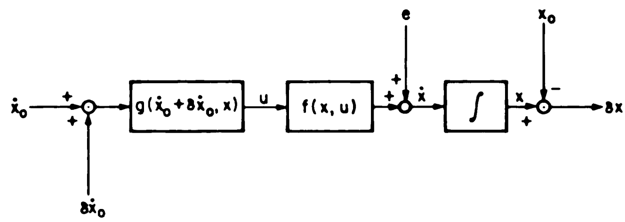

Figure 18.- Structure of proposed perturbation controller.

Now suppose that initially $x - x_o \neq 0$, but that the error can be removed by means of a flyable trajectory. Then there is an $\dot{x}_o + \delta\dot{x}_o$ that will take x into x_o by means of the control law given by equation (45). That is, the feedback for controlling the process uncertainties can be closed through the automatic trim logic as in figure 18 rather than after the trim logic as in figure 17. One immediate consequence is that envelope limiting is done within the trimmap. The other consequence is that, for any admissible $\delta\dot{x}_o$, the perturbation model is given anywhere inside F by

$$\delta\dot{x} = \delta\dot{x}_o + e \qquad (46)$$

where the magnitude of the error e depends on the accuracy of the automatic trim logic. Thus the emphasis is shifted from the N perturbation models required to cover F to the construction of flyable perturbations in the commanded trajectories. The latter task is considerably simplified by decision 7.

Consider the block diagram in figure 19, which represents the automatic flight-control system as viewed from one level in the hierarchy, namely, that

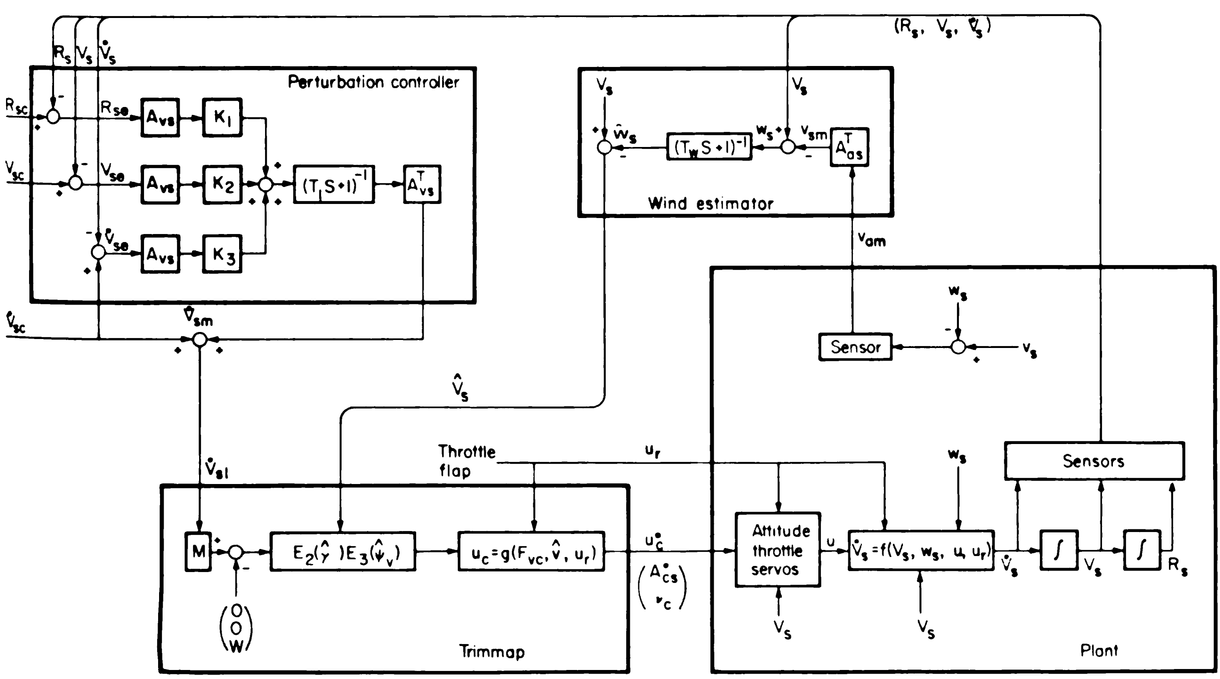

Figure 19.- Acceleration controller for the AWJSRA.

of the acceleration controller. The function of the acceleration controller is to accept commands from the command generator, which is one level higher, and transform them into commands to the flap, throttle, and nozzle servos, as well as to the attitude control system, all of which are one level lower. At the level of the acceleration controller, the servo systems are represented by relatively simple, possibly linear and low-order, input-output relations, which are treated as specifications to be met in the design of these subsystems. Of course, the subsystems may be quite complicated internally. For example, the attitude control system may have its own automatic trim logic and perturbation controller and may rely on simple input-output relations that describe the control surface servos, which are another step lower in the hierarchy.

The major blocks of the acceleration controller are the trimmap, wind filter, and compensator. The inertial coordinates $\dot{V}_{sI}$ of the input acceleration vector are transformed by the trimmap (fig. 16) into commanded flap, throttle, nozzle, and attitude.

The wind filter computes smoothed inertial coordinates $\hat{w}_s$ of aircraft velocity relative to the air mass from body-mounted air velocity v_{am} sensors and from the inertial velocity V_s and attitude A_{as} of the aircraft. Note that only the inertial coordinates of wind are filtered, while V_s is unaffected. Hence, in the absence of wind and, of course, sensor errors, $\hat{v}_s = V_s$.

The input-output relation, $\dot{V}_{sI} \rightarrow \dot{V}_s$, where the $\dot{V}_s$ terms are the inertial coordinates of aircraft acceleration vector, is given by (see eq. (46)),

$$\dot{V}_s = \dot{V}_{sI} + e \tag{47}$$

where e depends on the inaccuracies of the trimmap and the wind filter, the presence of unsteady aerodynamics such as $\dot{\alpha}$ effects, and on attitude and other subsystem dynamics. The purpose of the perturbation controller is to close the loop around such effects and thereby reduce e to a tolerable level. Inertial coordinates of position, velocity, and acceleration errors are transformed into approximately longitudinal, lateral, and normal errors by means of the direction cosine matrix A_{vs} computed from the commanded inertial velocity V_{sc}; the errors are weighted by constant gain matrices K_1, K_2, and K_3 commensurate with the acceleration capacities of the aircraft in these directions. The result is filtered to ensure compatibility with the attitude control system and other subsystem dynamics. The corrective acceleration is transformed back into inertial space and added to command $\dot{V}_{sc}$ to give input $\dot{V}_{sI}$. In this way, feedback is closed around the process uncertainties, e, so that

$$\dot{V}_s = \dot{V}_{sc} \tag{48}$$

is sufficiently accurate if the acceleration $\dot{V}_{sc}$ commanded by the command generator is admissible, namely, if $(V_{sc},\dot{V}_{sc})$ is flyable and the bandwidth of $\dot{V}_{sc}$ is suitably restricted. Coriolis terms due to the time rate of change of A_{vc} may be included in the perturbation controller if necessary using the techniques of the next section.

Angular Acceleration Controller

The discussion thus far has been concerned with controlling the motion of aircraft's center of mass. The concepts that led to the structure of the (translational) acceleration controller shown in figure 19 are also applied to formulate the structure of the angular acceleration controller. The function of the angular acceleration controller is to accept commands from the attitude command generator and transform them into commands to the wheel, elevator, and rudder servos. The structure is again hierarchical. The attitude command generator, one step above the angular acceleration controller, accepts attitude requests from the translational control system and, based on simple input-output representation, generates rotational trajectories $[A_{cs}(t), \omega_c(t), \dot{\omega}_c(t)]$ as input to the angular acceleration controller. The control surface servos, one step below the angular acceleration controller, are represented by relatively simple, input-output relations.

The structure of the angular acceleration controller is shown in figure 20. The major blocks are the moment trimmap, wind estimator, and attitude perturbation controller. The body coordinates $\dot{\omega}_{aI}$ of the input angular acceleration vector are transformed by the moment trimmap into commanded wheel δw_c, elevator δe_c, and rudder δ_{rc}.

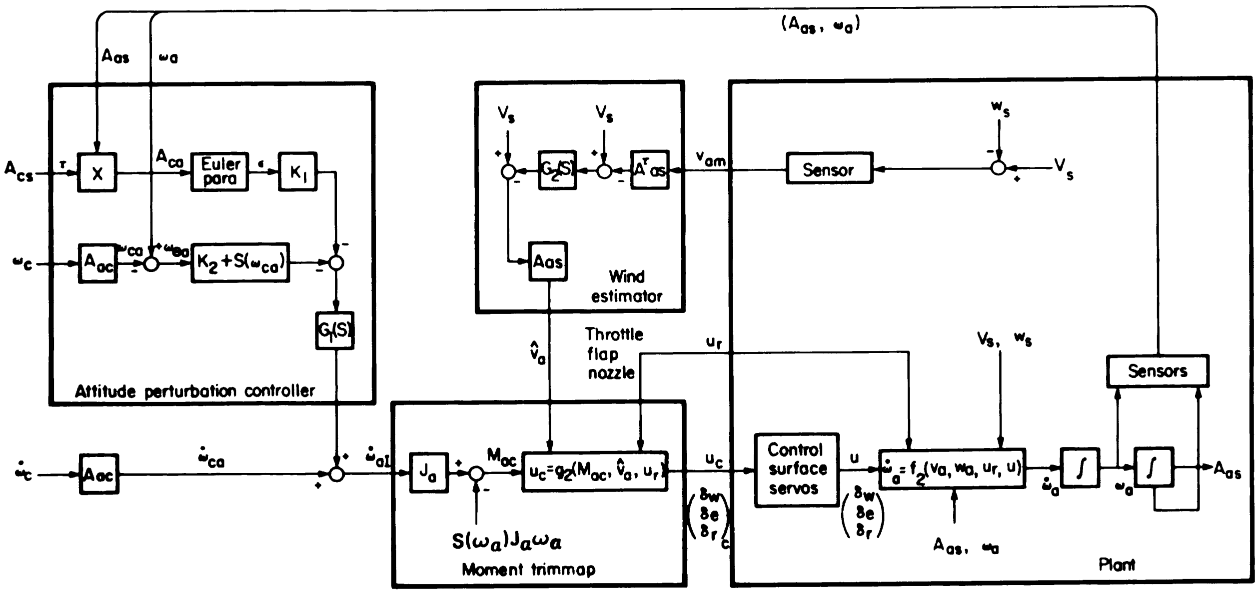

Figure 20.- Structure of the angular acceleration controller for the AWJSRA.

The wind estimator provides estimates of the body coordinates $\hat{v}_a$ of aircraft velocity relative to the air mass, which are needed in the moment trimmap calculations. The structure is very similar to that of the wind estimator in the translational control system. There may be differences in detail because of different bandwidth requirements.

The input-output relation, $\dot{\omega}_{ai} \rightarrow \dot{\omega}_a$, is given by

$$\dot{\omega}_a = \dot{\omega}_{ai} + e \tag{49}$$

where e depends on the inaccuracies of the moment trimmap and the wind estimator, the presence of unsteady aerodynamics such as $\dot{\alpha}$ effects and wind shear across the aircraft, and on the dynamics of control surface servos. The purpose of the attitude perturbation controller is to close the loop around such effects and thereby reduce the error e to a tolerable level. Following reference 4, attitude error is defined by the direction cosine matrix

$$A_{ac} = A_{as}A_{cs}^T \tag{50}$$

that represents the aircraft attitude relative to the commanded attitude. The time derivative is

$$\dot{A}_{ac} = \dot{A}_{as}A_{cs}^T + A_{as}\dot{A}_{cs}^T$$

But (see eq. (14)),

$$\dot{A}_{as} = S(\omega_a)A_{as}$$

and

$$\dot{A}_{cs} = S(\omega_c)A_{cs}$$

where ω_a represents (in body axes) the aircraft angular velocity relative to the runway, and ω_c represents (in the commanded body axes) the commanded angular velocity relative to the runway, Hence

$$\begin{aligned}\dot{A}_{ac} &= S(\omega_a)A_{ac} - A_{ac}S(\omega_c) \\ &= S(\omega_a)A_{ac} - A_{ac}S(\omega_c)A_{ac}^TA_{ac} \\ &= S(\omega_a)A_{ac} - S(A_{ac}\omega_c)A_{ac} \\ &= S(\omega_a - A_{ac}\omega_c)A_{ac}\end{aligned}$$

or, equivalently,

$$\dot{A}_{ac} = S(\omega_{ea})A_{ac} \tag{51}$$

where the body coordinates of angular velocity error are given by

$$\omega_{ea} = \omega_a - A_{ac}\omega_c \tag{52}$$

Therefore, the time derivative is

$$\dot{\omega}_{ea} = \dot{\omega}_a - S(\omega_{ea})A_{ac}\omega_c - A_{ac}\dot{\omega}_c$$

$$= \dot{\omega}_a + S(\omega_{ca})\omega_{ea} - A_{ac}\dot{\omega}_c$$

where $\omega_{ca} = A_{ac}\omega_c$ represents (in the body axes) the commanded angular velocity. The identity $S(x)y = -S(y)x$ was used in the last step above. Thus the body coordinates of angular acceleration are expressed in terms of the command and perturbations as

$$\dot{\omega}_a = A_{ac}\dot{\omega}_c - S(\omega_{ca})\omega_{ea} + \dot{\omega}_{ea} \tag{53}$$

Note that, since no small signal approximations are used to derive equation (53), it is universally valid.

Equation (53) can be interpreted as defining the required angular acceleration $\dot{\omega}_{aI}$ of the aircraft (which is the input to the moment trimmap), so that the command is executed with perturbation $(A_{ac},\omega_{ea},\dot{\omega}_{ea})$. An equation connecting $\dot{\omega}_{ea}$ to (A_{ac},ω_{ea}) closes the loop around the perturbations. Thus the remaining problem is to synthesize a control law $h = h(A_{ac},\omega_{ea})$ so that the system

$$\begin{aligned} \dot{A}_{ac} &= S(\omega_{ea})A_{ac} \\ \dot{\omega}_{ea} &= h \end{aligned} \tag{54}$$

has an acceptable relaxation transient response, $[A_{ac}(0),\omega_{ea}(0)] \to (I,0)$. This problem is treated in some detail in references 4 and 6. For example, the attitude error is defined by

$$\varepsilon = 0.5 \begin{pmatrix} a_{23} - a_{32} \\ a_{31} - a_{13} \\ a_{12} - a_{21} \end{pmatrix}$$

where $(a_{ij}) = A_{ac}$. According to Euler's theorem on rotations, every attitude can be attained with a single rotation. Let ϕ be the angle of A_{ac}, and let c be the unit vector along the axis of A_{ac}. It can be shown that $\varepsilon = (\sin\phi)c$. Thus, for small attitude errors ($\phi \le 0.5$ radian), ε gives both the magnitude and direction of attitude error. In addition, for small perturbations,

$$\dot{\varepsilon} = \omega_{ea}$$

is a good approximation to the kinematic equation, and the state equation (54) becomes

$$\dot{\varepsilon} = \omega_{ea}$$

$$\dot{\omega}_{ea} = h$$

There are many techniques for synthesizing the control law h. A simple example is

$$h = - K_1\varepsilon - K_2\omega_{ea} \tag{55}$$

where the constant gain matrices K_1 and K_2 are selected to provide the required bandwidth and damping in each axis.

With the control law (55), the input to the moment trimmap becomes

$$\dot{\omega}_{aI} = A_{ac}\dot{\omega}_c - \{K_1\varepsilon + [K_2 + S(\omega_{ca})]\omega_{ea}\} \tag{56}$$

(shown schematically in fig. 20). The dynamic element $G_1(s)$ is included in the attitude perturbation controller to provide high-frequency cutoff. Thus, a feedback is closed around the process uncertainties, e, in equation (49) so that

$$\dot{\omega}_a = \dot{\omega}_c \tag{57}$$

is sufficiently accurate if the angular acceleration command, $\dot{\omega}_c$, commanded by the attitude command generator is admissible, namely, if $(A_{cs},\omega_c,\dot{\omega}_c)$ is flyable and if the bandwidth of $\dot{\omega}_c$ is suitably restricted.

Now, consider the translation perturbation controller discussed at the end of the preceding section. The Coriolis effects may be included as follows. Let the matrix A define an axis system with respect to inertial space, and let $R_e = A(R_{sc} - R_s)$ and $V_e = A(V_{sc} - V_s)$ be the position and velocity errors, respectively. Then $\dot{A} = S(\omega)A$, where ω is the angular velocity of A, and

$$\dot{R}_e = S(\omega)R_e + V_e$$

$$\ddot{R}_e = S(\dot{\omega})R_e + S(\omega)[S(\omega)R_e + V_e] + S(\omega)V_e + A(\dot{V}_{sc} - \dot{V}_s)$$

Hence,

$$\dot{V}_s = \dot{V}_{sc} + A^T[S(\dot{\omega})R_e + S^2(\omega)R_e + 2S(\omega)V_e - \ddot{R}_e]$$

The designer is free to choose A and $\ddot{R}_e$. For example, let the error relax according to the linear law,

$$\ddot{R}_e = -K_1R_e - K_2\dot{R}_e$$

Then the input to the trimmap is given by

$$\dot{V}_{sI} = \dot{V}_{sc} + A^T\{[S(\dot{\omega}) + S^2(\omega) + K_2S(\omega) + K_1]R_e + [2S(\omega) + K_2]V_e\}$$

In particular, if $A = A_{vs}$, which aligns the first axis with the commanded velocity, V_{sc}, and maintains the second axis horizontal, then

$$\omega = \omega_v = -(A_{vs} + k\delta_1\delta_3^T)S(V_{sc})\dot{V}_{sc}/V_c^2$$

where

$$k = \frac{\delta_3^T u_{sc}}{1 - (\delta_3^T u_{sc})^2}, \qquad u_{sc} = \frac{V_{sc}}{V_c}, \qquad V_c = (V_{sc}^T V_{sc})^{-1/2}$$

The results of simulation tests suggest that all significant coriolis effects are accounted for by the approximation in which $k = 0$ and the gains in figure 19 are replaced as follows,

$$K_1 \leftarrow S^2(\omega_v) + K_2S(\omega_v) + K_1$$

$$K_2 \leftarrow 2S(\omega_v) + K_2$$

and K_3 is unchanged.

Trajectory Command Generator

The last two major blocks of the proposed structure of automatic flight-control systems are the trajectory command generator and the attitude command generator. Their function is to provide only admissible commands to the corresponding acceleration controllers. In this section, only the trajectory command generator is discussed. Since, within the scope of this report, the two generators may be considered to be very similar, the discussion applies also to the attitude command generator.

In the hierarchy of control logic, the command generator is one level above the acceleration controller and one level below the generalized air traffic control (which includes the pilot). Sufficiently smooth commands can be passed unmodified to the acceleration controller. However, in general, discontinuities will be present: the air traffic control may request a discontinuous change in trajectory; the pilot may switch to a different control mode; the set of active sensors may change; or a strong disturbance due to wind or a partial failure may force the aircraft too far from the commanded trajectory to be brought back by the perturbation controller. In such cases, the command generator must generate an acceptable transition (flare) trajectory that returns the aircraft on target. The transition may be generated by means of a dynamical system as shown in figure 21.

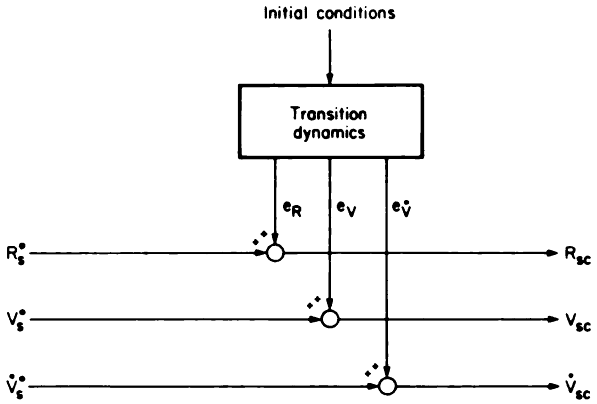

Figure 21.- Generation of transition (flare) trajectory.

The output of the command generator is given by

$$\begin{pmatrix} R_{sc} \\ V_{sc} \\ \dot{V}_{sc} \end{pmatrix} = \begin{pmatrix} R_s^* \\ V_s^* \\ \dot{V}_s^* \end{pmatrix} + \begin{pmatrix} e_R \\ e_V \\ e_{\dot{V}} \end{pmatrix} \tag{58}$$

where the quantities ( )* are the ATC command (see eq. (1)), and e_R, e_V, and $e_{\dot{V}}$ are the modifications of that command in position, velocity, and acceleration.

Let the differential equation of the transition dynamics be

$$\dot{e} = h(e) \tag{59}$$

with an output map

$$\begin{pmatrix} e_R \\ e_V \\ e_{\dot{V}} \end{pmatrix} = H(e) \tag{60}$$

If equation (59) is asymptotically stable and $H(0) = 0$, the output of the command generator will approach the ATC command with time. To have continuity in commanded position, velocity, and acceleration, the dimension of e must be at least 9, that is, 3 for each axis. If initial conditions are chosen so that

$$\begin{pmatrix} e_R(0) \\ e_V(0) \\ e_{\dot{V}}(0) \end{pmatrix} = \begin{pmatrix} R_s(0) - R_s^*(0) \\ V_s(0) - V_s^*(0) \\ \dot{V}_s(0) \quad \dot{V}_s^*(0) \end{pmatrix} \tag{61}$$

then, at the initiation of the transition, the command coincides with the actual position, velocity, and acceleration of the aircraft.

The detailed shape of the transition is controlled by means of the function $h(e)$ in the state equation (59). Generally, the state space will consist of at least two regions, one of which includes the origin $e = 0$. In this region, the function $h(e)$ may be linear. Thus, for example, let the small transitions be generated by three uncoupled, linear systems with constant coefficients,

$$\dot{e}_i = F_i e_i \tag{62}$$

where, for each $i = 1,2,3$, the dimension of e_i is 3 and the dimension of the constant matrices F_i is 3 × 3. If the initial conditions are defined by the rows of the matrix

$$e(0) = A_{vc}[e_R(0), e_V(0), e_{\dot{V}}(0)] \tag{63}$$

and the output map is defined by

$$[e_R(t), e_V(t), e_{\dot{V}}(t)] = A_{vc}^T e(t) \tag{64}$$

then the transition dynamics will be approximately invariant with respect to the commanded velocity axes given by the matrix A_{vc}. Since the acceleration controller tracks the output of the command generator with small error, equation (62) represents approximately the transition dynamics with respect to the longitudinal ($i = 1$), lateral ($i = 2$), and normal ($i = 3$) axes of the aircraft, respectively. The bandwidth of the transition can be made compatible with the restrictions of acceleration controller by a proper choice of matrices F_i.

Outside a neighborhood of $e = 0$, the function $h(e)$ must be modified; otherwise, the magnitude restrictions of the acceleration controller will be violated. In this region of the state space of e, the design of $h(e)$ may be based on such considerations as the optimization of transit time or transit energy with hard constraints on e.

In effect, trajectory tracking errors have been sorted into three levels. Small errors are corrected by the perturbation controller without reinitializing the command generator. Medium errors are corrected by means of the command generator with linear transition dynamics. Large errors are corrected by means of the command generator with nonlinear dynamics.

The total output of the command generator is given by equation (58). The generalized ATC command $(R_g^*, V_g^*, \dot{V}_g^*)^T$, when not provided explicitly as a function of time by ATC, must be generated onboard from a set of trajectory parameters that are either signaled by ATC or selected by the pilot.

Finally, the command generator must contain a subblock within which autopilot modes can be defined for the control logic. The essential function of the mode variable is to specify which parameters of the commanded trajectory are to be tracked. A very simple example is given in table 2.

TABLE 2.- EXAMPLE OF A MODE VARIABLE

Trajectory parameter to be tracked	Axis		
	Longitudinal	Lateral	Vertical
Acceleration	0	0	0
Velocity	1	1	1
Position	2	2	2

The mode variable M in this case is three-dimensional. Each coordinate can take one of three values. Thus, there are 27 possible modes: $M = (2,2,2)$ specifies position tracking in all three axes; $M = (0,1,2)$ specifies the tracking of longitudinal acceleration, lateral velocity, and vertical position; and $M = (1,1,1)$ represents velocity vector tracking mode, etc. Of course, other definitions of the mode variable are possible and are being investigated. Some of the commonly used modes can be included within the proposed structure by simply changing the set of active sensors. For example, if compass heading and barometric altitude are to be tracked instead of inertial heading and altitude, then compass and baro altimeter should be used for feedback instead of, say, MLS. Other modes, such as when the automatic flight-control system is allowed only limited authority and must interact with the pilot in the loop may be more difficult to include within the proposed structure, but present indications are that such inclusions are possible. For the present purposes, however, it is sufficient to note that the automatic control logic must include a mode definition subblock.

The proposed structure of the command generator is outlined in figure 22.

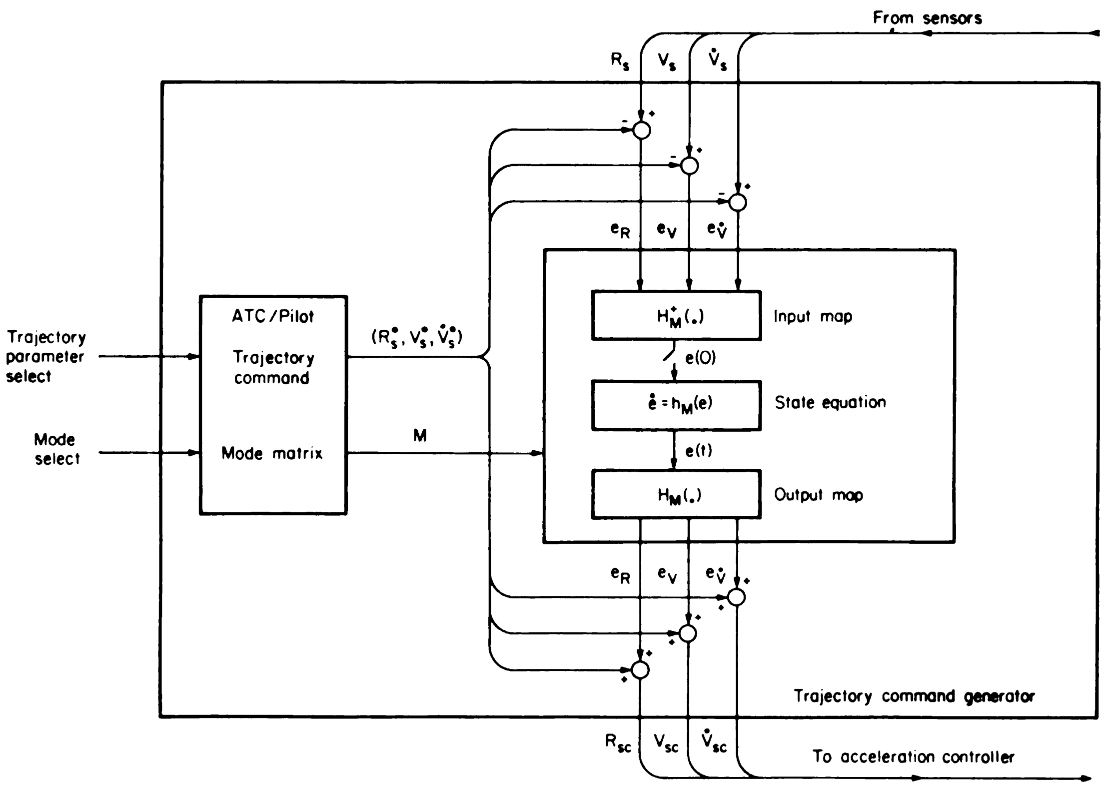

Figure 22.- Structure of the trajectory command generator.

PROPOSED STRUCTURE OF AUTOMATIC FLIGHT-CONTROL SYSTEM

The overall logical structure of the automatic flight-control system developed here is outlined in figure 23. The structure consists of five major subsystems, namely, the trimmap, wind filter, attitude and throttle control systems, perturbation controller, and command generator.

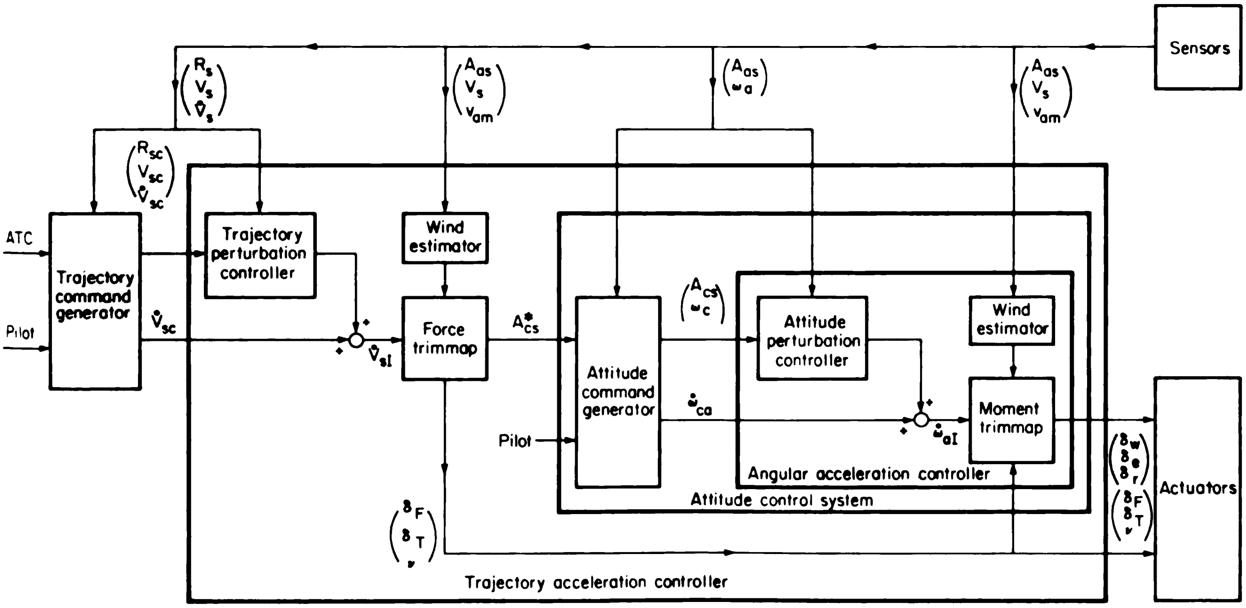

Figure 23.- Proposed structure of the automatic flight-control system for the AWJSRA.

The decision to include a trimmap is motivated by the need to provide automatic envelope limiting and by the impracticality of overcoming the highly nonlinear characteristics of the aircraft by means of high-gain feedback. In the trimmap, a priori information concerning the aircraft characteristics is used to generate open-loop control commands that trim the aircraft to a given acceleration vector.

The decision to include a wind filter is dictated by the fact that aerodynamic forces and moments are functions of the aircraft velocity relative to the air mass.

Considerations of reliability and simplicity motivated the decision to impose a hierarchy on the control logic. The six degrees of freedom of the rigid aircraft are partitioned into a three-dimensional translation system and a three-dimensional rotational system. The function of the attitude control system is to execute the attitude commands provided by the (translation) trimmap. The bandwidth of the attitude control system is an order of magnitude higher than the bandwidth of the translation control system.

Process uncertainties are controlled by means of a perturbation controller which closes the loop around the trimmap, wind filter, and attitude and throttle control systems. The design and implementation of the perturbation controller are drastically simplified by the decision to close the feedback through the trimmap.

The subsystem composed of the perturbation controller, trimmap, attitude and throttle control system, and wind filter is an acceleration controller. Its input-output relation between the commanded acceleration $\dot{V}_{sc}$ and actual aircraft acceleration $\dot{V}_s$ is approximately an identity everywhere on the flight envelope for suitably restricted acceleration commands. The function of the command generator is to give only admissible commands to the acceleration controller and to provide the interface between the control logic and the air traffic control or the pilot.

As stated in the introduction, the purpose of the present report is not to present a complete design of an automatic flight control system, but, rather, to outline a structure of such systems. The discussion in the report leads to the structure composed of five major subsystems which are interconnected as indicated in figure 23. Some of the details within these subsystems discussed in the report are intended primarily to further clarify the purpose of each subsystem rather than as final designs. Indeed, the detailed structure of each of the five subsystems is currently being developed and the results will be reported in forthcoming publications. However, the feasibility of the proposed structure has been tested by application to a simulation of the unmodified DHC-C8A and the Augmentor Wing Jet STOL Research Aircraft. The proposed logical structure has been shown to be feasible, and flight test evaluation will occur in the near future.

CONCLUSIONS

The proposed approach to the design of automatic flight control systems for advanced aircraft has several advantages, among which are the following.

The approach is applicable to a large class of aircraft.

The approach is nearly algorithmic.

The tracking accuracy enters as an independent variable which may be varied over a wide range.

There is an effective trade-off between tracking accuracy and flight computer requirements.

Because the approach leads to a hierarchical system, questions of reliability are tractable.

The approach has been shown to be feasible, and flight test evaluation will occur in the near future.

Ames Research Center
National Aeronautics and Space Administration
Moffett Field, Calif. 94035, February 12, 1975

REFERENCES

1. Erzberger, Heinz; and Lee, Homer Q.: Terminal-Area Guidance Algorithms for Automated Air-Traffic Control. NASA TN D-6773, 1972.

2. McGee, Leonard A.; Smith, Gerald L.; Hegarty, Daniel M.; Carson, Thomas M.; and Merrick, Robert B.: Flight Results from a Study of Aided Inertial Navigation Applied to Landing Operations. NASA TN D7302, 1973.

3. McRuer, Duane; Ashkenas, Irving; and Graham, Dunstan: Aircraft Dynamics and Automatic Control. Princeton University Press, 1973.

4. Meyer, George: On the Use of Euler's Theorem on Rotations for the Synthesis of Attitude Control Systems. NASA TN D-3643, 1966.

5. Anon.: Special Issue on Linear-Quadratic-Gaussian Estimation and Control Problem, IEEE Transactions on Automatic Control, vol. AC-16, no. 6, Dec. 1971, pp. 527-869.

6. Meyer, George: Design and Global Analysis of Spacecraft Attitude Control Systems. NASA TR R-361, 1971.

.TIONAL AERONAUTICS AND SPACE ADMINISTRATION
WASHINGTON, D.C. 20546

OFFICIAL BUSINESS
PENALTY FOR PRIVATE USE $300

SPECIAL FOURTH-CLASS RATE
BOOK

POSTAGE AND FEES PAID
NATIONAL AERONAUTICS AND
SPACE ADMINISTRATION
451

U.S.MAIL

553 001 C1 U AL 750516 S00606HU
UNIV OF MICHIGAN
ENGINEERING LIBRARY
ATTN: MR ROBERT T FREESE
ANN ARBOR MI 48104

POSTMASTER : If Undeliverable (Section 158 Postal Manual) Do Not Return

"The aeronautical and space activities of the United States shall be conducted so as to contribute . . . to the expansion of human knowledge of phenomena in the atmosphere and space. The Administration shall provide for the widest practicable and appropriate dissemination of information concerning its activities and the results thereof."

—NATIONAL AERONAUTICS AND SPACE ACT OF 1958

NASA SCIENTIFIC AND TECHNICAL PUBLICATIONS

TECHNICAL REPORTS: Scientific and technical information considered important, complete, and a lasting contribution to existing knowledge.

TECHNICAL NOTES: Information less broad in scope but nevertheless of importance as a contribution to existing knowledge.

TECHNICAL MEMORANDUMS: Information receiving limited distribution because of preliminary data, security classification, or other reasons. Also includes conference proceedings with either limited or unlimited distribution.

CONTRACTOR REPORTS: Scientific and technical information generated under a NASA contract or grant and considered an important contribution to existing knowledge.

TECHNICAL TRANSLATIONS: Information published in a foreign language considered to merit NASA distribution in English.

SPECIAL PUBLICATIONS: Information derived from or of value to NASA activities. Publications include final reports of major projects, monographs, data compilations, handbooks, sourcebooks, and special bibliographies.

TECHNOLOGY UTILIZATION PUBLICATIONS: Information on technology used by NASA that may be of particular interest in commercial and other non-aerospace applications. Publications include Tech Briefs, Technology Utilization Reports and Technology Surveys.

Details on the availability of these publications may be obtained from:

SCIENTIFIC AND TECHNICAL INFORMATION OFFICE

NATIONAL AERONAUTICS AND SPACE ADMINISTRATION

Washington, D.C. 20546

NASA TECHNICAL NOTE

NASA TN D-7941

NASA TN D-7941

DEVELOPMENT OF A REMOTE DIGITAL AUGMENTATION SYSTEM AND APPLICATION TO A REMOTELY PILOTED RESEARCH VEHICLE

John W. Edwards and Dwain A. Deets

Flight Research Center
Edwards, Calif. 93523

NATIONAL AERONAUTICS AND SPACE ADMINISTRATION • WASHINGTON, D. C. • APRIL 1975

1. Report No.	2. Government Accession No.	3. Recipient's Catalog No.
NASA TN D-7941		

4. Title and Subtitle	5. Report Date
DEVELOPMENT OF A REMOTE DIGITAL AUGMENTATION SYSTEM AND APPLICATION TO A REMOTELY PILOTED RESEARCH VEHICLE	April 1975
	6. Performing Organization Code
7. Author(s)	8. Performing Organization Report No.
John W. Edwards and Dwain A. Deets	H-854
	10. Work Unit No.
9. Performing Organization Name and Address	760-67-05
NASA Flight Research Center P. O. Box 273 Edwards, California 93523	11. Contract or Grant No.
	13. Type of Report and Period Covered
12. Sponsoring Agency Name and Address	Technical Note
National Aeronautics and Space Administration Washington, D. C. 20546	14. Sponsoring Agency Code

15. Supplementary Notes

A condensed version of this report was presented at the AIAA RPV Technology Symposium in Tucson, Ariz., November 12-14, 1974, and printed as NASA TM X-56029.

16. Abstract

A cost-effective approach to flight testing advanced control concepts with remotely piloted vehicles is described. The approach utilizes a ground-based digital computer coupled to the remotely piloted vehicle's motion sensors and control surface actuators through telemetry links to provide high bandwidth feedback control. The application of the system to the control of an unmanned 3/8-scale model of the F-15 airplane is described. The model was flown by a ground-based pilot from the remotely piloted research vehicle facility at the NASA Flight Research Center. The model was remotely augmented; that is, the F-15 mechanical and control augmentation flight control systems were simulated by the ground-based computer, rather than being in the vehicle itself. The results of flight tests of the model at high angles of attack are discussed.

17. Key Words (Suggested by Author(s))	18. Distribution Statement
Control systems Remotely piloted vehicle Digital flight control	Unclassified - Unlimited Category: 05

19. Security Classif. (of this report)	20. Security Classif. (of this page)	21. No. of Pages	22. Price*
Unclassified	Unclassified	52	$4.25

*For sale by the National Technical Information Service, Springfield, Virginia 22151

DEVELOPMENT OF A REMOTE DIGITAL AUGMENTATION SYSTEM AND APPLICATION TO A REMOTELY PILOTED RESEARCH VEHICLE

John W. Edwards and Dwain A. Deets
Flight Research Center

INTRODUCTION

The NASA Flight Research Center has developed a facility for flight testing aircraft using a remotely piloted research vehicle (RPRV) technique. This technique involves a pilot who controls the flight-test vehicle from a ground-based cockpit, and a ground-based digital computer for computation of command signals. The remote pilot cockpit and the computer are coupled to the flight-test vehicle through telemetry uplink and downlink data channels. This concept evolved from an interest in developing a low-cost alternative to full-scale manned prototype testing for high-risk flight tests such as stalls and spins.

The flight-test capability of the NASA Flight Research Center's RPRV facility is enhanced by its remotely augmented vehicle (RAV) system, which can provide remote augmentation for manned or unmanned test vehicles. In this system the ground-based digital computer provides closed-loop control law computation for the remote vehicle. The closed-loop control laws can be implemented on the computer by using FORTRAN programing, which removes much of the complexity from the onboard systems. The computer can simulate either digital flight control systems or analog flight control systems. The RAV system is not suitable for duplicating some flight control concepts such as redundancy management or multiple channel operation.

The RPRV technique was used at the NASA Flight Research Center in a flight-test program on a 3/8-scale model of the F-15 airplane. The RPRV systems used in this research program were checked out on a PA-30 airplane (ref. 1). The development of the RPRV testing technique is summarized in reference 2. The objective of the scale-model flight-test program was to investigate the high-angle-of-attack stall-spin region of the F-15 airplane. For this program the RAV system simulated the full-scale F-15 analog control system (both the open-loop mechanical control system and the closed-loop control augmentation system). It also provided basic control modes that enabled stability and control data to be obtained from the flight data.

This report describes the RPRV facility at the NASA Flight Research Center, the development of the digital RAV system, and its application to the scale-model F-15 flight-test program.

SYMBOLS

a	model scale factor
$a_i, b_i, c_i, d_i, \alpha_i, \beta_i$	coordinates of poles and zeros of general s-plane transfer function
b, c, d, β	coordinates of specific poles and zeros in s-plane transfer function
C^*	longitudinal performance index, $n_z - \frac{V_{co}}{g} q$
$F_{\delta_e}, F_{\delta_a}$	longitudinal and lateral stick force, respectively, N
$G(\cdot)$	general transfer function where $(\cdot)$ is (s), (w), or (z)
$G_0(s)$	zero-order hold transfer function
g	acceleration of gravity, m/sec^2
I	moment of inertia, N/m^2
I_X	moment of inertia about X-axis, kg-m^2
I_{XZ}	product of inertia, kg-m^2
I_Y	moment of inertia about Y-axis, kg-m^2
I_Z	moment of inertia about Z-axis, kg-m^2
i	index variable
$j = \sqrt{-1}$	
$K_{(\cdot)}$	feedback gain associated with $(\cdot)$
K', K''	general filter gain constants
k	difference between order of numerator and denominator of $G(s)$
l	length, m
M	Mach number
$M_\alpha, M_q, M_{\delta_e}, Z_\alpha, Z_{\delta_e}$	dimensionalized stability and control derivatives for longitudinal short-period equations of motion

m	mass, kg
n,t	number of complex pairs of roots in numerator and denominator, respectively, of general transfer function
n_z,n_y	airplane normal and lateral acceleration, respectively, g
Δn_z	incremental change in airplane normal acceleration, g
p,q,r	airplane roll, pitch, and yaw rate, respectively, deg/sec
$Re\ z, Im\ z$	abscissa and ordinate of z-plane, respectively
s	s-plane complex variable
T	sample period, sec
u,r	number of real roots in numerator and denominator, respectively, of general transfer function
V	velocity, m/sec
V_c	speed of sound, m/sec
V_{co}	crossover velocity for C^* index, m/sec
w	w-plane complex variable, $\frac{z-1}{z+1}$
z	z-plane complex variable, e^{sT}
α,β	angle of attack and angle of sideslip, respectively, deg
δ_a	aileron signal, $\frac{1}{2}\left(\delta_{a_L} - \delta_{a_R}\right)$, deg
$\delta_{a_L},\delta_{a_R}$	left and right aileron position, respectively, positive trailing edge down, deg
δ_{a_p}	pilot's lateral stick position, cm
δ_a/δ_{a_p}	lateral stick gearing ratio, deg/cm
δ_d	differential stabilator signal, $\frac{1}{2}\left(\delta_{h_L} - \delta_{h_R}\right)$, deg

$\delta_{d_{CAS}}$ contribution to δ_d from roll command augmentation system, deg

$\delta_{d_{MCS}}$ contribution to δ_d from roll mechanical control system, deg

δ_{e_p} pilot's longitudinal stick position, cm

$\delta_{e_{trim}}, \delta_{a_{trim}}, \delta_{r_{trim}}$ longitudinal, lateral, and yaw trim, respectively, cm

δ_h collective stabilator signal, $\frac{1}{2}\left(\delta_{h_L} + \delta_{h_R}\right)$, deg

$\delta_{h_{CAS}}$ pitch command augmentation system command, deg

$\delta_{h_L}, \delta_{h_R}$ left and right stabilator position, respectively, positive trailing edge down, deg

δ_{pb} pitch boost servo output, deg

δ'_{pb} lagged pitch boost servo output, deg

δ_r rudder position, deg

δ_{r_a} rudder command due to aileron interconnect, deg

δ_r/δ_{a_p} aileron-to-rudder interconnect gain, deg/cm

δ_{r_p} pilot's rudder pedal position, cm

$\delta_1, \delta_2, \delta_3, \delta_4$ general uplink commands of RPRV system, counts

ζ damping ratio

θ pitch angle, deg

$\ddot{\theta}$ angular acceleration, deg/sec^2

μ, η abscissa and ordinate of w-plane, respectively

ν kinematic viscosity, m^2/sec

ρ atmospheric density, kg/m^3

σ, ε abscissa and ordinate of s-plane, respectively

ω frequency, rad/sec

Subscripts:

c commanded variable

f full scale

max maximum value

s stability axis

sp short period

Abbreviations:

CAS control augmentation system

MCS mechanical control system

REMOTELY PILOTED RESEARCH VEHICLE FACILITY

A block diagram of the RPRV system is shown in figure 1. The vehicle response variables are telemetered to a ground station where they are routed to a ground computer, a ground cockpit instrument panel, and analog strip chart recorders for real-time flight monitoring. The ground cockpit proportional control functions (longitudinal and lateral stick and rudder pedals) are processed by the analog-to-digital converter and are trunked to the ground computer together with the mode panel signals. The ground computer calculates the command variables and provides them to the uplink encoder. Figure 2 shows the location of the components of the RPRV system in the RPRV facility. The ground cockpit (not shown) is adjacent to the cockpit electronics racks, which makes the RPRV system a self-contained, dedicated facility except for the uplink and downlink transmission and reception systems.

The RPRV system uses two uplink encoders (fig. 1). The computer encoder receives command variables from the computer, and the bypass encoder receives command variables directly from the ground cockpit. The RPRV pilot selects an encoder by means of a pushbutton on the mode control panel. The bypass encoder serves as a backup to the computer encoder if the computer malfunctions. The command signals are transmitted to the test vehicle, where they are decoded and sent to the appropriate servochannel.

The pilot may select one of two telemetry uplink antennas: an antenna slaved to a radar tracking antenna, or a fixed antenna. The uplink antennas and the uplink encoders are the only dualized components in the RPRV system. Since the system is intended for flight research, it was designed as a single channel system except for the critical uplink channel.

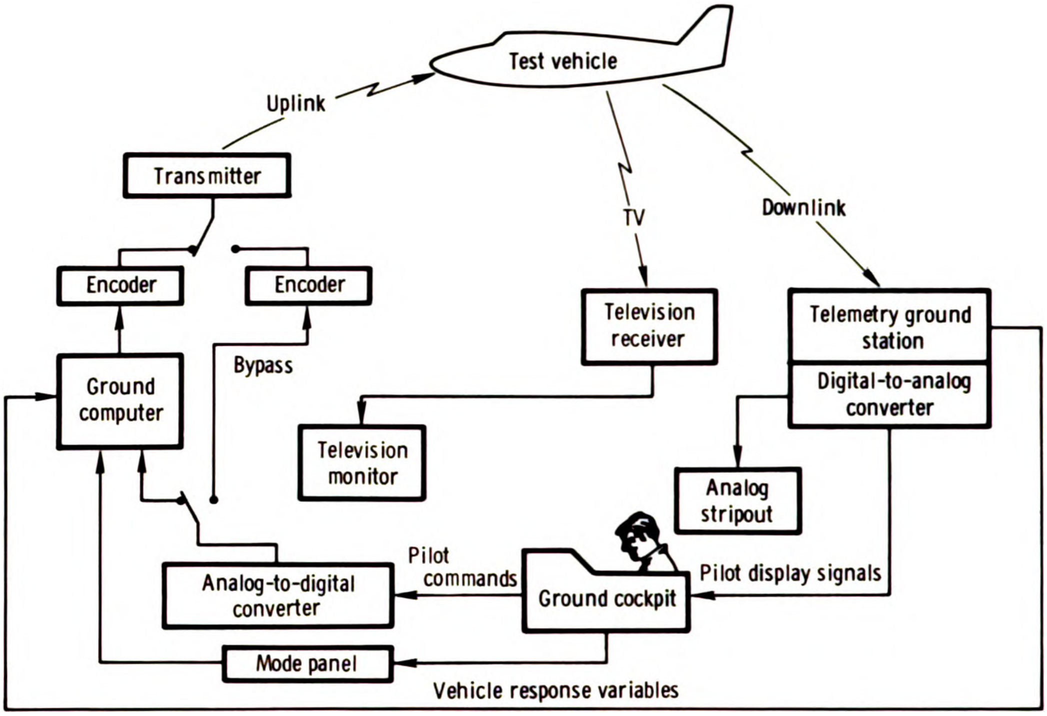

Figure 1. Functional block diagram of the RPRV system.

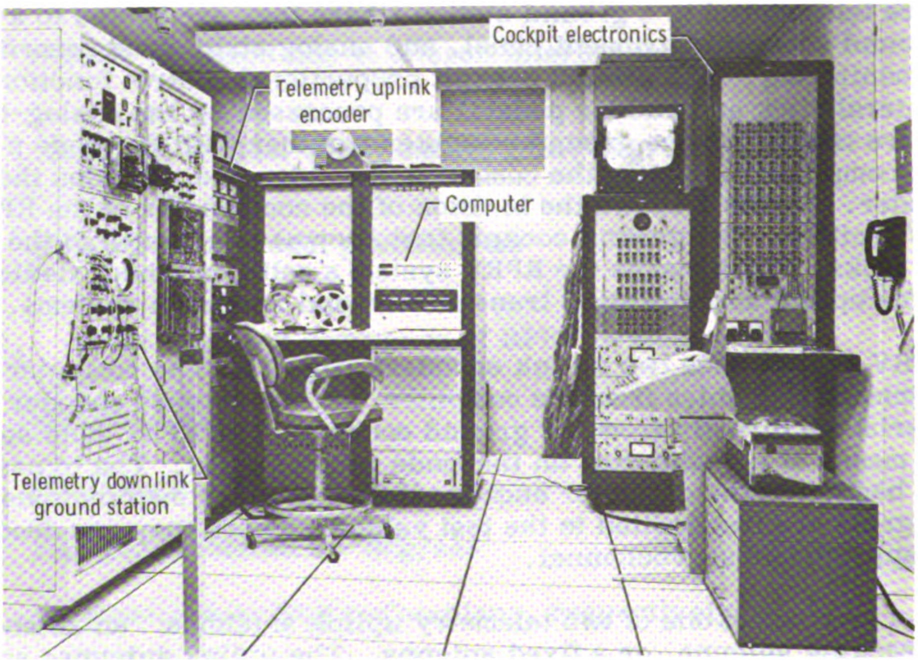

Figure 2. RPRV facility equipment. **E-26105**

Ground Cockpit

In the operation of the RPRV system, the remote pilot is given direct proportional control of the test vehicle. This makes it possible to use experienced test pilots so that the maximum research capability can be realized from the system. Accordingly, the ground cockpit is configured to provide the pilot with as much information as possible about the test vehicle and with complete control over the system. Figure 3 is a photograph of the ground cockpit showing the instrument panel, control stick, mode control panel, and pulse panel. The pilot controls the vehicle with a control stick and rudder pedals. The stick and pedals are part of an artificial feel system, and position limits and force gradients are adjustable. The pilot may select various control modes and gains on the mode control panel and apply control surface steps or doublets, under computer control, through the pulse panel. The mode control panel implements four control modes in three axes (pitch, roll, and yaw) and provides gain switches that can be programed in each axis. The panel also permits the pilot to select the bypass mode or computer modes and informs him if any downlink variable fails a window check. The mode control panel pushbutton switches are rear-lighted under computer control and indicate the control mode of the computer.

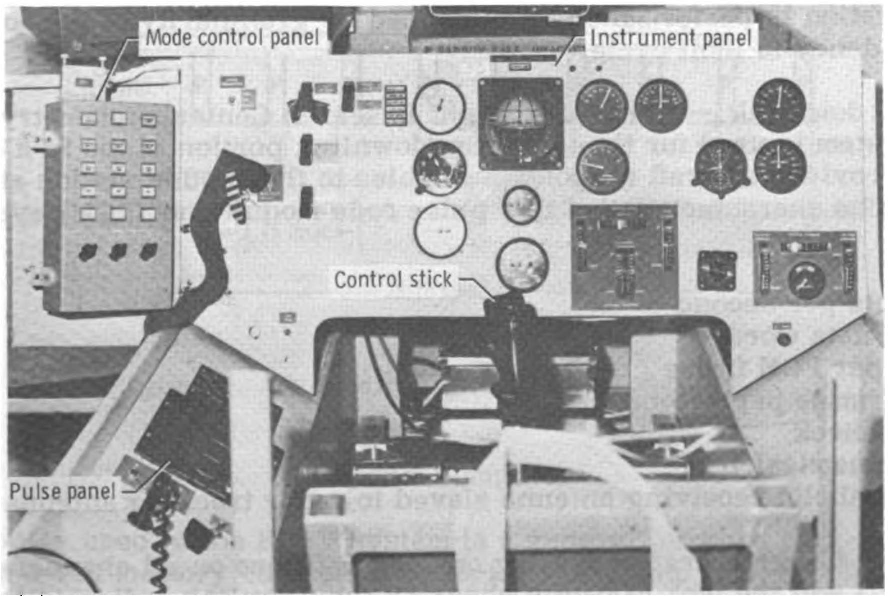

Figure 3. Remote pilot cockpit. *E-26991*

Telemetry Downlink and Uplink

Successful operation of the telemetry data links is critical to the RPRV/RAV system. The links must be highly reliable and not introduce unacceptable time delays. During operation in a closed-loop RAV system mode, transmission losses lasting more than several tenths of a second would be unacceptable. This is in contrast to typical remotely piloted drone military missions which involve the transmission of discrete commands to onboard analog autopilots and are capable of operating in hostile environments.

The time delay of the data links in the RPRV system is approximately 3.3 microseconds per kilometer, which yields a total time delay of approximately 0.5 millisecond through the downlink and uplink when the test vehicle is at a range of 75 kilometers. This is an acceptable time delay, compared to the total computational delay through the RAV system.

The telemetry links are essentially line-of-sight transmission paths, so the signal may be blocked by the wing of the test vehicle at extreme attitudes or by the horizon if the vehicle is at too low an altitude at extreme range. Thus the range of RPRV testing is a function of vehicle attitude and altitude. It was estimated that flight operations would be limited to approximately 55 kilometers at 1500 meters altitude and to approximately 185 kilometers at 13,700 meters altitude.

The number of bits in the downlink and uplink telemetry channels (9 bits in the downlink and 10 bits in the uplink) was chosen to permit valid implementation of typical closed-loop aircraft control laws. Simulator studies indicated that little increased performance was achieved with more than 10 bits, whereas less than 9 bits led to deterioration in performance as evidenced by granularity of the command signals and a tendency to limit cycle.

Telemetry downlink.— The NASA Flight Research Center's telemetry flight data acquisition system is used for the telemetry downlink portion of the RPRV system. This system provides aircraft response variables to the ground station at 200 samples per second. The characteristics of this pulse code modulation (PCM) system are as follows:

144,000 bits per second
9 bits per data word
80 words per PCM frame
200 PCM frames per second
No parity check
L-band transmission
12-foot parabolic receiving antenna slaved to radar tracking antenna

The system has 40-hertz first-order-lag analog prefilters on all channels. The low power (5 watts) and the lack of parity check on the downlink indicated the need for reasonability checks in the software to discriminate against incorrect telemetry data. The downlink is commonly used to obtain data at ranges as great as 320 kilometers for high-altitude aircraft.

Telemetry uplink.— The telemetry uplink used for the system was developed by the U.S. Navy for the remote control of drone aircraft. The system is capable of several modes of operation, from the control of a single drone to the time-multiplexed control of a fleet of drones. Because it can control more than one drone simultaneously, the update rate of the system when controlling a single aircraft is comfortably high. Consequently, the system has good research capability. The characteristics of the system are as follows:

16 bits per data frame (10-bit proportional command signal and 6 discrete signals)
4 data frames per cycle
53.33 cycles per second
2 parity checks per data frame
Synchronization and parity checks on each cycle
UHF band transmission
Frequency shift keying

The telemetry uplink cycle (fig. 4) consists of 4 data words (frames) and a sync word transmitted at 53.33 samples per second (18.75 milliseconds cycle time). The transfer of each data word from encoder to receiver output on board the test airplane requires 3.75 milliseconds. The four command signals are coded in the 10 most significant bits of the uplink words, with the remaining 6 bits being available for discrete signals to the test vehicle. Since parity checks are performed on each data word, intermittent dropout of the telemetry uplink signal was not expected to cause serious problems.

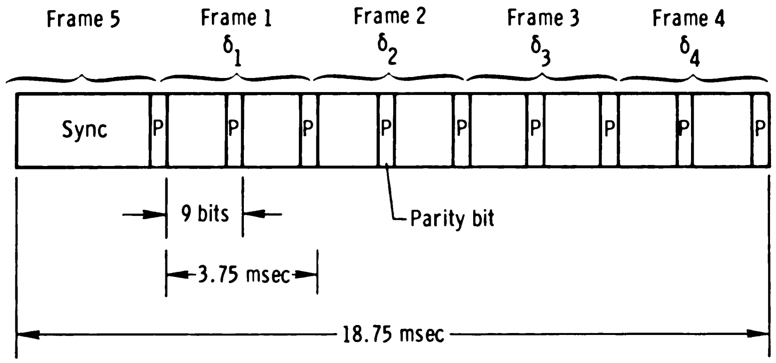

Figure 4. Telemetry uplink time schedule.

Ground Computer

The computer used in the RPRV system is a general purpose rack-mounted minicomputer with a 16K memory consisting of 16-bit words and with a 750-nanosecond cycle time. The peripheral equipment includes a card reader, line printer, magnetic tape unit, disc unit, teletype, paper tape reader/punch, and peripheral floating point processor. The software is composed of an assembler, a FORTRAN compiler, and a mathematical subroutine support library. During real-time RPRV operation, data inputs to the computer (cockpit data and downlink data) and data outputs from the computer (uplink commands) are initiated by means of input/output interrupts.

The peripheral floating point processor receives and transmits data associated with the hardware floating point operation over the input/output bus by means of the priority memory access unit. Although this operation consumes the major portion of the 75-microsecond hardware floating point execution time, it is faster than the computer's software floating point option. It is slower, though, than may be achieved with integrated floating point hardware. A floating point data word requires two memory locations and has an 8-bit exponent and a 22-bit mantissa (six-place accuracy).

The open-loop and closed-loop control law computations are implemented through an RPRV computer program which uses floating point FORTRAN. Thus the FORTRAN compiler is used to debug and check out programs, and the floating point feature eliminates the need for variable scaling. The obvious advantage of this mode of programing in a research environment is the ease with which programs may be written and modified by a control systems engineer. The RPRV computer program also contains the assembly language subroutines which perform all input and output of data, pass the data to the FORTRAN main program, and receive the uplink command signals from the main program.

As an indication of the capability of the RPRV computer to perform feedback control law computations, approximately 0.7 millisecond is required to sum two feedback variables and a pilot command signal (each multiplied by a gain) and to operate on the resulting error signal with a first-order digital filter.

Ground Computer Input/Output Interface

Figure 5 illustrates the RPRV system interface at the computer. The number of bits in the data words passed to and from the computer is indicated in the arrows. All input/output of data is performed by assembly language interrupt servicing subroutines. The FORTRAN main program tests for the occurrence of interrupts by calls to the assembly language subroutines. The data are transferred between the assembly language routines and the FORTRAN program through the common data block and subroutine calling lists.

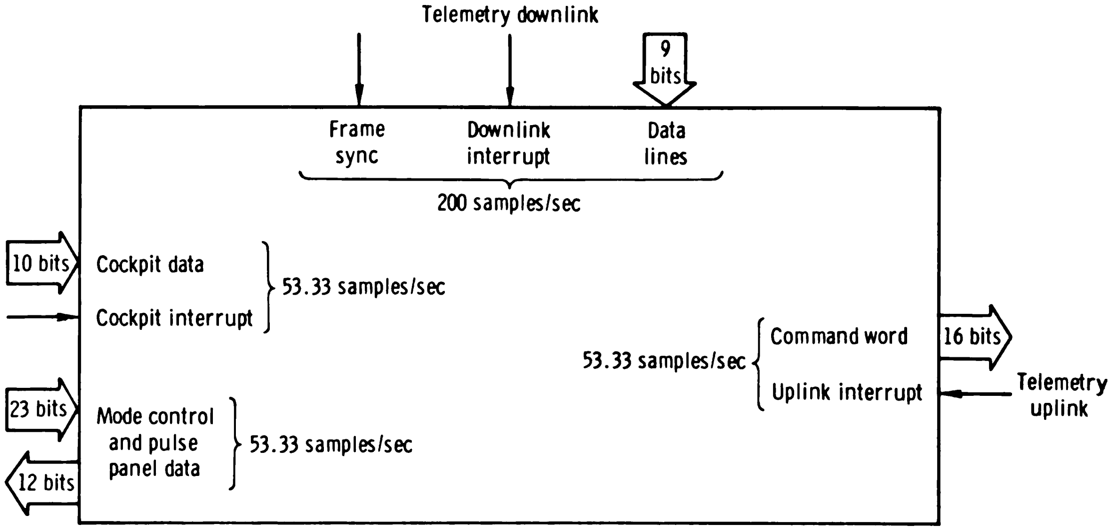

Figure 5. Input/output interface at the RPRV computer.

Telemetry downlink interface.— Downlink telemetry data are transferred to the computer by the downlink interrupt servicing routine at 200 samples per second for each variable. The program recognizes the variables by their sequence with respect to the FRAME SYNC PULSE which occurs once every PCM frame. The values of the variables are represented by a 0 to 511 decimal count format.

During on-line operation, the downlink interrupt servicing routine continuously updates the table of telemetry data. When the FORTRAN main program accesses the data, a window check is performed on the most recent data word to discriminate against bad data caused by loss of the downlink signal. If this word is within ±70 counts of the last "good" data word, it is accepted as valid.

Telemetry uplink interface.— The computer encoder interrupts the computer every 3.75 milliseconds to request one of the five 16-bit command words. The uplink interrupt servicing routine tests five sense lines to determine the correct variable to output. If the computer program and the uplink encoder should get out of synchronization, the computer sends the variable that the encoder requests, even though it may have anticipated sending a different variable.

Ground cockpit interface.— The pilot's proportional command signals and the mode control panel status are sampled by the computer once each cycle at a rate of 53.33 samples per second. The present mode control panel status is interrogated by the FORTRAN main program to determine if a mode change is being commanded by the pilot.

Timing and Synchronization of RPRV System

Figure 6 shows the time sequence of operations of the RPRV system. The FORTRAN program computation sequence is controlled by the uplink interrupt. For instance, during frame 1 the program computes the command signal δ_1. This command is passed to the uplink interrupt servicing subroutine, and the FORTRAN program then waits in an idle loop for an uplink interrupt. When the interrupt occurs, the FORTRAN program determines if δ_1 was requested and, if so, begins computing the next command signal, δ_2. If any other command was requested, the FORTRAN program branches to the appropriate frame in an attempt to get back into synchronization.

During frame 5, the FORTRAN program accepts the cockpit data, determines the mode control panel status, and performs mode switching initialization. The final function during frame 5 is a check to determine if the cockpit is in the bypass mode. If it is, the FORTRAN program continually loops in frame 5 awaiting the pilot's selection of a computer mode.

The downlink system is asynchronous with respect to the uplink system. The PCM data are provided at 200 samples per second, and the uplink commands are updated at 53.33 samples per second. The high data rate of the downlink system is used to minimize the time delay through the closed-loop system; all telemetry data are accepted but only the most recent value of a downlink variable is used. Thus the effective overall sample rate of the flight control system is that of the system with the lowest sample rate, in this instance, the uplink system.

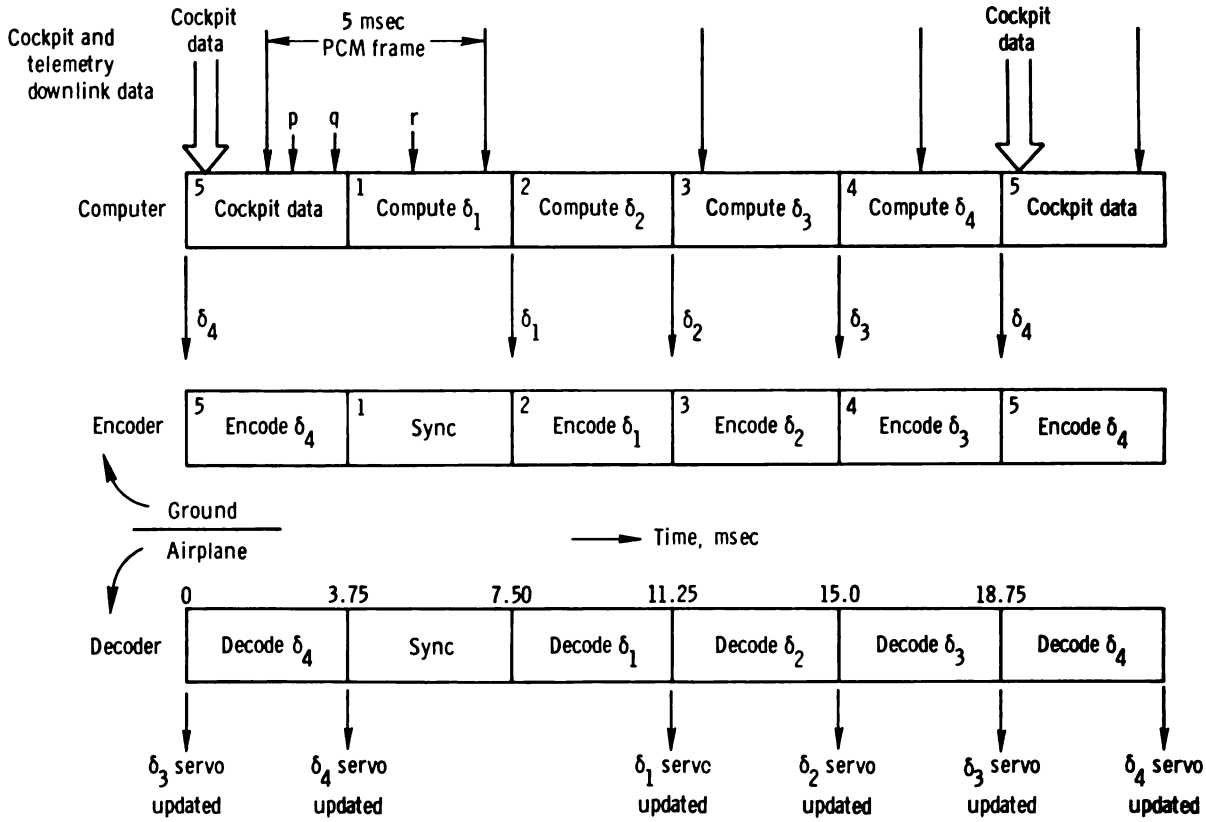

Figure 6. Computation sequence for RPRV system.

The throughput delay associated with the computer and encoder varies from 7.5 milliseconds to 12.5 milliseconds. The minimum delay occurs when a sensed variable enters the computer immediately before the beginning of the frame in which it would be used. The variable would be used to update the command signal during that 3.75-millisecond frame and would be transmitted to the test airplane to update the airplane's controls at the end of the following 3.75-millisecond frame. The maximum delay of 12.5 milliseconds occurs if the sensed variable is 5 milliseconds old before the current computation frame begins.

As an example of the approximate total lag through the system, from sensor output to control surface actuator command, the lag shown in the table on the next page would be accumulated for a 5-hertz signal with a vehicle located 75 kilometers from the ground station.

	Time delay, milliseconds
40-hertz analog prefilter	4.44
Downlink (PCM) encoding	.06
Transmittal to ground station	.25
Average computer/encoder throughput	10.00
Zero-order hold	9.40
Transmittal to airplane	.25
Average total delay	24.40

This time delay corresponds to a 44° phase lag at 5 hertz, an acceptable lag for most applications. If this lag is unacceptably large, some lead could be generated by programing a lead-lag filter in the digital computer.

All computations within a given frame, as well as background interrupt servicing (invisible to the FORTRAN program), must be performed within 3.75 milliseconds. If this time constraint is violated, the interrupt for that frame will occur before the FORTRAN program is ready to test for its occurrence. Then the FORTRAN program must wait for the next interrupt before it can begin the next computation frame. Thus the command in the following frame would not be updated.

SUBSCALE F-15 PROGRAM

The RPRV facility was used to flight test a 3/8-scale model of the F-15 airplane. The goal of the flight program was to investigate the model's high-angle-of-attack performance and its stalling and spinning characteristics. This program was an appropriate application of the RPRV technique to hazardous flight testing, in that it was possible to perform much of the model testing before spin flight tests were made on the full-scale F-15 airplane. The function of the RPRV ground computer in the subscale F-15 program was to simulate the full-scale F-15 flight control systems. The F-15 open-loop mechanical control system (MCS) and the closed-loop control augmentation system (CAS) modes, containing actuator dynamics, gearing schedules, gains, and shaping filters, were implemented by using the ground computer.

F-15 Model

A three-view drawing of the F-15 model is shown in figure 7. The model was built to be at least as stiff as the full-scale airplane to minimize structural resonance problems. Batteries powered all onboard systems, including the hydraulic actuators which positioned the control surfaces. The control surfaces consisted of left and right stabilators for pitch and roll control, ailerons for roll control, and twin rudders for yaw control. The control surface actuators had 10-hertz bandwidths. A detailed description of the model and instrumentation system is given in reference 3.

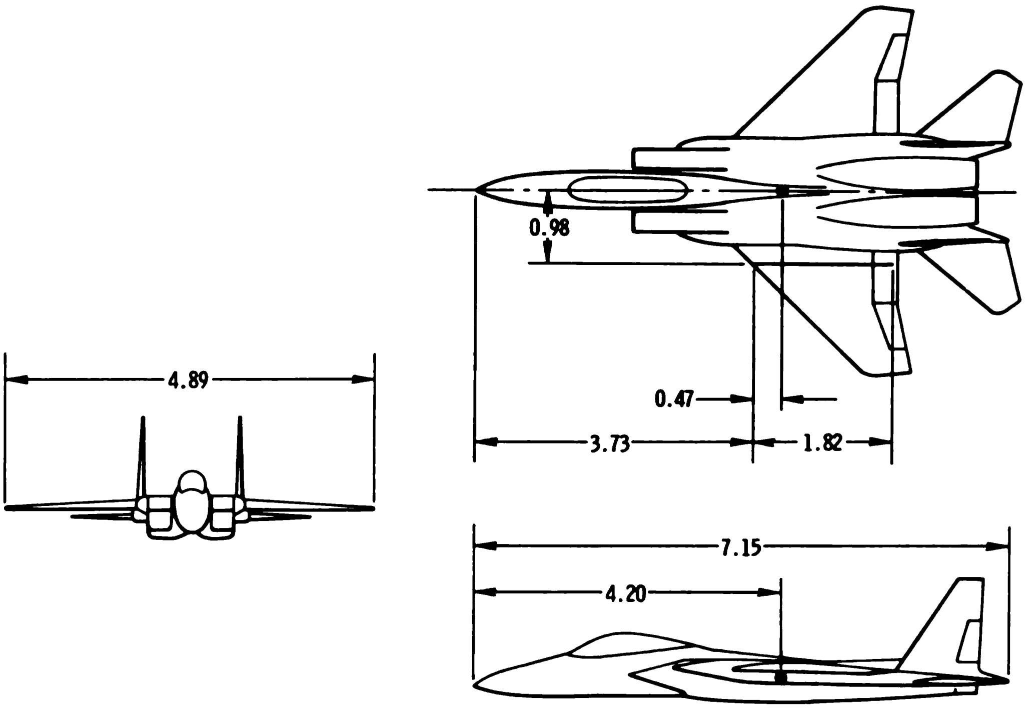

Figure 7. Three-view drawing of 3/8-scale-model F-15. Dimensions in meters.

Two center-of-gravity locations—at the 26-percent mean aerodynamic chord and at the 30-percent mean aerodynamic chord—were used. The 30-percent mean aerodynamic chord location is the most rearward center-of-gravity location in the full-scale F-15 airplane.

Weights and inertias were as close as practical to the values required for correct 3/8-scale inertial-force-to-gravitational-force scaling. Appendix A discusses this scaling technique and derives the corresponding scaling laws. The desired values of weight and inertia and the actual values for the two center-of-gravity locations are as follows:

	Desired value at 26-percent mean aero-dynamic chord	Actual value	
		26-percent mean aerodynamic chord	30-percent mean aerodynamic chord
Weight, N	7,668	10,964	10,951
I_X, kg-m^2	235	373	373
I_Y, kg-m^2	1,520	2,579	2,452
I_Z, kg-m^2	1,708	3,021	2,894
I_{XZ}, kg-m^2	-4.7	15.7	3.4

The differences between the actual and the desired values point up the difficulty of independently controlling the mass distribution of a flight vehicle while meeting all the proper geometrical and structural design load requirements. Strict adherence to the desired values was not necessary, since the ratio between model and full-scale atmospheric density is a factor in each of the mass and inertia scaling laws (table A2). Proper selection of model F-15 flight-test altitude could give a reasonable simulation of the full-scale F-15 at a different altitude.

To implement the full-scale F-15 CAS, the ground computer required three-axis rate signals, normal and lateral accelerations, and angle of attack from the model. Table 1 lists the input/output variables, and their ranges, required by the ground computer to implement the F-15 control system. The only analog prefiltering performed on board the model was with 40-hertz first-order low-pass filters on all signals. A simple wings-leveling autopilot was the only onboard control system. It was activated by loss of the carrier frequency of the uplink command signals.

Launch and Recovery Technique

The unpowered model was air-launched from a B-52 airplane at an altitude of 13,700 meters and had a flight time of approximately 5 minutes, depending on the number and types of maneuvers performed. The model was recovered with a midair parachute recovery system which was automatically deployed at 4600 meters altitude unless manual recovery was started earlier. The flight range of the model from the ground station was approximately 15 kilometers to 25 kilometers. During the launch sequence, the control surfaces of the model were locked in the launch configuration for 3 seconds. At the end of this interval, the uplink command signals became operative and the remote pilot took control of the model.

Simulation

A simulation of the RPRV system was required to check out RPRV programs and to provide pilot training and flight planning capability. The simulation was performed on the NASA Flight Research Center's central computer, utilizing its real-time simulation capability. The cockpit used in the simulation was designed to be as similar as possible to the RPRV facility cockpit. Six-degree-of-freedom equations of motion were mechanized, and the program was written to accept aerodynamic force and moment data in a general format. The airplane's continuous differential equations of motion were integrated numerically by the computer, using a second-order Runge-Kutta integration technique.

Two separate simulations of the RPRV system were implemented. The first, called the RPRV digital simulation, contained the basic aircraft simulation described above and a subroutine which simulated the control system modes of the RPRV computer program. The filters and actuator dynamics required for the basic modes and the F-15 control system modes were implemented in this subroutine by difference equations. The update rate of the difference equations was 53 samples per second. The processing of these equations simulated the operations performed by the RPRV computer.

TABLE 1.— INPUT/OUTPUT VARIABLES TO RPRV COMPUTER FOR 3/8-SCALE-MODEL F-15

Variable	Range
Cockpit inputs (10 bits)	
δ_{e_p}	-7.37 cm to 13.72 cm
δ_{a_p}	±10.16 cm
δ_{r_p}	±8.26 cm
F_{δ_e}	-111 N to 204 N
F_{δ_a}	±71 N
$\delta_{e_{trim}}$	-7.37 cm to 13.72 cm
$\delta_{a_{trim}}$	±10.16 cm
Telemetry downlink inputs (9 bits)	
α	-5° to 35°
p	±200 deg/sec
q	±100 deg/sec
r	±100 deg/sec
n_z	-3g to 6g
n_y	±1g
Telemetry uplink outputs (10 bits)	
δ_{a_c}	±20°
$\delta_{h_{L_c}}$	-27.5° to 15°
$\delta_{h_{R_c}}$	-27.5° to 15°
δ_{r_c}	±30°

The second simulation, called the analog CAS simulation, contained the basic aircraft simulation and a subroutine which simulated the operation of the F-15 analog CAS. The continuous differential equations which described the analog CAS were integrated, along with the airplane's equations of motion, at 200 samples per second. Both systems of equations were integrated by using the same second-order Runge-Kutta integration technique. The validity of the RAV system approach to flight testing was assessed by comparing the RPRV digital simulation of the F-15 CAS and the analog CAS simulation.

Since the subscale model flight program involved stalling and spinning, these maneuvers were simulated. Wind-tunnel aerodynamic data for angles of attack from 0° to 90° and angles of sideslip from -40° to 40° were used in the simulation, as well as a limited amount of wind-tunnel aerodynamic data for angles of attack from 0° to -90°. Thus stalls, departures, post-stall gyrations, and fully developed spins could be simulated to the extent of the validity of the aerodynamic data.

Because the RPRV computer program was coded in floating point FORTRAN, it was possible to incorporate the actual program into the RPRV digital simulation as a subroutine. Only minor modifications to the RPRV computer program were required to make it compatible with the flight planning simulation.

The central computer's UPDATE feature was another aid in modifying the RPRV program. An UPDATE file of the entire simulation program was created, including a representation of the actual RPRV program card deck as a subroutine. The UPDATE feature permitted individual cards to be inserted or deleted from the UPDATE file and the resulting file to be compiled by the FORTRAN compiler. This enabled modifications to be made in the RPRV program in less than 5 minutes. When a final configuration was attained for an RPRV flight, a hard-copy record of the individual changes to the original RPRV card deck was available. This method of operation, coupled with the debugging capability of the RPRV computer's FORTRAN compiler, provided a high level of confidence in the modified RPRV program software.

USE OF REMOTELY AUGMENTED VEHICLE SYSTEM WITH THE SCALE-MODEL F-15

The RAV system can be used to control remote vehicles in a closed-loop, high-bandwidth mode using telemetry downlink and uplink data. This capability gives the RPRV facility an added dimension over an open-loop uplink control mode but requires that attention be given to the stability of the system. This section discusses the use of the RPRV facility in this remote augmentation mode.

Digital Filtering Technique

Simulation of analog components of a flight control system on a digital computer requires the use of a technique of discrete representation of continuous transfer functions. The technique used in the RPRV/RAV system was to transform continuous transfer functions, $G(s)$, into discrete transfer functions, $G(z)$, which were then implemented in the control computer as difference equations. The digital filtering algorithm used to simulate the scale-model F-15 analog control system is described in appendix B. The algorithm is an extension of the technique referred to in reference 4 as "bilinear transformation with frequency prewarping" and in reference 5 as the matched z-transform. The algorithm implements an exact conformal mapping from the s-plane to the w-plane, followed by the bilinear transformation:

$$w = \frac{z - 1}{z + 1}$$

The exact mapping of the s-plane to the w-plane yielded digital filters with magnitude and phase characteristics which were good approximations of the original continuous transfer functions. The resulting digital filters were similar to those which would be obtained by using the Tustin method, an alternative filtering algorithm (ref. 5), but were superior in several respects, as noted in appendix B.

The filtering algorithm described was also used to implement required digital compensation, aside from any requirement for simulating an analog function. In this application, frequency domain requirements such as notch filters may be translated directly to a digital filter by the algorithm. For example, digital notch and low-pass filters were required for the closed-loop rate damper and CAS modes. The z-plane transfer functions of the digital filters were derived by the filtering algorithm. These transfer functions contained the coefficients required for mechanizing the filters by means of difference equations in the RPRV program control laws. The general form of the notch filter was

$$G(z) = \frac{K''(z^2 - 2 \cos bT\, z + 1)}{z^2 - 2e^{-cT} \cos dT\, z + e^{-2cT}}$$

where

$$K'' = \frac{1 - 2e^{-cT} \cos dT + e^{-2cT}}{2 - 2 \cos bT}$$

in which b specifies the notch frequency and location of the positive complex zero on the s-plane imaginary axis, and c and d specify the s-plane coordinates of the desired poles. The general form of the low-pass filter was

$$G(z) = \tfrac{1}{2}\left(1 - e^{-\beta T}\right)\frac{(z + 1)}{\left(z - e^{-\beta T}\right)}$$

where β specifies the s-plane coordinate of the desired real pole.

Remote Augmentation Modes for the Scale-Model F-15

Several tasks were required of the RPRV ground computer in the scale-model F-15 program. It was necessary to have two basic control modes available that were specifically designed for the research function of the scale model and not related to the full-scale airplane's control system. The MCS and CAS modes were not well suited to stability and control maneuvers because of gearing schedules and interconnects which modified and restricted control surface authority as a function of flight condition, particularly at high angles of attack. The computer was also required to simulate the full-scale airplane's open-loop MCS and closed-loop CAS for the stall and spin testing. Motion of the control surfaces can have a marked influence on an airplane's propensity to experience a spin departure. The basic control modes and the F-15 control system modes were implemented in the computer program as four different control modes and placed under the remote pilot's control by means of the mode control panel.

Basic modes.— As shown in figure 8, the two upper rows of selector buttons on the mode control panel are the basic modes, and the two lower rows are the F-15 control system modes. The basic modes were required to provide (1) a simple control system for the initial checkout of the RPRV systems and (2) the full control authority of the airplane throughout the model's flight envelope to obtain stability and control data. The open-loop airplane is lightly damped in both the longitudinal and lateral-directional axes at high angles of attack, so the requirement to obtain useful stability and control data necessitated high damper gains. These gains were implemented in the rate damper mode. Stability and control maneuvers were performed by using the damper system to establish a trimmed flight condition and switching the damper gain in one or more axes to a low value or zero before the maneuver was started.

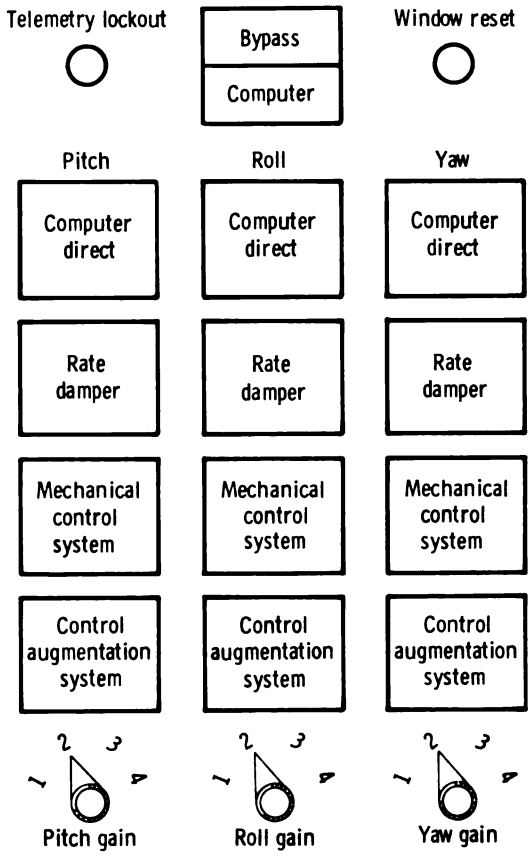

Figure 8. Mode control panel.

Block diagrams of the basic modes for the pitch axis are shown in figure 9(a) and for the roll and yaw axes in figure 9(b). The pilot's longitudinal stick displacement is modified by a nonlinear gearing schedule which commands the stabilators collectively. The nonlinear gearing schedule, shown in figure 10, was implemented to provide good model handling qualities in the launch condition ($\delta_h \approx 0°$) and full stabilator authority of 15° to -27.5° in the computer direct and rate damper modes. These are the maximum positive and negative stabilator deflections that can be commanded by the full-scale airplane's control system. Full stabilator authority was provided because it was intended to obtain stability and control data in these modes at the maximum angle of attack early in the flight program. The gearing schedule was mechanized in the RPRV computer as the sum of linear and quartic factors of δ_{e_p}.

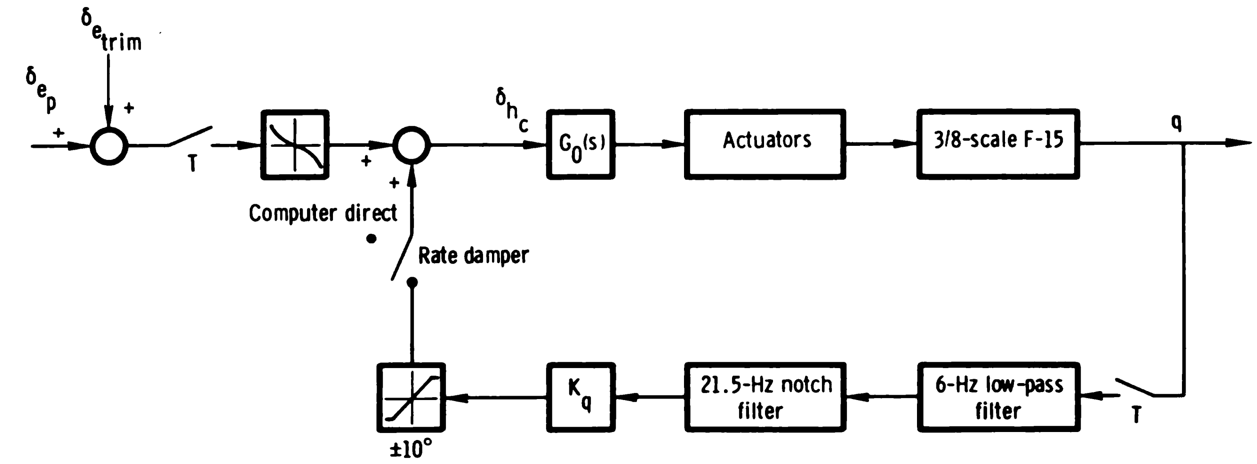

(a) Pitch axis.

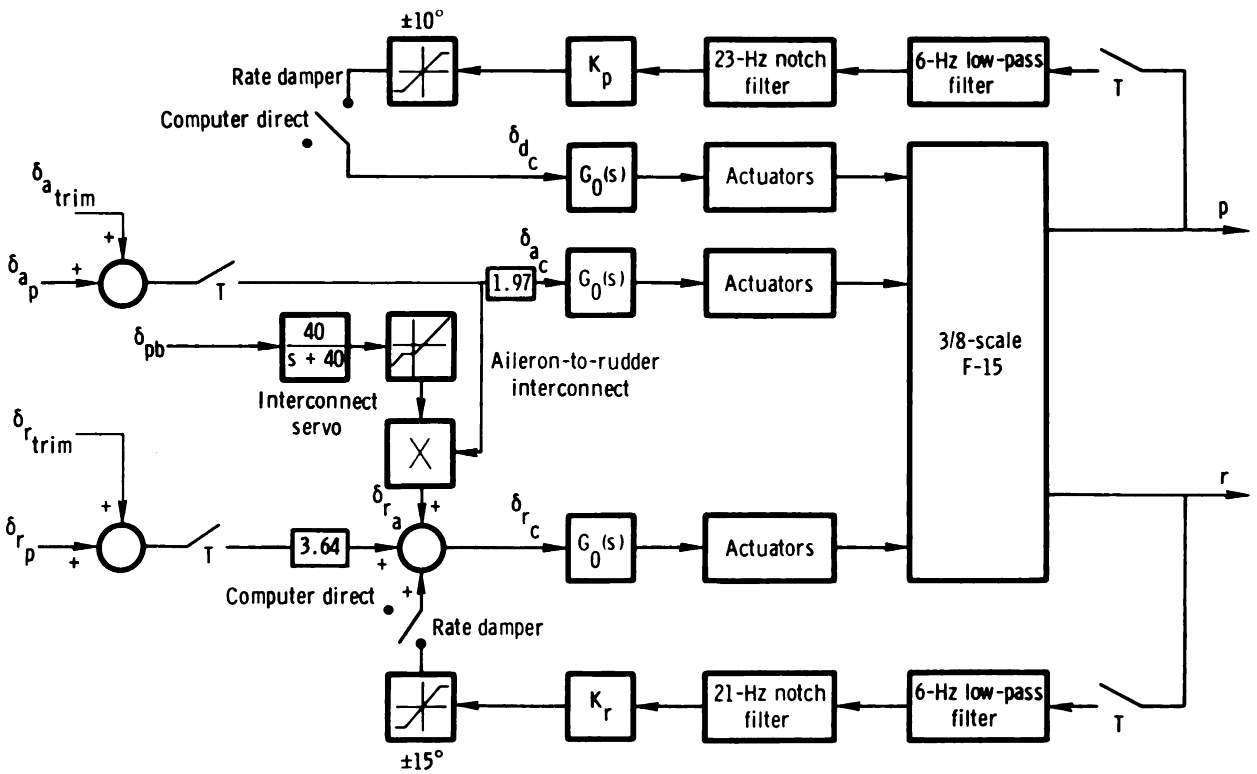

(b) Roll and yaw axes.

Figure 9. Block diagrams of the computer direct and rate damper modes.

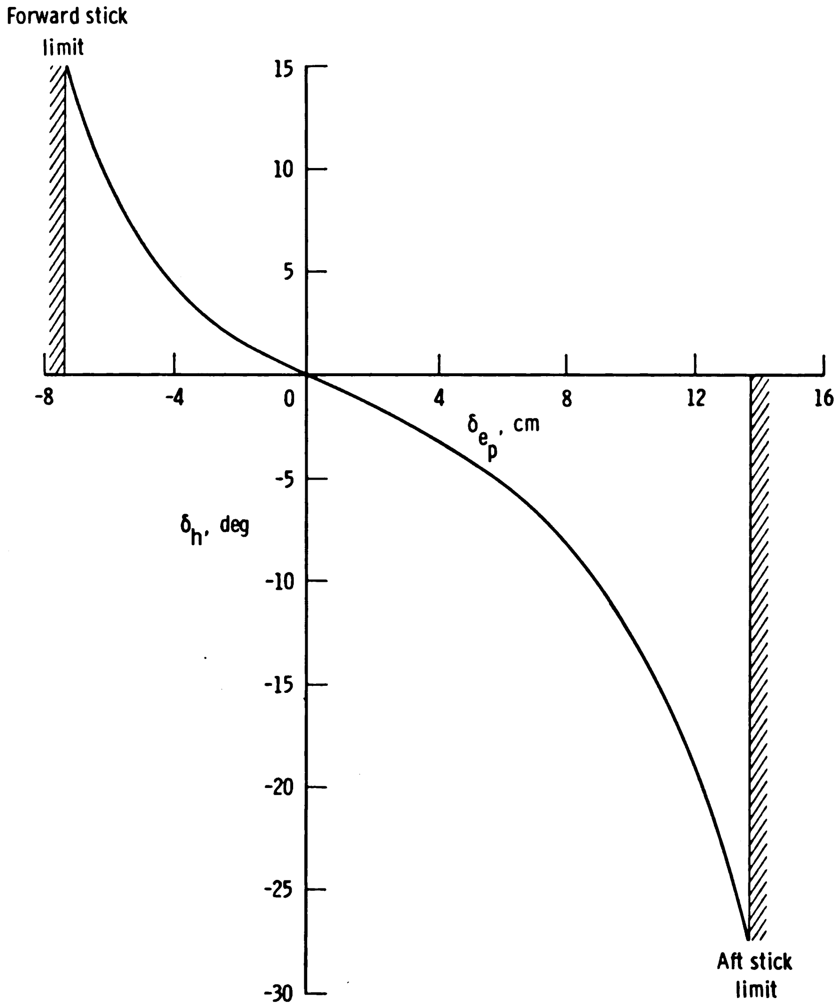

Figure 10. Nonlinear longitudinal stick-to-stabilator gearing for the computer direct and rate damper modes.

The pilot's lateral stick displacement, δ_{a_p}, commanded the ailerons and the rudders through an aileron-to-rudder interconnect. Since the F-15 MCS mode contained an interconnect schedule, the basic modes used this interconnect by executing the same code as used by the MCS mode for this function. The interconnect gain was scheduled as a function of pitch boost servo output, δ_{pb}, a parameter generated in the MCS code approximately proportional to the pilot's longitudinal stick position. The pilot's rudder pedals also controlled the rudders.

In the rate damper mode mechanization (fig. 9) damper commands were summed with the computer direct mode pilot commands. The rate damper mode implemented angular rate feedback in which pitch rate, q, was fed to the collective stabilators, roll rate, p, was fed to the differential stabilators, and yaw rate, r, was fed to the rudders. Each of the rate gyro signals was low-pass-filtered at 6 hertz and notch-filtered to eliminate the dominant structural resonance near 20 hertz. Amplitude authority limits of ±10°, ±10°, and ±15° were implemented in the pitch, roll, and yaw axes, respectively. Maximum rate damper gains used are listed in table 2 together with the gains implemented in the CAS mode, which will be discussed later All the functions of the computer direct and rate damper modes shown in figure 9 were programed in the RPRV computer.

TABLE 2.— MAXIMUM RATE DAMPER GAINS AND SCALE-MODEL F-15 CAS GAINS

Quantity	Maximum rate damper gain	Scale-model F-15 CAS gain
K_q, sec	0.4	0.133
K_p, sec	-0.8	-0.077
K_r, sec	4.0	- - -
K_{r_s}, sec	- -	0.613
K_{C*}, deg/g	- -	1.0
K_{n_y}, deg/g	- -	9.2

Scale-model F-15 modes.— Simulation of the full-scale F-15 control system required scaling of the system gains and characteristic frequencies in order to maintain the proper ratios of inertial to gravitational force. Appendix A derives scaling laws for the augmentation feedback control gains and shows that only angular rate feedback gains need modification. For example, the correct scaling for pitch rate feedback gain is

$$K_q = a^{\frac{1}{2}} K_{q_f}$$

where a is the model scale factor and K_{q_f} is the pitch rate feedback gain for the full-scale F-15 airplane. The decrease in gain reflects the increased angular rates experienced by the model. Also, all the critical frequencies of the full-scale airplane's flight control system dynamic components (actuators and filters) must be increased by $a^{-\frac{1}{2}}$ to reflect the time scaling of the model. Block diagrams of the F-15 MCS and CAS modes are shown in figures 11(a) and 11(b) for the pitch and the roll and yaw axes, respectively. The figures show the system implemented in the RPRV computer and include the critical frequency and rate feedback scaling.

The analog transfer functions of the servo actuators and shaping filters are also shown in figure 11 and are summarized in table 3. The transfer functions were simulated by difference equations which were implemented by using the digital filtering algorithm described in appendix B. The position limits and rate limits of the actuators were also simulated and are listed in table 3.

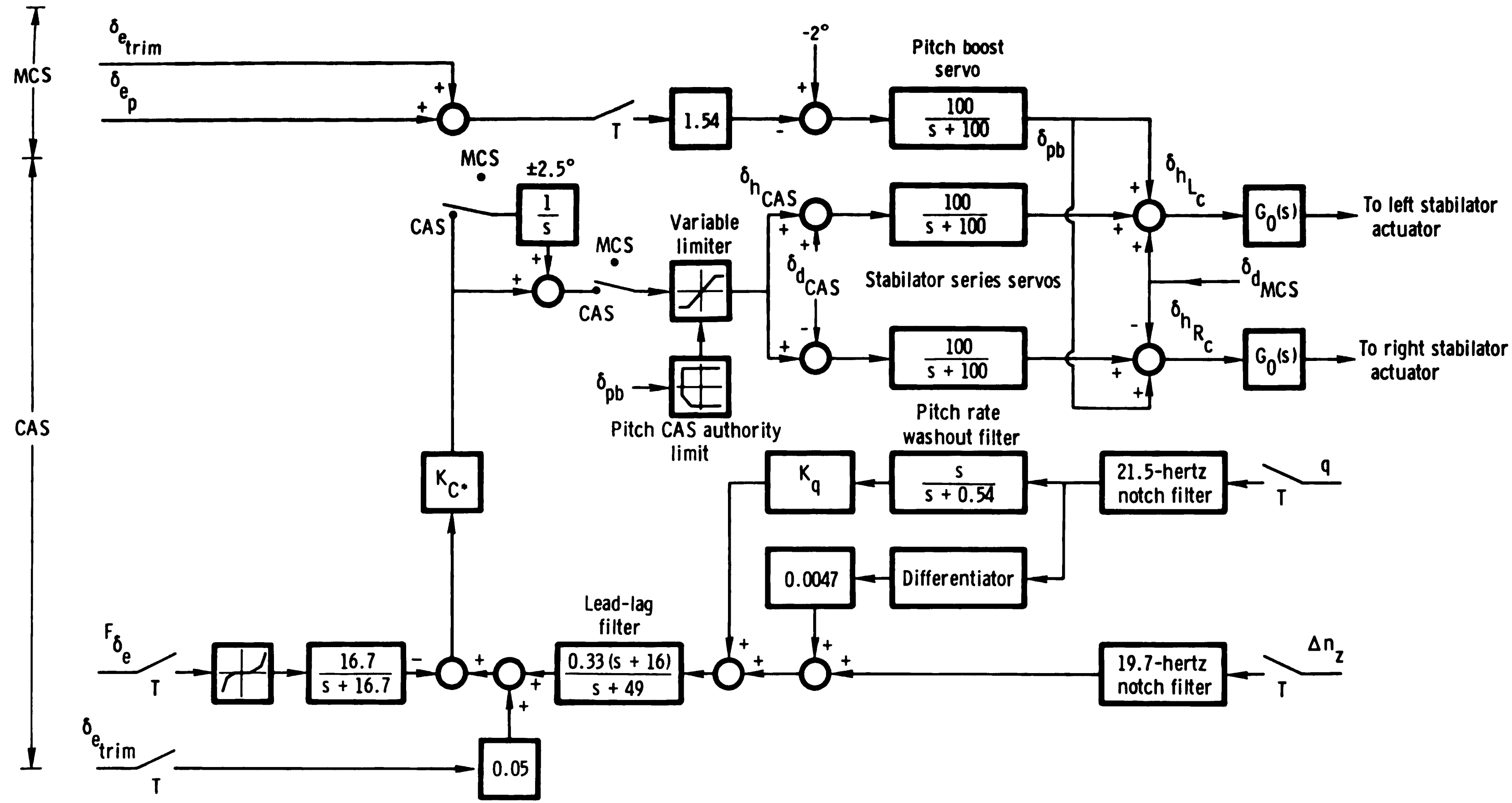

(a) *Pitch axis.*

Figure 11. Block diagram of the scale-model F-15 control system.

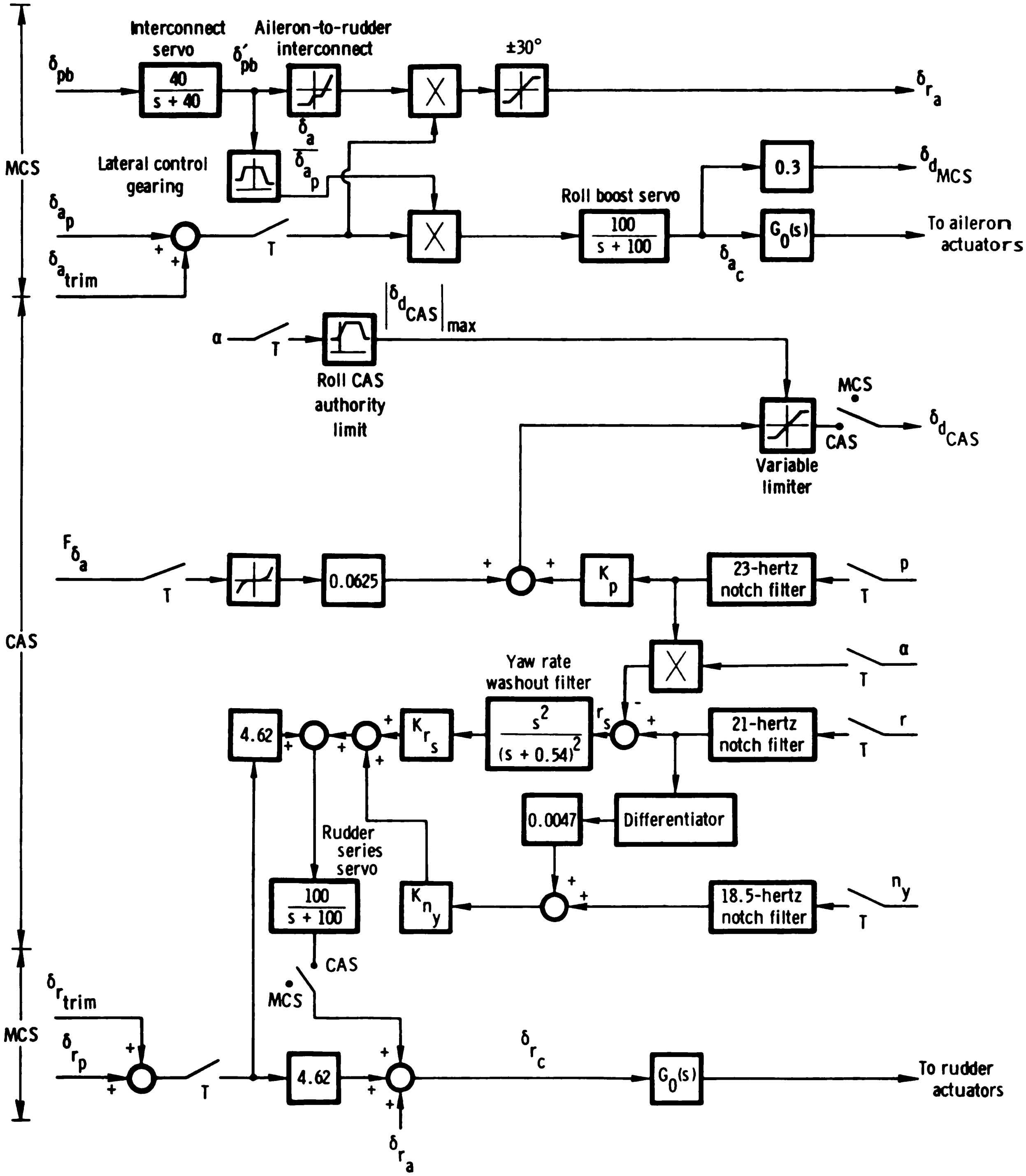

(b) Roll and yaw axes.

Figure 11. Concluded.

TABLE 3.— CHARACTERISTICS OF THE SERVOS AND SHAPING FILTERS FOR THE SCALED F-15 FLIGHT CONTROL SYSTEM

Servos and shaping filters	Transfer function	Position limit, deg	Rate limit, deg/sec
Pitch boost servo	$\frac{100}{s + 100}$	15, -25	±320
Roll boost servo (single surface)	$\frac{100}{s + 100}$	±20	±320
Stabilator series servos	$\frac{100}{s + 100}$	±10	±57
Rudder series servo	$\frac{100}{s + 100}$	±15	±146
Interconnect servo	$\frac{40}{s + 40}$	- - -	±57
Lead-lag filter	$\frac{0.33(s + 16)}{s + 49}$	- - -	- - -
Pitch rate washout filter	$\frac{s}{s + 0.54}$	- - -	- - -
Yaw rate washout filter	$\frac{s^2}{(s + 0.54)^2}$	- - -	- - -
Differentiator	$\frac{s}{1 + 2\frac{0.3s}{37} + \frac{s^2}{37^2}}$	- - -	- - -

Mechanical control system: The MCS mode was a simulation of the primary flight control system of the full-scale F-15 airplane in which the pilot was assisted in pitch and roll control by hydraulic power boost servos. These boost servos were simulated on the ground computer for the scale-model MCS mode. The pitch boost servo output, δ_{pb}, was combined with the roll MCS command, $\delta_{d_{MCS}}$, to form the commands to the left and right stabilizer power actuators, $\delta_{h_{L_c}}$ and $\delta_{h_{R_c}}$. These power actuators were duplicated on board the scale-model F-15 by the model's hydraulic actuators and were not simulated in the ground computer. Similar functions were performed by the aileron and rudder actuators.

The longitudinal stick position controlled the collective stabilators, and the lateral stick position controlled the ailerons and differential stabilators. The rudders were controlled by the rudder pedals and the aileron-to-rudder interconnect. Lateral control authority was scheduled as a function of the lagged pitch boost servo output, δ'_{pb}, and resulted in the authority being restricted at aft and forward longitudinal stick positions (fig. 12). The interconnect was also scheduled as a function of δ'_{pb} (fig. 13) and resulted in rudder commands proportional to lateral stick deflection.

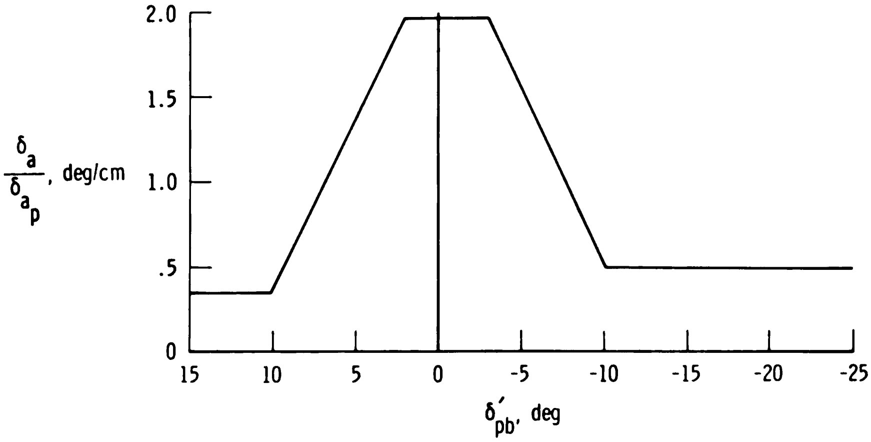

Figure 12. MCS lateral control gearing schedule as a function of lagged pitch boost servo output.

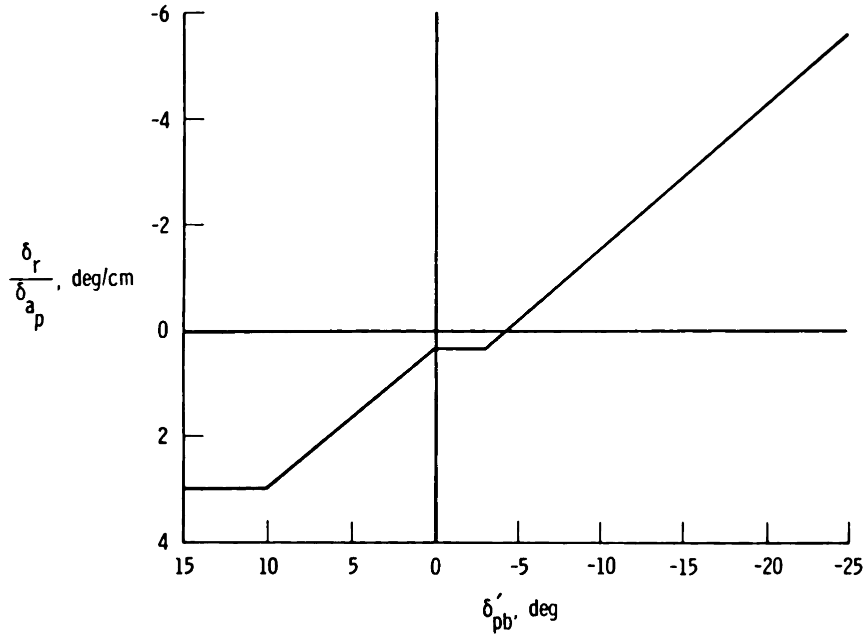

Figure 13. MCS aileron-to-rudder interconnect gearing as a function of lagged pitch boost servo output.

Control augmentation system: The CAS utilized pitch, roll, and yaw rates and normal and lateral accelerations as feedback variables. Each of these five signals was notch filtered to suppress the approximately 20-hertz resonance. The three rate gyro signals used the same notch filters as those for the rate damper mode (described previously).

The pitch CAS command was composed of a modified form of the blended normal acceleration and pitch rate response parameter, commonly referred to as C^* (ref. 6), and commanded normal acceleration derived from longitudinal stick force, F_{δ_e}. The commanded normal acceleration signal was derived by passing the longitudinal stick force, F_{δ_e}, through a dual-gradient gearing schedule and a first-order shaping filter. A stall inhibiter function is also included in the full-scale F-15 CAS to provide nose-down stabilator deflection when angle of attack or washed out pitch rate, or both, exceed a preset level. For the flight tests described in this report, this stall inhibiter function was disabled in the RPRV computer program because the intent of the program was to investigate the stalling and spinning characteristics of the model. The pitch CAS command was passed through a proportional plus integral feed-forward network and limited by the schedule shown in figure 14 to form the pitch CAS command, $\delta_{h_{CAS}}$, which was summed with the roll CAS command, $\delta_{d_{CAS}}$. The combined pitch and roll CAS commands positioned the series servos. The outputs of the servos were then summed with the pitch boost servo output and the MCS differential stabilator signal to form the left and right stabilator commands, $\delta_{h_{L_c}}$ and $\delta_{h_{R_c}}$, which were the uplink commands required for the RPRV system operation.

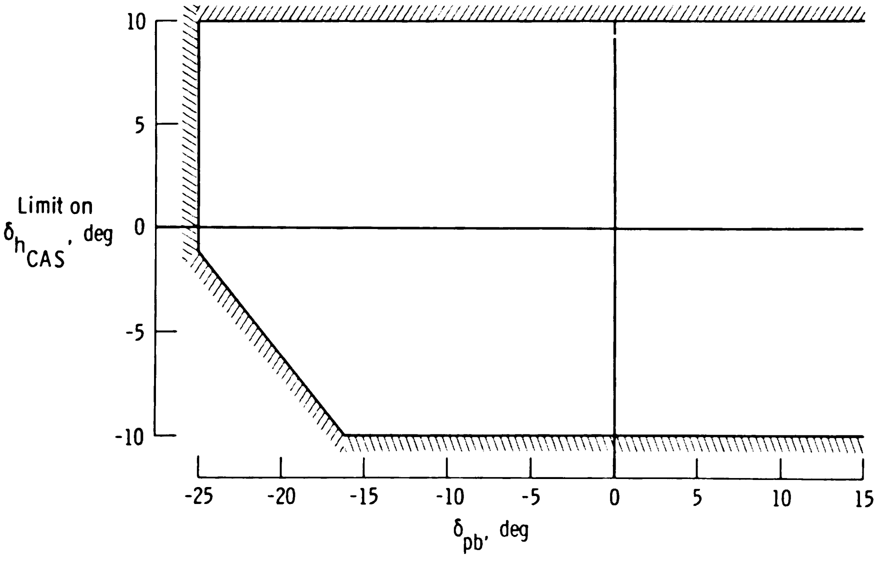

Figure 14. Pitch CAS authority limit as a function of pitch boost servo output.

The roll CAS command to the differential stabilator was formed by comparing roll rate to commanded roll rate from the lateral stick force. The commanded roll rate signal was derived by passing lateral stick force, F_{δ_a}, through a dual-gradient gearing schedule. The resulting roll rate error signal was limited by the roll CAS angle-of-attack schedule shown in figure 15 to form $\delta_{d_{CAS}}$ and summed with the pitch CAS command, $\delta_{h_{CAS}}$.

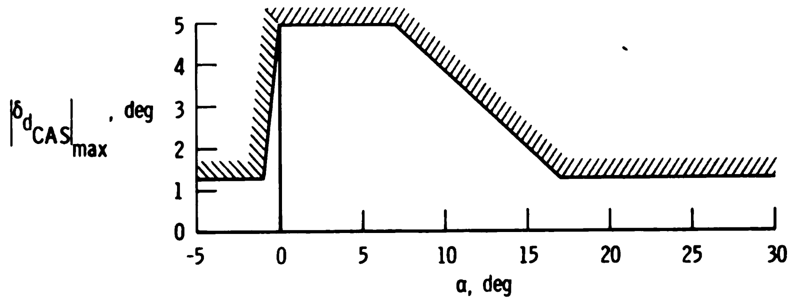

Figure 15. Roll CAS authority limit as a function of angle of attack.

In the yaw axis CAS mode, rudder pedal gearing was effectively doubled over that of the MCS mode. Lateral acceleration and washed out stability axis yaw rate were fed to the rudders. The stability axis yaw rate signal was computed as $r_s = r - \alpha p$.

To account for different accelerometer locations in the full-scale and scale-model F-15 vehicles, pitch rate and yaw rate were differentiated and summed with n_z and n_y, respectively, to simulate lever arm effects.

The full-scale CAS contained an automatic "downmoding" from CAS to MCS for spin departure prevention which was activated when the yaw rate exceeded ±42 deg/sec. For the scale-model F-15 the scaled yaw rate was ±70 deg/sec. The effect of the downmoding was to restrict control authority and deactivate feedback controls, since full control authority or feedback augmentation, or both, could enhance the departure rather than oppose it. This function was easily programed into the RPRV system.

Software Mechanization

The scale-model F-15 computer program occupied 100 percent of the available core of the RPRV program and had a duty cycle of approximately 90 percent of the available computation time. The allocation of the RPRV computer's 16K memory for the subscale F-15 flight program is shown in figure 16. Note that the FORTRAN main program was the largest single unit in the computer, requiring 6500 words.

The core required by the resident operating system and the loader could not be utilized during real-time RPRV operation and may be viewed as the cost of the FORTRAN programing capability. This was not really a disadvantage because the general purpose minicomputer memory could have been expanded if a larger flight program were required. All constants, digital filter coefficients, and combinations of constants required for the RPRV program were precomputed in a separate FORTRAN data program on the RPRV computer and processed in an off-line batch processing mode.

Words	
1,900	Resident operating system
800	Common
1,700	Loader
3,700	Run-time mathematics and utility routines
1,400	Assembly subroutines
6,500	FORTRAN main program
300	Pointers
Total 16,300	

Figure 16. RPRV computer memory map for scale-model F-15 program.

Wherever possible, the computations performed by the RPRV program were in engineering units using floating point arithmetic. This eliminated the requirement of variable scaling and problems with arithmetic overflow. The relatively slow floating point execution time (approximately 75 microseconds) of the RPRV computer did not permit the entire RPRV program to be coded in floating point, so several functions, including the digital notch filters, were coded in scaled fixed point FORTRAN.

Analysis and Design

Two primary objectives of the scale-model F-15 flight program were to obtain stability and control data for the full-scale airplane and to simulate the operation of the F-15 flight control system in the high-angle-of-attack stall-spin region. Both of these objectives required the use of the remote augmentation capability of the RPRV system. As noted previously, to obtain high-quality stability and control data at these high angles of attack, it was necessary to implement a relatively high gain rate damper mode to stabilize the vehicle before the maneuvers were started. Also, the CAS mode had significant effects on the high-angle-of-attack response of the vehicle. Thus it was necessary to make a limited analysis of both augmented modes to insure proper operation of the systems. The analysis discussed in this section is for the 26-percent mean aerodynamic chord center-of-gravity location on the model.

Figure 17 is a z-plane plot of the location of the response modes of the open-loop airplane as a function of trimmed angle of attack. The short-period, Dutch roll, phugoid, roll, and spiral modes are shown. The approximate s-plane coordinates are included for reference. The stability boundary is indicated by the portion of the unit circle. The open-loop natural frequencies of the airplane decrease with increasing angle of attack from $\alpha \approx 3°$ to $\alpha \approx 17°$. Above $\alpha \approx 17°$ the short-period and Dutch roll modes remain very lightly damped with a frequency of approximately 2 radians per second over a large range of angle of attack, whereas the roll and spiral modes continue toward a lateral phugoid mode. Minimum stability for the short-period mode is at $\alpha \approx 26°$ and for the Dutch roll mode at $\alpha \approx 28°$. The phugoid mode is only slightly affected by angle of attack. Obviously, the lightly damped oscillatory modes would respond to pilot inputs or aerodynamic buffet, so a damper system was required to augment the damping of the vehicle.

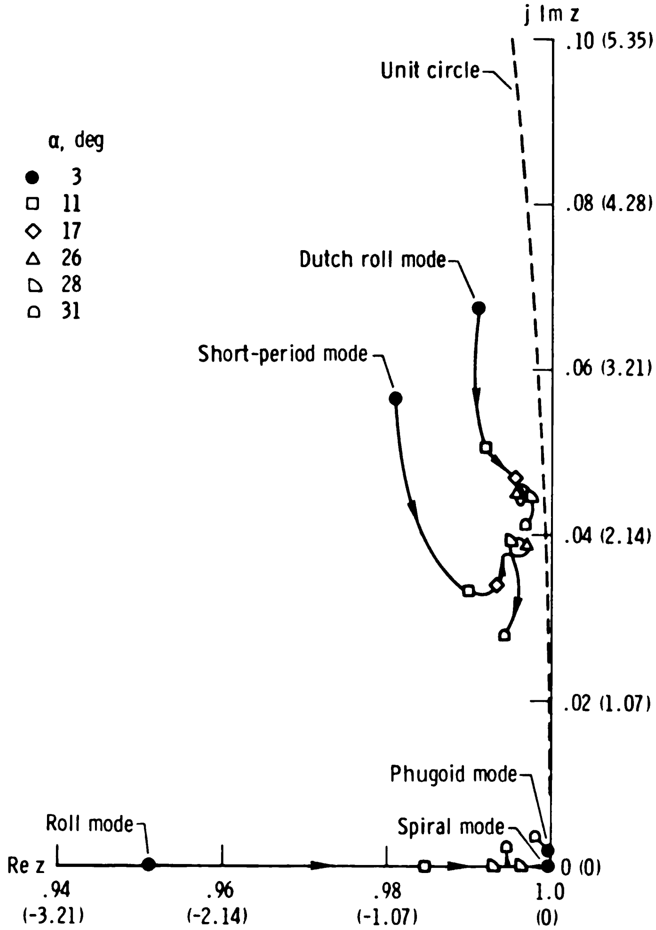

Figure 17. Root locus (z-plane) of response modes of scale-model F-15 as a function of trimmed angle of attack. (Approximate s-plane coordinates given in parentheses.)

Rate damper system.— The short-period mode was easily damped by using a pitch rate feedback to the stabilators. Figure 18 shows the z-plane root locus of this feedback for $\alpha = 3°$ and $\alpha = 26°$. The actuator dynamics and filters shown in figure 9(a) were included. A maximum gain of 0.4 second was chosen. The pilot was able to select lower gains by using the pitch gain switch on the mode control panel.

Damping the Dutch roll mode proved to be difficult because the yaw rate damper was ineffective at angles of attack above 15°. Figure 19 shows the z-plane root locus of yaw rate feedback to the rudders for $\alpha = 3°$ and $\alpha = 28°$. The actuator dynamics and filters shown in figure 9(b) were included. The complex zero of the $\frac{r}{\delta_r}(z)$ transfer function effectively cancels the Dutch roll pole at high angles of attack. In addition, the rudder control power drops rapidly at these angles of attack.

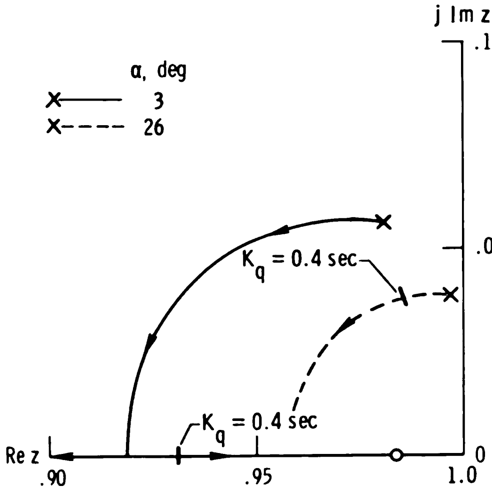

Figure 18. Root locus (z-plane) of pitch rate damper short-period mode for α = 3° and 26°.

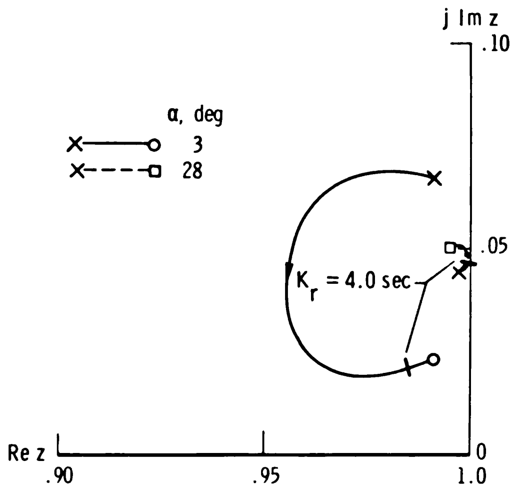

Figure 19. Root locus (z-plane) of yaw rate damper Dutch roll mode for α = 3° and 28°.

Although the yaw damper proved ineffective in damping the Dutch roll mode at high angles of attack, the roll damper was very effective. Figure 20 shows the z-plane root locus of roll rate feedback to the stabilators for $\alpha = 3°$ and $\alpha = 28°$. Actuator dynamics and filters were included. Although the roll damper has little effect on the Dutch roll pole below $\alpha \approx 15°$, it is very effective at higher angles of attack. A maximum gain of 0.8 second was selected, which is considerably higher than the scaled roll CAS gain of -0.077 second.

Although the high roll damper gain stabilized the Dutch roll mode, it aggravated the coupled roll-spiral mode (lateral phugoid) at $\alpha \approx 30°$ and caused a low-frequency heading stability problem. The yaw damper was beneficial

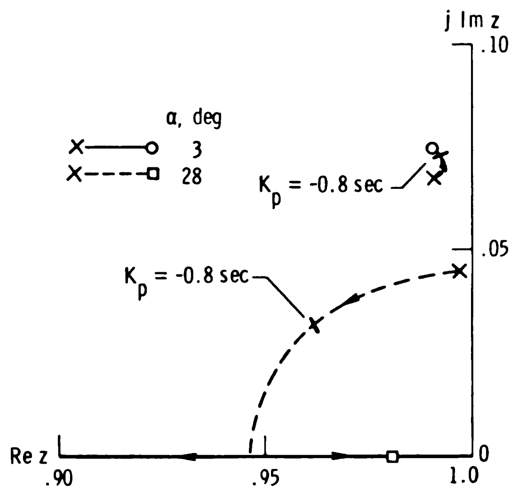

Figure 20. Root locus (z-plane) of roll rate damper Dutch roll mode for α = 3° and 28°.

in damping this lateral phugoid, as shown in figure 21. The figure shows the z-plane root locus of the lateral phugoid at $\alpha = 28°$ due to roll rate feedback to the stabilators, followed by the root locus of yaw rate feedback to the rudder. The maximum yaw rate gain of 4.0 seconds was selected to position the lateral phugoid roots.

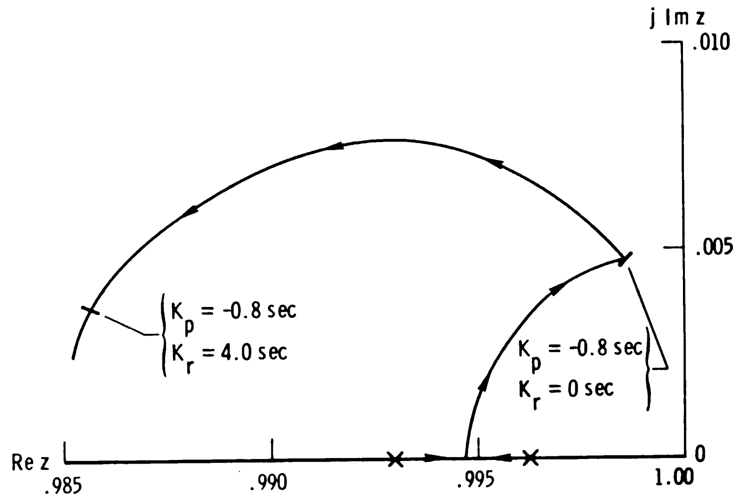

Figure 21. Root locus (z-plane) of lateral phugoid mode for roll rate feedback to stabilators followed by yaw rate feedback to rudder at $\alpha = 28°$.

The high maximum roll and yaw gains chosen for the rate damper mode reflected the relative uncertainty concerning the model's lateral-directional aerodynamics when trimmed at full aft longitudinal stick. The pilot was able to select lower roll and yaw damper gains through the gain switches on the mode control panel.

Control augmentation system.— The CAS mode introduced feedback variables into the remote augmentation system in addition to those required for the rate damper mode. Normal and lateral acceleration feedbacks and angle-of-attack scheduling of roll rate feedback were required, as shown in figure 11. The effectiveness of the rate feedbacks in the CAS mode in damping vehicle motions was similar to that for the rate damper mode. The crossfeed of roll rate to the rudder in the stability axis yaw rate feedback was a key difference between the rate damper mode and the CAS mode, aside from the higher gains used in the rate damper mode. The z-plane root locus of the Dutch roll mode for the stability axis yaw rate feedback to δ_r is shown in figure 22 for $\alpha = 3°$ and $28°$. The filters and actuator dynamics shown in figure 11 were included, and the yaw CAS gain ($K_{r_s} = 0.613$ sec) is indicated on the locus. The damping of the Dutch roll mode is increased at both angles of attack by the stability axis yaw rate feedback.

In addition to the rate feedbacks, the CAS uses normal and lateral acceleration feedbacks to provide good handling qualities. No difficulty was foreseen in using these signals for rigid body control; however, the use of acceleration feedbacks may have caused structural resonance problems. (The implementation of notch filters to suppress structural resonance was described previously.)

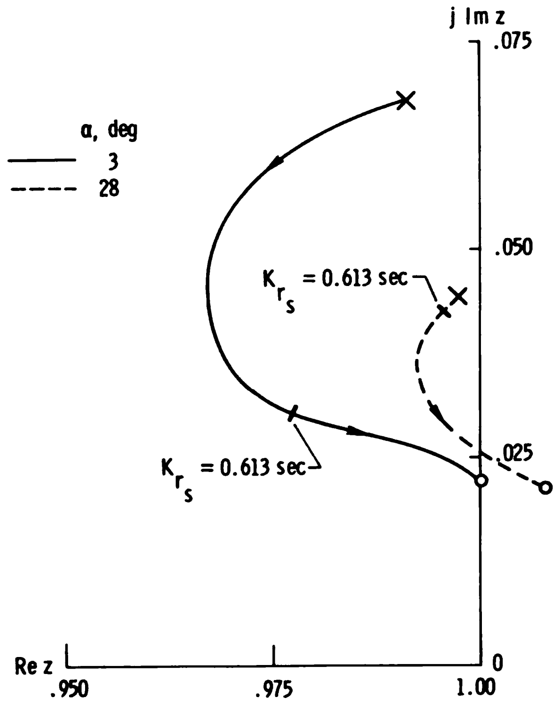

Figure 22. Root locus (z-plane) of stability axis yaw rate feedback to rudder for α = 3° and 28°.

A primary objective of the scale-model F-15 program was to achieve a valid simulation of the F-15 analog flight control systems. No attempt was made to investigate modifications to the CAS mode. The ability of the remote augmentation system to simulate the analog CAS of the full-scale F-15 airplane is indicated in figure 23, which compares step responses of the pitch CAS for the RPRV digital simulation and the analog CAS simulation. No attempt was made to adjust the gains or constants of the RPRV digital simulation to achieve a better "match" with the analog CAS simulation.

Ground Testing and Checkout

Before flight the RPRV program software was extensively checked and tested to insure that computation time was not excessive and that the gearing schedules and gain schedules operated correctly.

To identify resonance problems, a ground vibration test was made on the vehicle. Symmetric vibration modes were mapped with frequencies of 15.4 hertz, 16.2 hertz, 18.2 hertz, 21.0 hertz, 39.0 hertz, and 51.0 hertz. The 21.0-hertz mode had a noticeable horizontal-stabilator motion which was sensed by the pitch rate gyro and normal accelerometer. The 18.2-hertz mode was also prominent. The strong

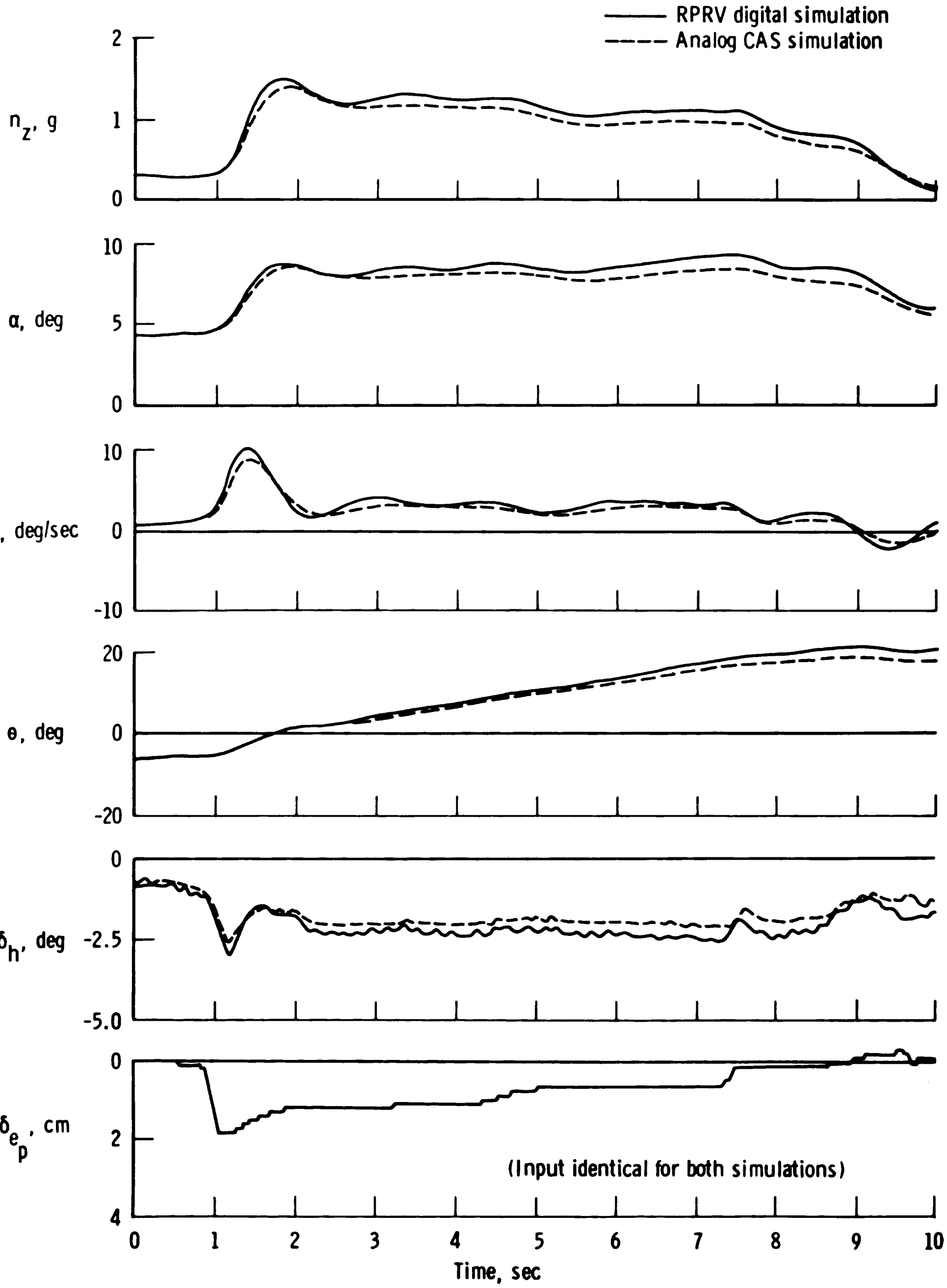

Figure 23. Comparison of scale-model F-15 pitch CAS response to pilot input for RPRV digital simulation and analog CAS simulation.

coupling between stabilator motion and sensor pickup of the modes near 20 hertz indicated a possible problem in the augmented modes.

Before the flights in which the rate damper and CAS modes were used, structural resonance tests were made on the closed-loop system to determine stability margins. The test feedback gains were several times larger than those to be used in flight. The RPRV flight program was coded to branch around the notch and low-pass filters in the feedback loops if a sense switch was set. Thus the effect of the filters on the system stability could be assessed. The only structural resonance observed in the tests was a symmetrical mode which was driven unstable by pitch rate feedback to the stabilators at a frequency of approximately 20 hertz. For the pitch rate damper mode with no notch or low-pass filtering, the instability occurred at a gain of 1.0 second. When the notch filter was added, the 20-hertz instability was no longer seen, but a 10-hertz neutrally damped oscillation occurred at a slightly higher gain. No structural mode had been identified at this frequency, and the oscillation was traced to a mass unbalance of the stabilators which caused a "tail-wags-dog" oscillation. In the fabrication of the model, primary importance had been placed on weight and strength constraints, rather than on duplicating mass and inertia effects. One result was a mass imbalance in the stabilators in which the center-of-gravity-location was 4.4 centimeters rearward of the hinge line.

When the low-pass filters were added to the rate damper mode, the 10-hertz oscillation did not occur until a gain of 3.0 seconds was used. This was 7.5 times the maximum gain selected for flight (table 2). A similar resonance was observed in testing the pitch CAS mode. The pitch rate CAS feedback excited a structural instability at approximately 20 hertz at a gain of 4.0 deg/g with no notch filtering on pitch rate or normal acceleration. When the notch filters were added, the 10-hertz oscillation was again observed at a gain of 4.0 deg/g. This gain is four times the pitch CAS gain (table 2).

No structural resonances were observed for the roll and yaw rate damper and CAS modes, although the roll rate damper mode did excite the tail-wags-dog oscillation at a gain of 4.0 seconds with the notch and low-pass filters. Again, this was five times the roll CAS gain (table 2). Thus the ground resonance checks established stability margins for all axes of the rate damper and CAS modes. A minimum stability margin of 12 decibels was verified for the pitch, roll, and yaw axes of the two augmented modes.

FLIGHT-TEST RESULTS

Before the scale-model F-15 was air launched, two captive flights were made to check the operation of the telemetry links, onboard systems, and RPRV facility. Data from the first nine drop flights are presented in this section. Additional data from the first four flights are presented in reference 3.

The flight program was scheduled so that the modes and components of the RPRV/RAV system could be activated gradually. Thus the remotely augmented rate damper and CAS modes were not activated until the open-loop operation of the system had been demonstrated. The early flights were devoted largely to obtaining basic stability and control data to verify the wind-tunnel data used in the simulation. These manuevers were performed using the computer direct and rate damper modes. After these stability and control flights were made, the model was flown in the MCS and CAS modes, and aggravated inputs were applied to investigate its stall, departure, and spin characteristics.

Basic Modes

The computer direct and rate damper modes were designed to permit the pilot to perform stability and control maneuvers efficiently. In the nine flights of the model (40 minutes of flight time), approximately 100 stability and control maneuvers have been performed using these control modes.

The unaugmented modes were used on the first flight of the model, and data were obtained from $\alpha = 5°$ to $26°$. Simulation studies had indicated very light damping of the Dutch roll and short-period modes, so use of the rate damper mode was planned for subsequent flights. Power spectra were obtained from the first flight for roll, pitch, and yaw rates and normal and lateral accelerations at several angles of attack. All the variables showed a strong resonance at approximately 20 hertz; the intensity of the resonance was a function of angle of attack. At $\alpha < 10°$ all the signals were clean, with the accelerations indicating a broad low-amplitude resonance of approximately 50 hertz. Above $\alpha = 10°$ the energy at approximately 20 hertz increased with angle of attack on all signals until an angle of attack of 20° was reached, after which it remained constant. The resonance may have been caused by buffet characterized by locally separated flow on the wing at high angles of attack which excited the approximately 20-hertz structural modes.

Before using the rate damper or CAS modes, it was necessary to consider the possibility of closed-loop structural resonance. The versatility of the RPRV computer permitted a simple solution to this problem: the implementation of digital notch filters in the control law computation.

The power spectra from the first flight were used to select frequencies for notch filters on roll, pitch, and yaw rates and normal and lateral accelerations. Five notch filters were added to the program between the first two drop flights. In addition, 6-hertz low-pass filters were applied to the roll, pitch, and yaw rates for the rate damper mode to aid in the attenuation of high-frequency structural resonances. The filter used to simulate the F-15 series servos performed a similar high-frequency attenuation in the CAS mode.

The rate damper mode was activated on the third flight and operated as expected. The operation of the pitch and the roll and yaw dampers is shown in figure 24. Figure 24(a) shows the open-loop pitch response to a stabilator doublet followed by the operation of the pitch damper after several oscillations. The pitch damper was effective in damping the short-period mode of the vehicle, as had been predicted. Figure 24(b) shows the operation of the roll and yaw rate dampers at angles of attack of 28° to 31°. Three successive open-loop manuevers are shown with the damper system operating between maneuvers. During the maneuvers, the model is excited by aileron, rudder, and differential stabilator doublets. The doublets are indicated

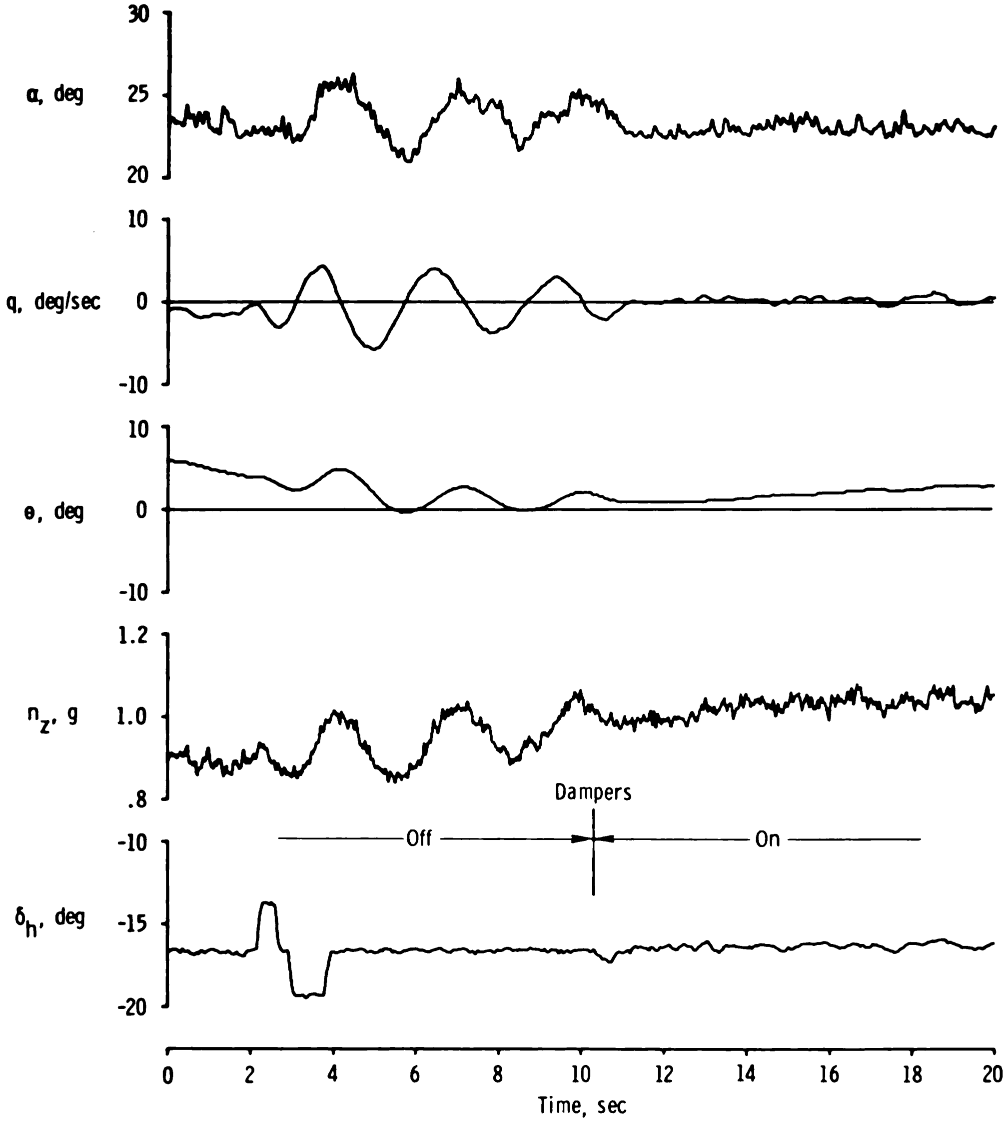

(a) Pitch rate damper, K_q = 0.4 sec.

Figure 24. Operation of rate damper system.

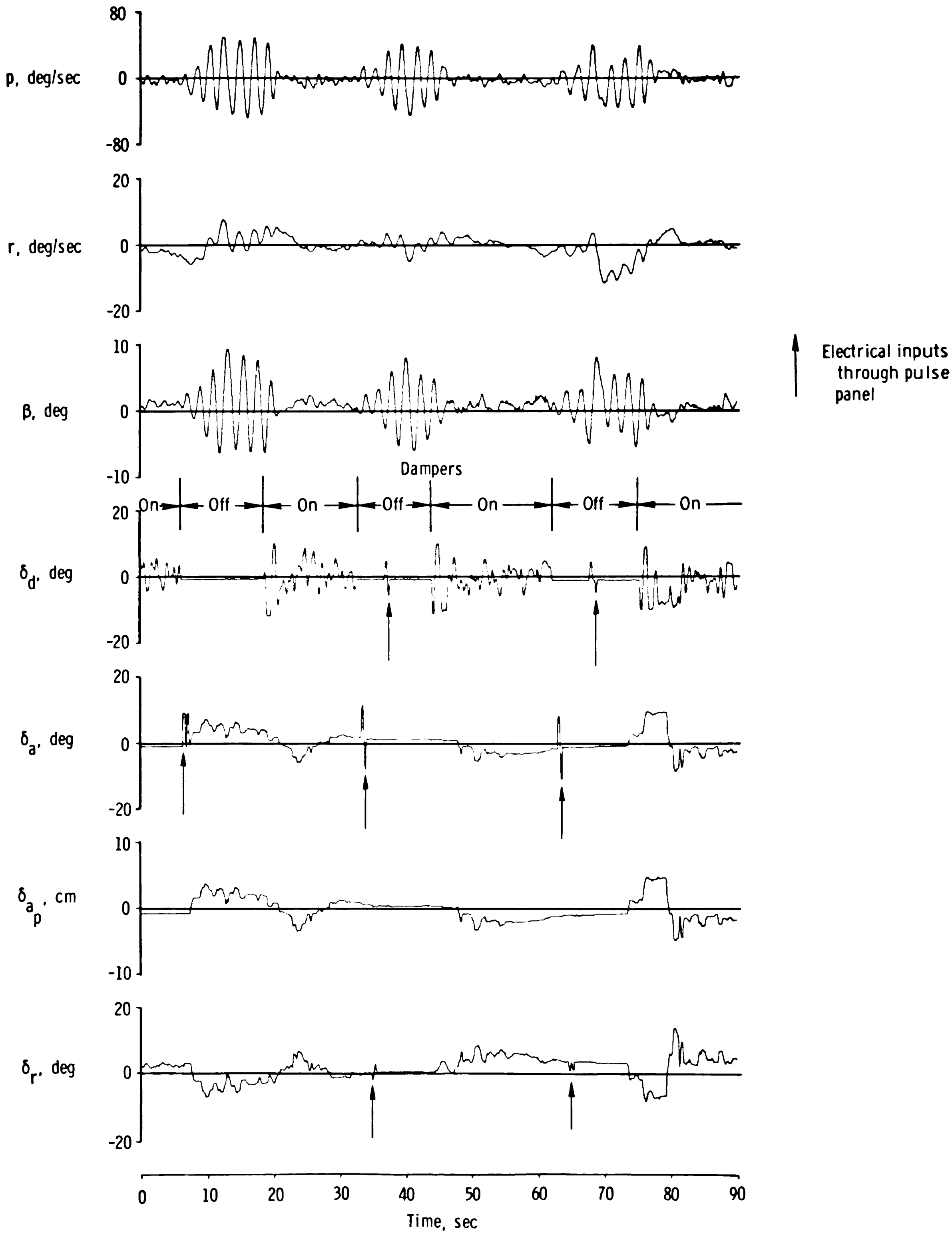

(b) Roll and yaw rate dampers, α = 28° to 31°, K_p = -0.8 sec, K_r = 1.0 sec.

Figure 24. Concluded.

by arrows on the δ_d, δ_a, and δ_r traces and were commanded electrically through the pulse panel. The pilot did not use the rudder pedals; all rudder motion is due to the aileron-to-rudder interconnect, the yaw damper, and the pulse panel inputs. The figure shows that the open-loop airplane's Dutch roll mode at this angle of attack was unstable for small oscillations in p, r, and β and that the dampers were effective in damping the oscillations.

The RPRV computer program was modified and recompiled between each flight. Most of the changes were associated with the computer direct and rate damper modes and were implemented to help the pilot obtain high-quality stability and control data. Stability and control derivatives have been identified over a range of angle of attack from -20° to 40°. Changes were made in the damper gain, control authority (for example, lateral stick gearing), and pulse panel software. Also, the aileron-to-rudder interconnect was incorporated to aid in turn coordination. To obtain the negative-angle-of-attack data, the model was flown inverted for prolonged periods and trimmed with forward stick inputs. No difficulty was experienced with the telemetry links in these maneuvers.

In preparation for the CAS flight tests, several maneuvers were performed in the basic modes at stick deflections equal to the maximum stabilator authority in CAS. For example, on the fourth flight the model was trimmed at $\alpha = 31°$ and flown in the computer direct mode with full aft stick ($\delta_h = -27.5°$), which is the maximum stabilator authority of the full-scale F-15 CAS mode. On the seventh flight, with the center of gravity at 30-percent mean aerodynamic chord, the model was trimmed at $\alpha = 40°$ with full aft stick.

F-15 Control System Modes

The MCS and CAS modes were fully exercised during the nine flights of the model. The MCS mode was used on every flight. The first five flights were flown with the center of gravity at the 26-percent mean aerodynamic chord location, and the following four flights at the 30-percent mean aerodynamic chord location. On the second flight the model was flown for several minutes in the MCS mode with full aft longitudinal stick ($\delta_h = 23°$) and trimmed at $\alpha = 28°$.

The CAS mode was used for the first time on the fifth flight and operated as expected. No problems were encountered in the use of acceleration feedbacks in the pitch and yaw axes. Figure 25 shows the model's pitch CAS response to pilot input during flight and in the RPRV digital simulation. The closed-loop bandwidth of the pitch CAS is approximately 4 radians per second. The pilot's input was the same as that in figure 23. Figure 25 shows good correlation between the flight and simulation responses.

Complete verification that the model F-15 under control of the digital RAV system in flight provides a valid scaled simulation of the full-scale F-15 airplane with onboard analog control system would entail a number of steps and require flight data from the full-scale F-15 airplane. Full-scale F-15 flight data were not available;

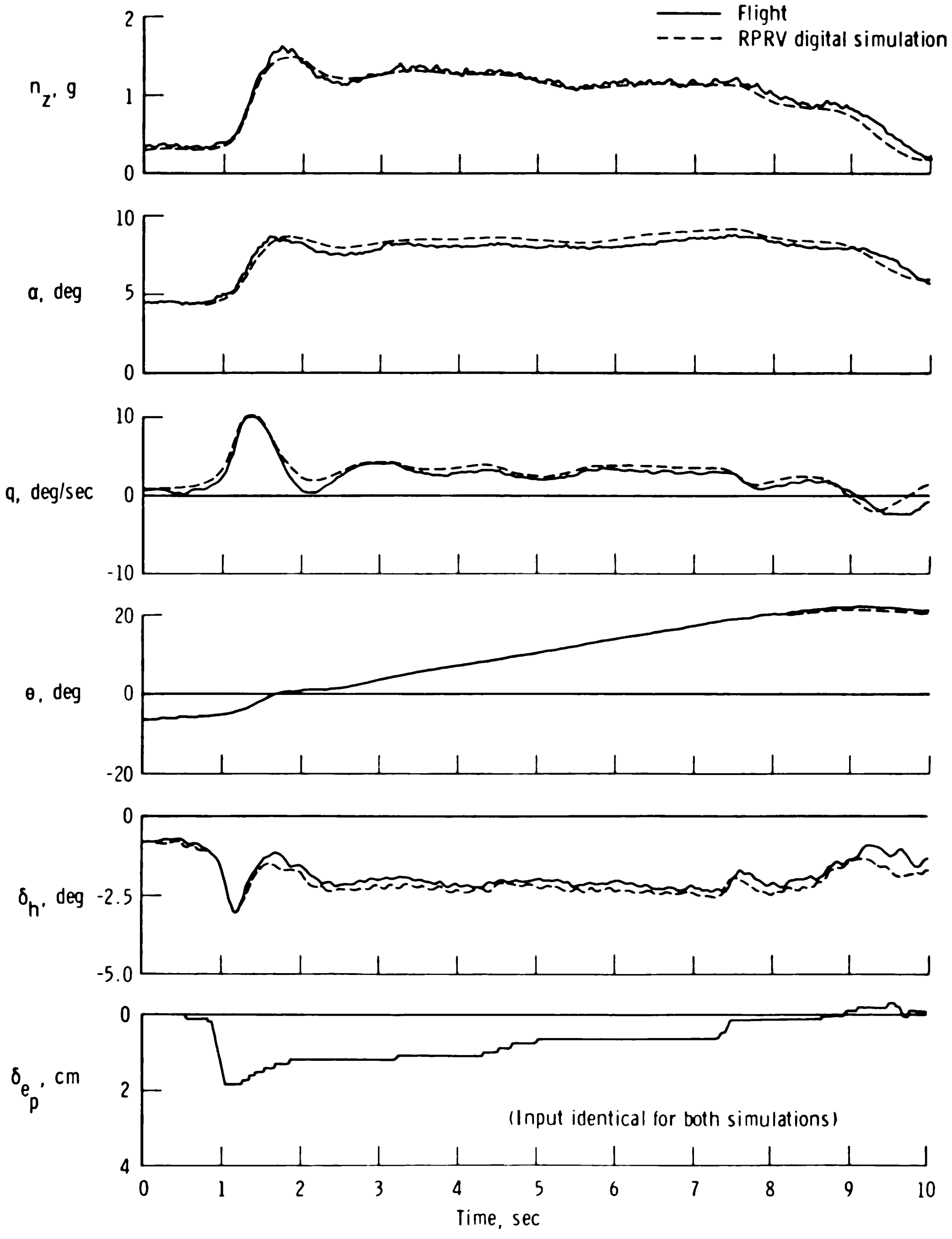

Figure 25. Comparison of pitch CAS response to pilot input during flight and in RPRV digital simulation.

however, most of the key steps were taken to verify the technique. The RPRV digital simulation was validated as an accurate simulation of the closed-loop model F-15 in flight (fig. 25) and then compared with the analog CAS simulation (fig. 23). Since both figures show close agreement in vehicle motion response for identical inputs and initial conditions, the assumption that the digital RAV system in control of the model F-15 in flight would provide a valid simulation of an onboard analog system in control of the same model can be made with confidence.

High-angle-of-attack stall and spin departure studies were started on the third flight, utilizing the MCS mode. Aggravated inputs (full aft and full lateral stick) were applied in this mode on the third and fourth flights, but no control problems were experienced. On the fifth flight, using the additional control surface authority provided by the CAS mode, attempts to spin the model were again unsuccessful. A spin was finally achieved on the seventh flight by using a spin entry control scheme developed on the simulation. The model recovered easily when spin recovery controls were applied. Two more spins were performed on the following flight, and again no difficulty was experienced in recovering. As noted previously, the stall inhibiter function of the full-scale F-15 CAS was not implemented in the RPRV computer program for these tests. The spin entries were started with the computer in the CAS mode, and the computer automatically downmoded to the MCS on each spin entry when the yaw rate exceeded 70 degrees per second.

The results of this series of flights, which involved high-risk flight testing and the use of the remote augmentation system to perform the control function, demonstrate the usefulness of the RPRV system. An approach this aggressive would not usually be attempted in a manned program.

RPRV FACILITY OPERATIONAL EXPERIENCE

The operation of the RPRV system during the first nine flights of the scale-model F-15 showed that the RPRV approach to flight testing is a promising method for advanced systems testing and hazardous flight testing. The remote augmentation system, which utilizes a ground-based computer, did not experience a failure during flight; however, problems did occur with the telemetry downlink and uplink.

On the second flight, the ground station receiver was slightly out of adjustment, which made the remote pilot's displays unusable because of downlink dropout. This adjustment was carefully monitored during the following flights, and the problem did not recur. No other downlink dropout was experienced during the test time on any of the other flights.

The uplink command system functioned perfectly during the first five flights; however, a problem which occurred during attempts to make the sixth flight resulted in two aborted flights. On both of the aborted flights and on the sixth flight, the uplink signal strength dropped below a preset threshold. Proper action was taken by the system in each instance: On the aborted flights a low signal level was indicated, and on the sixth flight the onboard autopilot system was activated. The difficulty was traced to a series of unrelated alinement and calibration problems. The most important of these was faulty boresighting of the uplink system ground antenna. Modifications were made to the onboard receiver to permit the signal strength level to be monitored through the telemetry downlink. After the system was properly alined and calibrated, three additional flights were made without incident.

The RPRV system operation has also provided information about the capability of a remote pilot to control a vehicle during unrestricted maneuvering. The F-15 model was flown through an extensive range of attitudes, including 360° rolls and 90° nose-down attitudes. High oscillatory rates of 200 deg/sec in roll, 100 deg/sec in pitch, and 200 deg/sec in yaw were sustained, and the model experienced elevated acceleration maneuvers up to its structural design limit (4g). As noted, the model was flown in an inverted attitude for prolonged periods to obtain data at negative angles of attack, and aggravated full authority control inputs in both the MCS and CAS modes were made in attempts to force the model into departures and spins.

The interaction between the remote pilot and the RPRV systems proved to be of great benefit in accomplishing the research objectives of the program. By utilizing the flight planning simulator and the control of the RPRV computer software afforded by the mode control panel and the pulse panel, the pilot was able to perform many high-quality stability and control maneuvers. The FORTRAN programing capability made it possible for suggestions by the pilot or required additions to the software to be implemented quickly and made available for the next flight. For example, it was necessary to add five notch filters and three low-pass filters in the rate damper mode to the computer program between the first and second flights. This was accomplished easily within the planned $1\frac{1}{2}$ weeks between the flights. Also, it was necessary to modify the scale-model F-15 modes in order to duplicate modifications made in the full-scale F-15 flight control system during its initial flight testing. These modifications were made easily in the RPRV computer software.

The RPRV system operation was enhanced by the use of floating point FORTRAN coding to write the RPRV computer programs. This capability was in keeping with the overall philosophy of low-cost subscale testing, in that the control system engineer was able to write the flight control system software directly. He thus had direct control of the software and could use the FORTRAN compiler to check out and debug the program. The ability to run the identical program card deck in the RPRV digital simulation was a further check on the software.

CONCLUDING REMARKS

The remote augmentation capability of the remotely piloted research vehicle (RPRV) facility at the NASA Flight Research Center was used in flight tests of a 3/8-scale model of the F-15 airplane. It was found that coupling the remote piloting task with the remote augmentation technique in a ground-based digital computer made it possible to achieve the research objectives of the subscale F-15 program. The use of FORTRAN programing made it easy to write and modify the program containing the control laws.

The validity of the remote augmentation concept of implementing closed-loop feedback control of a remotely piloted research vehicle in a ground-based digital computer was demonstrated. Rate damper and control augmentation systems were successfully implemented for the scale model.

The integrity of the RPRV facility's uplink and downlink telemetry systems was demonstrated for the control and remote augmentation of unmanned models. The telemetry links operated for extended periods and over an extensive range of vehicle attitudes without transmission difficulties.

The remote augmentation technique of simulating an analog flight control system was successful. The RPRV system accurately simulated the F-15 analog control augmentation system.

Flight Research Center
National Aeronautics and Space Administration
Edwards, Calif., January 6, 1975

APPENDIX A

MODEL SCALING TECHNIQUES

Scale-model flight testing requires an understanding of the scaling laws that relate the dynamic behavior of the scale model to that of the full-scale aircraft. It is important to realize that exact similitude between the model and the full-scale airplane cannot be achieved, and that a choice must be made between several available scaling techniques. Also, in designing remote augmentation systems for use with scale models, it is necessary to compensate for scaling effects in the closed-loop control laws by modifying feedback gains.

Figure A1 shows the forces, moments, and geometry relevant to the dynamic response of a model and a full-scale airplane. The functional dependencies of the forces and moments are indicated in the figure. Table A1 lists the scaling relationships which would have to be satisfied for exact similitude. Relation 1 is a statement of the model scale factor, and relation 2 is a statement of the requirement of matching helix angles so that the vehicles follow geometrically similar flightpaths. There are eight relations between the seven variables: model scale factor, a, frequency, ω, velocity, V, Mach number, M, mass, m, moment of inertia, I, and atmospheric density, ρ. Thus, in general, at least one of the relations will not be satisfied. The relations chosen to be matched are determined by the purpose of the scale-model test.

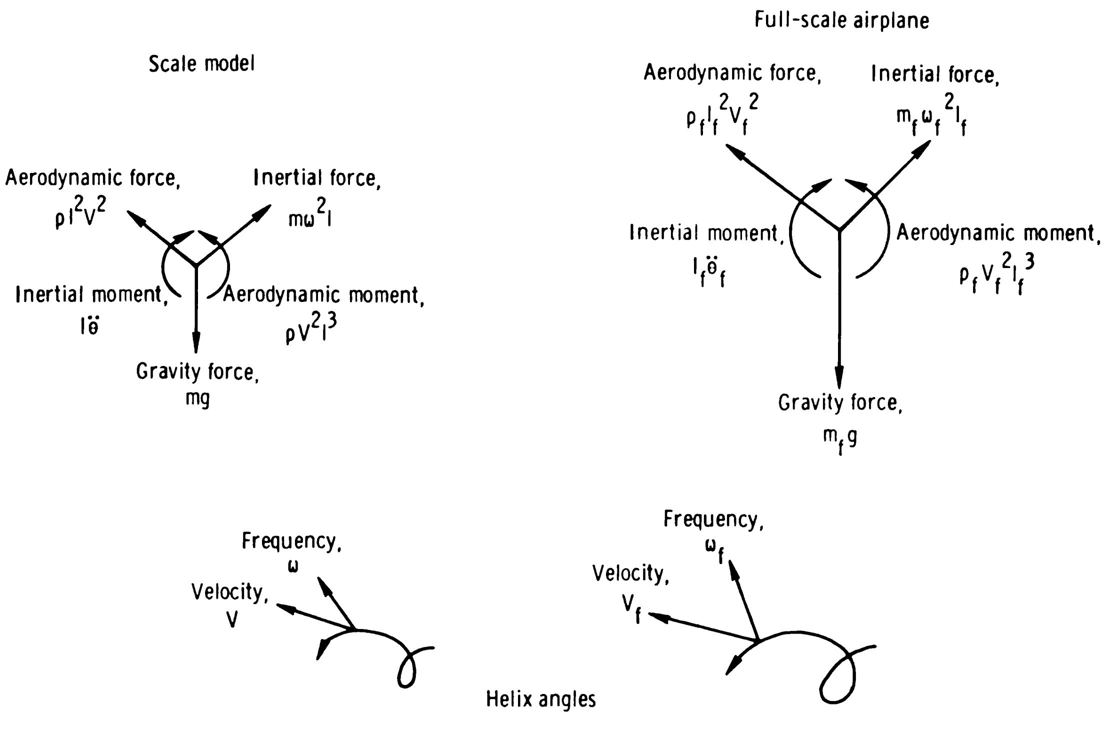

Figure A1. Force, moment, and helix diagrams of scale model and full-scale airplane.

TABLE A1.— SCALING RELATIONSHIPS IN MODEL TESTING

Relation	Quantity
1 $l = al_f$	Length
2 $\frac{\omega l}{V} = \frac{\omega_f l_f}{V_f}$	Helix angle
3 $\frac{V}{V_c} = \frac{V_f}{V_{c_f}}$	Mach number $\left(M = \frac{V}{V_c}\right)$
4 $\frac{Vl}{\nu} = \frac{V_f l_f}{\nu_f}$	Reynolds number
5 $\frac{I\ddot{\theta}}{\rho l^3 V^2} = \frac{I_f \ddot{\theta}_f}{\rho_f l_f^3 V_f^2}$	Ratio of inertial moments to aerodynamic moments
6 $\frac{m\omega^2 l}{\rho l^2 V^2} = \frac{m_f \omega_f^2 l_f}{\rho_f l_f^2 V_f^2}$	Ratio of inertial forces to aerodynamic forces
7 $\frac{m}{m\omega^2 l} = \frac{m_f}{m_f \omega_f^2 l_f}$	Ratio of gravitational forces to inertial forces
8 $\frac{m}{\rho l^2 V^2} = \frac{m_f}{\rho_f l_f^2 V_f^2}$	Ratio of gravitational forces to aerodynamic forces

For wind-tunnel testing, the length, Reynolds number, and Mach number relations are usually matched (refs. 7 and 8). For free-flight model testing, scaling relationships must be chosen on the basis of the dynamic pressure region being investigated. If compressibility effects are being investigated, the Mach number is matched (ref. 9). For dynamic testing at low dynamic pressures, the Froude number (ratio of inertial forces to gravitational forces) is held invariant (ref. 10). This inertia-gravity scaling technique was used for the scale-model F-15.

Requiring that the ratio of inertial forces to gravitational forces be held invariant while at the same time matching helix angles places a constraint upon the model velocity (relations 2 and 7, table A1). This constraint may be stated in the form of a scaling law, $V = a^{\frac{1}{2}} V_f$. The remaining relations between forces and moments (relations 5, 6, and 8) are matched by properly scaling the model's mass and inertias. Table A2 lists the complete set of scaling laws for an invariant inertia-gravity relationship. Note that mass and inertia scaling is a function of the ratio of atmospheric pressures, ρ/ρ_f. Proper selection of model altitude provides some independent control over these scaling ratios.

TABLE A2.— SCALING LAWS FOR INVARIANT INERTIA-GRAVITY RELATIONSHIP

Quantity	Scale factor
Model scale	a
Density	$\frac{\rho}{\rho_f}$
Mass	$a^3 \frac{\rho}{\rho_f}$
Inertia	$a^5 \frac{\rho}{\rho_f}$
Mach number	$a^{\frac{1}{2}} \frac{V_c}{V_{c_f}}$
Velocity	$a^{\frac{1}{2}}$
Linear acceleration	1
Angles	1
Angular velocity	$a^{-\frac{1}{2}}$
Angular acceleration	a^{-1}
Time	$a^{\frac{1}{2}}$
Reynolds number	$a^{\frac{3}{2}} \frac{\nu}{\nu_f}$

The scaling indicated in table A2 is particularly important in interpreting a scale model's dynamic response and the effect of scaling on closed-loop model operation. Using two-degree-of-freedom longitudinal equations of motion, reference 11 derives the short-period natural frequency and damping as

$$\omega_{sp} = \sqrt{M_q Z_\alpha - M_\alpha} \tag{A1}$$

$$\zeta_{sp} = \frac{-(Z_\alpha + M_q)}{2\omega_{sp}} \tag{A2}$$

Because the model is scaled to be geometrically similar to the full-scale airplane, the nondimensional stability derivatives of the two vehicles will be the same. Dimensionalizing the derivatives (as shown in ref. 11) at the same altitude and using the inertia-gravity scaling laws of table A2 gives the following relationship between model and full-scale dimensionalized derivatives:

$$Z_\alpha = a^{-\frac{1}{2}} Z_{\alpha_f}$$

$$Z_{\delta_e} = a^{-\frac{1}{2}} Z_{\delta_{e_f}}$$

$$M_\alpha = a^{-1} M_{\alpha_f}$$

$$M_q = a^{-\frac{1}{2}} M_{q_f}$$

$$M_{\delta_e} = a^{-1} M_{\delta_{e_f}}$$

Substitution in equations (A1) and (A2) gives

$$\omega_{sp} = a^{-\frac{1}{2}} \omega_{sp_f} \tag{A3}$$

$$\zeta_{sp} = \zeta_{sp_f} \tag{A4}$$

Thus the frequencies of the response modes of the model are increased by $a^{-\frac{1}{2}}$ over those of the full-scale vehicle, whereas the damping ratios are unchanged. This reflects the time scaling indicated in table A2.

For closed-loop control of scale models the airplane response is modified; however, it is necessary that the scaling relations of equations (A3) and (A4) hold for the closed-loop vehicle as well. To investigate the effect of scaling on the control system, the following general feedback control law is postulated:

$$\delta_h = K_\theta \theta + K_\alpha \alpha + K_q q + K_{n_z} n_z$$

When this general control law is substituted into the two-degree-of-freedom short-period mode approximation equations of reference 12 and the scaling laws of table A2 are applied, the closed-loop frequency and damping of the model will obey equations (A3) and (A4) if only the pitch rate feedback gain is scaled as

$$K_q = a^{\frac{1}{2}} K_{q_f}$$

None of the other feedback gains require scaling. In general, all angular rate feedback gains of the full-scale airplane must be reduced by the square root of the scaling ratio. Also, the critical frequencies of control system components such as shaping filters and actuators must be increased as in equation (A3). The critical parameters of nonlinear components must be adjusted according to the appropriate scaling law, as well. For example, angular rate limits must be increased by $a^{-\frac{1}{2}}$, corresponding to the angular velocity scale factor in table A2.

APPENDIX B

DIGITAL FILTERING TECHNIQUE

To utilize the RPRV system, the systems engineer must use digital filtering techniques to simulate analog systems, implement digital control systems, and suppress undesirable noise and structural resonances in the test vehicle's response signals. The problem of shaping the frequency content of a continuous signal with linear analog filters is well understood, and it is desirable to use this knowledge in designing digital filters. The resulting problem is that of approximating the filtering action of a continuous linear filter on a continuous waveform with a linear digital filter operating on a sampled continuous waveform. Many techniques are available, among them numerical integration and the standard z-transform. Numerical integration techniques are usually inefficient for real-time operations because they rely on repeated evaluations of functions to produce a solution and they do not take advantage of the known structure of linear filters. The standard z-transform technique is the natural choice for analyzing discrete system stability, but it has drawbacks when used for approximating continuous transfer functions (ref. 5). Two of these drawbacks are the aliasing of power about the Nyquist frequency and the difficulty of implementing some standard filter forms such as high-pass filters.

The derivation of the filtering algorithm used in the RPRV computer program is illustrated in figure B1. The poles and zeros of the continuous transfer function

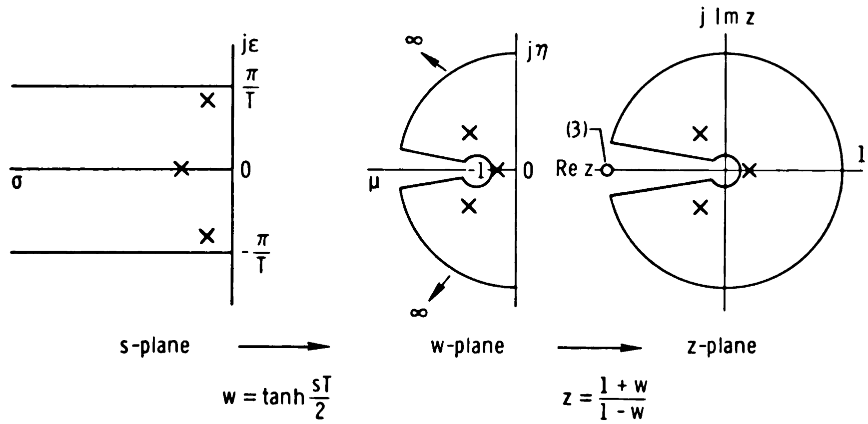

Figure B1. Conformal mappings between the s-, w-, and z-planes used in defining the digital filtering algorithm for the RPRV computer program.

$G(s)$ contained in the primary strip of the s-plane are mapped into the left half of the intermediate w-plane by means of the complex transformation

$$w = \tanh \frac{sT}{2}$$

The transformation maps a root located at $s = \sigma + j\varepsilon$ to a root located at $w = \mu + j\eta$ with

$$\mu = \frac{\sinh \sigma T}{\cosh \sigma T + \cos \varepsilon T}$$

$$\eta = \frac{\sin \varepsilon T}{\cosh \sigma T + \cos \varepsilon T}$$

Note that the imaginary s-plane axis from $-\frac{\pi}{T}$ to $\frac{\pi}{T}$ maps onto the entire imaginary axis of the w-plane. The negative real axis in the s-plane maps onto the negative segment of the real axis of the w-plane from -1 to 0. The final step of the algorithm maps the function $G(w)$ into the unit circle of the z-plane through the bilinear transformation

$$z = \frac{1 + w}{1 - w}$$

The transformation maps a root located at $w = \mu + j\eta$ to a root located at $z = Re\ z + j\ Im\ z$:

$$Re\ z = \frac{1 - \mu^2 + \eta^2}{(1 - \mu)^2 + \eta^2}$$

$$Im\ z = \frac{2\eta}{(1 - \mu)^2 + \eta^2}$$

It can be shown that the complete algorithm maps roots from the s-plane to the z-plane such that a real root located at $s = -\beta$ will map to a real root located at $z = e^{-\beta T}$, and a pair of complex conjugate roots with the characteristic polynomial $(s + c)^2 + d^2$ will map to a pair of complex conjugate roots with the characteristic polynomial $z^2 - 2e^{-cT} \cos dT\, z + e^{-2cT}$. Band-limited transforms, such as low-pass filters, with more poles than zeros have additional zeros inserted at $z = -1$ such that the orders of the denominator and the numerator of $G(z)$ are the same. The effect of these zeros at $z = -1$ (for low-pass filter forms) is to introduce a "notch" characteristic in the frequency response of the digital filter at the half-sample frequency. This is in addition to the desired low-pass characteristic for which the filter was designed and may be regarded as a "free" noise rejection capability of the digital filter at frequencies near the half-sample frequency.

The complete algorithm can be stated as follows: Given a continuous transfer function,

$$G(s) = \frac{K' \prod_{i=1}^{u} (s + \alpha_i) \prod_{i=1}^{n} \left[(s + a_i)^2 + b_i^2\right]}{\prod_{i=1}^{r} (s + \beta_i) \prod_{i=1}^{t} \left[(s + c_i)^2 + d_i^2\right]}$$

a digital filter approximating $G(s)$ is given by

$$G(z) = \frac{K''(z+1)^k \prod_{i=1}^{u}\left(z - e^{-\alpha_i T}\right)\prod_{i=1}^{n}\left(z^2 - 2e^{-a_i T}\cos b_i Tz + e^{-2a_i T}\right)}{\prod_{i=1}^{r}\left(z - e^{-\beta_i T}\right)\prod_{i=1}^{t}\left(z^2 - 2e^{-c_i T}\cos d_i Tz + e^{-2c_i T}\right)} \qquad \text{(B1)}$$

where $k = r + 2t - u - 2n$, $k \geq 0$, and K'' is the normalization constant. For unity gain low-pass filters, K'' is set by the condition $G(z)\Big|_{z=+1} = 1$, and for unity gain high-pass filters, by the condition $G(z)\Big|_{z=-1} = 1$.

The preceding digital filtering algorithm is an extension of algorithms described by Kaiser in reference 5 and Gold and Rader in reference 4. The algorithms discussed in these references are referred to as the bilinear transformation, although the algorithms are not the same. The algorithm described by Kaiser is also known as Tustin's method and involves trapezoidal integration of the differential equation describing the continuous transfer function. The algorithm described by Gold and Rader performs a prewarping of the critical frequencies of the filter transfer function before the application of the bilinear transformation. In both of these algorithms, the root locations of the resulting digital filters are approximations to those given by equation (B1). The matched z-transform algorithm (ref. 12) gives the same pole and zero locations as equation (B1) but does not account for the zeros added at $z = -1$ for band-limited functions. In the use of the matched z-transform, it is common to add these zeros in an *ad hoc* manner.

REFERENCES

1. Edwards, John W.: Flight-Test of a Remotely Piloted Research Vehicle Using a Remote Digital Computer for Control Augmentation. Transactions of the First NWC Symposium on the Application of Control Theory to Modern Weapons Systems - 9-10 May 1973. NWC TP 5522, Naval Weapons Center (China Lake, Calif.), June 1973, pp. 281-308.

2. Reed, R. Dale: RPRVs - The First and Future Flights. Astronaut. Aeron., Apr. 1974, pp. 26-42.

3. Holleman, Euclid C., compiler: Initial Results From Flight Testing a Large, Remotely Piloted Airplane Model. NASA TM X-56024, 1974.

4. Gold, Bernard; and Rader, Charles M.: Digital Processing of Signals. McGraw-Hill Book Co., Inc., c.1969, pp. 48-97.

5. Kaiser, J. F.: Digital Filters. Ch. 7 of Systems Analysis by Digital Computer, Franklin F. Kuo and James F. Kaiser, eds., John Wiley & Sons, Inc., c.1966, pp. 218-285.

6. Tobie, Harold N.; Malcom, Lawrence G.; and Elliott, Elden M.: A New Longitudinal Handling Qualities Criterion. NAECON/66; Proceedings of the IEEE 18th Annual National Aerospace Electronics Conference, May 1966, pp. 93-99.

7. Shapiro, Ascher H.: The Dynamics and Thermodynamics of Compressible Fluid Flow. Vol. I. The Ronald Press Co., c.1953, p. 56.

8. Kuethe, A. M.; and Schetzer, J. D.: Foundations of Aerodynamics. 2nd ed., John Wiley & Sons, Inc., c.1959, pp. 11, 243-244, 260-261.

9. Neihouse, Anshal I.; and Pepoon, Philip W.: Dynamic Similitude Between a Model and a Full-Scale Body for Model Investigation at Full-Scale Mach Number. NACA TN 2062, 1950.

10. Scherberg, Max; and Rhode, R. V.: Mass Distribution and Performance of Free Flight Models. NACA TN 268, 1927.

11. Northrop Servomechanisms Section and Aerodynamics Section: Dynamics of the Airframe. AE-61-4II, Bur. of Aeron., Navy Dept., Sept. 1952, pp. II-29 - III-7. (Available from Northrop Corp., Norair Div.)

12. Slater, G. L.: A Unified Approach to Digital Flight Control Algorithms. AIAA Paper No. 74-884, Aug. 1974.

NASA-Langley, 1975 H-854

"The aeronautical and space activities of the United States shall be conducted so as to contribute . . . to the expansion of human knowledge of phenomena in the atmosphere and space. The Administration shall provide for the widest practicable and appropriate dissemination of information concerning its activities and the results thereof."

—NATIONAL AERONAUTICS AND SPACE ACT OF 1958

NASA SCIENTIFIC AND TECHNICAL PUBLICATIONS

TECHNICAL REPORTS: Scientific and technical information considered important, complete, and a lasting contribution to existing knowledge.

TECHNICAL NOTES: Information less broad in scope but nevertheless of importance as a contribution to existing knowledge.

TECHNICAL MEMORANDUMS: Information receiving limited distribution because of preliminary data, security classification, or other reasons. Also includes conference proceedings with either limited or unlimited distribution.

CONTRACTOR REPORTS: Scientific and technical information generated under a NASA contract or grant and considered an important contribution to existing knowledge.

TECHNICAL TRANSLATIONS: Information published in a foreign language considered to merit NASA distribution in English.

SPECIAL PUBLICATIONS: Information derived from or of value to NASA activities. Publications include final reports of major projects, monographs, data compilations, handbooks, sourcebooks, and special bibliographies.

TECHNOLOGY UTILIZATION PUBLICATIONS: Information on technology used by NASA that may be of particular interest in commercial and other non-aerospace applications. Publications include Tech Briefs, Technology Utilization Reports and Technology Surveys.

Details on the availability of these publications may be obtained from:

SCIENTIFIC AND TECHNICAL INFORMATION OFFICE

NATIONAL AERONAUTICS AND SPACE ADMINISTRATION

Washington, D.C. 20546

NASA TECHNICAL NOTE

NASA TN D-7942

NASA TN D-7942

FORMULATION OF THE INFORMATION CAPACITY OF THE OPTICAL-MECHANICAL LINE-SCAN IMAGING PROCESS

Friedrich O. Huck and Stephen K. Park

Langley Research Center
Hampton, Va. 23665

NATIONAL AERONAUTICS AND SPACE ADMINISTRATION • WASHINGTON, D. C. • AUGUST 1975

1. Report No.	2. Government Accession No.	3. Recipient's Catalog No.
NASA TN D-7942		

4. Title and Subtitle	5. Report Date
FORMULATION OF THE INFORMATION CAPACITY OF THE OPTICAL-MECHANICAL LINE-SCAN IMAGING PROCESS	August 1975
	6. Performing Organization Code
7. Author(s)	8. Performing Organization Report No.
Friedrich O. Huck and Stephen K. Park	L-10118
9. Performing Organization Name and Address	10. Work Unit No.
NASA Langley Research Center Hampton, Va. 23665	506-18-21-02
	11. Contract or Grant No.
12. Sponsoring Agency Name and Address	13. Type of Report and Period Covered
National Aeronautics and Space Administration Washington, D.C. 20546	Technical Note
	14. Sponsoring Agency Code

15. Supplementary Notes

16. Abstract

An expression for the information capacity of the optical-mechanical line-scan imaging process is derived which includes the effects of blurring of spatial detail, photosensor noise, aliasing, and quantization. Both the information capacity for a fixed data density and the information efficiency (i.e., the ratio of information capacity to data density) exhibit a distinct single maximum when displayed as a function of sampling rate, and the location of this maximum is determined by the system frequency-response shape, signal-to-noise ratio, and quantization interval.

17. Key Words (Suggested by Author(s))	18. Distribution Statement
Information capacity and efficiency Optical-mechanical line-scan imaging process Facsimile camera Aliasing	Unclassified – Unlimited New Subject Category 35

19. Security Classif. (of this report)	20. Security Classif. (of this page)	21. No. of Pages	22. Price*
Unclassified	Unclassified	35	$3.75

*For sale by the National Technical Information Service, Springfield, Virginia 22161

FORMULATION OF THE INFORMATION CAPACITY OF THE OPTICAL-MECHANICAL LINE-SCAN IMAGING PROCESS

Friedrich O. Huck and Stephen K. Park
Langley Research Center

SUMMARY

The information capacity of the optical-mechanical line-scan imaging process is formulated by generally following the classical work of Fellgett and Linfoot who applied Shannon's theory of information to the assessment of film-camera images. Although images obtained with film cameras and optical-mechanical line-scan devices are both degraded by blurring of spatial detail and by noise, the latter images are also degraded by aliasing that results when spatial scene radiance variations are undersampled, and by quantization that results when the photosensor analog signal is converted to a digital signal for transmission.

Numerical evaluations of the derived expression reveal that both the information capacity for a fixed data density and the information efficiency (i.e., the ratio of information capacity to data density) exhibit a distinct single maximum when displayed as a function of sampling rate, and that the location of this maximum is determined by the system frequency-response shape, signal-to-noise ratio, and quantization interval. These results suggest a general design criteria for optical-mechanical line-scan devices: namely, the optimization of either their information capacity for a fixed data density or their information efficiency, especially if large quantities of data are involved or the data must be transmitted over long distances.

INTRODUCTION

Film and television cameras have generally been employed in the past to characterize spatial variations of scene brightness, whereas optical-mechanical line-scan devices have been employed to characterize spectral and radiometric variations. Little attention has, therefore, been paid to the image quality of spatial detail obtained with the latter devices. However, the spatial characterization of scenes has become in recent years an important objective in several applications of the optical-mechanical line-scan technique to multispectral imaging systems for Earth-orbiting spacecraft; and it is the most important objective in applications to the so-called facsimile cameras of the U.S.S.R. spacecraft Luna (ref. 1) and Lunakhod (ref. 2) and the U.S. spacecraft Viking Lander (ref. 3).

Data returned from Earth-orbiting spacecraft are constantly increasing, and data returned from planetary spacecraft will remain very expensive. In both cases, the quality of the data is most generally assessed by its information content, and the capability of the imaging system by its information capacity. The application of information theory to the assessment of optical-mechanical line-scan devices is particularly interesting because the quantity of data that is transmitted and the quantity of information that these data can contain are interrelated by two factors: the inevitable line-scan sampling process associated with this device, and the electronic sampling and quantization process required for digital data transmission.

The approach that is pursued here to formulate the information capacity of the optical-mechanical line-scan imaging process generally follows the classical work of Fellgett and Linfoot (ref. 4) who applied Shannon's theory of information (ref. 5) to the assessment of the image quality obtained with film cameras. Images obtained with film cameras and optical-mechanical line-scan devices are both degraded by blurring of small detail and by random noise. However, the latter images are also degraded by the aliasing that results when spatial scene radiance variations are undersampled and by the quantization that results when the photosensor analog signal is converted to a digital signal for transmission.

SYMBOLS

A	isoplanatism patch of camera field of view
$\lvert A \rvert$	solid angle of isoplanatism patch, sr
$\hat{B}$	sampling frequency passband
$\hat{F}$	camera frequency passband
$g(\chi,\psi)$	spatial function confined to A
$\hat{g}(\upsilon,\omega)$	frequency spectrum of $g(\chi,\psi)$ confined to $\hat{F}$
h_d	data density, bits/sr
h_i	information density or capacity, binits/sr
H_d	quantity of data in A, bits

H_g — entropy of $g(\chi,\psi)$, binits

H_i — quantity of information in A, binits

$I(\chi,\psi)$ — random variable, minus its average value, of all signal and noise components in A

k — filter-shape parameter (see fig. 3)

K — average signal, A

m,n — elevation and azimuth sampling counts, respectively

M,N — number of elevation and azimuth samples, respectively

n_e — magnitude of white Gaussian noise spectrum, A

$N(\chi,\psi)$ — random variable, minus its average value, of all noise components in A

$\bar{N}(\lambda)$ — average spectral radiance of object, W/m^2-sr-μm

$o(\chi,\psi)$ — normalized spatial distribution of object radiance

p,q — elevation and azimuth integers of mathematical sampling points in $\hat{F}$, respectively

$P(\chi,\psi)$ — random variable, minus its average value, of all signal components in A

$S(\chi,\psi)$ — spatial distribution of camera signal, A

$\hat{S}(\upsilon,\omega)$ — frequency spectrum of camera signal, A

X,Y — elevation and azimuth sampling intervals, respectively, rad

δ — delta or unit impulse function

η — number of binary encoding levels, bits

κ — number of quantization levels

λ wavelength, μm

σ standard deviation

$\tau(\chi,\psi)$ point-spread function

$\hat{\tau}(\upsilon,\omega)$ spatial frequency response

υ,ω elevation and azimuth spatial frequencies, respectively, rad^{-1}

υ_e cutoff frequency of electronic filter, rad^{-1}

$\hat{\Upsilon}(\upsilon,\omega)$ square root of $\hat{\tau}(\upsilon,\omega)$

$\hat{\phi}(\upsilon,\omega)$ Wiener spectrum, or power spectral density

χ,ψ elevation and azimuth angles of camera scanning coordinates, respectively, rad

$Ш(\chi,\psi)$ sampling or comb function

$(\bar{\ })$ average value or ensemble average

$(\hat{\ })$ spatial frequency domain

$(\ )*(\ )$ convolution

Subscripts:

an aliasing noise

c camera

e electronics

en electronic noise

g spatial function $g(\chi,\psi)$

l lens

o optics

ps proper signal

FORMULATION

The Optical-Mechanical Line-Scan Imaging Process

Consider an optical-mechanical line-scan imaging device such as the facsimile camera shown in figure 1. Radiation from the object field is reflected by the scanning mirror, captured by the objective lens, and projected onto a plane which contains a photosensor covered by a small aperture. The photosensor converts the radiation falling on the aperture into an electrical signal which is then amplified, sampled, and quantized for digital transmission. As the mirror rotates, the imaged object field moves past the aperture and thus permits the aperture to scan vertical strips. The camera rotates in small steps between each vertical line scan until the entire object field of interest is scanned. The distance between object and camera is assumed to be large compared with the distance between camera mirror and lens; thus, spherical coordinates with an origin at the center of the objective lens can be used as reference for the elevation and azimuth imaging coordinates, labeled "χ" and "ψ," respectively.

The process by which this device transfers the (continuous) object radiance distribution $o(\chi,\psi)$ into a (discrete) electrical signal $S(\chi,\psi)$ can be approximately formulated by the equation (ref. 6)

$$S(\chi,\psi) = K\left[o(\chi,\psi) * \tau_c(\chi,\psi)\right] \text{Ш}\left(\frac{\chi}{X},\frac{\psi}{Y}\right) \tag{1}$$

The symbol $*$ denotes convolution, K is the camera response to uniform radiance, and $\tau_c(\chi,\psi)$ is the camera point-spread function which, in turn, is given by

$$\tau_c(\chi,\psi) = \tau_l(\chi,\psi) * \tau_p(\chi,\psi) * \left[\tau_e(\chi)\ \delta(\psi)\right]$$

where $\tau_l(\chi,\psi)$, $\tau_p(\chi,\psi)$, and $\tau_e(\chi)\ \delta(\psi)$ are the point-spread functions of the lens, photosensor aperture, and signal electronics, respectively. The symbol $\text{Ш}\left(\frac{\chi}{X},\frac{\psi}{Y}\right)$ is the sampling (ref. 7) or comb (ref. 8) function. This function is an infinite sum of delta functions with spacings X and Y radians, which in this case correspond to the effective camera elevation and azimuth sampling intervals, respectively:

$$\text{Ш}\left(\frac{\chi}{X},\frac{\psi}{Y}\right) = \sum_{m=-\infty}^{\infty}\sum_{n=-\infty}^{\infty}\delta\left(\frac{\chi}{X}-m,\frac{\psi}{Y}-n\right) = XY\sum_{m=-\infty}^{\infty}\sum_{n=-\infty}^{\infty}\delta(\chi-Xm,\psi-Yn)$$

For facsimile cameras used on planetary landers, the spacing Y is equal to the azimuth stepping interval times the cosine of χ where χ is measured from a plane normal to the optical axis of the objective lens.

An approximation is introduced into the formulation of equation (1) by the separation of spectral and spatial object and camera characteristics, with the average signal K accounting for the spectral characteristics. Actually, $o(\chi,\psi)$ and $\tau_c(\chi,\psi)$ are functions of wavelength, and the spatial convolution should, therefore, be integrated over wavelength. However, it is convenient here to let (ref. 9)

$$K = A_c B_c \int_0^\infty \overline{N}(\lambda)\, \tau_c(\lambda)\, R(\lambda)\, d\lambda \tag{2}$$

where A_c is the area of the lens aperture, B_c is the solid angle of the field of view formed by the photosensor aperture (i.e., the solid angle that defines a picture element), $\overline{N}(\lambda)$ is the average spectral radiance of the object, $\tau_c(\lambda)$ is the transmittance of the camera optics, and $R(\lambda)$ is the responsivity of the photosensor. The use of K in equation (1) permits $o(\chi,\psi)$ and $\tau_c(\chi,\psi)$ to be expressed as normalized functions while $S(\chi,\psi)$ takes on the unit of K, which is amperes.

The optical-mechanical line-scan imaging process is implicitly a function of time. The formulation of equation (1) implies, therefore, that the convolution of the object radiance distribution with the camera point-spread function be performed for each picture element (pixel) in a picture to allow for changes of $o(\chi,\psi)$ or $\tau_c(\chi,\psi)$ with time. If neither object radiance distribution nor camera response varies with time (as is assumed here), then it is immaterial whether the pixels in a picture are formed simultaneously or in sequence, and the convolution needs to be performed only once for each picture.

Significant variations in defocus blur and in azimuth sampling intervals, however, may occur as a function of the elevation scanning angle. If such variations occur, it is necessary for the purpose of analysis to divide the camera field of view into isoplanatism patches (i.e., areas within which these variations become negligibly small) and restrict all formulations to such a patch. The total information contained in an image is the sum of the information contained in all the patches that make up the image.

An isoplanatism patch is denoted here by A and assumed to be rectangular and centered at $\chi = \psi = 0$. For M samples per line scan and N line scans in A, χ, and ψ are limited to

$$-XM/2 \leqq \chi \leqq XM/2$$

$$-YN/2 \leqq \psi \leqq YN/2$$

and the solid angle subtended by A is $|A| = XYMN$ steradians. Any spatial function $g(\chi,\psi)$ is then said to be confined to A if $g(\chi,\psi) = 0$ for all points outside A. The error that is introduced by confining the radiance distribution $o(\chi,\psi)$ to A is negligibly small everywhere in A except at a very narrow strip along the boundary of A. (See, for example, refs. 10 and 11.)

The imaging process formulated by equation (1) is generally more convenient to evaluate for the isoplanatism patch A in the frequency rather than spatial domain. Any spatial function $g(\chi,\psi)$ which is confined to A and its corresponding frequency function $\hat{g}(\upsilon,\omega)$ are related by the Fourier transform pair

$$\hat{g}(\upsilon,\omega) = \iint_A g(\chi,\psi)e^{-i2\pi(\upsilon\chi+\omega\psi)}d\chi\, d\psi$$

$$g(\chi,\psi) = \iint_{-\infty}^{\infty} \hat{g}(\upsilon,\omega)e^{i2\pi(\upsilon\chi+\omega\psi)}d\upsilon\, d\omega$$

By using this transformation, equation (1) becomes

$$\hat{S}(\upsilon,\omega) = K\left[\hat{o}(\upsilon,\omega)\,\hat{\tau}_c(\upsilon,\omega)\right] * XY\, III(X\upsilon,Y\omega) \tag{3a}$$

where

$$\hat{\tau}_c(\upsilon,\omega) = \hat{\tau}_l(\upsilon,\omega)\,\hat{\tau}_p(\upsilon,\omega)\,\hat{\tau}_e(\upsilon)$$

and

$$XY\, III(X\upsilon,Y\omega) = \sum_{m=-\infty}^{\infty}\sum_{n=-\infty}^{\infty} \delta\left(\upsilon-\frac{m}{X},\omega-\frac{n}{Y}\right)$$

Equation (3a) can be written more conveniently as

$$\hat{S}(\upsilon,\omega) = K\sum_{m=-\infty}^{\infty}\sum_{n=-\infty}^{\infty} \hat{o}\left(\upsilon-\frac{m}{X},\omega-\frac{n}{Y}\right)\hat{\tau}_c\left(\upsilon-\frac{m}{X},\omega-\frac{n}{Y}\right) \tag{3b}$$

or

$$\hat{S}(\upsilon,\omega) = K\,\hat{o}(\upsilon,\omega)\,\hat{\tau}_c(\upsilon,\omega) + K\sum_{\substack{m=-\infty \\ (m,n)\neq(0,0)}}^{\infty}\sum_{n=-\infty}^{\infty} \hat{o}\left(\upsilon-\frac{m}{X},\omega-\frac{n}{Y}\right)\hat{\tau}_c\left(\upsilon-\frac{m}{X},\omega-\frac{n}{Y}\right) \tag{3c}$$

The first term of the equation for $\hat{S}(\upsilon,\omega)$ given by equation (3c), $K\,\hat{o}(\upsilon,\omega)\,\hat{\tau}_c(\upsilon,\omega)$, is equal to the image frequency spectrum obtained with film cameras if $\hat{\tau}_c(\upsilon,\omega)$ is interpreted as the combined camera lens and film spatial frequency response and K as a (linear) film exposure-to-density transfer function. It is the existence of the sidebands given by the second term in equation (3c) that distinguishes the signal frequency spectrum generated by the optical-mechanical line-scan imaging process from the image frequency spectrum of the film camera.

In order to characterize the signal frequency spectrum $\hat{S}(\upsilon,\omega)$, it is convenient to make the following two definitions: First, let $\hat{F}$ be the camera passband; ultimately, this passband is limited by the diffraction limit of the camera objective lens $\left(\text{i.e., } \upsilon^2 + \omega^2 < \left(\frac{2 \sin \alpha}{\lambda}\right)^2, \text{ where } \sin \alpha \text{ is the lens numerical aperture}\right)$. Second, let $\hat{B}$ be the sampling passband with corner points $\upsilon = \pm\frac{1}{2X}$ and $\omega = \pm\frac{1}{2Y}$ and sides parallel to the frequency coordinates (υ,ω). Two cases must be recognized as illustrated in figure 2: (a) sufficient sampling when $\hat{F} \subset \hat{B}$; and (b) insufficient sampling, or undersampling, when $F \not\subset B$.

If sufficient sampling occurs (fig. 2(a)), then the "proper signal" term $K\,\hat{o}(\upsilon,\omega)\,\hat{\tau}_c(\upsilon,\omega)$ can, in the absence of noise, be completely recovered by passing the signal frequency spectrum through an ideal low-pass filter whose passband agrees with the camera passband $\hat{F}$ or sampling passband $\hat{B}$. However, if insufficient sampling occurs (fig. 2(b)), then the "proper signal" components cannot be completely recovered, because displaced, false-frequency components, called aliased signals, fall into the passband $\hat{F}$. These aliased signal components cannot be distinguished in practice from the proper-signal components but tend to mask spatial detail in the image just like noise. The aliased signal is consequently treated as noise whose power is additive.

Data Density

Recall that M is the number of samples per line scan and N is the number of line scans in the isoplanatism patch A, and let κ be the number of quantization levels of each sample. Then, the number of distinguishable states in A is κ^{MN}, and the amount of data in A is given by

$$H_d = MN \log_2 \kappa = \frac{|A|}{XY} \log_2 \kappa$$

The units of H_d are binary digits. It follows that the data density in A (i.e., the channel capacity of the optical-mechanical line-scan device for the field of view $|A|$) is given by

$$h_d = \frac{H_d}{|A|} = \frac{1}{XY} \log_2 \kappa \tag{4a}$$

The units of h_d are binary digits per steradian. For η-bit encoding, $\kappa = 2^\eta$ and

$$h_d = \frac{\eta}{XY} \tag{4b}$$

If all the image states κ^{MN} are independent and equally probable, then H_d is the amount of information contained in A and h_d is the information density. However, all image states are generally neither independent nor equally probable in practice. To distinguish between units of data and information, the unit "binary digits" will be abbreviated to "bits" for data and to "binits" for information.

Information Density

The spatial radiance distribution of natural scenes is generally not completely predictable and must be treated as a random phenomenon. Otherwise, of course, the image data of such a scene could not be considered to carry any information. Image data of a reference test chart, for example, are not intended to provide information about the chart but about the camera performance. Consequently, an imaging system (just like a communication or control system) must be designed for an ensemble of scene radiances (or messages) and an ensemble of noise, not a particular scene radiance (or message) and a particular realization of noise. Wiener has shown that power spectral density is a meaningful and useful statistical description of random phenomena (ref. 12). For optical systems, the power spectral density is often referred to as the Wiener spectrum to free the mathematical concept of a power spectral density from its physical implications in electrical engineering (ref. 13).

Before formulating these statistics for the optical-mechanical line-scan imaging process, it is convenient to review a general analytical representation of random phenomena as presented by Fellgett and Linfoot (ref. 4) and by Linfoot (ref. 10) for optical images. Pertinent scene and camera characteristics are then molded into this analytical presentation, leading directly to the desired formulation of the information density generated by the optical-mechanical line-scan imaging process.

Analytical representation.- Let the spatial function $g(\chi,\psi)$ be a random process that represents any signal or noise component confined to the isoplanatism patch A of the reconstructed line-scan image; let the Fourier transform of this function $\hat{g}(\upsilon,\omega)$ be the corresponding frequency spectrum confined to the camera passband $\hat{F}$; and let

$$\hat{\phi}_g(\upsilon,\omega) = \frac{1}{|A|} \overline{|\hat{g}(\upsilon,\omega)|^2} \tag{5}$$

be the corresponding Wiener spectrum. In other words, the Wiener spectrum can be calculated by averaging the modulus squared of the Fourier transform of $g(\chi,\psi)$, that is, $|\hat{g}(\upsilon,\omega)|^2$, over the ensemble to which $g(\chi,\psi)$ belongs and by dividing the result by the area $|A|$.

The function $g(\chi,\psi)$ is real for the case of incoherent radiation treated here, so that the complex conjugate of $\hat{g}(\upsilon,\omega)$ is equal to $\hat{g}(-\upsilon,-\omega)$. The Wiener spectrum is always real, nonnegative, and symmetric about the origin $\left(\text{i.e., } \hat{\phi}_g(\upsilon,\omega) = \hat{\phi}_g(-\upsilon,-\omega)\right)$.

Furthermore, let $\hat{g}_{pq} = \hat{g}\left(\upsilon_p,\omega_q\right)$ be the value of $\hat{g}(\upsilon,\omega)$ at the sampling points $\left(\upsilon_p,\omega_q\right) = (p/XM,q/YN)$, where p and q are integers. The sampling intervals $(1/XM,1/YN)$ assure sufficient (mathematical) sampling since $g(\chi,\psi)$ is confined to A (i.e., $|\chi| \leqq XM/2, |\chi| \leqq YN/2$). The frequency function $\hat{g}(\upsilon,\omega)$ can then be reconstructed from the sampled values according to Shannon's sampling theorem (ref. 5)

$$\hat{g}(\upsilon,\omega) \approx \sum_{pq\in\hat{F}}\sum \hat{g}_{pq} \operatorname{sinc}(XM\upsilon - p) \operatorname{sinc}(YN\omega - q)$$

where

$$\operatorname{sinc} \upsilon = \frac{\sin \pi\upsilon}{\pi\upsilon}$$

and the notation $pq \in \hat{F}$ indicates that the summation is performed over all sampling points in $\hat{F}$. The spatial function $g(\chi,\psi)$ can be reconstructed by the Fourier series expansion

$$g(\chi,\psi) = \begin{cases} \dfrac{1}{|A|} \displaystyle\sum_{pq\in F}\sum \hat{g}_{pq}\, e^{2\pi i\left(\frac{p\chi}{XM} + \frac{q\psi}{YN}\right)} & ((\chi,\psi) \in A) \\ 0 & ((\chi,\psi) \notin A) \end{cases}$$

To avoid possible confusion it should be pointed out that the sampling intervals $(1/XM,1/YN)$ in the frequency domain are not directly related to the camera sampling intervals (X,Y) in the spatial domain except through the somewhat arbitrarily defined solid angle $|A|$ of the isoplanatism patch A. The former sampling intervals are introduced to provide a convenient analytical representation of scene and camera characteristics as a summation of discrete sampling values. The latter sampling intervals are an inherent aspect of the optical-mechanical line-scan imaging process.

The statistical properties of any signal or noise component $g(\chi,\psi)$ confined to A can be characterized by the statistical properties of the finite collection of complex random variables $\hat{g}_{pq}$ for which $(\upsilon_p, \omega_q) \in \hat{F}$. If $\hat{g}_{pq}$ has a probability distribution $p_{pq}(\hat{g})$, the entropy of $\hat{g}_{pq}$ is defined as

$$H_{\hat{g}_{pq}} = -\iint p_{pq}(\hat{g}) \log_2 p_{pq}(\hat{g})\, d\zeta\, d\xi \tag{6}$$

where ζ and ξ are the real and imaginary components of $\hat{g}_{pq}$, respectively. Due to the conjugate symmetry of the collection of $\hat{g}_{pq}$, only one-half of them can be assumed to be independent. With this understanding, the joint entropy of the collection of $\hat{g}_{pq}$ (i.e., of $\hat{g}(\upsilon,\omega)$) is given by

$$H_g = \frac{1}{2} \sum_{pq \in \hat{F}}\sum H_{\hat{g}_{pq}} \tag{7}$$

Each sample value of $\hat{g}_{pq}$ is assumed to have a Gaussian (i.e., normal) probability density function with mean zero and variance $\sigma^2_{g,pq}$ equal to the average power of $\hat{g}_{pq}$; that is,

$$p_{pq}(\hat{g}) = \frac{1}{2\pi\sigma^2_{g,pq}} e^{-|\hat{g}|^2 / 2\sigma^2_{g,pq}} \tag{8}$$

where

$$\sigma^2_{g,pq} = |A| \hat{\phi}_g(\upsilon_p, \omega_q)$$

For a random variable with a specified variance, the Gaussian probability density function represents the maximum statistical uncertainty, or entropy, of the random variable. Substituting this function into equations (6) and (7) yields the following familiar results (ref. 5):

$$H_{\hat{g}_{pq}} = \log_2 4\pi\sigma^2_{g,pq} \tag{9}$$

$$H_g = \frac{1}{2} \sum_{pq \in \hat{F}}\sum \log_2 4\pi\sigma^2_{g,pq} \tag{10}$$

Now, let the spatial function $I(\chi,\psi)$ be the random variable, minus its average value, that represents all the signal and noise components that have been constructed (without loss of information) in the isoplanatism patch A of the image; let the Fourier transform of this function $\hat{I}(\upsilon,\omega)$ be the corresponding frequency spectrum confined to the camera passband $\hat{F}$; and let $\hat{\phi}_I(\upsilon,\omega)$ be the corresponding Wiener spectrum. Similarly, let $P(\chi,\psi)$ be the signal components of $I(\chi,\psi)$, minus its average value, with $\hat{P}(\upsilon,\omega)$ and $\hat{\phi}_P(\upsilon,\omega)$ the corresponding frequency and Wiener spectrum, respectively; and let $N(\chi,\psi)$ be the noise components of $I(\chi,\psi)$, with $\hat{N}(\upsilon,\omega)$ and $\hat{\phi}_N(\upsilon,\omega)$ the corresponding frequency and Wiener spectrum, respectively. It is assumed that the signal and noise components are additive and statistically independent, so that

$$\sigma^2_{I,pq} = \sigma^2_{P,pq} + \sigma^2_{N,pq}$$

In the sense that the information gained about a scene can be regarded as a reduction in the statistical uncertainty, or entropy, about the probable state of the scene, the quantity of information H_i contained in $I(\chi,\psi)$ is defined within the foregoing constraints as

$$H_i = H_I - H_N = \frac{1}{2} \sum\sum_{pq\in\hat{F}} \log_2 4\pi\sigma^2_{I,pq} - \frac{1}{2} \sum\sum_{pq\in\hat{F}} \log_2 4\pi\sigma^2_{N,pq}$$

$$H_i = \frac{1}{2} \sum\sum_{pq\in\hat{F}} \log_2 \frac{\sigma^2_{I,pq}}{\sigma^2_{N,pq}} = \frac{1}{2} \sum\sum_{pq\in\hat{F}} \log_2 \left(1 + \frac{\sigma^2_{P,pq}}{\sigma^2_{N,pq}}\right) \tag{11}$$

This summation can be approximated by an integration of a continuous function over $\hat{F}$ as

$$H_i = \frac{1}{2}|A| \iint_{\hat{F}} \log_2 \left[1 + \frac{\hat{\phi}_P(\upsilon,\omega)}{\hat{\phi}_N(\upsilon,\omega)}\right] d\upsilon\, d\omega$$

The information density in the isoplanatism patch A is then given by

$$h_i = \frac{H_i}{|A|} = \frac{1}{2} \iint_{\hat{F}} \log_2 \left[1 + \frac{\hat{\phi}_P(\upsilon,\omega)}{\hat{\phi}_N(\upsilon,\omega)}\right] d\upsilon\, d\omega \tag{12}$$

The units of h_i are binits per steradians.

Object radiance.- The radiance distribution of a natural scene is taken to be $\overline{N}(\lambda)\, o(\chi,\psi)$ with the spectral and spatial characteristics separated for convenience. The spatial characteristics are given by the random variable $o(\chi,\psi)$ which has the following two constraints: (1) The variations of $o(\chi,\psi)$ are effectively confined to the range

$$\left.\begin{array}{ll} 0 \leqq o(\chi,\psi) \leqq 2 & ((\chi,\psi) \in A) \\ o(\chi,\psi) = 0 & ((\chi,\psi) \notin A) \end{array}\right\} \tag{13}$$

(2) The average value of $o(\chi,\psi)$ is unity; that is,

$$\frac{1}{|A|}\iint_A o(\chi,\psi)d\chi\, d\psi = 1 \tag{14}$$

An ensemble of scenes may be regarded to contain all scenes that consist of the same composition and have undergone the same morphological processes. The information content of the scene is contained in the spatial distribution $o(\chi,\psi)$ of the radiance. However, it should be recognized that the average photosensor signal K is proportional to the spatial average value of the scene radiance $\overline{N}(\lambda)$ (see eq. (2)) and that $\overline{N}(\lambda)$ contributes, therefore, to the amount of information about the scene that can ultimately be recovered from the camera signal. With this understanding, the Wiener spectrum of the scene is defined as

$$\hat{\phi}_o(\upsilon,\omega) = \frac{1}{|A|}\overline{|\hat{o}(\upsilon,\omega)|^2} \tag{15}$$

where again $\overline{|\hat{o}(\upsilon,\omega)|^2}$ indicates that $|\hat{o}(\upsilon,\omega)|^2$ has been averaged over the ensemble to which $\hat{\phi}(\upsilon,\omega)$ belongs.

Camera signal.- The Wiener spectrum of the camera signal is defined as

$$\hat{\phi}_s(\upsilon,\omega) = \frac{1}{|A|}\overline{|\hat{S}(\upsilon,\omega)|^2}$$

where $\hat{S}(\upsilon,\omega)$ is given by equations (3). It is assumed on practical grounds that the aliased signals are to be treated as noise – similar, for example, to the noise generated by the photosensor. It may be pointed out to emphasize this analogy that the Wiener spectrum of the aliased signal, like that of the photosensor noise, may be assumed known; but a particular realization of either aliased signal or photosensor noise cannot be assumed known for any random process. The Wiener spectrum of the "proper signal" $\hat{\phi}_{ps}(\upsilon,\omega)$ (i.e., of that component which is contained in the camera passband $\hat{F}$ when sufficient sampling occurs) is defined as

$$\hat{\phi}_{ps}(\upsilon,\omega) = K^2\, \hat{\phi}_o(\upsilon,\omega)\left|\hat{\tau}_c(\upsilon,\omega)\right|^2 \tag{16}$$

Following Blackman and Tukey (ref. 14), the Wiener spectrum of the "aliased noise" $\hat{\phi}_{an}(\upsilon,\omega)$ (i.e., of those components that are contained in $\hat{F}$ only when insufficient sampling occurs) is defined as

$$\hat{\phi}_{an}(\upsilon,\omega) = K^2 \sum_{\substack{m=-\infty \\ (m,n)\neq(0,0)}}^{\infty} \sum_{n=-\infty}^{\infty} \hat{\phi}_o\left(\upsilon - \frac{m}{X}, \omega - \frac{n}{Y}\right)\left|\hat{\tau}_c\left(\upsilon - \frac{m}{X}, \omega - \frac{n}{Y}\right)\right|^2 \tag{17}$$

Electronic noise.- Noise is present in the object radiation itself, in the photosensor which transduces this radiation into an electrical signal, and in the electronic circuit which amplifies the small photosensor current into a signal large enough to be processed for transmission. Noise in the object radiation, referred to as photon noise, results from the random arrival of photons at the photosensor. However, the magnitude of this noise is significantly smaller than the noise generated in the solid-state photosensors and associated electronics that would generally be used with optical-mechanical line-scan devices. The noise generated in photosensors can be divided into noise affected in magnitude by the presence of the arriving radiation, referred to as shot noise, and noise not so affected, referred to as dark current. The noise generated by the electronics is independent of the magnitude of the arriving radiation. It is generally too complicated to account rigorously for variations in shot noise as a function of variations in signal level; instead, an average value for the shot noise based on an average signal current K can readily be accounted for. This approximation applies in particular to low-contrast scenes.

The electronic noise is amplified and sampled together with the signal for digital transmission. Just as undersampling of the signal frequency spectrum generates aliasing, so does undersampling of the noise frequency spectrum generate additional noise. However, severe undersampling of the electronic-noise frequency spectrum that would generate a significant increase in the magnitude of the noise samples should generally be avoidable by proper shaping of the electronic frequency response $\hat{\tau}_e(\upsilon)$. The Wiener spectrum of the sampled noise at the output of the electronics becomes then

$$\hat{\phi}'_{en}(\upsilon) = \hat{\phi}_{en}(\upsilon)\left|\hat{\tau}_e(\upsilon)\right|^2 \tag{18}$$

where $\hat{\phi}_{en}(\upsilon)$ is the Wiener spectrum of the unfiltered electronic noise.

Quantization noise.- After the electrical signal (and noise) that has been generated along the line-scan direction is sampled, each one of the samples is also quantized for digital transmission. The quantization effect is a basic limitation of digital systems in determining the true value of a signal, just as random noise is a limitation of analog systems.

In order to determine the loss of information that results from quantization, it is necessary to account for some of the assumptions that have already been made about the signal and noise. Pertinent assumptions are: The average value of the signal is K and of the noise is zero; the probability density functions of signal and noise are Gaussian; and the effective range of signal variations is $2K$. To form a valid model of the quantization process with these assumptions, it is necessary to assume also that the average-signal-to-rms-noise ratio is large – say, 10 or more. (This constraint is not serious in practice since only extremely poor images are reproduced from signals for which the signal-to-noise ratio is less than 10.)

Additional assumptions are as follows: The signal is linearly quantized over its effective range $2K$, so that the quantum levels have a uniform spacing of $2K/\kappa$ where κ is the number of quantization levels; the quantization error of any one sample is uncorrelated with that of any other sample; and the signal occurs equally likely anywhere in the quantization interval $-K/\kappa$ to K/κ. The last assumption is valid only if the number of quantization intervals is large – say, $\kappa \geqq 16$ (i.e., 4-bit encoding or more).

These assumptions imply that the quantization error n_κ has the uniform probability density function (ref. 15)

$$
\begin{aligned}
p(n_\kappa) &= \frac{\kappa}{2K} \qquad && \left(-K/\kappa \leqq n_\kappa \leqq K/\kappa\right) \\
&= 0 && \text{(Elsewhere)}
\end{aligned}
$$

In fact, a random variable which is constrained to a finite interval has maximum entropy when its probability density function is uniform.

A signal that is uniformly distributed between $-K/\kappa$ and K/κ has a mean equal to zero and a variance given by

$$\sigma^2_{\kappa n} = \int_{-K/\kappa}^{K/\kappa} n_\kappa^2 \, p(n_\kappa) \, dn_\kappa = \frac{K^2}{3\kappa^2}$$

Since quantization noise is uncorrelated (in the spatial domain), it has a Wiener spectrum equal to its variance; that is,

$$\hat{\phi}_{\kappa n}(\upsilon,\omega) = \frac{K^2}{3\kappa^2} \qquad (19)$$

Quantization noise will be treated as additive white Gaussian noise with the Wiener spectrum given by equation (19). The fact that this treatment of quantization leads to reasonable results is demonstrated in the next section.

Formulation of information density.- It remains now only to recognize that $\hat{\phi}_P(\upsilon,\omega)$ in equation (12) is equal to the Wiener spectrum of the proper signal component $\hat{\phi}_{ps}(\upsilon,\omega)$ given by equation (16) and that $\hat{\phi}_N(\upsilon,\omega)$ is equal to the sum of the Wiener spectrums of the aliased noise $\hat{\phi}_{an}(\upsilon,\omega)$, electronic noise $\hat{\phi}'_{en}(\upsilon)$, and quantization noise $\hat{\phi}_{\kappa n}(\upsilon,\omega)$ given by equations (17), (18), and (19), respectively. Substituting these results into equation (12) leads to the desired expression for the information density of the signal generated by the optical-mechanical line-scan imaging process:

$$h_i = \frac{1}{2}\iint_{\hat{F}} \log_2\left[1 + \frac{\hat{\phi}_o(\upsilon,\omega)\left|\hat{\tau}_c(\upsilon,\omega)\right|^2}{\sum\limits_{m=-\infty}^{\infty}\sum\limits_{\substack{n=-\infty \\ (m,n)\neq(0,0)}}^{\infty} \hat{\phi}_o\left(\upsilon - \frac{m}{X}, \omega - \frac{n}{Y}\right)\left|\hat{\tau}_c\left(\upsilon - \frac{m}{X}, \omega - \frac{n}{Y}\right)\right|^2 + K^{-2}\hat{\phi}_{en}(\upsilon)\left|\hat{\tau}_e(\upsilon)\right|^2 + \frac{1}{3}\kappa^{-2}}\right] d\upsilon\, d\omega \qquad (20)$$

In order to support the treatment of quantization as additive noise and, hence, to explore the validity of equation (20), consider the following idealized situation. Let the Wiener spectrum of the camera signal with an effective range of 2K be

$$K^2\hat{\phi}_o(\upsilon,\omega)\left|\hat{\tau}_c(\upsilon,\omega)\right|^2 = \frac{K^2}{4} \qquad \left(|\upsilon| \leq \frac{1}{2X}, |\omega| \leq \frac{1}{2Y}\right)$$

$$= 0 \qquad \text{(Elsewhere)}$$

Consequently, the camera passband and sampling passband are the same (i.e., $\hat{B} = \hat{F}$), and the aliasing noise term is zero. Similarly, let the Wiener spectrum of the electronic noise with an effective range $2n_e$ be

$$\phi_{en}(\upsilon)\left|\tau_e(\upsilon)\right|^2 = \frac{n_e^2}{4} \qquad \left(|\upsilon| \leq \frac{1}{2X}\right)$$

$$= 0 \qquad \text{(Elsewhere)}$$

Equation (20) reduces then to

$$h_i = \frac{1}{2}\iint_{\hat{B}} \log_2\left[1 + \frac{1}{\left(\frac{K}{n_e}\right)^{-2} + \frac{4}{3}\kappa^{-2}}\right] d\upsilon\, d\omega$$

Finally, let the electronic noise be small compared to the quantization interval; that is,

$$\left(\frac{K}{\kappa}\right)^2 >> n_e^2$$

Then, equation (20) reduces further to

$$h_i = \frac{1}{2}\iint_{\hat{B}} \log_2\left(1 + \frac{3}{4}\kappa^2\right) d\upsilon\, d\omega = \frac{1}{2XY}\log_2\left(1 + \frac{3}{4}\kappa^2\right)$$

If the number of quantization levels is large, then for this idealized situation

$$h_i \approx \frac{1}{2XY}\log_2 \frac{3}{4}\kappa^2 = \frac{1}{XY}\log_2\sqrt{\frac{3}{4}}\,\kappa$$

It is readily recognized that in this situation the information density h_i approaches – but remains slightly less than – the data density h_d given by equation (4a). The fact that the maximum possible value of the ratio h_i/h_d is slightly less than unity is consistent with the observation that h_d represents the maximum possible information density for a spatial radiance distribution which is uniform rather than Gaussian.

It is also informative to compare equation (20) with the general expression for information density derived by Fellgett and Linfoot (ref. 4, p. 399) for film-camera images as given here in the notation of this report:

$$h_{i,film} = \frac{1}{2}\iint_{\hat{F}} \log_2\left[1 + \frac{\hat{\phi}_o(\upsilon,\omega)\left|\hat{\tau}_{lf}(\upsilon,\omega)\right|^2}{\hat{\phi}_p(\upsilon,\omega)\left|\hat{\tau}_{lf}(\upsilon,\omega)\right|^2 + \hat{\phi}_f(\upsilon,\omega)}\right] d\upsilon\, d\omega$$

where $\hat{\phi}_o(\upsilon,\omega)$, $\hat{\phi}_p(\upsilon,\omega)$, and $\hat{\phi}_f(\upsilon,\omega)$ are the Wiener spectrum of the object radiance, photon noise, and film granularity, respectively, and $\hat{\tau}_{lf}(\upsilon,\omega)$ is the combined frequency response of the camera lens and film. It should be noted in particular that photon noise and aliased noise are similarly treated. Both are part of the object radiation, yet appear as statistically independent quantities. Furthermore, both their Wiener spectrums are modified by the frequency response of the camera.

Information Capacity and Efficiency

The information density h_i formulated by equation (20) is a function of scene as well as camera characteristics. It is convenient to assume here that the Wiener spectrum of the scene is constant out to some frequency beyond the system response $\hat{F}$. (See, for example, ref. 16.) Consistent with the previous assumption that the spatial radiance distribution of the scene $o(\chi,\psi)$ is Gaussian with an effective range of 2, its Wiener spectrum $\hat{\phi}_o(\upsilon,\omega)$ is 1/4. It is also convenient to assume that the Wiener spectrum of the electronic noise is constant within the frequency passband of the electrical filter $\hat{\tau}_e(\upsilon)$, with magnitude $\hat{\phi}_{en}(\upsilon) = n_e^2/4$.

With these assumptions, the (statistical mean) information capacity (in binits per steradian) of the optical-mechanical line-scan imaging process becomes

$$h_i = \frac{1}{2}\iint_{\hat{F}} \log_2\left[1 + \frac{\left|\hat{\tau}_c(\upsilon,\omega)\right|^2}{\displaystyle\sum_{\substack{m=-\infty \\ (m,n)\neq(0,0)}}^{\infty}\sum_{n=-\infty}^{\infty}\left|\hat{\tau}_c\left(\upsilon-\frac{m}{X},\omega-\frac{n}{Y}\right)\right|^2 + K^{-2}\, n_e^2\left|\hat{\tau}_e(\upsilon)\right|^2 + \frac{4}{3}\kappa^{-2}}\right] d\upsilon\, d\omega \qquad (21)$$

The data density (in bits per steradian) that is inevitably associated with this information capacity is given by equation (4a) as

$$h_d = \frac{1}{XY}\log_2 \kappa$$

It can be recognized that the objective to maximize the information capacity h_i without regard to the associated data density h_d would lead to sufficient sampling and very small quantization intervals, and, therefore, to large data requirements. It may often be more desirable either to maximize h_i for a fixed value of h_d or to maximize the ratio h_i/h_d. This ratio will be referred to as information efficiency.

EVALUATION

The foregoing formulation of the information capacity of the optical-mechanical line-scan imaging process was based in part on reasonable considerations of the effect of aliasing and quantization rather than on strictly mathematical grounds. It is, therefore, desirable to demonstrate that these assumptions lead to reasonable results.

Frequency-Response Shapes

The realizability of frequency-response shapes of optical apertures is constrained by the requirement that the aperture transmission is always greater than zero. This constraint may be generalized by noting that any aperture transmission function, being always positive, must have a square root; that is, $\tau(\chi,\psi) = \Upsilon^2(\chi,\psi)$, where $\tau(\chi,\psi)$ is the aperture response and $\Upsilon(\chi,\psi)$ is its square root. Taking the spatial Fourier transform and using the transform properties of the convolution yields

$$\hat{\tau}(\upsilon,\omega) = \int_{-\infty}^{\infty}\int_{-\infty}^{\infty} \hat{\Upsilon}(\upsilon',\omega')\,\hat{\Upsilon}(\upsilon-\upsilon',\omega-\omega')\,d\upsilon'\,d\omega'$$

In words, any realizable transfer function must, in the spatial-frequency domain, be representable as the convolution of a function with itself. Given any response function, realizable or not (it must, of course, be the transform of a real function), a fully realizable one can be generated simply by convolving it with itself (ref. 17).

The frequency-response characteristics of electrical filters are not similarly constrained. Consequently, the overall frequency response of electro-optical systems can be shaped with greater freedom along the line-scan direction than along the azimuth-stepping direction.

It is convenient here to consider only the simplified frequency-response shapes generated by the function

$$\left.\begin{aligned}\hat{\tau}(\upsilon,\omega) &= 1 - \left(\upsilon^2 + \omega^2\right)^{k/2} && \left(\upsilon^2 + \omega^2 \leqq 1\right)\\ &= 0 && \left(\upsilon^2 + \omega^2 > 1\right)\end{aligned}\right\} \tag{22}$$

where $k > 0$. (See fig. 3.) For electrical filters, $\hat{\tau}$ depends only on υ and for large k becomes the approximately rectangular-shaped frequency response of ideal low-pass electrical filters. A cylindrical-shaped frequency response (i.e., the rectangular shape with circular symmetry) is not realizable for optical apertures; however, an approximately cone-shaped frequency response is realizable as can be shown by convolving the cylindrical shape with itself. In fact, this convolution yields the frequency response of a diffraction-limited lens (see, for example, ref. 9), which is approximated by equation (22) for $k = 1$.

The remainder of this paper is concerned with four numerical examples. For convenience, in all but the first example, the camera passband $\hat{F}$ is normalized to be the set of points (υ,ω) with $\upsilon^2 + \omega^2 \leqq 1$. Consequently, the Nyquist elevation and azimuth sampling rates are $1/X = 2$ and $1/Y = 2$, respectively. In the first example only an electrical filter is considered for which the Nyquist rate is $1/X = 2$.

Examples

The performance of the optical-mechanical line-scan imaging process for fixed sampling rates ($1/X$ and $1/Y$) is determined – consistent with the assumptions that have been made – by the signal-to-noise ratio K/n_e, the digital encoding level η, the optical filter shape parameter k_o, the electrical filter shape parameter k_e, and the electrical filter cutoff frequency υ_e. Table I presents a summary of values for these five parameters that are used in the following examples.

Electrical filters.- Consider first a one-dimensional example that is representative of electrical filters. The information capacity analogous to equation (21) is

$$h_i = \int_0^{\upsilon_e} \log_2 \left[1 + \frac{\hat{\tau}_e^2(\upsilon)}{\sum\limits_{\substack{m=-\infty \\ m \neq 0}}^{\infty} \hat{\tau}_e^2\left(\upsilon - \frac{m}{X}\right) + \left(\frac{K}{n_e}\right)^{-2} \hat{\tau}_e^2(\upsilon) + \frac{4}{3}\kappa^{-2}} \right] d\upsilon \tag{23}$$

The frequency response of the electrical filter is given by

$$\left.\begin{aligned} \hat{\tau}_e(\upsilon) &= 1 - \left|\frac{\upsilon}{\upsilon_e}\right|^{k_e} & \quad & \left(|\upsilon| \leqq \upsilon_e\right) \\ &= 0 & & \left(|\upsilon| > \upsilon_e\right) \end{aligned}\right\} \tag{24}$$

where υ_e is the cutoff frequency. Analogous to equations (4), the associated data density is

$$h_d = \frac{1}{X} \log_2 \kappa = \frac{\eta}{X} \tag{25}$$

The units of h_i and h_d are binits/radian and bits/radian, respectively.

Often more useful and certainly more familiar is the information rate $\dot{h}_i = \dot{\chi}_s h_i$ binits/second and the data rate $\dot{h}_d = \dot{\chi}_s h_d$ bits/second, where $\dot{\chi}_s$ is the mirror line-scan rate in radians/second. The information efficiency remains the same $\left(\text{i.e., } h_i/h_d = \dot{h}_i/\dot{h}_d\right)$.

Figure 4 illustrates the variation of information capacity h_i, data density h_d, and information efficiency h_i/h_d with sampling rate $1/X$. For reference: $\upsilon_e = 1$; the Nyquist sampling rate is $1/X = 2$ cycles/radian; the root-mean-square (rms) magnitude of the electronic noise is

$$\sqrt{\left(\frac{K}{n_e}\right)^{-2} \int_0^1 \hat{\tau}_e^2(\upsilon)\, d\upsilon} = 1.3 \times 10^{-3}$$

for $K/n_e = 400$ and $k_e = 1$; and the rms magnitude of the quantization noise for $\eta = 8$ bits is

$$\sqrt{\frac{4}{3}\kappa^{-2}} = 2^{-\eta}\sqrt{\frac{4}{3}} = 4.5 \times 10^{-3}$$

The results shown in figure 4 are intuitively satisfying. It should be noted in particular in figure 4(c) that the information efficiency approaches unity $\left(h_i/h_d = 0.9\right)$ for a nearly ideal filter $\left(k_e = 4\right)$ and a nearly Nyquist sampling rate $\left(1/X = 1.95\right)$ and that the peak information efficiency not only decreases with a poorer filter response but also shifts toward lower sampling rates. Also, note in figure 4(b) that 10-bit encoding provides a significantly higher information capacity over 8-bit encoding, but that the latter provides a slightly higher information efficiency. Finally, note in figure 4(a) that a signal-to-noise ratio significantly higher than $K/n_e = 400$ does not appreciably increase either h_i or h_i/h_d.

Optical filters (symmetric sampling).- Consider next a two-dimensional example with circular symmetry that is representative of optical filters. The information capacity given by equation (21) becomes

$$h_i = 2\int_0^1 \int_0^{\sqrt{1-\omega^2}} \log_2 \left[1 + \frac{\hat{\tau}_o^2(\upsilon,\omega)}{\displaystyle\sum_{m=-\infty}^{\infty} \sum_{\substack{n=-\infty \\ (m,n)\neq(0,0)}}^{\infty} \hat{\tau}_o^2\left(\upsilon - \frac{m}{X}, \omega - \frac{n}{Y}\right) + \left(\frac{K}{n_e}\right)^{-2} + \frac{4}{3}\kappa^{-2}}\right] d\upsilon\, d\omega \qquad (26)$$

The frequency response of the optical filter is given by

$$\left.\begin{aligned} \hat{\tau}_o(\upsilon,\omega) &= 1 - \left(\upsilon^2 + \omega^2\right)^{k_o/2} & \left(\upsilon^2 + \omega^2 \leq 1\right) \\ &= 0 & \left(\upsilon^2 + \omega^2 > 1\right) \end{aligned}\right\} \qquad (27)$$

The associated data density given in equations (4) is

$$h_d = \frac{1}{XY} \log_2 \kappa = \frac{\eta}{XY}$$

The units of h_i and h_d are binits/steradian and bits/steradian, respectively.

Results for h_i, h_d, and h_i/h_d are plotted in figure 5 for symmetric elevation and azimuth sampling rates (i.e., $1/X = 1/Y$). It should be noted by comparing figures 4 and 5 that the information efficiency for optical filters tends to be substantially lower than for electrical filters. Also, the peak information efficiency tends to occur at substantially lower sampling rates than the Nyquist sampling rate $1/X = 1/Y = 2$.

Optical filters (unsymmetric sampling).- Consider next a two-dimensional example identical to the previous one except that the elevation and azimuth sampling rates, $1/X$ and $1/Y$, respectively, are not restricted to be equal. Since the information capacity h_i and efficiency h_i/h_d are then functions of two sampling rates, it is necessary to use a two-dimensional graphical representation of numerical solutions. Figure 6 presents a contour plot of information efficiency (i.e., lines of constant h_i/h_d) corresponding to the set of parameters $K/n_e = 400$, $\eta = 8$ bits, and $k_o = 1$. As would be expected, the contour lines have diagonal symmetry for a filter with circular symmetry. Consequently, the maximum information efficiency is obtained with symmetric sampling rates (i.e., $1/X = 1/Y$).

Figure 7(a) presents a contour plot of information capacity h_i and three contours of constant data density h_d. Figure 7(b) presents a plot of values of h_i along the three contours of constant h_d against the azimuth sampling rate $1/Y$. Again, the maximum information capacity is obtained with symmetric sampling rates.

Electro-optical systems.- Consider last a two-dimensional example without circular symmetry that is representative of electro-optical systems. The information capacity becomes

$$h_i = 2\int_0^1\int_0^{\sqrt{1-\omega^2}} \log_2\left[1 + \frac{\hat{\tau}_o^2(\upsilon,\omega)\,\hat{\tau}_e^2(\upsilon)}{\sum\limits_{m=-\infty}^{\infty}\sum\limits_{\substack{n=-\infty \\ (m,n)\neq(0,0)}}^{\infty} \hat{\tau}_o^2\left(\upsilon-\frac{m}{X},\omega-\frac{n}{Y}\right)\hat{\tau}_e^2\left(\upsilon-\frac{m}{X}\right) + \left(\frac{K}{n_e}\right)^{-2}\hat{\tau}_e^2(\upsilon) + \frac{4}{3}\kappa^{-2}}\right] d\upsilon\, d\omega \tag{28}$$

The frequency response of the electrical filter is given by equations (24) and of the optical filter by equations (27). The associated data density h_d is given by equations (4).

Figure 8 presents a contour plot of the information efficiency h_i/h_d analogous to figure 6, but for $K/n_e = 400$, $\eta = 8$ bits, $k_o = 1$, $k_e = 4$, and $\upsilon_e = 0.8$. Maximum values of h_i/h_d still occur at sampling rates below the Nyquist rate. However, as would be expected, the location of these maximum values occurs off the diagonal at an elevation sampling rate which is lower than the azimuth sampling rate because of the additional electrical filtering along the elevation direction.

Figure 9 presents information-capacity plots analogous to figure 7. Again, as in figure 8, the maximum information capacity for a fixed data density occurs at an elevation sampling rate lower than the azimuth sampling rate.

CONCLUDING REMARKS

Imaging systems cannot exactly reproduce a scene as an image. All images are degraded at least by some blurring of small detail and by random noise. As demonstrated by Fellgett and Linfoot, these two phenomena inevitably limit the amount of information density in an image. The optical-mechanical line-scan imaging process of many space-borne cameras almost unavoidably generates some additional image degradation due to aliasing and quantization. The results of Fellgett and Linfoot are extended here to include the effects of these degradations. All formulations are constrained by the assumption of statistically independent and additive Gaussian random processes, as have been all previous related analyses for incoherent radiation. This assumption includes here in particular the treatment of aliasing and quantization as noise sources.

The information density in an image depends not only on characteristics of the imaging system but also on statistical properties of the scene; namely, its random spatial radiance variation and power spectral density (i.e., Wiener spectrum). It is assumed that the radiance variation is Gaussian and that the Wiener spectrum is flat out to some spatial frequency beyond the optical passband of the imaging system. The information density of an image is then solely determined by the information capacity of the instrument used to obtain this image.

The objective to maximize the information capacity of the optical-mechanical line-scan imaging process without regard to the associated data density can lead to impractically large data requirements. It may be preferable either to maximize the information capacity for a fixed data density or to maximize the information efficiency (i.e., the ratio of information capacity to data density). Both the information capacity for a fixed data density and the information efficiency exhibit a distinct single maximum when displayed as a function of sampling rate.

It is shown that the information efficiency of an instrument can approach unity (i.e., that the information capacity of an instrument can approach the data density) under certain theoretical conditions. These conditions can be approximated in practice by electronic systems for time-varying signals but not by optical systems for space-varying signals. The reason for this is that the frequency response of electronic systems can approach a rectangular shape, whereas that of optical systems cannot approach a two-dimensional equivalent to this shape (i.e., a cylinderlike shape). In fact, the frequency response of an optical system is in practice generally limited by the conelike shape of a diffraction-limited lens, limiting the information efficiency of optical-mechanical line-scan devices to considerably less than unity. Nevertheless, within this limit, the information efficiency can vary significantly with sampling rate, signal-to-noise ratio, and quantization interval, as has been illustrated for a wide range of reasonable camera frequency-response shapes.

Langley Research Center,
National Aeronautics and Space Administration,
Hampton, Va., April 22, 1975.

REFERENCES

1. Selivanov, A. S.; Govorov, V. M.; Titov, A. S.; and Chemodanov, V. P.: Lunar Station Television Camera. Contract NAS 7-100, Reilly Translations, 1968. (Available as NASA CR-97884.)

2. Selivanov, A. S.; Govorov, V. M.; Zasetskii, V. V.; and Timokhin, V. A. (Morris D. Friedman, transl.): Chapter V. Peculiarities of the Construction and Fundamental Parameters of the "Lunokhod-1" Television Systems. Lockheed Missiles & Space Co. Transl. (From Peredvizhenaia Laboratoriia na Lune – Lunokhod-1, Acad. Sci. SSSR Press (Moscow), 1971, pp. 55-64.)

3. Mutch, T. A.; Binder, A. B.; Huck, F. O.; Levinthal, E. C.; Morris, E. C.; Sagan, Carl and Young, A. T.: Imaging Experiment: The Viking Lander. Icarus, vol. 16, no. 1, Feb. 1972, pp. 92-110.

4. Fellgett, P. B.; and Linfoot, E. H.: On the Assessment of Optical Images. Phil. Trans Roy. Soc. London, ser. A, vol. 247, no. 931, Feb. 17, 1955, pp. 369-407.

5. Shannon, C. E.: A Mathematical Theory of Communication. Bell Syst. Tech. J., vol. XXVII, no. 3, July 1948, pp. 379-423.

6. Huck, Friedrich O.; Wall, Stephen D.; and Burcher, Ernest E.: An Investigation of the Facsimile Camera Response to Object Motion. NASA TN D-7668, 1974.

7. Bracewell, R.: The Fourier Transform and Its Applications. McGraw-Hill Book Co., Inc., c.1965.

8. Goodman, Joseph W.: Introduction to Fourier Optics. McGraw-Hill Book Co., Inc., 1968.

9. Huck, Friedrich O.; and Lambiotte, Jules J., Jr.: A Performance Analysis of the Optical-Mechanical Scanner As an Imaging System for Planetary Landers. NASA TN D-5552, 1969.

10. Linfoot, E. H.: Information Theory and Optical Images. J. Opt. Soc. of America, vol. 45, no. 10, Oct. 1955, pp. 808-819.

11. Linfoot, E. H.: Fourier Methods in Optical Image Evaluation. The Focal Press, c.1964

12. Lee, Y. W.: Statistical Theory of Communication. John Wiley & Sons, Inc., c.1960.

13. Jones, R. Clark: Information Capacity of Radiation Detectors. J. Opt. Soc. of America vol. 50, no. 12, Dec. 1960, pp. 1166-1170.

14. Blackman, R. B.; and Tukey, J. W.: The Measurement of Power Spectra. Dover Publ., Inc., 1959.

15. Carlson, A. Bruce: Communications Systems. McGraw-Hill Book Co., c.1968.

16. O' Neill, Edward L.: Introduction to Statistical Optics. Addison-Wesley Pub. Co., Inc., c.1963.

17. Katzberg, Stephen J.; Huck, Friedrich O.; and Wall, Stephen D.: Photosensor Aperture Shaping To Reduce Aliasing in Optical-Mechanical Line-Scan Imaging Systems. Appl. Optics, vol. 12, no. 5, May 1973, pp. 1054-1060.

TABLE I.- SUMMARY OF EXAMPLES

Systems	Parameters				
	K/n_e	η, bits	k_o	k_e	υ_e
Electrical filter	100	6	Not applicable	0.25	1
	400	8		1	1
	1600	10		4	1
Optical filter, symmetric sampling	100	6	0.25	Not applicable	
	400	8	.5		
	1600	10	1		
Optical filter, unsymmetric sampling	400	8	1	Not applicable	
Electro-optical filter, unsymmetric sampling	400	8	1	4	0.8

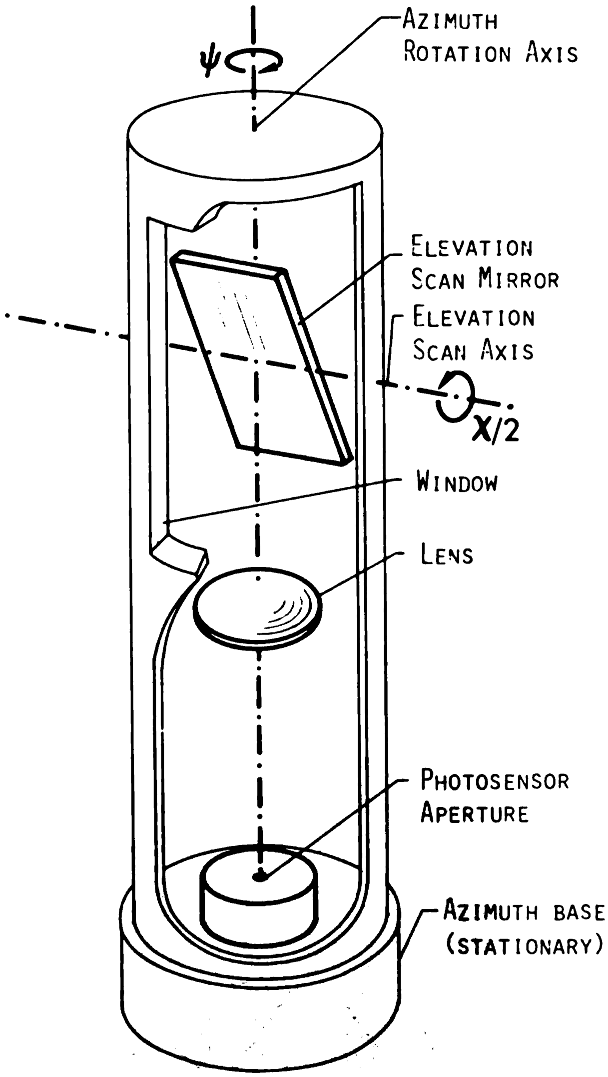

Figure 1.- Basic facsimile-camera configuration.

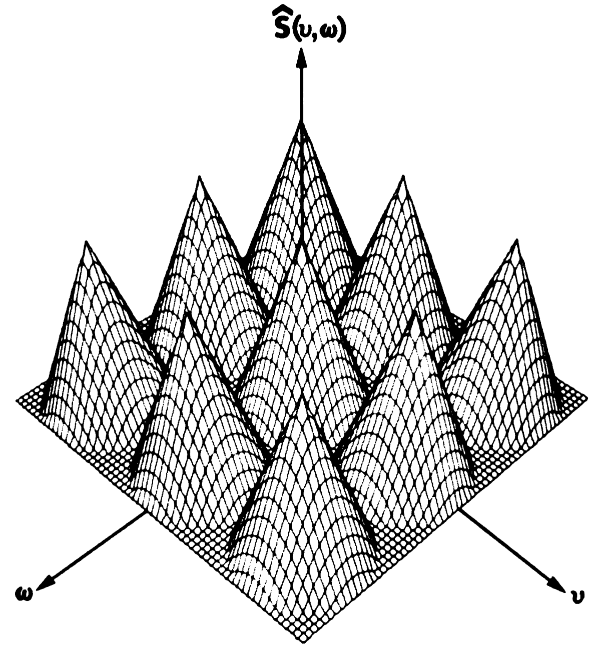

(a) Sufficient sampling.

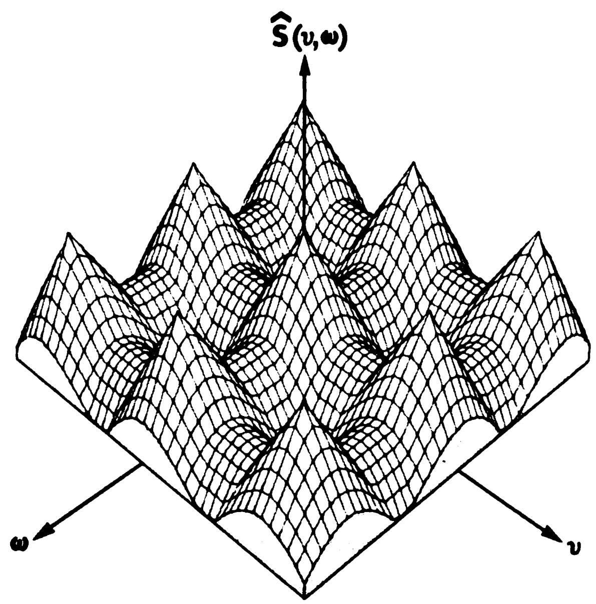

(b) Insufficient sampling.

Figure 2.- Frequency spectrum generated by the optical-mechanical line-scan imaging process.

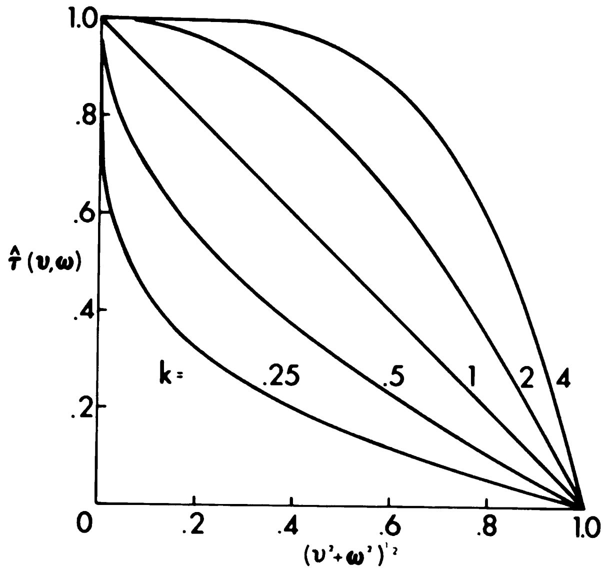

Figure 3.- Simplified frequency-response shapes.

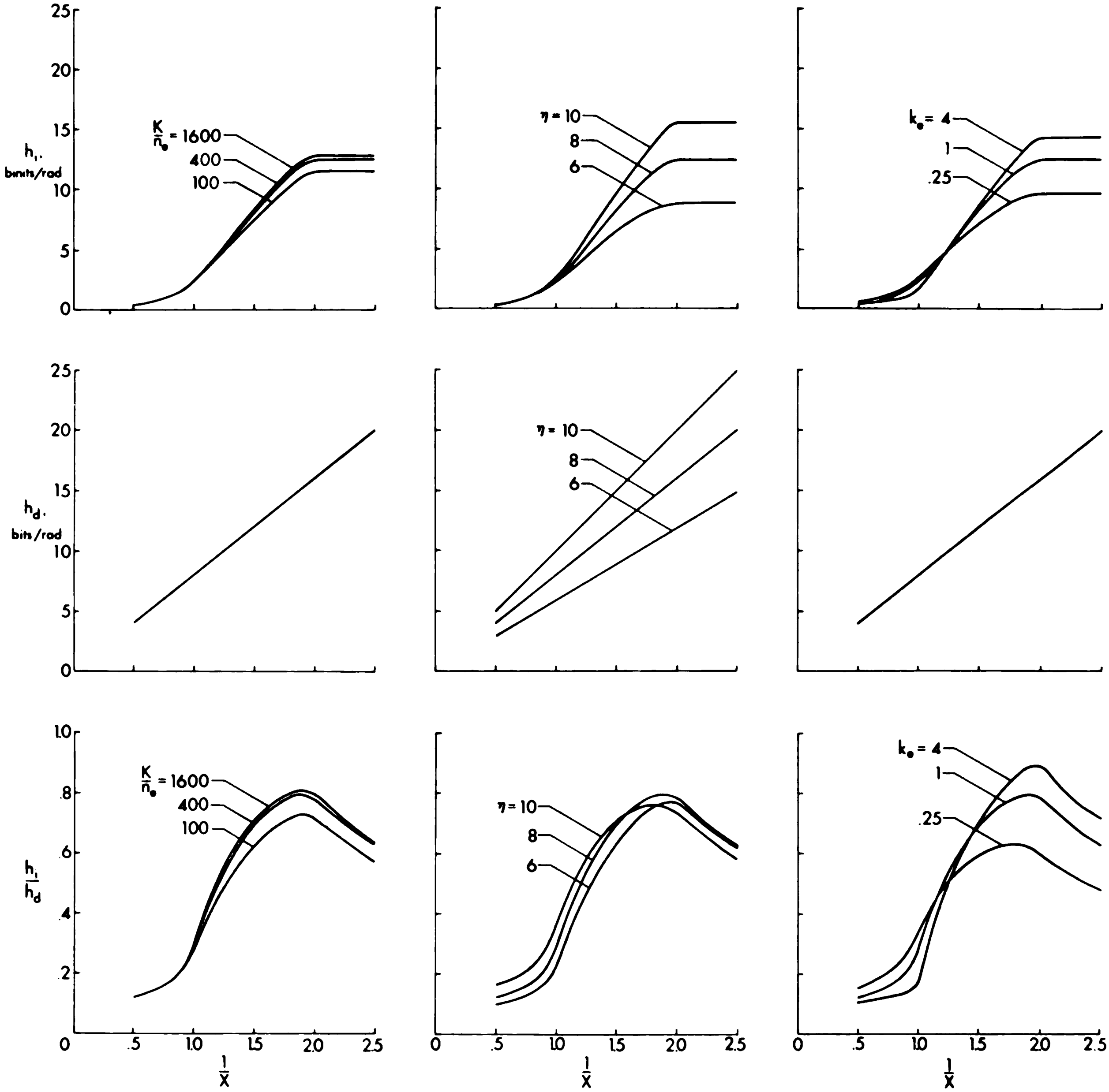

(a) $k_e = 1$; $\eta = 8$ bits.

(b) $K/n_e = 400$; $k_e = 1$.

(c) $K/n_e = 400$; $\eta = 8$ bits.

Figure 4.- Variation of information capacity h_i, data density h_d, and information efficiency h_i/h_d with sampling rate $1/X$ for electrical filters.

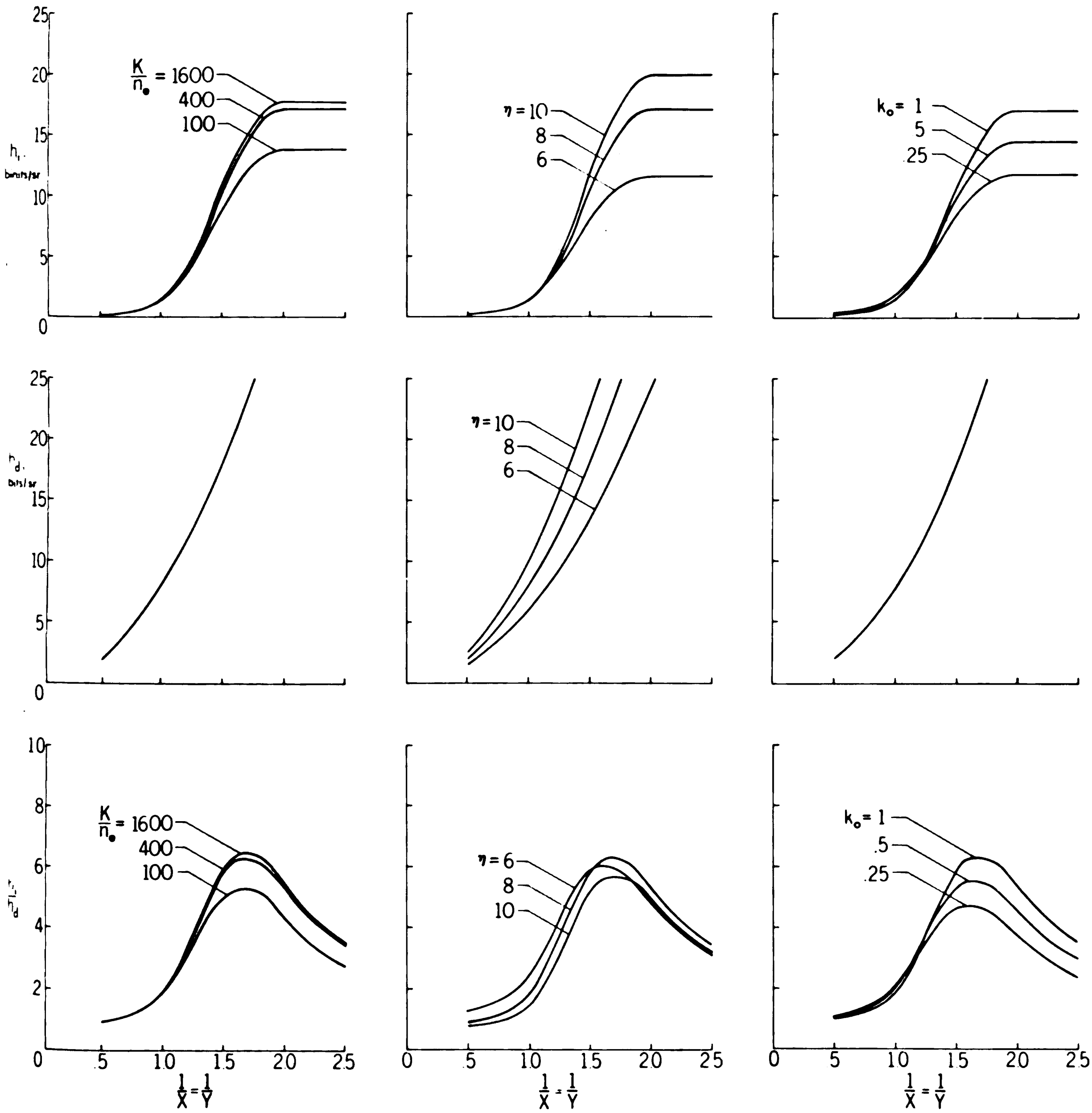

(a) $k_o = 1$; $\eta = 8$ bits.

(b) $K/n_e = 400$; $k_o = 1$.

(c) $K/n_e = 400$; $\eta = 8$ bits.

Figure 5.- Variation of information capacity h_i, data density h_d, and information efficiency h_i/h_d with symmetric sampling rates $1/X = 1/Y$ for optical filters.

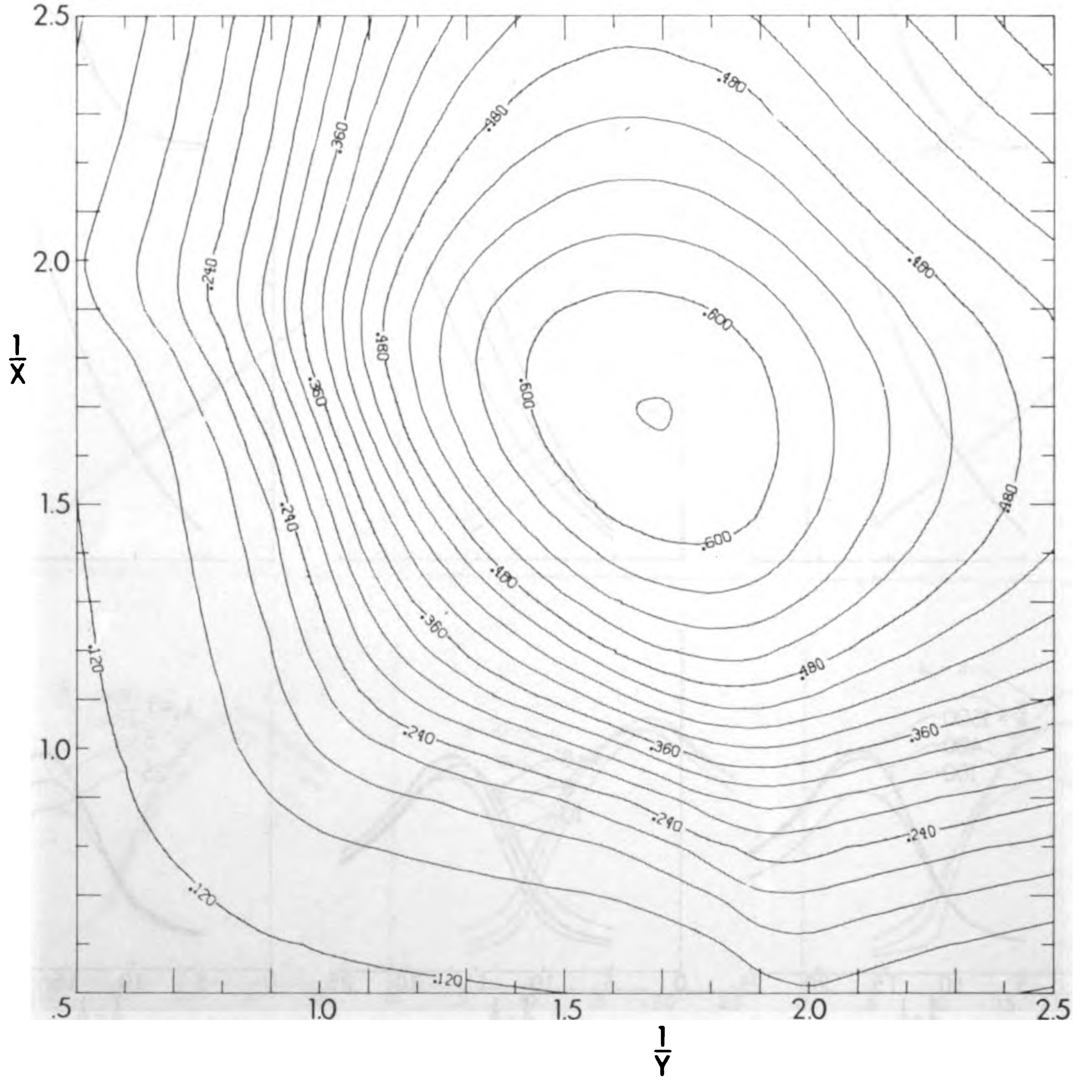

Figure 6.- Contour plot of information efficiency h_i/h_d as a function of sampling rates $1/X$ and $1/Y$ for optical filters. $K/n_e = 400$; $\eta = 8$ bits; and $k_o = 1$.

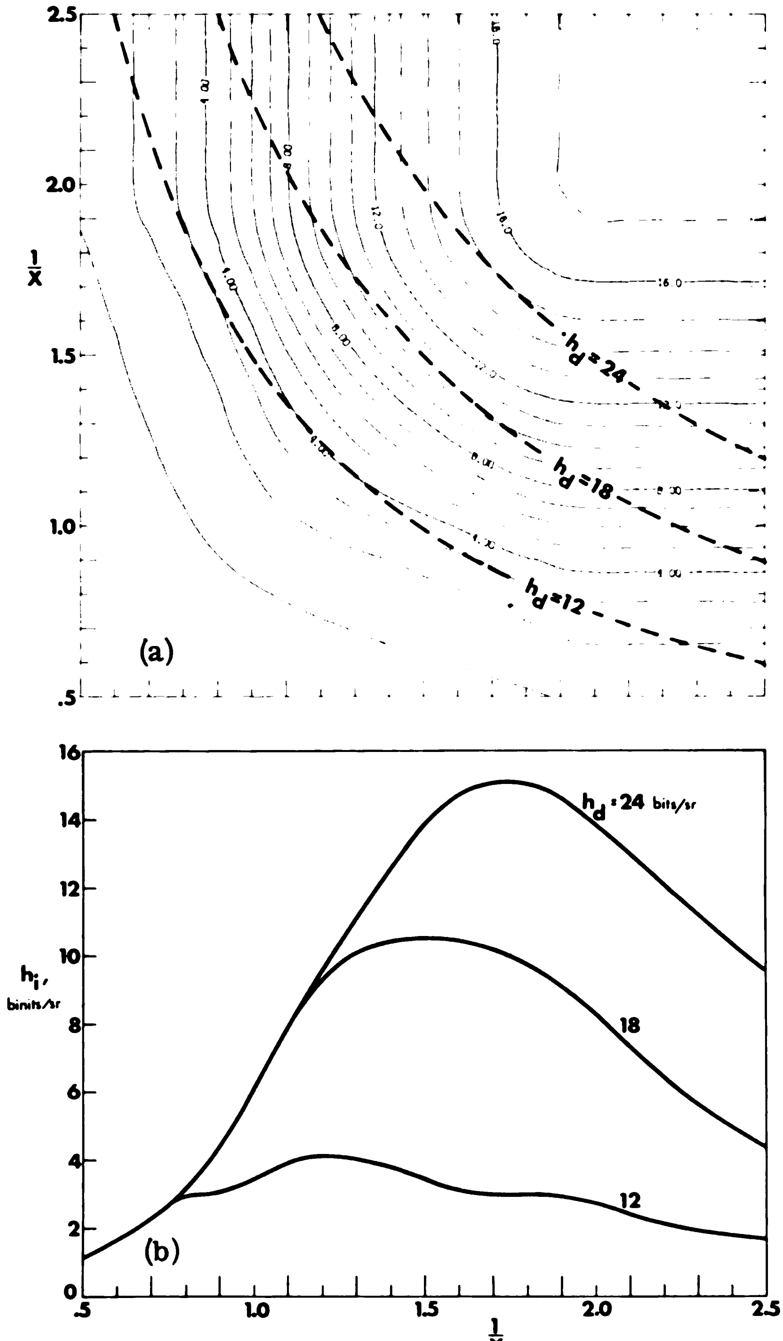

(a) Contour plot of information capacity h_i and three contours of constant data density h_d as a function of sampling rates $1/X$ and $1/Y$.

(b) Plot of h_i along the three contours of constant h_d against sampling rate $1/Y$.

Figure 7.- Plots of information capacity for optical filters. $K/n_e = 400$; $\eta = 8$ bits; and $k_o = 1$.

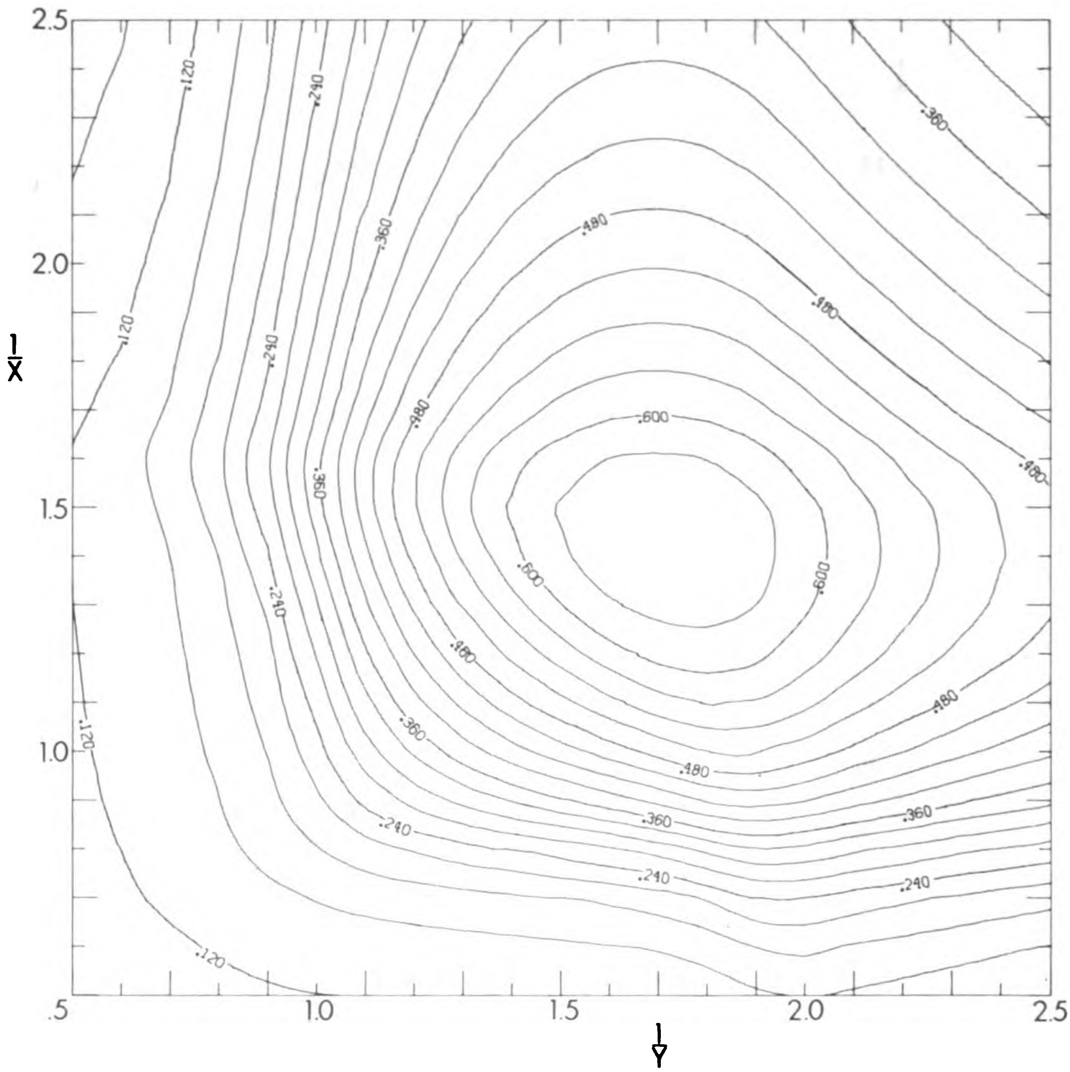

Figure 8.- Contour plot of information efficiency h_i/h_d as a function of sampling rates $1/X$ and $1/Y$ for electro-optical systems. $K/n_e = 400$; $\eta = 8$ bits; $k_o = 1$; $k_e = 4$; and $\upsilon_e = 0.8$.

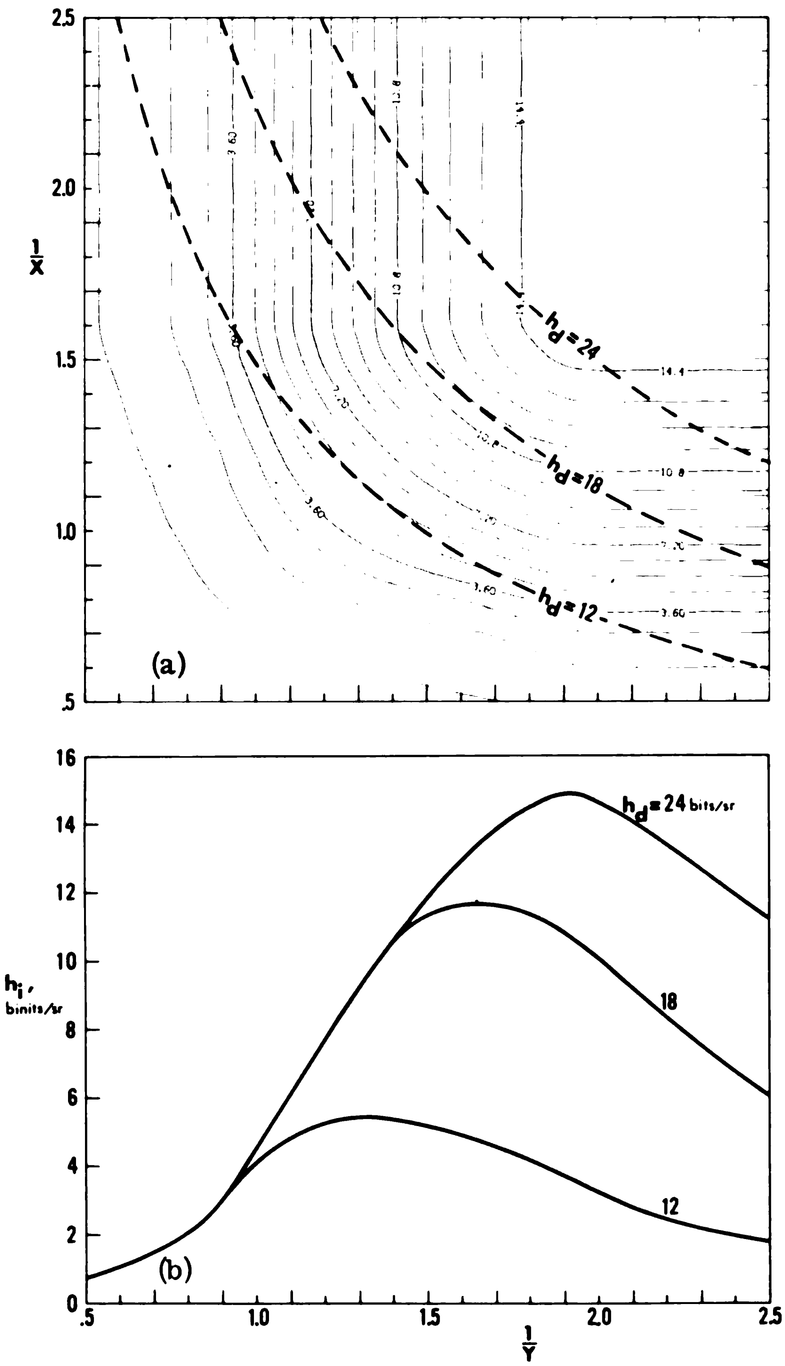

(a) Contour plot of information capacity h_i and three contours of constant data density h_d as a function of sampling rates $1/X$ and $1/Y$.

(b) Plot of h_i along the three contours of constant h_d against sampling rate $1/Y$.

Figure 9.- Plots of information capacity for electro-optical systems. $K/n_e = 400$; $\eta = 8$ bits; $k_o = 1$; $k_e = 4$; and $\upsilon_e = 0.8$.

NATIONAL AERONAUTICS AND SPACE ADMINISTRATION
WASHINGTON, D.C. 20546

OFFICIAL BUSINESS
PENALTY FOR PRIVATE USE $300

SPECIAL FOURTH-CLASS RATE
BOOK

POSTAGE AND FEES PAID
NATIONAL AERONAUTICS AND
SPACE ADMINISTRATION
451

U.S.MAIL

732 001 C1 U AL 750711 S00606HU
UNIV OF MICHIGAN
ENGINEERING LIBRARY
ATTN: MR ROBERT T FREESE
ANN ARBOR MI 48104

POSTMASTER: If Undeliverable (Section 158 Postal Manual) Do Not Return

---

"The aeronautical and space activities of the United States shall be conducted so as to contribute . . . to the expansion of human knowledge of phenomena in the atmosphere and space. The Administration shall provide for the widest practicable and appropriate dissemination of information concerning its activities and the results thereof."

—NATIONAL AERONAUTICS AND SPACE ACT OF 1958

NASA SCIENTIFIC AND TECHNICAL PUBLICATIONS

TECHNICAL REPORTS: Scientific and technical information considered important, complete, and a lasting contribution to existing knowledge.

TECHNICAL NOTES: Information less broad in scope but nevertheless of importance as a contribution to existing knowledge.

TECHNICAL MEMORANDUMS: Information receiving limited distribution because of preliminary data, security classification, or other reasons. Also includes conference proceedings with either limited or unlimited distribution.

CONTRACTOR REPORTS: Scientific and technical information generated under a NASA contract or grant and considered an important contribution to existing knowledge.

TECHNICAL TRANSLATIONS: Information published in a foreign language considered to merit NASA distribution in English.

SPECIAL PUBLICATIONS: Information derived from or of value to NASA activities. Publications include final reports of major projects, monographs, data compilations, handbooks, sourcebooks, and special bibliographies.

TECHNOLOGY UTILIZATION PUBLICATIONS: Information on technology used by NASA that may be of particular interest in commercial and other non-aerospace applications. Publications include Tech Briefs, Technology Utilization Reports and Technology Surveys.

Details on the availability of these publications may be obtained from:

SCIENTIFIC AND TECHNICAL INFORMATION OFFICE

NATIONAL AERONAUTICS AND SPACE ADMINISTRATION

Washington, D.C. 20546

NASA TECHNICAL NOTE

NASA TN D-7943

NASA TN D-7943

AEROTHERMAL PERFORMANCE AND STRUCTURAL INTEGRITY OF A RENÉ 41 THERMAL PROTECTION SYSTEM AT MACH 6.6

William D. Deveikis, Robert Miserentino,
Irving Weinstein, and John L. Shideler
Langley Research Center
Hampton, Va. 23665

NATIONAL AERONAUTICS AND SPACE ADMINISTRATION • WASHINGTON, D. C. • NOVEMBER 1975

1. Report No.	2. Government Accession No.	3. Recipient's Catalog No.
NASA TN D-7943		

4. Title and Subtitle	5. Report Date
AEROTHERMAL PERFORMANCE AND STRUCTURAL INTEGRITY OF A RENÉ 41 THERMAL PROTECTION SYSTEM AT MACH 6.6	November 1975
	6. Performing Organization Code
7. Author(s)	8. Performing Organization Report No.
William D. Deveikis, Robert Miserentino, Irving Weinstein, and John L. Shideler	L-9945
	10. Work Unit No.
9. Performing Organization Name and Address	506-17-22-01
NASA Langley Research Center Hampton, Va. 23665	11. Contract or Grant No.
	13. Type of Report and Period Covered
12. Sponsoring Agency Name and Address	Technical Note
National Aeronautics and Space Administration Washington, D.C. 20546	14. Sponsoring Agency Code

15. Supplementary Notes

16. Abstract

A flightweight (10.6 kg/m^2 (2.18 lb/ft^2)) 106.7 by 148.3 cm (42.0 by 58.4 in.) panel based on a metallic thermal-protection-system concept for hypersonic and reentry vehicles was subjected repeatedly to thermal cycling by quartz-lamp radiant heating using a thermal history representative of a reentry heat pulse and to aerodynamic heating at heating rates required to sustain a surface temperature of 1089 K (1960° R). The panel consisted of a corrugated heat shield and support members of 0.05-cm (0.02-in.) thick René 41 of riveted construction and 5.08-cm (2-in.) thick silica fibrous insulation packages covered by René 41 foil and inconel screening. All tests were conducted in the Langley 8-foot high-temperature structures tunnel with the heat-shield corrugations alined in the stream direction. Nominal free-stream Mach number was 6.6, and free-stream unit Reynolds number was 5.118×10^6 per meter (1.56×10^6 per foot). Local Mach numbers were from 6.2 to 4.4; surface pressures were from 3.5 to 11.7 kPa (0.5 to 1.7 psia); and local dynamic pressures were from 97 to 158 kPa (14 to 23 psi). The panel sustained 5.33 hr of intermittent radiant heating and 6.5 min of intermittent aerodynamic heating of up to 1-min duration for differential pressures up to 6.2 kPa (0.9 psi) with no apparent degradation of thermal or structural integrity, as indicated by temperature distributions and results from load-deflection tests and vibration surveys of natural frequencies.

17. Key Words (Suggested by Author(s))	18. Distribution Statement
Thermal protection system Hypersonic Corrugated surface Turbulent heat transfer	Unclassified – Unlimited Subject Category 18

19. Security Classif. (of this report)	20. Security Classif. (of this page)	21. No. of Pages	22. Price*
Unclassified	Unclassified	98	$4.75

*For sale by the National Technical Information Service, Springfield, Virginia 22161

CONTENTS

Page

AEROTHERMAL PERFORMANCE AND STRUCTURAL INTEGRITY OF A RENÉ 41 THERMAL PROTECTION SYSTEM AT MACH 6.6

William D. Deveikis, Robert Miserentino, Irving Weinstein,
and John L. Shideler
Langley Research Center

SUMMARY

A flightweight (10.6 kg/m^2 (2.18 lb/ft^2)) 106.7 by 148.3 cm (42.0 by 58.4 in.) panel of a corrugated René 41 thermal-protection-system concept for hypersonic and reentry vehicles was subjected to both radiant and aerodynamic heating in order to evaluate its thermal performance and structural integrity. The panel consisted of 0.05-cm (0.02-in.) thick heat shield and support members of riveted construction and 5.08-cm (2-in.) thick silica fibrous insulation packages covered with René 41 foil and inconel screening. It was designed to carry a uniform pressure of 20.7 kPa (3 psia) at a surface temperature of 1089 K (1960° R). Test goal was to protect a stainless-steel substructure from temperatures above 422 K (760° R) for 28 min. All tests were conducted in the Langley 8-foot high-temperature structures tunnel with the heat-shield corrugations alined in the stream direction. Nominal free-stream Mach number was 6.6, and free-stream unit Reynolds number was 5.118×10^6 per meter (1.56×10^6 per foot). Angle of attack was varied to produce local Mach numbers from 6.2 to 4.4, surface pressures from 3.5 to 11.7 kPa (0.5 to 1.7 psia), and local dynamic pressures from 97 to 158 kPa (14 to 23 psi). The panel sustained 5.33 hr of intermittent radiant heating and 6.5 min of intermittent aerodynamic heating of up to 1-min duration for differential pressures up to 6.2 kPa (0.9 psi) following radiant preheating. In addition, the panel endured tunnel start and shutdown acoustic loading of up to 157 dB for about 30 sec per test.

The panel suffered no apparent degradation of thermal or structural integrity and was tolerant of abuses from electrical arcing, water impingement on the hot surface, and accelerations up to 12g. The largest measured change in panel natural frequency was 6 Hz (3.5 percent). During radiant heating, the substructure temperature limit occurred 26 min after heating started, and panel thermal performance was predictable with reasonable accuracy. During aerodynamic heating, temperature-rise rates on support members approximated those obtained under radiant heating. However, as expected, thermal performance degraded when hot gases from the boundary layer were unrealistically forced through the panel interior. For the heating and loading conditions of the tests, analysis indicated stress concentrations within yield-stress limits but higher than the proportional

limit. The stress concentrations were located in the angles formed by the juncture of pairs of legs on the truss-shaped support members. Results of the investigation identified areas for improving panel design to enhance concept suitability for flight application.

INTRODUCTION

Hypersonic cruise and reentry vehicles (such as Space Shuttle) will require lightweight thermal protection systems that should endure many flights before requiring refurbishment. However, as reported in references 1 and 2, these systems present critical technological deficiencies in terms of materials, reuse potential, and, hence, economical refurbishment. Consequently, NASA has initiated a major effort to develop the necessary design technology for suitable thermal protection systems. As part of this effort, the Langley Research Center, through experiment and analysis, is evaluating several full-scale, flightweight panels of metallic and nonmetalic concepts. (See, for example, ref. 3.) Experimentally, thermal performance and structural integrity are assessed from repeated exposures to two types of heating. One type is radiant heating from quartz lamps for exposure times up to approximately 1/2 hr using a surface-temperature history representative of a reentry heat pulse from Earth orbit. The other type is aerodynamic heating with associated pressure loading for exposure times up to 1-min duration in the hypersonic stream of the Langley 8-foot high-temperature structures tunnel. Analytical tools employed are a finite-difference computer program (ref. 4) for thermal analysis and a finite-element computer program (ref. 5) for stress analysis.

The present investigation was the first of the series conducted and, therefore, served the twofold purpose of evaluating a metallic (René 41) thermal protection system and of verifying the test techniques (ref. 6) that were developed for the present evaluation program. The panel used was a corrugated heat shield with insulation packages. It was designed for service on a reentry surface where temperatures reach approximately 1089 K (1960° R), as depicted in figure 1, and to protect the load-carrying substructure from temperatures above 422 K (760° R). The metallic heat-shield design was based on a multisupported concept reported in reference 7. Its configuration is convenient for covering large areas uninterrupted by longitudinal (streamwise) panel-to-panel joints. Hence, the number of places requiring sealing against inflow of hot boundary-layer gases is minimized. Therefore, for the present investigation, the prime requirements were (1) to design and fabricate a panel which covered the largest area that could be accepted by the test fixture and (2) to test only for thermal and structural response. The resulting panel had no transverse (spanwise) thermal expansion joints, and problems of sealing the edges and the representation of a thermally realistic substructure were not addressed.

Prior to thermal testing, the structural characteristics of the panel were determined from static load-deflection tests and vibration surveys. Upon completion of these tests, the panel was subjected to the radiant-heating and aerodynamic-heating tests which were to be conducted alternately. Occasionally, panel structural integrity was checked by additional vibration surveys. For the aerodynamic-heating tests, nominal free-stream conditions were: Mach number, 6.6; total temperature, 1722 K (3100° R); and unit Reynolds number, 5.1×10^6 per meter (1.56×10^6 per foot). Surface temperatures, temperature distributions through the panel, surface deformations, natural frequencies, and results from thermal and stress analyses are presented herein. The test and analytical results are used to assess the thermal and structural performance of the thermal protection system and to identify potential areas for improving its design.

SYMBOLS

Values are given both in SI Units and in U.S. Customary Units. The measurements and calculations were made in U.S. Customary Units.

a panel length between supports in x-direction (streamwise)

D_x panel bending stiffness in x-direction (fig. 7)

F reaction force, N (lb)

f frequency, Hz

$K_d = \frac{k_d a^3}{D_x}, K_r = \frac{k_r a}{D_x}, K_t = \frac{k_t a}{D_x}$ nondimensional deflection, rotational, and torsional spring constants, respectively

k_d, k_r, k_t deflectional, rotational, and torsional spring constants, respectively, per unit length

l panel length, cm (in.)

M Mach number

m number of half-waves in x-direction (streamwise, fig. 7) between adjacent supports

n number of half-waves in y-direction (transverse to stream, fig. 7) over width of panel

p	pressure, Pa (psia)
q	dynamic pressure, Pa (psi)
R	Reynolds number
T	temperature, K (^{o}R)
t	time, sec
w	panel width, cm (in.)
x,y,z	panel coordinates (see fig. 7), cm (in.)
α	angle of attack, deg
β	compressibility parameter, $\sqrt{M^2 - 1}$
Δp	differential-pressure load on panel, Pa (psi)
δ	deflection, cm (in.)
σ	stress, Pa (psi)

Subscripts:

b	base of panel holder
l	local condition at edge of boundary layer
max	maximum
t	total condition in combustor
tu	tensile ultimate
ty	tensile yield
∞	free stream

PANEL, PANEL HOLDER, AND INSTRUMENTATION

Thermal-Protection-System Panel

Description and design. - The thermal-protection-system panel used in the present investigation is shown attached to a substructure of stainless-steel hat-section members in figure 2. The panel consisted of the following components: A rectangular René 41 sheet-metal heat shield with 60° circular-arc corrugations that ran longitudinally (streamwise); four continuous René 41 transverse support members that were alined laterally (spanwise); 14 René 41 V-shaped center support members that were oriented longitudinally; and a set of insulation packages placed at the bottom of the support members. Heat shield and support members were joined by rivets. The support members were arranged so that they divided the heat shield into bays of approximately equal length. Stainless-steel screening was placed across the hat-section members to take the place of a substructure wall and thus to support the insulation packages. For the present installation, the packages were tied to the screening with nickel chromium (Nichrome) wire. The support members were bolted directly to the hat-section members through holes cut in the screening. Combined unit mass of the heat shield and support members was approximately 6.4 kg/m^2 (1.30 lb/ft^2). Total unit mass of the thermal protection system was 10.6 kg/m^2 (2.18 lb/ft^2). Masses of panel elements are itemized in table I.

The simplicity of the heat-shield design and its low mass are attractive features of this system. Its configuration absorbs lateral thermal displacements and therefore obviates the need for heavy, built-up transverse beams. Thus, the corrugations in the heat shield allow free lateral thermal expansion, and flexible bents at the top and bottom of the transverse support members allow nearly unrestrained longitudinal thermal growth. The center supports carry the aerodynamic drag loads. In designing the heat shield, corrugation radius was governed by the stiffness needed to beam the loading produced by aerodynamic surface pressures to the support members. The support members were sized to carry a uniform pressure of 20.7 kPa (3 psia) at a temperature of 1089 K (1960° R) without buckling as columns and without yielding. Design calculations were based on temperature-dependent material properties given in appendix A.

Fabrication details. - The panel was fabricated from materials on hand. René 41 components were cut and die-formed from 0.05-cm (0.02-in.) thick sheet that, as a result of uncertainties in material properties, had been re-solution treated for 2 hours in air at 1339 K (2410° R). Cutting and forming operations were performed without difficulty. The components were then aged 4 hr in air at 1172 K (2110° R) and air cooled. Formed configurations did not distort during the aging process. Inasmuch as the properties of the René 41 material can be adversely affected by reactions with elements in other materials, including body chemicals (see ref. 8), the heat shield and support members were both freon and ultrasonically cleansed before aging and after assembly; degreased tools and rivets were used in assembling the components; and surgical rubber gloves were worn when components were handled.

Heat-shield details and dimensions are sketched in figure 3. The heat shield was 148.3 cm (58.4 in.) long and 106.7 cm (42.0 in.) wide. It contained 13 corrugations separated by narrow flat sections spaced at 8.01-cm (3.154-in.) intervals. Corrugation radius and height were 5.9 cm (2.32 in.) and 0.8 cm (0.31 in.), respectively. Inasmuch as there was no single sheet on hand large enough for the heat shield, two pieces of sheet were required to make up its width. The two pieces were overlapped along a flat section and were joined by two staggered rows of spotwelds spaced 1.27 cm (0.5 in.) apart. The spotwelds in each row were 0.64 cm (0.25 in.) apart. Five holes were drilled and dimpled through the heat shield along the center line of each flat at intervals of 35.56 cm (14 in.) to provide 70 attachment points for the support members. Each attachment point was reinforced by a 0.05-cm (0.02-in.) thick René 41 doubler approximately 2.03 cm (0.8 in.) square. Each doubler was spotwelded in four places to the underside of the heat shield.

The support members are sketched in figure 3(b) and are shown photographically in figure 4. The transverse support members were reinforced by 0.05-cm (0.02-in.) thick René 41 right-angle elements riveted at every attachment as illustrated in figure 3(b) and shown in figure 4(a). These elements prevented the introduction of eccentric loads at the top of the column-type supports and provided the desired stiffness in bending at the bottom. The center support members were assembled to give the box configuration shown in figure 4(b) for torsional stiffness in taking out the aerodynamic drag loads. The box configuration was obtained by overlapping and spotwelding top and bottom flanges of individual center support sections together at four places. All support members were attached to the heat shield with 0.40-cm (0.16-in.) diameter, A-286 stainless-steel countersunk blind rivets. The right-angle reinforcing elements were attached with brazier head rivets. This type of rivet was used in order to observe effects of aerodynamic heating on protruding rivet heads. Anchor nuts were fastened to the bottom flanges on all support members for convenient attachment to the hat-section substructure members. The hat sections were formed from 0.13-cm (0.05-in.) thick, type 347 stainless steel. Anchor nuts were fastened to the flanges of the hat sections for convenient attachment to the test fixture.

Insulation package.- In order to satisfy the requirement limiting substructure temperature to 422 K (760° R) after an exposure time of approximately 1/2 hr at a surface temperature of 1089 K (1960° R), a 5.08-cm (2-in.) thickness of layered silica fibrous (Micro-Quartz) insulation having a density of 67 kg/m^3 (4.2 lb/ft^3) was used in packages tailored to fit snugly between support members, as shown in figure 5. Rectangular packages were used between transverse support members, but the center packages were notched to fit around the center support members. A ship lap joint was also provided on the center packages as a means of interrupting a direct radiation path to the panel interior. Small packages were constructed to fit inside the box of the center support members. Photographs of insulation packages are shown in figure 6. The insulation material was enclosed in envelopes constructed of 200-mesh screen made of Inconel 650 on the sides and undersurface and a 0.005-cm (0.002-in.) thick René 41 foil reflector surface on the top as shown in figure 5 and in the photograph of figure 6(b). The screening provided soft corners and sides to fit around the legs of support members and also permitted package venting during the rapid pressure changes of the wind-tunnel start and shutdown periods. The envelopes were assembled by spotwelding. Each package was made up of 12 layers of insulation. Wafers of a single layer of insulation were inserted between the layers along two rows on approximately 12.7 cm (5 in.) centers as shown in the photograph of figure 6(a). These wafers provided "hard" points for attaching the package to the substructure screening (fig. 2(b)) and aided in maintaining overall package thickness. The "hard" points were capped at the top and bottom by 0.005-cm (0.002-in.) thick René 41 foil wafers that were held together with 0.05-cm (0.018-in.) diameter (26-gage) nickel chromium (Nichrome) wire looped through the package. Package weight was 4.3 kg/m^2 (0.88 lb/ft^2). A photograph of the fitted center packages is shown in figure 6(c).

Panel Holder

Description.- The panel was tested using the panel holder illustrated in figure 7. Details on the development of this test fixture are given in reference 9. The panel holder is rectangular in planform, 141 cm (55.4 in.) wide by 300 cm (118 in.) long, and is 30.5 cm (12 in.) deep. Its lower surface is bevelled 20° from the sharp leading edge. Exterior surfaces are covered with 2.54-cm (1-in.) thick Glasrock foam tiles which protect the internal structure from the aerodynamic heating environment produced in the wind tunnel. For wind-tunnel testing, the panel holder is sting mounted at its base. Test panels are mounted within a rectangular cavity 108 cm (42.5 in.) wide by 152 cm (60 in.) long located 102 cm (40 in.) downstream from the leading edge. Aerodynamic fences along the sides of the panel holder provide two-dimensional flow over the test area, and a boundary-layer trip of 0.24-cm (0.094-in.) diameter stainless-steel spheres near the leading edge generates turbulent flow over the panel surface. Surface pressures and aerodynamic heating rates are varied by pitching the panel holder. Differential-pressure loading of the panel is controlled by regulating the cavity pressure under the panel by means of spring-loaded vent doors in the boxes shown at the base of the panel holder. Details of the differential-pressure control system are described in the section entitled "Differential-Pressure Control" and in reference 6.

Panel installation.- The panel and hat-section substructure assembly was bolted through six 7.62-cm (3-in.) steel channel beams that, in turn, were bolted to the leading- and trailing-edge walls of the cavity in the panel holder. Spacing of the beams was as shown in figure 7(a). The panel was inclined 0.3° to the panel-holder surface. It was mounted so that the crests of corrugations intersected the Glasrock surface at the leading edge and the flats between corrugations intersected the Glasrock surface at the trailing edge. Thus, the corrugations provided rearward-facing steps at the trailing edge, as shown in figure 7(b). Panel inclination was accomplished by using hat sections of different heights (see fig. 3). This orientation was chosen because it presented fewer aerodynamic problems, especially with respect to interference heating at the leading and trailing edges.

No attempt was made to close the open corrugations at the trailing edge. Thus, the openings provided a natural interior venting capability in the event that the differential-pressure control system would not perform as expected. (The differential-pressure control system was to be proof tested in the present test program.) Total vent area of the open corrugations was 41.3 cm^2 (6.4 in^2). Panel side edges and the ends of the flat surfaces at the trailing edge rested on a frame formed by the flanges of René 41 closeouts configured as shown in figure 8. The closeouts (fig. 8(a)) were 0.05 cm (0.02 in.) thick and were bolted to the side and trailing-edge walls of the cavity. The leading edge of the heat shield was covered by the seal and fairing unit shown in figure 8(b). The flat sections between the corrugation closeouts ramped down from the Glasrock to the flats on the heat shield. In order to avoid separation of the leading-edge fairing from the heat-shield surface by thermal distortion, the crests of the fairing and the heat shield were clamped by a round-head rivet. As illustrated in figure 8(c), relative motion from thermal expansion between the fairing and heat-shield leading edge was allowed by slots cut in the crests of the fairing. A view of the panel and panel holder in the test chamber of the wing tunnel is shown in figure 9.

Instrumentation

Panel temperatures were sensed by eighty-two 30-gage, chromel-alumel thermocouples. Forty-six thermocouples were distributed over the back surface of the heat shield as shown in the sketch of figure 10; 30 were spaced at 2.54-cm (1-in.) intervals down the legs of the seven support members indicated in figure 10 by letter designations; four were placed inside the insulation package near the center of the panel – one each near the upper and lower surfaces and two at half depth; and two were used for sensing the air temperature within the cavity under the hat sections. Where temperatures were expected to be very hot, as on the heat shield and support members, stainless-steel-sheathed thermocouple assemblies were used. A typical thermocouple installation on the heat shield can be seen in the photograph of figure 4(a). The ends of the thermocouple wires were alined normal to the flow direction and were spotwelded to the heat shield to form the junction. The wires were slacked to allow for thermal growth of the heat shield and passed through a two-hole ceramic bead to maintain separation of the wires. The sheathing was strapped to the heat shield with small strips of stainless-steel foil that were spotwelded to the heat shield. It was then routed down the legs of support members and joined to glass-cloth-covered thermocouple extension wiring below the insulation package where temperatures were expected to be cooler. The thermocouple installation technique on the legs of support members was similar to that on the heat shield. Glass-cloth-covered thermocouple wires were used in the insulation packages. For that installation, individual thermocouple wires were spotwelded to 0.94 by 5.08 cm (0.37 by 2.0 in.) strips of 0.04-cm (0.016-in.) thick René 41 sheet. These strips were then placed between layers of insulation at the desired depth.

In addition to the use of thermocouples, detailed coverage of surface temperatures during aerodynamic heating was obtained remotely by means of infrared radiometry. The radiometer was located outside the test stream about 183 cm (72 in.) above the center of the heat shield and scanned a 76.2 cm (30 in.) square, as shown in figure 10. This area was surveyed by 150 scanlines every 5 sec. Details of the radiometer are reported in reference 6.

Six high-temperature (922 K (1660° R)) deflectometers that operated on the inductive principle were distributed under the heat shield, as shown by the circle symbols in figure 10, to sense static deflections and dynamic response of the heat shield. The deflectometers were mounted in stainless-steel holders that were bolted to the channel beams supporting the panel. The deflectometer face was set at a distance of 0.09 cm (0.035 in.) from the back surface of the heat shield. Deflectometer power supply units were housed in two nitrogen-gas-cooled containers located between the pairs of channel beams.

Surface pressures were measured at four orifices spaced around the periphery of the panel-holder cavity and one orifice in the Glasrock 8.57 cm (3.38 in.) upstream of the cavity leading edge. Also measured were the differential pressure between the surface and the airspace under the heat shield, the cavity static pressure under the hat sections, the panel-holder base pressure, and pitot pressure at the trailing edge of the heat shield. All these measurements were obtained from strain-gage pressure transducers connected to 0.15-cm (0.060-in.) inside diameter stainless-steel orifice tubing. The transducers were located in the cavity under the hat sections. Panel accelerations were measured with an accelerometer mounted under the panel near its center of gravity.

High-speed motion-picture cameras were used for photographing the heat shield during wind-tunnel tests, and still photography was used for recording panel surface appearance throughout the test series.

APPARATUS AND TESTS

Test Facility

The present tests were conducted in the Langley 8-foot high-temperature structures tunnel shown schematically in figure 11. This facility is a hypersonic blowdown wind tunnel that operates at a nominal Mach number of 7, at total pressures between 4.1 and 24.1 MPa (600 and 3500 psia), and at nominal total temperatures between 1389 and 2000 K (2500° and 3600° R). Corresponding free-stream unit Reynolds numbers are between 1×10^6 and 10×10^6 per meter (0.3×10^6 and 3.0×10^6 per foot). Within the operating envelope bounded by these conditions, the aerodynamic pressures and heating rates encountered in flight at Mach 7 in the altitude range between 25 and 40 km (80 000 and 130 000 ft) are obtained.

The high-energy test medium is the products of combustion of a mixture of methane and air which is burned within a pressurized combustion chamber. The combustion products are then expanded to the test-section Mach number through an axisymmetric contoured nozzle having an exit diameter of 2.4 m (8 ft). In the test section, the stream is a free jet with a usable test core approximately 1.2 m (4 ft) in diameter over a length of 4.3 m (14 ft) that is diffused and pumped to the atmosphere by means of a single-stage annular air ejector. Total temperature is controlled by regulating the fuel-to-air ratio. Air storage capacity is sufficient for run times up to 2 min. The combustion products are considered to be in chemical equilibrium and are oxidizing. Partial pressure of free oxygen is calculated to be 70 Pa (0.01 psia) over the range of stream conditions.

Test models are protected from adverse tunnel startup and shutdown transient loads by storing them in a pod below the test stream until the desired hypersonic flow conditions are established. The model is then inserted rapidly into the stream on a hydraulically actuated elevator having a mass of 13 608 kg (30 000 lbm) and can travel vertically over a distance of 2.1 m (7 ft) to the stream center line in 1 sec. A model pitch system provides a range of angles of attack up to $\pm 20^{\circ}$. Prior to tunnel shutdown, the model is withdrawn from the stream. Other details on this test facility are reported in reference 9.

Radiant Heaters

The present test program required the installation of two retractable, hydraulically actuated quartz-lamp radiators for thermal cycling and preheating the panel in the pod beneath the tunnel test chamber (ref. 6). Preheating was necessary because the relatively short aerodynamic exposure times available precluded obtaining desired temperature distributions through the panel. The radiators parted above the heat-shield longitudinal center line, retracted spanwise in opposite directions, as in the sketch of figure 12, and were transported on a steel framework carriage mounted on rails. Full travel time in each direction was 1 sec. Each radiator was made up of 10 gold-plated, water-cooled reflector units containing 16 tungsten filament quartz lamps rated at 2000 W. Lamp distance above the model surface was 10.2 cm (4 in.). This distance was dictated both by the height of the aerodynamic fences on the sides of the panel holder and by what was believed to be the minimum allowable clearance that would preclude arcing to the heat shield at the reduced pressures during wind-tunnel operations.

Both radiators were divided into three zones. Voltage to the outer zones was ratioed to the center zones to give the desired surface temperature distribution. An ignitron tube power supply controlled by a closed loop servosystem continuously compared the output from a heat-shield thermocouple and the desired temperature input which was plotted on a time-based curve. Three-phase electrical power was distributed to the lamps through a system of rubber-covered copper cables that were wrapped in glass tape behind the reflector units. Maximum power capacity available was 1 mW.

Acoustic and Buffet Protection

A pair of retractable baffles shown in figure 13 was mounted to the carriage of the quartz-lamp radiators to shield the panel from potentially damaging acoustic pressures that occur during tunnel startup and shutdown and from severe buffeting associated with abnormal shutdowns. Under the baffles, the acoustic energy is attenuated approximately from 168 dB to 157 dB over the range of combustor pressures for which the flow is subsonic. Other details on the baffles are given in reference 6.

Differential-Pressure Control

Provision for varying the differential-pressure loading normal to the panel surface was built into the panel holder both as a means of protecting the panel during tunnel startup and shutdown and of extending the range of test variables. The differential-pressure control system consists of spring-loaded vent and fill doors at the base of the panel holder, as shown in figures 7 and 14, and a supply of nitrogen gas. On tunnel start, the vent doors allow the pressure within the cavity to follow the test-chamber evacuation rate of 41.4 kPa (6.0 psia) per second. On tunnel shutdown, the fill doors allow the pressure in the cavity to follow the test-chamber compression rate of up to 1 atmosphere per second. With this system, either positive (inward acting) or negative (outward acting) differential-pressure loading can be applied when the panel is in the stream. Positive differential pressures as high as 17.2 kPa (2.5 psi) are achievable by varying angle of attack up to -18° and venting cavity pressure to panel-holder base pressure. Differential pressure can also be varied between positive and negative values independently of angle of attack by locking the vent doors closed and pumping nitrogen gas into the cavity. The door locks are pneumatically actuated pins.

Tests

Panel evaluation test program.- The present investigation focused on panel structural and thermal response during repeated exposures to both radiant and aerodynamic heating to observe cumulative effects of cyclic heating. Structural response was evaluated by comparing structural static and dynamic characteristics of the panel before and after the heating tests. These characteristics were determined from static load-deflection tests and vibration surveys of natural frequencies. Panel structural integrity was monitored during the heating test series by means of visual inspections, surface mapping, and vibration surveys. Details of the procedures, apparatus, and results from the characterization tests are presented in appendix B.

In the heating tests, the panel was subjected to the three types of surface heating profiles shown in figure 15. The profile of figure 15(a) illustrates a radiant heating thermal cycle. This profile approximated the surface temperature encountered during a reentry heat pulse from Earth orbit (ref. 10). The profile of figure 15(b) illustrates a combined radiant preheating and aerodynamic-heating (aerothermal) test. These two types of tests were interspersed throughout the test series. The profile of figure 15(c) illustrates an aerothermal shock test in which the panel was not preheated. This type of test was conducted to observe panel response to the most severe test that could be applied. A summary of all of the tests is presented in table II.

Thermal cycle.- For thermal cycling events (fig. 15(a)), the radiant heaters were programed to allow heatup and cooldown of the heat shield at a rate of 2.8 K/sec (5° R/sec) to 1089 K (1960° R) and to maintain a constant surface temperature for periods up to 28 min. However, surface cooldown was to commence when the substructure temperature reached 422 K (760° R). The programed cooldown rate was maintained by the radiant heaters until a surface temperature was reached below which natural (uncontrolled) cooling dominated.

Radiant-preheat—aerothermal test.- In the radiant-preheat—aerothermal test (fig. 15(b)), the heat shield was preheated at a rate of 2.8 K/sec (5° R/sec) to 1089 K (1960° R) and was maintained at that temperature until one of two desired temperature distributions through the panel was present. These were indicated when the substructure temperature reached either 311 K (560° R) or 422 K (760° R) and corresponded to distributions that occur early and late, respectively, in reentry. The panel was then exposed to the tunnel stream for as long as possible at conditions that would sustain the preheat surface temperature of 1089 K (1960° R). Surface cooldown following aerodynamic exposure was uncontrolled because arcing problems precluded use of the radiant heaters in the low-pressure environment of the tunnel prior to shutdown.

For these tests, the tunnel was started when the desired substructure temperature was reached. If nominal flow conditions could not be achieved, radiant heating was continued as in a thermal cycle. When the correct flow conditions were established, the procedure, as illustrated in figure 16, was to de-energize the quartz lamps, retract the radiators and acoustic baffles, and insert and simultaneously pitch the panel holder so that it attained the desired angle of attack on reaching the stream center line. At the end of aerodynamic exposure the procedure was reversed, and tunnel shutdown was initiated after the radiators and acoustic baffles covered the panel. The desired interval between radiator retraction and panel insertion was 5 sec for minimum interruption of panel heating. On insertion, the panel entered the edge of the stream 1 sec after the elevator began lifting and reached the stream center line after an additional second. Panel acceleration during insertion and withdrawal was usually approximately 6g.

A maximum duration tunnel run required operating at high total conditions. Consequently, the average combustor-chamber pressure was 18.2 MPa (2641 psia), and the average total temperature was 1762 K (3173° R). (Two tests, 4 and 11, table II, were inadvertently conducted at an average combustion pressure of 6.9 MPa (1005 psia).) Average free-stream Mach number was 6.6, and average free-stream unit Reynolds number was 5.1×10^6 per meter (1.56×10^6 per foot). For most tests, panel-holder angle of attack was -9°; its selection was based on the turbulent calibration data of reference 9 and an estimate of the heating rate required for the preheat surface temperature. However, during three tests (tests 26, 31, and 34, table II), panel-holder angle of attack was varied between -3° and -12° to obtain data on the variation of positive differential pressure with angle of attack. These tests resulted in local Mach numbers at the panel from 6.2 to 4.4, surface pressures from 3.5 to 11.7 kPa (0.5 to 1.7 psia), and local dynamic pressures from 97 to 158 kPa (14 to 23 psi). In tests 26 and 31, the cavity pressure was vented to panel-holder base pressure. In test 34, the vent doors were closed and the cavity was pressurized to maintain an unloaded panel at various angles of attack.

Aerothermal shock test.- In the aerothermal shock test (fig. 15(c)), the panel was not preheated prior to its insertion into the tunnel stream. The test was conducted to evaluate panel response to transient aerodynamic heating. In addition, panel-holder angle of attack was increased in steps to approximately -12° to obtain data on the variation of positive differential-pressure loading with angle of attack with the vent doors closed and then was decreased to -9° for the remainder of aerodynamic exposure. Surface cooling after withdrawal was uncontrolled. The radiant heaters and acoustic baffles covered the panel during tunnel transient periods, and free-stream conditions were the same as for the radiant-preheat-aerothermal test.

Data Acquisition

During thermal cycles and preheat events, thermocouple output was recorded at a sampling rate of once every 2 sec. When the wind tunnel was operating, thermocouple and pressure-transducer outputs were recorded at a sampling rate of 20 per second.

Outputs from the infrared radiometer and deflectometers were recorded on FM tape. All data were reduced to engineering quantities at the Langley central digital data recording facility. Analytical quantities reported herein for the wind-tunnel tests are based on the thermal, transport, and flow properties of the combustion products test medium as determined from reference 11. Free-stream conditions in the test section were determined from reference measurements in the combustion chamber by using results from tunnel stream survey tests such as reported in reference 9. Local Mach number was obtained from oblique-shock relations.

RESULTS AND DISCUSSION

Summary of Panel Test Experience

The panel was tested in the sequence given in table II. As indicated, a positive differential pressure of 6.9 kPa (1 psi) was applied statically to the panel at the beginning and at the conclusion of the test series. In addition, the panel was vibrated to obtain up to nine natural frequencies on 17 occasions throughout the test series. (Results from these structural characterization tests are presented in appendix B.) The panel was also subjected to 12 thermal cycles at a surface temperature of 1089 K (1960° R), 10 radiant-preheat—aerothermal tests, and one aerothermal shock test. However, in attempting radiant-preheat—aerothermal tests, there were 21 false starts of the wind tunnel during which the panel did not enter the test stream but which resulted in 14 additional thermal cycles. For those events, the panel was simultaneously subjected to the effects of rapid test-chamber evacuation to near-vacuum conditions of 0.7 and 2.1 kPa (0.1 and 0.3 psia) and to tunnel start and shutdown acoustics under the baffles for about 30 sec per test.

Heat-shield and substructure temperature histories from all the heating tests are presented in sequential order in figure 17. The interrupted histories from tests 2 and 5 reflect intermittent electrical power failures to the quartz-lamp radiators, whereas the interrupted history from test 33 was deliberate in order to photograph the radiantly heated heat-shield surface. Environmental conditions and panel exposure times are summarized in table III for each type of heating test. Thus, the panel endured the following: 5.33 hr at a surface temperature of 1089 K (1960° R); 6.5 min in a Mach 6.6 stream that loaded the panel externally to differential pressures of up to 6.2 kPa (0.9 psi) while maintaining a surface temperature of 1089 K (1960° R); 12.9 min at low pressures resulting from 22 rapid test-chamber evacuations during preheating; and 81 excursions on the elevator that produced panel accelerations of up to 12g on a few occasions. (The high accelerations that exceeded the nominal value of 6g were inadvertent and occurred during calibration of the elevator control system.) Moreover, the heat shield was struck by electrical arcing from the quartz-lamp radiators during nearly every evacuation of the test chamber. On at least two insertions, a cloud of steam wiped along the hot surface as the panel entered the stream boundary layer and momentarily decreased heat-shield temperatures by about 22 K (40° R). In those instances, water leaking from the tunnel nozzle cooling system sprayed onto the Glasrock surface upstream of the panel prior to insertion. The panel survived the foregoing with no apparent degradation of structural integrity. Therefore, these tests revealed an attribute inherent in this rather simple, lightweight thermal-protection-system concept – namely, ruggedness.

Panel Thermal Performance

Thermal cycle.- Panel thermal performance under radiant heating is demonstrated in figure 18 by thermocouple data obtained near the center of the panel during test 17 (table III). Variations of temperature with time are shown in figure 18 for the heat shield at flat 8 (fig. 10) from thermocouple 11 located 18 cm (7 in.) upstream of the center of the panel, for center support A (fig. 10), for the substructure, for the air in the cavity under the substructure, and for the insulation package. Calculated temperatures of support A obtained from a thermal analysis of this panel (presented in appendix C) are superimposed for comparison with the experimental values (fig. 18). The calculations were based on the output of heat-shield thermocouple 11 which was used as the surface heating input to the computer program. The very good agreement obtained between experiment and calculation indicates that a complex structural configuration can be modeled to predict interior temperatures resulting from heat conduction through the depth of the structure with reasonable accuracy.

During surface heatup at 2.8 K/sec (5° R/sec), 265 sec elapsed before the substructure temperature began increasing. In the constant-temperature period, temperatures on center support A were about 56 K (100° R) lower than in the insulation package (compare temperatures at locations 3 and 4 in fig. 18), indicating that excessive heat was not conducted down the support member. At 1268 sec into the constant-temperature period, the substructure temperature limit of 422 K (760° R) was reached, and surface cooldown was initiated at a rate of 2.8 K/sec (5° R/sec). At that time, average heat-shield temperature was 1089 K (1960° R) within a spread of ±35 K (±63° R). At 185 sec into the cooldown period, the substructure temperature peaked at 429 K (773° R), and cooldown using the quartz-lamp radiators terminated because the programed cooldown rate exceeded the natural surface cooldown rate. Panel heating and cooling processes are illustrated in figure 19 by temperature distributions on center support member A. During the constant surface-temperature period (fig. 19(a)), the temperatures on the support member increased to the approximately linear distributions of different slope above and below the top of the insulation package, as shown by the data at the end of that period. During panel cooldown (fig. 19(b)), the maximum temperature moved toward the substructure. The shaded band in figure 19(a) indicates the spread in temperatures obtained down all instrumented support members at the end of the constant surface-temperature period. The width of the band reflects thermal response to variations in heat-shield temperature, to the heat-sink effect of the cavity walls, and to variations in the amount of radiation blockage provided by the insulation packages at the support members. The cooler edge of the shaded band is the distribution obtained from support member E (fig. 10) at the heat-shield edge. The dashed curve in figure 19(a) was obtained from calculated values based on an assumed surface-temperature history similar to the output of heat-shield thermocouple 11. These values fall within the shaded band and were used in a stress analysis of the panel which is presented in appendix D.

Thermal growth during the thermal cycle was indicated by scratches on the trailing-edge closeout where the trailing edge of the heat shield had rubbed and by a change in color of the oxidized coating where the heat-shield leading edge was covered by the leading-edge fairing. The length of the scratches and of the discoloration as measured with a ruler showed that the heat shield grew longitudinally about 0.80 cm (0.31 in.) in either direction from the center support members. This result agrees with the calculated thermal displacement reported in appendix D.

The time at which the substructure temperature limit occurred fell 2 min short of the desired 28 min. However, the use of a more realistic substructure of aluminum alloy with its greater thermal capacity would have extended this protection time. Inasmuch as the current Space Shuttle guideline limits the substructure temperature to 450 K (810° R) after 28 min of heating, the thermal performance of the present thermal protection system in a radiant heating environment is considered excellent.

Radiant-preheat—aerothermal test.- The effect of aerodynamic heating on panel thermal performance following a radiant preheat is shown in figure 20 by thermocouple data plotted as a function of time. Calculated temperatures from the thermal analysis presented in appendix C are also included. As a companion to this figure, figure 21 is presented to show the thermal response during aerodynamic exposure on an expanded time scale. The data were obtained during test 19 (table III). In that test, the panel was preheated for 648 sec, at which time the substructure temperature was 318 K (573° R), and panel exposure time in the stream was the longest of the test series (61 sec). (Aerodynamic exposure times varied as a result of anomalies in test facility operation.) Panel-holder angle of attack was -9°, and the cavity pressure was vented to base pressure in order to apply maximum positive differential pressure on the panel.

The thermal response to this type of test is characterized as follows (figs. 20 and 21): panel cooling by aspiration during test-chamber evacuation on tunnel startup near the end of the radiant preheat; additional cooling at reduced ambient pressure (2.1 kPa (0.3 psia)) for a 5-sec interval between quartz-lamp radiator retraction and panel entry into the stream; substantially greater temperature rise rates throughout the interior after entry into the stream; heat-shield temperature recovery by aerodynamic heating; and uncontrolled cooldown after withdrawal from the stream. After approximately 16 sec in the stream, the heat-shield temperature (fig. 21) recovered from the 5-sec cooldown prior to insertion to an average value of 1089 K (1960° R) within a spread of ±28 K (±50° R). Thus, the preselected panel-holder angle of attack of -9° was approximately correct for the stream conditions of these tests. Positive differential pressure was 4.8 kPa (0.7 psi). At 220 sec into the cooldown period, the substructure temperature peaked at 382 K (688° R). The calculated curves in figure 20 show very good agreement with measured temperatures during radiant preheating, but the thermal modeling does not account for variations caused by the flow of hot gases through the interior of the panel during aerodynamic heating. Consequently, in the aerodynamic portion of the test, the calculated temperature at locations 3 and 4 on the support member and on the substructure underpredicted the corresponding measured temperature by about 83 K (150° R) and 44 K (80° R), respectively.

Although support-member temperatures increased after insertion, insulation temperatures appeared not to be affected by the insertion event (fig. 20(b)). The increase in heating along the support members after entry into the stream resulted from an unrealistic situation in which hot gases were drawn from the boundary layer by differential pressure between the surface and the cavity, through the gaps between the insulation packages, and out the vent doors at the base of the panel holder. (See fig. 7.) From the slope of the curve for the substructure temperature given in figure 20(a), it appears that if the time in the stream could have been extended, the substructure temperature limit would have occurred at a time far short of the desired 28 min. In fact, as demonstrated by the temperature distributions on the support member in figure 22, the distribution obtained after only 58 sec in the stream – following a relatively short radiant preheat – approximated that obtained after 1563 sec of radiant heating in the thermal cycle of test 17 (fig. 19(a)). However, the circulation of hot gases to the cavity under the hat sections can be retarded by keeping the vent doors closed. In that event, the cavity pressure primarily vents through the open corrugations at the heat-shield trailing edge with the result that the temperature rise rate on the lower part of the support member (location 4) is substantially less than when the vent doors are open, as indicated in figure 23. The data for this figure were obtained during test 31 (table III) in which the vent doors were closed for approximately 9 sec and then were opened while the panel holder was at $\alpha = -9^{\circ}$. This effect is further illustrated in figure 24, where slopes of the thermocouple output at location 4 are plotted as a function of time for 4-sec periods taken just before airflow began and before and after the vent doors opened. These results show the following: (1) when the vent doors were closed, the variation of temperature rise rate with time at the bottom of the support member (location 4) was the same both before airflow began near the end of the radiant preheat period and after panel insertion into the stream, and (2) when the vent doors were opened, the temperature rise rate increased markedly. At that time, the pressure under the open corrugations at the heat-shield trailing edge decreased by about 0.8 kPa (0.12 psia), and positive differential pressure loading of the panel increased by the same amount. This result indicated a diversion of some of the interior flow from the open corrugations to the base of the panel holder. Therefore, in a more realistic test setup, the present concept shows excellent potential for protecting a substructure from a severe aerodynamic-heating environment. In the present test series, no attempt was made to seal the side edges positively against boundary-layer inflow. Future development tests of this thermal-protection-system concept should address this problem.

Aerothermal shock test.- In order to observe panel response under transient aerodynamic heating, the panel was subjected to aerothermal shock by inserting it into the stream without preheating (test 35, table III). In this test, the vent doors were locked closed to minimize internal flow of hot gases and thus maximize thermal gradient. Exposure time in the stream was 46 sec. Positive differential pressures up to 6.2 kPa (0.9 psi) were obtained for panel-holder angles of attack up to approximately -12°. Maximum cold-wall heating rate to the surface was 158 kW/m^2 (14 Btu/ft^2-sec) as determined from heat-shield thermocouple data for $\alpha = -9^{\circ}$. This result is within 5 percent of the flat-plate turbulent cold-wall value determined from the calibration data of reference 9 for a panel angle of attack of -9.3°.

The thermal response of the panel to these conditions is shown in figure 25 by thermocouple data plotted as a function of time. As indicated, heat-shield temperature increased very rapidly from the initial room-temperature value on insertion into the stream. Just prior to withdrawal from the stream, the average heat-shield temperature was 1096 K (1972° R) within a spread of ±29 K (±53° R). The distribution of heat-shield temperatures at that time was similar to that obtained in test 19 (table III) in which the panel was preheated. The longer exposure time with the vent doors closed, relative to test 31 (previously discussed), afforded a better opportunity in test 35 to observe panel performance under conditions that would not force hot boundary-layer gases down the support member. That this, indeed, was the case is indicated by the relatively high temperatures on the portion of the support member located above the insulation package (locations 1 and 2) with respect to the very low temperatures <367 K (<660° R) on the lower portion of the support member (locations 3 and 4) adjacent to the insulation package. The temperature of the substructure and of the air under the substructure did not vary during the aerodynamic exposure period. These results indicate that the thermal performance of the present thermal-protection-system concept in a severe aerothermal shock environment is excellent.

Calculated support-member temperatures based on two different heat-shield temperature histories as input are also shown in figure 25. In addition to the calculations based on a measured heat-shield temperature history from thermocouple 11, calculations were performed using a heat-shield temperature history based on heat-transfer coefficient and adiabatic wall temperature as determined from tunnel stream conditions corresponding to the various angles of attack. The latter calculations were independent of any measured heat-shield temperature response and reflected the accuracy with which the heat-transfer coefficient and adiabatic wall temperature were determined. The calculated temperatures based on the measured heat-shield temperature history as input (dashed curves) considerably underpredicted temperatures on the upper half of the support member (locations 1 and 2). The calculations based on the heat-shield temperature history determined from flow conditions (dash-dot curves) showed good agreement at location 1 and better agreement at location 2 than was obtained by the former calculations. However, the latter calculations overpredicted the measured heat-shield temperature, and therefore, higher calculated support-member temperatures would be expected. The agreement obtained by both methods with experiment was much better at locations 3 and 4 and was excellent on the substructure. These calculated results indicate the need for better definition of the convective heat-transfer process that was obviously present to some extent under the heat shield even when the vent doors were closed.

Surface temperatures.- As indicated earlier, thermocouple data showed that aerodynamic heating tended to smooth out the heat-shield temperature distribution obtained by radiant preheating from a spread of ±35 K (±63° R) to ±28 K (±50° R). Digitized traces of scanlines obtained from the infrared radiometer in test 19 in figure 26 showed a much smaller spread in the heat-shield surface temperatures during aerodynamic exposure than did the thermocouple data – only ±8.3 K (±15° R). In this figure, the scanlines were obtained along the flat sections and along the crests of corrugations over approximately one-half of the infrared viewing area between the center-line corrugation 7 and corrugation 11. The data were taken after approximately 55 sec of aerodynamic exposure. Temperatures along corrugations appeared uniformly distributed, whereas the protruding brazier-head rivets produced peaks in the distributions along flat sections. The peaks indicated rivet temperatures that averaged at least 30 K (54° R) higher than the average surface temperature. Inasmuch as the size of the resolution element scanning the surface was larger than the rivet head, actual rivet temperatures were probably somewhat higher than indicated. As shown in figures 26(b), 26(d), and 26(e), good agreement was obtained between temperatures given by infrared radiometry and by thermocouples.

Spanwise surface-temperature distributions at various longitudinal stations are presented in figure 27. The data for this figure are cross plots of digitized data traces spaced at approximately 0.6-cm (0.25-in.) intervals. Between support members $x/l = 0.381$ and $x/l = 0.657$ (figs. 27(d) and 27(b)), the distributions appeared flat within a spread of ±8.3 K (±15° R) and show good agreement with thermocouple data. At $x/l = 0.281$ and $x/l = 0.736$ (figs. 27(e) and 27(a)), the effect of the hotter, protruding brazier-head rivets is clearly indicated. These results are pictorially represented in figure 28. A plot of the temperatures across the center-line corrugation 7 is presented in figure 29. Data from four thermocouples and from 14 infrared scans show that the temperatures were within ±5.6 K (±10° R) over the corrugation. Interestingly, the data from both systems reflected the same trends and indicated a small increase in temperature near the corners joining the corrugations and flat sections.

Under transient aerodynamic-heating conditions, rivets and support members are initially heat sinks; consequently, their temperatures lag those of the surrounding surface. This effect is seen as downward pointing spikes on scanlines of surface temperature obtained from the infrared radiometer during test 35 (table III), as shown in figure 30. The digitized trace shown in this figure was obtained 15 sec after panel insertion in the stream. The agreement of infrared and thermocouple data is within 28 K (50° R).

Panel Integrity

Thermal.- Panel thermal integrity can be evaluated from figure 31 by comparing the variations of temperature with time obtained from thermocouples on the heat shield and on center-support member A during thermal cycles conducted early and late in the test series (tests 13 and 33, table III). In figure 31, only the first heatup in test 33 (fig. 17) is plotted. Test 13 was the earliest thermal cycle of sufficient duration to allow adequate response at the bottom of the support member (location 4) for comparison with a subsequent test. Test 33 was the last thermal cycle that was free of radiant-heater output anomalies. Through test 13, the panel had been subjected to nine thermal cycles, of which six resulted from abortive tunnel runs, and to four radiant-preheat—aerothermal tests for approximately 1 hr of radiant heating at 1089 K (1960° R) and 2.3 min of aerodynamic heating. After the panel endured 14 additional thermal cycles, of which seven resulted from abortive tunnel runs, and five radiant-preheat—aerothermal tests for an additional 4.3 hr of radiant heating at 1089 K (1960° R) and 2.6 min of aerodynamic heating, no degradation in thermal response was evident during test 33. The similarity of the temperature histories along the support member indicates excellent thermal integrity for this panel.

Structural.- Panel structural integrity during the present test series can be assessed by comparing the natural frequencies obtained from vibration surveys taken between heating tests; these frequencies are presented in table IV. Details of the procedures for the vibration surveys are given in appendix B. Experimental and calculated natural frequencies and mode shapes obtained from the static characterization tests conducted prior to the heating tests are also given in appendix B. The tabulated frequencies are for one half-wave (m = 1) in the stream direction between support members and 1, 2, 6, and 9 half-waves in the cross-stream direction. The number of accumulated test events between vibration surveys is also given in table IV. The largest observed change in panel natural frequency between vibration surveys was 6 Hz, and changes in the natural frequency appeared to be independent of the type of event or the number of events between vibration surveys, which was as high as seven (between tests 29 and 32, table II). The maximum change in natural frequency throughout the test series was about 3.5 percent. Although some scatter and drifting in frequencies occurred, first downward and then upward, no indications of serious structural degradation were detectable from results of the vibration surveys. During aerodynamic exposures, no evidence of panel flutter by the heat shield was indicated, as might be expected for highly orthotropic panels where the flow is alined with the major stiffness. An estimate of the flutter parameter from reference 12 showed that the heat shield should flutter at a value of q/β above 5033 kPa (730 psi), whereas the maximum wind-tunnel test value was only approximately 34 kPa (5 psi). However, as reported in reference 13, the flutter parameter for highly orthotropic panels can reduce more than an order of magnitude for small angles of yaw. Thus in a flight application, this heat-shield concept may be flutter prone if the corrugations are not alined with the flow direction.

Surface deformation.- A contour map of the changes in heat-shield surface deformation made at the end of the test series is plotted in figure 32. Each contour represents a deviation of 0.025 cm (0.010 in.) with respect to pretest values. In general, variations in the surface were within only one or two skin thicknesses as a result of an outward warp along the trailing edge toward the left corner, looking upstream. The largest change in surface shape was a depression approximately 0.23 cm (0.09 in.) deep shown on the center-line crest in the leading-edge bay. This depression extended to the adjacent flat sections and is believed to have occurred during test 6 (table III); further discussion of this test follows in the next section. Data on static loads and deflections given in appendix B indicated no detectable changes in stiffness of the support members from the beginning to the end of the test series.

Posttest condition of panel.- Except for the appearance of the heat-shield surface, which became increasingly discolored and pitted as the tests progressed, the panel was in excellent structural condition at the conclusion of the test series. Photographs of the heat-shield surface taken prior to testing and after the final test are shown in figure 33. The large, lighter areas shown in figure 33(b) reflect a pattern produced by the quartz-lamp radiators during preheating and thermal cycling events. Temperatures from thermocouples in these areas during radiant heating were approximately 44 K (80° R) higher than in the darker areas. Rainbow-like color variations appeared at random intervals along the side edges of the panel from effects of burnt silicone rubber sealant used on the walls of the rectangular cutout in the panel holder. Other contaminants marked the surface with white, powdery deposits, which may have resulted from an occasional broken quartz lamp, and with dried streaks from liquid deposits – perhaps drops of hydraulic fluid. Extensive pitting and scratching resulted from electrical arcing, as in the photograph of figure 34, and from impacts by particles in the tunnel test stream. The particles were produced by flaking of a coating of plasma-sprayed alumina used for thermal protection on the combustor liner of the wind tunnel. All upstream surfaces of protruding rivet heads and the leading edge of some flush rivet heads were eroded, as shown in the photographs of figure 35.

At the back of the panel, most of the bolted connections between the support members and the stainless-steel substructure hat-section members had seized slightly so that an audible snap occurred as they were loosened using a ratchet wrench for disassembly. The heavy stainless-steel wire screen, the back surface of the Inconel 650 screen envelope covering the insulation material, the back surface of the heat shield, and the support members resembled their pretest appearance. The finish of the René 41 foil on the upper surface of the insulation packages, shown in figure 36, was oxidized to hues of blue and purple from repeated exposures to the test temperatures.

A careful visual inspection of the heat shield and support members showed no stretched or twisted support members, dimensional changes, or cracks other than a hairline crack around two (out of 112) spotweld craters at the top of the two outboard center support members. The origin of the cracks is not known, and it cannot be stated with certainty that they were not present prior to testing. Nevertheless, they were not structurally degrading. However, inasmuch as the cracks were located in both outboard center support members, they may have developed during testing from the unrealistic panel edge condition provided by the side-edge closeouts (fig. 8). These relatively rigid components impeded vertical motion of the heat-shield side edges induced by the thermal expansion of the outboard corrugations, acoustics, buffeting, and surface pressures encountered during aerodynamic testing. Such vertical motion would have occurred for an edge condition more representative of a heat-shield to heat-shield longitudinal joint in a reentry application. The only obvious indication of some structural change that could be attributed to an effect of testing was that all of the center support members could rotate freely about the countersunk rivets that fastened them to the heat shield. All other riveted connections appeared tight. It is believed that the rivets may have loosened during test 6 (table III). In that test, 12 thermocouples and six deflectometer probes were destroyed by heat-shield impact when the panel was subjected to combustor noise of at least 154 dB for at least 1 min during an aborted attempt to run the tunnel when the ejector failed to operate and tunnel shutdown was unusually severe.

Heat-shield and support-member stresses. - A stress analysis of the heat shield and support members using the SNAP (Structural Network Analysis Program of ref. 5) finite-element digital computer program is presented in appendix D. The analysis was based on material properties given in appendix A. The results indicated that for the loading and heating conditions of the present tests (excluding aerothermal shock), stresses in the heat shield were low and that the support members offered little resistance to thermal growth. However, in the transverse support members, maximum compressive inplane stresses of 552 MPa (80 ksi) were concentrated in the angles formed by the intersection of each pair of legs at the bottom of the support member. Tensile stresses of 241 MPa (35 ksi) were concentrated in the angles at the top of the support member. Although these stresses were well within yield-stress limits, they exceeded the proportional limit. An assessment of their severity in terms of life degradation is beyond the scope of the present investigation and would require a nonlinear analysis using a finer grid of finite elements. Nevertheless, further development work to reduce stress concentrations in the transverse support members is indicated.

Recommended Improvements in Design

The results from the present panel evaluation substantiated the viability of the René 41 thermal protection concept and also indicated where improvements in detail design would enhance its practicality for service on hypersonic vehicles. Thus, the transverse support member should be designed so that stress levels in the formed angles are reduced. As indicated in appendix D, design changes might include (1) dimpling the angle to allow thermal growth or (2) riveting separate legs together to form the truss-shaped support. Inasmuch as the heat shield was lightly loaded, its thickness could be reduced to save mass. Further development work should also concentrate on making this type of heat shield flutter free. Toward this end, consideration should be given to placing the insulation in contact with the heat shield so that it can assist in damping heat-shield vibrations. Placing the insulation against the heat shield should also eliminate the need to totally envelop the insulation in screening or foil and, thus, might result in further savings in mass.

CONCLUDING REMARKS

A large, flightweight panel for a metallic thermal-protection-system concept for reentry- and hypersonic-vehicle application was tested in the Langley 8-foot high-temperature structures tunnel to evaluate its aerothermal performance and its structural integrity. The panel consisted of a 106.7 by 148.3 cm (42.0 by 58.4 in.) corrugation-stiffened heat shield riveted to support members made of 0.05-cm (0.02-in.) thick heat treated and aged René 41 sheet material and 5.08-cm (2-in.) thick silica fibrous insulation packages that were covered with René 41 foil and Inconel 650 screening. The insulation packages were located at the bottom of the support members. The system was designed to protect the substructure from temperatures above 422 K (760° R) for 28 min and to carry a uniform pressure of 20.7 kPa (3 psi) at a surface temperature of 1089 K (1960° R). Total mass of the system was 10.6 kg/m^2 (2.18 lb/ft^2). The panel was subjected to the following tests: 12 thermal cycles by radiant heating at atmospheric pressure to a surface temperature of 1089 K (1960° R) for constant-temperature exposure times up to 21 min; 14 thermal cycles by radiant heating with intermittent pressure and acoustic pulses (rapid reduction in ambient pressure to 0.7 kPa (0.1 psia) and acoustic pressures to 162 dB); 10 radiant preheats followed by aerodynamic exposures that produced differential-pressure loading up to 6.2 kPa (0.9 psi), local Mach numbers from 6.2 to 4.4, local dynamic pressures from 97 to 158 kPa (14 to 23 psi), and aerodynamic heating rates that maintained a surface temperature of 1089 K (1960° R); and one aerothermal shock test at a cold-wall turbulent heating rate of 158 kW/m^2 (14 Btu/ft^2-sec). Aerodynamic exposure times were up to 1 min at a nominal free-stream Mach number of 6.6 and a nominal free-stream unit Reynolds number of 5.118×10^6 per meter (1.56×10^6 per foot). Heat-shield corrugations were alined with the stream.

During these tests, the panel sustained 5.33 hr at a surface temperature of 1089 K (1960° R), 6.5 min in the aerothermal environment, and accelerations of up to 12g without apparent degradation of thermal or structural integrity. The panel demonstrated that under radiant heating it can protect the substructure from temperatures above 422 K (760° R) for 26 min with a surface-heating history corresponding to a typical reentry heat pulse from Earth orbit. This is well within the current shuttle guideline that limits the substructure temperature to 450 K (810° R) after 28 min of heating. The panel also demonstrated excellent potential for thermal protection in a severe aerodynamic-heating environment by temperature rise rates on support members that approximated those obtained under radiant heating. However, as would be expected, panel thermal performance degraded when hot gases from the boundary layer were forced through the panel interior.

Thermal analysis demonstrated that this thermal-protection-system concept can be modeled to predict thermal response with reasonable accuracy. Stress analysis, based on the test pressures and heating rates, indicated stress concentrations in the angles formed by the intersection of support-member legs within yield-stress limits but greater than the proportional limit by as much as 30 percent. In view of these calculated stresses, further development work should consider redesigning support members to reduce the level of stress concentration. Design changes might include (1) dimpling the angle to allow thermal growth or (2) riveting separate legs together to form the truss-shaped support. Inasmuch as the stress analysis also showed that the heat shield was lightly loaded, mass can be saved by reducing the heat-shield thickness.

Although no evidence of panel flutter was indicated during the aerodynamic exposures, this heat-shield concept may be flutter prone at small angles of yaw, according to analysis. Therefore, further development work should also focus on making the heat shield flutter free. As a step toward this end, placing the insulation against the heat shield would aid in damping heat-shield vibrations. This action would eliminate the need for totally enveloping the insulation in screening or foil, which might also result in further mass saving.

Langley Research Center
National Aeronautics and Space Administration
Hampton, Va. 23665
July 18, 1975

APPENDIX A

MATERIAL PROPERTIES

This appendix presents the material properties which were used in the thermal and stress analyses of the test panel. Table V contains temperature-independent values of emittance and density which were determined by tests or were obtained from standard material handbooks. Figure 37 gives temperature-dependent properties, most of which were taken from reference 14. Values of thermal conductivity and specific heat in figures 37(a) and 37(b) are connected by straight lines since linear interpolation between known values is used in the program.

APPENDIX B

PANEL CHARACTERIZATION

Static Load-Deflection Tests and Results

Tests.- Panel static load-deflection data were obtained experimentally before and after the heating test series. A differential-pressure loading technique was employed, using the setup as shown in figure 38. With this technique, the heat shield was covered with a sheet of vinyl, and the edges of the vinyl were sealed to the Glasrock surface of the panel holder. A vacuum pump reduced the pressure within the cavity under the panel and thus induced a uniform load over the heat shield. Cavity pressure was reduced in increments of 1.4 kPa (0.2 psi) to a maximum differential pressure of 6.9 kPa (1 psi) and then was increased by the same increments. Panel deflections were recorded at each pressure level from the output of a deflectometer system mounted on a traversing trolley and bridge mechanism that can survey the entire heat-shield surface. The mechanism was operated so that the deflectometer was transported in the spanwise direction on the bridge which traversed the heat-shield length on rails. For these tests, the traversing mechanism surveyed heat-shield surface deflections along the length of only one flat and the crest of one corrugation near the longitudinal center line. Output of the deflectometer probe was recorded on an x-y plotter. Deflections were also recorded from the outputs of the six deflectometers mounted under the heat shield (fig. 10) and from readings of 12 dial micrometer gages on the surface; these gages were used to check symmetry of deflections.

Static loads and panel deflections.- Panel deflections measured along a flat nearest the center line are presented in figure 39 as a function of length. Inasmuch as the deflections varied linearly with loading, they were normalized with respect to the maximum loading of 6.9 kPa (1.0 psia) which totaled 10.9 kN (2453 lb). Support-member locations are indicated by a center line and dashed lines. The results obtained at the beginning and at the conclusion of the test series were virtually the same and so are shown as a single curve. The repeatability of results indicates that heat-shield and support stiffnesses did not change.

The raw data were corrected by the amount of the deflections of the heavy channel beams to which the hat-section substructure members were mounted. The correction was determined by using simple beam theory and was verified by the data from the fixed deflectometers. Deflections were symmetrical about the center support which deflected the least of the supports, i.e., about one-half the heat-shield thickness. Deflections of the transverse supports adjacent to the center support were approximately 63 percent greater than the deflection of the center support, whereas the deflections of the transverse supports adjacent to the leading and trailing edges were only about 27 percent greater than those of the center support.

Maximum deflections of the heat shield between supports, excluding support-member deflections, occurred in the leading- and trailing-edge bays and were approximately three times those that occurred in the interior bays. Maximum deflection of the heat shield in these outer bays amounted to a little more than one skin thickness.

Vibration Modes and Frequency Surveys

Tests.- Panel vibration modes and frequencies were obtained before and after the heating tests and intermittently during the test program. The surveys were conducted using the portable setup shown in the photograph of figure 40. The panel was excited by an electrodynamic shaker mounted above the heat shield. In order to define mode shapes, the entire surface was surveyed using the traversing trolley and bridge mechanism as was done during the static load-deflection tests. Resonant frequencies were indicated by the peak amplitude response shown on an oscilloscope, and modal frequencies were surveyed in the range between 50 and 500 Hz by using a frequency sweep technique. The natural frequencies thus obtained provided a convenient means of detecting panel structural degradation after a thermal cycle or a wind-tunnel test, as indicated by significant changes in natural frequency.

Panel vibration modes and frequencies.- Some of the experimentally observed nodal patterns and frequencies determined from vibration surveys of the panel that were conducted at the beginning of the test series are presented in figure 41. Up to two heat-shield bays were surveyed. Although the interplay of heat-shield and support-member responses often precluded clear definition of the mode shapes, sufficient information was generated to indicate that mode shapes are complex, a characteristic that was identified in reference 15 for a corrugated panel constructed of René 41 similar to the present panel.

Experimental and calculated natural frequencies (calculations based on theory of ref. 13) of the panel are given in table VI and are plotted in figure 42 as a function of the mode number n up to 10 modes. The measured natural frequencies varied between 222 and 376 Hz, and their agreement with calculated values is fairly good (within 5.5 percent) through the mode $n = 7$. After the seventh mode, the agreement between experiment and calculation diverges. The boundary conditions assumed in the calculations were that the streamwise edges of the heat shield were simply supported and that the other two edges were supported by deflectional, rotational, and torsional springs of equal stiffness, respectively. The approach used in obtaining calculated frequencies was to identify the deflectional spring constant K_d from the deflection data determined by the static load tests as shown in figure 43. In that figure, calculated and measured heat-shield and support-member deflections in half of an interior bay bounded by a center support member are compared and show good agreement; although the other half of the bay would be different since, on the panel, the leading- and trailing-edge supports are unequal. Rotational and torsional constraints were then adjusted for a "best fit" of the vibration data. The calculated frequencies were obtained using $K_d = 75.5$, $K_r = 10$, and $K_t = 5$. The technique used is described in reference 16.

APPENDIX C

THERMAL ANALYSIS OF RENÉ 41 THERMAL PROTECTION SYSTEM

A thermal analysis was made to predict the temperatures on the surface and through the depth of a metallic thermal protection system for comparison with the experimental results. The program used for the analysis was MITAS (Martin Interactive Thermal Analysis System) which is described in reference 4. The panel is divided into a network of nodes where each node is considered to be a constant temperature region. The network solution is obtained by using a finite differencing technique. The region modeled for the thermal analysis was a symmetrical section in the center of the panel (see fig. 10) over a length of 17.8 cm (7.0 in.) and width of 4.0 cm (1.6 in.) and included a center support member and a node containing a surface thermocouple.

A schematic for the section modeled is shown in figure 44. The modeling included a node representing the rivet that attached the support member to the heat shield and a node representing the bolt that attached the support member to the hat section. The insulation blanket was divided into a number of nodes through the thickness.

Figure 45 shows a section through the panel identifying the various components and the modes of heat transfer considered in the analysis. The preheating tests allowed the quartz lamps to radiate to the heat-shield surface to maintain a controlled surface temperature. The modeling allowed for a radiation interchange between the heat-shield surface, the support members, and the insulation package as indicated in the figure. Conduction was considered to have occurred along all surface and support nodes, through the insulation package, and along the hat sections. A radiation heat loss was allowed from the lower surface of the thermal protection system.

Temperature-dependent thermal properties for the materials used as components in the thermal-protection system are presented in figure 37. The material density and the constant-value emittance of these materials are given in table V.

The following assumptions were made for the analysis: (1) The initial starting temperature for all nodes was taken as the local ambient condition, (2) The emittance values used for radiation were taken as a constant value for each material involved, (3) There was no thermal interchange considered between the support nodes and the ends of the insulation nodes since the temperature at adjacent locations were nearly the same, and (4) An aluminum plate 1.3 cm (0.5 in.) thick was placed below the system to represent an equivalent structure to which heat radiated (this plate represented the mesh screens on the lower surface of the insulation package, the instrumentation wiring, and the cavity walls of the panel holder). Calculated temperatures are compared with thermocouple measurements through the depth of the panel in the main text.

APPENDIX D

STRESS ANALYSIS OF RENÉ 41 THERMAL PROTECTION SYSTEM

A stress analysis of the René 41 heat shield was performed by using the SNAP (Structural Network Analysis Program of ref. 5) finite-element digital computer program. The length of the portion modeled by finite elements (see fig. 10) represents the aft 20.96 cm (8.25 in.) of the total heat-shield length of approximately 147.32 cm (58 in.). Lengthwise (x-direction) rigid body displacements of the entire heat shield are prevented by the center supports, and thermal growth of the heat shield occurs from the center supports. The transverse supports, located every 35.56 cm (14 in.) from the center supports, prevent lateral (y-direction) displacements, carry pressure loads, and flex to accommodate thermal growth of the heat shield. The end portion of the heat shield was selected for modeling since the greatest displacement due to thermal growth occurs at the end.

The grid used for modeling is shown in figure 46. The 4-node elements contain both membrane and bending stiffness and, consequently, the stresses calculated are the sum of membrane and bending stresses. All elements were 0.05 cm (0.020 in.) thick except that the elements around support attachments (nodes 59 and 112) were 0.10 cm (0.040 in.) to include doublers at these locations. A beam 0.10 cm (0.040 in.) long with extremely high stiffness properties connected nodes 45 and 112 to represent the attachment of the heat shield to the support. The right-angle reinforcing elements were added after the stress analysis was performed (compare fig. 46 with fig. 3) and so were not modeled. Conditions of symmetry were used at the nodes along cut edges to represent the remainder of the heat shield and support member. Node 59 was completely restrained from motion to represent a riveted attachment to the substructure. An initial longitudinal displacement (x-direction) was assigned to nodes 1 to 5 to represent the thermal growth of the portion of the heat shield upstream of that location. Temperature-dependent values of material modulus of elasticity, coefficient of thermal expansion, and Poisson's ratio used in this analysis are given in figure 37.

Loading and heating conditions applied to the structure were a 3.5-kPa (0.5-psi) differential pressure pushing the heat shield inward, a uniform surface temperature of 1089 K (1960° R), and a temperature gradient of 1089 K (1960° R) at the top of the support to 450 K (810° R) at the bottom of the support member. An assumed surface-temperature history was used with the MITAS program described in appendix C to calculate the temperature distribution shown by the dashed line in figure 19(a). An initial temperature of 294 K (530° R) was assumed for the temperature history followed by a 2.8 K/sec (5° R/sec) rise to 1089 K (1960° R). The surface temperature was held constant for approximately 1300 sec and then was reduced to 294 K (530° R) at a rate of

2.8 K/sec (5^o R/sec). The temperature distribution shown in figure 19(a) (dashed line) was calculated at a time corresponding to the end of the constant-temperature period. These loading conditions were selected because a 3.5-kPa (0.5-psi) differential pressure load was expected during wind-tunnel tests and because maximum thermal expansion of the support was expected at the end of the constant-temperature period of the surface-temperature history. The agreement of the calculated temperature gradient with the experimental scatter band from test 17 (table III) indicates that the calculated results represent a reasonable temperature distribution.

The resulting longitudinal displacement and reaction forces of the support members at the trailing edge are given in figure 47. The displacement of 0.85 cm (0.335 in.) agrees closely with the measured value of 0.80 cm (0.313 in.). The small reaction force, 3.58 N (0.803 lb), which results entirely from thermal growth of the heat shield, indicates that the support members are highly flexible in the length direction.

Inplane stress contours showing the summation of membrane and bending stress are plotted on the developed surface of the support member in figure 48 and show that the maximum stress is compressive and occurs in the angle formed by the intersection of each pair of support-member legs at the bottom of the support (see 552-MPa (80-ksi) contour). The stress appears to be primarily a result of constrained thermal expansion rather than a result of the temperature gradient. The stress level in the upper angle formed by the intersection of each pair of support-member legs exceeds 345-MPa (50-ksi) tension and appears to be caused, at least in part, by the temperature gradient down the top portion of the support. The right-angle reinforcing element, which was not modeled, was attached near this location of maximum stress. However, this element should have had negligible effect on the thermal stresses in this region since the element was attached by a single rivet. These stresses fall well within yield-stress limits (see appendix A) but exceed the proportional limit. Although these stresses may not be critical for short duration tests (no evidence of failure was found as a result of the tests reported herein), their level is such that a nonlinear analysis and a finer grid of finite elements in the regions of maximum stress would be required to assess their severity accurately. For example, such a detailed study might be necessary if a heat-shield support of the design considered herein were to be used for a specific life application. Furthermore, any additional development of this type of support should probably consider design changes to reduce stress levels in the formed angles. Such changes might include (1) dimpling the angle to allow thermal growth or (2) riveting separate legs together to form the truss-shaped support.

APPENDIX D

Heat-shield stresses, plotted on the developed surface of the heat shield, are shown in figure 49. They are relatively low compared with the stresses in the support members because the high flexibility of the support allowed essentially unrestrained thermal growth. The maximum shear stresses for the heat shield and the support were small and are not shown. In each case they were about one-tenth the value of the previously mentioned maximum stresses.

REFERENCES

1. Anderson, Roger A.; Brooks, William A., Jr.; Leonard, Robert W.; and Maltz, Joseph: Structures – A Technology Overview. Astronaut. & Aeronaut., vol. 9, no. 2, Feb. 1971, pp. 38-47.

2. Stein, Bland A.; Bohon, Herman L.; and Rummler, Donald R.: An Assessment of Radiative Metallic Thermal Protection Systems for Space Shuttle. NASA Space Shuttle Technology Conference – Dynamics and Aeroelasticity; Structures and Materials, NASA TM X-2570, 1972, pp. 267-302.

3. Hunt, L. Roane; and Bohon, Herman L.: Performance of LI-1542 Reusable Surface Insulation System in a Hypersonic Stream. NASA TM X-71955, 1974.

4. Martin Interactive Thermal Analyzer System – Version 1.0. User's Manual. MDS-SPLPD-71-FD238 (REV 3), Martin Marietta Corp., Mar. 1972.

5. Whetstone, W. D.: Structural Network Analysis Program – User's Manual. Static Analysis Version V70E. LMSC-HREC D162812. Lockheed Missiles & Space Co., Dec. 14, 1970.

6. Deveikis, William D.; Bruce, Walter E., Jr.; and Karns, John R.: Techniques for Aerothermal Tests of Large, Flightweight Thermal Protection Panels in a Mach 7 Wind Tunnel. NASA TM X-71983, 1974.

7. Plank P. P.; Sakata, I. F.; Davis, G. W.; and Richie, C. C.: Hypersonic Cruise Vehicle Wing Structure Evaluation. NASA CR-1568, 1970.

8. Lyman, T., ed.: Metals Handbook. Volume 2.- Heat Treating, Cleaning and Finishing. 8th ed. American Soc. Metals, c.1964.

9. Deveikis, William D.; and Hunt, L. Roane: Loading and Heating of a Large Flat Plate at Mach 7 in the Langley 8-Foot High-Temperature Structures Tunnel. NASA TN D-7275, 1973.

10. Eidinoff, H. L.; and Rose, L.: Thermal-Structural Evaluation of TD Ni-20Cr Thermal Protection System Panels. NASA CR-132487, 1974.

11. Leyhe, E. W.; and Howell, R. R.: Calculation Procedure for Thermodynamic, Transport, and Flow Properties of the Combustion Products of a Hydrocarbon Fuel Mixture Burned in Air With Results for Ethylene-Air and Methane-Air Mixtures. NASA TN D-914, 1962.

12. Erickson, Larry L.: Supersonic Flutter of Flat Rectangular Orthotropic Panels Elastically Restrained Against Edge Rotation. NASA TN D-3500, 1966.

13. Sawyer, James Wayne: Flutter of Elastically Supported Orthotropic Panels Including the Effects of Flow Angle. NASA TN D-7491, 1974.

14. Mechanical Properties Data Center, Belfour Stulen, Inc.: Aerospace Structural Metals Handbook – 1974 Publication. AFML-TR-68-115, U.S. Air Force, c.1974.

15. Carden, Huey D.; Durling, Barbara J.; and Walton, William C., Jr.: Space Shuttle TPS Panel Vibration Studies. NASA Space Shuttle Technology Conference, Volume III – Dynamics and Aeroelasticity, NASA TM X-2274, 1971, pp. 27-48.

16. Heard, Walter L., Jr.; and Bohon, Herman L.: Natural Vibration and Flutter of Elastically Supported Corrugation-Stiffened Panels – Experiment and Theory. NASA TN D-5986, 1970.

TABLE I.- MASS OF PANEL ELEMENTS

Item	Mass		Unit mass		Thickness	
	kg	lb	kg/m^2	lb/ft^2	cm	in.
Corrugated René 41 heat shield with 70 doublers	7.60	16.76	4.81	0.98	(a)	(a)
4 René 41 transverse support members	.86	1.90	----	---	0.05	0.020
14 René 41 upper reinforcing elements	[b].04	[b].09	----	---	.05	.020
13 René 41 lower reinforcing elements	[b].05	[b].11	----	---	.05	.020
14 René 41 center support members	1.17	2.58	----	---	.05	.020
52 floating anchor nuts	.08	.18	----	---	----	----
14 rigid anchor nuts	.01	.02	----	---	----	----
70 countersunk rivets	.06	.13	----	---	----	----
156 brazier head rivets	.18	.40	----	---	----	----
Heat shield and support assembly	10.05	22.17	6.36	1.30	10.6	4.16
Insulation packages	7.12	15.69	4.26	.88	5.1	2.00
Thermal protection system	17.17	37.86	10.62	2.18	10.6	4.16

[a]Corrugated heat shield, 0.05 cm (0.020 in.); doublers, 0.05 cm (0.020 in.).
[b]Calculated.

TABLE II.- SUMMARY OF TESTS

Test	Type of test	Remarks
	Static load deflection	Four tests conducted at $\Delta p = 6.9$ kPa (1 psi); natural vibration modes and frequencies obtained; panel surface deformations mapped at zero load
1	Thermal cycle	
2	Thermal cycle	Vibration survey followed this test
3	Thermal cycle from aborted tunnel run[a]	Vibration survey followed this test
4	Radiant preheat and aerothermal	Low total pressure
5	Thermal cycle from aborted tunnel run	
6	Thermal cycle from aborted tunnel run	Hard shutdown destroyed 12 thermocouples and 6 deflectometers; vibration survey followed this test
7	Thermal cycle from aborted tunnel run	
8	Thermal cycle from aborted tunnel run	Vibration survey followed this test
9	Thermal cycle from aborted tunnel run	
10	Radiant preheat and aerothermal	Vibration survey followed this test
11	Radiant preheat and aerothermal	Low total pressure
12	Radiant preheat and aerothermal	Vibration survey followed this test
13	Thermal cycle	
14	Thermal cycle from aborted tunnel run	
15	Thermal cycle from two aborted tunnel runs	Hard shutdown; vibration survey and surface mapping followed this test
16	Thermal cycle from three aborted tunnel runs	
17	Thermal cycle	
18	Thermal cycle from two aborted tunnel runs	Vibration survey and surface mapping followed this test

[a]False tunnel start resulted in no aerodynamic exposure but subjected the panel to rapid test-section evacuation and recompression; also to acoustic loading of 157 dB.

TABLE II.- SUMMARY OF TESTS – Concluded

Test	Type of test	Remarks
19	Radiant preheat and aerothermal	Vibration survey followed this test
20	Radiant preheat and aerothermal	Test aborted after 2 sec in tunnel stream
21	Thermal cycle	Vibration survey followed this test
22	Thermal cycle	
23	Thermal cycle	
24	Radiant preheat and aerothermal	
25	Thermal cycle	Vibration survey followed this test
26	Radiant preheat and aerothermal	Pitch angle varied
27	Thermal cycle	
28	Thermal cycle	Vibration survey followed this test
29	Thermal cycle from three aborted tunnel runs	Vibration survey followed this test
30	Thermal cycle from aborted tunnel run	
31	Radiant preheat and aerothermal	False tunnel start preceded aerodynamic exposure; pitch angle varied; vent doors closed initially, then opened
32	Thermal cycle from two aborted tunnel runs	Vibration survey followed this test
33	Thermal cycle	
34	Radiant preheat and aerothermal	Pitch angle varied; vent door closed; cavity pressurized
35	Aerothermal shock	Pitch angle varied; vent doors closed; vibration survey followed
36	Thermal cycle	
	Static load deflection	Two tests conducted at $\Delta p = 6.9$ kPa (1 psi); natural vibration modes and frequencies obtained; panel surface deformations mapped at zero load

TABLE III.- TEST CONDITIONS

(a) Thermal cycles[a]

Test	Time at 1089 K (1960° R), sec	Peak substructure temperature	
		K	°R
1	60	---	---
2	272	---	---
13	930	---	---
17	1268	429	773
21	1227	428	770
22	1225	433	779
23	1198	443	798
25	1033	438	788
27	1204	433	780
28	1138	446	803
33	815	---	---
36	593	409	737

[a]2.8 K/sec (5° R/sec) heatup and cooldown with a constant surface temperature period at 1089 K (1960° R).

TABLE III.- TEST CONDITIONS – Continued

(b) Thermal cycles from aborted tunnel runs

Test	Time at 1089 K (1960° R), sec	Peak substructure temperature		False tunnel starts	Test chamber evacuations[a]	Time between 148 dB and 157 dB,[b] sec	Time between 159 dB and 168 dB,[c] sec
		K	°R				
3	195	---	---	1	1	---	
5	295	---	---	1	1	40	
6	603	---	---	1	0	57	
7	94	---	---	1	1	27	
8	87	---	---	1	1	18	17
9	90	---	---	1	1	29	
14	237	---	---	1	1	25	
15	483	375	675	2	1	333	
16	857	404	727	3	0	32	
18	815	409	736	2	1	100	[d]180
29	786	404	728	3	1	42	
30	345	361	650	1	1	30	
[e]31	378	---	---	1	0	13	
32	301	346	622	2	1	39	

[a]Static pressure in test chamber between 0.7 and 2.1 kPa (0.1 and 0.3 psia).
[b]Panel covered during subsonic flow periods of tunnel operation.
[c]Panel uncovered during subsonic flow periods of tunnel operation.
[d]Panel exposed to subsonic flow during air storage depletion.
[e]Aerothermal test followed the false tunnel start.

TABLE III. - TEST CONDITIONS – Concluded

(c) Aerothermal tests

Test	Preheat time at 1089 K (1960° R), sec	Time between 148 dB and 157 dB, sec (a)	Time in hypersonic stream, sec	Peak substructure temperature		α, deg (b)	Time at α, sec	Δp		p_b		p_l		q_l		M_l	M_∞	p_∞		p_t		T_t		R	
				K	°R			kPa	psi	kPa	psia	kPa	psia	kPa	psi			kPa	psia	MPa	psia	K	°R	Per meter	Per foot
4	73	35	24	---	---	-8.7	20	1.2	0.17	0.8	0.11	---	---	---	----	5.56	7.03	1.0	0.14	6.8	993	1897	3414	2.07×10^6	0.63×10^6
10	113	29	32	---	---	-9.6	27	4.6	.66	2.3	.33	---	---	---	----	5.10	6.59	1.9	.28	18.22	2643	1765	3177	5.09	1.55
11	52	27	47	---	---	-9.3	42	1.1	.16	.8	.11	---	---	---	----	5.26	6.86	.8	.12	7.01	1017	1796	3232	1.97	.60
12	642	27	37	---	---	-9.3	32	4.1	.60	2.3	.33	---	---	---	----	5.10	6.58	1.9	.28	18.23	2644	1769	3184	4.99	1.52
19	322	27	61	382	688	-9.3	55	4.9	.71	2.3	.34	8.0	1.16	146	21.12	5.10	6.52	2.1	.31	18.17	2635	1723	3102	5.09	1.55
20	1201	28	2	438	788	-5.3	2	3.0	.44	--	---	5.8	.84	---	----	---	---	2.1	.30	----	----	----	----	---------	---------
24	1289	38	34	444	800	-9.3	30	4.7	c.68	2.1	.30	8.9	1.29	162	23.49	5.10	6.52	2.1	.31	18.13	2630	1716	3089	5.45	1.66
26	317	29	18	358	644	-9.3	5	5.4	.78	3.4	.49	8.6	1.25	157	22.76	5.10	6.53	2.2	.32	18.45	2676	1718	3092	4.92	1.50
						-7.3	3	4.0	.58	2.9	.42	6.7	.97	131	19.07	5.30	6.56	2.2	.32	18.33	2659	1741	3133	5.18	1.58
31	378	27	43	376	676	-9.3	4.5, 4.5	c4.3, 5.2	c0.63, 0.75	2.4	.35	8.3	1.20	157	22.71	5.20	6.71	2.3	.33	18.23	2644	1831	3295	5.02	1.53
						-7.5	4	4.8	.54	1.7	.25	6.4	.93	130	18.84	5.38	6.63	2.3	.33	18.20	2640	1783	3210	4.79	1.46
						-5.5	3	2.6	.38	1.2	.18	4.8	.70	112	16.20	5.75	6.63	2.3	.33	18.20	2640	1780	3204	4.95	1.51
						-3.1	2	1.5	.22	1.2	.18	3.6	.52	95	13.77	6.15	6.64	2.3	.33	18.15	2632	1711	3080	5.54	1.69
						-5.5	7	2.6	.38	1.2	.18	4.8	.69	108	15.69	5.70	6.58	2.3	.33	18.20	2640	1749	3148	5.41	1.65
34	60	28	50	342	616	-9.3	19.3	.1	c.02	2.3	.33	7.9	1.15	147	21.35	5.15	6.67	2.1	.31	18.18	2637	1802	3243	5.05	1.54
						-11.0	8	.6	c.09	2.1	.30	9.9	1.44	157	22.74	4.75	6.52	2.2	.32	18.14	2631	1728	3111	5.15	1.57
						-12.3	8	.6	c.09	7.4	1.07	11.7	1.69	158	22.90	4.40	6.29	2.6	.38	18.12	2628	1596	2873	5.25	1.60
						-9.3	3	-.6	c-.08	2.1	.31	8.1	1.17	136	19.66	4.90	6.25	2.2	.32	18.12	2628	1574	2833	5.28	1.61
35	0	36+	46	319	574	-9.5	6	4.4	c.64	2.1	.31	8.5	1.23	156	22.66	5.13	6.68	1.9	.29	18.24	2646	1806	3251	5.05	1.54
						-10.5	7	5.4	c.78	2.2	.32	9.7	1.41	170	24.68	5.00	6.70	1.9	.29	18.22	2642	1834	3302	5.02	1.53
						-11.6	7	6.2	c.90	1.8	.26	11.0	1.60	178	25.80	4.80	6.70	1.9	.29	18.20	2640	1840	3312	4.99	1.52
						-9.5	15	4.6	c.66	2.1	.31	8.3	1.21	158	22.90	5.20	6.76	1.9	.29	18.20	2639	1856	3340	4.95	1.51

[a] Panel covered during subsonic flow periods of tunnel operation.
[b] Includes model inclination relative to panel holder.
[c] Vent doors locked closed.

TABLE IV.- PANEL FREQUENCIES AFTER SPECIFIED TEST EVENTS

Test	f, Hz				Number of accumulated test events		
	m = 1, n = 1	m = 1, n = 2	m = 1, n = 6	m = 1, n = 9	Static loading	Thermal cycle	Aerothermal
Static load-deflection test	222	232	291	376	4		
2	222	233	288	372		2	
3	221	229	291	374		3	
6	221	231	289	373		6	1
8	219	231	292	373		8	
10	218	229	286	374		10	2
12	218	232	289	372		12	4
15	218	231	285	369		13	
18	218	231	281	371		18	
19	219	232	283	371		19	5
21	220	231	286	372		21	
25	222	233	286	375		25	6
28	221	232	285	374		28	7
29	221	234	284	373		29	
32	221	233	284	375	7	35	8
35	222	234	286	375		37	10

TABLE V.- DENSITY AND EMITTANCE OF PANEL MATERIALS

Material	Emittance	Density	
		kg/m^3	lb/ft^3
René 41 (oxidized)	0.75	8250	515
René 41 foil	.55	8250	515
347 stainless steel	.4	7690	480
Silica fibrous insulation (Micro-Quartz)	.5	67	4.2

TABLE VI.- MEASURED AND CALCULATED FREQUENCIES OF PANEL BEFORE THERMAL TESTS

Modes		f, Hz	
m	n	Experiment	Calculated
1	1	222	221
1	2	232	235
1	3	245	252
1	4	258	271
1	5	272	287
1	6	291	302
1	7	---	314
1	8	355	326
1	9	376	337
1	10	---	348

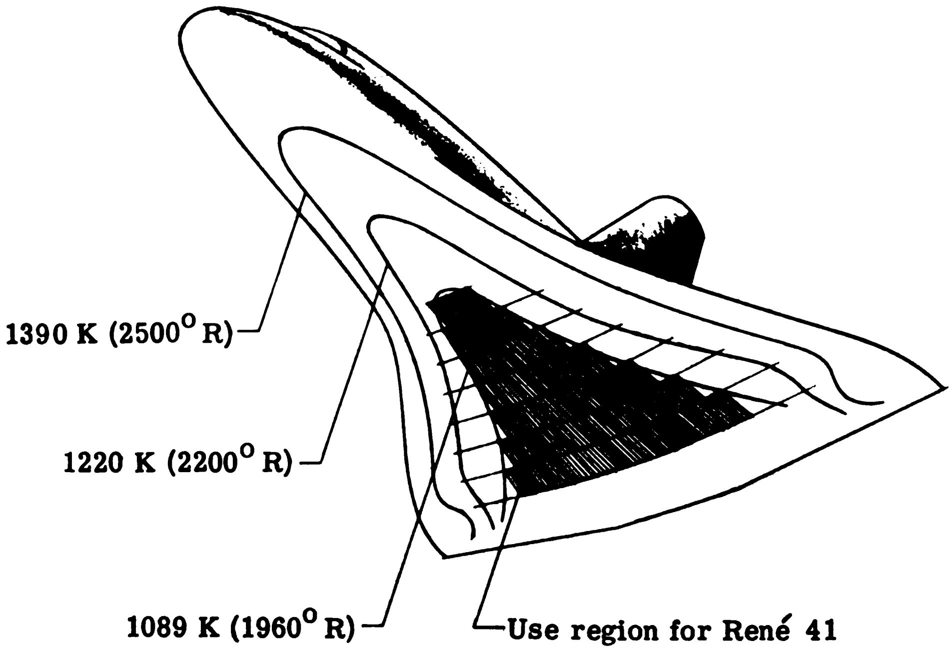

Figure 1.- Isotherms on reentry surface.

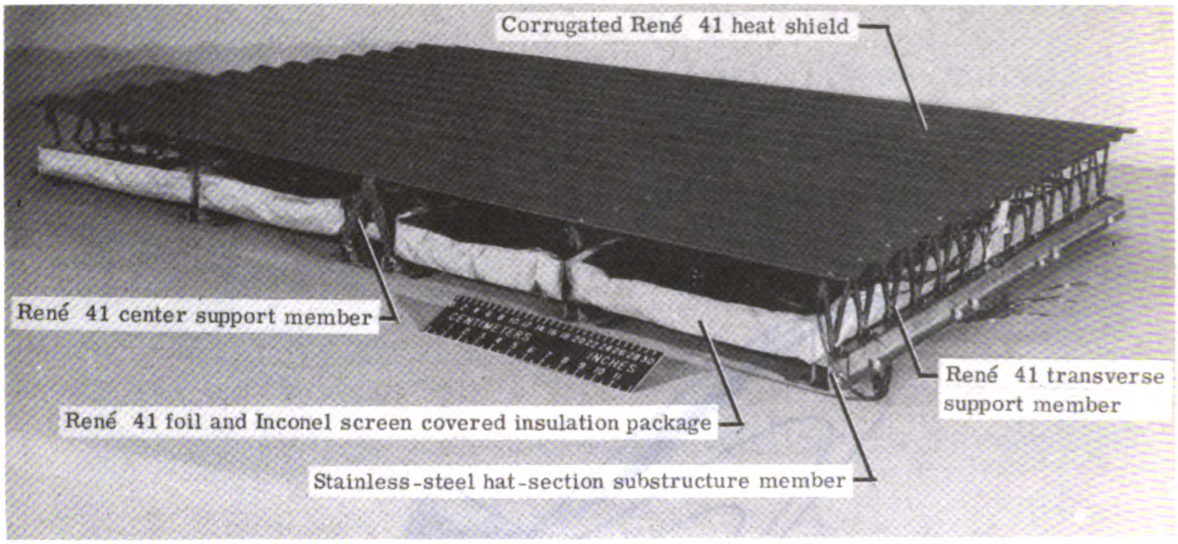

(a) Heat-shield surface view.

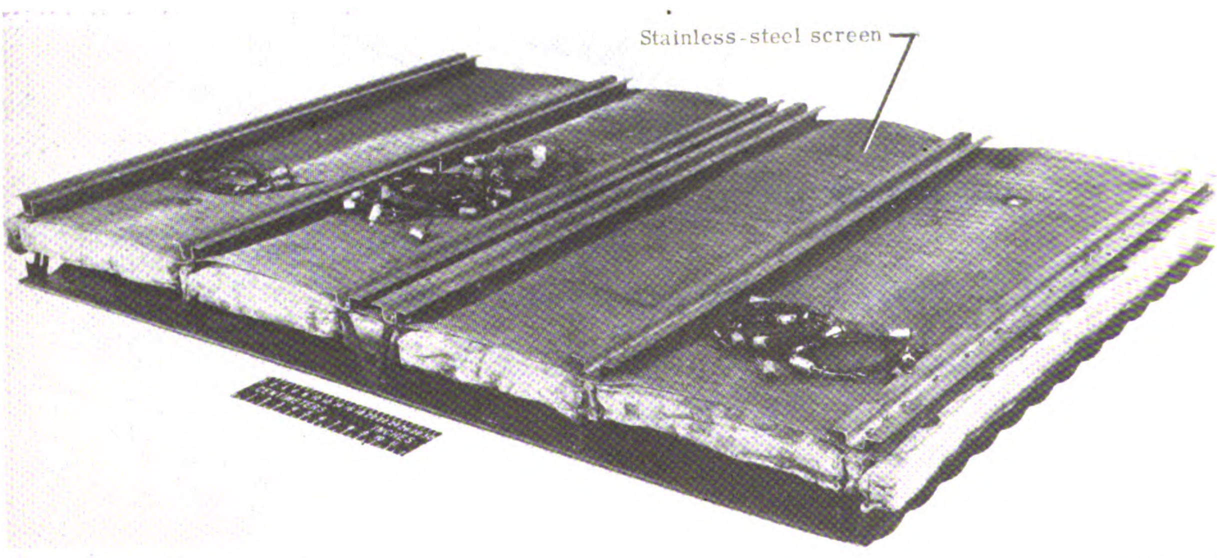

L-75-186

(b) Back surface view.

Figure 2.- René 41 thermal-protection-system model.

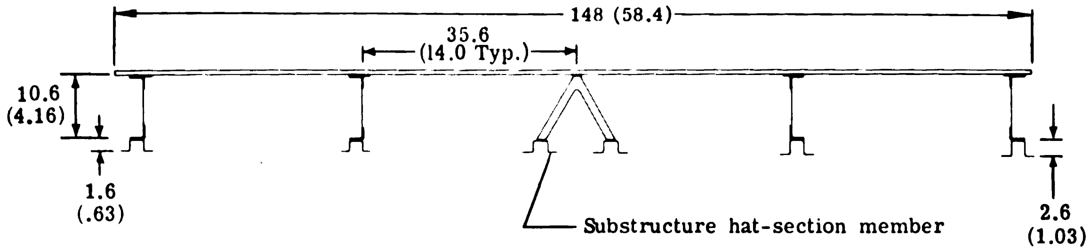

(a) Heat-shield support member arrangement.

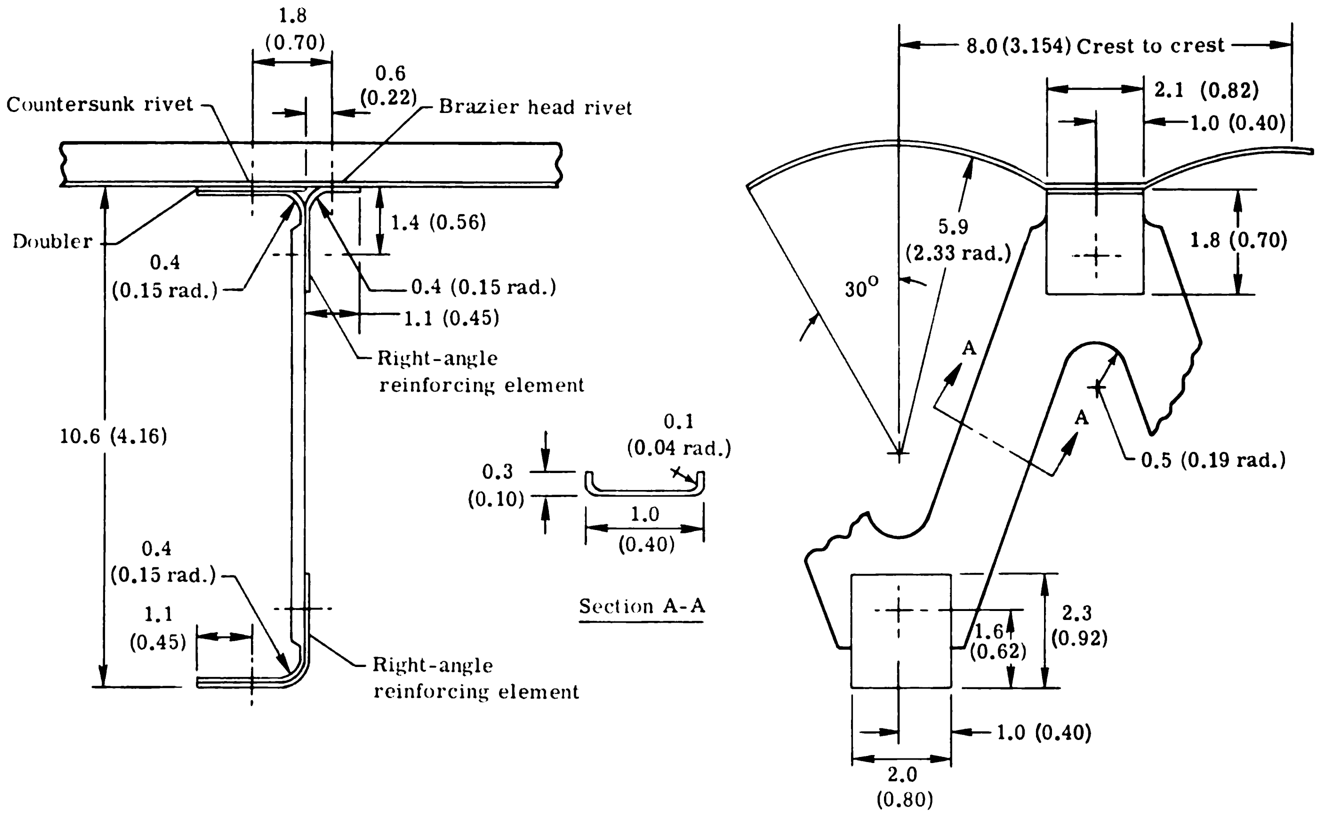

(b) Transverse support member.

Figure 3.- Details of René 41 heat shield. Dimensions in cm (in.).

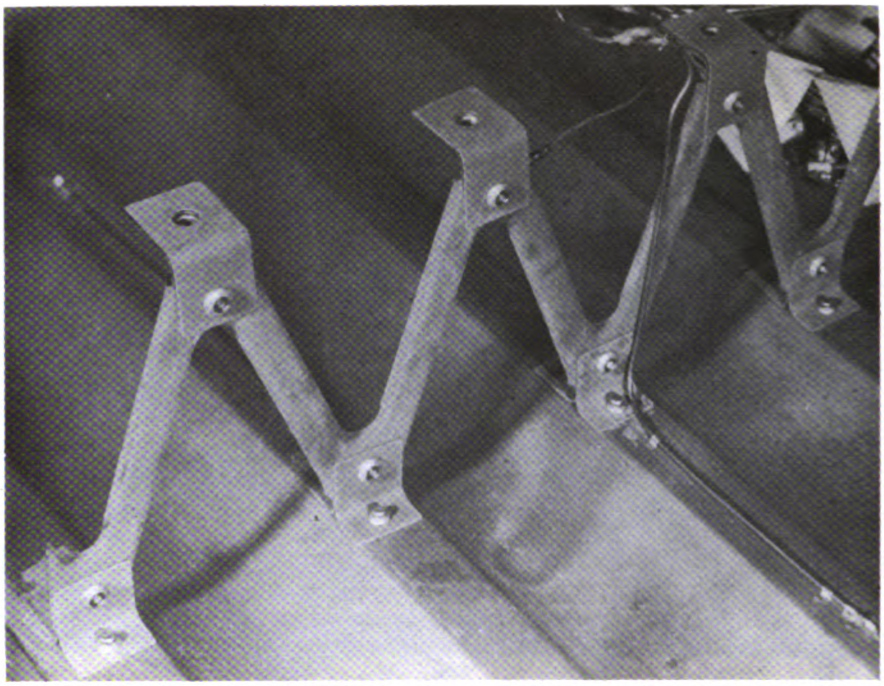

(a) Transverse support member.

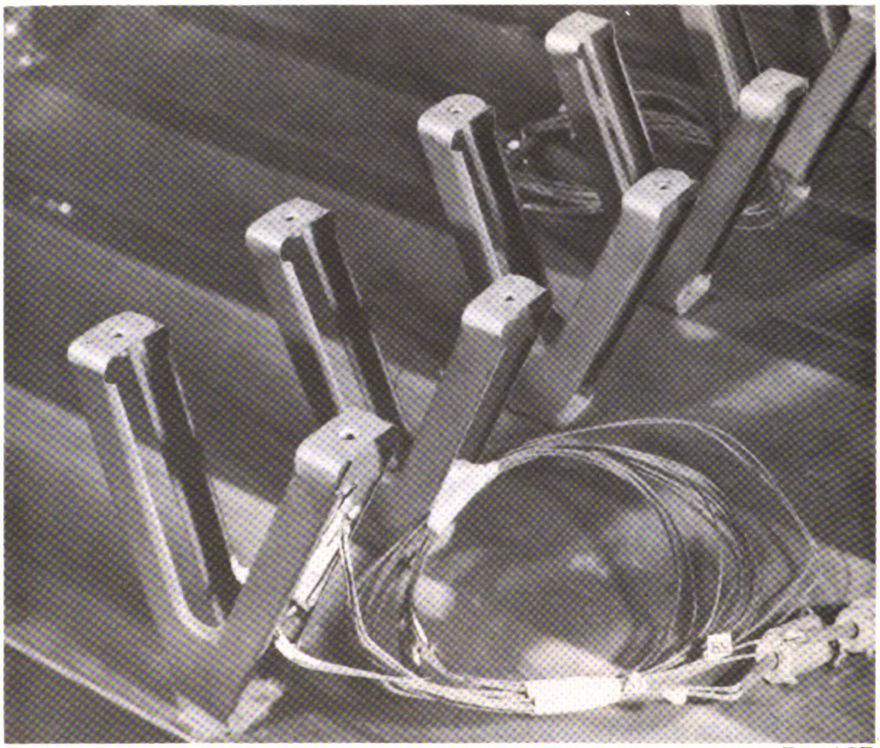

L-75-187

(b) Center support members.

Figure 4.- Heat-shield support members.

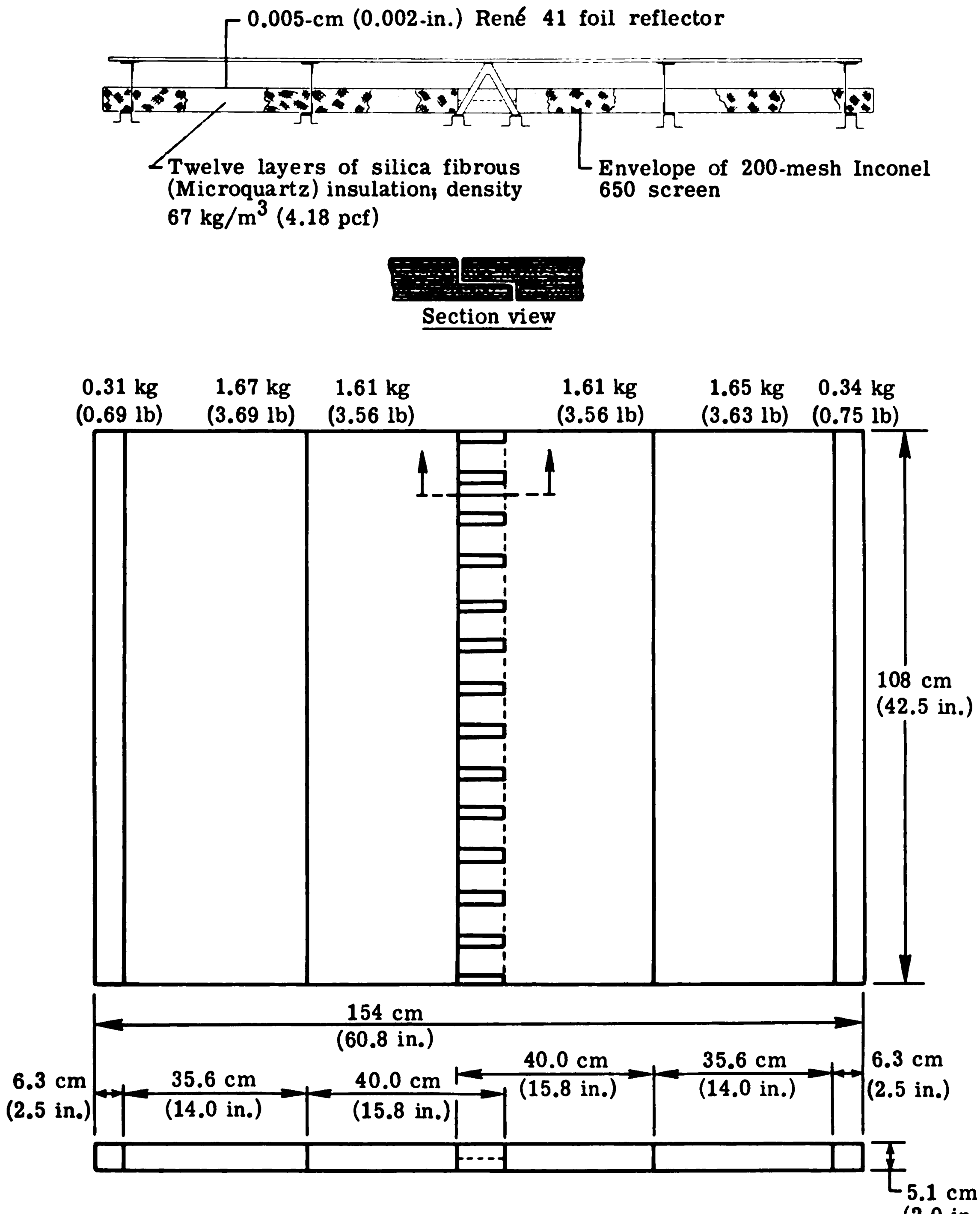

Figure 5.- Insulation-package configuration. Package weight, 4.3 kg/m^2 (0.88 lb/ft^2).

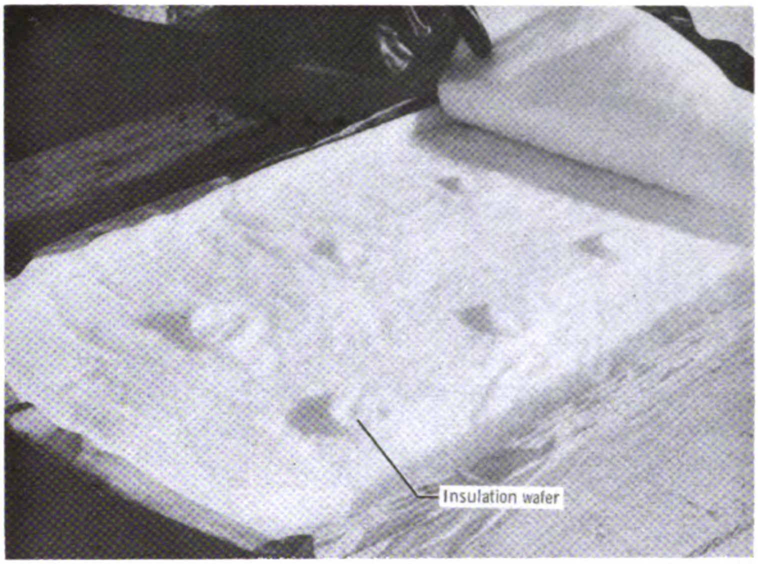

(a) Fabrication.

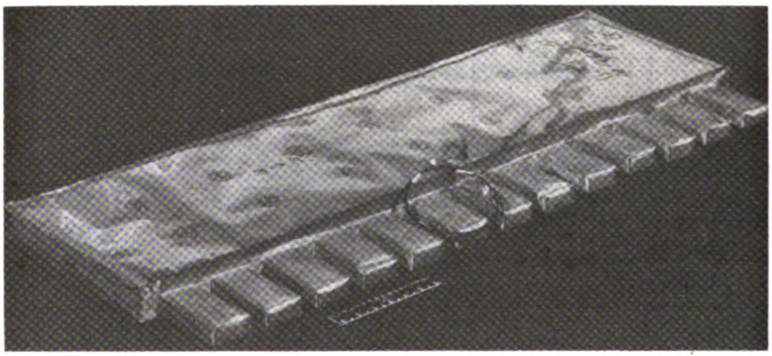

(b) Fabricated center section.

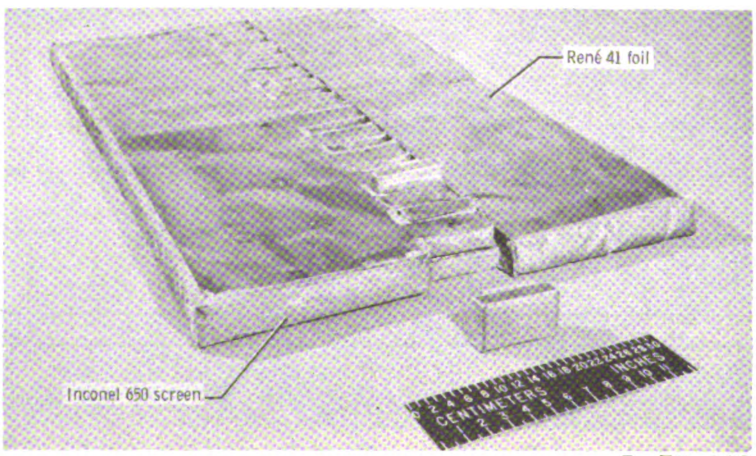

L-75-188

(c) Fitted center sections.

Figure 6.- Insulation packages.

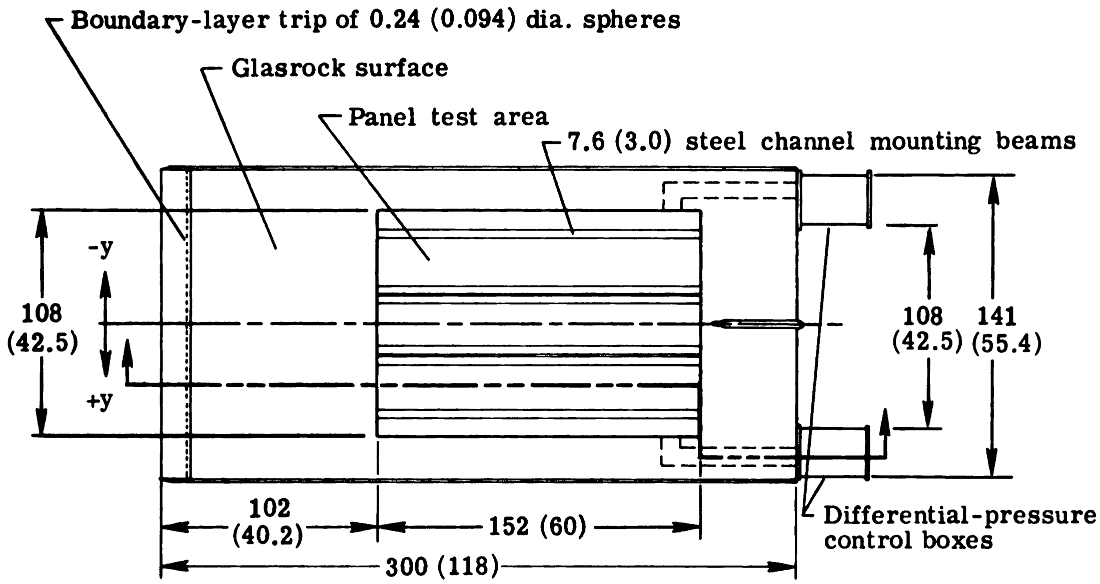

(a) Planview without panel.

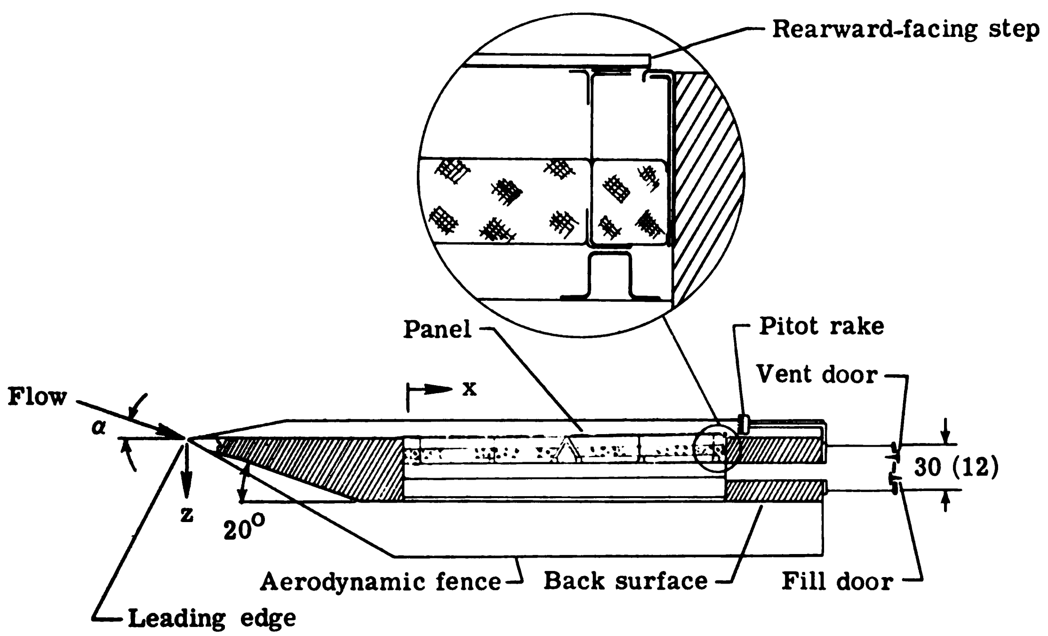

(b) Longitudinal cross section with panel in place.

Figure 7.- Details of panel holder. Dimensions are in cm (in.).

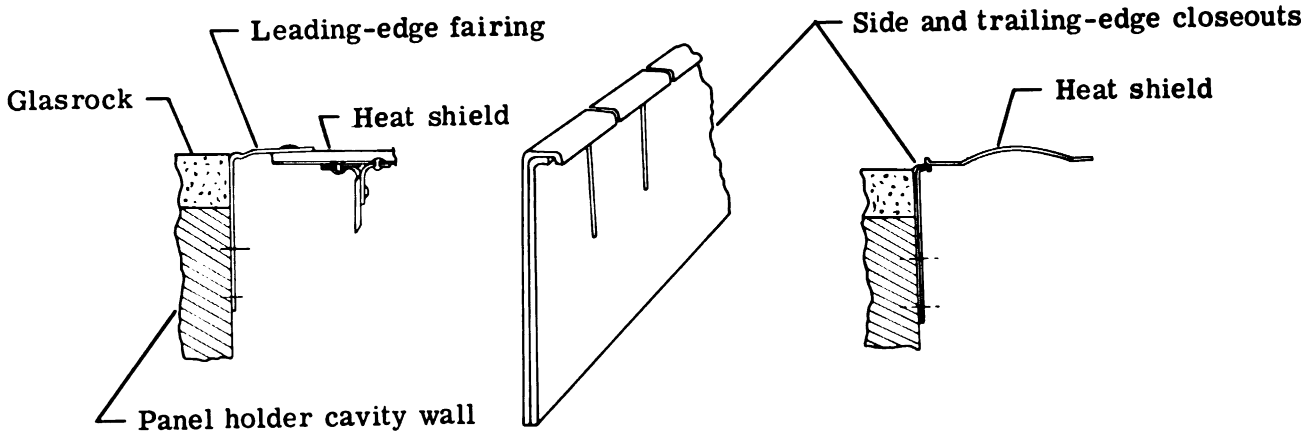

(a) Heat-shield edge closeouts.

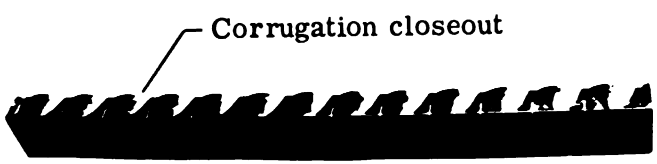

(b) Leading-edge fairing.

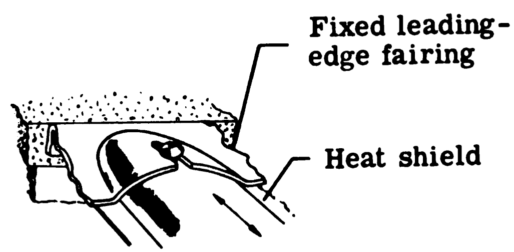

(c) Thermal expansion guide at heat-shield leading edge.

Figure 8.- Edge closeouts.

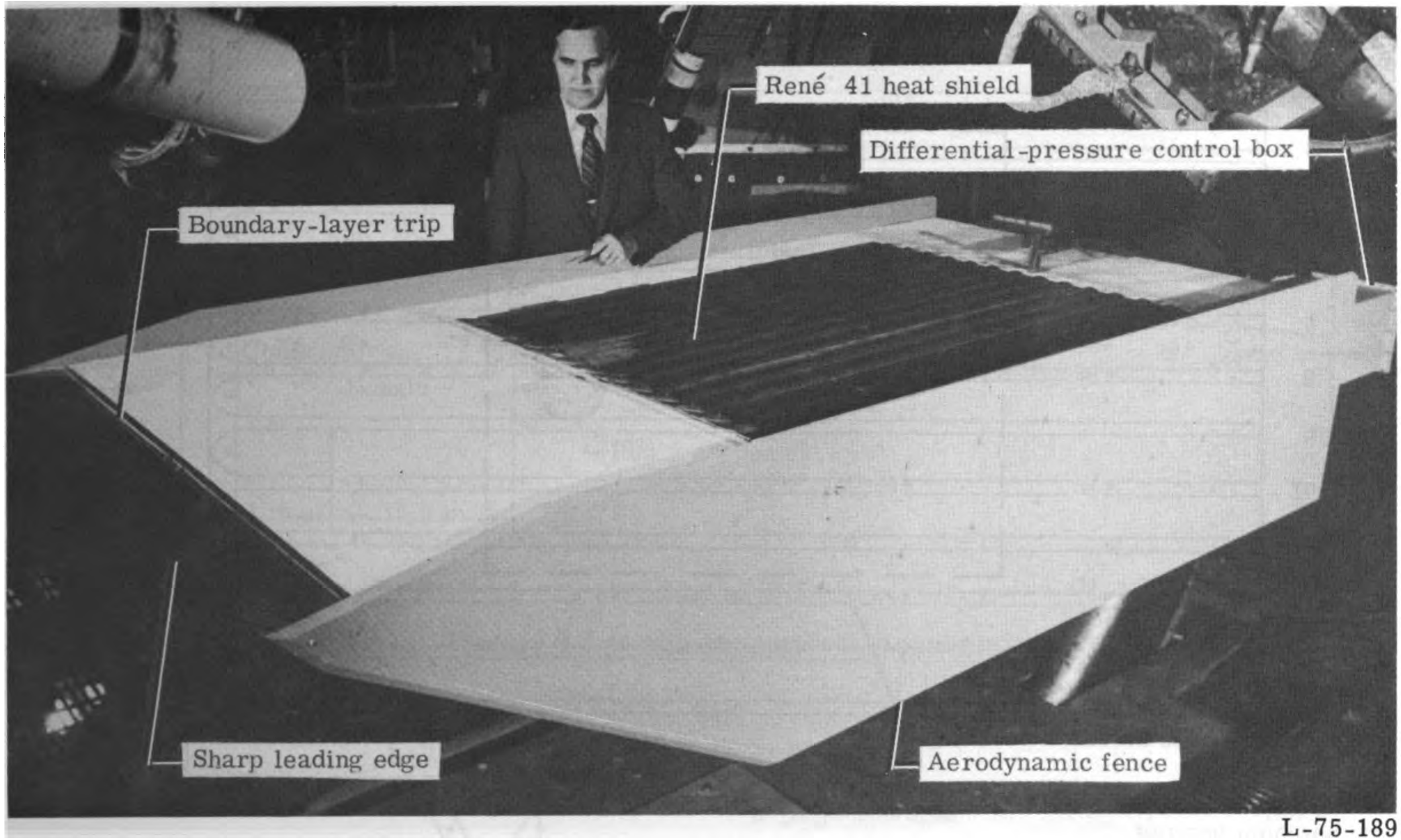

L-75-189

Figure 9.- René 41 thermal protection panel in test section.

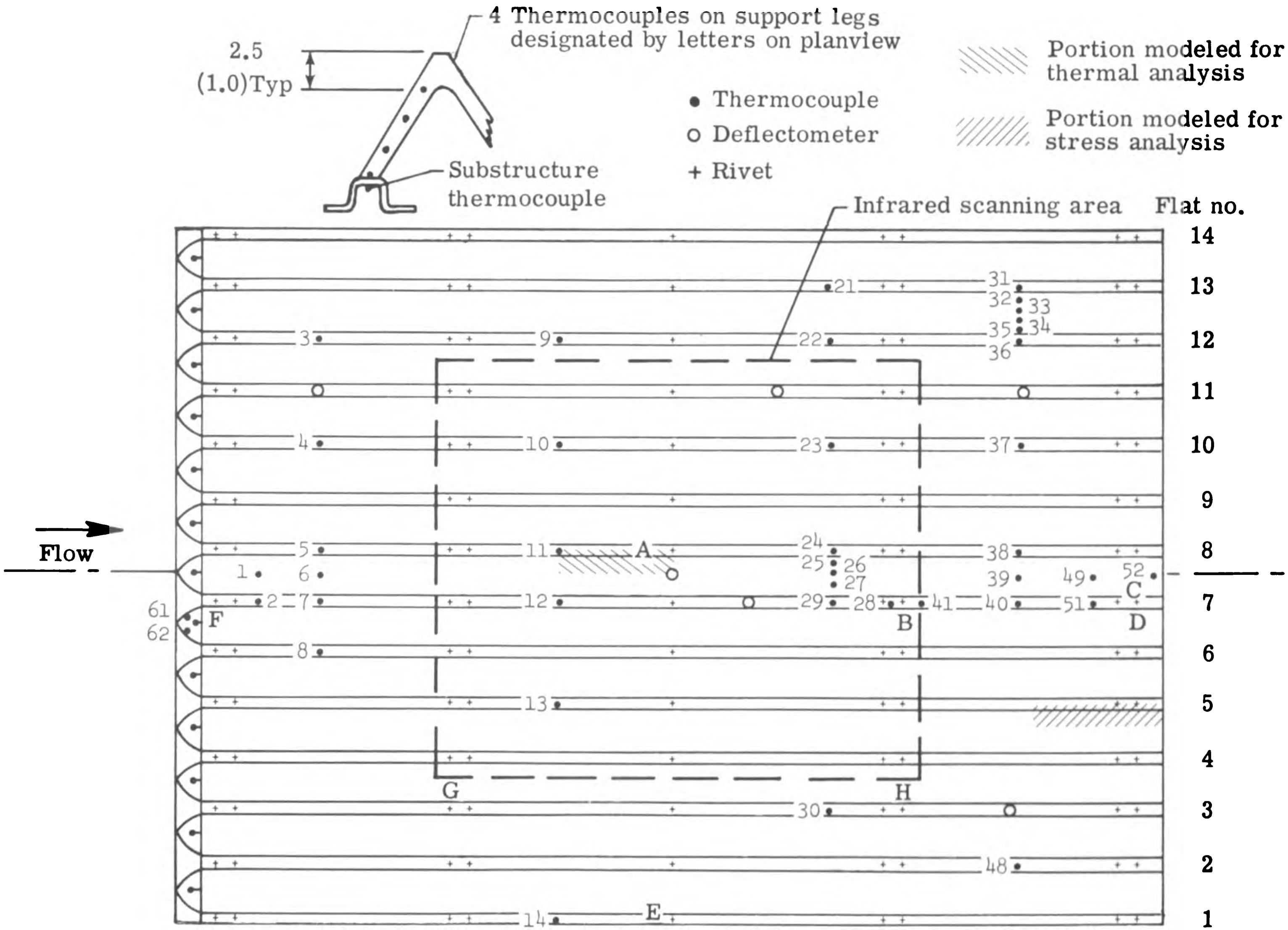

Figure 10.- Distribution of thermocouples and deflectometers under René 41 heat shield.

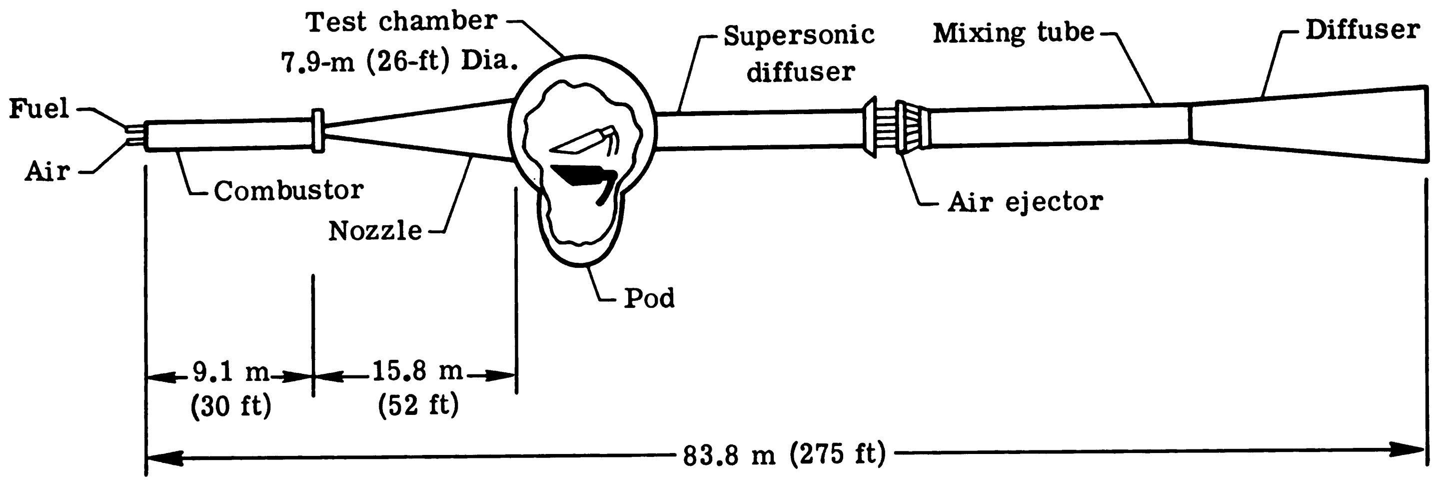

Figure 11.- Langley 8-foot high-temperature structures tunnel.

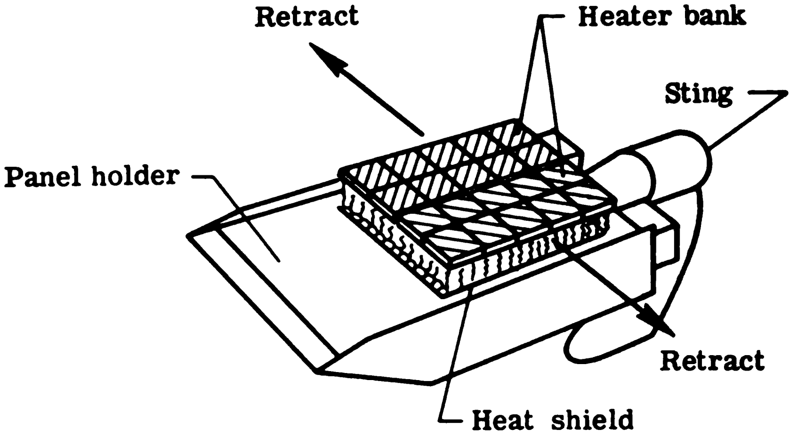

Figure 12.- Retractable quartz-lamp radiant heaters.

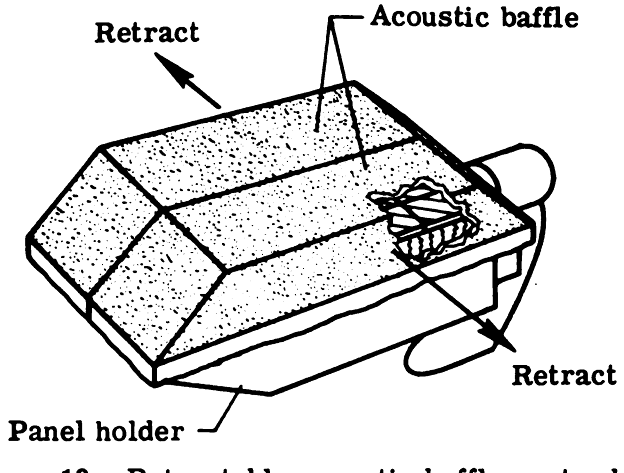

Figure 13.- Retractable acoustic baffles extended over panel holder.

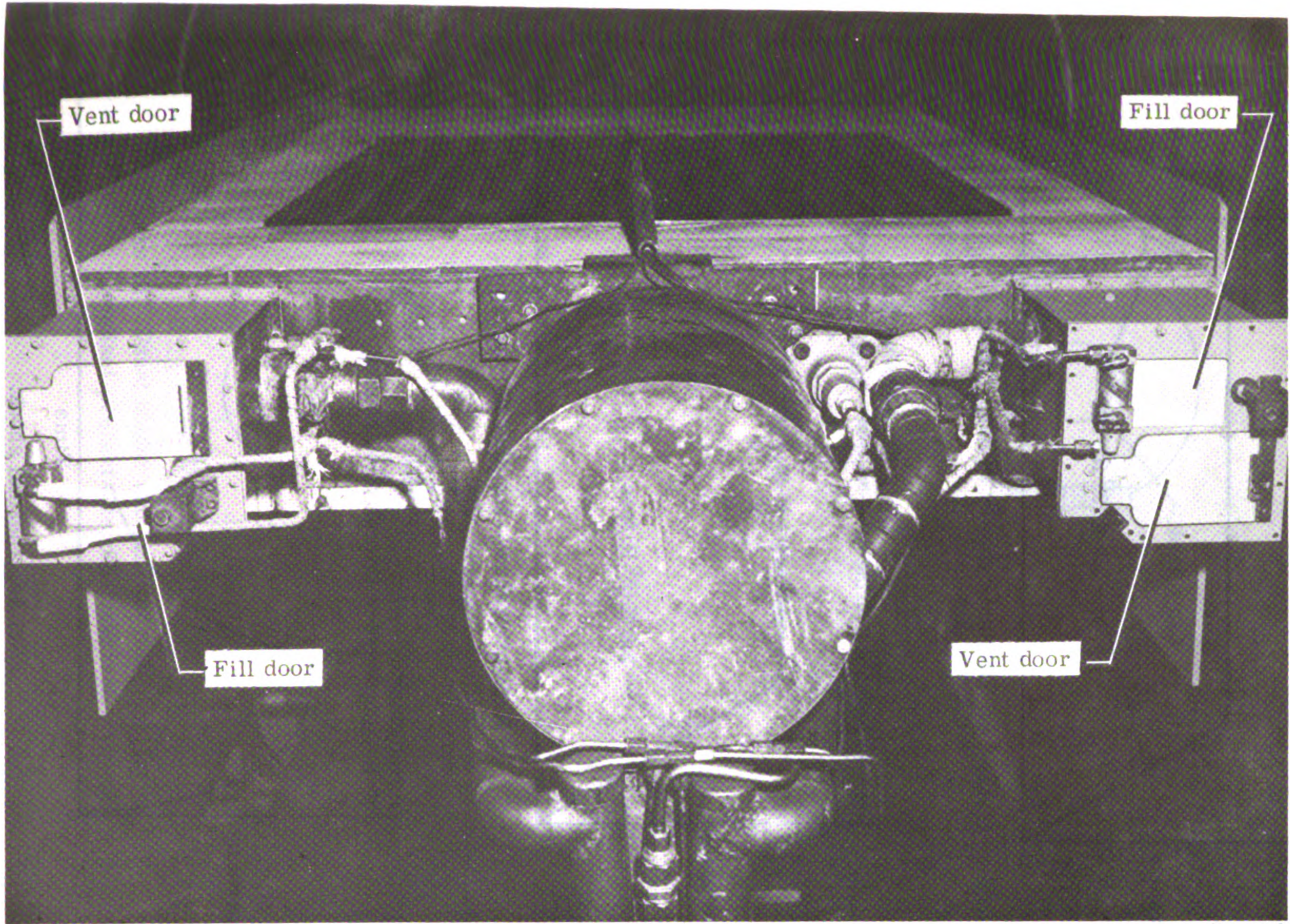

L-75-190

Figure 14.- Differential-pressure apparatus of panel holder.

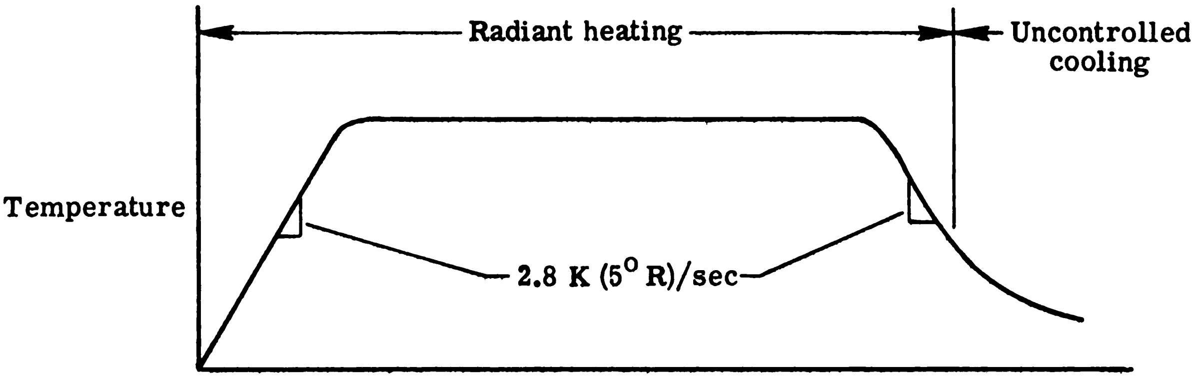

(a) Thermal cycle by radiant heating.

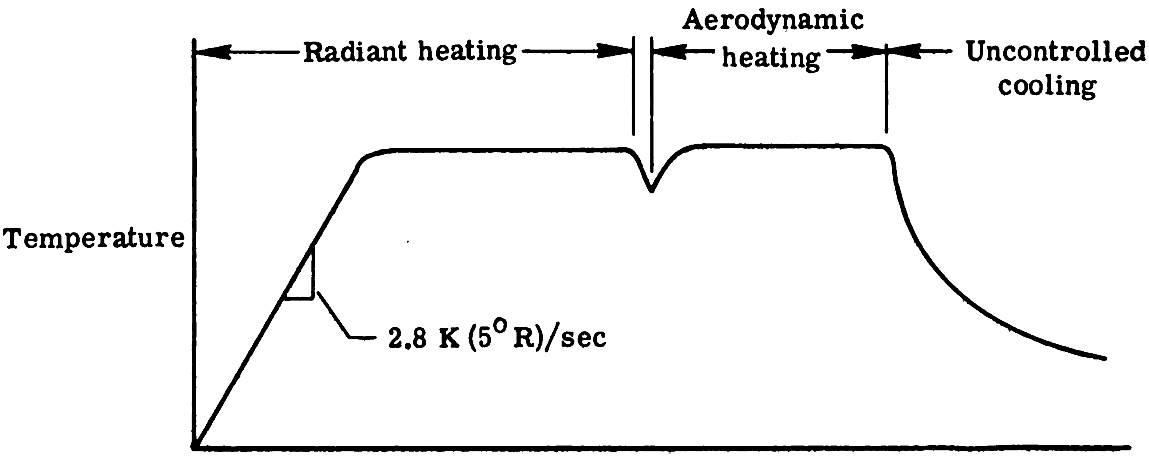

(b) Radiant-preheat—aerothermal exposure.

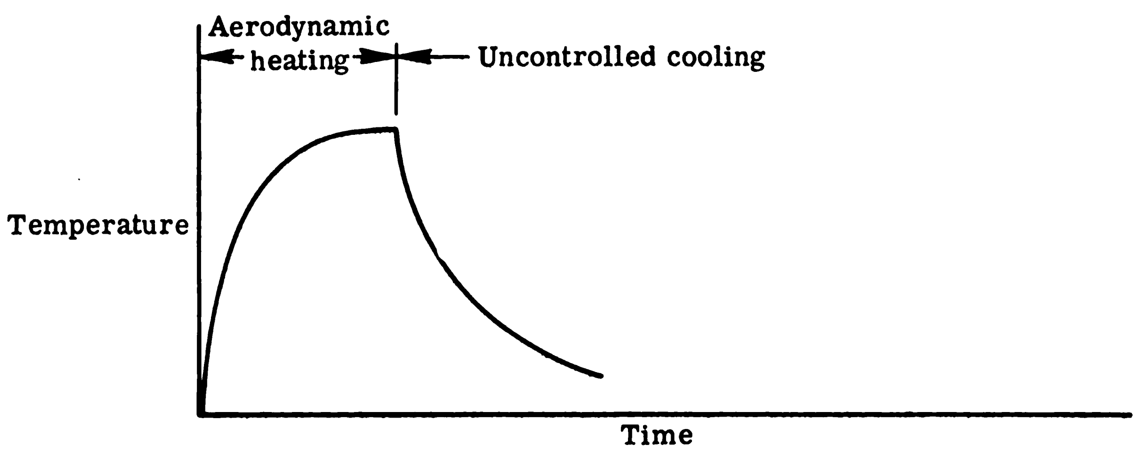

(c) Aerothermal shock.

Figure 15. - Typical surface temperature histories.

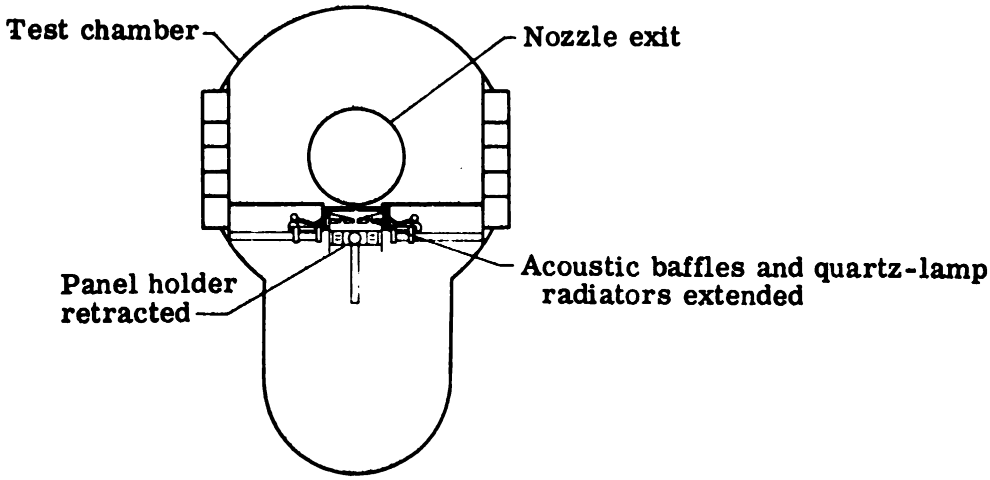

(a) Preheat and posttest.

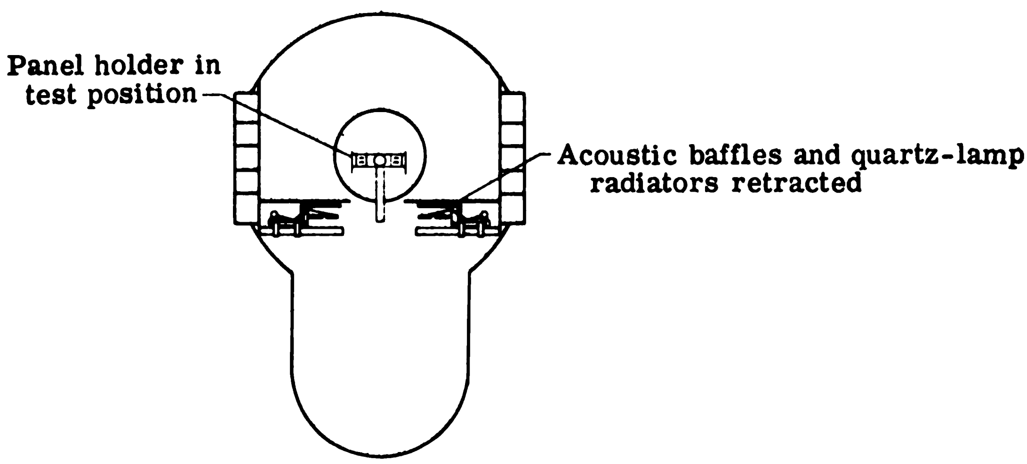

(b) During test.

Figure 16.- Panel holder and radiator positions during radiant-preheat—aerothermal test.

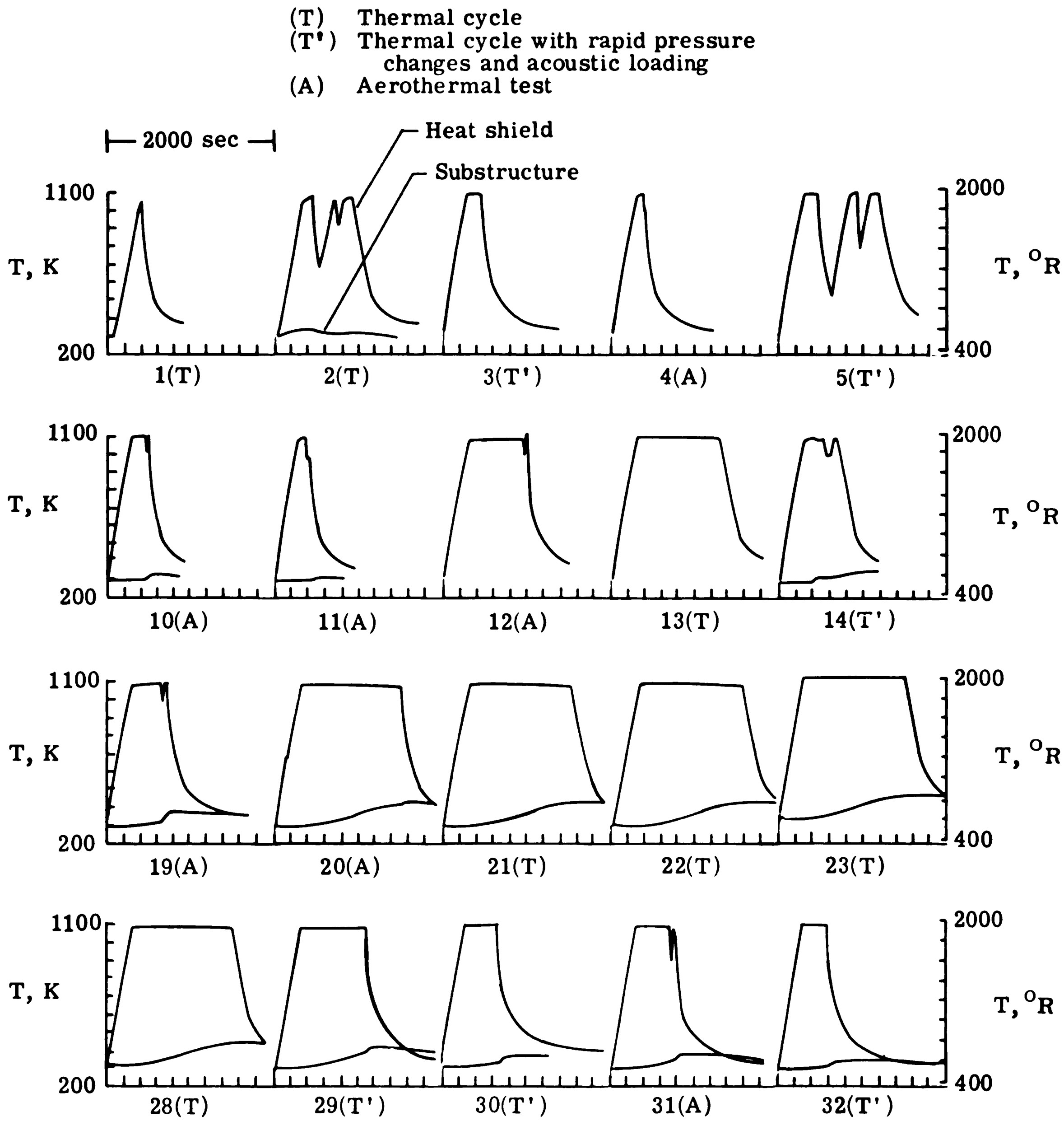

Figure 17.- Summary of heat-shield and substructure temperature responses.

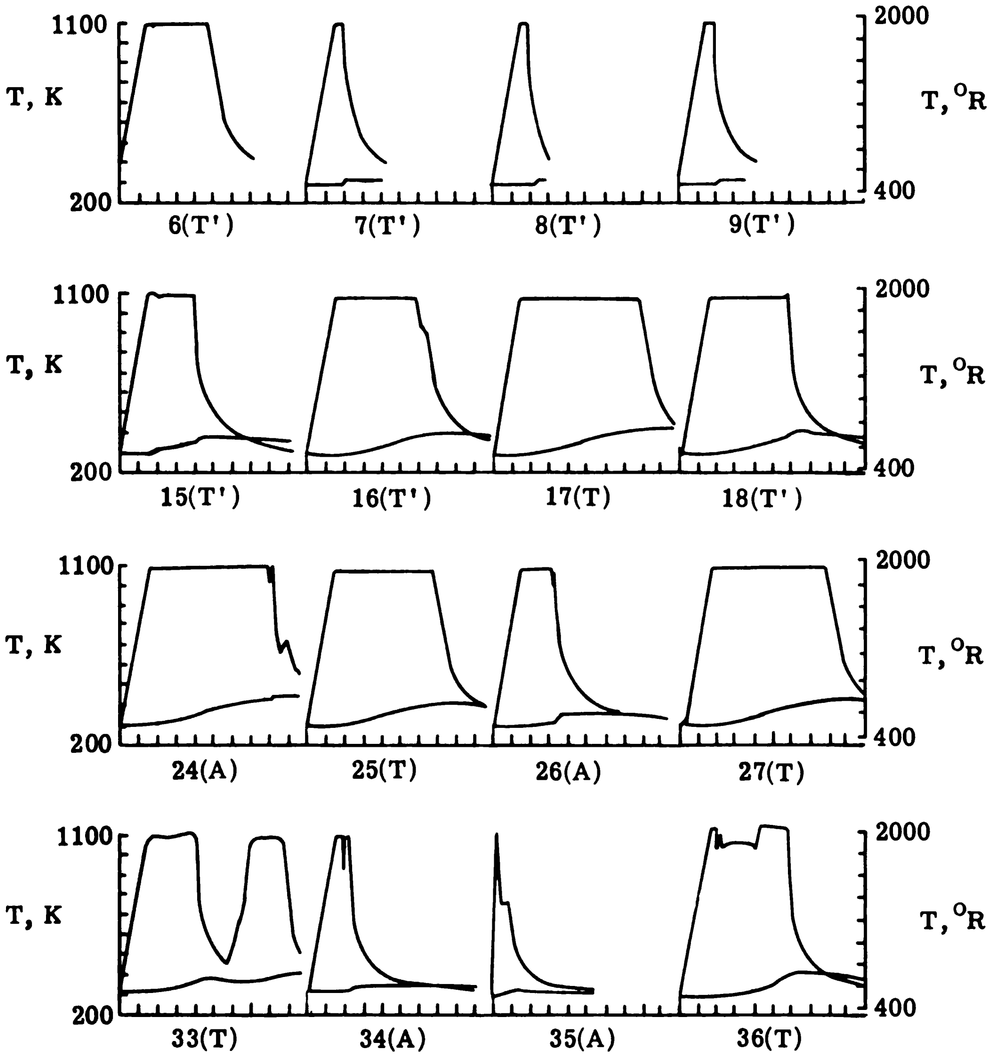

Figure 17.- Concluded.

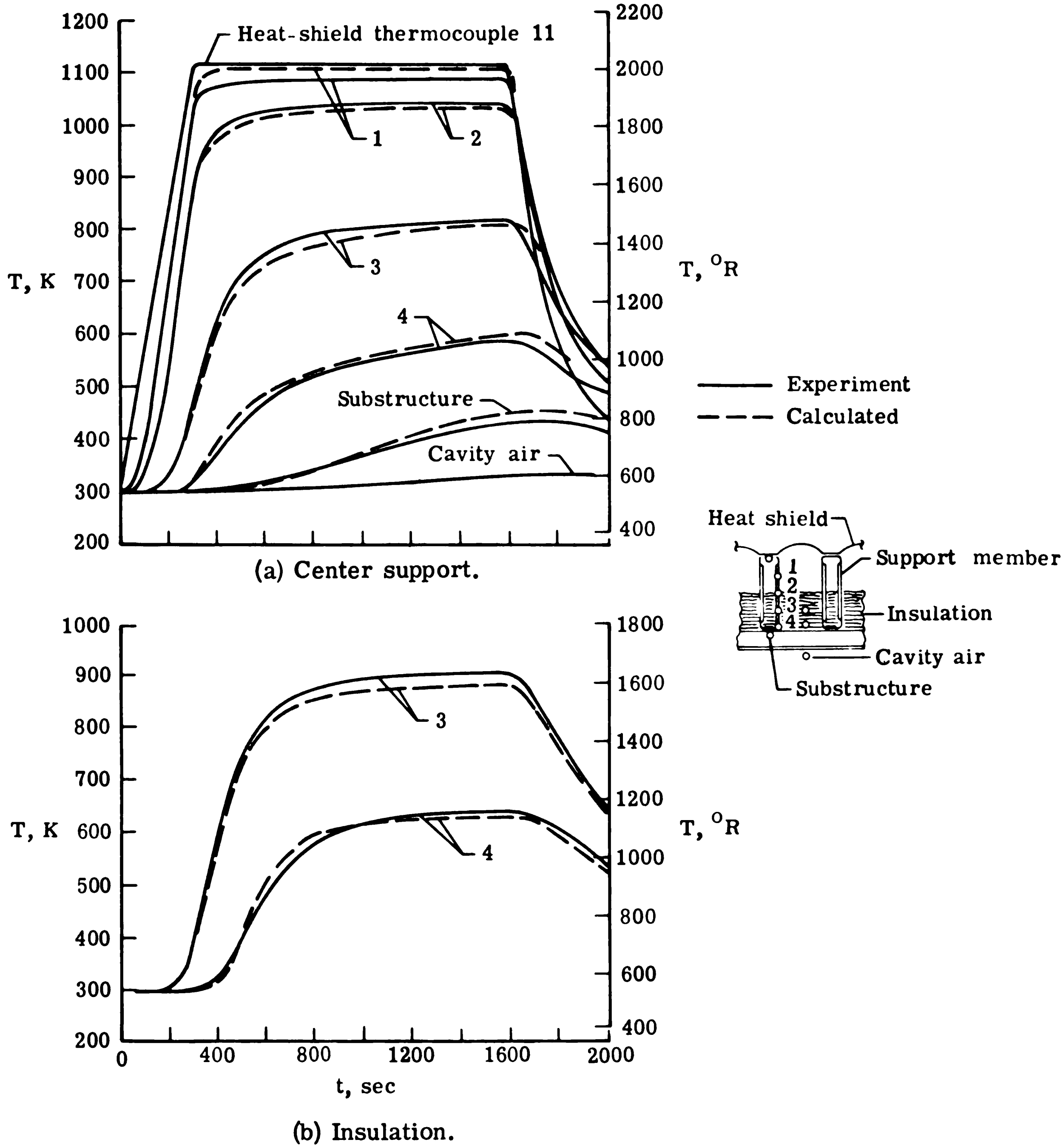

Figure 18.- Response of panel to radiant heating (test 17).

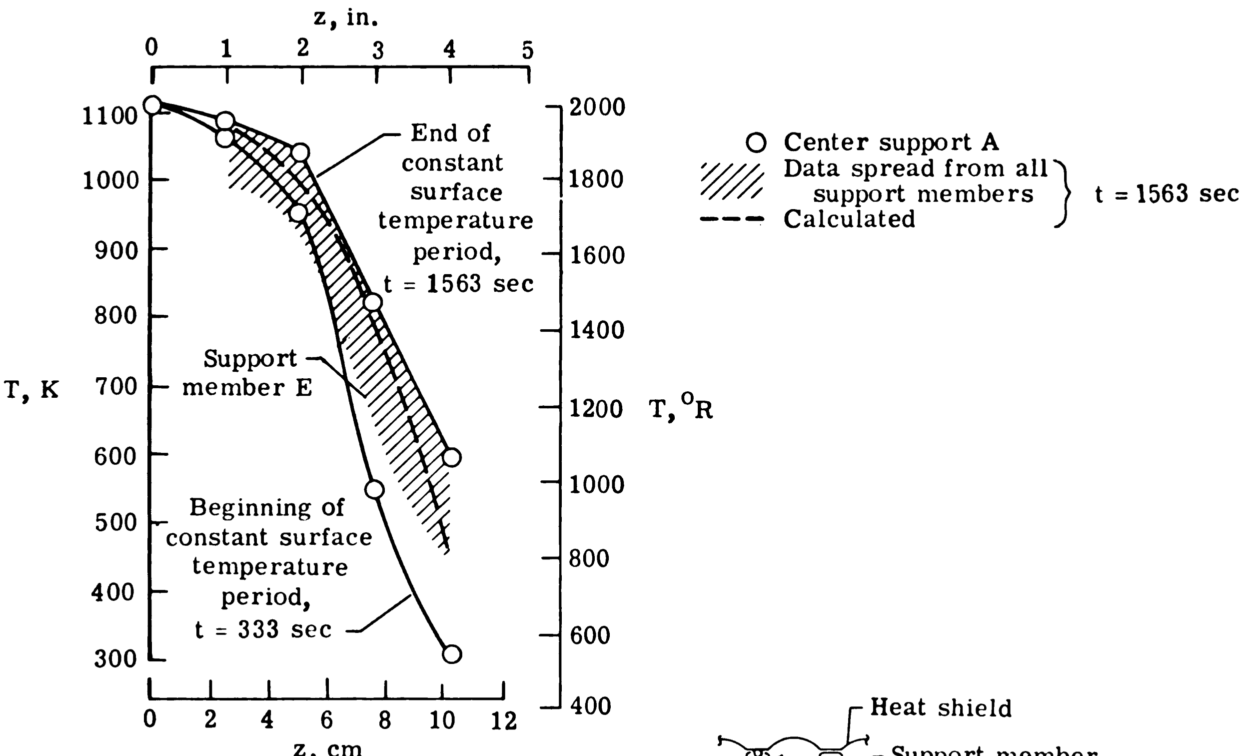

(a) Constant surface temperature.

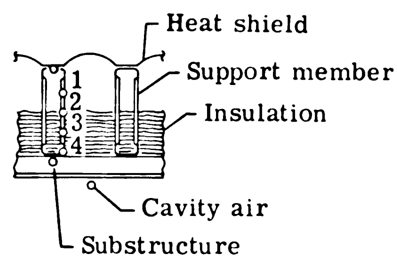

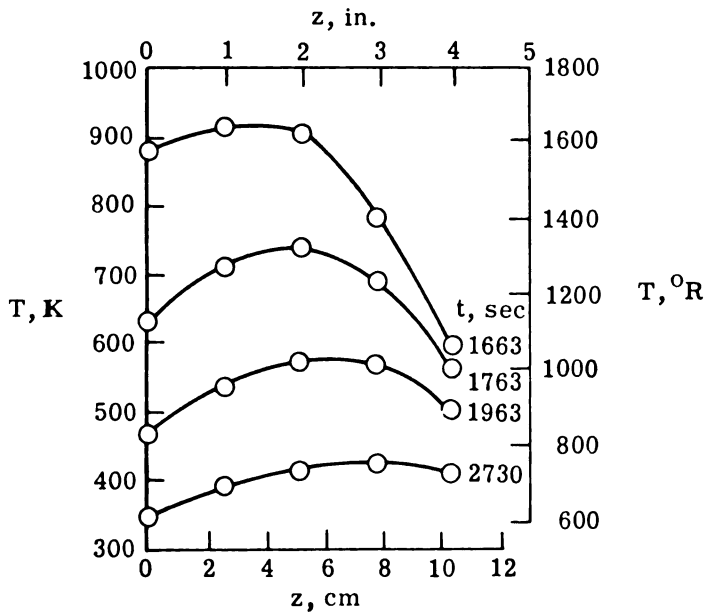

(b) Cooldown.

Figure 19.- Comparison of support-member temperatures during heating and cooling.

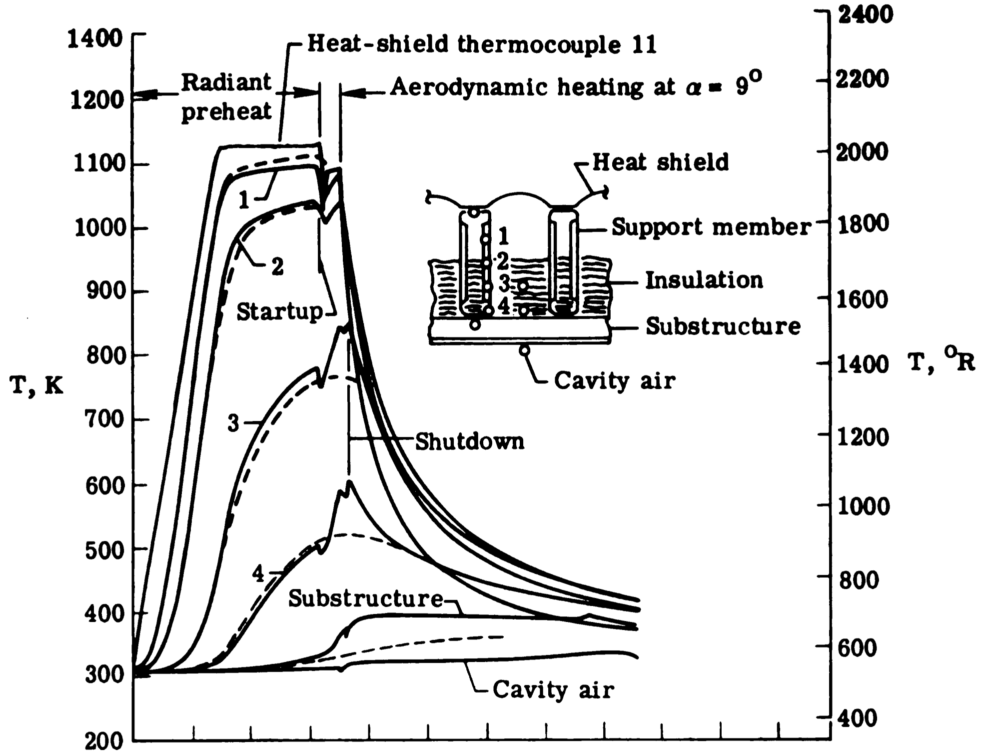

(a) Center support.

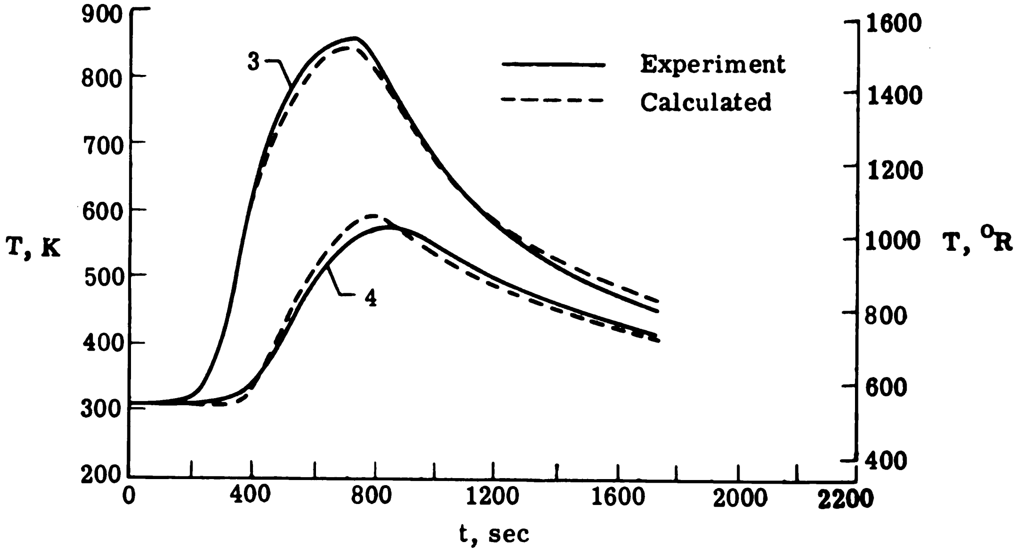

(b) Insulation.

Figure 20.- Response of panel to radiant preheating followed by exposure to aerodynamic heating; vent doors open (test 19).

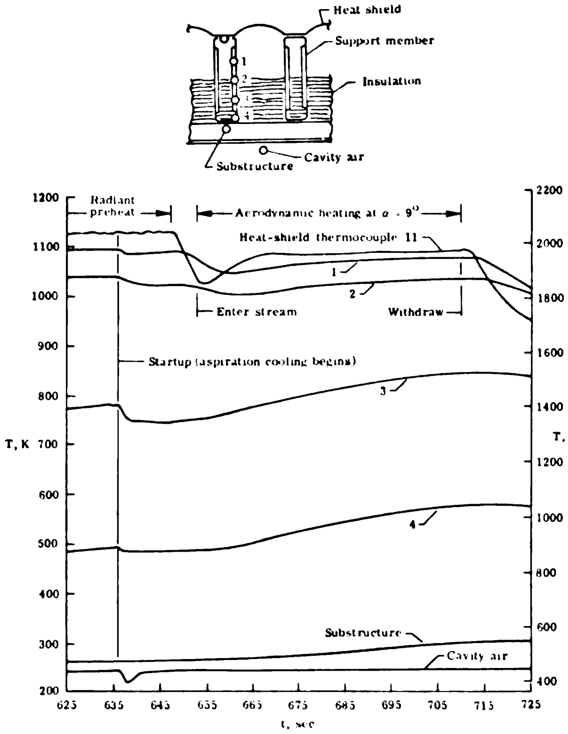

Figure 21.- Thermal response of panel to aerodynamic heating; vent doors open (test 19).

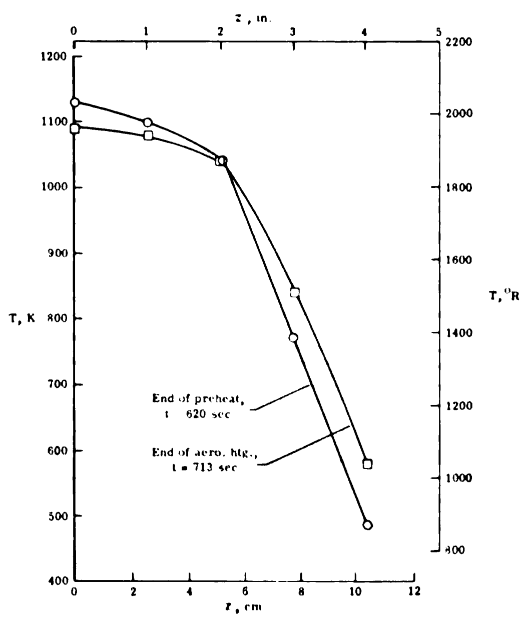

Figure 22.- Temperature distributions on center support during radiant-preheat—aerothermal test; vent doors open (test 19).

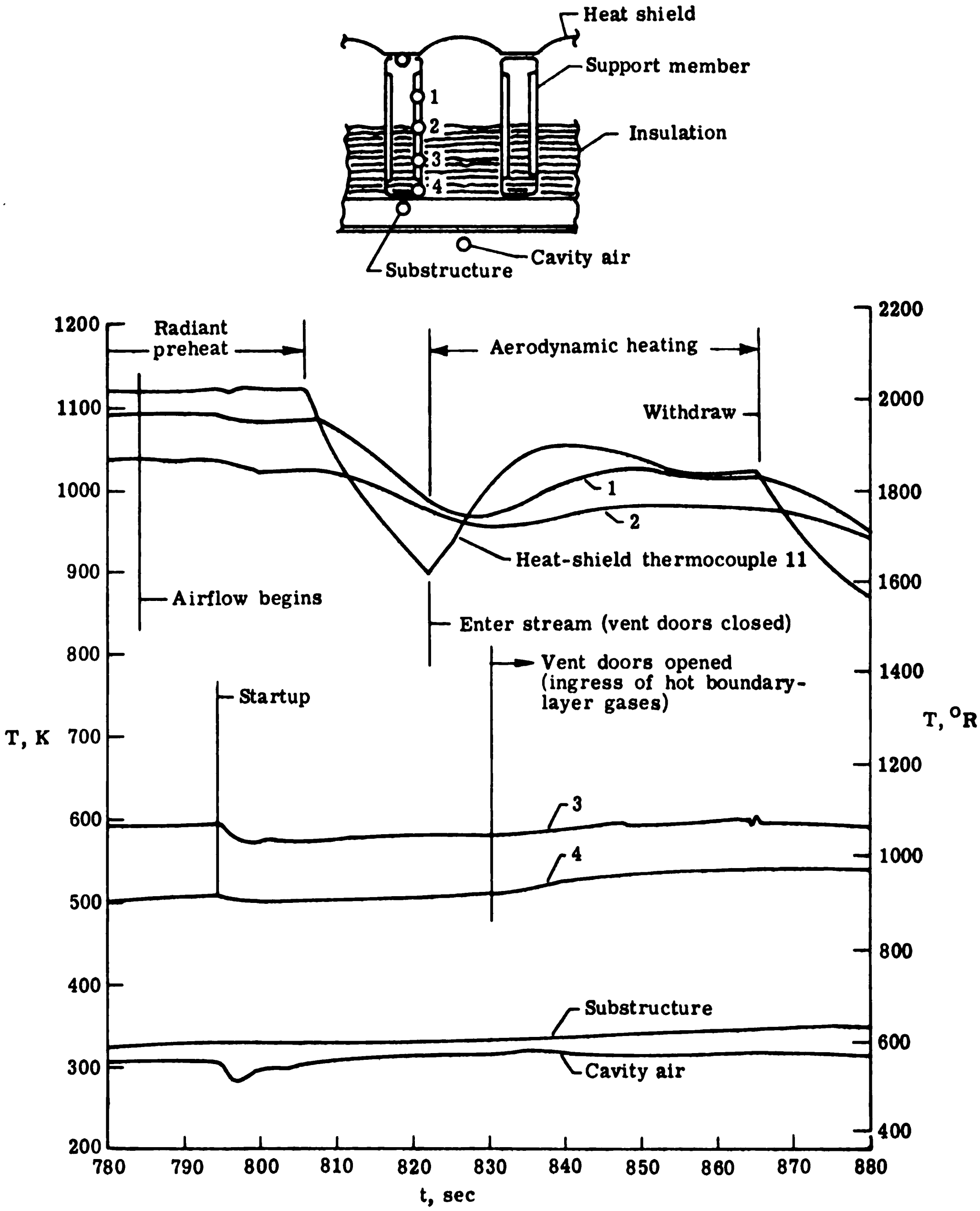

Figure 23.- Thermal response of panel during test 31 showing effect of vent door position.

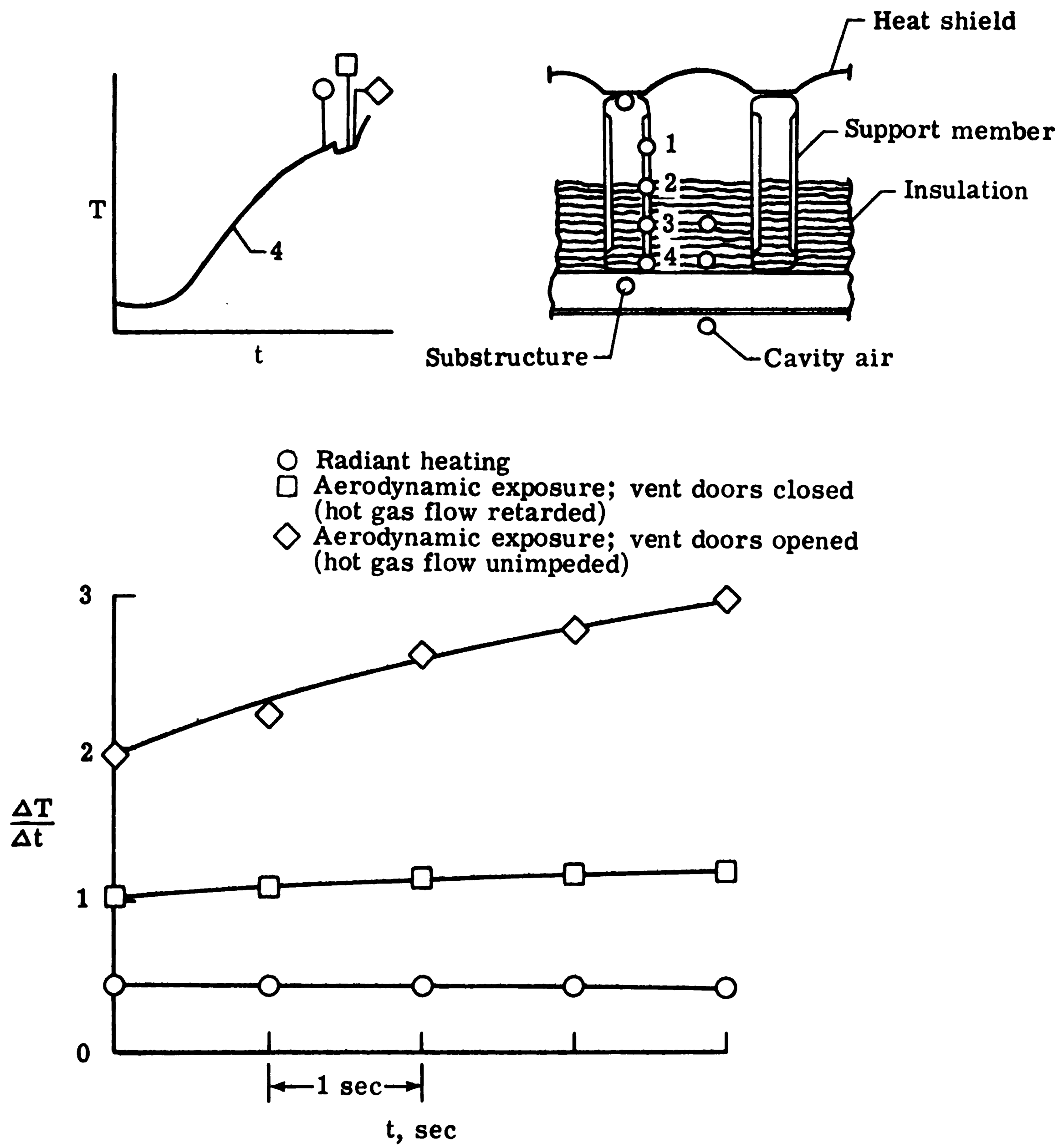

Figure 24.- Effect of hot-gas flow on thermal response at bottom of support member (location 4), test 31.

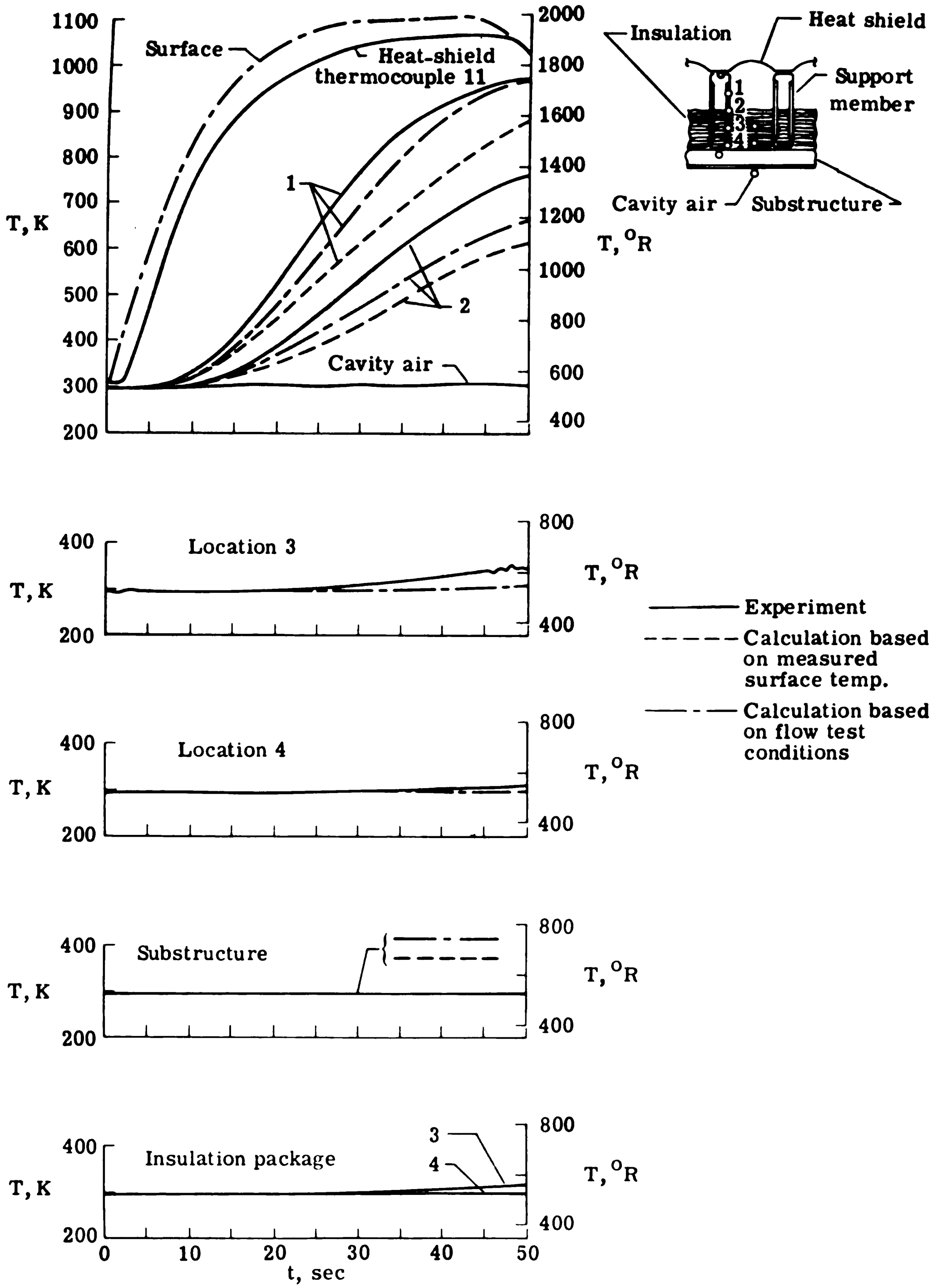

Figure 25.- Response of panel to aerothermal shock at $M_\infty \approx 7$; vent doors closed (test 35).

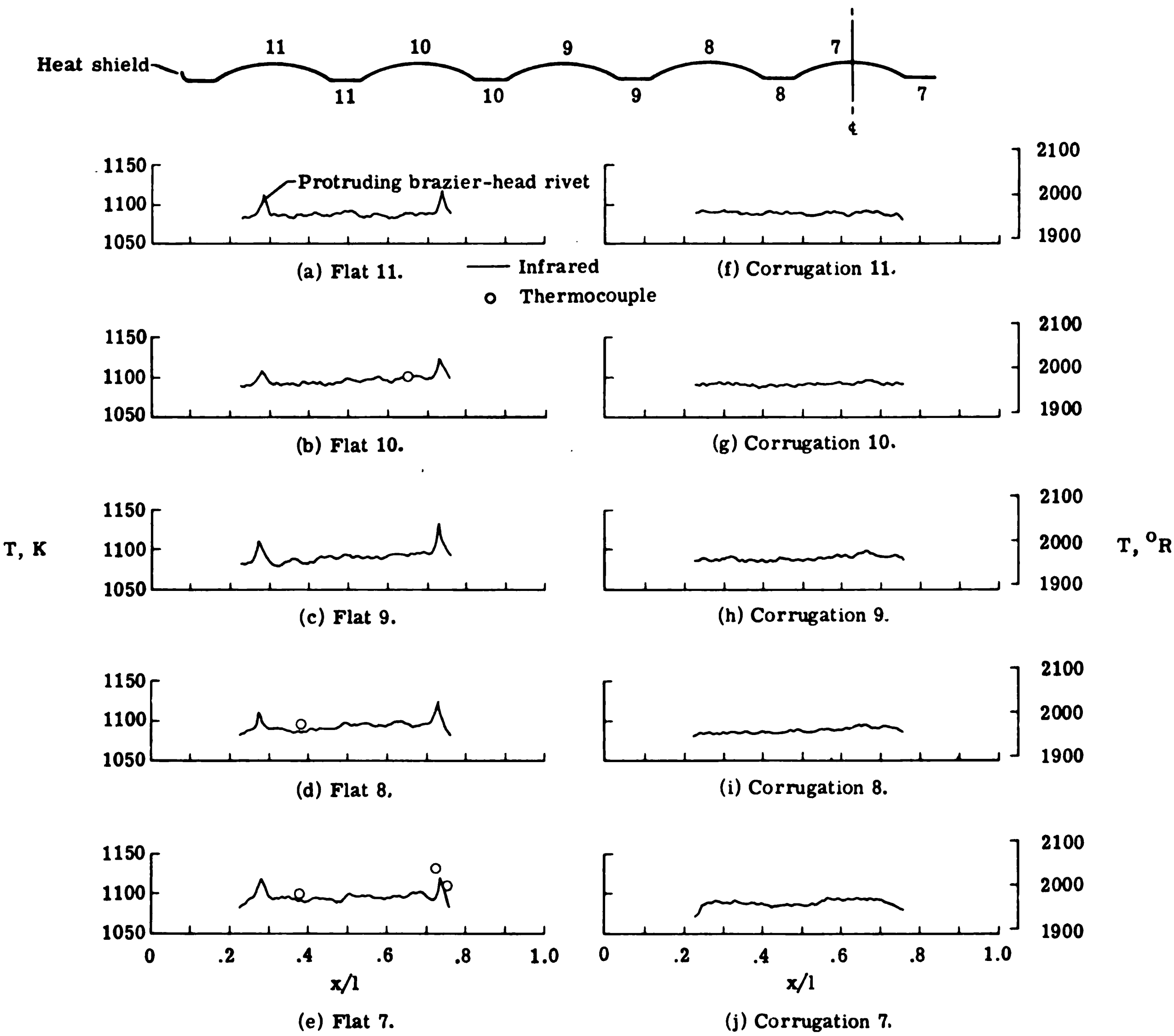

Figure 26.- Infrared scanlines of René 41 heat-shield surface temperatures after approximately 55 sec of aerodynamic heating following radiant preheating (test 19).

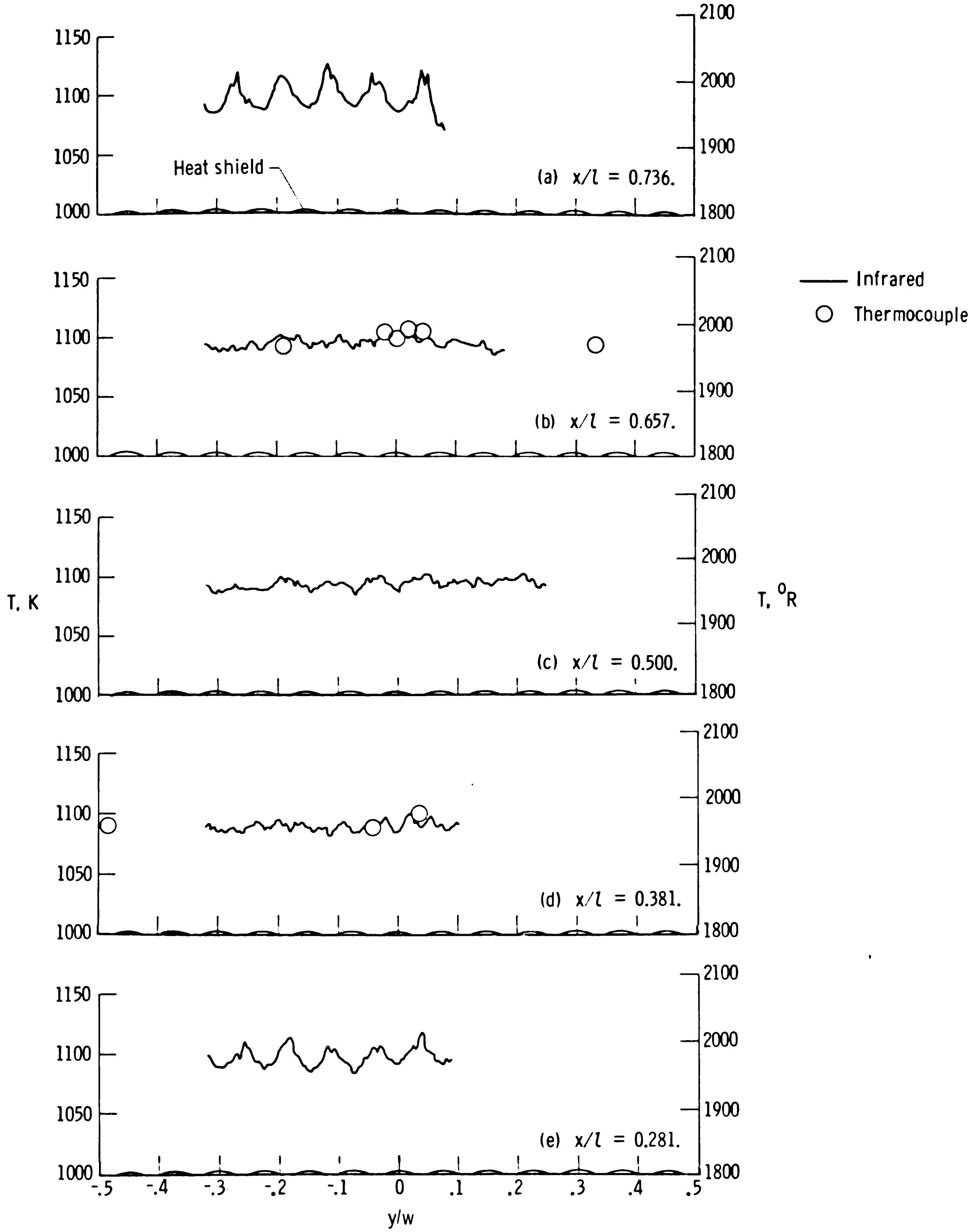

Figure 27.- Spanwise surface temperature distributions of René 41 heat shield by infrared radiometry after approximately 55 sec of aerodynamic heating following radiant preheating (test 19).

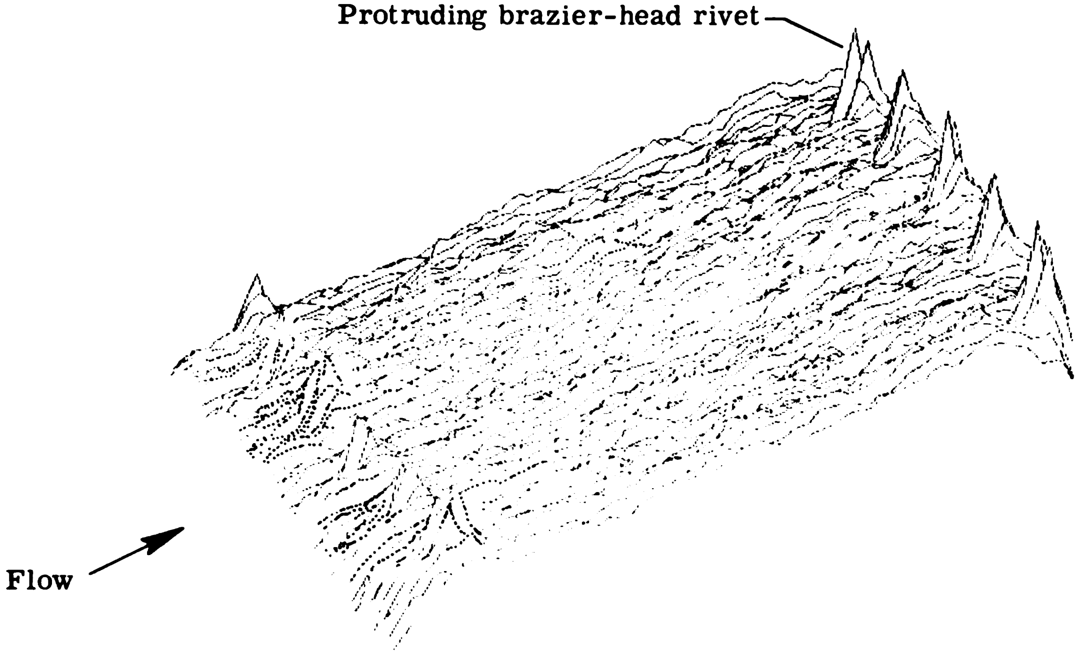

Figure 28.- Pictorial representation of aerodynamically heated René 41 heat-shield surface from infrared radiometry.

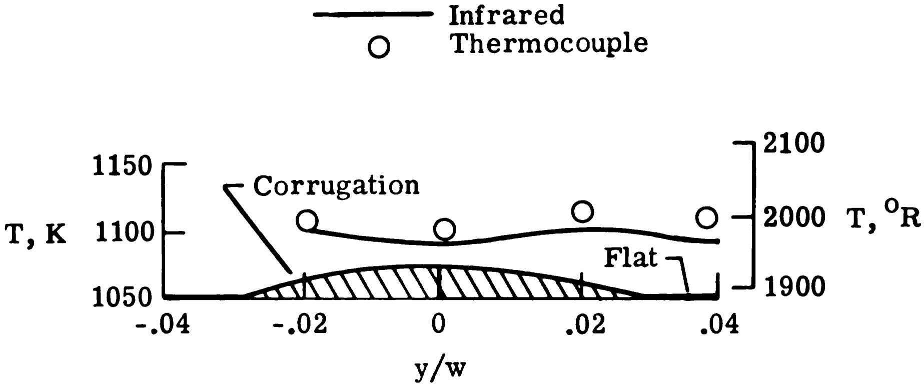

Figure 29.- Temperature distribution across center-line corrugation of René 41 heat shield during aerodynamic heating.

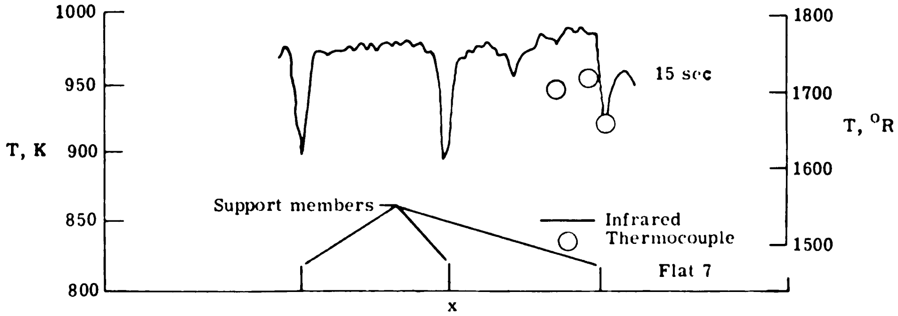

Figure 30.- Infrared scanline of René 41 heat shield during transient aerodynamic heating (test 35).

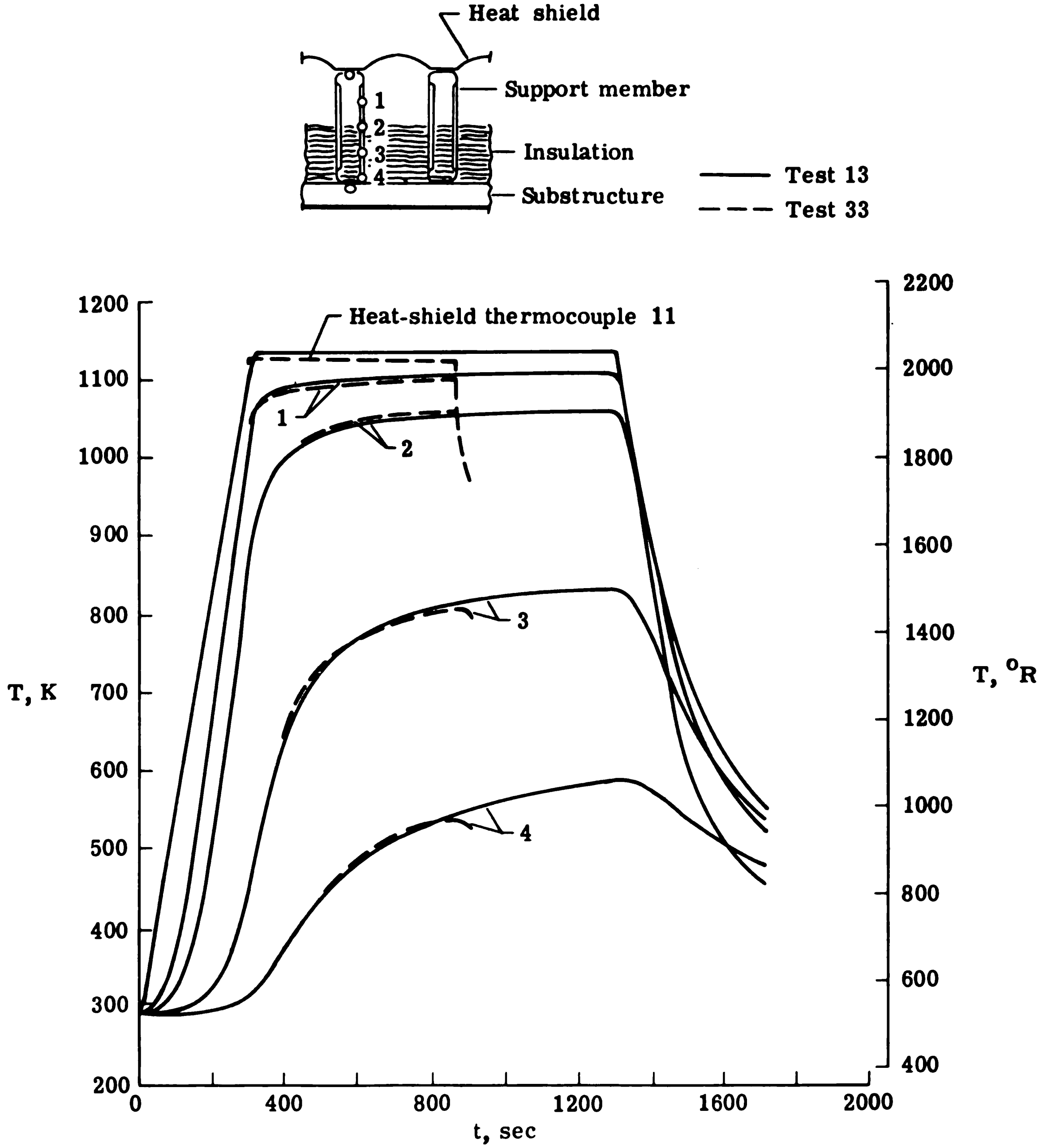

Figure 31.- Comparison of temperatures obtained early and late in heating-test series on René 41 heat shield and support members.

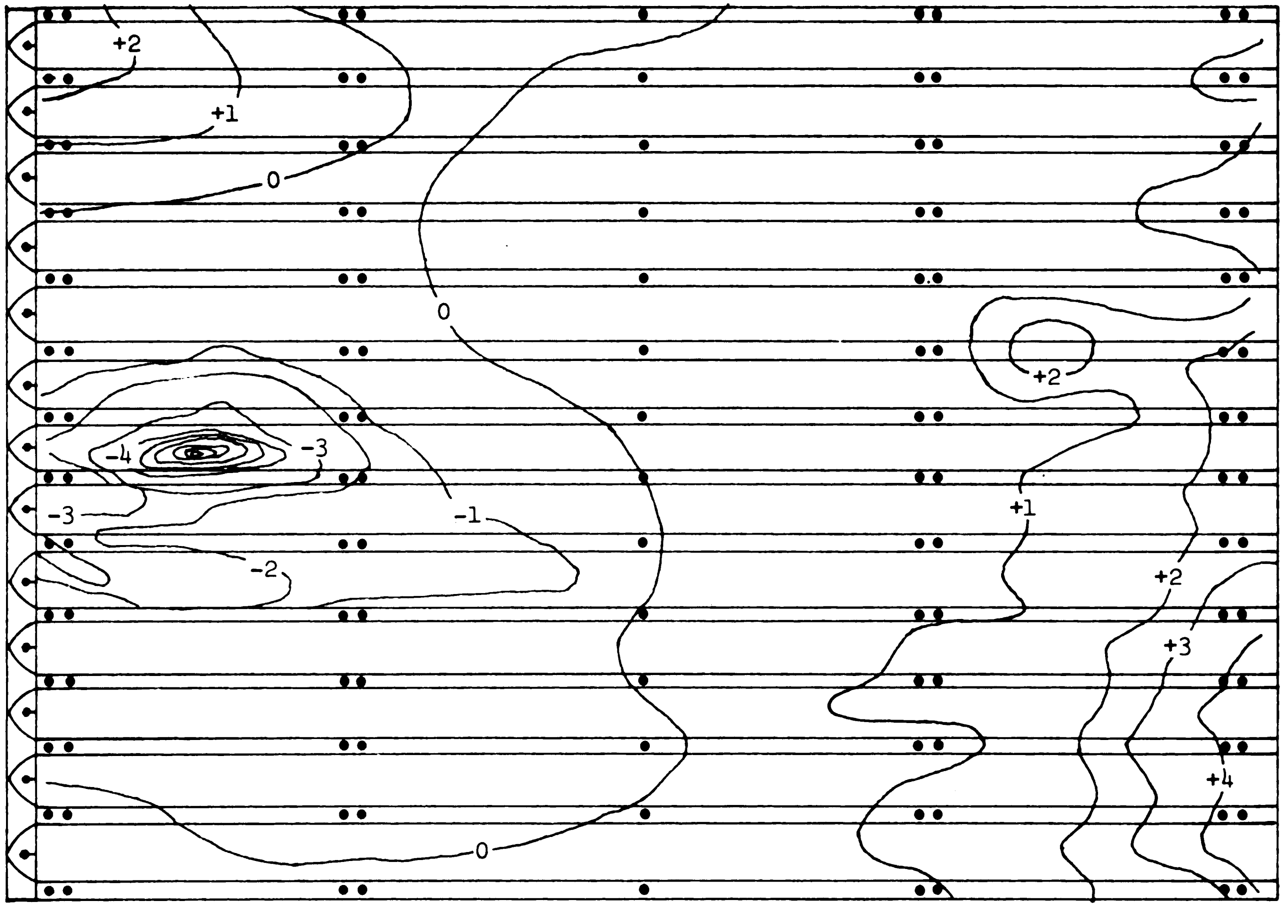

Figure 32.- Map of changes in surface deformations of René 41 heat shield at end of heating test series. Each contour represents 0.025-cm (0.010-in.) change.

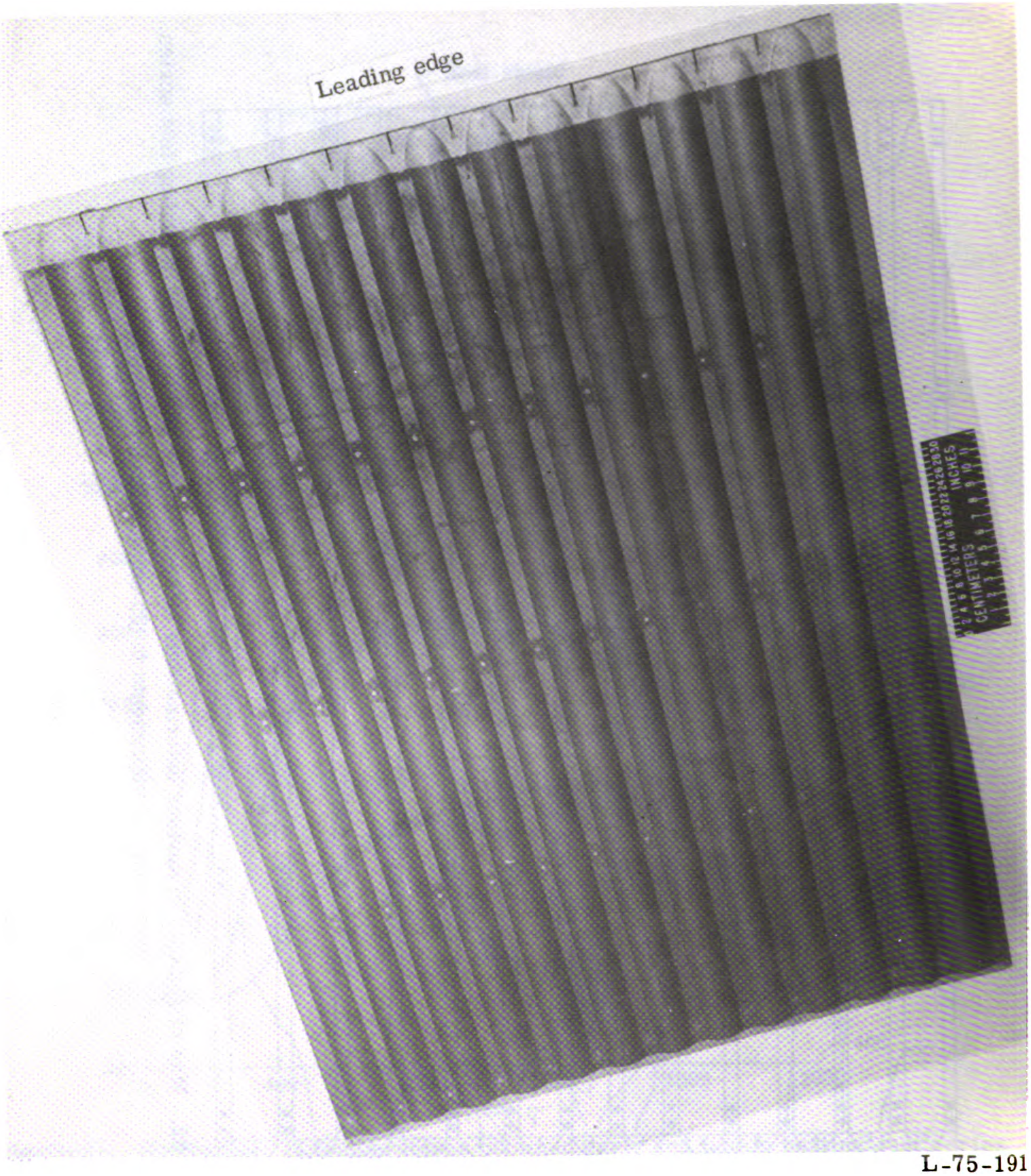

L-75-191

(a) Before testing.

Figure 33.- René 41 heat-shield surface before and after testing.

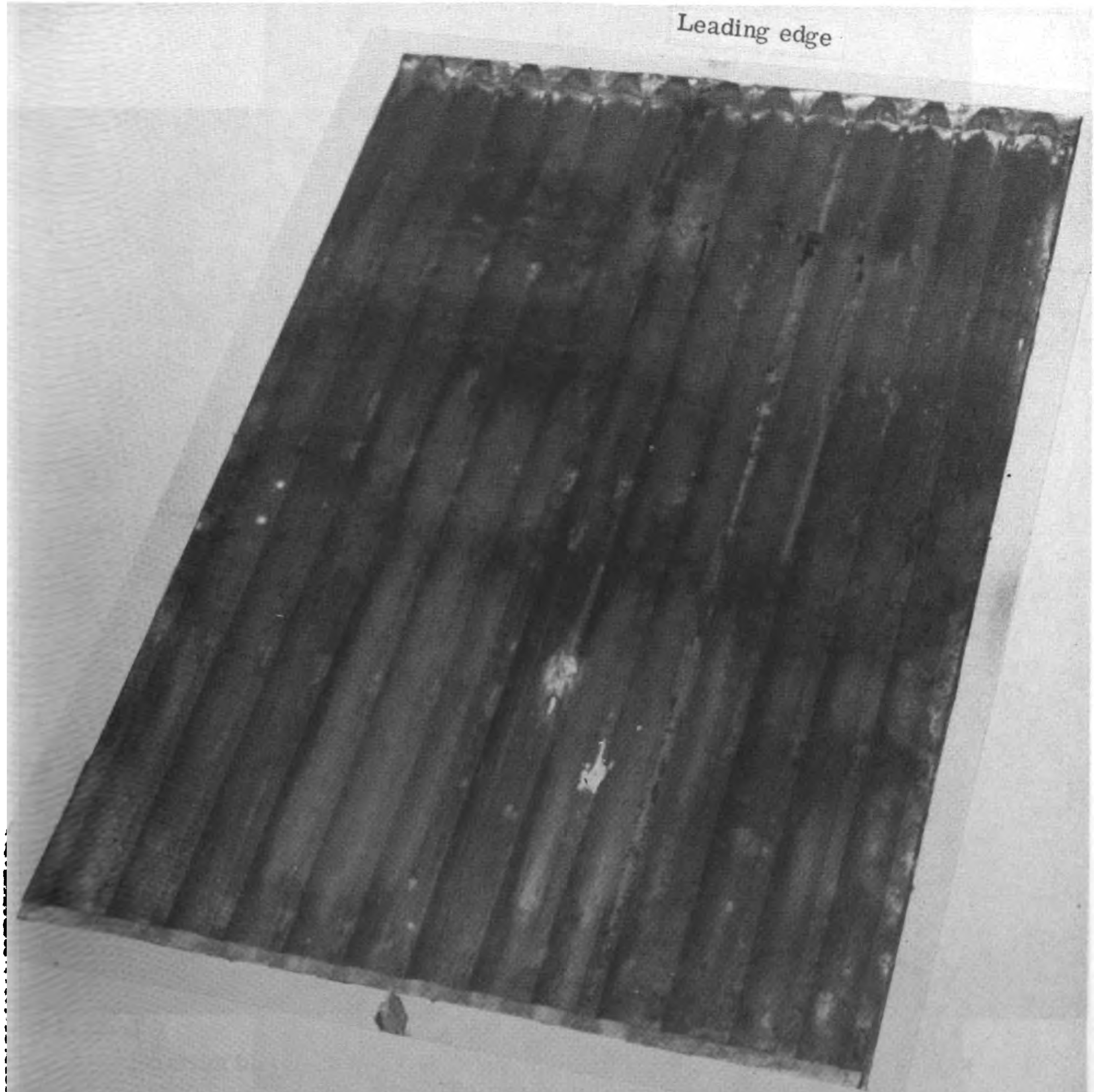

L-75-192

(b) After testing.

Figure 33.- Concluded.

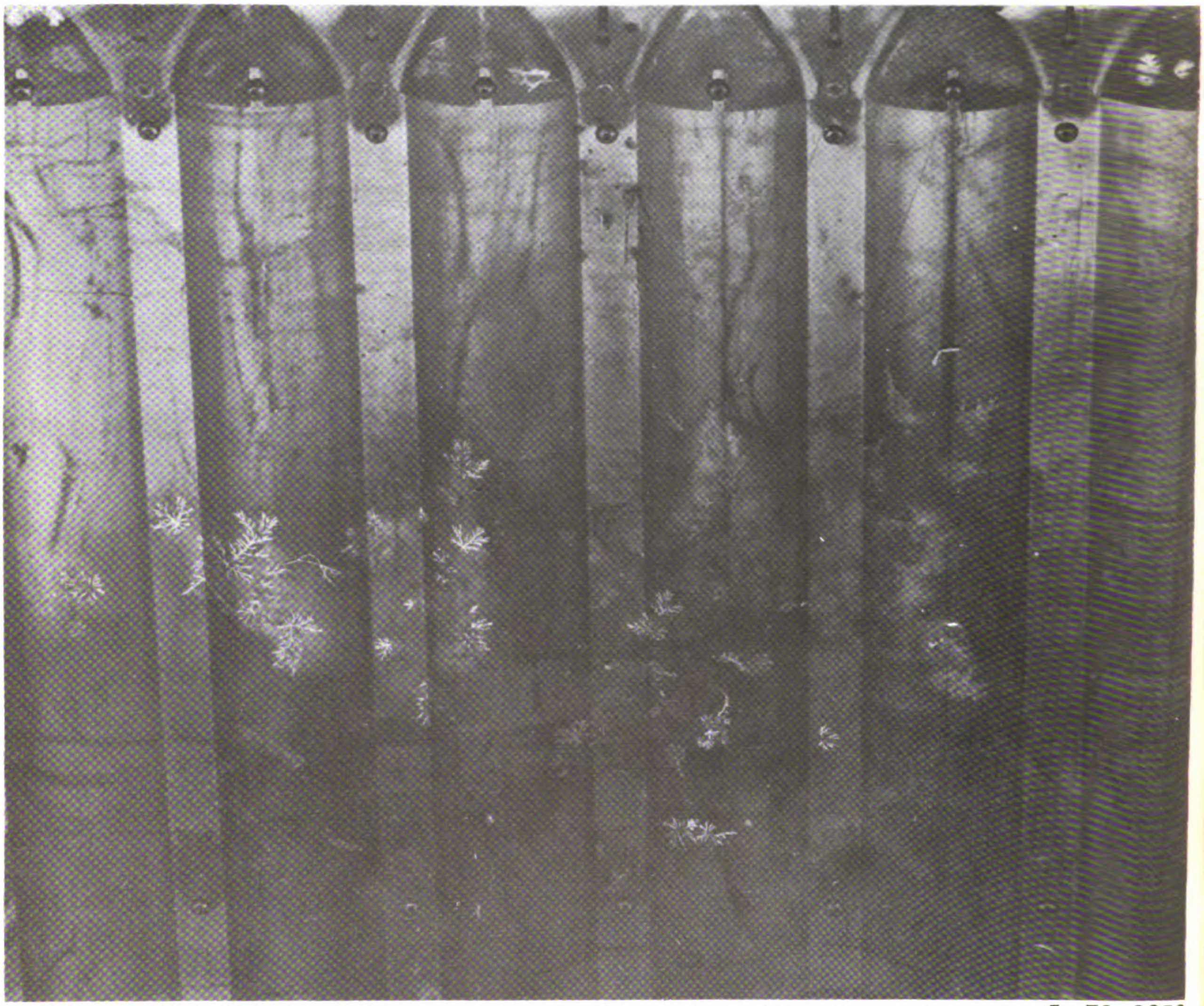

L-73-2258

Figure 34.- Electrical arcing patterns on René 41 heat-shield surface.

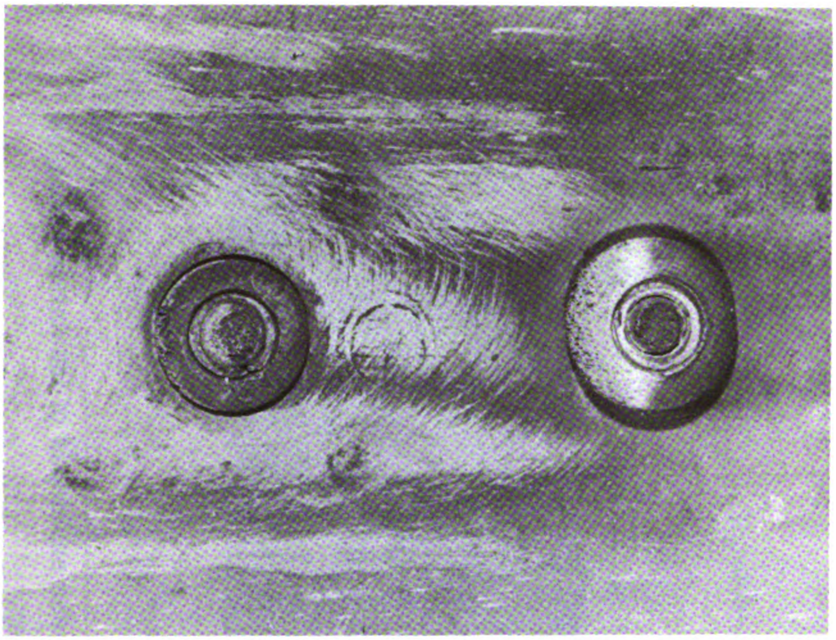

(a) At upstream support member.

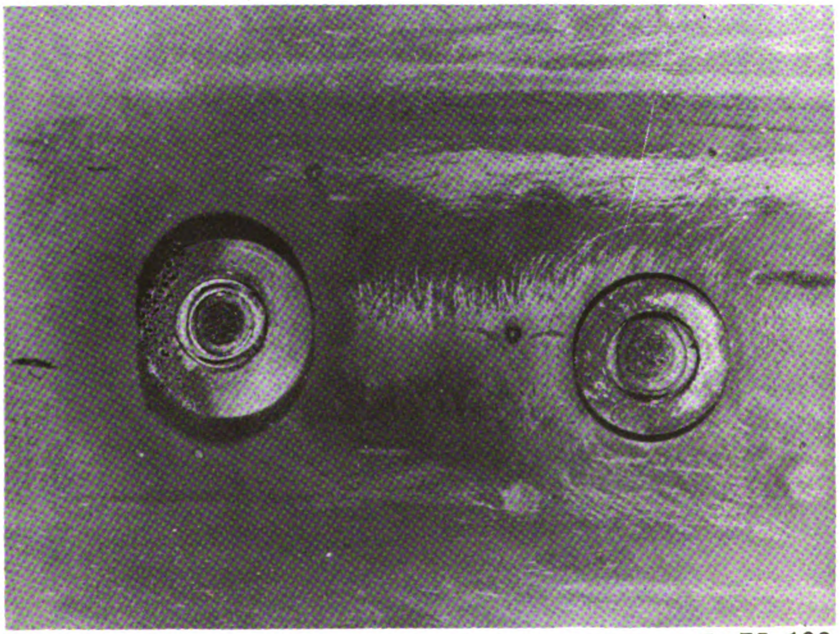

L-75-193

(b) At downstream support member.

Figure 35.- Eroded rivets after exposure to aerodynamic heating at $M_\infty = 6.7$ and $T_t \approx 1722$ K (3100° R); maximum rivet-head diameter, 0.8 cm (0.3 in.).

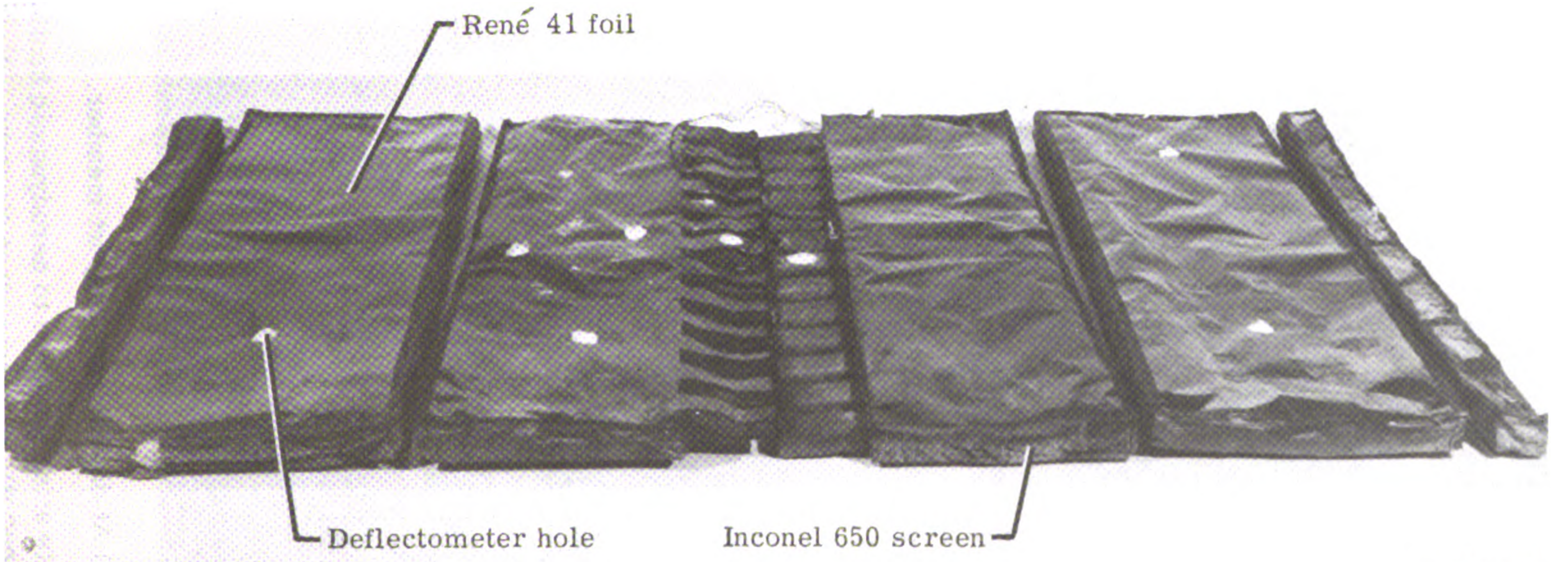

L-75-194

Figure 36.- Oxidized surfaces of René 41 foil and Inconel 650 screen envelopes of insulation packages after exposure to radiant heating.

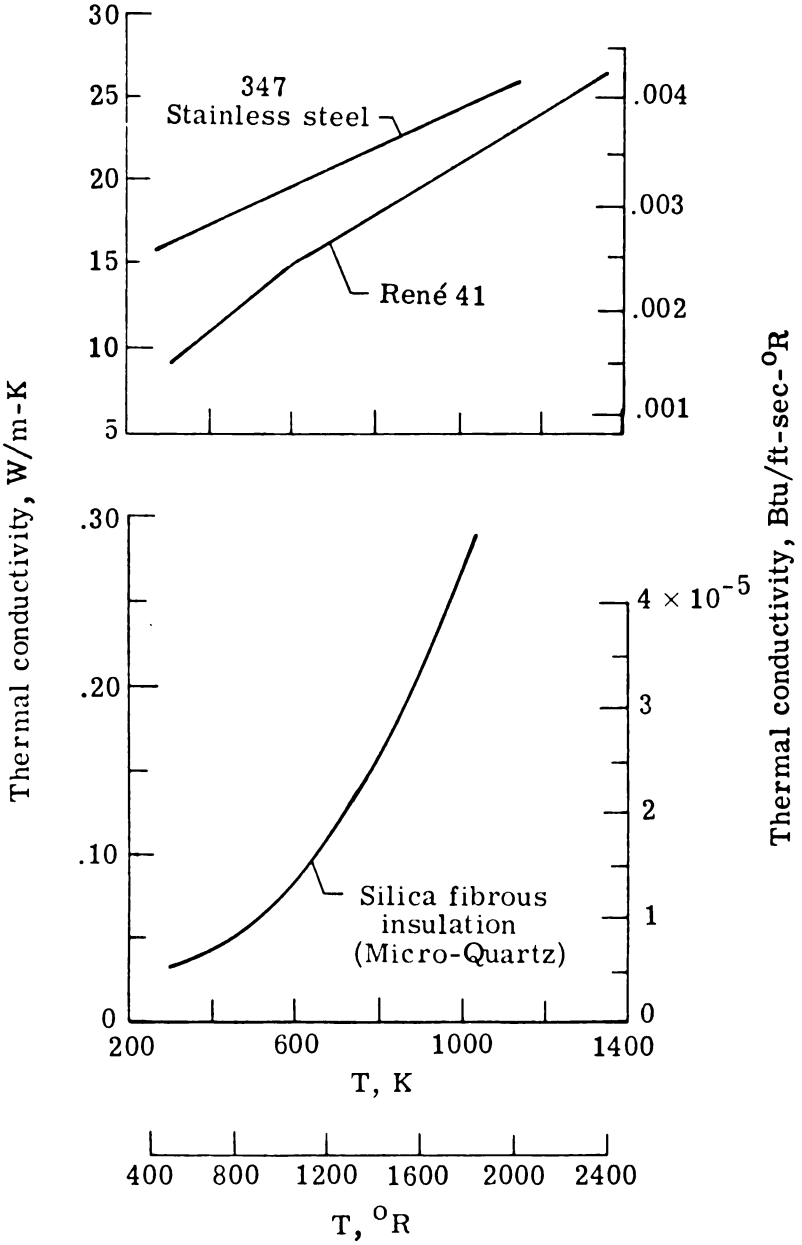

(a) Thermal conductivity.

Figure 37.- Temperature-dependent properties of panel materials.

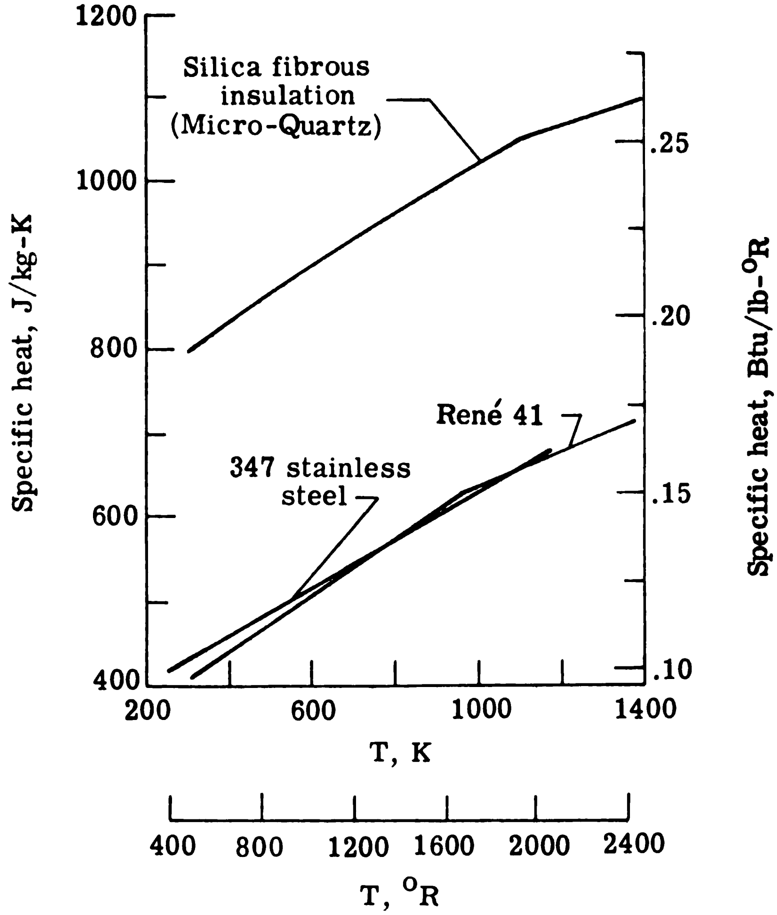

(b) Specific heat.

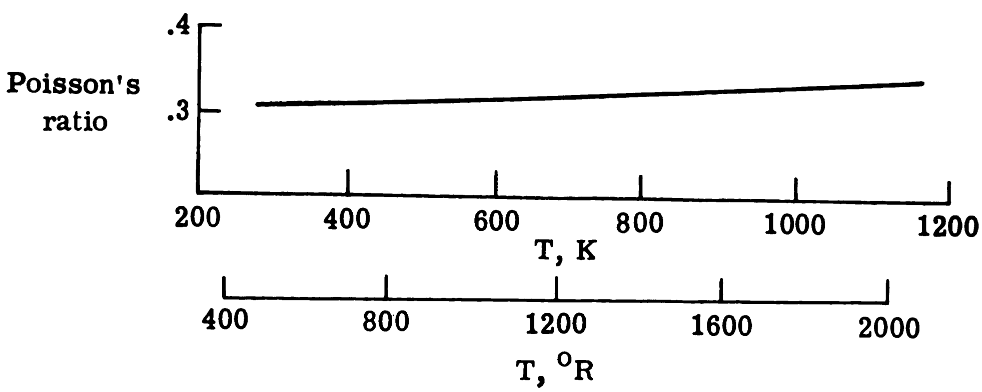

(c) Poisson's ratio for René 41.

Figure 37. - Continued.

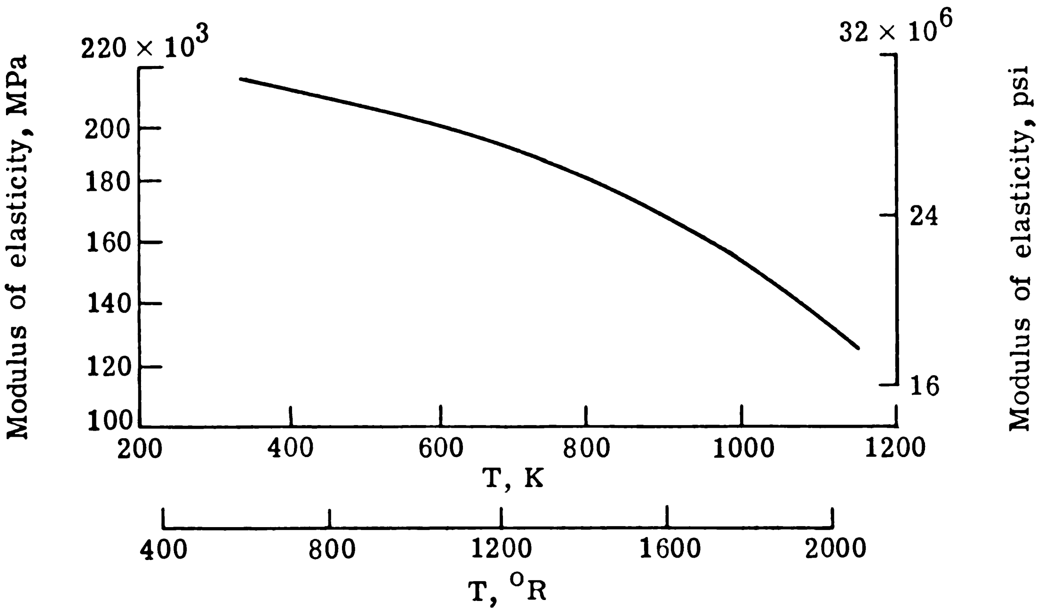

(d) Modulus of elasticity for René 41.

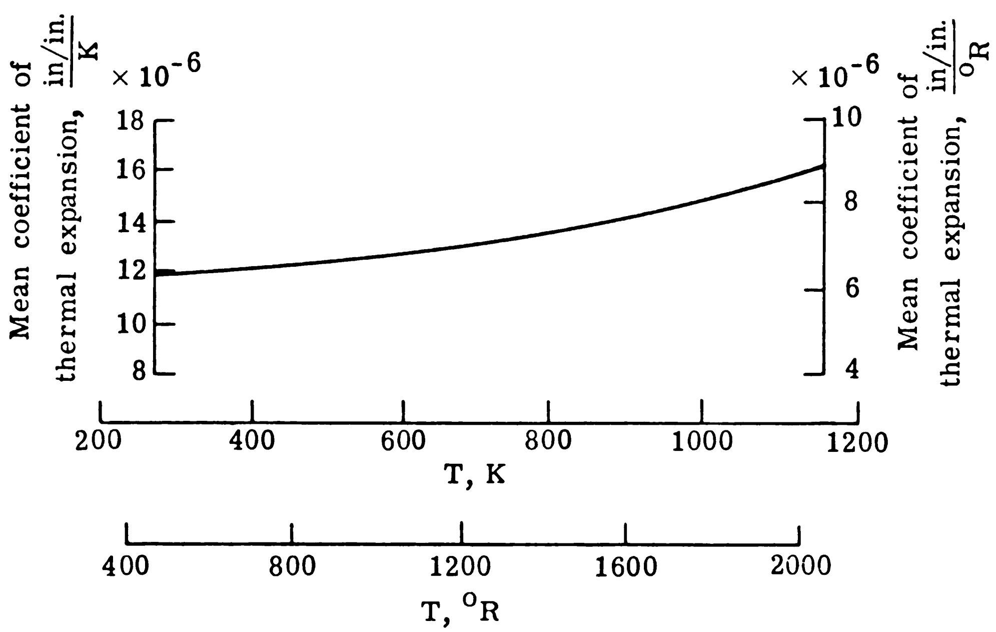

(e) Mean coefficient of thermal expansion from 294 K (530° R) for René 41.

Figure 37.- Continued.

Ni-19Cr-11Co-10Mo-3Ti-1.5Al
Sheet and plate 0.013 to 0.79 (0.005 to 0.312 in.)
1353 to 1450 K (2435 to 2610° R)
30 min to 4 hr at 1172 K (2110° R), 4 hr air cooled

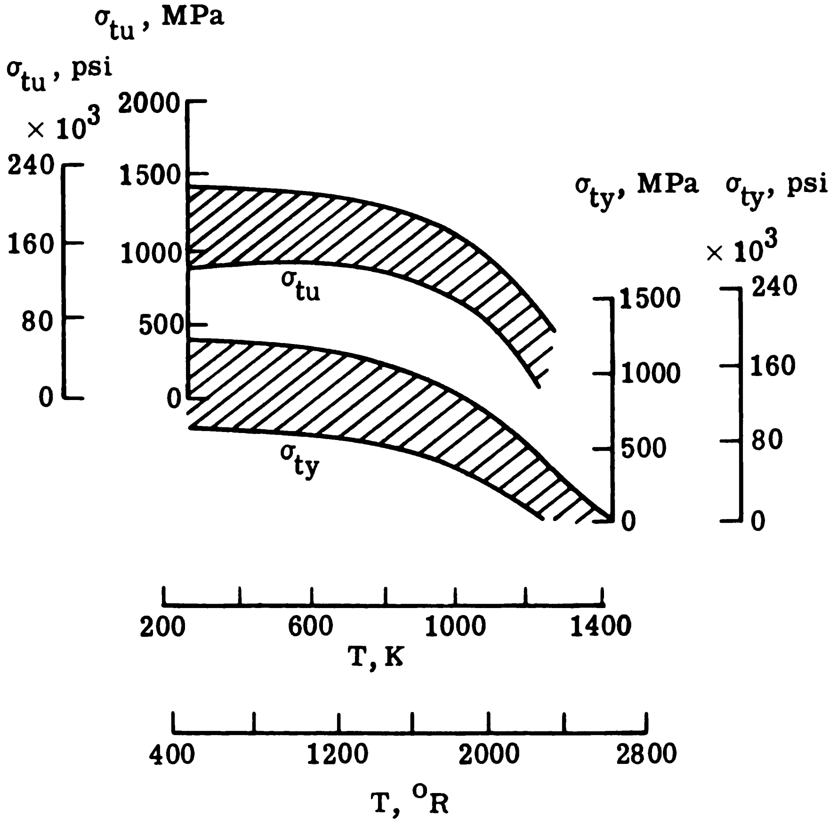

(f) Tensile properties for René 41.

Figure 37. - Concluded.

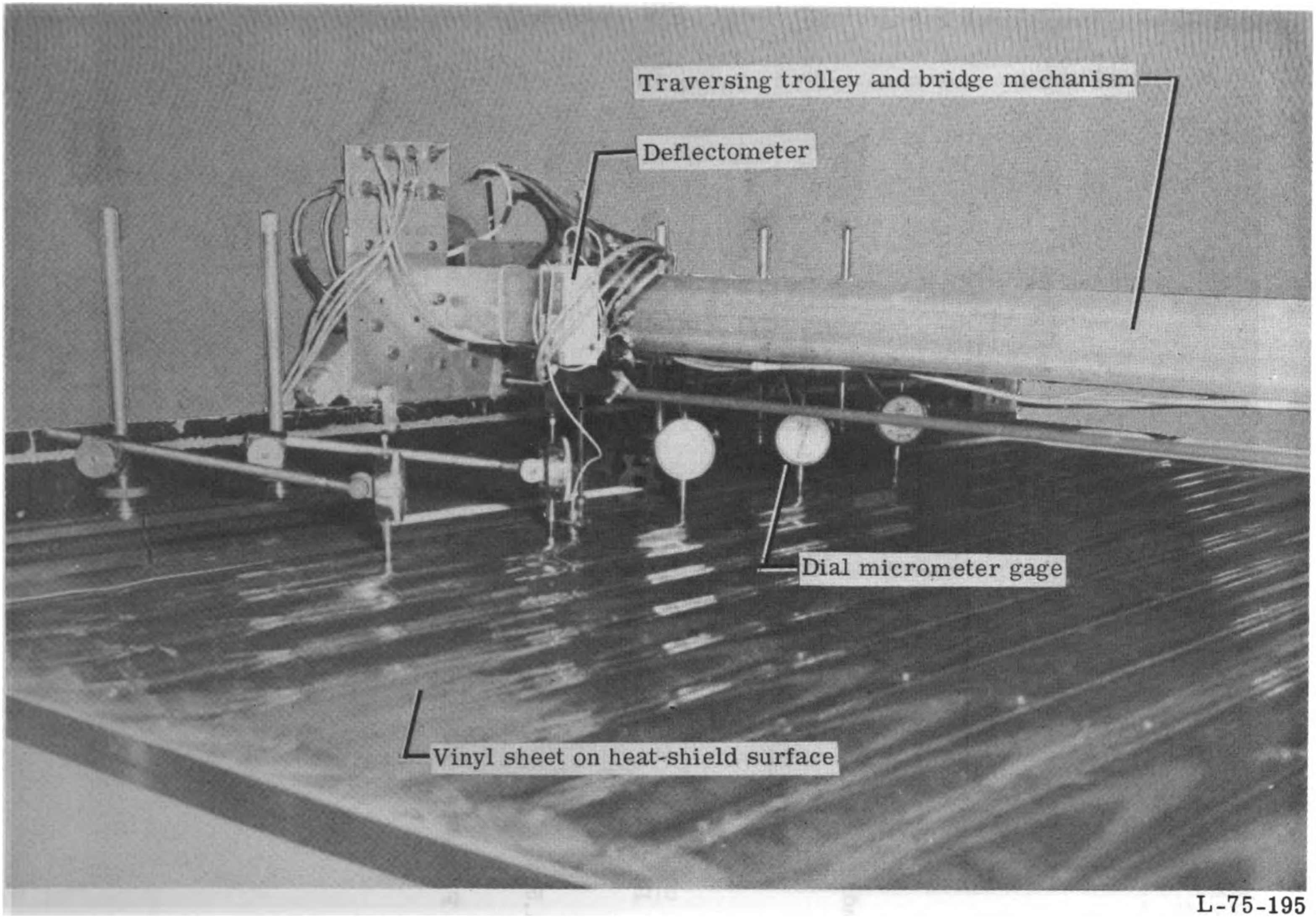

Figure 38.- Apparatus for measuring heat-shield deflections under differential-pressure loading.

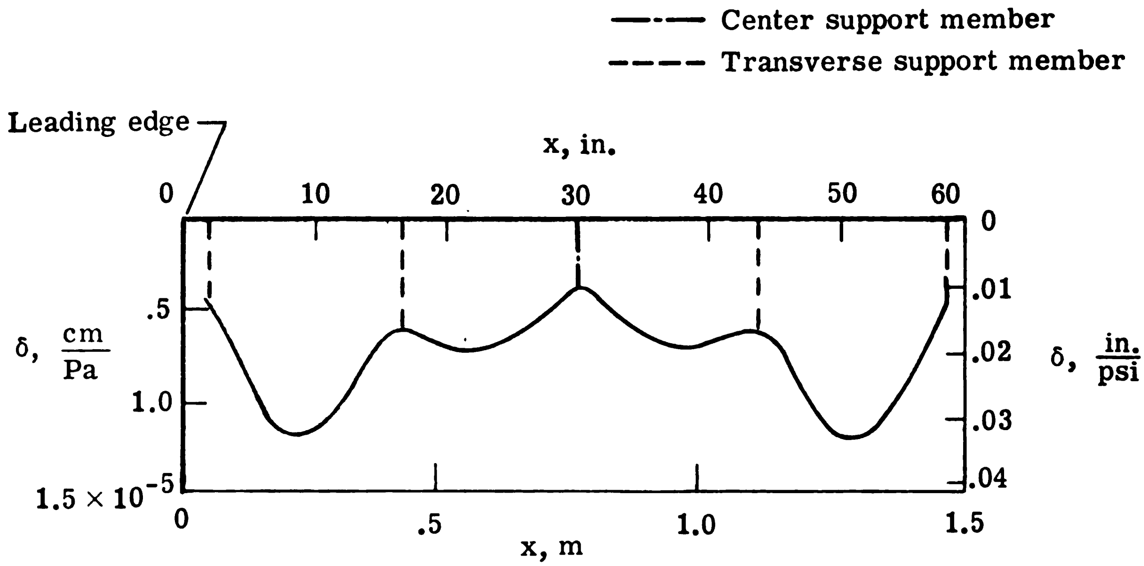

Figure 39.- Measured deflections of the heat shield and support members for a differential pressure of 6.9 kPa (1.0 psi).

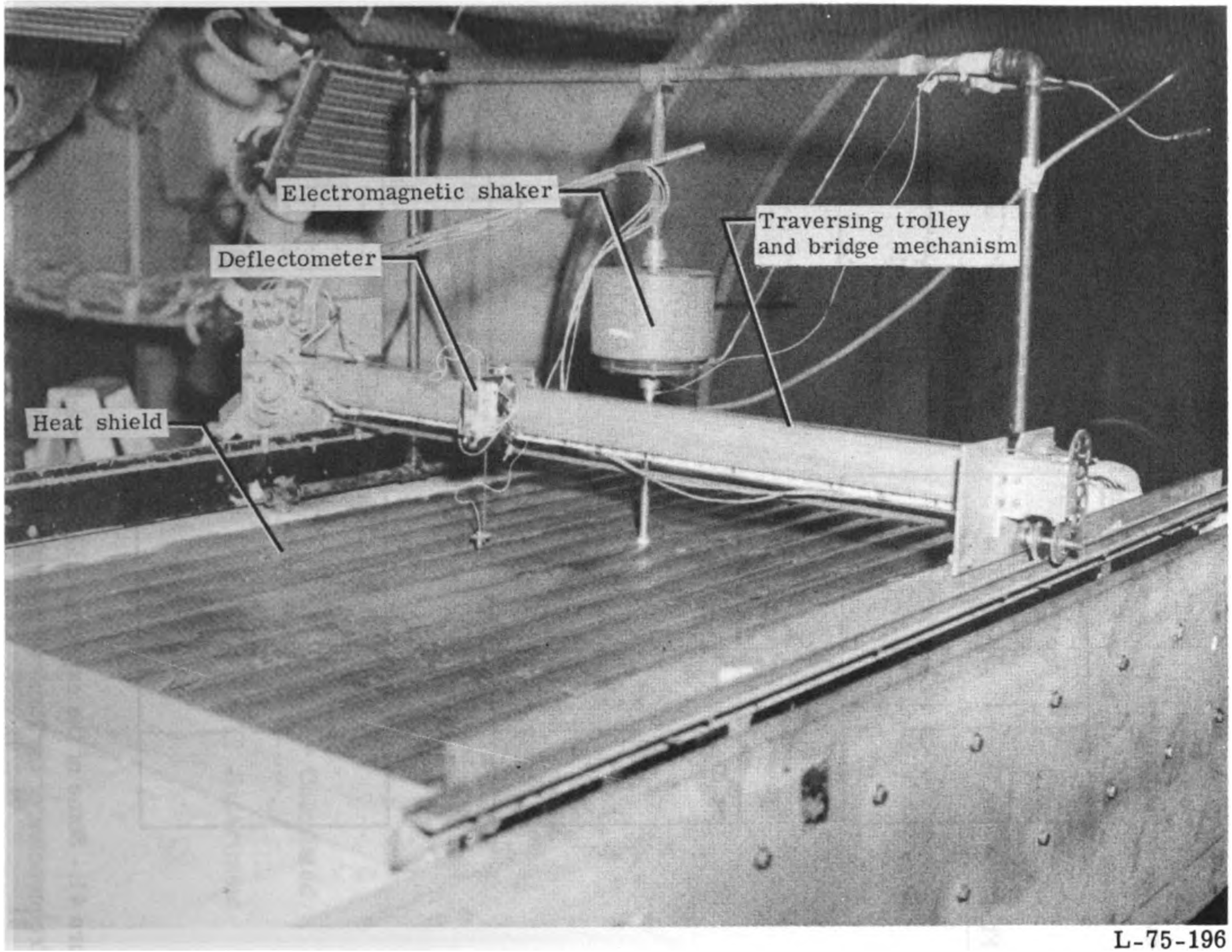

L-75-196

Figure 40.- Apparatus for surveying vibration modes and frequencies.

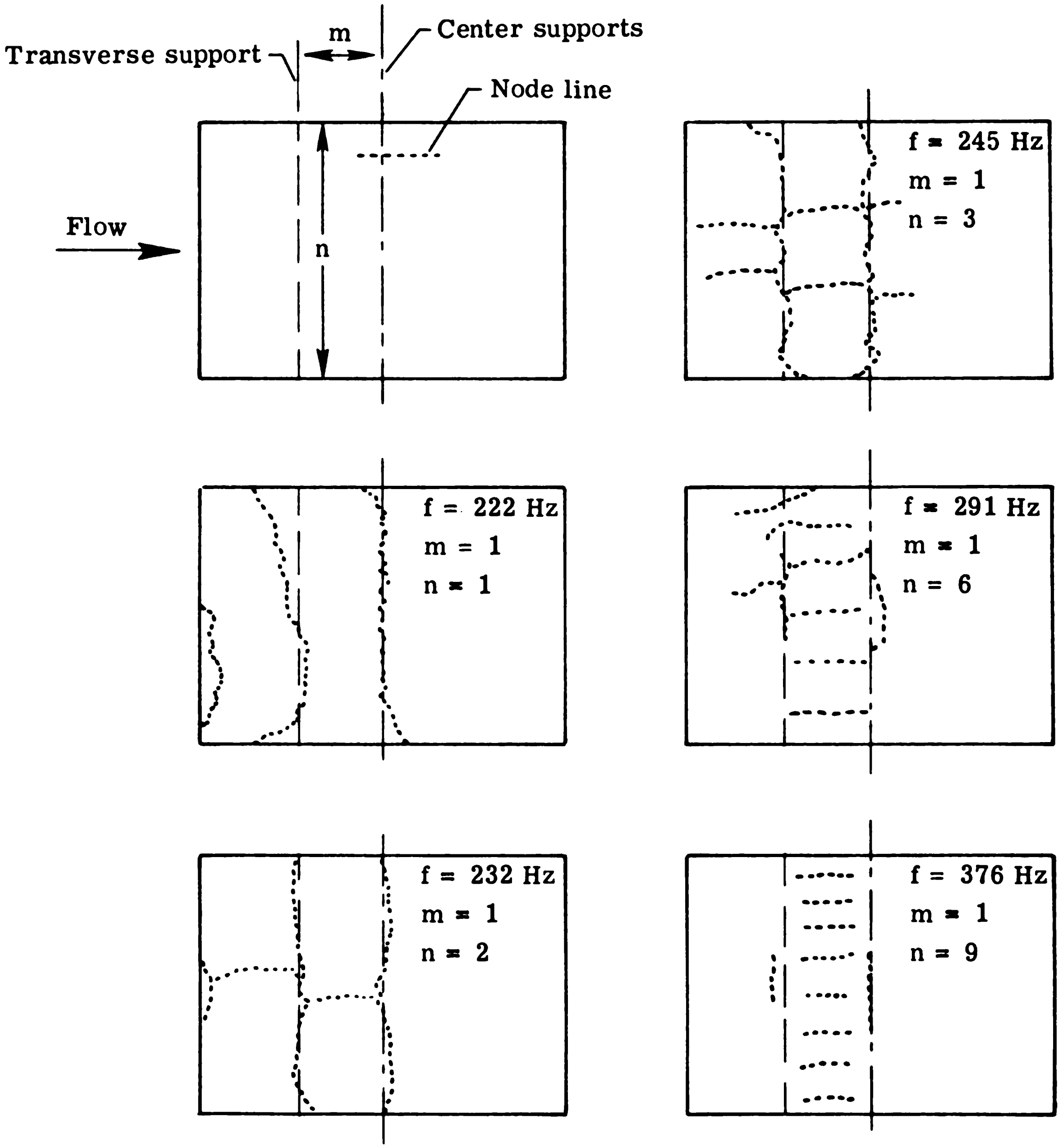

Figure 41.- Some of the experimentally observed nodal patterns and associated frequencies of the René 41 heat shield obtained prior to the heating tests.

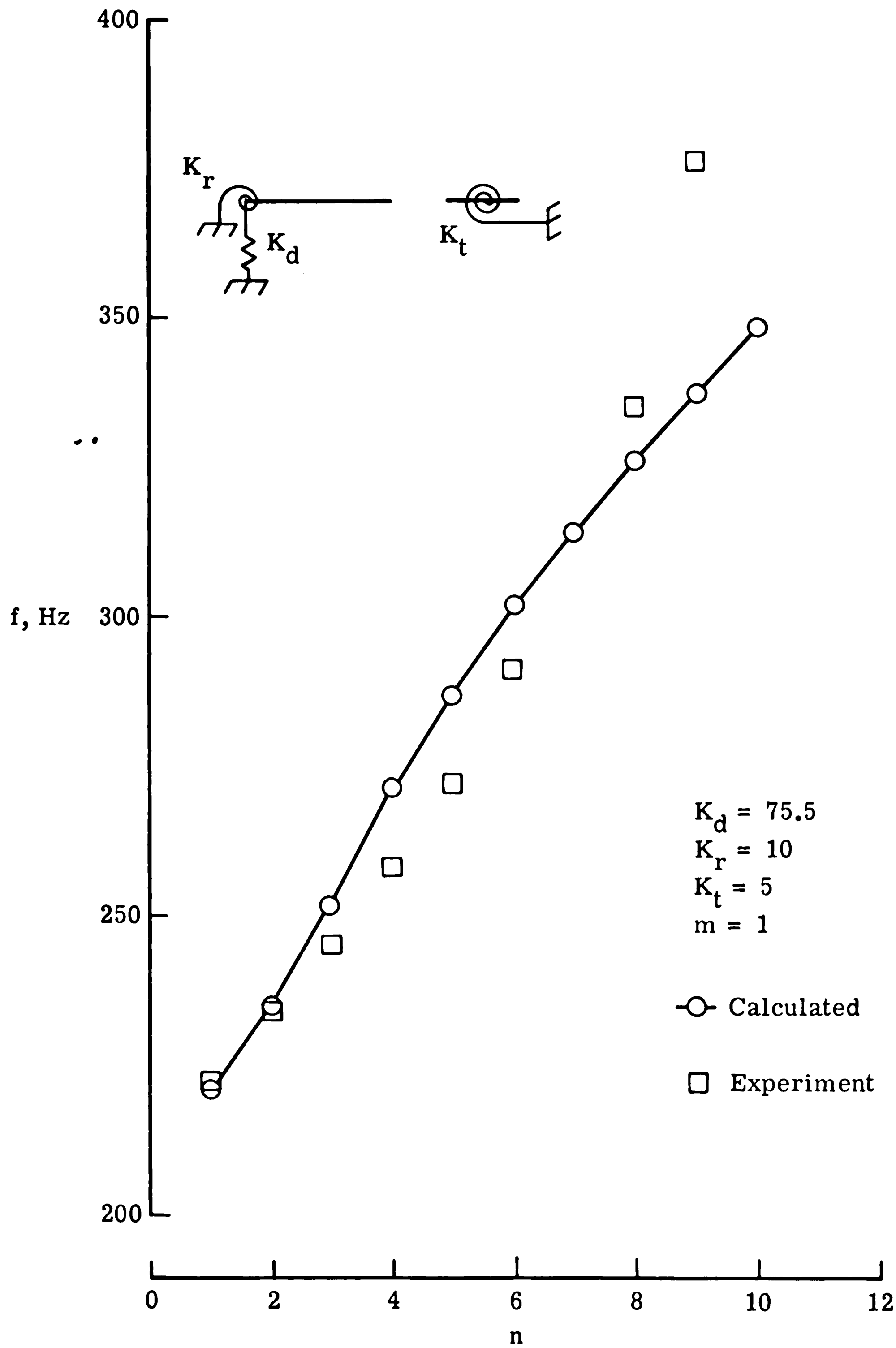

Figure 42.- Calculated and experimental frequencies for different modes in a single bay of the René 41 heat shield.

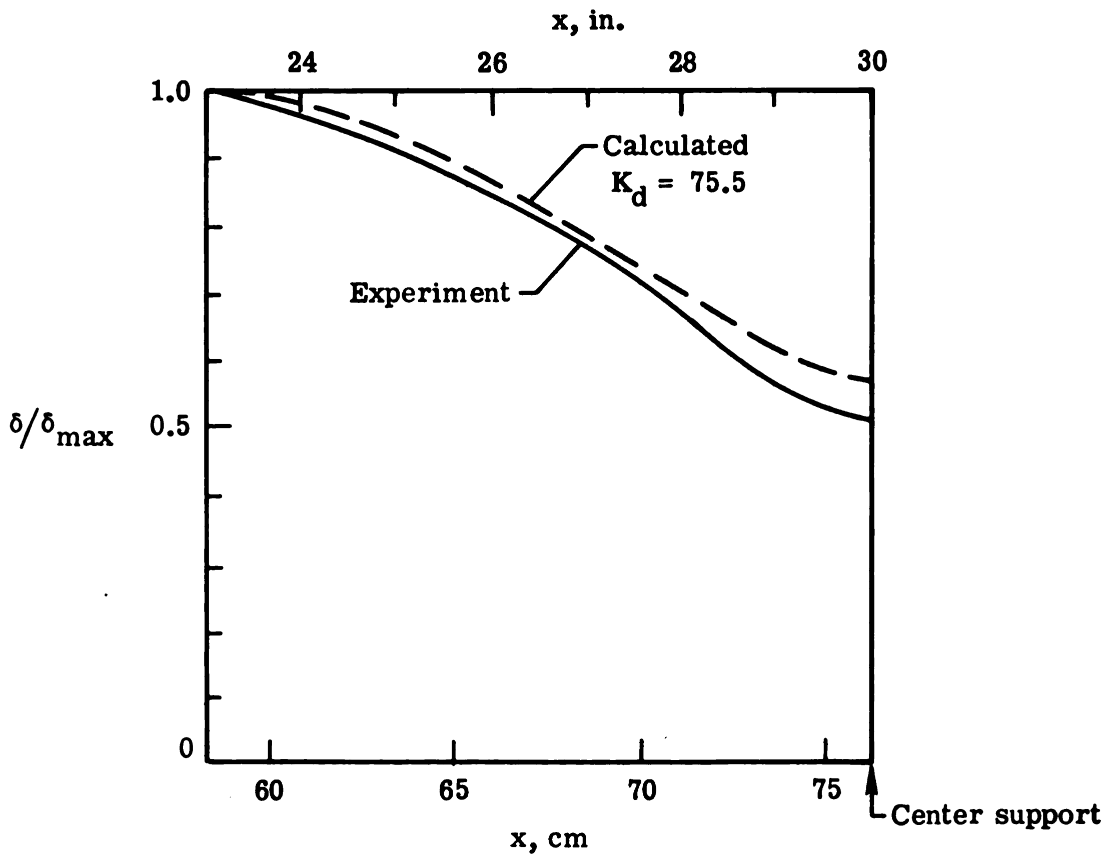

Figure 43.- Normalized static deflections of one-half of the second bay of the René 41 heat shield.

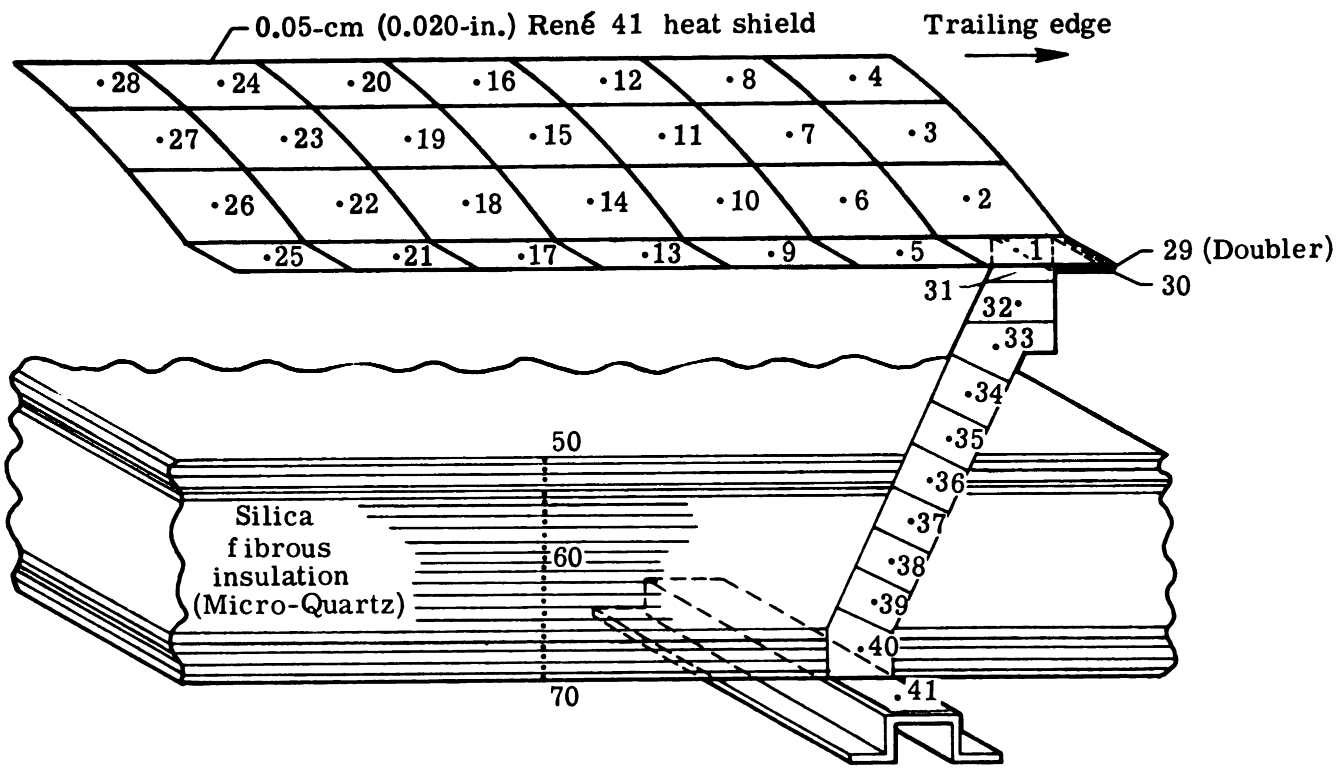

Figure 44.- Nodal representation for thermal analysis of René 41 thermal protection system.

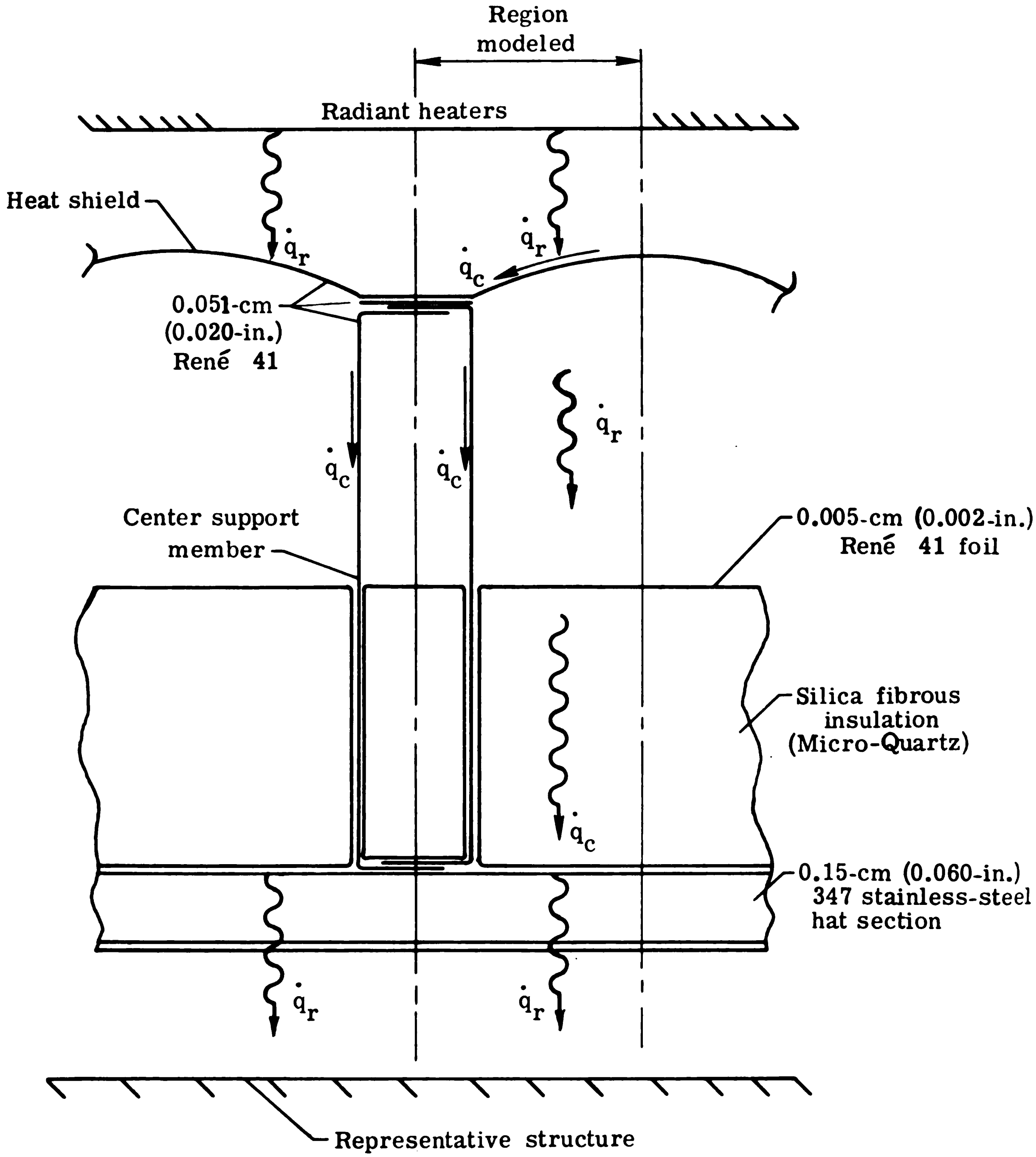

Figure 45.- Section identifying panel components and heating modes used for thermal analysis. ($\dot{q}_r$ is radiative heating rate; $\dot{q}_c$ is convective heating rate.)

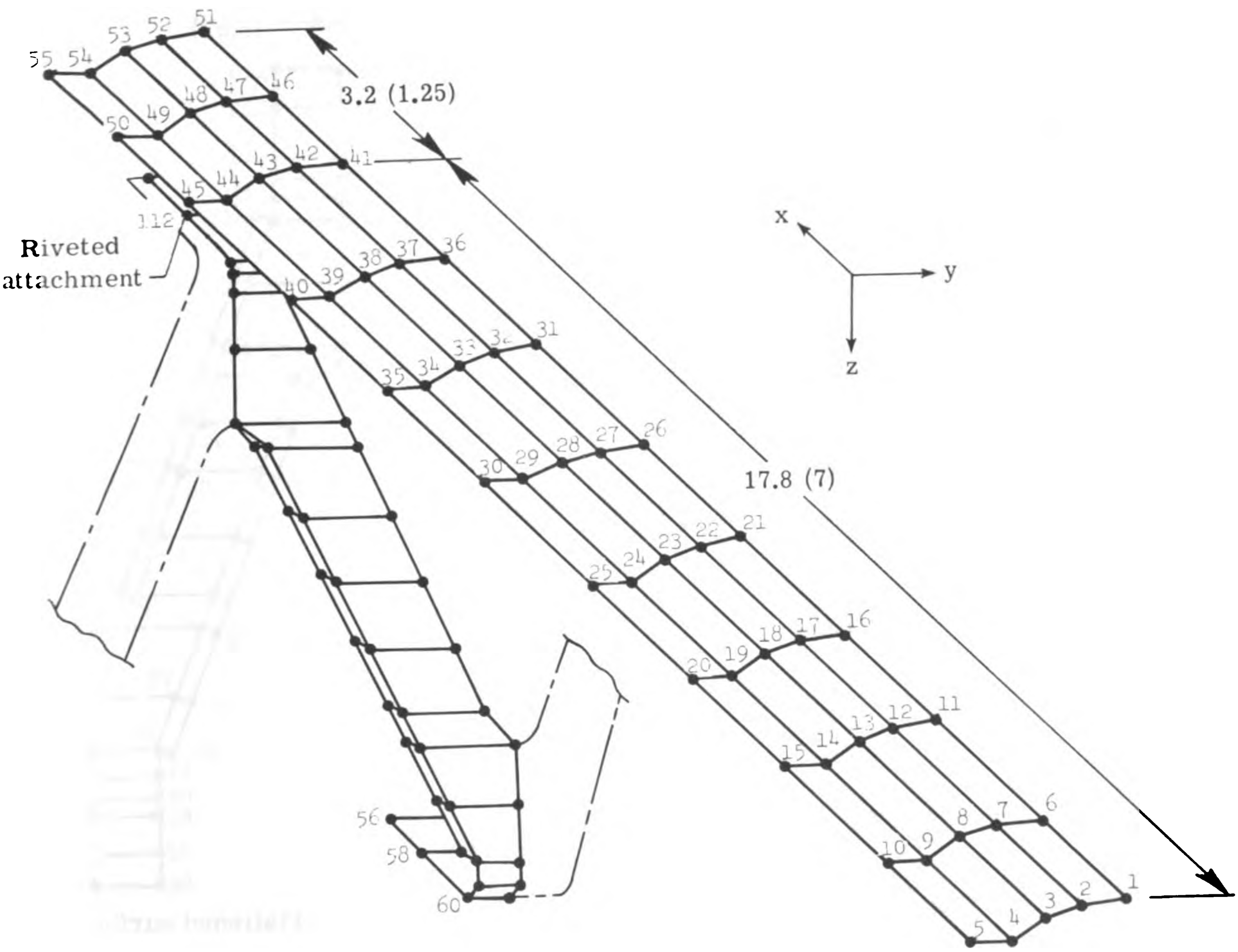

(a) Heat-shield elements.

Figure 46.- Finite element grid used for stress analysis of René 41 heat shield and support member.

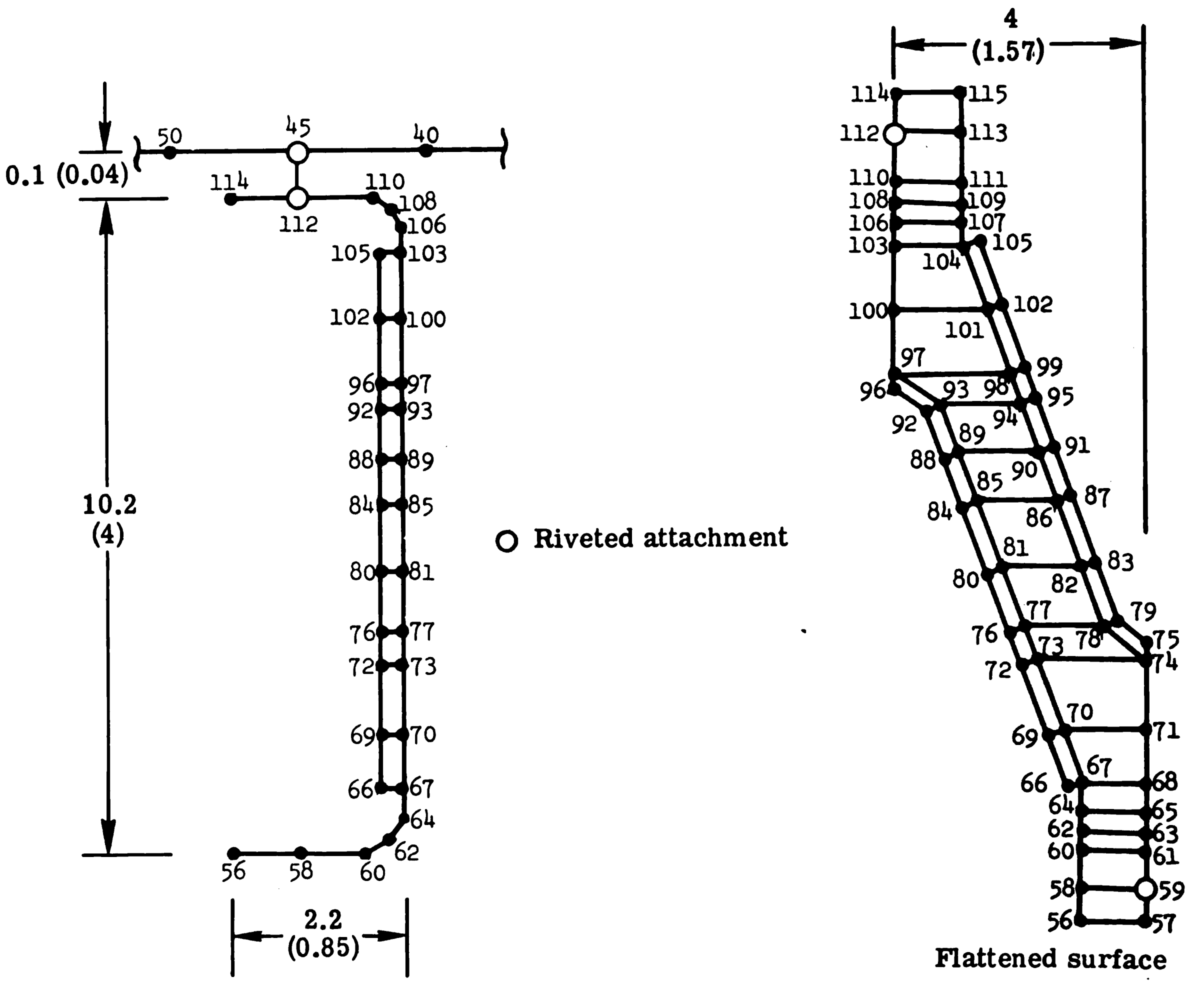

(b) Support-member elements.

Figure 46.- Concluded.

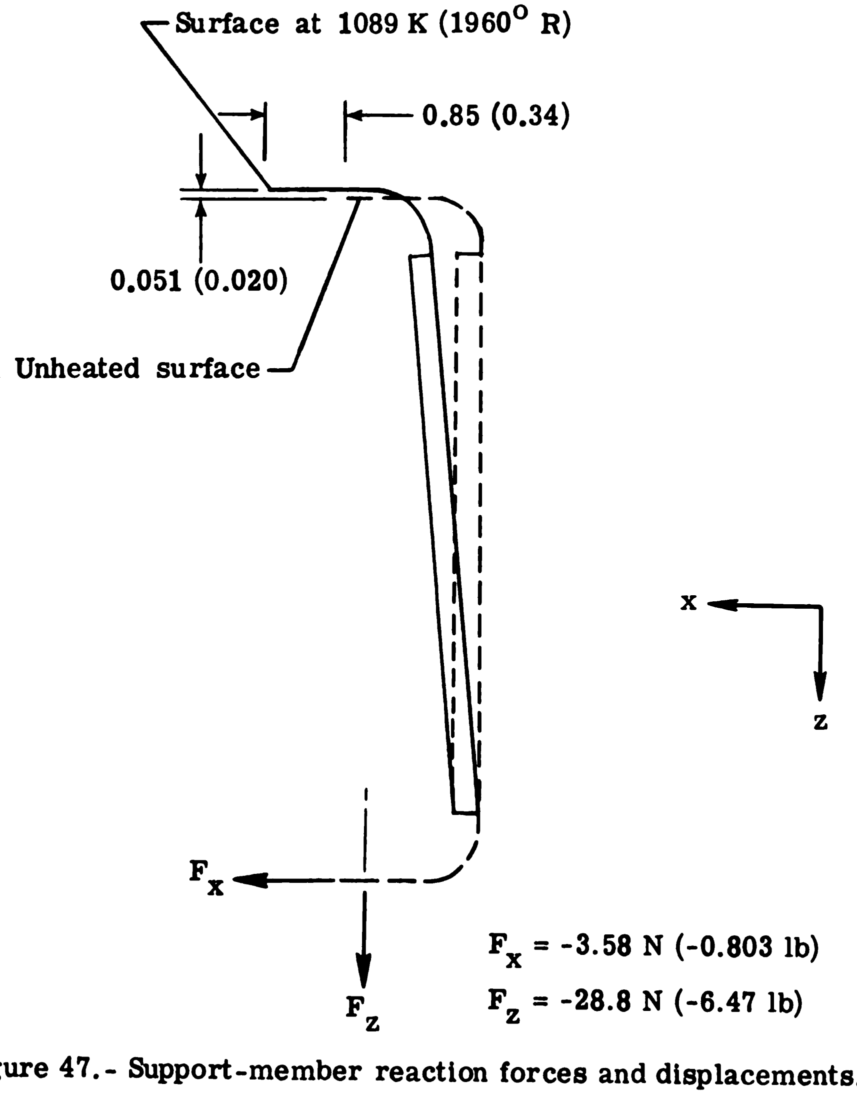

Figure 47.- Support-member reaction forces and displacements.

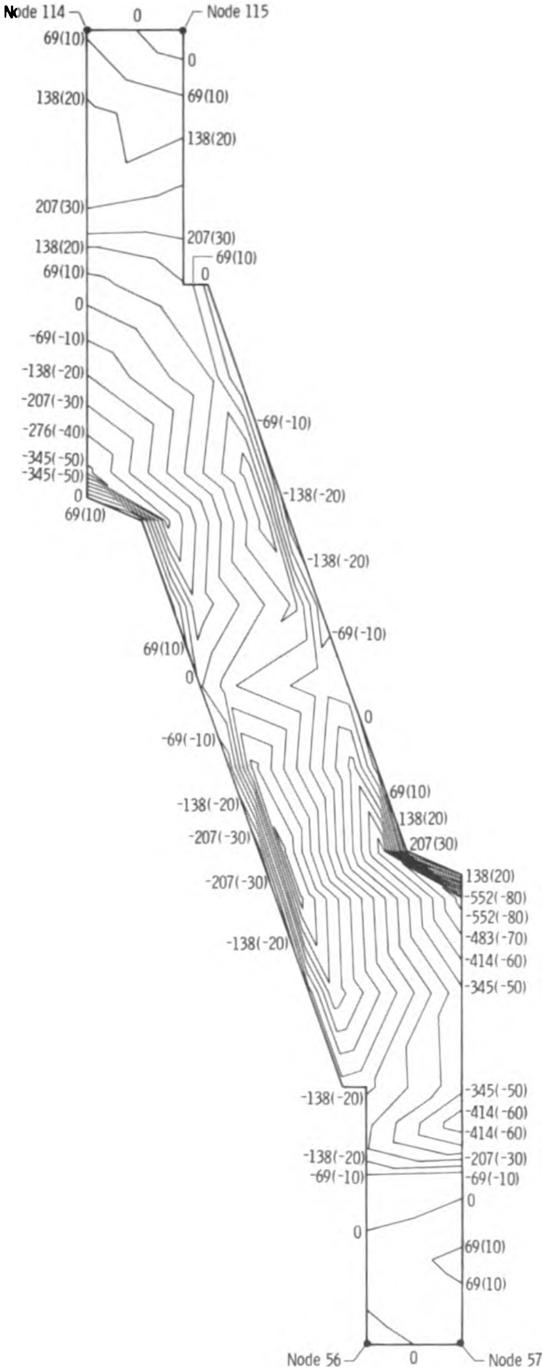

(a) Support-member stress in z-direction for σ_{max} = -583 MPa (-84.6 ksi).

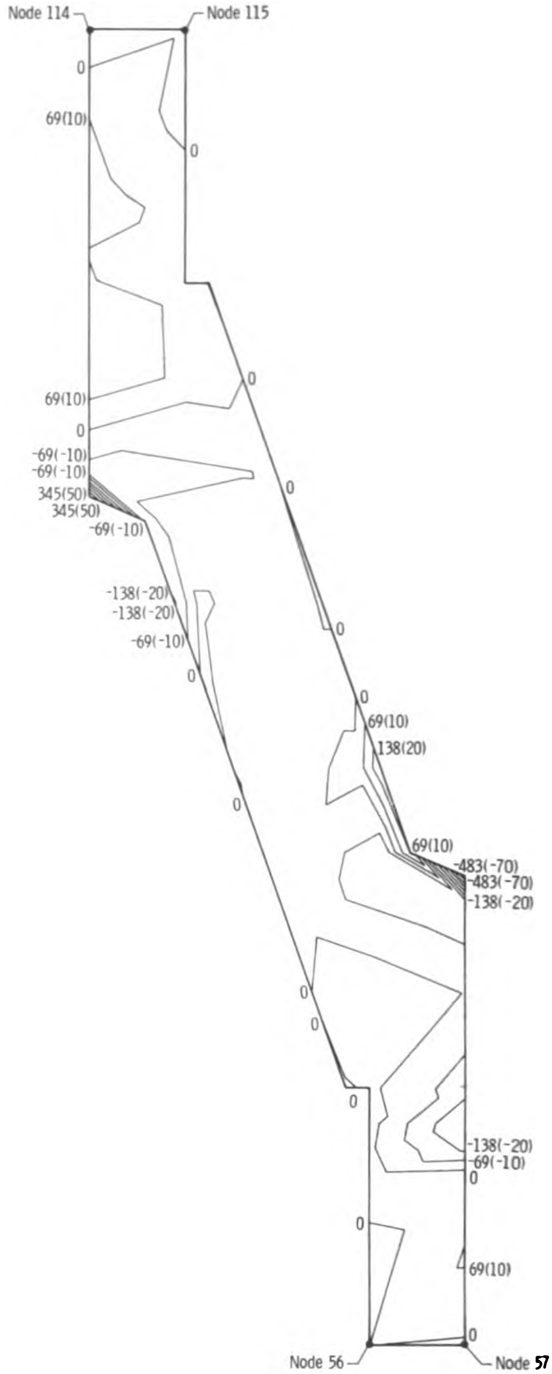

(b) Support-member stress in y-direction for σ_{max} = -539 MPa (-78.1 ksi).

Figure 48.- Stress contours for René 41 support member.

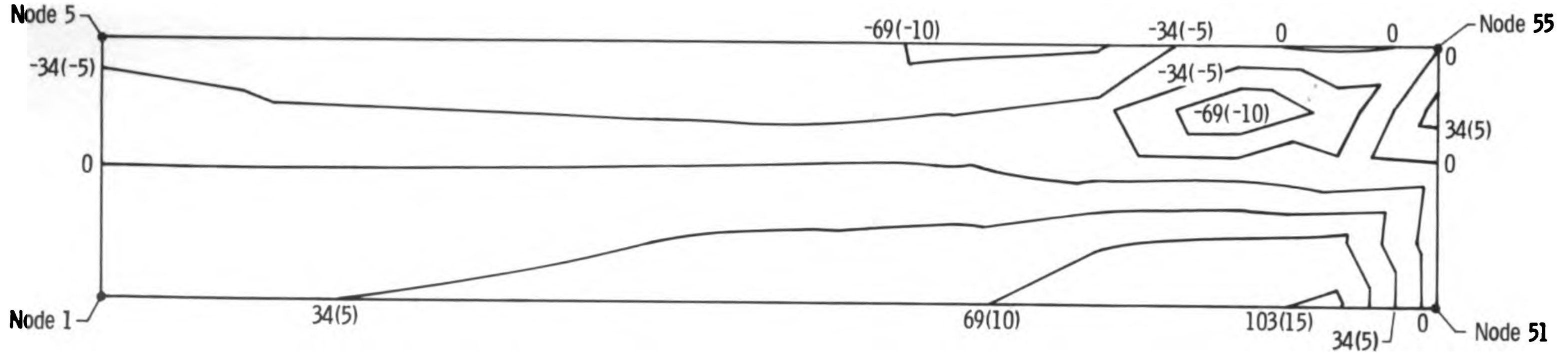

(a) Heat-shield stress in x-direction for σ_{max} = 113 MPa (16.3 ksi).

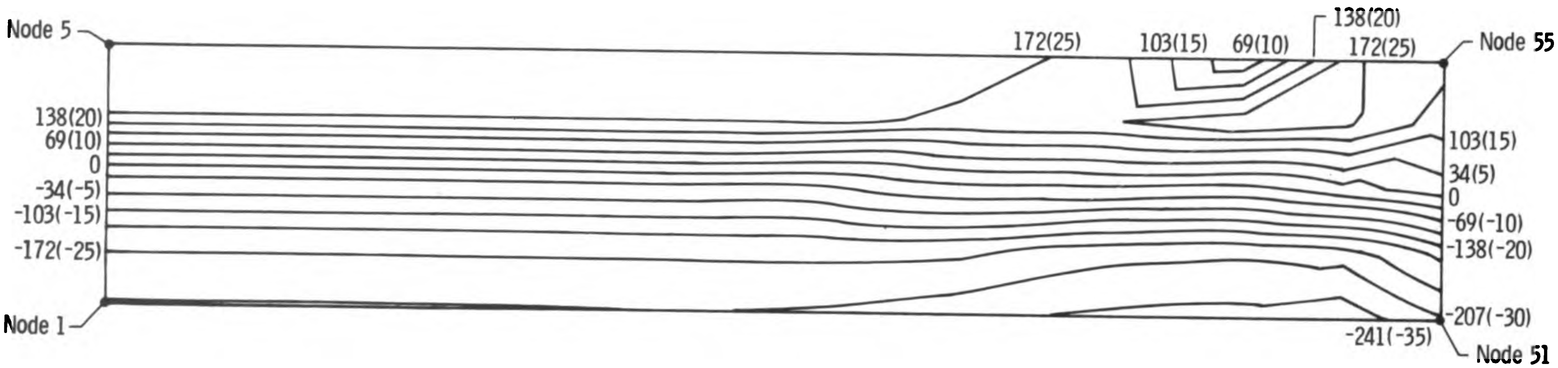

(b) Heat-shield stress in y-direction for σ_{max} = -267 MPa (-38.7 ksi).

Figure 49.- Stress contours for René 41 heat shield.

NASA-Langley, 1975 L-9945

ATIONAL AERONAUTICS AND SPACE ADMINISTRATION
WASHINGTON, D.C. 20546

OFFICIAL BUSINESS
PENALTY FOR PRIVATE USE $300

SPECIAL FOURTH-CLASS RATE
BOOK

POSTAGE AND FEES PAID
NATIONAL AERONAUTICS AND
SPACE ADMINISTRATION
451

U.S.MAIL

024 001 C1 U AL 751031 S00606HU
UNIV OF MICHIGAN
ENGINEERING LIBRARY
ATTN: MR ROBERT T FREESE
ANN ARBOR MI 48104

POSTMASTER: If Undeliverable (Section 158 Postal Manual) Do Not Return

"The aeronautical and space activities of the United States shall be conducted so as to contribute . . . to the expansion of human knowledge of phenomena in the atmosphere and space. The Administration shall provide for the widest practicable and appropriate dissemination of information concerning its activities and the results thereof."

—NATIONAL AERONAUTICS AND SPACE ACT OF 1958

NASA SCIENTIFIC AND TECHNICAL PUBLICATIONS

TECHNICAL REPORTS: Scientific and technical information considered important, complete, and a lasting contribution to existing knowledge.

TECHNICAL NOTES: Information less broad in scope but nevertheless of importance as a contribution to existing knowledge.

TECHNICAL MEMORANDUMS: Information receiving limited distribution because of preliminary data, security classification, or other reasons. Also includes conference proceedings with either limited or unlimited distribution.

CONTRACTOR REPORTS: Scientific and technical information generated under a NASA contract or grant and considered an important contribution to existing knowledge.

TECHNICAL TRANSLATIONS: Information published in a foreign language considered to merit NASA distribution in English.

SPECIAL PUBLICATIONS: Information derived from or of value to NASA activities. Publications include final reports of major projects, monographs, data compilations, handbooks, sourcebooks, and special bibliographies.

TECHNOLOGY UTILIZATION PUBLICATIONS: Information on technology used by NASA that may be of particular interest in commercial and other non-aerospace applications. Publications include Tech Briefs, Technology Utilization Reports and Technology Surveys.

Details on the availability of these publications may be obtained from:

SCIENTIFIC AND TECHNICAL INFORMATION OFFICE

NATIONAL AERONAUTICS AND SPACE ADMINISTRATION

Washington, D.C. 20546

NASA TECHNICAL NOTE

NASA TN D-7944

NASA TN D-7944

DESIGN AND PERFORMANCE AT A LOCAL MACH NUMBER OF 6 OF AN INLET FOR AN INTEGRATED SCRAMJET CONCEPT

Carl A. Trexler and Sue W. Souders

Langley Research Center
Hampton, Va. 23665

NATIONAL AERONAUTICS AND SPACE ADMINISTRATION • WASHINGTON, D. C. • AUGUST 1975

1. Report No. NASA TN D-7944	2. Government Accession No.	3. Recipient's Catalog No.
4. Title and Subtitle DESIGN AND PERFORMANCE AT A LOCAL MACH NUMBER OF 6 OF AN INLET FOR AN INTEGRATED SCRAMJET CONCEPT		5. Report Date August 1975 6. Performing Organization Code
7. Author(s) Carl A. Trexler and Sue W. Souders		8. Performing Organization Report No. L-10000
9. Performing Organization Name and Address NASA Langley Research Center Hampton, Va. 23665		10. Work Unit No. 505-05-41-01 11. Contract or Grant No.
12. Sponsoring Agency Name and Address National Aeronautics and Space Administration Washington, D.C. 20546		13. Type of Report and Period Covered Technical Note 14. Sponsoring Agency Code
15. Supplementary Notes		

16. Abstract

A research program on hypersonic propulsion at the NASA Langley Research Center is focused on the development of a concept for a modular supersonic combustion ramjet (Langley Scramjet Module), which is designed to integrate with the airframe of a hypersonic vehicle. The present paper reports the design philosophy and results of experiments at Mach 6 to evaluate the performance of the scramjet inlet. The inlet was designed with modest contraction ratio, fixed geometry, and three fuel injection struts which contribute to the inlet flow compression and provide a short combustor design that results in low internal cooling requirements. The baseline inlet configuration is rectangular in cross-sectional shape, has planar compression surfaces swept at 48°, and has an opening upstream of the cowl leading edge through which spillage occurs for starting. The inlet model has a projected geometric capture area measuring 19.05 cm high by 15.24 cm wide. The average throat Mach number was 3.1. The kinetic energy efficiency was 97.7 percent, and the average inlet aerodynamic contraction ratio was 7.0, which does not include the compression expected from the vehicle bow shock. The inlet captured 94 percent of the flow at its face; and, overall, the inlet performance was well within the acceptable range for high engine performance.

17. Key Words (Suggested by Author(s)) Hypersonic inlet Integrated scramjet Hypersonic propulsion	18. Distribution Statement Unclassified – Unlimited New Subject Category 07		
19. Security Classif. (of this report) Unclassified	20. Security Classif. (of this page) Unclassified	21. No. of Pages 140	22. Price* $5.75

*For sale by the National Technical Information Service, Springfield, Virginia 22151

CONTENTS

Page

DESIGN AND PERFORMANCE AT A LOCAL MACH NUMBER OF 6 OF AN INLET FOR AN INTEGRATED SCRAMJET CONCEPT

Carl A. Trexler and Sue W. Souders
Langley Research Center

SUMMARY

A research program on hypersonic propulsion at the NASA Langley Research Center is focused on the development of a concept for a modular supersonic combustion ramjet (Langley Scramjet Module). The modular engine concept is designed to integrate with the airframe; precompression of the engine airflow will be produced by the vehicle bow shock and additional expansion of the nozzle exhaust will be produced by the vehicle afterbody. As part of this research program, component investigations are in progress on the baseline inlet configuration and the present paper reports the design philosophy and results of experiments at Mach 6 to evaluate the performance of the inlet.

With the integration advantages, the inlet was designed with modest contraction ratios and fixed geometry. Three fuel injection struts contribute to the inlet flow compression and provide a short combustor design that results in low internal cooling requirements. The baseline inlet configuration is rectangular in cross-sectional shape, has sweptback sidewall planar compression surfaces, has an opening upstream of the cowl leading edge through which spillage occurs for starting and normal operation, and has the external cowl surface alined with the local flow to provide a minimal external drag. The inlet model had a projected geometric capture area measuring 19.05 cm high by 15.24 cm wide. The sidewalls and struts had 48° swept leading edges and nominal compression surface angles of 6°.

Tests were conducted in the Langley 20-inch Mach 6 tunnel and the inlet model was instrumented to obtain both wall and survey pressure measurements which were used in computing performance and capture flow. The data-reduction system provided integrated performance data as well as contour maps of parameters such as total-pressure recovery and Mach number in the inlet throat. The difficulty and importance of properly positioning the shock waves in the throats of hypersonic inlets were demonstrated, but no adverse effects were noted as a result of the inlet ingesting a boundary layer on the top surface which simulated the boundary layer that would be ingested from the vehicle forebody.

The average throat Mach number was 3.1 compared with the predicted value of 3.4. The kinetic energy efficiency was 97.7 percent (0.59 recovery) compared with prediction

of 98.3 percent (0.67 recovery), which did not account for all sources of total-pressure loss. The average inlet aerodynamic contraction ratio was 7.0, which does not include the compression expected from the vehicle bow shock. The inlet captured 94 percent of the flow at its face; and, overall, the inlet performance was well within the acceptable range for high engine performance.

INTRODUCTION

The attractive potential of hypersonic flight with air-breathing propulsion has been recognized for the past 15 years; however, major advances in technology are required. Exploratory research on concepts for hypersonic air-breathing engines has been pursued in substantial research and development programs and a broad technology base has been established. See, for example, references 1 to 4. The investigation of several small-scale, hydrogen fueled, supersonic combustion ramjet (scramjet) engine designs has shown that the scramjet is a feasible engine concept and practical levels of thrust have been demonstrated (ref. 5). Hypersonic research and technology programs have been conducted (refs. 6 and 7) which illustrate the next logical step in scramjet evolution, which is the development of engine concepts which will integrate with the airframe. Integration includes the use of the vehicle forebody to precompress the engine airflow before it enters the inlet and the use of the vehicle afterbody for additional expansion and thrust vectoring of the nozzle exhaust gas. Other principal design criteria for hypersonic systems are minimum engine cooling requirements to make part of the heat sink of the hydrogen fuel available for active cooling of the airframe, fixed geometry to reduce weight and system complexity, and minimum external drag.

Detailed analytical and experimental studies at the Langley Research Center have resulted in the definition of the Langley Scramjet Module, with design features in both the inlet and combustor which will satisfy the engine design criteria, when the benefits of vehicle and propulsion system integration are included. This report deals primarily with the design and performance evaluation for the hypersonic inlet concept for the Langley Scramjet Module. The design criteria were met with the use of swept compression surfaces, which produced oblique shock waves, and a matching swept throat and combustor. Because of the complexity of the flow, it was necessary to optimize the selected inlet configuration from the experimental results of several earlier configuration studies. Once the concept was derived, computer programs aided in locating shock waves within the inlet, determined boundary-layer corrections to the interior walls, provided theoretical performance results, and reduced experimental test data.

A model of the inlet portion of the Langley Scramjet Module, 19.05 cm high by 15.24 cm wide, was tested in the Langley 20-inch Mach 6 wind tunnel. This test condition represents local inlet face conditions for a flight Mach number of approximately 7.6 after compression from the vehicle forebody. The tunnel free-stream total temperature and pressure were 467 K and 11.9 atm (1 atm = 101.3 KN/m^2), respectively, and provided a Reynolds number per meter of approximately 9.8×10^6. One run was made at a reduced Reynolds number per meter of 3.3×10^6.

SYMBOLS

When two symbols are given for the same concept, the second one is that used for the computer data.

A	cross-sectional area of a stream tube
A*	cross-sectional area of a stream tube with sonic velocity
A/A_1	aerodynamic contraction ratio, $\frac{A_1}{A_1^*} \frac{p_t}{p_{t,1}} \frac{A^*}{A}$
c,C	distance from cowl tip (fig. 13(d))
c',C'	distance from cowl leading edge (fig. 13(d))
H	inlet height, 19.05 cm (7.5 in.)
M	Mach number
p,P	static pressure
p_1,P1	static pressure in front of inlet
p_t	total pressure
p_{pitot},PITOT	pitot pressure
R	Reynolds number
s	distance from foreplate leading edge (fig. 13(a))

s'	distance from sidewall leading edge (fig. 13(c))
s"	distance from strut leading edge (figs. 13(e) to 13(g))
T	temperature
T_{aw}	adiabatic wall temperature
T_t	total temperature
V	velocity vector
v	velocity
W	throat gap or width of capture measurement station, cm (figs. 11 and 25)
X	distance downstream of intersection of sidewall with foreplate (fig. 13(b))
x	axis parallel to free-stream flow (fig. 57)
Y	distance from foreplate (fig. 13(c))
y	axis perpendicular to free-stream flow (fig. 57)
Z	distance away from model center line (figs. 13(a) and 13(d))
Z'	distance across throat or across duct (fig. 11)
z	axis perpendicular to free-stream flow and y-axis (figs. 4 and 57)
δ	boundary-layer thickness
δ_n	flow turning angle normal to leading edge of swept wedge (fig. 57)
δ_{xy}	cross-flow angle (fig. 57)
δ_{xz}	wedge angle or flow turning angle in xz-plane (fig. 57)

ϵ_{xz} — shock-wave angle in xz-plane (fig. 57)

η_k — kinetic energy efficiency

Λ — sweep angle measured in xy-plane, deg

λ — distance around capture measurement station (fig. 62)

ρ — density

ϕ — dihedral angle measured perpendicular to ridge line, deg

ψ — dihedral parameter

Subscripts:

1 — conditions at inlet face or ahead of a shock wave

2,3,4 — conditions behind 1st, 2d, and 3d shock waves, respectively

n — normal to leading edge (fig. 57)

t — tangential to leading edge (fig. 57)

∞ — free stream (in front of vehicle)

INLET DESIGN CRITERIA AND CONCEPT

Airframe-Engine Integration

The advantages of integrating the airframe and engine of a hypersonic vehicle are well known. The parametric analysis of reference 8 indicates that the contributions of the vehicle forebody and afterbody are responsible for up to 70 percent of the thrust. At hypersonic speeds very large engine airflows are required for adequate thrust in spite of the high-energy potential of the hydrogen fuel. These engine airflow requirements are best met by utilizing the precompression obtained from the vehicle forebody and locating the engine on the underside of the vehicle toward the aft end. (See fig. 1.) A method of designing the forebody is discussed in reference 6. The propulsion system inlet area is therefore restricted to the space between the vehicle undersurface and the bow shock and is several times wider than it is high, as shown in the cross section of figure 1. This geometry concept suggests the arrangement of a number of adjacent rectangular engine modules, and the use of modules also permits development in ground test facilities of reasonable size. The relatively thick turbulent boundary layer generated on the vehicle forebody is an unfavorable characteristic which must be considered in the inlet design. The design of the vehicle afterbody, discussed in reference 7, is also important because of the large gross-thrust and moment forces involved, which can generate large trim drag penalties if not correctly considered.

The Scramjet Engine

The primary objectives of the scramjet engine design are: to provide a high level of thrust and specific impulse with efficient capture over the flight Mach number range from 3.5 to 10, to have low cooling requirements in order to make a portion of the fuel heat sink available for active cooling of the vehicle structure at high Mach numbers, to have satisfactory operating characteristics over the Mach number range including the establishment of supersonic flow (starting) within the inlet at the low end of the Mach number range, to have fixed geometry in order to reduce system complexity as well as joint and seal problems, to ingest successfully the vehicle-forebody boundary layer, and to produce low external drag. Many of these objectives are interrelated and trade-offs discussed in reference 7 indicate that a fixed geometry inlet with moderate contraction for starting at a low Mach number is desirable. A moderate contraction and low internal pressure will not only mean a reduction in engine weight and cooling requirements but also an increased ability for the engine to ingest the vehicle-forebody boundary layer.

Because the use of only fuel injection from the sidewalls would produce very long mixing lengths for this type of modular design, the scramjet engine concept of figure 2 has three struts to provide six planes of instream fuel injection. This feature not only reduces cooling and shortens the combustor but also the inlet, since the struts provide a significant part of the inlet flow compression. The sidewalls are the main inlet compression surfaces, whereas the top surface partially eliminates expansions produced by the downflow created by the swept shock-wave system, which is a unique characteristic of the swept inlet design. The cowl is kept nearly parallel to the vehicle underbody to minimize external drag.

The Inlet Concept

The inlet must efficiently compress the airflow captured for the combustor. Reference 7 indicates that a contraction ratio between 6 and 10 would be satisfactory for a fixed geometry inlet at a flight Mach number of about $7\frac{1}{2}$, and several inlet configurations were investigated which would fit into the area provided beneath the vehicle. Inlet interior walls consisting of swept planar surfaces were assumed; this assumption simplifies the analysis and avoids the need for three-dimensional characteristic computer programs.

Compression angles between 6° and 8° were employed; these angles are a compromise between high angles which contribute to high total-pressure losses from shock waves and increase the possibility of shock-induced boundary-layer separation and low compression angles which make the inlet long.

Prior to the development of the inlet shown in figure 2, a design utilizing swept compression surfaces in which the top surface was the primary compression surface was considered and is discussed in reference 9. Disadvantages to this design were: a corner flow problem originating at the top surface and covering much of the inlet throat; difficulty in obtaining good capture characteristics over the Mach number range; and no effective way of dealing with the vehicle-forebody boundary layer. Therefore sidewalls with swept leading edges were made the primary compression surface for the inlet in figure 2. Because planes of constant flow properties tend to be parallel to the sweep lines, the fuel injection struts and all downstream stations are also swept at the same angle. This design generates a system of swept shock waves which turns the flow away from the top surface and thus reduces the corner flow and boundary-layer problems on that surface. A cowl design which would provide 100-percent capture at high Mach numbers was tested on a preliminary design, and those results indicated that better starting and operating performance could be obtained with the pointed cowl leading edge located near the struts as shown in figure 2. Good capture characteristics can be obtained over the Mach number range with the fixed geometry design; and spillage, produced by the flow being turned toward the opening in front of the cowl by a transient shock system, permits starting at a low Mach number. The downflow produced by the sweep during normal operation tends to reduce the static-pressure rise near the top surface and should make possible the ingestion of the vehicle-forebody boundary layer without separation.

Inlet Starting

Inlet starting at the low end of the Mach number range is primarily a function of contraction ratio, which is influenced by the amount of sweep, the strut design, and the cowl leading-edge location. From simple one-dimensional considerations at an entrance Mach number of 3.0, an area contraction of less than 30 percent is necessary downstream of the plane of closure corresponding to the cowl leading edge. However, in figure 3 the normal plane B-B having the minimum cross-sectional flow area is shown to be located at the cowl leading edge; therefore, on the average there is no contraction downstream of the cowl leading edge. This is a strong indication that the inlet will have no starting problem, and early investigations of similar designs substantiate this conclusion.

The frontal height-width ratio also contributes to the starting characteristics of the inlet. If the width is greater than the height, the inlet is longer and end effects from the top surface and cowl begin to dominate the throat. If the width is much less than the height, the struts become slender and structural problems can appear. Based on preliminary investigations, a width-height ratio of 0.8 was selected for the inlet design to reduce end effects and to permit a reasonable flight weight structure.

INLET MODEL DESIGN

Sweep Angle

In order to develop the swept shock-wave system for these inlet configurations, it was necessary to understand the process that the supersonic flow undergoes as it strikes a swept wedge. A detailed discussion of the calculation procedure for obtaining the shock-wave angle ϵ_{xz}, downflow δ_{xy}, and the flow properties behind the shock wave is given in reference 9, and a method for predicting the complete shock-wave train for the inlet is developed in appendix A.

A shock wave may be attached or detached depending on the sweep angle and Mach number; consequently, the sweep angle determines the lowest Mach number at which the shock waves can be attached at the strut leading edges. If the sweep is too high, low Mach number operation will result in shock waves being detached well upstream in the inlet ahead of the struts. These detached shock waves may create a situation where disturbances originating in the combustor may extend upstream of the struts locally and produce an undesirable inlet combustor interaction. Too little sweep means the internal contraction is high and no mechanism is provided for sufficient flow spillage for inlet starting at low Mach numbers. Because of the difficulty in analyzing inlet performance at low Mach numbers when the shock waves become detached, two models with struts were built and tested over the Mach number range of 2.3 to 6.0. These models had sweep angles of 60° and 56°. Several smaller models without struts but with sweeps of 50° and 0° were also tested at Mach 4. The results of these tests indicated that a sweep angle lower than 50° could be obtained with adequate starting capability and a sweep angle of 48° was selected.

Mach 6 Shock-Wave System

The theoretical shock diagram for a Mach number of 6 is shown in figure 4 with tables for the various flow passages and struts within the inlet. Section A-A is a horizontal plane parallel to the vehicle underbody and cowl. The sidewall compression angle was kept low to prevent the possibility of boundary-layer separation due to boundary-layer—shock interactions. (See ref. 10.) A detail of the predicted shock-wave structure in the vicinity of the struts is given in figure 5, and the properties of each numbered bay are listed in table I. The struts provide approximately 75 percent of the inlet static-pressure rise (46-percent decrease in throat area measured in the xz-plane). The side struts were positioned within the inlet so that two-thirds of the flow area available was in front of the center passages. This flow division permits the fuel to be injected equally from the surfaces of both the center strut and side struts (only six injection planes).

Boundary-layer transition on the sidewalls is expected to occur ahead of the struts, and the correction of 0.4° (based on flat-plate predictions) in conjunction with the sidewall angle provides a nominal turning of 6°. Because the chords of the struts are small, the thin boundary layer of the struts is expected to be largely laminar in front of the throats, and separation of this thin boundary layer is expected to be of little consequence. Although it is impossible to prevent the sidewall shocks from merging with the strut shocks at some flight Mach number, the situation is relieved for the Mach 6 shock-wave system by changing the wall slope of the struts at appropriate locations and either canceling or reducing the shock strength.

Inlet Design Performance

As previously mentioned, cooling requirements are a major consideration in combustor design and tend to limit the inlet contraction ratio. The inviscid design aerodynamic contraction ratio (which is computed from Mach number at the face of the inlet, throat Mach number, and total-pressure recovery) for the inlet at Mach 6 was 6.85 for the side passage (bay 6) and 7.57 for the center passage (bay 10) and yielded a mass flow weighted average theoretical contraction of 7.3. The geometric throat gaps between the struts are greater than those for a two-dimensional inlet of the same contraction, because a portion of the contraction is produced when the flow is turned toward the cowl (δ_{xy} in table I). In this inlet design the ratio of throat gap to inlet height is 0.042 for each center passage and 0.041 for each boundary-layer-corrected side passage. The width ratio measured in the xz-plane sidewall leading edges to the throats is 5.74 for the inviscid side passages and 6.17 for the center passages when the predicted flow split of 67 percent for the center passage and 33 percent for the side passage is assumed.

In the inviscid flow the average throat Mach number is 3.4 and the total-pressure recovery is 0.88; as a result, there is an adiabatic kinetic energy efficiency of 99.5 percent. The inclusion of the estimated boundary-layer losses on the struts, sidewalls, and top surface reduces the total-pressure recovery to approximately 0.67 (η_k = 98.3 percent); but this value still does not include corner effects. Inlet capture at Mach 6 was predicted to be 93 percent for the cowl location discussed in the next section. This predicted capture is based on the spillage generated when the flow is turned toward the opening in front of the cowl which is computed from matching pressure and flow direction between the external and internal streams.

End Effects

Although no attempt was made to analyze viscous corner boundary-layer interaction regions in the inlet throat, inviscid calculations of the flow near the top surface and cowl were made. Because the flow is turned away from the top surface as it proceeds through the inlet, a fillet was added as shown in figure 6(a). To match precisely the downflow, the top-surface contour must vary with local Mach number, but to avoid this complication, a single contour angle and position was selected. The angle was kept small (4°) to avoid shock interactions which could lead to separation of the thick, top-surface boundary layer. The leading edge of the top-surface fillet coincides with the location of the sidewall shocks with a Mach number of 5 in front of the inlet. With Mach 6 in front of the inlet, the top-surface fillet is upstream of the sidewall shock wave, and a 4° shock wave is produced as illustrated in section B-B of figure 6(a). At the throat the fillet displaces approximately the same amount or cross-sectional area as it would have if it had been on design for each bay, the Mach number in front of the inlet being equal to 6. The corrected values of flow parameters near the top surface for this constant-angle fillet are given in table II(a), where the angle of flow δ_{xy} in each bay has been corrected to match the 4° slope.

When the internal flow strikes the cowl, the flow must be turned back parallel to the cowl internal surface; as a result, a cowl shock wave and a high-pressure region are produced. The results of this flow turning are given in table II(b) where $\delta_{xy} = 0^{\circ}$. To compensate partially for this high pressure, the throat area next to the cowl was opened by relieving the struts and sidewalls. (See fig. 6(b).) This relief area begins where the shock wave from the cowl leading edge strikes the struts and sidewalls, and because the center strut is located downstream of the cowl leading edge, the strut does not extend to the cowl surface. For the inlet model, this cantilevered center strut was secured to the cowl with a pin located behind the strut maximum thickness.

Selection of the proper cowl leading-edge shape was based upon previous model testing. Cowls which enclosed the area behind the sidewall shock waves providing 100-percent capture made the model difficult to start, produced a cowl shock covering most of the inlet throat, and generated a very large corner interaction region between the sidewalls and cowl. A partial cowl whose leading edges were swept back at 50° (fig. 6(c)) was selected, which provided an open area near the inlet throats. This open area permits spillage for low Mach number inlet starting and provides for some sidewall boundary-layer bleed. The exact location of the cowl relative to the struts was determined from additional model testing as described in a later section.

Off-Design Performance

Although the inlet is not a point design at a local Mach 6 in the conventional sense, it is designed to give the highest relative performance at this Mach number. As the Mach number is decreased as shown in figure 7, the shock-wave system shifts forward, and experimental observations on previous models indicate an increased spillage and lower aerodynamic contraction. For this design at a Mach number of about 3.5, the shock waves become detached from the strut leading edges. With this swept inlet concept, the aerodynamic contraction will increase with increasing Mach number until the shock waves are fully attached in the throat region. At still higher Mach numbers the number of shock waves in the inlet decreases as they pass through the throat and the contraction begins to decrease slightly.

The combination of detached shock waves, with resulting spillage and variable contraction with Mach number, permits the inlet to have fixed geometry, to start at a low Mach number, and to provide enough contraction for successful operation at a high Mach number.

APPARATUS AND TEST PROCEDURE

The Inlet Model

A photograph of the inlet model designed with regard to the aforementioned concepts appears in figure 8. One sidewall has been removed in figure 8(a) and several pressure rakes can be seen. The model is shown upside down, and the 45.72-cm (18-in.) plate extending ahead of the sidewalls generates a simulated vehicle-forebody boundary layer. The boundary layer from this plate encounters early transition by trips located near the leading edge and the resulting boundary-layer profile entering the inlet is measured by a three-prong adjustable rake.

The model is 90.2 cm (35.5 in.) long not including the foreplate, and inlet frontal dimensions are 19.05 cm (7.5 in.) high by 15.24 cm (6.0 in.) wide. The aluminum top surface was machined in one piece, the foreplate being detachable. Assembly consisted of pinning and bolting the aluminum sidewalls to the top surface and then the stainless-steel cowl to the sidewalls in any one of three possible positions. Three stainless-steel struts were bolted in slots machined in the top surface which were then sealed. The struts were attached to the cowl by pins instead of bolts to reduce thermal stresses created by changes in the lengths of the struts and heights of the sidewalls. The normal to the leading-edge radii of the sidewalls, cowl, and struts was about 0.01 cm (0.004 in.), whereas the foreplate leading-edge radius was 0.06 cm (0.023 in.). Partially visible in the upper left of figure 8(b) is the actuator mechanism which moved pressure survey rakes inside the model.

Schematic drawings of the model are given in figure 9. Stainless-steel cheeks attached to the exterior of the sidewalls simulated adjacent inlet modules up to the inlet closeoff station next to the cowl. A survey station for measuring inlet capture was provided by a swept flat section of sidewall located downstream of the struts. A sidewall relief area next to the cowl is also illustrated, along with the footprint of the side struts on the cowl in section D-D. Detailed strut dimensions (fig. 10) and the relative positions of the struts and cowl (fig. 11) are measured in any xz-plane parallel to the foreplate and away from the relieved area near the cowl. The "station" positions are relative to the sidewall leading edges in the same xz-plane. A second center strut, which provides an increase in contraction, is also described in figure 10. The difference in contour for this second center strut is similarly shown by the dashed lines on some subsequent figures in the report.

Boundary-Layer Trips

To insure a turbulent boundary layer entering the throat passages, boundary-layer trips were attached to the sidewalls as well as to the foreplate. (See fig. 12.) The diameter of the steel balls (0.159 cm) was approximately equal to the estimated, flat-plate, boundary-layer thickness measured 7.6 cm downstream from the foreplate leading edge. The balls were spotwelded to steel strips which were in turn fastened with epoxy to the aluminum surfaces. The trips on the foreplate were utilized to increase the thickness of the boundary layer which would be entering the inlet, to determine whether there were any adverse effects associated with ingesting the boundary layer of a vehicle forebody.

Model Instrumentation

Figure 13 locates the 116 static-pressure orifices distributed throughout the inlet model. The orifices were strategically located to determine inlet starting, pinpoint shock-wave position, and aid in evaluating inlet contraction. Because of the variety of locations, the position reference varies for each group of orifices. Iron-constantan thermocouples were installed in the right sidewall as shown in figure 14. Each thermocouple lead was spotwelded to the aluminum surface instead of the leads being welded together, in order to determine more precisely the surface temperature.

Pressure Survey Rakes

The three-pronged foreplate boundary-layer probe is described in figure 15. This probe, alined with the sidewall leading edge at $Y/H = 0$ and $Z/H = 0.133$, was adjusted in height between tests to obtain detailed inlet entrance conditions near the top surface. The remaining survey probes were positioned laterally, by an electric motor and actuator attached to the model (fig. 16), in one of five access locations. Locations 1 to 4 provided for probe surveys across the inlet's throats, whereas location 5 provided access to the capture measurement station downstream of the struts. Tubing for the throat survey probes (fig. 17) was routed through the hollow actuator shaft, whereas capture measurement probe (fig. 18) tubes were carried out the rear of the model as illustrated in figure 8(a). The throat pitot probes were designed to survey one side and one center passage simultaneously, and the static survey probe surveyed only one center passage. It was necessary to rely on wall static data for the side passage. The capture measurement station 6.35 cm (2.5 in.) downstream from the struts was surveyed by the seven-prong pitot and static probes of figure 18(a). A single, stationary tube (0.102 cm I.D.) extended through the top surface and was bent toward the flow to obtain pitot pressure data in the front of a center passage near the top surface. This tube was bent to different locations across the passage between test runs.

Because of the static-pressure gradients in the small throat area to be surveyed, a conventional static-pressure probe, with the orifices located 10 to 20 diameters downstream from the tip, was found to be unsatisfactory. Therefore, a new static probe design (ref. 11), with the orifices approximately 3 tube diameters downstream from the probe tip and on a 3° conical shoulder, was used for both the throat and capture measurement surveys. These static-pressure probes were calibrated at a Mach number of 4.0, and the recorded pressures were found to be in error by less than 5 percent.

Mach 6 Test Facility

Figure 19 is a sketch of the Langley 20-inch Mach 6 tunnel. Tunnel test-section characteristics and flow calibrations can be found in the appendix of reference 12. The tunnel total temperature and pressure were normally 467 K and 11.9 atm, respectively, and provided a Reynolds number per meter of 9.8×10^6. One run was made at a reduced Reynolds number per meter of 3.3×10^6 at a pressure of 4.4 atm, and all runs in the blowdown tunnel were restricted to less than 2 min. The model was mounted upside down in the center of the 50.8-cm-square test section with two 15.24-cm steel channels bolted to the tunnel floor as shown in figure 20.

Facility Instrumentation

Tunnel pressure was recorded with strain-gage pressure transducers, and model static pressures were divided between six 48-port scanivalves. Pitot pressures and all survey data were measured by either strain-gage pressure transducers or multirange capacitance-type pressure transducers. Pitot position was determined with an electronic bridge circuit, and all data were processed by an electronic data processing system.

Because of the short time in which data could be taken $\left(\text{less than } 1\frac{1}{2} \text{ min}\right)$, the scanivalve stepping mechanism was used to trigger the recording system, once each second, while the survey probe was moved continuously across the flow. Before the test the speed of the throat probes was selected by varying the voltage to the dc motor until the probe would span the flow in one test run. At the capture measurement station two test runs were required to span the flow area with the probe. An analysis of the survey data also indicated that pressure lag was not significant even though the connecting tubing was up to ≈ 3 m in length.

DATA-REDUCTION PROCEDURE

A curve-fitting interpolation procedure was utilized to expand the pitot and static survey data into a grid network. Mach number, total pressure, and unit mass flow were calculated for each grid point; and contour maps of each parameter were plotted by the computer's graphic system. Inserted into the program for each grid point was an upper limit on total-pressure recovery which was obtained from the inviscid shock diagram. (See fig. 5.) If the total pressure was greater than this limit, the measured pitot pressure and the limiting total pressure were used to compute the flow parameters including the static pressure. The measured static pressure was discarded when the recovery limit was exceeded for any particular grid point because of the relative inaccuracy of the static-pressure measurements. After completing the grid, numerical integrations were performed to compute a mass-weighted Mach number and total-pressure recovery for the inlet throats and a value for a capture parameter $\rho v/\rho_1 v_1$ at the capture measurement station.

RESULTS AND DISCUSSION

Initial Inlet Tests

The results of the first inlet tests at Mach 6 indicated the model was not operating as expected. Initial testing of the model at Mach 6 indicated too much compression and possible choking was occurring within the center passage as indicated in figure 21. Upon investigation, it was discovered that the 6° sidewall shock wave was striking the side strut too near the leading edge. This shock wave then combined with the 4° side-strut shock wave and produced a 10° wave which reflected between the side and center struts (fig. 22) unlike the expected pattern of figure 5. The location of this sidewall shock wave was also determined by removing the struts and observing the sidewall static-pressure distribution (fig. 23). The error in shock-wave position as measured in the xz-plane was only about 0.64 cm ($\Delta/H \approx 0.033$) measured approximately 36 cm from the sidewall leading edge. The effect of the increased compression of the center passage extended across the inlet in the vicinity of the cowl to the sidewall, as indicated by the disturbance in the oil-streak photograph of figure 24(a). More detail concerning the oil study is provided in a later section, but proof that the sidewall disturbance was created by the center passage is illustrated in figure 24(b) with the center strut removed. This photograph shows no disturbance next to the cowl. The measured capture was only 81 percent with the choked cowl compared with 92 percent with the center strut removed.

Modified Inlet Configuration

To deal with the miscalculated sidewall shock-wave location, the strut arrangement was altered to move the shock waves toward the center-passage throat. The three struts and cowl were moved forward $\Delta X/H = 0.213$ ($\Delta X = 4.06$ cm); and the side struts were moved toward the sidewalls $\Delta Z/H = 0.022$ ($\Delta Z = 0.43$ cm) to maintain the same contraction and percent of flow in the side passage. The resulting configuration is shown in figure 25. It was also observed that the experimentally determined location of the sidewall shock waves could be duplicated theoretically by the addition of 0.83° to the sidewall compression angle. This correction is necessary because of end effects from the top surface, or model misalinement, or the use of flat-plate boundary-layer calculations on the swept sidewalls and struts. There was some concern for the inlet operation at lower Mach numbers when the shock wave moved forward along the side strut. However, the shock waves become detached from the swept compression surfaces and should prevent boundary-layer separation and choking by spreading the static-pressure rise along the strut surfaces. In fact, unpublished data from low Mach number tests support this conclusion.

The shock waves were recomputed with the new strut locations and the corrected inviscid sidewall compression angle, and the results are given in figures 26, 27, and in tables III and IV. Compression in the side passage increased because of the stronger sidewall shock wave. Mach number, recovery, and aerodynamic contraction changed from 3.51, 87.9 percent, and 6.85 to 3.45, 86.2 percent, and 7.07, respectively. The center-passage throat is now divided between bays 10, 14, and 16. The predicted, inviscid, mass-weighted average Mach number, recovery, and aerodynamic contraction for the inlet changed from 3.44, 88 percent, and 7.3 to 3.37, 85 percent, and 7.6, respectively, for the modified design.

From the initial inlet tests, moving the cowl to the forward position (fig. 11) aggravated the choking situation next to the cowl; and the cowl at the most rearward position failed to help the design. Therefore, the center position of the cowl relative to the struts (fig. 25) was maintained for the new configuration. This movement of the cowl forward ($\Delta X/H = 0.213$) relative to the sidewalls increased the theoretical capture by 2 percent to 95 percent.

The center-passage-throat gap was increased when the struts were moved forward, although the inlet aerodynamic contraction increased slightly. The purpose of center strut 2 was to decrease again the center-passage-throat gap and to determine operating sensitivity of the inlets on this parameter.

Inlet Entrance Conditions

The foreplate static-pressure distribution and the Mach number profile for the flow entering the inlet are given in figure 28. The static pressure on the foreplate was above the free-stream value because no boundary-layer correction was applied; in addition, the boundary layer was thicker than predicted by the flat-plate calculations probably as a result of trip losses.

Wall Static-Pressure Distribution

Figures 29 to 41 present the results of the static-pressure data throughout the model, which are compared with the predicted results of figures 26 and 27, and of tables III and IV. The solid symbols are data from orifices used to check flow symmetry with the two passages on the right side of the model. The round symbols are data obtained with the initial configuration and the x-position of this data has been shifted to correspond to the new strut locations. These data indicate in figures 29 to 33 that there was reasonable agreement between predicted and measured operation of the side passage away from the cowl. Some additional compression was observed on the cowl of the modified configuration (fig. 32) that was probably due to corner interaction phenomenon and blunt leading-edge effects. The static-pressure distribution along the side-passage throat is summarized in figure 33. The symbols of figure 33(b) were obtained from orifices located on the side strut; and, because no static surveys were made in the side passage, a linear pressure distribution was assumed across the throat between the strut and sidewall for data analysis. The data from the sidewall throat (squares in fig. 33(a)) of the new configuration were neglected because these orifices were no longer at the throat but downstream of the struts.

Data in the center passage are given in figures 34 to 41. The center passage of the initial design also operated as anticipated near the top surface (fig. 34), unlike the evidence of too much compression on the side strut at $Y/H = 0.43$ (fig. 21 or 35). The cowl pressures were greatly reduced with the modified configuration (figs. 38 and 39), but no theoretical value is shown because of the complicated flow generated by the strut relief (fig. 6(b)). The hump in the center-passage-throat pressure distribution (fig. 40) is attributed to a corner effect from the top surface creating a relocation of the strut shock waves. In general the center-passage compression was slightly greater than that predicted because no boundary-layer correction was made on the struts. The diamond symbols of figures 33 to 41 correspond to the larger center strut. From figure 27 it is clear that the larger center strut reduces the gap between the struts and moves the throat downstream. None of the experimental measurements would be expected to be affected by the larger strut except wall statics on the side strut in the downstream portion of bay 16 (fig. 27). Figure 35 does, in fact, show a higher pressure on the most downstream static orifice. In all other instances the larger strut had a negligible effect on the pressure measurements and it is concluded that the strut could be used successfully at Mach 6 to provide added contraction ratio. The static pressure on the small center strut (fig. 41) is lower because the orifices were located downstream of the strut shoulder. Appendix B presents pressure levels found within the model for a low-pressure test ($R = 3.3 \times 10^6$ per meter) and also an unstarted condition.

Oil-Flow Study

Although static pressures could be, and were, monitored to detect inlet starting, the most rapid and reliable method was to observe, by closed circuit television, the oil-flow pattern formed as the blackened oil droplets moved across the model's surface under the approaching flow. If the model did not start, all the oil on the sidewall moved in a curved path toward the bottom of the model. The only evidence of any shock wave was observed well upstream of the sidewall leading edges on the top surface. With the started inlet (fig. 42), the oil on the sidewall moves toward the throat along a line parallel to the line of intersection between the top surface and the sidewall. The exception was the oil near the bottom edge of the sidewall which followed the path of the flow spilled from the inlet. When the oil reached the high-pressure region formed by the side strut shock wave on the sidewall, it turned toward the cowl along a line approximately parallel to the swept leading edges. This oil accumulation line extended out the bottom of the inlet in front of the cowl with no interruptions, unlike the original strut configuration (fig. 24(a)).

Wall Surface Temperature and Boundary-Layer Analysis

The inlet did not reach an equilibrium temperature (fig. 43) because of a test time limit; however, the temperature was fairly uniform because of the high thermal conductivity of the aluminum. The dashed lines of figure 43 represent the wall temperature distribution selected for the boundary-layer analysis conducted with a modified version of the boundary-layer program of reference 13. This integral method computer program provided a viscous correction to the top-surface sidewalls and struts and reduced the total-pressure recovery from 86.2 percent to 54 percent for the side passage. The center-passage recovery changed from 84 percent to 73 percent, and the inlet average recovery was decreased from 85 percent to 67 percent. Because the surface of the cowl was small, it was neglected in the analysis, but the computed boundary-layer thickness for the rest of the inlet was nondimensionalized by the inlet height and plotted in figure 44. Transition was forced on the top surface 7.62 cm from the foreplate leading edge because of the trips. Natural transition was assumed at $s'/H \approx 0.8$ for the sidewall where the Reynolds number based on momentum thickness was equal to 1000. The sidewall boundary-layer trips had been removed prior to the modified configuration test when it was observed that they had little effect on the side-passage experimental data. The boundary-layer flow over the struts was assumed to be turbulent from the swept leading edges.

Throat Surveys

Pitot pressure distributions for both the side and center passage are presented in figure 45, where W is the throat gap and Z' is equal to zero at the sidewall for the side-passage throat and equal to zero at the side strut for the center-passage throat. At the top of the model ($Y/H = 0.14$), the center throat data were obtained from the fixed tube, which was bent to a new Z' position for each test. The side-passage pitot profile ($Y/H = 0.17$) was obtained from the theoretical boundary-layer profile at $Z/W = 0.5$ and then assumed similarity with the profile at the adjacent side throat station of $Y/H = 0.26$. The solid symbols were not data points but depended on theoretical boundary-layer calculations to extend each survey (dashed lines) to the wall static value for data reduction.

Data station $Y/H = 0.43$ was considered the station least influenced by top-surface and cowl flow effects, and surveys for the low Reynolds number test and the large center strut test are presented for this station in figures 45(g) and 45(h). The dashed lines in these two figures were taken from the standard tests (fig. 45(c)) and indicate that neither the large center strut nor the low Reynolds number tests had any significant effect on inlet operation.

The static survey data (fig. 46), obtained for the center passage, were faired to the wall values as indicated by the solid symbols. As mentioned earlier, when the measured static pressure was low and the total-pressure recovery exceeded the set upper limit (88 percent), a new static pressure based on the upper recovery limit was computed as illustrated by the dashed lines. To check the effect of this restriction, it was determined that a 10-percent increase in the limit increased the mass-weighted total-pressure recovery by approximately 3 percent. The straight lines are the static-pressure distributions assumed for the side passage and are based on neighboring wall static values. Other static-pressure data estimated from neighborhood statics for both the center- and side-passage throats near the top surface and cowl are given in figure 47. These additional estimated distributions made possible an analysis of a greater part of the throat flow area as defined by the pitot surveys.

The throat stations at $Y/H = 0.43$ were selected to be compared with the theoretical inviscid and boundary-layer calculations, and the resulting Mach number profiles are found in figure 48. The agreement is good for both passages; the dip next to the center-passage side strut may be caused by a probe-tip shock-wave interaction. The small hash marks indicate the pitot measurement closest to the sidewall or strut, and the remainder of the curve is the result of fairing the pitot pressure to the wall static-pressure level.

Throat Contour Maps

Contour maps of the results of compiling the throat pitot and static data are given in figures 49 to 52. Figures 49 and 50 are maps of the data input used to compute the Mach number and recovery maps of figures 51 and 52. Each map is shown with the width scale seven times the height, which makes the relief area next to the cowl (illustrated in fig. 51) appear to be out of proportion. The side-passage Mach number contours (fig. 51) are relatively symmetrical, and the prediction of boundary-layer thickness δ agrees well for the top and side surface. The top-surface boundary-layer thickness for the side passage had to agree because of the imposed boundary conditions. A nearly horizontal shock of about 8° turning was generated by the cowl leading edge and is still near the cowl surface at the throat. This discrete shock is smeared by the computer programs interpolation process; and consequently a vertical Mach number gradient extending well beyond the predicted δ for the cowl is indicated. There is some rounding of the contours at the corners, but no flow separation is detected. The Mach number contours for the center passage are not as symmetrical because of the greater shock-wave concentration (fig. 51(b)); however, the Mach 3 (mass-weighted average equals 3.11) contour encloses the major portion of the total area. The mass-weighted total-pressure recovery recorded in figure 52 for both the throat passages was obtained by a computer program which averaged the values of approximately 1000 grid points, evenly spaced over the throat area. One case was also integrated by hand with negligible difference, and the results verified the computed results. The mass-weighted average recovery for the two passages is 59 percent when the losses on the foreplate are included and 61 percent when they are neglected. The central area of nearly constant total-pressure recovery in figure 52(b) is in part a result of the assumption of a total-pressure recovery limit in regions where the measured static-pressure level was too low (fig. 46); however, this assumption is considered to be justified on a phenomenological basis as well as by the similarity in shape between the measured and derived static-pressure profiles (fig. 46) and the reasonable agreement between theory and data (for example, fig. 48).

Capture Measurement Results

The procedure for analyzing the flow at the capture measurement station was identical to that of the inlet throats. At this station static survey data were taken at each pitot survey location. Each rake had seven probe tips. The data from which the Mach number and capture parameter $\rho v/\rho_1 v_1$ were derived for figures 53 and 54 are discussed in appendix C. The wakes of the three struts, which are about 7.5 cm upstream, are detectable in the Mach number map (fig. 53); in general, lines of constant Mach number are parallel to the sidewalls. Besides measuring inlet capture flow, the capture parameter (fig. 54) is a good indicator of flow gradient direction because it is less sensitive to static-pressure error than either Mach number or recovery. The average value of $\rho v/\rho_1 v_1$ was 3.18 for the inlet at the capture measurement station; before capture flow could be calculated, however, some estimate of flow direction to determine cross-sectional area had to be made. The assumptions in figure 55 are: flow parallel to the top surface in the top-surface boundary layer; flow parallel to the cowl below the estimated location of the cowl shock wave; and flow down at 8° for the remainder of the area. This 8° downflow was the flow turning which was computed from the rise in static pressure due to the cowl shock. The flow was also assumed to be parallel to the sidewalls at this station. With these restrictions a capture of about 94 percent was computed for the inlet at Mach 6.

Performance Results

Because the struts were positioned within the inlet to provide two-thirds of the flow to the center passage, the captured flow (94 percent) was assumed to be split between the center and side passages in the ratio of 63/31. With this criteria the Mach 6 integrated performance parameters based on the tunnel free-stream conditions are tabulated for each passage, and the total inlet, in figure 56. The side-passage total-pressure recovery was lower than the center-passage recovery because of the relatively thicker boundary layer on the sidewalls. The average viscous total-pressure recovery was 0.59 compared with the predicted value of 0.67 for the initial inlet configuration, which did not include corner effects. The aerodynamic contraction ratio, which is based on the average throat Mach number and total pressure, is 7.0 instead of the design value of 7.3. This is because moving the struts upstream increased the throat width somewhat and because the measured total-pressure recovery was slightly lower. The larger center strut increased the contraction, but no data were taken at the new center-passage throat location. Included in figure 56 are curves from reference 7 predicting the inlet kinetic energy efficiency and capture over the flight Mach number range of 4 to 10. The Mach 6.0 inlet data have been entered in the figure for a flight Mach number of 7.6, which indicates a representative amount of vehicle forebody compression. The measured kinetic energy efficiency as determined by adiabatic process was 97.7 percent compared with the predicted tunnel value of 98.3 percent. The predicted curve is slightly high primarily because the cowl shock and viscous corner interactions were not included. The measured captured mass flow from in front of the inlet was 94 percent and matched the predicted value. The theory is expected to be less accurate at low Mach numbers because of the formation of detached shock waves. (See fig. 7.)

CONCLUDING REMARKS

As part of a Langley research and technology program focused on the development of a concept for an airframe-integrated scramjet engine (Langley Scramjet Module), a detailed performance evaluation of the baseline inlet configuration at Mach 6 (simulated flight Mach number of approximately 7.6) has been conducted.

Mach number profiles in the inlet throat agreed reasonably well with the predicted results both for the inviscid flow and the boundary-layer calculations on the struts and sidewall. The mass-weighted average throat Mach number was 3.0 for the side passage and 3.1 for the center passage. This value compares with the inviscid values of 3.4 for each of the two passages. This additional compression was produced by the boundary layer, viscous corner interactions, and other end effects (for example, the internal cowl shock).

An adiabatic kinetic energy efficiency of 97.7 percent (0.59 recovery) was measured and compared with a predicted value of 98.3 percent (0.67), which does not include corner or end effects.

The average inlet aerodynamic contraction ratio was 7.0 instead of the predicted value of 7.3 because of the slightly lower total-pressure recovery. However, the results indicated that the contraction ratio can be increased by the use of a larger center strut, which operated successfully but no survey data were taken.

The measured inlet capture flow was 94 percent which agrees with the predicted value of 95 percent.

The difficulty and importance of properly positioning the shock waves in the throats of hypersonic inlets were demonstrated, but no adverse effects were noted as a result of the inlet ingesting a boundary layer on the top surface which simulated the boundary layer that would be ingested from the vehicle forebody. Overall, the inlet performance is well within the acceptable range for high engine performance.

Langley Research Center,
National Aeronautics and Space Administration,
Hampton, Va., April 22, 1975.

APPENDIX A

ANALYTICAL CALCULATIONS OF SWEPT SHOCK WAVES

Shock-wave systems for swept inlet configurations require a three-dimensional coordinate system to locate the shock waves correctly and to compute the flow properties. A selected two-dimensional coordinate system (the xz-plane of fig. 4) is also helpful in maintaining visual contact with the problem. Figure 57 illustrates the flow striking a swept wedge (surface AGFED) and helps to describe the development of the swept shock wave. Points A, H, I, and D lie in the xy-plane and points A, H, G, and B lie in the xz-plane. The flow strikes the leading edge at point A; and if the wedge were not swept, the flow would only be turned away from the xy-plane by angle δ_{xz} and would follow the path AG. However, sweeping the wedge requires the flow to traverse the surface along AF, the flow also being turned away from the xz-plane as shown by angle δ_{xy} which is measured in the xy-plane. A swept shock wave (plane ABCD) attached to the leading edge is produced and is located with angle ϵ_{xz} which is measured in the xz-plane. As long as the wedge is assumed to be of infinite length, no end effects are encountered; if the wedge is assumed to extend from the xz-plane, a reduced pressure, nonuniform flow region will exist in the proximity of the xz-plane. To eliminate this region, a fillet (AGFB) is added which extends out to the shock wave and fills the void left by the flow being turned away from the xz-plane.

A detailed discussion of the calculation procedure for obtaining the shock wave angle ϵ_{xz}, downflow δ_{xy}, and the flow properties behind the shock wave is given in reference 9, which describes the flow velocity being broken into vector components normal and tangential to the leading edge as shown in the sketch of figure 57. Although the velocity component tangential to the leading edge V_t remains unchanged $\left(V_{t,1} = V_{t,2}\right)$, the component perpendicular to the leading edge $V_{n,1}$ is reduced because it is turned by δ_n when it encounters the wedge. The vectors on the wedge surface, $V_{n,2}$, and $V_{t,2}$, are then combined to obtain the velocity and direction of flow on the wedge surface. One limitation to the procedure occurs when either the sweep angle or the wedge angle is too great, and the velocity component $V_{n,2}$ becomes subsonic. The shock wave may become detached from the wedge leading edge, as illustrated in the sketch, and the downstream flow is not uniform.

The Swept Shock-Wave System

To determine the shock-wave orientation and flow properties for a train of shock waves as illustrated in figure 58, additional steps are required to compute the shock angles in the xz-plane. The computation must include the change in sweep angle and normal turning angle as the flow crosses each successive shock wave and is turned further from the xz-plane.

A computer program has been written to compute an inviscid shock wave system for an inlet, when the inlet geometry and the initial Mach number are specified. Inlet geometry consists of plane wedges defined by sweep angle measured in the xy-plane and flow turning angles which are measured in the xz-plane. The shock-wave computational procedure is described for the three shock waves of figure 58. The second shock wave reflects from a plane of symmetry along line AB, strikes the sidewall (line BB), and is again reflected. The flow vectors behind the three shock waves are labeled V_2, V_3, and V_4, respectively. Because the flow angle with respect to the top surface (xz-plane) increases as the flow crosses each successive shock wave, a new fillet is required to eliminate three-dimensional end effects. The downstream fillets have complex orientations which are functions of Mach number; but, because they are small and considered to have minimal influence on the flow, these effects were neglected in the inlet design.

The sidewall is the generator of the first shock wave and may be considered to be a wedge or wing with sweep Λ_1 measured in the xy-plane, angle of attack δ_{xz} and dihedral as measured by the angle ϕ_1. The second shock wave is reflected from the plane of symmetry along line AA and is illustrated in detail in figure 59. For this reflected wave the computer program solves the problem of flow across a wedge or wing with sweep Λ_2, angle of attack $\delta_{(xz)'}$, and zero dihedral $(\phi_2 = 0)$. The reference axes are x', y', and z'. Because the flow has been turned toward the y-axis by the first shock wave, the sweep angle Λ_2 increased from the value of Λ_1. Once V_3 and the shock-wave angle $\epsilon_{(xz)'}$ have been computed, the shock wave is defined in the original xz-plane with angle ϵ_{xz}.

The third shock wave is illustrated in detail in figure 60, where the flow in front of the wave V_3 approaches a swept wedge (sidewall) which is in the x'', y'', and z'' coordinate system. The sweep angle is Λ_3. The angle of attack is $\delta_{(xz)''}$, and the dihedral is ϕ_3. The computer program treats this wave in the same manner as the first wave to compute $\epsilon_{(xz)''}$, and then defines the shock wave in the xz-plane with ϵ_{xz}.

The first and third shock waves are coded "type A" waves by the program whereas waves reflected from the plane of symmetry are coded "type B." The flow turning across each wave, measured in the xz-plane, can be put into the program, which means the strength of the reflected wave (type B) may be made different from the strength of the incident (type A) wave. To compute a shock train, the program always begins with a wave of type A, but the wave types do not have to alternate as the wave type of each shock wave is input to the program. When two type B waves are together, the nomenclature must be reversed and the second type B wave considered to be type A; then this new orientation is continued.

The program transfers all shock angles back to the xz-plane, where the angle is measured with respect to the flow direction in front of the wave for a type A wave; and the shock angle is measured with respect to the flow direction behind the wave for a type B wave. For a selected path of shock waves the sweep angle and dihedral for the first wave are input to the program. Subsequent sweep angles are internally computed, as is the dihedral, which is a function of the wave type. The number of shock waves in the train is input, and the program will continue to calculate across successive shock waves until shock-wave detachment occurs.

Because the flow properties in oblique shock-wave systems are path dependent, it may become necessary to iterate on pressure and flow direction, when waves of different turning strengths are encountered. Usually, however, the differences in shock-wave turning angles are small enough to insure that such effects can be neglected. If a correction is deemed to be necessary, an iteration can be done either by hand as the program computes across one wave at a time, or by following several flow paths with the program and averaging the results in the selected downstream flow bay.

The Computer Program

The program is written in FORTRAN IV and is adapted to the CDC 6600 computer located at the Langley Research Center, Hampton, Virginia. Although the primary purpose of the program is to compute flow properties for swept, weak, oblique shock-wave systems, additional versatility is available as shown in the input listing attached to this appendix. Either perfect-gas or thermally perfect-gas (gas with caloric imperfections as defined in ref. 14) problems may be computed by the listed program. Also operational, but not included in the program listing, is a subroutine for real-air calculations. This real-air subroutine uses either thermodynamic tables or equations of air in thermochemical equilibrum to compute flow properties behind shock waves.

For the thermally perfect gas, the local total properties are computed; and the specific heat ratio γ is computed as a function of static temperature from equation (180) of reference 14. The gas characteristics that are assumed for air and are used currently in the program are:

Molecular vibrational-energy constant, θ_v	3076 K
Perfect gas specific heat ratio, γ_p	1.4
Gas constant, $\overline{R}$	1545.31
Molecular weight	28.9644

Both weak and strong shock waves and perfect-gas Prandtl-Meyer expansion calculations are possible. For the expansion fan, the angles of the leading, trailing, and average waves are printed.

The dihedral ϕ is measured in a plane perpendicular to the wedge ridge line (line AG of fig. 57) and is defined in a parameter ψ where

$$\psi \equiv 1 - \frac{\cot \Lambda \tan \phi}{\sin \delta_{xz}}$$

This parameter is defined in reference 9 as the ratio of the lengths of two line segments (DE/AD) and is used to define the location of the wedge leading edge with respect to the xy-plane. For the first wave of a shock train, the wedge dihedral ϕ does not have to be calculated because the leading edge is assumed to lie in the xy-plane and ψ has a value of zero. For a single-wave calculation the leading edge may be lifted out of the xy-plane; and when the dihedral is zero, ψ has a value of 1.

Program Input

Card 1 – FORMAT(4F10.4,2F5.2,2F10.4,5I1)

OC Number of successive waves (Maximum = 20) (cols. 1 to 10)

XM Initial Mach number, M (cols. 11 to 20)

ALP Sweep angle, Λ, deg (cols. 21 to 30)

E1 Wedge ridge angle, δ_{xz}, deg (cols. 31 to 40)

DEADR Dihedral parameter, $\psi \equiv 1 - \frac{\cot \Lambda \tan \phi}{\sin \delta_{xz}}$ (cols. 41 to 45)

GAM Specific heat ratio, γ, for perfect gas (cols. 46 to 50)

P1 Static pressure, p_1, psia (cols. 51 to 60)
Set equal to 1.0 if left blank

T1 Static temperature, T_1, $^{\circ}R$ (cols. 61 to 70)
Set equal to 500° R if left blank

K1 Type of gas calculation (col. 71)
- 0 perfect gas
- 2 thermally perfect gas

K2 Flag indicates value of turning angle for each shock wave to follow on card 2 (col. 72)
- 0 all waves will have δ_{xz} = E1
- 2 OC values of δ_{xz} will follow on card 2

K3 Flag indicates wave type for each shock wave to follow on card 3 (col. 73)
- 0 no card 3 necessary, waves will alternate Type A and Type B
- 2 OC wave types to follow on card 3

K4 Flag indicates strength of shock wave (col. 74)

- 0 weak shock waves
- 2 strong shock wave (limited to OC = 1)

K5 Special input case for dihedral (col. 75)

- 0 DEADR = Dihedral parameter, ψ
- 2 DEADR = Dihedral angle, deg

Card 2 – FORMAT (16F5.3). Do not use if K2 = 0

E11A Value of δ_{xz} for each wave, deg
Expansion waves are entered as negative

Card 3 – FORMAT (16F5.3). Do not use if K3 = 0

TYPE Wave types

- 1. Type A
- -1. Type B

The first wave of a shock train must be type A.

A listing of the computer program follows:

```
          PROGRAM INLET    (INPUT,OUTPUT,TAPE5=INPUT,TAPE6=OUTPUT,TAPE8)
      C
      C        SWEPT SHOCK WAVE PROGRAM   A1991        BY C.A. TREXLER     10/22/74
      C
      C    INPUT FOR CARD 1    FORMAT(4F10.4,2F5.2,2F10.4,5I1)
      CNO.WAVES MACH NO.  SWEEP      DELTA      DIH  GAM  P1         T1        KKKKK
      C                   DEG.       DEG.       DE/AD     PSIA       DEG.R     12345
      C
      C        SWEEP= SWEEP ANGLE MEASURED IN XY PLANE
      C        DELTA= FLOW TURNING ANGLE IN XZ PLANE
      C        DIH=   DIHEDRAL PARAMETER  (DE/AD)
      C        GAM=   SPECIFIC HEAT RATIO      **  SET EQUAL TO 1.4 IF LEFT BLANK
      C        P1=    STATIC PRESSURE, PSIA    **  SET EQUAL TO 1.0 IF LEFT BLANK
      C        T1=    STAT TEMP., DEG R        **  SET EQUAL TO 500. IF LEFT BLANK
      C        ADDITIONAL ENGLISH UNITS
      C               DENSITY -- LBM/FT**3
      C               VELOCITY - FT/SEC
      C               ENTHALPY - BTU/LBM
      C
      C    K1= BLANK, PERFECT GAS               ///    K1= 2, THERMALLY PERFECT GAS
      C               K1= 4, REAL AIR - EQUATIONS  (IF T1=0  P1= ALTITUDE, FT.)
      C               K1= 6, REAL AIR - TABLES     (IF T1=0  P1= ALTITUDE, FT.)
      C    K2= BLANK, WAVE STRENGTHS NOT INPUT  ///    K2= 2, WAVE STRENGTHS INPUT
      C    K3= BLANK, WAVE TYPES NOT INPUT      ///    K3= 2, WAVE TYPES INPUT
      C    K4= BLANK, WEAK SHOCK WAVE           ///    K4= 2, STRONG SHOCK WAVE
      C    K5= BLANK, DIH = DE/AD               ///    K5= 2, SPECIAL CASE
      C      *SPECIAL CASE* DIHEDRAL (DIH) DEFINED BY AN ANGLE MEASURED
      C                     IN A PLANE PERPENDICULAR TO RIDGE LINE.
      C                     SWEEP MEASURED WITH LEADING EDGE IN XY PLANE,
      C                     AND WEDGE AT ZERO ANGLE OF ATTACK.
      C
      C    INPUT FOR CARD 2   FORMAT(16F5.2)    NOT INPUT IF K2= BLANK
      CD(1) D(2) D(3) D(4).....D(NW)
      C        D=      FLOW TURNING ANGLE IN XZ PLANE (DEG)
      C        NW=     NO. WAVES
      C
      C    INPUT FOR CARD 3   FORMAT(16F5.2)    NOT INPUT IF K3= BLANK
      CT(1) T(2) T(3) T(4).....T(NW)
      C        T=      WAVE TYPE ****** T= 1. FOR TYPE A    ///    T= -1. FOR TYPE B
      C        NW=     NO. WAVES
      C
000003          COMMON C,THV,GAMP,RBAR,XMWT,P1,T1,XM,XMNORM,TO
```

```
000003          COMMON P2,T2,DELTN,GAM,XM2N,EPD,RHOR
000003          COMMON EMAX,DELTNM,N,KGAS,MC
000003          COMMON EPDF,TPKA,AR,XM1T,XM2T
000003          COMMON NDEBUG
000003          DIMENSION E11A(20), TYPE(20)
000003          C=3.14159265/180.0
000005          GAM=1.400
000006          THV=5537.0
000007          GAMP=1.4
000010          RBAR=1545.31
000012          XMWT=28.9644
000013          NDEBUG=0
000014          JJ=0
000016        5 READ(5,101)OC,XM,ALP,E1,DEADR,GAM,P1,T1,KGAS,NDELT,NORDER,N,KSP
000054      101 FORMAT(4F10.4,2F5.2,2F10.4,5I1)
000054          IF(EOF,5)6,70
000057        6 STUP
000061       70 CONTINUE
000061          T0=0.
000062          DIH=DEADR
000063          NSTR=N
000065          IF(GAM.LT..001)GAM=1.4
000071          IF(KGAS.GT.3)GO TO 400
000075          IF(P1.EQ.0.)P1=1.
000077          IF(T1.EQ.0.)T1=500.
000101      400 CONTINUE
000101          IF(KGAS.EQ.0)KGAS=0
000103          IF(NDELT.EQ.0)NDELT=0
000105          IF(NORDER.EQ.0)NORDER=0
000107          IF(NSTR.EQ.0)NSTR=)
000111          IF(KSP.EQ.0)KSP=0
000113          IF(ALP.EQ.0.)GO TO 700
000114          IF(E1.EQ.0.)GO TO 700
000115          IF(KSP.EQ.2)DEADR=1.-TAN(DEADR*C)/(SIN(E1*C)*TAN(ALP*C))
000136      700 CONTINUE
000136          XMINF=XM
000137          PINFR=1.0
000141          TINFR=1.0
000141          RINFR=1.0
000142          KKGAS=KGAS
000144          IF(KGAS.EQ.0)KGAS=1
000146          MC=OC
000150          DO 3 I=1,MC
000152          E11A(I)=E1
000154          TYPE(I)=0.
000155        3 CONTINUE
000157          IF(NDELT.EQ.0)GO TO 4
000160          READ(5,102)(E11A(NO),NO=1,MC)
000172          E1=E11A(1)
000174      102 FORMAT(16F5.3)
000174        4 CONTINUE
000174          IF(NORDER.EQ.2)READ(5,102)(TYPE(NO),NO=1,MC)
000211          OC=1.0
000212          I=1
000213          CO13PT=0.0
000214          ARCA=1.0
000215          TPRA=1.0
000216          K=1
000217          NN=0
000220          JJ=JJ+1
000222          AL1=ALP
000224        7 CONTINUE
000224          PRINT 106
000230      106 FORMAT(1H1)
000230          PRINT 126, JJ,K
000240      126 FORMAT(1X,7HCASE NO,I3,10X,7HWAVE NO,I3,39X2HK1,2X2HK2,2X2HK3,2X
              1 2HK4,2X2HK5)
000240          IF(NSTR.EQ.2.AND.E1.GE..01)PRINT 121,KKGAS,NDELT,NORDER,NSTR,KSP
000257          IF(NSTR.NE.2.AND.E1.GE.0.)PRINT 122,KKGAS,NDELT,NORDER,NSTR,KSP
000315          IF(NSTR.NE.2.AND.E1.LT.0.)PRINT 123,KKGAS,NDELT,NORDER,NSTR,KSP
000343          IF(NSTR.EQ.2.AND.E1.LT..01)PRINT 124,KKGAS,NDELT,NORDER,NSTR,KSP
000372          IF(KSP.EQ.2)PRINT 125, DIH
000402      121 FORMAT(45X14H(STRONG SHOCK),9X6I4)
000402      122 FORMAT(45X14H(WEAK SHOCK)  ,9X6I4)
000402      123 FORMAT(45X14H(EXPANSION)   ,9X6I4)
000402      124 FORMAT(45X14H(NORMAL SHOCK),9X6I4)
000402      125 FORMAT(70X26H(DIHEDRAL = SPECIAL CASE =,F7.3,5H DEG))
000402          J=1
```

```
000403    600 CONTINUE
000403        ALPH=ALP*C
000405        E=E1*C
000406        IF(ALPH.GT..001)GO TO 9
000412        XM1N=XM
000412        XM1T=0.
000413        XMNORM=XM
000414        DELTN=E
000416        DELTNP=DELTN
000420        GO TO 14
000420      9 CONTINUE
000420        ACOD=90.*C-ALPH
000423        CD=OC*TAN(ACOD)
000426        OD=OC/COS(ACOD)
000431        BC=OC*TAN(E)
000434        AD=BC
000436        DE=AD*DEADR
000437        PSI=ATAN2(DE,OD)
000442        OE=(OD**2+DE**2)**.5
000450        OB=(BC**2+OC**2)**.5
000456        AE=ABS(AD-DE)
000461        BE=(CD**2+AE**2)**.5
000467        THETA=ACOS(OC/OE)
000473        ABOE=ACOS((OB**2+OE**2-BE**2)/(2.0*OB*OE))
000504        XM1T=XM*OC/OE
000507        XM1N=XM*SIN(THETA)
000512        IF(XM1N-1.0)203,203,8
000515      8 CONTINUE
000515        OG=OC*OC/OE
000517        CG=OC*SIN(THETA)
000522        HG=OG*TAN(ABOE)
000525        OH=(HG**2+OG**2)**.5
000532        HC=(OH**2+OC**2-2.0*OH*OC*COS(E))**.5
000544        DELTN=ACOS((HG**2+CG**2-HC**2)/(2.0*HG*CG))
000554        IF(E11A(K).LT.0.)DELTN=-DELTN
000560        DELTNP=DELTN
000561        XMNORM=XM1N
000563     14 CONTINUE
000563        GR=(GAM+1.)/(GAM-1.)
000567        EMAX=SQRT((GAM+1.)*(1.+(GAM-1.)/2.*XM1N**2+(GAM+1.)/16.*XM1N**4))
000605        EMAX=(1./(GAM*XM1N**2))*((GAM+1.)/4.*XM1N**2-1.+EMAX)
000620        EMAX=ASIN(SQRT(EMAX))
000624        DELTNM =(GAM+1.)*XM1N**2/(2.*(XM1N**2* (SIN(EMAX)**2)-1.))
000635        DELTNM=(DELTNM-1.)*TAN(EMAX)
000642        DELTNM=ATAN(1./DELTNM)
000645        DLIMIT=DELTNM+10.*C
000650        IF(XM1N.LT.2.)DLIMIT=DELTNM+2.*C
000656        IF(DLIMIT.GT.DELTN)GO TO 15
000662        KGAS=1
000663     15 CONTINUE
000663        IF(KGAS-1)10,10,11
000666     11 CONTINUE
000666        IF(KGAS.GT.3)CALL RAIR(ZFT,NSTR)
000673        IF(KGAS.GT.3)GO TO 16
000677        CALL REALG (NSTR)
000700        IF(N.LT.100)GO TO 16
000703        KGAS=1
000703        IF(DELTNM.LT.DELTN)GO TO 10
000706        IF(N.EQ.100)GO TO 5
000707     16 CONTINUE
000707        TR=T2/T1
000711        PR1=P2/P1
000713        RR=RHOR
000714        EP=EPD*C
000716        EPF=EPDF*C
000717        IF(ALPH.LT..001)GO TO 21
000722     10 CONTINUE
000722        IF(KGAS-1)12,12,25
000725     12 CALL PGAS
000726        IF(N.EQ.100)GO TO 5
000730        TR=T2/T1
000732        PR1=P2/P1
000734        RR=RHOR
000735        EP=EPD*C
000737        EPF=EPDF*C
000740        IF(ALPH.GT..001)GO TO 13
000744     21 CONTINUE
000744        ARCA=ARCA*AR
```

```
000746         DELTN1=DELTNP/C
000747         DELTM=DELTNM/C
000751         EMAX1=EMAX/C
000752         EEF=1.-(2./((GAM-1.)*((1./TPRA)**((GAM-1.)/GAM)-1.)/XMINF**2)
000766         PINFR=PINFR*PR1
000770         TINFR=TINFR*TR
000771         RINFR=RINFR*RR
000773         PRINT 115
000777     115 FORMAT(// *         SUMMARY OF FLOW PROPERTIES ACROSS UNSWEPT WEDGE
              1  *)
000777         PRINT 17, XM,ALP,DELTN1,EPD,P1,T1
001017      17 FORMAT(/1X,3HM1=,F8.3,7X6HSWEEP=,F7.3,7X6HDELTA=,F7.3,12X4HEPS=,
              1 F7.3,7X3HP1=,F8.4,6X3HT1=,F8.2)
001017         PRINT 19, XM2N,PINFR,RINFR,TINFR,GAM
001035      19 FORMAT(/1X,3HM2=,F8.3,6X,7HP/PINF=,F8.4,5X7HR/RINF=,F8.4,9X7HT/TIN
              1F=,F8.4,5X4HGAM=,F7.4)
001035         PRINT 120,TPRA,EEF
001045     120 FORMAT(/1X,22HRECOVERY (PT/PTINF)  =,F8.4,7X20HKINETIC ENERGY EFF.
              1=,F9.5)
001045         PRINT 18,ARCA,DELTM,EMAX1
001057      18 FORMAT(/1X,22HCONTRACTION (AINF/A) =,  F8.4,27X10HDELTA MAX=,F8.4,
              14X8HEPS MAX=,F8.4)
001057         IF(DELTN1.GT.DELTM)PRINT 119
001065     119 FORMAT(60X28H***SHOCK WAVE IS DETACHED***)
001065         IF(DELTN.GT.DELTNM)GO TO 5
001071         I=I+1
001072         IF(MC-I)5,20,20
001074      20 CONTINUE
001074         K=K+1
001076         P1=P2
001077         T1=T2
001100         XM=XM2N
001102         E1=E11A(K)
001104         GO TO 7
001104      13 CONTINUE
001104         XM2T= XM1T*(1./TR)**.5
001112      25 CONTINUE
001112         XM2=(XM2T**2+XM2N**2)**.5
001120         ARC=AR*XMNORM*XM2/(XM2N*XM)
001124         ARCA=ARCA*ARC
001126         ACHG=ACOS((HC**2+HG**2-CG**2)/(2.*HC*HG))
001136         AJHG=180.*C-ACHG
001141         IF(E11A(K).LT.0.)AJHG=ACHG
001145         AJGH = EP - DELTN
001147         AHJG=180.*C-(AJHG+AJGH)
001153         GJ=HG*(SIN(AJHG)/SIN(AHJG))
001161         HJ=HG*(SIN(AJGH)/SIN(AHJG))
001167         CJ=HC+HJ
001171         IF(E11A(K).LT.0.)CJ=HJ-HC
001175         OJ=(GJ**2+OG**2)**.5
001203         EPXZP=ACOS((OJ**2+OC**2-CJ**2)/(2.*OJ*OC))
001214         EXZPF=EPXZP
001216         EXZAVG=0.0
001216         IF(E11A(K))505,500,500
001221     505 AJGHF=EPF
001222         AHJGF=180.*C-(AJHG+AJGHF)
001226         GJF=HG*(SIN(ACHG)/SIN(AHJGF))
001234         HJF=HG*(SIN(AJGHF)/SIN(AHJGF))
001242         CJF=HJF-HC
001244         IF((EPF+DELTN).LT.0.)CJF=HC-HJF
001251         OJF=(GJF**2+OG**2)**.5
001257         EXZPF =ACOS((OJF**2+OC**2-CJF**2)/(2.*OJF*OC))
001270         IF((EPF+DELTN).LE.0.)EXZPF=-EXZPF
001274         EXZAVG= EPXZP-.5*(EPXZP- EXZPF)
001300     500 CONTINUE
001300     300 FORMAT(10F10.5)
001300         AEOI1P=ATAN2(XM2N,XM2T)
001302         ABOI1P=ABOE-AEOI1P
001304         ABEO=ASIN(OB*SIN(ABOE)/BE)
001312         AOBE=180.*C-(ABEO+ABOE)
001316         ABI1PO=180.*C-(AOBE+ABOI1P)
001321         IF(ABOI1P)304,303,303
001322     304 ABI1PO=AOBE- ABS(ABOI1P)
001325     303 CONTINUE
001325         BI1P=OB*(SIN(ABOI1P)/SIN(ABI1PO))
001333         AABE=ATAN(AE/CD)
001337         T1P12P= BI1P*COS(AABE)
001342         ACOI3P = ATAN(T1P12P/OC)
001346         AFOC= ATAN2(DE,OC)
```

```
001351            ABOF= ABS(E-AFOC)
001354            BI2P=(BI1P**2-T1PI2P**2)**.5
001362            IF(DEADR-1.)200,200,201
001365        200 CI2P = BC -BI2P
001367            ACOI2P=ATAN(CI2P/OC)
001374            GO TO 203
001374        201 CI2P = BC +BI2P
001376            ACOI2P=ATAN(CI2P/OC)
001403        203 CONTINUE
001403            EQ=EP/C
001405            THET1=THETA/C
001406            DELTN1=DELTN/C
001410            EPX1=EPXZP/C
001411            EPX1F=EXZPF/C
001413            EXZ1AV=EXZAVG/C
001415            COI3P= ACOI3P/C
001416            OUT2=COI3P
001420            COI2P=ACOI2P/C
001421            EOI1P= AEOI1P/C
001423            AABE1=AABE/C
001425            DELTM=DELTNM/C
001426            EMAX1=EMAX/C
001430            ABOE1=ABOE/C
001431            ABEO1=ABEO/C
001433            DELTN1=DELTNP/C
001435            EEF=1.-(2./(GAM-1.)*((1./TPRA)**((GAM-1.)/GAM)-1.)/XMINF**2)
001451            PINFR=PINFR*PR1
001453            TINFR=TINFR*TR
001454            RINFR=RINFR*RR
001456            PRINT 114
001462        114 FORMAT(// *         FLOW PROPERTIES REFERENCED TO SWEPT WEDGE*)
001462            PRINT 110
001466        110 FORMAT(/4X,3HM1N,7X3HM1T,7X3HM2N,7X3HM2T,8X2HM2,6X6HP/PINF,5X6HR/R
                 1INF,5X6HT/TINF,6X3HGAM)
001466            PRINT 111, XM1N,XM1T,XM2N,XM2T,XM2,PINFR,RINFR,TINFR,GAM
001514        111 FORMAT(1X,9F10.5)
001514            PRINT 112
001520        112 FORMAT(/3X6HDELTAN,5X4HEPSN,6X4HAJOC,5X6HACOI2P,4X6HACOI3P,
                 14X6HAEOI1P,5X5HTHETA,4X10HDELTAN MAX,3X8HEPSN MAX,3X1HN)
001520            PRINT 113, DELTN1,EQ,EPX1,COI2P,COI3P,EOI1P,THET1,DELTM,EMAX1,N
001550        113 FORMAT(1X,9F10.5,I7)
001550            IF(DELTN1.GT.DELTM)PRINT 119
001556            PRINT 109, XM,ALP,E1,DEADR,P1,T1
001576        109 FORMAT(                      /1X,3HM1=,F8.3, 7X6HSWEEP=,F8.3, 7X12HR
                 1IDGE ANGLE=,F8.3,7X6HDE/AD=,F6.3,7X3HP1=,F8.4,7X3HT1=,F8.2)
001576            PRINT 19, XM2, PINFR,RINFR,TINFR,GAM
001614            PRINT 120,TPRA,EEF
001624            PRINT 108, ARCA,EPX1,COI3P
001636        108 FORMAT(/1X,22HCONTRACTION (AINF/A) =,  F8.4,7X4HEPS=,F8.3,7X11HCRO
                 1SS FLOW=,F8.3)
001636            IF(DELTN1.LT.0.)PRINT 508,EPX1,EPX1F,EXZ1AV
001651        508 FORMAT(/2X,14HEXPANSION FAN*,9X,10HLEAD WAVE=,F8.4,5X11HFINAL WAVE
                 1=,F8.4,5X9HAVG WAVE=,F8.4)
001651            PRINT 118
001655        118 FORMAT(// *        FLOW PROPERTIES REFERENCED TO INITIAL XYZ COORDI
                 1NATE SYSTEM*)
001655            WR=ARCA*SIN((90.-AL1-COI3P)*C)/COS(AL1*C)
001671            IF(K.EQ.1)PRINT 117,XM2,E11A(K),EPX1
001705        117 FORMAT(/1X3HM2=,F8.3,3X9HDELTA XZ=,F8.3,10X7HEPS XZ=,F8.3)
001705            IF(K.EQ.1.AND.DELTN1.LT.0.)PRINT 508,EPX1,EPX1F,EXZ1AV
001727            IF(K.EQ.1)PRINT 116,COI3P,WR
001741        116 FORMAT(/1X28HTOTAL CROSS FLOW (DELTA XY)=,F8.3,10X
                 118HGAP RATIO (W1/W2)=,F8.3)
001741            IF(MC.EQ.1)GO TO 5
001743        274 IF(NN)276,606,275
001745        606 IF(TYPE(K+1))601,601,602
001750        276 CONTINUE
001750            XJOC2=EPXZP
001751            ACOI2P=COI2P*C
001753            COI3P1=COI3PT*C
001755            ALP1=(90.-AL1)*C
001757            EXZP = TAN(XJOC2-ACOI2P)*TAN(ALP1)/(COS(COI3P1)*(TAN(ALP1)-TAN(COI
                 13P1)))
002000            EXZP=ATAN(EXZP)/C
002003            XJMUP = EXZPF-ACOI2P
002005            IF(EXZPF.LT.0.)XJMUP=EXZPF
002010            EXZPF=TAN(  XJMUP      )*TAN(ALP1)/(COS(COI3P1)*(TAN(ALP1)-TAN(COI3
                 1P1)))
```

```
002027        EXZPF=ATAN(EXZPF)/C
002032        EXZAVG=EXZP-.5*(EXZP-EXZPF)
002036        OUT2= (ABUE-AEOI1P)/C
002041        OUTT=COI3PT+OUT2
002043        WR = ARCA*SIN((90.-AL1-OUTT)*C)/COS(AL1*C)
002057        PRINT 117, XM2,E11A(K),EXZP
002070        IF(DELTN1.LT.0.)PRINT 508,EXZP,EXZPF,EXZAVG
002103        PRINT 116, OUTT,WR
002113        IF(DELTN.GT.DELTNM)GO TO 5
002117        I=I+1
002120        IF(MC-I)5,5,604
002122    604 IF(TYPE(K+1))601,602,602
002125    275 CONTINUE
002125        OFT=COI3PT*C
002127        XJOC3=EPXZP
002130        CAP1=(90.-AL1)*C
002133        EXZP=TAN(CAP1)*TAN(OFT)*TAN(XJOC3)/(SIN(OFT)*(TAN(CAP1)-TAN(OFT)))
002155        EXZP=ATAN(EXZP)/C
002160        EXZPF=TAN(CAP1)*TAN(OFT)*TAN( EXZPF)/(SIN(OFT)*(TAN(CAP1)-TAN(OFT)
             1))
002202        EXZPF = ATAN(EXZPF)/C
002205        EXZAVG= EXZP - .5*(EXZP-EXZPF)
002211        OUTF=COI3PT+COI3P
002213        WR = ARCA*SIN((90.-AL1-OUTF)*C)/COS(AL1*C)
002230        PRINT 117, XM2,E11A(K),EXZP
002241        IF(DELTN1.LT.0.)PRINT 508,EXZP,EXZPF,EXZAVG
002254        PRINT 116, OUTF,WR
002264        IF(DELTN.GT.DELTNM)GO TO 5
002270        I=I+1
002271        IF(MC-I)5,5,605
002273    605 IF(TYPE(K+1))601,601,602
002275    601 CONTINUE
002275        NN=-1
002276        COI3PT=COI3PT+COI3P
002300        AIOI3P=ATAN(TAN(COI2P*C)*COS(COI3PT*C))/C
002313        ALP=ATAN((TAN((90.-AL1-COI3PT)*C))/COS(AIOI3P*C))
002330        ALP=90.-ALP/C
002333        K=K+1
002335        E11=E11A(K-1)
002336        TE1=(TAN(E11*C)-TAN(E11*C-E11A(K)*C))*TAN(AIOI3P*C)/TAN(E11*C)
002363        E1=ATAN(TE1)/C
002366        XM=XM2
002370        T1=T2
002371        P1=P2
002373        DEADR=ABS(TAN(AIOI3P*C)/TAN(E1*C))
002405        GO TO 7
002405    602 CONTINUE
002405        NN=1
002406        COI3PT=COI3PT+OUT2
002410        ALP=AL1+COI3PT
002411        SIGMA=(90.-AL1)*C
002414        SIGMA1=COI3PT*C
002415        K=K+1
002417        E12 = E11A(K)
002420        E1=ATAN(TAN(E12*C)*(TAN(SIGMA)-TAN(SIGMA1))*SIN(SIGMA1)/(TAN(SIGMA
             1)*TAN(SIGMA1)))
002446        E1=E1/C
002450        XM=XM2
002452        T1=T2
002453        P1=P2
002455        DEADR=0.0
002456        GO TO 7
002456        END
              SUBROUTINE REALG (NSTR)
        C     THIS SUBROUTINE COMPUTES WAVE PROPERTIES FOR A THERMALLY PERFECT GAS
000003        COMMON C,THV,GAMP,RBAR,XMWT,P1,T1,XM,XMNORM,TO
000003        COMMON P2,T2,DELTN,GAM,XM2N,EPD,RHOR
000003        COMMON EMAX,DELTNM,N,KGAS,MC
000003        COMMON EPDF,TPRA,AR,XM1T,XM2T
000003        COMMON NDEBUG
000003        DIMENSION P(4),T(4),PD(4)
000003        FGA(T )=1.+(GAMP-1.)/(1.+(GAMP-1.)*(THETA/T)**2*EXP(THETA/T)/(
             2EXP(THETA/T)-1.)**2)
000035        FW(T2)=A**2-Q*(A**2-4.*R*T2)**.5-2.*R*T2-DD+GG*R*(T2-T1)+4.*R*
             1THETA*(1./(EXP(THETA/T2)-1.)-E1)
000075        EPDF=0.
000076        EPDAVG=0.
000076        GC=32.1741
000100        GG=4.0*GAMP/(GAMP-1.)
```

```
000103        R=GC*PBAR/XMWT
000106        R1=P1*144./(RBAR/XMWT*T1)
000112        THETA=THV
000114        XM1=XMNORM
000115        ARA=1.0
000117        J=1
000120        I=N
000122   117  CONTINUE
000122        DELT=DELTN
000123        IF(DELTN.LT.0.)PRINT 118
000132   118  FORMAT(1X27H***THERMALLY PERFECT GAS***,14X16HAPPROX. SOLUTION)
000132        IF(DELTN.GE.0.)PRINT 6
000141     6  FORMAT(1X27H***THERMALLY PERFECT GAS***)
000141        PRINT 9
000145     9  FORMAT(38X16HIN FRONT OF WAVE)
000145        CALL TOTAL (P1,T1,XM,TO,PT1)
000151        GAM1=FGA(T1)
000154        XM1N=XM1
000156        GAM=GAM1
000157        SOUND =(R*T1*GAM1)**.5
000165        IF(DELTN.LT.0.) GO TO 446
000167        EMAX= SQRT((GAM+1.)*(1.+(GAM-1.)/2.*XM1N**2+(GAM+1.)/16.*XM1N**4))
000204        EMAX=(1./(GAM*XM1N**2))*((GAM+1.)/4.*XM1N**2-1.+EMAX)
000217        EMAX=ASIN(SQRT(EMAX))
000223        DELTNM =(GAM+1.)*XM1N**2/(2.*(XM1N**2* (SIN(EMAX)**2)-1.))
000234        DELTNM=(DELTNM-1.)*TAN(EMAX)
000241        DELTNM=ATAN(1./DELTNM)
000244        V1=XM1*SOUND
000246        PIE=3.141592654
000250        N2=4
000251        IF(I.EQ.2)N2=0
000255        IF(MC.GT.1)N2=4
000261        DEL2=DELTN
000262        IF(DELTNM.LT.DELTN)DEL2=DELTNM
000266        GAN=GAM1
000267        XM12=XM1**2
000271        XM14=XM1**4
000272        BB=-(XM12+2.)/XM12-GAN*SIN(DEL2)**2
000301        CC=(2.*XM12+1)/XM14+((GAN+1.)**2/4.+(GAN-1.)/XM12)*SIN(DEL2)**2
000320        D2=-COS(DEL2)**2/XM14
000324        EX=     (9.*BB*CC/2.-BB**3-27.*D2/2.)/(BB**2-3.*CC)**1.5
000344        IF(EX.GT.1)EX=1.
000352        IF(EX.LT.-1)EX=-1
000357        EE=ACOS(EX)
000361        FF=COS((EE+N2*PIE)/3.)
000370        G2=(-BB/3.+(2*(BB**2-3.*CC)**.5/3.)*FF)**.5
000406        EPS=ASIN(G2)
000410        IF(NSTR.EQ.2.AND.DEL2.LT..01)GO TO 1000
000423        GO TO 1001
000423  1000  EPS=90.*C
000425        GO TO 1004
000426  1001  CONTINUE
000426        RR=TAN(EPS)/TAN(EPS-DEL2)
000435        PR1=1.+GAN* XM1**2*SIN(EPS)**2*(1.-1./RR)
000447  1004  CONTINUE
000447        EP1=EPS/C
000451        M=1
000452        N=1
000453        NN=1
000454        E1=1./(EXP(THETA/T1)-1.)
000462        NT=1
000464   111  CONTINUE
000464        KK=-1
000465        U1=V1*SIN(EPS)
000470        A=U1+R*T1/U1
000474        Q=A
000475        DD=2.0*U1**2
000477        HH=XM1**2*(SIN(EPS))**2
000503        HK=(2.*GAM1*HH-(GAM1-1.))*((GAM1-1.)*HH+2.)/((GAM1+1.)**2*HH)
000516        STR=((-.2/9000.)*T0+1.0)*HK
000523        TMAX=A**2/(4.*R)-.000001
000530        IF(N.EQ.1.AND.NDEBUG.GT.0)PRINT 223
000544   223  FORMAT(/)
000544        IF(NDEBUG.EQ.0)GO TO 120
000545        PRINT 222, TMAX,A,R,U1,T1,V1,EP1,PR1,PR2
000573   222  FORMAT(1X9HSUB REALG,9F12.4)
000573   120  CONTINUE
000573        WMAX=FW(TMAX)
```

```
000576          IF(WMAX)140,10,143
000600     140  Q=-Q
000601          NT=2
000602          T21=TMAX
000603          T22=T21
000605          W1=FW(TMAX)
000610     703  T22=T22-.1*(T21-T1)
000614          W2=FW(T22)
000616          NT=NT+1
000620          IF(NT-12)803,803,802
000622     803  IF(W2)703,19,707
000624     707  T21=T22+.1*(T21-T1)
000630          W1=FW(T21)
000632          T21=-W1/(W2-W1)*(T22-T21)+T21
000640          IF(T21-TMAX)706,706,708
000642     708  T21=TMAX-.00001
000644     706  CONTINUE
000644          W1=FW(T21)
000646          T22=T21-.01*(T21-T1)
000652          W2=FW(T22)
000655          T21=-W1/(W2-W1)*(T22-T21)+T21
000663          IF(T21-TMAX)712,711,711
000665     711  T21=TMAX
000667     712  CONTINUE
000667          W1=FW(T21)
000672          GO TO 802
000672      19  CONTINUE
000672          W1=W2
000673          T21=T22
000675          GO TO 802
000676     143  CONTINUE
000676          T21=STR*T1+40.
000701          IF(T21-TMAX)300,300,301
000704     301  T21=TMAX
000706     300  T22=T21-10.*XM1
000711          W1=FW(T21)
000713          W2=FW(T22)
000716          T21=-W1/(W2-W1)*(T22-T21)+T21
000724          IF(T21-TMAX)11,11,14
000726      14  T21=TMAX
000730      11  T22=T21-2.*XM1
000733          W1=FW(T21)
000735          W2=FW(T22)
000740          T21=-W1/(W2-W1)*(T22-T21)+T21
000746          IF(T21-TMAX)141,141,305
000750     305  T21=TMAX
000752     141  T22=T21-.8*XM1
000755          W1=FW(T21)
000757          W2=FW(T22)
000762          T21=-W1/(W2-W1)*(T22-T21)+T21
000770          IF(T21-TMAX)12,12,142
000772     142  T21=TMAX
000774      12  T22=T21-.1*XM1
000777          W1=FW(T21)
001001          W2=FW(T22)
001004          T21=-W1/(W2-W1)*(T22-T21)+T21
001012          IF(T21-TMAX)15,15,10
001014      10  T21=TMAX
001016   15     CONTINUE
001016          W1=FW(T21)
001021     802  CONTINUE
001021          XNT=NT
001022          XNN=NN
001024          TRR=T21/T1
001026          T2=T21
001027      13  CONTINUE
001027          GAM2=FGA(T2)
001031          XM2=2.0*T1/(GAM2*T2)*((GAM1*XM1**2/2.0)+(GAMP/(GAMP-1.0))*(1.0-
               2T2/T1)+THETA/T1*(1./(EXP(THETA/T1)-1.0)-1./(EXP(THETA/T2)-1.0)))
001067          IF(XM2)28,28,307
001072     307  CONTINUE
001072          XM2=XM2**.5
001076          PR2=1./2.*((1.+GAM2*XM2**2)-T1/T2*(1.+GAM1*XM1**2)+(((((1.+GAM2*
               2XM2**2)-T1/T2*(1.+GAM1*XM1**2))**2)+4.*T1/T2)**.5))
001123          PR2=1./PR2
001125          ROR=(((GAM2/GAM1)*(T2/T1)*(XM2/XM1)**2-1.)/SIN(EPS)**2)+1.
001137          IF(ROR)100,101,102
```

```
001143       101 CONTINUE
001143           ROR=.000001
001145       102 CONTINUE
001145           ROR=ROR**.5
001151       100 CONTINUE
001151           ROR=1./ROR
001153           PR3=ROR*T2/T1
001155           EP1=EPS/C
001157           IF(NSTR.EQ.2.AND.DEL2.LT..01)GO TO 1002
001170           GO TO 1003
001170      1002 PR1=PR2
001172           GO TO 25
001172      1003 CONTINUE
001172           IF(ABS(PR2-PR1)-.001)25,25,27
001177     27    N=N+1
001201           NAP=N
001201           IF(M-2)55,56,56
001204     55    PRY=PR2
001205           PRX=PR1
001207           IF(NN-2)304,303,303
001212       304 PR1=PR1+.5*(PR2-PR1)
001216           NN=2
001217       303 CONTINUE
001217           PR1=PR1+.01*(PR2-PR1)
001223           M=M+1
001225           GO TO 191
001225     56    S=(PRY-PR2)/(PRX-PR1)
001231           PR1=(1./(1.-S))*(-S*PRX+PRY)
001237           M=M-1
001241       306 CONTINUE
001241       191 CONTINUE
001241           COTD=1.0/TAN(DELT)
001244           EPS=ATAN(COTD/(GAM1*XM1**2/(PR1-1.)-1.))
001254           EP1=EPS/C
001256           IF(EP1.LT.1.)GO TO 28
001262           IF(N-20)111,28,28
001265        28 PRINT 112,EP1,T2,JJ,J,JAA,NN,N,XM2
001311     112   FORMAT(//21H PR DID NOT CONVERGE ,3X4HEP1=,F10.4,3X3HT2=,F10.4,3X3
                2HJJ=,I4,3X2HJ=,I4,3X4HJAA=,3I6,F10.4)
001311           N=100
001312           RETURN
001313     25    CONTINUE
001313           P2=PR1*P1
001315           R2=ROR*R1
001317           GO TO 447
001321       446 CONTINUE
           C     C  EXPANSION WAVE CALCULATIONS FOR TPG
001321           XNUDF=-DELTN/C
001323           XNUD=XNUDF
001324           XMI=XM1
001326           T02=T0
001327           AW=SQRT((GAM+1.)/(GAM-1.))
001336           AAW=SQRT((GAM-1.)/(GAM+1.)*(XMI**2-1.))
001350           XMU=90.-ACOS(1./XMI)/C
001357           XNUS=AW*ATAN(AAW)/C-(90.-XMU)
001366           XNUB=XNUS+XNUDF
001367           BW=1./AW
001371           CW=(GAM-1.)/2.
001374           DW=(GAM+1.)/(2.*(GAM-1.))
001377           EW=-GAM/(GAM-1.)
001402           XMW=XMI
001403           XNUX=XNUS*C
001405           NW=0
001406       444 DO 445 JW=1,30
001411           XNU=AW*ATAN(BW*SQRT(XMW*XMW-1.))-ATAN(SQRT(XMW*XMW-1.))
001432           DIFF=XNUX-XNU
001433           IF(ABS(DIFF)-.00001)22,22,33
001440        33 DM=(XMW/SQRT(XMW*XMW-1.))*(1.+CW*XMW*XMW)*DIFF
001452           XMW=XMW+DM
001453       445 CONTINUE
001456           PRINT80
001462        80 FORMAT(30H MAX NO OF ITERATIONS EXCEEDED)
001462        22 XMU=ATAN(1./SQRT(XMW*XMW-1.))/C
001472           PR=(1.+CW*XMW*XMW)**EW
001501           IF(NW)64,64,66
001504        64 CONTINUE
001504           XMU1=XMU
001505           PRT1=PR
```

```
001507         XNUD=XNUDF
001510         NW=NW+1
001512         XNUX=(XNUS+FLOAT(NW)*XNUD)*C
001516         IF(XNUX-XNUB*C)444,444,66
001522      66 CONTINUE
001522         XM2N=XMW
001523         XM2=XM2N
001525         TR=(1.+(GAM-1.)/2.*XM1N**2)/(1.+(GAM-1.)/2.*XM2N**2)
001537         T2=T1*TR
001541         GAM2=FGA(T2)
001543         PR1=PR/PRT1
001545         P2=P1*PR1
001547         R2=P2*144./(RBAR/XMWT*T2)
001553         RHOR=R2/R1
001555         EPD=XMU1
001556         EP1=EPD
001557         EPDF=XMU
001561         EPDAVG=EPD-.5*(EPD-EPDF)
001564         B=1.0
001566         N=JW
001567         AR=RHOR*(XM2N/XMNORM)*TR**.5
001576         RNFR=RHOR*XM2N/(XMNORM*TR**.26)
001604         GAMM1=GAM-1.
001606         TPR=((GAM+1.)*B/(GAMM1*B+2.))**(GAM/GAMM1)*((GAM+1.)/(2.*GAM*
              1B-(GAMM1)))**(1./GAMM1)
001630         TPRA=TPRA*TPR
001632         DELTN1=DELTN/C
         C     THIS PACKAGE OVER RIDES PERFECT GAS PRESSURE RATIO AND USES TPG EQ
001634         GAX = GAMP/(GAMP-1.)
001636         ETT=EXP(THETA/T2)
001642         ETTM1=ETT-1.
001644         ETTT=EXP(THETA/T02)
001650         ETTTM1=ETTT-1.
001652         ETR=ETTTM1/ETTM1
001654         TTTR=T2/T02
001656         THTR=THETA/T2
001660         THTTR=THETA/T02
001661         EX1=ETT/ETTM1
001663         EX2=ETTT/ETTTM1
001665         PTPR=ETR*TTTR**GAX*EXP(THTR*EX1-THTTR*EX2)
001700         P2=PT1*PTPR
001702         R2=P2*144./(RBAR/XMWT*T2)
001706         RHOR=R2/R1
001710     447 CONTINUE
001710         TR=T2/T1
001712         XM2T=XM1T*((GAM1*T1)/(GAM2*T2))**.5
001717         XM2F=(XM2T**2+XM2**2)**.5
001725         PRINT 7
001731       7 FORMAT(/38X11HBEHIND WAVE)
001731         CALL TOTAL(P2,T2,XM2F,T02,PT2)
001735         PTR=PT2/PT1
001737         TPRA=TPRA*PTR
001740         DELTD=DELT/C
001742         SND2=(R*T2*GAM2)**.5
001747         AR=R2*XM2*SND2/(R1*XM1*SCUND)
001754         ARA=ARA*AR
001755         PRINT 8
001761       8 FORMAT(// *        FLOW PROPERTIES MEASURED NORMAL TO WEDGE LEADING
              1 EDGE     *)
001761         PRINT113,XM1,DELTD,P1,R1,T1,PT1,GAM1
002003     113 FORMAT(/2X4HM1N=,F6.3,4X7HDELTAN=,F7.3,5X3HP1=,F8.4,6X3HR1=,F8.4,
              26X3HT1=,F8.2,6X4HPT1=,F10.4,6X5HGAM1=,F6.4)
002003         PRINT114,XM2,EP1,P2,R2,T2,PT2,GAM2
002025     114 FORMAT(2X4HM2N=,F6.3,7X4HEPN=,F7.3,5X3HP2=,F8.4,6X3HR2=,F8.4,
              26X3HT2=,F8.2,6X4HPT2=,F10.4,6X5HGAM2=,F6.4)
002025         RHOR=R2/R1
002027         RNFR=RHOR*XM2/(XM1*(T2/T1)**0.26)
002036         PRINT 115,RNFR,AR,PR1,RHOR,TR,PTR,NAP
002060     115 FORMAT(1X,5HREYR=,F6.3,5X6HA1/A2=,F7.3,2X6HP2/P1=,F8.4,3X6HR2/R1=,
              1F8.4,3X6HT2/T1=,F8.4,6X4HTPR=,F10.4,9X2HN=,I6)
002060         IF(DELTD .LT.0.)PRINT 116, EPD,EPDF,EPDAVG
002075     116 FORMAT(/2X,14HEXPANSION FAN*,9X,10HLEAD WAVE=,F8.4,5X11HFINAL WAVE
              1=,F8.4,5X9HAVG WAVE=,F8.4)
002075         J=J+1
002077         XM2N=XM2
002100         EPD=EP1
002102         RETURN
002103     109 STOP
002105         END
```

```
                 SUBROUTINE PGAS
          C    THIS SUBROUTINE COMPUTES WAVE PROPERTIES FOR A PERFECT GAS
          C     INPUT= XM1,  DELT,  N          OUTPUT= EP
          C     NN= 0 FOR  STRONG  SHOCK
          C     NN= 4 FOR  WEAK  SHOCK
000002           COMMON C,THV,GAMP,RBAR,XMWT,P1,T1,XM,XMNORM,TO
000002           COMMON P2,T2,DELTN,GAM,XM2N,EPD,RHOR
000002           COMMON EMAX,DELTNM,N,KGAS,MC
000002           COMMON EPDF,TPRA,AR,XM1T,XM2T
000002           COMMON NDEBUG
000002           RBAR=1545.31
000003           XMWT=28.9644
000005           XM1N=XMNORM
000006           EPDF=0.
000007           EPDAVG=0.
000010           GR=(GAM+1.)/(GAM-1.)
000015           NN=4
000016           IF(MC.GT.1)N=0
000022           IF(N.EQ.2)NN=0
000025           IF(N.EQ.0)NN=4
000027           IF(DELTNM.LT.DELTN)DELTN=DELTNM
000032           XM1=XM1N
000033           DELT=DELTN
000035           PRINT 6
000040         6 FORMAT(1X17H***PERFECT GAS***)
000040           PRINT 9
000044         9 FORMAT(38X16HIN FRONT OF WAVE)
000044           CALL TOPG(P1,T1,XM,TO,PT1)
000050           IF(DELTN.LT.0.)GO TO 500
000052           PIE=3.141592654
000053           XM12=XM1**2
000054           XM14=XM1**4
000055           BB=-(XM12+2.)/XM12-GAM*SIN(DELT)**2
000064           CC=(2.*XM12+1.)/XM14+((GAM+1.)**2/4.+(GAM-1.)/XM12)*SIN(DELT)**2
000102           DD=-COS(DELT)**2/XM14
000106           EX=      (9.*BB*CC/2.-BB**3-27.*DD/2.)/(BB**2-3.*CC)**1.5
000126           IF(EX.GT.1)EX=1.
000133           IF(EX.LT.-1)EX=-1
000140           EE=ACOS(EX)
000142           FF=COS((EE+NN*PIE)/3.)
000151           GG=(-BB/3.+(2*(BB**2-3.*CC)**.5/3.)*FF)**.5
000167           EP=ASIN(GG)
000171           EPD=EP/C
000173           IF(EPD.GE.89.999)GO TO 25
000176           RR=TAN(EP)/TAN(EP-DELTN)
000206        25 CONTINUE
000206           IF(EPD.GT.89.999)RR= (GAM+1.)*XM1**2/(((GAM-1.)*XM1**2)+2.)
000220           PR1=1.+GAM*XM1N**2*SIN(EP)**2*(1.-1./RR)
000231           N=NN
000232           B=XM1N**2*SIN(EP)**2
000236           BB=((GAM-1.)*B+2.)/(2.*GAM*B-(GAM-1.))
000244           XM2N = (BB/(SIN(EP-DELTN))**2)**.5
000255           TR=((2.0*GAM*B-(GAM-1.))*((GAM-1.)*B+2.))/((GAM+1.)**2*B)
000270           T2=TR*T1
000272           P2=PR1*P1
000274           PR=P2/P1
000275           RHOR=RR
000276           EPD=EP/C
000300           GO TO 502
000301       500 CONTINUE
          C      EXPANSION WAVE CALCULATION
000301           XMI=XM1N
000302           XNUDF=-DELTN/C
000304           XNUD=XNUDF
000306           AW=SQRT((GAM+1.)/(GAM-1.))
000314           AAW=SQRT((GAM-1.)/(GAM+1.)*(XMI**2-1.))
000326           XMU=90.-ACOS(1./XMI)/C
000335           XNUS=AW*ATAN(AAW)/C-(90.-XMU)
000344           XNUB=XNUS+XNUDF
000345           BW=1./AW
000347           CW=(GAM-1.)/2.
000352           DW=(GAM+1.)/(2.*(GAM-1.))
000355           EW=-GAM/(GAM-1.)
000360           XMW=XMI
000361           XNUX=XNUS*C
000363           NW=0
000364       444 DO10JW=1,30
```

```
000365          XNU=AW*ATAN(BW*SQRT(XMW*XMW-1.))-ATAN(SQRT(XMW*XMW-1.))
000407          DIFF=XNUX-XNU
000410          IF(ABS(DIFF)-.00001)22,22,33
000414       33 DM=(XMW/SQRT(XMW*XMW-1.))*(1.+CW*XMW*XMW)*DIFF
000426          XMW=XMW+DM
000427       10 CONTINUE
000432          PRINT80
000435       80 FORMAT(30H MAX NO OF ITERATIONS EXCEEDED)
000435       22 XMU=ATAN(1./SQRT(XMW*XMW-1.))/C
000445          PR=(1.+CW*XMW*XMW)**EW
000454          IF(NW)55,55,66
000456       55 CONTINUE
000456          XMU1=XMU
000457          PRT1=PR
000461          XNUD=XNUDF
000462          NW=NW+1
000464          XNUX=(XNUS+FLOAT(NW)*XNUD)*C
000470          IF(XNUX-XNUB*C)444,444,66
000474       66 CONTINUE
000474          XM2N=XMW
000475          PR1=PR/PRT1
000477          TR=(1.+(GAM-1.)/2.*XM1N**2)/(1.+(GAM-1.)/2.*XM2N**2)
000512          T2=T1*TR
000514          P2=P1*PR1
000516          RHOR=PR1/TR
000517          EPD=XMU1
000521          EPDF=XMU
000522          EPDAVG=EPD-.5*(EPD-EPDF)
000526          B=1.0
000530          N=JW
000532      502 CONTINUE
000532          AR=RHOR*(XM2N/XMNORM)*TR**.5
000541          RNFR=RHOR*XM2N/(XMNORM*TR**.26)
000547          GAMM1=GAM-1.
000551          TPR=((GAM+1.)*B/(GAMM1*B+2.))**(GAM/GAMM1)*((GAM+1.)/(2.*GAM*
               1B-(GAMM1)))**(1./GAMM1)
000573          XM2T=XM1T*(T1/T2)**.5
000600          XM2F=(XM2T**2+XM2N**2)**.5
000606          PRINT 7
000612        7 FORMAT(/38X11HBEHIND WAVE)
000612          CALL TOPG(P2,T2,XM2F,TO2,PT2)
000615          TPRA=TPRA*TPR
000620          DELTN1=DELTN/C
000621          ACR=0.
000622          GAM1=GAM
000624          GAM2=GAM
000624          R1=P1*144./(RBAR*T1/XMWT)
000630          R2=P2*144./(RBAR*T2/XMWT)
000634          RHOR=R2/R1
000636          PRINT 8
000642        8 FORMAT(// *         FLOW PROPERTIES MEASURED NORMAL TO WEDGE LEADING
               1 EDGE     *)
000642          PRINT 3,XMNORM,DELTN1,P1,R1,T1,PT1,GAM1
000664        3 FORMAT(/2X4HM1N=,F6.3,4X7HDELTAN=,F7.3,5X3HP1=,F8.4,6X3HR1=,F8.4,
               26X3HT1=,F8.2,6X4HPT1=,F10.4,6X5HGAM1=,F6.4)
000664          PRINT 4, XM2N,EPD,P2,R2,T2,PT2,GAM2
000706        4 FORMAT(2X4HM2N=,F6.3,7X4HEPN=,F7.3,5X3HP2=,F8.4,6X3HR2=,F8.4,
               26X3HT2=,F8.2,6X4HPT2=,F10.4,6X5HGAM2=,F6.4)
000706          PRINT     2,RNFR,AR,PR1,RHOR,TR,TPR,N
000730        2 FORMAT(1X,5HREYR=,F6.3,5X6HA1/A2=,F7.3,2X6HP2/P1=,F8.4,3X6HR2/R1=,
               1F8.4,3X6HT2/T1=,F8.4,6X4HTPR=,F10.4,9X2HN=,I6)
000730          IF(DELTN1.LT.0.)PRINT 5, EPD,EPDF,EPDAVG
000743        5 FORMAT(/2X,14HEXPANSION FAN*,9X,10HLEAD WAVE=,F8.4,5X11HFINAL WAVE
               1=,F8.4,5X9HAVG WAVE=,F8.4)
000743          RETURN
000744          END

                SUBROUTINE TOTAL(P,T,YM,TTOT,PO)
          C  THIS SUBROUTINE COMPUTES TOTAL PROPERTIES FOR A THERMALLY PERFECT GAS
000010          COMMON C,THV,GAMP,RBAR,XMWT,P1,T1,XM,XMNORM,TO
000010          COMMON P2,T2,DELTN,GAM,XM2N,EPD,RHOR
000010          COMMON EMAX,DELTNM,N,KGAS,MC
000010          COMMON EPDF,TPRA,AR,XM1T,XM2T
000010          COMMON NDEBUG
000010          FGA(T )=1.+(GAMP-1.)/(1.+(GAMP-1.)*(THETA/T)**2*EXP(THETA/T)/(
               2EXP(THETA/T)-1.)**2)
000044          FXM(TO) = SQRT((A*TO-7./GAM)+B*(1./(EXP(THV/TO)-1.)-E))
```

```
000072           THETA=THV                                                               90000000
000074           PRINT2                                                                  90100000
000077         2 FORMAT( 49X,*TOTAL PROPERTIES*)                                         90200000
000077           PRINT3                                                                  90300000
000103         3 FORMAT(8X1HM,9X6HMCHECK,7X2HTO,9X4HT/TO,8X2HPO,10X4HP/PO,9X1HR,         90400000
                11OX4HR/RO,8X3HGAM,6X1HN)                                                90500000
000103           N=1                                                                     90600000
000104           GAM=FGA(T)                                                              90700000
000111           RHO=P*144./(RBAR*T/XMWT)                                                90800000
000115           A= 7./(GAM*T)                                                           90900000
000120           B= 2.*THV/(GAM*T)                                                       91000000
000122           ET= EXP(THV/T)                                                          91100000
000130           E=1./(ET-1.)                                                            91200000
000133           T01 = T*(1.+(GAM-1.)*YM**2/2.)                                          91300000
000140           T02=T01-50.                                                             91400000
000142         8 XM1=FXM(T01)                                                            91500000
000144           XM2= FXM(T02)                                                           91600000
000147           TO=(YM-XM1)/(XM2-XM1)*(T02-T01)+T01                                     91700000
000156           XM3=FXM(TO)                                                             91800000
000161           IF(ABS(YM-XM3)-.0001)10,10,5                                            91900000
000166         5 T01=TO                                                                  92000000
000167           T02=TO-10.                                                              92100000
000171           N=N+1                                                                   92200000
000173           IF(N-25)9,9,10                                                          92300000
000175         9 GO TO 8                                                                 92400000
000176        10 CONTINUE                                                                92500000
000176           ETO=EXP(THV/TO)                                                         92600000
000202           ETO1=ETO-1.                                                             92700000
000204           ET1=ET-1.                                                               92800000
000206           APR=EXP((THV*ET/(T*ET1))-(THV*ETO/(TO*ETO1)))                           92900000
000225           PR= ETO1*(T/TO)**(GAMP/(GAMP-1.))*APR/ET1                               93000000
000236           RHOR =  ETO1*(T/TO)**(1./(GAMP-1.))*APR/ET1                             93100000
000247           TR=T/TO                                                                 93200000
000251           PO=P/PR                                                                 93300000
000253           TTOT=TO                                                                 93400000
000253           PRINT1,YM,XM3,TO,TR,PO,PR,RHO,RHOR,GAM,N                                93500000
000303         1 FORMAT(1X,2F12.5,F12.3,F10.5,F13.3,F13.9,F12.6,F13.9,F9.5,I5)           93600000
000303           RETURN                                                                  93700000
000304           END                                                                     93800000
                 SUBROUTINE TOPG(P,T,YM,TTOT,PO)                                         93900000
             C   THIS SUBROUTINE COMPUTES TOTAL PROPERTIES FOR A PERFECT GAS             94000000
000010           COMMON C,THV,GAMP,RBAR,XMWT,P1,T1,XM,XMNORM,TO                          94100000
000010           COMMON P2,T2,DELTN,GAM,XM2N,EPD,RHOR                                    94200000
000010           COMMON EMAX,DELTNM,N,KGAS,MC                                            94300000
000010           COMMON EPDF,TPRA,AR,XM1T,XM2T                                           94400000
000010           COMMON NDEBUG                                                           94500000
000010           PRINT2                                                                  94600000
000013         2 FORMAT( 49X,*TOTAL PROPERTIES*)                                         94700000
000013           PRINT3                                                                  94800000
000017         3 FORMAT(8X1HM,9X6HMCHECK,7X2HTO,9X4HT/TO,8X2HPO,10X4HP/PO,9X1HR,         94900000
                110X4HR/RO,8X3HGAM,6X1HN)                                                95000000
000017           RBAR=1545.31                                                            95100000
000020           XMWT=28.9644                                                            95200000
000022           RHO=P*144./(RBAR*T/XMWT)                                                95300000
000030           A = (GAM-1.)/2.*YM**2                                                   95400000
000034           TR = 1./(1.+A)                                                          95500000
000036           PR = (1./(1.+A))**(GAM/(GAM-1.))                                        95600000
000045           RHOR = (1./(1.+A))**(1./(GAM-1.))                                       95700000
000055           TO=T/TR                                                                 95800000
000057           PO=P/PR                                                                 95900000
000060           TTOT=TO                                                                 96000000
000061           XM3=YM                                                                  96100000
000062           PRINT1,YM,XM3,TO,TR,PO,PR,RHO,RHOR,GAM                                  96200000
000110         1 FORMAT(1X,2F12.5,F12.3,F10.5,F13.3,F13.9,F12.6,F13.9,F9.5,I5)           96300000
000110           RETURN                                                                  96400000
000111           END                                                                     96500000
```

```
****     SAMPLE CASES     ****

CASE NO. 1 -- FOR AN INITIAL SWEEP ANGLE OF 48 DEGREES, THIS CASE COMPUTES
              FLOW PROPERTIES ACROSS 3 SUCCESSIVE SHOCK WAVES.  THE WAVES
              ALTERNATE TYPE A, TYPE B, AND TYPE A, WITH THE FLOW TURNING
              ACROSS EACH SHOCK WAVE EQUAL TO 6 DEGREES WHEN MEASURED IN
              THE XZ PLANE.

          INPUT FOR CASE NO. 1
  3.        6.0       48.       6.0       0.    1.4                    02200
  6.   6.   6.
  1.  -1.   1.

CASE NO. 2 -- THIS IS ALSO A PERFECT GAS CASE, WITH AN INITIAL SWEEP ANGLE
              OF 48 DEGREES.  THE FIRST WAVE IS A SHOCK FOLLOWED BY AN
              EXPANSION FAN.  BOTH WAVES ARE TYPE A, AND THE FLOW TURNING
              ACROSS EACH WAVE IS EQUAL TO 6 DEGREES WHEN MEASURED IN THE
              XZ PLANE.

          INPUT FOR CASE NO. 2
  2.        6.0       48.       6.0       0.    1.4                    02200
  6.  -6.
  1.   1.

CASE NO. 3 -- THIS CASE IS A REPEAT OF CASE NO. 1, BUT FOR A THERMALLY
              PERFECT GAS AND AT A FLIGHT DYNAMIC PRESSURE OF 1000 PSF.

          INPUT FOR CASE NO. 3
  3.        6.0       48.       6.0       0.        .2775     402.     22200
  6.   6.   6.
  1.  -1.   1.
```

CASE NO 1 WAVE NO 1 (WEAK SHOCK)

K1	K2	K3	K4	K5
0	2	2	0	0

PERFECT GAS

IN FRONT OF WAVE

TOTAL PROPERTIES

M	MCHECK	TO	T/TO	PO	P/PO	R	R/RO	GAM	N
6.00000	6.00000	4100.000	.12195	1578.878	.000633361	.005398	.005193563	1.40000	

BEHIND WAVE

TOTAL PROPERTIES

M	MCHECK	TO	T/TO	PO	P/PO	R	R/RO	GAM	N
5.17681	5.17681	4100.000	.15724	1490.317	.001541448	.009618	.009803422	1.40000	

FLOW PROPERTIES MEASURED NORMAL TO WEDGE LEADING EDGE

M1N= 4.015	DELTAN= 8.927	P1= 1.0000	R1= .0054	T1= 500.00	PT1= 1578.8777	GAM1=1.4000
M2N= 3.373	EPN= 21.221	P2= 2.2972	R2= .0096	T2= 644.67	PT2= 1490.3174	GAM2=1.4000
REYR= 1.401	A1/A2= 1.700	P2/P1= 2.2972	R2/R1= 1.7817	T2/T1= 1.2893	TPR= .9439	N= 4

FLOW PROPERTIES REFERENCED TO SWEPT WEDGE

M1N	M1T	M2N	M2T	M2	P/PINF	R/RINF	T/TINF	GAM
4.01478	4.45887	3.37334	3.92683	5.17681	2.29725	1.78173	1.28933	1.40000

DELTAN	EPSN	AJOC	ACOI2P	ACOI3P	AEOI1P	THETA	DELTAN MAX	EPSN MAX	N
8.92684	21.22146	14.56494	5.80584	1.68065	40.66416	42.00000	38.82060	66.06870	4

M1= 6.000 SWEEP= 48.000 RIDGE ANGLE= 6.000 DE/AD= 0.000 P1= 1.0000 T1= 500.00

M2= 5.177 P/PINF= 2.2972 R/RINF= 1.7817 T/TINF= 1.2893 GAM= 1.4000

RECOVERY (PT/PTINF) = .9439 KINETIC ENERGY EFF.= .99769

CONTRACTION (AINF/A) = 1.7456 EPS= 14.565 CROSS FLOW= 1.681

FLOW PROPERTIES REFERENCED TO INITIAL XYZ COORDINATE SYSTEM

M2= 5.177 DELTA XZ= 6.000 EPS XZ= 14.565

TOTAL CROSS FLOW (DELTA XY)= 1.681 GAP RATIO (W1/W2)= 1.688

CASE NO 1 WAVE NO 2

K1	K2	K3	K4	K5
0	2	2	0	0

(WEAK SHOCK)

PERFECT GAS

IN FRONT OF WAVE

TOTAL PROPERTIES

M	MCHECK	TO	T/TO	PO	P/PO	R	R/RO	GAM	N
5.17681	5.17681	4100.000	.15724	1490.317	.001541448	.009618	.009803422	1.40000	

BEHIND WAVE

TOTAL PROPERTIES

M	MCHECK	TO	T/TO	PO	P/PO	R	R/RO	GAM	N
4.54388	4.54388	4100.000	.19496	1436.267	.003271737	.015867	.016781921	1.40000	

FLOW PROPERTIES MEASURED NORMAL TO WEDGE LEADING EDGE

M1N= 3.373	DELTAN= 8.927	P1= 2.2972	R1= .0096	T1= 644.67	PT1= 1490.3174	GAM1=1.4000	
M2N= 2.865	EPN= 24.092	P2= 4.6991	R2= .0159	T2= 799.32	PT2= 1436.2673	GAM2=1.4000	
REYR= 1.325	A1/A2= 1.560	P2/P1= 2.0455	R2/R1= 1.6498	T2/T1= 1.2399	TPR= .9637	N= 4	

FLOW PROPERTIES REFERENCED TO SWEPT WEDGE

M1N	M1T	M2N	M2T	M2	P/PINF	R/RINF	T/TINF	GAM	
3.37334	3.92683	2.85536	3.52655	4.54388	4.69909	2.93943	1.59864	1.40000	

DELTAN	EPSN	AJOC	ACOI2P	ACOI3P	AEOI1P	THETA	DELTAN MAX	EPSN MAX	N
9.92684	24.09216	15.75064	5.80336	1.23139	39.09427	40.66416	36.26086	65.58180	4

M1= 5.177 SWEEP= 49.535 RIDGE ANGLE= 5.803 DE/AD= 1.000 P1= 2.2972 T1= 644.67

M2= 4.544 P/PINF= 4.6991 R/RINF= 2.9394 T/TINF= 1.5986 GAM= 1.4000

RECOVERY (PT/PTINF) = .9997 KINETIC ENERGY EFF.= .99619

CONTRACTION (AINF/A) = 2.8146 EPS= 15.751 CROSS FLOW= 1.231

FLOW PROPERTIES REFERENCED TO INITIAL XYZ COORDINATE SYSTEM

M2= 4.544 DELTA XZ= 6.000 EPS XZ= 10.280

TOTAL CROSS FLOW (DELTA XY)= 2.906 GAP RATIO (W1/W2)= 2.653

```
CASE NO  1          WAVE NO  3                                          K1  K2  K3  K4  K5
                                          (WEAK SHOCK)                   0   2   2   0   0
***PERFECT GAS***
                                   IN FRONT OF WAVE
                                            TOTAL PROPERTIES
        M          MCHECK       TO         T/TO         PO          P/PO            R           R/RO          GAM        N
     4.54388      4.54388    4100.000     .19496     1436.267    .003271737      .015867     .016781921    1.40000

                                   BEHIND WAVE
                                            TOTAL PROPERTIES
        M          MCHECK       TO         T/TO         PO          P/PO            R           R/RO          GAM        N
     4.03831      4.03831    4100.000     .23465     1401.402    .006258880      .024607     .026672824    1.40000

        FLOW PROPERTIES MEASURED NORMAL TO WEDGE LEADING EDGE

  M1N= 2.865    DELTAN=  8.927     P1=  4.6991      R1=    .0159      T1=  799.32      PT1= 1436.2673       GAM1=1.4000
  M2N= 2.444       EPN= 27.434     P2=  8.7712      R2=    .0246      T2=  962.08      PT2= 1401.4016       GAM2=1.4000
 REYR= 1.261     A1/A2=  1.451  P2/P1=  1.8666   R2/R1=  1.5508    T2/T1=  1.2036      TPR=      .9757          N=     4

        FLOW PROPERTIES REFERENCED TO SWEPT WEDGE

    M1N      M1T      M2N       M2T       M2      P/PINF    R/RINF    T/TINF     GAM
  2.86536  3.52655  2.44447   3.21443  4.03831   8.77120   4.55846   1.92416   1.40000

   DELTAN    EPSN      AJOC     ACOI2P    ACOI3P    AEOI1P    THETA    DELTAN MAX  EPSN MAX   N
  8.92684  27.43391  18.12559  5.39357   2.17835  37.25179  39.09427  33.10175   65.11211   4

M1=   4.544        SWEEP=  50.906         RIDGE ANGLE=   5.657         DE/AD= 0.000         P1=  4.6991         T1=  799.32

M2=   4.038       P/PINF=  8.7712       R/RINF=  4.5585          T/TINF=  1.9242       GAM= 1.4000

RECOVERY (PT/PTINF)  =   .8876        KINETIC ENERGY EFF.=    .99519

CONTRACTION (AINF/A)  =  4.2559        EPS=  18.126        CROSS FLOW=   2.178

        FLOW PROPERTIES REFERENCED TO INITIAL XYZ COORDINATE SYSTEM

M2=   4.038        DELTA XZ=   6.000          EPS XZ=  19.155

TOTAL CROSS FLOW (DELTA XY)=   5.084          GAP RATIO (W1/W2)=   3.820
```

```
CASE NO  2          WAVE NO  1                                            K1  K2  K3  K4  K5
                                          (WEAK SHOCK)                     0   2   2   0   0
***PERFECT GAS***
                                IN FRONT OF WAVE
                                          TOTAL PROPERTIES
       M           MCHECK        TO         T/TO        PO          P/PO          R          R/RO         GAM      N
    6.00000       6.00000     4100.000     .12195    1578.878   .000633361     .005398   .005193563   1.40000

                                BEHIND WAVE
                                          TOTAL PROPERTIES
       M           MCHECK        TO         T/TO        PO          P/PO          R          R/RO         GAM      N
    5.17681       5.17681     4100.000     .15724    1490.317   .001541448     .009618   .009803422   1.40000

     FLOW PROPERTIES MEASURED NORMAL TO WEDGE LEADING EDGE

  M1N= 4.015      DELTAN=  8.927     P1=  1.0000     R1=   .0054     T1=  500.00     PT1= 1578.8777       GAM1=1.4000
  M2N= 3.373         EPN= 21.221     P2=  2.2972     R2=   .0096     T2=  644.67     PT2= 1490.3174       GAM2=1.4000
 KEYR= 1.401       A1/A2=  1.700  P2/P1=  2.2972  R2/R1= 1.7817   T2/T1= 1.2893     TPR=       .9439        N=     4

     FLOW PROPERTIES REFERENCED TO SWEPT WEDGE

    M1N       M1T       M2N       M2T       M2       P/PINF     R/RINF     T/TINF      GAM
    4.01478   4.45887   3.37334   3.92683   5.17681  2.29725    1.78173    1.28933    1.40000

   DELTAN     EPSN      AJOC      ACOI2P    ACOI3P    AEOI1P     THETA     DELTAN MAX  EPSN MAX    N
    8.92684  21.22146  14.56494   5.80584   1.68065  40.66416   42.00000   38.82060   66.06870    4

 M1=    6.000        SWEEP=  46.000        RIDGE ANGLE=   6.000        DE/AD= 0.000        P1=  1.0000        T1=  500.00

 M2=    5.177       P/PINF=  2.2972      R/RINF=  1.7817        T/TINF=  1.2893      GAM= 1.4000

 RECOVERY (PT/PTINF)  =   .9439      KINETIC ENERGY EFF.=    .99769

 CONTRACTION (AINF/A)  =  1.7456      EPS=  14.565       CROSS FLOW=   1.681

     FLOW PROPERTIES REFERENCED TO INITIAL XYZ COORDINATE SYSTEM

 M2=    5.177         DELTA XZ=    6.000          EPS XZ=   14.565

 TOTAL CROSS FLOW (DELTA XY)=   1.681             GAP RATIO (W1/W2)=    1.688
```

```
CASE NO  2          WAVE NO  2                                          K1  K2  K3  K4  K5
                                        (EXPANSION)                      0   2   2   0   0
***PERFECT GAS***
                              IN FRCNT OF WAVE
                                           TOTAL PROPERTIES
     M          MCHECK        TO         T/TO        PO          P/PO            R            R/RO        GAM       N
   5.17681     5.17681     4100.000     .15724     1490.317   .001541448      .009618     .009803422   1.40000

                              BEHIND WAVE
                                           TOTAL PROPERTIES
     M          MCHECK        TO         T/TO        PO          P/PO            R            R/RO        GAM       N
   5.93700     5.93700     4100.000     .12423     1490.317   .000675761      .005337     .005439594   1.40000

     FLOW PROPERTIES MEASURED NORMAL TO WEDGE LEADING EDGE

 M1N= 3.350    DELTAN= -8.927     P1=  2.2972     R1=   .0096     T1=  644.67     PT1= 1490.3174      GAM1=1.4000
 M2N= 3.941       EPN= 17.370     P2=  1.0071     R2=   .0053     T2=  5J9.34     PT2= 1490.3174      GAM2=1.4000
REYR=  .694     A1/A2=   .580  P2/P1=   .4384  R2/R1=   .5549  T2/T1=   .7901     TPR=     1.0000        N=     4

  EXPANSION FAN*         LEAD WAVE= 17.3699      FINAL WAVE= 14.7001      AVG WAVE= 16.0350

     FLOW PROPERTIES REFERENCED TO SWEPT WEDGE

    M1N        M1T        M2N        M2T        M2       P/PINF      R/RINF     T/TINF      GAM
  3.34964    3.94706    3.94075    4.44054    5.93700    1.00710     .98862    1.01869    1.40000

   DELTAN      EPSN       AJOC       ACOI2P     ACOI3P     AEOI1P      THETA    DELTAN MAX   EPSN MAX    N
  -8.92684   17.35989   11.44203   -5.91259    -.92163   41.58737   40.31935   36.14072   65.56125     4

M1=   5.177       SWEEP=  49.681       RIDGE ANGLE=  -5.803       DE/AD= 0.000       P1=  2.2972       T1=  644.67

M2=   5.937       P/PINF=  1.0071      R/RINF=    .9886        T/TINF=  1.0187     GAM= 1.4000

RECOVERY (PT/PTINF)  =   .9439       KINETIC ENERGY EFF.=    .99769

CONTRACTION (AINF/A) =   .9973       EPS=  11.442       CROSS FLOW=   -.922

  EXPANSION FAN*         LEAD WAVE= 11.4420      FINAL WAVE=  3.7429      AVG WAVE=  7.5925

     FLOW PROPERTIES REFERENCED TO INITIAL XYZ COORDINATE SYSTEM

M2=   5.937       DELTA XZ=  -6.000           EPS XZ=  11.822

  EXPANSION FAN*         LEAD WAVE= 11.8217      FINAL WAVE=  3.8703      AVG WAVE=  7.8460

TOTAL CROSS FLOW (DELTA XY)=     .759        GAP RATIO (W1/W2)=     .973
```

CASE NO 3 WAVE NO 1 (WEAK SHOCK)

K1	K2	K3	K4	K5
2	2	2	0	0

THERMALLY PERFECT GAS

IN FRONT OF WAVE

TOTAL PROPERTIES

M	MCHECK	TO	T/TO	PO	P/PO	R	R/RO	GAM	N
6.00000	5.99999	2999.707	.13401	528.661	.000524911	.001863	.003916865	1.39997	2

BEHIND WAVE

TOTAL PROPERTIES

M	MCHECK	TO	T/TO	PO	P/PO	R	R/RO	GAM	N
5.17765	5.17764	2999.706	.17273	498.361	.001277606	.003320	.007394459	1.39958	2

FLOW PROPERTIES MEASURED NORMAL TO WEDGE LEADING EDGE

M1N= 4.015	DELTAN= 8.927	P1= .2775	R1= .0019	T1= 402.00	PT1= 528.6610	GAM1=1.4000
M2N= 3.374	EPN= 21.221	P2= .6375	R2= .0033	T2= 518.29	PT2= 498.9614	GAM2=1.3996
REYR= 1.402	A1/A2= 1.700	P2/P1= 2.2972	R2/R1= 1.7819	T2/T1= 1.2893	TPR= .9438	N= R

FLOW PROPERTIES REFERENCED TO SWEPT WEDGE

M1N	M1T	M2N	M2T	M2	P/PINF	R/RINF	T/TINF	GAM
4.01478	4.45887	3.37387	3.92747	5.17765	2.29721	1.78194	1.28927	1.39958

DELTAN	EPSN	AJOC	ACOI2P	ACOI3P	AEOI1P	THETA	DELTAN MAX	EPSN MAX	N
8.92684	21.22136	14.56486	5.80582	1.68078	40.66402	42.00000	38.82164	66.06918	2

M1= 6.000 SWEEP= 48.000 RIDGE ANGLE= 6.000 DE/AD= 0.000 P1= .2775 T1= 402.00

M2= 5.178 P/PINF= 2.2972 R/RINF= 1.7819 T/TINF= 1.2893 GAM= 1.3996

RECOVERY (PT/PTINF) = .9438 KINETIC ENERGY EFF.= .99769

CONTRACTION (AINF/A) = 1.7458 EPS= 14.565 CROSS FLOW= 1.681

FLOW PROPERTIES REFERENCED TO INITIAL XYZ COORDINATE SYSTEM

M2= 5.178 DELTA XZ= 6.000 EPS XZ= 14.565

TOTAL CROSS FLOW (DELTA XY)= 1.681 GAP RATIO (W1/W2)= 1.688

```
CASE NO  3          WAVE NO  2                                         K1  K2  K3  K4  K5
                                            (WEAK SHOCK)                2   2   2   0   0
***THERMALLY PERFECT GAS***
                                   IN FRONT OF WAVE
                                              TOTAL PROPERTIES
      M          MCHECK        TO         T/TO        PO          P/PO           R           R/RO         GAM       N
   5.17765      5.17764    2999.706     .17278     498.961    .001277606     .003320    .007394459   1.39958    2

                                   BEHIND WAVE
                                              TOTAL PROPERTIES
      M          MCHECK        TO         T/TO        PO          P/PO           R           R/RO         GAM       N
   4.54805      4.54804    2999.706     .21416     480.627    .002712833     .005478    .012667153   1.39786    2


      FLOW PROPERTIES MEASURED NORMAL TO WEDGE LEADING EDGE

  M1N= 3.374    DELTAN=  8.927     P1=    .6375      R1=    .0033     T1=  518.29     PT1=  498.9614     GAM1=1.3996
  M2N= 2.868       EPN= 24.088     P2=  1.3039      R2=    .0055     T2=  642.43     PT2=  480.6274     GAM2=1.3979
 REYR= 1.327     A1/A2=  1.561  P2/P1=  2.0454   R2/R1=  1.6508  T2/T1=  1.2395     TPR=      .9633       N=    R


      FLOW PROPERTIES REFERENCED TO SWEPT WEDGE

    M1N       M1T       M2N       M2T        M2      P/PINF     R/RINF     T/TINF      GAM
   3.37387   3.92747   2.86794   3.52982   4.54805   4.69860   2.94169   1.59807   1.39786

   DELTAN     EPSN      AJOC      ACOI2P    ACOI3P    AEOI1P     THETA    DELTAN MAX   EPSN MAX   N
   8.92684  24.08782  15.74766   5.80334   1.23208  39.09345  40.66402  36.27601   65.58788    2

 M1=   5.178        SWEEP=  49.535          RIDGE ANGLE=   5.803          DE/AD= 1.000         P1=   .6375        T1=  518.29

 M2=   4.548       P/PINF=  4.6986        R/RINF=  2.9417          T/TINF=  1.5981       GAM= 1.3979

 RECOVERY (PT/PTINF)  =    .9091          KINETIC ENERGY EFF.=    .99616

 CONTRACTION (AINF/A)  =  2.8167          EPS=  15.748          CROSS FLOW=   1.232


      FLOW PROPERTIES REFERENCED TO INITIAL XYZ COORDINATE SYSTEM

 M2=   4.548         DELTA XZ=   6.000            EPS XZ=  10.277

 TOTAL CROSS FLOW (DELTA XY)=   2.907            GAP RATIO (W1/W2)=   2.654
```

```
CASE NO  3          WAVE NO  3                                        K1  K2  K3  K4  K5
                                          (WEAK SHOCK)                 2   2   2   0   0
***THERMALLY PERFECT GAS***
                               IN FRONT OF WAVE
                                     TOTAL PROPERTIES
      M          MCHECK        TC         T/TO        PO         P/PO           R          R/RO        GAM       N
   4.54805      4.54804    2999.706     .21415     480.627    .002712833     .005478    .012667153   1.39786     2

                               BEHIND WAVE
                                     TOTAL PROPERTIES
      M          MCHECK        TO         T/TO        PO         P/PO           R          R/RO        GAM       N
   4.05131      4.05130    2999.707     .25739     468.389    .005185326     .008502    .020146935   1.39377     2

     FLOW PROPERTIES MEASURED NORMAL TO WEDGE LEADING EDGE

  M1N= 2.868     DELTAN=  8.927     P1=  1.3039     R1=    .0055     T1=  642.43     PT1=  480.6274     GAM1=1.3979
  M2N= 2.453        EPN= 27.384     P2=  2.4319     R2=    .0085     T2=  772.05     PT2=  468.9891     GAM2=1.3938
 REYR= 1.265     A1/A2=  1.453   P2/P1=  1.8651  R2/R1=   1.5520  T2/T1=  1.2018     TPR=      .9758       N=     3

     FLOW PROPERTIES REFERENCED TO SWEPT WEDGE

    M1N        M1T        M2N        M2T        M2       P/PINF     R/RINF     T/TINF      GAM
  2.86794    3.52982    2.45253    3.22462    4.05131    8.76346    4.56542    1.92052    1.39377

   DELTAN      EPSN       AJOC      ACOI2P     ACOI3P     AEOI1P      THETA    DELTAN MAX  EPSN MAX   N
  8.92684   27.38449   18.08956    5.39400    2.17396   37.25537   39.09345   33.17773   65.13902    2

 M1=    4.548        SWEEP=  50.907          RIDGE ANGLE=    5.657         DE/AD= 0.000          P1=  1.3039        T1=  642.43

 M2=    4.051       P/PINF=  8.7635       R/RINF=  4.5654          T/TINF=  1.9205        GAM= 1.3938

 RECOVERY (PT/PTINF)  =    .9871          KINETIC ENERGY EFF.=    .99514

 CONTRACTION (AINF/A) =  4.2626           EPS=  18.090          CROSS FLOW=   2.174

     FLOW PROPERTIES REFERENCED TO INITIAL XYZ COORDINATE SYSTEM

 M2=    4.051          DELTA XZ=   6.000             EPS XZ=  19.117

 TOTAL CROSS FLOW (DELTA XY)=   5.081              GAP RATIO (W1/W2)=   3.827
```

APPENDIX B

INLET PERFORMANCE FOR LOW REYNOLDS NUMBER AND UNSTARTED OPERATION

In order to evaluate the inlets operating characteristics better, one test was made with the Reynolds number reduced by a factor of 1/3 to 3.3×10^6 per meter. The resulting static-pressure distributions within the inlet are found in figure 61 where they are compared with the high-pressure tests. Also given in figure 61 are the results of a test in which the model failed to start because of blockage produced by a survey rake.

The low Reynolds number tests had only a small effect on inlet operation as determined by static-pressure level changes produced by slight alterations in shock-wave positions. In the side passage these effects were seen near the cowl in figures 61(f) and 61(h), whereas the center-passage effects are observed in figure 61(k). The high-pressure level indicated on the foreplate (fig. 61(a)) is in error because of the difficulty in measuring the extremely low pressures.

Alterations in static-pressure levels for the unstarted choked inlet were observed throughout the model. High pressures were found on the foreplate (fig. 61(a)), top surface (figs. 61(b) and 61(c)), sidewalls in front of the struts (fig. 61(d)), and on the cowl (figs. 61(f) and 61(g)). The pressure level in the center passage was low and uniform and indicated the absence of shock waves (figs. 61(i) and 61(k)).

APPENDIX C

CAPTURE MEASUREMENT DATA

The primary conclusions from the capture measurement data (Mach number and capture parameter contour maps) taken downstream from the struts are presented in the report in figures 53 and 54. The purpose of this appendix is to include the data from pitot and static-pressure surveys used to produce those results. Like the data taken at the inlet throat, the program used to analyze these data and generate the contour maps is discussed in appendix B.

The static-pressure distribution around the walls of the inlet at the capture measurement station is given in figure 62 where λ is the peripheral distance around the area as defined in the sketch. The static probe survey data are found in figure 63 which also includes the wall values of figure 62. A nominal value of 80 percent was selected for the total-pressure recovery limit at the capture measurement location downstream of the struts. When the static surveys were combined with the pitot surveys of figure 64, the computed total-pressure recovery was above the imposed limit of 80 percent only in the very small region indicated by the dashed line in figure 63(d). The data are seen in contour map form in figures 65 and 66, and a total-pressure recovery map is given in figure 67.

REFERENCES

1. Henry, J. R.; and McLellan, C. H.: Air-Breathing Launch Vehicle for Earth-Orbit Shuttle – New Technology and Development Approach. AIAA Paper No. 70-269, Feb. 1970. (Also J. Aircraft, vol. 8, no. 5, May 1971, pp. 381-387.)
2. Ferri, A.: Review of SCRAMJET Propulsion Technology. J. Aircraft, vol. 5, no. 1, Jan.-Feb. 1968, pp. 3-10.
3. Becker, John V.: New Approaches to Hypersonic Aircraft. Paper presented at Seventh Congress of the International Council of the Aeronautical Sciences (Rome, Italy), Sept. 1970.
4. Becker, John V.: Prospects for Actively Cooled Hypersonic Transports. Astronaut. & Aeronaut., vol. 9, no. 8, Aug. 1971, pp. 32-39.
5. Development of Liquid-Hydrogen Scramjet Key to Hypersonic Flight. Aviat. & Space Technol., vol. 99, no. 12, Sept. 17, 1973, pp. 75-78.
6. Edwards, C. L. W.: A Forebody Design Technique for Highly Integrated Bottom-Mounted Scramjets With Application to a Hypersonic Research Airplane. NASA TM X-71971, 1974.
7. Small, William J.; Weidner, John P.; and Johnston, P. J.: Scramjet Nozzle Design and Analysis as Applied to a Highly Integrated Hypersonic Research Airplane. NASA TM X-71972, 1974.
8. Henry, John R.; and Anderson, Griffin Y.: Design Considerations for the Airframe-Integrated Scramjet. NASA TM X-2895, 1973.
9. Trexler, Carl Arthur: An Experimental Investigation of the Forebody of a Hypersonic Inlet Model and a Comparison With Theory. M.S. Thesis, Virginia Polytech. Inst. & State Univ., Apr. 1971.
10. Pinckney, S. Z.: Semiempirical Method for Predicting Effects of Incident-Reflecting Shocks on the Turbulent Boundary Layer. NASA TN D-3029, 1965.
11. Pinckney, S. Z.: An Improved Static Probe Design. AIAA J., vol. 12, no. 4, Apr. 1974, pp. 562-564.
12. Goldberg, Theodore J.; and Hefner, Jerry N. (With appendix by James C. Emery) Starting Phenomena for Hypersonic Inlets With Thick Turbulent Boundary Layers at Mach 6. NASA TN D-6280, 1971.
13. Pinckney, S. Z.: Turbulent Heat-Transfer Prediction Method for Application to Scramjet Engines. NASA TN D-7810, 1974.
14. Ames Research Staff: Equations, Tables, and Charts for Compressible Flow. NASA Rep. 1135, 1953. (Supersedes NACA TN 1428.)

TABLE I.- THEORETICAL FLOW FIELD PROPERTIES USED FOR FIGURE 5

Bay	M	p/p_1	$p_t/p_{t,1}$	δ_{xz}	δ_{xy}	A/A_1	p_{pitot}/p_1	
1	6.0	1.0	1.0	0	0	1.0	46.8	← Free stream
2	5.18	2.30	.944	6.0	1.7	1.75	80.4	
3	4.54	4.70	.910	0	2.9	2.81	127.0	
4	4.04	8.77	.888	6.0	5.1	4.26	188.0	
5	3.76	12.74	.883	2.0	6.2	5.25	237.0	
6	3.51	18.02	.879	6.0	7.9	6.85	294.0	← Side-passage throat
7	4.75	3.74	.933	10.0	2.8	2.43	110.0	
8	4.21	7.16	.903	4.0	4.5	3.74	167.0	
9	3.77	12.67	.891	10.0	6.9	5.45	238.0	
10	3.40	20.99	.879	6.0	8.95	7.57	322.0	← Center-passage throat
11	3.17	28.91	.871	2.0	10.5	9.29	388.0	
12	4.54	4.70	.910	0	2.9	2.81	127.0	
13	4.04	8.77	.888	-6.0	5.1	4.26	188.0	
14	3.76	12.77	.886	-2.0	6.2	5.46	238.0	
15	3.51	18.02	.879	-6.0	7.9	6.85	294.0	
16	3.08	33.26	.870	10.0	12.2	10.16	422.0	

TABLE II.- THEORETICAL END EFFECTS USED FOR FIGURE 5

(a) Top surface $\left(\delta_{xy} = 4^{\circ}\right)$

Bay	M	p/p_1	$p_t/p_{t,1}$	p_{pitot}/p_1
2	4.92	3.07	0.939	97.1
3	4.46	5.22	.910	136.0
4	4.13	7.79	.888	175.0
5	3.92	10.25	.883	208.0
6	3.77	12.53	.879	235.0
7	4.67	4.26	.933	122.0
8	4.25	6.80	.903	161.0
9	3.98	9.53	.891	199.0
10	3.72	13.58	.879	248.0
11	3.56	16.47	.871	277.0
12	4.46	5.22	.910	136.0
13	4.13	7.79	.888	175.0
14	3.92	10.27	.886	208.0
On plow*	5.33	1.98	.968	73.3

*In front of bay number 2.

(b) Cowl $\left(\delta_{xy} = 0^{\circ}\right)$

Bay	M	p/p_1	$p_t/p_{t,1}$	p_{pitot}/p_1
2	4.99	2.82	0.942	91.7
3	4.28	6.48	.907	156.0
4	3.67	14.40	.877	256.0
5	3.35	22.30	.867	333.0
6	3.04	34.90	.854	432.0
7	4.48	5.17	.930	136.0
8	3.86	11.30	.894	222.0
9	3.31	23.60	.870	344.0
10	2.88	43.40	.846	484.0
11	2.62	63.60	.829	592.0
12	4.28	64.80	.907	156.0
13	3.67	14.40	.877	257.0
14	3.35	22.40	.870	334.0

TABLE III.- CORRECTED THEORETICAL FLOW FIELD PROPERTIES USED FOR FIGURE 27

Bay	M	p/p_1	p_t/p_1	δ_{xz}	δ_{xy}	A/A_1	p_{pitot}/p_1
1	6.00	1.00	1.000	0	0	1.00	46.8
2	5.07	2.54	.922	6.83	2.00	1.80	85.2
3	4.46	5.12	.891	0	3.18	2.96	133.0
4	3.97	9.44	.870	6.00	5.40	4.44	196.0
5	3.70	13.61	.866	2.00	6.52	5.66	246.0
6	3.45	19.14	.862	6.00	8.27	7.07	302.0
7	4.66	4.09	.912	10.83	3.19	2.56	116.0
8	4.07	8.37	.879	4.00	5.20	4.11	182.0
9	3.59	15.55	.858	10.83	8.14	6.16	265.0
10	3.24	25.52	.842	4.83	10.28	8.45	357.0
11	---	----	----	----	----	---	----
12	4.38	5.59	.879	0	3.44	3.13	141.0
13	3.90	10.19	.859	-6.00	5.71	4.65	204.0
14	3.64	14.62	.857	-2.00	6.87	5.91	256.0
*15	3.40	20.40	.852	-6.00	8.66	7.34	313.0
16	3.24	25.28	.835	4.83	11.30	8.38	354.0

*For large center strut.

TABLE IV.- CORRECTED THEORETICAL END EFFECTS USED FOR FIGURE 27

(a) Top surface $\left(\delta_{xy} = 4^{o}\right)$

Bay	M	p/p_1	$p_t/p_{t,1}$	p_{pitot}/p_1
2	4.86	3.25	0.921	100.0
3	4.39	5.61	.891	142.0
4	4.07	8.26	.870	180.0
5	3.88	10.60	.866	210.0
6	3.73	12.90	.862	522.0
7	4.58	4.46	.912	123.0
8	4.17	7.34	.879	168.0
9	3.87	10.60	.858	209.0
10	3.63	14.60	.842	254.0
11	---	----	----	----
12	4.33	5.95	.878	146.0
13	4.03	8.56	.859	183.0
14	3.84	11.10	.857	216.0
*15	3.70	13.40	.852	242.0
16	3.69	13.80	.835	248.0

*For large center strut.

(b) Cowl $\left(\delta_{xy} = 0^{o}\right)$

Bay	M	p/p_1	$p_t/p_{t,1}$	p_{pitot}/p_1
2	4.86	3.25	0.921	100.0
3	4.18	7.22	.996	166.0
4	3.57	15.80	.858	267.0
5	3.28	24.30	.849	348.0
6	2.97	37.80	.835	447.0
7	4.35	6.52	.902	162.0
8	3.68	13.40	.867	240.0
9	3.10	31.10	.829	399.0
10	2.69	56.30	.801	551.0
11	---	----	----	----
12	4.11	8.08	.873	180.0
13	3.50	17.40	.845	283.0
14	3.22	26.60	.838	368.0
*15	2.90	41.10	.822	465.0
16	2.63	59.90	.783	562.0

*For large center strut.

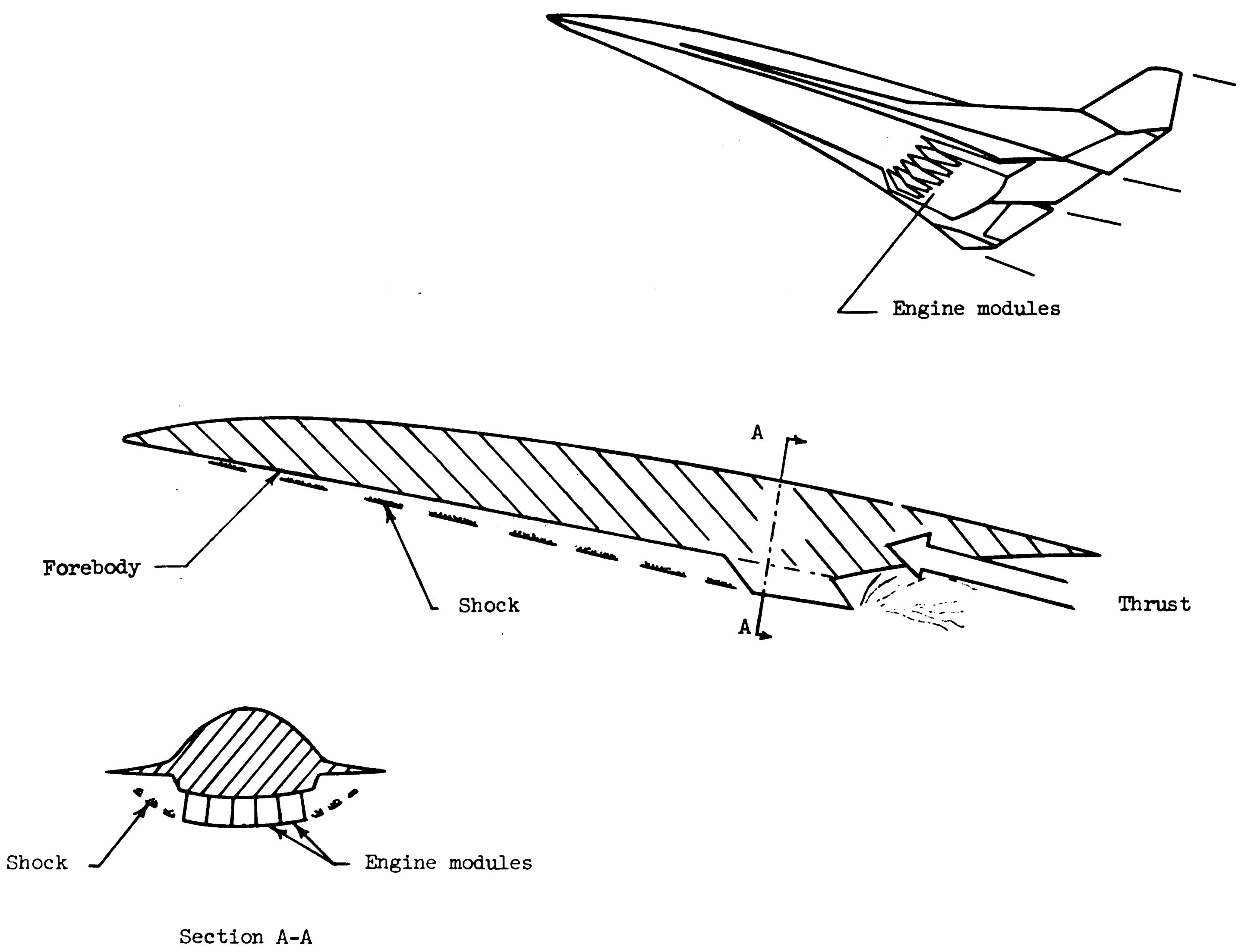

Figure 1.- Airframe-scramjet-engine integration.

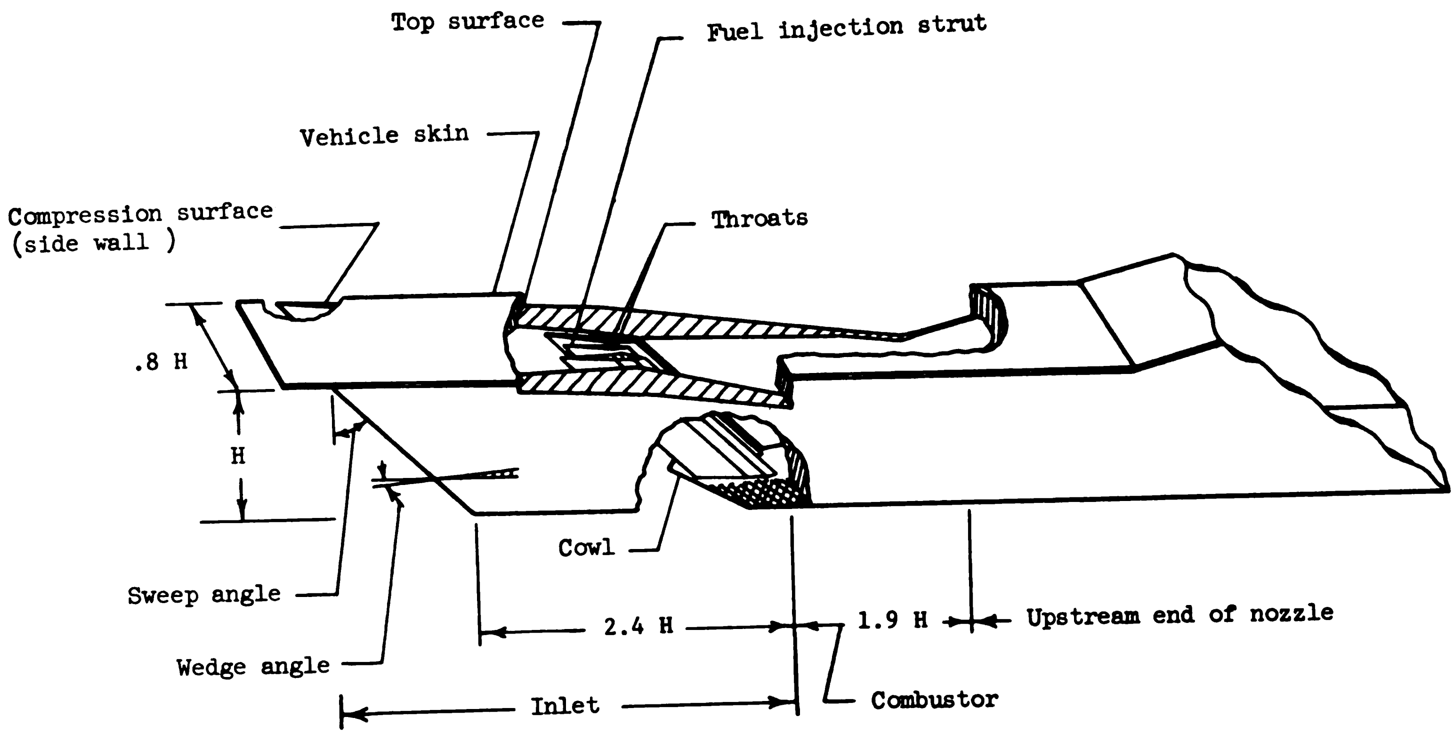

Figure 2.- Inner module of scramjet engine concept (ref. 8).

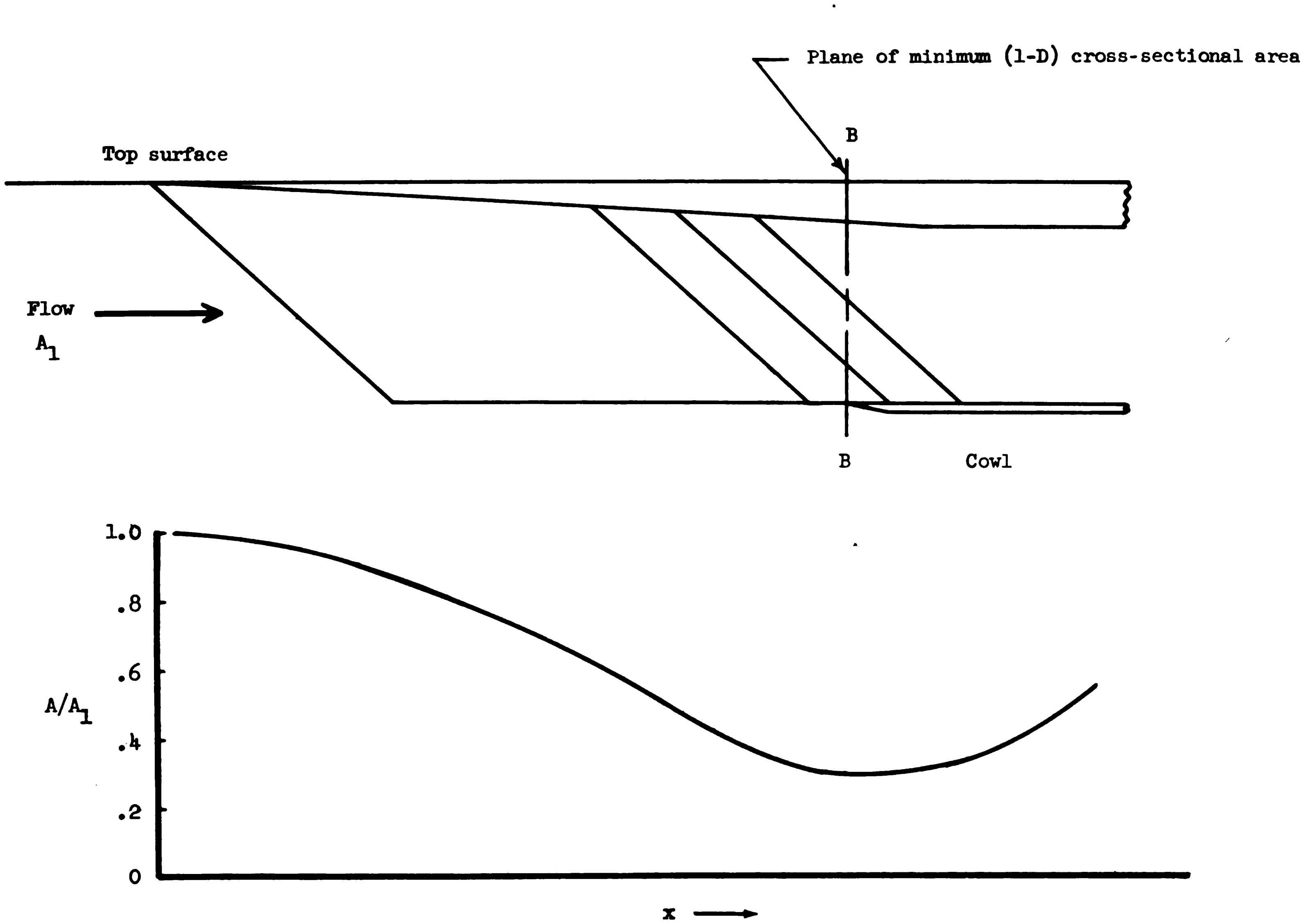

Figure 3.- One-dimensional inlet contraction.

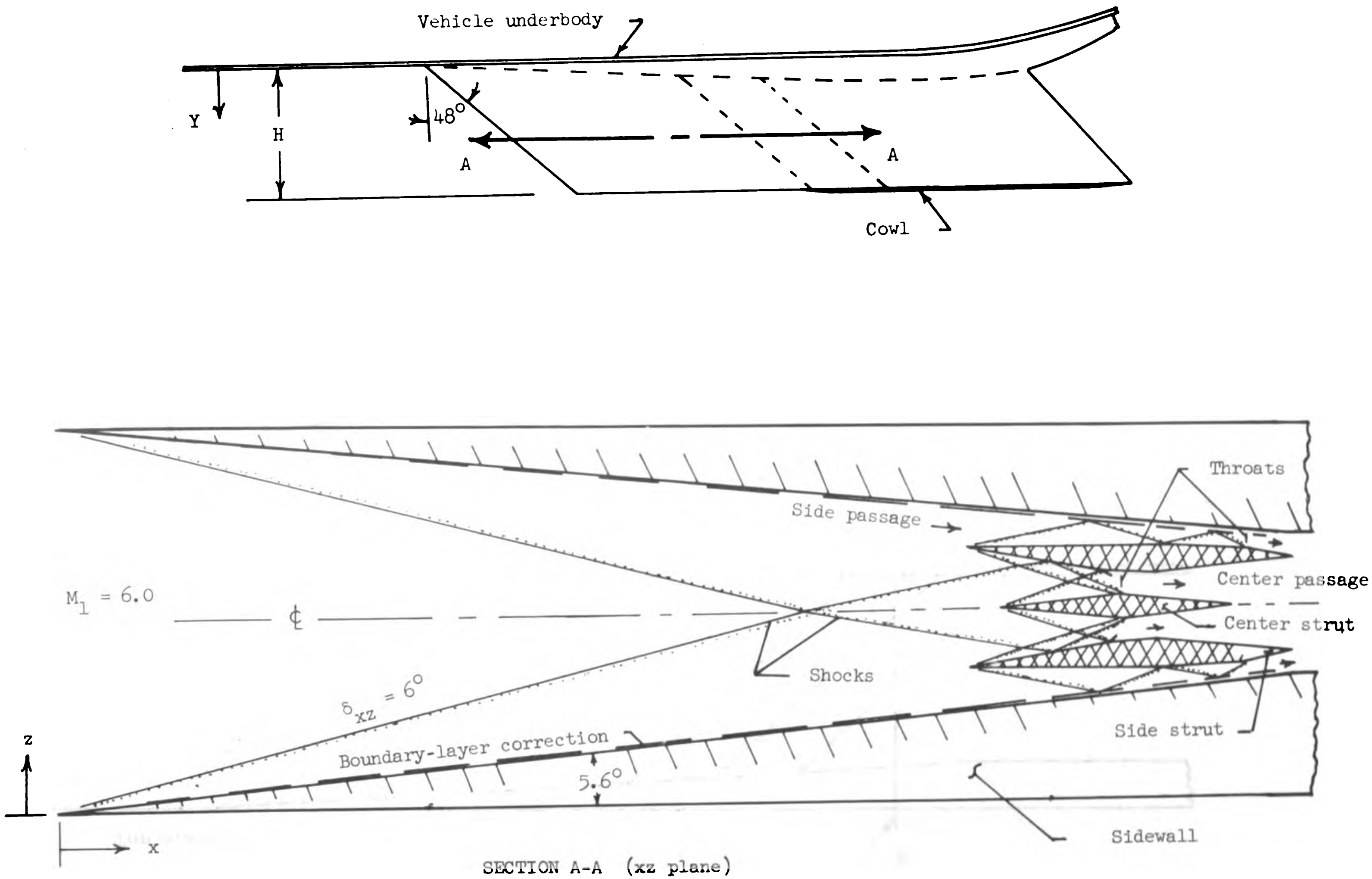

Figure 4.- Inlet model sketch and Mach 6 shock diagram.

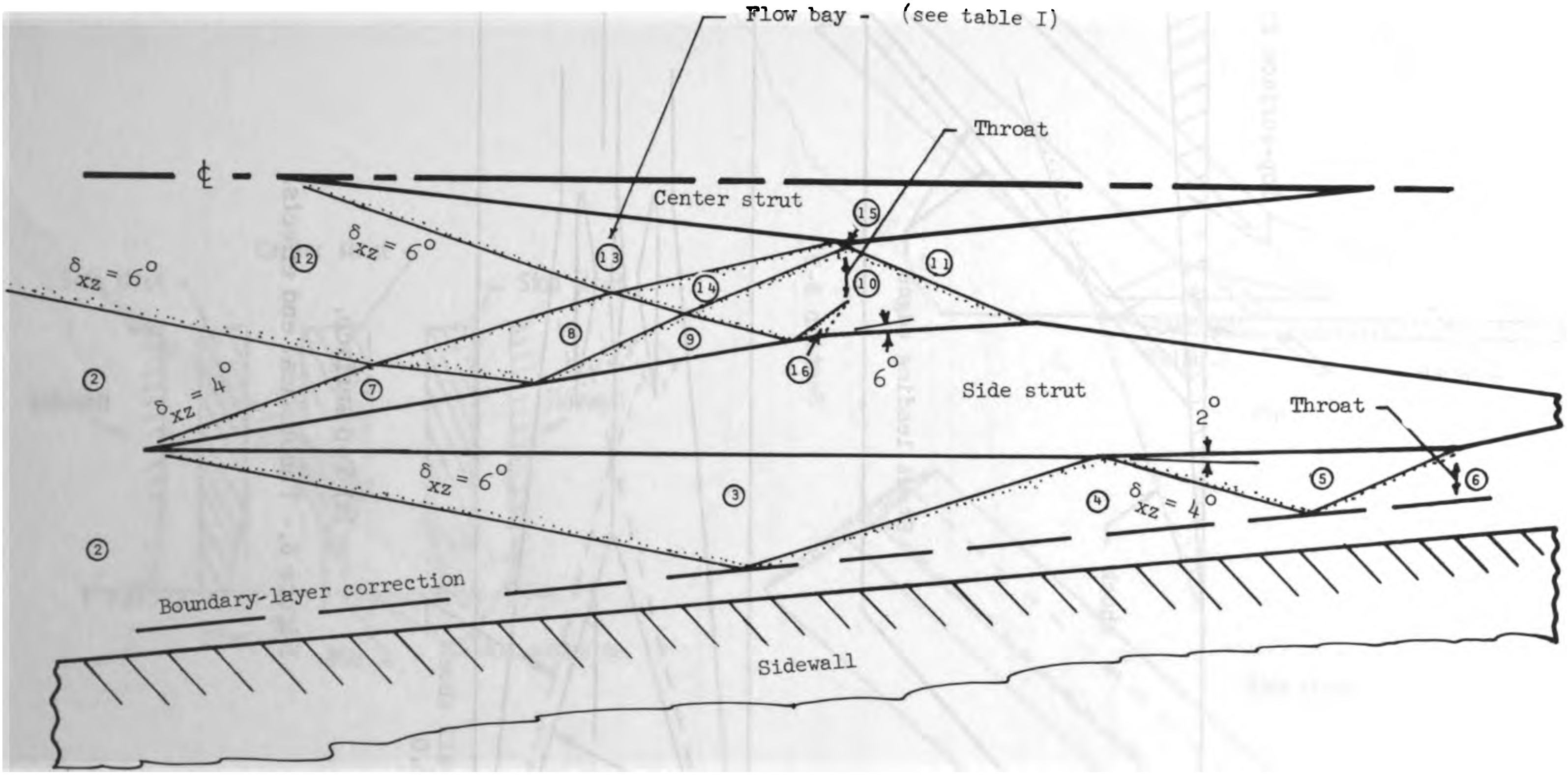

Figure 5.- Shock-wave detail in vicinity of struts. $M_1 = 6.0$.

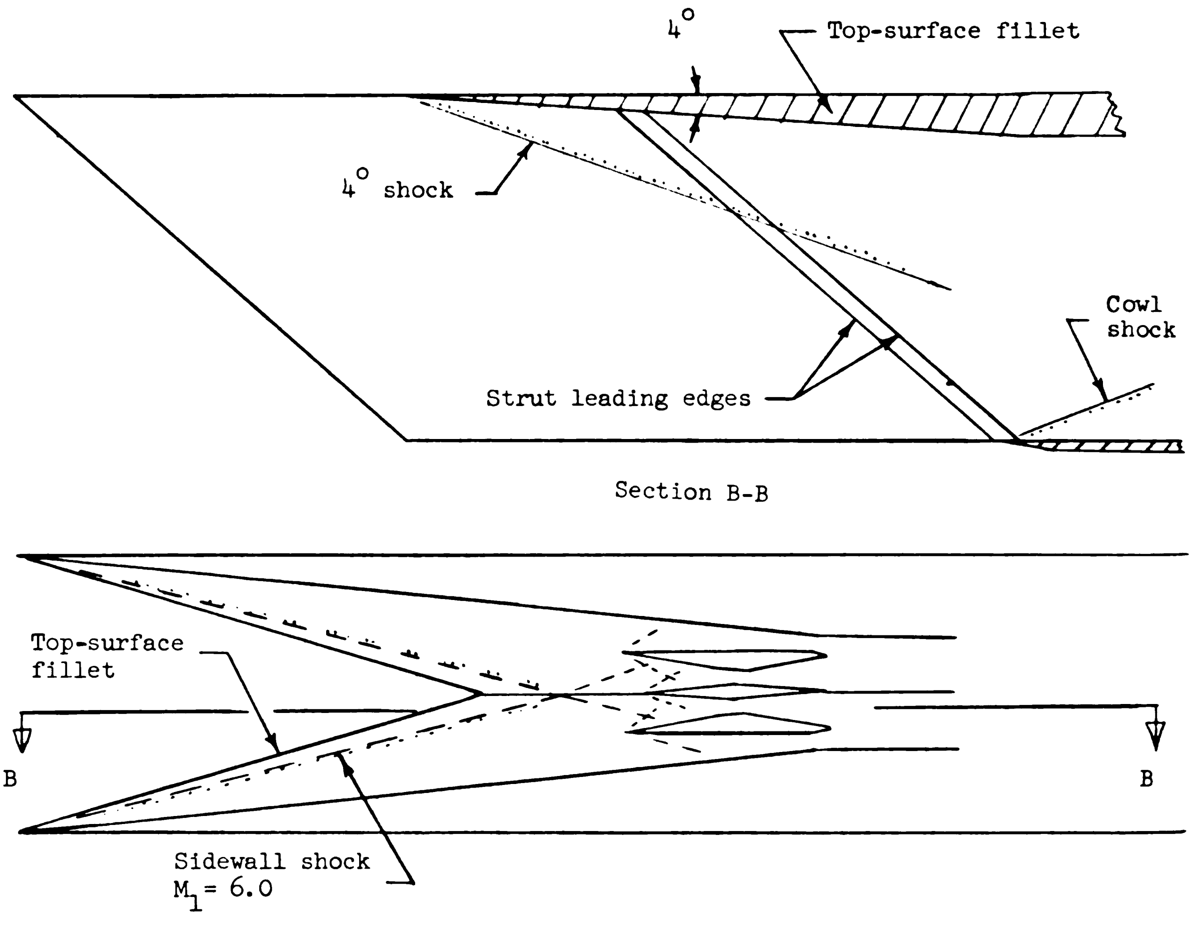

(a) Top surface.

Figure 6.- Theoretical end effects.

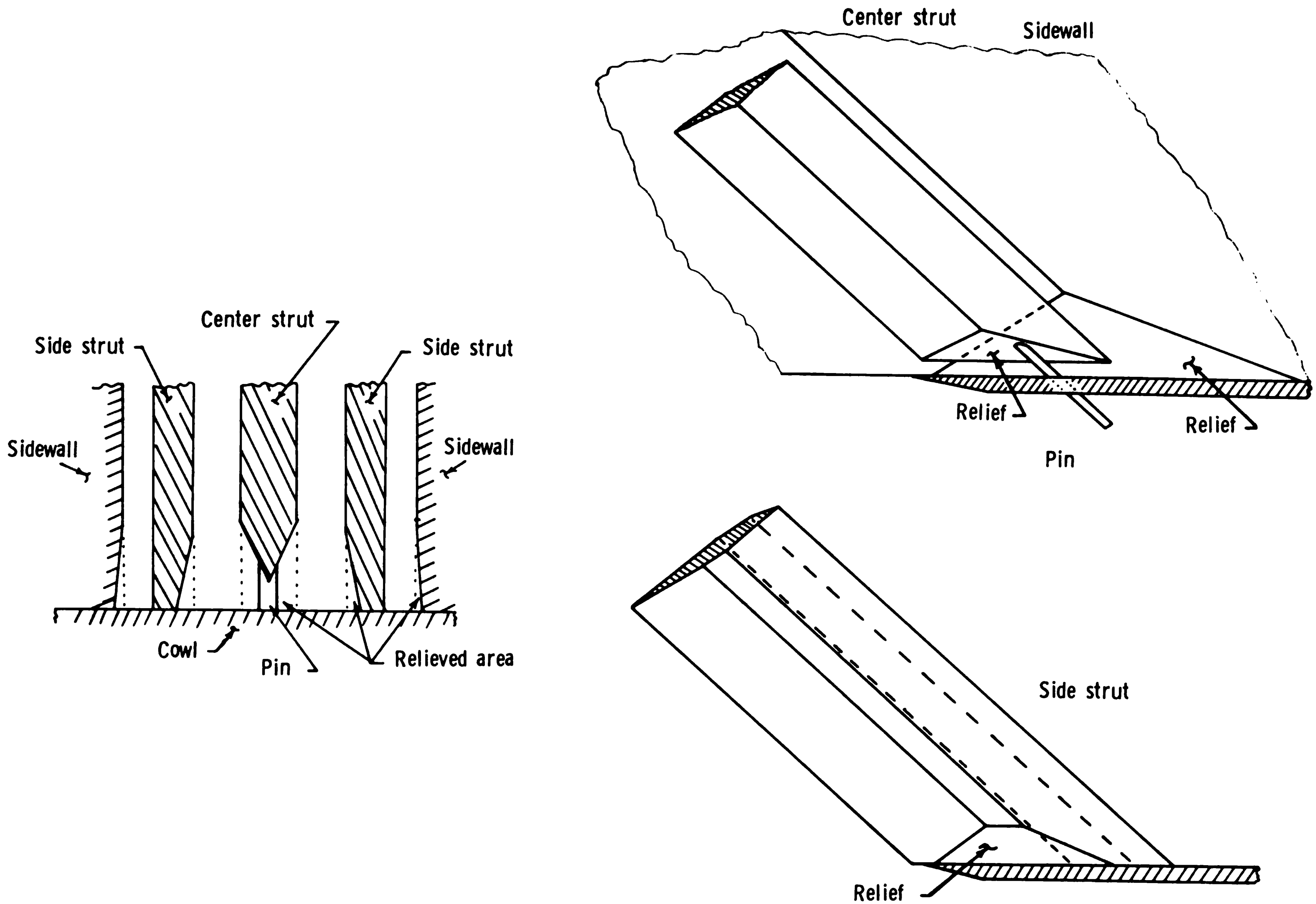

(b) Throat relief next to cowl.

Figure 6.- Continued.

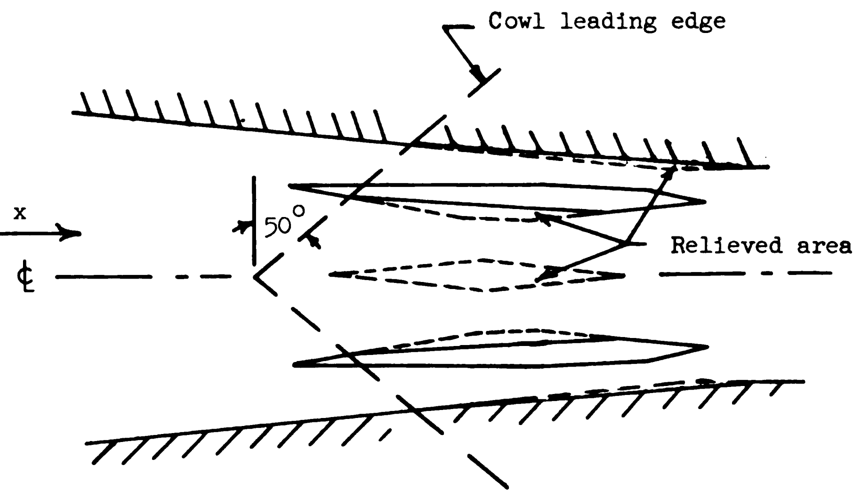

(c) Cowl leading-edge design.

Figure 6.- Concluded.

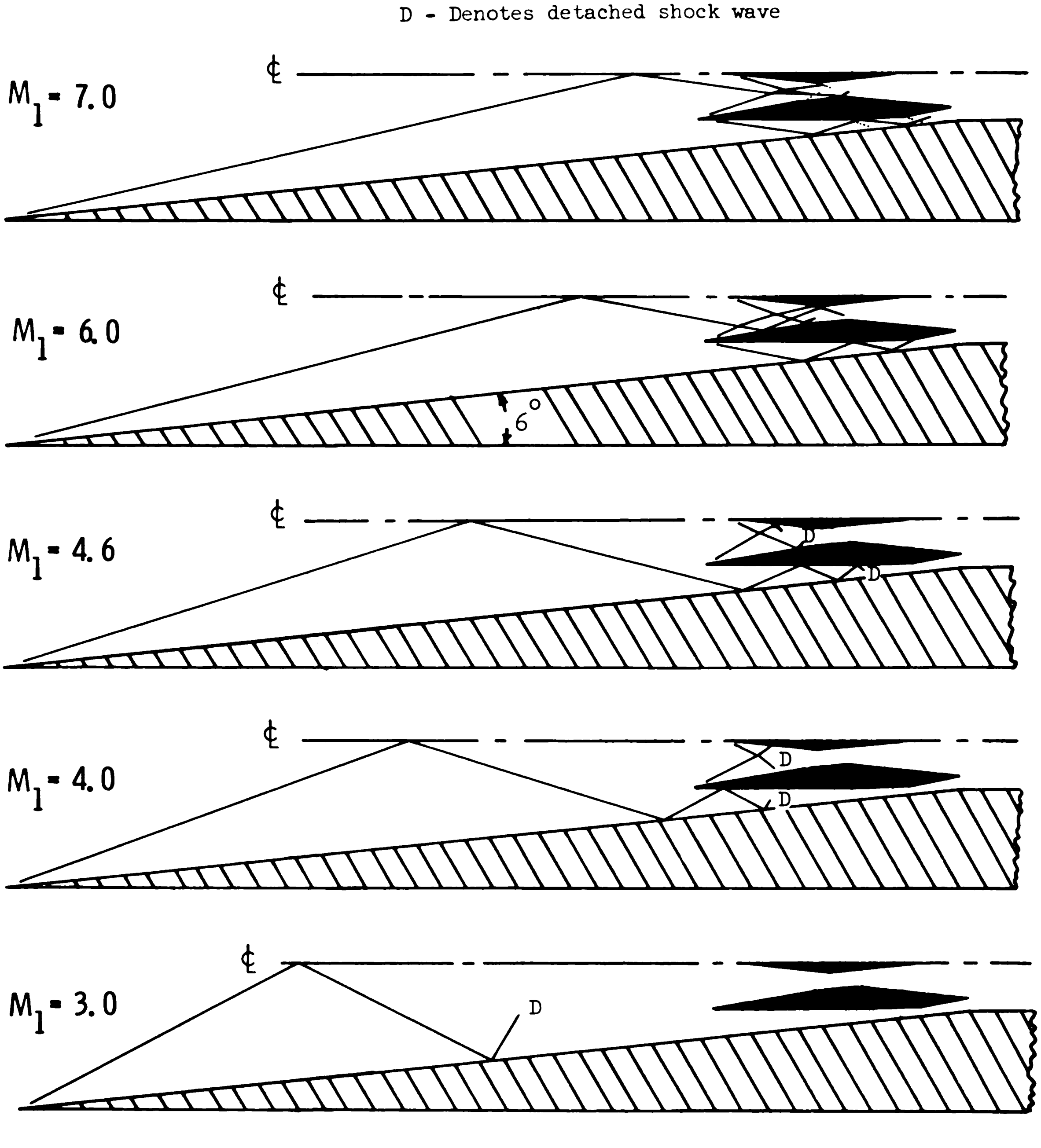

Figure 7.- Off-design shock wave systems (xz-plane). Sweep = 48°.

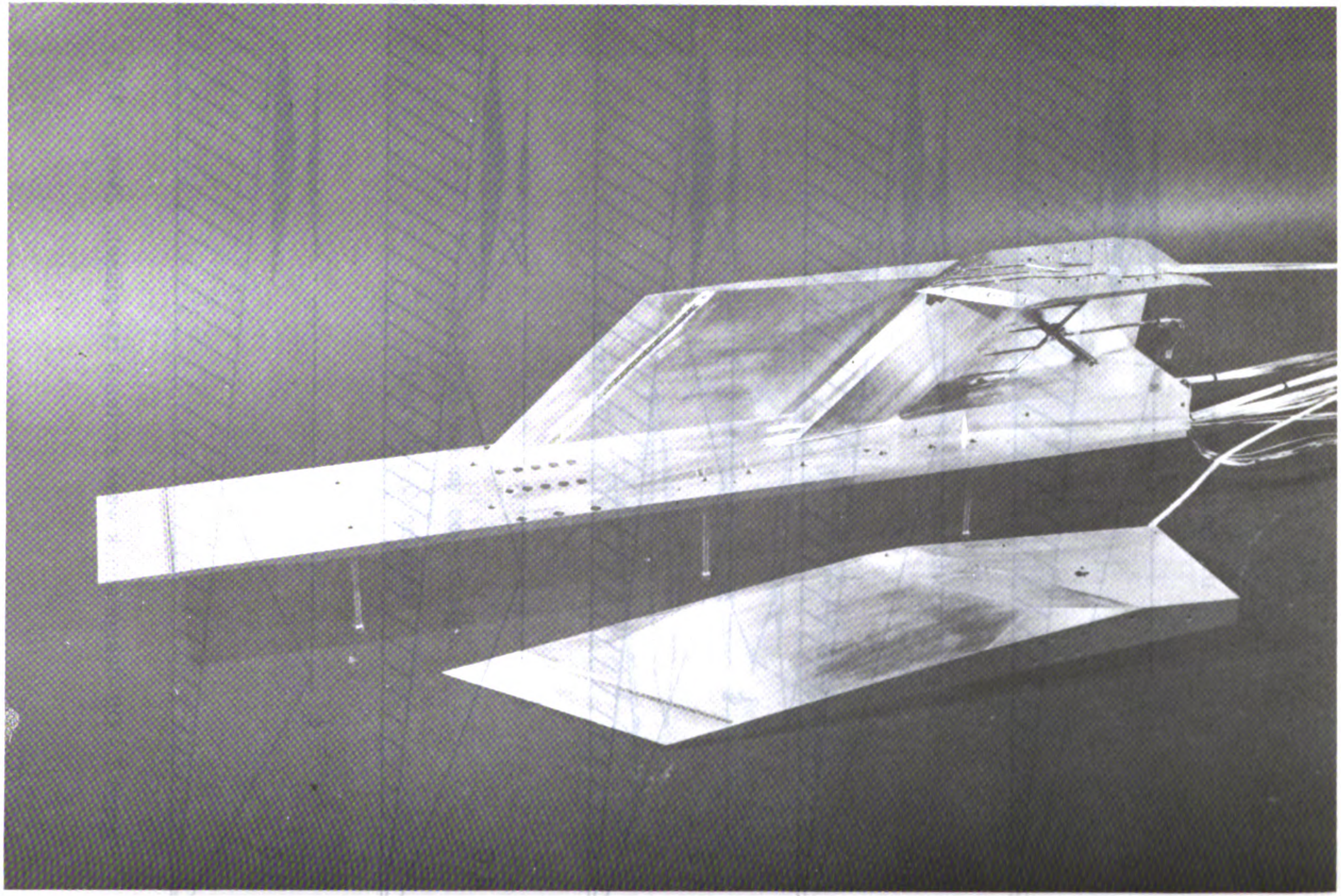

L-72-7495

(a) Side view.

Figure 8.- Model photograph.

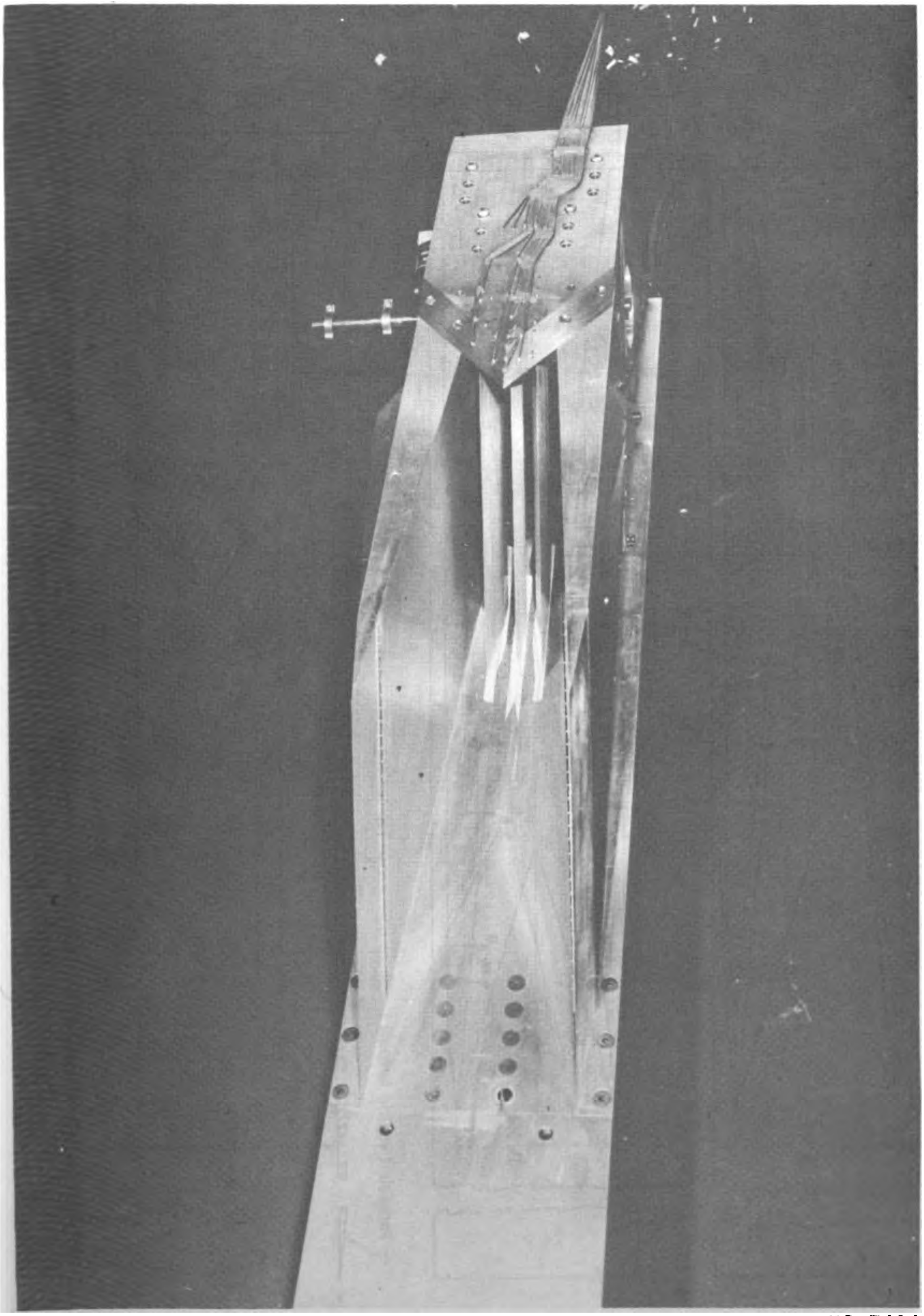

L-72-7494

(b) Front view.

Figure 8.- Concluded.

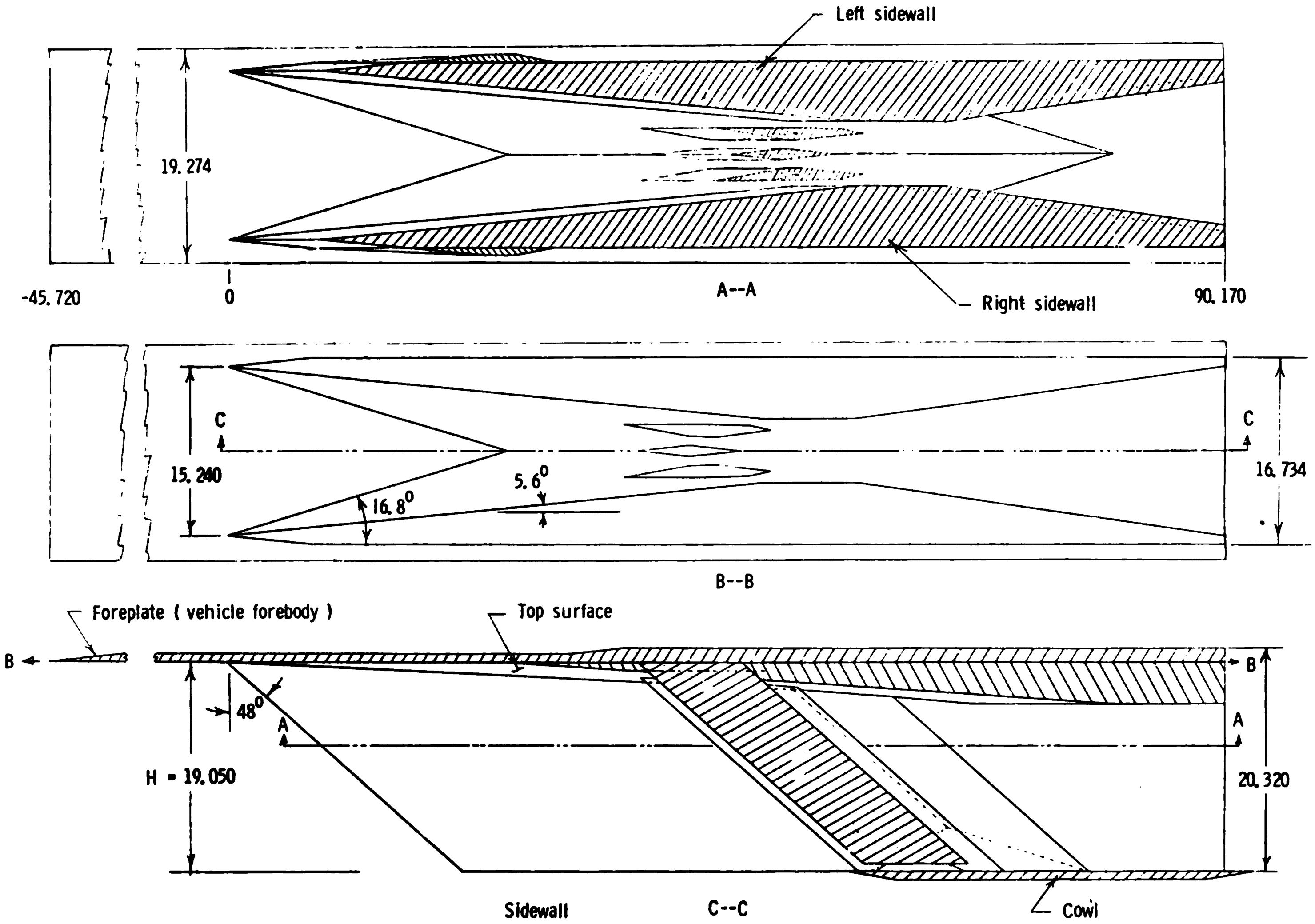

Figure 9.- Model schematics. All dimensions are in centimeters.

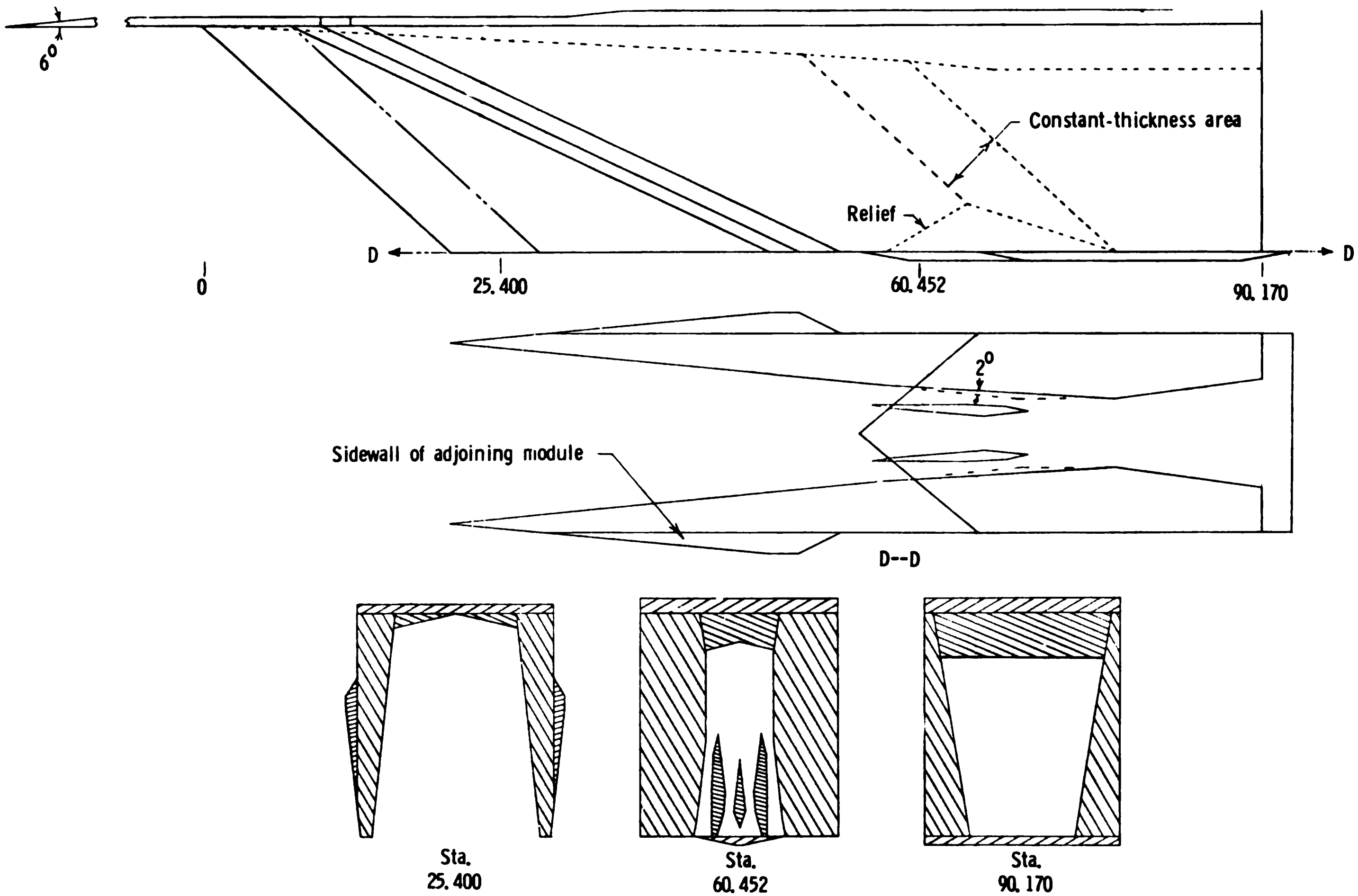

Figure 9.- Concluded.

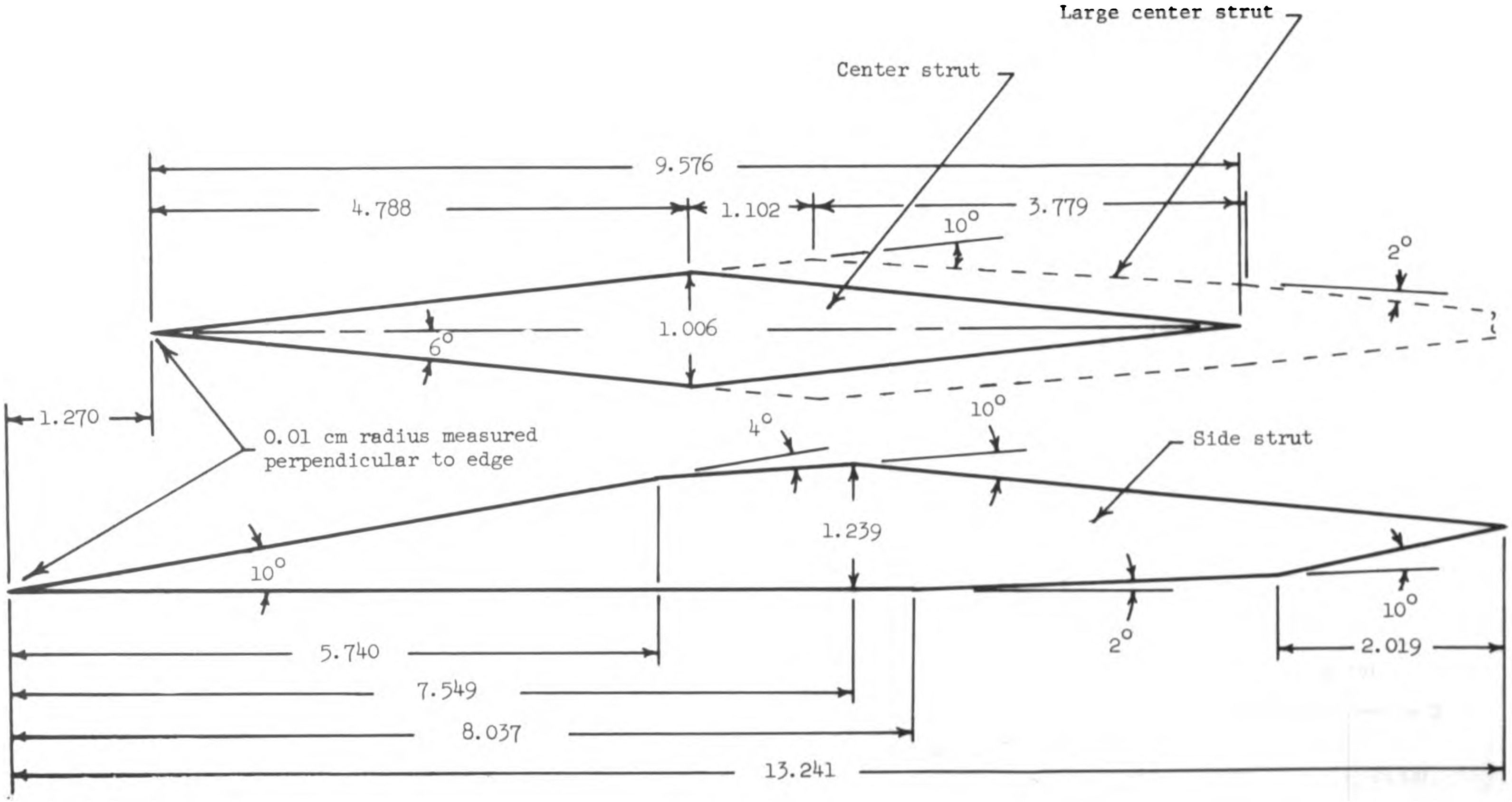

Figure 10.- Side and center strut dimensions as measured in the xz-plane. All dimensions are in centimeters.

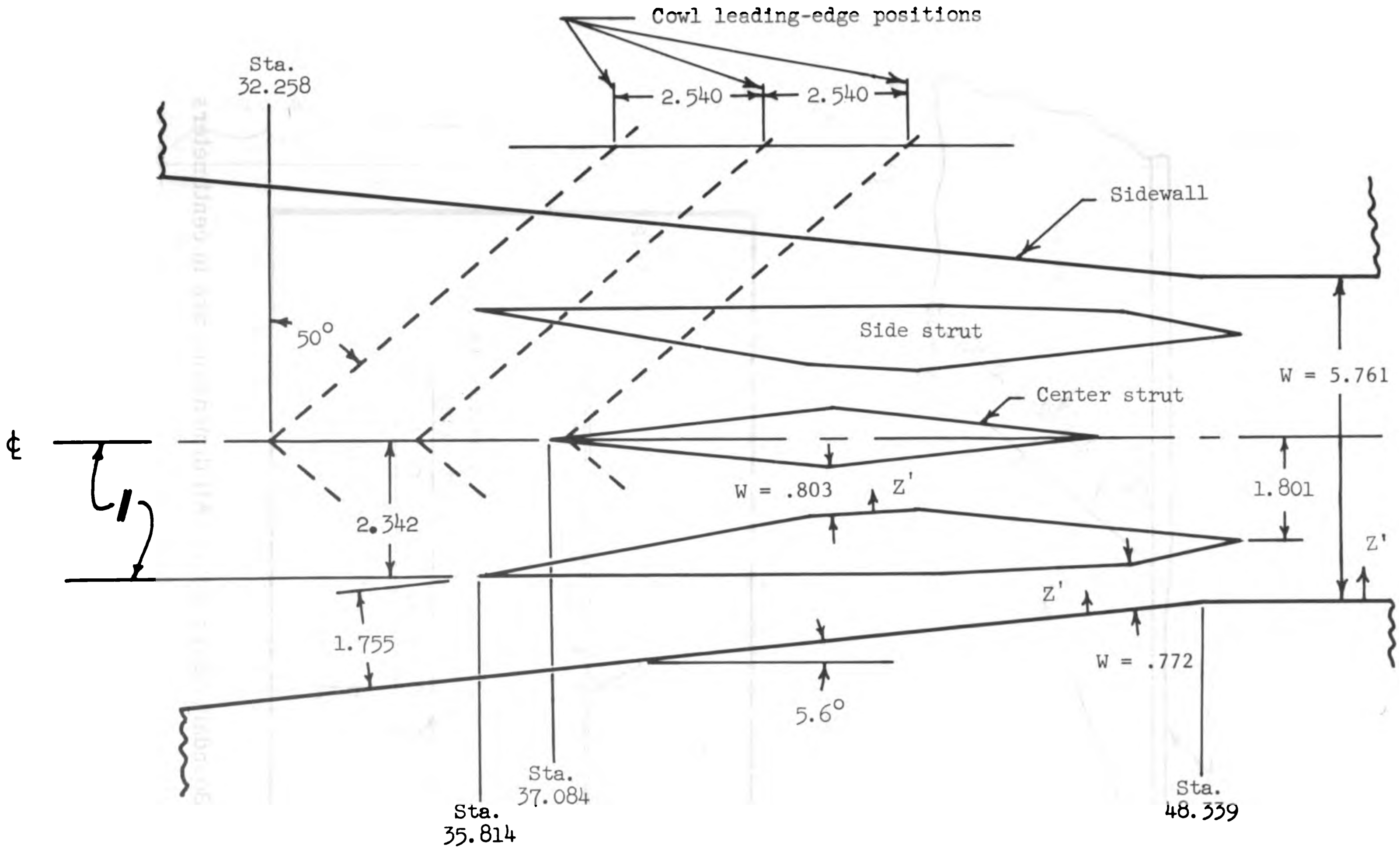

Figure 11.- Relative positions of struts and cowl in xz-planes. All dimensions are in centimeters. Stations are measured relative to sidewall leading edge; cowl leading edge shown at y = H.

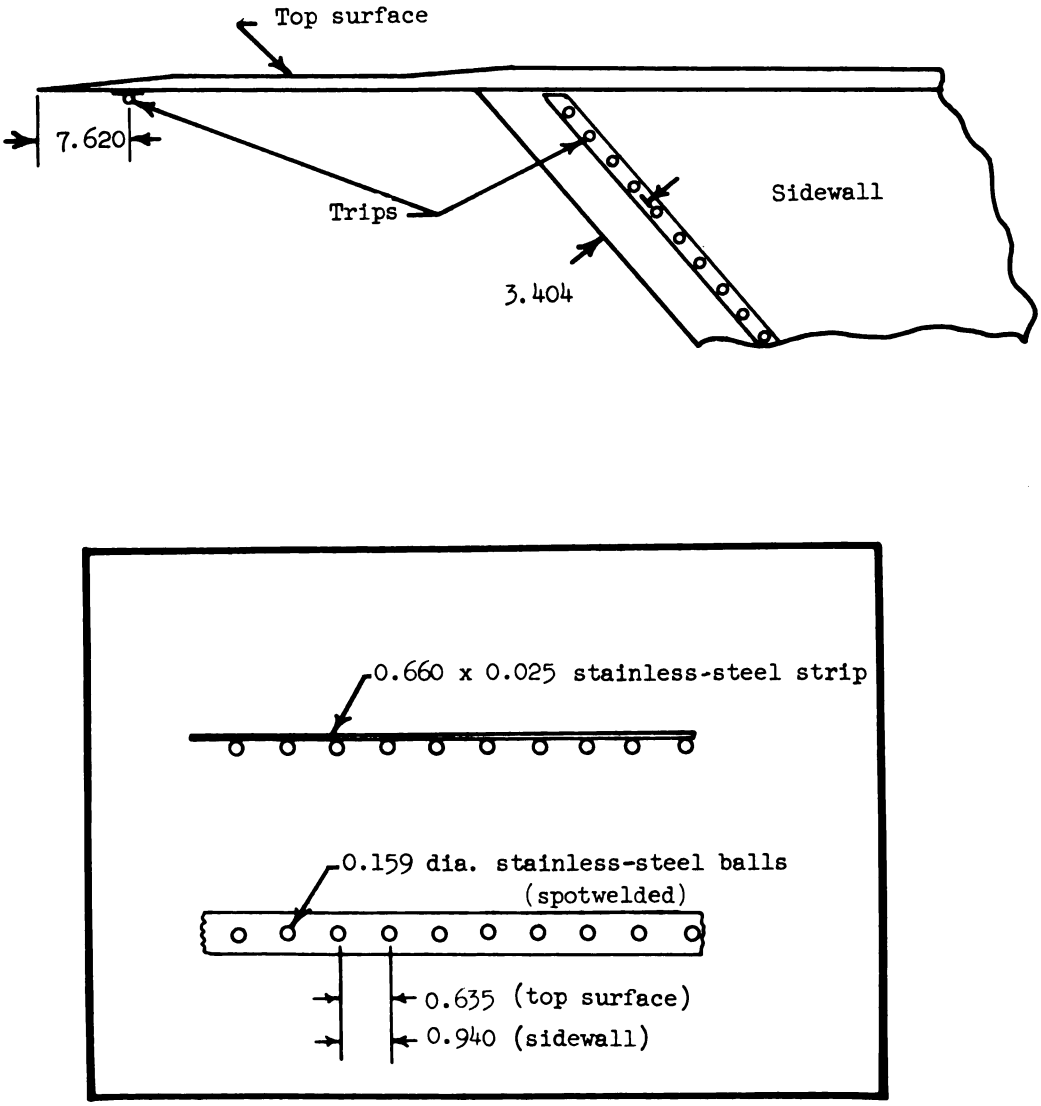

Figure 12.- Boundary-layer trips. All dimensions are in centimeters.

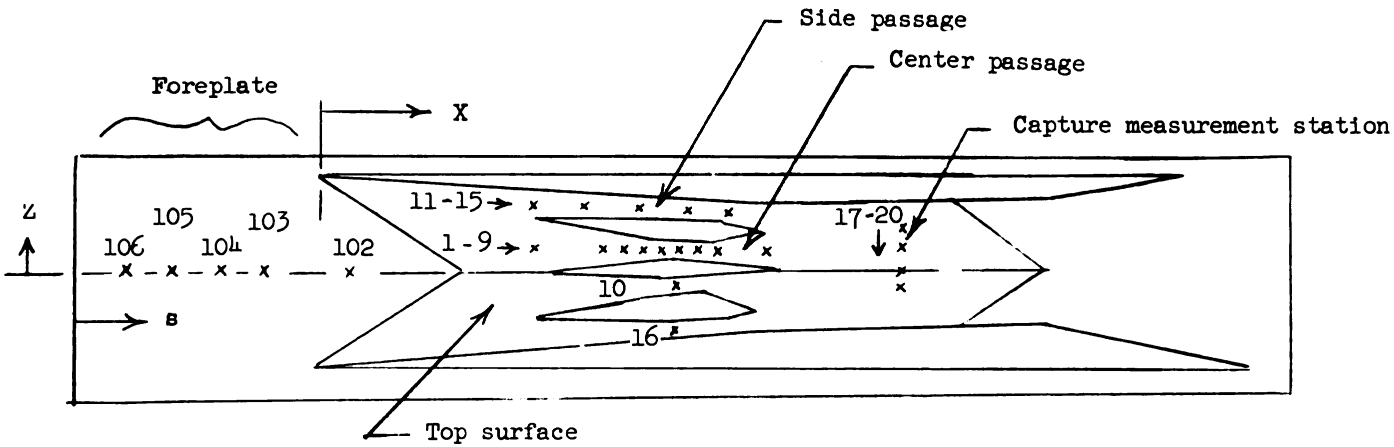

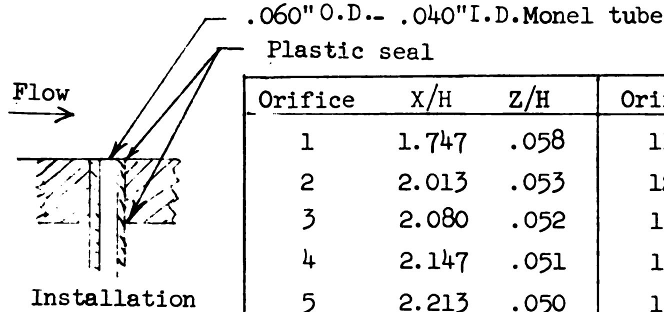

Orifice	s/H	Z/H
106	.733	0
105	1.267	0
104	1.800	0
103	2.333	0
102	3.040	0

Orifice	X/H	Z/H	Orifice	X/H	Z/H
1	1.747	.058	11	1.693	.175
2	2.013	.053	12	1.960	.163
3	2.080	.052	13	2.227	.151
4	2.147	.051	14	2.427	.142
5	2.213	.050	15	2.560	.136
6	2.280	.049	16	2.227	-.151
7	2.347	.048	17	3.040	.107
8	2.480	.045	18	3.040	.053
9	2.747	.041	19	3.040	0
10	2.213	.050	20	3.040	-.053

(a) Foreplate. (b) Top surface.

Figure 13.- Static orifice locations. H = 19.05 cm.

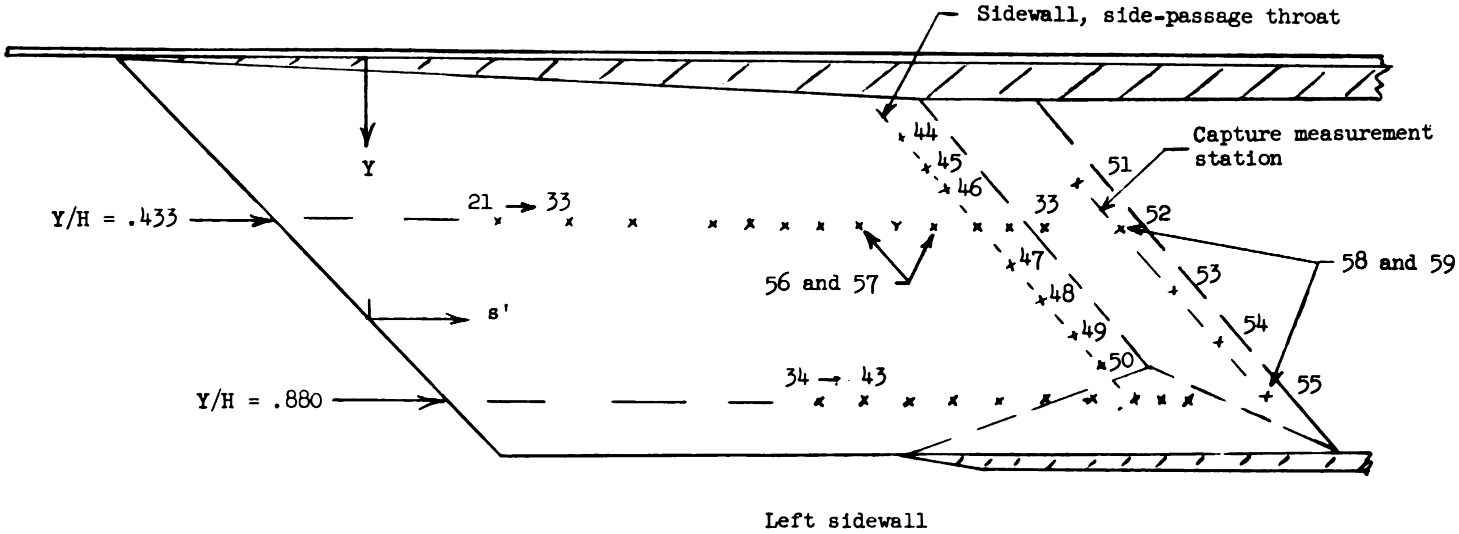

Orifice	s'/H	Y/H
21	.924	.433
22	1.191	.433
23	1.457	.433
24	1.724	.433
25	1.857	.433
26	1.991	.433
27	2.124	.433
28	2.257	.433
29	2.324	.433
30	2.391	.433

Orifice	s'/H	Y/H
31	2.457	.433
32	2.524	.433
33	2.591	.433
34	1.591	.880
35	1.724	.880
36	1.857	.880
37	1.991	.880
38	2.124	.880
39	2.257	.880
40	2.391	.880

Orifice	s'/H	Y/H
41	2.457	.880
42	2.524	.880
43	2.591	.433
44	2.457	.166
45	2.457	.255
46	2.457	.344
47	2.497	.522
48	2.457	.612
49	2.457	.701
50	2.457	.790

Orifice	s'/H	Y/H
51	2.907	.284
52	2.907	.433
53	2.907	.582
54	2.907	.731
55	2.907	.880
*56	2.257	.433
*57	2.391	.433
*58	2.907	.433
*59	2.907	.880

*Right sidewall

(c) Sidewall.

Figure 13.- Continued.

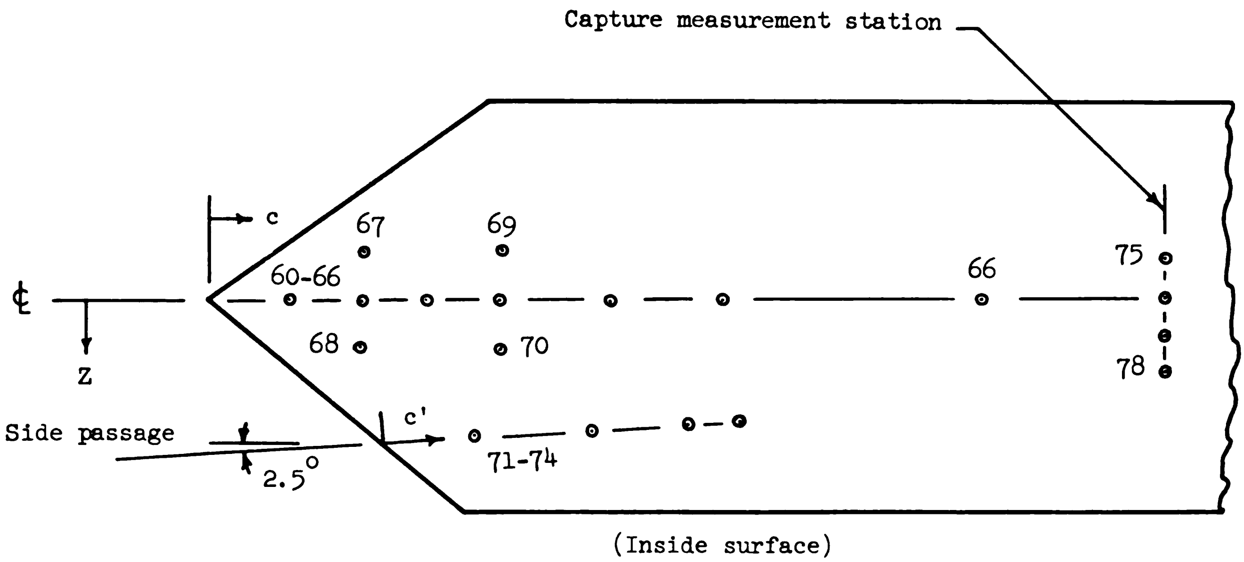

Orifice	c/H	Z/H
60	.093	0
61	.160	0
62	.227	0
63	.293	0
64	.427	0
65	.560	0
66	.827	0
67	.160	-.056
68	.160	.056
69	.293	-.056
70	.293	.056

Orifice	c'/H	Z/H
71	.087	.163
72	.220	.157
73	.353	.151
74	.420	.149
Orifice	c /H	Z/H
75	1.080	-.053
76	1.080	0
77	1.080	.053
78	1.080	.107

(d) Cowl.

Figure 13.- Continued.

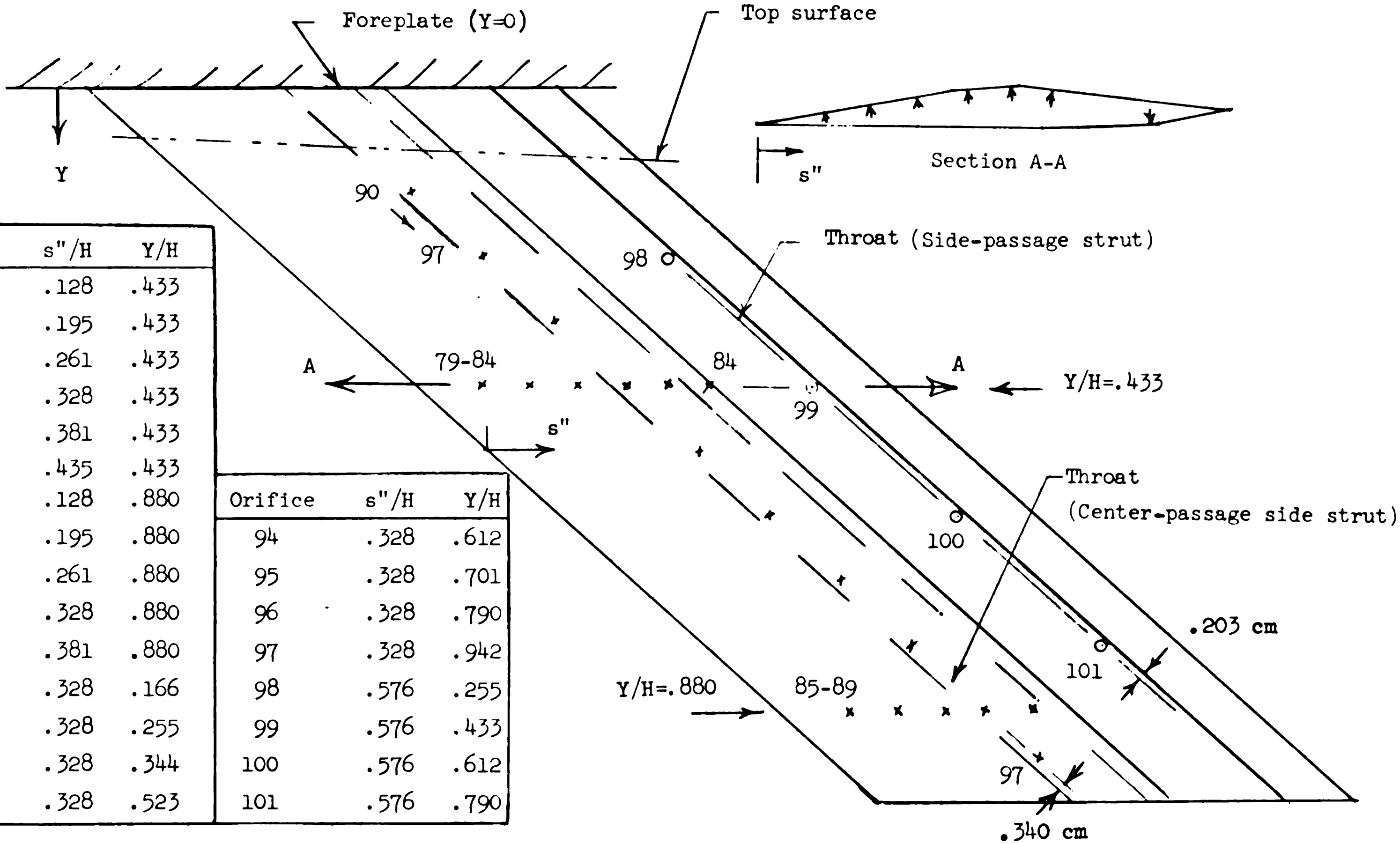

Orifice	s"/H	Y/H
79	.128	.433
80	.195	.433
81	.261	.433
82	.328	.433
83	.381	.433
84	.435	.433
85	.128	.880
86	.195	.880
87	.261	.880
88	.328	.880
89	.381	.880
90	.328	.166
91	.328	.255
92	.328	.344
93	.328	.523

Orifice	s"/H	Y/H
94	.328	.612
95	.328	.701
96	.328	.790
97	.328	.942
98	.576	.255
99	.576	.433
100	.576	.612
101	.576	.790

(e) Left side strut.

Figure 13.- Continued.

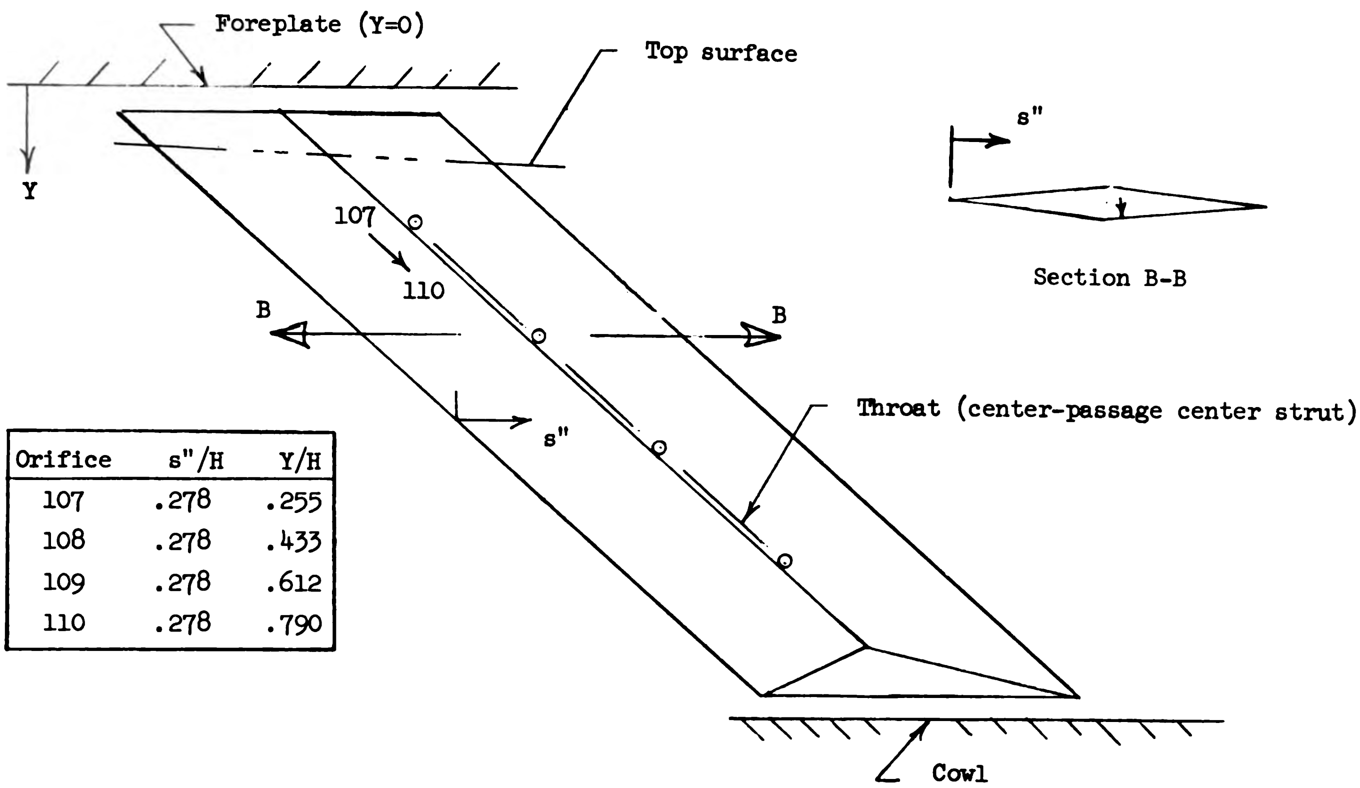

Orifice	s"/H	Y/H
107	.278	.255
108	.278	.433
109	.278	.612
110	.278	.790

(f) Center strut.

Figure 13.- Continued.

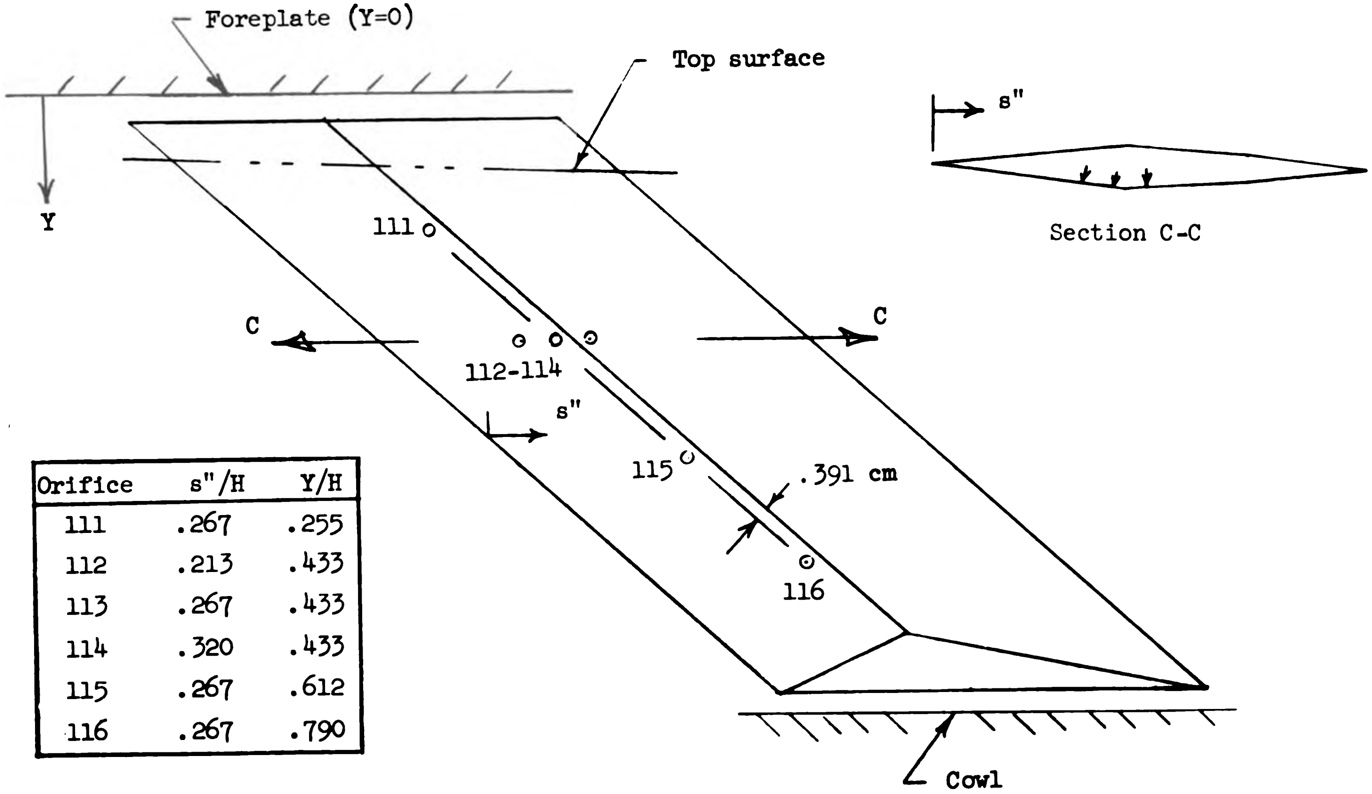

Orifice	s"/H	Y/H
111	.267	.255
112	.213	.433
113	.267	.433
114	.320	.433
115	.267	.612
116	.267	.790

(g) Large center strut.

Figure 13.- Concluded.

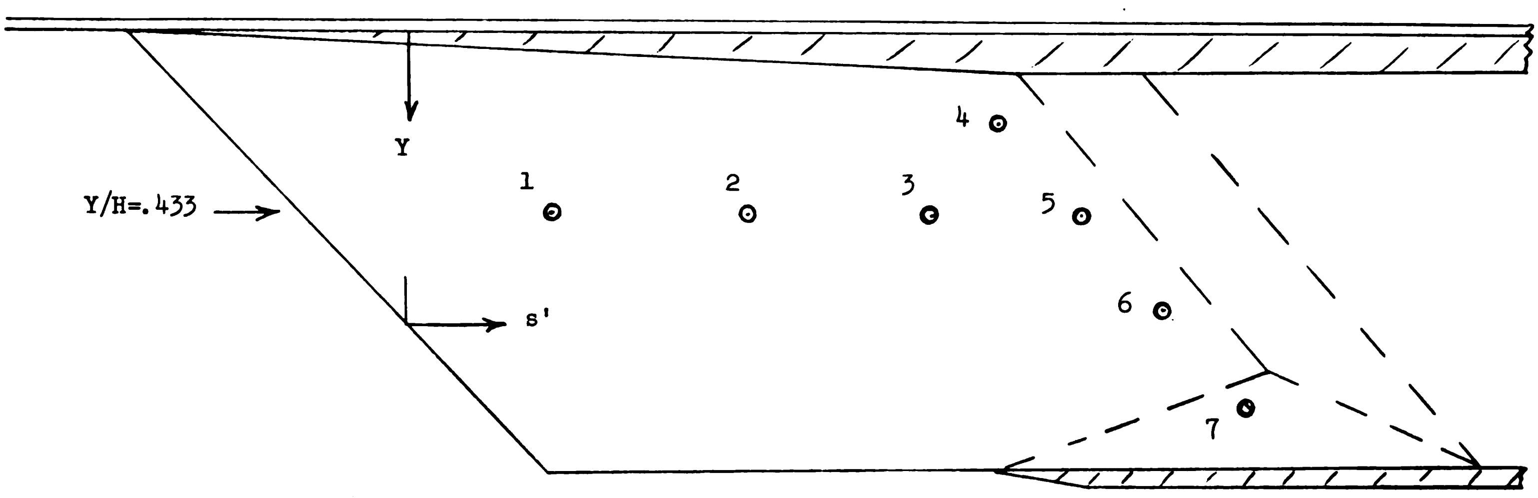

Thermocouple	s'/H	Y/H
1	.924	.433
2	1.591	.433
3	2.057	.433
4	2.457	.210
5	2.457	.433
6	2.457	.656
7	2.457	.880

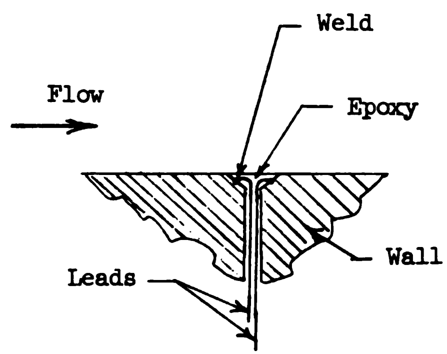

Thermocouple installation

Figure 14.- Thermocouple locations. H = 19.05 cm; 24-gage iron-constantan.

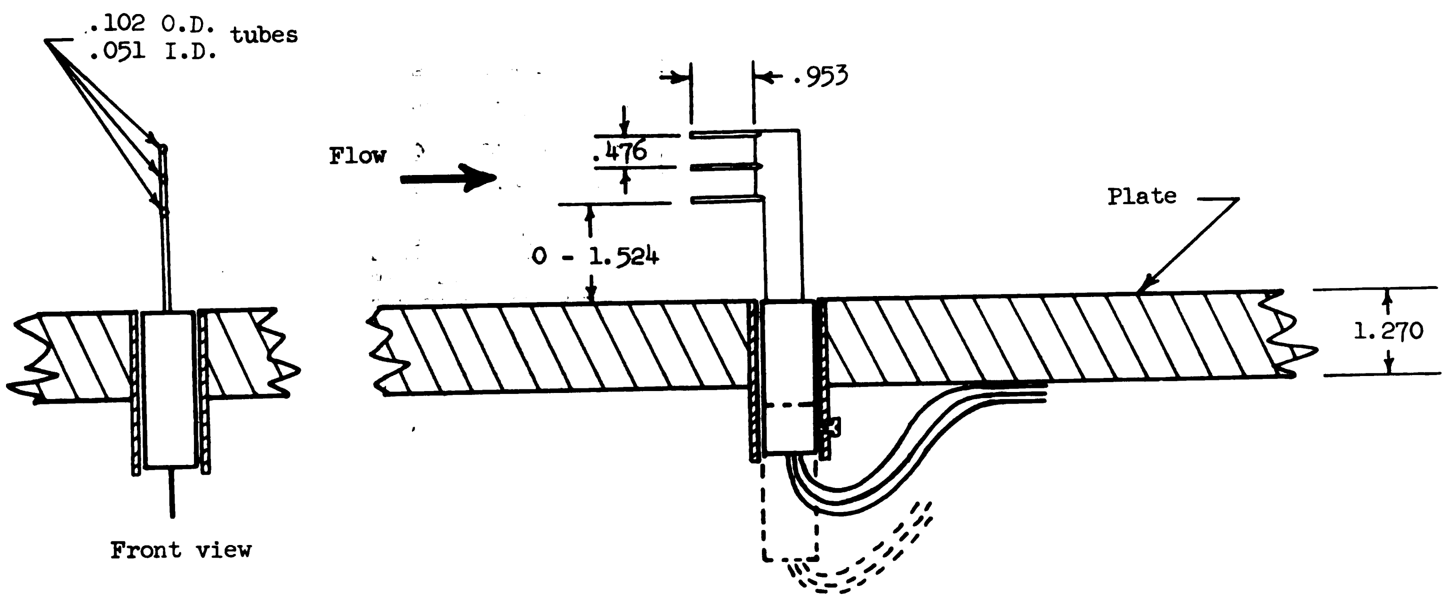

Figure 15.- Foreplate boundary-layer probe. All dimensions are in centimeters.

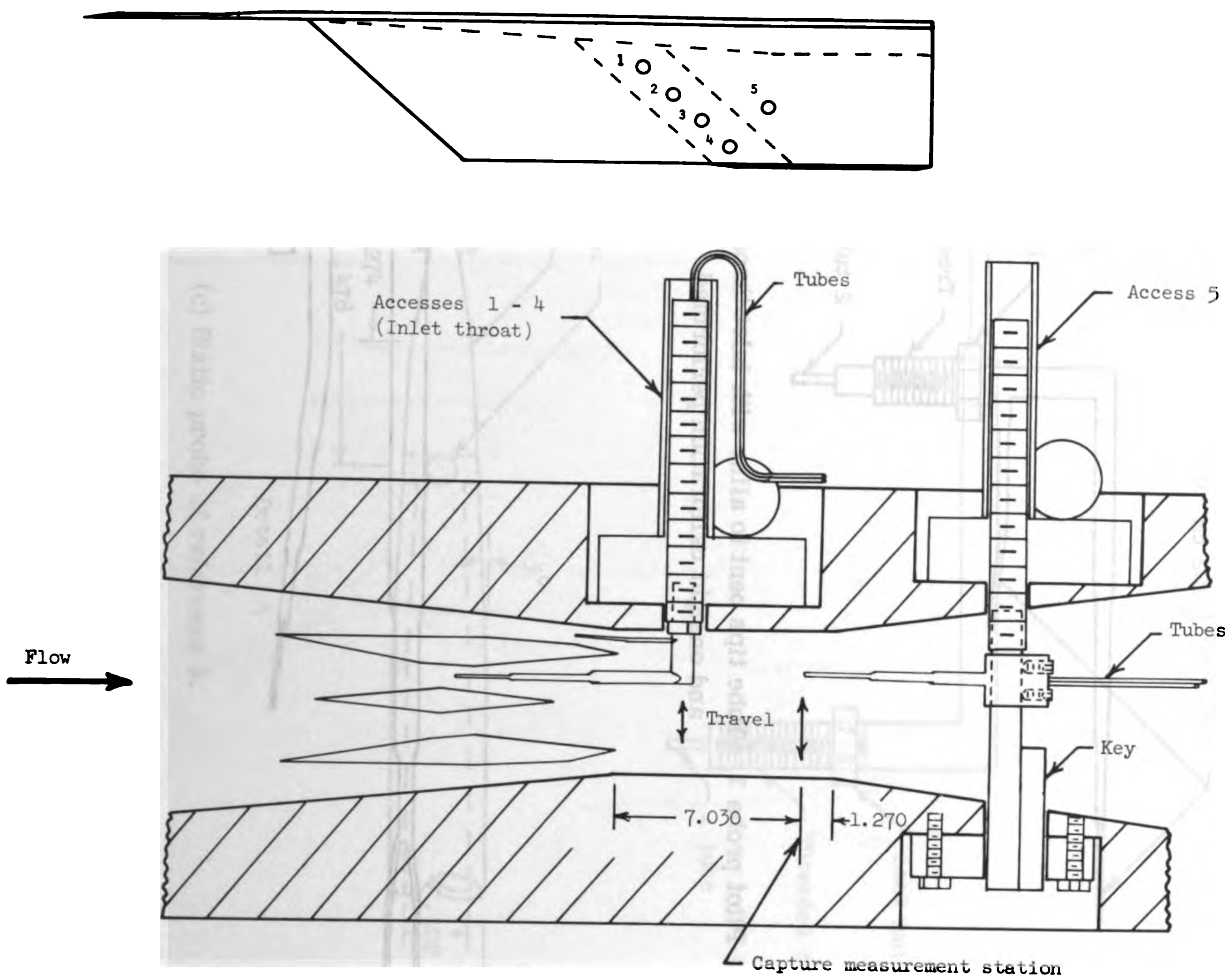

Figure 16.- Survey probe mechanism and access locations. All dimensions are in centimeters.

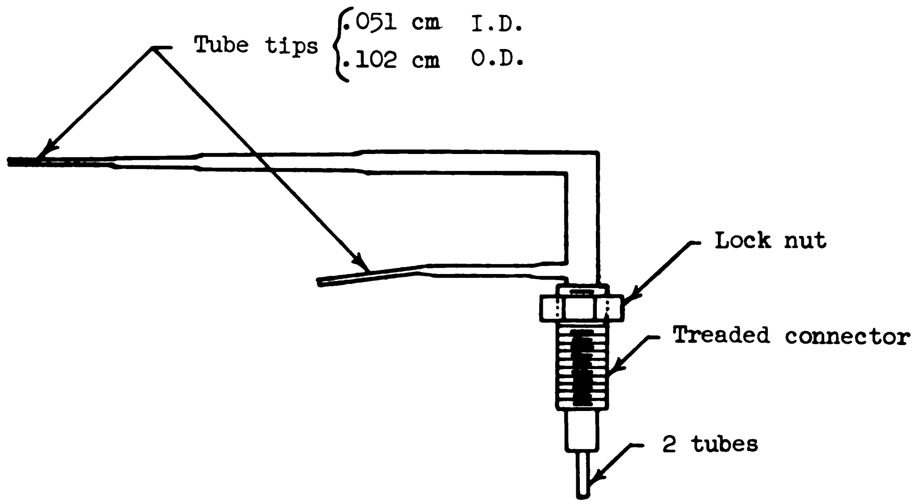

(a) Pitot probe 1. Tube tips bent to aline with inlet throats for each test, and onsight calibration performed.

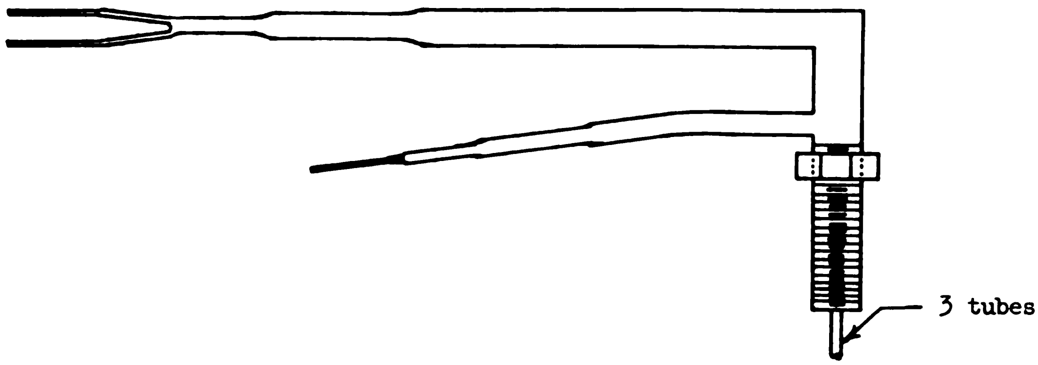

(b) Pitot probe 2. This probe used with modified strut configuration which had wider gap in center passage.

Figure 17.- Throat survey probes. All dimensions are in centimeters.

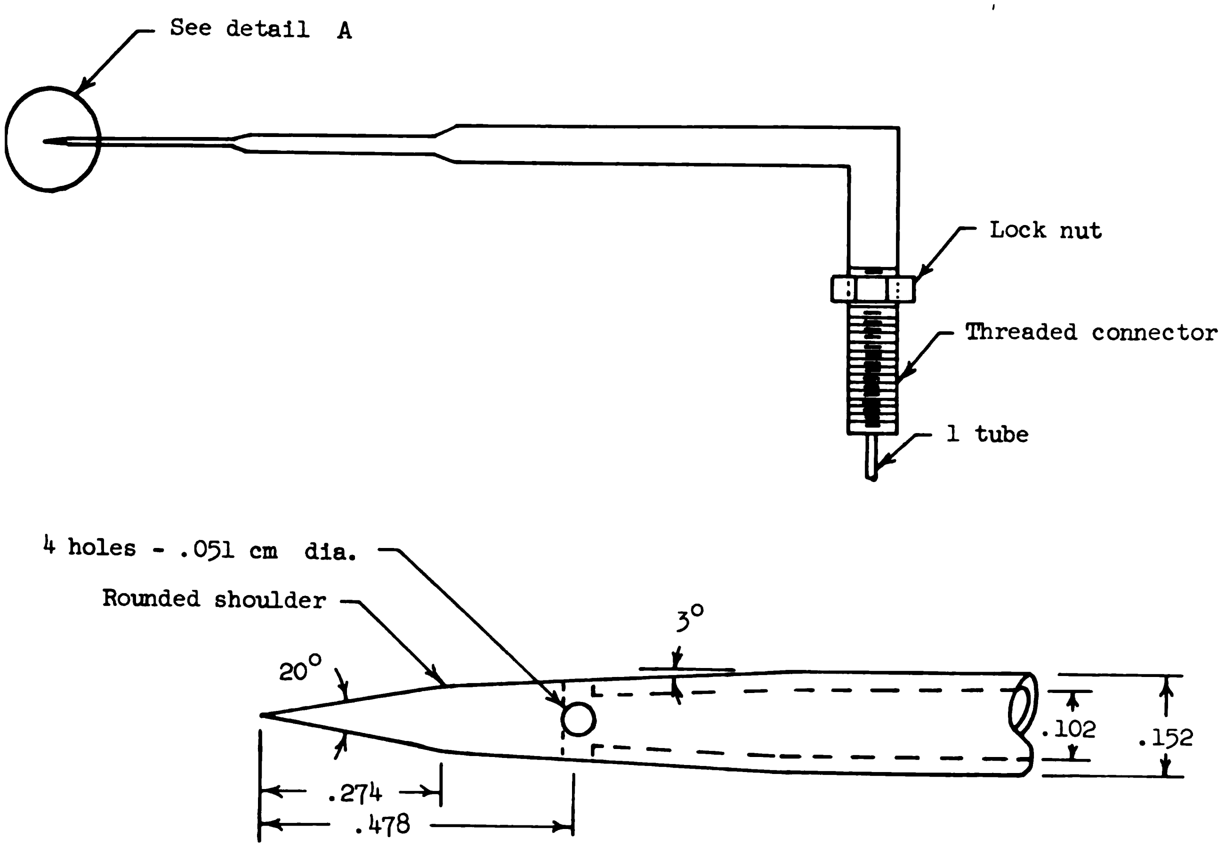

Detail A

(c) Static probe of reference 9.

Figure 17.- Concluded.

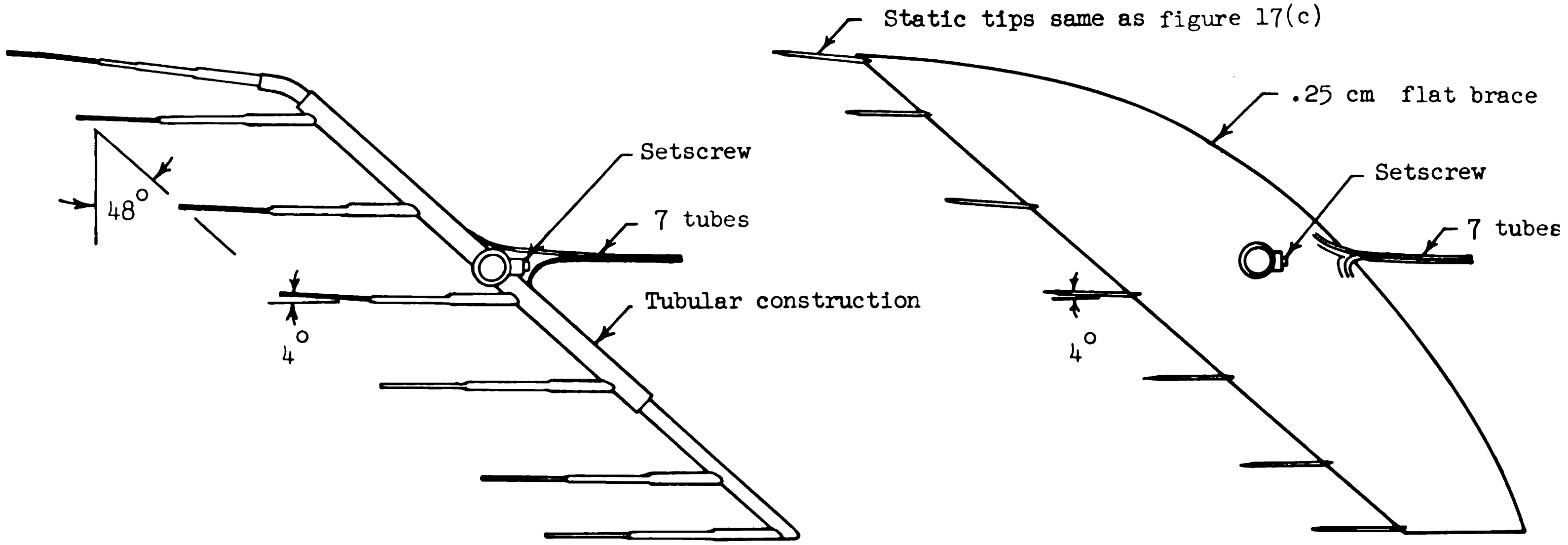

(a) Pitot probe.

(b) Static probes.

Figure 18.- Capture measurement survey probes.

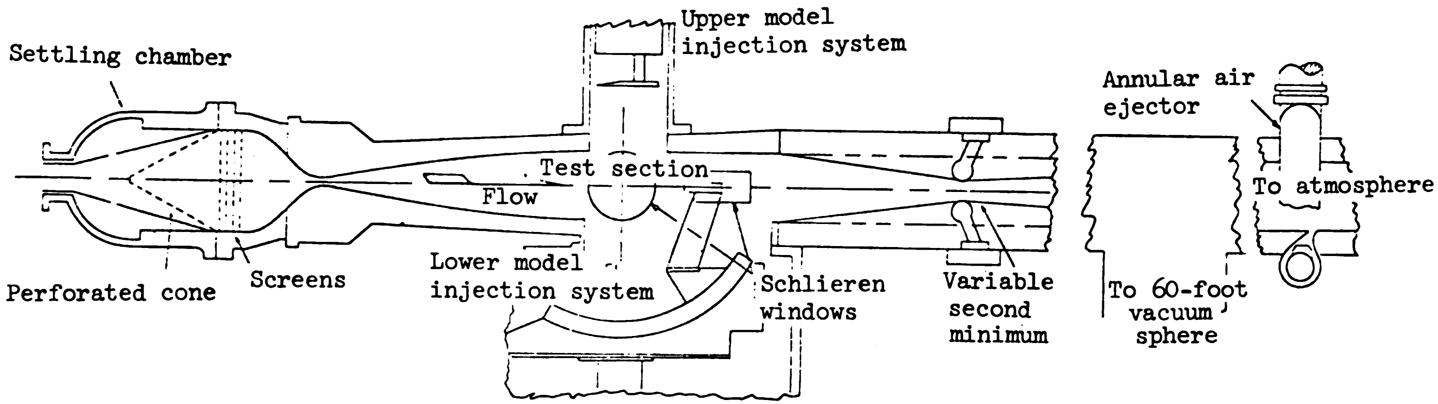

Figure 19.- Langley 20-inch Mach 6 test facility. (See ref. 12.)

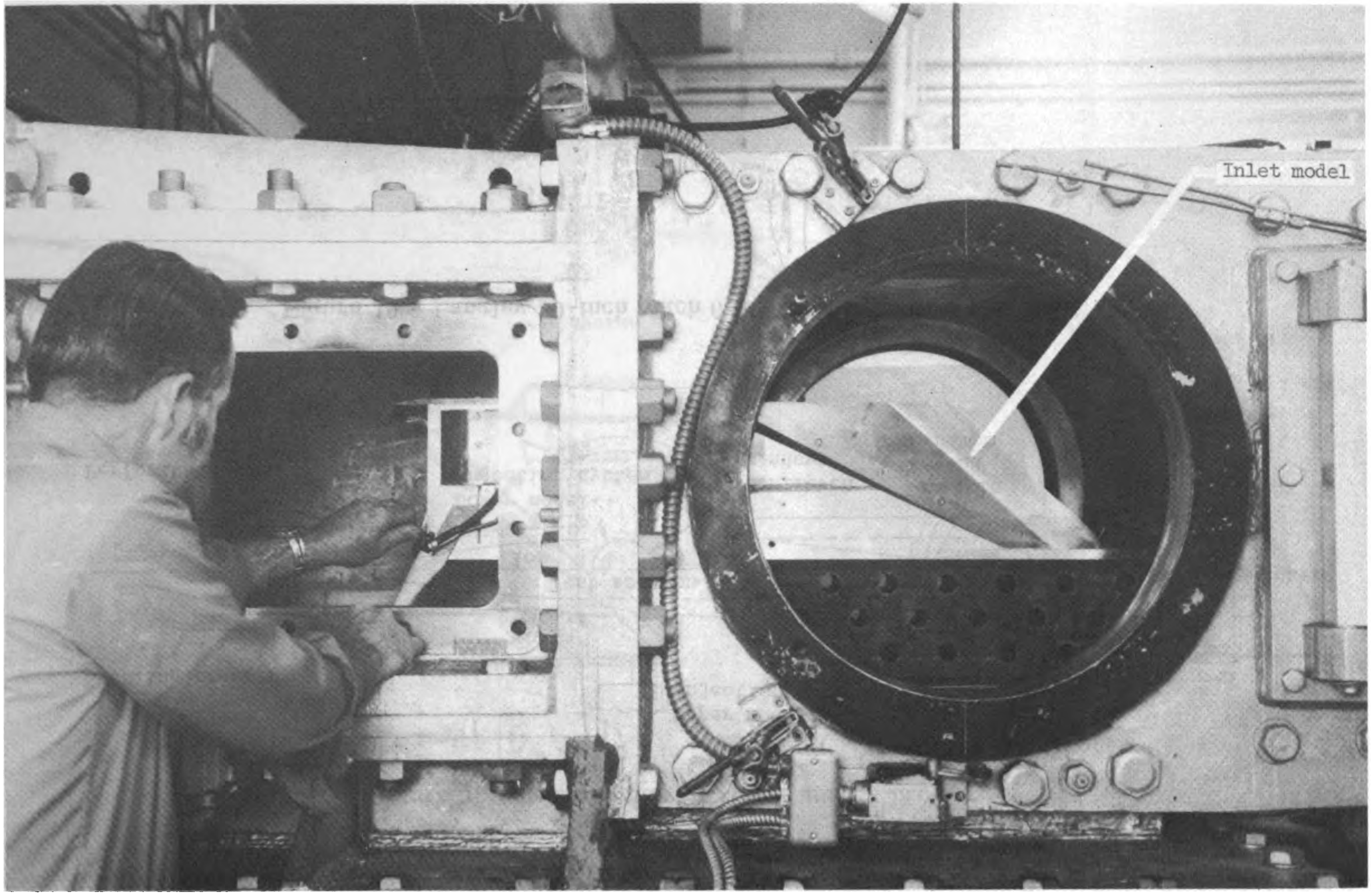

L-75-152

Figure 20.- Inlet model mounted in test facility.

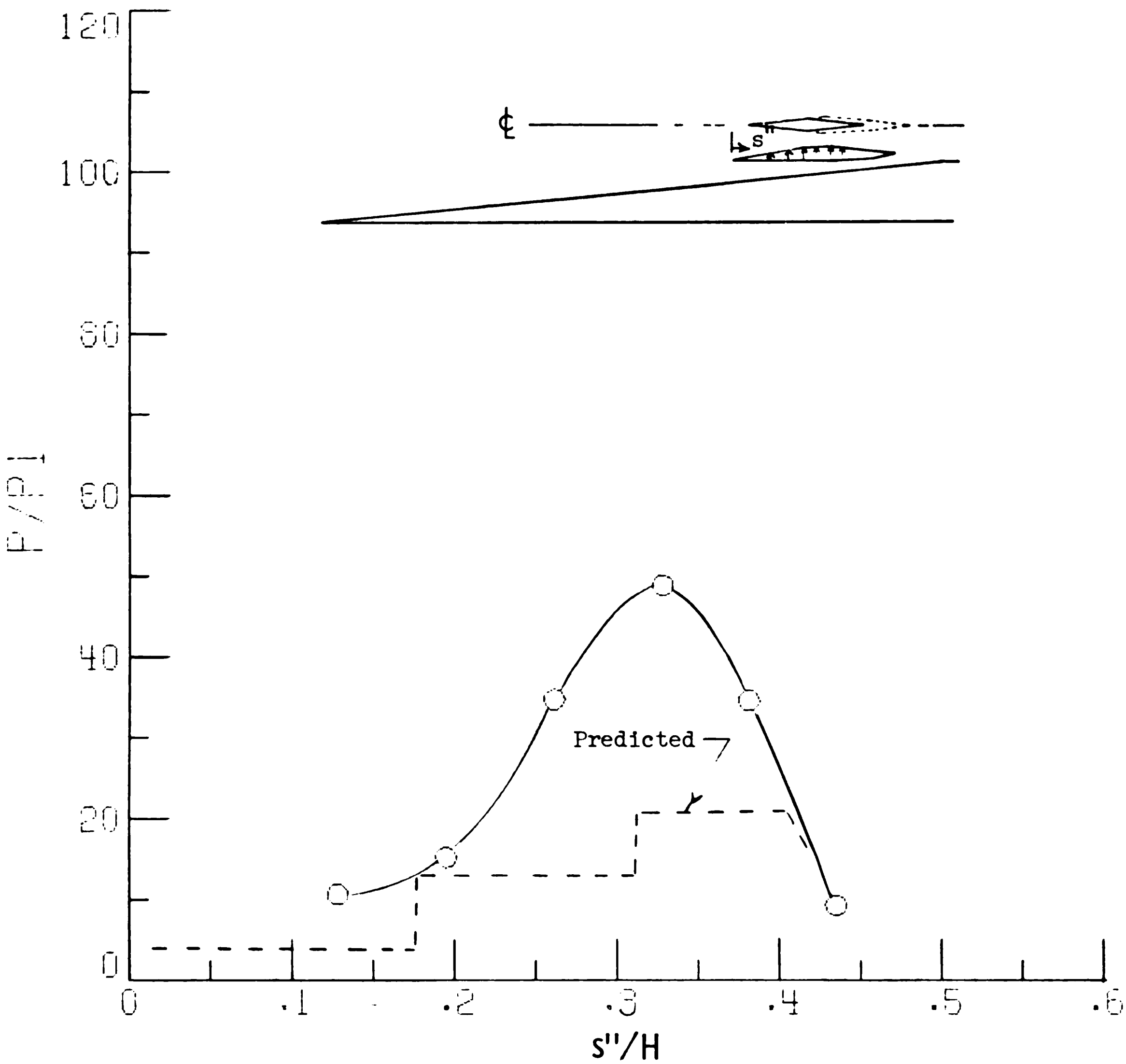

(a) Side strut; Y/H = 0.43.

Figure 21.- Center-passage static-pressure distribution.

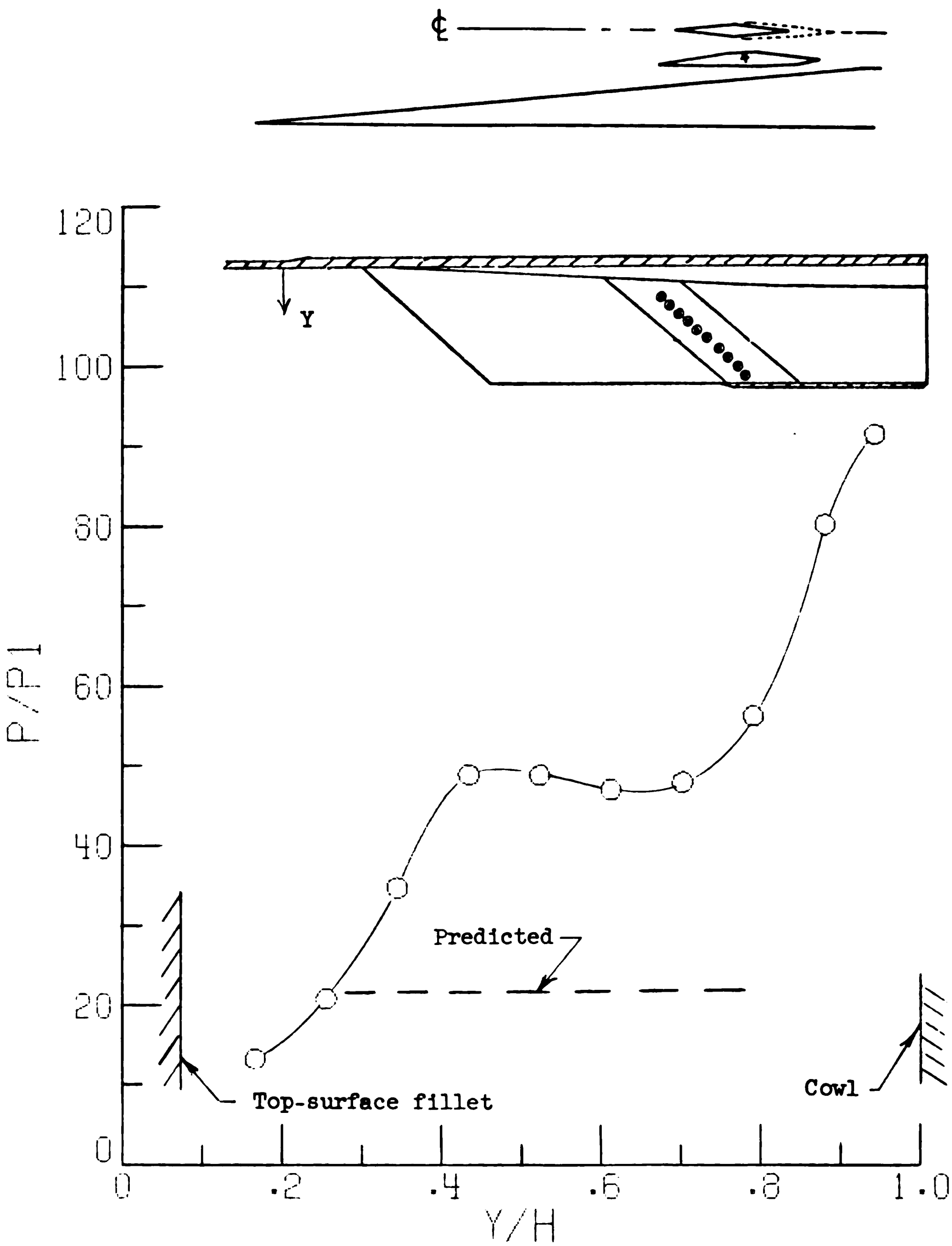

(b) Side strut; throat.

Figure 21.- Concluded.

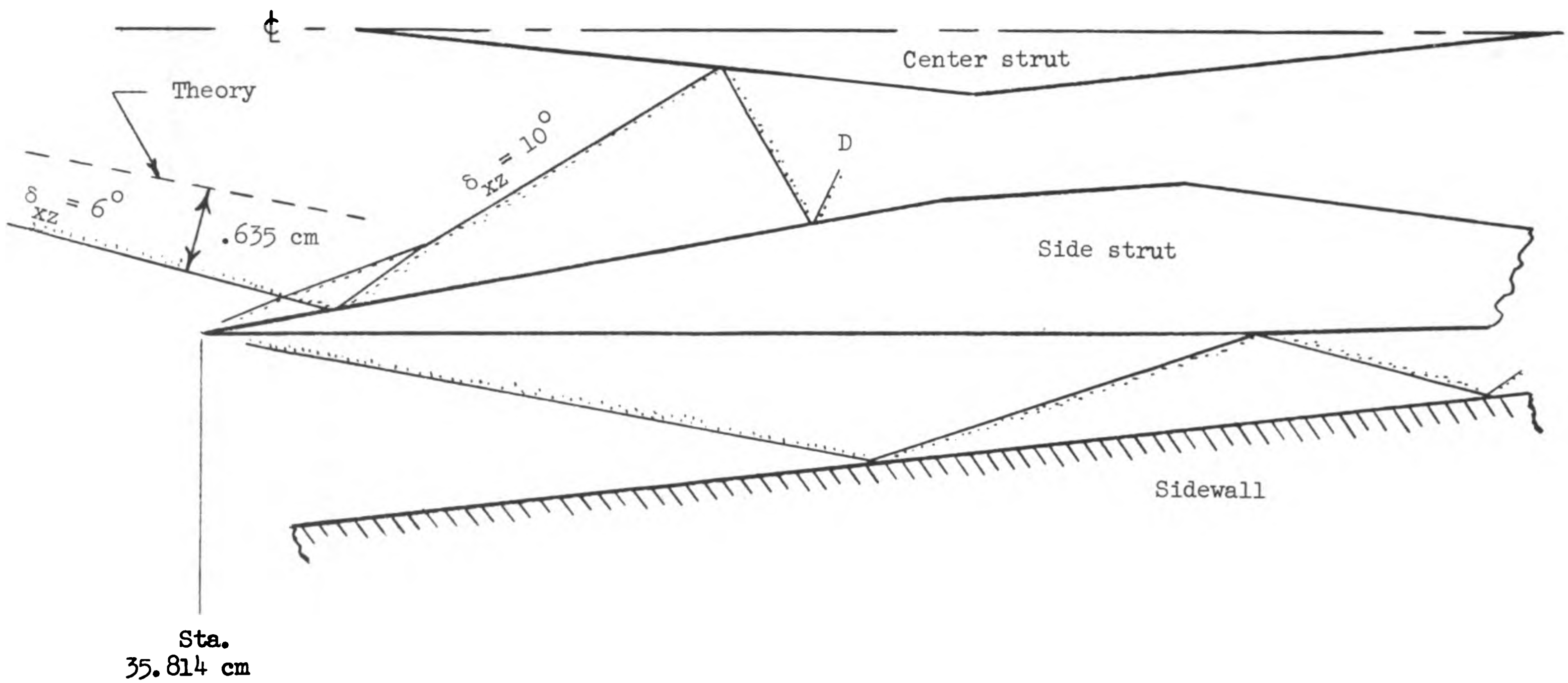

Figure 22.- Effect of shifted shock wave on center passage (xz-plane).

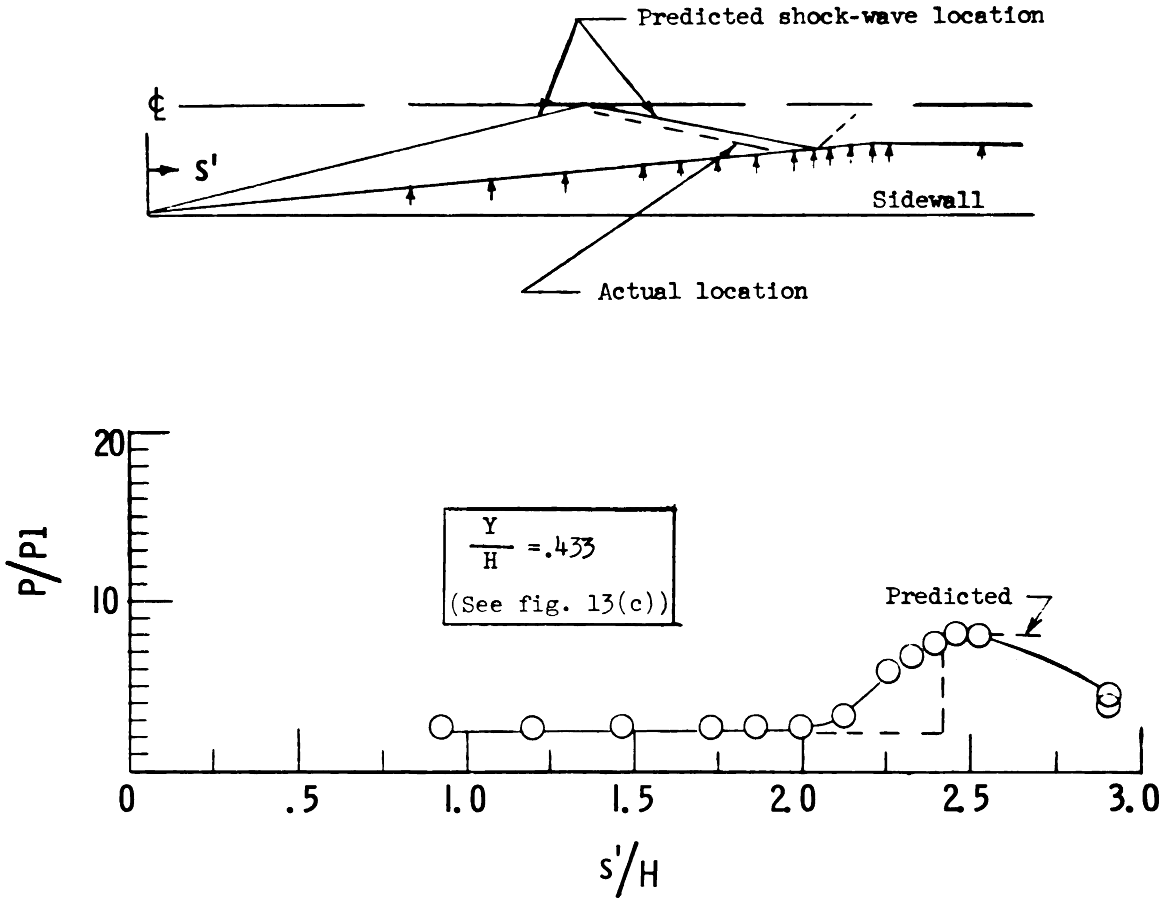

Figure 23.- Sidewall static-pressure distribution. No struts.

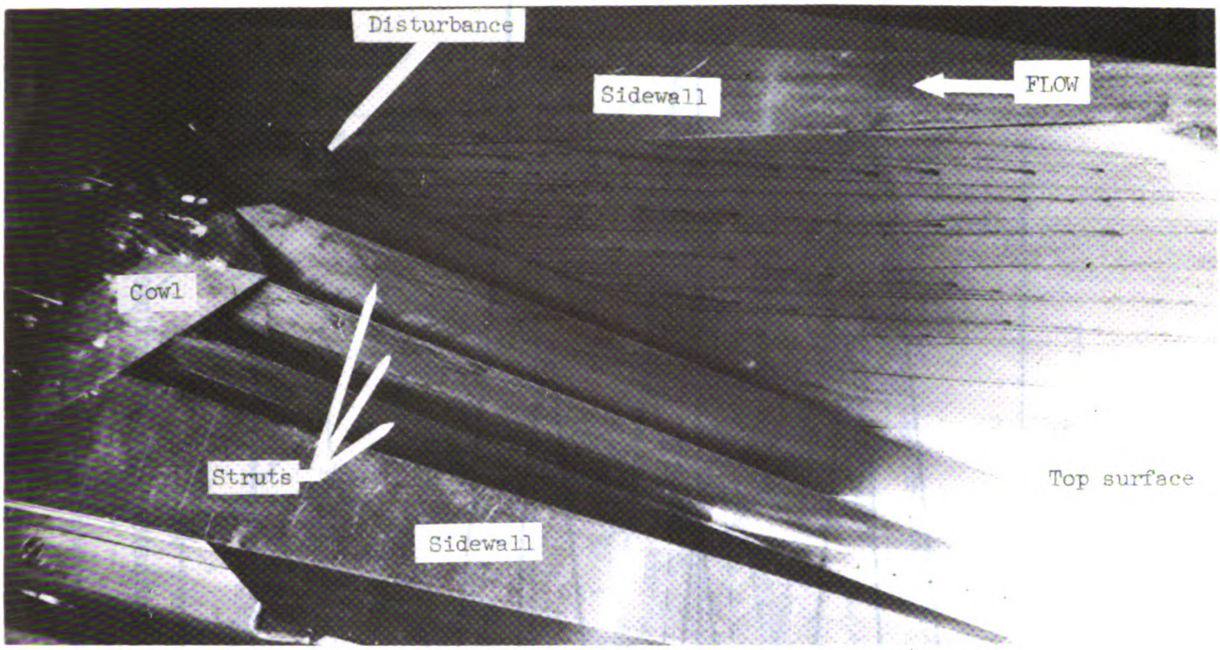

(a) Three-strut configuration (Capture = 81 percent).

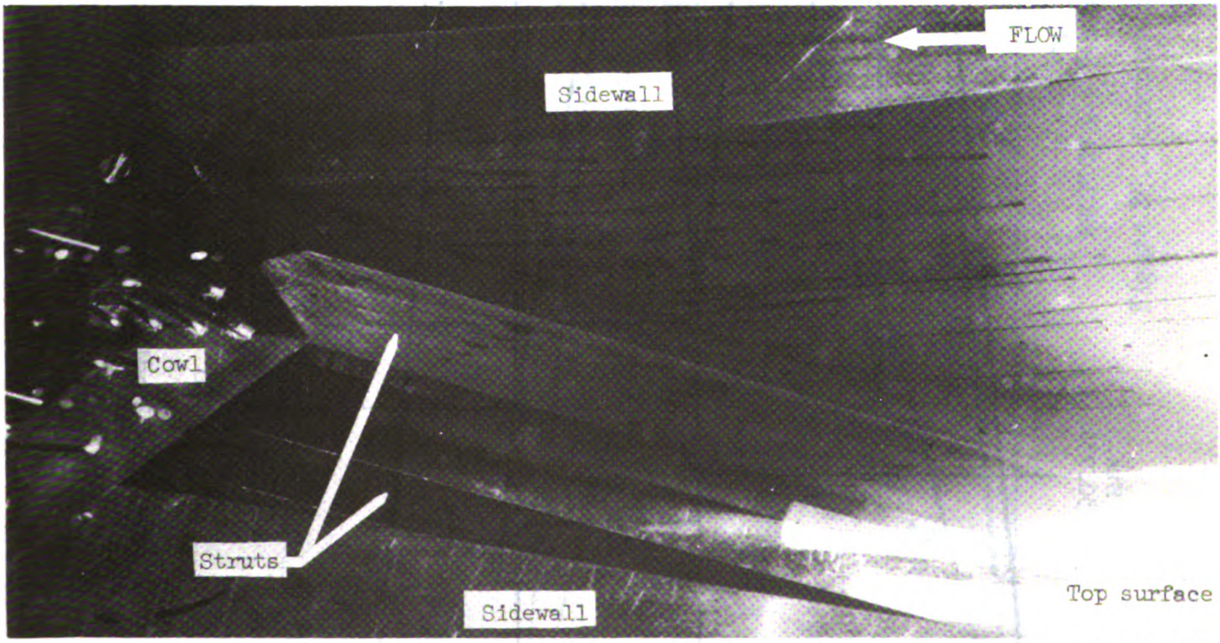

L-75-153

(b) No center strut (Capture = 92 percent).

Figure 24.- Oil-streak photograph.

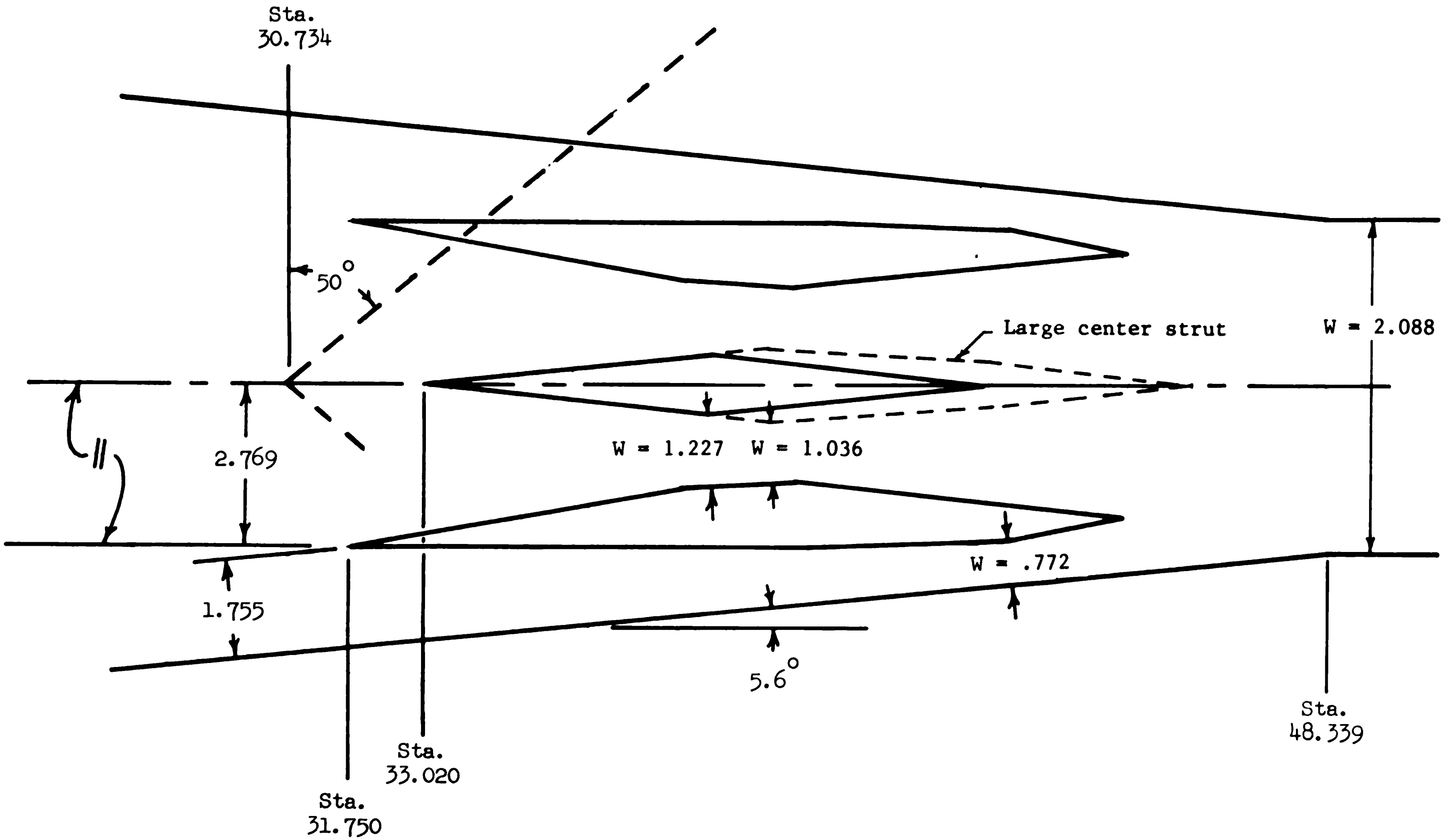

Figure 25.- Modified strut positions (xz-plane). All dimensions are in centimeters.

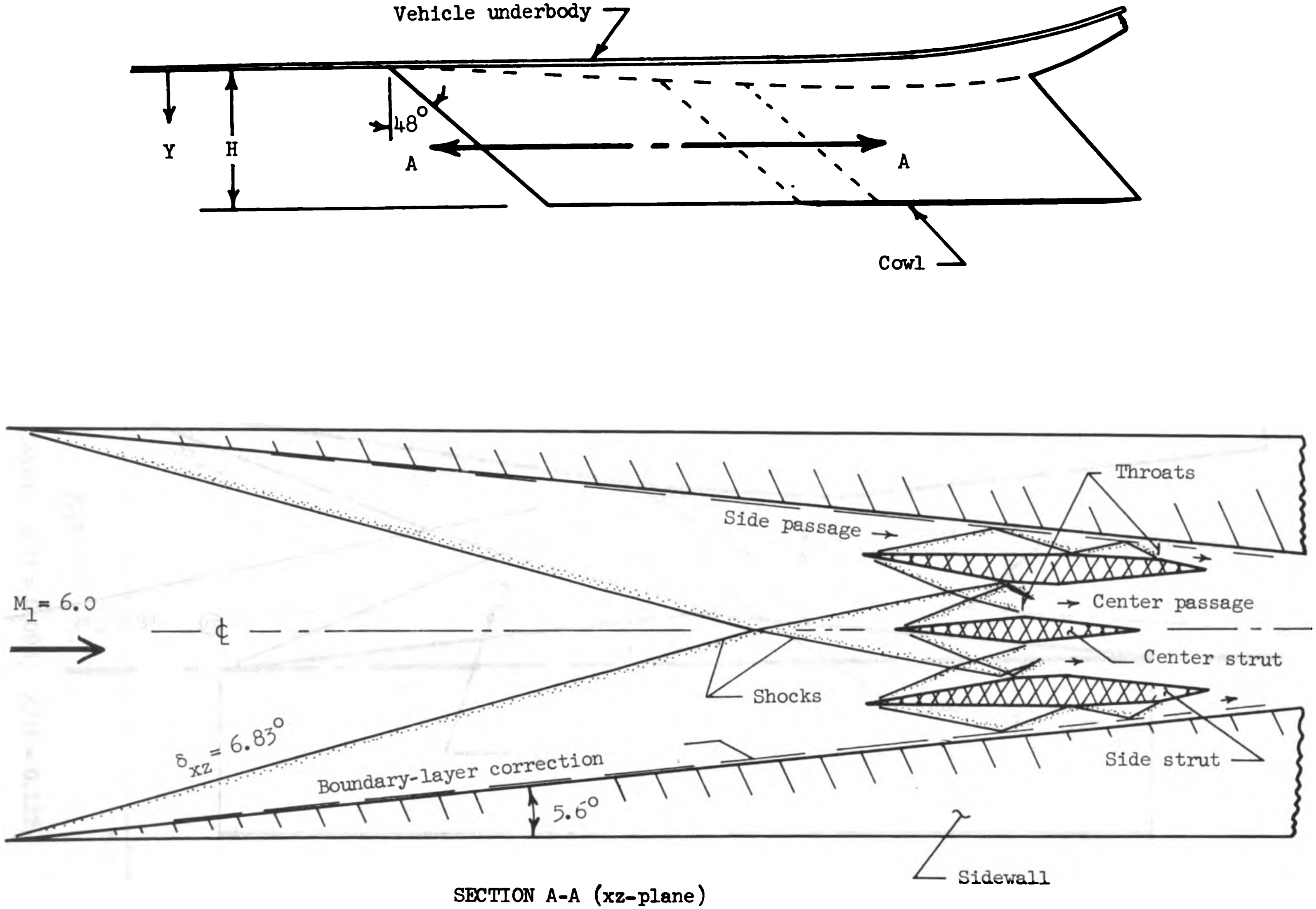

Figure 26.- Corrected Mach 6 shock diagram.

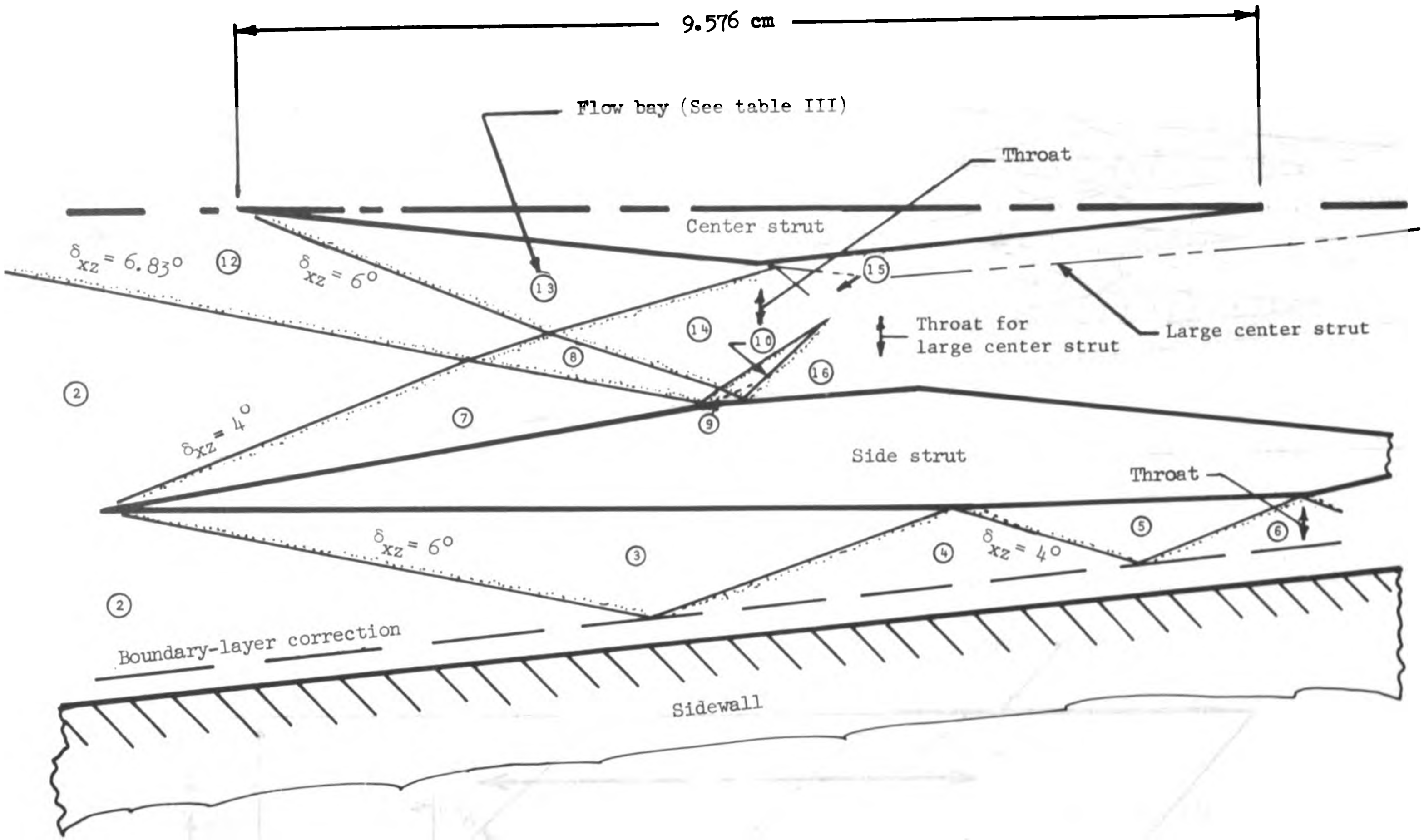

Figure 27.- Corrected shock-wave detail in vicinity of struts. $M_1 = 6.0$.

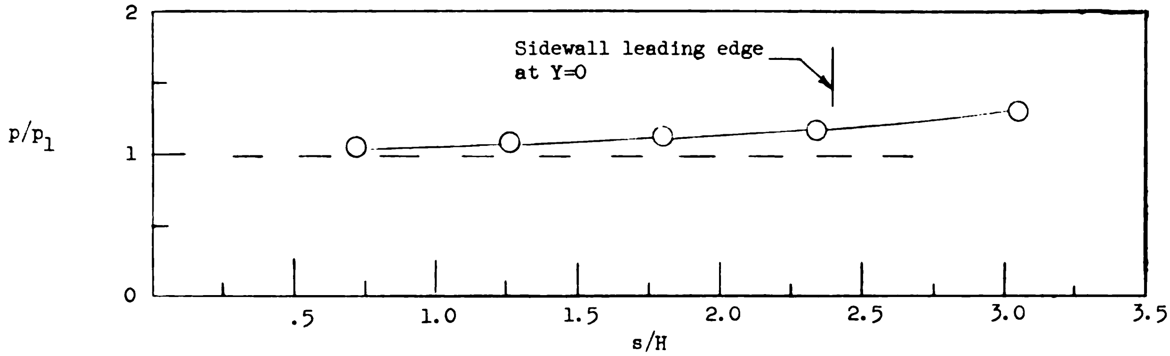

(a) Static pressure on foreplate. Z/H = 0.

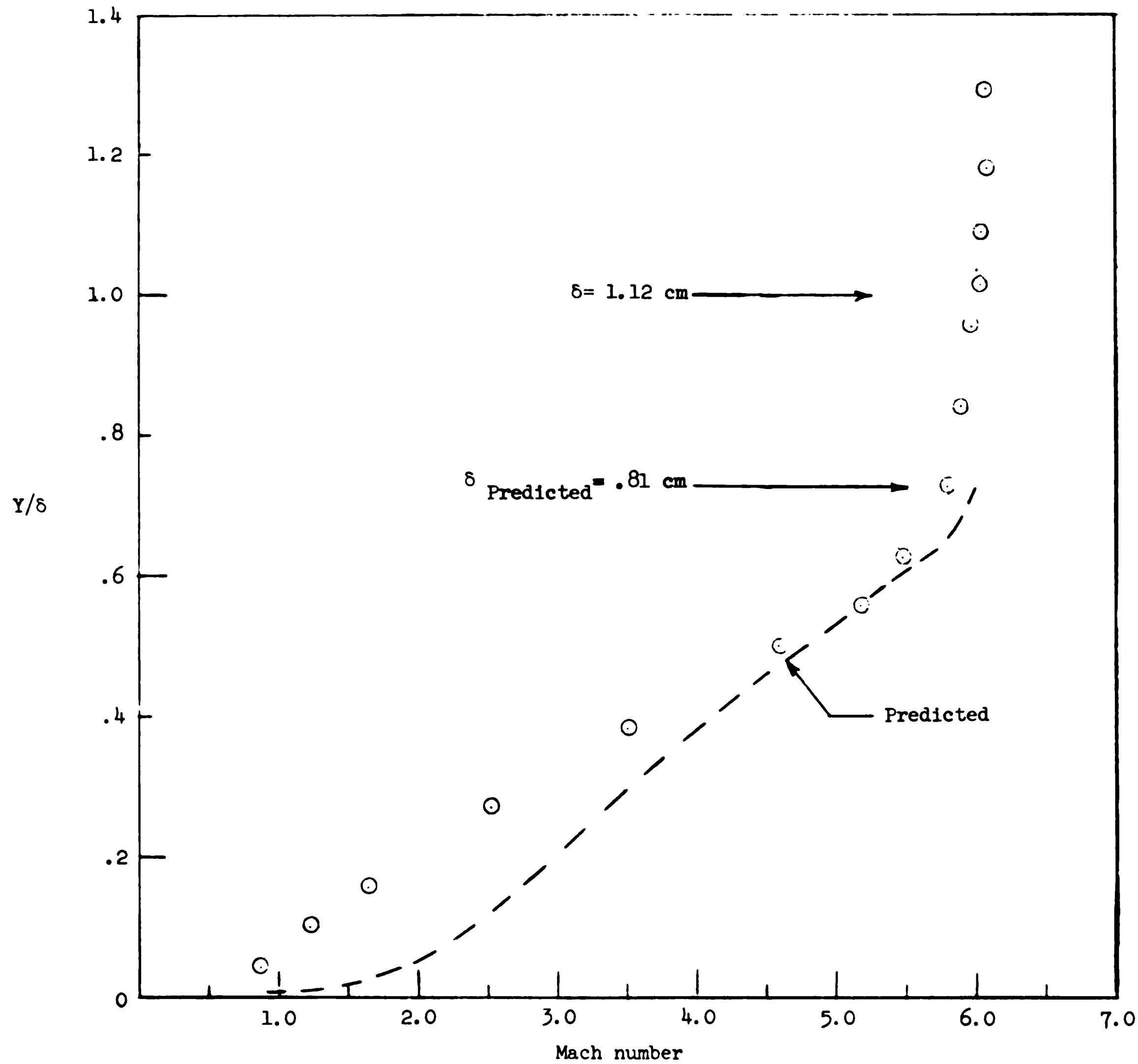

(b) Foreplate boundary layer. s/H = 6.096; Z/H = 0.133.

Figure 28.- Foreplate conditions.

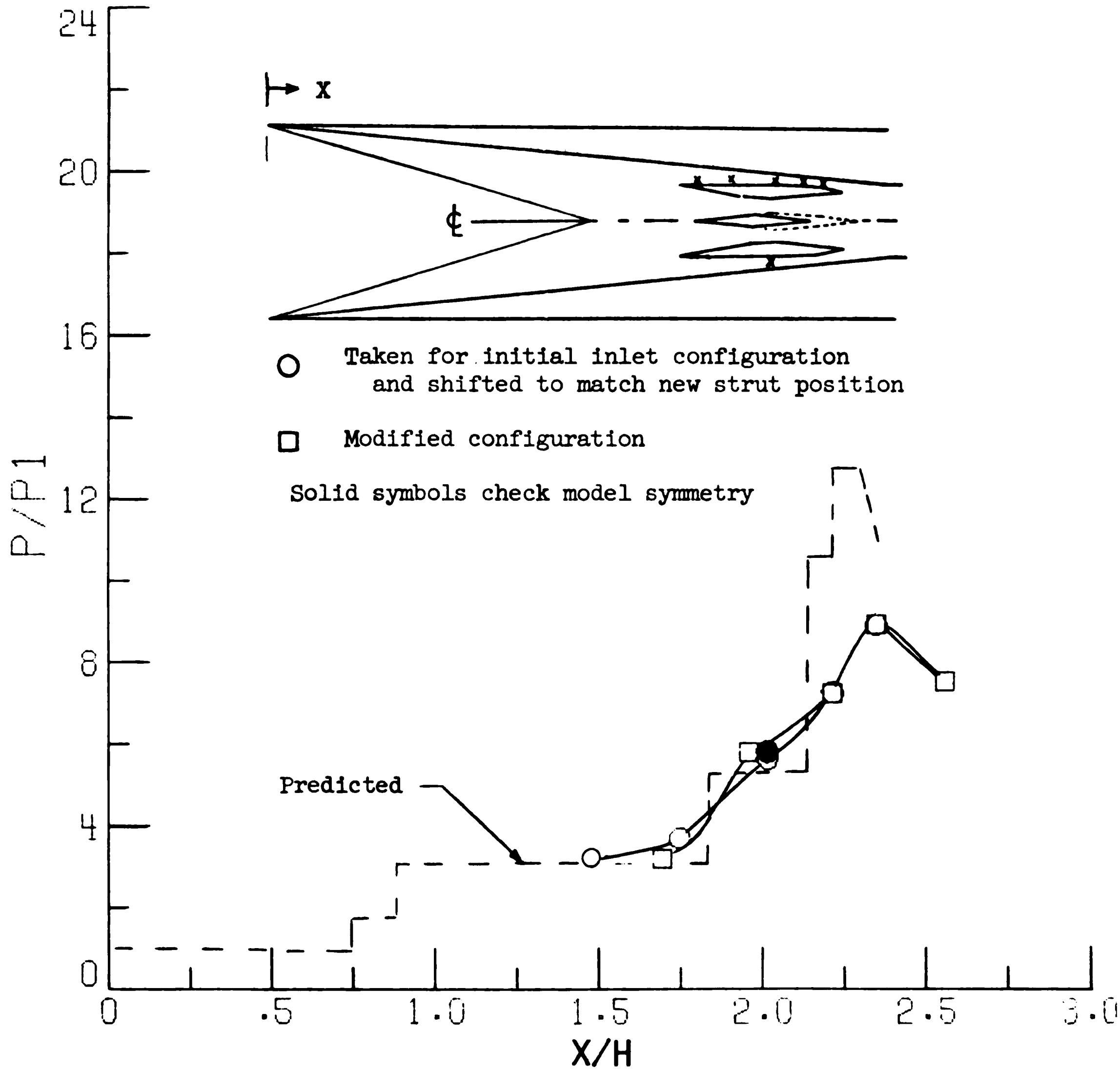

Figure 29.- Static-pressure distribution. Top surface (side passage).

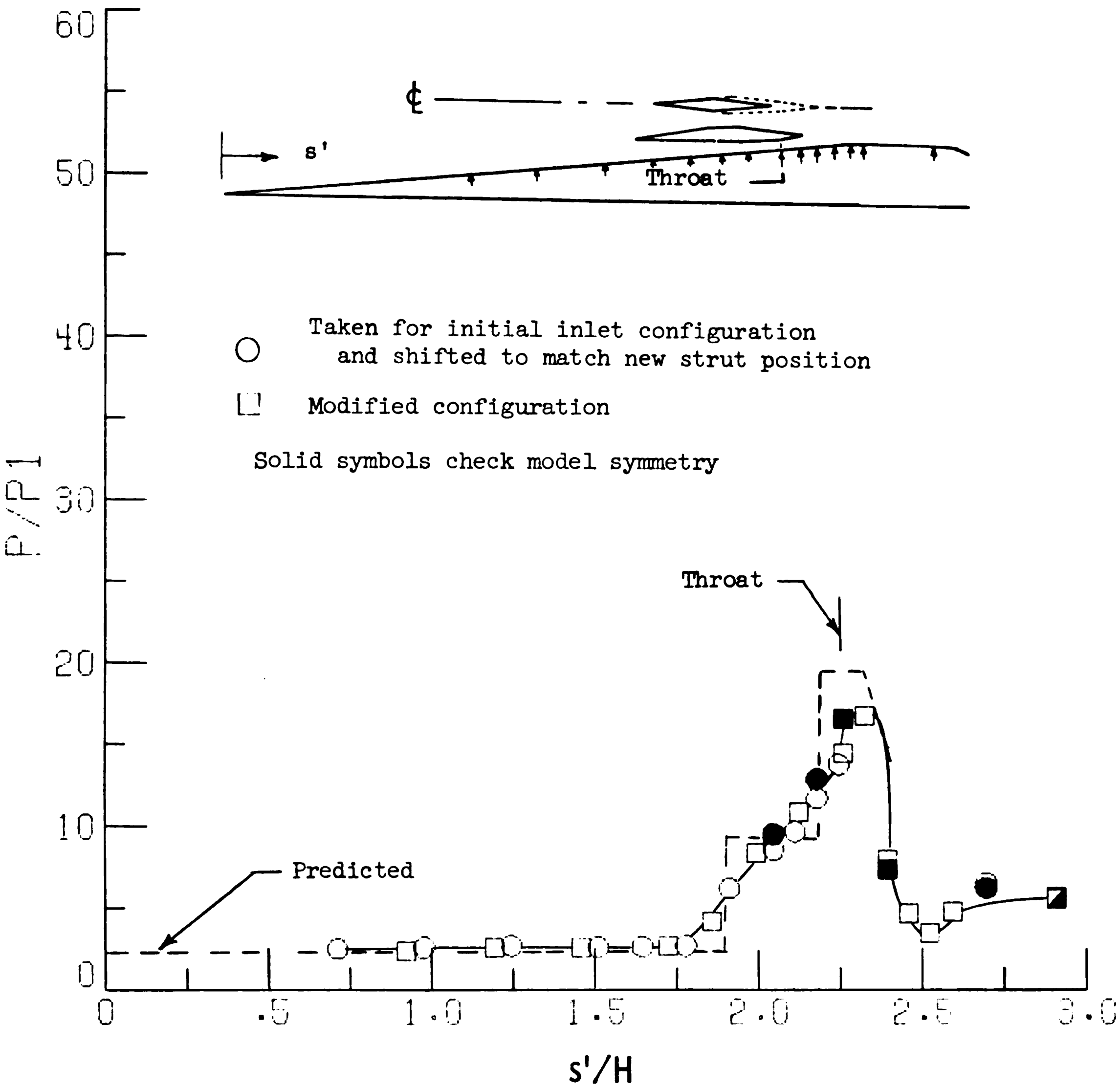

Figure 30.- Static-pressure distribution. Sidewall; Y/H = 0.43.

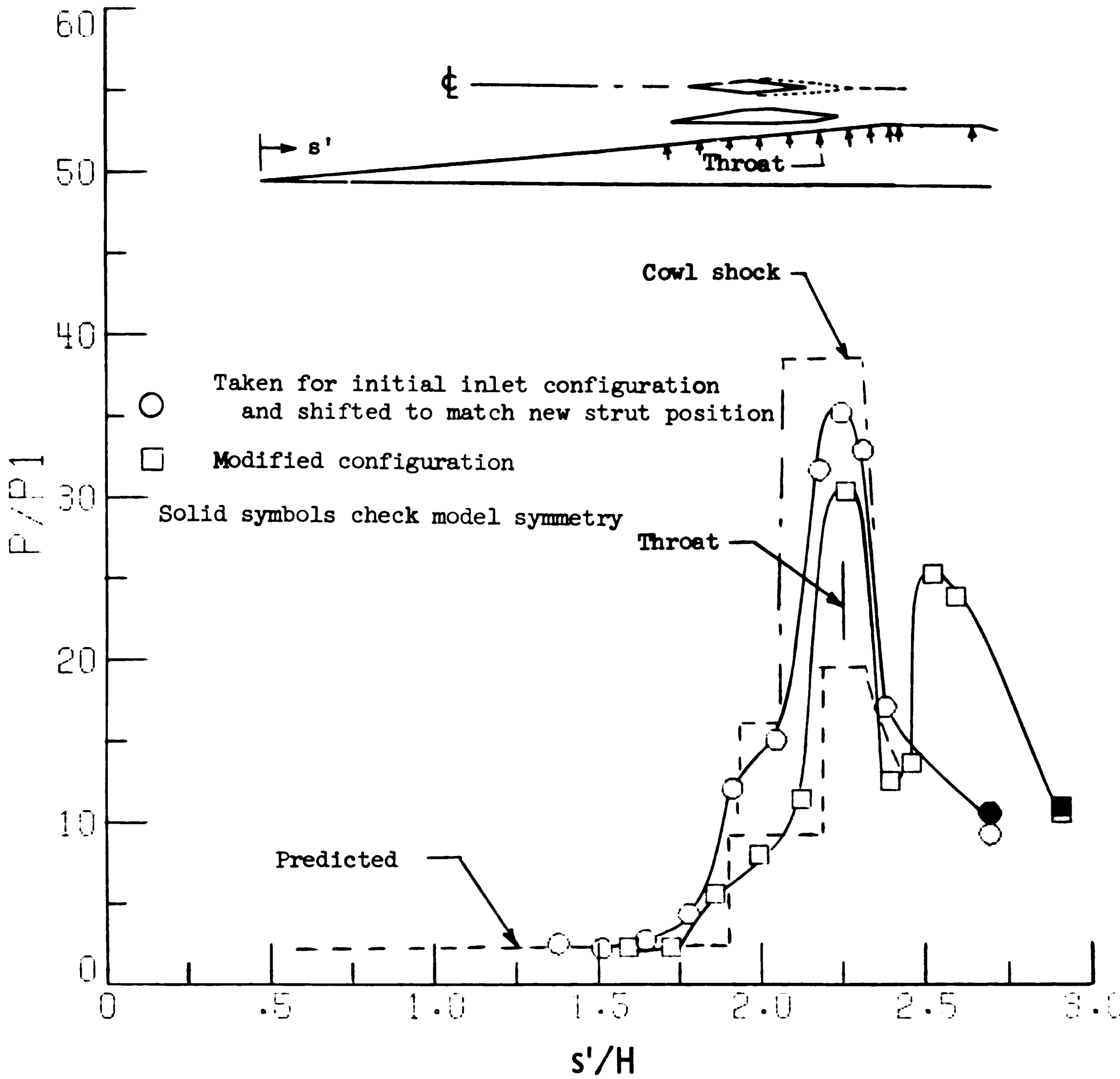

Figure 31.- Static-pressure distribution. Sidewall; Y/H = 0.88.

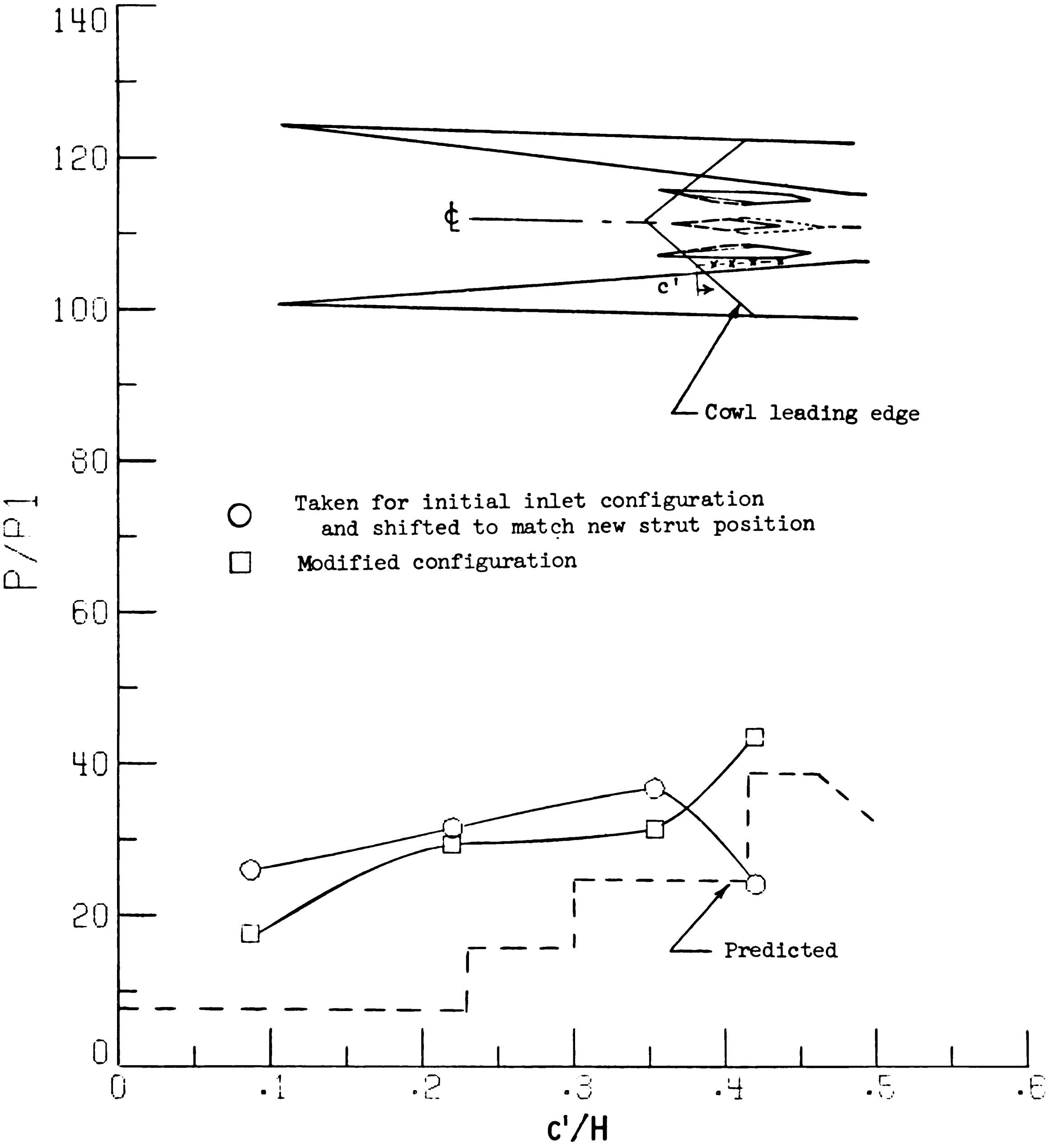

Figure 32. - Static-pressure distribution cowl. Side passage.

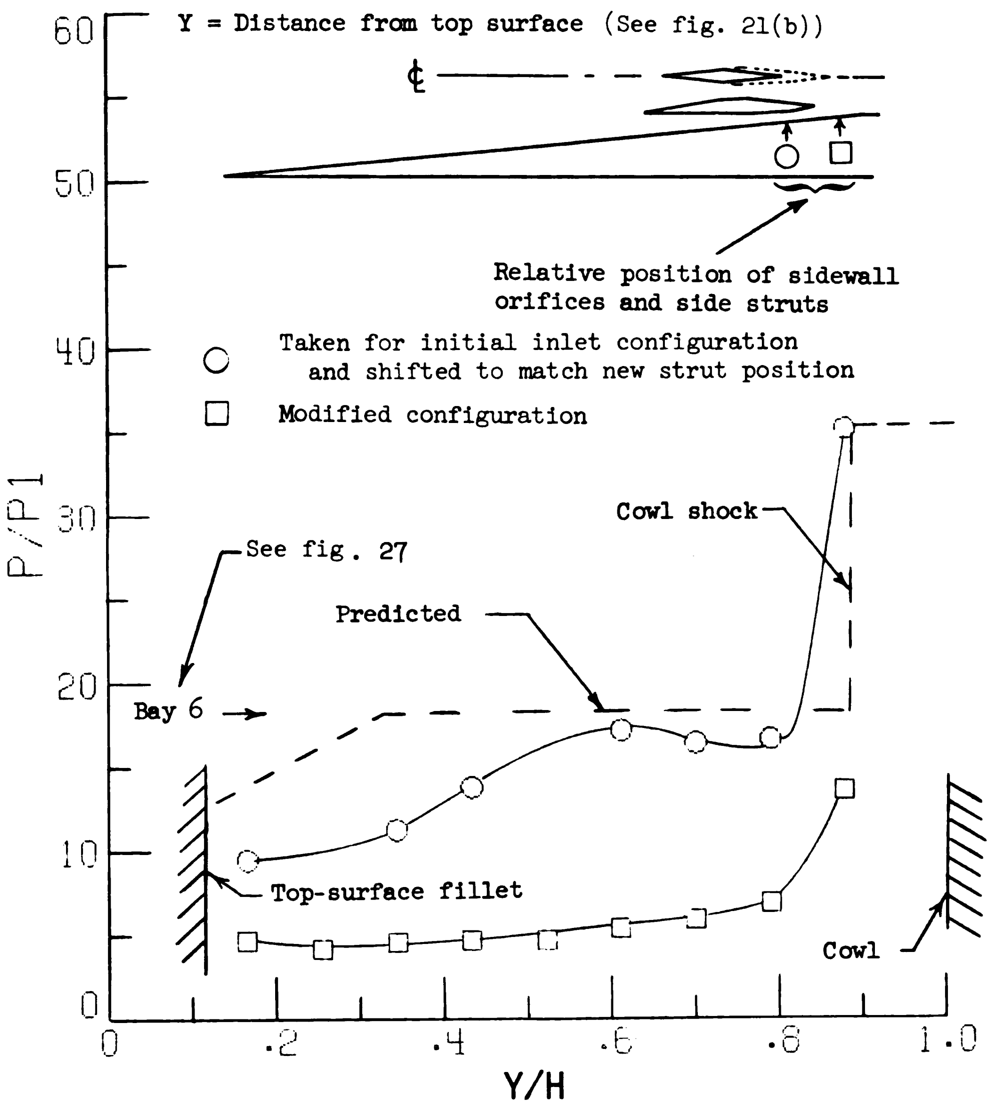

(a) Sidewall.

Figure 33.- Static-pressure distribution. Side passage throat.

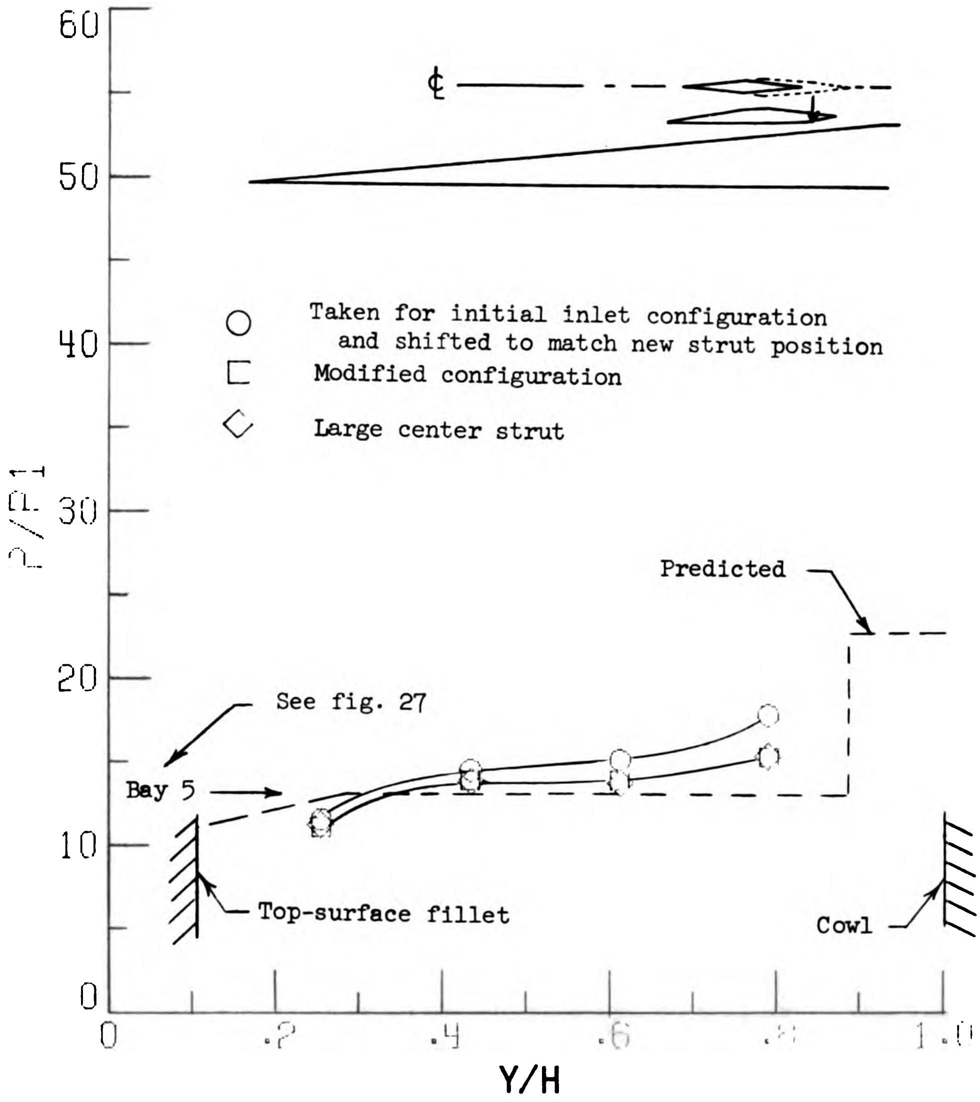

(b) Side strut.

Figure 33.- Concluded.

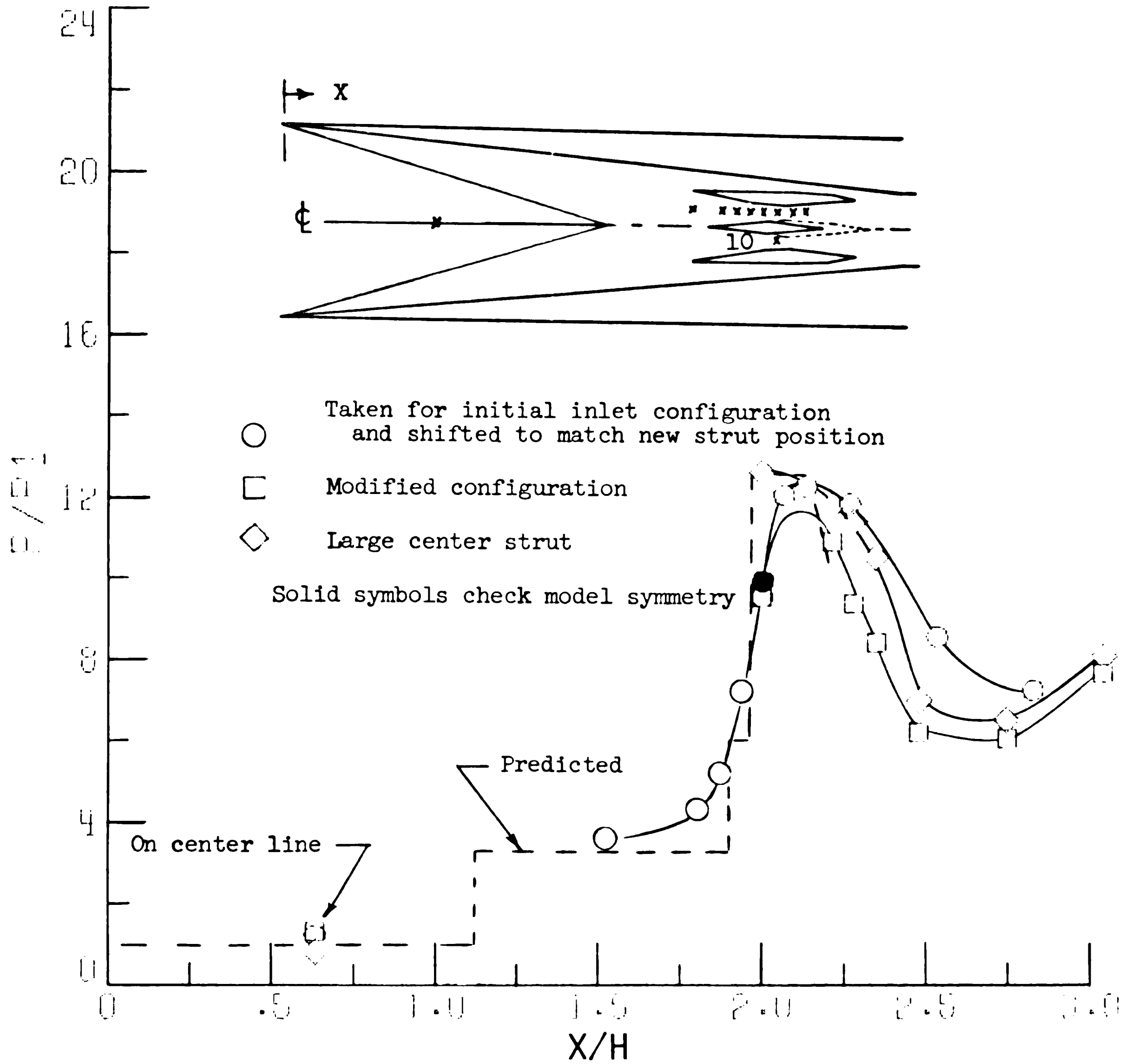

Figure 34.- Static-pressure distribution top surface. Center passage.

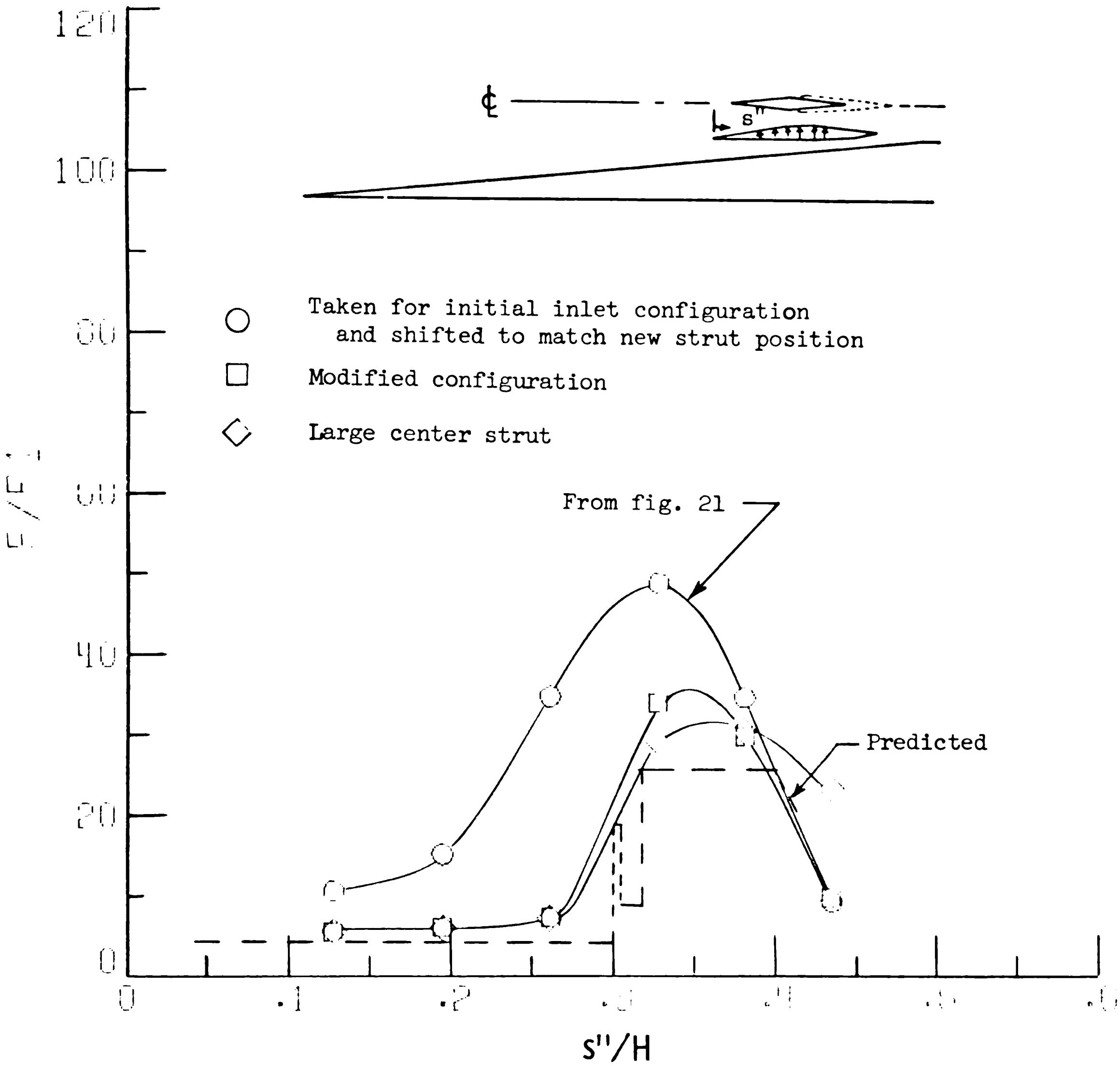

Figure 35.- Static-pressure distribution center passage. Side strut; Y/H = 0.43.

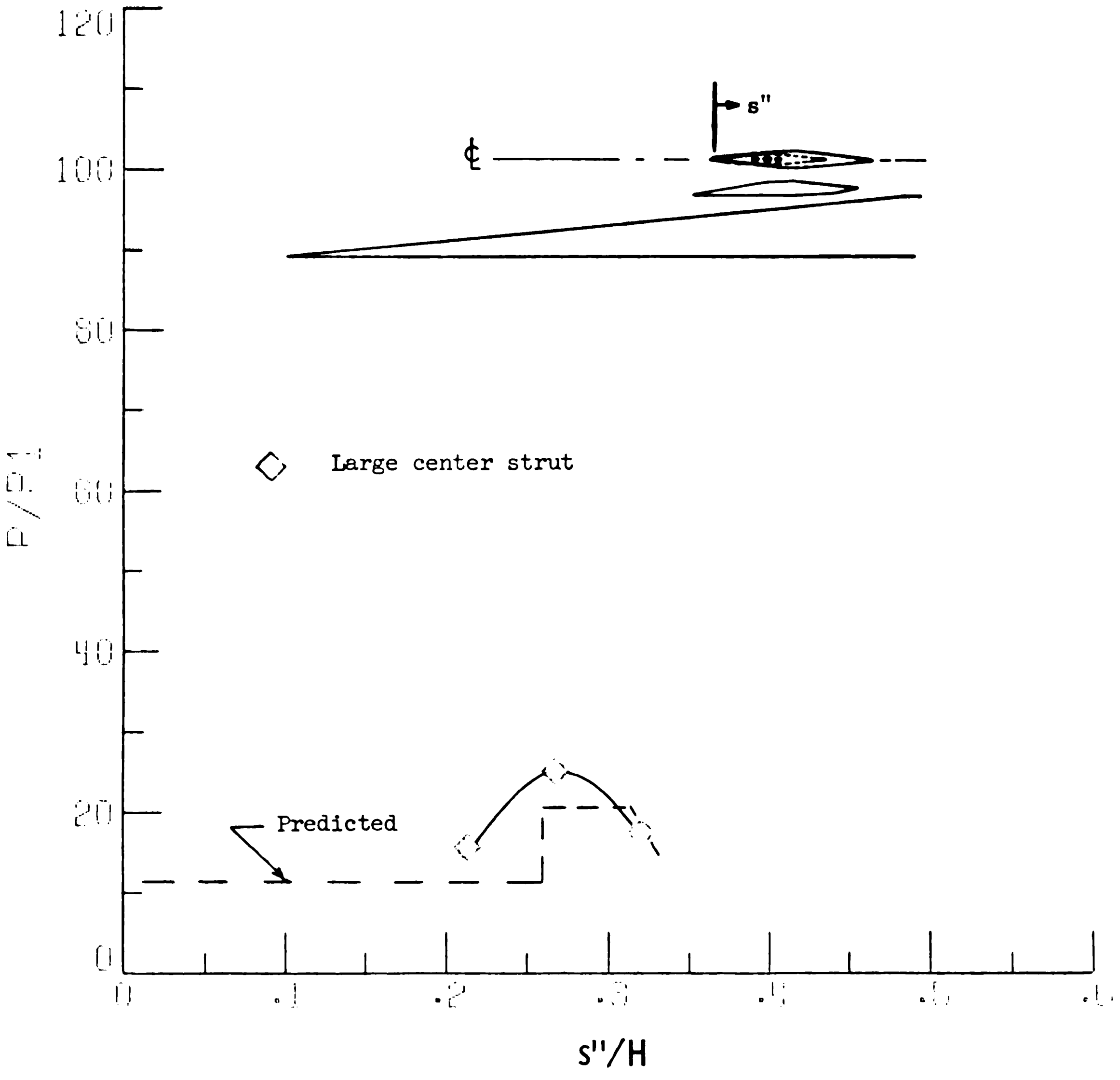

Figure 36.- Static-pressure distribution center passage. Center strut 2; Y/H = 0.43.

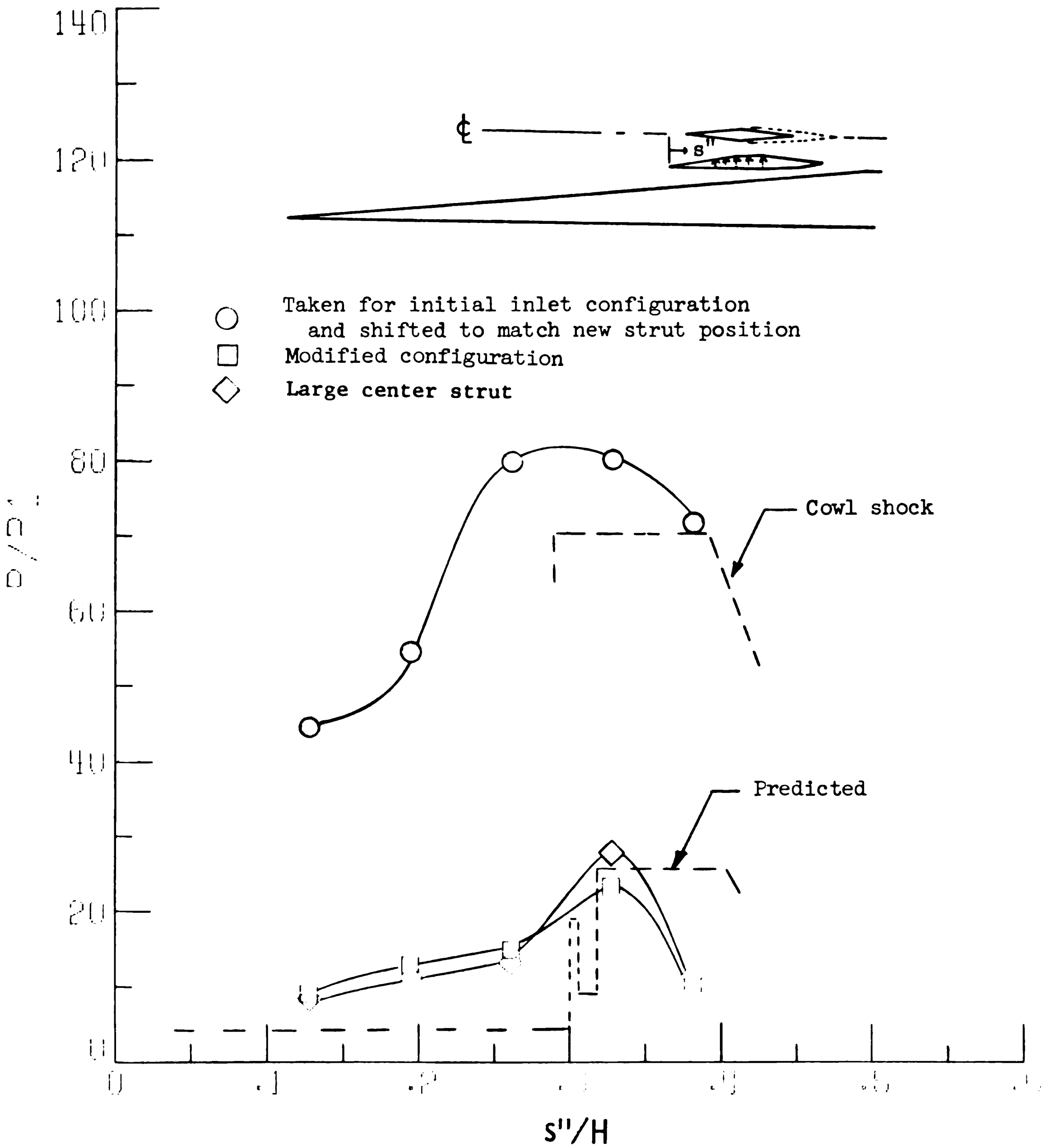

Figure 37.- Static-pressure distribution center passage. Side strut; Y/H = 0.88.

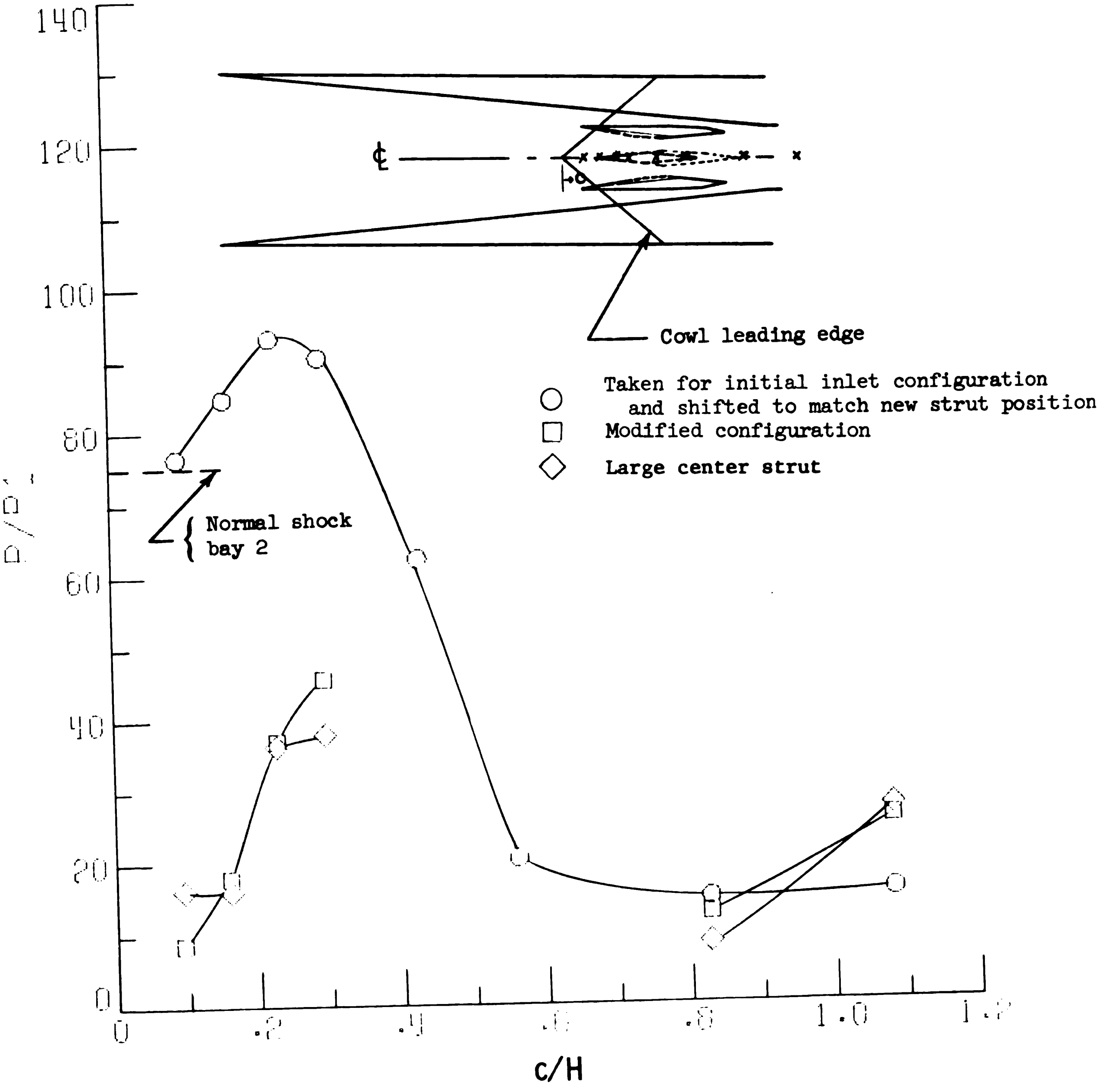

Figure 38.- Static-pressure distribution. Cowl (center line).

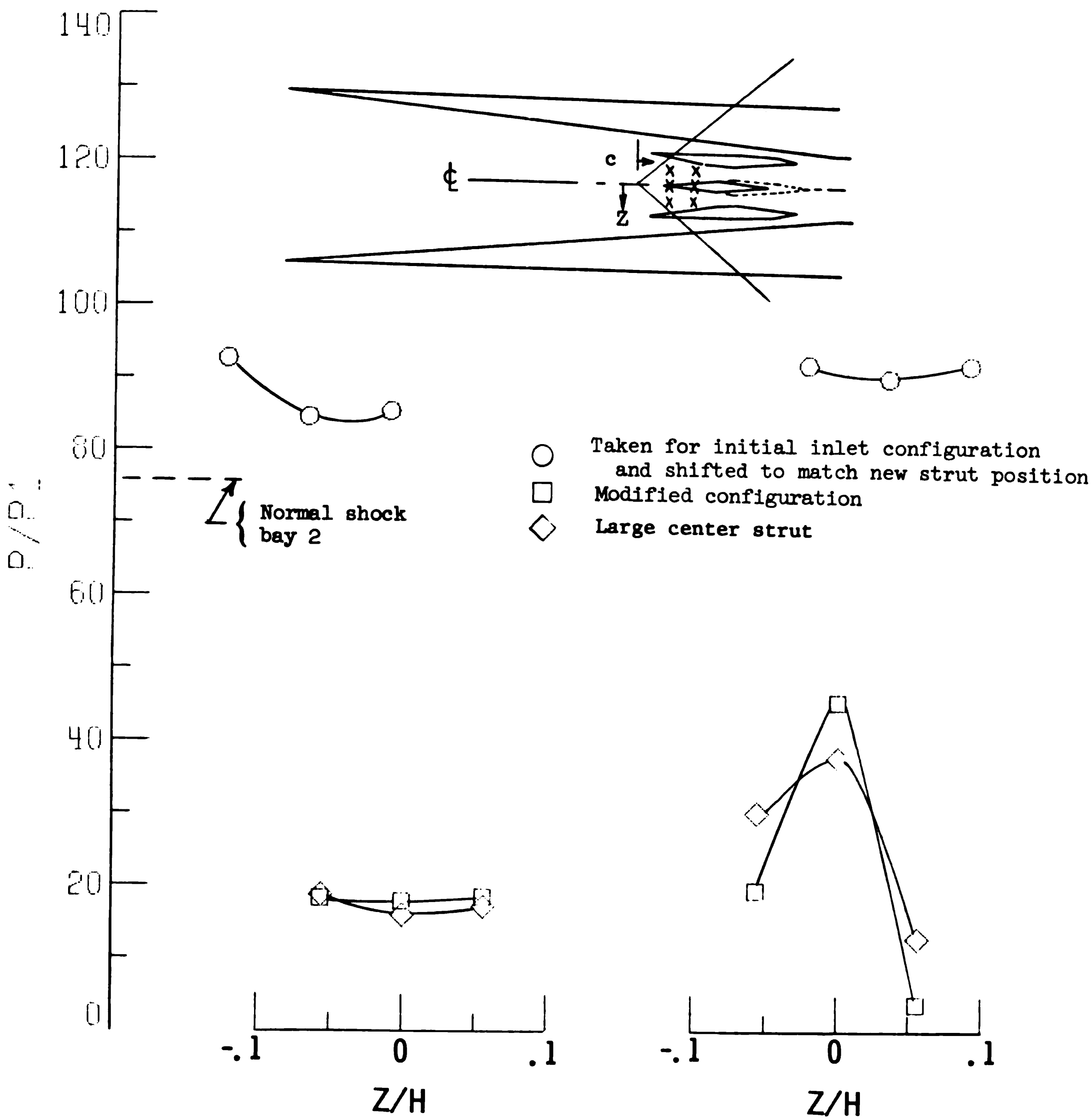

(a) c/H = 0.160. (b) c/H = 0.293.

Figure 39.- Static-pressure distribution. Cowl (Z-direction).

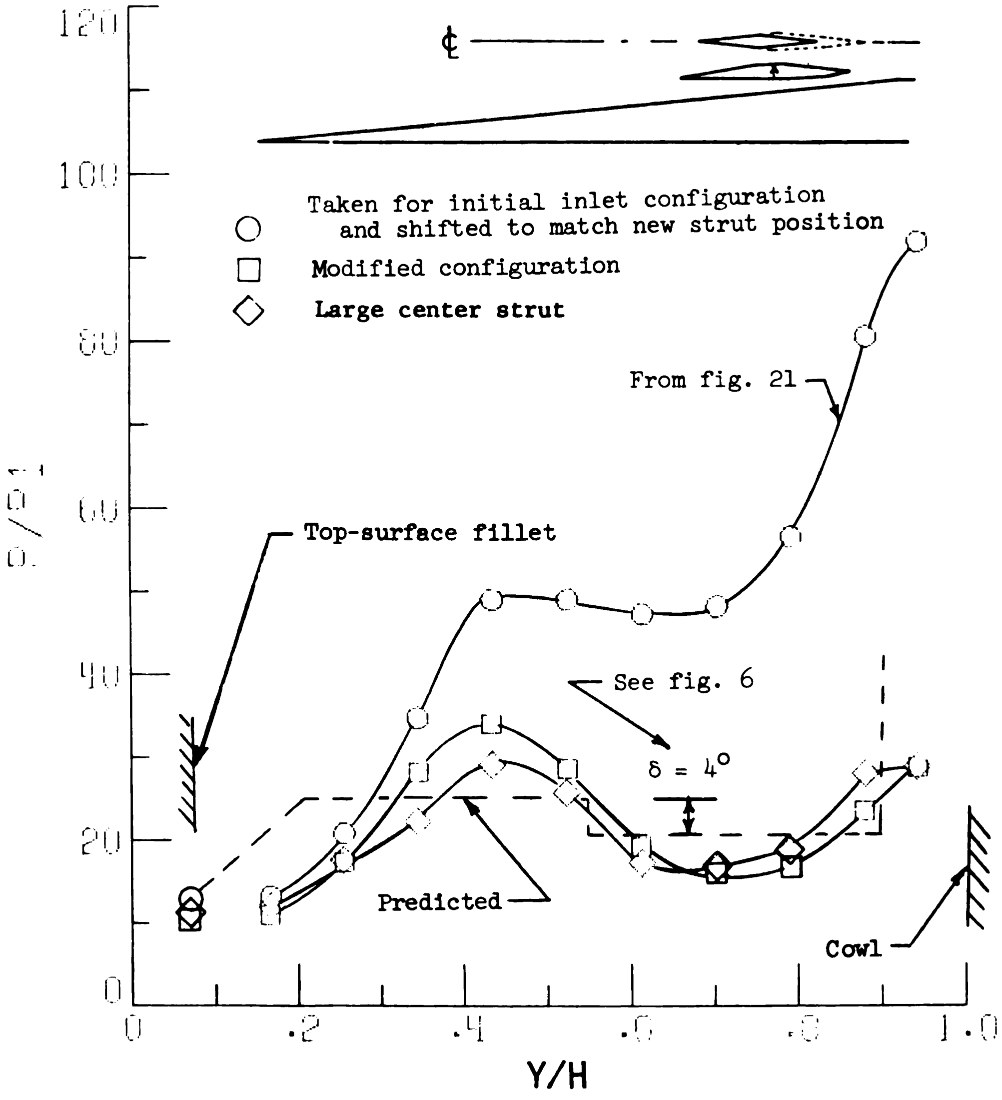

Figure 40.- Static-pressure distribution. Throat (center-passage side strut).

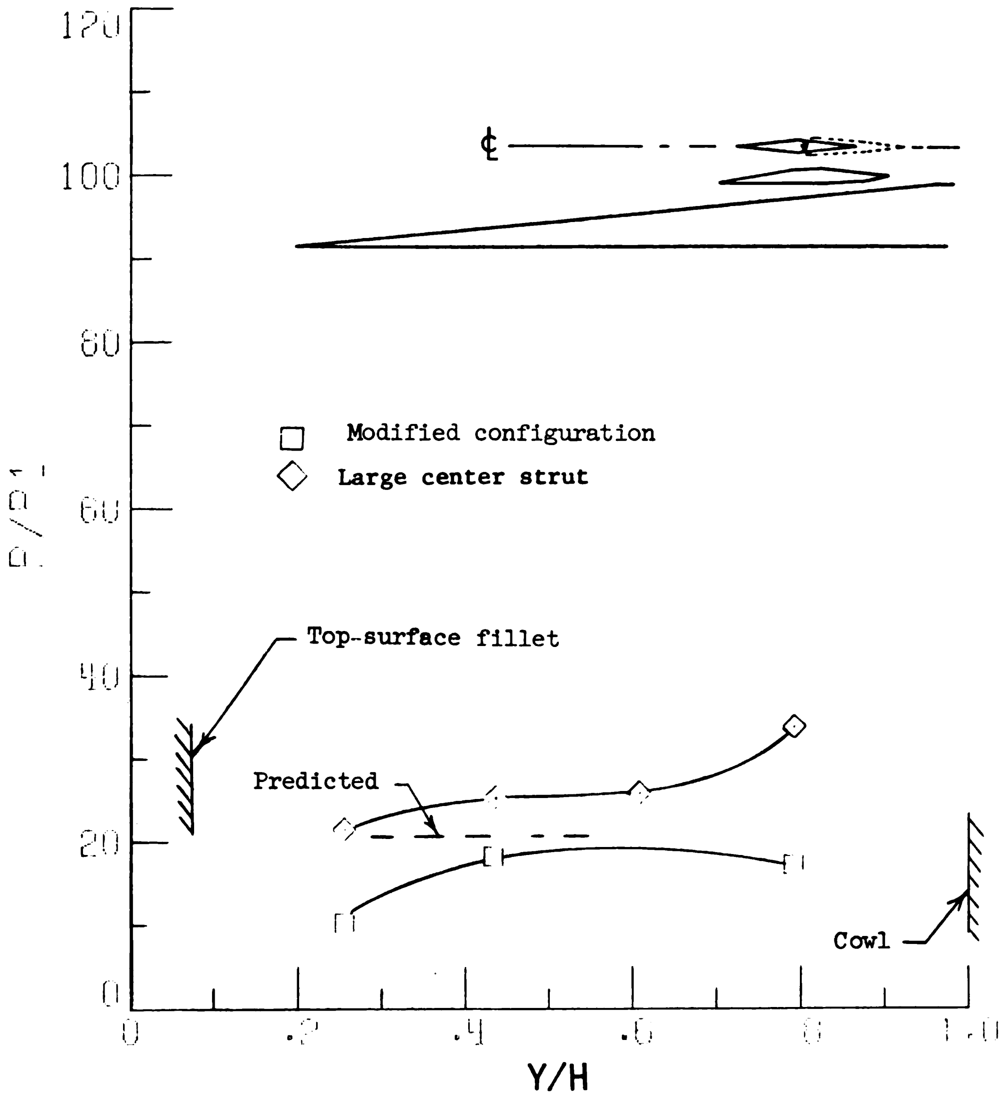

Figure 41.- Static-pressure distribution. Throat (center-passage center strut).

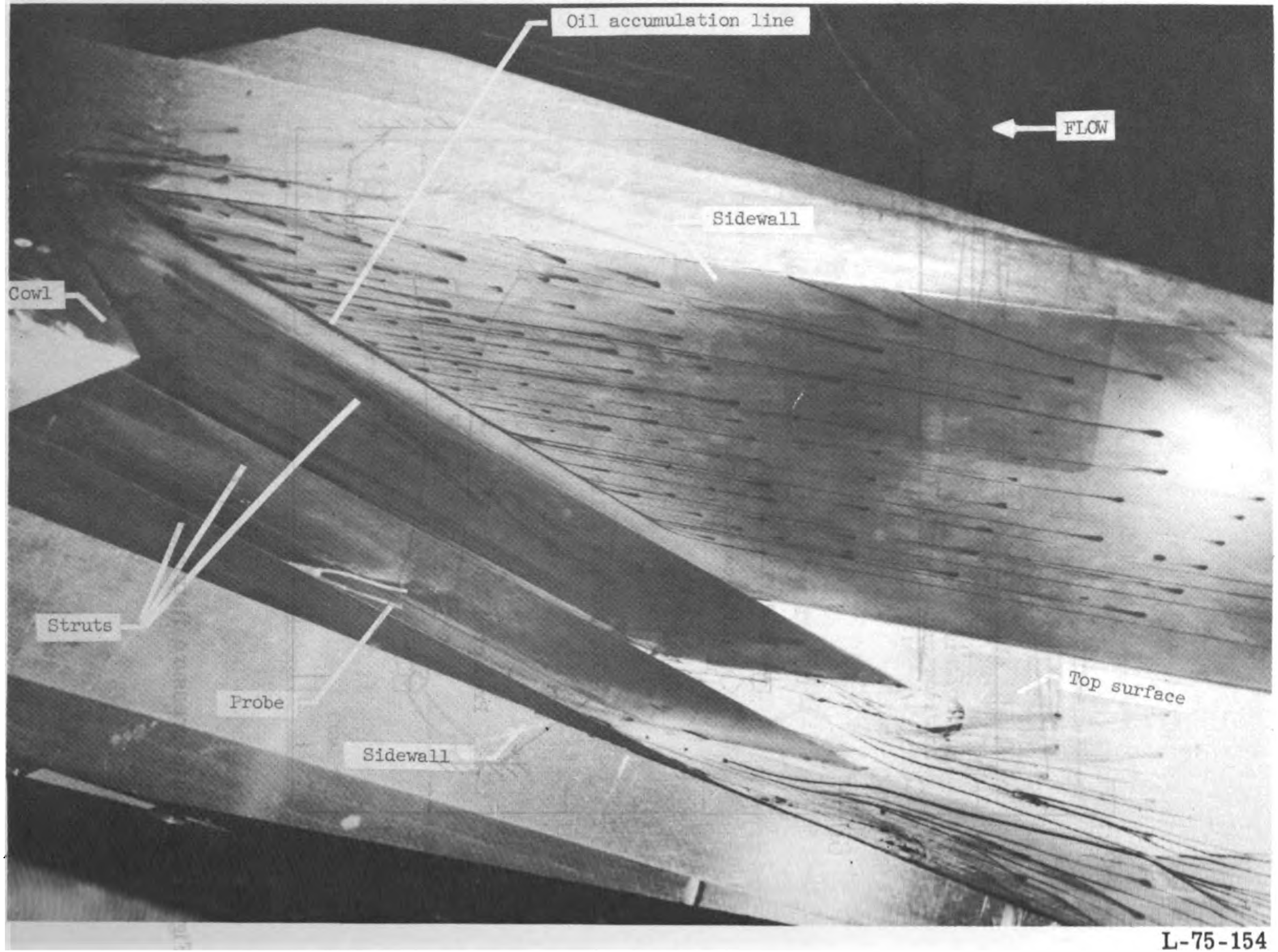

L-75-154

Figure 42.- Oil-flow study.

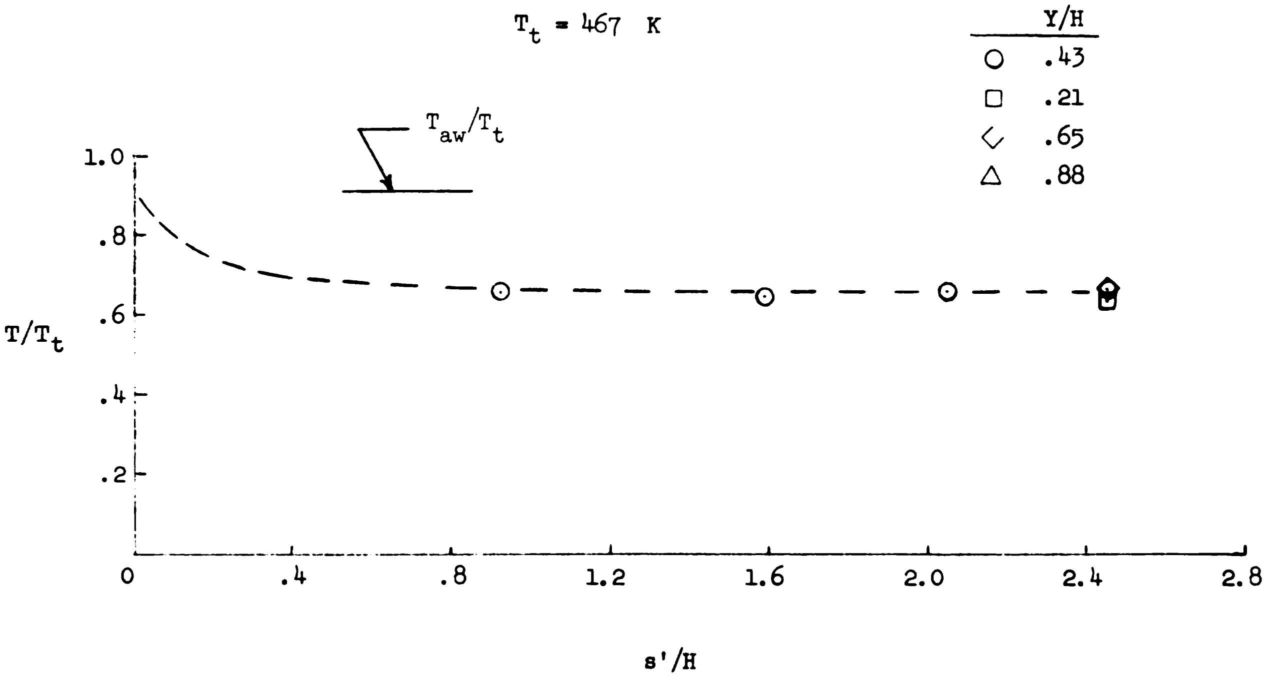

(a) Sidewall.

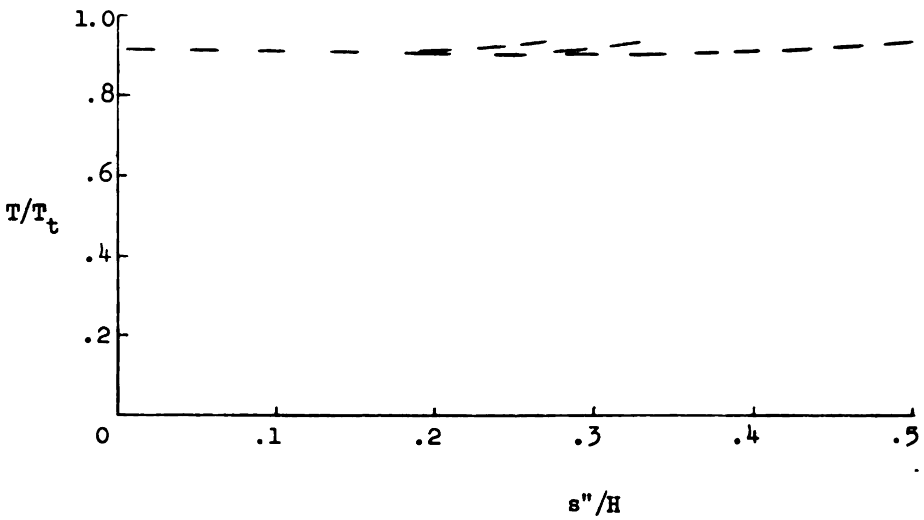

(b) Struts.

Figure 43.- Temperature distributions after 80 sec. M_1 = 6.0.

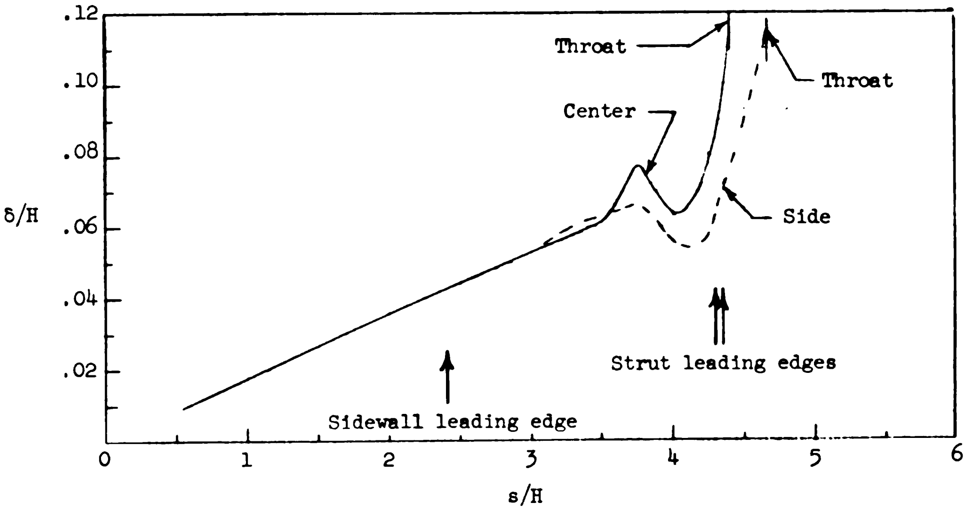

(a) Top surface.

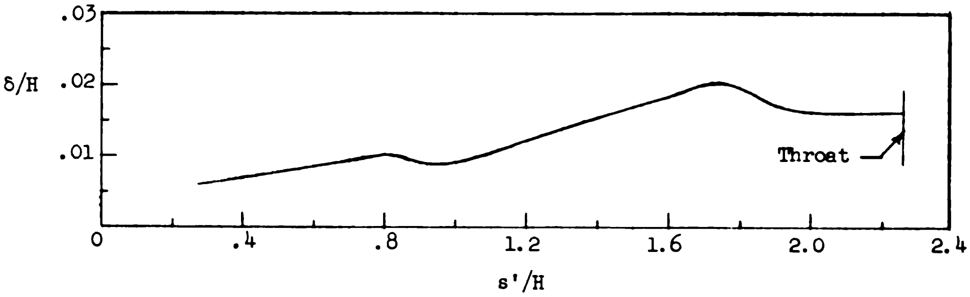

(b) Sidewall (xz-plane).

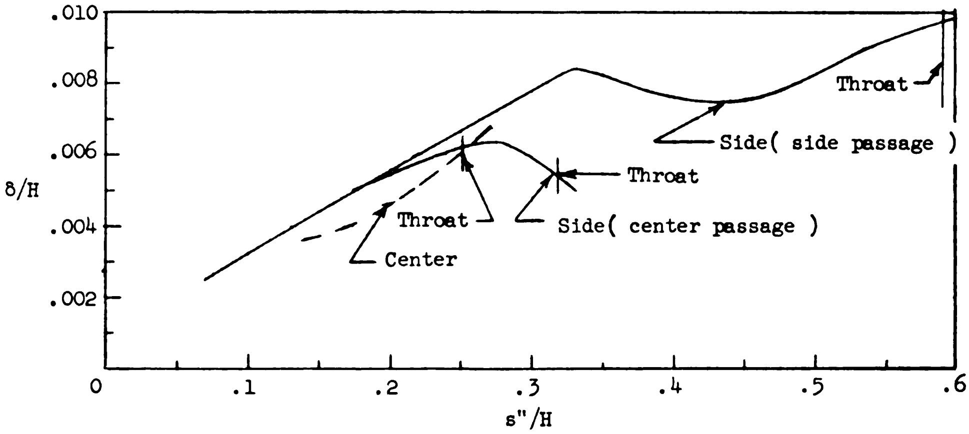

(c) Struts (xz-plane).

Figure 44.- Inlet boundary layers.

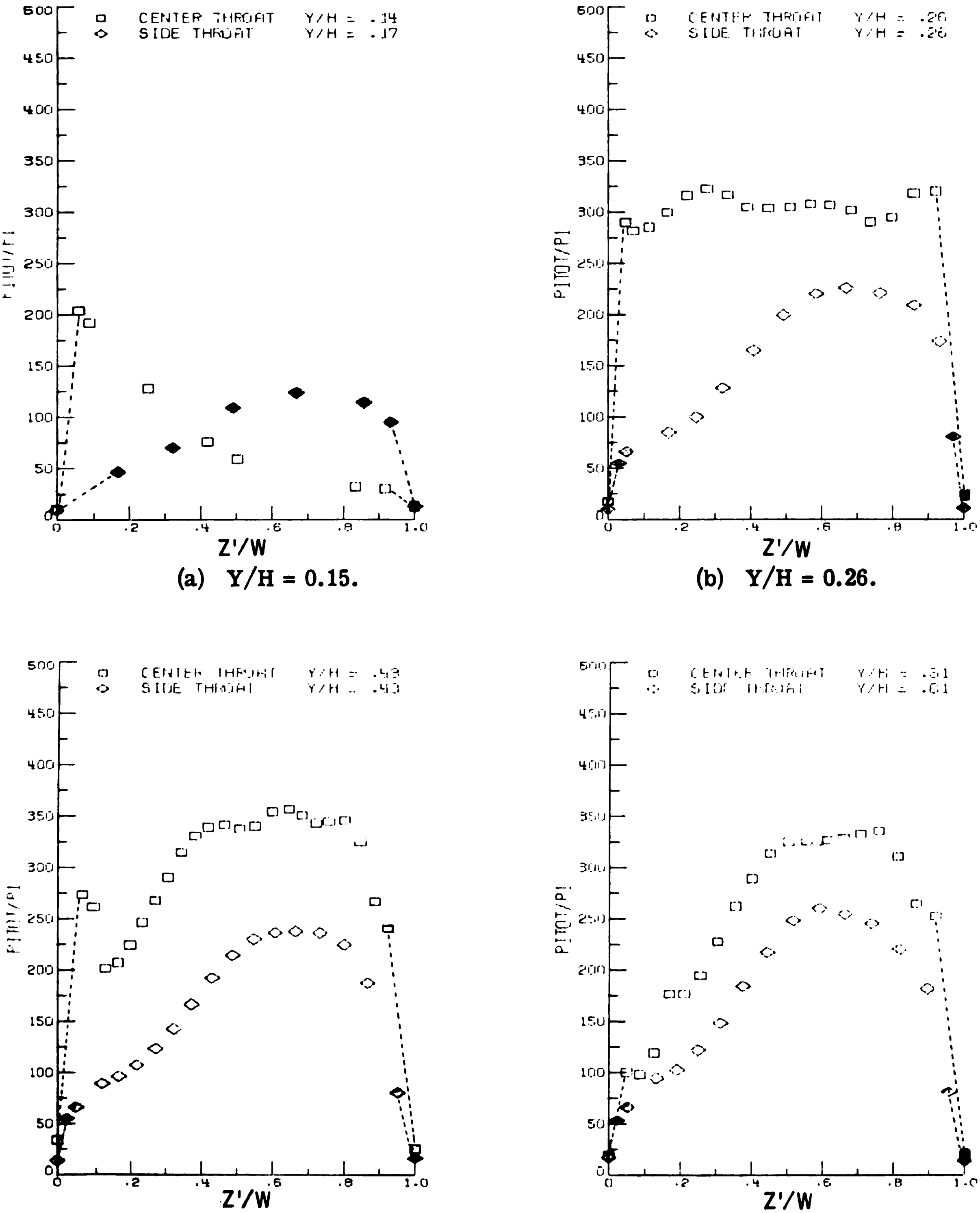

(a) Y/H = 0.15.

(b) Y/H = 0.26.

(c) Y/H = 0.43.

(d) Y/H = 0.61.

Figure 45.- Throat pitot pressure surveys. The solid symbols represent theoretical boundary-layer calculations.

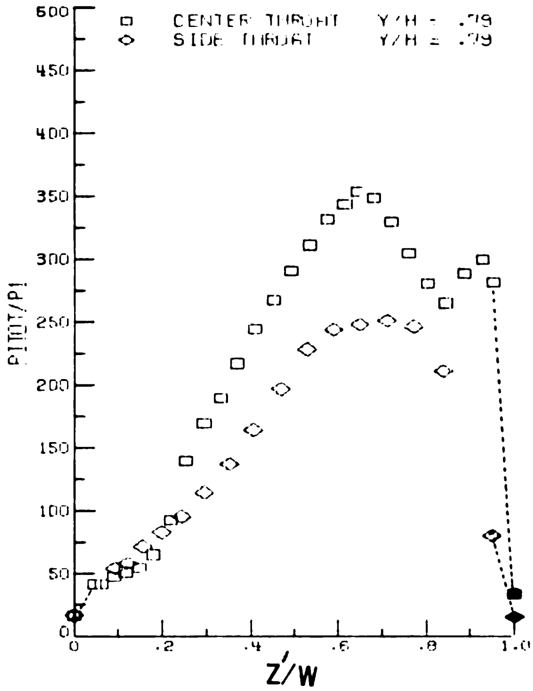

(e) Y/H = 0.79.

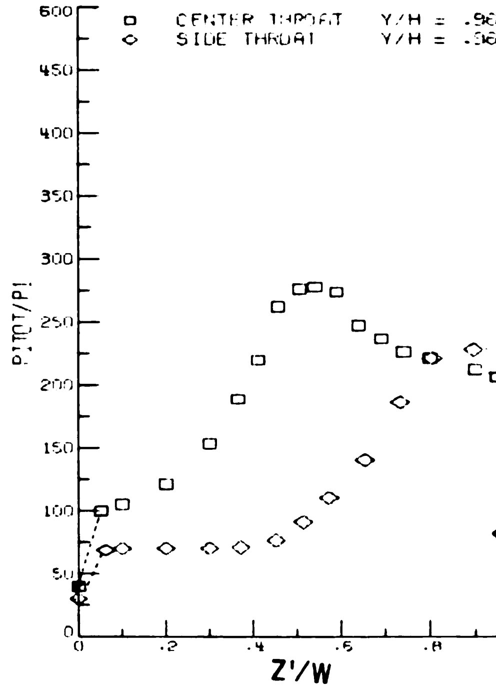

(f) Y/H = 0.96.

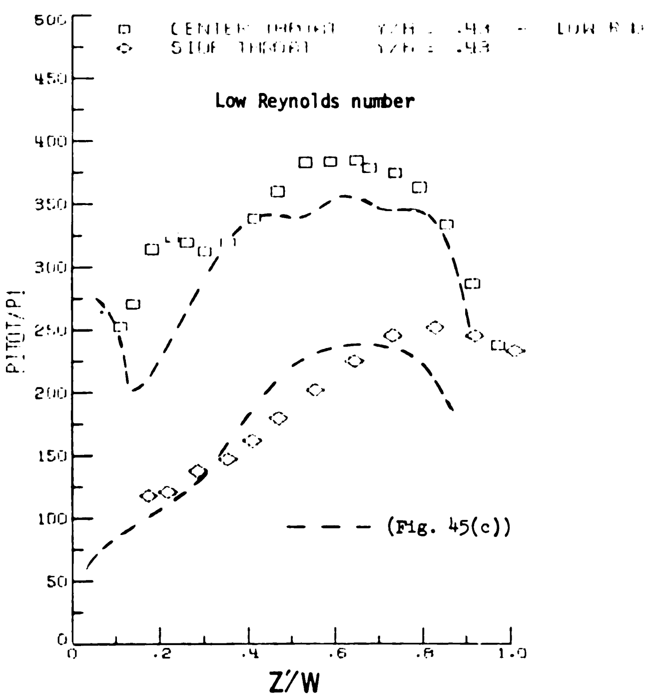

(g) Y/H = 0.43.

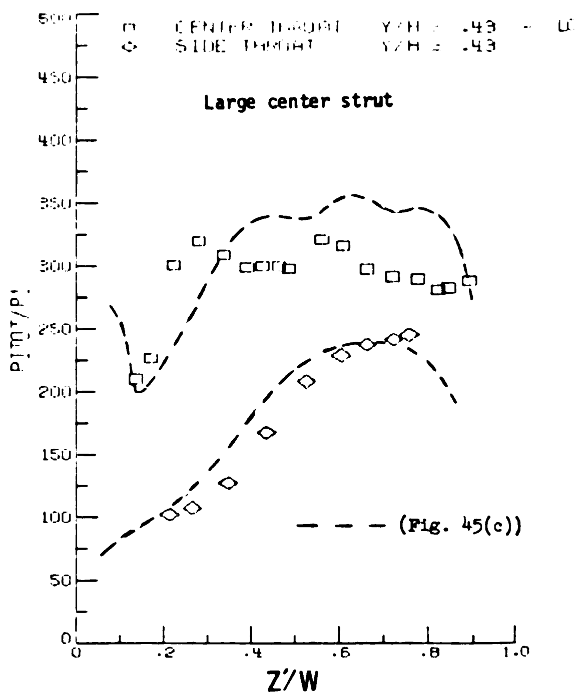

(h) Y/H = 0.43.

Figure 45.- Concluded.

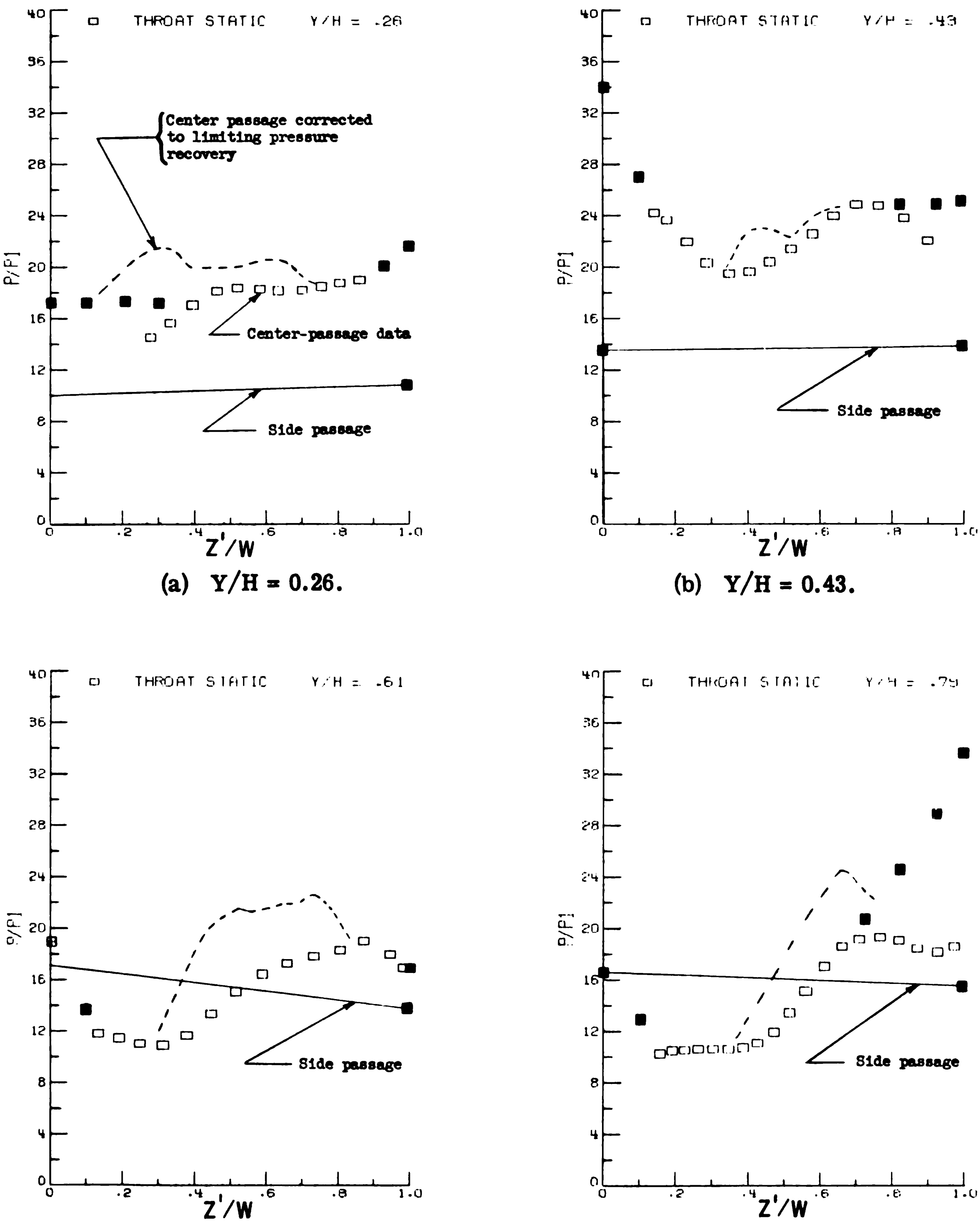

(a) Y/H = 0.26.

(b) Y/H = 0.43.

(c) Y/H = 0.61.

(d) Y/H = 0.79.

Figure 46.- Throat static-pressure surveys. The solid symbols represent data faired to the wall static pressure.

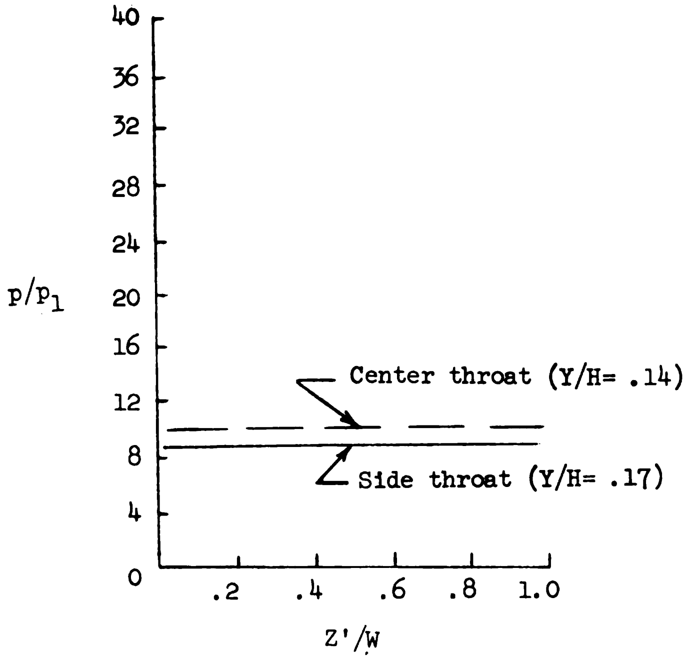

(a) Near top surface.

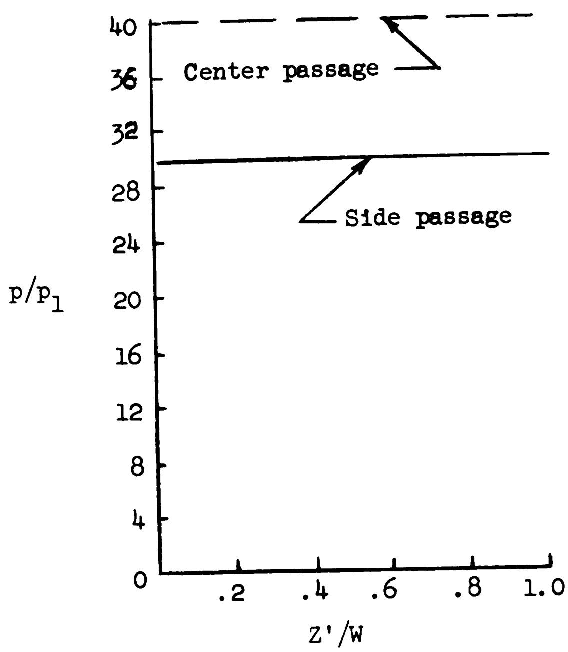

(b) Near cowl; Y/H = 0.96.

Figure 47.- Additional estimated throat static distributions.

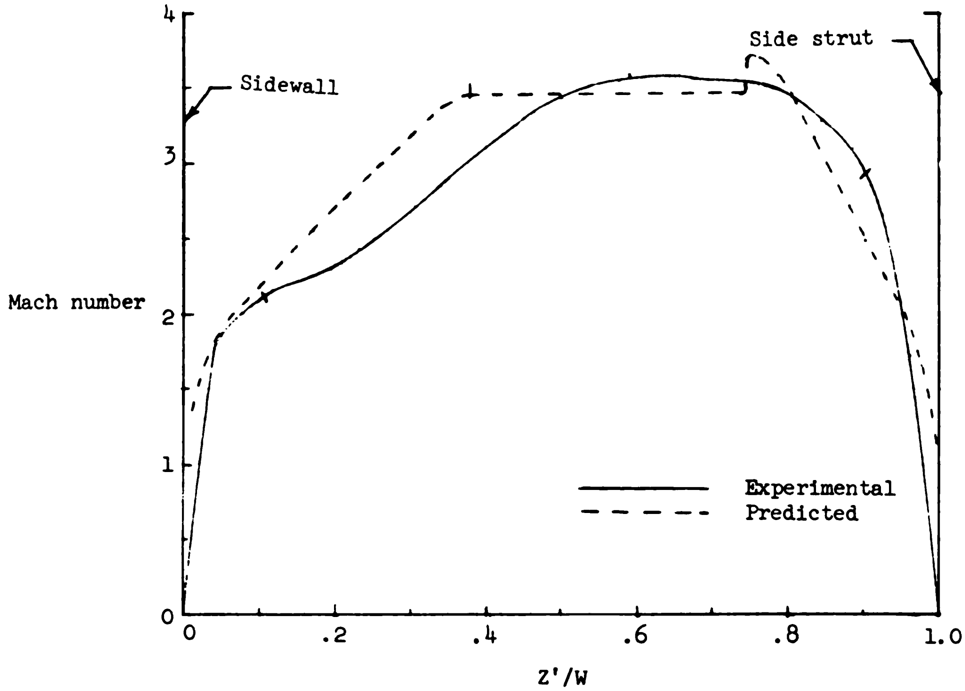

(a) Side passage; Throat gap = 0.772 cm.

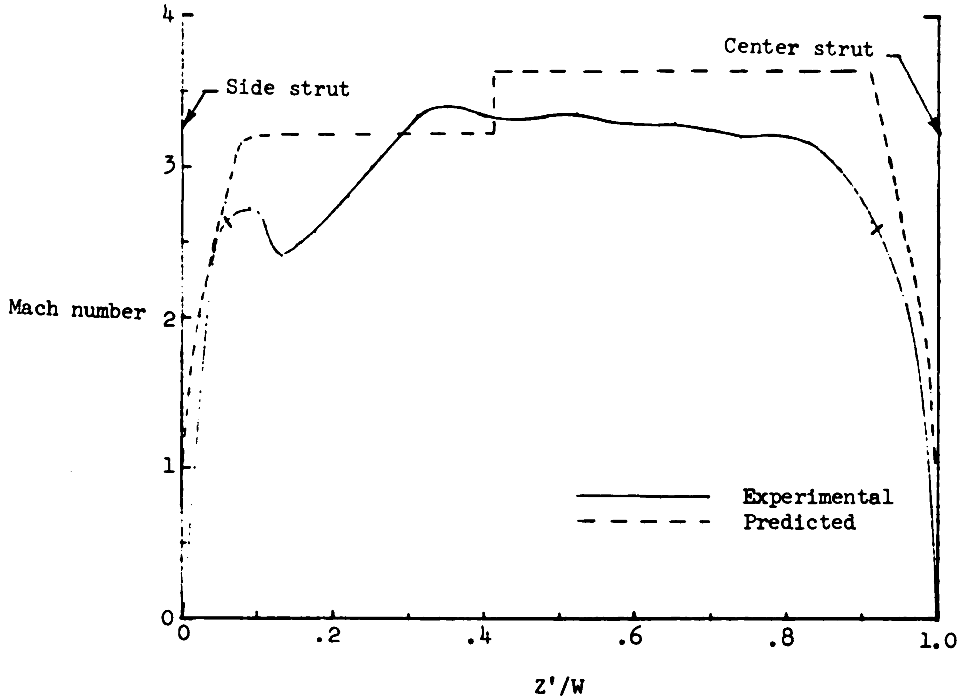

(b) Center passage; Throat gap = 1.227 cm.

Figure 48.- Mach number distribution at throat. Y/H = 0.43.

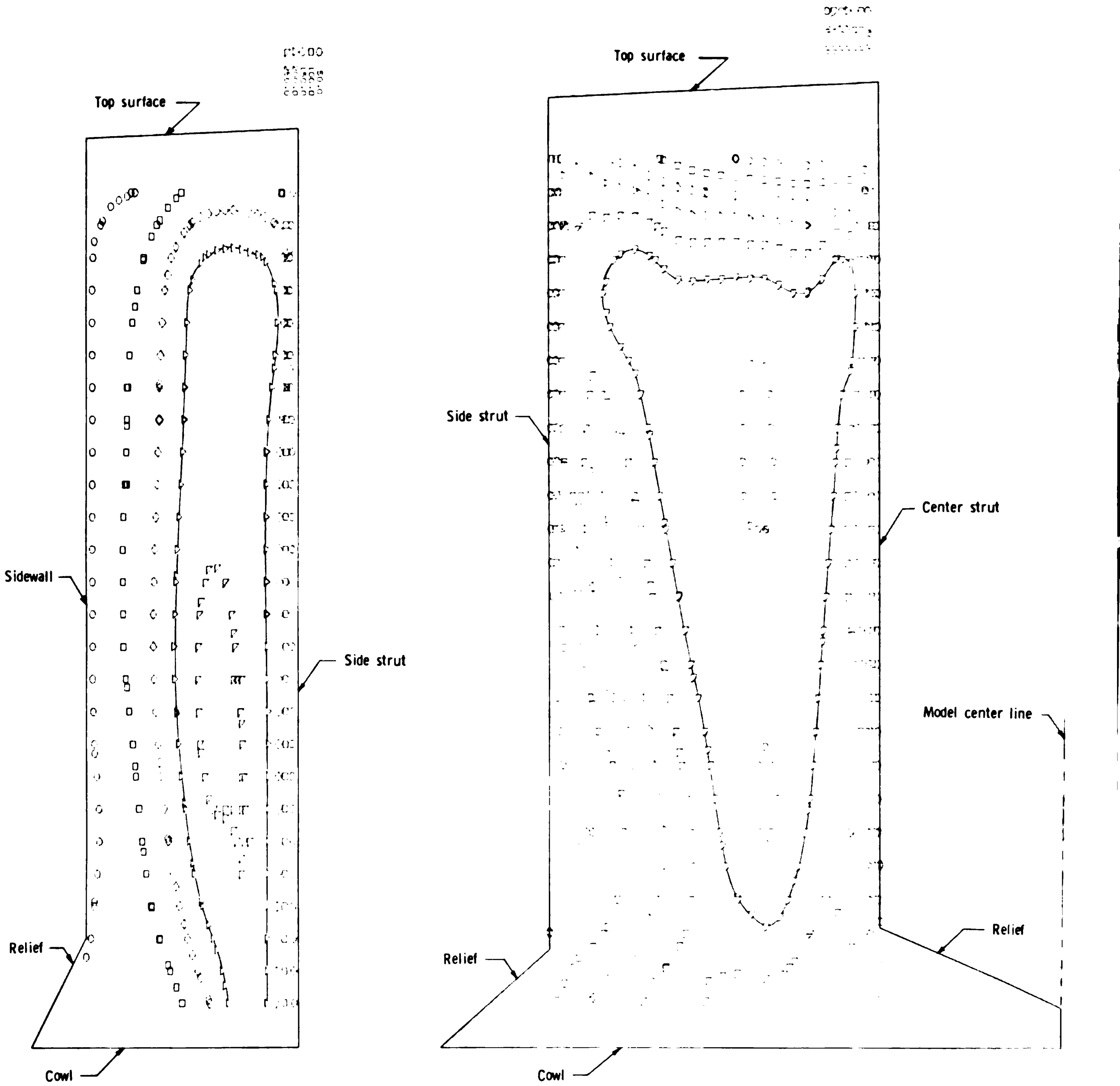

(a) Side passage.

(b) Center passage.

Figure 49.- Throat map of p_{pitot}/p_1.

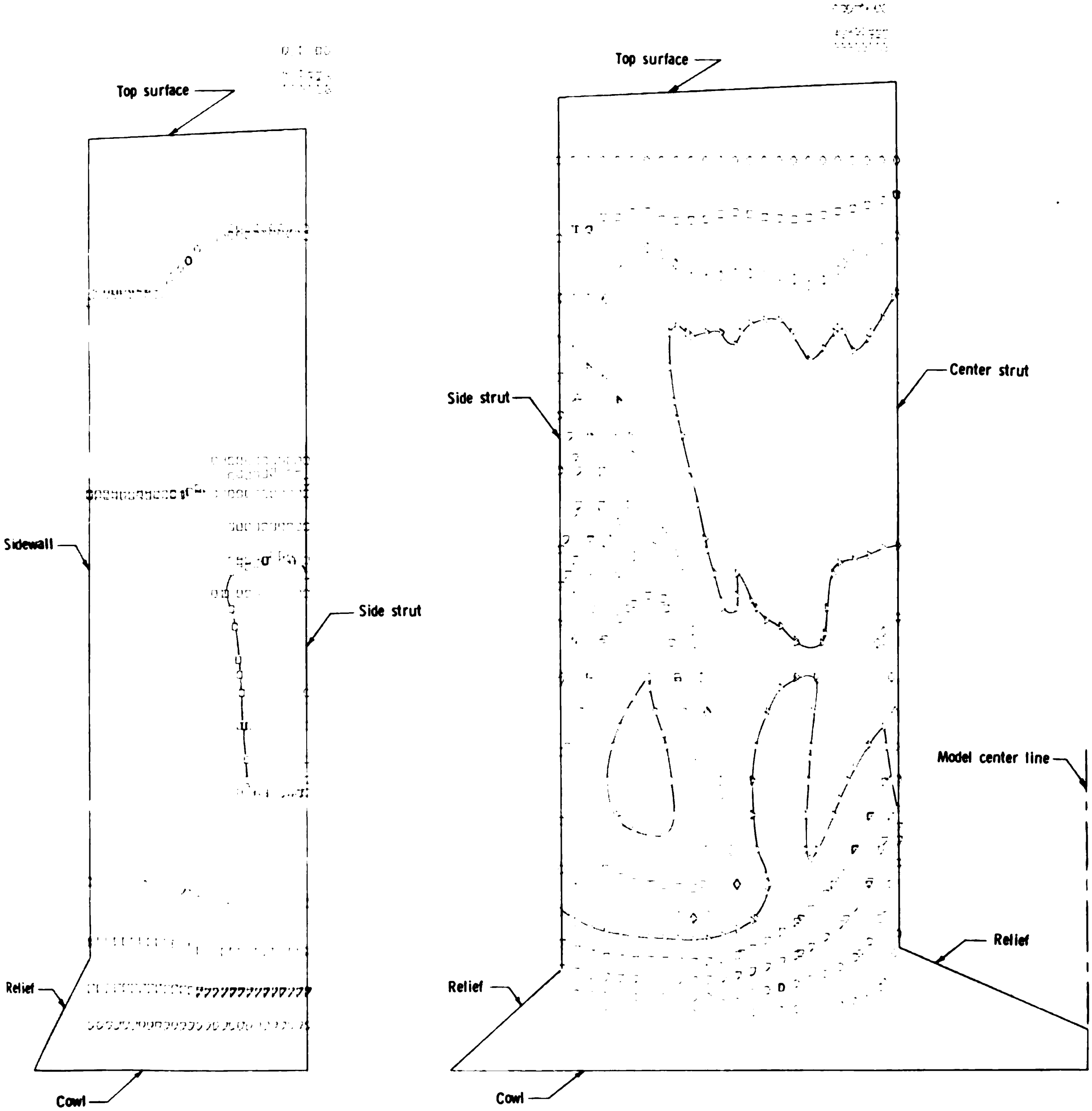

(a) Side passage.

(b) Center passage.

Figure 50.- Throat map of p/p_1.

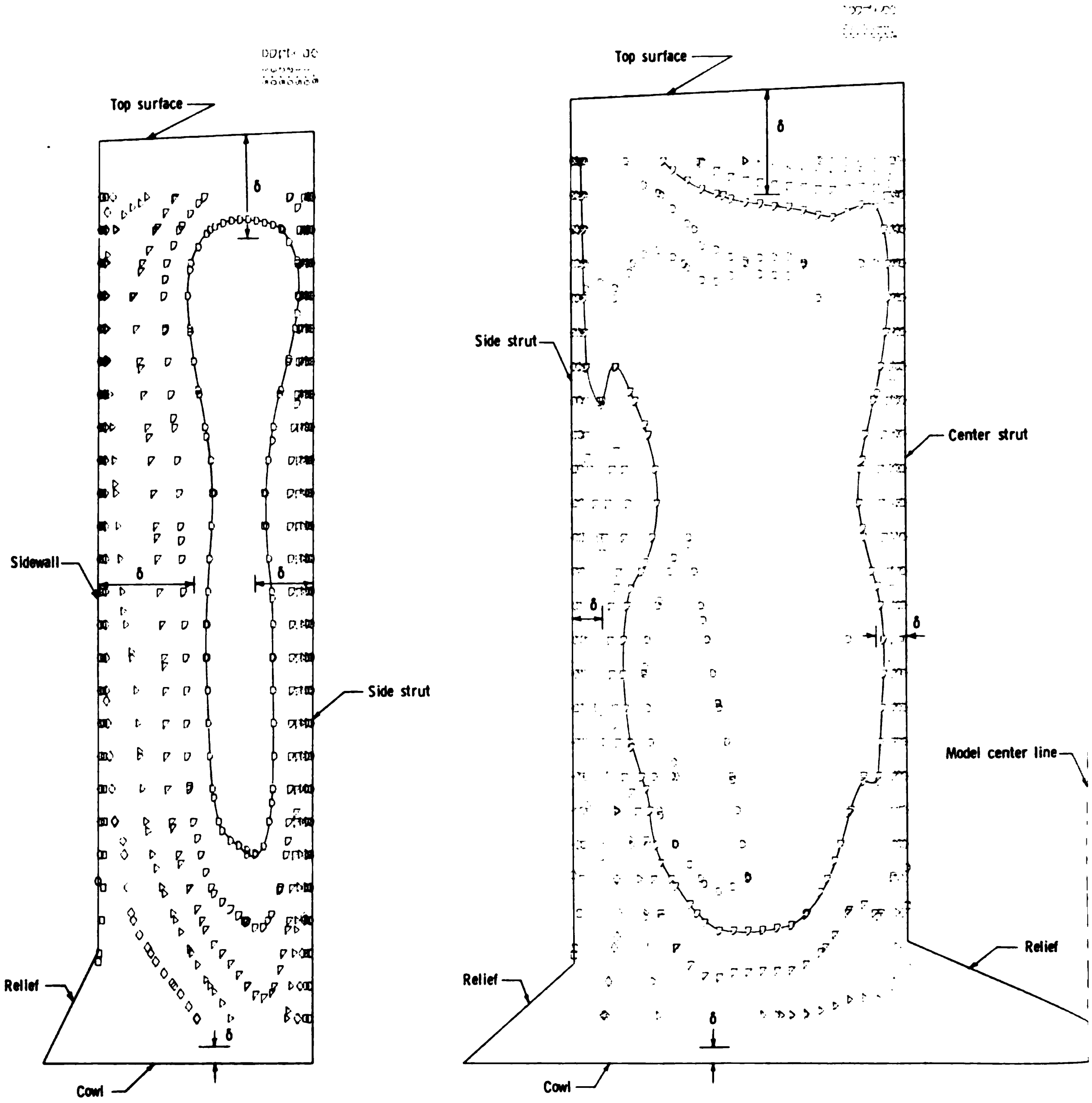

Figure 51.- Throat map of Mach number. $M_1 = 6.0$.

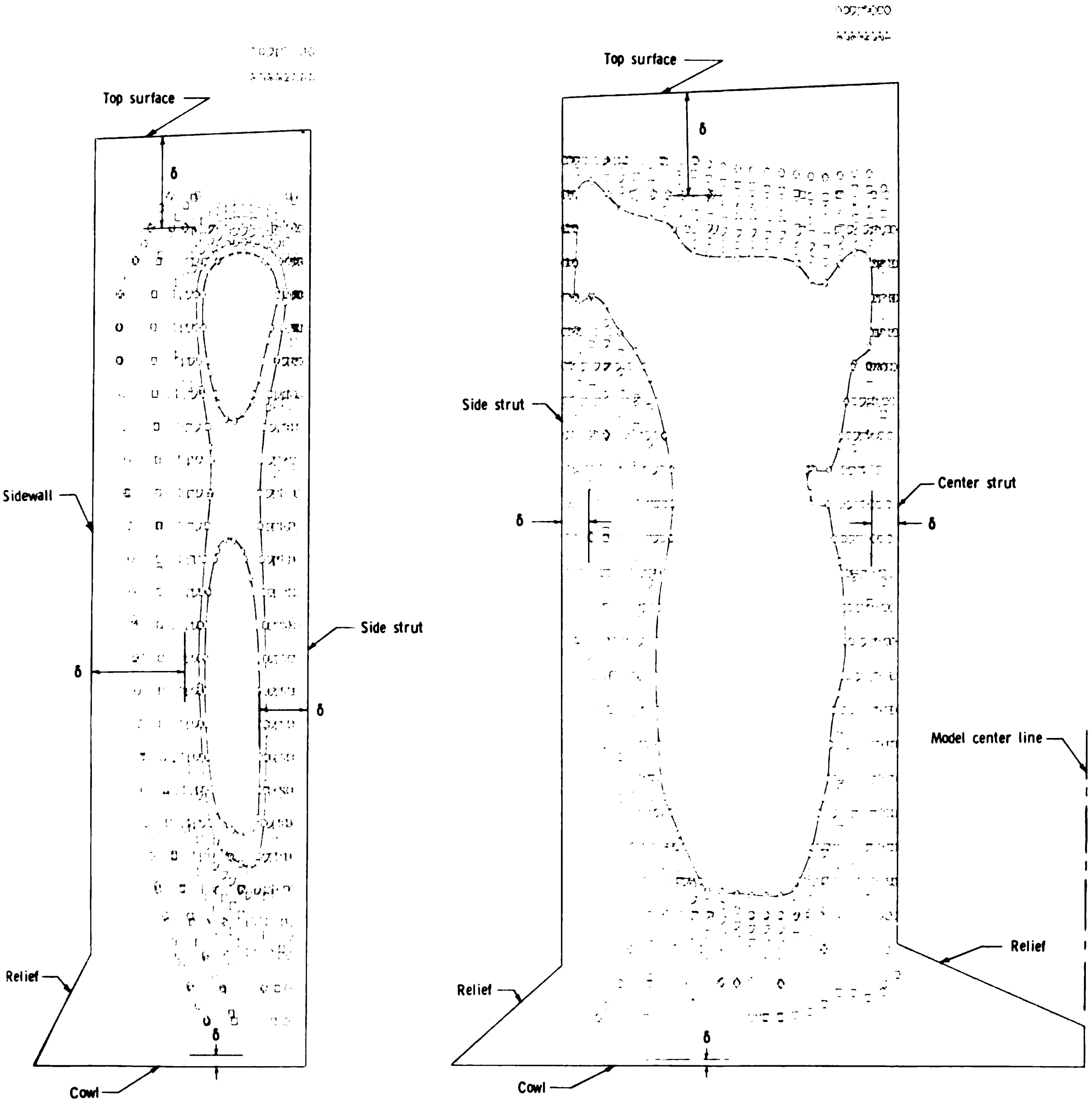

(a) Side passage. **(b) Center passage.**

Figure 52.- Throat map of total-pressure recovery.

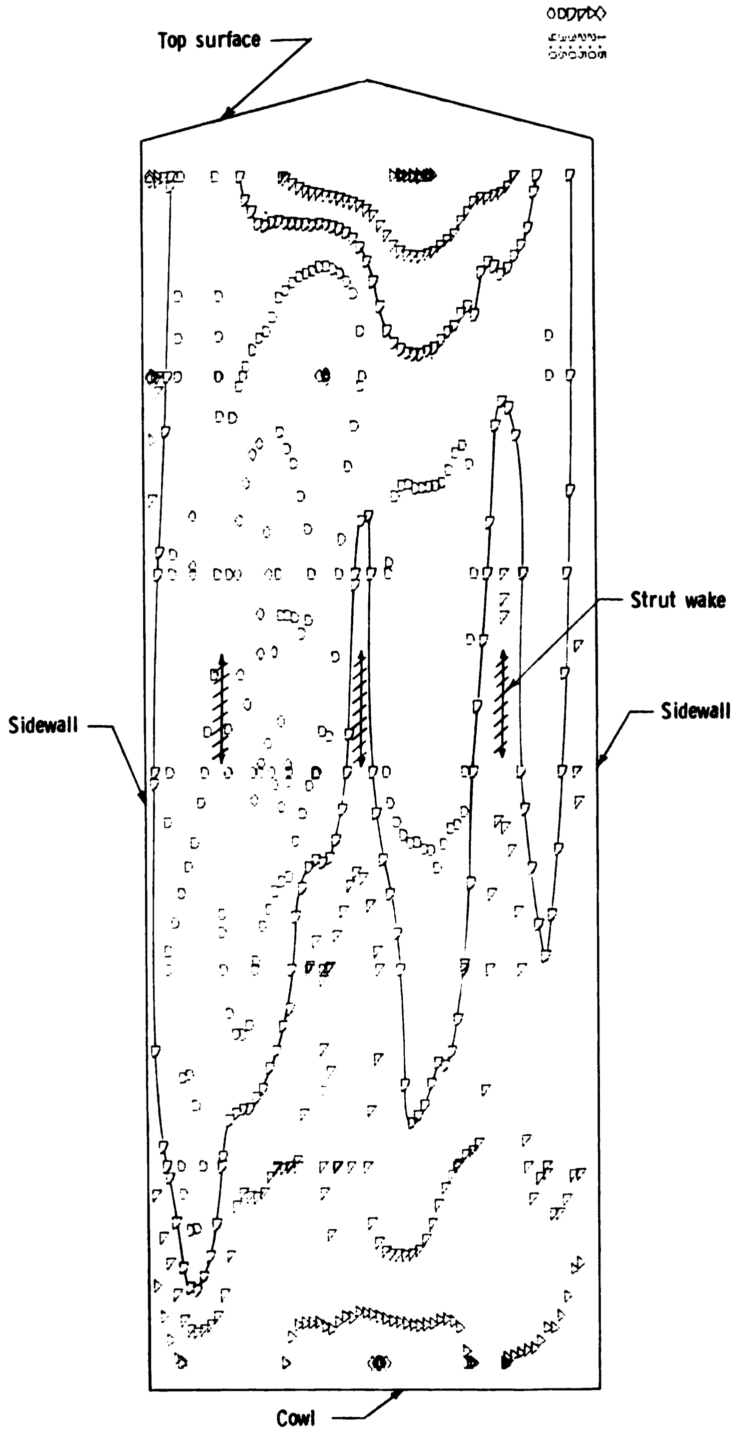

Figure 53.- Mach number distribution at capture station. $M_1 = 6.0$.

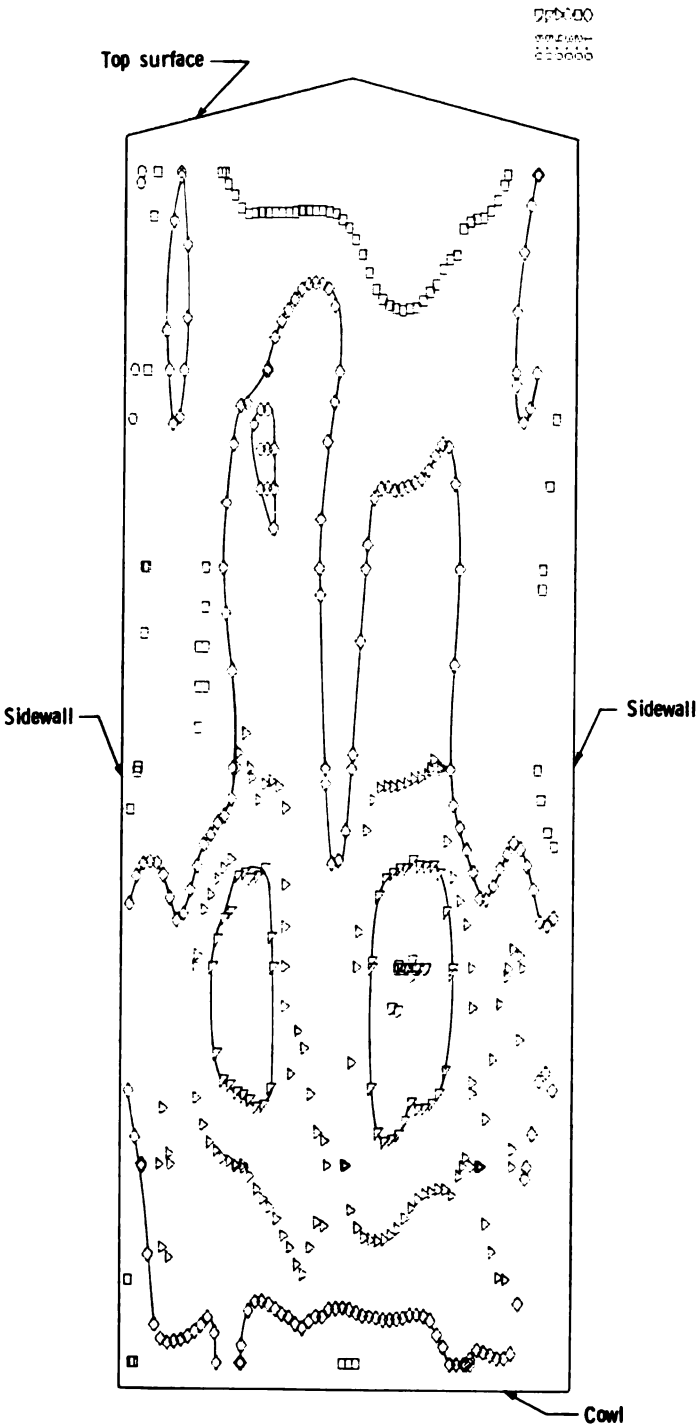

Figure 54.- Capture parameter $\rho v/\rho_1 v_1$.

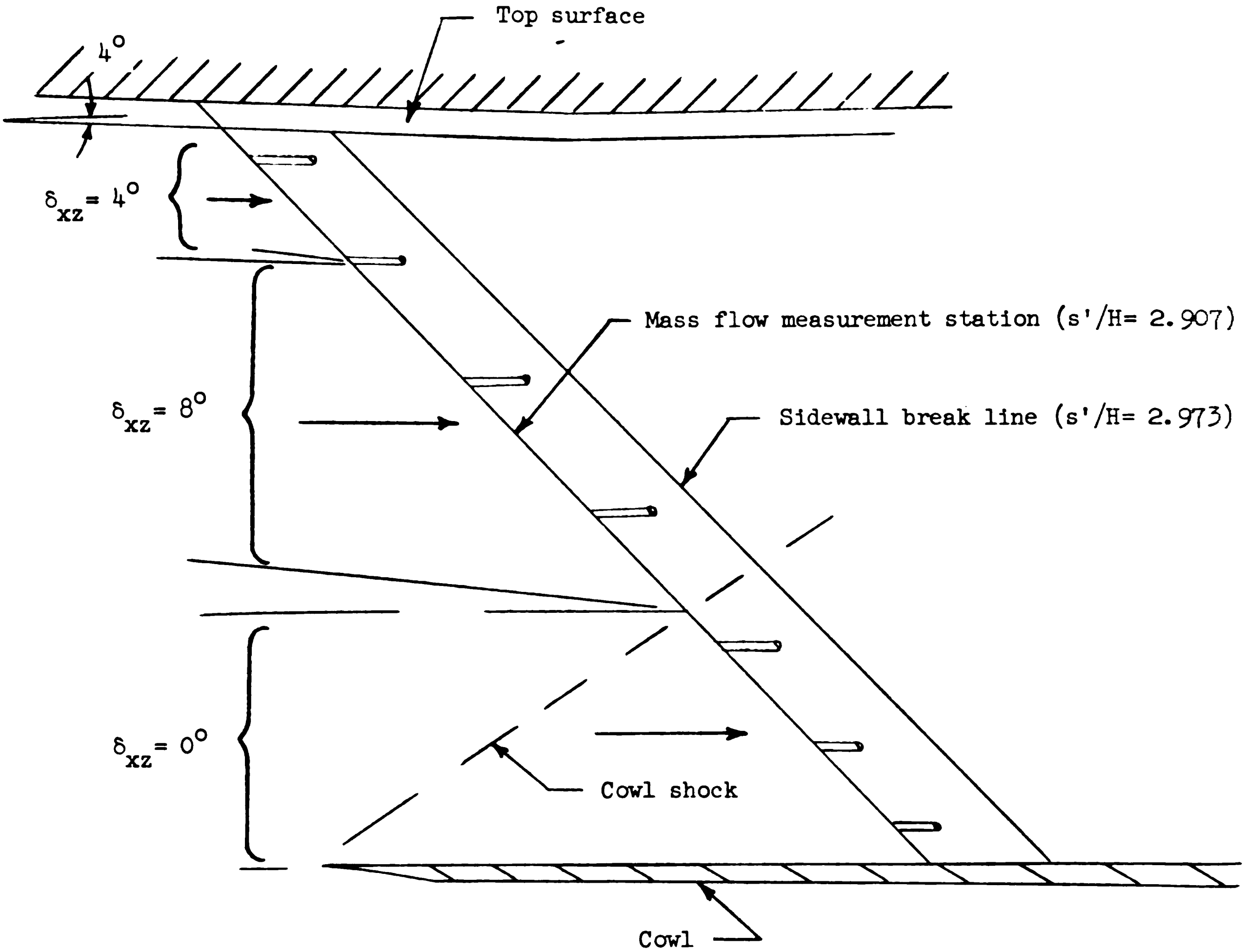

Figure 55.- Assumed flow directions used to compute capture.

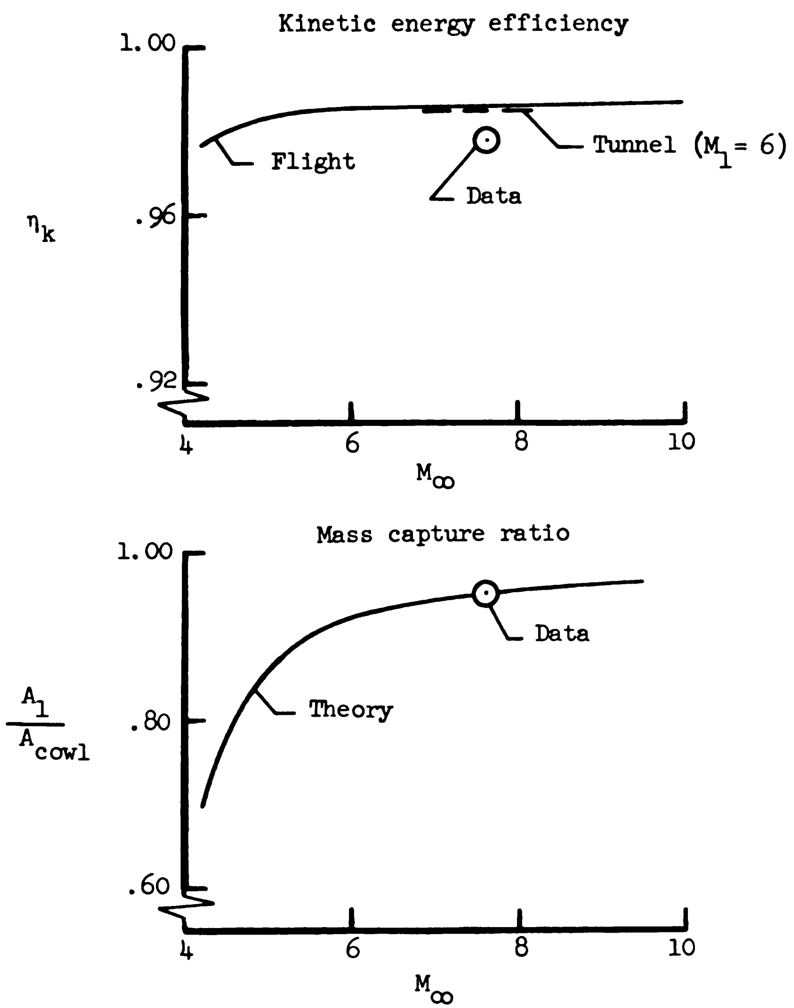

Mass weighted data (M_1 = 6.0)

	Passage		Total*
	Side	Center	Inlet
Contraction ratio	5.8	7.5	7.0
Throat Mach number	3.0	3.1	3.1
Recovery	.46	.66	.59
η_k	.965	.982	.977
Mass capture	.31	.63	.94

* Flow split based on design

Figure 56.- Integrated performance parameters.

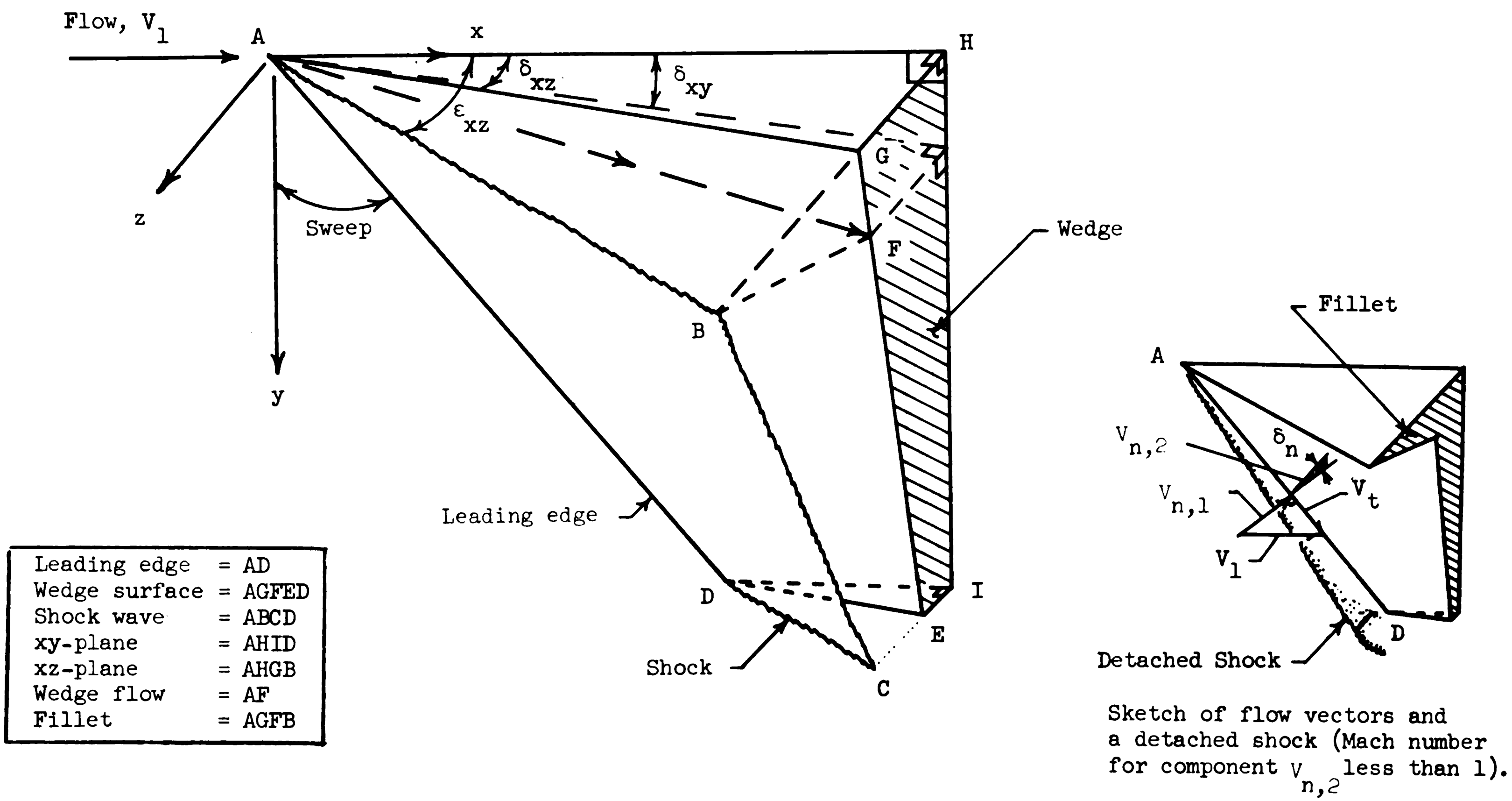

Figure 57.- Swept compression wedge.

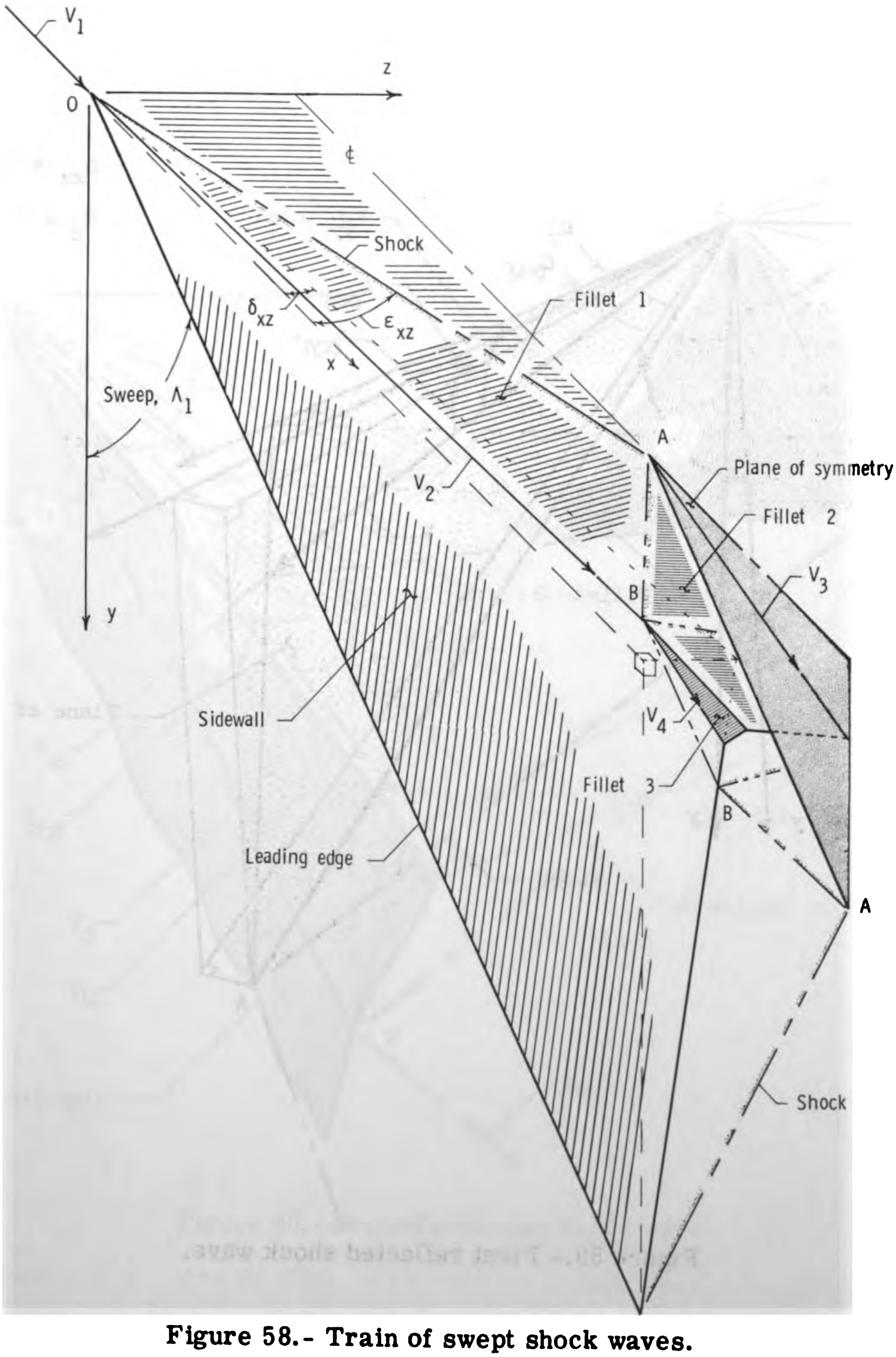

Figure 58.- Train of swept shock waves.

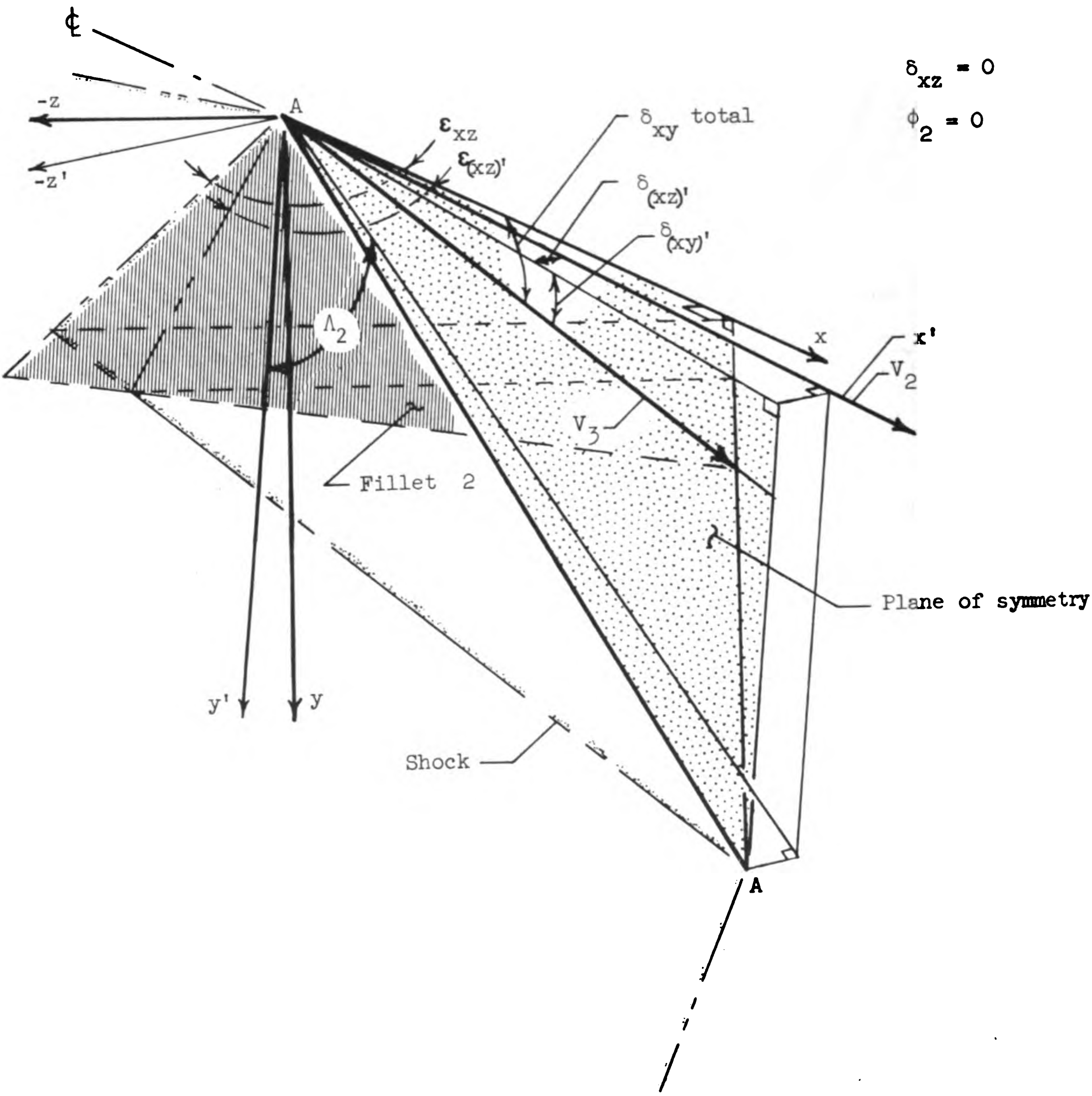

Figure 59.- First reflected shock wave.

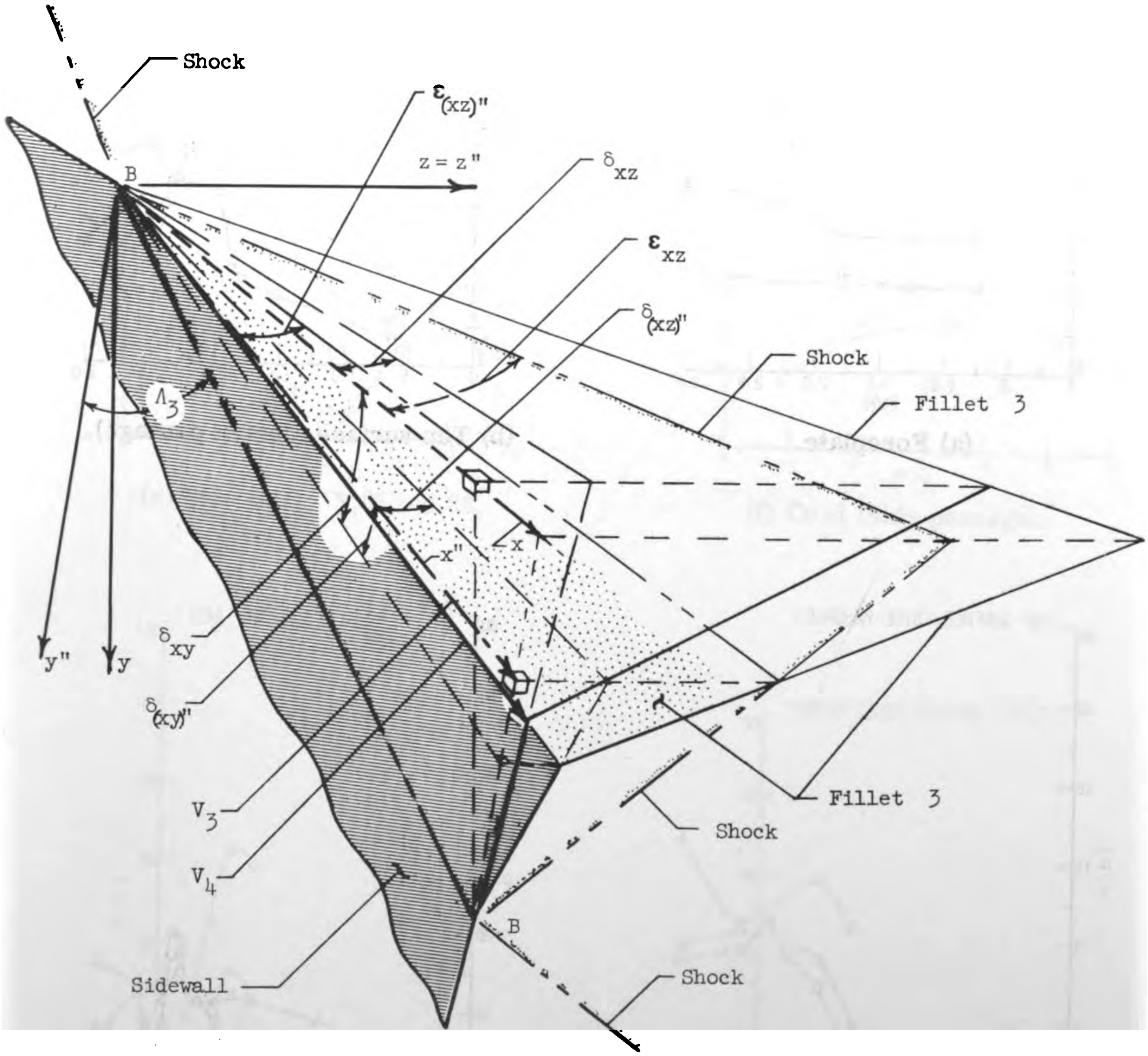

Figure 60.- Second reflected shock wave.

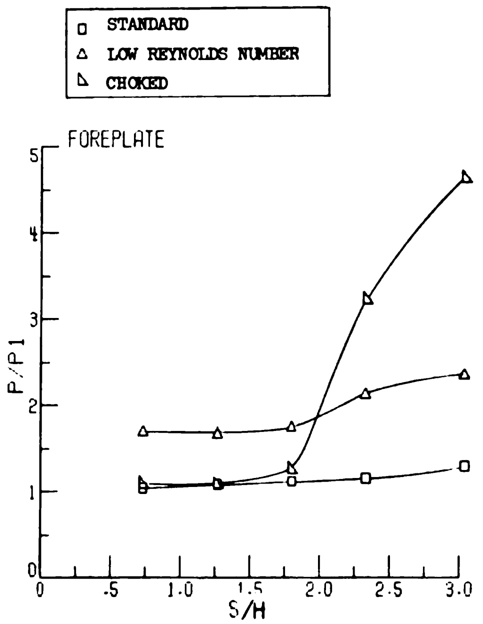

(a) Foreplate.

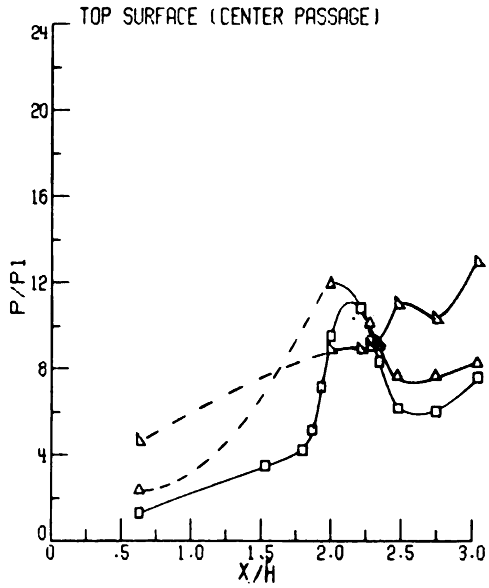

(b) Top surface (center passage).

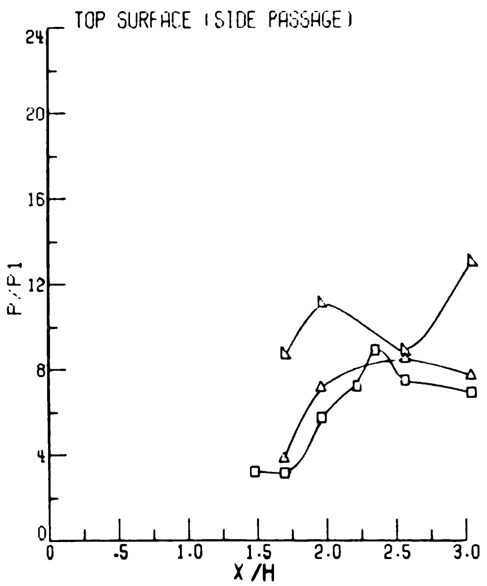

(c) Top surface (side passage).

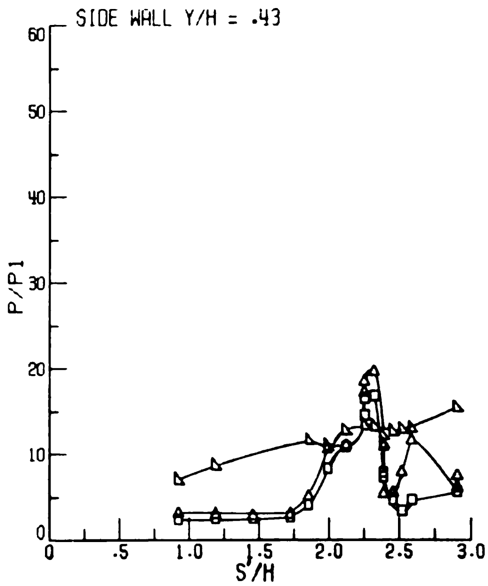

(d) Side wall; Y/H = 0.43.

Figure 61.- Static pressure distributions for low pressure and choked inlet tests. $M_1 = 6.0$.

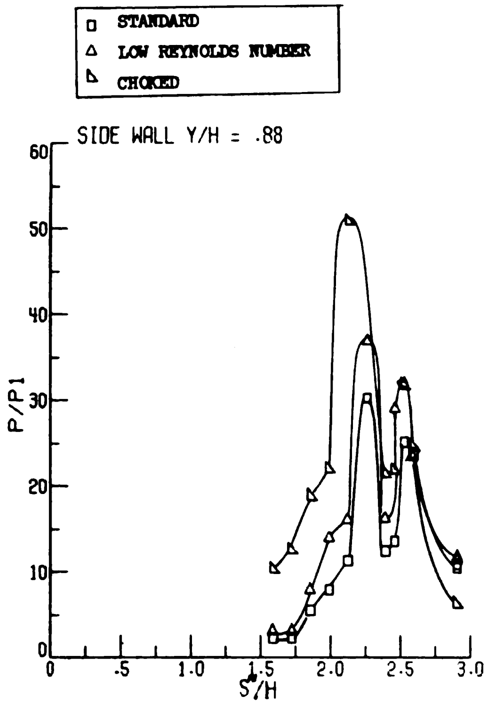

(e) Side wall; Y/H = 0.88.

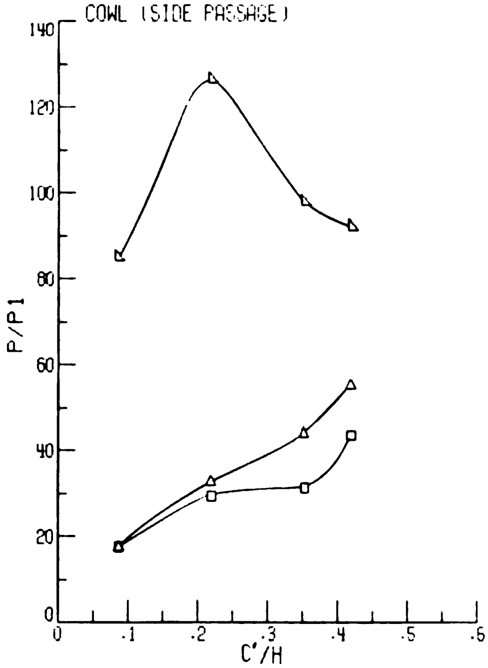

(f) Cowl (side passage).

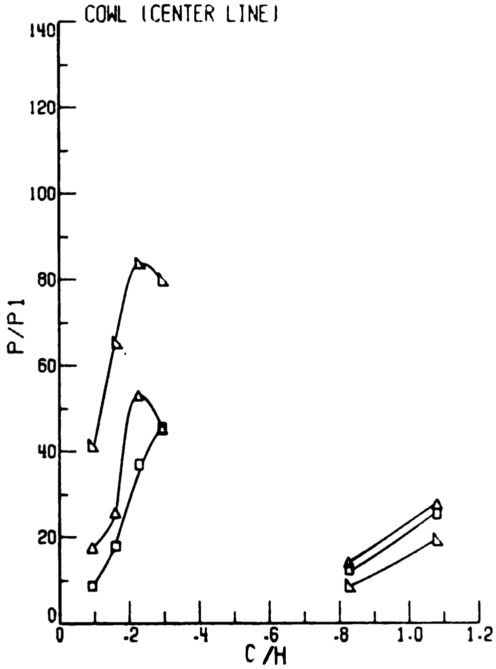

(g) Cowl (center line).

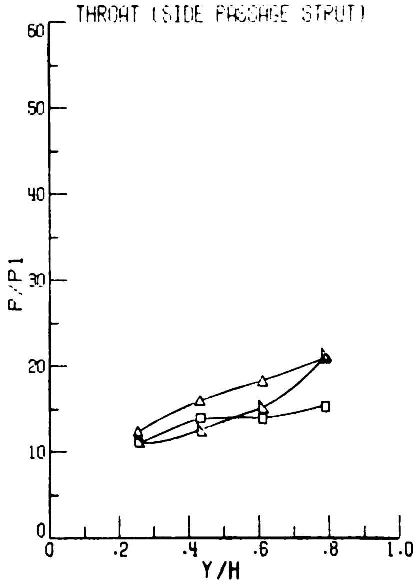

(h) Throat (side-passage strut).

Figure 61.- Continued.

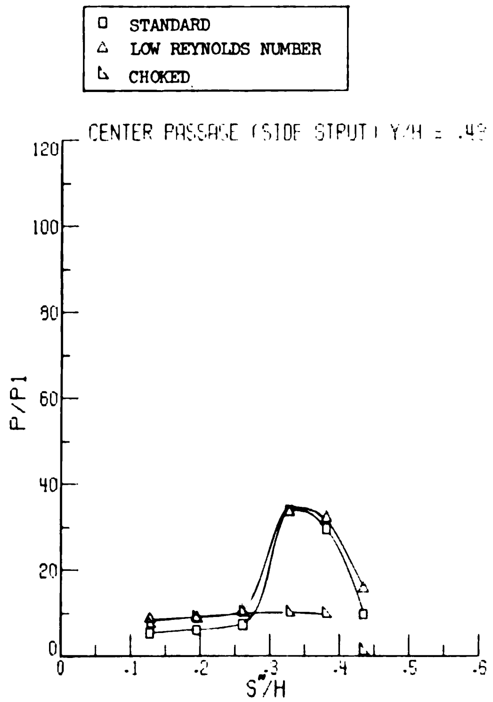

(i) Center passage (side strut); Y/H = 0.43.

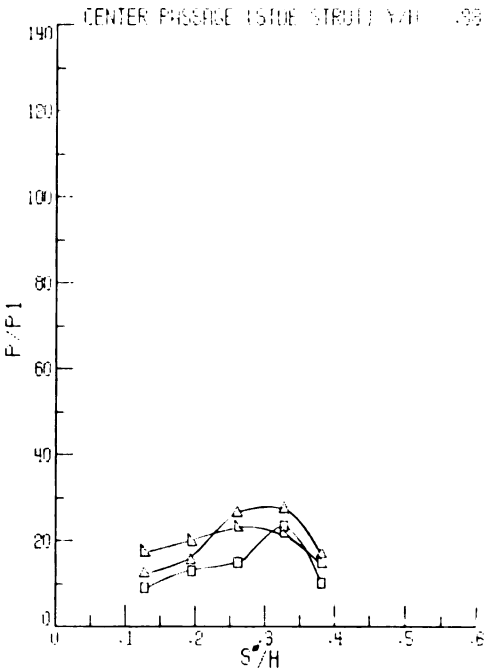

(j) Center passage (side strut); Y/H = 0.88.

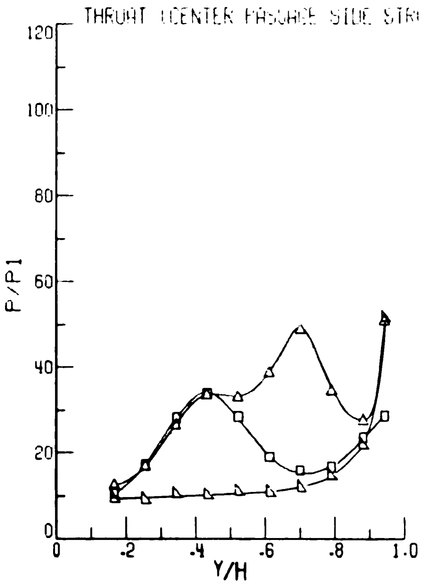

(k) Throat (center-passage side strut).

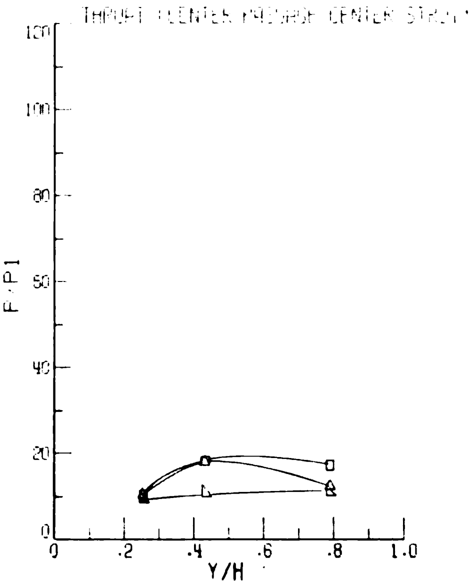

(l) Throat (center-passage center strut).

Figure 61.- Concluded.

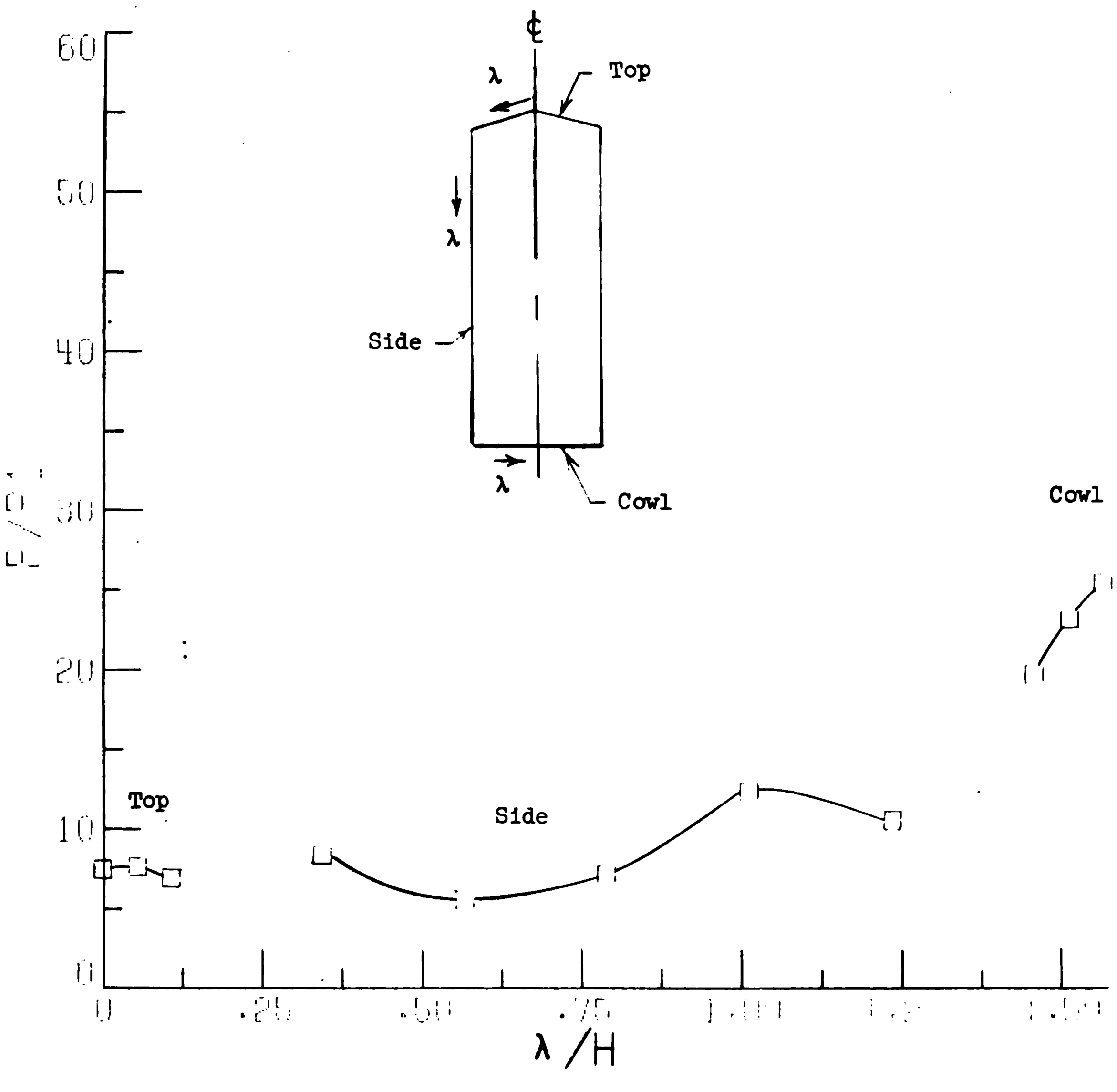

Figure 62.- Wall static-pressure distribution at capture station.

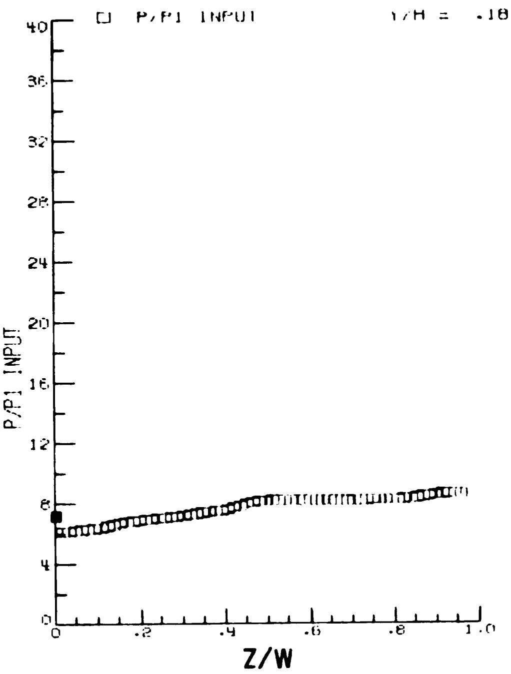

(a) Y/H = 0.18.

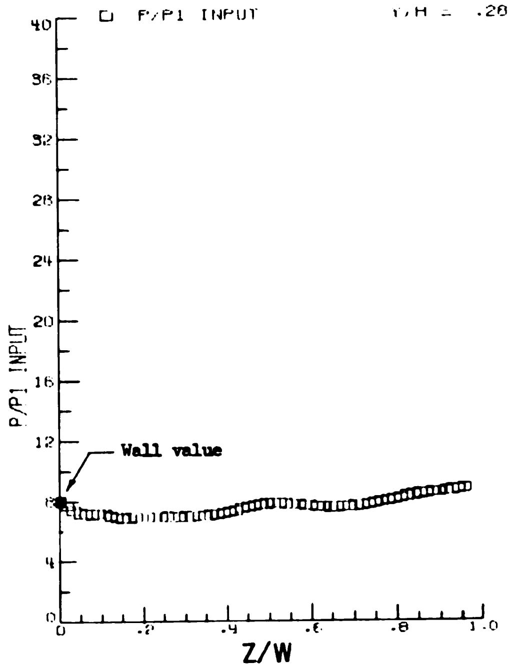

(b) Y/H = 0.28.

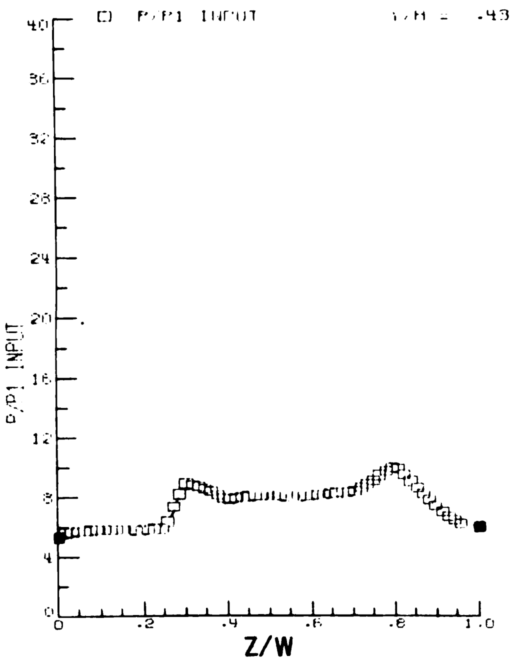

(c) Y/H = 0.43.

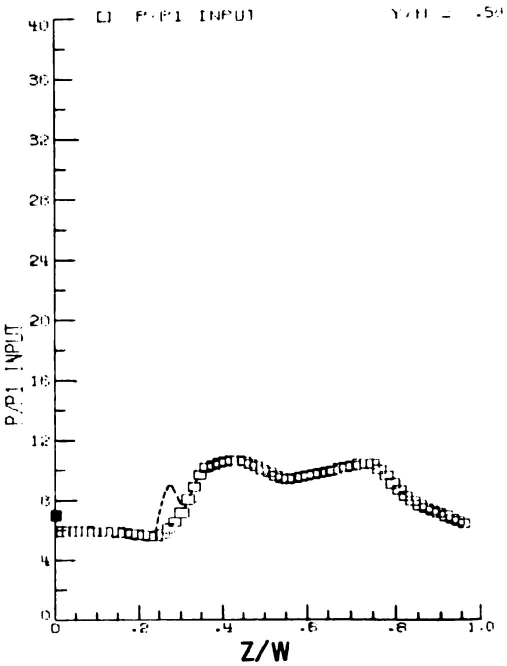

(d) Y/H = 0.58.

Figure 63.- Static-pressure surveys at capture station. $M_1 = 6.0$.

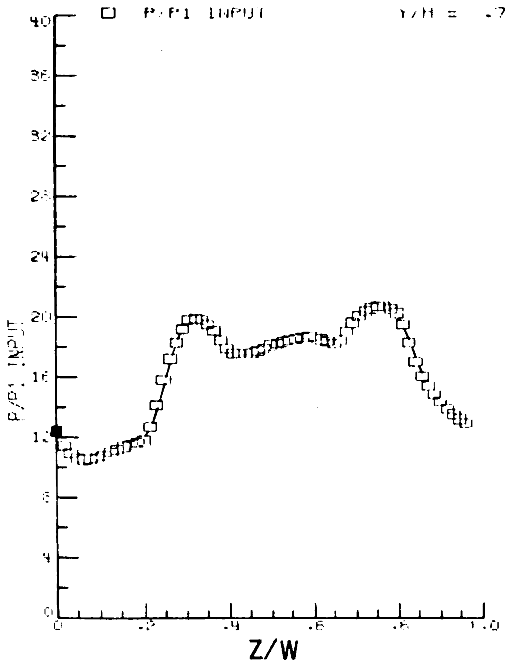

(e) Y/H = 0.73.

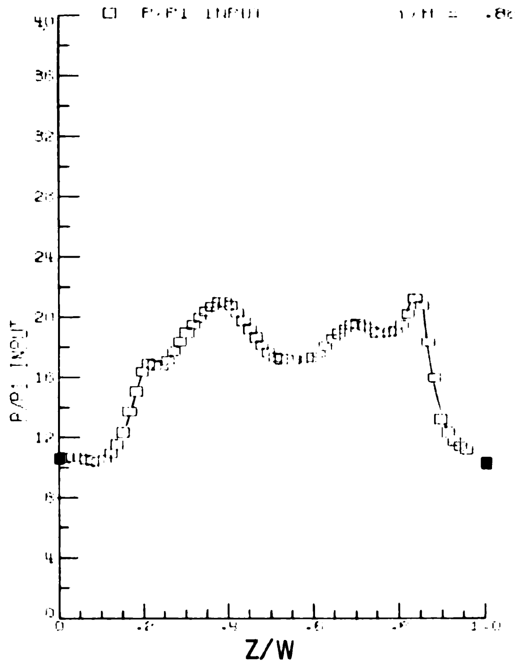

(f) Y/H = 0.88.

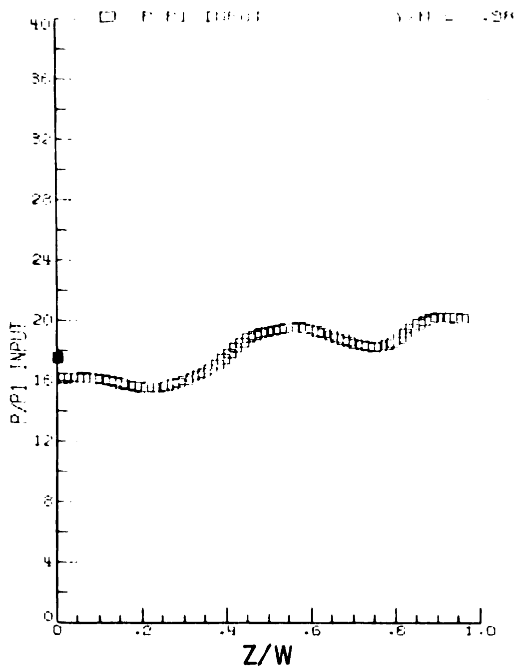

(g) Y/H = 0.98.

Figure 63.- Concluded.

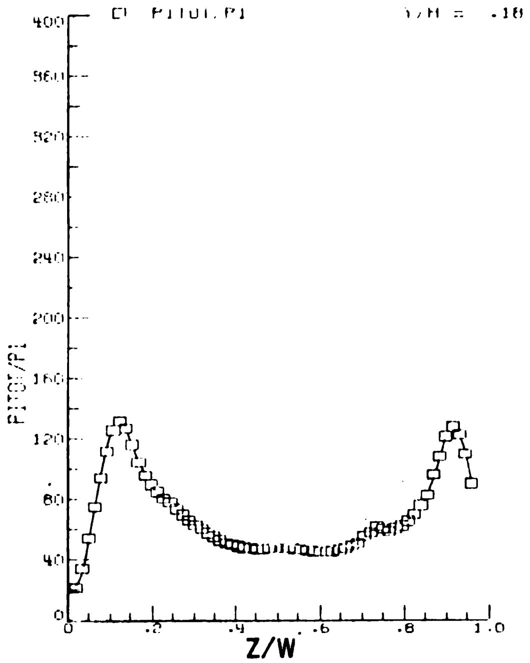

(a) Y/H = 0.18.

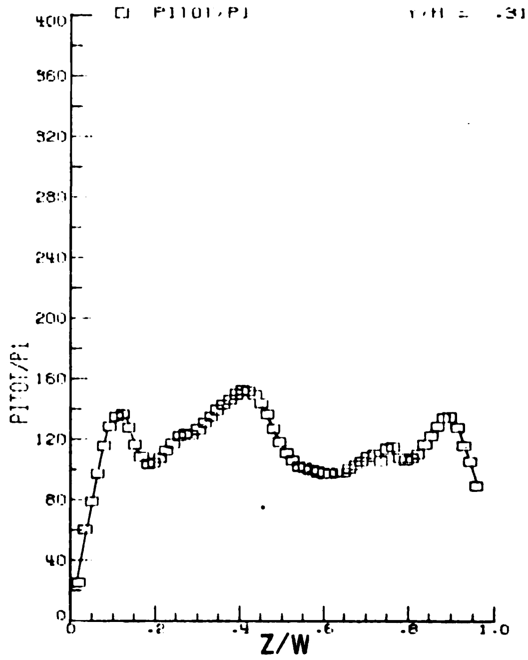

(b) Y/H = 0.31.

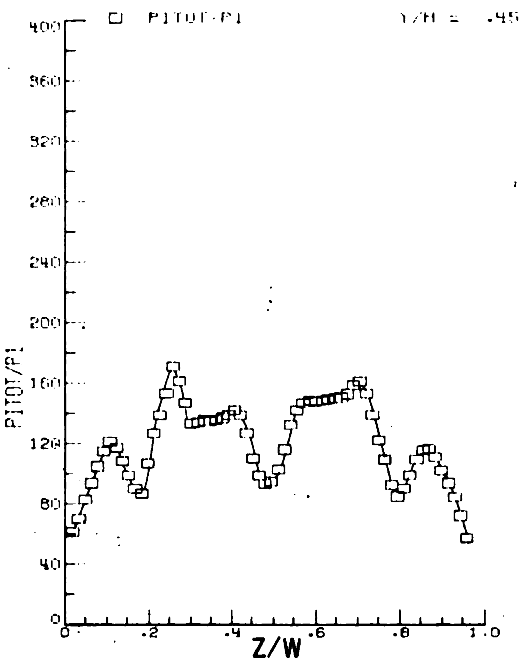

(c) Y/H = 0.45.

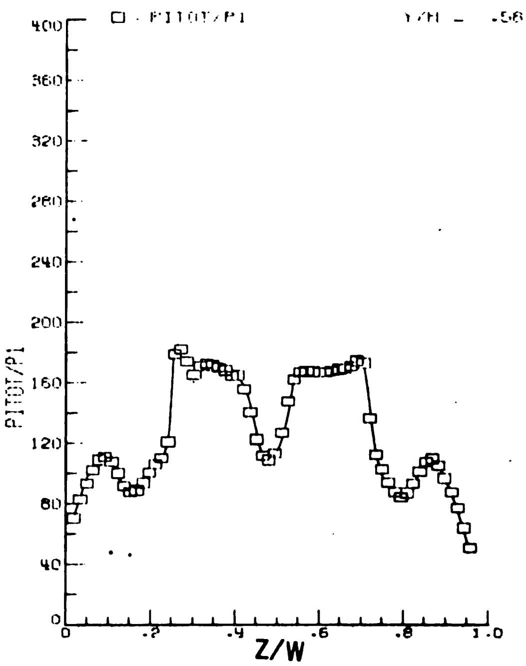

(d) Y/H = 0.58.

Figure 64.- Pitot-pressure surveys at capture station. $M_1 = 6.0$.

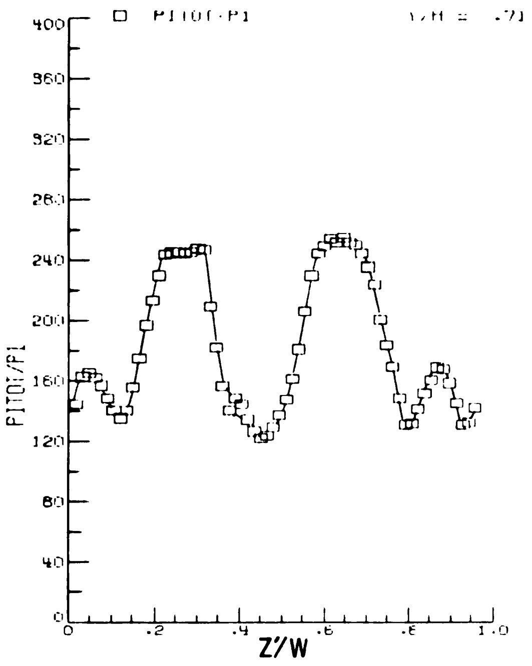

(e) Y/H = 0.71.

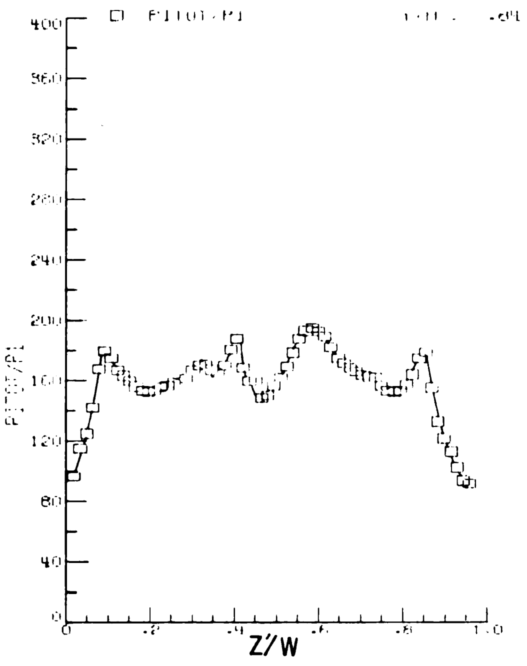

(f) Y/H = 0.84.

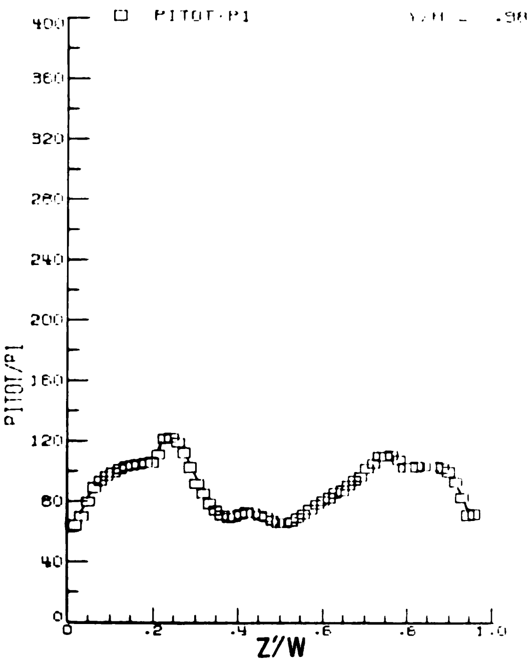

(g) Y/H = 0.98.

Figure 64.- Concluded.

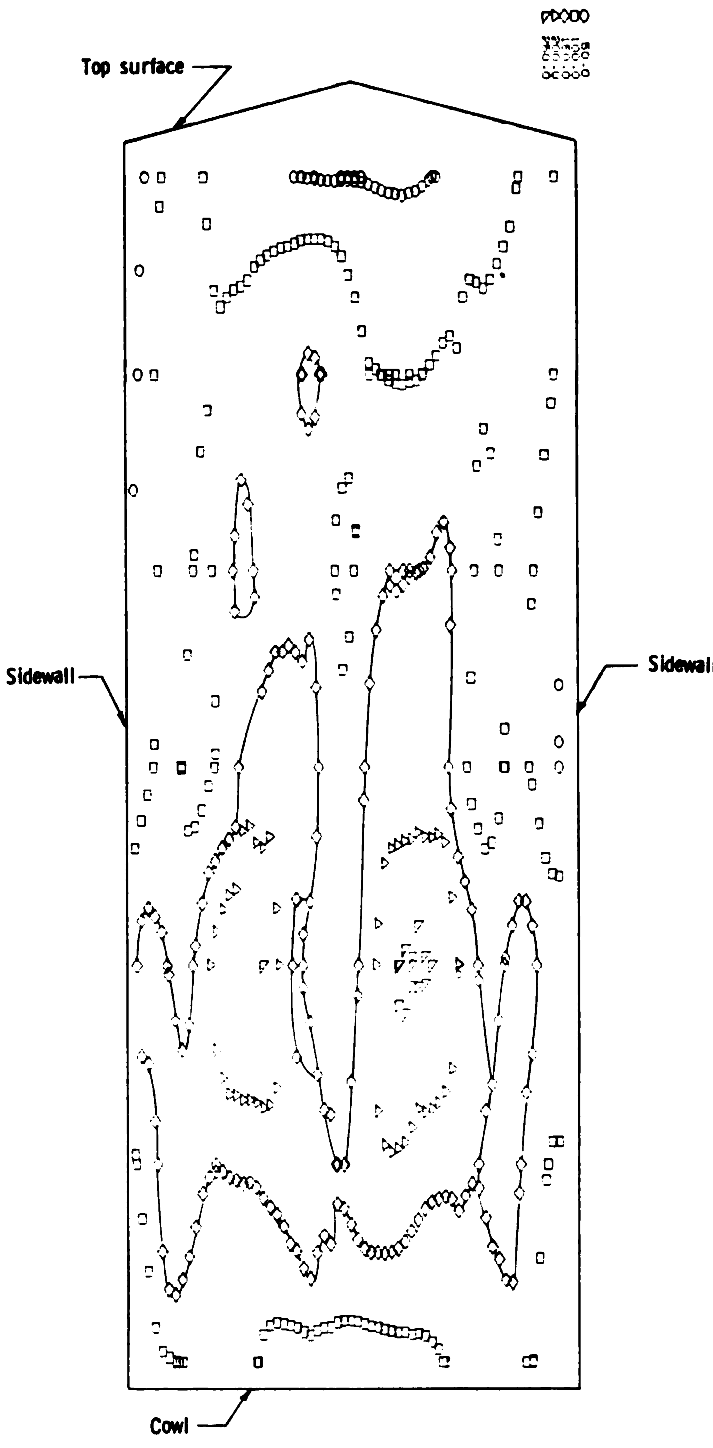

Figure 65.- Capture station. p_{pitot}/p_1.

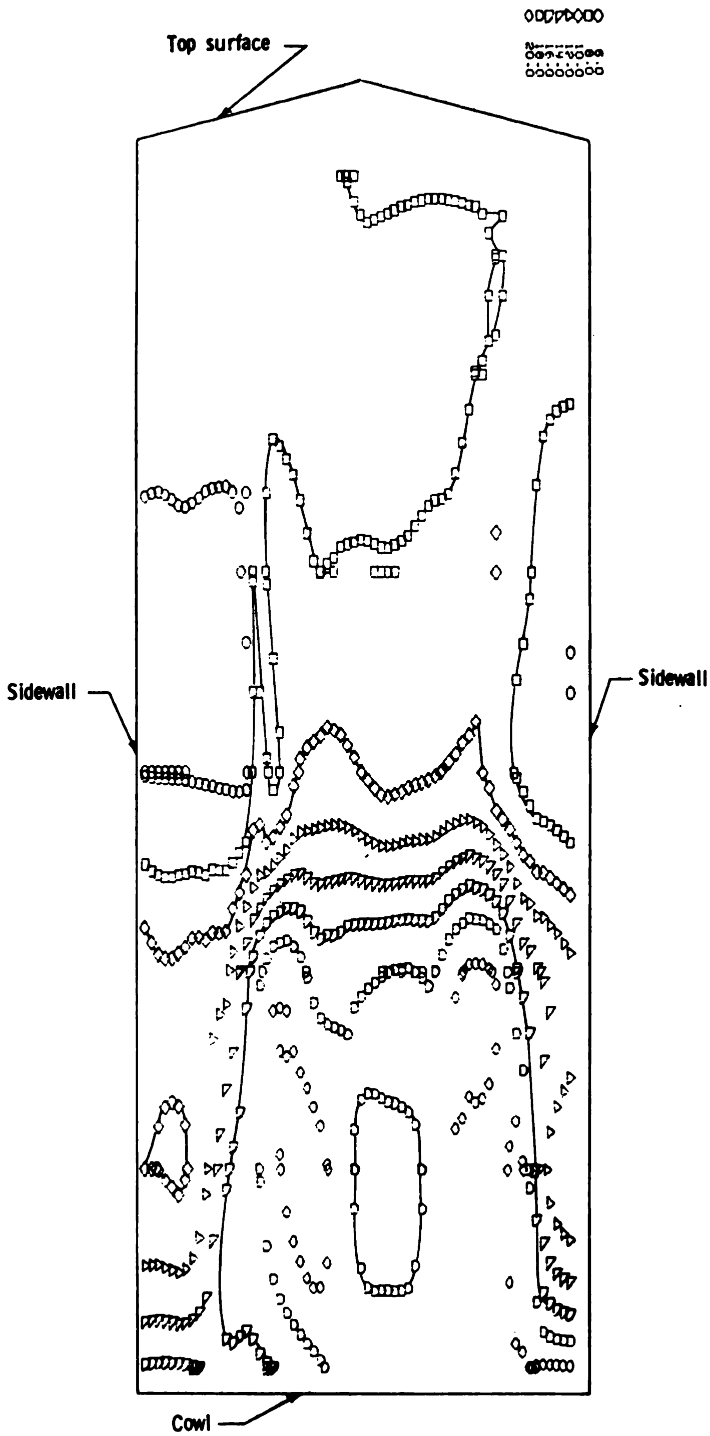

Figure 66.- Capture station. p/p_1.

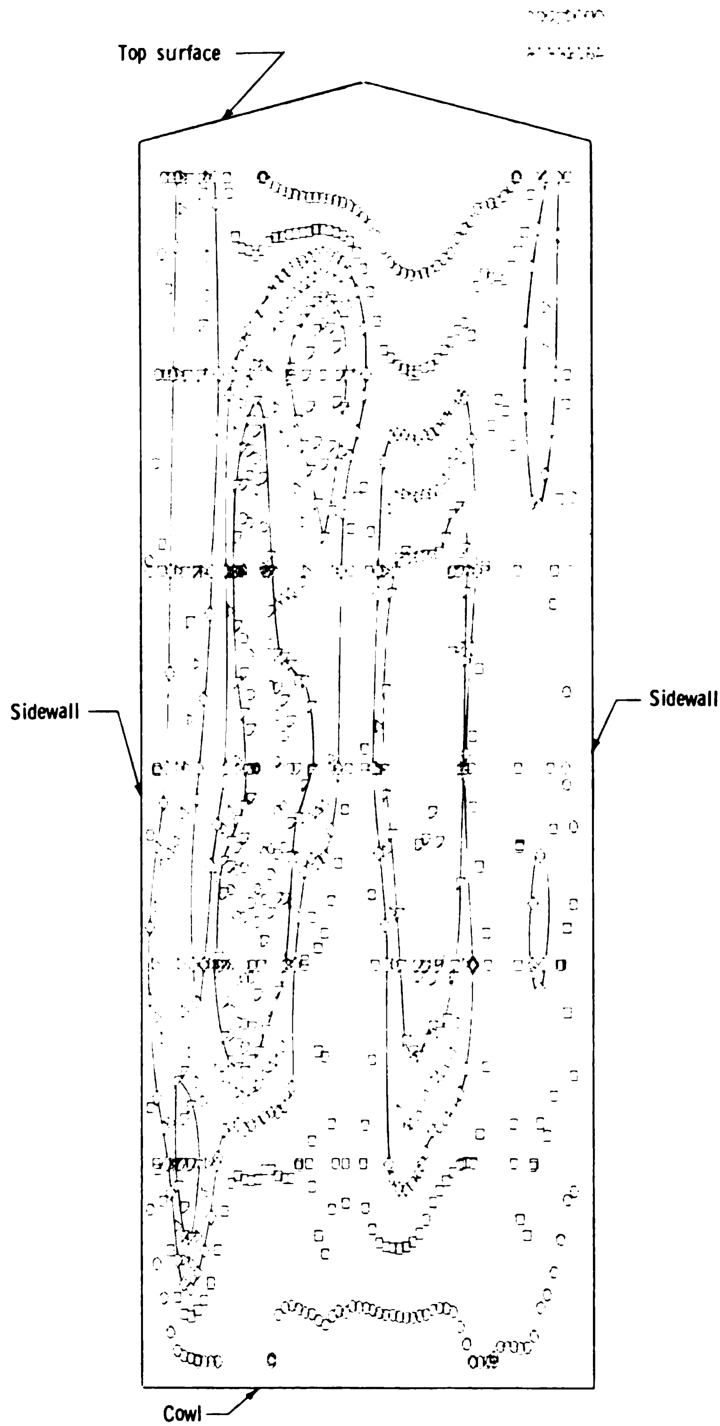

Figure 67.- Capture station total-pressure recovery.

NASA-Langley, 1975 L-10000

"The aeronautical and space activities of the United States shall be conducted so as to contribute . . . to the expansion of human knowledge of phenomena in the atmosphere and space. The Administration shall provide for the widest practicable and appropriate dissemination of information concerning its activities and the results thereof."

—NATIONAL AERONAUTICS AND SPACE ACT OF 1958

NASA SCIENTIFIC AND TECHNICAL PUBLICATIONS

TECHNICAL REPORTS: Scientific and technical information considered important, complete, and a lasting contribution to existing knowledge.

TECHNICAL NOTES: Information less broad in scope but nevertheless of importance as a contribution to existing knowledge.

TECHNICAL MEMORANDUMS: Information receiving limited distribution because of preliminary data, security classification, or other reasons. Also includes conference proceedings with either limited or unlimited distribution.

CONTRACTOR REPORTS: Scientific and technical information generated under a NASA contract or grant and considered an important contribution to existing knowledge.

TECHNICAL TRANSLATIONS: Information published in a foreign language considered to merit NASA distribution in English.

SPECIAL PUBLICATIONS: Information derived from or of value to NASA activities. Publications include final reports of major projects, monographs, data compilations, handbooks, sourcebooks, and special bibliographies.

TECHNOLOGY UTILIZATION PUBLICATIONS: Information on technology used by NASA that may be of particular interest in commercial and other non-aerospace applications. Publications include Tech Briefs, Technology Utilization Reports and Technology Surveys.

Details on the availability of these publications may be obtained from:

SCIENTIFIC AND TECHNICAL INFORMATION OFFICE

NATIONAL AERONAUTICS AND SPACE ADMINISTRATION

Washington, D.C. 20546

NASA TECHNICAL NOTE NASA TN D-7945

NASA TN D-7945

AN AUTOMATIC DATA SYSTEM FOR VIBRATION MODAL TUNING AND EVALUATION

Robert A. Salyer, Ed J. Jung, Jr., Stacy L. Huggins, and Barry L. Stephens

Lyndon B. Johnson Space Center
Houston, Texas 77058

NATIONAL AERONAUTICS AND SPACE ADMINISTRATION • WASHINGTON, D. C. • APRIL 1975

1. Report No. NASA TN D-7945	2. Government Accession No.	3. Recipient's Catalog No.
4. Title and Subtitle AN AUTOMATIC DATA SYSTEM FOR VIBRATION MODAL TUNING AND EVALUATION		5. Report Date April 1975
		6. Performing Organization Code JSC-09249
7. Author(s) Robert A. Salyer, TRW Systems Group; Ed J. Jung, Jr., JSC; and Stacy L. Huggins and Barry L. Stephens, Northrop Services, Inc.		8. Performing Organization Report No. JSC S-435
9. Performing Organization Name and Address Lyndon B. Johnson Space Center Houston, Texas 77058		10. Work Unit No. 961-21-31-05-72
		11. Contract or Grant No.
12. Sponsoring Agency Name and Address National Aeronautics and Space Administration Washington, D.C. 20546		13. Type of Report and Period Covered Technical Note
		14. Sponsoring Agency Code

15. Supplementary Notes

16. Abstract

A digitally based automatic modal tuning and analysis system developed to provide an operational capability beginning at 0.1 hertz is described. The elements of the system, which provides unique control features, maximum operator visibility, and rapid data reduction and documentation, are briefly described; and the operational flow is discussed to illustrate the full range of capabilities and the flexibility of application. The successful application of the system to a modal survey of the Skylab payload is described. Information about the Skylab test article, coincident-quadrature analysis of modal response data, orthogonality, and damping calculations is included in the appendixes. Recommendations for future application of the system are also made.

17. Key Words (Suggested by Author(s))	18. Distribution Statement
·Structural Vibration ·Forced Vibration ·Digital Servomechanisms ·Harmonic Excitation ·Strain Gage Accelerometers ·Orthogonality ·Fourier Analysis ·Shakers	STAR Subject Category: 18 (Spacecraft Design, Testing and Performance)

19. Security Classif. (of this report)	20. Security Classif. (of this page)	21. No. of Pages	22. Price*
Unclassified	Unclassified	44	$3.75

*For sale by the National Technical Information Service, Springfield, Virginia 22151

CONTENTS

Section | Page

TABLES

FIGURES

AN AUTOMATIC DATA SYSTEM FOR

VIBRATION MODAL TUNING AND EVALUATION

By Robert A. Salyer,[*] Ed J. Jung, Jr.,
Stacy L. Huggins,[†] and Barry L. Stephens[†]
Lyndon B. Johnson Space Center

SUMMARY

A state-of-the-art data system was developed to achieve the objectives of the ͻration modal survey phase of the Skylab vibroacoustic test program. The ν-frequency requirements dictated a digital-based system capable of operation ›m 0.1 to 100 hertz.

An automatic modal tuning and analysis system was conceived and developed meet the stringent test requirements and to achieve the objectives of the modal rvey. The system uses digital techniques to provide positive control of test nditions, a high degree of specimen safety, rapid data acquisition and reduction, d immediate documentation of modal response characteristics. Man-computer teractive control allows ample operational flexibility.

The system was sucessfully used to perform a modal survey of the Skylab yload in the launch and orbital configurations. The system incorporates analyti- l and experimental procedures to fully close the circle of modal survey plementation: pretest analysis, test implementation, and posttest loads analysis. ıta derived during pretest analysis are an integral part of the data base available complement and assess the data obtained experimentally during system plication. The system output consists of a complete data package that may be ımediately used for loads analysis without further reduction or manipulation. This chnique provided the foundation for the automatic modal tuning and analysis 'stem design criteria and contributed significantly to the success and wide accept- ıce of the system.

INTRODUCTION

The NASA Lyndon B. Johnson Space Center (JSC) Vibration and Acoustic est Facility (VATF) was built in 1964 and was equipped for performing a wide ınge of structural dynamic testing. Since the inception of the VATF, test operations

---

*TRW Systems Group, Redondo Beach, California.

†Northrop Services, Inc., Houston, Texas.

have involved both acoustic and mechanical excitation of complex elastic structures inherent in manned spacecraft. In the intervening years, the facility test capabilities have been constantly refined to meet the diverse requirements of numerous Apollo spacecraft test programs. In turn, the subsequent Skylab vibroacoustic test program, recently completed at VATF, stimulated development of a high-performance system for performing vibration modal surveys.

The computer-based automatic modal tuning and analysis system (AMTAS) is a major advance in the state of the art of such systems available within NASA. The AMTAS uses a greater complexity of digital techniques to perform excitation force control and data acquisition, processing, and display than was previously available. These digital techniques eliminate the low-frequency processing limits of analog instruments and provide substantial improvements in the quality of the resulting data. The system includes a large number of automated functions to expedite test operations, to provide maximum test article safety during test operations, and to eliminate excessive test article exposure and program delays by providing rapid data acquisition and reduction capabilities.

The AMTAS has been used on two Skylab modal surveys involving the largest and most complex spacecraft built by NASA. Data were obtained from the surveys of two configurations of the Skylab orbiting laboratory, which consists of an assembly of six modules. The Skylab test article is discussed in appendix A. These configurations, both approximately 21 meters (70 feet) high, embodied complex, unsymmetrical structural arrangements that weigh approximately 54 430 kilograms (120 000 pounds). These modal surveys, which required documenting all modes in the range of 1 to 45 hertz, were performed despite severe limitations due to schedule time, number of shaker excitation points, and response measurements available. The complexity of the Skylab structure and the urgency of the survey results warranted development of the AMTAS, which is nearly as complex as the Skylab structure. Through these Skylab surveys, AMTAS concepts and capabilities were verified, and a highly mature modal survey system consisting of sophisticated test equipment and software resulted. The purpose of this paper is to present a general overview of the hardware and software components of the AMTAS. A functional description of the system capabilities also is given.

As an aid to the reader, where necessary the original units of measure have been converted to the equivalent value in the Système International d'Unités (SI). The SI units are written first, and the original units are written parenthetically thereafter.

SYSTEM DESCRIPTION

The system description includes AMTAS general features, the computer, support subsystems, the excitation and excitation control subsystems, the data acquisition subsystem, and the monitoring subsystem.

General Features

Digital techniques are used to provide a low-frequency operating bound of virtually zero hertz without compromise of capability. Positive excitation control is achieved through force feedback digital control of the forcing function. The narrow-band filtering and coincident-quadrature (co-quad) capabilities are extended to essentially zero hertz through software for digital filtering and data reduction.

Six elements constitute the AMTAS: a computer, a software support package, an excitation control subsystem, an excitation subsystem, a data acquisition subsystem, and a monitoring subsystem. Concise information about data storage and presentation is presented in table I. The conceptual layout of the AMTAS is shown in figure 1. Some ancillary support systems used in the application of AMTAS to perform related tasks are discussed in the latter part of this section.

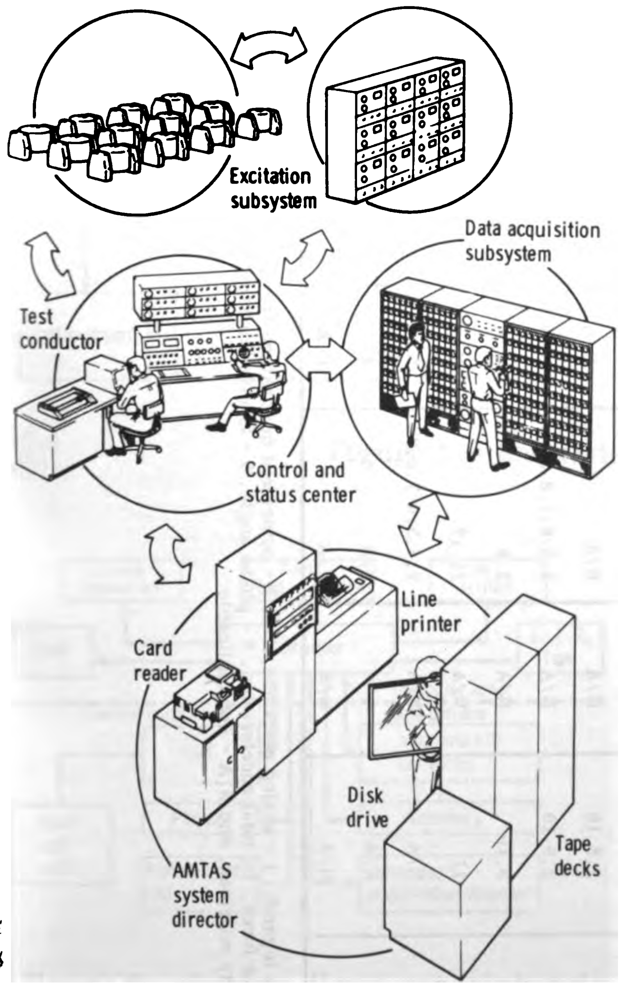

Figure 1.- Conceptual layout of AMTAS.

The control, data acquisition, and excitation subsystems are interconnected with the computer through the peripherals (fig. 2). Man-computer interactive control of system functions is provided by the keyboard display units at the control console. Real-time data reduction, modal purity, and data validity assessment results are displayed on the alphanumeric cathode-ray-tube (CRT) display. Quick-look graphic documentation is presented on the graphic CRT hard-copy unit and digital plotter.

Computer

A general-purpose computer having 32 000 words of core memory is used to direct the system. The computer supports the following peripherals: a card reader, a card punch, a line printer, a disk drive, tape decks, a console typewriter, input signal selectors, a multiplexer (MUX) and analog-to-digital (A/D) converter, an alphanumeric CRT with keyboard, an alphanumeric-graphic CRT with keyboard, a force and acceleration detector, and digital plotters. The physical placement of the computer and the peripherals is indicated in figure 3.

TABLE I.- DATA STORAGE AND PRESENTATION MATRIX

Operation	Presentation medium[a]						Storage medium[a]		
	Alphanumeric CRT	Graphic CRT and hard copy	Line printer	Digital plotter	Oscillograph	Card	Digital magnetic tape	Analog magnetic tape	Disk
SUPSS	2,9,10	N/A	2,5,6,7,9	3	N/A	N/A	2,5,6,7	N/A	N/A
SUPTS	2,9,10	N/A	N/A	N/A	N/A	N/A	N/A	N/A	N/A
SUPTM	2,9,10	N/A	N/A	N/A	N/A	N/A	N/A	N/A	N/A
SUPSM	2,9,10	N/A	2,5,6,7,9	3	N/A	N/A	2,5,6,7	N/A	N/A
SUPMD	2,9,10	N/A	N/A	N/A	1	N/A	N/A	1,6	N/A
SUPDW	2,9,10	N/A	2,5,6,7,8,9	N/A	N/A	N/A	2,5,6,7,8	N/A	2,4,5,6,7,8,9
ASUPS	9,10	N/A	2,9	N/A	N/A	N/A	N/A	1,6	N/A
ORTHO	11	N/A	11,12	N/A	N/A	N/A	N/A	N/A	N/A
Print	N/A	N/A	2,4,5,6,7,8,9	N/A	N/A	N/A	N/A	N/A	N/A
Plot	N/A	4	N/A	4	N/A	N/A	N/A	N/A	N/A
Punch	N/A	N/A	N/A	N/A	N/A	5,2	N/A	N/A	N/A

[a]Data legend: 1 - analog response data, 2 - coincident quadrature (co-quad), 3 - co-quad × 10 000, 4 - translated co-quad, 5 - bookkeeping data, 6 - reference force, 7 - total acceleration, 8 - phase angle, 9 - forcing distribution, 10 - high-limit acceleration, 11 - orthogonality result, 12 - 2 × 2 orthogonality matrices, and N/A - not applicable.

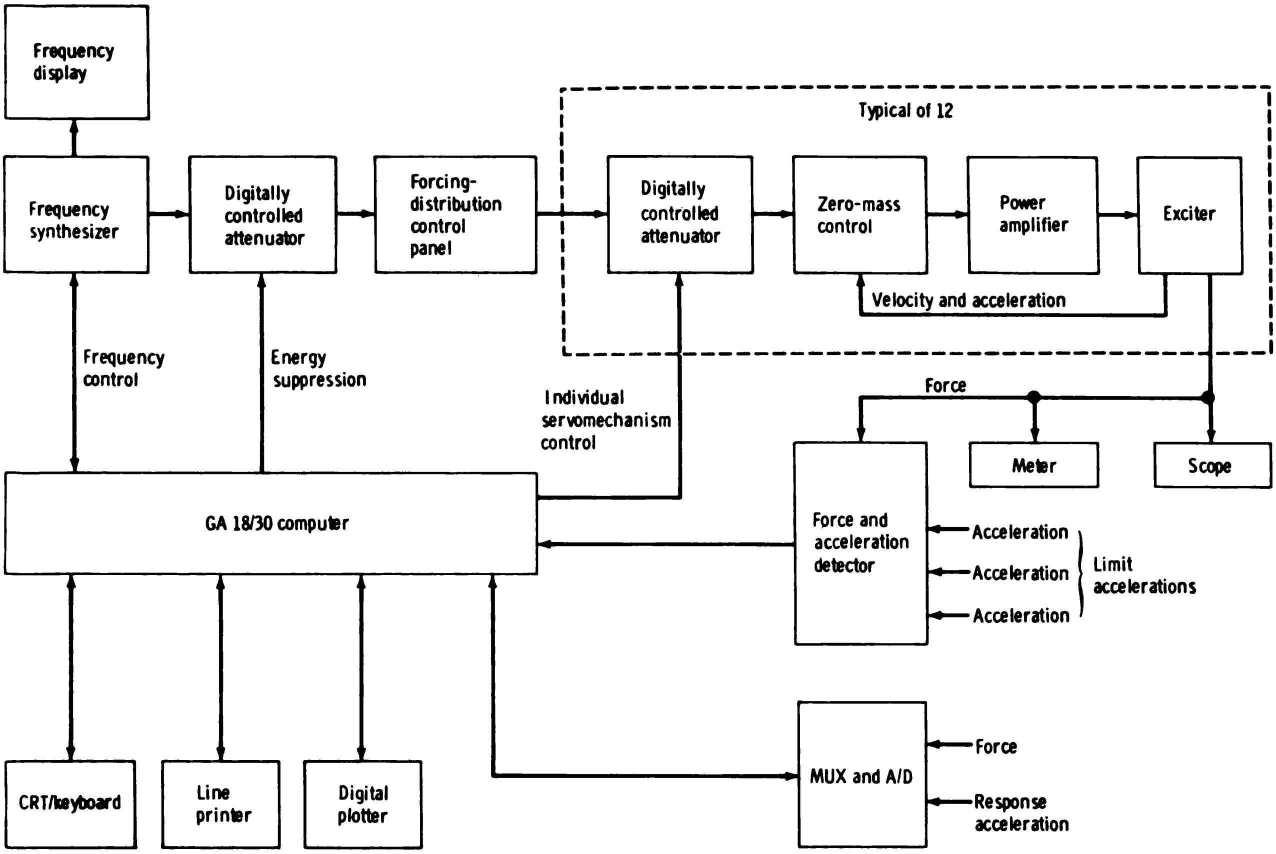

Figure 2.- Excitation control subsystem.

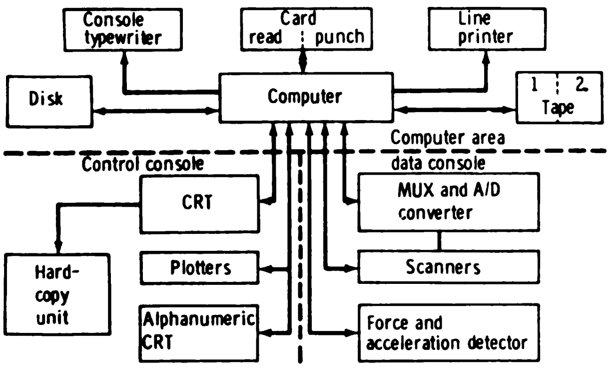

Figure 3.- System director peripherals.

The computer operates under a group of programs (supplied by the manufacturer) for generating, organizing, testing, and executing programs for real-time data acquisition and control. The major components of this software include a machine language assembler, a FORTRAN compiler, a loader, a disk utility program, a supervisor, and a real-time system director.

The system director, which controls the real-time data acquisition and control programs, consists of time-sharing control, program sequence control, master interrupt control, interval timer control, and error alert control. A subroutine library consists of programs for input-output conversion and for performing arithmetic, functional, selective dump, debug, and miscellaneous operations. In addition, three other categories of software are required for the system: input-output handlers for nonstandard peripherals, application programs (real time and off line), and test and validation routines. These three groups of software, referred to as the software support package, were written specifically for the AMTAS application.

Software Support Package

Five process control functions are provided by the software support package: sweep direction and linear rate, response channel selection, phase-lock control, force distribution control, and limiting of critical accelerations. Data acquisition is inhibited when any servomechanism (servo) correction (force level or frequency) is in progress. The software support package also provides the data acquisition, data reduction, and modal documentation features of the system.

A modular structure for the software support package is dictated by several realities of test performance. Core memory limitations are greatly diminished by the use of overlay and disk-resident structured coreloads that are loaded on demand. Subroutines are used to the greatest possible extent, and many are reentrant. File data must be installed early (with final corrections expected before the survey commences) to enable performance of the system confidence test. These files (e.g., the mass model of the structure) are sometimes corrected during the course of the test. These requirements are accommodated by separate data files in the software support package. The organization of the software support package is shown in figure 4.

All structure-dependent data exist in files that are easily maintained during model updates and revisions. The operational program, the file creation program, and the file input program with data modules are stored and maintained separately. For a future modal test, only the file input modules need be revised to include the structure-peculiar data; other modules are independent of structure.

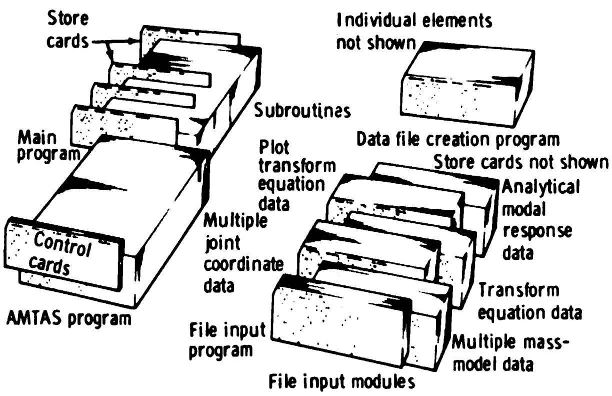

Figure 4.- Organization of software support package.

The data file creation module creates the files required for program execution, including the structure-dependent data. The structure-dependent data files can be revised at any time without disturbing the other programs by replacing the data deck and reloading and executing the file input program.

Process control.- The process control sequence during modal sweeps is shown in figure 5. The sweep parameters and reference transducers are selected by keyboard entry. Frequency incrementing is initiated by command. The individual force distribution and

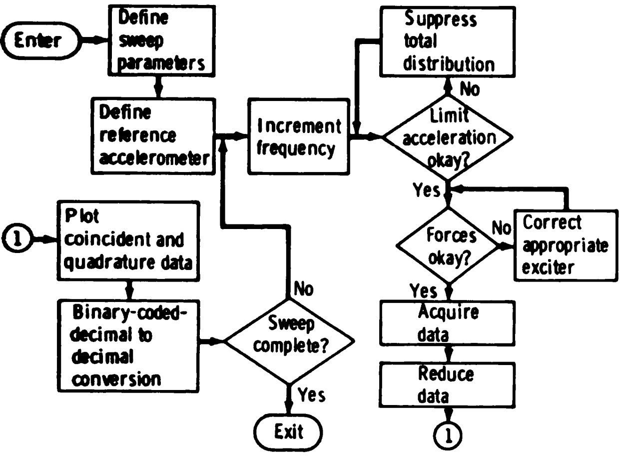

Figure 5.- Process control, sweep mode.

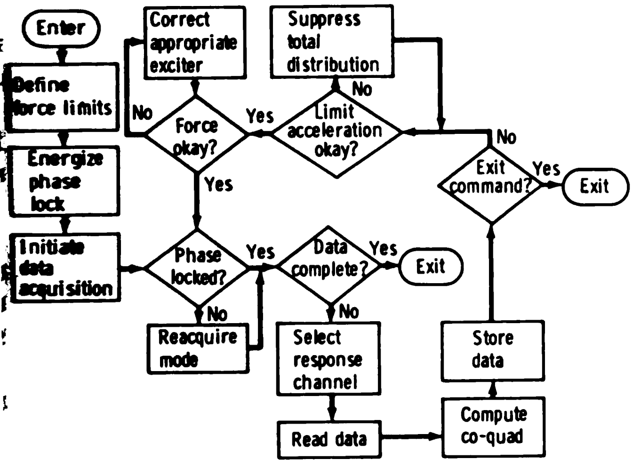

Figure 6.- Process control, dwell mode.

limit accelerations are checked and corrected if required. Data samples are acquired, and total-response data from three reference accelerometers are resolved into co-quad components. The co-quad data are plotted, and the frequency is incremented. This sequence is repeated until the sweep is completed.

The process control sequence during a modal dwell is shown in figure 6. After the modal decay indicates that the desired mode has been separated from adjacent modes, the run number and the mode number are entered on the CRT keyboard. All other bookkeeping and test data are acquired by the computer to completely eliminate manual recording errors. Phase lock and data acquisition are initiated by keyboard entry. The first set of three response channels is selected for co-quad analysis. When data sampling is complete, the next set of response accelerometers is selected for priority level sampling, while data reduction, documentation, and storage continue on the main-line level of software operation. If an exit command has not been entered on the keyboard, the force distribution and limit acceleration are corrected, if required. The sequence is repeated until all response data are acquired or until an exit command is received. Fourteen digital servos are active during the modal dwell: twelve individual force servos, the total energy servo, and the frequency servo (phase lock).

Data acquisition.- Several data acquisition functions are common to both sweep and dwell modes of operation. Bookkeeping data (run number and mode number) are entered by means of the manual CRT keyboard, shown at the left of figure 2. The format is printed out on the display such that the letter "X" appears where data must be entered by the operator. After data entry, the send key is depressed to initiate read in by the computer. The format is updated and the input stored on disk. The run and mode numbers are used to subscript the incoming data for proper organization and storage in disk and tape files.

A view of the control console is given in figure 7. The keyboard display units are shown on the right side of the control console. Overall views of the AMTAS are shown in figures 8 and 9.

Figure 7.- The AMTAS control console.

Figure 8.- Overview of AMTAS looking toward the shaker amplifier console.

Figure 9.- Overview of AMTAS looking toward the narrow-band filters.

The force level of each active exciter is displayed on the alphanumeric CRT. Limit acceleration status is displayed at the bottom of the CRT at each force-level update time.

Response data are acquired by a keyboard-selected load cell and a set of three accelerometers. These transducers are fixed throughout a sweep. However, in the tuning mode, the load cell and the response accelerometers may be selected or changed at any time to examine response characteristics of the structure as the forcing distribution and frequency are varied to optimize a desired mode. In the dwell mode, the reference load cell is selected by keyboard entry. The data acquisition sequence, initiated on the keyboard, consists of acquiring response data from all accelerometers (maximum of 200) in groups of 3.

Data reduction.- The software support package provides maximum real-time visibility and immediate posttest documentation within minutes after response data from all transducers are acquired. This result is achieved by maximizing the data reduction that is performed as the data from each transducer are acquired.

The raw voltage data are converted to engineering unit data, and any direct-current component introduced by the signal-conditioning equipment is eliminated. These converted data are then processed by a Fourier analysis routine to digitally filter the data and to obtain the real and imaginary Fourier coefficients required for co-quad component resolution. Co-quad reduction techniques are described in appendix B. The co-quad components are derived and stored in core and magnetic tape files. These co-quad data are normalized to input force to remove this dependence.

After all data are acquired and reduced to co-quad components, the normalized quadrature data are translated to the mass-model (generalized) coordinates, and the generalized mass is computed. The generalized quadrature deflections are then normalized to unity generalized mass. These normalized, generalized quadrature deflection data are used for all data documentation.

Data documentation.- Documentation (fig. 10) consists of co-quad plots, decay curves, listing of raw voltage, engineering unit and generalized coordinate data, orthogonality matrix printout, modal plots, and a punched-card deck of modal response data. This documentation is available immediately after modal acquisition is completed.

The CRT display unit affords a dynamic, real-time status display. Parameters included are force levels, frequency, error, and status messages. Subroutine execution is initiated by a command entered on the keyboard.

Data listing by the line printer is initiated by keyboard entry. This listing is available for single modes or a total set of modes and includes status and bookkeeping, raw voltage, and engineering unit and generalized coordinate (normal mode) data. An additional keyboard entry will result in an orthogonality printout.

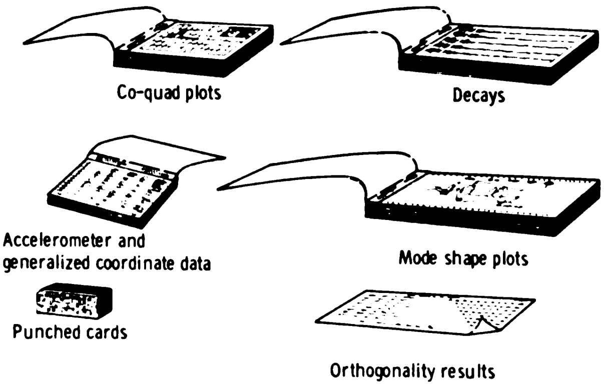

Figure 10.- Modal documentation.

Modal deflections for a given mode can be produced in the form of cards by means of a nonprocess program in an off-line, time-share computer mode. A set of stick plots (15 maximum) documents a mode in the form of node deflections as functions of vehicle station.

Excitation Control Subsystem

The use of digital feedback force-control techniques avoids the need for constant-bandwidth tracking analyzers and an analog servo unit, either of which imposes a low-frequency limit on the system. The frequency synthesizer, controlled by the computer (fig. 2), provides the desired frequency. The finest resolution is 0.01 hertz. The system master gain, which controls the total forcing distribution, is manually initialized but is adjusted under direct program control to suppress the total energy supplied to the structure if critical acceleration levels are exceeded. The signal from the ensemble of critical-location sensors, which sense the highest signal level, is selected with a force and acceleration detector. The output of this unit is fed to the computer to control the total energy level.

The forcing distribution is manually programed by level set and phase selection for each individual exciter. Phase adjustment is by sense only (0° or 180°). Other phase manipulation is undesirable because normal mode motions and damping forces act, respectively, in a 0° or 180° sense. The driving forces are continuously variable to cancel the internal damping shears and moments and thus to preserve the steady-state natural mode. To ensure preservation of the forcing distribution and natural mode, a detected signal from each amplifier representing force is monitored by the computer to allow computer adjustment of the current supplied to each individual exciter. If the system total amplitude is corrected by the computer, the individual forcing-distribution digital control output is factored to prevent recompensation.

A separate component of the excitation control subsystem is the zero-mass control. This unit eliminates the effects of armature and mechanical force-input coupler (stinger) mass during modal decays or when a zero-drive signal is applied to the exciter. In addition, because the armature circuit remains active during a modal decay, the unit must compensate for back electromotive force generated by the moving coil. A secondary effect of the control unit is to transform a voltage amplifier into an approximation of a current amplifier. A velocity transducer measures the differential velocity between the exciter body and the armature. (Back electromotive force is directly proportional to the differential velocity.) Mass cancellation is directly proportional to the acceleration of the armature-stinger assembly. Therefore, use of the acceleration signal measured on the vehicle at the stinger interface is appropriate. The signals generated by the two transducers are correctly phased and summed with the excitation drive signal, if present, to produce a positive-feedback system. The feedback signal is summed with the drive signal instead of switching the feedback signal into the amplifier input circuit on initiating a decay.

Excitation Subsystem

A single channel of the excitation subsystem consists of a solid-state, direct-coupled power amplifier; a field supply and control unit; a low-frequency, long-stroke exciter assembly; and a stinger. A maximum of 12 channels can be excited simultaneously by using a combination of 16 power amplifiers/field supplies and 24 exciters. A patching network provides access from a given exciter to any power amplifier.

The primary consideration in the design of the excitation system is to ensure that no phase shift occurs between any of the inputs to the structure. Phase shifts may occur electrically in the input circuitry to the power amplifiers or within the power amplifiers. A phase shift can also occur mechanically in the shaker support structure or the stinger. Direct coupling is advantageous in minimizing or deleting phase shifts in the input and drive circuits and is necessary for very-low-frequency operation. Direct coupling is used in the system principally because of the low-frequency design criterion.

The stinger assemblies were designed to be stiff enough to transmit the force input without the occurrence of an appreciable phase shift (less than 5°) at frequencies as high as the upper frequency limit. Nominal guidelines are to have the first mode of the stinger, axial or bending, at a minimum frequency of three times the upper frequency limit of the test band.

Data Acquisition Subsystem

A diagram of the data acquisition subsystem is shown in figure 11. The analog front end of the subsystem includes the following systems.

1. A strain gage signal-conditioning system capable of being patched into the test laboratory junction boxes supplies power, signal amplification, calibration capability, and bridge balancing capability for one to four active-element strain gage circuits and strain gage transducers, such as load cells.

2. A servo accelerometer signal-conditioning system capable of being patched into the test laboratory junction boxes supplies power, output signal balancing, and calibration for sensitive servo-type acceleration transducers.

The analog front end conditions the acceleration and force signals. Groups of transducers are selected automatically by the computer as inputs to the low-pass antialiasing filters. Digitized samples of the inputs are acquired by an MUX and A/D converter. Fourier analysis of these digitized data provides complex Fourier transform coefficients for the computation of coincident and quadrature values.

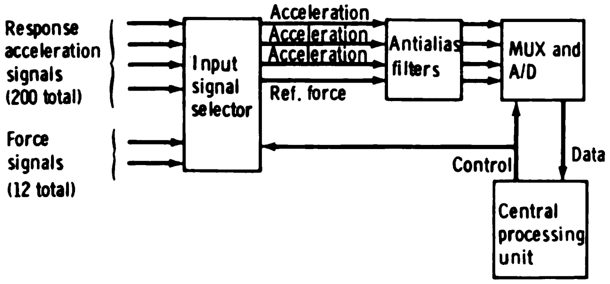

Figure 11.- Data acquisition subsystem.

Monitoring Subsystem

The peripheral monitoring subsystem consists of a group of analog meters, analyzers, and display units that aid tuning operations and provide continuous verification of system operation. The function of the monitoring subsystem is to display 12 Lissajous patterns simultaneously to aid the operator in tuning.

Twelve dual-channel dynamic analyzers act as narrow-band filters (5 hertz) to provide high-quality output signals of force and acceleration to the display units. In addition, a 90° phase shift is introduced between the two channels of the analyzer so that the Lissajous figure at resonance is a straight line rather than an ellipse. The paired outputs of the analyzers are hard wired to signal multiplexing units and then to bistable storage display units, which display four patterns on a single unit. (Storage display units are superior to standard oscilloscopes when operating at frequencies of less than 5 hertz.) Two options are available to the operators for tuning at frequencies of less than 3 hertz, where the analyzers cannot function. Because response signals are of much higher quality at lower frequencies, the main function of the analyzers is to provide the 90° phase shift between the force and acceleration signals. Therefore, the raw acceleration can be used to tune on elliptical patterns. An alternative is to use the raw velocity signal available from the shaker-mounted velocity transducers. By using these transducers only at the very-low frequencies, the phase problems associated with shaker body motion are avoided.

Other features of the monitoring subsystem include miniature oscilloscopes for continuous display of the raw force wave shape and analog voltmeters connected through a signal selector from the analyzer outputs. The analog meters are used to monitor force and acceleration when the central processor is not on line and to cross-check the digital data acquisition system during dwell operations by comparing analog and digital readings.

Ancillary Support Systems

The soft-spring suspension system provides a simulated free-free environment in which to excite and measure the natural elastic vibration modes of a structure. A maximum of 16 units can be used to suspend the test article. Each unit can support as much as 22 700 kilograms (50 000 pounds) while maintaining a very low resonance frequency.

The closed-circuit television capability consists of eight video channels, including cameras and controls. The video control console permits adjusting the position of each camera image. Patch panel and pushbutton selection capability are available for matching cameras and monitors. Scan conversion, split-screen special effects, waveform monitoring, and video signal conditioning are also available.

Analog data recording systems include the following:

1. Analog magnetic tape recorders having frequency multiplex input capability are used to record data for off-line co-quad reduction.

2. Oscillograph chart recorders that include dry-development, light-sensitive papers for recording galvanometer deflections are used to acquire unfiltered accelerometer data during modal decays.

An off-line co-quad analysis capability was developed to process data acquired from many transducers during an incremental sinusoidal sweep over a wide frequency band. The wide-band sweep is performed to define the structural modes. The processed data are used in conjunction with the analytical data to define target modes and to predict optimum forcing distributions.

SYSTEM APPLICATION

Two keyboard CRT terminals are used for entering test parameters, initiating commands to the software system, and displaying data and computations. When the computer is brought on line to support AMTAS operations, the system controller format (fig. 12) is displayed on the alphanumeric CRT. Several key features are programed into the display. As shown in the controller format, the correct page of the operating procedure that applies to the operation in progress is displayed, the allowed options are defined, and instructions for entering these options are given to the operator. The general scheme is to present the system operating instructions as follows.

```
ENTER DATA INTO  ·XX·  FIELDS USING FOLLOWING PROCEDURE:
     1- PRESS LOCAL KEY                    3- PRESS HOME KEY
     2- ENTER DATA                         4- PRESS HDX KEY
                                           5- PRESS SEND KEY

                                                  PROCEDURE SEQ:  01
                     -- AMTAS CONTROLLER --

        SELECTED MODULE WILL BE EXECUTED UPON ENTRY DEFINED BELOW:

-SD- EXC CONTROL AND DATA ACQ SUPVR    -PL- PLOT QWKLOOK AND HDCOPY DATA
-RE- REDUCE, STORE DATA FROM TAPE      -OR- ORTHOGONALITY BETWEEN MODES
-PR- HDCOPY PRINT OUT OF DATA          -EX- EXIT TO NON-PROCESS MONITOR
-CR- INITIATE CHECK POINT RESTART

(XX / )
```

Figure 12.- System controller CRT display.

1. Alphanumeric CRT

a. Line 1 consists of messages pertaining to general system operation and required entries (to be exercised by AMTAS control). Error messages are also displayed on this line.

b. Lines 2 to 19 are used for definition of allowed entries. (During real-time operations, this area is used for display of dynamic test parameters and the definitions are presented on the graphic CRT display.)

c. Line 20 consists of messages pertaining to vibration control (initializing gains, phases and level, etc.).

2. Graphic CRT

a. The storage area is used for definition of allowed entries when the alphanumeric CRT is displaying test parameters.

b. The scratch pad area is used to enter option messages. (The alphanumeric keyboard cannot be used when test parameters are being continuously updated.)

This scheme ensures that the correct operation is performed at the proper time so that manual functions are performed synchronously with programed operations. Operator directions and error messages (lines 1 and 20 of the alphanumeric CRT) are blinked on and off to capture the operator's attention.

The system controller provides a logic procedure (fig. 13) for selecting the basic options for tuning and acquiring data for a mode or manipulating and displaying modal response data for assessing the purity and validity of a previously acquired mode. In the following paragraphs, the options are discussed in the nominal operational sequence.

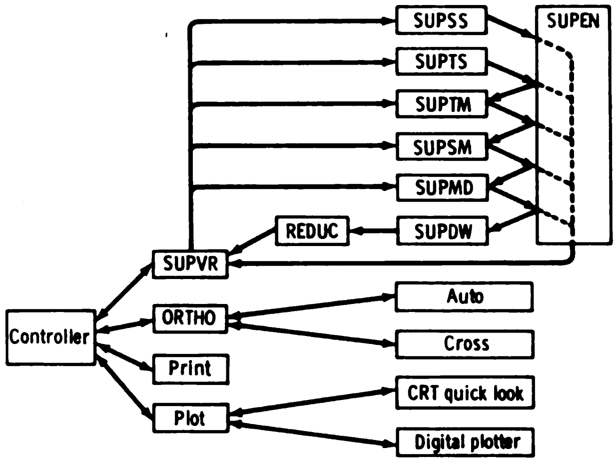

Figure 13.- Application software logic.

```
ENTER 'C' ON TEK KBD TO CONTINUE S/W SEQUENCE

AMTAS INITIALIZATION PROCEDURE:                    PROCEDURE SEQ: 01

1- PATCH LIMIT ACCELS                7- SUMDET IN COMPUTER MODE
2- NORMALIZE WEIGHTING AMPLIFIERS    8- MASTER GAIN FULL CCW
3- PATCH INPUTS TO SUMDET            9- INDIV GAINS FULL CCW
4- PATCH SCOPE AND METER PANELS      10-PHASE CONTROLS TO OFF
5- READY DIGITAL PLOTTER             11-ZERO MASS ENABLED
6- SYNCON IN REMOTE MODE             12-MAG. TAPES INITIALIZED


          S/W HOLD-PERFORM LISTED OPERATIONS
```

Figure 14.- The AMTAS initialization procedure CRT display.

```
ENTER DATA INTO (XX) FIELDS USING FOLLOWING PROCEDURE:
    1- PRESS LOCAL KEY                  3- PRESS HOME KEY
    2- ENTER DATA                       4- PRESS HDX KEY
                                        5- PRESS SEND KEY

CH 00 LOC (XXX )  G=(+X.XXE+XX )    CH 01 LOC (XXX )  G=(+X.XXE+XX )
CH 02 LOC (XXX )  G=(+X.XXE+XX )    CH 03 LOC (XXX )  G=(+X.XXE+XX )
CH 04 LOC (XXX )  G=(+X.XXE+XX )    CH 05 LOC (XXX )  G=(+X.XXE+XX )
CH 06 LOC (XXX )  G=(+X.XXE+XX )    CH 07 LOC (XXX )  G=(+X.XXE+XX )
CH 08 LOC (XXX )  G=(+X.XXE+XX )    CH 09 LOC (XXX )  G=(+X.XXE+XX )
CH 10 LOC (XXX )  G=(+X.XXE+XX )    CH 11 LOC (XXX )  G=(+X.XXE+XX )
CH 12 LOC (XXX )  G=(+X.XXE+XX )    CH 13 LOC (XXX )  G=(+X.XXE+XX )
CH 14 LOC (XXX )  G=(+X.XXE+XX )    CH 15 LOC (XXX )  G=(+X.XXE+XX )
CH 16 LOC (XXX )  G=(+X.XXE+XX )    CH 17 LOC (XXX )  G=(+X.XXE+XX )
CH 18 LOC (XXX )  G=(+X.XXE+XX )    CH 19 LOC (XXX )  G=(+X.XXE+XX )
CH 20 LOC (XXX )  G=(+X.XXE+XX )    CH 21 LOC (XXX )  G=(+X.XXE+XX )
CH 22 LOC (XXX )  G=(+X.XXE+XX )    CH 23 LOC (XXX )  G=(+X.XXE+XX )
          LIMIT ACCEL F.S. A/D COUNT=(+X.XXXE+XX / ) VOLTS
```

Figure 15.- Patch correspondence table CRT display.

Supervisor Option

The excitation control and data acquisition supervisor option (SUPVR) is composed of the software modules for system initialization, modal tuning, and data acquisition. All excitation, real-time monitoring and control, and data acquisition are performed with this supervisor. The remaining options of the controller are associated with data analysis, display, and assessment. The initialization procedure (fig. 14) is displayed immediately after the supervisor is selected. After the initialization is completed, the patch correspondence table (fig. 15) is displayed. Completion of this table is necessary to select 24 limit accelerometers from the 200 total-response accelerometers. After this table is completed, the supervisor options are displayed (fig. 16). Eight operational possibilities are available within the supervisor.

1. The SUPSS option consists of a single-shaker, wide-band sinusoidal sweep with digital data acquisition. Three accelerometers can be selected for generating co-quad plots (fig. 17) on the digital plotter during one sweep. The raw co-quad data are stored on magnetic tape and listed on the line printer.

```
TO CONTINUE S/W SEQUENCE:
    1- DO NOT MOVE CURSOR
    2- ENTER APPROPRIATE CHARACTERS
    3- HOLD CTRL KEY DOWN, PRESS 'ETX' KEY
    4- PRESS SEND KEY
ENTRIES DEFINED BELOW ARE ALLOWED:
    SS- SWEEP SINGLE /DIGITAL DATA ACQ/
    AS- SWEEP SINGLE /ANALOG DATA ACQ/
    TS- TUNE SINGLE
    TM- TUNE MULTIPLE
    SM- SWEEP MULTIPLE
    MD- MODAL DECAY
    DW- MODAL DWELL
    RT- RETURN TO AMTAS
```

Figure 16.- Operation selection table CRT display.

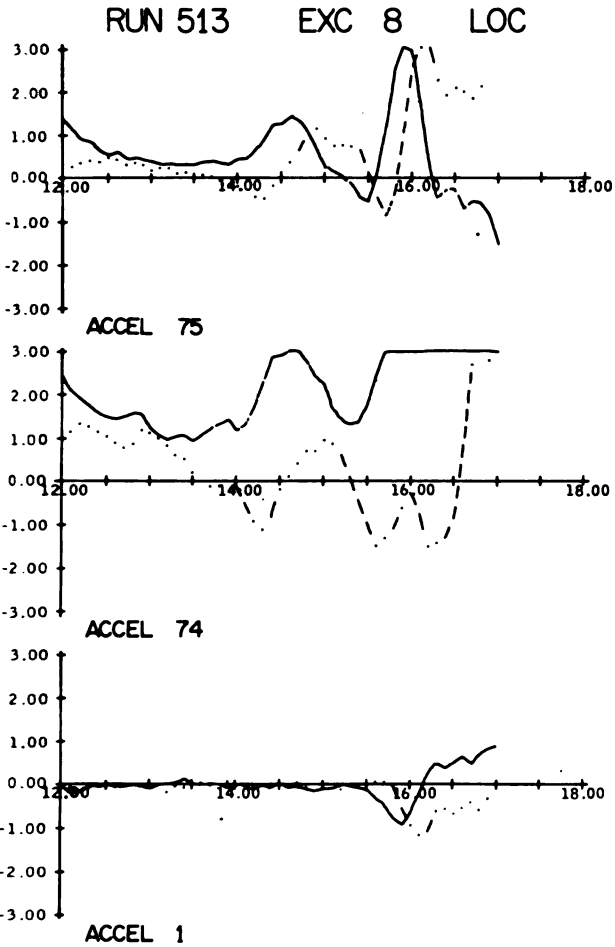

Figure 17.- Portion of wide-band sweep co-quad plot.

2. The ASUPS option consists of a single-shaker, wide-band sinusoidal sweep with analog data acquisition for off-line co-quad reduction (not shown in fig. 13). Typical data reduced with the off-line software are given in figure 18.

3. The SUPTS option consists of tuning operations with a single shaker for approximate frequency settings.

4. The SUPTM option consists of tuning operations with multiple shakers (maximum of 12). Fine tuning is accomplished with this software module. The alphanumeric CRT display of test parameters, similar to those displayed for other supervisor options, is given in figure 19. Appropriate entries for this option are shown in figure 20. The line-printer listing of the sequence log obtained during a tune multiple (SUPTM) operation is shown as run 642 in figure 21. This listing is similar to sequence-log data obtained during SUPSS, ASUPS, and SUPTS operations.

5. The SUPSM option consists of a multiple-shaker, narrow-band sinusoidal sweep to define the resonance condition. Three accelerometers can be selected for generating co-quad plots on the digital plotter during one sweep. The raw co-quad data are stored on magnetic tape and listed on the line printer. Plots similar to those shown in figure 18 result from this operation.

6. The SUPMD option consists of modal decay with signals from a maximum of 24 selected accelerometers recorded on an oscillograph. Sequence-log output from this operation is shown in figure 21 (runs 643 and 644).

7. The SUPDW option consists of modal dwell operation for digital data acquisition in coincident and quadrature format. The system director checks the phase lock, if in use, and the force distribution status while selecting input signals and resolving the data into coincident and quadrature components. The data are stored on magnetic tape, displayed on the CRT, listed on the line printer, and transferred to cards as a backup data file. A portion of the sequence log generated during an SUPDW operation is shown in figure 21 (run 645).

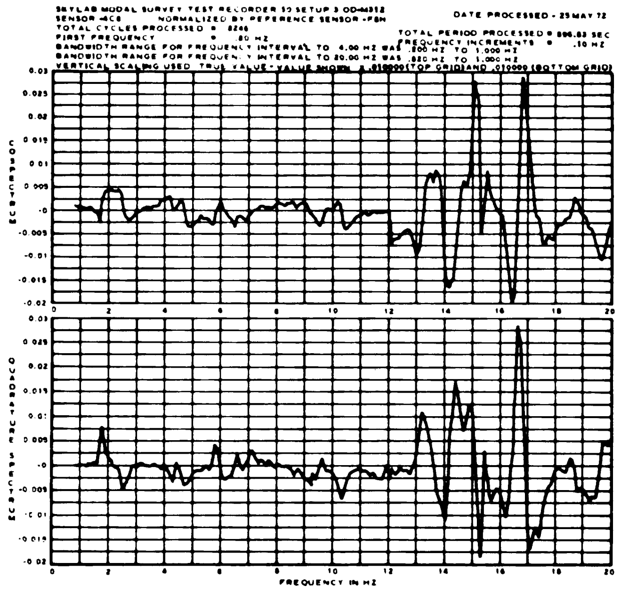

Figure 18.- Off-line co-quad reduction: typical plots of coincident and quadrature components of total acceleration. Top: coincident component (normalized to reference force); bottom: quadrature component (normalized to reference force).

```
ENTER DESIRED OPTION ON TEK KBD TO CONTINUE S/W SEQUENCE
TM OPERATION     RUN (XXX )  FREQ: +X.XXXX+XX HZ.  PROCEDURE SEQ:  04
SWP--ST:(+X.XXE+XX )
C/Q ACCELS---(XXX ) CO:+D.DD+DD  (XXX ) CO:+D.DD+DD  (XXX ) CO:+D.DD+DD
 BW= +X.XX+XX     QUAD:+D.DD+DD        QUAD:+D.DD+DD        QUAD:+D.DD+DD
 REF CH=(XX)     RATIO:+D.DD+DD       RATIO:+D.DD+DD       RATIO:+D.DD+DD
 CH 01       LOC:(XXX )        SET ϕ= +E.EE+EE    ACTUAL ϕ= +F.FF+FF   PH J
 CH 02       LOC:(XXX )        SET ϕ= +E.EE+EE    ACTUAL ϕ= +F.FF+FF   PH J
 CH 03       LOC:(XXX )        SET ϕ= +E.EE+EE    ACTUAL ϕ= +F.FF+FF   PH J
 CH 04       LOC:(XXX )        SET ϕ= +E.EE+EE    ACTUAL ϕ= +F.FF+FF   PH J
 CH 05       LOC:(XXX )        SET ϕ= +E.EE+EE    ACTUAL ϕ= +F.FF+FF   PH J
 CH 06       LOC:(XXX )        SET ϕ= +E.EE+EE    ACTUAL ϕ= +F.FF+FF   PH J
 CH 07       LOC:(XXX )        SET ϕ= +E.EE+EE    ACTUAL ϕ= +F.FF+FF   PH J
 CH 08       LOC:(XXX )        SET ϕ= +E.EE+EE    ACTUAL ϕ= +F.FF+FF   PH J
 CH 09       LOC:(XXX )        SET ϕ= +E.EE+EE    ACTUAL ϕ= +F.FF+FF   PH J
 CH 10       LOC:(XXX )        SET ϕ= +E.EE+EE    ACTUAL ϕ= +F.FF+FF   PH J
 CH 11       LOC:(XXX )        SET ϕ= +E.EE+EE    ACTUAL ϕ= +F.FF+FF   PH J
 CH 12       LOC:(XXX / )      SET ϕ= +E.EE+EE    ACTUAL ϕ= +F.FF+FF   PH J
HI LIMIT ACCEL--LOC: GGG    LEVEL:+H.HH+HH G    .XX OF LIMIT VALUE
   ADJUST FORCING DIST AND FREQ AS REQD TO OPTIMIZE MODAL RESPONSE
```

Figure 19.- Modal tuning (SUPTM) format CRT display.

```
TO CONTINUE S/W SEQUENCE:
   1- DO NOT MOVE CURSOR
   2- ENTER APPROPRIATE CHARACTERS
   3- HOLD CTRL KEY DOWN. PRESS 'ETX' KEY
   4- PRESS SEND KEY
ENTRIES DEFINED BELOW ARE ALLOWED:
   CO- COMPUTE CO/QUAD
   ST- STOP OPERATION
   FRBSXXX -DELTA FREQ IN +/- .01 INCR. AND COMPUTE CO/QUAD
   PR- PROCEED TO NEXT OPERATION
   AFCCCBDDDBEEEBFF - NEW ACCELS AND FG
       CCC- NEW ACCEL, POS 1, FOR C/Q ANAL
       DDD- NEW ACCEL, POS 2, FOR C/Q ANAL
       EEE- NEW ACCEL, POS 3, FOR C/Q ANAL
       FF-  NEW REF FG FOR CO/QUAD ANAL
       D-   DENOTES REQUIRED BLANK
   HI- RAPID UPDATE
   LO- NORMAL UPDATE---ONLY ENTRY ALLOWED WHEN IN 'HI' UPDATE MODE
```

Figure 20.- The CRT display of modal tuning options.

8. In the REDUC option, following the completion of the SUPDW operation (assuming that no exit entry was received during the operation), the logic flows automatically into the reduction module to prevent loss of these data caused by an inadvertent entry. In this module, all remaining data reduction is performed without any operator intervention or direction required. These reduction operations consist of translation of data to generalized coordinates, computation of generalized mass, and normalization of generalized quadrature data to unity generalized mass. The reduced data are automatically stored in the correct primary disk storage area and backup magnetic tape file area.

The "return to controller" function provides the initial display on the CRT and awaits a selection by the operator (not shown in fig. 13).

```
175/ 3/10/ 6                 AMTAS COLDSTART INITIATED

175/ 3/10/33                 AMTAS INITIALIZATION COMPLETE

175/ 3/10/55                 MD OPERATION SELECTED

175/ 3/14/44    RUN 642      TM OPERATION COMPLETED
                             FREQUENCY = 16.20 HZ.

                             ACCEL-           - 31-             - 2-              -117-
                               CO-       -0.197584E-03    -0.874546E-05    -0.164480E-04
                              QUAD-      -0.113400E-03    -0.620806E-05     0.857374E-04
                             RATIO-       0.174236E 01     0.140872E 01    -0.191841E 00

                             REF FG  6      .    ANALYSIS B/W   0.95

                             FORCING DISTRIBUTION

                             EX  1     LOC  13     SET LBS =    2.17      PHASE  0
                             EX  2     LOC  14     SET LBS =    2.17      PHASE  0
                             EX  3     LOC  18     SET LBS =    1.08      PHASE  0
                             EX  4     LOC   4     SET LBS =    2.17      PHASE  0
                             EX  5     LOC   5     SET LBS =    0.00      PHASE  0
                             EX  6     LOC   6     SET LBS =   73.84      PHASE  +
                             EX  7     LOC   7     SET LBS =  142.25      PHASE  -
                             EX  8     LOC   8     SET LBS =    0.00      PHASE  0
                             EX  9     LOC   9     SET LBS =    0.00      PHASE  0
                             EX 10     LOC  10     SET LBS =    1.08      PHASE  0
                             EX 11     LOC  17     SET LBS =    1.08      PHASE  0
                             EX 12     LOC  12     SET LBS =  117.27      PHASE  -

175/ 3/20/43    RUN 643      MODAL DECAY INITIATED

175/ 3/24/14    RUN 644      MODAL EXCITATION REINSTATED

175/ 3/25/15    RUN 644      MODAL DECAY INITIATED

175/ 3/27/42    RUN 645      MODAL EXCITATION REINSTATED

175/ 3/27/59    RUN 645      DW OPERATION STARTED---MODE      25
                                   LOC      CO              QUAD          FORCE          TOTAC
                                    1   -0.844E-04      -0.536E-04     0.748E 02      0.749E-02
                                    2   -0.967E-05      -0.213E-04     0.748E 02      0.175E-02
                                    3    0.839E-04      -0.214E-04     0.748E 02      0.649E-02
                                    4    0.126E-05      -0.213E-04     0.749E 02      0.160E-02
                                    5   -0.222E-04       0.640E-05     0.749E 02      0.173E-02
                                    6    0.102E-04       0.448E-04     0.749E 02      0.344E-02
```

Figure 21.- Portion of sequence log.

Print Option

The print option entry from the controller provides for additional printing of the generalized coordinate data from the disk unit to the line printer. Any mode previously stored on disk can be printed. Three pages excerpted from a total printout are presented in figures 22(a) to 22(c). All bookkeeping data required to define the frequency and forcing distribution are presented in figure 22(a). The format used to document the response data in accelerometer coordinates is shown in figure 22(b). The response data in generalized coordinates are given in figure 22(c).

SKYLAB MODAL SURVEY ORBITAL CONFIGURATION

MODE 25 RUN 645 DAY 175 HR 3 MIN 27 SEC 59

PERIOD 0.617284E-01 SEC. FREQUENCY 16.200 HZ.

REFERENCE FORCE EXCITER 6

EXCITER	LOCATION	PHASE(REL)	FORCE(LBS)
1	13	0	2.171
2	14	0	2.171
3	18	0	1.085
4	4	0	2.171
5	5	0	0.000
6	6	+	73.840
7	7	-	142.250
8	8	0	0.000
9	9	0	0.000
10	10	0	1.085
11	17	0	1.085
12	12	-	117.275

GENERALIZED MASS 0.504447E-05

(a) Housekeeping data.

Figure 22.- Typical modal data summary.

LOCATION	ID	CO (G/LB)	QUAD (G/LB)	RATIO	PHASE ANGLE (DEG)	TOTAL ACCEL. (G)
1	427-426X	-0.8447E-04	-0.5365E-04	0.1574E 01	32.42	0.7494E-02
2	428-426Y	-0.9672E-05	-0.2132E-04	0.4535E 00	65.60	0.1754E-02
3	789-426Z	0.8397E-04	-0.2143E-04	-0.3916E 01	165.67	0.6490E-02
4	430-426X	0.1269E-05	-0.2137E-04	-0.5939E-01	93.39	0.1603E-02
5	788-426Y	-0.2222E-04	0.6406E-05	-0.3469E 01	163.92	0.1732E-02
6	432-426X	0.1025E-04	0.4483E-04	0.2286E 00	77.12	0.3445E-02
7	439-602X	-0.6942E-04	-0.4221E-04	0.1644E 01	31.30	0.6073E-02
8	440-602Y	0.5228E-06	-0.4483E-04	-0.1166E-01	90.66	0.3351E-02
9	443-602Z	-0.5373E-04	-0.4101E-05	0.1310E 02	4.36	0.4028E-02
10	442-602X	0.6597E-05	-0.1340E-04	-0.4921E 00	116.20	0.1116E-02
11	793-602Y	-0.1940E-04	0.2513E-04	-0.7718E 00	127.66	0.2372E-02
12	444-601X	0.3343E-04	0.3655E-04	0.9147E 00	47.55	0.3700E-02
13	445-602X	-0.1098E-04	0.3689E-05	-0.2978E 01	161.43	0.8658E-03
14	446-602Y	-0.2971E-05	-0.2431E-04	0.1222E 00	83.03	0.1830E-02
15	449-602Z	0.9323E-05	0.1953E-04	0.4771E 00	64.49	0.1617E-02
16	448-602X	0.7421E-05	-0.2183E-05	-0.3398E 01	163.60	0.5776E-03
17	794-601Y	-0.9456E-05	0.3739E-04	-0.2528E 00	104.19	0.2880E-02
18	450-601X	-0.4292E-04	-0.3409E-04	0.1258E 01	38.46	0.4092E-02
19	468-509X	0.8118E-04	0.5229E-04	0.1552E 01	32.78	0.7173E-02
20	467-509Y	-0.2444E-04	-0.3622E-04	0.6749E 00	55.98	0.3246E-02
21	465-509Z	-0.3525E-05	0.3702E-04	-0.9520E-01	95.43	0.2762E-02
22	474-509X	-0.9403E-04	0.1353E-04	-0.6948E 01	171.81	0.7061E-02
23	473-509Y	-0.9890E-04	0.5342E-04	-0.1851E 01	151.62	0.8355E-02
24	471-509Z	-0.2043E-03	0.8176E-04	-0.2498E 01	158.18	0.1635E-01
25	480-509X	-0.6726E-04	-0.1025E-03	0.6561E 00	56.72	0.9122E-02
26	479-509Y	-0.8163E-04	-0.4754E-04	0.1717E 01	30.21	0.7028E-02
27	477-509Z	-0.1769E-03	-0.8392E-04	0.2108E 01	25.37	0.1457E-01
28	486-509X	0.1968E-03	0.1122E-03	0.1752E 01	29.70	0.1683E-01
29	485-509Y	-0.9424E-05	0.1077E-03	-0.8746E-01	94.99	0.8034E-02
30	483-509Z	0.7245E-04	0.7113E-04	0.1018E 01	44.47	0.7543E-02
31	492-509X	-0.1681E-03	-0.1299E-03	0.1294E 01	37.69	0.1577E-01
32	491-509Y	-0.8458E-04	-0.7199E-04	0.1174E 01	40.40	0.8244E-02
33	489-509Z	-0.6427E-04	-0.9301E-04	0.6910E 00	55.35	0.8391E-02
34	498-509X	-0.7677E-04	-0.1162E-04	0.6605E 01	8.60	0.5749E-02
35	497-509Y	-0.1387E-04	0.1299E-04	-0.1067E 01	136.87	0.1407E-02
36	495-509Z	0.1120E-03	0.8861E-04	0.1264E 01	38.34	0.1057E-01
37	770-509X	0.2546E-04	-0.3152E-05	-0.8077E 01	172.94	0.1903E-02
38	771-509Y	0.4462E-04	0.2943E-04	0.1516E 01	33.40	0.3966E-02
39	772-509Z	-0.1113E-03	-0.7089E-04	0.1570E 01	32.48	0.9792E-02
40	773-509X	-0.7189E-05	-0.3411E-04	0.2107E 00	78.09	0.2588E-02

(b) Accelerometer response data.

Figure 22.- Continued.

DEG. OF FREEDOM	QUAD ACCEL. (G/LB) OR (G/LB-IN)	NORM. QUADS (G(2)SEC(2)/LB-IN)	DEG. OF FREEDOM	QUAD ACCEL. (G/LB) OR (G/LB-IN)	NORM. QUADS (G(2)SEC(2)/LB-IN)
1	-0.4559E-05	-0.2029E-02	41	0.2854E-04	0.1270E-01
2	-0.1409E-04	-0.6277E-02	42	0.1016E-03	0.4527E-01
3	0.2030E-04	0.9038E-02	43	0.2450E-04	0.1091E-01
4	0.5616E-07	0.2500E-04	44	-0.6191E-05	-0.2756E-02
5	-0.3729E-06	-0.1660E-03	45	0.5436E-04	0.2420E-01
6	0.1365E-06	0.6081E-04	46	0.1659E-04	0.7388E-02
7	-0.2831E-05	-0.1260E-02	47	0.4181E-04	0.1861E-01
8	-0.9865E-05	-0.4392E-02	48	0.9985E-04	0.4445E-01
9	-0.3908E-04	-0.1740E-01	49	0.4711E-04	0.2097E-01
10	0.2671E-06	0.1189E-03	50	0.4350E-04	0.1936E-01
11	-0.2955E-06	-0.1315E-03	51	0.1130E-03	0.5031E-01
12	0.8567E-07	0.3814E-04	52	-0.1648E-05	-0.7339E-03
13	-0.1520E-04	-0.6771E-02	53	0.4782E-04	0.2129E-01
14	0.6882E-05	0.3064E-02	54	0.4993E-04	0.2223E-01
15	-0.1145E-04	-0.5101E-02	55	0.7522E-05	0.3349E-02
16	0.2342E-06	0.1042E-03	56	0.7464E-06	0.3323E-03
17	0.1415E-06	0.6304E-04	57	0.7948E-04	0.3538E-01
18	-0.9882E-07	-0.4400E-04	58	0.4160E-06	0.1852E-03
19	0.5229E-04	0.2328E-01	59	0.7798E-07	0.3472E-04
20	0.3622E-04	0.1612E-01	60	0.1290E-06	0.5745E-04
21	-0.3702E-04	-0.1648E-01	61	0.1023E-04	0.4555E-02
22	0.1353E-04	0.6025E-02	62	0.1555E-04	0.6924E-02
23	-0.5342E-04	-0.2378E-01	63	0.1024E-03	0.4560E-01
24	-0.8176E-04	-0.3640E-01	64	0.3845E-06	0.1712E-03
25	-0.1025E-03	-0.4564E-01	65	0.1070E-05	0.4765E-03
26	-0.4734E-04	-0.2116E-01	66	-0.1446E-06	-0.6442E-04
27	0.8392E-04	0.3736E-01	67	0.7210E-05	0.3210E-02
28	0.1122E-03	0.4999E-01	68	0.1895E-05	0.8437E-03
29	0.1077E-03	0.4797E-01	69	0.4526E-04	0.2015E-01
30	-0.7113E-04	-0.3167E-01	70	0.2743E-06	0.1221E-03
31	-0.1299E-03	-0.5786E-01	71	0.1289E-05	0.5741E-03
32	-0.7199E-04	-0.3205E-01	72	-0.1103E-06	-0.4913E-04
33	-0.9301E-04	-0.4141E-01	73	0.4494E-05	0.2001E-02
34	-0.1162E-04	-0.5174E-02	74	-0.2593E-04	-0.1154E-01
35	0.1299E-04	0.5786E-02	75	-0.1545E-03	-0.6879E-01
36	0.8861E-04	0.3945E-01	76	0.3529E-06	0.1571E-03
37	-0.3152E-05	-0.1403E-02	77	0.1431E-05	0.6371E-03
38	0.2943E-04	0.1310E-01	78	0.3243E-07	0.1444E-04
39	0.7089E-04	0.3156E-01	79	0.6714E-04	0.2989E-01
40	-0.3411E-04	-0.1518E-01	80	-0.1512E-04	-0.6733E-02

(c) Generalized response data.

Figure 22.- Concluded.

Plot Option

The plot option provides access to the plot routines. The following two options are available.

1. Stick plots on the digital plotter or graphic CRT generated by this routine are composed of node displacements or rotations as functions of elevation or station number about three mutually perpendicular axes. The shape of the perturbed structure is derived from the deflection data of the mass points. A typical stick plot is shown in figure 23. The columns of numbers at the bottom of each stick

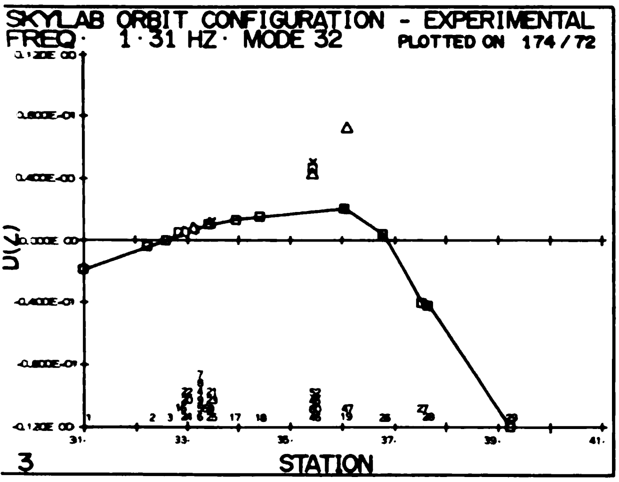

Figure 23.- Typical stick plot.

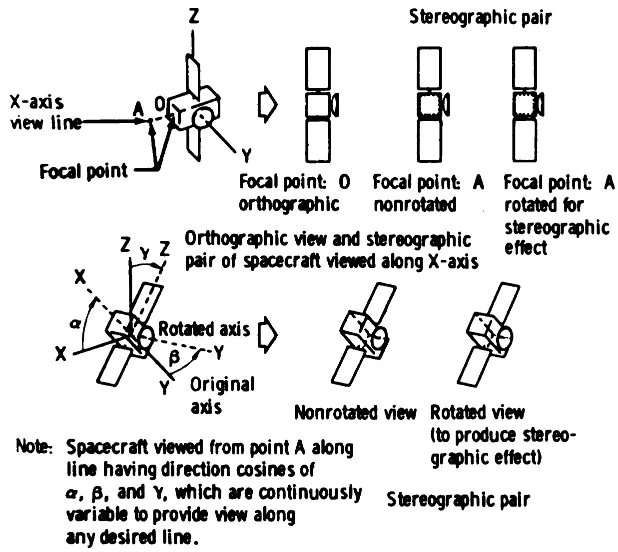

Figure 24.- Effect of varying plot parameters.

plot consist of the node numbers, arranged in the order of deflection. Only six plots (three translation and three rotation) are required to describe a structure, but the capability of plotting separate parts of the structure on different plots was developed to increase the clarity of presentation.

2. The routine for orthographic and stereographic plots on the digital plotter generates three orthographic and two stereographic views of the structure. Plotting parameters are manually entered on the keyboard to enable viewing of the structure at any angle and at any focal point. The utility provided by parameter selection is shown in figure 24. The stereographic plots, when viewed with a stereoscope, provide a three-dimensional view of the structure.

Orthogonality Option

The orthogonality routine (ORTHO) provides for selecting the type of check, automatic or cross, to be made between analytical or experimental modes. In addition, the particular set of desired modes for orthogonality is entered through the CRT keyboard. Orthogonality is discussed in appendix C.

TEST TECHNIQUES

The test techniques section comprises a discussion of several techniques used in testing with the AMTAS.

Modal Tuning and Data Acquisition

The supervisor provides the algorithms for excitation control, real-time monitoring, and data acquisition for all modal operations. Upon selection of the supervisor through the controller, the initialization procedure is performed, followed by keyboard entry of the limit accelerometer parameters and respective response limits. The first operational entry is used to perform a wide-band sinusoidal sweep with a selected exciter to obtain preliminary data of vehicle response to uniaxial, single-point force input. These data provide modal definition for use during tuning. Generally, most of these sweeps are performed before advancing to the other sequences. (In either the SUPSS or the ASUPS mode, two shakers can be driven simultaneously, although only one is actively servo controlled. The second shaker improves the quality of the excitation for better definition of bending or torsional modes when driving tangentially attached shakers.) In the SUPSS mode, three accelerometers can be selected for digital recording and concurrent co-quad plotting. Any number of accelerometers can be selected for analog tape recording in the ASUPS mode for subsequent off-line data reduction. This mode of operation is advantageous when many accelerometers are used for preliminary data analysis. The information resulting from wide-band sweeps consists of gross mode shapes or pairing with predicted analytical modes, approximate frequency of a mode, preferred shakers for a mode, and initial phase settings for shakers.

Modal tuning follows the initial wide-band sweeps and subsequent data analysis. The next four selection options, SUPTS, SUPTM, SUPSM, and SUPMD, are associated with the tuning operation. Modal tuning with multiple exciters, SUPTM, is the main process of modal excitation and mode identification and separation. Tuning with a single exciter, SUPTS, is a short form of tune multiple operation.

The modal tuning and acquisition sequence is initiated by selecting a target mode and determining the appropriate forcing distribution. A nominal force level is manually initialized on the master (primary) exciter. This exciter is selected by analysis of the analytical model data (plots and listings) and the experimental co-quad data derived from the single-exciter (ASUPS and SUPSS) sinusoidal sweeps.

The operator directs the operation by keyboard entry. After manual initialization of the forcing distribution, the low (LO) command returns the display update rate to the slow mode. The high (HI) update mode is automatically activated upon entry to a software module; therefore, forcing-distribution initialization is required. Returning to the slow update mode allows most of the computer time to be devoted to acquiring and reducing data. The data identifying the response accelerometers and reference load cell are entered into the CRT format before the operation begins. These transducers can be changed by the appropriate entry at any time during a given operation.

The modal response of the structure is optimized by varying the frequency of excitation and the forcing distribution (phase and level of the active exciters). While increasing quadrature values are noted on the co-quad displays, the frequency is incremented to maximize the quadrature value and to close the Lissajous pattern. The Lissajous pattern complements the co-quad displays and is useful in approaching an effective distribution. However, fine tuning is best achieved by observing small changes in the quadrature values because these effects cannot be detected in the Lissajous patterns. Lissajous patterns are normally formed by pairing exciter forces and respective driving-point accelerations. However, accelerations from other points of the structure may also be used, particularly when fine tuning the mode. As more exciters are activated, the resonance frequency will tend to shift downward. As this shift occurs, the frequency is incremented to below resonance, then increased in fine steps to peak the quadrature values. (See the following comments on hysteresis.)

In some instances, it may be advantageous to suppress participation of a neighboring mode rather than to attempt excitation of the target mode. A decrease in the coincident values indicates suppression of the undesired mode. The quadrature values must not decrease appreciably during the process.

After the forcing distribution is optimized, the frequency of resonance is established from a lower frequency to eliminate effects of hysteresis; hysteresis often distorts curves of response level as a function of frequency and may result in erroneous indications of resonance conditions.

Accelerometers at key points of the structure are surveyed to assess the adequacy of tuning. Co-quad values from several primary locations are tabulated for reference during subsequent operations.

The four options of the tuning process automatically sequence in a logical order: tune single proceeds to tune multiple, then to sweep multiple, and then to modal decay. However, any desired operation can be entered directly through the operation selection table, as shown in figure 13.

A sweep multiple operation can be performed at any time in the tuning process as an aid in defining the resonance condition, particularly if difficulties arise in the tune multiple operation. Performance of a narrow-band sweep can identify any neighboring problem mode and provide insight on suppression techniques. After completion of the final tune multiple sequence, a sweep multiple operation is normally performed for data purposes. The co-quad plots from these narrow-band sinusoidal sweeps are used in posttest analysis for an index of modal separation and for the calculation of damping values. Damping calculations are discussed in appendix D. One or more sweeps can be performed depending on the number of different accelerometers to be plotted.

When the co-quad data of the tune multiple and sweep multiple operations indicate that a mode has been properly separated and tuned, a modal decay is performed. Shaker excitation is removed, and the unfiltered signals from selected accelerometers are recorded on an oscillograph. The quality of the decay curves (fig. 25) provides another index of modal purity. If the structure decays smoothly with the absence of beating for the tuned mode, modal purity is good. If the modal purity is satisfactory, the sequence will be cycled automatically to the modal dwell operation for data acquisition. If modal purity is poor, the tuning iterations can be repeated. In tuning problem modes, it is sometimes helpful to acquire dwell data despite the impurities and to generate plots of the existing mode. These plots provide the visibility to define problem areas and to assess the adequacy of the existing exciter locations to properly excite the target mode.

The modal dwell operation begins with operator entry of bookkeeping data, mode identifier, and run number for documentation and data retrieval purposes. Excitation is reinstated, and the force servo maintains the predetermined forcing distribution. The automatic phase-lock feature can be activated if desired. After stabilization of the forcing distribution and response, data are acquired on the operator's CRT. Upon completion of data acquisition, the data are automatically reduced and stored on disk. (Note the position of the REDUC module in fig. 13.)

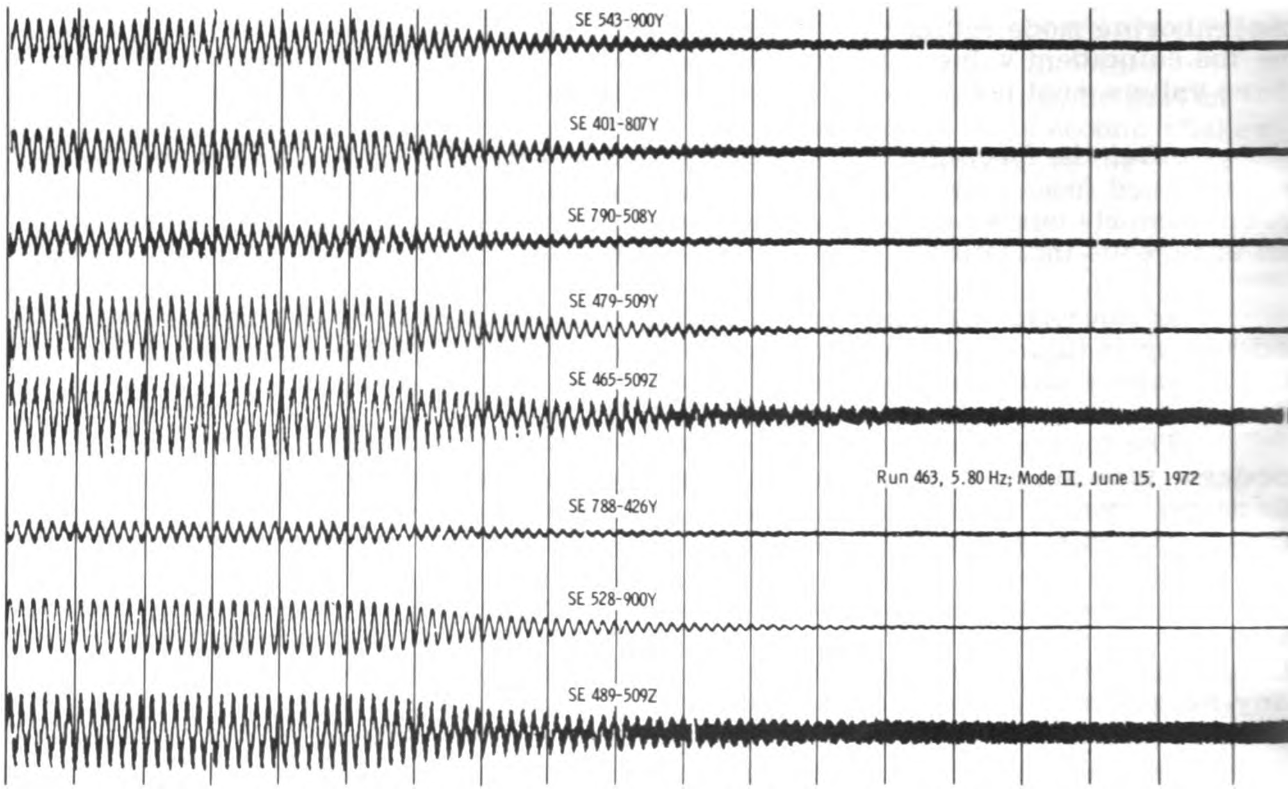

Figure 25.- Skylab orbital configuration modal decay curve.

Co-Quad Plots

The data obtained from a typical sine sweep are in the form of three sets of force-normalized coincident and quadrature component values displayed on a digital X-Y plotter. The wide-band, force-normalized co-quad plots provide a means of identifying the resonant frequencies of the structure.

At a resonance frequency, the quadrature component of the data rises to a peak value and then declines while the coincident component decreases to a minimum, rises sharply crossing the zero axis when the quadrature is at a peak value, increases to a maximum, and gradually returns to the zero axis, assuming a positive quadrature peak. Polarities of the coincident value will reverse for a negative quadrature peak.

Modal Plots

The stick plots are useful as a diagnostic tool, in addition to their normal function of providing a graphic description of a mode. Appropriate calibration values may be inserted on the data bus to simulate unit accelerations on all transducers and unit forces on all load cells, and the SUPDW module may be used to acquire these calibration data. After reduction, the plotted data must appear as rigid-body translations on the stick plots. If not, there are errors in the translation equations. The trimetric (three planar views) set and stereographic pair provide a graphic capability for assessing the adequacy of a particular forcing distribution in exciting a given mode.

An automatic scaling feature provides maximum resolution. (The operator may override this feature and specify a particular scale, if desired.) For comparison purposes, however, scaling for the total set of translation plots is calculated on the basis of all data to be plotted. Similarly, the scale for rotation is calculated for all plots.

A set of stick plots may be made on the alphanumeric-graphic CRT (quick look) or the digital plotter (report-quality hard copy). These instruments plot degree of freedom as a function of station number; the plots are formatted to provide perturbation definition along each axis.

Decay Curves

Decay curves are used to assess the purity of a mode by noting the amount of beating present. Curves generated during a modal decay with only the target mode excited will reflect no beating.

Off-Line Co-Quad Analysis

The off-line co-quad processing (by a central reduction laboratory) is accomplished by digitizing and reducing the taped analog data to the desired engineering unit output. These reduced data permit assessment of the force-servo subsystem operation and detection of the approximate frequencies at which the response of the structure is significant.

RECOMMENDATIONS FOR FUTURE APPLICATIONS

During the application of AMTAS to the Skylab modal survey, several improvements to the system were defined. Improvements that represent significant increases to overall capability are discussed in the following paragraphs.

Test Article Suspension System

The ancillary suspension system should become an integral part of the AMTAS to permit computer control of the suspension system. Single-parameter (position) or dual-parameter (load or pressure and position) feedback can be used for positive control of the test article suspension.

Technical Writer's Log Input

An additional CRT/keyboard display unit should be incorporated for use by the technical writer. Test comments could be composed in the local mode using the edit features of the unit. After the text is completed, the comments could be entered by a send command. The entire sequence log, including comments, should be displayed on the line printer and stored on digital magnetic tape.

Modal Survey Simulator

Training could be facilitated if a simulator software package were developed and included as an on-line option. Data stored during the Skylab modal survey could be used for a realistic simulation of a modal survey, including wide-band and narrow-band sweeps, tuning operations, modal decays, and dwells. This approach would eliminate the need for a structure for training purposes.

Test Procedure Display

A separate CRT (monitor only) unit should be incorporated to display the test procedure with slaved monitor units at each test station. This arrangement would eliminate the complexity of following the test operation, because the main-line program will automatically display the correct page of the procedure and scroll it forward as the test progresses.

CONCLUDING REMARKS

The design goals of the automatic modal tuning and analysis system — providing positive control of test conditions, rapid data acquisition and reduction, immediate documentation of modal response characteristics, and a high degree of specimen safety — were achieved. This unique system provided data in a meaningful form to the data evaluation team, which rapidly evaluated the data and selected specific modes from the numerous candidate modes observed. The selected modes were individually excited, and pertinent data were acquired. The automatic modal tuning and analysis system described herein is capable of meeting the requirements for a modal survey of any structure comparable in size and complexity to the Skylab payload. The techniques and methods employed in the system will enable expansion to meet the requirements of larger structures.

Lyndon B. Johnson Space Center
National Aeronautics and Space Administration
Houston, Texas, January 16, 1975
961-21-31-05-72

APPENDIX A

SKYLAB TEST ARTICLE

The automatic modal tuning and analysis system provides the capability for performing a modal test survey of a large and complex test article having resonance frequencies from 0.1 to 100 hertz. The Skylab orbital assembly, shown in figure A-1, is an example of such a test article to which the system has been applied.

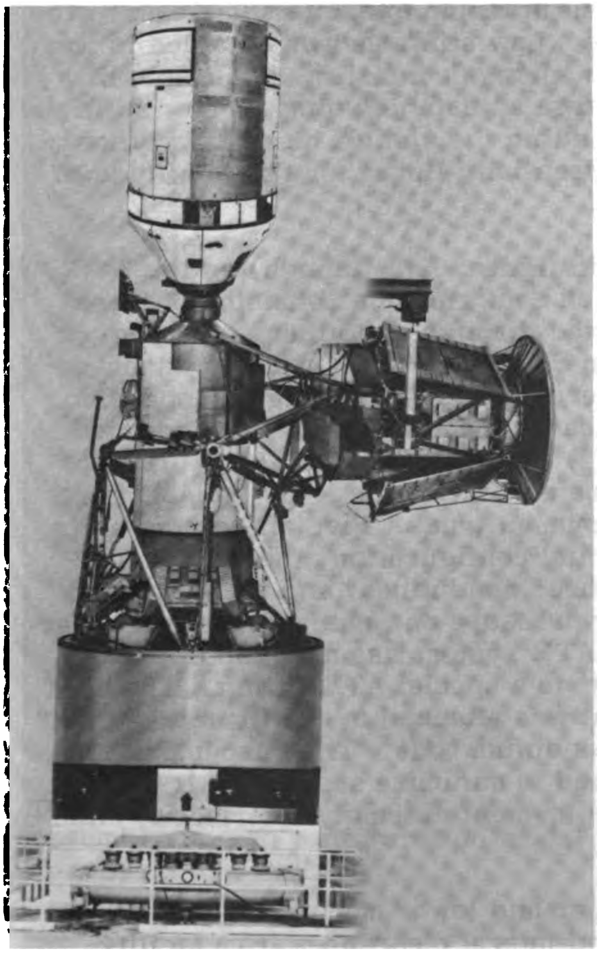

Figure A-1.- Skylab payload in orbital configuration.

The Skylab assembly orbital test configuration consisted of the Vibration and Acoustic Test Facility (VATF) base ring, the orbital workshop (OWS) forward skirt, the instrumentation unit (IU), the fixed airlock shroud (FAS), the airlock module (AM), the deployed Apollo telescope mount (ATM), and the inverted command and service module (CSM). The ATM includes engaged launch and orbital locks and four undeployed solar arrays. The entire cluster was suspended axially by air springs. With the exception of the CSM, the launch test configuration had all the same subassemblies plus the payload shroud. The test article in each configuration weighed approximately 54 400 kilograms (120 000 pounds) and was approximately 21 meters (70 feet) high.

The vehicle suspension systems used for the Skylab launch and orbital test configurations were designed to provide free-free support and made use of soft pneumatic spring units. Although to rigidly support the vehicle in the test facility would have permitted analysis of the test vehicle as a cantilevered beam, the soft suspension was preferred. Some of the reasons for this preference are as follows.

1. Before modal testing, the launch configuration was subjected to a high-force dynamics test of 444 800 newtons (100 000 pounds) force peak. For this test, isolation of the vehicle and the

excitation system from the facility was required for facility protection. Therefore, a soft pneumatic spring system was necessary.

2. If a rigid support had been used, boundary conditions would have been extremely difficult to define, but definition would have been necessary to determine the effects and contributions of the support to modal responses of the test article.

3. Regardless of the type of support used for the remainder of the vehicle stack, a vertically soft spring was required for the deployed ATM in the orbital configuration. A vertical spring allowed for correct relative displacements during modal excitation. Failure of the ATM air spring with the remainder of the stack rigidly supported could have damaged the ATM and attaching hardware.

The two Skylab vehicle configurations in the vertical position provided a simulated free-free or unrestrained environment in which to excite and measure the natural elastic vibration modes of the structure. Low stiffness was obtained in the vertical direction through the use of pneumatic springs consisting of multiple lift elements mounted on a plenum tank having a large adjustable volume. Low stiffness in the lateral directions was obtained by suspending the vehicle on relatively long rods to produce pendulum motions that were essentially linear for the amplitude of the motions experienced during the modal test.

The two suspension systems are shown in figures A-2 (launch) and A-3 (orbital). The suspension system for the launch configuration consisted of three identical air-spring units mechanically connected through pendulums to a ring fixture to which the lower surface of the Saturn S-IVB forward skirt was attached. These three air-spring units functioned and were operated as a single suspension system. For the orbital configuration, the spacecraft modules were divided into three subassemblies: (1) the inverted CSM; (2) the deployed ATM; and (3) a subassembly consisting of an OWS forward dome and skirt, the FAS, the AM, the multiple docking adapter (MDA), and the deployment truss. Five air-spring units were used, as shown in figure A-3. In the orbital configuration, the airlock subassembly was suspended on the same ring fixture, pendulums, and plenums used for the launch configuration, but the operating pressure and natural frequency were adjusted to match the other two systems. The ATM system was made up of one air-spring unit attached with a single pendulum to a special ATM fitting. The CSM system consisted of a single air-spring unit but was attached to two fittings on the aft bulkhead of the service module using two pendulum rods. The suspension systems including control systems were designed to minimize static-load transfers across the CSM/MDA interface and the ATM/deployment assembly interface to eliminate degrading effects on modal response data.

Safety features of the system include upper and lower mechanical stops for each air-spring unit or vehicular subsystem and lateral clearances from facility structures. The most important safety feature is inherent in the soft-spring suspension. If an air spring failed, the maximum load across the vehicle interface would not exceed the load required to displace the remaining air springs to their lower stops. These stops were set at 3.8 centimeters (1.5 inches) below the nominal operating height of each subassembly, and the maximum interface loads would have been well below the allowable spacecraft design limits. A separate safety feature of the controls is an overtravel monitor that is used to terminate excitation automatically when the vehicle approaches one of the mechanical stops.

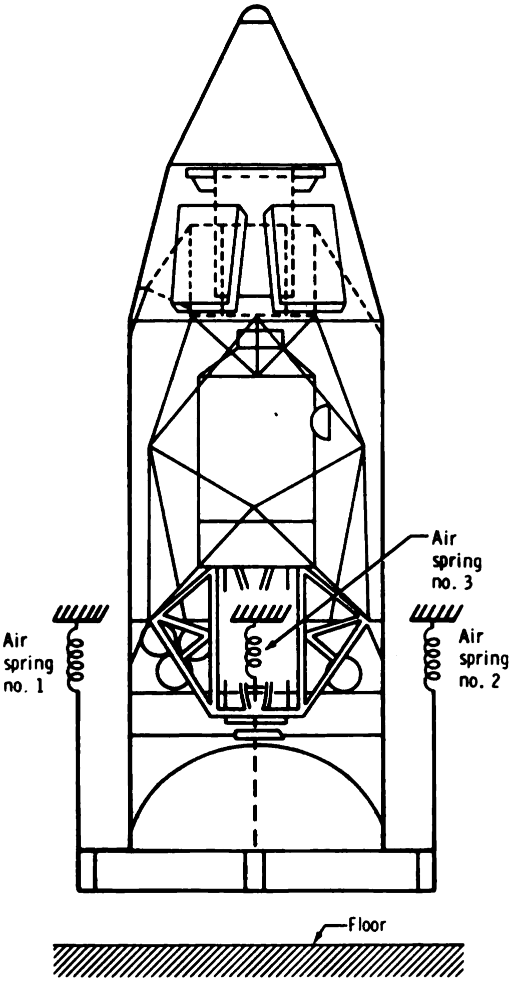

Figure A-2.- Suspension of payload assembly launch configuration modal survey.

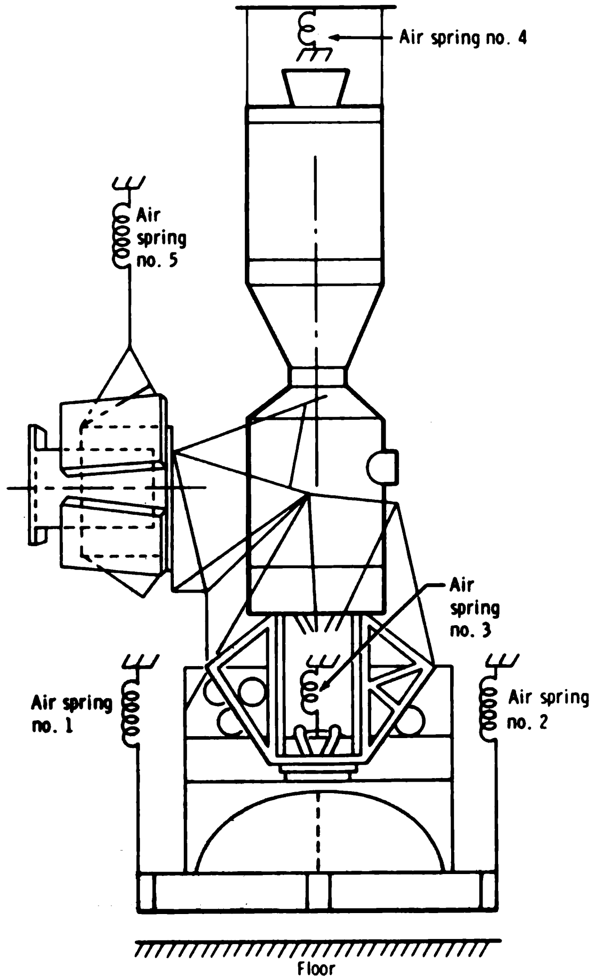

Figure A-3.- Suspension of payload assembly orbital configuration modal survey.

The exciter supports were soft mounted for one test and hard mounted for the other because of the differing frequency ranges of the Skylab launch (5 to 50 hertz) and orbital (0.8 to 20 hertz) test configurations. For the launch configuration, all horizontal exciters were pendulum mounted with soft (35 N/cm (20 lb/in.)) mechanical springs in series with the support rod. The same springs were used for supporting the vertically oriented exciters. The exciters weighed approximately 150 kilograms (330 pounds); this weight resulted in a vertical natural frequency of 0.75 hertz.

For the orbital configuration, most of the exciters were hard mounted. However, in a few locations, pendulum mounting was used because of poor exciter position relative to adequate support structure. The pendulum-mounted exciters required additional reaction mass loading to maintain adequate stroke capability at the lower frequency limit. Additional mass of approximately 900 kilograms (2000 pounds) was attached to these exciters. The arrangement of exciters for the orbital configuration modal survey is depicted in figure A-4.

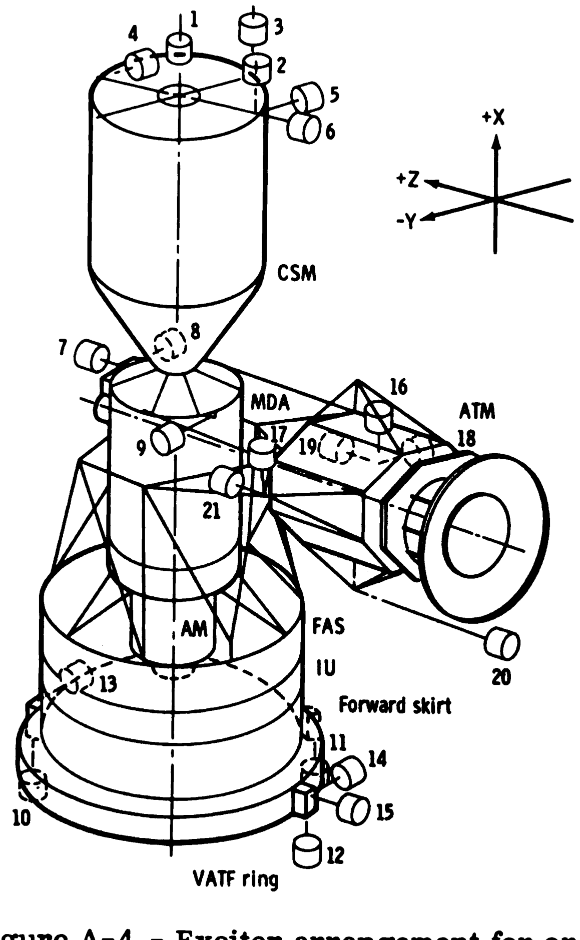

Figure A-4.- Exciter arrangement for orbital configuration modal survey.

APPENDIX B

CO-QUAD ANALYSIS OF MODAL RESPONSE DATA

Co-quad analysis represents a recent and important advance in modal survey technology. The term co-quad is used to refer to the in-phase (coincident) and out-of-phase (quadrature) components of one signal that are in phase and out of phase, respectively, with another signal. In applying the co-quad technique to reducing modal survey data, the acceleration response signal is resolved into coincident and quadrature components with respect to the signal representing the force applied to the structure under test. (See fig. B-1.)

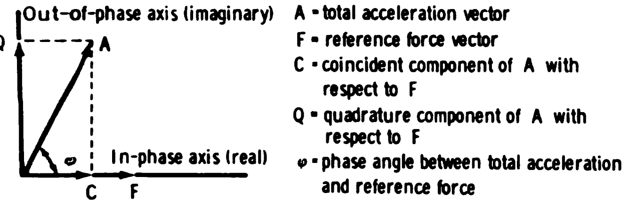

Figure B-1.- Co-quad component definition.

It is appropriate to examine the phase relationships that exist during steady-state vibration to acquire the background necessary to fully appreciate the power of co-quad analysis. W. T. Thomson (ref. 1) succinctly interprets these phase relationships for cases of steady-state excitation at frequencies below resonance, at resonance, and above resonance.

Force and acceleration signals are used for co-quad analysis because they are readily available from force transducers and response accelerometers. Signals from velocity or displacement transducers, or from another accelerometer, could be used as a reference for resolving response accelerations into their coincident and quadrature components. However, the proper phase relationships between the reference signal and the response acceleration must be known to interpret the results properly. The phase relationships for force F, acceleration A, velocity V, and displacement D for conditions below resonance, at resonance, and above resonance are given in table B-I. As shown in table B-I, with force as the reference signal and acceleration as the response signal, acceleration is 90° out of phase with force at resonance. Below resonance, the phase angle ϕ is between 90° and 180°; above resonance, the phase angle is between 0° and 90°. As a function of frequency, the co-quad response of acceleration with respect to force is shown in figure B-2. At resonance, the quadrature value is at a maximum and the coincident value is at a minimum. Data resulting from a slow sweep through a resonant frequency point, at a linear rate, are useful in assessing the modal qualities in the following ways. First, such data indicate the frequency of resonance (maximum quadrature point); second, such data give a clear picture of any modal content at adjacent frequencies (minor quadrature peaks or other perturbations to a smooth rise and fall of the quadrature curve); and, third, data that may be used to calculate the percent of critical damping are contained in the coincident spectrum.

TABLE B-I.- PHASE RELATIONSHIPS FOR BASIC STRUCTURAL CONDITIONS

Phase relationship	Basic structural conditions[a]		
	Below resonance (spring control)	At resonance	Above resonance (mass control)
F lags A by	$90° < \phi \leq 180°$	90°	$0° \leq \phi < 90°$
F lags V by	$0° < \phi_1 \leq 90°$	0°	$-90° \leq \phi_1 < 0°$
F lags D by	$-90° < \phi_2 \leq 0°$	-90°	$-180° \leq \phi_2 < -90°$

[a]Where $\phi_1 = \phi - 90°$; $\phi_2 = \phi_1 - 90°$.

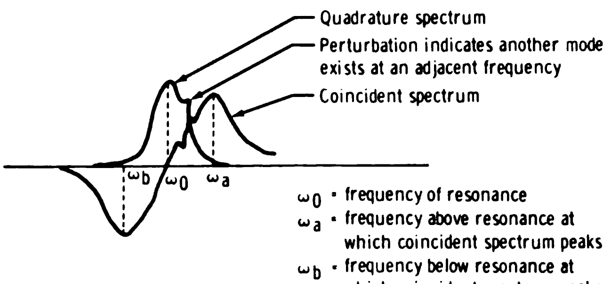

Figure B-2.- Narrow-band co-quad spectrum.

Digital filtering of the data with a tuned center frequency and a variable bandwidth enables performance of co-quad analysis not only during data acquisition at a resonance frequency but also during a sweep operation in which the band-pass filter must track the frequency of excitation. The variable-bandwidth filter is most useful during acquisition of response data from a structure having a high modal density, during which the adjacent modes cannot be completely suppressed with the available exciters.

Aliasing, or foldover, of data into the frequency range in which data must be accurate (within the filter bandwidth) is prevented by using low-pass filters to eliminate input signal components above a given frequency. This result is achieved by maintaining the 3-decibel cutoff frequency at a value less than half the sampling rate. The case in which the cutoff frequency F_c of the low-pass antialiasing filter is set to greater than half the sampling rate SR is illustrated in figure B-3. Any value is permissible for F_c as long as the resulting image frequencies do not fall below the value obtained by adding one-half the filter bandwidth BW to the frequency of excitation F_e.

The total acceleration vector is resolved into its coincident and quadrature components in two steps. First, the complex Fourier transform coefficients are computed for both the reference and response signal. The terms used are as follows: A_f is the real coefficient for force, B_f is the imaginary coefficient for force, A_a is the real coefficient for acceleration, and B_a is the imaginary coefficient for acceleration. The coincident and quadrature components are obtained by the following cross-multiplication process.

$$\left.\begin{aligned} \text{Co} &= A_f \cdot A_a + B_f \cdot B_a \\ \text{Quad} &= A_a \cdot B_f - A_f \cdot B_a \end{aligned}\right\} \tag{B1}$$

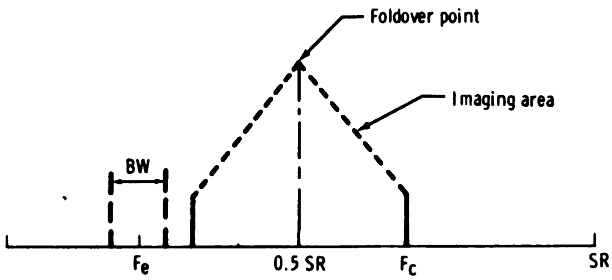

Figure B-3.- Antialiasing of input data.

APPENDIX C

ORTHOGONALITY

The modal deflections of a measured mode are the elements of a column matrix. This modal column of the n degree-of-freedom system in the rth mode is represented by $[\Theta_r]$ where each element $\Theta_{i,r}$ equals deflection at point i (where $i = 1, n$). This modal column is also called the rth eigenvector and can be thought of as a vector in n-dimensional space where each element of the column is a component of the vector in the corresponding coordinate direction. For an n degree-of-freedom system, there are n such eigenvectors. Each eigenvector and associated eigenvalue (resonance frequency) will satisfy the equation of motion for the system in free vibration.

The generalized mass G_r of the system for the rth measured mode is given by

$$G_r = \left[\Theta_r\right]^T [M] \left[\Theta_r\right] \tag{C1}$$

where T denotes the transpose of the mass matrix [M]. The set of eigenvectors obtained experimentally should be orthogonal with respect to the mass (or stiffness) weighting matrix. This orthogonality relationship, with mass as the weighting matrix between the rth and sth modes, is expressed as

$$\left[\Theta_r\right]^T [M] \left[\Theta_s\right] = 0 \tag{C2}$$

Mass coupling between the rth and sth modes results in a value other than zero. Therefore, the mass coupling C between the rth and sth measured modes is defined as

$$C_{r,s} = \left[\Theta_r\right]^T [M] \left[\Theta_s\right] \tag{C3}$$

The magnitude of mass coupling $\delta_{r,s}$ between the rth and sth measured modes can be assessed by comparison with the rth and sth generalized masses.

$$\delta_{r,s} = \frac{C_{r,s}}{\left(G_r \cdot G_s\right)^{\frac{1}{2}}} \tag{C4}$$

The generalized mass matrix $[G]$ is defined as $[G] = [\Theta]^T[M][\Theta]$ where the lack of a subscript for the modal matrices signifies that the complete set of eigenvectors is included. The generalized mass matrix will contain diagonal elements representing the generalized mass for each mode and off-diagonal elements representing the mass coupling terms. The generalized mass matrix can be characterized by

$$\left[G_{r,s}\right] = \begin{bmatrix} G_r & C_{r,s} \\ C_{r,s} & G_s \end{bmatrix} \tag{C5}$$

where G_r and G_s are the generalized masses of modes r and s, respectively, and $C_{r,s}$ is the coupling between modes r and s. The nondimensional magnitude of mass coupling $\delta_{r,s}$ can be computed by using the elements of the mass matrix. It is desirable to normalize the elements of each modal column to unity generalized mass for the particular measured mode. Normalization is possible because amplitude is not a property of normal modes. Denoting the normalized modal column of the rth measured mode as $[\phi_r]$, each element is obtained by dividing by the root of the rth generalized mass.

$$\phi_{i,r} = \frac{\Theta_{i,r}}{\left(G_r\right)^{\frac{1}{2}}} \tag{C6}$$

The generalized masses of each normalized mode will be unity.

The difficulty in attempting to obtain absolutely orthogonal modes (with zero-mass coupling) can be realized by noting the causes of error. The distributed mass of the structure is represented by discrete mass elements to form a mass model. The transformation equations include terms to determine the displacements of the center of gravity and rotations about the principal axes of inertia of each mass element from components of acceleration measured at various physical locations. The accuracy of the determined mass coupling, or orthogonality, depends on the accuracy of the theoretical mass model, the transformation equations, and the experimental data. Two modes can be orthogonal, but it is possible that these modes are not normal to the remaining modes of a set even though they appear to meet orthogonality conditions when considered as a pair without regard to the other normal modes. Orthogonality is a necessary but not sufficient condition that the mode under consideration is a normal mode of the structure.

In a frequency range having a high modal density, the auto-orthogonality check is a convenient method of comparing analytically predicted and experimentally derived modes. This comparison is made by using orthogonality checks between the mode being investigated and all analytical modes predicted to be within the general frequency area of the mode of interest.

APPENDIX D

DAMPING CALCULATIONS

The most convenient method for calculating the damping factor is to determine e frequency points of maximum and mimimum coincident response. In figure B-2, e minimum frequency ω_b occurs below resonance and the maximum frequency occurs above resonance. The damping factor ξ is a function of the ratio of ese frequencies.

$$\xi = \frac{\left[\left(\frac{\omega_a}{\omega_b}\right)^2 - 1\right]}{2\left[\left(\frac{\omega_a}{\omega_b}\right)^2 + 1\right]} \qquad \text{(D1)}$$

An alternate method is to use the relationship based on the logarithmic decre- ent of the decay curve given as

$$\xi = \frac{1}{2\pi n} \log \frac{Y_0}{Y} \qquad \text{(D2)}$$

which the damping factor is a function of the initial amplitude Y_0 and the final nplitude Y of the peaks of a decay curve, as shown in figure D-1, and n is the ımber of cycles included within the initial and final amplitude peaks.

Figure D-1.- Modal decay curve.

REFERENCE

1. Thomson, William Tyrrell: Vibration Theory and Applications. Third ed., Prentice-Hall, Inc., 1965, ch. 3, pp. 51-98.

BIBLIOGRAPHY

Salyer, R. A.: Hybrid Techniques for Modal Survey Control and Data Appraisal. The Shock and Vibration Bulletin of the 41st Shock and Vibration Symposium, Air Force Academy (Colorado Springs, Colo.), Oct. 27-29, 1970, pp. 25-42.

Salyer, R. A.: Purity Criteria for Modal Survey Data. Proceedings of the 17th Annual Technical Meeting and Equipment Exposition, Institute of Environmental Sciences (Los Angeles, Calif.), Apr. 26-30, 1971, pp. 163-168.

NASA-Langley, 1975 S-435

"The aeronautical and space activities of the United States shall be conducted so as to contribute . . . to the expansion of human knowledge of phenomena in the atmosphere and space. The Administration shall provide for the widest practicable and appropriate dissemination of information concerning its activities and the results thereof."

—NATIONAL AERONAUTICS AND SPACE ACT OF 1958

NASA SCIENTIFIC AND TECHNICAL PUBLICATIONS

TECHNICAL REPORTS: Scientific and technical information considered important, complete, and a lasting contribution to existing knowledge.

TECHNICAL NOTES: Information less broad in scope but nevertheless of importance as a contribution to existing knowledge.

TECHNICAL MEMORANDUMS: Information receiving limited distribution because of preliminary data, security classification, or other reasons. Also includes conference proceedings with either limited or unlimited distribution.

CONTRACTOR REPORTS: Scientific and technical information generated under a NASA contract or grant and considered an important contribution to existing knowledge.

TECHNICAL TRANSLATIONS: Information published in a foreign language considered to merit NASA distribution in English.

SPECIAL PUBLICATIONS: Information derived from or of value to NASA activities. Publications include final reports of major projects, monographs, data compilations, handbooks, sourcebooks, and special bibliographies.

TECHNOLOGY UTILIZATION PUBLICATIONS: Information on technology used by NASA that may be of particular interest in commercial and other non-aerospace applications. Publications include Tech Briefs, Technology Utilization Reports and Technology Surveys.

Details on the availability of these publications may be obtained from:

SCIENTIFIC AND TECHNICAL INFORMATION OFFICE

NATIONAL AERONAUTICS AND SPACE ADMINISTRATION

Washington, D.C. 20546

NASA TECHNICAL NOTE

NASA TN D-7946

NASA TN D-7946

PRESSURE DISTRIBUTIONS ON A CAMBERED WING-BODY CONFIGURATION AT SUBSONIC MACH NUMBERS

William P. Henderson

Langley Research Center
Hampton, Va. 23665

AMERICAN REVOLUTION BICENTENNIAL 1776-1976

NATIONAL AERONAUTICS AND SPACE ADMINISTRATION • WASHINGTON, D. C. • JULY 1975

1. Report No. NASA TN D-7946	2. Government Accession No.	3. Recipient's Catalog No.
4. Title and Subtitle PRESSURE DISTRIBUTIONS ON A CAMBERED WING-BODY CONFIGURATION AT SUBSONIC MACH NUMBERS		5. Report Date July 1975
		6. Performing Organization Code
7. Author(s) William P. Henderson		8. Performing Organization Report No. L-10105
9. Performing Organization Name and Address NASA Langley Research Center Hampton, Va. 23665		10. Work Unit No. 505-11-21-02
		11. Contract or Grant No.
12. Sponsoring Agency Name and Address National Aeronautics and Space Administration Washington, D.C. 20546		13. Type of Report and Period Covered Technical Note
		14. Sponsoring Agency Code
15. Supplementary Notes		

16. Abstract

An investigation has been conducted in the Langley high-speed 7- by 10-foot tunnel at Mach numbers of 0.20 and 0.40 and angles of attack up to about 22° to measure the pressure distributions on two cambered-wing configurations. The wings had the same planform (aspect ratio of 2.5 and a leading-edge-sweep angle of 44°) but differed in amounts of camber and twist (wing design lift coefficient of 0.35 and 0.70). The effects of wing strake on the wing pressure distributions were also studied. The results indicate that the experimental chordwise pressure distribution agrees reasonably well with the design distribution over the forward 60 percent of nearly all the airfoil sections for the lower cambered wing. The measured lifting pressures are slightly less than the design pressures over the aft part of the airfoil. For the highly cambered wing, there is a significant difference between the experimental and the design pressure level. The experimental distribution, however, is still very similar to the prescribed distribution. At angles of attack above 12°, the addition of a wing-fuselage strake results in a significant increase in lifting pressure coefficient at all wing stations outboard of the strake-wing intersection.

17. Key Words (Suggested by Author(s)) Pressure distributions; Cambered wing; Wing-fuselage strake; Subsonic	18. Distribution Statement Unclassified – Unlimited New Subject Category 02

19. Security Classif. (of this report) Unclassified	20. Security Classif. (of this page) Unclassified	21. No. of Pages 151	22. Price* $6.25

*For sale by the National Technical Information Service, Springfield, Virginia 22151

PRESSURE DISTRIBUTIONS ON A CAMBERED WING-BODY CONFIGURATION AT SUBSONIC MACH NUMBERS

William P. Henderson
Langley Research Center

SUMMARY

An investigation has been conducted in the Langley high-speed 7- by 10-foot tunnel at Mach numbers of 0.20 and 0.40 and angles of attack up to about 22° to measure the pressure distributions on two cambered-wing configurations. The wings had the same planform (aspect ratio of 2.5 and a leading-edge-sweep angle of 44°) but differed in amounts of camber and twist (wing design lift coefficient of 0.35 and 0.70). The effects of wing strake on the wing pressure distributions were also studied. The results indicate that the experimental chordwise pressure distribution agrees reasonably well with the design distribution over the forward 60 percent of nearly all the airfoil sections for the lower cambered wing. The measured lifting pressures are slightly less than the design pressures over the aft part of the airfoil. For the highly cambered wing, there is a significant difference between the experimental and the design pressure level. The experimental distribution, however, is still very similar to the prescribed distribution. At angles of attack above 12°, the addition of a wing-fuselage strake results in a significant increase in lifting pressure coefficient at all wing stations outboard of the strake-wing intersection.

INTRODUCTION

The National Aeronautics and Space Administration is currently conducting wind-tunnel investigations to provide information useful in developing fighter aircraft concepts possessing desirable stability, control, and performance characteristics over a wide range of flight conditions. Two approaches for achieving high lift-drag ratios at maneuvering lift coefficients are discussed in reference 1. The first approach involved design of the wing camber and twist to support a load distribution for which the extent of regions of adverse pressure gradients is minimized; hence, the tendency for flow separation at the wing design lift coefficient is suppressed. The second approach utilizes the vortex lift produced by leading-edge separation from a sharp highly swept wing strake to enhance the wing lift.

The experimental results of reference 1 indicate that the wings performed well at the design conditions and confirmed that proper design of wing camber and twist can provide levels of drag commensurate with an elliptical span load distribution at reasonably high design lift coefficients. However, it is not known whether the desired load distribution on the wings was actually obtained. The benefits derived from the strakes were shown to be dependent upon wing design lift coefficient since its success depends on the mutual interaction of the strake vortex and the main wing, a phenomenon which is difficult to predict analytically.

For the foregoing reasons, it appeared desirable to measure the pressure distribution on these cambered wings both with and without a strake in order to validate the design procedures used to determine the camber surface of the wings, and to study the effect of the strake vortex on the pressure distributions.

Therefore, an investigation was conducted in the Langley high-speed 7- by 10-foot tunnel to determine the pressure distributions on wings having design lift coefficients of 0.35 and 0.70. The measurements were made at Mach numbers of 0.20 and 0.40 at angles of attack up to 22°.

SYMBOLS

Second symbol denotes computer printout symbol. The coefficients and symbols are defined as follows:

b	semispan, cm
C_l	section lift coefficient
$C_{L,d}$	wing design lift coefficient
C_p,CP	pressure coefficient, $\frac{p_l - p_\infty}{q_\infty}$
ΔC_p,ΔCP	differential pressure coefficient, $C_{p,u} - C_{p,l}$
c,C	local wing chord, cm
M	Mach number

p_l local static pressure, Pa

p_∞ free-stream static pressure, Pa

q_∞ free-stream dynamic pressure, Pa

x,X distance behind leading edge of wing, cm

y distance along span from center line, cm

α angle of attack, deg

Subscripts:

u,U upper surface

l,L lower surface

MODEL DESCRIPTION

A three-view drawing of the basic model is presented in figure 1(a) and a drawing showing the model with the wing strake is presented in figure 1(b). A photograph of the model sting mounted in the Langley high-speed 7- by 10-foot tunnel is presented in figure 2. The model, as illustrated in figure 1(a), consists of a simple wing-fuselage configuration with the wing having an aspect ratio of 2.5, a taper ratio of 0.20, a wing leading-edge sweep angle of 44°, and an NACA 64A series airfoil section (measured streamwise) with a thickness ratio of 6 percent at the fuselage, juncture, and 4 percent at the wing tip. Two variations in wing camber and twist corresponding to design lift coefficients of 0.35 and 0.70 were studied. At these lift coefficients the wings were designed to support an elliptical span load and a rectangular chord load distribution. Ordinates for the cambered airfoils are presented in reference 1. The wing strake was constructed of a 0.159-cm-thick flat plate with sharp leading edges. A total of 140 pressure orifices (70 on the upper surface and 70 on the lower) were placed on the wing in rows at six spanwise stations as shown in figure 1.

TEST AND CORRECTIONS

The investigation was conducted in the Langley high-speed 7- by 10-foot tunnel at Mach numbers of 0.20 and 0.40 and at angles of attack of up to 22°. The test Reynolds number, based on the wing mean geometric chord, was 1.03×10^6 at a Mach number of 0.20 and 1.96×10^6 at a Mach number of 0.40. Transition strips 0.32 cm wide of No. 100 carborundum grains were placed 1.14 cm streamwise from the leading edge of the wings and 2.54 cm behind the nose of the fuselage. Corrections to the model angle of attack have been made for deflections of the balance and sting support system under aerodynamic load. Blockage corrections were found to be negligible and therefore were not applied to the data.

PRESENTATION OF RESULTS

All the pressure data obtained in this investigation are presented in tabulated form in tables I to VIII. Because of the large volume of data obtained, only the data for a Mach number of 0.40 are presented in plotted form. On the left-hand side of each data figure, the pressure coefficients measured for the upper and lower surfaces at each span station are presented; whereas on the right-hand side the differences in pressure between the upper and lower surface are presented. As an aid in locating a particular part of the data, the following index of figures is presented.

RESULTS AND DISCUSSION

Since the volume of data obtained during this study is very large, the discussion is limited to the more significant observations. However, a tabulation of all the pressure data obtained during this investigation is presented in tables I to VIII.

Comparison of Experimental and Design Pressure Distributions

The wings for this study, as indicated in reference 1, were designed to support an elliptical span load and a rectangular chord load distribution at the design conditions $\left(M = 0.40 \text{ at } C_{L,d} = 0.35 \text{ and } 0.70\right)$. The chord load distribution was specified in the design program by a Fourier series having four terms. The small number of terms accounts for the oscillation in the design pressure distribution (solid curve) presented in figure 9. Considerably more terms would be required to match a rectangular distribution exactly. Designing the camber surface to support this type of pressure distribution did not, however, result in any significant irregularities in the camber distribution. The design chordwise pressure distribution is compared with experimental data for the wing with a $C_{L,d}$ of 0.35 in figure 9(a) and a $C_{L,d}$ of 0.70 in figure 9(b). The experimental pressure distribution agrees reasonably well with the prescribed chordwise pressure distribution over the forward 60 percent of nearly all of spanwise stations for the wing with the lower camber $\left(C_{L,d} = 0.35\right)$. The measured lifting pressures are slightly lower than the design pressures on the aft part of the airfoil at nearly all the stations where pressure data were obtained. This is not surprising since the theory used to design the wing camber surface (see ref. 2) does not account for the effects of wing or boundary-layer thickness. For the wing with higher camber $\left(C_{L,d} = 0.70\right)$, there is a significant difference between the experimental and the design pressure distributions. The experimental chordwise pressure distribution, however, is very similar to the prescribed distribution. Even though the experimental chordwise pressure distributions are somewhat different from the prescribed pressure distributions, the drag levels for this wing, based on data presented in reference 1, are still commensurate with the values for full leading-edge suction and an elliptical span load distribution. These data presented in figure 10, which are discussed in more detail in the next section, again illustrate that the experimental span load agrees extremely well with the theoretical lift distribution corresponding to an elliptical span load.

Effect of Wing Strake

The difference in pressure coefficient ΔC_p between the wing upper and lower surfaces is presented for the configuration with the strake on and off in figures 7 and 8. Figure 7 is for the configuration with the cambered wing for a $C_{L,d} = 0.35$ and figure 8 is for $C_{L,d} = 0.70$. At the lower angles of attack, below 4°, there is no effect of the strake on the pressure distributions over the wing surface. In the intermediate angle-of-attack range (4° to 12°), the only significant effect of the strake on the wing pressure is isolated to the station immediately behind the strake (station 1). This effect (see fig. 8(h), for example) can undoubtedly be attributed to downwash off the strake. At the higher angles of attack, above 12°, significant increases in lifting pressure coefficient are noted at all wing stations outboard of the strake-wing intersection. Small effects are noted even at the most outboard wing station, which is located at 97 percent of the wing semispan. A somewhat more definitive analysis of these results can be made with the aid of figure 10. This figure presents the variation of section lift (determined by integrating wing pressures at the various stations over the wing with $C_{L,d} = 0.70$) across the wing span for the strake on and off, compared with a theoretical estimate made for the wing alone at several angles of attack. The estimate was determined by use of the methods presented in reference 3. As noted in figure 10 at the lower angles of attack, there is very little difference in the variation of section lift over the wing with the strake on or off. The experimental variation of section lift is in close agreement with the estimated potential flow solution. At the higher angle of attack ($\alpha = 21.5^{\circ}$), the section lift characteristics developed on the wing with the strake on is considerably higher than those for the wing with the strake off. It was initially believed that the vortex created by the wing-fuselage strake was interacting with the wing flow field to keep the wing flow from separating up to higher angles of attack. However, the pressure distributions (for example, see fig. 7(m) or 8(m)) at an angle of attack of 21.5° show large lift increases over the forward part of the airfoil section. These pressure distributions (on stations 2 and 3) appear to be typical of the type expected with a leading-edge vortex-type flow. The existence of a wing-leading-edge vortex was substantiated by a flow-visualization study conducted on a similar model. Figure 10 indicates, however, that although the wing lift was increased by the strake, the total lift developed is only slightly higher than the value expected if potential flow has been maintained at the inboard stations and significantly less at the outboard stations. Since fully developed leading-edge vortex flow usually provides lift greater than fully attached flow, it appears that the wing vortex system is weak and probably does not extend to the tip. It is obvious, however, that the interaction of the strake vortex flow field with the wing flow field allowing the creation of a vortex on the wing has a significantly beneficial effect on the lift developed by the wing at the higher angles of attack.

CONCLUSIONS

A wind-tunnel study has been conducted to measure the pressure distribution on two cambered-wing configurations with and without a wing-fuselage strake. As a result of this study the following conclusions can be made:

1. The experimental chordwise pressure distribution agrees reasonably well with the design distribution over the forward 60 percent of nearly all the airfoil sections for the lower cambered wing. The measured lifting pressures are slightly less than the design pressures over the aft part of the airfoil section.

2. For the highly cambered wing, there is a significant difference between the experimental and the design pressure level. The experimental distribution, however, is still very similar to the prescribed distribution.

3. At angles of attack above 12°, the addition of a wing-fuselage strake results in a significant increase in the lifting pressure coefficient at all wing stations outboard of the strake-wing intersection.

Langley Research Center,
National Aeronautics and Space Administration,
Hampton, Va., April 30, 1975.

REFERENCES

1. Henderson, William P.; and Huffman, Jarrett K.: Effect of Wing Design on the Longitudinal Aerodynamic Characteristics of a Wing-Body Model at Subsonic Speeds. NASA TN D-7099, 1972.

2. Lamar, John E.: A Modified Multhopp Approach for Predicting Lifting Pressures and Camber Shape for Composite Planforms in Subsonic Flow. NASA TN D-4427, 1968.

3. Margason, Richard J.; and Lamar, John E.: Vortex-Lattice FORTRAN Program for Estimating Subsonic Aerodynamic Characteristics of Complex Planforms. NASA TN D-6142, 1971.

TABLE I.- PRESSURE COEFFICIENTS AT A MACH NUMBER OF 0.20 FOR MODEL WITH STRAKE OFF. $C_{L,d} = 0.35$

(a) $\alpha = -3.79^{\circ}$

STATION 1

X/C	CPU	CPL
.005	.5877	-1.2956
.010	.5850	-1.2654
.025	.4541	-1.3957
.050	.3499	-.2245
.100	.2444	-.1693
.200	.1131	-.1186
.300	.0302	-.0720
.400	-.0144	-.0690
.500	-.0197	-.0367
.600	-.0427	-.0301
.700	-.0319	.0769
.800	.0011	.0827
.900	.0270	-.0281
.950	-.0093	.1832
.970	.0176	

STATION 2

X/C	CPU	CPL
.005	.5668	-.8059
.010	.5634	-.8200
.025	.4646	-.7954
.050	.3635	-.8250
.100	.2480	-.8672
.200	.1075	-.5535
.300	-.0055	.0301
.400	-.0556	.0245
.500	-.0485	.0334
.600	-.0684	.1100
.700	-.0744	
.800	-.0292	.1727
.900	-.0108	.2347
.925	-.0222	.2589
.950	-.0208	.2858

STATION 3

X/C	CPU	CPL
.010	.5720	-.6227
.025	.4941	-.6148
.050	.3924	-.6147
.100	.2418	-.6346
.200	.0960	-.6494
.400	-.0419	.0323
.600	-.0791	.1630
.800	-.0437	.1918
.900	-.0103	.2386
.925	-.0287	.2744

STATION 4

X/C	CPU	CPL
.010	.5732	-.5122
.025	.4857	-.5211
.050	.3671	-.5100
.100	.2678	-.5023
.200	.1097	-.5067
.400	-.0555	-.4971
.600	-.1002	-.0571
.800	-.0892	.0746
.900	-.0539	.0831
.925	-.0772	.0770

STATION 5

X/C	CPU	CPL
.025	.4361	.0869
.050	.3380	.0713
.075	.2746	.0430
.150	.1466	.0387
.300	-.0502	.0389
.450	-.1063	.0359
.600	-.1462	-.0722
.750	-.1312	-.0756
.800	-.1123	-.0811
.850	-.1006	-.0717

STATION 6

X/C	CPU	CPL
.025	.3815	-.0665
.050	.2713	-.1540
.100	.1771	-.1277
.200	.0424	-.1192
.300	-.0488	-.0847
.400	-.0852	-.0607
.500	-.1059	-.0466
.600	-.1232	-.0202
.700	-.1261	-.0061
.800	-.0983	.0165

(b) $\alpha = -1.95^{\circ}$

STATION 1

X/C	CPU	CPL
.005	.5746	-.9997
.010	.4719	-.9764
.025	.3444	-.6318
.050	.2159	-.1619
.100	.1383	-.1393
.200	.0385	-.0730
.300	-.0336	-.0307
.400	-.0687	-.0208
.500	-.0646	-.0193
.600	-.0787	-.0114
.700	-.0695	.0832
.800	-.0298	.0913
.900	.0025	-.0238
.950	-.0149	.2044
.970	.0198	

STATION 2

X/C	CPU	CPL
.005	.5751	-.9561
.010	.4955	-.9308
.025	.3770	-.9919
.050	.2699	-.8311
.100	.1485	-.0284
.200	.0309	-.0256
.300	-.0525	-.0127
.400	-.1145	-.0034
.500	-.1046	.0290
.600	-.1122	.0652
.700	-.1030	
.800	-.0542	.1627
.900	-.0188	.2065
.925	-.0359	.2249
.950	-.0303	.2551

STATION 3

X/C	CPU	CPL
.010	.5392	-.6093
.025	.3868	-.5919
.050	.2823	-.6135
.100	.1458	-.6234
.200	.0102	-.2187
.400	-.0924	.0607
.600	-.1092	.1156
.800	-.0543	.1715
.900	-.0270	.2205
.925	-.0369	.2502

STATION 4

X/C	CPU	CPL
.010	.5326	-.5203
.025	.3544	-.5226
.050	.2891	-.5268
.100	.1653	-.5311
.200	.0088	-.5346
.400	-.1129	-.5190
.600	-.1382	.0538
.800	-.1105	.0552
.900	-.0705	.0618
.925	-.0837	.0780

STATION 5

X/C	CPU	CPL
.025	.3561	.0833
.050	.2419	.0762
.075	.1818	.0024
.150	.0888	.0363
.300	-.1140	.0447
.450	-.1432	.0307
.600	-.1677	.0231
.750	-.1457	.0262
.800	-.1033	.1812
.850	-.0697	.1885

STATION 6

X/C	CPU	CPL
.025	.3266	.1859
.050	.2206	-.1584
.100	.1279	-.1325
.200	.0212	-.1015
.300	-.0729	-.0767
.400	-.0956	-.0551
.500	-.1158	-.0419
.600	-.1219	-.0290
.700	-.1107	-.0417
.800	-.0851	-.0253

TABLE I.- Continued

(c) $\alpha = -0.02^{\circ}$

STATION 1

X/C	CPU	CPL
.005	.4842	-.5618
.010	.3064	-.2750
.025	.1916	-.1175
.050	.1085	-.0754
.100	.0470	-.0432
.200	-.0209	-.0070
.300	-.1025	.0126
.400	-.1063	.0150
.500	-.1[illegible]39	.0178
.600	-.1161	-.0126
.700	-.0712	.1012
.800	-.0252	.1211
.900	.0056	-.0146
.950	-.0197	.2079
.970	.0272	

STATION 2

X/C	CPU	CPL
.005	.5074	-.6533
.010	.3621	-.6399
.025	.2265	-.6305
.050	.1229	-.1359
.100	.0375	-.0535
.200	-.0576	-.0053
.300	-.1346	.0350
.400	-.1623	.0350
.500	-.1287	.0409
.600	-.1427	.1057
.700	-.1229	
.800	-.0694	.1628
.900	-.0260	.1965
.925	-.0361	.2308
.950	-.0333	.2502

STATION 3

X/C	CPU	CPL
.010	.4334	-.5303
.025	.2574	-.5132
.050	.1496	-.2824
.100	.0329	-.1030
.200	-.0724	.0039
.400	-.1563	.0528
.600	-.1389	.1160
.800	-.0699	.1569
.900	-.0432	.2109
.925	-.0350	.2409

STATION 4

X/C	CPU	CPL
.010	.4152	-.5795
.025	.2498	-.5910
.050	.1269	-.3921
.100	.0345	-.2296
.200	-.0673	-.0290
.400	-.1826	-.0216
.600	-.1741	.1367
.800	-.1200	.1607
.900	-.0775	.1563
.925	-.0910	.1761

STATION 5

X/C	CPU	CPL
.025	.2258	.1550
.050	.1406	.1478
.075	.0827	-.4584
.150	-.0283	-.4598
.300	-.1727	-.4294
.450	-.1898	-.4163
.600	-.2090	-.0088
.750	-.1474	-.0159
.800	-.1184	.0731
.850	-.0806	.0821

STATION 6

X/C	CPU	CPL
.025	.2313	-.3245
.050	.1293	-.3217
.100	.0483	-.3048
.200	-.0323	-.2051
.300	-.1212	-.1554
.400	-.1531	.0365
.500	-.1596	.0896
.600	-.1521	.1027
.700	-.1447	.1234
.800	-.1091	.1248

(d) $\alpha = 1.94^{\circ}$

STATION 1

X/C	CPU	CPL
.005	.2917	-.0559
.010	.0939	.0062
.025	.0105	.0519
.050	-.0303	.0575
.100	-.0778	.0585
.200	-.0974	.0669
.300	-.1520	.0787
.400	-.1720	.0618
.500	-.1327	.0707
.600	-.1276	.0109
.700	-.0835	.1407
.800	-.0472	.1390
.900	.0014	-.0205
.950	-.0169	.2175
.970	.0086	

STATION 2

X/C	CPU	CPL
.005	.3208	-.1995
.010	.1106	-.0639
.025	-.0127	-.0447
.050	-.0401	.0244
.100	-.1113	.0254
.200	-.1469	.0772
.300	-.2129	.0919
.400	-.2317	.0834
.500	-.1802	.0808
.600	-.1730	.1282
.700	-.1484	
.800	-.0805	.1756
.900	-.0344	.2100
.925	-.0400	.2290
.950	-.0310	.2606

STATION 3

X/C	CPU	CPL
.010	.2038	-.0708
.025	.0190	-.0724
.050	-.0650	-.0514
.100	-.0878	.0148
.200	-.1645	.0617
.400	-.2237	.0895
.600	-.1916	.1326
.800	-.1039	.1609
.900	-.0438	.1851
.925	-.0522	.2310

STATION 4

X/C	CPU	CPL
.010	.1976	-.1114
.025	.0164	-.0901
.050	-.0719	-.0112
.100	-.0963	-.0102
.200	-.1847	.0025
.400	-.2469	.0073
.600	-.2076	.1458
.800	-.1335	.1606
.900	-.0737	.1687
.925	-.0875	.1989

STATION 5

X/C	CPU	CPL
.025	.0174	.1820
.050	-.0527	.1815
.075	-.0709	.1744
.150	-.1367	.2443
.300	-.2612	.2386
.450	-.2292	.2405
.600	-.2297	.1621
.750	-.1616	.1662
.800	-.1282	.1843
.850	-.0882	.1786

STATION 6

X/C	CPU	CPL
.025	.0350	-.4091
.050	-.0301	-.2676
.100	-.0509	-.0333
.200	-.1192	-.0248
.300	-.1706	-.0296
.400	-.1989	.0751
.500	-.2035	.0828
.600	-.1853	.1209
.700	-.1749	.1371
.800	-.1370	.1456

TABLE I. - Continued

(e) $\alpha = 3.89^{\circ}$

STATION 1

X/C	CPU	CPL
.005	-.0043	.3059
.010	-.1607	.2277
.025	-.2075	.1973
.050	-.1743	.1705
.100	-.1749	.1152
.200	-.1786	.1247
.300	-.2087	.1176
.400	-.1989	.0910
.500	-.1719	.0934
.600	-.1646	.0159
.700	-.0947	.1557
.800	-.0471	.1571
.900	-.0075	-.0068
.950	-.0033	.2308
.970	.0212	

STATION 2

X/C	CPU	CPL
.005	-.0142	.2343
.010	-.1967	.2338
.025	-.2289	.2002
.050	-.2133	.1615
.100	-.2140	.1321
.200	-.2396	.1386
.300	-.2788	.1358
.400	-.2705	.1291
.500	-.2126	.1075
.600	-.1931	.1382
.700	-.1780	
.800	-.0885	.1831
.900	-.0445	.2063
.925	-.0450	.2342
.950	-.0308	.2616

STATION 3

X/C	CPU	CPL
.010	-.1880	.2157
.025	-.2623	.2073
.050	-.2248	.1719
.100	-.2396	.1294
.200	-.2552	.1380
.400	-.2674	.1369
.600	-.2098	.1531
.800	-.1000	.1842
.900	-.0548	.2130
.925	-.0638	.2589

STATION 4

X/C	CPU	CPL
.010	-.2311	.2419
.025	-.2743	.1772
.050	-.2709	.1814
.100	-.2716	.1573
.200	-.2830	.1573
.400	-.2995	.1421
.600	-.2487	.1876
.800	-.1575	.1871
.900	-.0859	.1996
.925	-.0972	.2188

STATION 5

X/C	CPU	CPL
.025	-.3428	.2275
.050	-.3123	.2232
.075	-.2905	.2157
.150	-.2851	.2583
.300	-.3533	.2501
.450	-.3065	.2511
.600	-.2850	.1677
.750	-.1980	.1715
.800	-.1605	.1786
.850	-.1208	.1605

STATION 6

X/C	CPU	CPL
.025	-.2664	.1786
.050	-.2277	.0867
.100	-.1858	.0795
.200	-.2208	.0691
.300	-.2403	.0966
.400	-.2530	.0819
.500	-.2567	.0909
.600	-.2609	.1059
.700	-.2660	.1287
.800	-.2393	.1320

(f) $\alpha = 5.94^{\circ}$

STATION 1

X/C	CPU	CPL
.005	-.4300	.4843
.010	-.5092	.4048
.025	-.4607	.3241
.050	-.3195	.2648
.100	-.2901	.2040
.200	-.2654	.1674
.300	-.2548	.1651
.400	-.2443	.1266
.500	-.1973	.1223
.600	-.1623	.0250
.700	-.0905	.1665
.800	-.0569	.1513
.900	-.0045	-.0082
.950	-.0096	.2291
.970	.0274	

STATION 2

X/C	CPU	CPL
.005	-.6091	.5302
.010	-.6463	.4404
.025	-.5859	.3448
.050	-.4592	.2893
.100	-.3700	.2277
.200	-.3472	.1977
.300	-.3364	.1806
.400	-.3259	.1535
.500	-.2438	.1468
.600	-.2428	.1844
.700	-.1941	
.800	-.0953	.2120
.900	-.0463	.2453
.925	-.0515	.2677
.950	-.0325	.2704

STATION 3

X/C	CPU	CPL
.010	-.7516	.4910
.025	-.6403	.3788
.050	-.5068	.3232
.100	-.4320	.2771
.200	-.3758	.2393
.400	-.3387	.2001
.600	-.2549	.2055
.800	-.1306	.2088
.900	-.0508	.2387
.925	-.0691	.2807

STATION 4

X/C	CPU	CPL
.010	-.8652	.5183
.025	-.7311	.3904
.050	-.5904	.3390
.100	-.4678	.3186
.200	-.4079	.2787
.400	-.3708	.2340
.600	-.2898	.2274
.800	-.1895	.2255
.900	-.1107	.2169
.925	-.1150	.2487

STATION 5

X/C	CPU	CPL
.025	-.7177	.2578
.050	-.5804	.2654
.075	-.5283	.2701
.150	-.4525	.2778
.300	-.4505	.2749
.450	-.3752	.2706
.600	-.3288	.2359
.750	-.2373	.2292
.800	-.2023	.2111
.850	-.1586	.2083

STATION 6

X/C	CPU	CPL
.025	-.6339	.2092
.050	-.4634	.2095
.100	-.3696	.2224
.200	-.3230	.1925
.300	-.3594	.1053
.400	-.3637	.0881
.500	-.3784	.0906
.600	-.3813	.1005
.700	-.3918	.1176
.800	-.3600	.1291

TABLE I. - Continued

(g) $\alpha = 7.94^{\circ}$

STATION 1

X/C	CPU	CPL
.005	-.9047	.5899
.010	-.8971	.5332
.025	-.7257	.4375
.050	-.4432	.3651
.100	-.4125	.2835
.200	-.3365	.2447
.300	-.3157	.2166
.400	-.2886	.1686
.500	-.2395	.1629
.600	-.1978	.0342
.700	-.1003	.1894
.800	-.0637	.1795
.900	-.0036	-.0218
.950	-.0088	.2412
.970	.0314	

STATION 2

X/C	CPU	CPL
.005	-1.3482	.5700
.010	-1.1200	.5612
.025	-1.0626	.4746
.050	-.5912	.3993
.100	-.5411	.3224
.200	-.4561	.2593
.300	-.4336	.2358
.400	-.3889	.2127
.500	-.3103	.1784
.600	-.2643	.2230
.700	-.2048	
.800	-.1202	.2377
.900	-.0409	.2577
.925	-.0483	.2829
.950	-.0223	.2919

STATION 3

X/C	CPU	CPL
.010	-1.5352	.5910
.025	-1.0603	.5053
.050	-.7542	.4471
.100	-.5968	.3649
.200	-.5017	.3039
.400	-.4135	.2563
.600	-.2900	.2465
.800	-.1433	.2398
.900	-.0746	.2530
.925	-.0661	.2655

STATION 4

X/C	CPU	CPL
.010	-2.2485	.6031
.025	-1.0160	.5732
.050	-.8563	.4452
.100	-.6544	.3856
.200	-.5368	.3819
.400	-.4354	.3168
.600	-.3253	.2574
.800	-.1985	.2316
.900	-.1055	.2425
.925	-.1125	.2750

STATION 5

X/C	CPU	CPL
.025	-1.6795	.2896
.050	-1.4377	.3035
.075	-1.1653	.2988
.150	-.5347	.3049
.300	-.5150	.3056
.450	-.4333	.3025
.600	-.3846	.2952
.750	-.2758	.2834
.800	-.2336	.2492
.850	-.1878	.2287

STATION 6

X/C	CPU	CPL
.025	-.9763	.2996
.050	-.9337	.3374
.100	-.8467	.3189
.200	-.5479	.2129
.300	-.4650	.1032
.400	-.4595	.0782
.500	-.4880	.0797
.600	-.4858	.0935
.700	-.5275	.1097
.800	-.4986	.1294

(h) $\alpha = 10.02^{\circ}$

STATION 1

X/C	CPU	CPL
.005	-1.5520	.6007
.010	-1.2948	.6095
.025	-1.1927	.5421
.050	-.6675	.4338
.100	-.5353	.3627
.200	-.4105	.3009
.300	-.3743	.2632
.400	-.3376	.2166
.500	-.2562	.1976
.600	-.2094	.0465
.700	-.1208	.2171
.800	-.0869	.2018
.900	-.0217	-.0125
.950	.0007	.2461
.970	.0184	

STATION 2

X/C	CPU	CPL
.005	-2.7909	.4891
.010	-1.6361	.5735
.025	-1.2904	.5520
.050	-.9426	.4763
.100	-.7446	.4005
.200	-.5686	.3176
.300	-.5104	.2833
.400	-.4389	.2523
.500	-.3506	.2089
.600	-.2866	.2515
.700	-.2157	
.800	-.1378	.2628
.900	-.0479	.2561
.925	-.0398	.2871
.950	-.0260	.2974

STATION 3

X/C	CPU	CPL
.010	-3.0798	.5844
.025	-2.1179	.5821
.050	-1.0609	.5249
.100	-.7344	.4502
.200	-.5963	.3601
.400	-.4642	.2808
.600	-.3085	.2561
.800	-.1500	.2542
.900	-.0737	.2474
.925	-.0594	.2818

STATION 4

X/C	CPU	CPL
.010	-1.8562	.5859
.025	-1.8949	.5959
.050	-1.8963	.5805
.100	-1.4697	.4885
.200	-.4846	.4657
.400	-.4683	.3591
.600	-.3526	.2747
.800	-.2099	.2455
.900	-.1148	.2585
.925	-.1196	.2866

STATION 5

X/C	CPU	CPL
.025	-1.1991	.2741
.050	-1.2284	.2899
.075	-1.1936	.3024
.150	-1.1549	.2961
.300	-.9981	.2937
.450	-.6443	.2975
.600	-.4479	.2909
.750	-.3408	.2900
.800	-.2926	.2632
.850	-.2375	.2374

STATION 6

X/C	CPU	CPL
.025	-.9159	.2804
.050	-.9017	.2813
.100	-.8795	.2876
.200	-.8425	.2704
.300	-.7641	.1485
.400	-.6819	.0668
.500	-.6754	.0668
.600	-.6481	.0826
.700	-.7140	.0898
.800	-.7183	.0946

TABLE I. - Continued

(i) $\alpha = 12.20^{\circ}$

STATION 1

X/C	CPU	CPL
.005	-2.8343	.5192
.010	-1.6062	.6290
.025	-1.3390	.6099
.050	-.8855	.5296
.100	-.7075	.4517
.200	-.5127	.3682
.300	-.4337	.3198
.400	-.3648	.2670
.500	-.2975	.2333
.600	-.2466	.0410
.700	-.1326	.2391
.800	-.0871	.2074
.900	-.0211	-.0522
.950	-.0058	.2501
.970	.0154	

STATION 2

X/C	CPU	CPL
.005	-2.2755	.2343
.010	-2.2708	.5183
.025	-2.3314	.5896
.050	-2.3678	.5557
.100	-1.7610	.4657
.200	-.4649	.3843
.300	-.5199	.3364
.400	-.4700	.2757
.500	-.3590	.2466
.600	-.3109	.2677
.700	-.2235	
.800	-.1177	.2552
.900	-.0368	.2578
.925	-.0388	.2659
.950	-.0124	.2770

STATION 3

X/C	CPU	CPL
.010	-1.7496	.5431
.025	-1.7248	.6294
.050	-1.7657	.5741
.100	-1.8026	.4840
.200	-1.3255	.4111
.400	-.3776	.3141
.600	-.3113	.2676
.800	-.1799	.2441
.900	-.0950	.2450
.925	-.1017	.2729

STATION 4

X/C	CPU	CPL
.010	-1.4450	.5431
.025	-1.4077	.6199
.050	-1.3631	.6001
.100	-1.3833	.5395
.200	-1.3769	.5141
.400	-.9170	.3778
.600	-.4703	.2734
.800	-.2621	.2359
.900	-.1697	.2306
.925	-.1812	.2720

STATION 5

X/C	CPU	CPL
.025	-.9808	.2739
.050	-.9593	.2808
.075	-.9542	.2851
.150	-.9313	.3001
.300	-.8337	.2890
.450	-.7406	.2856
.600	-.6216	.2759
.750	-.5108	.2726
.800	-.4726	.2697
.850	-.4325	.2462

STATION 6

X/C	CPU	CPL
.025	-.7693	.4079
.050	-.7464	.4019
.100	-.7578	.3891
.200	-.7629	.3707
.300	-.7347	.1379
.400	-.7182	.0633
.500	-.6289	.0652
.600	-.6216	.0631
.700	-.6275	.0655
.800	-.5993	.0507

(j) $\alpha = 14.33^{\circ}$

STATION 1

X/C	CPU	CPL
.005	-3.9404	.3515
.010	-2.6490	.6172
.025	-1.7500	.6713
.050	-1.1161	.6016
.100	-.8671	.5312
.200	-.6022	.4282
.300	-.4974	.3699
.400	-.4251	.3083
.500	-.3610	.2713
.600	-.3033	.0536
.700	-.1608	.2665
.800	-.1276	.2351
.900	-.0529	-.0257
.950	-.0486	.2679
.970	.0097	

STATION 2

X/C	CPU	CPL
.005	-1.8875	.3139
.010	-1.9056	.5658
.025	-1.9244	.6476
.050	-1.8888	.6063
.100	-1.9753	.5244
.200	-1.5670	.4195
.300	-.6979	.3746
.400	-.4460	.3189
.500	-.3535	.2825
.600	-.3213	.2963
.700	-.2776	
.800	-.1928	.2693
.900	-.1214	.2528
.925	-.1378	.2889
.950	-.1194	.2951

STATION 3

X/C	CPU	CPL
.010	-1.3705	.5753
.025	-1.3278	.6635
.050	-1.3610	.6176
.100	-1.3517	.5409
.200	-1.2288	.4552
.400	-.9868	.3540
.600	-.5918	.2898
.800	-.3698	.2378
.900	-.2314	.2457
.925	-.2401	.2640

STATION 4

X/C	CPU	CPL
.010	-1.0551	.5520
.025	-1.1221	.6330
.050	-1.0923	.6422
.100	-1.0194	.5816
.200	-.9256	.5858
.400	-.8347	.4271
.600	-.6669	.2867
.800	-.5330	.2112
.900	-.4198	.1853
.925	-.4141	.2031

STATION 5

X/C	CPU	CPL
.025	-.7530	.2070
.050	-.7537	.2133
.075	-.7315	.2244
.150	-.7451	.2282
.300	-.6788	.2418
.450	-.6291	.2409
.600	-.5959	.2337
.750	-.5172	.2303
.800	-.5129	.2206
.850	-.4901	.2188

STATION 6

X/C	CPU	CPL
.025	-.6140	.2433
.050	-.6166	.4007
.100	-.6071	.4079
.200	-.6680	.3992
.300	-.6723	.1463
.400	-.6248	.0876
.500	-.5886	.0940
.600	-.5694	.0772
.700	-.5369	.0828
.800	-.5310	.0445

TABLE I. - Continued

(k) $\alpha = 16.39^{\circ}$

STATION 1

X/C	CPU	CPL
.005	-4.2487	.1609
.010	-4.2457	.5864
.025	-3.5021	.6892
.050	-1.0088	.6524
.100	-.8715	.5640
.200	-.6233	.4522
.300	-.5376	.4080
.400	-.4650	.3265
.500	-.3801	.2921
.600	-.3453	.0287
.700	-.2134	.2510
.800	-.1723	.2301
.900	-.0810	-.0521
.950	-.0618	.2562
.970	-.0380	

STATION 2

X/C	CPU	CPL
.005	-1.4405	.3262
.010	-1.4483	.5582
.025	-1.4113	.6463
.050	-1.4186	.6260
.100	-1.3445	.5372
.200	-1.2981	.4408
.300	-1.1610	.3828
.400	-.9563	.3333
.500	-.7496	.2812
.600	-.5800	.2979
.700	-.4938	
.800	-.3929	.2399
.900	-.2405	.2214
.925	-.2417	.2485
.950	-.1951	.2573

STATION 3

X/C	CPU	CPL
.010	-1.0907	.5742
.025	-1.0871	.6461
.050	-1.0762	.6356
.100	-1.0296	.5688
.200	-.9686	.4672
.400	-.8822	.3632
.600	-.7087	.2848
.800	-.5506	.2171
.900	-.4423	.1639
.925	-.4263	.1910

STATION 4

X/C	CPU	CPL
.010	-.8612	.5688
.025	-.8844	.6418
.050	-.8620	.6374
.100	-.8503	.6251
.200	-.8372	.6040
.400	-.7542	.4414
.600	-.6615	.2780
.800	-.6023	.1782
.900	-.5190	.1584
.925	-.5348	.1382

STATION 5

X/C	CPU	CPL
.025	-.6990	.1535
.050	-.7083	.1579
.075	-.6982	.3133
.150	-.6924	.3387
.300	-.6876	.3253
.450	-.6680	.3286
.600	-.6072	.3238
.750	-.5971	.3093
.800	-.5704	.2723
.850	-.5748	.2684

STATION 6

X/C	CPU	CPL
.025	-.6122	.5122
.050	-.6256	.4345
.100	-.5891	.4457
.200	-.6289	.4414
.300	-.6355	.1385
.400	-.5849	.0949
.500	-.5530	.0716
.600	-.5600	.0634
.700	-.5233	.0575
.800	-.5453	.0346

(l) $\alpha = 18.44^{\circ}$

STATION 1

X/C	CPU	CPL
.005	-3.4285	.1540
.010	-3.2297	.6030
.025	-3.2123	.7286
.050	-2.6253	.6968
.100	-1.7805	.6098
.200	-.6288	.5018
.300	-.5561	.4281
.400	-.4978	.3611
.500	-.4527	.3024
.600	-.3951	.0344
.700	-.2485	.2635
.800	-.2523	.2302
.900	-.1741	-.0481
.950	-.1524	.2299
.970	-.0756	

STATION 2

X/C	CPU	CPL
.005	-1.2054	.3240
.010	-1.2554	.5628
.025	-1.2190	.6525
.050	-1.1886	.6469
.100	-1.1467	.5812
.200	-1.0822	.4672
.300	-1.0597	.4050
.400	-.9592	.3542
.500	-.8149	.2887
.600	-.7433	.3108
.700	-.6336	
.800	-.5553	.2203
.900	-.4207	.2073
.925	-.3968	.1985
.950	-.3605	.1903

STATION 3

X/C	CPU	CPL
.010	-.9713	.5683
.025	-.9563	.6647
.050	-.9310	.6537
.100	-.9490	.5975
.200	-.8790	.5001
.400	-.8347	.3740
.600	-.7331	.2931
.800	-.5910	.1927
.900	-.5142	.1421
.925	-.4780	.1426

STATION 4

X/C	CPU	CPL
.010	-.8447	.5441
.025	-.8543	.6356
.050	-.8236	.6356
.100	-.7983	.6399
.200	-.7838	.6084
.400	-.7442	.4527
.600	-.6927	.2832
.800	-.6283	.1768
.900	-.5537	.1439
.925	-.5407	.1175

STATION 5

X/C	CPU	CPL
.025	-.6507	.1624
.050	-.6675	.1782
.075	-.6442	.3501
.150	-.6571	.3545
.300	-.6769	.3627
.450	-.6275	.3517
.600	-.6241	.3377
.750	-.6052	.3329
.800	-.6206	.2547
.850	-.6027	.1788

STATION 6

X/C	CPU	CPL
.025	-.5620	.5157
.050	-.5752	.4532
.100	-.5674	.4097
.200	-.6158	.4083
.300	-.6219	.1514
.400	-.5930	.0922
.500	-.5752	.0914
.600	-.5616	.0686
.700	-.5463	.0498
.800	-.5661	.0252

TABLE I. - Concluded

(m) $\alpha = 20.47^{\circ}$

STATION 1

X/C	CPU	CPL
.005	-2.1779	.2706
.010	-2.2116	.6277
.025	-2.1388	.7566
.050	-2.0530	.7272
.100	-1.9792	.6533
.200	-1.2651	.5301
.300	-.8075	.4692
.400	-.6402	.3981
.500	-.5299	.3358
.600	-.4571	.0387
.700	-.3428	.2805
.800	-.3432	.2358
.900	-.2524	-.0353
.950	-.2080	.2319
.970	-.1739	

STATION 2

X/C	CPU	CPL
.005	-1.1247	.3000
.010	-1.1435	.5533
.025	-1.1173	.6646
.050	-1.0578	.6683
.100	-1.0440	.5984
.200	-1.0041	.5104
.300	-.9816	.4397
.400	-.8945	.3813
.500	-.8407	.3273
.600	-.7949	.3208
.700	-.6833	
.800	-.6389	.2325
.900	-.5286	.2074
.925	-.4865	.1639
.950	-.4821	.1470

STATION 3

X/C	CPU	CPL
.010	-.8901	.5314
.025	-.9308	.6714
.050	-.9127	.6595
.100	-.8984	.6261
.200	-.8378	.5160
.400	-.7827	.3965
.600	-.7355	.3061
.800	-.6352	.1953
.900	-.5976	.1050
.925	-.5623	.1196

STATION 4

X/C	CPU	CPL
.010	-.8039	.5238
.025	-.7876	.6416
.050	-.7709	.6612
.100	-.7738	.6485
.200	-.7478	.6416
.400	-.7412	.5104
.600	-.6852	.3024
.800	-.6527	.1861
.900	-.6019	.1315
.925	-.5992	.1023

STATION 5

X/C	CPU	CPL
.025	-.6432	.0931
.050	-.6302	.1163
.075	-.6527	.3781
.150	-.6639	.3897
.300	-.6296	.3868
.450	-.6248	.3853
.600	-.6114	.3663
.750	-.6056	.3647
.800	-.5949	.1338
.850	-.5940	.1396

STATION 6

X/C	CPU	CPL
.025	-.5527	.5050
.050	-.5408	.4673
.100	-.5597	.4395
.200	-.5465	.4464
.300	-.5798	.1541
.400	-.5767	.0952
.500	-.5703	.0802
.600	-.5696	.0805
.700	-.5427	.0419
.800	-.5427	.0196

TABLE II.- PRESSURE COEFFICIENTS AT A MACH NUMBER OF 0.40 FOR MODEL STRAKE OFF. $C_{L,d} = 0.35$

(a) $\alpha = -3.90^{\circ}$

STATION 1

X/C	CPU	CPL
.005	.5572	-1.6053
.010	.5289	-1.5996
.025	.4165	-1.5267
.050	.2847	-.3711
.100	.1996	-.2424
.200	.0739	-.1918
.300	-.0290	-.1302
.400	-.0764	-.1176
.500	-.0934	-.0930
.600	-.1151	-.0722
.700	-.1102	.0238
.800	-.0720	.0522
.900	-.0522	-.0779
.950	-.0802	.1568
.970	-.0457	

STATION 2

X/C	CPU	CPL
.005	.5166	-.8758
.010	.5165	-.8691
.025	.4292	-.8866
.050	.3237	-.8870
.100	.1933	-.9853
.200	.0442	-.6250
.300	-.0658	-.0306
.400	-.1272	-.0002
.500	-.1219	-.0104
.600	-.1459	.0406
.700	-.1501	
.800	-.1028	.1084
.900	-.0808	.1590
.925	-.1001	.1966
.950	-.0993	.2253

STATION 3

X/C	CPU	CPL
.010	.5266	-.7469
.025	.4447	-.7335
.050	.3420	-.7430
.100	.2102	-.7350
.200	.0413	-.7422
.400	-.1127	-.2747
.600	-.1506	.0915
.800	-.1134	.1308
.900	-.0870	.1762
.925	-.1003	.2148

STATION 4

X/C	CPU	CPL
.010	.5203	-.6383
.025	.4397	-.6180
.050	.3351	-.6222
.100	.2166	-.6073
.200	.0448	-.6107
.400	-.1287	-.5909
.600	-.1748	-.0938
.800	-.1486	.0903
.900	-.1070	.1715
.925	-.1201	.2316

STATION 5

X/C	CPU	CPL
.025	.4118	-.0083
.050	.3166	-.1983
.075	.2587	-.3573
.150	.1190	-.3408
.300	-.0783	-.3354
.450	-.1487	-.3340
.600	-.2021	-.3294
.750	-.1759	-.3234
.800	-.1592	-.3178
.850	-.1467	-.3073

STATION 6

X/C	CPU	CPL
.025	.3527	-.2950
.050	.2503	-.2873
.100	.1579	-.2854
.200	.0285	-.2742
.300	-.0845	-.1991
.400	-.1309	-.1873
.500	-.1589	-.1674
.600	-.1703	-.1172
.700	-.1708	-.1024
.800	-.1416	-.0903

(b) $\alpha = -1.96^{\circ}$

STATION 1

X/C	CPU	CPL
.005	.5404	-1.1779
.010	.4325	-1.0786
.025	.3093	-.5682
.050	.1844	-.2273
.100	.0953	-.1803
.200	-.0122	-.1227
.300	-.0895	-.0792
.400	-.1244	-.0804
.500	-.1282	-.0588
.600	-.1396	-.0618
.700	-.1170	.0425
.800	-.0804	.0661
.900	-.0528	-.0787
.950	-.0768	.1605
.970	-.0486	

STATION 2

X/C	CPU	CPL
.005	.5334	-.9248
.010	.4600	-.9107
.025	.3394	-.9240
.050	.2138	-.9802
.100	.0999	-.3068
.200	-.0214	-.0724
.300	-.1219	-.0558
.400	-.1852	-.0472
.500	-.1575	-.0315
.600	-.1769	.0311
.700	-.1696	
.800	-.1191	.1020
.900	-.0835	.1541
.925	-.0968	.1771
.950	-.0942	.1897

STATION 3

X/C	CPU	CPL
.010	.4853	-.6993
.025	.3513	-.7030
.050	.2430	-.7010
.100	.1137	-.7199
.200	-.0330	-.2641
.400	-.1663	.0088
.600	-.1842	.0610
.800	-.1245	.1131
.900	-.0900	.1529
.925	-.1022	.2059

STATION 4

X/C	CPU	CPL
.010	.4862	-.5982
.025	.3583	-.5826
.050	.2411	-.5895
.100	.1145	-.5899
.200	-.0341	-.5906
.400	-.1741	-.0614
.600	-.2043	.0680
.800	-.1613	.0752
.900	-.1157	.0961
.925	-.1297	.1813

STATION 5

X/C	CPU	CPL
.025	.3375	.1730
.050	.2214	-.2805
.075	.1580	-.3939
.150	.0400	-.3904
.300	-.1491	-.3872
.450	-.1915	-.3879
.600	-.2280	-.1699
.750	-.1746	-.1324
.800	-.1478	.0676
.850	-.1227	.0865

STATION 6

X/C	CPU	CPL
.025	.2966	-.0722
.050	.1748	-.1861
.100	.0921	-.1940
.200	-.0090	-.1852
.300	-.1269	-.1616
.400	-.1578	-.1600
.500	-.1814	-.1202
.600	-.1759	-.1018
.700	-.1660	-.0971
.800	-.1331	-.0942

TABLE II. - Continued

(c) $\alpha = 0.03^{\circ}$

STATION 1

X/C	CPU	CPL
.005	.4507	-.6513
.010	.2709	-.3059
.025	.1291	-.1918
.050	.0571	-.1259
.100	-.0172	-.0891
.200	-.0876	-.0518
.300	-.1550	-.0241
.400	-.1736	-.0385
.500	-.1712	-.0195
.600	-.1724	-.0512
.700	-.1362	.0657
.800	-.0943	.0785
.900	-.0590	-.0713
.950	-.0752	.1715
.970	-.0435	

STATION 2

X/C	CPU	CPL
.005	.4725	-.8075
.010	.3107	-.8162
.025	.1669	-.7089
.050	.0774	-.1526
.100	-.0178	-.1174
.200	-.1164	-.0480
.300	-.1955	-.0225
.400	-.2451	-.0134
.500	-.1963	.0000
.600	-.2103	.0672
.700	-.1920	
.800	-.1356	.1271
.900	-.0926	.1696
.925	-.1036	.1898
.950	-.0942	.2171

STATION 3

X/C	CPU	CPL
.010	.3829	-.6930
.025	.2090	-.5782
.050	.1009	-.3598
.100	-.0142	-.1214
.200	-.1336	-.0448
.400	-.2165	.0082
.600	-.2196	.0707
.800	-.1419	.1255
.900	-.0983	.1675
.925	-.1064	.2055

STATION 4

X/C	CPU	CPL
.010	.3808	-.7373
.025	.2081	-.4537
.050	.0843	-.2918
.100	-.0010	-.1677
.200	-.1396	-.1656
.400	-.2424	-.1633
.600	-.2421	.0496
.800	-.1720	.0695
.900	-.1235	.0820
.925	-.1361	.1268

STATION 5

X/C	CPU	CPL
.025	.2051	-.0937
.050	.0879	-.4065
.075	.0273	-.5804
.150	-.0667	-.5189
.300	-.2282	-.3831
.450	-.2497	-.1334
.600	-.2600	-.0195
.750	-.1968	-.0003
.800	-.1638	.0747
.850	-.1316	.1016

STATION 6

X/C	CPU	CPL
.025	.2030	-.2683
.050	.0725	-.4496
.100	.0086	-.4426
.200	-.0678	-.2626
.300	-.1852	-.0690
.400	-.2048	-.0049
.500	-.2126	.0436
.600	-.2071	.0771
.700	-.1892	.1091
.800	-.1599	.1197

(d) $\alpha = 2.12^{\circ}$

STATION 1

X/C	CPU	CPL
.005	.2413	-.1262
.010	.0454	-.0526
.025	-.0454	.0003
.050	-.0808	.0225
.100	-.1319	.0050
.200	-.1710	.0248
.300	-.2209	.0279
.400	-.2339	.0046
.500	-.2103	.0114
.600	-.2007	-.0397
.700	-.1434	.0877
.800	-.1082	.0927
.900	-.0635	-.0628
.950	-.0766	.1796
.970	-.0383	

STATION 2

X/C	CPU	CPL
.005	.2630	-.2570
.010	.0573	-.1857
.025	-.0534	-.0698
.050	-.1124	-.0094
.100	-.1543	.0021
.200	-.2275	.0218
.300	-.2769	.0381
.400	-.3130	.0336
.500	-.2560	.0322
.600	-.2515	.0791
.700	-.2173	
.800	-.1500	.1334
.900	-.1008	.1715
.925	-.1073	.2005
.950	-.0954	.2209

STATION 3

X/C	CPU	CPL
.010	.1482	-.1670
.025	-.0458	-.0843
.050	-.0920	-.0325
.100	-.1563	-.0038
.200	-.2312	.0396
.400	-.2934	.0561
.600	-.2557	.0837
.800	-.1613	.1317
.900	-.1142	.1677
.925	-.1186	.2100

STATION 4

X/C	CPU	CPL
.010	.1269	-.1349
.025	-.0487	-.1215
.050	-.1094	-.0723
.100	-.1731	-.0013
.200	-.2481	-.0020
.400	-.3108	.0499
.600	-.2851	.1145
.800	-.1945	.1158
.900	-.1311	.1155
.925	-.1453	.2021

STATION 5

X/C	CPU	CPL
.025	-.0372	.1968
.050	-.1329	-.0361
.075	-.1403	-.0189
.150	-.1966	-.1451
.300	-.3233	-.1405
.450	-.3042	-.0694
.600	-.3027	.0706
.750	-.2181	.0848
.800	-.1883	.1253
.850	-.1486	.1282

STATION 6

X/C	CPU	CPL
.025	-.0304	-.3217
.050	-.1138	-.1517
.100	-.1187	-.0544
.200	-.1485	-.0201
.300	-.2435	.0125
.400	-.2618	.0138
.500	-.2542	.0601
.600	-.2524	.0726
.700	-.2330	.0909
.800	-.2141	.0964

TABLE II. - Continued

(e) $\alpha = 4.09^{\circ}$

STATION 1

X/C	CPU	CPL
.005	-.0633	.2346
.010	-.2229	.1819
.025	-.2678	.1656
.050	-.2389	.1236
.100	-.2479	.0983
.200	-.2398	.0808
.300	-.2742	.0737
.400	-.2761	.0517
.500	-.2507	.0458
.600	-.2329	-.0315
.700	-.1658	.1092
.800	-.1179	.1084
.900	-.0682	-.0688
.950	-.0720	.1874
.970	-.0323	

STATION 2

X/C	CPU	CPL
.005	-.0924	.2450
.010	-.2617	.2034
.025	-.3560	.1583
.050	-.2934	.1362
.100	-.2960	.0946
.200	-.3285	.1002
.300	-.3564	.0979
.400	-.3660	.0750
.500	-.2961	.0706
.600	-.2759	.1160
.700	-.2369	
.800	-.1559	.1518
.900	-.1030	.1806
.925	-.1144	.2070
.950	-.1006	.2305

STATION 3

X/C	CPU	CPL
.010	-.2404	.2006
.025	-.3458	.1409
.050	-.3239	.1201
.100	-.3232	.1036
.200	-.3491	.1064
.400	-.3650	.0974
.600	-.2953	.1201
.800	-.1775	.1443
.900	-.1214	.1844
.925	-.1232	.2124

STATION 4

X/C	CPU	CPL
.010	-.3944	.2328
.025	-.3799	.1368
.050	-.3759	.1357
.100	-.3379	.1232
.200	-.3705	.1232
.400	-.3860	.1148
.600	-.3271	.1372
.800	-.2129	.1399
.900	-.1406	.1441
.925	-.1480	.1913

STATION 5

X/C	CPU	CPL
.025	-.4242	.1950
.050	-.3744	.1938
.075	-.3502	.1268
.150	-.3456	.0320
.300	-.4117	.0337
.450	-.3818	.0596
.600	-.3556	.1046
.750	-.2622	.1055
.800	-.2219	.1350
.850	-.1841	.1336

STATION 6

X/C	CPU	CPL
.025	-.3298	.0646
.050	-.3195	.0456
.100	-.2817	.0367
.200	-.2698	.0260
.300	-.3296	.0561
.400	-.3323	.0332
.500	-.3353	.0496
.600	-.3353	.0655
.700	-.3396	.0809
.800	-.3205	.0855

(f) $\alpha = 6.21^{\circ}$

STATION 1

X/C	CPU	CPL
.005	-.4922	.4861
.010	-.5776	.3846
.025	-.5630	.3058
.050	-.3947	.2300
.100	-.3746	.1740
.200	-.3281	.1510
.300	-.3352	.1299
.400	-.3157	.0967
.500	-.2785	.0823
.600	-.2506	-.0297
.700	-.1689	.1299
.800	-.1256	.1231
.900	-.0707	-.0684
.950	-.0673	.1933
.970	-.0327	

STATION 2

X/C	CPU	CPL
.005	-.7400	.4846
.010	-.7637	.4120
.025	-.6964	.3285
.050	-.5792	.2616
.100	-.4676	.1905
.200	-.4400	.1595
.300	-.4404	.1453
.400	-.4204	.1198
.500	-.3411	.1054
.600	-.3097	.1450
.700	-.2600	
.800	-.1758	.1684
.900	-.1113	.1967
.925	-.1114	.2134
.950	-.0956	.2249

STATION 3

X/C	CPU	CPL
.010	-.9088	.4405
.025	-.7971	.3461
.050	-.6523	.2967
.100	-.4758	.2238
.200	-.4774	.1849
.400	-.4367	.1388
.600	-.3396	.1520
.800	-.1956	.1626
.900	-.1268	.1882
.925	-.1249	.2216

STATION 4

X/C	CPU	CPL
.010	-1.0323	.4655
.025	-.8765	.3692
.050	-.7386	.2900
.100	-.5334	.2724
.200	-.5032	.2023
.400	-.4638	.1658
.600	-.3702	.1689
.800	-.2328	.1612
.900	-.1475	.1732
.925	-.1584	.2095

STATION 5

X/C	CPU	CPL
.025	-.8373	.2117
.050	-.7152	.2132
.075	-.5982	.2262
.150	-.5176	.1643
.300	-.5208	.1678
.450	-.4466	.1680
.600	-.4079	.1589
.750	-.3073	.1623
.800	-.2701	.1502
.850	-.2265	.1459

STATION 6

X/C	CPU	CPL
.025	-.6876	.1799
.050	-.5897	.1907
.100	-.4667	.1801
.200	-.4001	.0908
.300	-.4453	.0598
.400	-.4579	.0188
.500	-.4646	.0299
.600	-.4673	.0410
.700	-.4849	.0574
.800	-.4520	.0667

TABLE II. - Continued

(g) $\alpha = 8.31^{\circ}$

STATION 1

X/C	CPU	CPL
.005	-1.0280	.5695
.010	-.9898	.5017
.025	-.8677	.4218
.050	-.5544	.3308
.100	-.5015	.2635
.200	-.4173	.2147
.300	-.3955	.1790
.400	-.3598	.1352
.500	-.3063	.1198
.600	-.2739	-.0084
.700	-.1877	.1560
.800	-.1393	.1436
.900	-.0774	-.0674
.950	-.0640	.2050
.970	-.0283	

STATION 2

X/C	CPU	CPL
.005	-1.6449	.5401
.010	-1.3896	.5270
.025	-1.1133	.4409
.050	-.7963	.3655
.100	-.6511	.2768
.200	-.5475	.2305
.300	-.5269	.1951
.400	-.4815	.1677
.500	-.3778	.1449
.600	-.3365	.1701
.700	-.2807	
.800	-.1860	.1818
.900	-.1104	.1982
.925	-.1080	.2182
.950	-.0874	.2340

STATION 3

X/C	CPU	CPL
.010	-1.5431	.5333
.025	-1.1579	.4686
.050	-.9005	.3965
.100	-.7153	.3086
.200	-.6023	.2410
.400	-.4954	.1751
.600	-.3661	.1709
.800	-.2091	.1706
.900	-.1299	.1911
.925	-.1248	.2276

STATION 4

X/C	CPU	CPL
.010	-2.4321	.5375
.025	-1.2467	.4738
.050	-.9987	.4171
.100	-.7626	.3410
.200	-.6518	.2785
.400	-.5469	.2204
.600	-.4127	.1897
.800	-.2573	.1722
.900	-.1682	.1830
.925	-.1666	.2181

STATION 5

X/C	CPU	CPL
.025	-1.7982	.2295
.050	-1.7221	.2373
.075	-1.4478	.3312
.150	-.6157	.3273
.300	-.5951	.3107
.450	-.5068	.2641
.600	-.4688	.1609
.750	-.3651	.1590
.800	-.3236	.1442
.850	-.2738	.1350

STATION 6

X/C	CPU	CPL
.025	-1.0526	.3891
.050	-1.0246	.3291
.100	-.9611	.2162
.200	-.7420	.0720
.300	-.5712	.0402
.400	-.5578	.0145
.500	-.5863	.0119
.600	-.5803	.0220
.700	-.6410	.0355
.800	-.6268	.0394

(h) $\alpha = 10.51^{\circ}$

STATION 1

X/C	CPU	CPL
.005	-1.9164	.5906
.010	-1.4752	.5870
.025	-1.1140	.5253
.050	-.7856	.4273
.100	-.6589	.3574
.200	-.5044	.2827
.300	-.4717	.2468
.400	-.4161	.1913
.500	-.3442	.1637
.600	-.3026	.0005
.700	-.1953	.1851
.800	-.1507	.1686
.900	-.0874	-.0469
.950	-.0789	.2207
.970	-.0406	

STATION 2

X/C	CPU	CPL
.005	-3.3356	.4417
.010	-1.9389	.5503
.025	-1.4982	.5409
.050	-1.1215	.4759
.100	-.8773	.3793
.200	-.6764	.2947
.300	-.6067	.2691
.400	-.5498	.2172
.500	-.4386	.1932
.600	-.3800	.2064
.700	-.3018	
.800	-.2004	.2010
.900	-.1185	.2090
.925	-.1085	.2256
.950	-.0809	.2475

STATION 3

X/C	CPU	CPL
.010	-2.6434	.5333
.025	-2.4752	.5433
.050	-1.9358	.4901
.100	-.8447	.4060
.200	-.6707	.3171
.400	-.5496	.2422
.600	-.3961	.2014
.800	-.2198	.1938
.900	-.1382	.2011
.925	-.1254	.2312

STATION 4

X/C	CPU	CPL
.010	-1.8212	.5430
.025	-1.8293	.5531
.050	-1.8453	.4918
.100	-1.8366	.4100
.200	-1.0511	.3961
.400	-.5254	.2905
.600	-.4254	.2180
.800	-.2698	.1841
.900	-.1754	.1958
.925	-.1849	.2362

STATION 5

X/C	CPU	CPL
.025	-1.2462	.2345
.050	-1.2519	.2441
.075	-1.2109	.3787
.150	-1.1852	.3753
.300	-1.0649	.3644
.450	-.8315	.3294
.600	-.6133	.1673
.750	-.4448	.1667
.800	-.4002	.1440
.850	-.3620	.1319

STATION 6

X/C	CPU	CPL
.025	-.9698	.3594
.050	-.9587	.3580
.100	-.9434	.3528
.200	-.9058	.1304
.300	-.8655	.0384
.400	-.8070	-.0041
.500	-.7798	.0039
.600	-.7560	.0115
.700	-.8082	.0230
.800	-.7838	.0226

TABLE II.- Continued

(i) $\alpha = 12.70^\circ$

STATION 1

X/C	CPU	CPL
.005	-3.0849	.5164
.010	-1.9882	.6129
.025	-1.4965	.5845
.050	-1.0163	.5095
.100	-.8272	.4148
.200	-.6281	.3419
.300	-.5390	.2927
.400	-.4637	.2342
.500	-.3847	.1925
.600	-.3276	-.0051
.700	-.2165	.2041
.800	-.1731	.1776
.900	-.1024	-.0703
.950	-.0962	.2247
.970	-.0623	

STATION 2

X/C	CPU	CPL
.005	-2.2771	.3031
.010	-2.2699	.5356
.025	-2.2319	.5726
.050	-2.2552	.5336
.100	-2.1721	.4333
.200	-.4299	.3454
.300	-.5646	.2957
.400	-.5697	.2522
.500	-.4517	.2135
.600	-.3996	.2138
.700	-.3338	
.800	-.2308	.1979
.900	-.1501	.2011
.925	-.1437	.2160
.950	-.1197	.2284

STATION 3

X/C	CPU	CPL
.010	-1.7294	.5210
.025	-1.6829	.5740
.050	-1.6953	.5402
.100	-1.6850	.4498
.200	-1.6034	.3581
.400	-.5891	.2698
.600	-.3795	.2131
.800	-.2666	.1878
.900	-.2051	.1946
.925	-.2148	.2160

STATION 4

X/C	CPU	CPL
.010	-1.3689	.5173
.025	-1.3498	.5726
.050	-1.3424	.5218
.100	-1.2837	.4464
.200	-1.2286	.4407
.400	-1.0222	.3251
.600	-.7186	.2179
.800	-.4751	.1636
.900	-.3563	.1586
.925	-.3416	.1916

STATION 5

X/C	CPU	CPL
.025	-.9399	.2102
.050	-.9592	.3788
.075	-.9306	.4213
.150	-.9098	.4222
.300	-.8322	.3653
.450	-.7404	.2921
.600	-.6528	.1564
.750	-.5816	.1419
.800	-.5481	.0901
.850	-.5256	.0851

STATION 6

X/C	CPU	CPL
.025	-.7612	.4115
.050	-.7613	.4131
.100	-.7555	.2534
.200	-.7953	.0936
.300	-.7766	.0499
.400	-.7152	.0036
.500	-.6867	.0016
.600	-.6692	.0054
.700	-.6383	.0085
.800	-.6216	-.0118

(j) $\alpha = 14.94^\circ$

STATION 1

X/C	CPU	CPL
.005	-3.6650	.4051
.010	-3.4455	.6222
.025	-2.6575	.6459
.050	-1.0277	.5722
.100	-.8813	.4880
.200	-.6454	.3974
.300	-.5667	.3404
.400	-.5061	.2724
.500	-.4296	.2289
.600	-.3763	.0014
.700	-.2728	.2145
.800	-.2375	.1828
.900	-.1449	-.1033
.950	-.1294	.2139
.970	-.0895	

STATION 2

X/C	CPU	CPL
.005	-1.6385	.3776
.010	-1.6102	.5640
.025	-1.5815	.6053
.050	-1.5321	.5712
.100	-1.4819	.4838
.200	-1.4861	.3908
.300	-1.2302	.3332
.400	-.9049	.2791
.500	-.7071	.2309
.600	-.5706	.2321
.700	-.4469	
.800	-.3743	.1883
.900	-.2508	.1618
.925	-.2811	.1974
.950	-.2703	.2121

STATION 3

X/C	CPU	CPL
.010	-1.2664	.5395
.025	-1.2332	.5946
.050	-1.2047	.5592
.100	-1.1524	.4895
.200	-1.0787	.3919
.400	-.9669	.2820
.600	-.7518	.2237
.800	-.5699	.1616
.900	-.4757	.1412
.925	-.4536	.1494

STATION 4

X/C	CPU	CPL
.010	-.9879	.5308
.025	-.9832	.5808
.050	-.9624	.5467
.100	-.9518	.4782
.200	-.9080	.4687
.400	-.7926	.3763
.600	-.7105	.2101
.800	-.6015	.1263
.900	-.5198	.0927
.925	-.5183	.0974

STATION 5

X/C	CPU	CPL
.025	-.7622	.2964
.050	-.7449	.3928
.075	-.7350	.4466
.150	-.7390	.3763
.300	-.7272	.3689
.450	-.6949	.3337
.600	-.6407	.1420
.750	-.5949	.1328
.800	-.5949	.0619
.850	-.5755	.0592

STATION 6

X/C	CPU	CPL
.025	-.6390	.3690
.050	-.6656	.3660
.100	-.6683	.2679
.200	-.7086	.1931
.300	-.6945	.0619
.400	-.6529	.0056
.500	-.6270	.0059
.600	-.6211	.0079
.700	-.6035	-.0098
.800	-.5870	-.0349

TABLE II. - Continued

(k) $\alpha = 17.05^{\circ}$

STATION 1

X/C	CPU	CPL
.005	-3.4021	.3453
.010	-3.5227	.6340
.025	-3.3065	.6876
.050	-2.0778	.6205
.100	-.8812	.5443
.200	-.6676	.4435
.300	-.6325	.3716
.400	-.5595	.2970
.500	-.4898	.2518
.600	-.4457	-.0070
.700	-.3389	.2224
.800	-.3042	.1732
.900	-.2229	-.0919
.950	-.1881	.2072
.970	-.1414	

STATION 2

X/C	CPU	CPL
.005	-1.3212	.3681
.010	-1.3399	.5499
.025	-1.2930	.6178
.050	-1.2857	.5939
.100	-1.2614	.5052
.200	-1.2176	.4096
.300	-1.1098	.3505
.400	-.9929	.2858
.500	-.8694	.2433
.600	-.7576	.2440
.700	-.6582	
.800	-.5614	.1752
.900	-.4712	.1412
.925	-.4333	.1597
.950	-.4260	.1481

STATION 3

X/C	CPU	CPL
.010	-1.0306	.5372
.025	-.9982	.6105
.050	-1.0318	.5877
.100	-.9870	.5146
.200	-.9510	.4214
.400	-.8871	.3064
.600	-.7463	.2232
.800	-.6448	.1371
.900	-.5660	.1002
.925	-.5551	.0987

STATION 4

X/C	CPU	CPL
.010	-.8721	.5273
.025	-.8663	.5854
.050	-.8770	.5839
.100	-.8808	.4982
.200	-.8542	.4957
.400	-.7920	.3912
.600	-.7261	.2209
.800	-.6532	.1010
.900	-.5954	.0618
.925	-.5915	.0669

STATION 5

X/C	CPU	CPL
.025	-.7217	.2731
.050	-.7144	.4153
.075	-.7080	.4710
.150	-.7162	.4538
.300	-.7010	.4491
.450	-.6852	.4081
.600	-.6601	.1424
.750	-.6400	.1139
.800	-.6368	.0471
.850	-.6322	.0505

STATION 6

X/C	CPU	CPL
.025	-.6298	.3590
.050	-.6215	.3826
.100	-.6306	.3218
.200	-.6472	.1327
.300	-.6628	.0810
.400	-.6348	.0169
.500	-.5962	.0116
.600	-.5993	-.0011
.700	-.5814	-.0118
.800	-.5681	-.0425

(l) $\alpha = 19.16^{\circ}$

STATION 1

X/C	CPU	CPL
.005	-2.4057	.3658
.010	-2.4539	.6524
.025	-2.2439	.7151
.050	-2.3406	.6670
.100	-2.0889	.5826
.200	-1.0917	.4734
.300	-.6735	.4014
.400	-.5826	.3248
.500	-.5502	.2754
.600	-.5292	.0129
.700	-.3987	.2303
.800	-.3848	.1739
.900	-.3073	-.1061
.950	-.2705	.1761
.970	-.2215	

STATION 2

X/C	CPU	CPL
.005	-1.1760	.3458
.010	-1.1872	.5439
.025	-1.1463	.6180
.050	-1.1243	.6073
.100	-1.0998	.5346
.200	-1.0316	.4354
.300	-1.0205	.3775
.400	-.9440	.3157
.500	-.8697	.2562
.600	-.8089	.2361
.700	-.7354	
.800	-.6546	.1588
.900	-.5700	.1004
.925	-.5462	.0972
.950	-.5252	.0790

STATION 3

X/C	CPU	CPL
.010	-.9405	.5245
.025	-.9271	.6124
.050	-.9065	.6033
.100	-.9274	.5371
.200	-.9057	.4508
.400	-.8506	.3215
.600	-.7624	.2311
.800	-.6745	.1212
.900	-.6256	.0861
.925	-.6210	.0443

STATION 4

X/C	CPU	CPL
.010	-.8590	.4850
.025	-.8655	.5833
.050	-.8353	.5858
.100	-.8233	.5155
.200	-.8114	.5121
.400	-.7766	.4297
.600	-.7320	.2191
.800	-.6768	.0850
.900	-.6298	.0383
.925	-.6251	.0371

STATION 5

X/C	CPU	CPL
.025	-.6838	.2248
.050	-.6910	.3967
.075	-.6825	.4797
.150	-.6668	.4615
.300	-.6717	.4609
.450	-.6607	.3405
.600	-.6736	.1483
.750	-.6493	.1219
.800	-.6364	.0473
.850	-.6392	.0420

STATION 6

X/C	CPU	CPL
.025	-.5980	.3484
.050	-.6059	.3902
.100	-.6254	.3260
.200	-.6351	.2141
.300	-.6387	.0658
.400	-.6504	.0050
.500	-.6031	.0020
.600	-.6167	-.0238
.700	-.6100	-.0227
.800	-.6030	-.0565

TABLE II. - Concluded

(m) $\alpha = 21.20^{\circ}$

STATION 1

X/C	CPU	CPL
.005	-1.8744	.3693
.010	-1.9408	.6607
.025	-1.8048	.7279
.050	-1.8071	.6980
.100	-1.7219	.6192
.200	-1.3956	.5109
.300	-1.0003	.4389
.400	-.8050	.3625
.500	-.6742	.2922
.600	-.6246	-.0000
.700	-.4863	.2405
.800	-.4865	.1792
.900	-.3608	-.1145
.950	-.3574	.1491
.970	-.2819	

STATION 2

X/C	CPU	CPL
.005	-1.0569	.3151
.010	-1.0287	.5259
.025	-1.0665	.6221
.050	-1.0268	.6320
.100	-1.0286	.5618
.200	-.9928	.4744
.300	-.9460	.4054
.400	-.9346	.3495
.500	-.8918	.2760
.600	-.8369	.2689
.700	-.7735	
.800	-.6997	.1560
.900	-.6246	.0767
.925	-.5954	.0564
.950	-.6072	.0473

STATION 3

X/C	CPU	CPL
.010	-.9173	.4940
.025	-.9066	.6123
.050	-.9112	.6129
.100	-.8988	.5615
.200	-.8843	.4607
.400	-.8313	.3454
.600	-.7787	.2401
.800	-.7091	.1153
.900	-.6573	.0369
.925	-.6672	.0419

STATION 4

X/C	CPU	CPL
.010	-.8093	.4713
.025	-.8362	.5958
.050	-.8285	.5905
.100	-.7979	.5890
.200	-.7871	.5750
.400	-.7739	.4975
.600	-.7343	.2353
.800	-.6901	.0862
.900	-.6652	.0387
.925	-.6666	.0260

STATION 5

X/C	CPU	CPL
.025	-.6938	.3098
.050	-.6873	.3945
.075	-.6951	.5022
.150	-.6855	.4925
.300	-.6861	.4942
.450	-.6698	.4451
.600	-.6739	.1540
.750	-.6735	.1099
.800	-.6652	.0356
.850	-.6693	.0374

STATION 6

X/C	CPU	CPL
.025	-.6104	.3618
.050	-.6028	.4066
.100	-.6054	.3767
.200	-.6020	.1381
.300	-.6217	.0806
.400	-.6345	.0245
.500	-.6220	.0032
.600	-.6217	-.0090
.700	-.6225	-.0317
.800	-.6065	-.0461

TABLE III.- PRESSURE COEFFICIENTS AT A MACH NUMBER OF 0.20 FOR MODEL WITH STRAKE ON. $C_{L,d} = 0.35$

(a) $\alpha = -3.79^{\circ}$

STATION 1

X/C	CPU	CPL
.005	.2744	.0581
.010	.2711	.0124
.025	.2403	-.0340
.050	.1875	-.0725
.100	.1605	-.0945
.200	.0987	-.0840
.300	.0235	-.0490
.400	-.0141	-.0339
.500	-.0130	-.0226
.600	-.0332	-.0277
.700	-.0290	.0813
.800	.0084	.0991
.900	.0333	-.0340
.950	.0087	.2028
.970	.0366	

STATION 2

X/C	CPU	CPL
.005	.5747	-1.0211
.010	.5908	-1.0409
.025	.4886	-1.0644
.050	.3846	-1.1769
.100	.2724	-.9811
.200	.1143	.0230
.300	.0036	-.0021
.400	-.0489	-.0026
.500	-.0449	.0023
.600	-.0779	.0687
.700	-.0622	
.800	-.0272	.1750
.900	.0004	.2171
.925	-.0188	.2427
.950	-.0220	.2531

STATICN 3

X/C	CPU	CPL
.010	.5916	-.7746
.025	.5039	-.7846
.050	.4025	-.7900
.100	.2755	-.8466
.200	.1137	-.7729
.400	-.0325	.1357
.600	-.0712	.1364
.800	-.0369	.1840
.900	-.0100	.2275
.925	-.0270	.2676

STATION 4

X/C	CPU	CPL
.010	.5777	-.6064
.025	.5104	-.6143
.050	.4114	-.6157
.100	.2793	-.6234
.200	.1213	-.6383
.400	-.0434	-.2361
.600	-.0977	.2213
.800	-.1025	.2181
.900	-.0620	.2360
.925	-.0660	.3071

STATION 5

X/C	CPU	CPL
.025	.4444	-.0502
.050	.3440	-.1885
.075	.2836	-.2786
.150	.1591	.0201
.300	-.0411	.0163
.450	-.0994	.0027
.600	-.1491	-.2631
.750	-.1310	-.2219
.800	-.1078	-.1233
.850	-.0842	-.0924

STATICN 6

X/C	CPU	CPL
.025	.4026	-.0958
.050	.2962	-.1463
.100	.2034	-.1265
.200	.0640	-.1208
.300	-.0390	-.0748
.400	-.0810	-.0674
.500	-.1014	-.0419
.600	-.1192	-.0323
.700	-.1223	-.0136
.800	-.0971	-.0028

(b) $\alpha = -1.91^{\circ}$

STATION 1

X/C	CPU	CPL
.005	.2518	.1290
.010	.2499	.0588
.025	.1988	.0244
.050	.1546	-.0123
.100	.1087	-.0418
.200	.0434	-.0325
.300	-.0104	-.0174
.400	-.0473	-.0060
.500	-.0475	-.0094
.600	-.0514	-.0079
.700	-.0250	.0914
.800	-.0032	.0985
.900	.0311	-.0450
.950	.0206	.2033
.970	.0396	

STATION 2

X/C	CPU	CPL
.005	.5935	-.8845
.010	.5163	-.9127
.025	.4083	-.9155
.050	.2910	-1.0425
.100	.1469	-.0061
.200	.0348	-.0492
.300	-.0505	-.0101
.400	-.0860	.0130
.500	-.0720	.0168
.600	-.0900	.0951
.700	-.0711	
.800	-.0262	.1607
.900	.0005	.2026
.925	-.0169	.2215
.950	-.0187	.2450

STATICN 3

X/C	CPU	CPL
.010	.5616	-.6080
.025	.4099	-.6363
.050	.3047	-.6313
.100	.1776	-.6580
.200	.0265	-.1225
.400	-.0928	.0670
.600	-.0918	.1239
.800	-.0369	.1797
.900	-.0133	.2141
.925	-.0214	.2530

STATION 4

X/C	CPU	CPL
.010	.5488	-.5084
.025	.4051	-.5021
.050	.3080	-.5014
.100	.1744	-.5452
.200	.0322	-.5375
.400	-.0938	-.0170
.600	-.1189	.1589
.800	-.1107	.1800
.900	-.0701	.1773
.925	-.0818	.2176

STATION 5

X/C	CPU	CPL
.025	.3583	-.1012
.050	.2476	-.2379
.075	.1979	-.3287
.150	.0810	-.2120
.300	-.1049	-.2189
.450	-.1431	-.2321
.600	-.1696	.0442
.750	-.1207	.1183
.800	-.0989	.1805
.850	-.0660	.1871

STATICN 6

X/C	CPU	CPL
.025	.3338	-.0795
.050	.2205	-.1655
.100	.1301	-.1475
.200	.0133	-.1063
.300	-.0719	-.0739
.400	-.0991	-.0666
.500	-.1275	-.0457
.600	-.1270	-.0607
.700	-.1180	-.0553
.800	-.0805	-.0378

TABLE III. - Continued

(c) α = -0.02°

STATION 1

X/C	CPU	CPL
.005	.2328	.1327
.010	.2273	.0792
.025	.1733	.0441
.050	.1066	.0186
.100	.0547	-.0034
.200	-.0158	-.0004
.300	-.0688	.0153
.400	-.0942	.0032
.500	-.0925	.0181
.600	-.0808	-.0130
.700	-.0526	.0894
.800	-.0187	.1043
.900	.0098	-.0256
.950	.0137	.1789
.970	.0321	

STATION 2

X/C	CPU	CPL
.005	.5334	-.6663
.010	.3787	-.6687
.025	.2658	-.6323
.050	.1472	-.1331
.100	.0604	-.0624
.200	-.0432	-.0134
.300	-.1253	.0188
.400	-.1497	.0272
.500	-.1176	.0316
.600	-.1235	.1109
.700	-.1056	
.800	-.0499	.1720
.900	-.0061	.2077
.925	-.0241	.2330
.950	-.0084	.2495

STATION 3

X/C	CPU	CPL
.010	.4571	-.4918
.025	.2732	-.5074
.050	.1719	-.3146
.100	.0645	-.0445
.200	-.0523	.0119
.400	-.1403	.0640
.600	-.1358	.1179
.800	-.0583	.1738
.900	-.0201	.2062
.925	-.0383	.2376

STATION 4

X/C	CPU	CPL
.010	.4485	-.5411
.025	.2652	-.5518
.050	.1676	-.4395
.100	.0512	-.1009
.200	-.0624	.0001
.400	-.1690	.0399
.600	-.1506	.1403
.800	-.1359	.1668
.900	-.0842	.1846
.925	-.0947	.2252

STATION 5

X/C	CPU	CPL
.025	.2127	-.1145
.050	.1231	-.2643
.075	.0667	-.4434
.150	-.0281	-.3577
.300	-.1880	-.3655
.450	-.2115	-.2469
.600	-.2055	.0851
.750	-.1604	.0883
.800	-.1280	.0906
.850	-.1009	.0837

STATION 6

X/C	CPU	CPL
.025	.2293	-.1067
.050	.1061	-.3206
.100	.0353	-.2882
.200	-.0521	-.1940
.300	-.1327	.0275
.400	-.1667	.0716
.500	-.1579	.1018
.600	-.1649	.1313
.700	-.1588	.1607
.800	-.1146	.1748

(d) α = 1.91°

STATION 1

X/C	CPU	CPL
.005	.2271	.1761
.010	.2198	.1221
.025	.1590	.0876
.050	.0781	.0532
.100	.0170	.0438
.200	-.0590	.0589
.300	-.1189	.0608
.400	-.1251	.0514
.500	-.1170	.0491
.600	-.1105	-.0017
.700	-.0548	.1175
.800	-.0244	.1199
.900	.0139	-.0266
.950	-.0019	.1910
.970	.0422	

STATION 2

X/C	CPU	CPL
.005	.3638	-.2379
.010	.1498	-.0955
.025	.0338	-.0338
.050	-.0113	.0306
.100	-.0770	.0371
.200	-.1396	.0533
.300	-.1890	.0784
.400	-.2106	.0784
.500	-.1568	.0723
.600	-.1493	.1334
.700	-.1263	
.800	-.0698	.1802
.900	-.0134	.2126
.925	-.0206	.2409
.950	-.0103	.2684

STATION 3

X/C	CPU	CPL
.010	.2320	-.1051
.025	.0325	-.0245
.050	-.0071	.0256
.100	-.0751	.0558
.200	-.1495	.0822
.400	-.1956	.1057
.600	-.1666	.1552
.800	-.0810	.1786
.900	-.0313	.2270
.925	-.0340	.2578

STATION 4

X/C	CPU	CPL
.010	.2348	-.0964
.025	.0266	-.0642
.050	-.0089	-.0100
.100	-.0905	-.0072
.200	-.1562	-.0137
.400	-.2108	-.0014
.600	-.1875	.1633
.800	-.1480	.1767
.900	-.0925	.1814
.925	-.1000	.1889

STATION 5

X/C	CPU	CPL
.025	-.0016	.1684
.050	-.0626	.1001
.075	-.0743	.0297
.150	-.1509	-.1153
.300	-.2575	.0586
.450	-.2480	.0997
.600	-.2416	.1720
.750	-.1722	.1851
.800	-.1375	.1833
.850	-.1063	.1847

STATION 6

X/C	CPU	CPL
.025	.0232	-.3573
.050	-.0208	-.0168
.100	-.0571	.0135
.200	-.1367	.0624
.300	-.1897	.1062
.400	-.2039	.1078
.500	-.2011	.1156
.600	-.2052	.1319
.700	-.1889	.1487
.800	-.1488	.1571

TABLE III. - Continued

(e) $\alpha = 3.89^{\circ}$

STATION 1

X/C	CPU	CPL
.005	.1519	.2050
.010	.1682	.1501
.025	.1374	.1143
.050	.0755	.0976
.100	.0096	.0945
.200	-.0933	.0938
.300	-.1456	.1051
.400	-.1691	.0825
.500	-.1504	.0676
.600	-.1339	.0070
.700	-.0777	.1408
.800	-.0520	.1358
.900	.0056	-.0248
.950	-.0181	.2105
.970	.0214	

STATION 2

X/C	CPU	CPL
.005	.0070	.2375
.010	-.1962	.1865
.025	-.2585	.1693
.050	-.1929	.1664
.100	-.2027	.1326
.200	-.2236	.1232
.300	-.2482	.1117
.400	-.2519	.1102
.500	-.1950	.1046
.600	-.1752	.1686
.700	-.1411	
.800	-.0699	.2101
.900	-.0045	.2321
.925	-.0108	.2628
.950	.0063	.2773

STATION 3

X/C	CPU	CPL
.010	-.1657	.2572
.025	-.2349	.1943
.050	-.2260	.1920
.100	-.2218	.1709
.200	-.2491	.1640
.400	-.2592	.1491
.600	-.1925	.1859
.800	-.0931	.2055
.900	-.0410	.2395
.925	-.0474	.2671

STATION 4

X/C	CPU	CPL
.010	-.2390	.2862
.025	-.2826	.2629
.050	-.2843	.1845
.100	-.2422	.1792
.200	-.2787	.1691
.400	-.2804	.1640
.600	-.2260	.2017
.800	-.1667	.2083
.900	-.0975	.2238
.925	-.1002	.2713

STATION 5

X/C	CPU	CPL
.025	-.3601	.2685
.050	-.3005	.2754
.075	-.2915	.1905
.150	-.2879	.0871
.300	-.3559	.1119
.450	-.3134	.1291
.600	-.2817	.1858
.750	-.2088	.1858
.800	-.1789	.2045
.850	-.1284	.1971

STATION 6

X/C	CPU	CPL
.025	-.2666	.1886
.050	-.2524	.0909
.100	-.2163	.0928
.200	-.2462	.0933
.300	-.2750	.1096
.400	-.2791	.1122
.500	-.2639	.1244
.600	-.2722	.1346
.700	-.2869	.1398
.800	-.2544	.1578

(f) $\alpha = 5.91^{\circ}$

STATION 1

X/C	CPU	CPL
.005	-.0367	.2295
.010	.0148	.1826
.025	-.0013	.1477
.050	-.0196	.1378
.100	-.0568	.1276
.200	-.1499	.1378
.300	-.1790	.1253
.400	-.1987	.1122
.500	-.1613	.1041
.600	-.1494	.0039
.700	-.0788	.1559
.800	-.0563	.1459
.900	-.0013	-.0314
.950	-.0367	.2089
.970	.0137	

STATION 2

X/C	CPU	CPL
.005	-.5138	.4880
.010	-.5950	.4157
.025	-.5380	.3292
.050	-.4056	.2704
.100	-.3341	.2009
.200	-.2960	.1773
.300	-.3005	.1642
.400	-.2895	.1422
.500	-.2107	.1417
.600	-.1856	.2041
.700	-.1429	
.800	-.0610	.2244
.900	-.0147	.2256
.925	-.0087	.2691
.950	.0014	.2847

STATION 3

X/C	CPU	CPL
.010	-.7587	.5026
.025	-.5934	.3769
.050	-.4947	.3357
.100	-.4156	.2710
.200	-.3593	.2357
.400	-.3082	.1990
.600	-.2310	.2103
.800	-.0882	.2071
.900	-.0308	.2508
.925	-.0242	.2804

STATION 4

X/C	CPU	CPL
.010	-.8634	.5153
.025	-.7150	.4946
.050	-.5739	.3388
.100	-.4424	.2894
.200	-.3960	.2527
.400	-.3572	.2136
.600	-.2634	.2217
.800	-.1647	.2216
.900	-.1008	.2382
.925	-.1028	.2810

STATION 5

X/C	CPU	CPL
.025	-.7553	.2980
.050	-.5892	.2962
.075	-.5019	.3008
.150	-.4435	.2259
.300	-.4548	.2256
.450	-.3712	.2161
.600	-.3295	.2004
.750	-.2394	.2030
.800	-.2014	.1972
.850	-.1605	.2004

STATION 6

X/C	CPU	CPL
.025	-.7034	.2095
.050	-.4639	.2156
.100	-.3639	.2122
.200	-.3365	.2018
.300	-.3711	.1095
.400	-.3769	.0971
.500	-.3745	.0996
.600	-.3759	.1099
.700	-.3848	.1208
.800	-.3695	.1284

TABLE III. - Continued

(g) $\alpha = 7.94^{\circ}$

STATION 1

X/C	CPU	CPL
.005	-.2288	.1993
.010	-.1873	.1500
.025	-.2028	.1247
.050	-.1528	.1028
.100	-.1867	.1093
.200	-.2491	.1154
.300	-.2418	.1079
.400	-.2305	.0837
.500	-.2221	.0774
.600	-.1853	-.0327
.700	-.1048	.1123
.800	-.0788	.1077
.900	-.0204	-.0855
.950	-.0415	.1697
.970	-.0071	

STATION 2

X/C	CPU	CPL
.005	-1.0944	.4808
.010	-.9622	.4459
.025	-.8839	.3680
.050	-.5207	.3013
.100	-.4299	.2261
.200	-.3661	.1779
.300	-.3548	.1558
.400	-.3156	.1430
.500	-.2383	.1181
.600	-.2126	.1785
.700	-.1604	
.800	-.0865	.1991
.900	-.0177	.2166
.925	-.0228	.2378
.950	-.0276	.2558

STATION 3

X/C	CPU	CPL
.010	-1.4522	.5391
.025	-.9663	.4613
.050	-.6825	.3977
.100	-.5483	.3128
.200	-.4386	.2576
.400	-.3538	.1987
.600	-.2366	.1936
.800	-.0917	.1936
.900	-.0237	.2096
.925	-.0057	.2444

STATION 4

X/C	CPU	CPL
.010	-2.0129	.5541
.025	-.9943	.5585
.050	-.8383	.4312
.100	-.6028	.3392
.200	-.4979	.2718
.400	-.3865	.2279
.600	-.2658	.2075
.800	-.2398	.1990
.900	-.1532	.2033
.925	-.1476	.2472

STATION 5

X/C	CPJ	CPL
.025	-1.7294	.2794
.050	-1.5334	.2688
.075	-1.2512	.2835
.150	-.5885	.2731
.300	-.5659	.2701
.450	-.4898	.2677
.600	-.4376	.2011
.750	-.3403	.1895
.800	-.3058	.1722
.850	-.2573	.1708

STATION 6

X/C	CPU	CPL
.025	-1.0383	.2472
.050	-1.0122	.2495
.100	-.8769	.2397
.200	-.6309	.2127
.300	-.5101	.0742
.400	-.5186	.0483
.500	-.5322	.0435
.600	-.5349	.0589
.700	-.5857	.0722
.800	-.5718	.0959

(h) $\alpha = 10.03^{\circ}$

STATION 1

X/C	CPU	CPL
.005	-.3768	.2715
.010	-.3644	.2456
.025	-.3608	.2002
.050	-.3233	.2006
.100	-.3514	.2083
.200	-.3711	.2102
.300	-.3415	.2100
.400	-.3144	.1840
.500	-.2715	.1606
.600	-.2202	.0194
.700	-.1259	.1973
.800	-.0904	.1729
.900	-.0327	-.0421
.950	-.0518	.2313
.970	-.0014	

STATION 2

X/C	CPU	CPL
.005	-2.2015	.4502
.010	-1.5755	.5267
.025	-.9965	.5008
.050	-.7505	.4291
.100	-.5854	.3552
.200	-.4307	.2869
.300	-.3967	.2610
.400	-.3671	.2253
.500	-.3005	.1876
.600	-.2345	.2435
.700	-.1833	
.800	-.0909	.2422
.900	-.0167	.2615
.925	-.0317	.2801
.950	-.0234	.2934

STATION 3

X/C	CPU	CPL
.010	-2.8370	.5578
.025	-1.7428	.5649
.050	-.9229	.5013
.100	-.6697	.4236
.200	-.5199	.3430
.400	-.3828	.2747
.600	-.2521	.2543
.800	-.1155	.2279
.900	-.0552	.2529
.925	-.0516	.2742

STATION 4

X/C	CPU	CPL
.010	-1.7898	.5798
.025	-1.8201	.5880
.050	-1.8026	.5679
.100	-1.6268	.4326
.200	-.4063	.4203
.400	-.4221	.3210
.600	-.3013	.2623
.800	-.1789	.2396
.900	-.0972	.2476
.925	-.0991	.2702

STATION 5

X/C	CPU	CPL
.025	-1.2235	.2920
.050	-1.2211	.3011
.075	-1.2355	.3995
.150	-1.1487	.4022
.300	-.9897	.3378
.450	-.6831	.2931
.600	-.4596	.2220
.750	-.3172	.2247
.800	-.2789	.2031
.850	-.2313	.1941

STATION 6

X/C	CPU	CPL
.025	-.9090	.4445
.050	-.8807	.4326
.100	-.8668	.4119
.200	-.7918	.4084
.300	-.7319	.1011
.400	-.6857	.0718
.500	-.6906	.0741
.600	-.6439	.0794
.700	-.7203	.0988
.800	-.7359	.0998

TABLE III. - Continued

(i) $\alpha = 12.17^{\circ}$

STATION 1

X/C	CPU	CPL
.005	-.5493	.3076
.010	-.5238	.2736
.025	-.5068	.2455
.050	-.4815	.2369
.100	-.4912	.2411
.200	-.5252	.2627
.300	-.4546	.2613
.400	-.3831	.2253
.500	-.3158	.2004
.600	-.2612	.0170
.700	-.1528	.2226
.800	-.1219	.1957
.900	-.0503	-.0313
.950	-.0518	.2302
.970	.0012	

STATION 2

X/C	CPU	CPL
.005	-2.3702	.2835
.010	-2.4572	.4781
.025	-2.6979	.5210
.050	-1.0248	.4776
.100	-.5035	.4064
.200	-.4343	.3414
.300	-.4137	.3068
.400	-.3952	.2546
.500	-.3073	.2248
.600	-.2646	.2562
.700	-.2068	
.800	-.1240	.2477
.900	-.0436	.2530
.925	-.0335	.2789
.950	-.0136	.2945

STATION 3

X/C	CPU	CPL
.010	-1.8606	.5292
.025	-1.8825	.6038
.050	-1.9581	.5609
.100	-2.1854	.4754
.200	-.3065	.3823
.400	-.3459	.3016
.600	-.2554	.2657
.800	-.1204	.2355
.900	-.0497	.2553
.925	-.0517	.2738

STATION 4

X/C	CPU	CPL
.010	-1.5525	.5379
.025	-1.5389	.5681
.050	-1.5496	.5637
.100	-1.6089	.5357
.200	-1.6656	.5072
.400	-.3658	.3282
.600	-.2593	.2802
.800	-.2165	.2463
.900	-.1388	.2462
.925	-.1487	.2817

STATION 5

X/C	CPU	CPL
.025	-1.0104	.3853
.050	-1.0147	.3858
.075	-.9780	.4100
.150	-.9342	.4086
.300	-.8657	.3683
.450	-.7943	.3360
.600	-.7230	.2201
.750	-.6186	.2219
.800	-.5824	.1822
.850	-.5209	.1632

STATION 6

X/C	CPU	CPL
.025	-.7901	.5049
.050	-.7815	.4707
.100	-.7809	.4707
.200	-.7212	.1826
.300	-.6735	.1126
.400	-.6177	.0720
.500	-.5819	.0743
.600	-.5524	.0855
.700	-.5403	.0882
.800	-.5247	.0586

(j) $\alpha = 14.37^{\circ}$

STATION 1

X/C	CPU	CPL
.005	-.7005	.3389
.010	-.6644	.3193
.025	-.6799	.2789
.050	-.6658	.2762
.100	-.6877	.2955
.200	-.6834	.3026
.300	-.5680	.2871
.400	-.4743	.2673
.500	-.3964	.2372
.600	-.3062	.0388
.700	-.1747	.2414
.800	-.1540	.2030
.900	-.0721	-.0322
.950	-.0576	.2374
.970	-.0184	

STATION 2

X/C	CPU	CPL
.005	-2.4558	.1507
.010	-2.5253	.4478
.025	-2.5961	.5578
.050	-3.4041	.5391
.100	-.3393	.4732
.200	-.4584	.3867
.300	-.4331	.3430
.400	-.4032	.2979
.500	-.3455	.2518
.600	-.3341	.2618
.700	-.2671	
.800	-.1568	.2657
.900	-.0669	.2596
.925	-.0472	.2823
.950	-.0258	.2908

STATION 3

X/C	CPU	CPL
.010	-1.9924	.4838
.025	-2.0019	.6192
.050	-1.9797	.6107
.100	-2.4441	.5435
.200	-1.0218	.4493
.400	-.3275	.3466
.600	-.2973	.2894
.800	-.1657	.2600
.900	-.1116	.2610
.925	-.1121	.2794

STATION 4

X/C	CPU	CPL
.010	-1.4570	.5063
.025	-1.4621	.6296
.050	-1.4811	.6339
.100	-1.5133	.6209
.200	-1.7164	.5551
.400	-.9704	.3407
.600	-.4865	.2977
.800	-.3103	.2521
.900	-.2234	.2565
.925	-.2373	.2768

STATION 5

X/C	CPU	CPL
.025	-.8614	.4721
.050	-.8537	.4999
.075	-.8579	.5254
.150	-.8232	.5182
.300	-.7567	.4094
.450	-.7284	.3524
.600	-.7178	.2425
.750	-.6570	.2194
.800	-.6421	.1498
.850	-.6068	.1472

STATION 6

X/C	CPU	CPL
.025	-.6775	.5208
.050	-.6796	.5157
.100	-.6767	.5117
.200	-.6507	.5056
.300	-.6422	.1491
.400	-.6111	.1062
.500	-.5820	.1039
.600	-.5552	.0922
.700	-.5327	.0906
.800	-.5112	.0680

TABLE III. - Continued

(k) $\alpha = 16.42^{\circ}$

STATION 1

X/C	CPU	CPL
.005	-.8492	.3653
.010	-.8111	.3370
.025	-.8252	.3135
.050	-.7949	.3145
.100	-.8418	.3342
.200	-.8292	.3497
.300	-.6942	.3417
.400	-.5744	.3060
.500	-.4582	.2741
.600	-.3858	.0357
.700	-.2004	.2628
.800	-.1710	.2210
.900	-.0839	-.0475
.950	-.0593	.2482
.970	-.0144	

STATION 2

X/C	CPU	CPL
.005	-2.6029	.0268
.010	-2.6585	.3833
.025	-2.7853	.5557
.050	-4.2220	.5682
.100	-.8181	.5133
.200	-.4670	.4294
.300	-.4783	.3777
.400	-.4783	.3304
.500	-.4521	.2824
.600	-.3994	.2944
.700	-.2989	
.800	-.1935	.2666
.900	-.1226	.2464
.925	-.0904	.2564
.950	-.0630	.2614

STATION 3

X/C	CPU	CPL
.010	-2.0375	.4219
.025	-2.0365	.6013
.050	-2.0916	.6147
.100	-2.5592	.5495
.200	-1.5839	.4756
.400	-.4190	.3639
.600	-.3249	.2957
.800	-.2172	.2518
.900	-.1429	.2429
.925	-.1506	.2679

STATION 4

X/C	CPU	CPL
.010	-1.4018	.4568
.025	-1.4036	.6173
.050	-1.4386	.6300
.100	-1.5105	.6225
.200	-1.6721	.6116
.400	-1.1169	.3612
.600	-.6379	.3103
.800	-.4229	.2377
.900	-.2863	.2250
.925	-.3072	.2410

STATION 5

X/C	CPU	CPL
.025	-.8683	.4216
.050	-.8702	.4724
.075	-.8745	.5348
.150	-.8765	.5380
.300	-.8005	.3806
.450	-.7876	.3146
.600	-.7757	.2254
.750	-.7071	.2014
.800	-.6664	.1384
.850	-.6651	.1349

STATION 6

X/C	CPU	CPL
.025	-.6391	.5107
.050	-.6519	.4951
.100	-.6148	.5003
.200	-.6169	.2287
.300	-.5919	.1493
.400	-.5736	.0942
.500	-.5559	.0884
.600	-.5440	.0795
.700	-.5186	.0728
.800	-.5045	.0594

(l) $\alpha = 18.50^{\circ}$

STATION 1

X/C	CPU	CPL
.005	-1.0041	.3836
.010	-.9540	.3521
.025	-.9710	.3399
.050	-.9456	.3497
.100	-.9744	.3502
.200	-.9472	.3780
.300	-.7959	.3723
.400	-.6601	.3234
.500	-.5408	.2849
.600	-.4237	.0298
.700	-.2265	.2703
.800	-.1915	.2279
.900	-.0867	-.0380
.950	-.0454	.2500
.970	.0002	

STATION 2

X/C	CPU	CPL
.005	-2.8121	-.1634
.010	-2.8158	.3014
.025	-2.9421	.5339
.050	-4.1444	.5882
.100	-1.5380	.5500
.200	-.5541	.4610
.300	-.5656	.4146
.400	-.6146	.3619
.500	-.5637	.3167
.600	-.4650	.3222
.700	-.3885	
.800	-.3009	.2670
.900	-.2576	.2344
.925	-.2614	.2345
.950	-.2486	.2391

STATION 3

X/C	CPU	CPL
.010	-2.0309	.3764
.025	-1.9923	.6068
.050	-2.0806	.6265
.100	-2.0033	.5942
.200	-1.9594	.5085
.400	-.6123	.3962
.600	-.3977	.3139
.800	-.2859	.2492
.900	-.2145	.2182
.925	-.1989	.2480

STATION 4

X/C	CPU	CPL
.010	-1.5049	.4064
.025	-1.5009	.6243
.050	-1.5150	.6418
.100	-1.5716	.6337
.200	-1.6424	.6296
.400	-1.1999	.3854
.600	-.7456	.3267
.800	-.4936	.2305
.900	-.3361	.2131
.925	-.3742	.2333

STATION 5

X/C	CPU	CPL
.025	-.9159	.4187
.050	-.9207	.4601
.075	-.9105	.5800
.150	-.8795	.5729
.300	-.8075	.3965
.450	-.8322	.3256
.600	-.8158	.2494
.750	-.7546	.2258
.800	-.7396	.1592
.850	-.6544	.1616

STATION 6

X/C	CPU	CPL
.025	-.6105	.5201
.050	-.6070	.5130
.100	-.5961	.5021
.200	-.5758	.2484
.300	-.5820	.1658
.400	-.5690	.1223
.500	-.5613	.1067
.600	-.5406	.0968
.700	-.5181	.1087
.800	-.4853	.0743

TABLE III. - Concluded.

(m) $\alpha = 20.60^{\circ}$

STATION 1

X/C	CPU	CPL
.005	-1.1620	.4108
.010	-1.1296	.3910
.025	-1.1530	.3794
.050	-1.1367	.3844
.100	-1.1599	.4059
.200	-1.1449	.4224
.300	-.9440	.4172
.400	-.7650	.3674
.500	-.6065	.3182
.600	-.4743	.0330
.700	-.2535	.2919
.800	-.1777	.2487
.900	-.0289	-.0643
.950	.0015	.2684
.970	.0360	

STATION 2

X/C	CPU	CPL
.005	-2.8614	-.3765
.010	-2.9041	.1881
.025	-3.0901	.5040
.050	-4.1486	.5978
.100	-2.3452	.5761
.200	-.7144	.5072
.300	-.7292	.4473
.400	-.8028	.3967
.500	-.7065	.3339
.600	-.6796	.3290
.700	-.6691	
.800	-.6756	.2495
.900	-.6566	.1762
.925	-.6206	.1635
.950	-.5987	.1385

STATION 3

X/C	CPU	CPL
.010	-1.9338	.2868
.025	-1.9479	.5829
.050	-1.9681	.6467
.100	-1.8229	.6258
.200	-2.1744	.5352
.400	-.8526	.4214
.600	-.5814	.3335
.800	-.4553	.2381
.900	-.3699	.1706
.925	-.3727	.1787

STATION 4

X/C	CPU	CPL
.010	-1.4674	.3208
.025	-1.4826	.6084
.050	-1.5416	.6434
.100	-1.5427	.6403
.200	-1.5443	.6401
.400	-1.1923	.4121
.600	-.8029	.3318
.800	-.5689	.2222
.900	-.4287	.2009
.925	-.4378	.1883

STATION 5

X/C	CPU	CPL
.025	-.8957	.4251
.050	-.9049	.4877
.075	-.9242	.5777
.150	-.9114	.5682
.300	-.8628	.4124
.450	-.8133	.3347
.600	-.7745	.2618
.750	-.7250	.2166
.800	-.6848	.1648
.850	-.6375	.1686

STATION 6

X/C	CPU	CPL
.025	-.5696	.5084
.050	-.5859	.4984
.100	-.5789	.4909
.200	-.5839	.4909
.300	-.5717	.1948
.400	-.5554	.1350
.500	-.5296	.1177
.600	-.5113	.1162
.700	-.4780	.1089
.800	-.4529	.0877

TABLE IV.- PRESSURE COEFFICIENTS AT A MACH NUMBER OF 0.40 FOR MODEL WITH STRAKE ON. $C_{L,d} = 0.35$

(a) $\alpha = -3.94^{\circ}$

STATION 1

X/C	CPU	CPL
.005	.2205	-.0059
.010	.2217	-.0453
.025	.1654	-.0808
.050	.1317	-.1402
.100	.0975	-.1666
.200	.0328	-.1457
.300	-.0434	-.0983
.400	-.0841	-.0948
.500	-.0989	-.0773
.600	-.1129	-.0758
.700	-.1094	.0298
.800	-.0733	.0425
.900	-.0454	-.0818
.950	-.0682	.1617
.970	-.0367	

STATION 2

X/C	CPU	CPL
.005	.5049	-1.0839
.010	.5231	-1.0868
.025	.4413	-1.1221
.050	.3266	-1.2344
.100	.2017	-1.2444
.200	.0457	-.0266
.300	-.0547	-.0574
.400	-.1324	-.0616
.500	-.1200	-.0492
.600	-.1438	.0158
.700	-.1454	
.800	-.1024	.1066
.900	-.0785	.1626
.925	-.1018	.1842
.950	-.1028	.2021

STATION 3

X/C	CPU	CPL
.010	.5283	-.8550
.025	.4475	-.8710
.050	.3513	-.8647
.100	.2109	-.9489
.200	.0485	-.9885
.400	-.1018	.0648
.600	-.1485	.0735
.800	-.1090	.1185
.900	-.0841	.1686
.925	-.1011	.2099

STATION 4

X/C	CPU	CPL
.010	.5154	-.6947
.025	.4492	-.6954
.050	.3450	-.7021
.100	.2173	-.7045
.200	.0561	-.7110
.400	-.1137	-.4757
.600	-.1646	.0684
.800	-.1544	.1593
.900	-.1143	.2019
.925	-.1366	.2504

STATION 5

X/C	CPU	CPL
.025	.4215	-.1303
.050	.3080	-.2503
.075	.2476	-.3939
.150	.1096	-.3159
.300	-.0857	-.3423
.450	-.1614	-.3873
.600	-.2132	-.3669
.750	-.1907	-.3000
.800	-.1683	-.2215
.850	-.1515	-.1778

STATION 6

X/C	CPU	CPL
.025	.3580	-.1825
.050	.2491	-.1938
.100	.1563	-.1933
.200	.0308	-.1829
.300	-.0897	-.1795
.400	-.1375	-.1668
.500	-.1671	-.1239
.600	-.1773	-.1217
.700	-.1778	-.0996
.800	-.1587	-.0947

(b) $\alpha = -1.87^{\circ}$

STATION 1

X/C	CPU	CPL
.005	.1929	.0950
.010	.1889	.0265
.025	.1340	-.0255
.050	.0925	-.0609
.100	.0490	-.0947
.200	-.0263	-.0875
.300	-.0881	-.0603
.400	-.1308	-.0629
.500	-.1330	-.0527
.600	-.1414	-.0595
.700	-.1186	.0453
.800	-.0817	.0584
.900	-.0524	-.0754
.950	-.0707	.1613
.970	-.0358	

STATION 2

X/C	CPU	CPL
.005	.5325	-.8861
.010	.4470	-.8789
.025	.3142	-.9002
.050	.2104	-.8917
.100	.1011	-.3606
.200	-.0368	-.0698
.300	-.1303	-.0493
.400	-.1837	-.0367
.500	-.1579	-.0251
.600	-.1738	.0342
.700	-.1723	
.800	-.1183	.1069
.900	-.0855	.1572
.925	-.1042	.1801
.950	-.1001	.2016

STATION 3

X/C	CPU	CPL
.010	.4767	-.6895
.025	.3389	-.6864
.050	.2228	-.6933
.100	.1014	-.7185
.200	-.0461	-.3252
.400	-.1667	.0045
.600	-.1864	.0580
.800	-.1257	.1098
.900	-.0910	.1640
.925	-.1045	.2015

STATION 4

X/C	CPU	CPL
.010	.4840	-.5973
.025	.3444	-.5838
.050	.2293	-.5907
.100	.1062	-.5932
.200	-.0338	-.5894
.400	-.1788	-.0502
.600	-.2063	.0869
.800	-.1619	.0892
.900	-.1146	.1463
.925	-.1328	.2045

STATION 5

X/C	CPU	CPL
.025	.3320	-.1595
.050	.2213	-.2634
.075	.1564	-.4053
.150	.0365	-.3667
.300	-.1567	-.3711
.450	-.1989	-.3404
.600	-.2301	-.0776
.750	-.1814	.0429
.800	-.1502	.1106
.850	-.1218	.1241

STATION 6

X/C	CPU	CPL
.025	.2850	-.1296
.050	.1752	-.2315
.100	.0892	-.2149
.200	-.0196	-.1812
.300	-.1321	-.1445
.400	-.1620	-.1212
.500	-.1764	-.1163
.600	-.1855	-.1131
.700	-.1715	-.0940
.800	-.1381	-.1063

TABLE IV. - Continued

(c) α = 0.03°

STATION 1

X/C	CPU	CPL
.005	.2000	.1066
.010	.1645	.0501
.025	.1043	.0144
.050	.0361	-.0154
.100	-.0057	-.0439
.200	-.0831	-.0389
.300	-.1482	-.0214
.400	-.1724	-.0325
.500	-.1649	-.0187
.600	-.1688	-.0496
.700	-.1314	.0604
.800	-.0989	.0745
.900	-.0586	-.0632
.950	-.0671	.1586
.970	-.0314	

STATION 2

X/C	CPU	CPL
.005	.4701	-.8017
.010	.3173	-.8326
.025	.1790	-.5663
.050	.0826	-.1485
.100	-.0072	-.1041
.200	-.1153	-.0538
.300	-.2074	-.0150
.400	-.2443	-.0058
.500	-.2006	.0028
.600	-.2093	.0592
.700	-.1917	
.800	-.1317	.1213
.900	-.0902	.1632
.925	-.1035	.1901
.950	-.0973	.2127

STATION 3

X/C	CPU	CPL
.010	.3877	-.6668
.025	.1850	-.4927
.050	.0995	-.3303
.100	-.0184	-.1243
.200	-.1255	-.0495
.400	-.2203	-.0001
.600	-.2216	.0671
.800	-.1486	.1195
.900	-.1026	.1627
.925	-.1058	.1974

STATION 4

X/C	CPU	CPL
.010	.3918	-.7552
.025	.1939	-.4706
.050	.0789	-.2713
.100	-.0060	-.1460
.200	-.1299	-.0639
.400	-.2421	-.0022
.600	-.2385	.0836
.800	-.1805	.0833
.900	-.1201	.1405
.925	-.1364	.1570

STATION 5

X/C	CPU	CPL
.025	.1756	-.1539
.050	.0872	-.4464
.075	.0437	-.5572
.150	-.0631	-.4868
.300	-.2299	-.2337
.450	-.2427	-.0584
.600	-.2603	.1009
.750	-.1976	.1252
.800	-.1694	.1350
.850	-.1352	.1364

STATION 6

X/C	CPU	CPL
.025	.1953	-.2794
.050	.0858	-.4222
.100	.0030	-.4263
.200	-.0707	-.2565
.300	-.1798	-.0133
.400	-.1990	.0026
.500	-.2083	.0460
.600	-.2036	.0706
.700	-.1948	.1060
.800	-.1583	.1279

(d) α = 2.04°

STATION 1

X/C	CPU	CPL
.005	.2059	.1417
.010	.1607	.0872
.025	.0876	.0473
.050	.0094	.0242
.100	-.0552	.0163
.200	-.1421	.0150
.300	-.2034	.0246
.400	-.2181	.0074
.500	-.2057	.0172
.600	-.1981	-.0427
.700	-.1453	.0791
.800	-.1103	.0844
.900	-.0666	-.0652
.950	-.0754	.1626
.970	-.0413	

STATION 2

X/C	CPU	CPL
.005	.2523	-.2570
.010	.0638	-.2094
.025	-.0476	-.0658
.050	-.1033	-.0119
.100	-.1627	-.0039
.200	-.2184	.0137
.300	-.2730	.0348
.400	-.2961	.0339
.500	-.2423	.0339
.600	-.2374	.0798
.700	-.2120	
.800	-.1420	.1287
.900	-.0890	.1649
.925	-.0997	.1914
.950	-.0903	.2133

STATION 3

X/C	CPU	CPL
.010	.1570	-.1864
.025	-.0419	-.0913
.050	-.0931	-.0476
.100	-.1615	-.0050
.200	-.2317	.0289
.400	-.2908	.0399
.600	-.2572	.0879
.800	-.1581	.1255
.900	-.1069	.1670
.925	-.1099	.2011

STATION 4

X/C	CPU	CPL
.010	.1379	-.1794
.025	-.0570	-.1054
.050	-.1043	-.0487
.100	-.1591	-.0193
.200	-.2419	-.0183
.400	-.3123	.0090
.600	-.2784	.1073
.800	-.1964	.1056
.900	-.1333	.1463
.925	-.1423	.1607

STATION 5

X/C	CPU	CPL
.025	-.0759	-.0599
.050	-.1123	-.0889
.075	-.1331	-.0466
.150	-.2011	-.1234
.300	-.3209	-.0115
.450	-.3112	.0380
.600	-.3052	.1105
.750	-.2232	.1311
.800	-.1917	.1276
.850	-.1554	.1299

STATION 6

X/C	CPU	CPL
.025	-.0079	-.3234
.050	-.0981	-.0936
.100	-.1262	-.0507
.200	-.1504	-.0033
.300	-.2405	.0390
.400	-.2578	.0401
.500	-.2660	.0520
.600	-.2525	.0654
.700	-.2398	.0866
.800	-.2063	.0941

TABLE IV. - Continued

(e) $\alpha = 4.10^{\circ}$

STATION 1

X/C	CPU	CPL
.005	.1168	.1654
.010	.1062	.1126
.025	.0658	.0777
.050	.0083	.0607
.100	-.0692	.0552
.200	-.1780	.0617
.300	-.2356	.0581
.400	-.2539	.0439
.500	-.2344	.0414
.600	-.2153	-.0360
.700	-.1576	.1027
.800	-.1170	.1020
.900	-.0723	-.0730
.950	-.0923	.1766
.970	-.0537	

STATION 2

X/C	CPU	CPL
.005	-.0940	.2153
.010	-.2746	.1836
.025	-.3262	.1542
.050	-.2905	.1303
.100	-.2805	.1021
.200	-.3152	.0884
.300	-.3484	.0831
.400	-.3465	.0711
.500	-.2809	.0653
.600	-.2613	.1094
.700	-.2247	
.800	-.1455	.1485
.900	-.0882	.1784
.925	-.0891	.2039
.950	-.0734	.2214

STATION 3

X/C	CPU	CPL
.010	-.2916	.2175
.025	-.3602	.1587
.050	-.3276	.1339
.100	-.3123	.1253
.200	-.3486	.1198
.400	-.3572	.0940
.600	-.2869	.1254
.800	-.1713	.1440
.900	-.1121	.1791
.925	-.1138	.2127

STATION 4

X/C	CPU	CPL
.010	-.3901	.2437
.025	-.3902	.1402
.050	-.3774	.1385
.100	-.3429	.1251
.200	-.3684	.1256
.400	-.3819	.1168
.600	-.3170	.1368
.800	-.2142	.1433
.900	-.1423	.1603
.925	-.1491	.2074

STATION 5

X/C	CPU	CPL
.025	-.4716	.2083
.050	-.4150	.1961
.075	-.3705	.1766
.150	-.3660	.1033
.300	-.4177	.1223
.450	-.3710	.1146
.600	-.3446	.1311
.750	-.2596	.1496
.800	-.2221	.1405
.850	-.1862	.1335

STATION 6

X/C	CPU	CPL
.025	-.4009	.0663
.050	-.3119	.0437
.100	-.2807	.0313
.200	-.2740	.0309
.300	-.3229	.0508
.400	-.3356	.0402
.500	-.3382	.0451
.600	-.3351	.0566
.700	-.3530	.0757
.800	-.3176	.0824

(f) $\alpha = 6.22^{\circ}$

STATION 1

X/C	CPU	CPL
.005	-.0689	.1968
.010	-.0725	.1473
.025	-.0997	.1128
.050	-.0855	.1025
.100	-.1376	.0940
.200	-.2371	.1056
.300	-.2734	.1100
.400	-.2846	.0800
.500	-.2618	.0725
.600	-.2477	-.0254
.700	-.1781	.1281
.800	-.1349	.1146
.900	-.0810	-.0712
.950	-.1040	.1904
.970	-.0655	

STATION 2

X/C	CPU	CPL
.005	-.6420	.4666
.010	-.7532	.3898
.025	-.6596	.3066
.050	-.5488	.2469
.100	-.4373	.2036
.200	-.4136	.1494
.300	-.4128	.1469
.400	-.3925	.1210
.500	-.3069	.1076
.600	-.2776	.1404
.700	-.2318	
.800	-.1521	.1656
.900	-.0942	.1955
.925	-.0874	.2159
.950	-.0665	.2351

STATION 3

X/C	CPU	CPL
.010	-.9153	.4410
.025	-.7906	.3326
.050	-.6098	.2721
.100	-.4692	.2193
.200	-.4513	.1785
.400	-.4124	.1372
.600	-.3165	.1508
.800	-.1766	.1626
.900	-.1108	.1903
.925	-.1066	.2199

STATION 4

X/C	CPU	CPL
.010	-1.0484	.4852
.025	-.8537	.3439
.050	-.7083	.2834
.100	-.5248	.2458
.200	-.5000	.1855
.400	-.4469	.1675
.600	-.3520	.1587
.800	-.2188	.1565
.900	-.1398	.1752
.925	-.1456	.2219

STATION 5

X/C	CPU	CPL
.025	-.8491	.2261
.050	-.6967	.2297
.075	-.6047	.2321
.150	-.5267	.1645
.300	-.5233	.1654
.450	-.4426	.1612
.600	-.4043	.1437
.750	-.3036	.1479
.800	-.2615	.1431
.850	-.2163	.1389

STATION 6

X/C	CPU	CPL
.025	-.7419	.2798
.050	-.5920	.2746
.100	-.4513	.1303
.200	-.4206	.0582
.300	-.4465	.0520
.400	-.4702	.0283
.500	-.4735	.0338
.600	-.4685	.0385
.700	-.4906	.0599
.800	-.4518	.0698

TABLE IV. - Continued

(g) $\alpha = 8.39^{\circ}$

STATION 1

X/C	CPU	CPL
.005	-.2857	.2248
.010	-.2902	.1818
.025	-.3053	.1496
.050	-.2689	.1382
.100	-.2944	.1406
.200	-.3583	.1500
.300	-.3463	.1497
.400	-.3348	.1252
.500	-.3108	.1123
.600	-.2873	-.0194
.700	-.2106	.1439
.800	-.1630	.1266
.900	-.1006	-.0699
.950	-.1226	.1971
.970	-.0822	

STATION 2

X/C	CPU	CPL
.005	-1.5069	.5042
.010	-1.2299	.4854
.025	-1.0221	.4137
.050	-.6642	.3416
.100	-.5697	.2606
.200	-.4743	.2045
.300	-.4562	.1882
.400	-.4161	.1603
.500	-.3426	.1362
.600	-.3082	.1695
.700	-.2525	
.800	-.1681	.1767
.900	-.0967	.1990
.925	-.1008	.2215
.950	-.1042	.2432

STATION 3

X/C	CPU	CPL
.010	-1.4589	.5198
.025	-1.1287	.4533
.050	-.8542	.3895
.100	-.6858	.2984
.200	-.5722	.2346
.400	-.4650	.1813
.600	-.3401	.1699
.800	-.1803	.1703
.900	-.1045	.1913
.925	-.0971	.2185

STATION 4

X/C	CPU	CPL
.010	-2.5509	.5299
.025	-1.2559	.4681
.050	-1.0045	.3980
.100	-.7611	.3288
.200	-.6320	.3183
.400	-.5179	.2712
.600	-.3846	.1879
.800	-.2294	.1650
.900	-.1430	.1865
.925	-.1459	.2258

STATION 5

X/C	CPU	CPL
.025	-1.7874	.4214
.050	-1.7019	.4220
.075	-1.5208	.4124
.150	-.7686	.3219
.300	-.5684	.3051
.450	-.4971	.2452
.600	-.4566	.1515
.750	-.3544	.1554
.800	-.3068	.1377
.850	-.2586	.1345

STATION 6

X/C	CPU	CPL
.025	-1.0478	.4011
.050	-1.0134	.3090
.100	-.9597	.2204
.200	-.7862	.0712
.300	-.5954	.0372
.400	-.5467	.0095
.500	-.5770	.0108
.600	-.5664	.0161
.700	-.6366	.0311
.800	-.6129	.0438

(h) $\alpha = 10.61^{\circ}$

STATION 1

X/C	CPU	CPL
.005	-.4249	.2507
.010	-.4406	.2048
.025	-.4774	.1807
.050	-.4431	.1734
.100	-.4433	.1799
.200	-.5200	.1978
.300	-.4599	.1867
.400	-.4206	.1619
.500	-.3789	.1425
.600	-.3235	-.0150
.700	-.2258	.1598
.800	-.1871	.1450
.900	-.1144	-.0737
.950	-.1183	.1974
.970	-.0771	

STATION 2

X/C	CPU	CPL
.005	-2.9439	.4075
.010	-1.5400	.4976
.025	-1.2126	.4733
.050	-.9028	.4153
.100	-.7108	.3269
.200	-.5622	.2679
.300	-.5402	.2340
.400	-.4866	.1919
.500	-.3862	.1668
.600	-.3244	.1984
.700	-.2631	
.800	-.1684	.2016
.900	-.1012	.2203
.925	-.1071	.2399
.950	-.1016	.2575

STATION 3

X/C	CPU	CPL
.010	-2.4870	.5141
.025	-2.3376	.5292
.050	-1.9538	.4670
.100	-.7221	.3978
.200	-.6144	.3111
.400	-.4691	.2279
.600	-.3472	.2069
.800	-.2009	.2003
.900	-.1335	.2065
.925	-.1233	.2382

STATION 4

X/C	CPU	CPL
.010	-1.8142	.5329
.025	-1.7785	.5471
.050	-1.7938	.4914
.100	-1.8138	.4186
.200	-1.0878	.3835
.400	-.4880	.3393
.600	-.3799	.2167
.800	-.2381	.1834
.900	-.1445	.2003
.925	-.1622	.2349

STATION 5

X/C	CPU	CPL
.025	-1.2282	.3631
.050	-1.2159	.4057
.075	-1.1719	.4086
.150	-1.1459	.4084
.300	-1.0708	.4064
.450	-.9068	.3099
.600	-.6459	.1696
.750	-.4674	.1598
.800	-.4272	.1419
.850	-.3830	.1363

STATION 6

X/C	CPU	CPL
.025	-.9433	.3997
.050	-.9440	.3659
.100	-.8956	.2424
.200	-.8781	.0970
.300	-.8171	.0483
.400	-.7666	.0165
.500	-.7684	.0147
.600	-.7296	.0222
.700	-.7474	.0324
.800	-.7556	.0267

TABLE IV.- Continued

(i) $\alpha = 12.86^{\circ}$

STATION 1

X/C	CPU	CPL
.005	-.6133	.2862
.010	-.6317	.2462
.025	-.6351	.2169
.050	-.6114	.2155
.100	-.6340	.2248
.200	-.6801	.2375
.300	-.5892	.2333
.400	-.5190	.2067
.500	-.4405	.1800
.600	-.3789	.0060
.700	-.2587	.1903
.800	-.2166	.1611
.900	-.1386	-.0783
.950	-.1250	.2035
.970	-.0809	

STATION 2

X/C	CPU	CPL
.005	-2.2778	.2616
.010	-2.3303	.4673
.025	-2.5504	.5097
.050	-2.8554	.4691
.100	-.4721	.4000
.200	-.5420	.3200
.300	-.5014	.2737
.400	-.4757	.2384
.500	-.4065	.2028
.600	-.3636	.2186
.700	-.3144	
.800	-.2183	.2019
.900	-.1322	.2064
.925	-.1248	.2227
.950	-.1087	.2386

STATION 3

X/C	CPU	CPL
.010	-1.9348	.4937
.025	-1.9370	.5581
.050	-1.9424	.5313
.100	-2.1555	.4440
.200	-1.0498	.3523
.400	-.3809	.2583
.600	-.3594	.2192
.800	-.2379	.1914
.900	-.1603	.2070
.925	-.1626	.2361

STATION 4

X/C	CPU	CPL
.010	-1.5567	.4903
.025	-1.5416	.5536
.050	-1.5778	.5209
.100	-1.5742	.4648
.200	-1.6659	.3945
.400	-.8529	.3236
.600	-.4594	.2244
.800	-.3459	.1753
.900	-.2569	.1931
.925	-.2765	.2234

STATION 5

X/C	CPU	CPL
.025	-.9577	.3614
.050	-.9454	.4256
.075	-.9295	.4455
.150	-.8904	.4429
.300	-.7941	.3918
.450	-.7561	.2964
.600	-.7059	.1678
.750	-.6421	.1545
.800	-.6201	.0942
.850	-.5977	.0983

STATION 6

X/C	CPU	CPL
.025	-.7482	.3698
.050	-.7391	.3754
.100	-.7237	.3332
.200	-.7130	.1132
.300	-.6925	.0688
.400	-.6360	.0213
.500	-.6188	.0261
.600	-.5943	.0164
.700	-.5737	.0214
.800	-.5538	.0035

(j) $\alpha = 15.18^{\circ}$

STATION 1

X/C	CPU	CPL
.005	-.7510	.3062
.010	-.7857	.2736
.025	-.8023	.2519
.050	-.7809	.2497
.100	-.7882	.2666
.200	-.8205	.2847
.300	-.7037	.2710
.400	-.5969	.2352
.500	-.5182	.2117
.600	-.4315	.0001
.700	-.2873	.2054
.800	-.2459	.1721
.900	-.1536	-.0798
.950	-.1392	.2096
.970	-.0969	

STATION 2

X/C	CPU	CPL
.005	-2.3689	.1861
.010	-2.4167	.4443
.025	-2.4372	.5278
.050	-2.9927	.5239
.100	-1.5514	.4461
.200	-.5095	.3673
.300	-.5269	.3112
.400	-.5281	.2691
.500	-.4784	.2232
.600	-.4663	.2378
.700	-.3895	
.800	-.2694	.2069
.900	-.1683	.1994
.925	-.1527	.2140
.950	-.1236	.2282

STATION 3

X/C	CPU	CPL
.010	-1.9183	.4624
.025	-1.8936	.5734
.050	-1.9140	.5535
.100	-2.4279	.4858
.200	-1.6470	.3999
.400	-.4861	.2932
.600	-.3958	.2364
.800	-.2971	.1914
.900	-.2182	.1908
.925	-.2215	.2198

STATION 4

X/C	CPU	CPL
.010	-1.4115	.4687
.025	-1.4257	.5781
.050	-1.4417	.5593
.100	-1.4977	.4927
.200	-1.5764	.4817
.400	-1.1334	.3711
.600	-.7220	.2355
.800	-.4997	.1654
.900	-.3553	.1563
.925	-.3765	.1786

STATION 5

X/C	CPU	CPL
.025	-.8609	.3578
.050	-.8724	.4244
.075	-.8565	.4522
.150	-.8412	.4445
.300	-.7875	.4139
.450	-.7646	.2839
.600	-.7493	.1681
.750	-.7048	.1539
.800	-.6808	.0826
.850	-.6595	.0826

STATION 6

X/C	CPU	CPL
.025	-.6949	.3625
.050	-.7098	.3913
.100	-.7012	.2947
.200	-.6841	.1318
.300	-.6751	.0775
.400	-.6462	.0342
.500	-.6257	.0205
.600	-.6054	.0137
.700	-.5665	.0112
.800	-.5623	-.0110

TABLE IV. - Continued

(k) $\alpha = 17.37^{\circ}$

STATION 1

X/C	CPU	CPL
.005	-.9162	.3475
.010	-.9246	.3190
.025	-.9364	.3010
.050	-.9362	.2952
.100	-.9819	.3099
.200	-.9857	.3366
.300	-.8315	.3216
.400	-.7289	.2829
.500	-.6181	.2487
.600	-.5222	.0035
.700	-.3320	.2287
.800	-.2865	.1946
.900	-.1764	-.0781
.950	-.1394	.2229
.970	-.0921	

STATION 2

X/C	CPU	CPL
.005	-2.5614	.0811
.010	-2.5683	.3850
.025	-2.6151	.5378
.050	-3.2379	.5475
.100	-2.0968	.4886
.200	-.5986	.4097
.300	-.5958	.3574
.400	-.6328	.3094
.500	-.6076	.2609
.600	-.5281	.2638
.700	-.4476	
.800	-.3504	.2153
.900	-.2719	.1876
.925	-.2528	.1917
.950	-.2270	.2043

STATION 3

X/C	CPU	CPL
.010	-2.0677	.4057
.025	-2.0512	.5757
.050	-2.0355	.5840
.100	-2.0452	.5280
.200	-2.1329	.4436
.400	-.7610	.3156
.600	-.4835	.2566
.800	-.3396	.1986
.900	-.2748	.1735
.925	-.2752	.2055

STATION 4

X/C	CPU	CPL
.010	-1.3822	.4085
.025	-1.3855	.5877
.050	-1.4046	.5783
.100	-1.4645	.5397
.200	-1.5544	.4628
.400	-1.2175	.3847
.600	-.8319	.2670
.800	-.5899	.1689
.900	-.4153	.1623
.925	-.4483	.1766

STATION 5

X/C	CPU	CPL
.025	-.9288	.3529
.050	-.9163	.4229
.075	-.9163	.4604
.150	-.8907	.4538
.300	-.8480	.4073
.450	-.8215	.2635
.600	-.8126	.1860
.750	-.7782	.1659
.800	-.7352	.0890
.850	-.7230	.0902

STATION 6

X/C	CPU	CPL
.025	-.7357	.3729
.050	-.7297	.4171
.100	-.7251	.3675
.200	-.7240	.1708
.300	-.6889	.1051
.400	-.6562	.0503
.500	-.6250	.0338
.600	-.5964	.0281
.700	-.5669	.0217
.800	-.5373	.0068

(l) $\alpha = 19.58^{\circ}$

STATION 1

X/C	CPU	CPL
.005	-1.0459	.3763
.010	-1.0710	.3479
.025	-1.0873	.3314
.050	-1.0970	.3331
.100	-1.1263	.3507
.200	-1.1403	.3724
.300	-.9617	.3580
.400	-.8330	.3233
.500	-.6942	.2807
.600	-.5638	.0208
.700	-.3828	.2529
.800	-.2996	.2073
.900	-.1322	-.0767
.950	-.0882	.2279
.970	-.0462	

STATION 2

X/C	CPU	CPL
.005	-2.5267	-.0995
.010	-2.5310	.3001
.025	-2.7221	.5163
.050	-3.0186	.5656
.100	-3.0565	.5228
.200	-.7524	.4466
.300	-.7001	.3923
.400	-.8563	.3401
.500	-.7898	.2909
.600	-.6959	.2847
.700	-.6326	
.800	-.6016	.2072
.900	-.5725	.1509
.925	-.5683	.1395
.950	-.5587	.1355

STATION 3

X/C	CPU	CPL
.010	-1.9865	.3580
.025	-1.9858	.5623
.050	-1.9320	.5915
.100	-1.8237	.5606
.200	-2.0923	.4716
.400	-.9938	.3516
.600	-.6251	.2721
.800	-.5397	.1819
.900	-.4111	.1419
.925	-.3909	.1476

STATION 4

X/C	CPU	CPL
.010	-1.3227	.3566
.025	-1.3450	.5756
.050	-1.3658	.5947
.100	-1.4425	.5889
.200	-1.4634	.5121
.400	-1.1802	.4449
.600	-.8597	.2658
.800	-.6564	.1618
.900	-.4767	.1407
.925	-.5175	.1486

STATION 5

X/C	CPU	CPL
.025	-.8636	.3734
.050	-.8737	.4599
.075	-.8948	.5260
.150	-.8942	.4950
.300	-.8414	.4090
.450	-.8078	.3197
.600	-.7848	.1985
.750	-.7255	.1936
.800	-.7113	.1048
.850	-.6872	.1069

STATION 6

X/C	CPU	CPL
.025	-.7028	.3654
.050	-.7022	.4287
.100	-.7125	.3617
.200	-.7122	.1830
.300	-.6812	.1133
.400	-.6591	.0604
.500	-.6200	.0420
.600	-.6087	.0410
.700	-.5785	.0323
.800	-.5388	.0118

TABLE IV. - Concluded.

(m) $\alpha = 21.80^{\circ}$

STATION 1

X/C	CPU	CPL
.005	-1.1978	.3994
.010	-1.2239	.3808
.025	-1.2571	.3624
.050	-1.2576	.3622
.100	-1.2932	.3961
.200	-1.3064	.4192
.300	-1.0904	.4073
.400	-.9187	.3642
.500	-.7713	.3251
.600	-.6443	.0294
.700	-.3883	.2951
.800	-.2570	.2430
.900	-.0608	-.0977
.950	-.0611	.2704
.970	-.0048	

STATION 2

X/C	CPU	CPL
.005	-2.7178	-.2373
.010	-2.7494	.2389
.025	-2.9059	.5037
.050	-3.1640	.5748
.100	-3.5280	.5568
.200	-1.0875	.4852
.300	-.8853	.4315
.400	-.9753	.3726
.500	-.9861	.3203
.600	-.9567	.2994
.700	-.9671	
.800	-.9646	.2107
.900	-1.0022	.1181
.925	-.9182	.0898
.950	-.8548	.0592

STATION 3

X/C	CPU	CPL
.010	-2.0448	.2612
.025	-2.0466	.5398
.050	-2.0644	.6007
.100	-1.9768	.5854
.200	-2.4878	.5057
.400	-1.2354	.3839
.600	-.8340	.2823
.800	-.6554	.1593
.900	-.6094	.0806
.925	-.6147	.0955

STATION 4

X/C	CPU	CPL
.010	-1.2923	.2771
.025	-1.3367	.5466
.050	-1.3493	.5977
.100	-1.4434	.5931
.200	-1.6457	.5940
.400	-1.3679	.4081
.600	-.9664	.2807
.800	-.7050	.1433
.900	-.5509	.0962
.925	-.5792	.0966

STATION 5

X/C	CPU	CPL
.025	-.9329	.4486
.050	-.9376	.4672
.075	-.9486	.5528
.150	-.9818	.5140
.300	-.8861	.4671
.450	-.8449	.3718
.600	-.7897	.2215
.750	-.7373	.1888
.800	-.7215	.1121
.850	-.6584	.1146

STATION 6

X/C	CPU	CPL
.025	-.7521	.3751
.050	-.7202	.4487
.100	-.7244	.3743
.200	-.7208	.2267
.300	-.7047	.1401
.400	-.6879	.0698
.500	-.6621	.0569
.600	-.6252	.0428
.700	-.5861	.0413
.800	-.5636	.0256

TABLE V.- PRESSURE COEFFICIENTS AT A MACH NUMBER OF 0.20 FOR THE MODEL WITH STRAKE OFF. $C_{L,d} = 0.70$

(a) $\alpha = -3.78^{\circ}$

STATION 1

X/C	CPU	CPL
.005	.4742	-1.6884
.010	.5758	-1.7865
.025	.4920	-2.0209
.050	.3544	-1.4967
.100	.2163	-.1194
.200	.0637	-.0956
.300	-.0841	-.0425
.400	-.1180	-.0441
.500	-.1447	-.0118
.600	-.1635	.0607
.700	-.2006	.1227
.800	-.1696	-.0654
.900	-.1411	.2049
.950	-.1869	.2548
.970	-.1180	

STATION 2

X/C	CPU	CPL
.005	.4490	-.6499
.010	.5442	-.7841
.025	.4790	-.8066
.050	.3980	-.8779
.100	.2282	-.9614
.200	.0312	-.5235
.300	-.1222	-.2894
.400	-.1775	.1229
.500	-.1889	.1687
.600	-.2470	.2166
.700		
.800	-.1796	.2693
.900	-.1902	.3128
.925	-.2268	.3820
.950	-.2209	.3868

STATION 3

X/C	CPU	CPL
.010	.5412	-.5635
.025	.4843	-.5790
.050	.4040	-.5911
.100	.2426	-.6145
.200	.0253	-.7940
.400	-.1934	-.4748
.600	-.2682	.1918
.800	-.2016	.3310
.900	-.1902	.3887
.925	-.2337	.4276

STATION 4

X/C	CPU	CPL
.010	.5361	-.3923
.025	.4835	-.3776
.050	.3976	-.3887
.100	.2484	-.4332
.200	.0234	-.4560
.400	-.2003	-.5415
.600	-.3306	-.2870
.800	-.2513	-.2185
.900	-.2496	.1655
.925	-.2922	.1728

STATION 5

X/C	CPU	CPL
.025	.4342	.1745
.050	.3631	
.075	.2731	-.1758
.150	.1555	-.1888
.300	-.1844	-.1985
.450	-.2582	-.2048
.600	-.3668	-.1996
.750	-.4003	-.2008
.800	-.3512	-.2089
.850	-.3242	-.2053

STATION 6

X/C	CPU	CPL
.025	.4346	
.050	.3464	-.0308
.100	.2107	
.200	.0304	-.0380
.300	-.1058	-.0398
.400	-.1528	-.0428
.500	-.2328	
.600	-.2898	-.0497
.700	-.3422	-.0614
.800	-.3440	-.1069

(b) $\alpha = -1.91^{\circ}$

STATION 1

X/C	CPU	CPL
.005	.5432	-1.2943
.010	.5187	-1.2957
.025	.4152	-1.5897
.050	.2455	-.6357
.100	.1278	-.0645
.200	-.0239	-.0436
.300	-.1558	.0026
.400	-.1777	-.0005
.500	-.1810	.0291
.600	-.1946	.0935
.700	-.2277	.1526
.800	-.1958	-.0491
.900	-.1493	.2060
.950	-.2003	.2580
.970	-.1192	

STATION 2

X/C	CPU	CPL
.005	.5211	-.5649
.010	.5187	-.6583
.025	.4166	-.6812
.050	.3101	-.7169
.100	.1339	-.8324
.200	-.0465	-.3157
.300	-.2137	.0268
.400	-.2314	.1728
.500	-.2220	.1805
.600	-.2799	.2251
.700		
.800	-.2057	.2731
.900	-.1996	.3293
.925	-.2492	.3759
.950	-.2297	.3817

STATION 3

X/C	CPU	CPL
.010	.5199	-.4638
.025	.4172	-.4836
.050	.3023	-.4877
.100	.1571	-.5359
.200	-.0618	-.6280
.400	-.2568	-.1415
.600	-.3189	.2863
.800	-.2285	.3220
.900	-.2083	.3779
.925	-.2560	.4253

STATION 4

X/C	CPU	CPL
.010	.5089	-.3382
.025	.4148	-.3400
.050	.3171	-.3589
.100	.1643	-.3740
.200	-.0738	-.3854
.400	-.2643	-.3727
.600	-.3403	-.1466
.800	-.2600	.2966
.900	-.2339	.3284
.925	-.2782	.3264

STATION 5

X/C	CPU	CPL
.025	.4139	.3272
.050	.3021	
.075	.2143	-.1474
.150	.0937	-.1562
.300	-.2318	-.1827
.450	-.2922	-.1655
.600	-.3954	-.1530
.750	-.3896	-.1406
.800	-.3226	-.1375
.850	-.2813	-.0937

STATION 6

X/C	CPU	CPL
.025	.4162	
.050	.3150	-.0407
.100	.1668	
.200	.0042	-.0348
.300	-.1435	-.0397
.400	-.1871	-.0410
.500	-.2434	
.600	-.2920	-.0521
.700	-.3399	-.0874
.800	-.3402	-.1211

TABLE V. - Continued

(c) $\alpha = 0.0^o$

STATION 1

X/C	CPU	CPL
.005	.5334	-.9818
.010	.4483	-.9571
.025	.2750	-1.2154
.050	.1353	.0319
.100	.0276	-.0525
.200	-.0986	.0052
.300	-.2005	.0339
.400	-.2253	.0493
.500	-.2155	.0531
.600	-.2342	.1216
.700	-.2465	.1613
.800	-.2055	-.0524
.900	-.1527	.2233
.950	-.1871	.2649
.970	-.1046	

STATION 2

X/C	CPU	CPL
.005	.5272	-.4306
.010	.4480	-.4976
.025	.3090	-.5195
.050	.1815	-.5592
.100	.0345	-.5688
.200	-.1311	-.1434
.300	-.2846	.1017
.400	-.2844	.1537
.500	-.2726	.1645
.600	-.3324	.2180
.700		
.800	-.2244	.2686
.900	-.2193	.3117
.925	-.2489	.3543
.950	-.2225	.3919

STATION 3

X/C	CPU	CPL
.010	.4549	-.3746
.025	.3156	-.3866
.050	.1946	-.3969
.100	.0643	-.4341
.200	-.1552	-.3461
.400	-.3333	.0905
.600	-.3455	.2501
.800	-.2446	.2927
.900	-.2156	.3489
.925	-.2528	.3865

STATION 4

X/C	CPU	CPL
.010	.4759	-.2988
.025	.3099	-.3012
.050	.2125	-.3012
.100	.0475	-.2923
.200	-.1613	-.3263
.400	-.3341	-.0743
.600	-.3893	.1466
.800	-.2729	.2169
.900	-.2594	.2773
.925	-.2938	.2674

STATION 5

X/C	CPU	CPL
.025	.3327	.2424
.050	.2109	
.075	.1447	-.1047
.150	.0073	-.1389
.300	-.3073	-.1469
.450	-.3533	-.1432
.600	-.4178	-.0772
.750	-.3919	.0615
.800	-.3104	.0917
.850	-.2555	.1456

STATION 6

X/C	CPU	CPL
.025	.3701	
.050	.2504	-.0498
.100	.1084	
.200	-.0566	-.0319
.300	-.2030	-.0360
.400	-.2483	-.0346
.500	-.2806	
.600	-.3282	-.0834
.700	-.3637	-.1163
.800	-.3712	-.1163

(d) $\alpha = 1.92^o$

STATION 1

X/C	CPU	CPL
.005	.4553	-.6606
.010	.3143	-.6880
.025	.1428	-.3410
.050	.0070	-.0171
.100	-.0619	.0130
.200	-.1621	.0548
.300	-.2623	.0928
.400	-.2734	.0942
.500	-.2430	.0897
.600	-.2536	.1449
.700	-.2550	.1838
.800	-.2042	-.0233
.900	-.1472	.2397
.950	-.1590	.2942
.970	-.0887	

STATION 2

X/C	CPU	CPL
.005	.4766	-.3159
.010	.3318	-.3653
.025	.1757	-.3831
.050	.0622	-.4119
.100	-.0729	-.2912
.200	-.2085	-.0116
.300	-.3592	.1338
.400	-.3442	.1420
.500	-.3085	.1740
.600	-.3516	.2279
.700		
.800	-.2180	.2746
.900	-.2076	.3210
.925	-.2377	.3677
.950	-.2125	.3842

STATION 3

X/C	CPU	CPL
.010	.3730	-.2808
.025	.2015	-.2779
.050	.0653	-.2899
.100	-.0510	-.3132
.200	-.2519	.0342
.400	-.3743	.1997
.600	-.3757	.2526
.800	-.2430	.2845
.900	-.2200	.3218
.925	-.2544	.3677

STATION 4

X/C	CPU	CPL
.010	.3763	-.2130
.025	.1990	-.2194
.050	.0754	-.2243
.100	-.0538	-.2214
.200	-.2685	-.2514
.400	-.4018	.2650
.600	-.4359	.2732
.800	-.2999	.2861
.900	-.2753	.3292
.925	-.3109	.3405

STATION 5

X/C	CPU	CPL
.025	.2093	.3287
.050	.0846	
.075	.0202	-.1058
.150	-.1006	-.1090
.300	-.4031	-.1323
.450	-.4218	.0583
.600	-.4807	.2702
.750	-.4341	.3449
.800	-.3484	.3474
.850	-.2944	.3350

STATION 6

X/C	CPU	CPL
.025	.2852	
.050	.1444	-.0472
.100	.0147	
.200	-.1424	-.0486
.300	-.2804	-.0775
.400	-.3318	-.1146
.500	-.3536	
.600	-.4355	-.0888
.700	-.4862	.0295
.800	-.4533	.1272

TABLE V. - Continued

(e) $\alpha = 3.90^{\circ}$

STATION 1

X/C	CPU	CPL
.005	.2987	-.2349
.010	.0730	-.1969
.025	-.0532	-.0241
.050	-.1513	.0609
.100	-.1884	.0864
.200	-.2562	.1105
.300	-.3333	.1297
.400	-.3315	.1171
.500	-.2901	.1129
.600	-.2889	.1430
.700	-.2832	.2026
.800	-.2123	-.0253
.900	-.1602	.2407
.950	-.1713	.2861
.970	-.0859	

STATION 2*

X/C	CPU	CPL
.005	.3182	-.2556
.010	.1299	-.2845
.025	-.0280	-.2284
.050	-.1079	.0443
.100	-.1957	.0928
.200	-.3250	-.0051
.300	-.4403	.1544
.400	-.4267	.1637
.500	-.3647	.1807
.600	-.3932	.2393
.700		
.800	-.2481	.2776
.900	-.2192	.3133
.925	-.2406	.3557
.950	-.2231	.3748

STATION 3

X/C	CPU	CPL
.010	.1149	-.1889
.025	-.0311	-.2122
.050	-.1094	-.0913
.100	-.2082	.1317
.200	-.3631	.1959
.400	-.4580	.2053
.600	-.4350	.2574
.800	-.2808	.2909
.900	-.2388	.3253
.925	-.2710	.3638

STATION 4

X/C	CPU	CPL
.010	.1797	-.1727
.025	-.0184	-.1659
.050	-.1067	-.1740
.100	-.2243	.0749
.200	-.4045	.1865
.400	-.4869	.2317
.600	-.4972	.2759
.800	-.3278	.2844
.900	-.2878	.3282
.925	-.3131	.3569

STATION 5

X/C	CPU	CPL
.025	.0065	.2771
.050	-.0830	
.075	-.1380	-.1561
.150	-.2474	.0186
.300	-.5230	.2164
.450	-.5081	.2357
.600	-.5463	.2671
.750	-.4770	.2980
.800	-.4042	.2883
.850	-.3426	.2785

STATION 6

X/C	CPU	CPL
.025	.1364	
.050	.0060	-.1787
.100	-.1106	
.200	-.2641	-.0651
.300	-.3891	.0984
.400	-.4247	.1559
.500	-.4481	
.600	-.5221	.1709
.700	-.5826	.1837
.800	-.5468	.1848

(f) $\alpha = 5.90^{\circ}$

STATION 1

X/C	CPU	CPL
.005	.0459	.1526
.010	-.1490	.1429
.025	-.2864	.1650
.050	-.2884	.1515
.100	-.2815	.1545
.200	-.3430	.1801
.300	-.4050	.1714
.400	-.3683	.1576
.500	-.3137	.1419
.600	-.2985	.1925
.700	-.2834	.2157
.800	-.2189	-.0192
.900	-.1525	.2531
.950	-.1398	.3040
.970	-.0655	

STATION 2

X/C	CPJ	CPL
.005	.0088	.0716
.010	-.1595	.1009
.025	-.2724	.1394
.050	-.3068	.1718
.100	-.3256	.1900
.200	-.4266	.0438
.300	-.5243	.2065
.400	-.4927	.1978
.500	-.4096	.2107
.600	-.4166	.2709
.700		
.800	-.2497	.2930
.900	-.2093	.3329
.925	-.2393	.3676
.950	-.1973	.3795

STATION 3

X/C	CPU	CPL
.010	-.1714	.1078
.025	-.2720	.1695
.050	-.3086	.2301
.100	-.3559	.2164
.200	-.4824	.2503
.400	-.5237	.2437
.600	-.4676	.2911
.800	-.2870	.3104
.900	-.2383	.3462
.925	-.2604	.3873

STATION 4

X/C	CPU	CPL
.010	-.1483	.1171
.025	-.3110	.1819
.050	-.3269	.2222
.100	-.3886	.1764
.200	-.5076	.2467
.400	-.5595	.2600
.600	-.5412	.2856
.800	-.3380	.3006
.900	-.2984	.3337
.925	-.3155	.3558

STATION 5

X/C	CPU	CPL
.025	-.2593	.3547
.050	-.3426	
.075	-.3592	.1874
.150	-.3844	.1897
.300	-.6253	.2200
.450	-.5827	.2457
.600	-.6006	.2716
.750	-.5250	.2962
.800	-.4367	.2926
.850	-.3734	.2785

STATION 6

X/C	CPU	CPL
.025	-.1480	
.050	-.1934	.0566
.100	-.2446	
.200	-.3642	.1314
.300	-.4810	.1576
.400	-.5094	.1501
.500	-.5346	
.600	-.6184	.1543
.700	-.7050	.1421
.800	-.6963	.1265

TABLE V.- Continued

(g) $\alpha = 7.94^\circ$

STATION 1

X/C	CPU	CPL
.005	-.3407	.4139
.010	-.4694	.3327
.025	-.4937	.2844
.050	-.5038	.2486
.100	-.4087	.2389
.200	-.4102	.2221
.300	-.4597	.2194
.400	-.41[illegible]6	.1908
.500	-.3611	.1684
.600	-.3359	.2093
.700	-.2994	.2362
.800	-.2266	-.0265
.900	-.1416	.2557
.950	-.1412	.3107
.970	-.0763	

STATION 2

X/C	CPU	CPL
.005	-.5367	.3332
.010	-.6052	.3050
.025	-.5997	.2964
.050	-.5390	.2891
.100	-.4949	.2704
.200	-.5493	.0496
.300	-.6164	.2499
.400	-.5516	.2323
.500	-.4558	.2426
.600	-.4607	.2763
.700		
.800	-.2643	.3003
.900	-.2094	.3307
.925	-.2135	.3692
.950	-.1902	.3832

STATION 3

X/C	CPU	CPL
.010	-.6504	.4044
.025	-.6568	.3294
.050	-.6223	.3466
.100	-.5333	.2910
.200	-.6072	.2848
.400	-.6046	.2836
.600	-.5075	.2945
.800	-.3085	.3029
.900	-.2393	.3447
.925	-.2573	.3823

STATION 4

X/C	CPU	CPL
.010	-.6130	.4182
.025	-.6989	.3353
.050	-.6666	.3353
.100	-.6058	.2949
.200	-.6670	.3007
.400	-.6429	.2924
.600	-.5867	.3099
.800	-.3711	.3089
.900	-.3045	.3446
.925	-.3324	.3720

STATION 5

X/C	CPU	CPL
.025	-.6863	.3747
.050	-.6438	
.075	-.6064	.2337
.150	-.5883	.2517
.300	-.7825	.2671
.450	-.7064	.2501
.600	-.6914	.2664
.750	-.6048	.2892
.800	-.5078	.2773
.850	-.4493	.2633

STATION 6

X/C	CPU	CPL
.025	-.5152	
.050	-.4975	.2176
.100	-.4543	
.200	-.5177	.1315
.300	-.6292	.1365
.400	-.6746	.1100
.500	-.7179	
.600	-.8069	.0882
.700	-.9390	.1116
.800	-.9198	.1036

(h) $\alpha = 10.01^\circ$

STATION 1

X/C	CPU	CPL
.005	-.7925	.5551
.010	-.8622	.4863
.025	-.8058	.3901
.050	-.7148	.3401
.100	-.5361	.3086
.200	-.4917	.2841
.300	-.5195	.2686
.400	-.4694	.2332
.500	-.3834	.2123
.600	-.3503	.2411
.700	-.3186	.2660
.800	-.2262	-.0210
.900	-.1427	.2704
.950	-.1402	.3265
.970	-.0819	

STATION 2

X/C	CPU	CPL
.005	-1.2050	.4528
.010	-1.1323	.4800
.025	-.9673	.4238
.050	-.8369	.3711
.100	-.6572	.3393
.200	-.6773	.0801
.300	-.7122	.2879
.400	-.6170	.2673
.500	-.5150	.2757
.600	-.4899	.3063
.700		
.800	-.2849	.3176
.900	-.2049	.3376
.925	-.2115	.3825
.950	-.1770	.3908

STATION 3

X/C	CPU	CPL
.010	-1.2372	.5275
.025	-1.0497	.4677
.050	-.8853	.4276
.100	-.7204	.3710
.200	-.7546	.3421
.400	-.6668	.3110
.600	-.5467	.3091
.800	-.3146	.3102
.900	-.2444	.3385
.925	-.2526	.3978

STATION 4

X/C	CPU	CPL
.010	-1.2040	.5609
.025	-1.0680	.4718
.050	-.9357	.4206
.100	-.7944	.3534
.200	-.8237	.3490
.400	-.7326	.3180
.600	-.6307	.3162
.800	-.3897	.3196
.900	-.3128	.3457
.925	-.3117	.3650

STATION 5

X/C	CPU	CPL
.025	-.9647	.3685
.050	-.9026	
.075	-.8638	.2353
.150	-.7825	.2376
.300	-.9019	.2682
.450	-.7793	.2734
.600	-.7587	.2775
.750	-.6472	.2914
.800	-.5500	.2871
.850	-.4801	.2614

STATION 6

X/C	CPU	CPL
.025	-1.3298	
.050	-.6773	.2931
.100	-.6302	
.200	-.6458	.1332
.300	-.7836	.1208
.400	-.8418	.0731
.500	-.8962	
.600	-.9888	.0486
.700	-1.0890	.0630
.800	-1.1146	.0630

TABLE V. - Continued

(i) $\alpha = 12.14^{\circ}$

STATION 1

X/C	CPU	CPL
.005	-1.4384	.5934
.010	-1.2886	.5724
.025	-1.1202	.4986
.050	-.8877	.4265
.100	-.6703	.3863
.200	-.5865	.3315
.300	-.5718	.3073
.400	-.4976	.2677
.500	-.4076	.2457
.600	-.3690	.2611
.700	-.3258	.2870
.800	-.2429	-.0178
.900	-.1605	.2856
.950	-.1533	.3309
.970	-.0901	

STATION 2

X/C	CPU	CPL
.005	-2.1784	.4246
.010	-1.6566	.5507
.025	-1.2864	.4878
.050	-1.0989	.4544
.100	-.8664	.3944
.200	-.8025	.1080
.300	-.7961	.3219
.400	-.6706	.3017
.500	-.5516	.3000
.600	-.5149	.3275
.700		
.800	-.2795	.3184
.900	-.2000	.3399
.925	-.1880	.3839
.950	-.1521	.3919

STATION 3

X/C	CPU	CPL
.010	-2.1728	.5728
.025	-1.4150	.5422
.050	-1.2030	.4970
.100	-.9616	.4401
.200	-.8768	.3847
.400	-.7497	.3433
.600	-.5823	.3440
.800	-.3346	.3363
.900	-.2479	.3462
.925	-.2475	.3865

STATION 4

X/C	CPU	CPL
.010	-2.8108	.5215
.025	-1.5492	.5574
.050	-1.2642	.5130
.100	-1.0263	.4608
.200	-.9696	.4150
.400	-.8139	.3529
.600	-.6666	.3445
.800	-.4032	.3346
.900	-.2980	.3451
.925	-.3037	.3649

STATION 5

X/C	CPU	CPL
.025	-1.8753	.3656
.050	-1.8204	
.075	-1.7374	.2580
.150	-1.1690	.3412
.300	-.9118	.3374
.450	-.8212	.2946
.600	-.7988	.2908
.750	-.6836	.2864
.800	-.6014	.2743
.850	-.5174	.2450

STATION 6

X/C	CPU	CPL
.025	-1.4132	
.050	-1.4139	.3649
.100	-1.2179	
.200	-.8413	.1305
.300	-.9156	.0869
.400	-.9864	.0366
.500	-1.0491	
.600	-1.1516	.0077
.700	-1.2824	.0197
.800	-1.3587	.0227

(j) $\alpha = 14.32^{\circ}$

STATION 1

X/C	CPU	CPL
.005	-2.5841	.5321
.010	-1.4873	.6291
.025	-1.3865	.5746
.050	-1.0838	.5045
.100	-.8154	.4441
.200	-.6708	.4029
.300	-.6469	.3647
.400	-.5483	.3232
.500	-.4443	.2889
.600	-.3976	.2943
.700	-.3558	.3138
.800	-.2648	-.0029
.900	-.1637	.3027
.950	-.1869	.3477
.970	-.1062	

STATION 2

X/C	CPU	CPL
.005	-3.7514	.2739
.010	-2.4500	.5380
.025	-1.6929	.5563
.050	-1.3715	.5078
.100	-1.0648	.4632
.200	-.9131	.1364
.300	-.8657	.3752
.400	-.7352	.3491
.500	-.5847	.3298
.600	-.5414	.3487
.700		
.800	-.2941	.3344
.900	-.1967	.3482
.925	-.1667	.3840
.950	-.1406	.3857

STATION 3

X/C	CPU	CPL
.010	-3.0958	.5377
.025	-2.9870	.5898
.050	-2.3177	.5609
.100	-1.0739	.4967
.200	-.9401	.4338
.400	-.7886	.3731
.600	-.5940	.3657
.800	-.3044	.3393
.900	-.2014	.3454
.925	-.2010	.3919

STATION 4

X/C	CPU	CPL
.010	-2.3585	.4405
.025	-2.3247	.5849
.050	-2.4161	.5526
.100	-2.1947	.5343
.200	-.8597	.4579
.400	-.7827	.3712
.600	-.6710	.3653
.800	-.4057	.3437
.900	-.3322	.3556
.925	-.3483	.3699

STATION 5

X/C	CPU	CPL
.025	-1.6183	.3670
.050	-1.5894	
.075	-1.5846	.3201
.150	-1.5299	.3836
.300	-1.2876	.3805
.450	-1.0022	.2869
.600	-.8321	.2855
.750	-.7014	.2803
.800	-.6499	.2598
.850	-.5819	.2210

STATION 6

X/C	CPU	CPL
.025	-1.3343	
.050	-1.3646	.3707
.100	-1.3886	
.200	-1.2968	.0830
.300	-1.0719	.0473
.400	-1.0976	-.0159
.500	-1.1304	
.600	-1.2541	-.0228
.700	-1.4572	-.0091
.800	-1.5169	-.0008

TABLE V.- Continued

(k) $\alpha = 16.36^{\circ}$

STATION 1

X/C	CPU	CPL
.005	-3.9054	.3902
.010	-2.0815	.6160
.025	-1.7354	.6187
.050	-1.3743	.5575
.100	-1.0123	.5064
.200	-.7849	.4393
.300	-.7162	.4012
.400	-.6013	.3530
.500	-.4969	.3146
.600	-.4282	.3201
.700	-.3690	.3313
.800	-.2632	.0077
.900	-.1642	.3110
.950	-.1804	.3613
.970	-.1068	

STATION 2

X/C	CPU	CPL
.005	-2.7507	.1023
.010	-2.7915	.4770
.025	-2.7878	.5804
.050	-2.7484	.5667
.100	-1.9748	.5133
.200	-.7875	.1464
.300	-.8610	.4152
.400	-.7437	.3680
.500	-.6072	.3535
.600	-.5611	.3590
.700		
.800	-.2871	.3450
.900	-.1944	.3450
.925	-.1787	.3833
.950	-.1362	.3874

STATION 3

X/C	CPU	CPL
.010	-2.1756	.5151
.025	-2.1846	.6189
.050	-2.2024	.6038
.100	-2.2258	.5577
.200	-1.7833	.4862
.400	-.7536	.4105
.600	-.5949	.3874
.800	-.3733	.3467
.900	-.2932	.3568
.925	-.3571	.3877

STATION 4

X/C	CPU	CPL
.010	-1.8216	.4160
.025	-1.7724	.6130
.050	-1.7758	.5924
.100	-1.6504	.5614
.200	-1.6543	.4958
.400	-1.2788	.4066
.600	-.9069	.3698
.800	-.6055	.3472
.900	-.4637	.3374
.925	-.4832	.3676

STATION 5

X/C	CPU	CPL
.025	-1.3173	.3571
.050	-1.3106	
.075	-1.3134	.3140
.150	-1.2715	.4049
.300	-1.1983	.3950
.450	-1.0873	.3059
.600	-.9339	.2961
.750	-.7912	.2703
.800	-.7542	.2494
.850	-.7029	.1937

STATION 6

X/C	CPU	CPL
.025	-1.1010	
.050	-1.1205	.3805
.100	-1.1852	
.200	-1.2029	.0774
.300	-1.1652	.0765
.400	-1.1103	.0022
.500	-1.1415	
.600	-1.1493	.0135
.700	-1.1323	.0278
.800	-1.0796	.0242

(l) $\alpha = 18.42^{\circ}$

STATION 1

X/C	CPU	CPL
.005	-4.5790	.2125
.010	-3.4964	.5720
.025	-2.0343	.6635
.050	-1.4940	.6032
.100	-1.0840	.5538
.200	-.8496	.4854
.300	-.7675	.4310
.400	-.6522	.3878
.500	-.5672	.3362
.600	-.4926	.3384
.700	-.4342	.3389
.800	-.3354	.0026
.900	-.2120	.3192
.950	-.2195	.3584
.970	-.1344	

STATION 2

X/C	CPU	CPL
.005	-2.0184	.1954
.010	-2.1308	.5334
.025	-1.9948	.6210
.050	-2.0573	.5956
.100	-1.9167	.5465
.200	-1.8121	.1530
.300	-1.2823	.4269
.400	-1.0521	.3895
.500	-.7552	.3774
.600	-.6896	.3881
.700		
.800	-.4277	.3389
.900	-.3521	.3429
.925	-.3878	.3697
.950	-.3462	.3744

STATION 3

X/C	CPU	CPL
.010	-1.5634	.5516
.025	-1.5915	.6285
.050	-1.5462	.6164
.100	-1.5462	.5734
.200	-1.4240	.5088
.400	-1.1869	.4264
.600	-.8976	.3883
.800	-.6287	.3246
.900	-.5155	.3210
.925	-.4661	.3628

STATION 4

X/C	CPU	CPL
.010	-1.2834	.4632
.025	-1.3080	.6158
.050	-1.2511	.6031
.100	-1.2287	.6032
.200	-1.2239	.5126
.400	-1.0709	.4188
.600	-.9220	.3721
.800	-.7431	.3162
.900	-.6288	.2794
.925	-.6084	.3049

STATION 5

X/C	CPU	CPL
.025	-1.0276	.2994
.050	-1.0716	
.075	-1.0390	.5225
.150	-1.0431	.4542
.300	-1.0623	.4026
.450	-1.0097	.3000
.600	-.9049	.2884
.750	-.7624	.2546
.800	-.7542	.2186
.850	-.7174	.1770

STATION 6

X/C	CPU	CPL
.025	-.9667	
.050	-.9766	.4071
.100	-1.0304	
.200	-1.0331	.1554
.300	-.9855	.1106
.400	-.9505	.0647
.500	-.9353	
.600	-.8840	.0623
.700	-.8282	.0554
.800	-.8433	.0371

TABLE V. - Concluded

(m) $\alpha = 20.48^{\circ}$

STATION 1

X/C	CPU	CPL
.005	-4.2877	.1155
.010	-4.2240	.5727
.025	-3.8796	.6931
.050	-2.2431	.6678
.100	-1.0305	.5969
.200	-.8625	.5315
.300	-.7781	.4618
.400	-.6832	.4098
.500	-.587[illegible]	.3582
.600	-.5513	.3515
.700	-.5213	.3462
.800	-.4222	.0009
.900	-.3015	.2960
.950	-.2760	.3529
.970	-.1999	

STATION 2

X/C	CPU	CPL
.005	-1.5266	.2767
.010	-1.4962	.5549
.025	-1.5274	.6124
.050	-1.5393	.6032
.100	-1.3888	.5579
.200	-1.3276	.1470
.300	-1.2619	.4322
.400	-1.1774	.3881
.500	-1.0111	.3814
.600	-.8710	.3814
.700		
.800	-.6246	.3247
.900	-.5226	.2939
.925	-.5076	.3260
.950	-.4814	.3330

STATION 3

X/C	CPU	CPL
.010	-1.2135	.5737
.025	-1.2472	.6461
.050	-1.1958	.6321
.100	-1.2342	.5806
.200	-1.1598	.5105
.400	-1.0563	.4249
.600	-.9339	.3884
.800	-.7279	.3011
.900	-.6493	.2773
.925	-.6394	.2846

STATION 4

X/C	CPU	CPL
.010	-1.1284	.4814
.025	-1.1328	.6088
.050	-1.1255	.6146
.100	-1.0845	.6092
.200	-1.0372	.5290
.400	-.9748	.4176
.600	-.9014	.3751
.800	-.7881	.3021
.900	-.6942	.2366
.925	-.6914	.2683

STATION 5

X/C	CPU	CPL
.025	-.8743	.3049
.050	-.8820	
.075	-.8627	.5399
.150	-.8770	.4562
.300	-.9261	.3914
.450	-.8682	.3132
.600	-.7900	.2856
.750	-.7586	.2482
.800	-.7443	.2073
.850	-.7177	.1474

STATION 6

X/C	CPU	CPL
.025	-.8296	
.050	-.8536	.4044
.100	-.8258	
.200	-.9024	.1681
.300	-.9136	.1128
.400	-.7903	.0792
.500	-.7653	
.600	-.7122	.0667
.700	-.7475	.0578
.800	-.7102	.0220

TABLE VI.- PRESSURE COEFFICIENTS AT A MACH NUMBER OF 0.40 FOR THE MODEL WITH STRAKE OFF. $C_{L,d} = 0.70$

(a) $\alpha = -3.92^{o}$

STATION 1

X/C	CPU	CPL
.005	.5007	-1.0987
.010	.5752	-1.7573
.025	.4944	-2.0865
.050	.3782	-1.6803
.100	.2139	-.1513
.200	.0490	-.1104
.300	-.0914	-.0605
.400	-.1467	-.0396
.500	-.1589	-.0184
.600	-.1973	.0575
.700	-.2428	.1213
.800	-.2079	-.0625
.900	-.1755	.1966
.950	-.2329	.2581
.970	-.1442	

STATION 2

X/C	CPU	CPL
.005	.4516	-.6962
.010	.5301	-.7960
.025	.4769	-.8182
.050	.3801	-.8740
.100	.2217	-.9306
.200	.0150	-.6920
.300	-.1599	-.4695
.400	-.2020	.0772
.500	-.2145	.1298
.600	-.2946	.1880
.700		
.800	-.2203	.2455
.900	-.2251	.3064
.925	-.2757	.3626
.950	-.2574	.3870

STATION 3

X/C	CPU	CPL
.010	.5267	-.5694
.025	.4721	-.5885
.050	.3862	-.6125
.100	.2348	-.6632
.200	.0050	-.8187
.400	-.2256	-.5697
.600	-.3145	.0446
.800	-.2382	.3022
.900	-.2321	.3693
.925	-.2756	.4195

STATION 4

X/C	CPU	CPL
.010	.5242	-.4256
.025	.4617	-.4424
.050	.3841	-.4467
.100	.2392	-.4486
.200	.0025	-.4468
.400	-.2477	-.5469
.600	-.3502	-.3799
.800	-.2762	-.0977
.900	-.2759	.1753
.925	-.3278	.2317

STATION 5

X/C	CPU	CPL
.025	.4550	.1665
.050	.3636	
.075	.3026	-.2248
.150	.1552	-.2185
.300	-.1634	-.2269
.450	-.2712	-.2406
.600	-.4008	-.2451
.750	-.4315	-.2703
.800	-.3755	-.2648
.850	-.3584	-.2744

STATION 6

X/C	CPU	CPL
.025	.4420	
.050	.3521	-.0843
.100	.2195	
.200	.0478	-.0764
.300	-.1223	-.0860
.400	-.1921	-.0874
.500	-.2374	
.600	-.2965	-.1016
.700	-.3474	-.1185
.800	-.3553	-.1597

(b) $\alpha = -1.95^{o}$

STATION 1

X/C	CPU	CPL
.005	.5499	-1.3215
.010	.5471	-1.3333
.025	.4059	-1.6495
.050	.2811	-.7662
.100	.1280	-.0960
.200	-.0253	-.0584
.300	-.1601	-.0099
.400	-.1973	-.0003
.500	-.2041	.0136
.600	-.2321	.0807
.700	-.2628	.1461
.800	-.2171	-.0542
.900	-.1754	.2132
.950	-.2241	.2673
.970	-.1340	

STATION 2

X/C	CPU	CPL
.005	.5043	-.5849
.010	.5123	-.6653
.025	.3948	-.6813
.050	.2893	-.7359
.100	.1284	-.8592
.200	-.0637	-.4396
.300	-.2375	-.0580
.400	-.2637	.1729
.500	-.2548	.1502
.600	-.3202	.2025
.700		
.800	-.2251	.2473
.900	-.2244	.3089
.925	-.2742	.3586
.950	-.2567	.3809

STATION 3

X/C	CPU	CPL
.010	.5133	-.5181
.025	.4173	-.5300
.050	.3005	-.5414
.100	.1507	-.5820
.200	-.0686	-.6952
.400	-.2868	-.2766
.600	-.3438	.2703
.800	-.2468	.3034
.900	-.2324	.3514
.925	-.2823	.4100

STATION 4

X/C	CPU	CPL
.010	.5144	-.3741
.025	.3944	-.3928
.050	.3012	-.3902
.100	.1751	-.3961
.200	-.0833	-.4532
.400	-.2991	-.4732
.600	-.3821	-.1873
.800	-.2713	.2134
.900	-.2576	.3803
.925	-.3058	.4410

STATION 5

X/C	CPU	CPL
.025	.4104	.2789
.050	.3051	
.075	.2254	-.1876
.150	.0899	-.1977
.300	-.2476	-.2083
.450	-.3257	-.2099
.600	-.4242	-.2152
.750	-.4227	-.2066
.800	-.3458	-.1909
.850	-.3117	-.1738

STATION 6

X/C	CPU	CPL
.025	.4145	
.050	.3013	-.0750
.100	.1623	
.200	-.0041	-.0653
.300	-.1689	-.0722
.400	-.2300	-.0747
.500	-.2552	
.600	-.3162	-.0982
.700	-.3619	-.1373
.800	-.3753	-.1586

TABLE VI. - Continued

(c) $\alpha = 0.05^{\circ}$

STATION 1

X/C	CPU	CPL
.005	.5453	-.9963
.010	.4550	-1.0243
.025	.2733	-1.2580
.050	.1649	.0380
.100	.0213	-.0612
.200	-.1048	-.0111
.300	-.2341	.0270
.400	-.2568	.0296
.500	-.2421	.0420
.600	-.2632	.1065
.700	-.2778	.1589
.800	-.2301	-.0450
.900	-.1811	.2204
.950	-.2152	.2772
.970	-.1250	

STATION 2

X/C	CPU	CPL
.005	.5134	-.4743
.010	.4480	-.5271
.025	.2923	-.5443
.050	.1765	-.5897
.100	.0323	-.5868
.200	-.1613	-.1669
.300	-.3130	.0582
.400	-.3282	.1412
.500	-.3107	.1320
.600	-.3620	.1957
.700		
.800	-.2475	.2457
.900	-.2459	.2976
.925	-.2804	.3534
.950	-.2582	.3773

STATION 3

X/C	CPU	CPL
.010	.4640	-.4220
.025	.3152	-.4407
.050	.2002	-.4245
.100	.0392	-.4545
.200	-.1801	-.3944
.400	-.3572	.0497
.600	-.3903	.2241
.800	-.2702	.2745
.900	-.2518	.3248
.925	-.2970	.3726

STATION 4

X/C	CPU	CPL
.010	.4724	-.3224
.025	.3228	-.3299
.050	.2146	-.3299
.100	.0651	-.3330
.200	-.1913	-.3288
.400	-.3752	-.1594
.600	-.4328	.1550
.800	-.3003	.2571
.900	-.2791	.3254
.925	-.3296	.3654

STATION 5

X/C	CPU	CPL
.025	.3408	.3590
.050	.2270	
.075	.1337	-.1890
.150	.0147	-.1932
.300	-.3243	-.1924
.450	-.3853	-.1858
.600	-.4553	-.1404
.750	-.4206	-.0200
.800	-.3441	.0373
.850	-.2839	.0920

STATION 6

X/C	CPU	CPL
.025	.3701	
.050	.2432	-.0962
.100	.0987	
.200	-.0600	-.0773
.300	-.2301	-.0741
.400	-.2735	-.0731
.500	-.3062	
.600	-.3700	-.1240
.700	-.4249	-.1657
.800	-.4167	-.1782

(d) $\alpha = 2.07^{\circ}$

STATION 1

X/C	CPU	CPL
.005	.4813	-.7283
.010	.3087	-.7665
.025	.1232	-.2758
.050	.0234	-.0257
.100	-.0812	-.0115
.200	-.1871	.0432
.300	-.2970	.0760
.400	-.3101	.0745
.500	-.2842	.0789
.600	-.2976	.1331
.700	-.3073	.1846
.800	-.2444	-.0308
.900	-.1887	.2331
.950	-.2062	.2935
.970	-.1163	

STATION 2

X/C	CPU	CPL
.005	.4649	-.3453
.010	.3094	-.3879
.025	.1452	-.4181
.050	.0283	-.4346
.100	-.0960	-.2809
.200	-.2504	-.0284
.300	-.4035	.1198
.400	-.4039	.1316
.500	-.3605	.1386
.600	-.4073	.1976
.700		
.800	-.2711	.2470
.900	-.2459	.2991
.925	-.2777	.3485
.950	-.2513	.3654

STATION 3

X/C	CPU	CPL
.010	.3405	-.3270
.025	.1659	-.3264
.050	.0601	-.3331
.100	-.0848	-.3633
.200	-.2779	.0231
.400	-.4274	.1650
.600	-.4372	.2179
.800	-.2903	.2612
.900	-.2589	.3040
.925	-.3006	.3460

STATION 4

X/C	CPU	CPL
.010	.3440	-.2641
.025	.1673	-.2652
.050	.0519	-.2617
.100	-.0490	-.2617
.200	-.3047	-.2669
.400	-.4616	.2278
.600	-.4777	.2543
.800	-.3257	.2272
.900	-.2974	.3133
.925	-.3432	.3193

STATION 5

X/C	CPU	CPL
.025	.1899	.3077
.050	.0886	
.075	-.0034	-.1313
.150	-.1084	-.1526
.300	-.4376	-.1758
.450	-.4640	-.0223
.600	-.5292	.1697
.750	-.4786	.3198
.800	-.3899	.3044
.850	-.3274	.2871

STATION 6

X/C	CPU	CPL
.025	.2670	
.050	.1321	-.0976
.100	-.0126	
.200	-.1488	-.1084
.300	-.3228	-.1296
.400	-.3693	-.1519
.500	-.4006	
.600	-.4782	-.1065
.700	-.5416	-.0021
.800	-.4957	.1384

TABLE VI. - Continued

(e) $\alpha = 4.13^{\circ}$

STATION 1

X/C	CPU	CPL
.005	.3070	-.2867
.010	.0906	-.1533
.025	-.0735	-.0034
.050	-.1306	.0760
.100	-.2035	.0771
.200	-.2842	.1136
.300	-.3746	.1242
.400	-.3793	.1121
.500	-.3299	.1095
.600	-.3291	.1563
.700	-.3268	.1977
.800	-.2556	-.0236
.900	-.1868	.2371
.950	-.1882	.2980
.970	-.1068	

STATION 2

X/C	CPU	CPL
.005	.3029	-.3778
.010	.0922	-.3912
.025	-.0573	-.0537
.050	-.1527	.0371
.100	-.2488	.0902
.200	-.3761	.0053
.300	-.5025	.1462
.400	-.4717	.1549
.500	-.4107	.1628
.600	-.4451	.2189
.700		
.800	-.2801	.2540
.900	-.2480	.3002
.925	-.2761	.3400
.950	-.2405	.3552

STATION 3

X/C	CPU	CPL
.010	.1437	-.3424
.025	-.0721	-.3037
.050	-.1357	.0360
.100	-.2242	.0927
.200	-.4037	.1540
.400	-.5077	.1785
.600	-.4836	.2393
.800	-.3107	.2682
.900	-.2686	.3101
.925	-.2988	.3515

STATION 4

X/C	CPU	CPL
.010	.1577	-.2307
.025	-.0713	-.2295
.050	-.1326	-.2196
.100	-.2090	.0771
.200	-.4395	.1458
.400	-.5421	.1956
.600	-.5270	.1980
.800	-.3486	.2637
.900	-.3087	.2753
.925	-.3499	.3504

STATION 5

X/C	CPU	CPL
.025	-.0247	.3494
.050	-.1123	
.075	-.1839	-.0825
.150	-.2674	-.0733
.300	-.5651	.0585
.450	-.5558	.1628
.600	-.5977	.1814
.750	-.5291	.2683
.800	-.4382	.2589
.850	-.3751	.2583

STATION 6

X/C	CPU	CPL
.025	.1093	
.050	-.0269	-.1624
.100	-.1392	
.200	-.2683	.0903
.300	-.4323	.1382
.400	-.4697	.1377
.500	-.4911	
.600	-.5774	.1389
.700	-.6439	.1333
.800	-.6105	.1152

(f) $\alpha = 6.24^{\circ}$

STATION 1

X/C	CPU	CPL
.005	.0212	.2027
.010	-.1794	.1598
.025	-.2911	.1467
.050	-.3088	.1525
.100	-.3339	.1599
.200	-.3692	.1641
.300	-.4487	.1725
.400	-.4184	.1507
.500	-.3644	.1426
.600	-.3540	.1796
.700	-.3316	.2210
.800	-.2590	-.0249
.900	-.1782	.2524
.950	-.1744	.3061
.970	-.0977	

STATION 2

X/C	CPU	CPL
.005	-.0325	.0905
.010	-.2109	.1228
.025	-.3405	.1629
.050	-.3653	.1693
.100	-.3978	.1944
.200	-.4830	.0373
.300	-.5899	.1974
.400	-.5440	.1909
.500	-.4642	.1945
.600	-.4822	.2425
.700		
.800	-.2960	.2730
.900	-.2504	.3113
.925	-.2712	.3559
.950	-.2345	.3667

STATION 3

X/C	CPU	CPL
.010	-.2666	.1144
.025	-.3451	.1350
.050	-.3681	.1902
.100	-.4171	.1946
.200	-.5409	.2198
.400	-.6034	.2191
.600	-.5275	.2607
.800	-.3283	.2785
.900	-.2729	.3203
.925	-.2979	.3621

STATION 4

X/C	CPU	CPL
.010	-.2402	.0900
.025	-.3690	.1716
.050	-.4376	.2031
.100	-.4008	.1829
.200	-.5819	.2256
.400	-.6346	.2375
.600	-.5816	.2675
.800	-.3708	.2783
.900	-.3188	.3233
.925	-.3525	.3637

STATION 5

X/C	CPU	CPL
.025	-.3787	.3633
.050	-.3909	
.075	-.4264	.1393
.150	-.4099	.1630
.300	-.7028	.1952
.450	-.6487	.2117
.600	-.6591	.2282
.750	-.5882	.2608
.800	-.4845	.2589
.850	-.4213	.2472

STATION 6

X/C	CPU	CPL
.025	-.1841	
.050	-.2484	.0827
.100	-.3142	
.200	-.3708	.1095
.300	-.5417	.1214
.400	-.5786	.1073
.500	-.5975	
.600	-.7001	.1012
.700	-.7886	.0990
.800	-.7898	.0911

TABLE VI. - Continued

(g) $\alpha = 8.37^{o}$

STATION 1

X/C	CPU	CPL
.005	-.3660	.4461
.010	-.5309	.3773
.025	-.5985	.3046
.050	-.5146	.2563
.100	-.4608	.2461
.200	-.4634	.2318
.300	-.5125	.2284
.400	-.4651	.1997
.500	-.3976	.1781
.600	-.3735	.2161
.700	-.3493	.2466
.800	-.2595	-.0212
.900	-.1786	.2643
.950	-.1643	.3159
.970	-.0938	

STATION 2

X/C	CPU	CPL
.005	-.5751	.4003
.010	-.6829	.3494
.025	-.7026	.3089
.050	-.6481	.2914
.100	-.5776	.2643
.200	-.6170	.0713
.300	-.6926	.2411
.400	-.6092	.2289
.500	-.5159	.2245
.600	-.5170	.2679
.700		
.800	-.3040	.2881
.900	-.2410	.3204
.925	-.2548	.3624
.950	-.2101	.3735

STATION 3

X/C	CPU	CPL
.010	-.8231	.4031
.025	-.7547	.3369
.050	-.6766	.3230
.100	-.6039	.2783
.200	-.6780	.2780
.400	-.6681	.2581
.600	-.5769	.2837
.800	-.3503	.2914
.900	-.2800	.3264
.925	-.2989	.3692

STATION 4

X/C	CPU	CPL
.010	-.7977	.4326
.025	-.7898	.3602
.050	-.7552	.3229
.100	-.5940	.2473
.200	-.7518	.2868
.400	-.7366	.2691
.600	-.6336	.2820
.800	-.3972	.2900
.900	-.3319	.3270
.925	-.3493	.3696

STATION 5

X/C	CPU	CPL
.025	-.7810	.3708
.050	-.6997	
.075	-.6701	.2500
.150	-.6440	.2486
.300	-.8467	.2495
.450	-.7450	.2420
.600	-.7499	.2481
.750	-.6523	.2667
.800	-.5543	.2605
.850	-.4823	.2581

STATION 6

X/C	CPU	CPL
.025	-.6474	
.050	-.5667	.2238
.100	-.5116	
.200	-.5112	.1098
.300	-.7039	.1010
.400	-.7537	.0717
.500	-.7840	
.600	-.9025	.0564
.700	-1.0134	.0587
.800	-1.0441	.0568

(h) $\alpha = 10.54^{o}$

STATION 1

X/C	CPU	CPL
.005	-.9181	.5648
.010	-.9702	.5093
.025	-.8497	.4278
.050	-.7416	.3610
.100	-.5897	.3162
.200	-.5603	.2947
.300	-.5807	.2679
.400	-.5107	.2451
.500	-.4217	.2118
.600	-.3932	.2455
.700	-.3590	.2691
.800	-.2629	-.0057
.900	-.1754	.2754
.950	-.1759	.3276
.970	-.1109	

STATION 2

X/C	CPU	CPL
.005	-1.3552	.4673
.010	-1.3126	.5059
.025	-1.1140	.4337
.050	-.9139	.3775
.100	-.7504	.3404
.200	-.7381	.0991
.300	-.7830	.2879
.400	-.6855	.2732
.500	-.5680	.2558
.600	-.5504	.2866
.700		
.800	-.3112	.2973
.900	-.2371	.3245
.925	-.2395	.3644
.950	-.1916	.3743

STATION 3

X/C	CPU	CPL
.010	-1.4561	.5227
.025	-1.3008	.4479
.050	-.9292	.4272
.100	-.8268	.3541
.200	-.8126	.3265
.400	-.7552	.2990
.600	-.6106	.3046
.800	-.3632	.2997
.900	-.2772	.3306
.925	-.2838	.3692

STATION 4

X/C	CPU	CPL
.010	-1.2397	.5330
.025	-1.2935	.4614
.050	-1.0616	.4496
.100	-.8872	.3732
.200	-.9181	.3360
.400	-.8167	.2986
.600	-.6838	.3028
.800	-.4254	.2977
.900	-.3365	.3254
.925	-.3429	.3619

STATION 5

X/C	CPU	CPL
.025	-1.2648	.3602
.050	-1.0705	
.075	-.9731	.3020
.150	-.8472	.3214
.300	-.9710	.3183
.450	-.8440	.2469
.600	-.8290	.2556
.750	-.7042	.2711
.800	-.6043	.2549
.850	-.5234	.2356

STATION 6

X/C	CPU	CPL
.025	-1.4327	
.050	-.9255	.2880
.100	-.7372	
.200	-.7342	.1093
.300	-.8816	.0884
.400	-.9456	.0425
.500	-.9719	
.600	-1.0778	.0237
.700	-1.2119	.0263
.800	-1.2570	.0183

TABLE VI. - Continued

(i) $\alpha = 12.73^{o}$

STATION 1

X/C	CPU	CPL
.005	-1.5661	.6003
.010	-1.4758	.6024
.025	-1.2164	.5220
.050	-.9968	.4476
.100	-.7490	.3826
.200	-.6438	.3554
.300	-.6390	.3306
.400	-.5563	.2830
.500	-.4638	.2539
.600	-.4243	.2766
.700	-.3758	.2918
.800	-.2822	-.0091
.900	-.1935	.2945
.950	-.2106	.3443
.970	-.1349	

STATION 2

X/C	CPU	CPL
.005	-2.7605	.4330
.010	-1.6066	.5577
.025	-1.4582	.5125
.050	-1.1837	.4622
.100	-.9554	.4061
.200	-.8646	.1366
.300	-.8754	.3356
.400	-.7419	.3161
.500	-.6069	.2913
.600	-.5744	.3153
.700		
.800	-.3175	.3144
.900	-.2244	.3261
.925	-.2148	.3680
.950	-.1705	.3776

STATION 3

X/C	CPU	CPL
.010	-2.5863	.5536
.025	-1.6270	.5353
.050	-1.3627	.4849
.100	-1.0885	.4284
.200	-.9690	.3859
.400	-.8278	.3301
.600	-.6429	.3301
.800	-.3723	.3160
.900	-.2704	.3330
.925	-.2494	.3747

STATION 4

X/C	CPU	CPL
.010	-2.9382	.4964
.025	-2.2505	.5261
.050	-1.7319	.5065
.100	-1.1117	.4372
.200	-1.0461	.3879
.400	-.8769	.3362
.600	-.7159	.3250
.800	-.4296	.3158
.900	-.3323	.3261
.925	-.3258	.3477

STATION 5

X/C	CPU	CPL
.025	-1.8107	.3516
.050	-1.8215	
.075	-1.7697	.4302
.150	-1.6117	.4058
.300	-1.0444	.3691
.450	-.8885	.2621
.600	-.8416	.2673
.750	-.7325	.2658
.800	-.6616	.2510
.850	-.5798	.2503

STATION 6

X/C	CPU	CPL
.025	-1.4543	
.050	-1.4595	.3449
.100	-1.4295	
.200	-1.0500	.1015
.300	-.9924	.0615
.400	-1.0935	.0034
.500	-1.1369	
.600	-1.2675	-.0108
.700	-1.4156	-.0082
.800	-1.5099	-.0126

(j) $\alpha = 15.01^{o}$

STATION 1

X/C	CPU	CPL
.005	-2.9454	.5444
.010	-1.8004	.6332
.025	-1.5227	.5851
.050	-1.2015	.5232
.100	-.9174	.4524
.200	-.7529	.3965
.300	-.7241	.3642
.400	-.6216	.3295
.500	-.5183	.2970
.600	-.4612	.3019
.700	-.4139	.3206
.800	-.3122	.0030
.900	-.2022	.3119
.950	-.2296	.3617
.970	-.1441	

STATION 2

X/C	CPU	CPL
.005	-3.1612	.3131
.010	-3.3368	.5451
.025	-2.5846	.5633
.050	-1.6030	.5295
.100	-1.1224	.4803
.200	-.9783	.1661
.300	-.9278	.3837
.400	-.7840	.3496
.500	-.6429	.3190
.600	-.5931	.3429
.700		
.800	-.3203	.3184
.900	-.2055	.3337
.925	-.1843	.3751
.950	-.1467	.3738

STATION 3

X/C	CPU	CPL
.010	-2.6022	.5378
.025	-2.6430	.5774
.050	-2.3849	.5339
.100	-2.2184	.4828
.200	-.8707	.4226
.400	-.8290	.3539
.600	-.6482	.3363
.800	-.3764	.3163
.900	-.2863	.3288
.925	-.2786	.3703

STATION 4

X/C	CPU	CPL
.010	-2.0665	.4578
.025	-2.1143	.5725
.050	-2.0275	.5714
.100	-1.9876	.4928
.200	-1.8538	.4287
.400	-.9838	.3561
.600	-.7015	.3365
.800	-.4633	.3081
.900	-.4015	.3269
.925	-.4346	.3686

STATION 5

X/C	CPU	CPL
.025	-1.5284	.4036
.050	-1.5326	
.075	-1.5429	.3405
.150	-1.4761	.3914
.300	-1.3413	.3395
.450	-1.1619	.2578
.600	-.9741	.2612
.750	-.8189	.2540
.800	-.7772	.2321
.850	-.7048	.1715

STATION 6

X/C	CPU	CPL
.025	-1.3396	
.050	-1.3005	.3382
.100	-1.3608	
.200	-1.3647	.0785
.300	-1.2393	.0261
.400	-1.1554	-.0313
.500	-1.1853	
.600	-1.2693	-.0293
.700	-1.3631	-.0318
.800	-1.3912	-.0338

TABLE VI. - Continued

(k) $\alpha = 17.12^{o}$

STATION 1

X/C	CPU	CPL
.005	-3.9018	.4440
.010	-2.9208	.6365
.025	-1.8841	.6387
.050	-1.4468	.5981
.100	-1.0563	.5214
.200	-.8328	.4616
.300	-.7831	.4217
.400	-.6712	.3730
.500	-.5846	.3417
.600	-.5200	.3431
.700	-.4551	.3457
.800	-.3476	.0056
.900	-.2264	.3220
.950	-.2377	.3718
.970	-.1532	

STATION 2

X/C	CPU	CPL
.005	-2.1953	.2198
.010	-2.2274	.5258
.025	-2.1926	.5976
.050	-2.1488	.5669
.100	-2.1431	.5211
.200	-1.5940	.1911
.300	-.9161	.4136
.400	-.7814	.3685
.500	-.6513	.3594
.600	-.6337	.3657
.700		
.800	-.4022	.3423
.900	-.3334	.3392
.925	-.3702	.3883
.950	-.3415	.3818

STATION 3

X/C	CPU	CPL
.010	-1.7330	.5453
.025	-1.7110	.6145
.050	-1.6969	.5869
.100	-1.6351	.5319
.200	-1.5228	.4697
.400	-1.2009	.3940
.600	-.8740	.3648
.800	-.5965	.3296
.900	-.4843	.3285
.925	-.4647	.3833

STATION 4

X/C	CPU	CPL
.010	-1.4693	.4495
.025	-1.4414	.5952
.050	-1.3773	.5915
.100	-1.4145	.5933
.200	-1.3549	.4666
.400	-1.1768	.3881
.600	-.9317	.3529
.800	-.7245	.3017
.900	-.6163	.3050
.925	-.5910	.3245

STATION 5

X/C	CPU	CPL
.025	-1.1265	.3578
.050	-1.0623	
.075	-1.1147	.4832
.150	-1.1474	.4326
.300	-1.1085	.3684
.450	-1.0343	.2915
.600	-.9192	.2805
.750	-.8013	.2462
.800	-.7580	.2353
.850	-.7320	.1621

STATION 6

X/C	CPU	CPL
.025	-1.0293	
.050	-1.0471	.3870
.100	-1.0589	
.200	-1.0770	.1173
.300	-1.0113	.0725
.400	-.9667	.0196
.500	-.9694	
.600	-.9289	.0210
.700	-.9221	.0082
.800	-.8752	-.0114

(l) $\alpha = 19.22^{o}$

STATION 1

X/C	CPU	CPL
.005	-3.7156	.3656
.010	-3.7521	.6344
.025	-3.3680	.6805
.050	-1.9625	.6355
.100	-.9772	.5610
.200	-.8516	.4956
.300	-.7999	.4405
.400	-.6917	.3851
.500	-.6049	.3369
.600	-.5829	.3380
.700	-.5501	.3388
.800	-.4581	-.0040
.900	-.3270	.2987
.950	-.3248	.3402
.970	-.2372	

STATION 2

X/C	CPU	CPL
.005	-1.6228	.1548
.010	-1.6498	.4843
.025	-1.6051	.5985
.050	-1.6070	.5916
.100	-1.4856	.5470
.200	-1.4044	.2024
.300	-1.2586	.4260
.400	-1.1396	.3779
.500	-1.0217	.3725
.600	-.8995	.3606
.700		
.800	-.6534	.3205
.900	-.5328	.3089
.925	-.5379	.3472
.950	-.5037	.3527

STATION 3

X/C	CPU	CPL
.010	-1.2471	.5372
.025	-1.2714	.6174
.050	-1.2610	.6069
.100	-1.2367	.5448
.200	-1.1844	.4797
.400	-1.0485	.4077
.600	-.9408	.3586
.800	-.7577	.2986
.900	-.6707	.2794
.925	-.6348	.3072

STATION 4

X/C	CPU	CPL
.010	-1.1389	.4454
.025	-1.1339	.6082
.050	-1.1356	.5960
.100	-1.0780	.5936
.200	-1.0829	.4751
.400	-.9874	.3856
.600	-.8842	.3417
.800	-.7780	.2668
.900	-.7052	.2482
.925	-.6974	.2791

STATION 5

X/C	CPU	CPL
.025	-.9057	.3365
.050	-.9187	
.075	-.8999	.3798
.150	-.9235	.4314
.300	-.9672	.3636
.450	-.9127	.2854
.600	-.8615	.2648
.750	-.7779	.2343
.800	-.7567	.1877
.850	-.7434	.1324

STATION 6

X/C	CPU	CPL
.025	-.8457	
.050	-.8502	.3825
.100	-.9096	
.200	-.9111	.1314
.300	-.9139	.0962
.400	-.8480	.0578
.500	-.7969	
.600	-.7712	.0462
.700	-.7479	.0311
.800	-.7513	.0091

TABLE VI. - Concluded

(m) $\alpha = 21.28^{\circ}$

STATION 1

X/C	CPU	CPL
.005	-2.7469	.3794
.010	-2.7595	.6646
.025	-2.5972	.7107
.050	-2.6190	.6684
.100	-2.0387	.5977
.200	-1.0078	.5185
.300	-.8039	.4598
.400	-.7440	.3951
.500	-.6641	.3426
.600	-.6323	.3374
.700	-.6122	.3307
.800	-.5356	-.0308
.900	-.4465	.2782
.950	-.4159	.3057
.970	-.3390	

STATION 2

X/C	CPU	CPL
.005	-1.3519	.3312
.010	-1.3250	.5760
.025	-1.2886	.6282
.050	-1.2674	.5957
.100	-1.2223	.5536
.200	-1.1733	.2088
.300	-1.1293	.4336
.400	-1.0708	.3857
.500	-1.0208	.3595
.600	-.9277	.3500
.700		
.800	-.7627	.2785
.900	-.6738	.2397
.925	-.6515	.2778
.950	-.6391	.2724

STATION 3

X/C	CPU	CPL
.010	-1.1075	.5539
.025	-1.1232	.6095
.050	-1.0969	.5963
.100	-1.0863	.5484
.200	-1.0678	.4892
.400	-.9799	.3888
.600	-.8989	.3492
.800	-.7965	.2625
.900	-.7100	.2226
.925	-.7029	.2481

STATION 4

X/C	CPU	CPL
.010	-1.0301	.4702
.025	-.9965	.6002
.050	-.9916	.5814
.100	-.9878	.5878
.200	-.9475	.4684
.400	-.9142	.3891
.600	-.8800	.3194
.800	-.7986	.2325
.900	-.7568	.2051
.925	-.7583	.2402

STATION 5

X/C	CPU	CPL
.025	-.8354	.2739
.050	-.8578	
.075	-.8224	.3319
.150	-.8506	.4303
.300	-.8294	.3557
.450	-.8137	.2692
.600	-.7921	.2584
.750	-.7608	.2180
.800	-.7759	.1934
.850	-.7454	.1286

STATION 6

X/C	CPU	CPL
.025	-.7454	
.050	-.7637	.3708
.100	-.7871	
.200	-.8168	.1455
.300	-.8102	.1018
.400	-.7811	.0560
.500	-.7368	
.600	-.7141	.0482
.700	-.6992	.0258
.800	-.7245	.0036

TABLE VII.- PRESSURE COEFFICIENTS AT A MACH NUMBER OF 0.20 FOR THE MODEL WITH STRAKE ON. $C_{L,d} = 0.70$

(a) $\alpha = -3.80^{\circ}$

STATION 1

X/C	CPU	CPL
.005	.3018	-.1029
.010	.3048	-.1146
.025	.2469	-.1589
.050	.1820	-.1312
.100	.1360	-.1560
.200	.0384	-.0534
.300	-.0789	-.0024
.400	-.1203	.0307
.500	-.1258	.0524
.600	-.1689	.1059
.700	-.1880	.1694
.800	-.1534	-.0376
.900	-.1254	.2373
.950	-.1741	.2974
.970	-.0887	

STATION 2

X/C	CPU	CPL
.005	.4095	-.8591
.010	.5450	-1.0270
.025	.5092	-1.0713
.050	.4235	-1.1788
.100	.2451	-1.8908
.200	.0521	-.0647
.300	-.1346	.0426
.400	-.1588	.0465
.500	-.1671	.0615
.600	-.2300	.1155
.700		
.800	-.1825	.1033
.900	-.1947	.2396
.925	-.2362	.3079
.950	-.2260	.3509

STATION 3

X/C	CPU	CPL
.010	.5431	-.6905
.025	.5127	-.7085
.050	.4351	-.7167
.100	.2663	-.7638
.200	.0400	-1.5216
.400	-.1797	.1769
.600	-.2536	.2472
.800	-.1815	.2581
.900	-.1846	.2757
.925	-.2319	.3266

STATION 4

X/C	CPU	CPL
.010	.5499	-.4820
.025	.5078	-.4779
.050	.4409	-.4709
.100	.2918	-.4783
.200	.0473	-.4853
.400	-.1785	-.6882
.600	-.3217	-.0985
.800	-.2378	.1842
.900	-.2386	.3147
.925	-.2979	.3132

STATION 5

X/C	CPU	CPL
.025	.4733	.2650
.050	.3885	
.075	.3307	-.2100
.150	.1735	-.2100
.300	-.1368	-.2211
.450	-.2431	-.2629
.600	-.3464	-.3929
.750	-.3670	-.3212
.800	-.3115	-.2852
.850	-.2747	-.2350

STATION 6

X/C	CPU	CPL
.025	.4712	
.050	.3701	-.0303
.100	.2539	
.200	.0775	-.0193
.300	-.0827	-.0318
.400	-.1559	-.0215
.500	-.2159	
.600	-.2836	-.0374
.700	-.3353	-.0668
.800	-.3544	-.1392

(b) $\alpha = -1.91^{\circ}$

STATION 1

X/C	CPU	CPL
.005	.2736	-.0654
.010	.2642	-.0839
.025	.2168	-.1282
.050	.1587	-.1198
.100	.0739	-.1351
.200	-.0170	-.0763
.300	-.1411	-.0170
.400	-.1777	-.0031
.500	-.1800	.0093
.600	-.1999	.0756
.700	-.2107	.1095
.800	-.1791	-.0725
.900	-.1446	.1809
.950	-.1743	.2441
.970	-.0931	

STATION 2

X/C	CPU	CPL
.005	.5101	-.7314
.010	.5159	-.8783
.025	.4343	-.8697
.050	.3192	-1.0135
.100	.1615	-1.5961
.200	-.0293	-.0507
.300	-.1915	.0801
.400	-.2217	.0684
.500	-.2221	.1267
.600	-.2756	.1881
.700		
.800	-.1919	.2446
.900	-.1862	.2773
.925	-.2347	.3277
.950	-.2201	.3377

STATION 3

X/C	CPU	CPL
.010	.5432	-.5907
.025	.4410	-.6050
.050	.3401	-.6004
.100	.1796	-.6406
.200	-.0561	-1.0088
.400	-.2522	.2413
.600	-.2986	.2684
.800	-.2091	.2972
.900	-.1994	.3540
.925	-.2468	.3753

STATION 4

X/C	CPU	CPL
.010	.5296	-.3978
.025	.4392	-.3982
.050	.3320	-.4024
.100	.1807	-.4076
.200	-.0562	-.4094
.400	-.2543	-.3856
.600	-.3828	.3007
.800	-.2897	.3664
.900	-.2665	.4018
.925	-.3251	.4528

STATION 5

X/C	CPU	CPL
.025	.3829	.4128
.050	.2840	
.075	.2056	-.1888
.150	.0529	-.1973
.300	-.2640	-.2165
.450	-.3350	-.3204
.600	-.4163	-.3273
.750	-.4219	-.1768
.800	-.3419	-.1475
.850	-.2943	-.0749

STATION 6

X/C	CPU	CPL
.025	.4070	
.050	.2827	-.0351
.100	.1329	
.200	-.0195	-.0279
.300	-.1690	-.0314
.400	-.2367	-.0292
.500	-.2752	
.600	-.3308	-.1036
.700	-.4024	-.1843
.800	-.4317	-.2488

TABLE VII. - Continued

(c) $\alpha = 0.0^{o}$

STATION 1

X/C	CPU	CPL
.005	.2530	.0397
.010	.2404	.0109
.025	.1830	-.0248
.050	.1061	-.0207
.100	.0368	-.0231
.200	-.0883	.0026
.300	-.1942	.0369
.400	-.2194	.0431
.500	-.2052	.0558
.600	-.2218	.1125
.700	-.2328	.1495
.800	-.1867	-.0350
.900	-.1318	.2070
.950	-.1572	.2506
.970	-.0790	

STATION 2

X/C	CPU	CPL
.005	.5349	-.5440
.010	.4873	-.6734
.025	.3263	-.6998
.050	.2185	-.7240
.100	.0492	-.6900
.200	-.1270	.0382
.300	-.2783	.1534
.400	-.2852	.1544
.500	-.2687	.1509
.600	-.3064	.2156
.700		
.800	-.2006	.2550
.900	-.1978	.3142
.925	-.2428	.3528
.950	-.2212	.3672

STATION 3

X/C	CPU	CPL
.010	.4836	-.4489
.025	.3289	-.4543
.050	.2291	-.4626
.100	.0799	-.5012
.200	-.1478	-.3900
.400	-.3081	.2350
.600	-.3453	.2604
.800	-.2360	.3060
.900	-.2095	.3381
.925	-.2421	.3939

STATION 4

X/C	CPU	CPL
.010	.4834	-.3290
.025	.3422	-.3272
.050	.2512	-.3313
.100	.0895	-.3258
.200	-.1139	-.3382
.400	-.2852	-.0516
.600	-.3958	.1386
.800	-.2693	.2501
.900	-.2623	.3244
.925	-.3041	.3175

STATION 5

X/C	CPU	CPL
.025	.3423	.3230
.050	.2144	
.075	.1309	-.1667
.150	.0051	-.1667
.300	-.3042	-.1962
.450	-.3510	-.1519
.600	-.4212	-.0713
.750	-.3943	.0743
.800	-.3079	.1227
.850	-.2603	.1649

STATION 6

X/C	CPU	CPL
.025	.3893	
.050	.2341	-.0576
.100	.1107	
.200	-.0638	-.0314
.300	-.2011	-.0249
.400	-.2588	-.0119
.500	-.2863	
.600	-.3357	-.0593
.700	-.3742	-.0902
.800	-.3701	-.0731

(d) $\alpha = 1.92^{o}$

STATION 1

X/C	CPU	CPL
.005	.2500	.0659
.010	.2330	.0406
.025	.1615	.0056
.050	.0757	.0296
.100	-.0212	.0354
.200	-.1480	.0620
.300	-.2534	.0751
.400	-.2646	.0793
.500	-.2413	.0897
.600	-.2533	.1419
.700	-.2624	.1728
.800	-.2112	-.0210
.900	-.1460	.2211
.950	-.1571	.2637
.970	-.0843	

STATION 2

X/C	CPU	CPL
.005	.4795	-.3904
.010	.3264	-.4782
.025	.1753	-.4929
.050	.0701	-.4805
.100	-.0604	-.1214
.200	-.2272	.0049
.300	-.3516	.1310
.400	-.3422	.1253
.500	-.3144	.1608
.600	-.3488	.2205
.700		
.800	-.2329	.2599
.900	-.1965	.3091
.925	-.2291	.3509
.950	-.2038	.3624

STATION 3

X/C	CPU	CPL
.010	.3676	-.3348
.025	.1903	-.3297
.050	.0844	-.3428
.100	-.0490	-.3479
.200	-.2466	.1264
.400	-.3770	.1975
.600	-.3853	.2518
.800	-.2444	.2809
.900	-.2180	.3215
.925	-.2578	.3696

STATION 4

X/C	CPU	CPL
.010	.4011	-.2548
.025	.1856	-.2525
.050	.0929	-.2552
.100	-.0565	-.2596
.200	-.2579	-.2397
.400	-.3558	.2577
.600	-.4454	.2521
.800	-.3009	.2481
.900	-.2735	.2476
.925	-.3145	.2417

STATION 5

X/C	CPU	CPL
.025	.2151	.2547
.050	.0802	
.075	.0124	-.1224
.150	-.1086	-.1494
.300	-.4107	-.1536
.450	-.4306	.0621
.600	-.4939	.2671
.750	-.4565	.3439
.800	-.3528	.3410
.850	-.3042	.3201

STATION 6

X/C	CPU	CPL
.025	.2733	
.050	.1433	-.0590
.100	.0075	
.200	-.1433	-.0488
.300	-.2835	-.0900
.400	-.3417	-.1219
.500	-.3862	
.600	-.4468	-.0506
.700	-.4831	.0024
.800	-.4637	.1533

TABLE VII. - Continued

(e) $\alpha = 3.90^{\circ}$

STATION 1

X/C	CPU	CPL
.005	.2327	.1059
.010	.2240	.1009
.025	.1698	.0547
.050	.0964	.0751
.100	-.0221	.0848
.200	-.1700	.1061
.300	-.2770	.1237
.400	-.3003	.1231
.500	-.2645	.1231
.600	-.2728	.1644
.700	-.2665	.1950
.800	-.2067	-.0105
.900	-.1385	.2254
.950	-.1782	.2868
.970	-.0899	

STATION 2

X/C	CPU	CPL
.005	.3341	-.2366
.010	.1494	-.2824
.025	-.0106	-.1863
.050	-.0942	.0313
.100	-.1843	.1066
.200	-.2989	.0275
.300	-.4232	.1646
.400	-.3892	.1688
.500	-.3406	.1827
.600	-.3631	.2422
.700		
.800	-.2163	.2801
.900	-.1776	.3235
.925	-.1845	.3634
.950	-.1509	.3835

STATION 3

X/C	CPU	CPL
.010	.1698	-.1935
.025	-.0212	-.1869
.050	-.0921	-.0502
.100	-.1885	.1415
.200	-.3488	.1925
.400	-.4353	.2259
.600	-.4168	.2669
.800	-.2522	.2997
.900	-.2125	.3330
.925	-.2369	.3680

STATION 4

X/C	CPU	CPL
.010	.2011	-.1615
.025	-.0182	-.1670
.050	-.0867	-.1443
.100	-.2073	-.1071
.200	-.3783	.0438
.400	-.4636	.1799
.600	-.4827	.1980
.800	-.3151	.2075
.900	-.2693	.2180
.925	-.3078	.2817

STATION 5

X/C	CPU	CPL
.025	.0321	.2770
.050	-.0865	
.075	-.1432	-.1109
.150	-.2387	-.0708
.300	-.5062	.1637
.450	-.5034	.2347
.600	-.5345	.2678
.750	-.4744	.2913
.800	-.3814	.2952
.850	-.3279	.2732

STATION 6

X/C	CPU	CPL
.025	.1559	
.050	.0099	-.2895
.100	-.1008	
.200	-.2541	.0856
.300	-.3806	.1013
.400	-.4247	.1051
.500	-.4432	
.600	-.5198	.1611
.700	-.5757	.1733
.800	-.5452	.1566

(f) $\alpha = 5.93^{\circ}$

STATION 1

X/C	CPU	CPL
.005	.0621	.1387
.010	.0493	.1177
.025	.0428	.0868
.050	.0322	.1199
.100	-.0683	.1219
.200	-.1884	.1473
.300	-.2889	.1594
.400	-.3064	.1554
.500	-.2779	.1482
.600	-.2789	.1867
.700	-.2820	.2159
.800	-.2201	-.0150
.900	-.1588	.2496
.950	-.2104	.2939
.970	-.1182	

STATION 2

X/C	CPU	CPL
.005	.0373	.0268
.010	-.1664	.1034
.025	-.2498	.1591
.050	-.2775	.1756
.100	-.2871	.1795
.200	-.3950	.0426
.300	-.4830	.1989
.400	-.4363	.2046
.500	-.3661	.2218
.600	-.3716	.2530
.700		
.800	-.2074	.2952
.900	-.1580	.3296
.925	-.1655	.3734
.950	-.1318	.3845

STATION 3

X/C	CPU	CPL
.010	-.1652	.1394
.025	-.2599	.1736
.050	-.3140	.2180
.100	-.3346	.2149
.200	-.4539	.2549
.400	-.4938	.2514
.600	-.4355	.2921
.800	-.2548	.3087
.900	-.2045	.3459
.925	-.2195	.3872

STATION 4

X/C	CPU	CPL
.010	-.1523	.1261
.025	-.3499	.1959
.050	-.3472	.2442
.100	-.3867	.2338
.200	-.5091	.2563
.400	-.5412	.2630
.600	-.5139	.2947
.800	-.3368	.3044
.900	-.2720	.3452
.925	-.3046	.3846

STATION 5

X/C	CPU	CPL
.025	-.2868	.3752
.050	-.3545	
.075	-.3586	.1944
.150	-.3829	.1956
.300	-.6143	.2246
.450	-.5753	.2505
.600	-.5950	.2739
.750	-.5098	.3031
.800	-.4333	.2880
.850	-.3710	.2791

STATION 6

X/C	CPU	CPL
.025	-.1346	
.050	-.2116	.0485
.100	-.2665	
.200	-.3553	.1297
.300	-.4915	.1662
.400	-.4997	.1428
.500	-.5387	
.600	-.6143	.1431
.700	-.6886	.1428
.800	-.6969	.1402

TABLE VII. - Continued

(g) $\alpha = 7.98^{o}$

STATION 1

X/C	CPU	CPL
.005	-.1187	.1695
.010	-.1285	.1474
.025	-.1381	.1238
.050	-.1402	.1349
.100	-.1944	.1634
.200	-.2734	.1833
.300	-.3477	.1994
.400	-.3691	.1802
.500	-.3202	.1788
.600	-.3160	.1980
.700	-.3189	.2375
.800	-.2577	-.0208
.900	-.1859	.2596
.950	-.2333	.3094
.970	-.1407	

STATION 2

X/C	CPU	CPL
.005	-.3905	.3102
.010	-.5155	.3256
.025	-.5170	.2802
.050	-.4779	.2709
.100	-.4237	.2582
.200	-.4908	.0646
.300	-.5413	.2324
.400	-.4847	.2327
.500	-.4005	.2272
.600	-.3950	.2895
.700		
.800	-.2179	.2957
.900	-.1635	.3365
.925	-.1790	.3690
.950	-.1576	.3833

STATION 3

X/C	CPU	CPL
.010	-.6135	.3668
.025	-.6054	.3461
.050	-.5750	.3281
.100	-.5084	.2903
.200	-.5626	.3002
.400	-.5548	.2781
.600	-.4557	.3041
.800	-.2571	.3138
.900	-.1859	.3502
.925	-.1918	.3795

STATION 4

X/C	CPU	CPL
.010	-.6456	.4276
.025	-.6980	.3981
.050	-.6135	.3321
.100	-.5947	.3296
.200	-.6455	.3108
.400	-.6218	.2901
.600	-.5671	.3108
.800	-.3335	.3136
.900	-.2743	.3509
.925	-.2955	.3974

STATION 5

X/C	CPU	CPL
.025	-.7062	.3887
.050	-.6418	
.075	-.6226	.1520
.150	-.5955	.2137
.300	-.7506	.2400
.450	-.6667	.2524
.600	-.6659	.2522
.750	-.5758	.2767
.800	-.4876	.2864
.850	-.4122	.2754

STATION 6

X/C	CPU	CPL
.025	-.5239	
.050	-.4725	.2258
.100	-.4501	
.200	-.5067	.1417
.300	-.6122	.1431
.400	-.6599	.1076
.500	-.7104	
.600	-.8053	.1032
.700	-.9239	.1144
.800	-.9308	.1034

(h) $\alpha = 10.06^{o}$

STATION 1

X/C	CPU	CPL
.005	-.2685	.1924
.010	-.2768	.1868
.025	-.3123	.1495
.050	-.3025	.1774
.100	-.3440	.1883
.200	-.3841	.2323
.300	-.4141	.2342
.400	-.4174	.2217
.500	-.3592	.2062
.600	-.3380	.2328
.700	-.3372	.2659
.800	-.2679	-.0158
.900	-.1887	.2770
.950	-.2556	.3223
.970	-.1596	

STATION 2

X/C	CPU	CPL
.005	-.9389	.4068
.010	-.9317	.4391
.025	-.8102	.3811
.050	-.6826	.3515
.100	-.5100	.3139
.200	-.5497	.0900
.300	-.5718	.2803
.400	-.4967	.2707
.500	-.4192	.2772
.600	-.4007	.3201
.700		
.800	-.2210	.3217
.900	-.1667	.3494
.925	-.1960	.3923
.950	-.1809	.3954

STATION 3

X/C	CPU	CPL
.010	-1.1915	.5191
.025	-.9826	.4602
.050	-.8586	.4175
.100	-.6797	.3658
.200	-.6603	.3480
.400	-.6022	.3164
.600	-.4681	.3211
.800	-.2458	.3289
.900	-.1641	.3604
.925	-.1624	.3945

STATION 4

X/C	CPU	CPL
.010	-1.2082	.5599
.025	-1.0336	.5629
.050	-.9039	.4339
.100	-.7348	.4280
.200	-.7592	.3552
.400	-.6790	.3181
.600	-.5770	.3305
.800	-.3343	.3217
.900	-.2539	.3575
.925	-.2551	.3949

STATION 5

X/C	CPU	CPL
.025	-.9637	.4035
.050	-.8947	
.075	-.8472	.2121
.150	-.7523	.2929
.300	-.8726	.3026
.450	-.7450	.2870
.600	-.7180	.2845
.750	-.5977	.3053
.800	-.5088	.2845
.850	-.4417	.2679

STATION 6

X/C	CPU	CPL
.025	-1.3582	
.050	-.6460	.3078
.100	-.6336	
.200	-.6322	.1301
.300	-.7618	.1235
.400	-.8104	.0676
.500	-.8649	
.600	-.9508	.0625
.700	-1.0455	.0680
.800	-1.0690	.0694

TABLE VII. - Continued

(i) $\alpha = 12.18^{\circ}$

STATION 1

X/C	CPU	CPL
.005	-.4293	.2224
.010	-.4294	.2117
.025	-.4584	.1852
.050	-.4898	.2114
.100	-.5374	.2238
.200	-.5425	.2610
.300	-.5196	.2635
.400	-.4773	.2480
.500	-.4172	.2339
.600	-.3780	.2532
.700	-.3822	.2902
.800	-.2982	-.0034
.900	-.2031	.2650
.950	-.2332	.3167
.970	-.1406	

STATION 2

X/C	CPU	CPL
.005	-1.5869	.3866
.010	-1.4007	.5087
.025	-1.0559	.4590
.050	-.8028	.4109
.100	-.6517	.3692
.200	-.5968	.1071
.300	-.6025	.3126
.400	-.5366	.2963
.500	-.4553	.2971
.600	-.4263	.3201
.700		
.800	-.2260	.3306
.900	-.1666	.3409
.925	-.1970	.3871
.950	-.1887	.3970

STATION 3

X/C	CPU	CPL
.010	-2.2101	.5591
.025	-1.2662	.5213
.050	-1.0496	.4842
.100	-.8503	.4260
.200	-.7554	.3869
.400	-.6230	.3423
.600	-.4837	.3440
.800	-.2734	.3355
.900	-.2084	.3526
.925	-.2128	.3822

STATION 4

X/C	CPU	CPL
.010	-2.7789	.4561
.025	-1.4632	.4707
.050	-1.1832	.4642
.100	-.9486	.4637
.200	-.8872	.4529
.400	-.7189	.4208
.600	-.5809	.3460
.800	-.3320	.3266
.900	-.2392	.3408
.925	-.2014	.3792

STATION 5

X/C	CPU	CPL
.025	-1.8199	.3847
.050	-1.7769	
.075	-1.6928	.1814
.150	-1.1592	.3126
.300	-.8683	.3178
.450	-.7849	.3037
.600	-.7545	.3023
.750	-.6279	.3075
.800	-.5414	.2804
.850	-.4663	.2496

STATION 6

X/C	CPU	CPL
.025	-1.3450	
.050	-1.3456	.3535
.100	-1.2015	
.200	-.8501	.1305
.300	-.8665	.1000
.400	-.9526	.0367
.500	-.9854	
.600	-1.0966	.0131
.700	-1.2364	.0308
.800	-1.3193	.0394

(j) $\alpha = 14.37^{\circ}$

STATION 1

X/C	CPU	CPL
.005	-.5475	.2630
.010	-.5808	.2585
.025	-.6127	.2278
.050	-.6191	.2530
.100	-.7014	.2655
.200	-.6782	.3100
.300	-.6295	.3197
.400	-.5679	.2896
.500	-.4927	.2627
.600	-.4196	.2890
.700	-.4092	.2959
.800	-.3236	.0081
.900	-.2179	.2920
.950	-.2052	.3374
.970	-.1306	

STATION 2

X/C	CPU	CPL
.005	-2.7298	.2917
.010	-1.9757	.4998
.025	-1.2173	.5034
.050	-.9868	.4546
.100	-.7693	.4246
.200	-.7014	.1354
.300	-.6612	.3515
.400	-.5882	.3266
.500	-.4769	.3270
.600	-.4446	.3534
.700		
.800	-.2417	.3454
.900	-.1678	.3659
.925	-.1845	.3984
.950	-.1536	.4101

STATION 3

X/C	CPU	CPL
.010	-2.7852	.5368
.025	-2.6868	.5524
.050	-1.7005	.5424
.100	-.8219	.4803
.200	-.7873	.4316
.400	-.6210	.3768
.600	-.4903	.3714
.800	-.3217	.3602
.900	-.2524	.3678
.925	-.2801	.4146

STATION 4

X/C	CPU	CPL
.010	-2.1881	.4557
.025	-2.1842	.5865
.050	-2.2101	.5602
.100	-2.1177	.5560
.200	-.7651	.5574
.400	-.6898	.3817
.600	-.5814	.3701
.800	-.3295	.3565
.900	-.2396	.3617
.925	-.2226	.3989

STATION 5

X/C	CPU	CPL
.025	-1.5665	.3950
.050	-1.5513	
.075	-1.5113	.4452
.150	-1.4649	.4523
.300	-1.3249	.3956
.450	-1.0512	.3034
.600	-.9120	.2993
.750	-.7533	.2951
.800	-.6535	.2729
.850	-.5495	.2482

STATION 6

X/C	CPU	CPL
.025	-1.2401	
.050	-1.2567	.3784
.100	-1.2409	
.200	-1.1975	.1015
.300	-1.0712	.0606
.400	-1.0338	.0024
.500	-1.1044	
.600	-1.2483	.0079
.700	-1.3978	.0193
.800	-1.4434	.0166

TABLE VII.- Continued

(k) $\alpha = 16.44^{o}$

STATION 1

X/C	CPU	CPL
.005	-.6989	.2797
.010	-.7444	.2692
.025	-.7781	.2530
.050	-.8044	.2766
.100	-.8551	.2860
.200	-.8275	.3197
.300	-.7592	.3333
.400	-.6659	.3153
.500	-.5336	.2962
.600	-.4656	.3003
.700	-.4486	.3134
.800	-.3631	-.0035
.900	-.2575	.2869
.950	-.2668	.3415
.970	-.1672	

STATION 2

X/C	CPU	CPL
.005	-2.7756	.1420
.010	-2.8843	.4590
.025	-3.1934	.5243
.050	-.6475	.5061
.100	-.7324	.4676
.200	-.6740	.1366
.300	-.7027	.3821
.400	-.6336	.3527
.500	-.5243	.3540
.600	-.4970	.3709
.700		
.800	-.2680	.3564
.900	-.1831	.3638
.925	-.1772	.4039
.950	-.1294	.3931

STATION 3

X/C	CPU	CPL
.010	-2.4466	.4772
.025	-2.4494	.5793
.050	-2.5124	.5823
.100	-2.9107	.5234
.200	-.5184	.4573
.400	-.6295	.4078
.600	-.5075	.3817
.800	-.2827	.3661
.900	-.2230	.3656
.925	-.2274	.4178

STATION 4

X/C	CPU	CPL
.010	-2.0208	.3967
.025	-2.0298	.5857
.050	-2.0652	.5808
.100	-2.1392	.5808
.200	-2.1149	.5727
.400	-.6243	.4939
.600	-.5535	.3753
.800	-.3810	.3444
.900	-.3272	.3589
.925	-.3638	.3998

STATION 5

X/C	CPU	CPL
.025	-1.4497	.4318
.050	-1.4374	
.075	-1.4321	.3164
.150	-1.3642	.4078
.300	-1.2649	.3995
.450	-1.1889	.3191
.600	-1.1200	.3080
.750	-.9831	.2850
.800	-.9196	.2660
.850	-.8263	.1989

STATION 6

X/C	CPU	CPL
.025	-1.1511	
.050	-1.1632	.3814
.100	-1.1561	
.200	-1.1386	.1036
.300	-1.0850	.1067
.400	-1.0534	.0564
.500	-1.0673	
.600	-1.0904	.0460
.700	-1.0615	.0557
.800	-.9510	.0429

(l) $\alpha = 18.52^{o}$

STATION 1

X/C	CPU	CPL
.005	-.8422	.3123
.010	-.8625	.2981
.025	-.9227	.2872
.050	-.9513	.3037
.100	-1.0276	.3323
.200	-1.0004	.3706
.300	-.8808	.3642
.400	-.7599	.3518
.500	-.6396	.3216
.600	-.5508	.3253
.700	-.5140	.3352
.800	-.4026	-.0099
.900	-.2900	.3003
.950	-.2839	.3489
.970	-.2022	

STATION 2

X/C	CPU	CPL
.005	-2.8810	.0270
.010	-2.9228	.4036
.025	-3.7477	.5342
.050	-2.7613	.5289
.100	-.6611	.5026
.200	-.6984	.1648
.300	-.7090	.4232
.400	-.6840	.3882
.500	-.5926	.3755
.600	-.5431	.3855
.700		
.800	-.3164	.3591
.900	-.2187	.3605
.925	-.1806	.3950
.950	-.1367	.3833

STATION 3

X/C	CPU	CPL
.010	-2.4550	.4396
.025	-2.4977	.5804
.050	-2.6147	.6000
.100	-3.4540	.5601
.200	-.6840	.4958
.400	-.6238	.4239
.600	-.5629	.3971
.800	-.3537	.3597
.900	-.2674	.3663
.925	-.2729	.4095

STATION 4

X/C	CPU	CPL
.010	-2.0018	.3271
.025	-2.0046	.5773
.050	-2.0465	.6059
.100	-2.0858	.6059
.200	-2.2162	.6020
.400	-1.2113	.4134
.600	-.7148	.3865
.800	-.4829	.3696
.900	-.4168	.3443
.925	-.4829	.3706

STATION 5

X/C	CPU	CPL
.025	-1.2922	.3692
.050	-1.2748	
.075	-1.2785	.5479
.150	-1.2577	.4739
.300	-1.1603	.4105
.450	-1.1450	.3278
.600	-1.1259	.3122
.750	-1.0358	.2753
.800	-.9923	.2380
.850	-.9217	.1839

STATION 6

X/C	CPU	CPL
.025	-1.0612	
.050	-1.0866	.4266
.100	-1.0695	
.200	-1.0573	.1744
.300	-1.0073	.1234
.400	-.9856	.0728
.500	-.9621	
.600	-.9506	.0700
.700	-.9200	.0617
.800	-.8785	.0424

TABLE VII. - Concluded

(m) $\alpha = 20.60^{\circ}$

STATION 1

X/C	CPU	CPL
.005	-.9586	.3566
.010	-1.0022	.3479
.025	-1.0697	.3228
.050	-1.0931	.3446
.100	-1.1731	.3755
.200	-1.1212	.4122
.300	-.9756	.4155
.400	-.8458	.3900
.500	-.6969	.3425
.600	-.5912	.3662
.700	-.5292	.3729
.800	-.4337	.0099
.900	-.3141	.3250
.950	-.2880	.3762
.970	-.1941	

STATION 2

X/C	CPU	CPL
.005	-3.0991	-.0762
.010	-3.1488	.3631
.025	-3.7095	.5365
.050	-4.3858	.5607
.100	-.6991	.5342
.200	-.7286	.1716
.300	-.7569	.4535
.400	-.7420	.4214
.500	-.6539	.3955
.600	-.5917	.4054
.700		
.800	-.3706	.3737
.900	-.2618	.3628
.925	-.2478	.3943
.950	-.2121	.3918

STATION 3

X/C	CPU	CPL
.010	-2.6108	.3953
.025	-2.6628	.5788
.050	-2.7444	.6186
.100	-3.5323	.6035
.200	-1.1705	.5304
.400	-.6871	.4474
.600	-.5847	.4142
.800	-.3838	.3674
.900	-.2969	.3547
.925	-.3229	.3960

STATION 4

X/C	CPU	CPL
.010	-1.8444	.2936
.025	-1.8665	.5999
.050	-1.8934	.6223
.100	-1.9703	.6248
.200	-2.1054	.6267.
.400	-1.4481	.4852
.600	-.9227	.4226
.800	-.5864	.3700
.900	-.5179	.3363
.925	-.5248	.3526

STATION 5

X/C	CPU	CPL
.025	-1.2444	.3745
.050	-1.2339	
.075	-1.2030	.5268
.150	-1.2010	.5081
.300	-1.1157	.4367
.450	-1.1314	.3323
.600	-1.0901	.3243
.750	-1.0195	.2893
.800	-1.0047	.2495
.850	-.9333	.1940

STATION 6

X/C	CPU	CPL
.025	-.9827	
.050	-1.0078	.4407
.100	-1.0071	
.200	-.9763	.1905
.300	-.9457	.1356
.400	-.9134	.0770
.500	-.8864	
.600	-.8581	.0694
.700	-.8265	.0676
.800	-.8035	.0465

TABLE VIII.- PRESSURE COEFFICIENTS AT A MACH NUMBER OF 0.40 FOR THE MODEL WITH STRAKE ON. $C_{L,d} = 0.70$

(a) $\alpha = -3.94^{\circ}$

STATION 1

X/C	CPU	CPL
.005	.3166	-.1078
.010	.3009	-.1459
.025	.2421	-.1997
.050	.1890	-.1576
.100	.1286	-.2066
.200	.0210	-.1116
.300	-.1051	-.0305
.400	-.1516	.0072
.500	-.1595	.0303
.600	-.1964	.0957
.700	-.2342	.1528
.800	-.2035	-.0540
.900	-.1673	.2229
.950	-.2154	.2884
.970	-.1340	

STATION 2

X/C	CPU	CPL
.005	.4039	-.8973
.010	.5191	-1.0391
.025	.4956	-1.0794
.050	.3984	-1.2065
.100	.2221	-1.7874
.200	.0263	-.1660
.300	-.1514	-.0191
.400	-.2006	.0118
.500	-.2103	.0341
.600	-.2896	.0476
.700		
.800	-.2202	.1134
.900	-.2323	.2680
.925	-.2653	.3312
.950	-.2707	.3533

STATION 3

X/C	CPU	CPL
.010	.5262	-.7500
.025	.4976	-.7457
.050	.4071	-.7712
.100	.2510	-.8216
.200	.0173	-1.5934
.400	-.2256	.0777
.600	-.3089	.2237
.800	-.2448	.2053
.900	-.2491	.2625
.925	-.3083	.2931

STATION 4

X/C	CPU	CPL
.010	.5251	-.5266
.025	.4832	-.5305
.050	.4079	-.5277
.100	.2629	-.5307
.200	.0100	-.5265
.400	-.2352	-.9393
.600	-.3353	-.1694
.800	-.2619	.2888
.900	-.2596	.3474
.925	-.3213	.4017

STATION 5

X/C	CPU	CPL
.025	.4750	.2533
.050	.3884	
.075	.3153	-.1857
.150	.1779	-.2122
.300	-.1525	-.2515
.450	-.2584	-.2242
.600	-.3860	-.3421
.750	-.4154	-.4402
.800	-.3563	-.4399
.850	-.3229	-.3594

STATION 6

X/C	CPU	CPL
.025	.4644	
.050	.3704	-.0948
.100	.2397	
.200	.0685	-.0667
.300	-.1025	-.0712
.400	-.1738	-.0817
.500	-.2258	
.600	-.2996	-.0970
.700	-.3553	-.1146
.800	-.3751	-.1531

(b) $\alpha = -1.95^{\circ}$

STATION 1

X/C	CPU	CPL
.005	.2756	-.0479
.010	.2654	-.0695
.025	.2092	-.1098
.050	.1503	-.1089
.100	.0754	-.1324
.200	-.0389	-.0600
.300	-.1617	.0025
.400	-.1963	.0112
.500	-.1975	.0290
.600	-.2308	.0915
.700	-.2522	.1529
.800	-.2142	-.0461
.900	-.1626	.2170
.950	-.2096	.2737
.970	-.1288	

STATION 2

X/C	CPU	CPL
.005	.4948	-.7356
.010	.5225	-.8563
.025	.4196	-.8456
.050	.3100	-.9775
.100	.1423	-1.5214
.200	-.0544	-.0513
.300	-.2288	.1001
.400	-.2627	.0859
.500	-.2540	.0867
.600	-.3192	.1620
.700		
.800	-.2311	.1916
.900	-.2365	.2499
.925	-.2826	.3046
.950	-.2609	.3284

STATION 3

X/C	CPU	CPL
.010	.5252	-.6209
.025	.4307	-.6221
.050	.3236	-.6247
.100	.1694	-.6925
.200	-.0631	-1.2404
.400	-.2894	.2194
.600	-.3485	.2440
.800	-.2558	.2735
.900	-.2407	.3311
.925	-.2945	.3797

STATION 4

X/C	CPU	CPL
.010	.5186	-.4336
.025	.4141	-.4353
.050	.3284	-.4352
.100	.1882	-.4362
.200	-.0750	-.4986
.400	-.3039	-.5190
.600	-.3830	.1120
.800	-.2775	.3406
.900	-.2623	.3868
.925	-.3208	.4385

STATION 5

X/C	CPU	CPL
.025	.4243	.3015
.050	.3168	
.075	.2337	-.2048
.150	.1020	-.2310
.300	-.2329	-.2408
.450	-.3205	-.3687
.600	-.4207	-.3713
.750	-.4149	-.2864
.800	-.3390	-.2449
.850	-.2860	-.1466

STATION 6

X/C	CPU	CPL
.025	.4311	
.050	.3246	-.0802
.100	.1777	
.200	.0073	-.0718
.300	-.1565	-.0823
.400	-.2181	-.0840
.500	-.2613	
.600	-.3309	-.1267
.700	-.4040	-.2078
.800	-.4394	-.2991

TABLE VIII.- Continued

(c) $\alpha = 0.05^{o}$

STATION 1

X/C	CPU	CPL
.005	.2463	.0195
.010	.2343	.0012
.025	.1695	-.0411
.050	.1096	-.0245
.100	.0085	-.0351
.200	-.1158	.0016
.300	-.2278	.0267
.400	-.2531	.0336
.500	-.2439	.0438
.600	-.2620	.1055
.700	-.2780	.1560
.800	-.2300	-.0336
.900	-.1751	.2138
.950	-.1986	.2537
.970	-.1188	

STATION 2

X/C	CPU	CPL
.005	.5185	-.5795
.010	.4550	-.6939
.025	.3143	-.7170
.050	.1811	-.7667
.100	.0343	-.7899
.200	-.1446	.0062
.300	-.3211	.1233
.400	-.3272	.1170
.500	-.3048	.1140
.600	-.3645	.1808
.700		
.800	-.2468	.2414
.900	-.2366	.2916
.925	-.2804	.3369
.950	-.2555	.3514

STATION 3

X/C	CPU	CPL
.010	.4702	-.4902
.025	.3089	-.4945
.050	.2122	-.5010
.100	.0415	-.5574
.200	-.1721	-.5457
.400	-.3539	.2262
.600	-.3893	.2344
.800	-.2694	.2679
.900	-.2484	.3237
.925	-.2982	.3746

STATION 4

X/C	CPU	CPL
.010	.4716	-.3517
.025	.2968	-.3505
.050	.2114	-.3561
.100	.0696	-.3556
.200	-.1844	-.4361
.400	-.3731	-.1501
.600	-.4324	.2333
.800	-.3006	.3080
.900	-.2802	.3541
.925	-.3310	.4069

STATION 5

X/C	CPU	CPL
.025	.3355	.2917
.050	.2100	
.075	.1237	-.1662
.150	.0074	-.1977
.300	-.3400	-.2212
.450	-.3897	-.2420
.600	-.4675	-.2024
.750	-.4256	-.0197
.800	-.3429	.0331
.850	-.2851	.1442

STATION 6

X/C	CPU	CPL
.025	.3689	
.050	.2416	-.0791
.100	.0926	
.200	-.0603	-.0773
.300	-.2277	-.0791
.400	-.2750	-.0935
.500	-.2969	
.600	-.3618	-.1532
.700	-.4138	-.1973
.800	-.4049	-.2045

(d) $\alpha = 2.09^{o}$

STATION 1

X/C	CPU	CPL
.005	.2582	.0651
.010	.2387	.0504
.025	.1548	.0121
.050	.0737	.0222
.100	-.0408	.0243
.200	-.1776	.0537
.300	-.2823	.0747
.400	-.3010	.0702
.500	-.2864	.0788
.600	-.2941	.1289
.700	-.2971	.1744
.800	-.2371	-.0295
.900	-.1745	.2214
.950	-.1987	.2650
.970	-.1167	

STATION 2

X/C	CPU	CPL
.005	.4551	-.4101
.010	.3282	-.4849
.025	.1362	-.5191
.050	.0361	-.5034
.100	-.0973	-.1081
.200	-.2596	-.0099
.300	-.3975	.1162
.400	-.3937	.1280
.500	-.3504	.1354
.600	-.4017	.1943
.700		
.800	-.2606	.2402
.900	-.2328	.2872
.925	-.2623	.3294
.950	-.2342	.3453

STATION 3

X/C	CPU	CPL
.010	.3478	-.3648
.025	.1729	-.3658
.050	.0408	-.3772
.100	-.0957	-.3993
.200	-.2833	.0973
.400	-.4308	.1664
.600	-.4339	.2234
.800	-.2854	.2614
.900	-.2568	.3054
.925	-.2993	.3518

STATION 4

X/C	CPU	CPL
.010	.3576	-.2770
.025	.1575	-.2844
.050	.0589	-.2843
.100	-.0546	-.2872
.200	-.3042	-.2808
.400	-.4515	.2213
.600	-.4786	.2400
.800	-.3292	.2519
.900	-.2955	.2758
.925	-.3460	.3053

STATION 5

X/C	CPU	CPL
.025	.1841	.3120
.050	.0687	
.075	-.0056	-.1150
.150	-.1047	-.1667
.300	-.4477	-.1780
.450	-.4717	-.0054
.600	-.5269	.1072
.750	-.4771	.3306
.800	-.3878	.3119
.850	-.3314	.2934

STATION 6

X/C	CPU	CPL
.025	.2663	
.050	.1212	-.0693
.100	-.0045	
.200	-.1545	-.1087
.300	-.3182	-.1369
.400	-.3720	-.1552
.500	-.4098	
.600	-.4828	-.0739
.700	-.5363	-.0201
.800	-.4942	.1328

TABLE VIII.- Continued

(e) $\alpha = 4.16^{o}$

STATION 1

X/C	CPU	CPL
.005	.2148	.1028
.010	.2152	.0865
.025	.1544	.0488
.050	.0813	.0682
.100	-.0488	.0745
.200	-.2050	.1007
.300	-.3238	.1106
.400	-.3441	.1121
.500	-.3153	.1137
.600	-.3203	.1589
.700	-.3198	.1987
.800	-.2606	-.0188
.900	-.1900	.2354
.950	-.2329	.2865
.970	-.1379	

STATION 2

X/C	CPU	CPL
.005	.2940	-.3640
.010	.1091	-.4124
.025	-.0489	-.0847
.050	-.1349	.0323
.100	-.2232	.0873
.200	-.3535	.0102
.300	-.4801	.1480
.400	-.4580	.1554
.500	-.3968	.1621
.600	-.4212	.2189
.700		
.800	-.2606	.2568
.900	-.2166	.2951
.925	-.2259	.3429
.950	-.1849	.3624

STATION 3

X/C	CPU	CPL
.010	.1238	-.3266
.025	-.0570	-.2584
.050	-.1373	.0515
.100	-.2192	.0954
.200	-.4061	.1567
.400	-.5033	.1884
.600	-.4734	.2395
.800	-.2969	.2713
.900	-.2535	.3109
.925	-.2835	.3460

STATION 4

X/C	CPU	CPL
.010	.1615	-.2065
.025	-.0502	-.2350
.050	-.1408	-.1917
.100	-.2181	.0389
.200	-.4360	.1283
.400	-.5388	.1949
.600	-.5232	.1917
.800	-.3434	.2556
.900	-.2989	.2824
.925	-.3397	.3504

STATION 5

X/C	CPU	CPL
.025	-.0043	.3465
.050	-.1135	
.075	-.1746	-.1046
.150	-.2521	-.0095
.300	-.5612	.1749
.450	-.5541	.2123
.600	-.5866	.2390
.750	-.5243	.2781
.800	-.4276	.2721
.850	-.3702	.2454

STATION 6

X/C	CPU	CPL
.025	.1115	
.050	-.0416	-.1606
.100	-.1447	
.200	-.2637	.0075
.300	-.4249	.0691
.400	-.4577	.1158
.500	-.4827	
.600	-.5696	.1517
.700	-.6394	.1331
.800	-.6073	.1674

(f) $\alpha = 6.31^{o}$

STATION 1

X/C	CPU	CPL
.005	.0107	.1379
.010	.0058	.1229
.025	-.0012	.0792
.050	-.0187	.1058
.100	-.1053	.1134
.200	-.2392	.1507
.300	-.3529	.1614
.400	-.3772	.1514
.500	-.3514	.1485
.600	-.3537	.1801
.700	-.3520	.2179
.800	-.2880	-.0151
.900	-.2082	.2513
.950	-.2665	.2993
.970	-.1687	

STATION 2

X/C	CPU	CPL
.005	-.0601	.0813
.010	-.2203	.0892
.025	-.3107	.1429
.050	-.3550	.1600
.100	-.3612	.1848
.200	-.4661	.0431
.300	-.5526	.1958
.400	-.5115	.1933
.500	-.4303	.1820
.600	-.4430	.2363
.700		
.800	-.2616	.2608
.900	-.2078	.3022
.925	-.2092	.3463
.950	-.1667	.3564

STATION 3

X/C	CPU	CPL
.010	-.2669	.1224
.025	-.3618	.1500
.050	-.3895	.1952
.100	-.3976	.1919
.200	-.5345	.2172
.400	-.5737	.2202
.600	-.5036	.2530
.800	-.3079	.2750
.900	-.2436	.3137
.925	-.2587	.3547

STATION 4

X/C	CPU	CPL
.010	-.2133	.1156
.025	-.3868	.1463
.050	-.4168	.2165
.100	-.3880	.2104
.200	-.5974	.2188
.400	-.6273	.2308
.600	-.5698	.2584
.800	-.3583	.2649
.900	-.3020	.2978
.925	-.3329	.3469

STATION 5

X/C	CPU	CPL
.025	-.3702	.3468
.050	-.3933	
.075	-.4156	.1564
.150	-.4217	.1556
.300	-.7011	.1624
.450	-.6506	.1732
.600	-.6600	.1766
.750	-.5785	.2362
.800	-.4806	.2384
.850	-.4163	.2405

STATION 6

X/C	CPU	CPL
.025	-.2074	
.050	-.2878	.0286
.100	-.3259	
.200	-.3719	.1011
.300	-.5437	.1101
.400	-.5663	.0914
.500	-.6127	
.600	-.6816	.0889
.700	-.7997	.0952
.800	-.7925	.0889

TABLE VIII.- Continued

(g) $\alpha = 8.46^{o}$

STATION 1

X/C	CPU	CPL
.005	-.1795	.1635
.010	-.1763	.1489
.025	-.2372	.1088
.050	-.2272	.1372
.100	-.2680	.1521
.200	-.3413	.1958
.300	-.4119	.2005
.400	-.4244	.1887
.500	-.3898	.1726
.600	-.3801	.2075
.700	-.3790	.2372
.800	-.3152	-.0202
.900	-.2306	.2571
.950	-.2886	.3170
.970	-.1910	

STATION 2

X/C	CPU	CPL
.005	-.4951	.3287
.010	-.6380	.3275
.025	-.6108	.2938
.050	-.5619	.2632
.100	-.5108	.2563
.200	-.5559	.0644
.300	-.6096	.2390
.400	-.5448	.2280
.500	-.4583	.2119
.600	-.4579	.2541
.700		
.800	-.2711	.2796
.900	-.2158	.3089
.925	-.2307	.3572
.950	-.2129	.3670

STATION 3

X/C	CPU	CPL
.010	-.7547	.3825
.025	-.7572	.3206
.050	-.6903	.3150
.100	-.5787	.2745
.200	-.6547	.2759
.400	-.6383	.2567
.600	-.5303	.2806
.800	-.3003	.2919
.900	-.2242	.3238
.925	-.2193	.3609

STATION 4

X/C	CPU	CPL
.010	-.8188	.4376
.025	-.8063	.3621
.050	-.7111	.3315
.100	-.6210	.2474
.200	-.7351	.2677
.400	-.7102	.2709
.600	-.6186	.2736
.800	-.3783	.2793
.900	-.3039	.2985
.925	-.3211	.3554

STATION 5

X/C	CPU	CPL
.025	-.7927	.3541
.050	-.7086	
.075	-.6805	.2385
.150	-.6516	.2529
.300	-.8502	.2526
.450	-.7460	.2442
.600	-.7386	.2472
.750	-.6394	.2621
.800	-.5376	.2537
.850	-.4635	.2354

STATION 6

X/C	CPU	CPL
.025	-.7121	
.050	-.5854	.1858
.100	-.5326	
.200	-.5191	.1039
.300	-.6938	.0972
.400	-.7582	.0638
.500	-.7931	
.600	-.8900	.0583
.700	-1.0022	.0481
.800	-1.0295	.0516

(h) $\alpha = 10.65^{o}$

STATION 1

X/C	CPU	CPL
.005	-.3346	.1965
.010	-.3458	.1830
.025	-.3618	.1425
.050	-.3987	.1710
.100	-.4261	.1879
.200	-.4654	.2275
.300	-.4988	.2307
.400	-.4886	.2180
.500	-.4331	.2030
.600	-.4076	.2304
.700	-.4103	.2535
.800	-.3416	-.0151
.900	-.2472	.2636
.950	-.3146	.3244
.970	-.2159	

STATION 2

X/C	CPU	CPL
.005	-1.1022	.4147
.010	-1.0873	.4458
.025	-.9237	.3982
.050	-.7569	.3521
.100	-.6232	.3179
.200	-.6311	.0967
.300	-.6661	.2786
.400	-.5852	.2616
.500	-.4946	.2528
.600	-.4775	.2873
.700		
.800	-.2783	.3009
.900	-.2170	.3266
.925	-.2548	.3734
.950	-.2474	.3833

STATION 3

X/C	CPU	CPL
.010	-1.4072	.5090
.025	-1.2290	.4420
.050	-.8675	.4011
.100	-.7666	.3444
.200	-.7550	.3228
.400	-.6817	.2863
.600	-.5439	.3032
.800	-.3037	.3016
.900	-.2137	.3265
.925	-.2036	.3670

STATION 4

X/C	CPU	CPL
.010	-1.2663	.5298
.025	-1.2695	.4683
.050	-1.0728	.4172
.100	-.8684	.4152
.200	-.8884	.3301
.400	-.7821	.2952
.600	-.6268	.3015
.800	-.3658	.2955
.900	-.2711	.3295
.925	-.2687	.3694

STATION 5

X/C	CPU	CPL
.025	-1.3368	.3699
.050	-1.1235	
.075	-.9467	.3117
.150	-.8435	.3190
.300	-.9547	.3039
.450	-.8225	.2541
.600	-.8012	.2573
.750	-.6686	.2680
.800	-.5734	.2564
.850	-.4917	.2246

STATION 6

X/C	CPU	CPL
.025	-1.4842	
.050	-1.0079	.2985
.100	-.7324	
.200	-.7217	.0966
.300	-.8578	.0788
.400	-.9315	.0335
.500	-.9692	
.600	-1.0946	.0194
.700	-1.1957	.0212
.800	-1.2450	.0192

TABLE VIII.- Continued

(i) $\alpha = 12.90^{\circ}$

STATION 1

X/C	CPU	CPL
.005	-.4752	.2299
.010	-.5041	.2164
.025	-.5448	.1867
.050	-.5601	.2145
.100	-.6205	.2268
.200	-.6138	.2643
.300	-.6115	.2760
.400	-.5696	.2540
.500	-.4956	.2340
.600	-.4500	.2553
.700	-.4378	.2796
.800	-.3735	-.0006
.900	-.2583	.2731
.950	-.2798	.3249
.970	-.1724	

STATION 2

X/C	CPU	CPL
.005	-2.0886	.3988
.010	-1.3757	.5023
.025	-1.1698	.4619
.050	-.9358	.4195
.100	-.7642	.3794
.200	-.6951	.1308
.300	-.7050	.3229
.400	-.6256	.2967
.500	-.5340	.2855
.600	-.5072	.3127
.700		
.800	-.2657	.3145
.900	-.2142	.3386
.925	-.2404	.3824
.950	-.2270	.3925

STATION 3

X/C	CPU	CPL
.010	-2.1148	.5326
.025	-1.4992	.4984
.050	-1.2401	.4637
.100	-.9808	.4090
.200	-.8663	.3620
.400	-.7077	.3200
.600	-.5596	.3252
.800	-.3582	.3219
.900	-.2884	.3365
.925	-.3037	.3749

STATION 4

X/C	CPU	CPL
.010	-2.7074	.4720
.025	-2.3181	.5161
.050	-1.7389	.5125
.100	-1.0315	.4092
.200	-.9639	.3807
.400	-.7994	.3334
.600	-.6200	.3235
.800	-.3379	.3092
.900	-.2315	.3172
.925	-.2095	.3554

STATION 5

X/C	CPU	CPL
.025	-1.7410	.3581
.050	-1.7052	
.075	-1.6729	.3167
.150	-1.5964	.3746
.300	-1.0528	.3269
.450	-.8387	.2600
.600	-.8015	.2584
.750	-.6983	.2624
.800	-.6157	.2456
.850	-.5345	.2081

STATION 6

X/C	CPU	CPL
.025	-1.3633	
.050	-1.3734	.3120
.100	-1.3519	
.200	-1.1672	.0951
.300	-.9773	.0477
.400	-1.0659	.0049
.500	-1.1085	
.600	-1.2347	-.0230
.700	-1.3738	-.0162
.800	-1.4666	-.0160

(j) $\alpha = 15.22^{\circ}$

STATION 1

X/C	CPU	CPL
.005	-.6297	.2610
.010	-.6618	.2502
.025	-.7059	.2149
.050	-.7464	.2422
.100	-.7894	.2567
.200	-.8106	.3025
.300	-.7503	.3175
.400	-.6675	.2881
.500	-.5733	.2725
.600	-.5060	.2812
.700	-.4824	.3007
.800	-.3922	-.0088
.900	-.2828	.2917
.950	-.2856	.3308
.970	-.1962	

STATION 2

X/C	CPU	CPL
.005	-3.1911	.2783
.010	-2.3433	.4965
.025	-1.3938	.4986
.050	-1.0965	.4723
.100	-.8951	.4274
.200	-.8085	.1585
.300	-.7727	.3569
.400	-.6638	.3324
.500	-.5506	.3104
.600	-.5329	.3414
.700		
.800	-.3009	.3300
.900	-.2212	.3514
.925	-.2297	.3869
.950	-.1948	.3944

STATION 3

X/C	CPU	CPL
.010	-2.4908	.5081
.025	-2.5562	.5406
.050	-2.5015	.5265
.100	-1.7357	.4717
.200	-.7508	.4160
.400	-.7042	.3556
.600	-.5614	.3471
.800	-.3508	.3431
.900	-.2910	.3533
.925	-.3139	.3978

STATION 4

X/C	CPU	CPL
.010	-2.0954	.4330
.025	-2.1329	.5621
.050	-2.1577	.5556
.100	-2.1867	.4864
.200	-1.8146	.4238
.400	-.6939	.3587
.600	-.6204	.3419
.800	-.3784	.3248
.900	-.3094	.3413
.925	-.3380	.3665

STATION 5

X/C	CPU	CPL
.025	-1.5742	.3649
.050	-1.5425	
.075	-1.5133	.3469
.150	-1.4881	.4115
.300	-1.3620	.3463
.450	-1.2105	.2755
.600	-1.0687	.2718
.750	-.8903	.2525
.800	-.8321	.2333
.850	-.7236	.1928

STATION 6

X/C	CPU	CPL
.025	-1.2739	
.050	-1.2685	.3149
.100	-1.2620	
.200	-1.2449	.0813
.300	-1.1592	.0222
.400	-1.1001	-.0271
.500	-1.1449	
.600	-1.2826	-.0133
.700	-1.3171	-.0235
.800	-1.2146	-.0220

TABLE VIII.- Continued

(k) $\alpha = 17.42^{\circ}$

STATION 1

X/C	CPU	CPL
.005	-.7829	.3036
.010	-.8131	.2857
.025	-.8733	.2623
.050	-.8950	.2947
.100	-.9908	.3091
.200	-.9765	.3506
.300	-.8775	.3574
.400	-.7678	.3304
.500	-.6753	.3095
.600	-.5838	.3220
.700	-.5297	.3277
.800	-.4392	.0077
.900	-.3257	.3005
.950	-.3329	.3498
.970	-.2302	

STATION 2

X/C	CPU	CPL
.005	-2.7371	.1628
.010	-2.7774	.4689
.025	-3.2401	.5364
.050	-2.5162	.5158
.100	-.7594	.4798
.200	-.7384	.1832
.300	-.7403	.4019
.400	-.6883	.3656
.500	-.6106	.3391
.600	-.6074	.3487
.700		
.800	-.3626	.3309
.900	-.2478	.3376
.925	-.2254	.3745
.950	-.1732	.3816

STATION 3

X/C	CPU	CPL
.010	-2.3499	.4811
.025	-2.3956	.5562
.050	-2.4301	.5447
.100	-2.9414	.5018
.200	-.5960	.4446
.400	-.6840	.3758
.600	-.6185	.3556
.800	-.4038	.3574
.900	-.3346	.3454
.925	-.3438	.3865

STATION 4

X/C	CPU	CPL
.010	-1.9466	.3902
.025	-1.9561	.5686
.050	-1.9462	.5635
.100	-1.9808	.5619
.200	-2.0255	.4530
.400	-1.2889	.3830
.600	-.7831	.3496
.800	-.5510	.3173
.900	-.4760	.3226
.925	-.5205	.3566

STATION 5

X/C	CPU	CPL
.025	-1.2529	.3803
.050	-1.2333	
.075	-1.2470	.3415
.150	-1.2113	.4248
.300	-1.1326	.3607
.450	-1.0594	.2846
.600	-1.0168	.2723
.750	-.9490	.2409
.800	-.9238	.2109
.850	-.8626	.1534

STATION 6

X/C	CPU	CPL
.025	-1.0880	
.050	-1.0625	.3826
.100	-1.0683	
.200	-1.0564	.1192
.300	-1.0404	.0754
.400	-1.0005	.0306
.500	-.9847	
.600	-.9409	.0286
.700	-.9014	.0163
.800	-.8734	-.0047

(l) $\alpha = 19.61^{\circ}$

STATION 1

X/C	CPU	CPL
.005	-.9241	.3255
.010	-.9587	.3191
.025	-1.0099	.2953
.050	-1.0450	.3224
.100	-1.1386	.3428
.200	-1.1222	.3850
.300	-1.0169	.3924
.400	-.8799	.3658
.500	-.7486	.3372
.600	-.6455	.3427
.700	-.5846	.3455
.800	-.4865	.0095
.900	-.3527	.3135
.950	-.3526	.3610
.970	-.2484	

STATION 2

X/C	CPU	CPL
.005	-2.7042	.0968
.010	-2.7712	.4310
.025	-3.0454	.5419
.050	-3.6204	.5421
.100	-.6933	.5150
.200	-.7460	.2016
.300	-.7879	.4283
.400	-.7696	.3860
.500	-.7050	.3635
.600	-.6714	.3753
.700		
.800	-.4269	.3388
.900	-.3135	.3316
.925	-.2899	.3653
.950	-.2407	.3708

STATION 3

X/C	CPU	CPL
.010	-2.3192	.4512
.025	-2.3541	.5700
.050	-2.4167	.5821
.100	-3.0980	.5460
.200	-1.5662	.4873
.400	-.7610	.4062
.600	-.6808	.3776
.800	-.4705	.3458
.900	-.3896	.3373
.925	-.4033	.3746

STATION 4

X/C	CPU	CPL
.010	-1.7493	.3730
.025	-1.7677	.5808
.050	-1.7913	.5832
.100	-1.8245	.5793
.200	-1.8871	.4797
.400	-1.4194	.4042
.600	-1.0386	.3636
.800	-.6847	.3226
.900	-.5802	.3094
.925	-.6283	.3453

STATION 5

X/C	CPU	CPL
.025	-1.2098	.3421
.050	-1.2101	
.075	-1.1821	.3594
.150	-1.1775	.4535
.300	-1.1158	.3788
.450	-1.0877	.3066
.600	-1.0326	.2877
.750	-.9968	.2496
.800	-.9701	.2099
.850	-.8869	.1521

STATION 6

X/C	CPU	CPL
.025	-1.0368	
.050	-1.0541	.3642
.100	-1.0289	
.200	-1.0266	.1463
.300	-.9816	.0921
.400	-.9311	.0497
.500	-.8971	
.600	-.8749	.0333
.700	-.8485	.0261
.800	-.8218	-.0011

TABLE VIII.- Concluded

(m) $\alpha = 21.77^{\circ}$

STATION 1

X/C	CPU	CPL
.005	-1.0632	.3611
.010	-1.0886	.3459
.025	-1.1664	.3248
.050	-1.2085	.3625
.100	-1.3000	.3822
.200	-1.2717	.4247
.300	-1.1445	.4247
.400	-.9987	.3951
.500	-.8550	.3636
.600	-.7281	.3607
.700	-.6674	.3626
.800	-.5586	.0086
.900	-.4153	.3239
.950	-.3799	.3651
.970	-.2689	

STATION 2

X/C	CPU	CPL
.005	-3.0079	-.0021
.010	-3.0312	.3981
.025	-3.0579	.5501
.050	-3.5501	.5690
.100	-1.3002	.5446
.200	-.8017	.2196
.300	-.9670	.4588
.400	-.9251	.4159
.500	-.8691	.3681
.600	-.8196	.3725
.700		
.800	-.6028	.3191
.900	-.4942	.2934
.925	-.4945	.3301
.950	-.4454	.3238

STATION 3

X/C	CPU	CPL
.010	-2.0299	.4464
.025	-2.0047	.5776
.050	-1.9358	.6029
.100	-2.0440	.5628
.200	-1.9889	.5030
.400	-.9736	.4120
.600	-.8094	.3682
.800	-.6068	.2988
.900	-.5003	.2840
.925	-.5308	.3191

STATION 4

X/C	CPU	CPL
.010	-1.6584	.3582
.025	-1.6604	.5785
.050	-1.6738	.5799
.100	-1.6152	.5793
.200	-1.5387	.5371
.400	-1.2906	.4135
.600	-1.0412	.3515
.800	-.7916	.2894
.900	-.7361	.2508
.925	-.7841	.2863

STATION 5

X/C	CPU	CPL
.025	-1.1574	.2999
.050	-1.1472	
.075	-1.1303	.3600
.150	-1.1218	.4044
.300	-1.0581	.3832
.450	-.9918	.3003
.600	-.9467	.2735
.750	-.8828	.2360
.800	-.8756	.1926
.850	-.8277	.1467

STATION 6

X/C	CPU	CPL
.025	-.9243	
.050	-.9166	.3537
.100	-.9147	
.200	-.9082	.1578
.300	-.8638	.1021
.400	-.8369	.0579
.500	-.8078	
.600	-.7905	.0374
.700	-.7584	.0204
.800	-.7430	-.0016

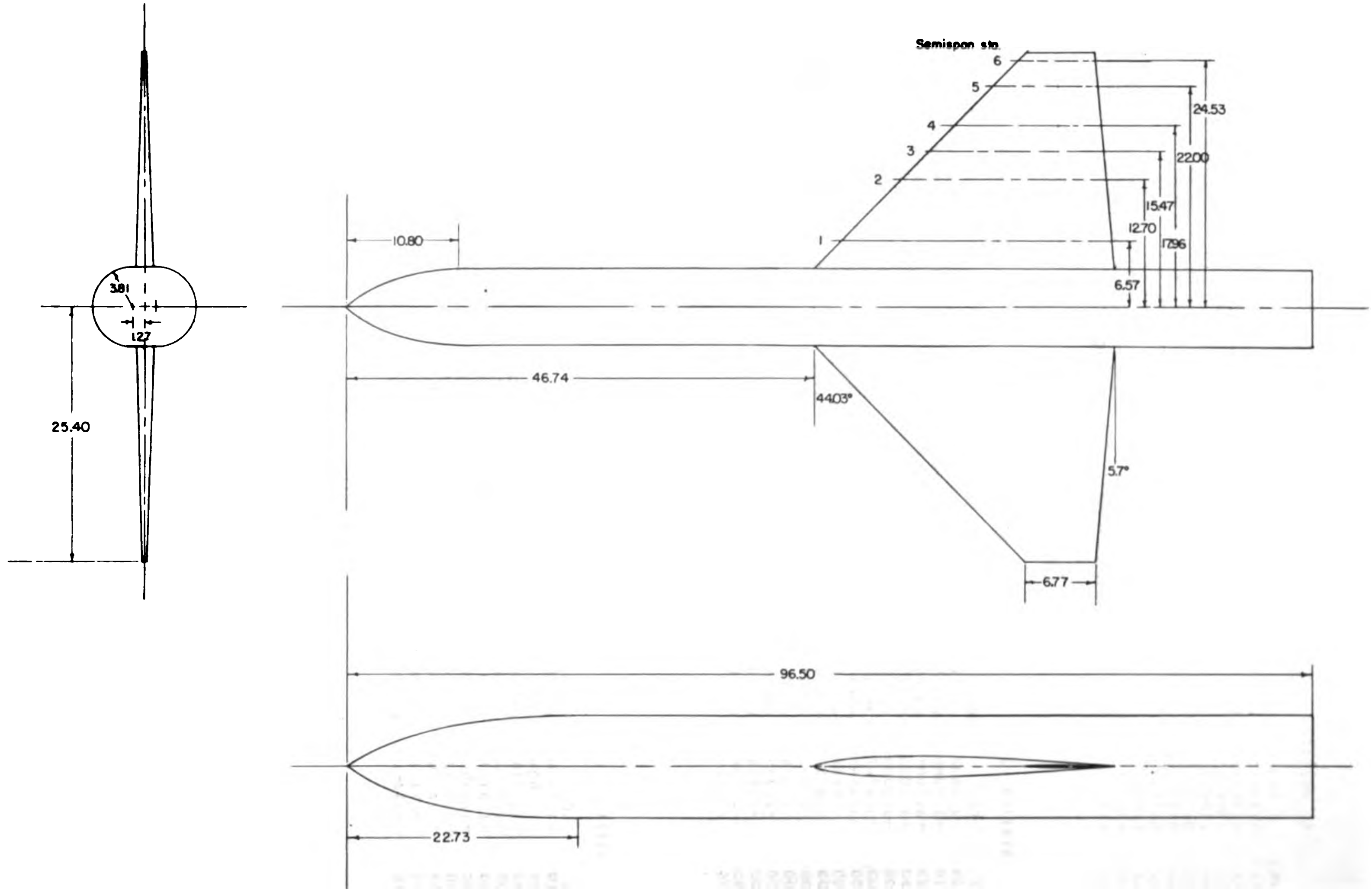

(a) Model with strake off.

Figure 1.- Drawing of the model. All dimensions are in centimeters.

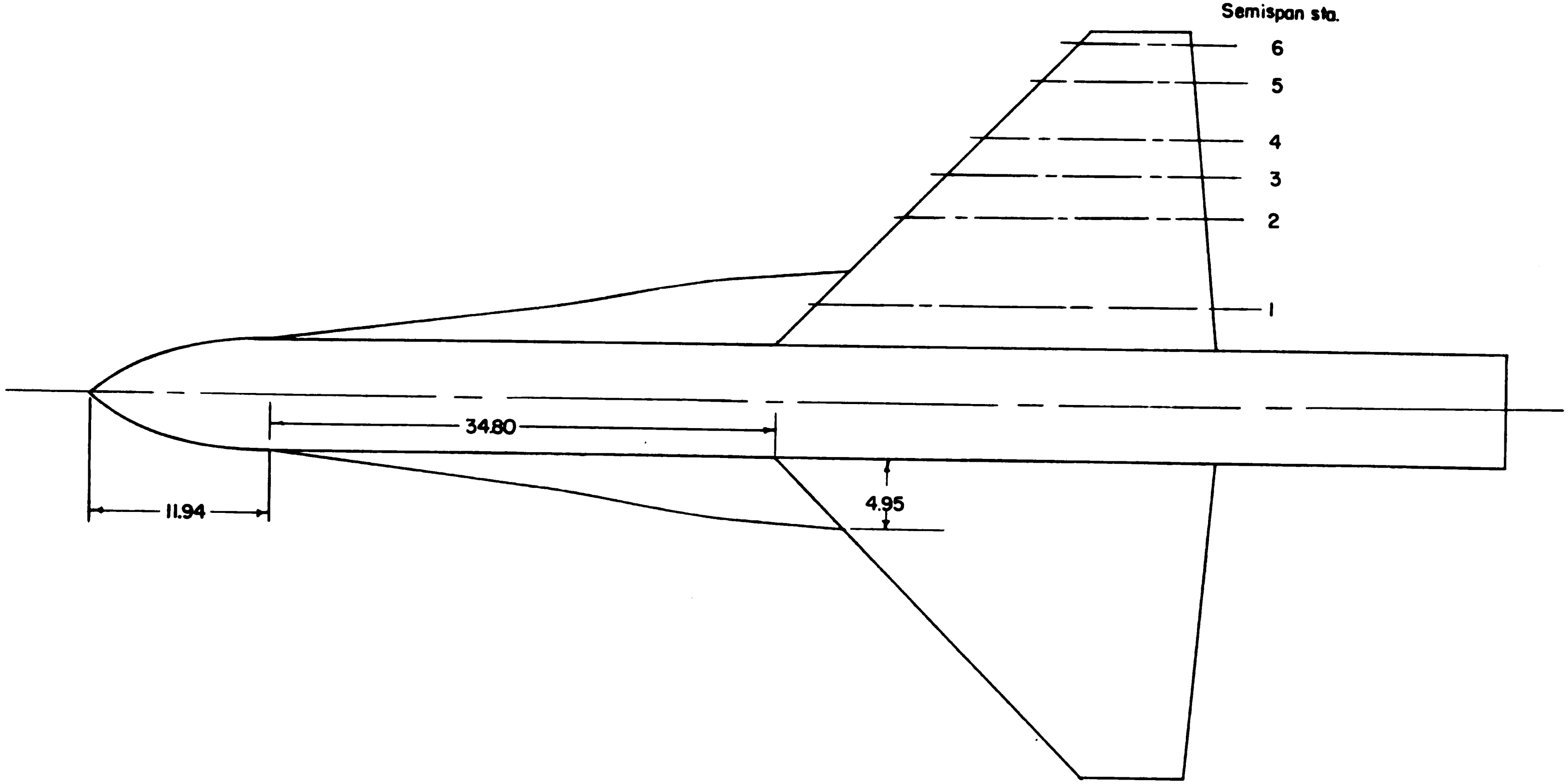

(b) Model with strake on.

Figure 1.- Concluded.

L-71-8385

Figure 2.- Photograph of model in Langley high-speed 7- by 10-foot tunnel.

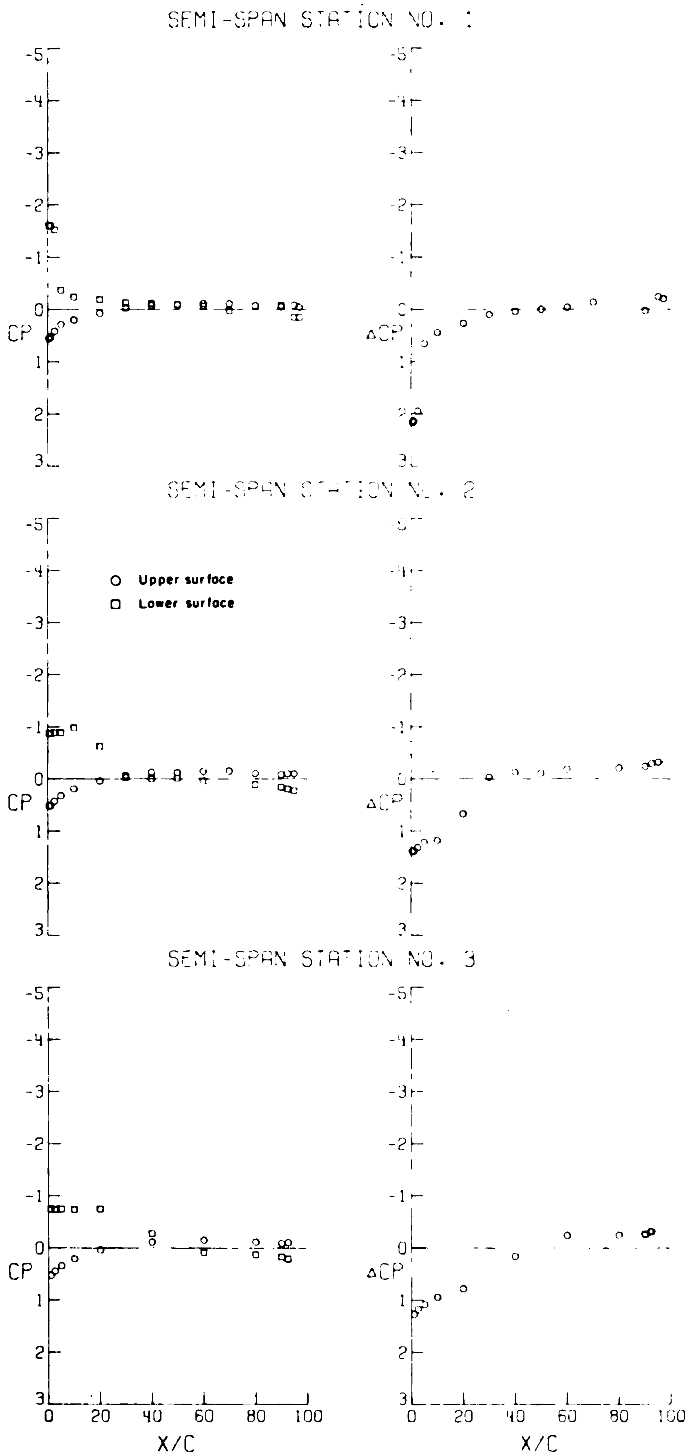

(a) $\alpha = -3.90^{o}$.

Figure 3.- Pressure distributions at a Mach number of 0.40 for the model with strakes off. $C_{L,d} = 0.35$.

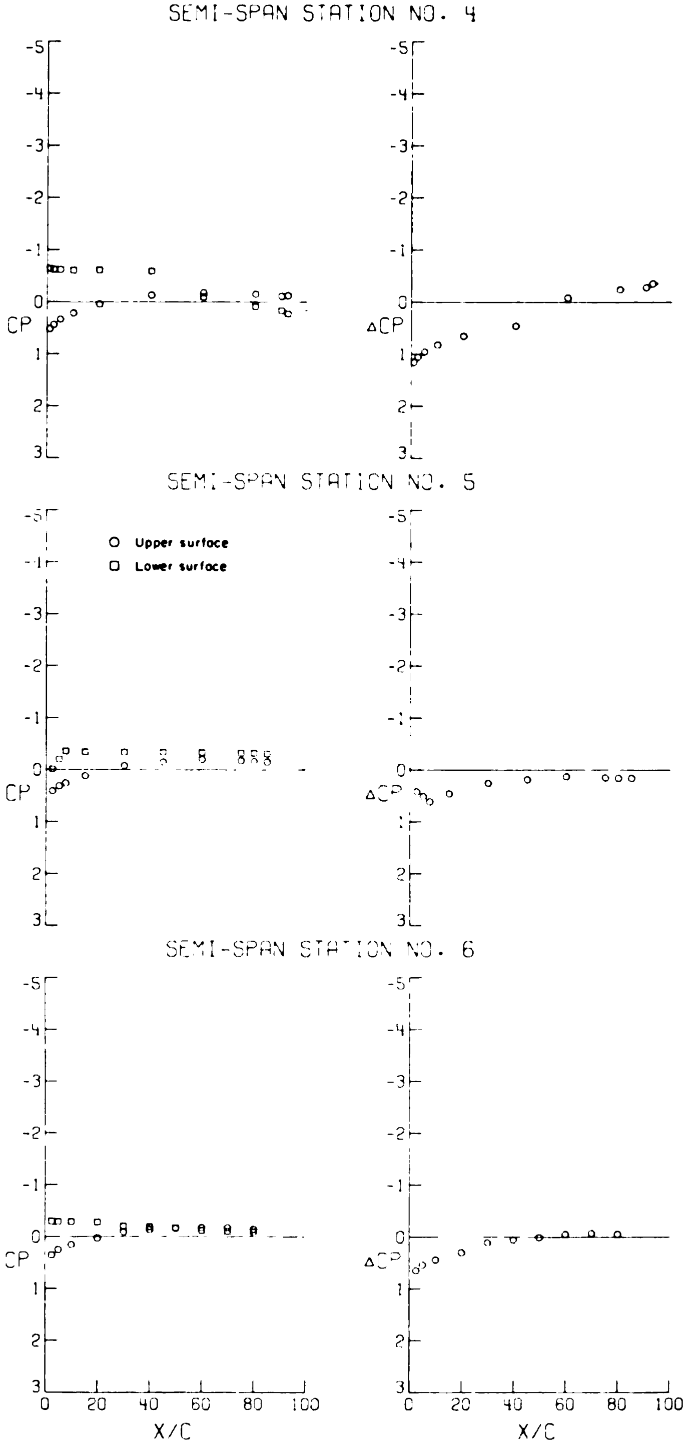

(a) Concluded.

Figure 3.- Continued.

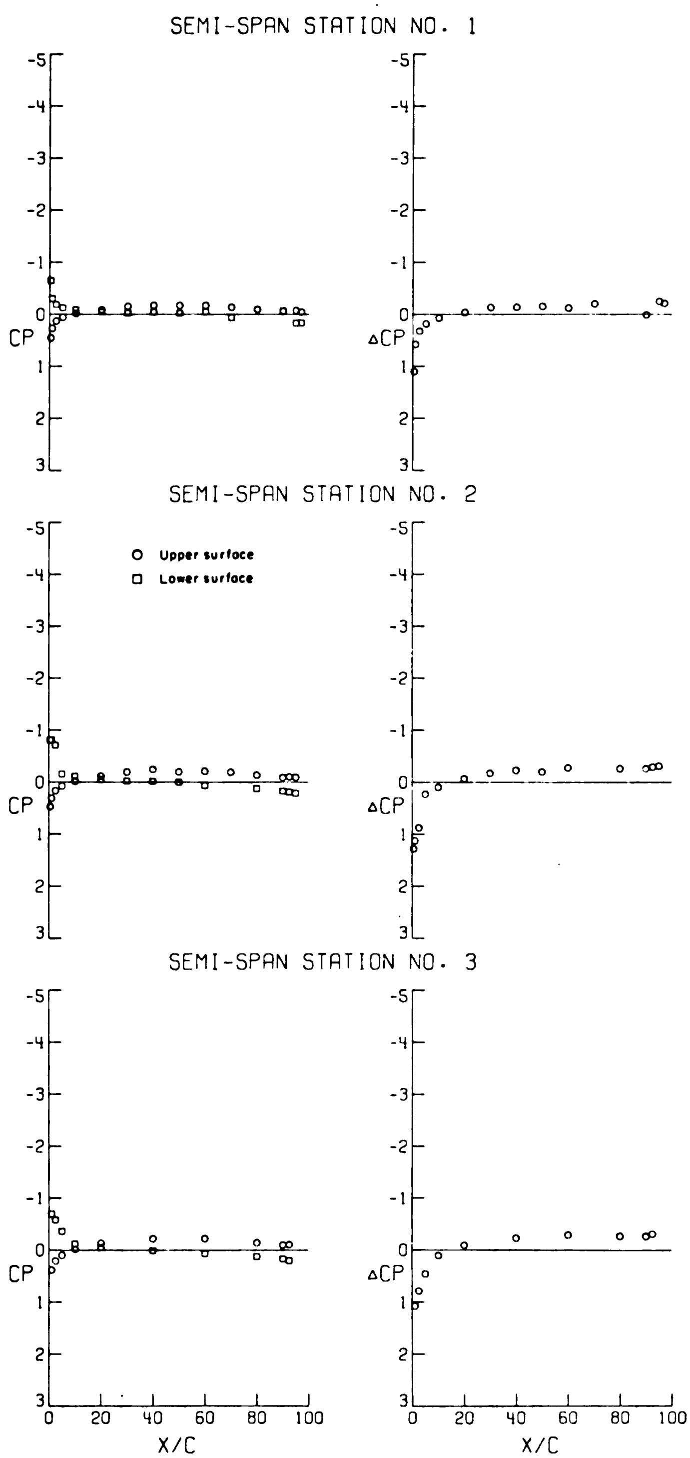

(b) $\alpha = 0.03°$.

Figure 3.- Continued.

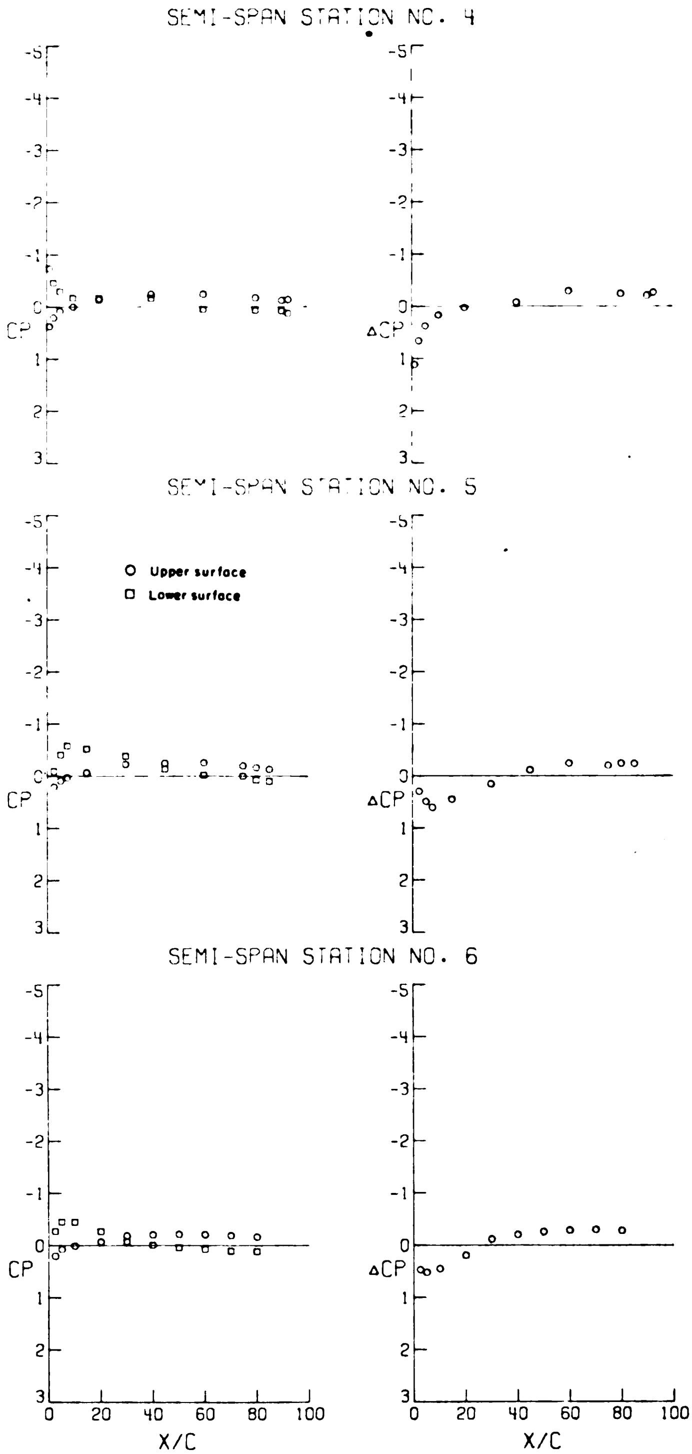

(b) Concluded.

Figure 3.- Continued.

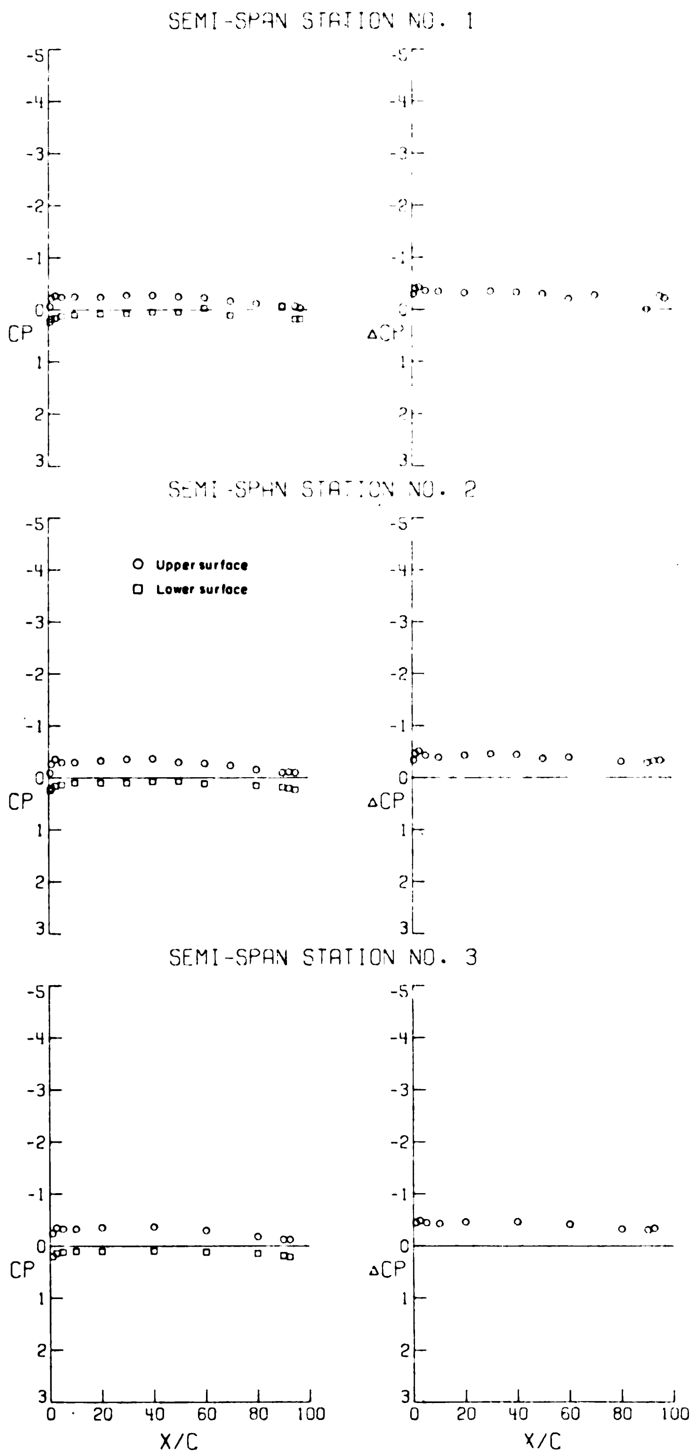

(c) $\alpha = 4.09^{\circ}$.

Figure 3.- Continued.

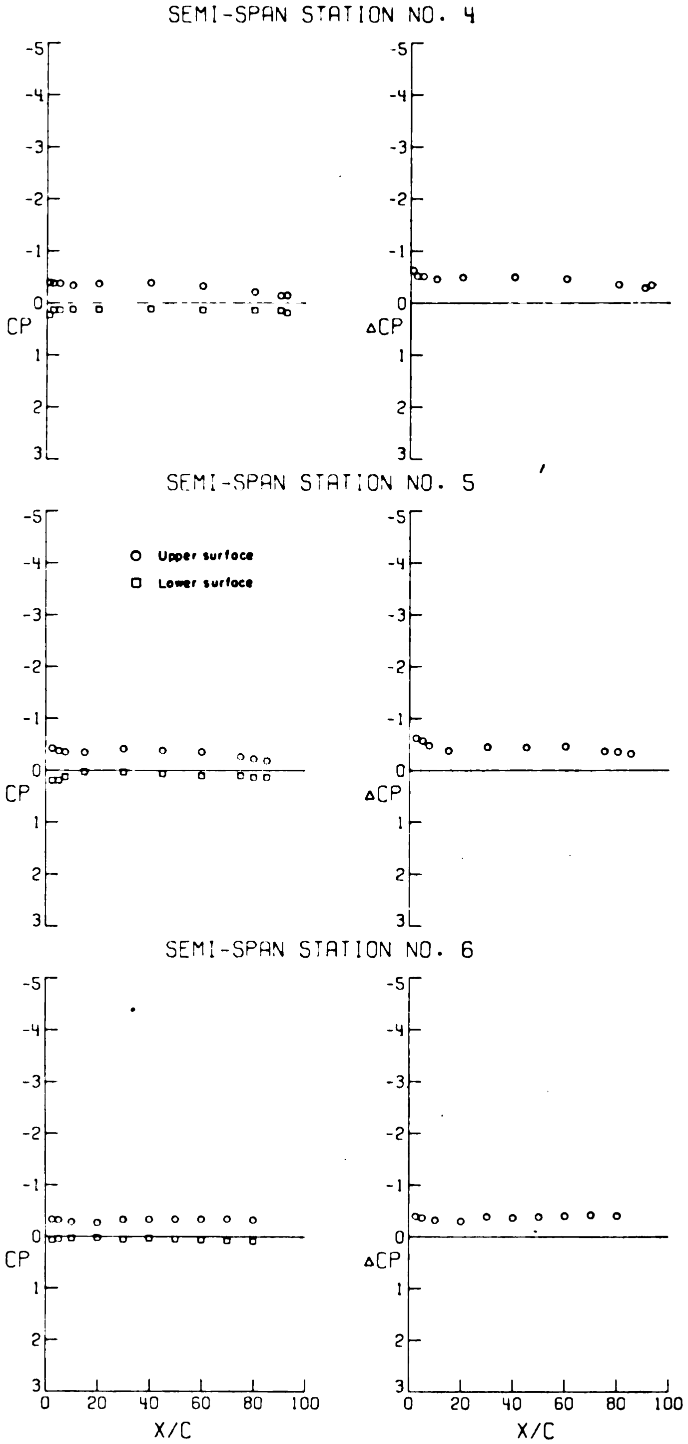

(c) Concluded.

Figure 3.- Continued.

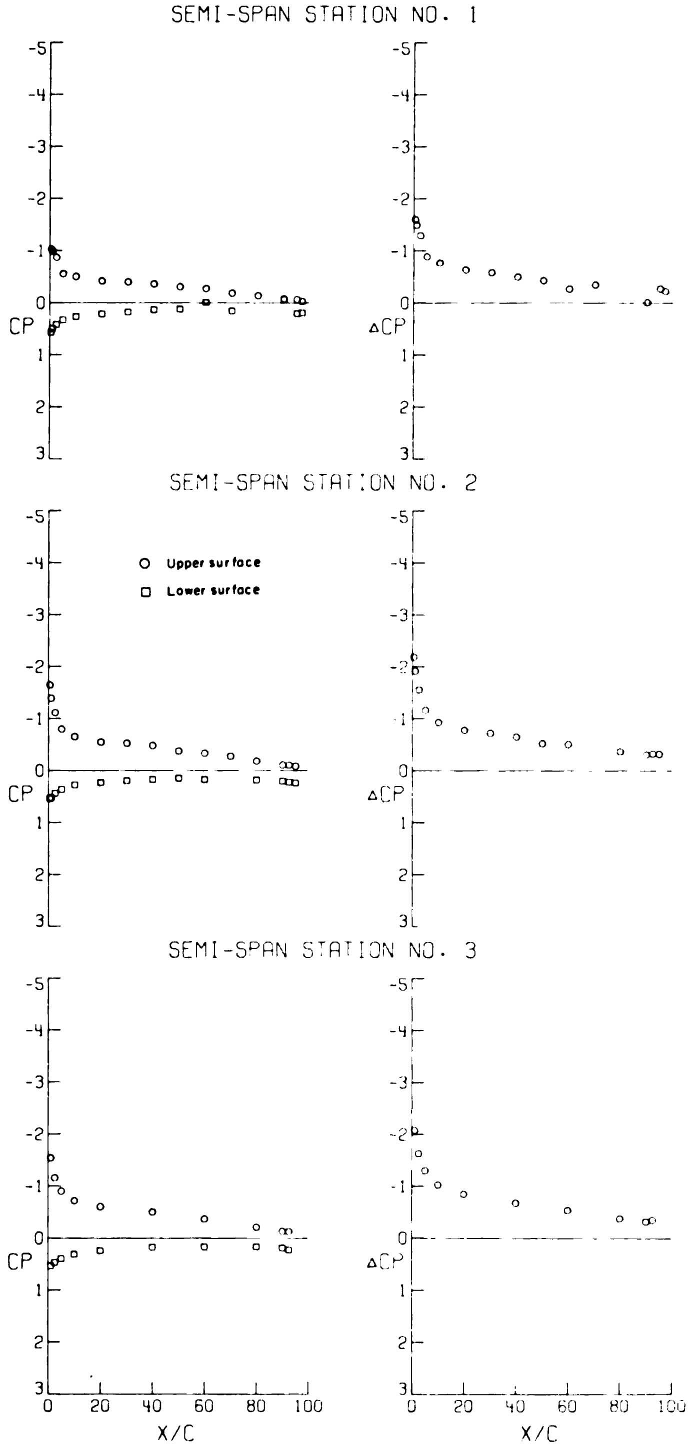

(d) $\alpha = 8.31^{\circ}$.

Figure 3.- Continued.

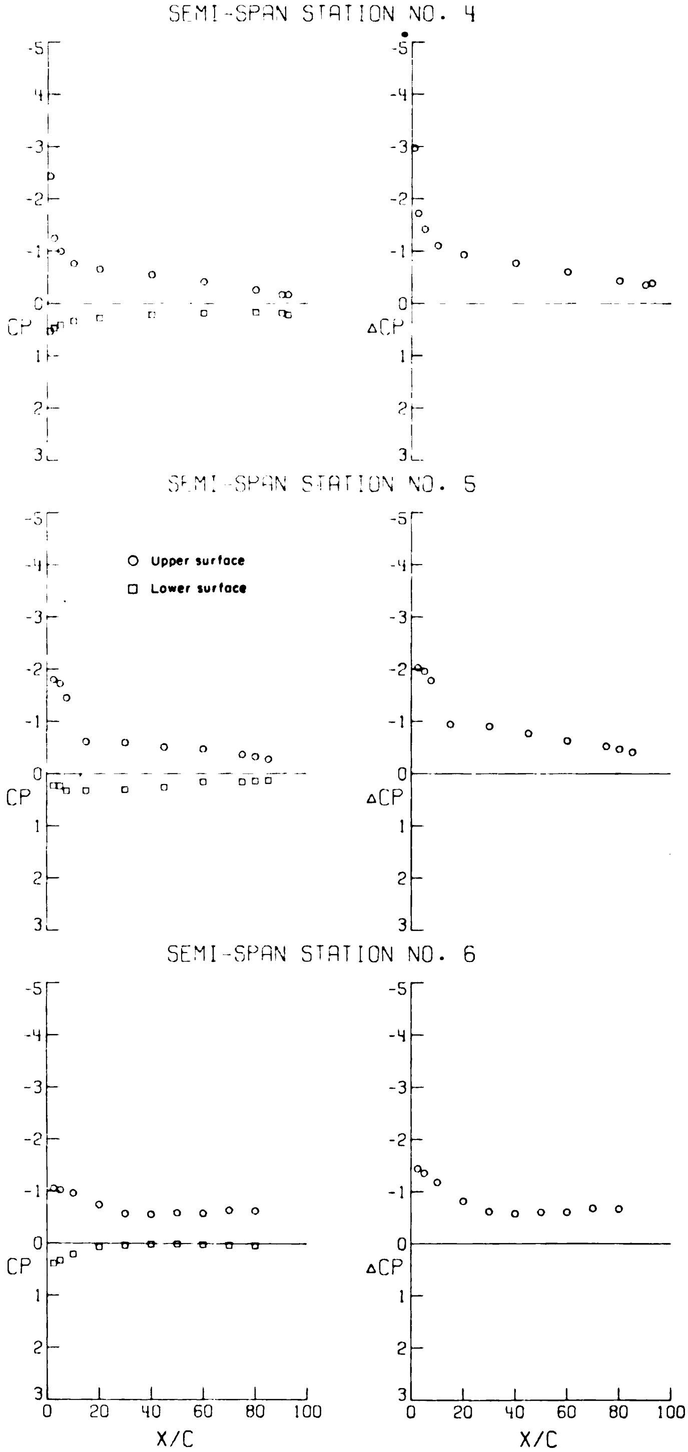

(d) Concluded.

Figure 3.- Continued.

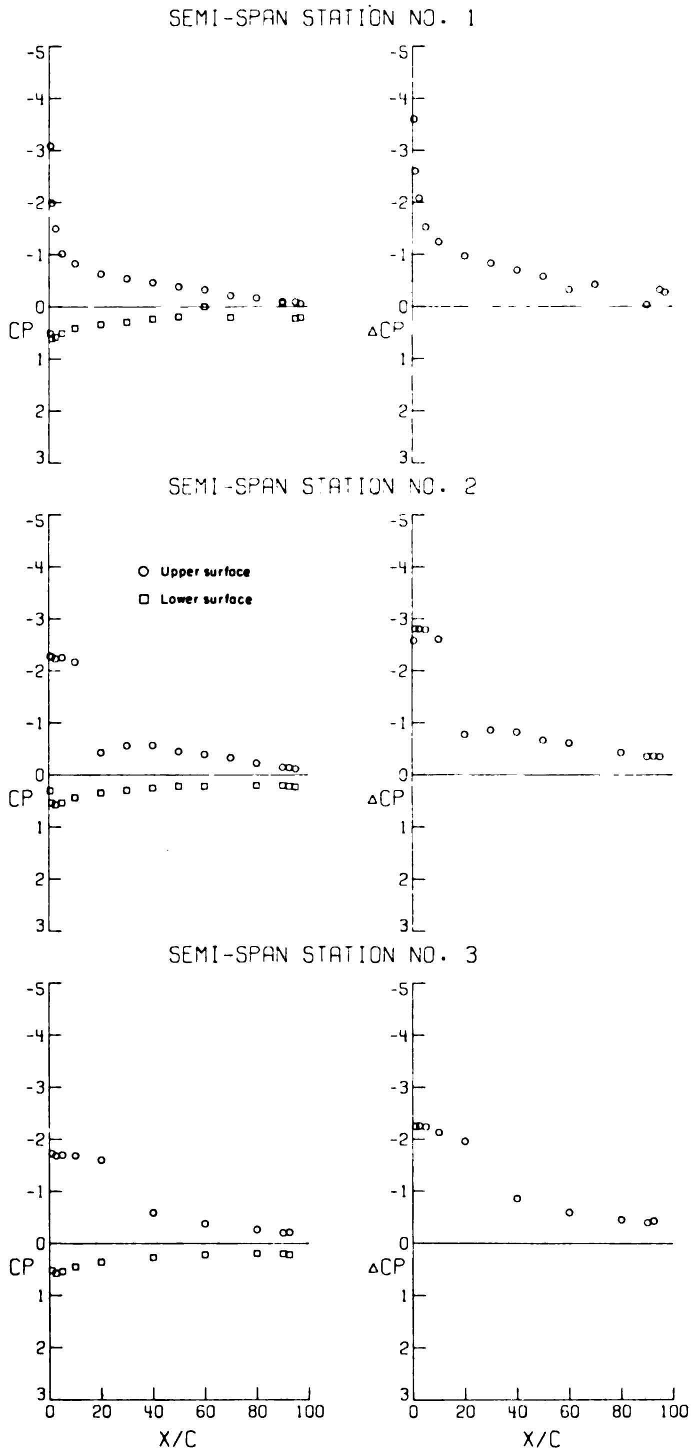

(e) $\alpha = 12.70^{o}$.

Figure 3.- Continued.

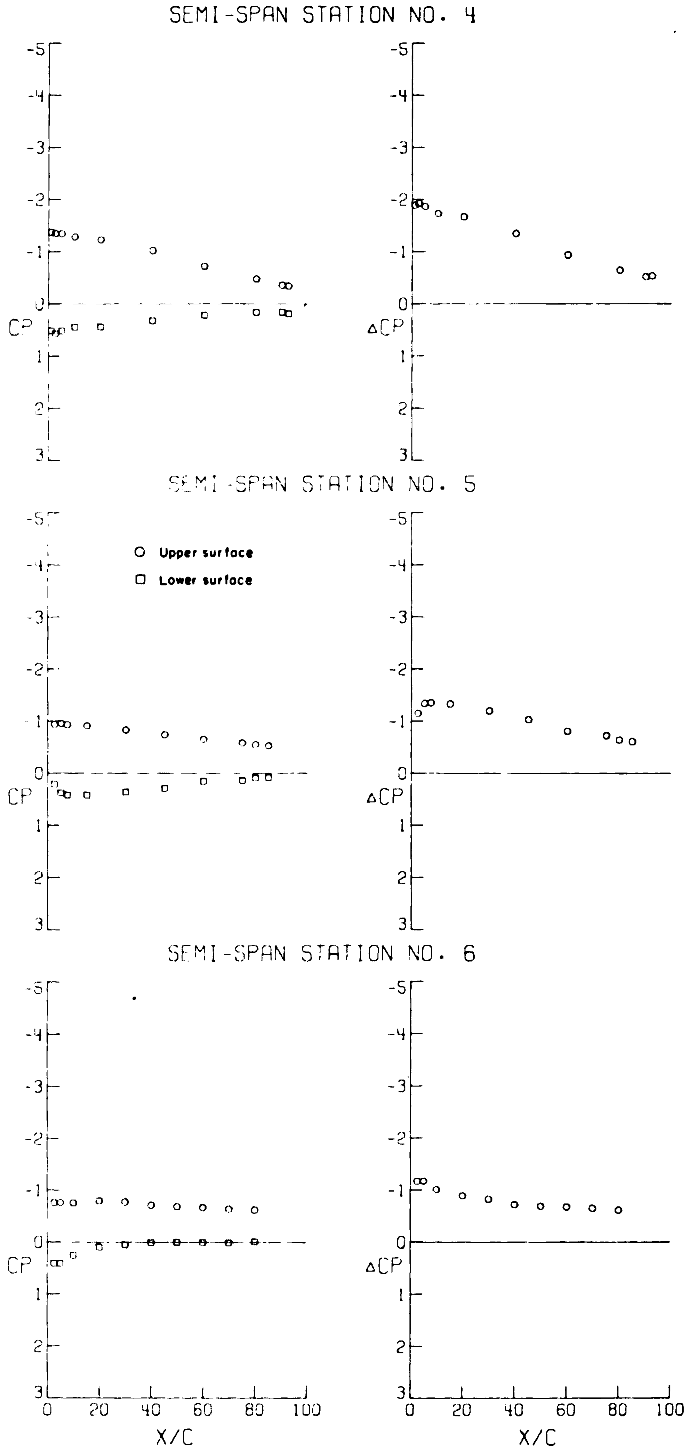

(e) Concluded.

Figure 3.- Continued.

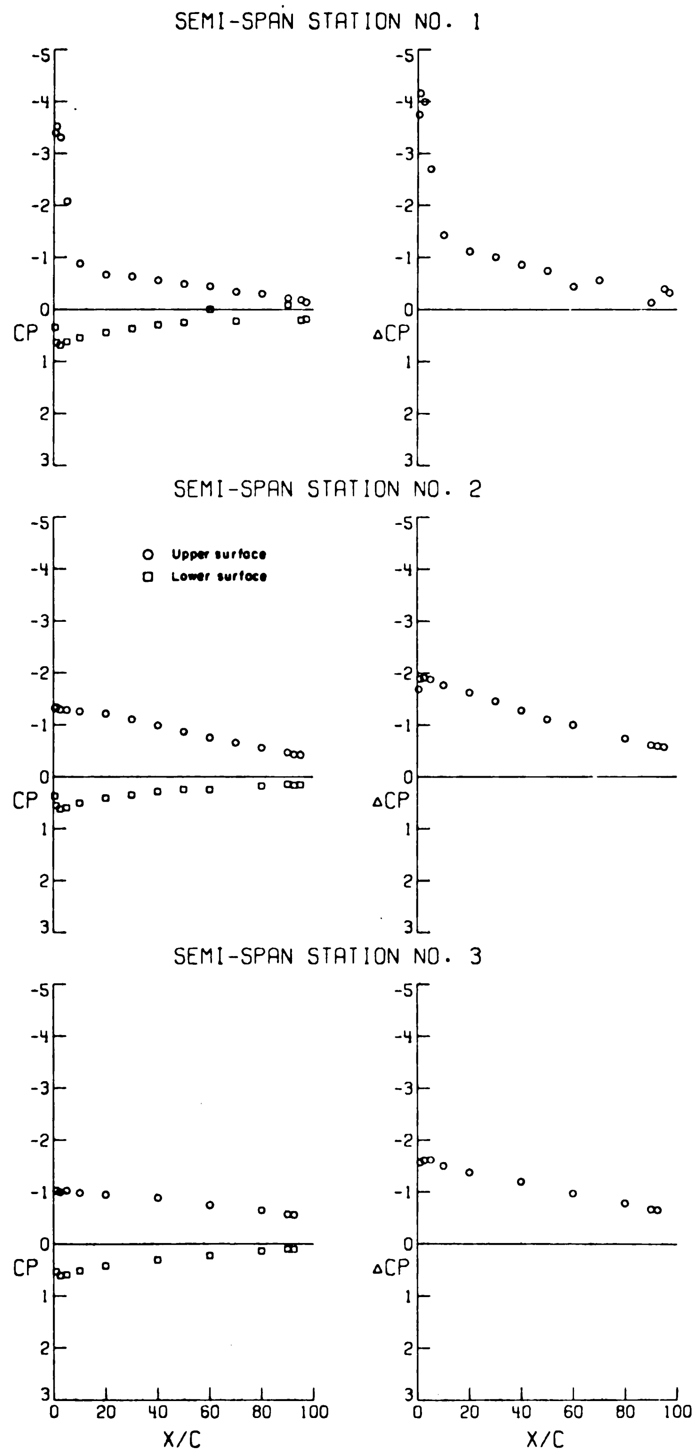

(f) $\alpha = 17.05^{\circ}$.

Figure 3.- Continued.

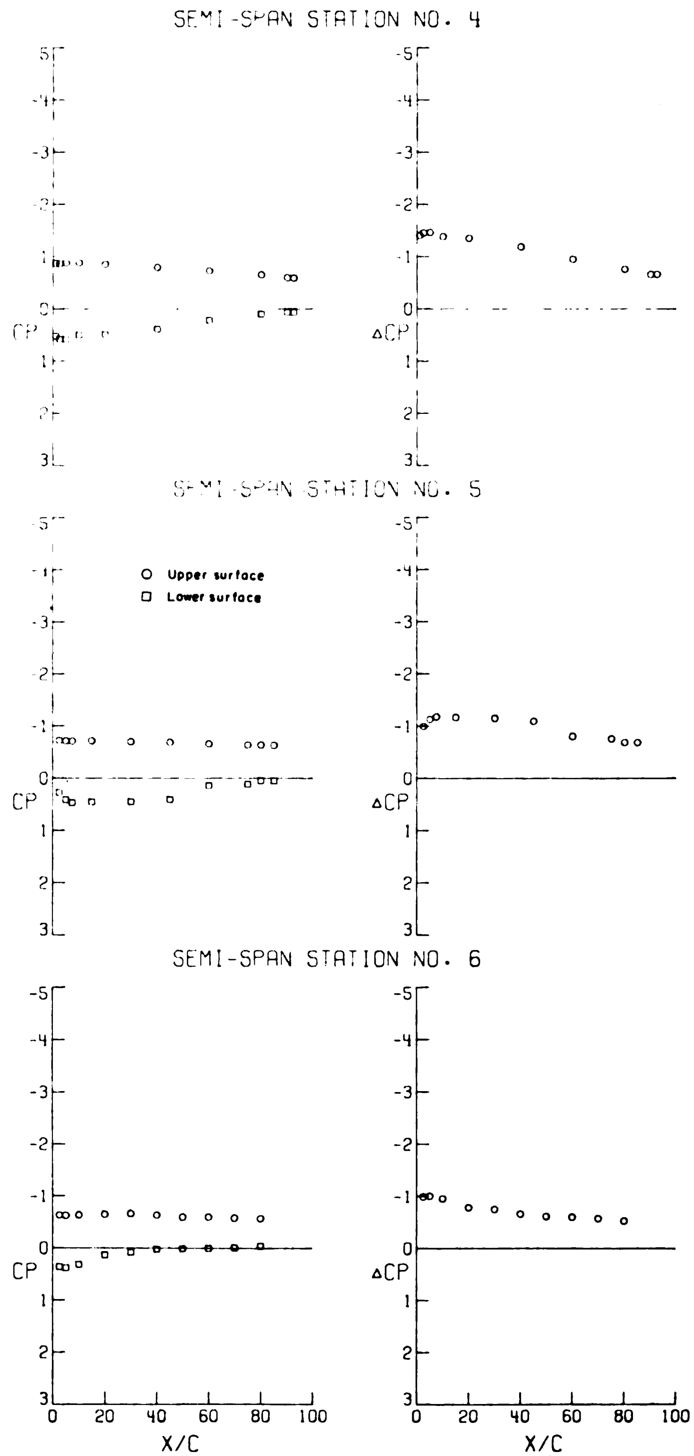

(f) Concluded.

Figure 3.- Continued.

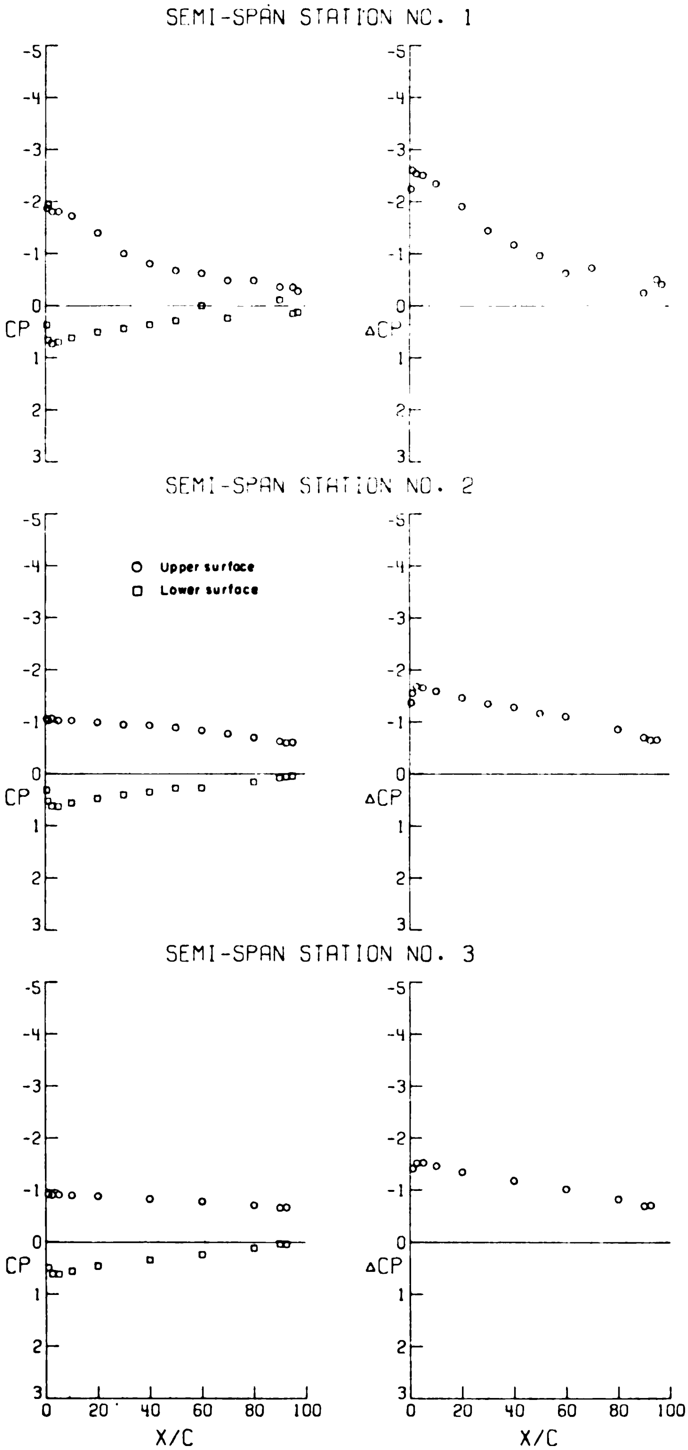

(g) $\alpha = 21.20^{\circ}$.

Figure 3.- Continued.

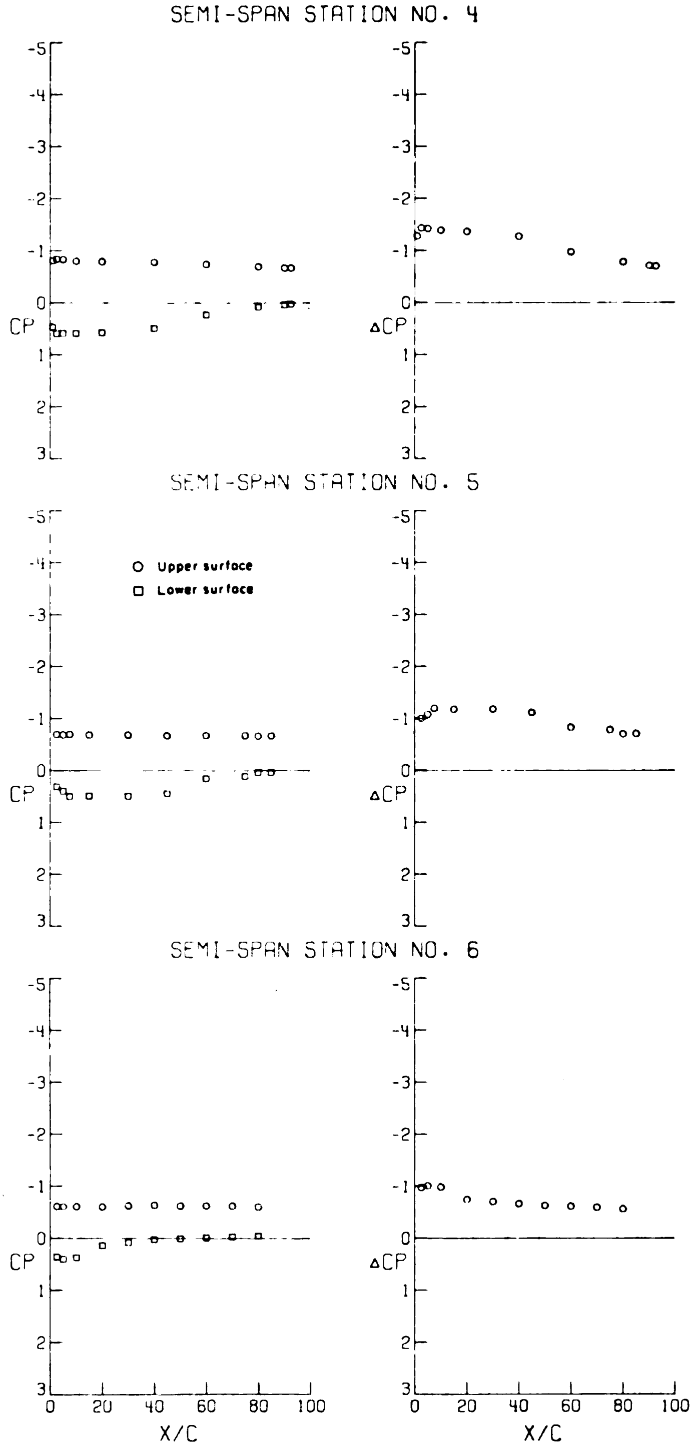

(g) Concluded.

Figure 3.- Concluded.

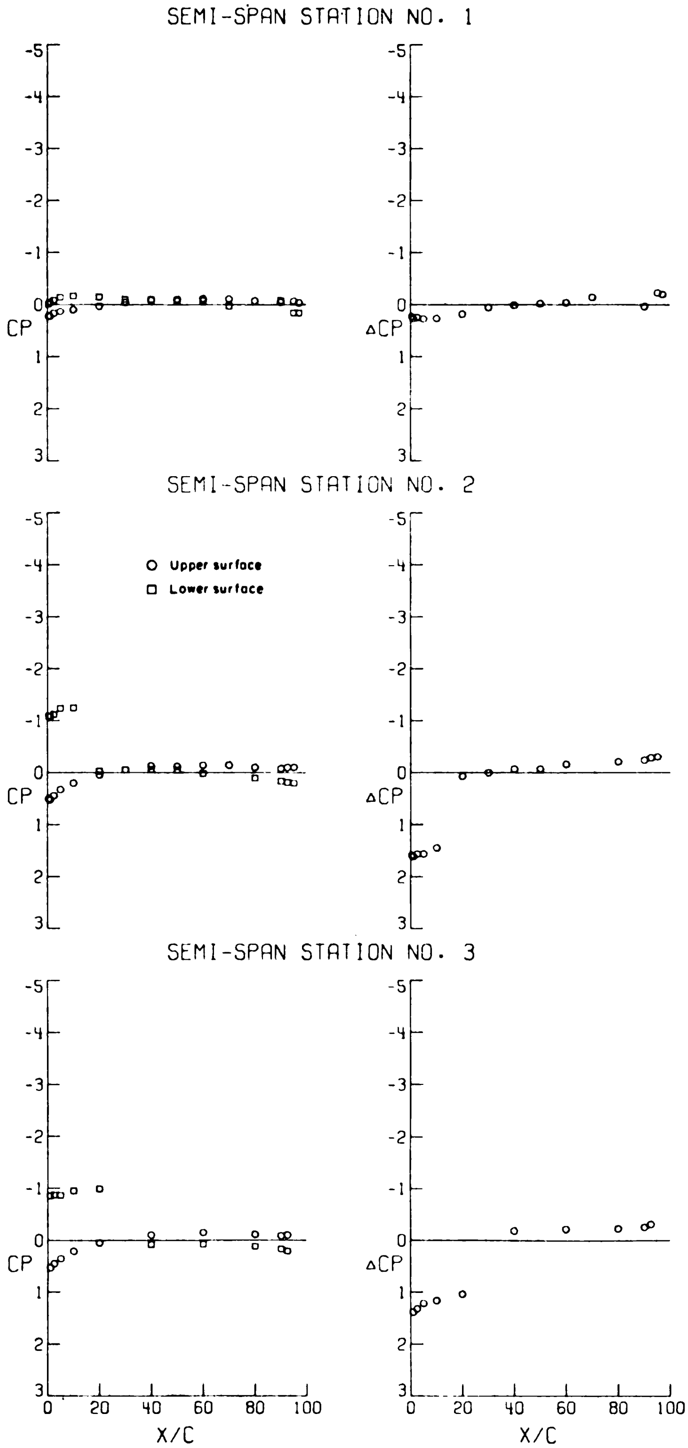

(a) α = -3.94°.

Figure 4.- Pressure distributions at a Mach number of 0.40 for the model with strakes on. $C_{L,d}$ = 0.35.

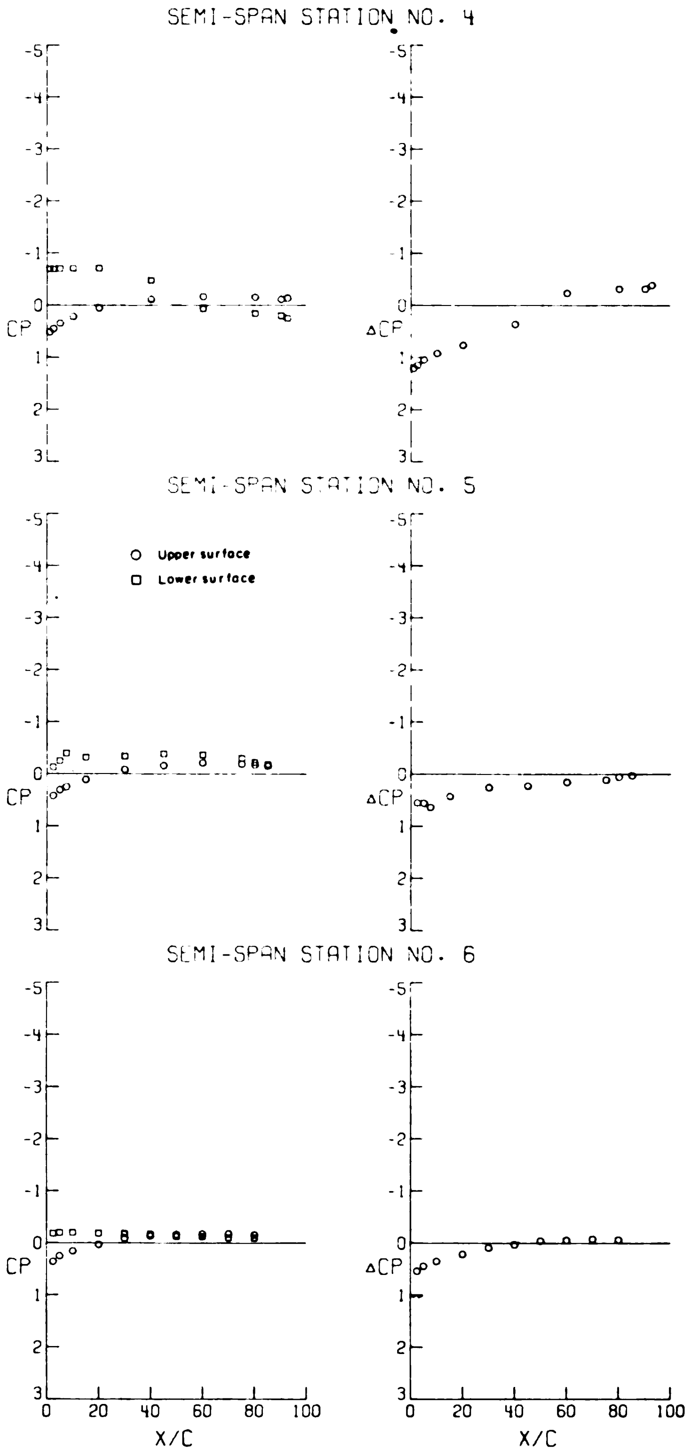

(a) Concluded.

Figure 4.- Continued.

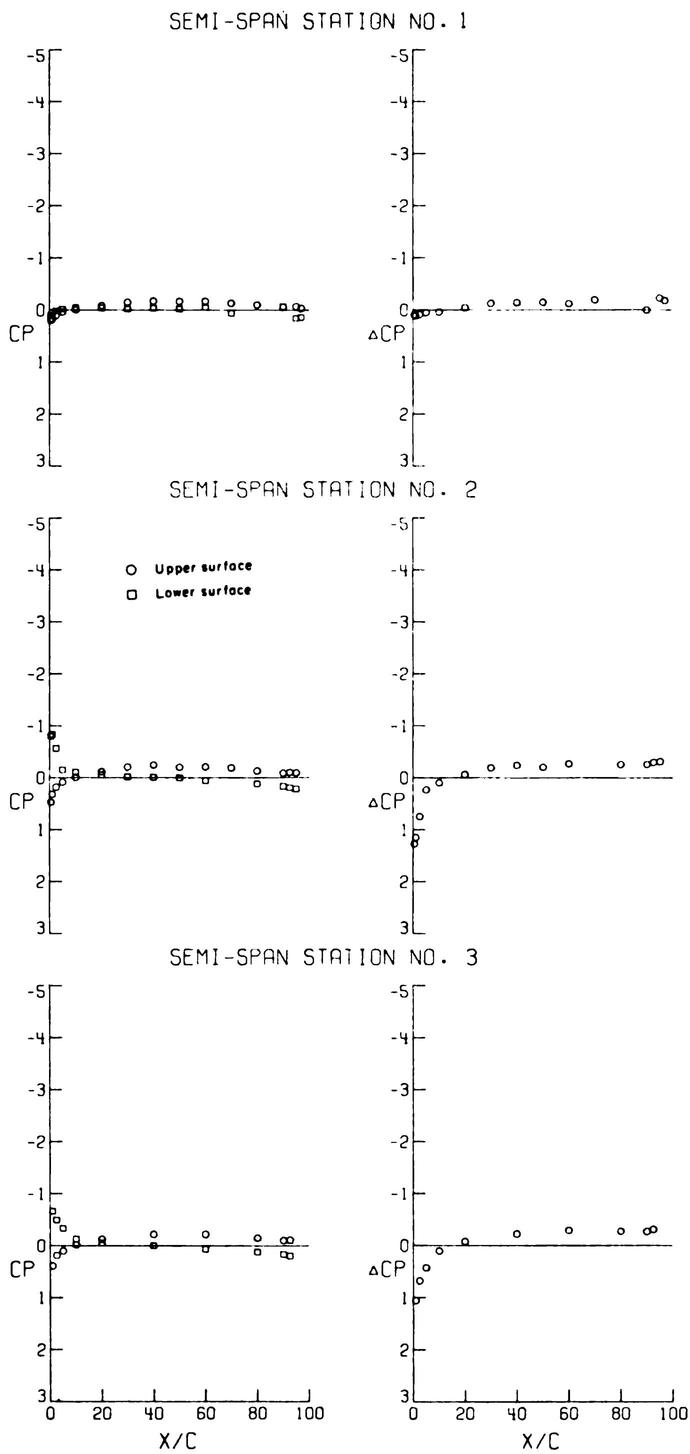

(b) $\alpha = 0.03^{\circ}$.

Figure 4.- Continued.

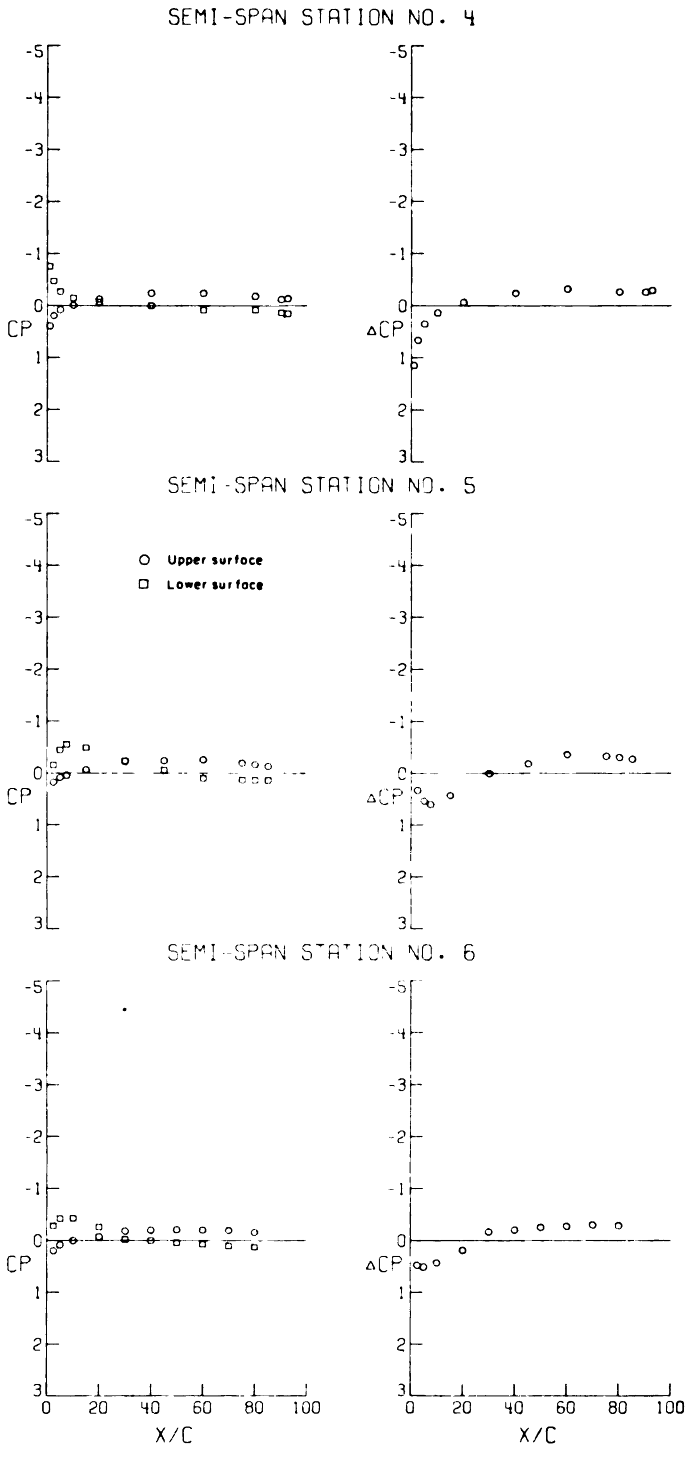

(b) Concluded.

Figure 4.- Continued.

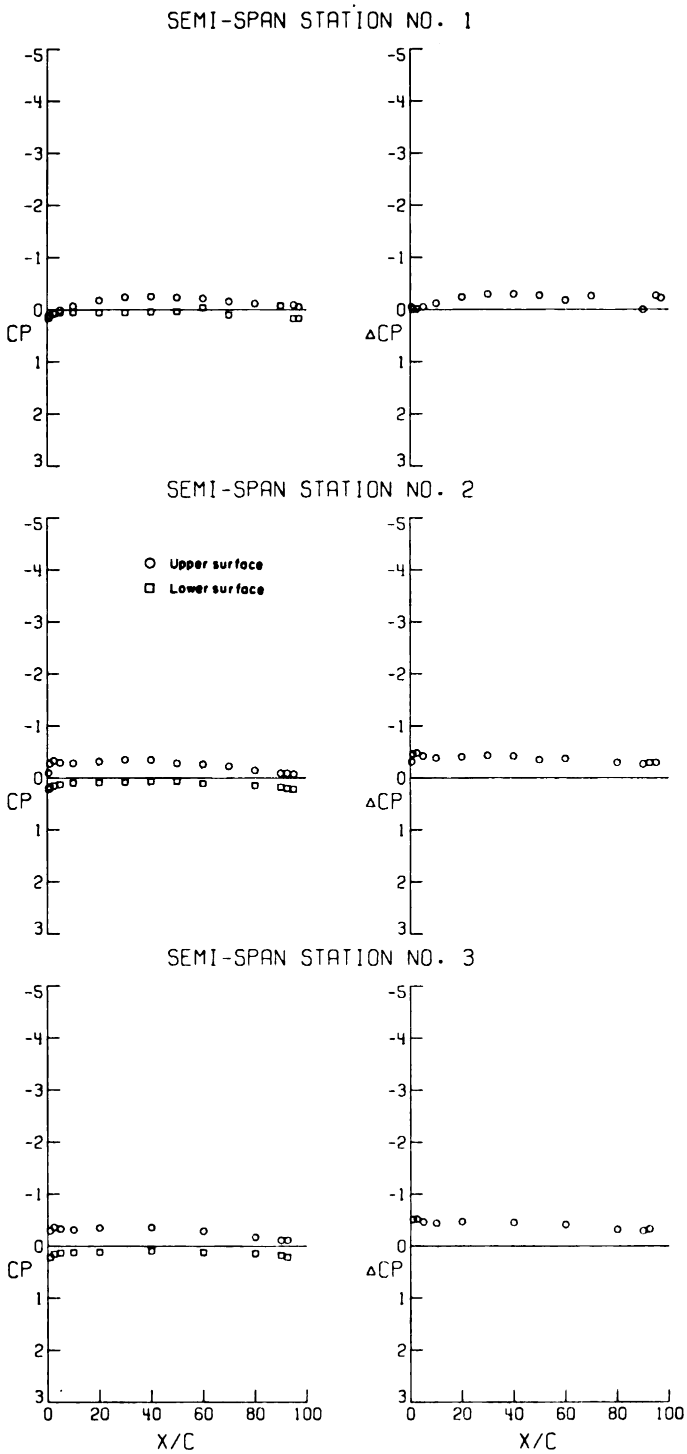

(c) $\alpha = 4.10^{\circ}$.

Figure 4.- Continued.

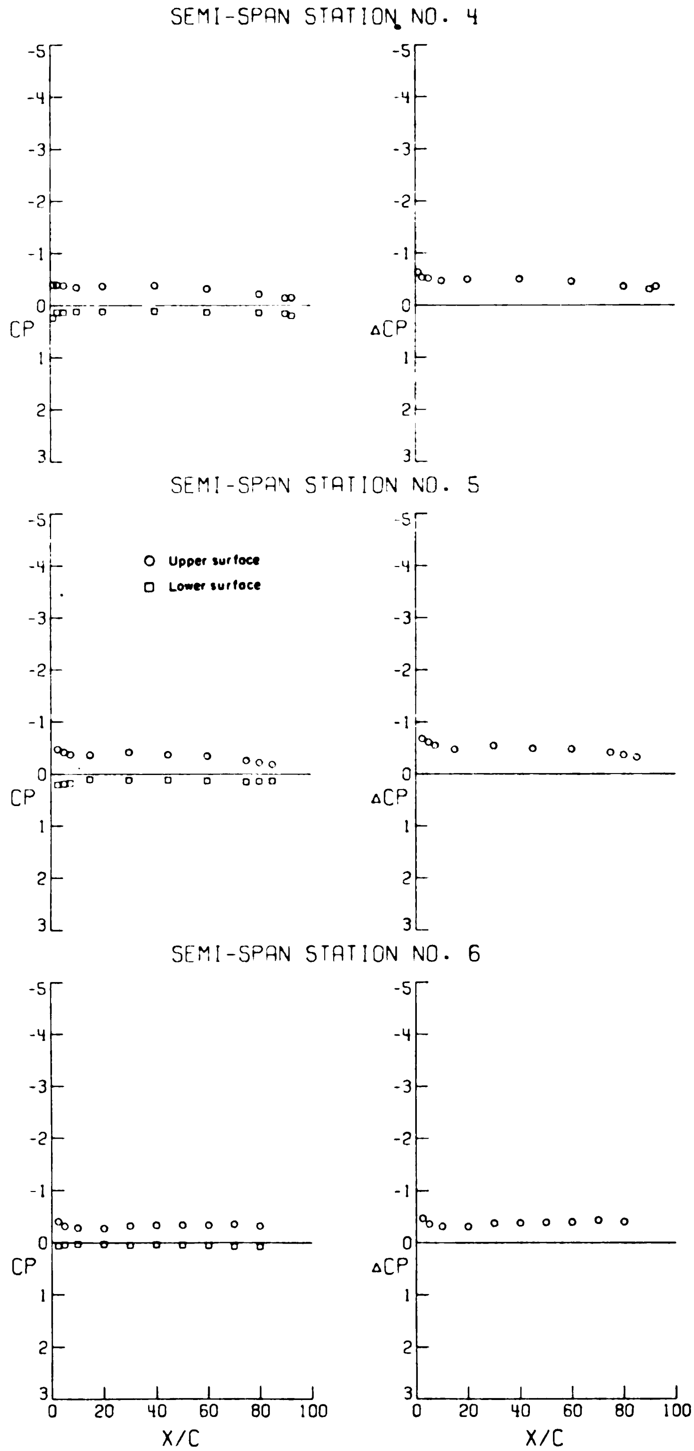

(c) Concluded.

Figure 4.- Continued.

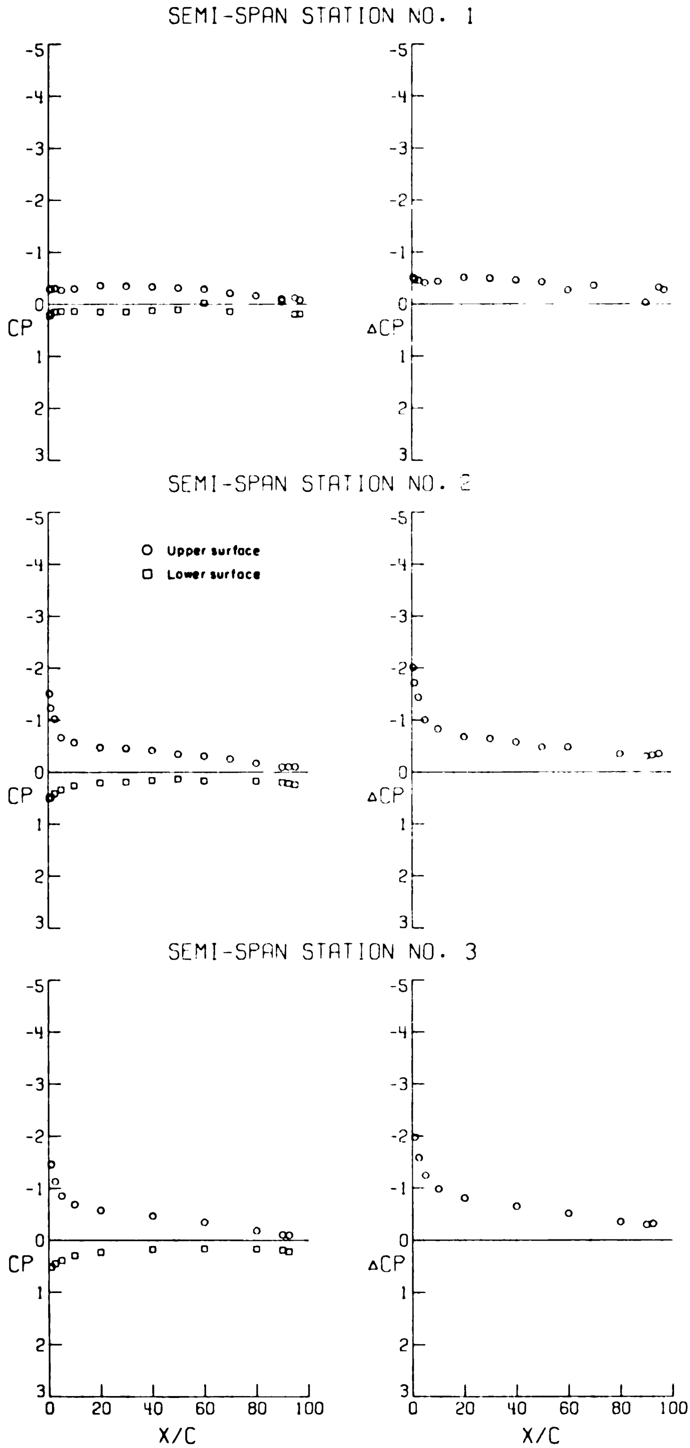

(d) $\alpha = 8.39^{\circ}$.

Figure 4.- Continued.

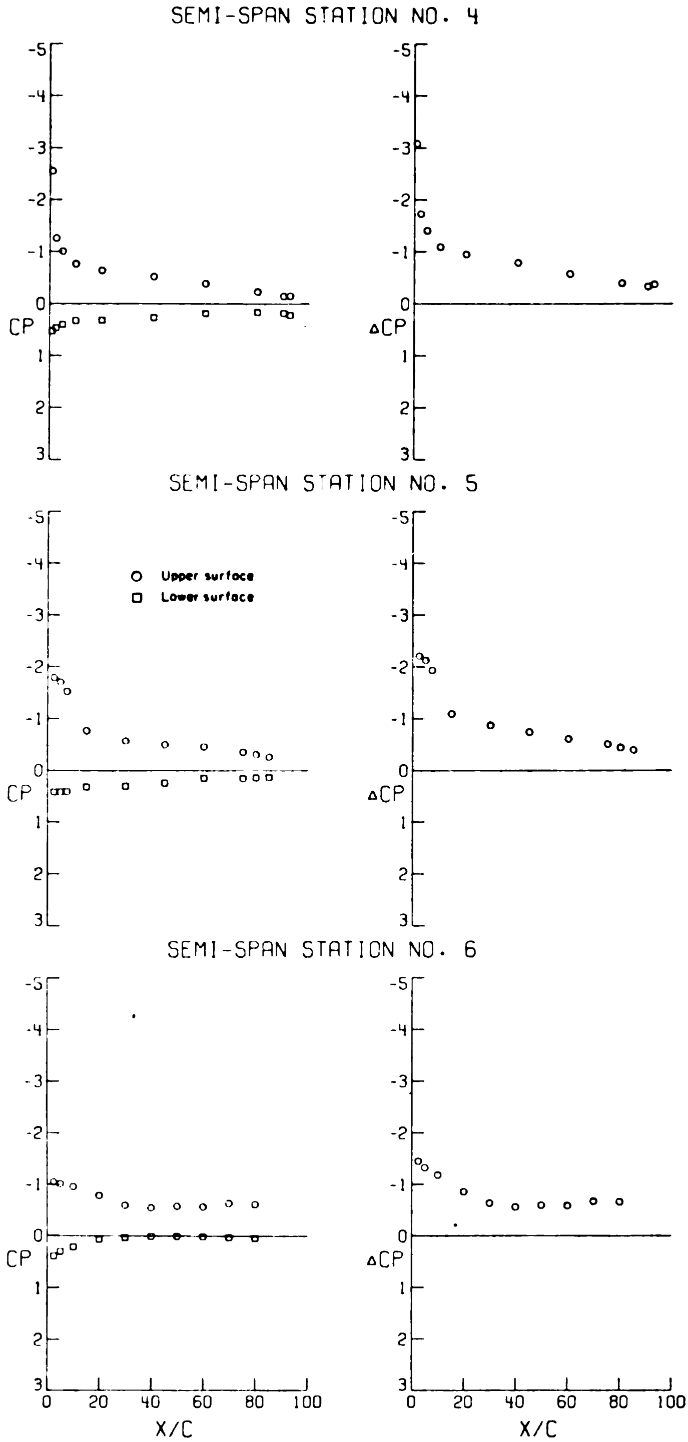

(d) Concluded.

Figure 4.- Continued.

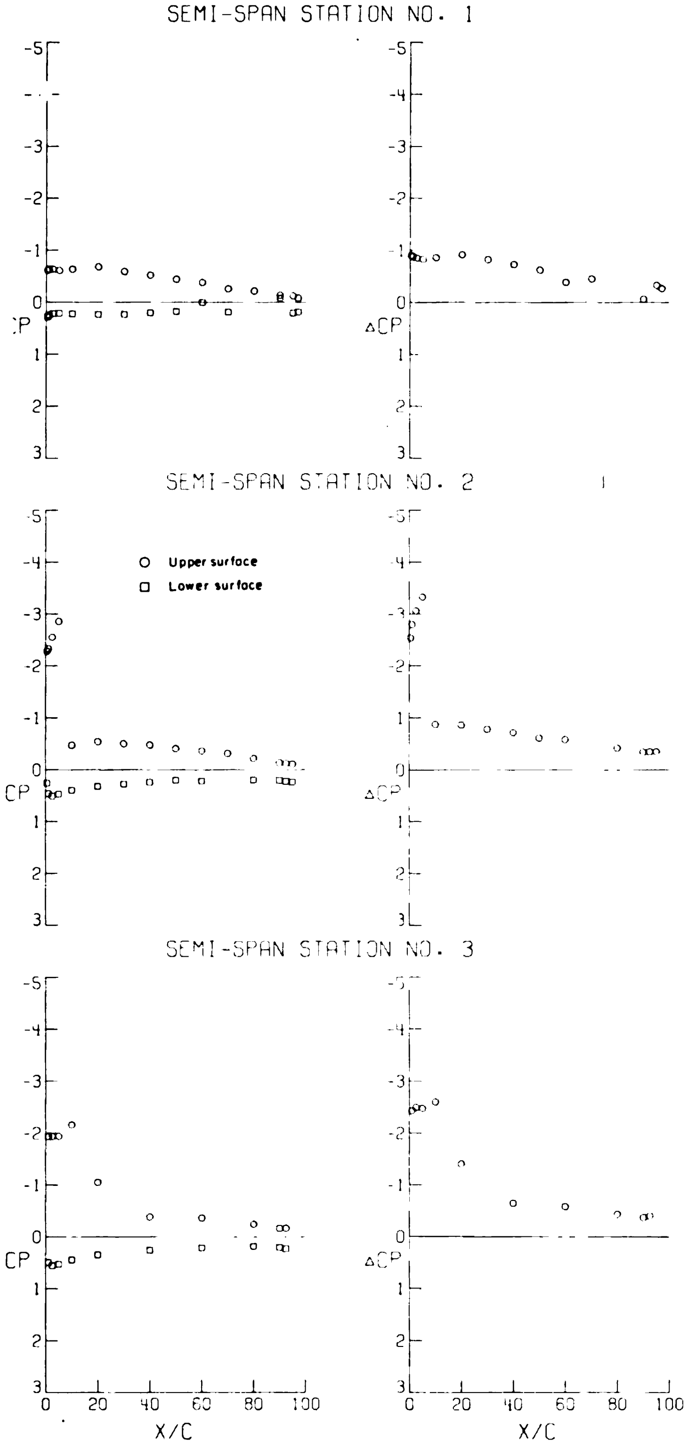

(e) $\alpha = 12.86^{\circ}$.

Figure 4.- Continued.

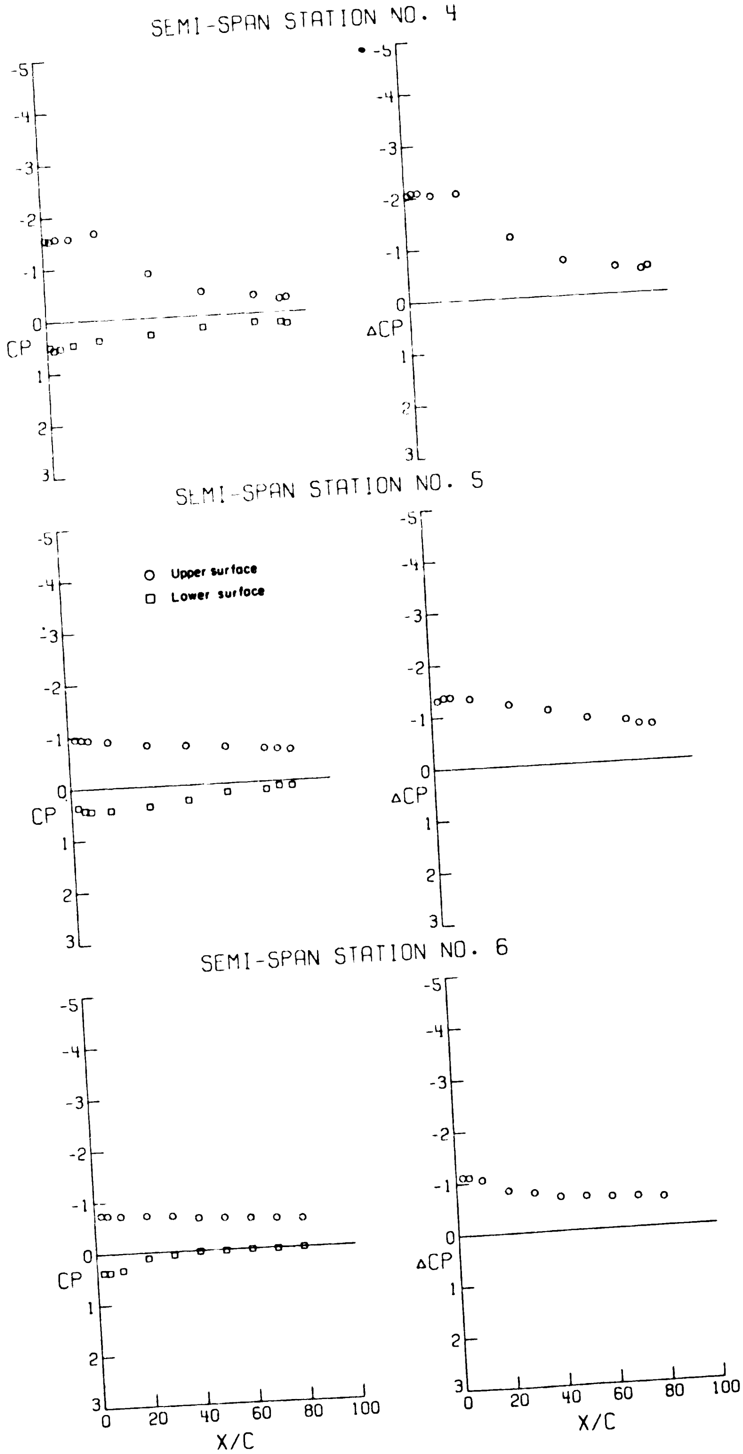

(e) Concluded.

Figure 4.- Continued.

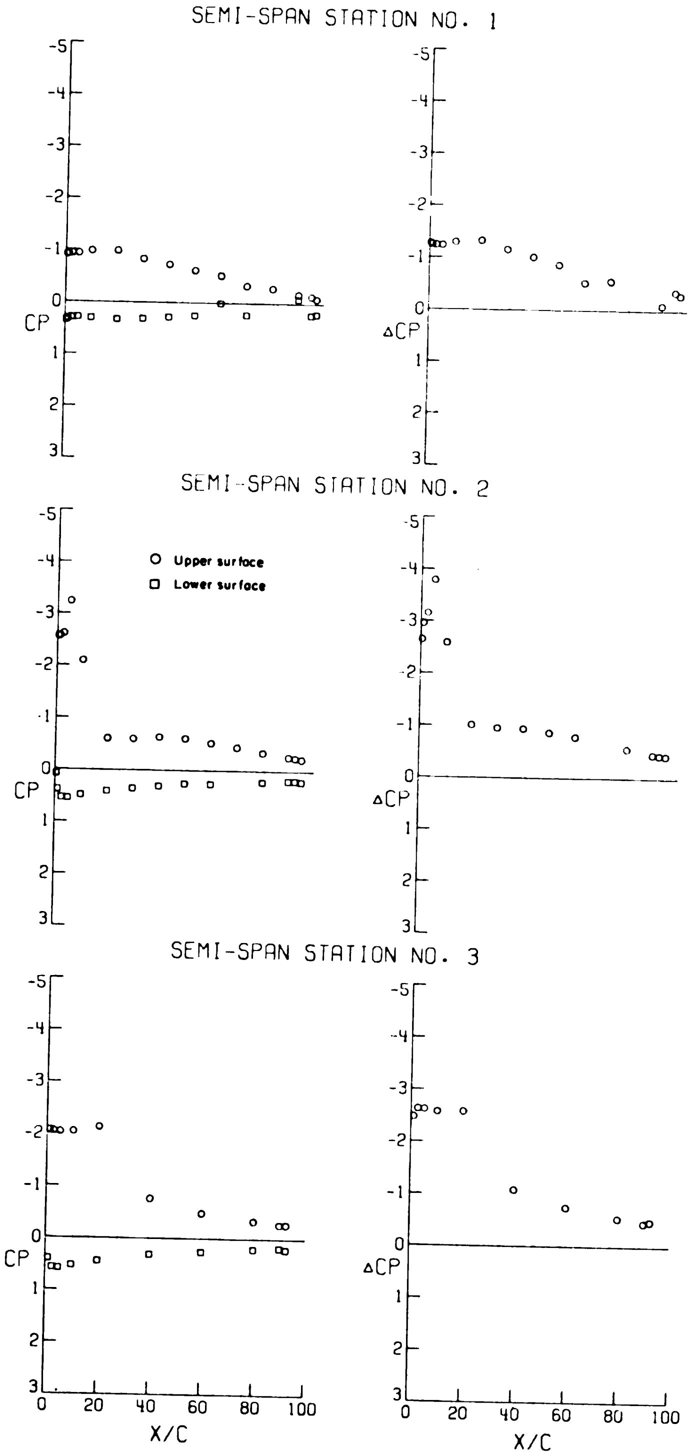

(f) $\alpha = 17.37°$.

Figure 4.- Continued.

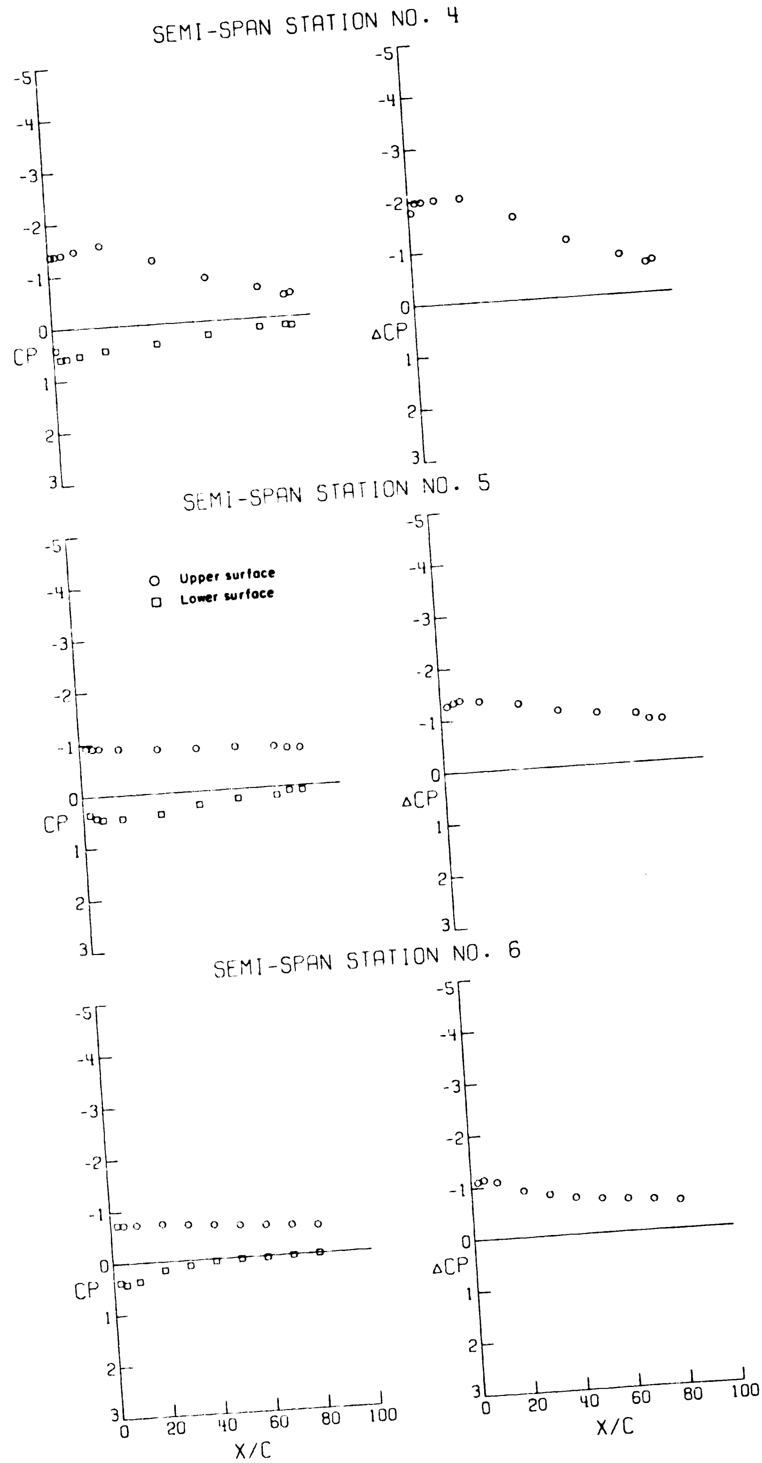

(f) Concluded.

Figure 4.- Continued.

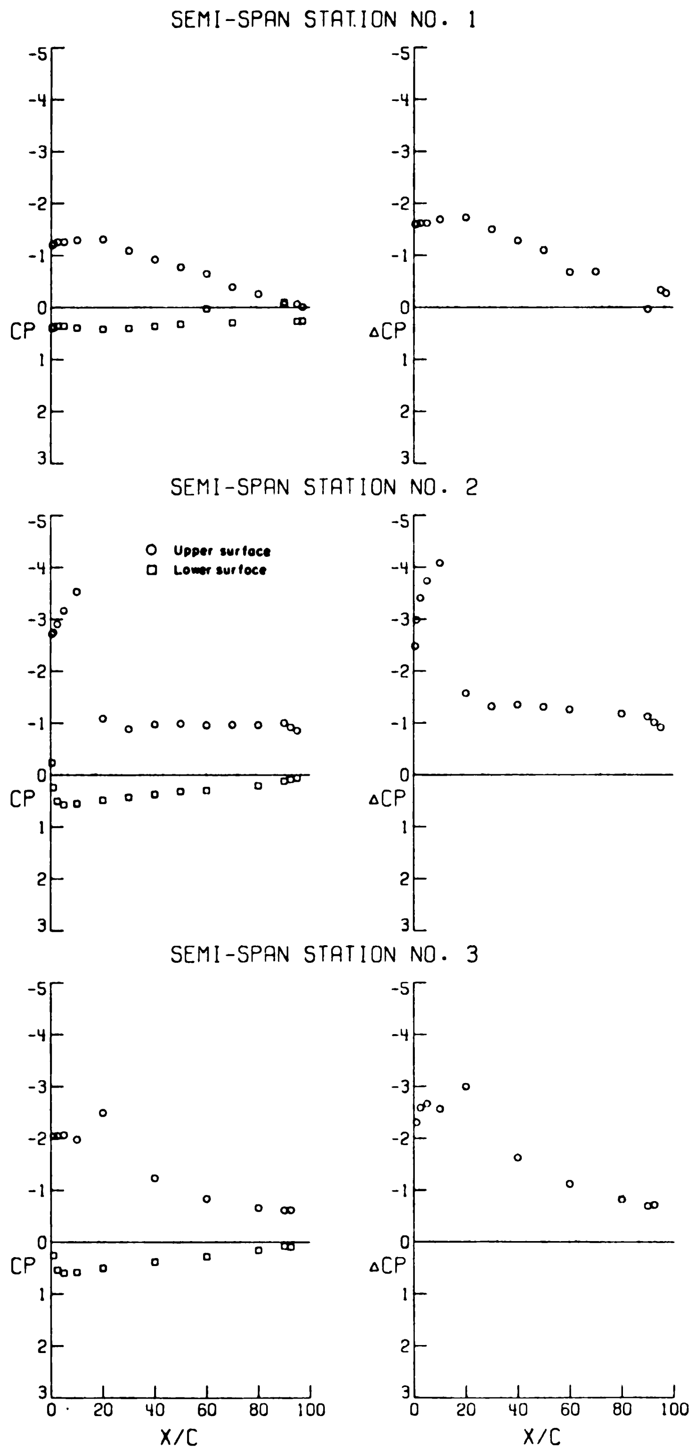

(g) $\alpha = 21.80^{\circ}$.

Figure 4.- Continued.

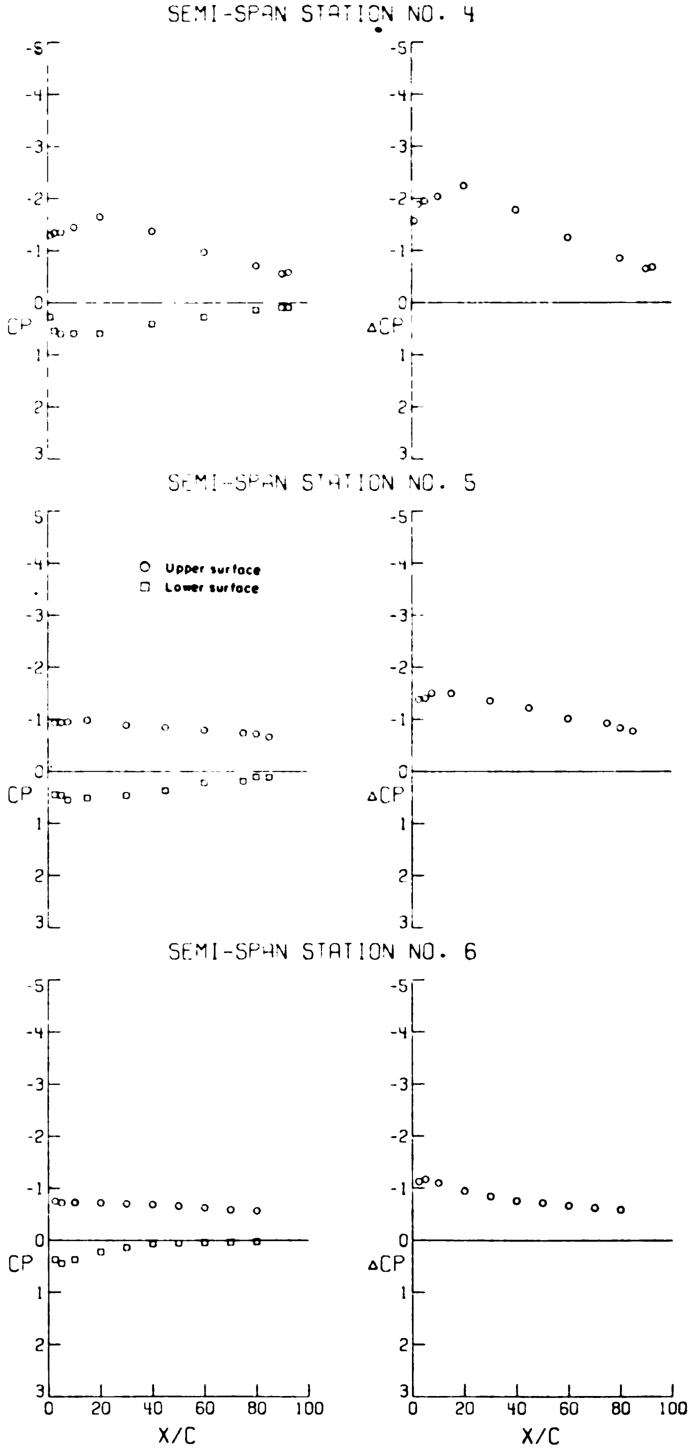

(g) Concluded.

Figure 4.- Concluded.

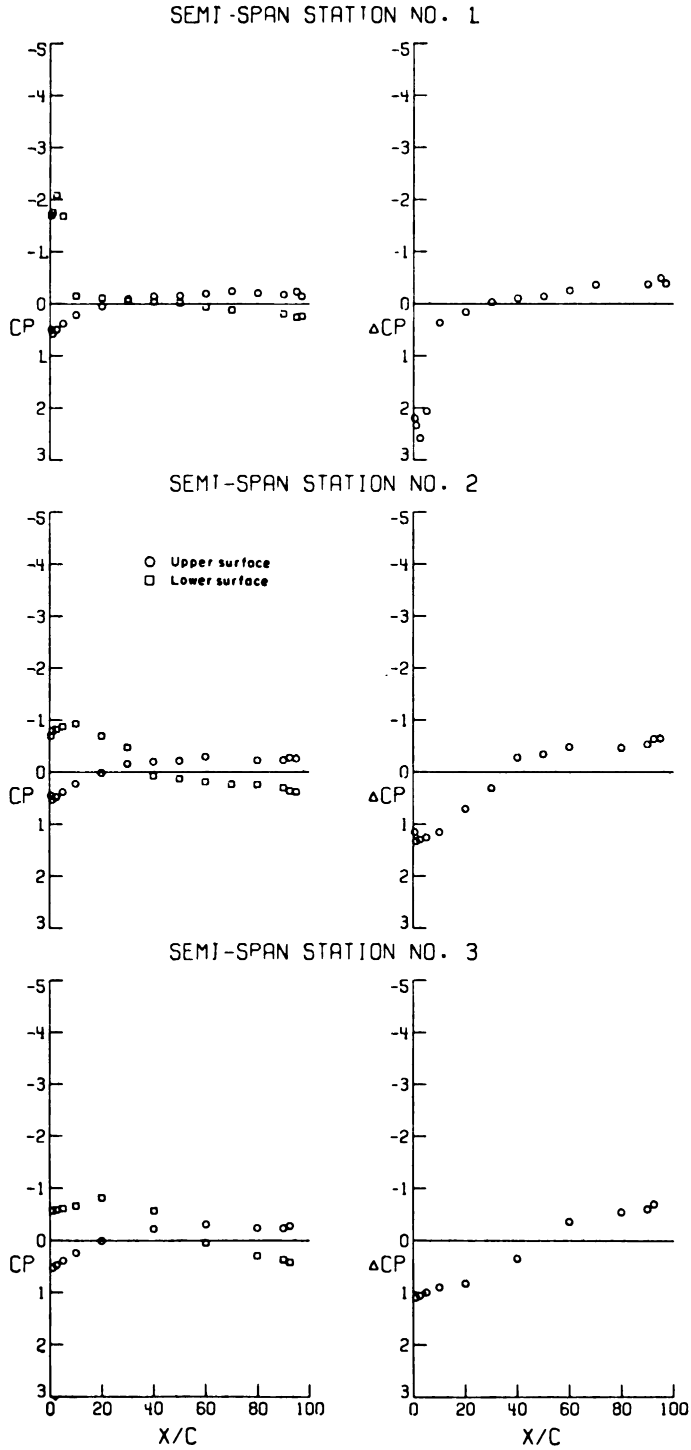

(a) $\alpha = -3.92^{\circ}$.

Figure 5.- Pressure distributions at a Mach number of 0.40 for the model with strakes off. $C_{L,d} = 0.70$.

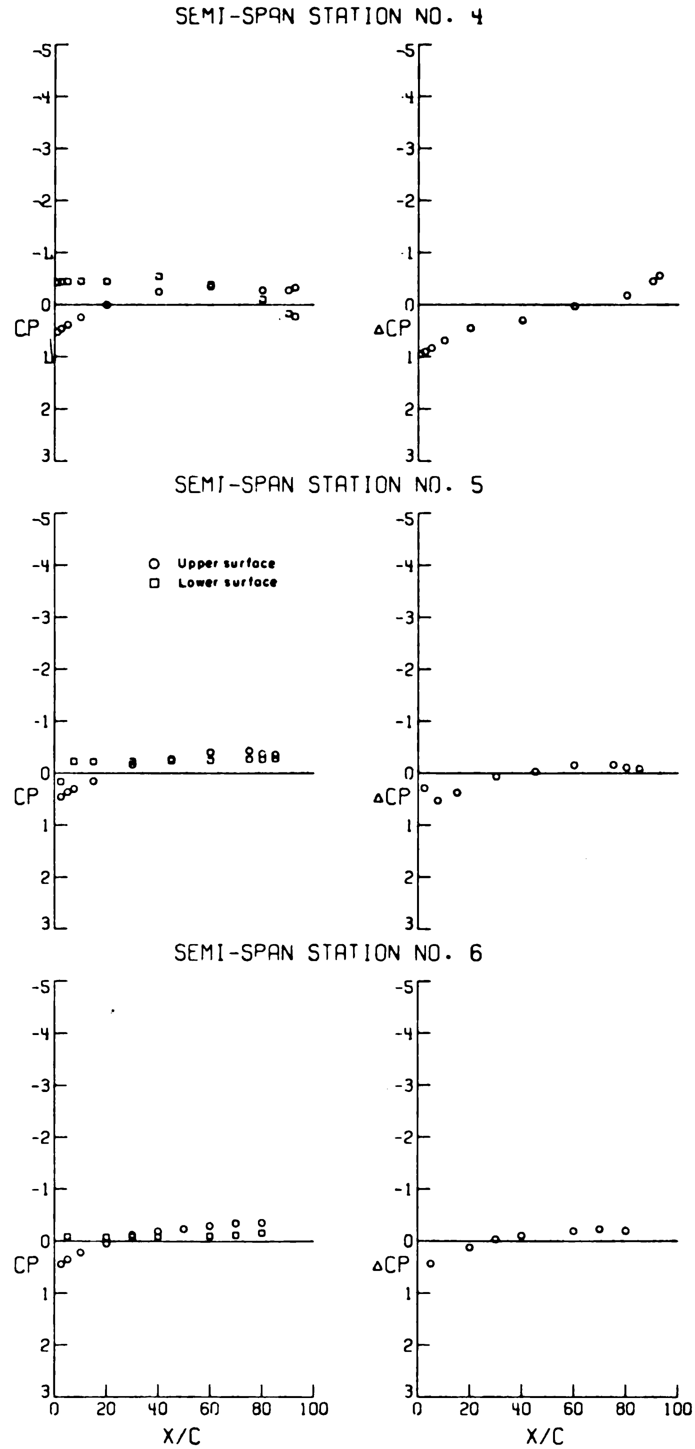

(a) Concluded.

Figure 5.- Continued.

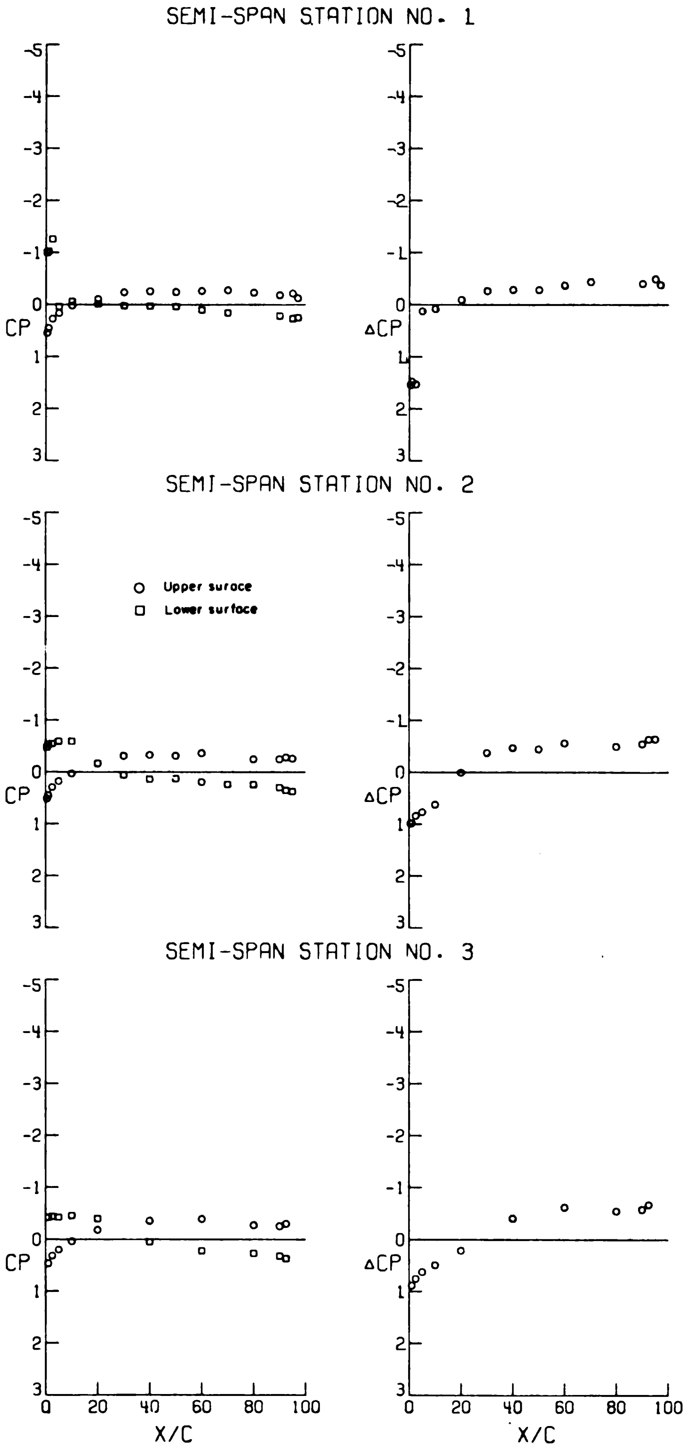

(b) $\alpha = 0.05^{\circ}$.

Figure 5.- Continued.

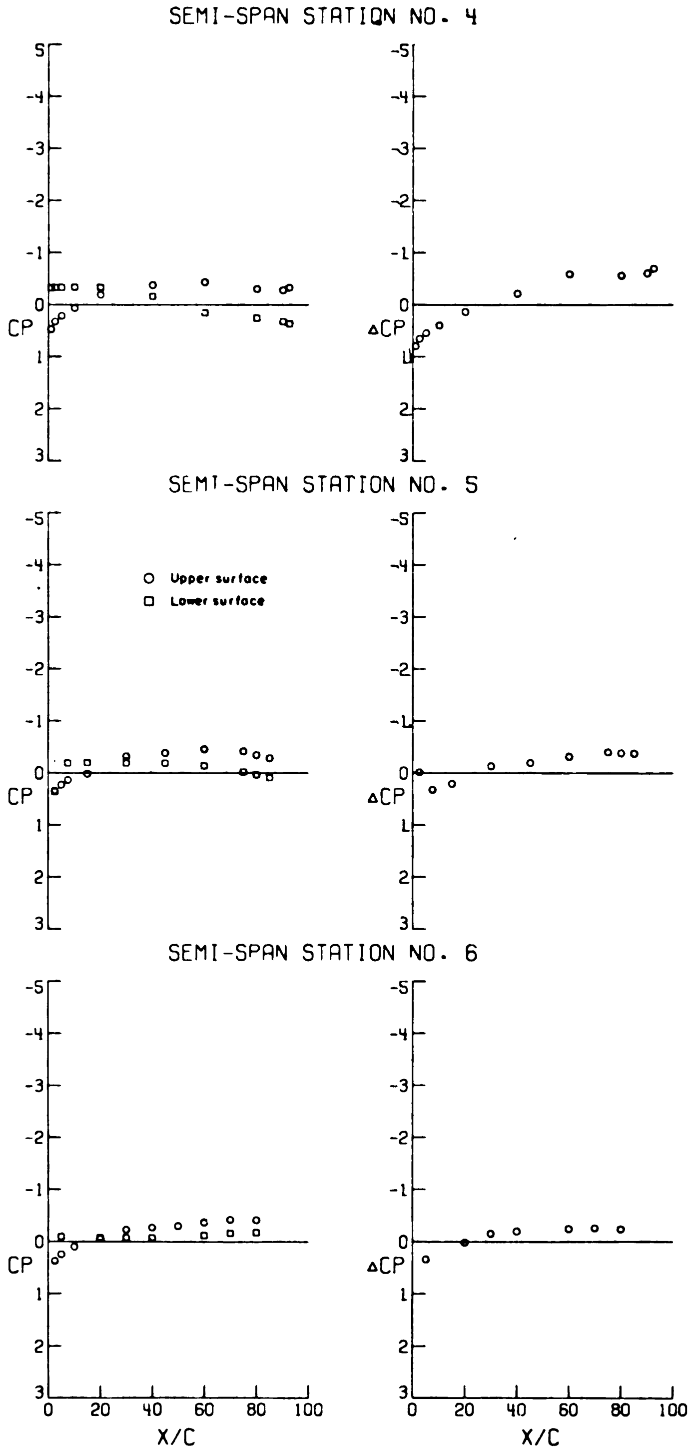

(b) Concluded.

Figure 5.- Continued.

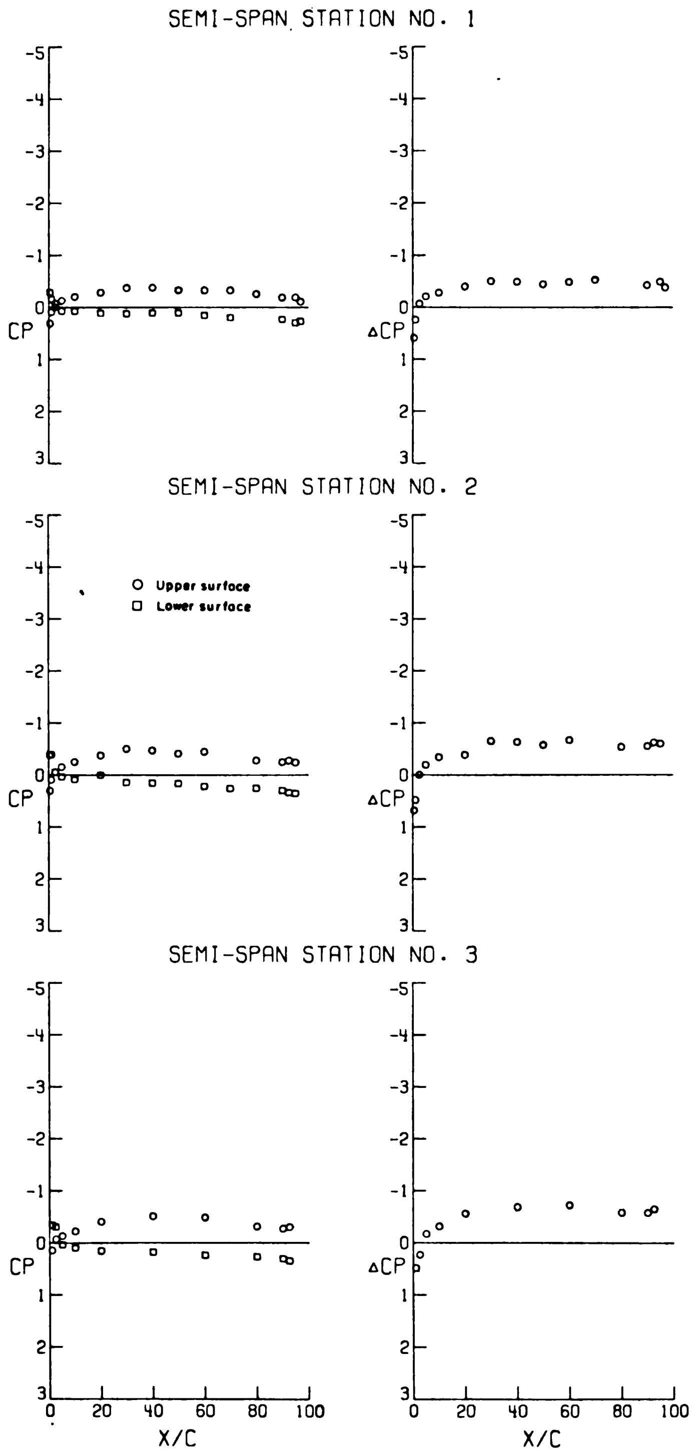

(c) $\alpha = 4.13^{\circ}$.

Figure 5.- Continued.

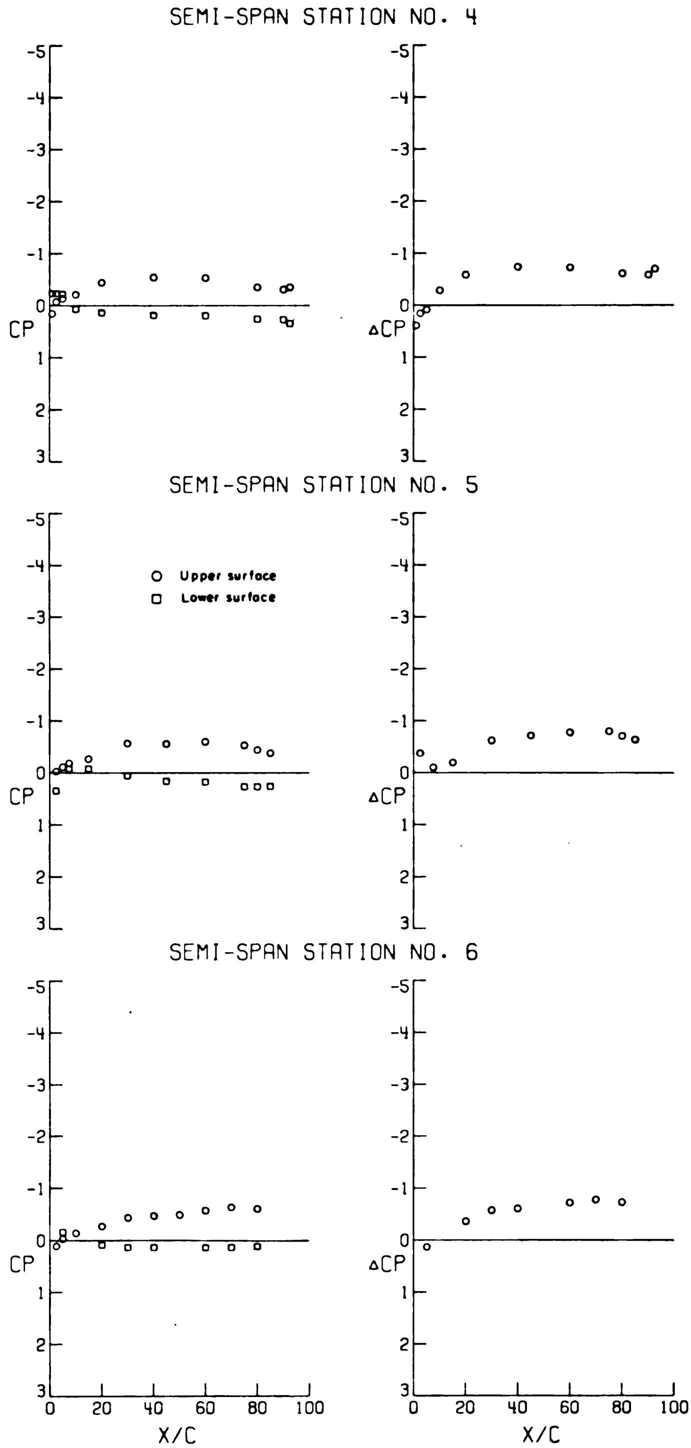

(c) Concluded.

Figure 5.- Continued.

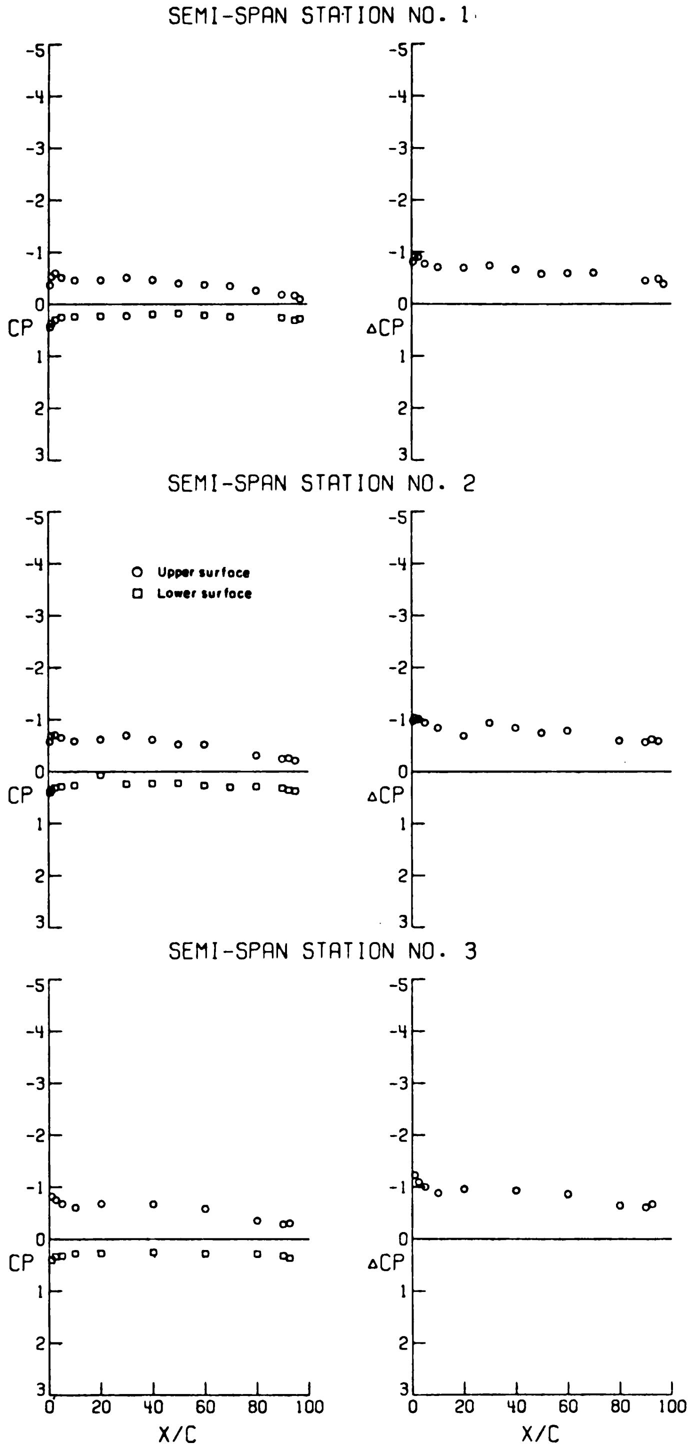

(d) $\alpha = 8.37^{\circ}$.

Figure 5.- Continued.

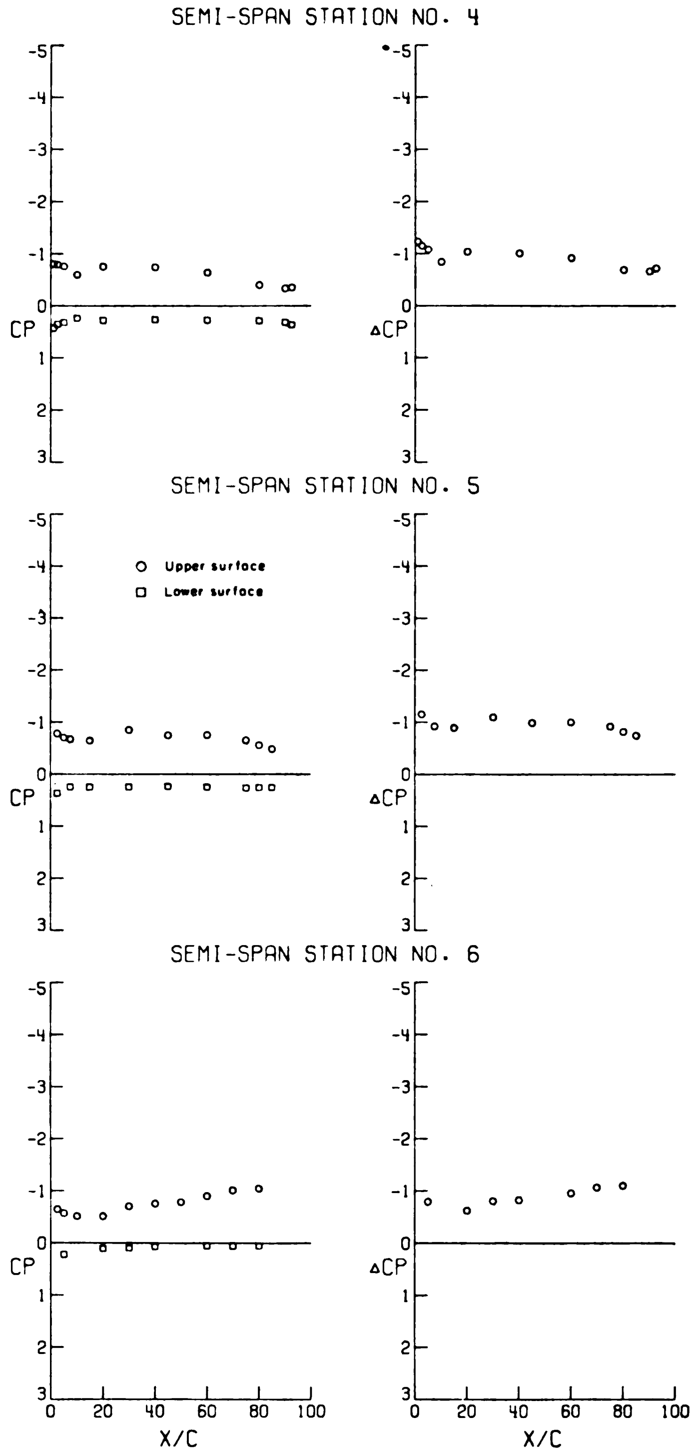

(d) Concluded.

Figure 5.- Continued.

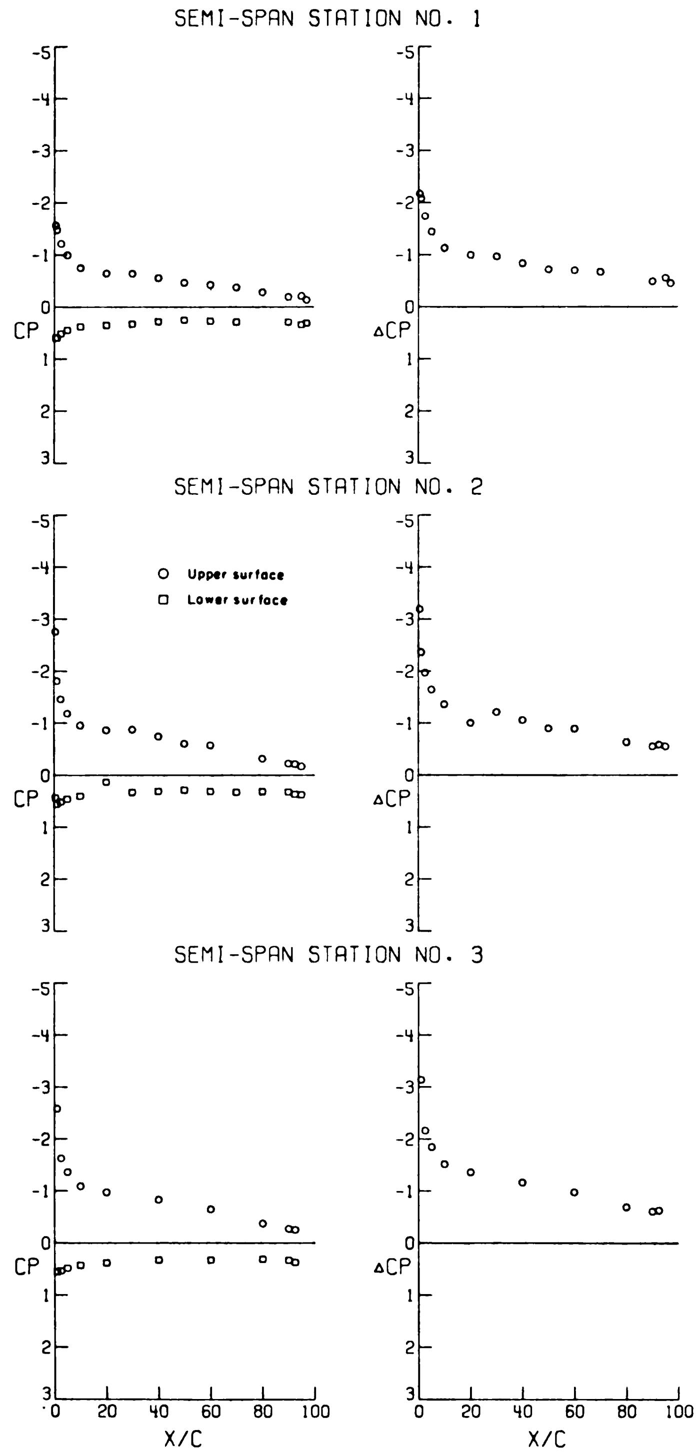

(e) $\alpha = 12.73^{\circ}$.

Figure 5.- Continued.

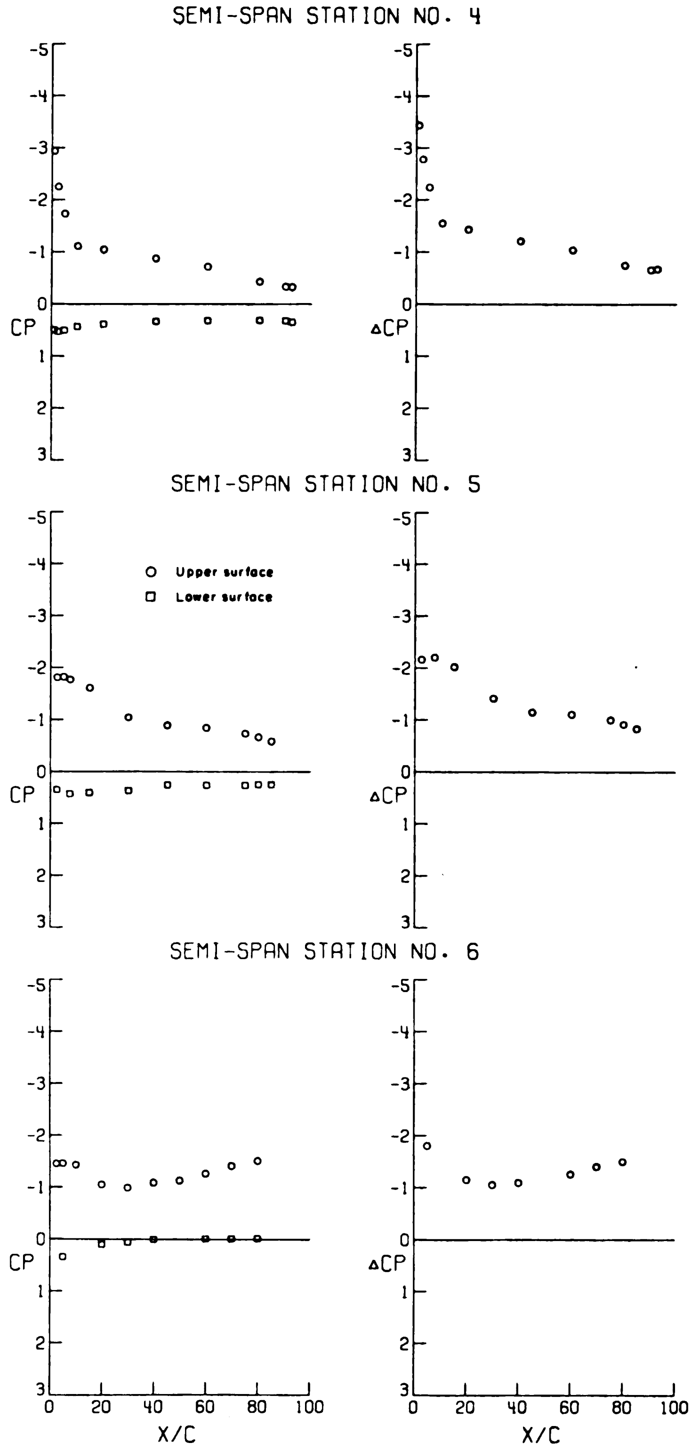

(e) Concluded.

Figure 5.- Continued.

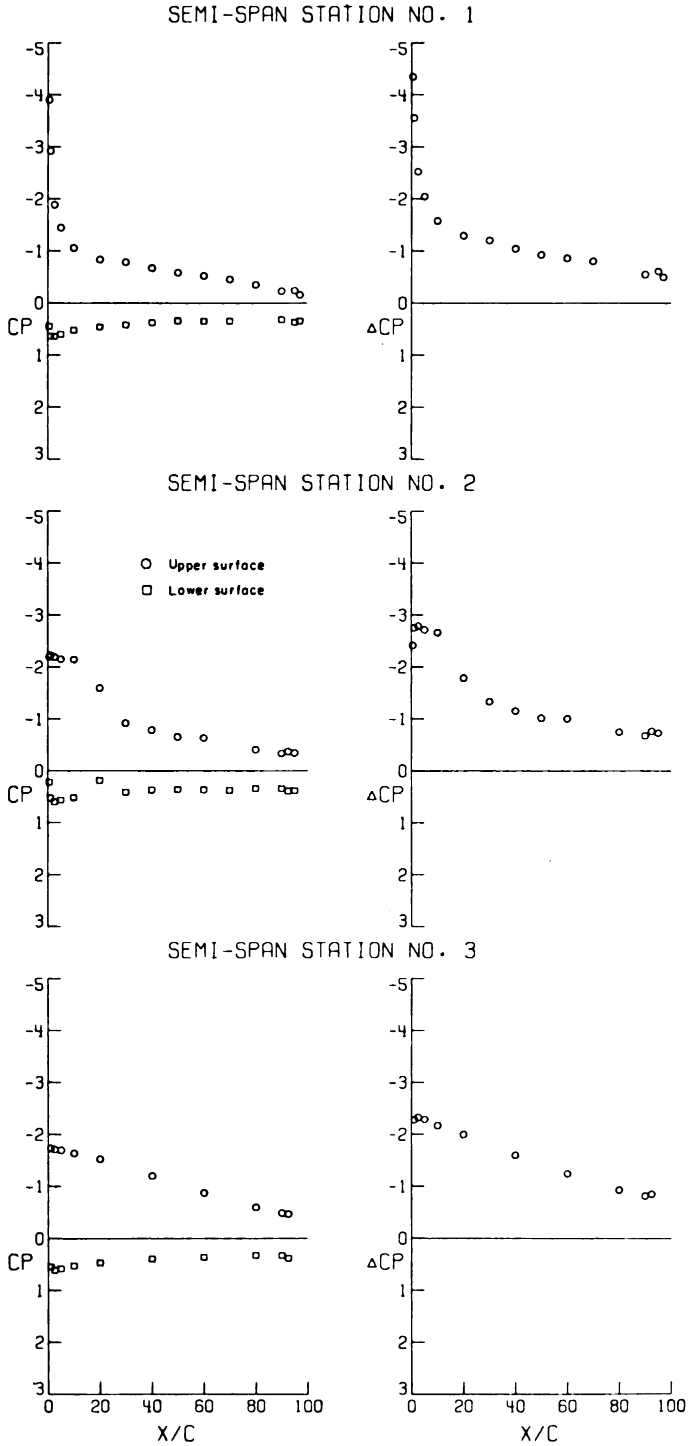

(f) $\alpha = 17.12^{\circ}$.

Figure 5.- Continued.

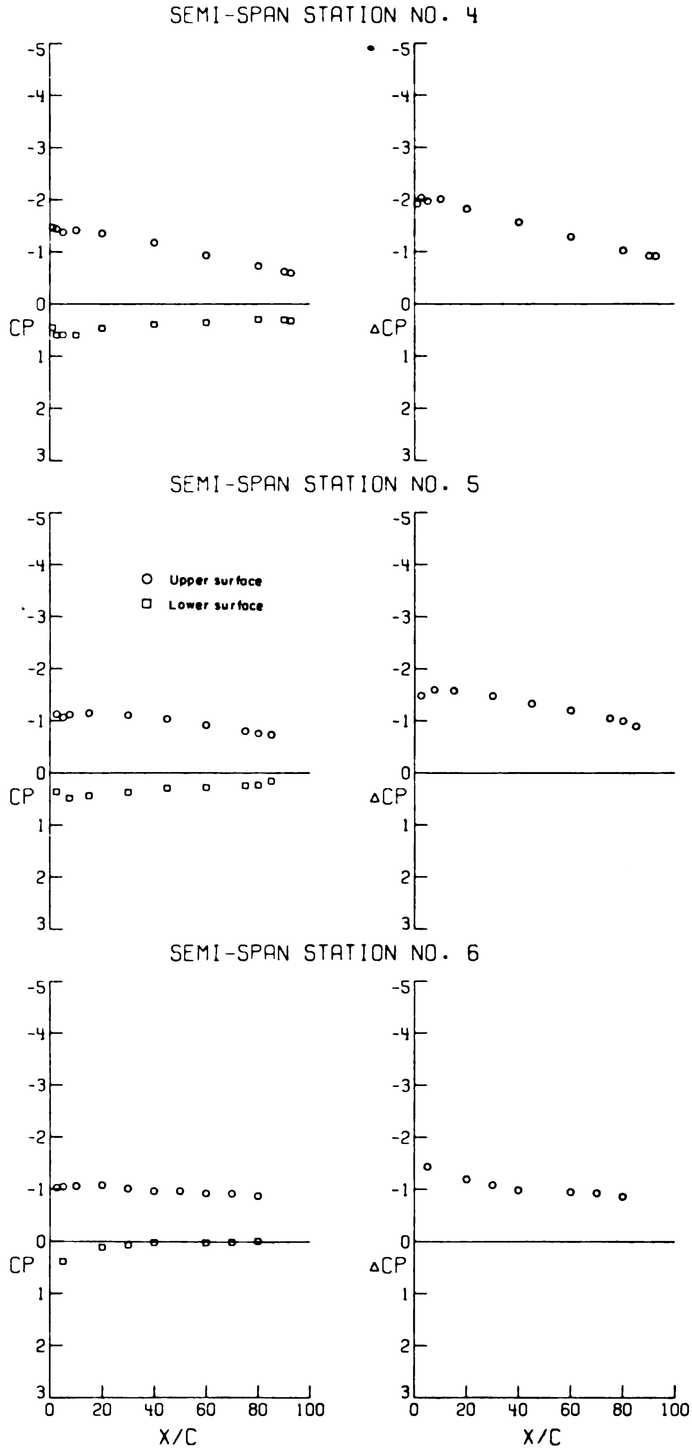

(f) Concluded.

Figure 5.- Continued.

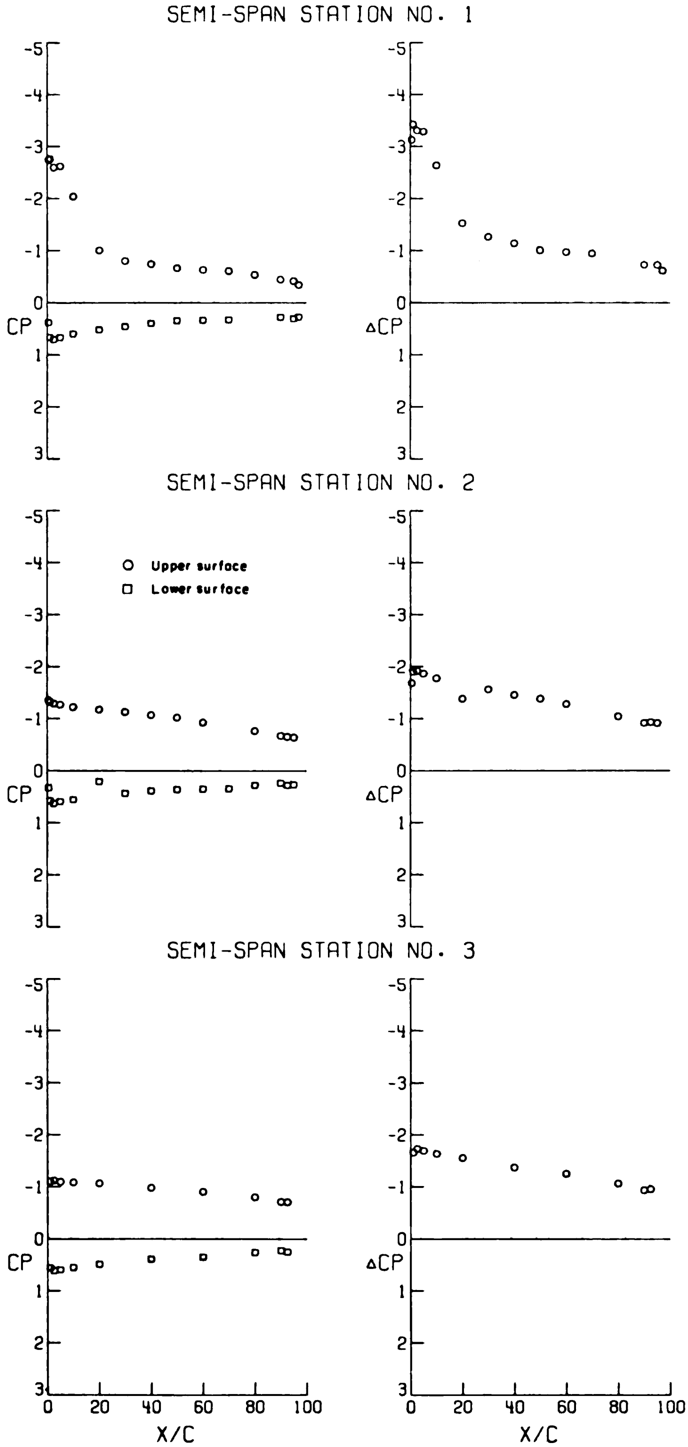

(g) $\alpha = 21.28^{o}$.

Figure 5.- Continued.

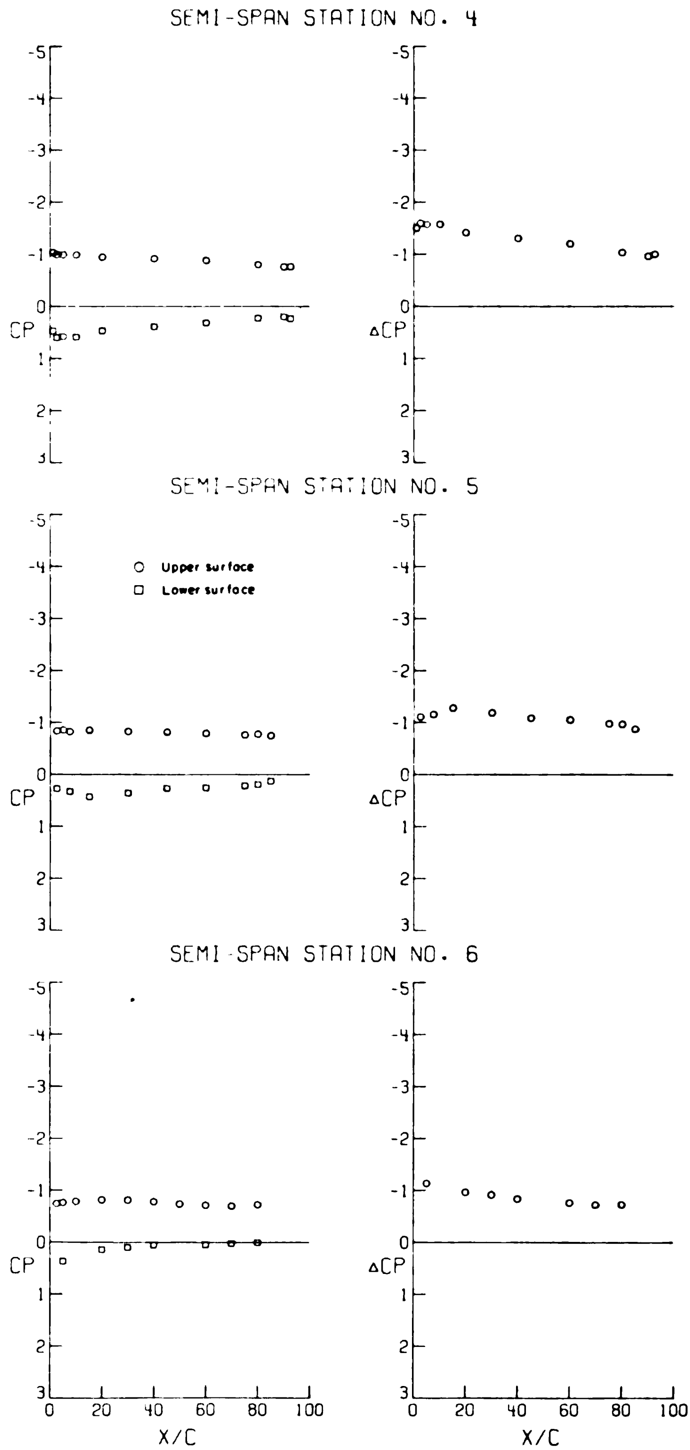

(g) Concluded.

Figure 5.- Concluded.

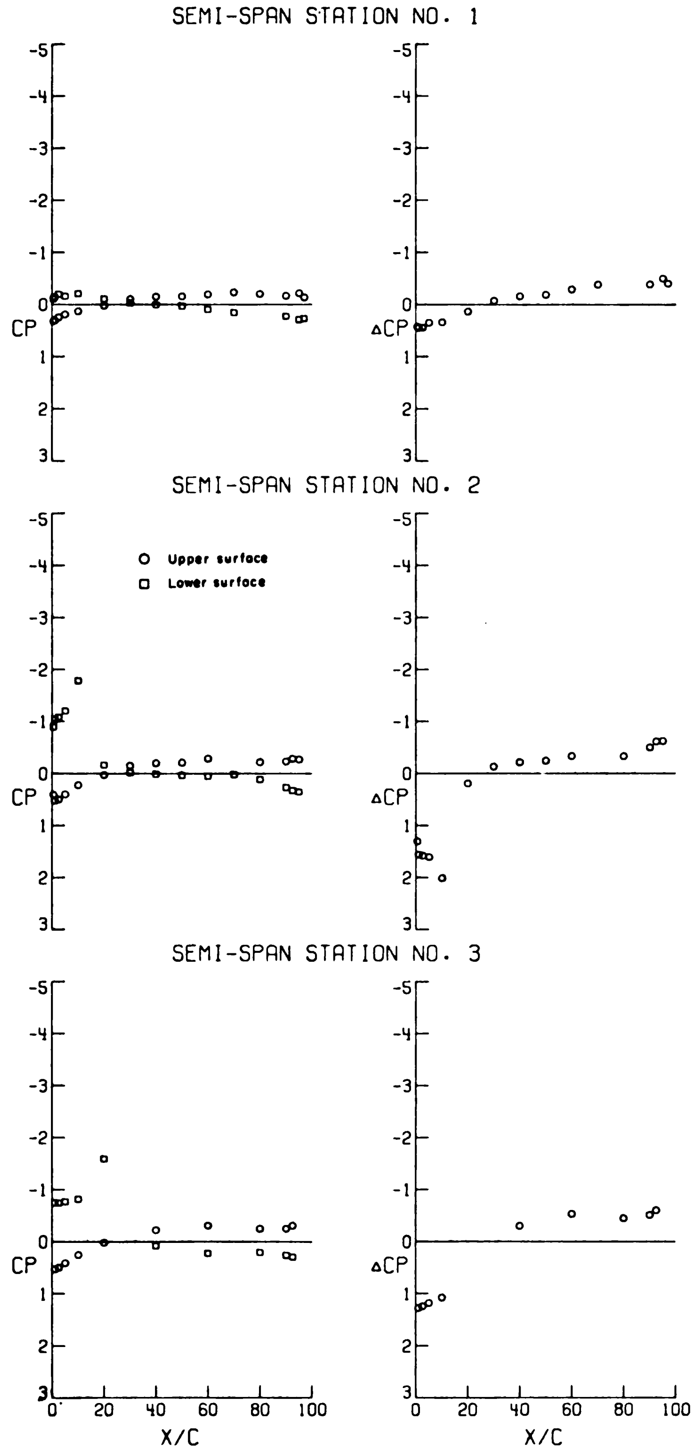

(a) $\alpha = -3.94^{\circ}$.

Figure 6.- Pressure distributions at a Mach number of 0.40 for the model with strakes on. $C_{L,d} = 0.70$.

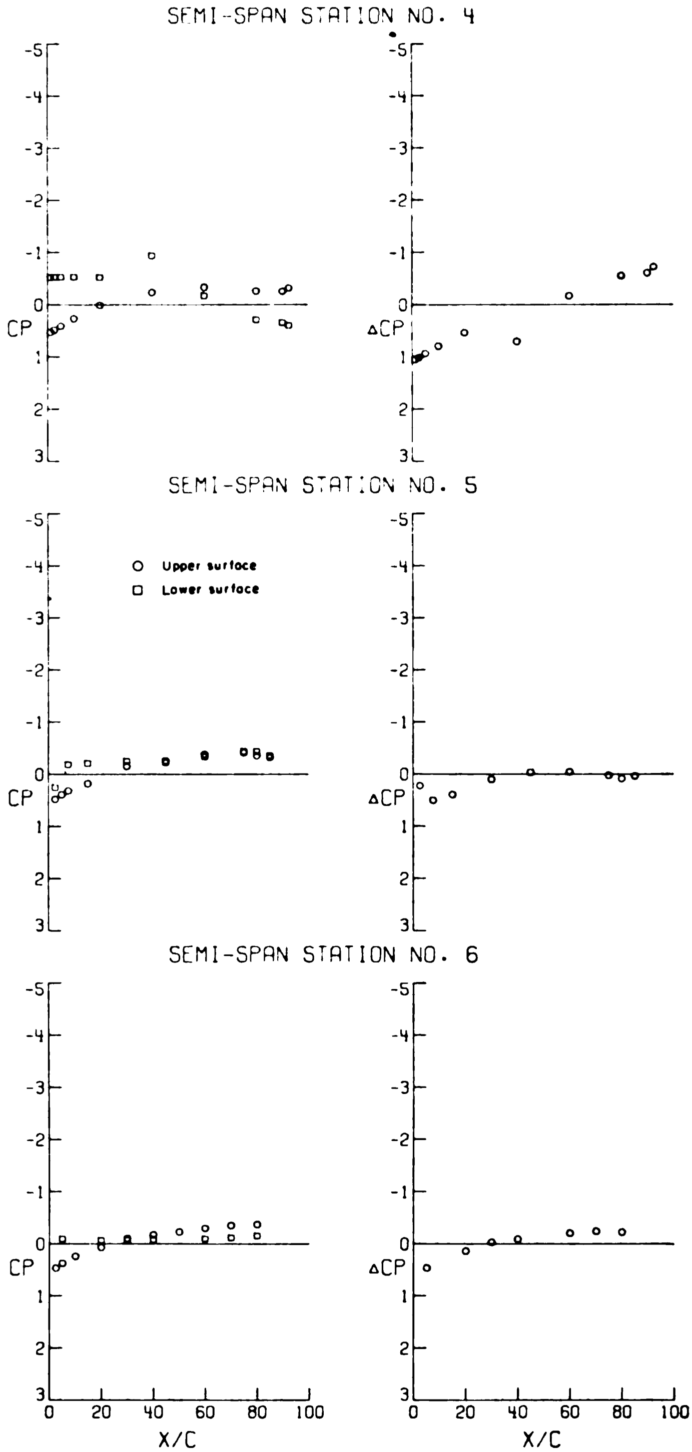

(a) Concluded.

Figure 6.- Continued.

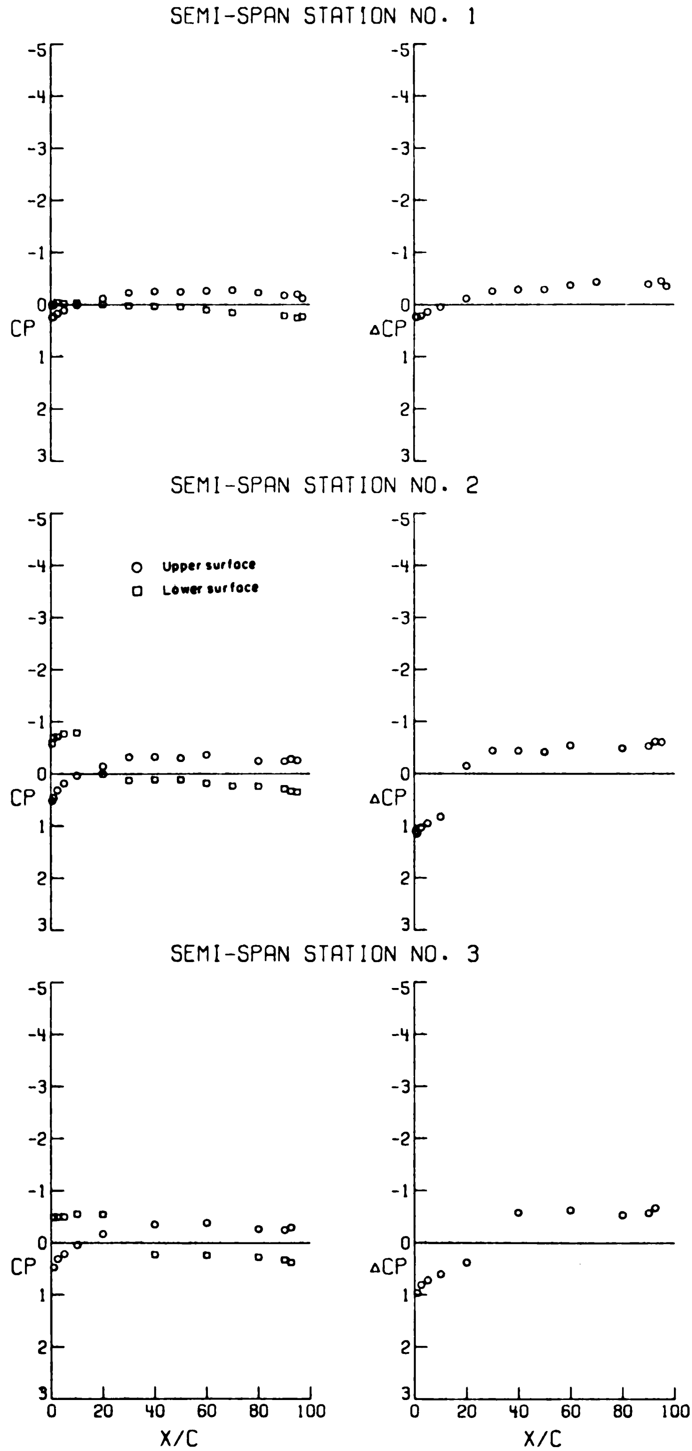

(b) $\alpha = 0.05^{\circ}$.

Figure 6. - Continued.

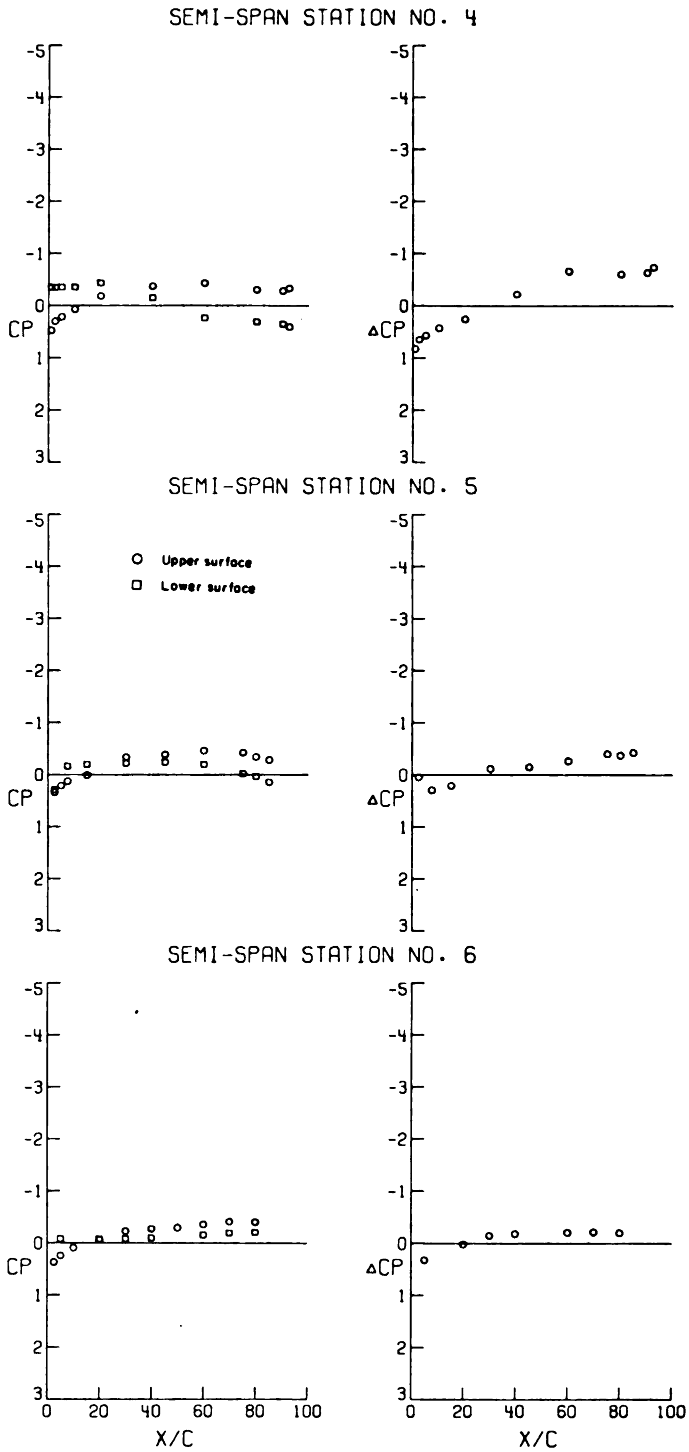

(b) Concluded.

Figure 6.- Continued.

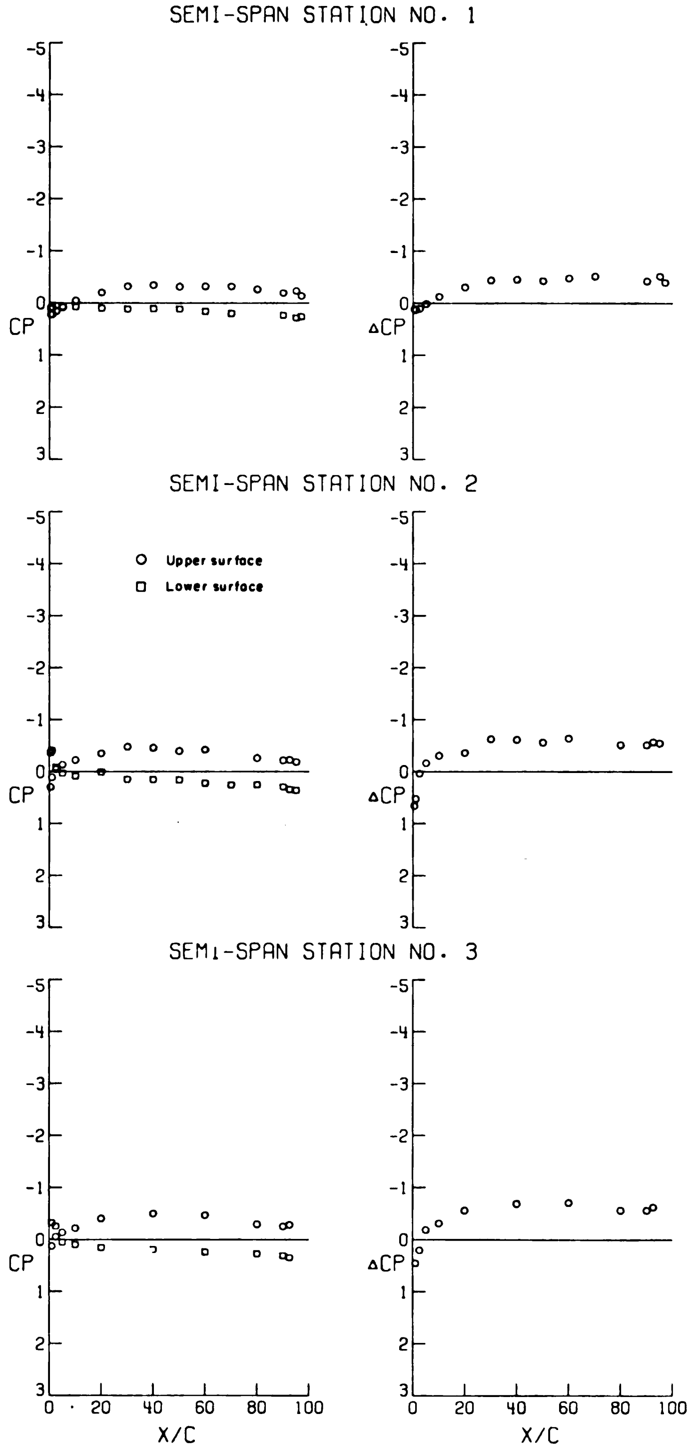

(c) $\alpha = 4.16^{\circ}$.

Figure 6.- Continued.

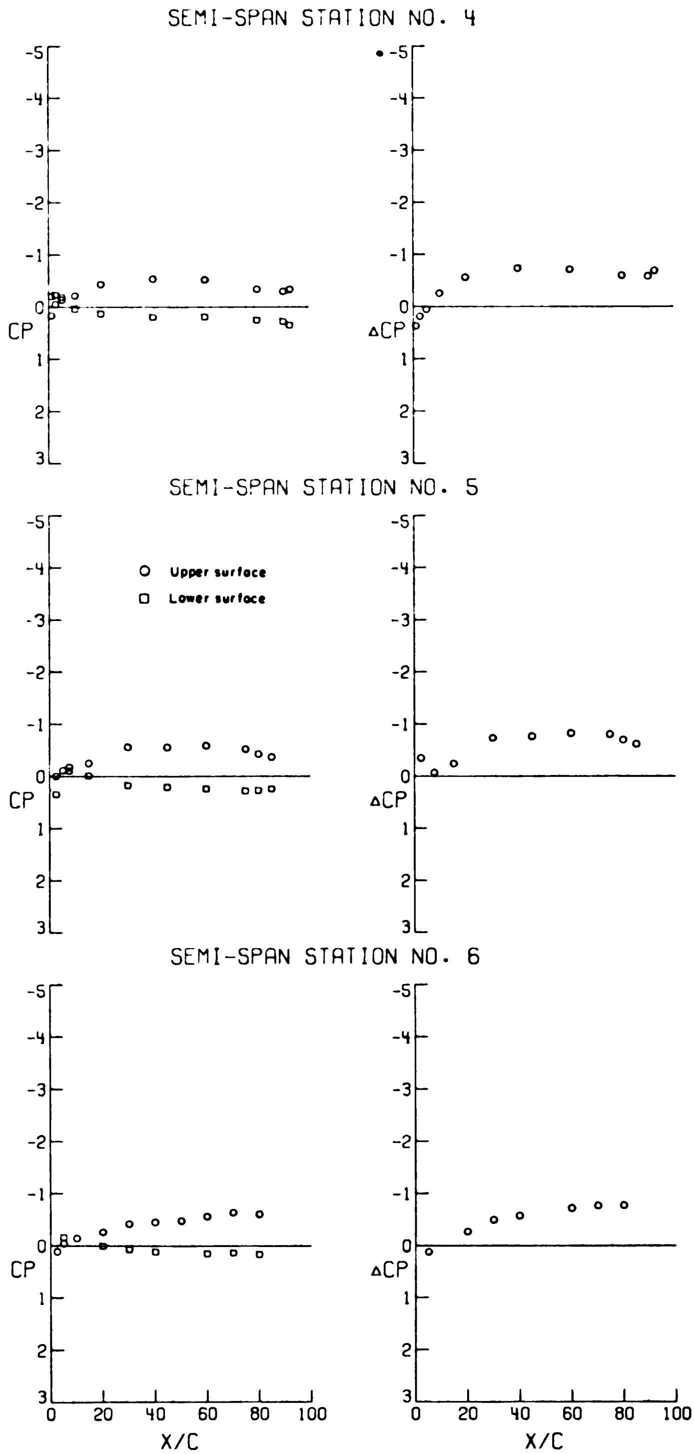

(c) Concluded.

Figure 6.- Continued.

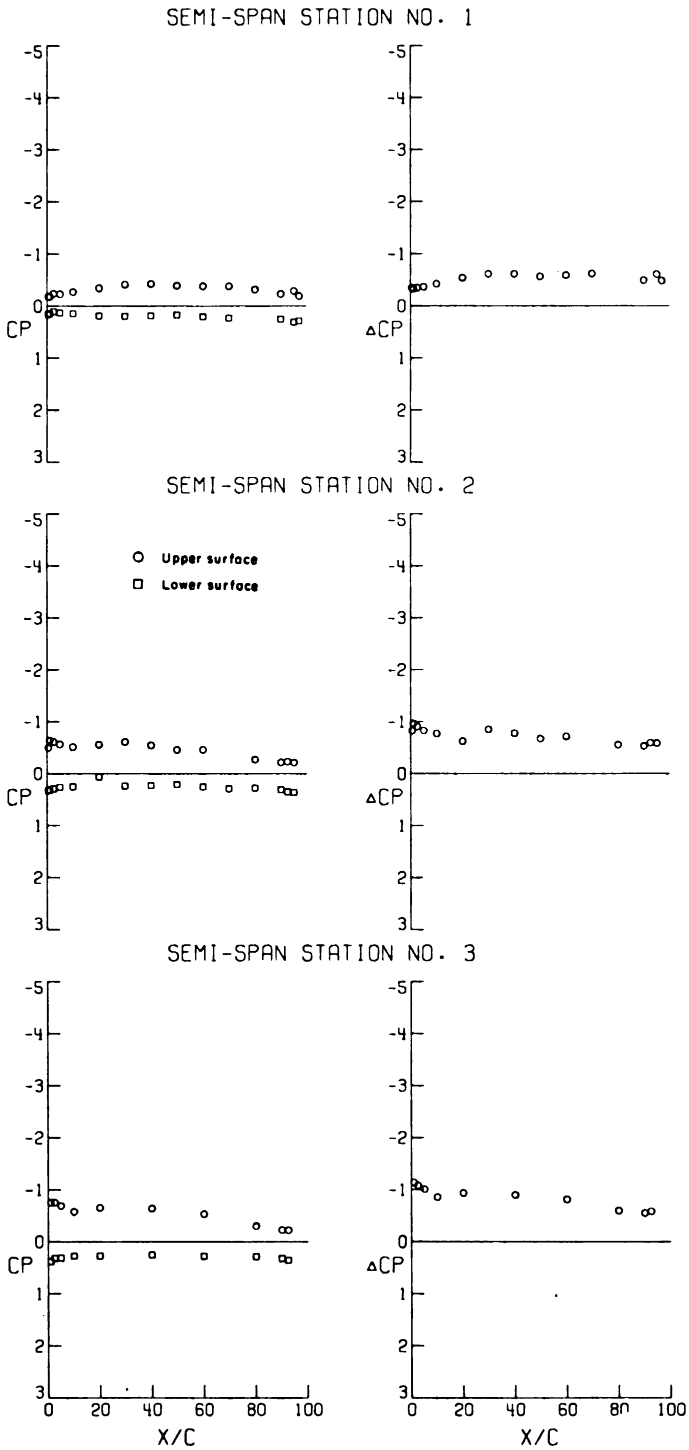

(d) $\alpha = 8.46^{\circ}$.

Figure 6.- Continued.

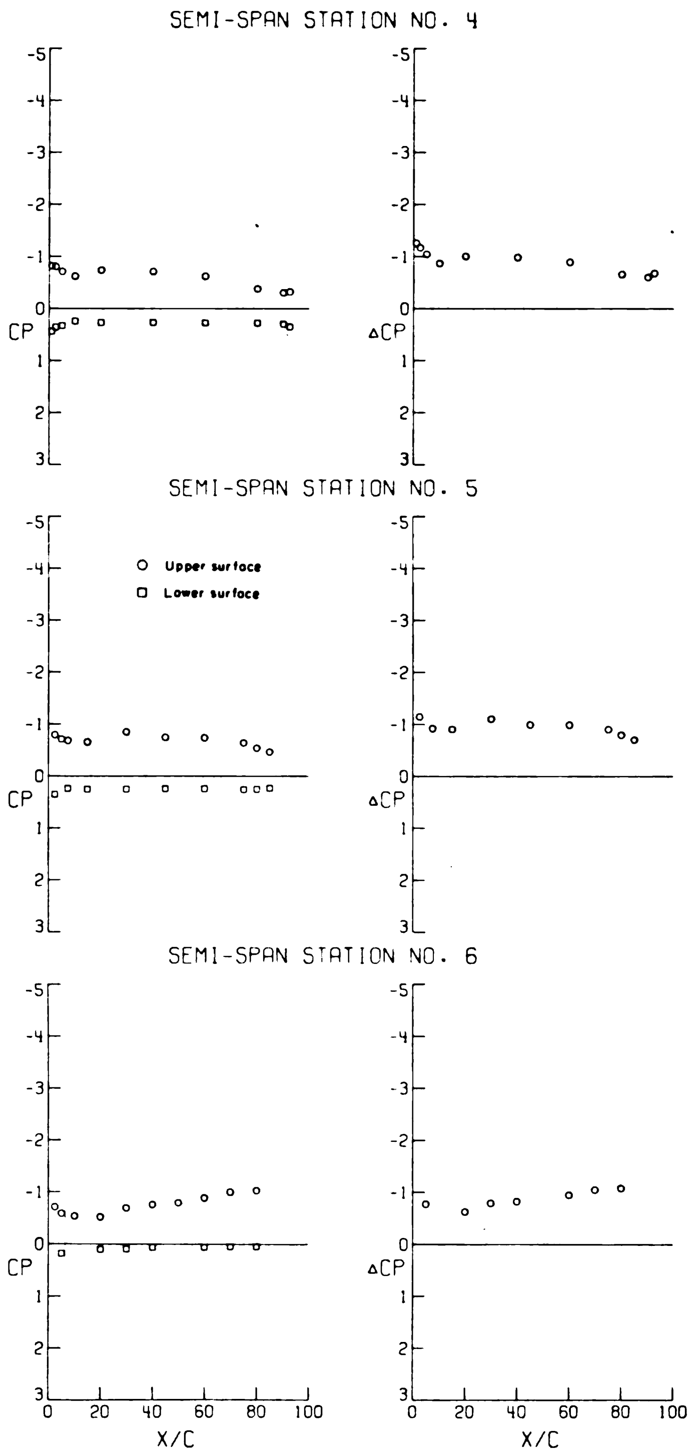

(d) Concluded.

Figure 6.- Continued.

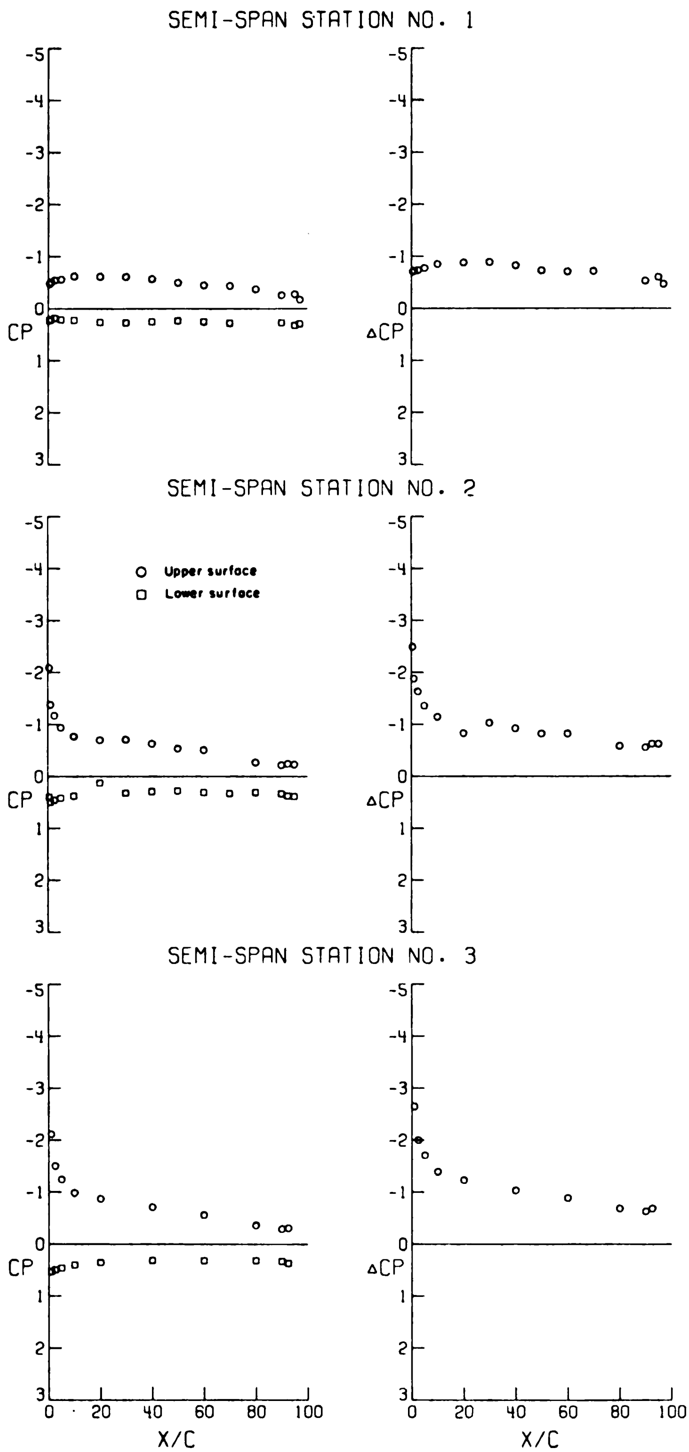

(e) $\alpha = 12.90^{\circ}$.

Figure 6.- Continued.

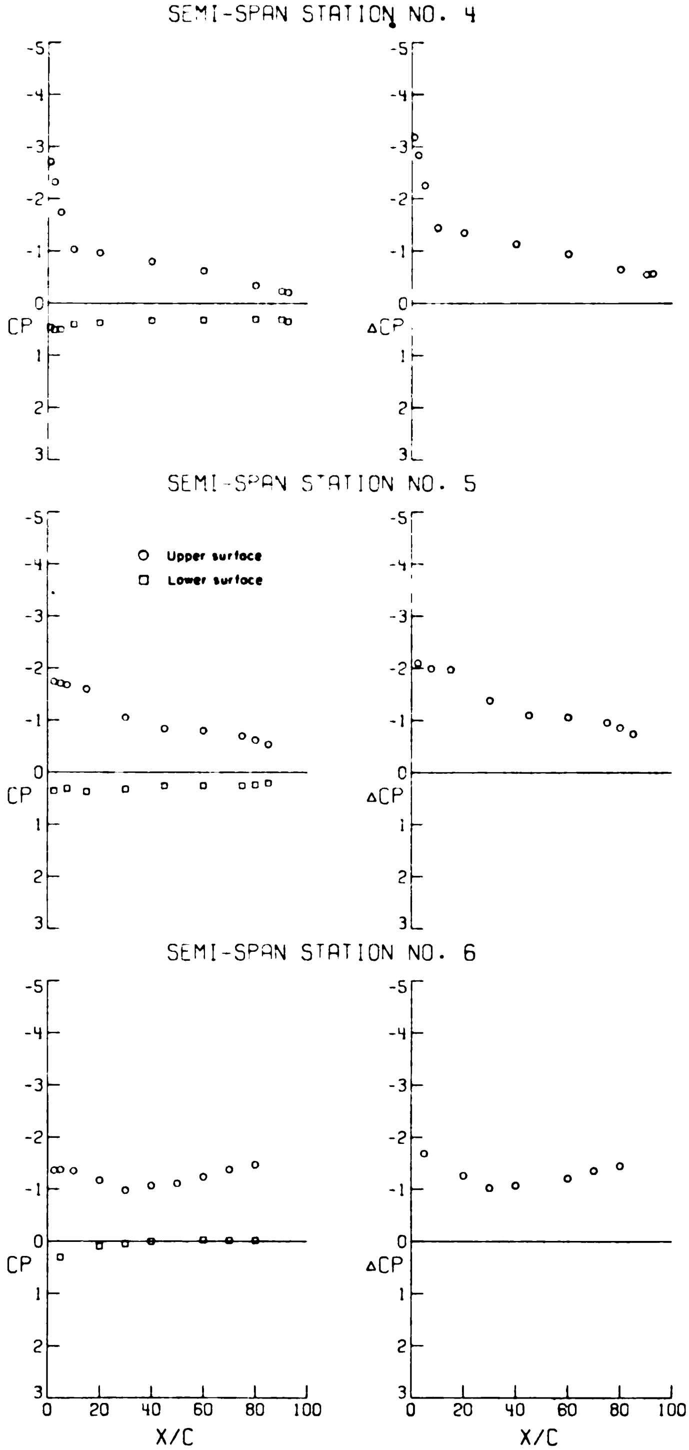

(e) Concluded.

Figure 6.- Continued.

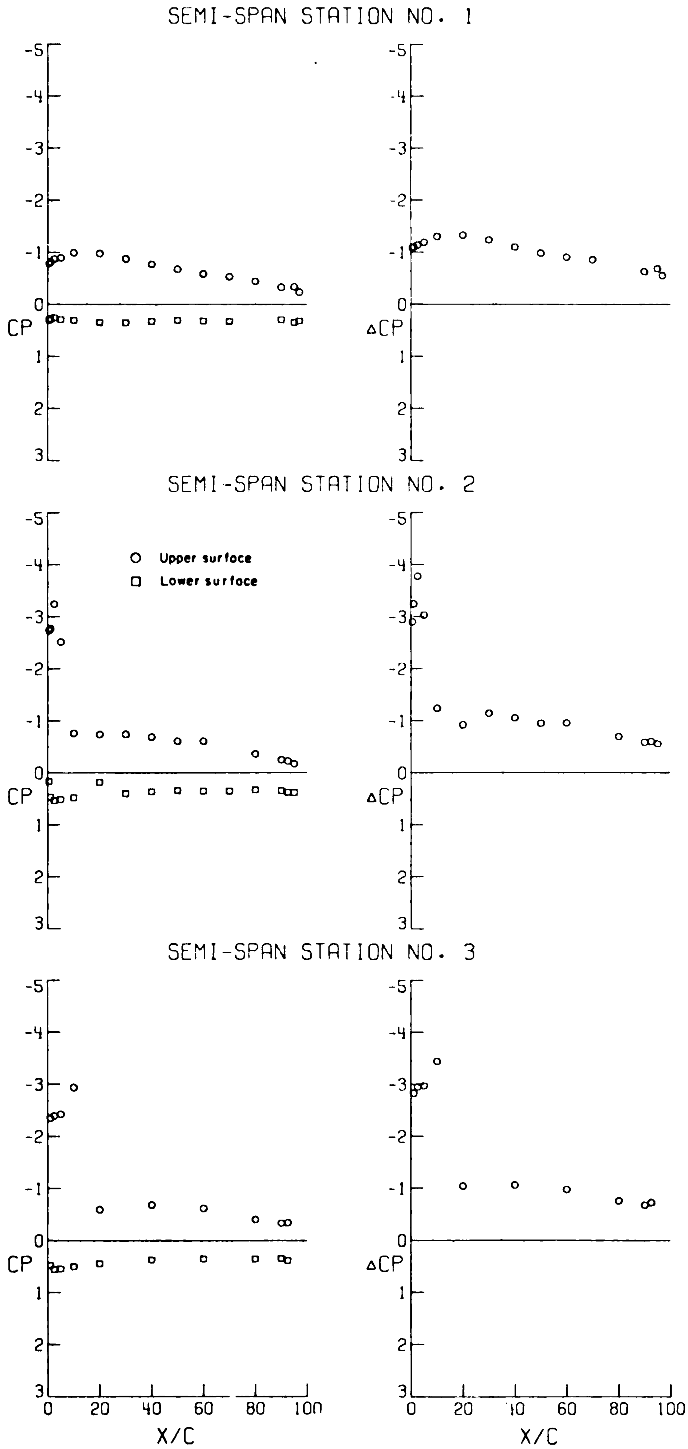

(f) $\alpha = 17.42^{\circ}$.

Figure 6.- Continued.

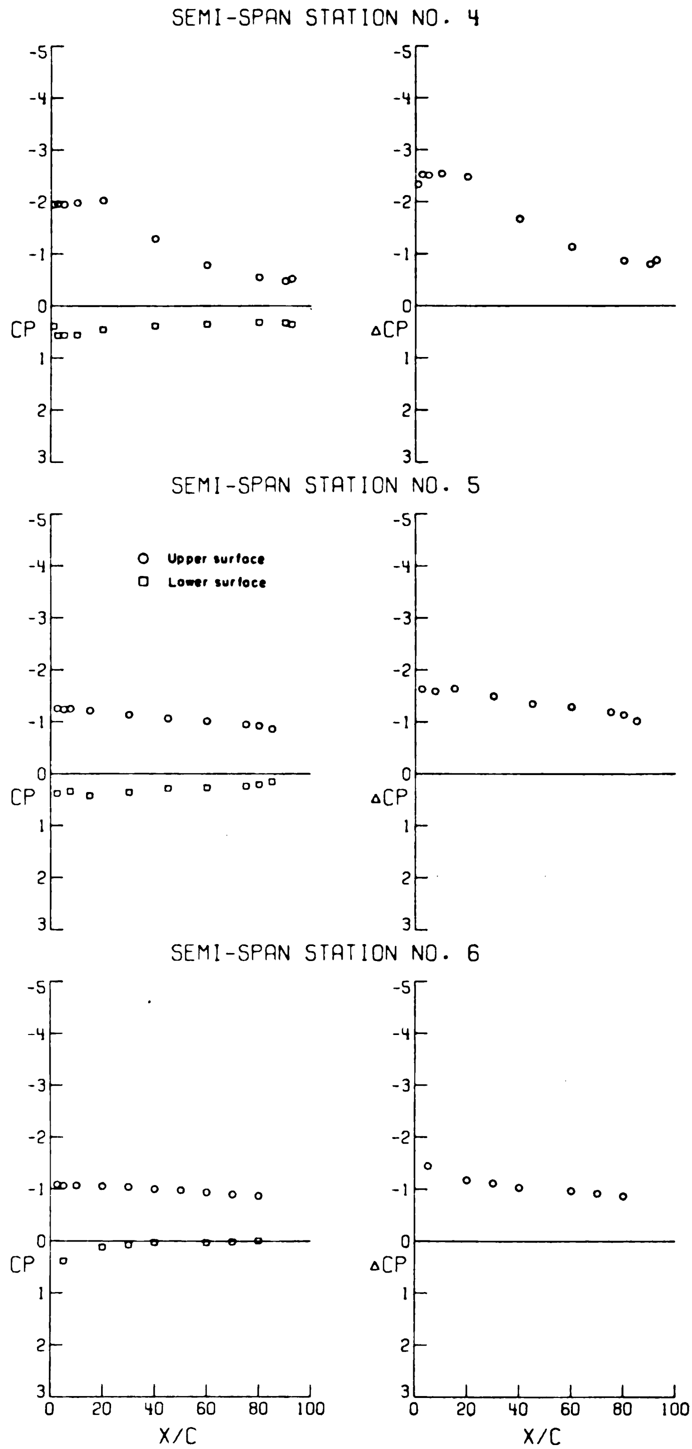

(f) Concluded.

Figure 6.- Continued.

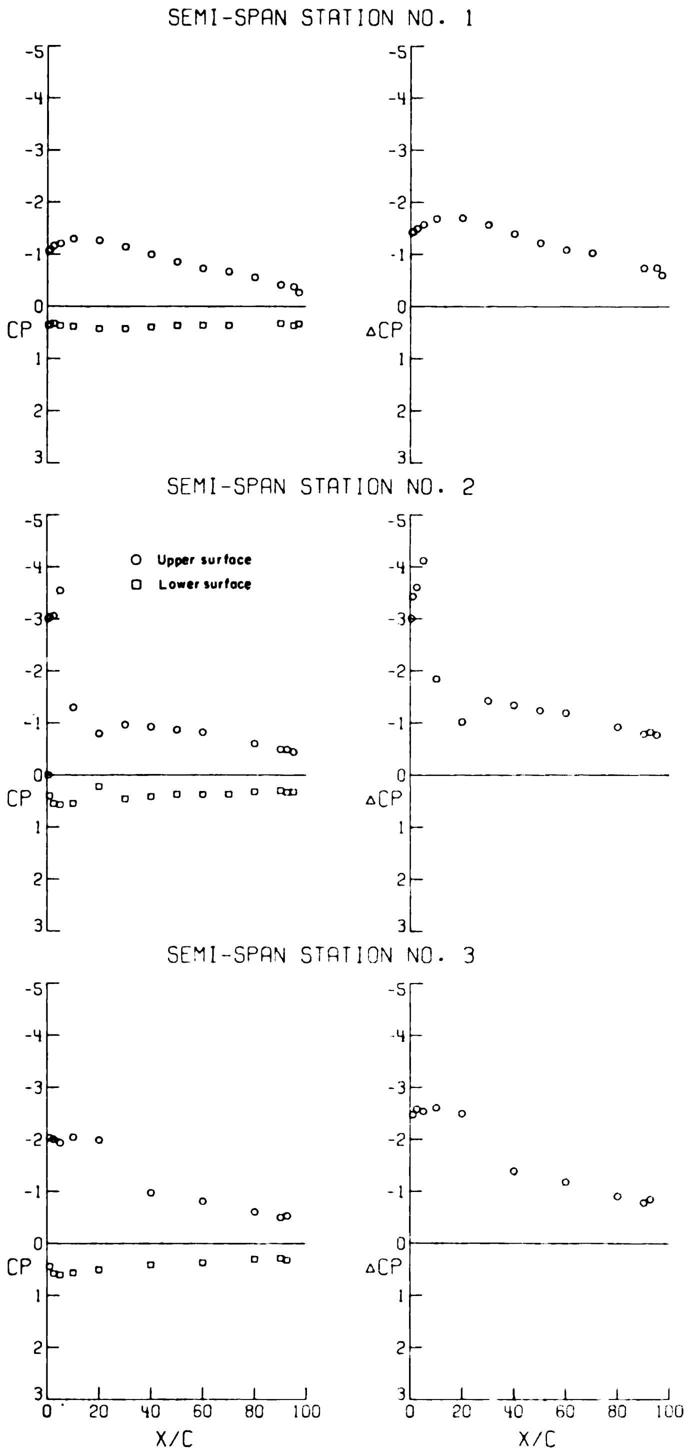

(g) $\alpha = 21.77^{\circ}$.

Figure 6.- Continued.

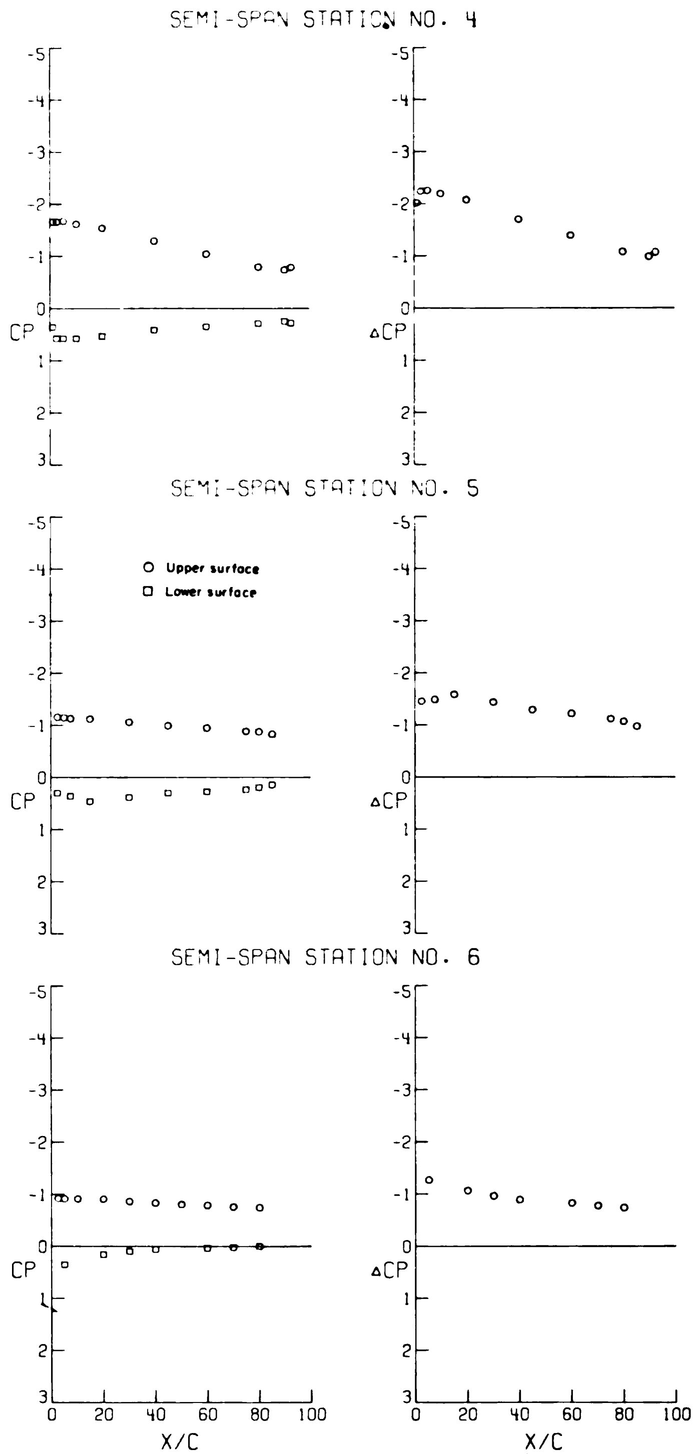

(g) Concluded.

Figure 6.- Concluded.

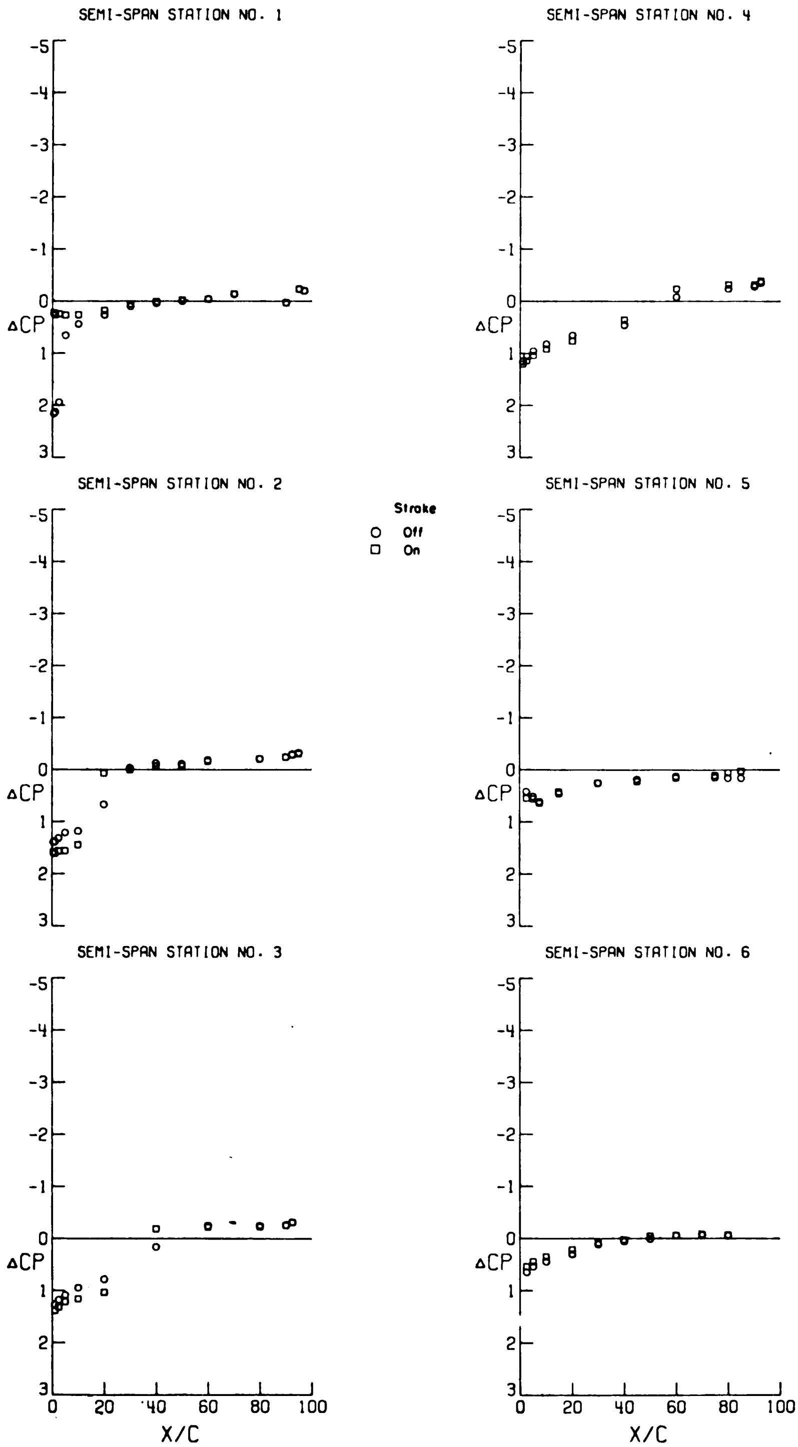

(a) $\alpha = -3.92^{\circ}$.

Figure 7.- Effect of strakes on the incremental pressure coefficients at a Mach number of 0.40. $C_{L,d} = 0.35$.

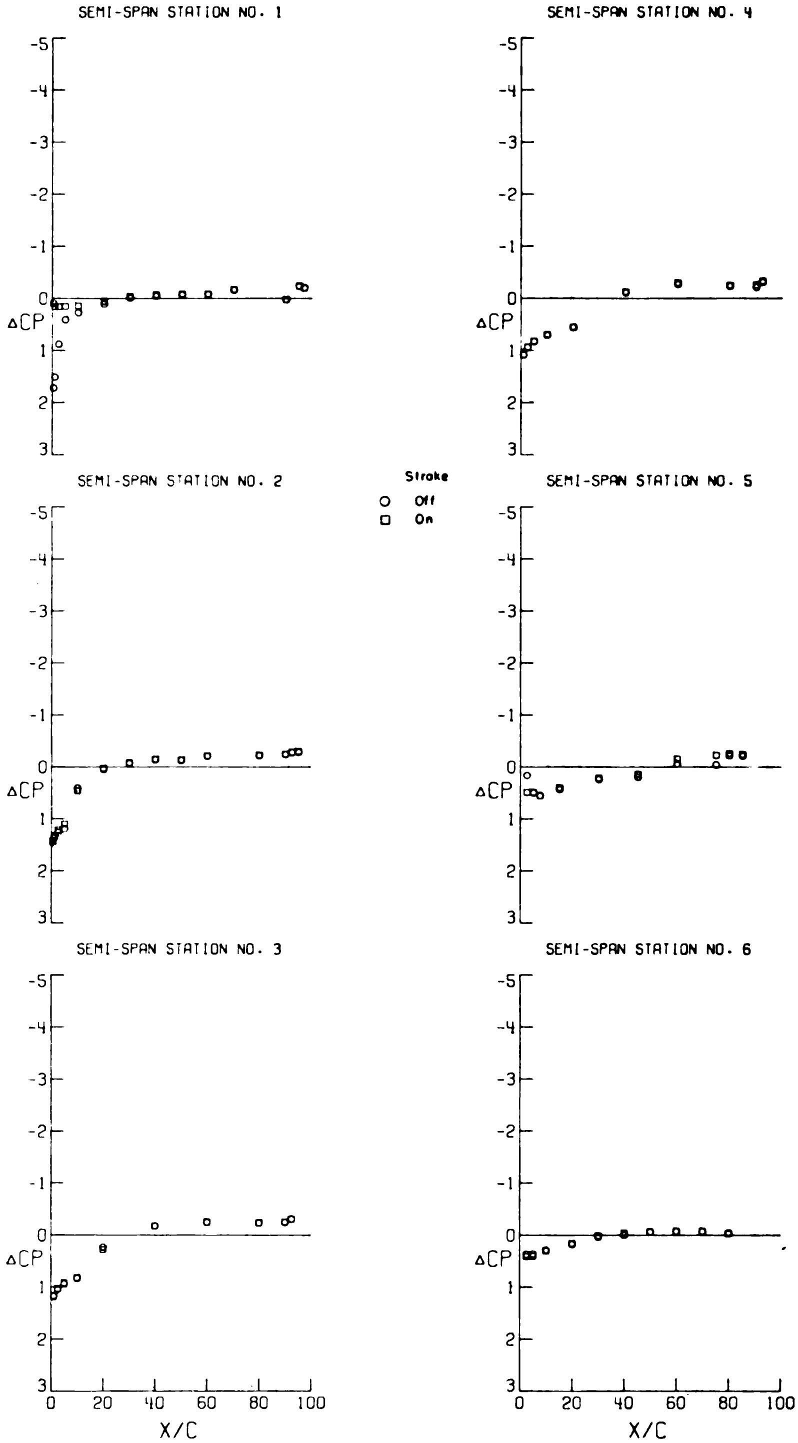

(b) $\alpha = -1.92^{o}$.

Figure 7.- Continued.

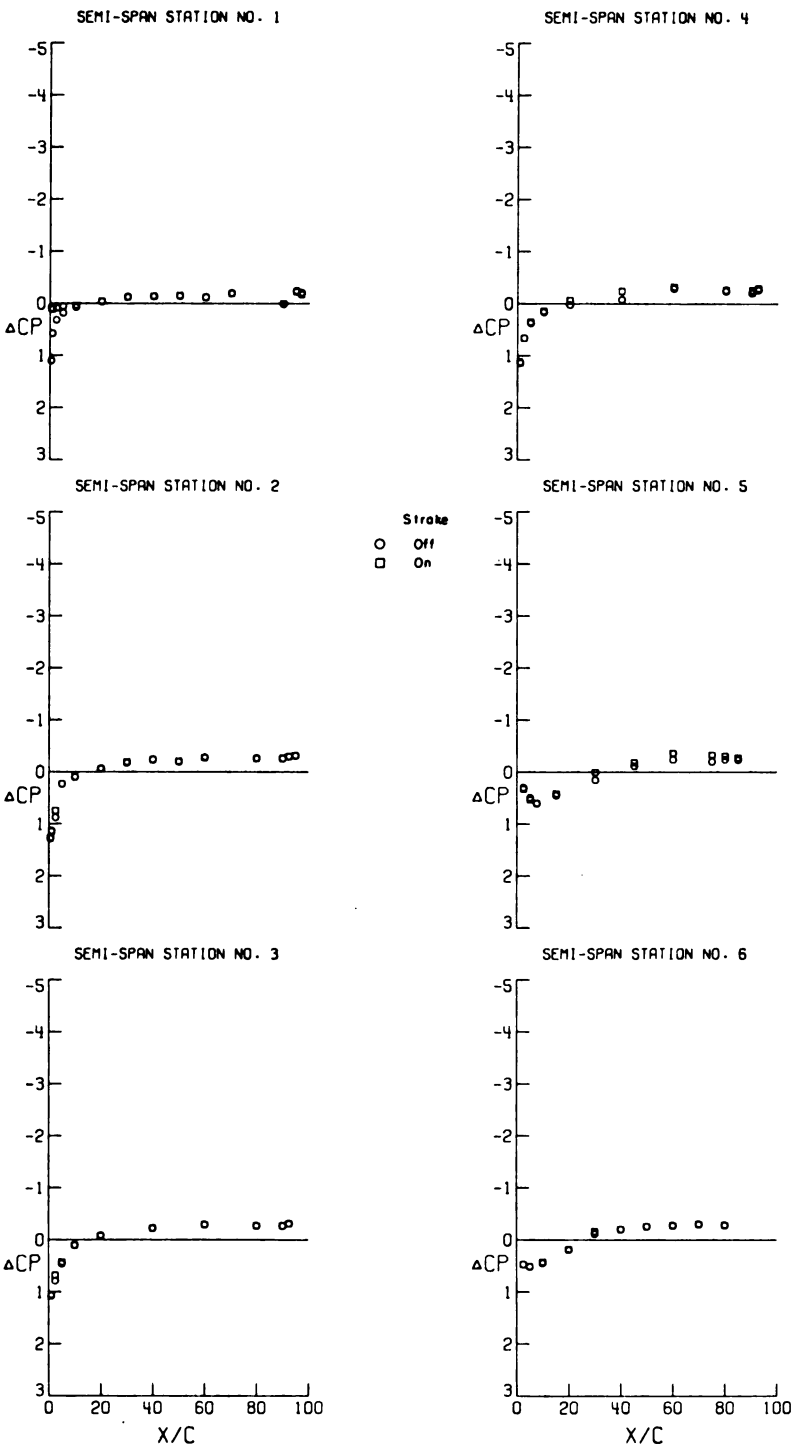

(c) $\alpha = 0.03^o$.

Figure 7.- Continued.

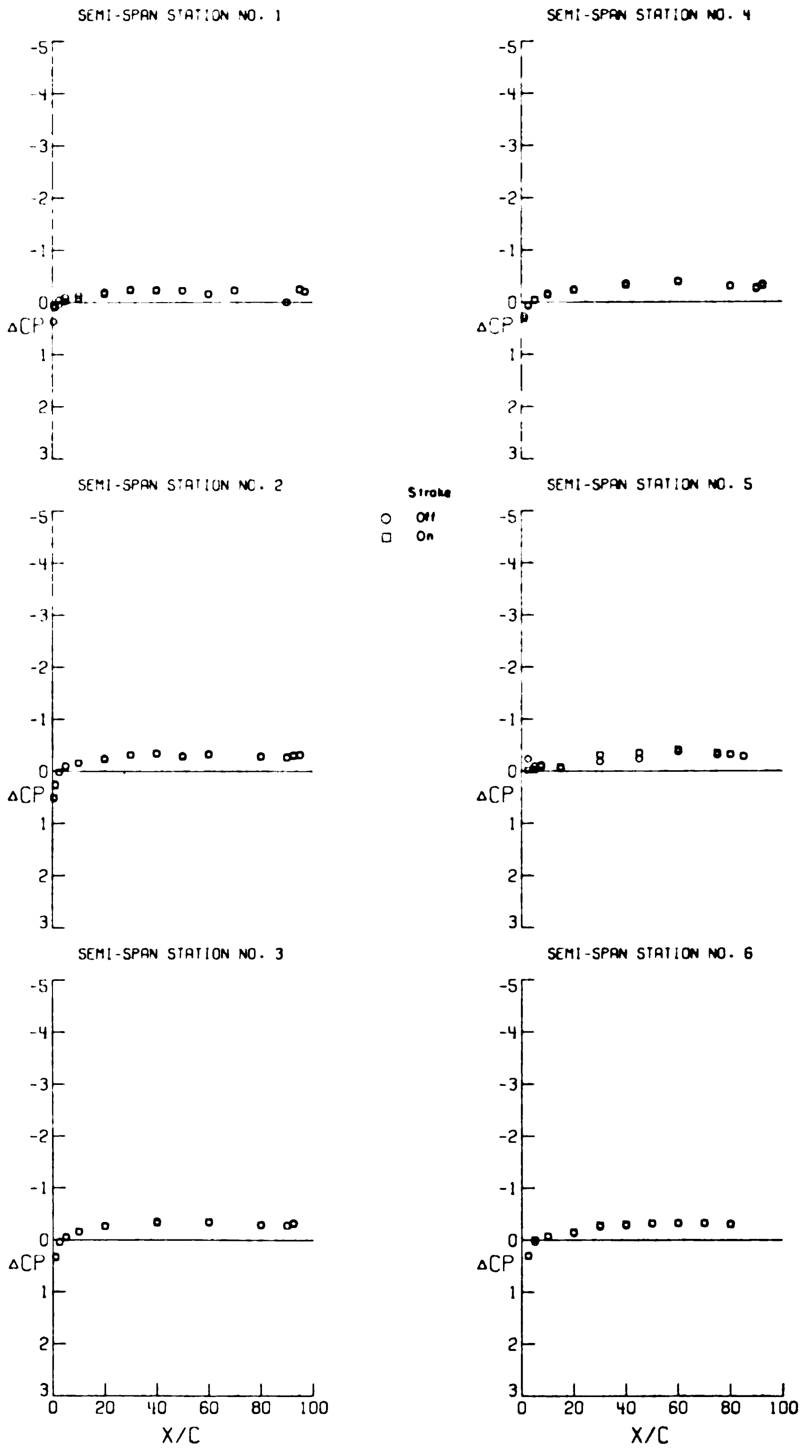

(d) $\alpha = 2.08^{\circ}$.

Figure 7.- Continued.

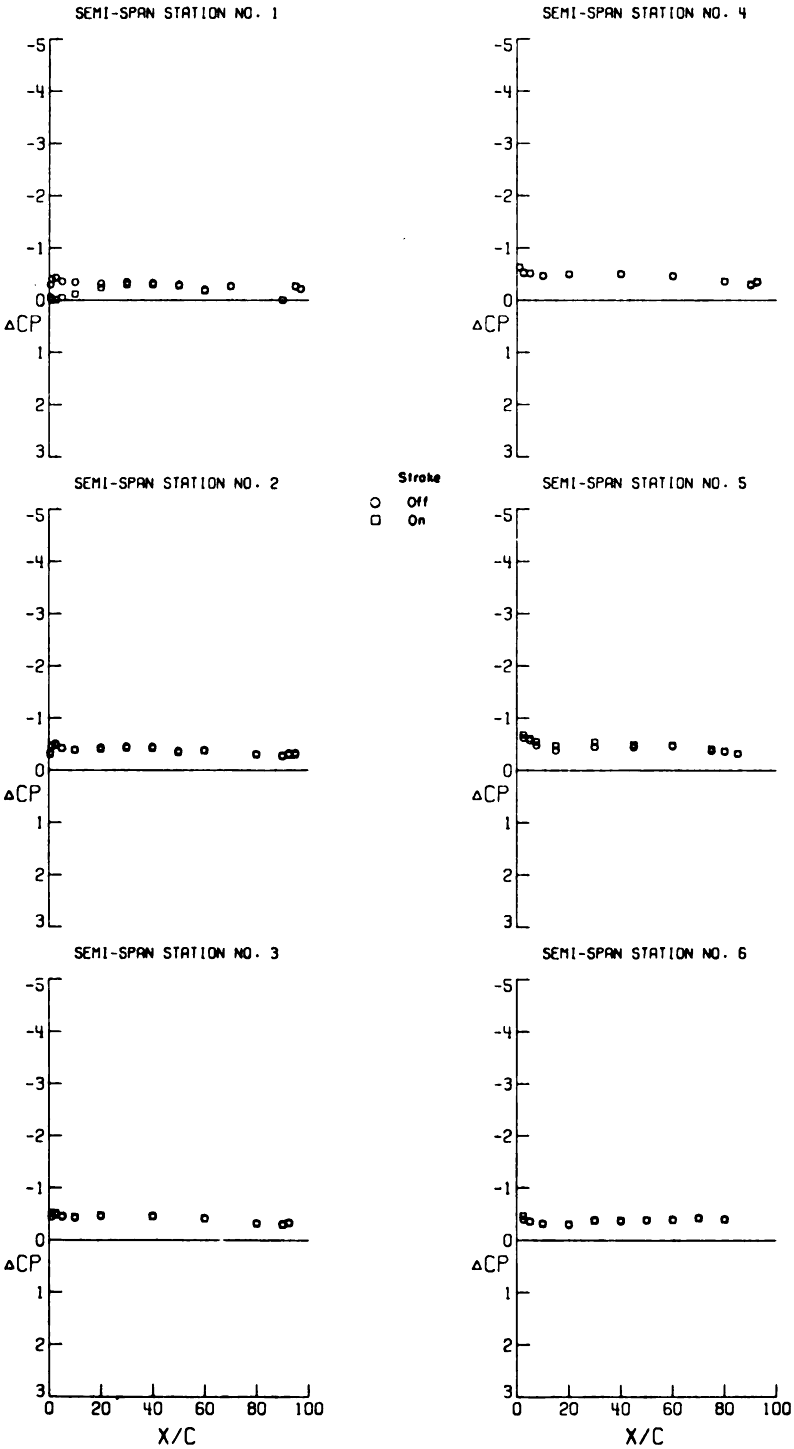

(e) $\alpha = 4.09°$.

Figure 7.- Continued.

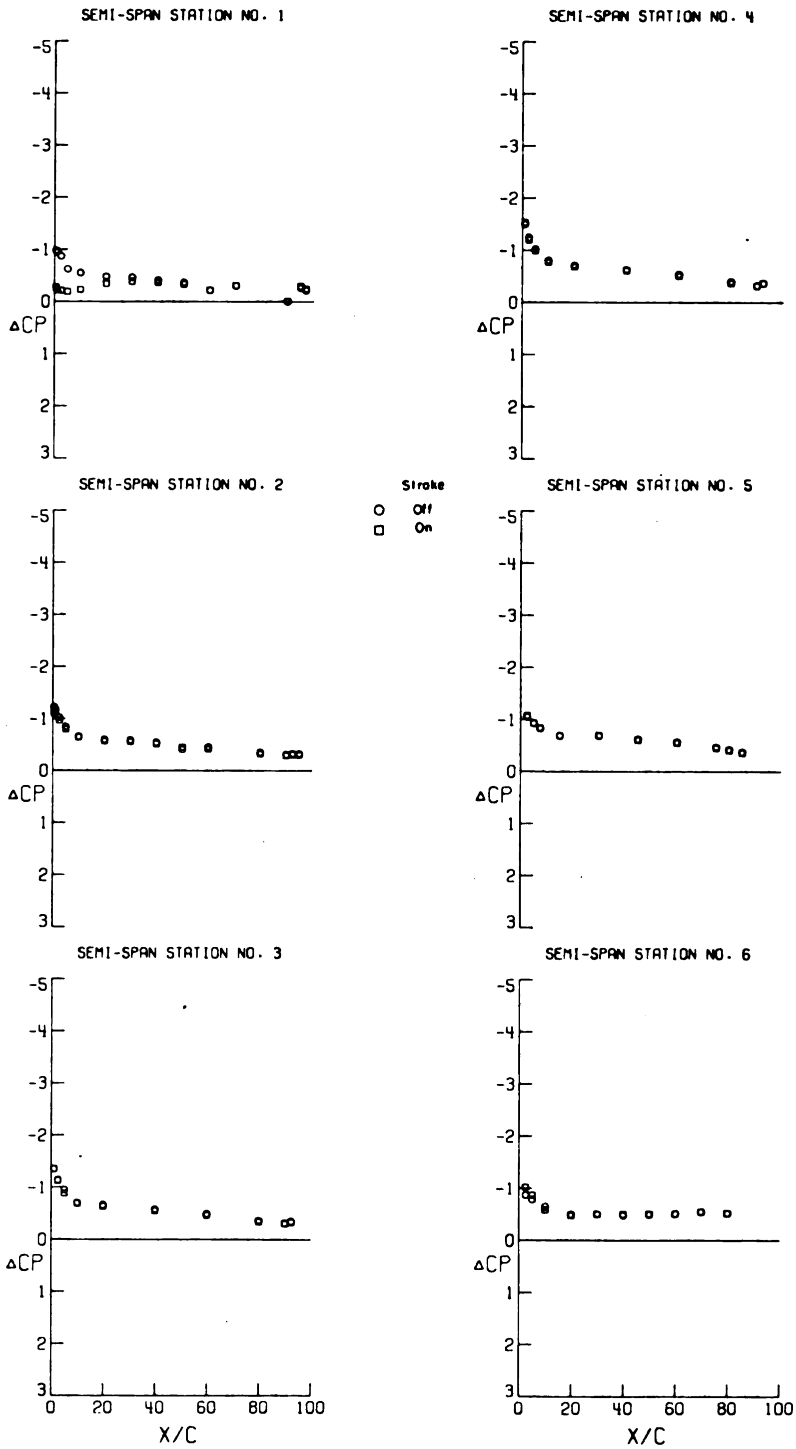

(f) $\alpha = 6.21^{\circ}$.

Figure 7.- Continued.

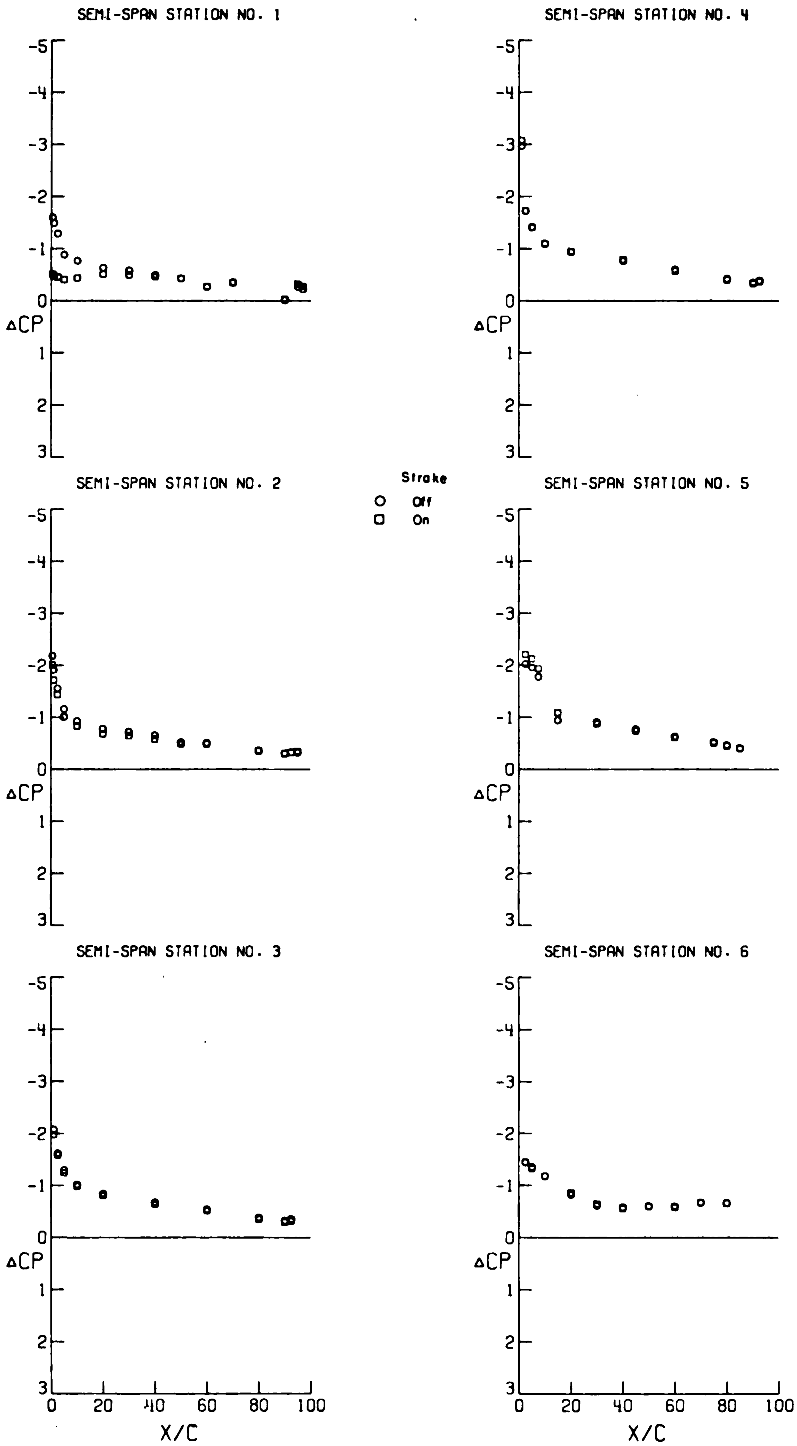

(g) $\alpha = 8.35^{o}$.

Figure 7.- Continued.

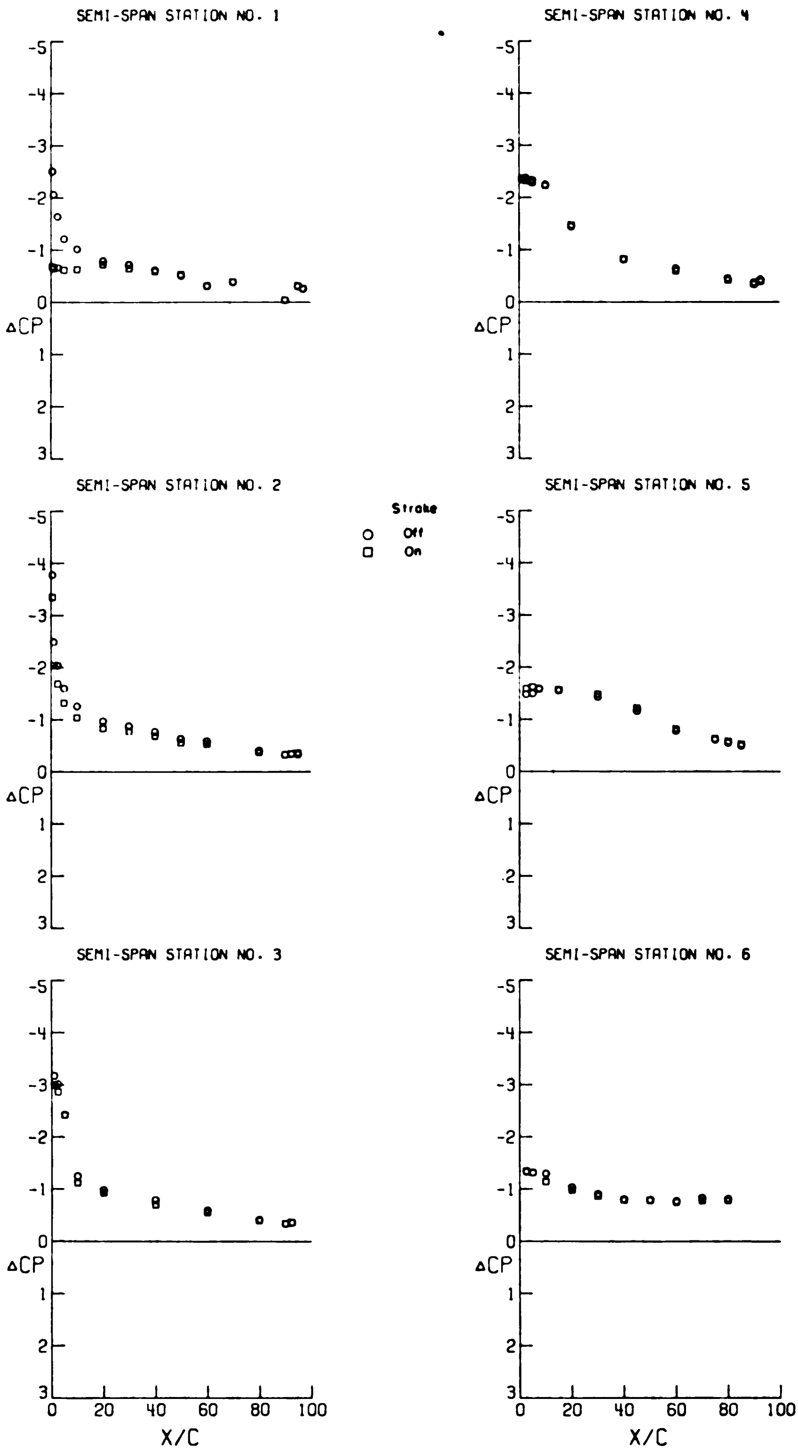

(h) $\alpha = 10.56^{\circ}$.

Figure 7.- Continued.

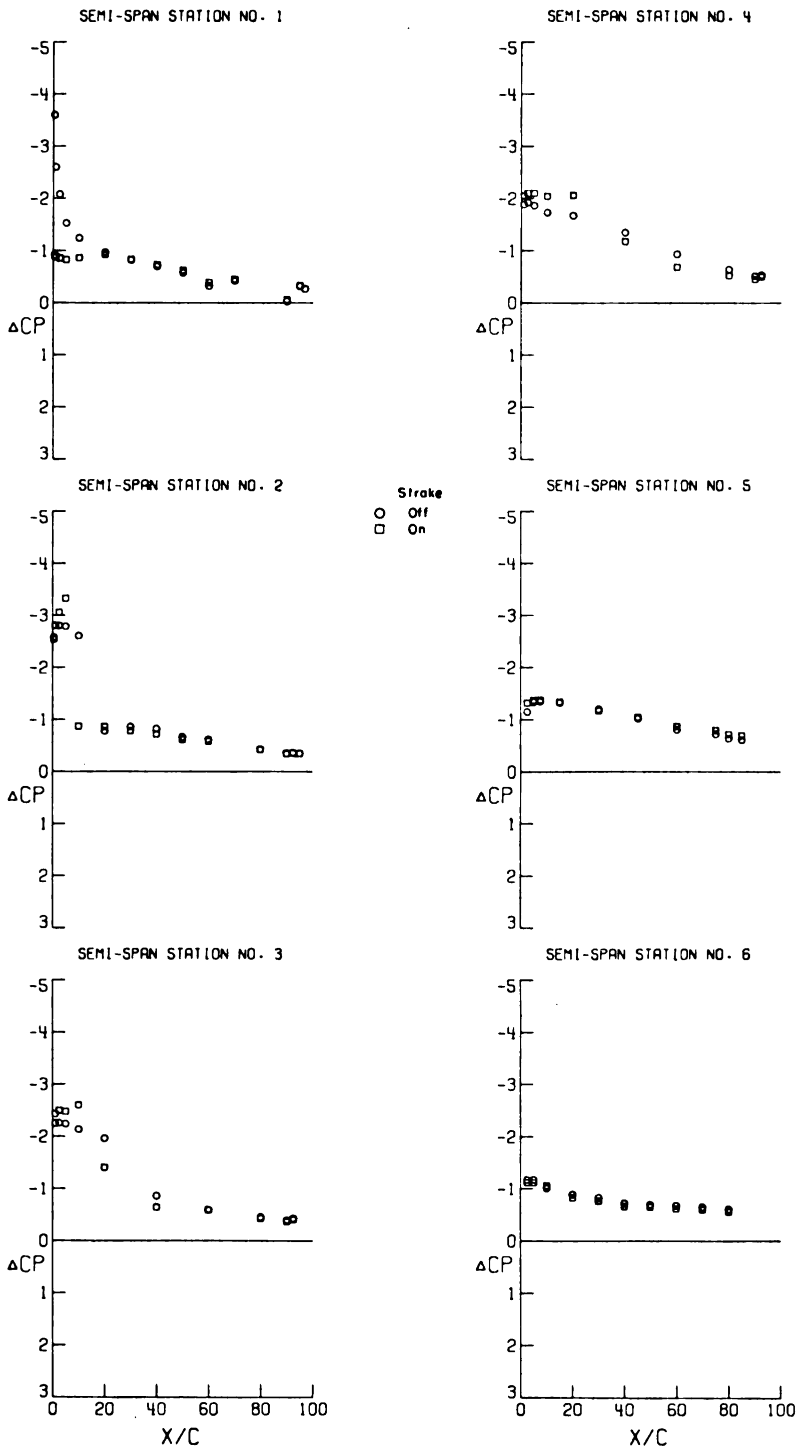

(i) $\alpha = 12.78^{\circ}$.

Figure 7.- Continued.

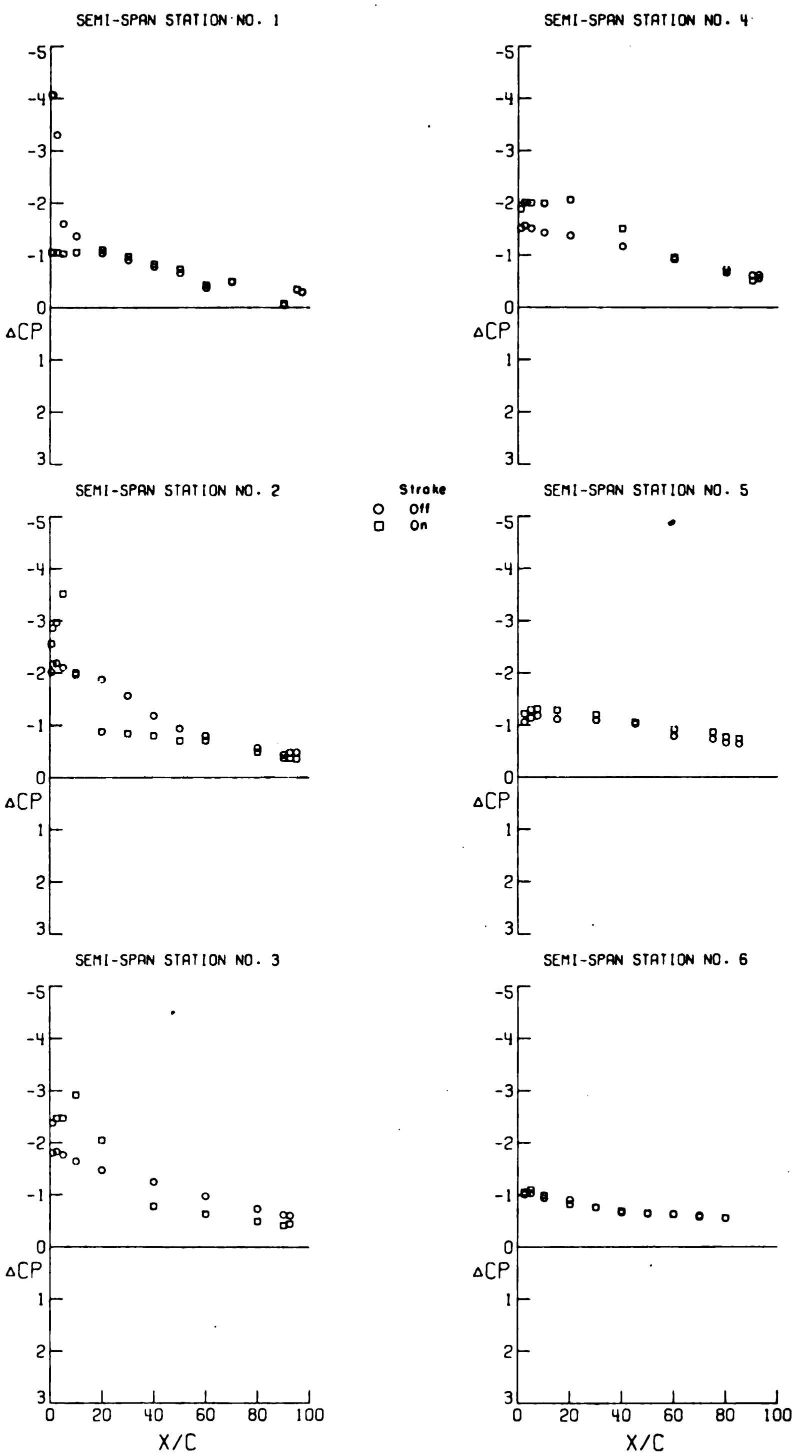

(j) $\alpha = 15.06^{\circ}$.

Figure 7.- Continued.

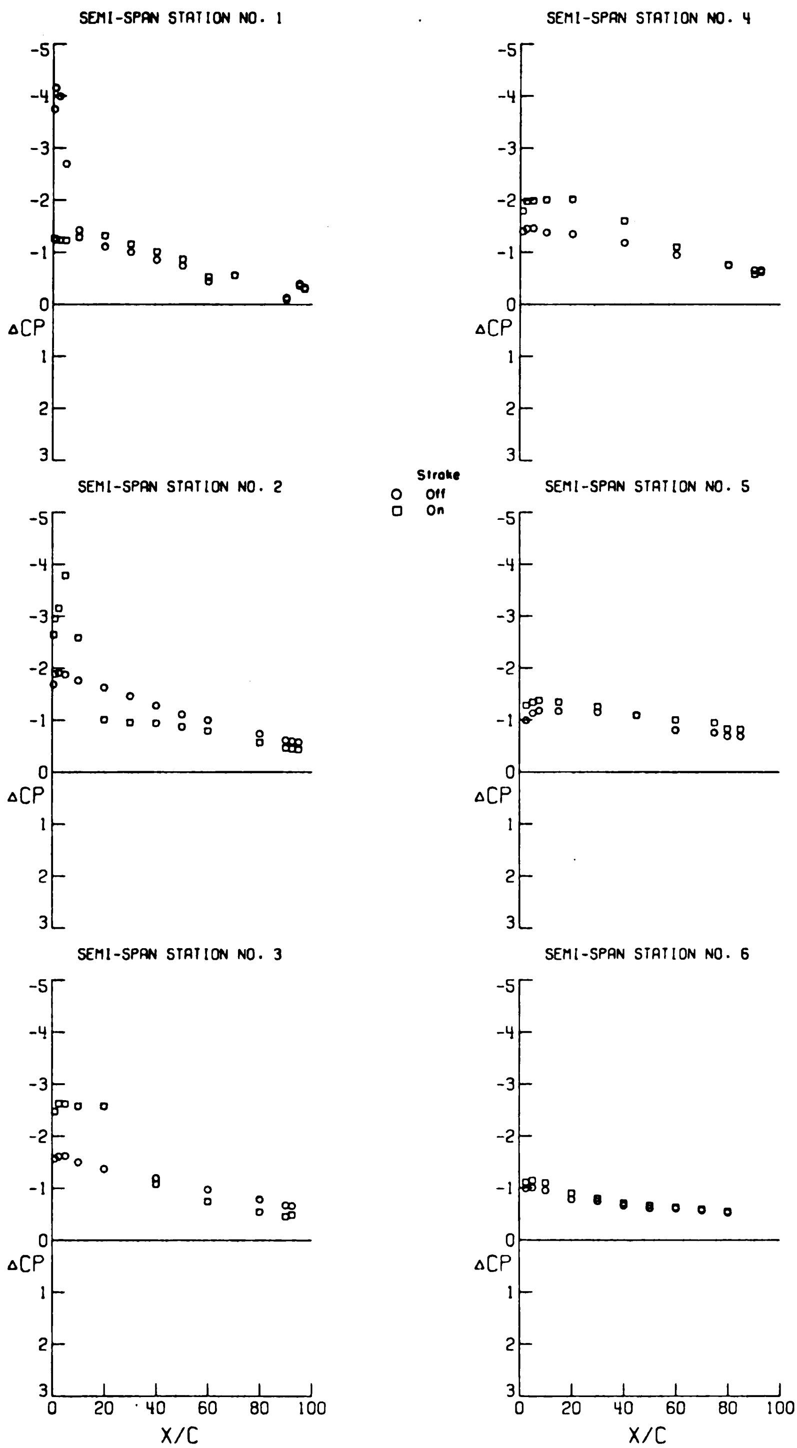

(k) $\alpha = 17.21^{\circ}$.

Figure 7.- Continued.

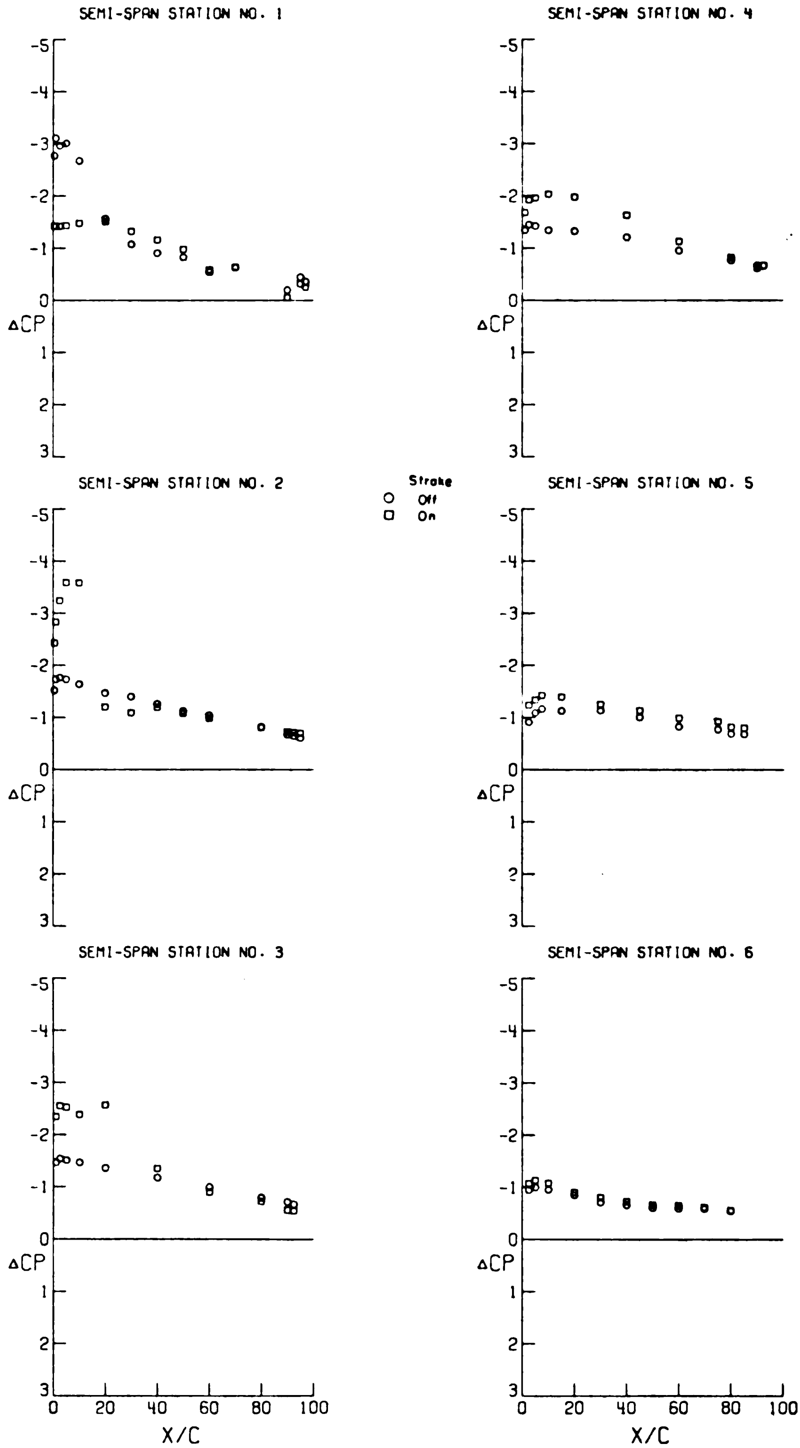

(l) $\alpha = 19.37^{\circ}$.

Figure 7.- Continued.

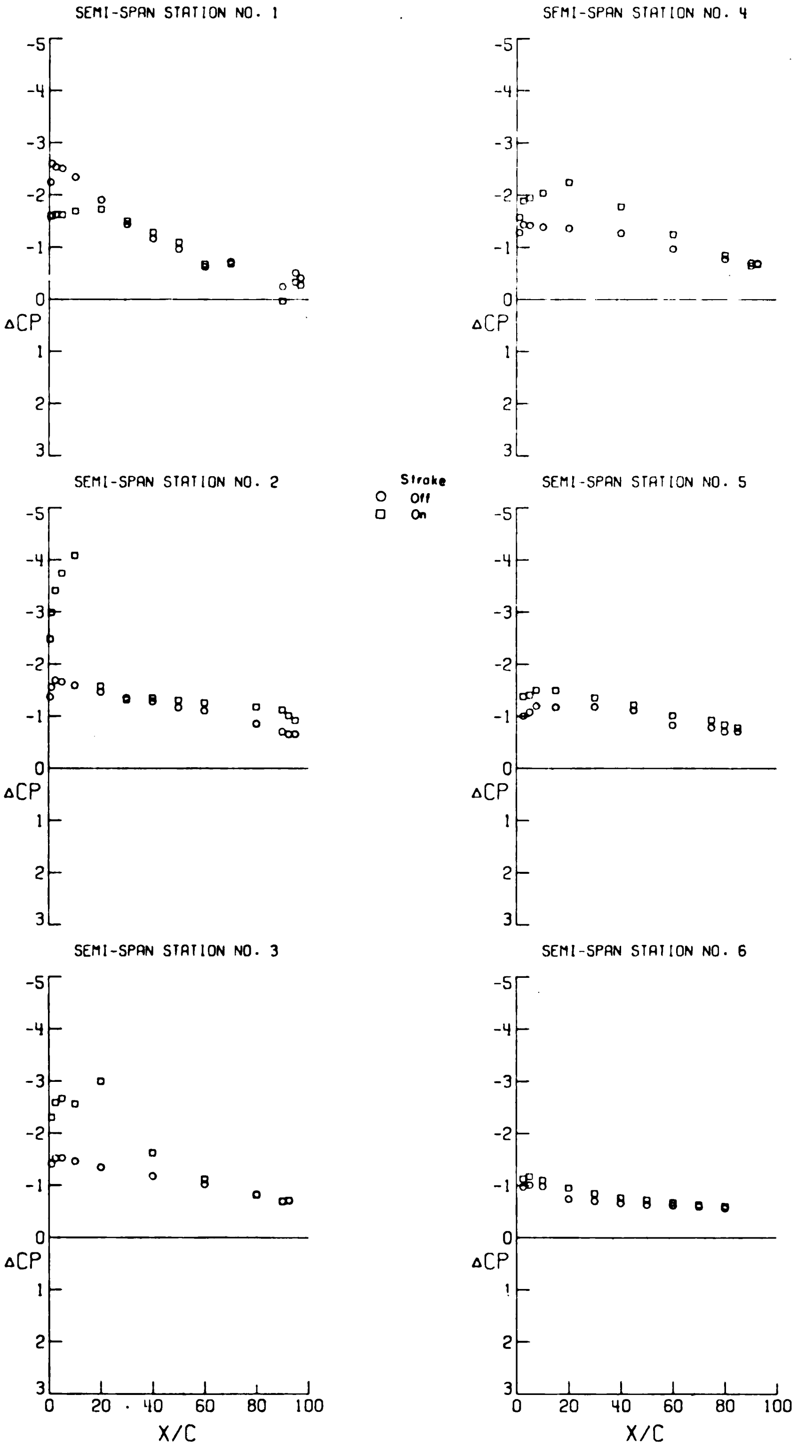

(m) α = 21.50°.

Figure 7.- Concluded.

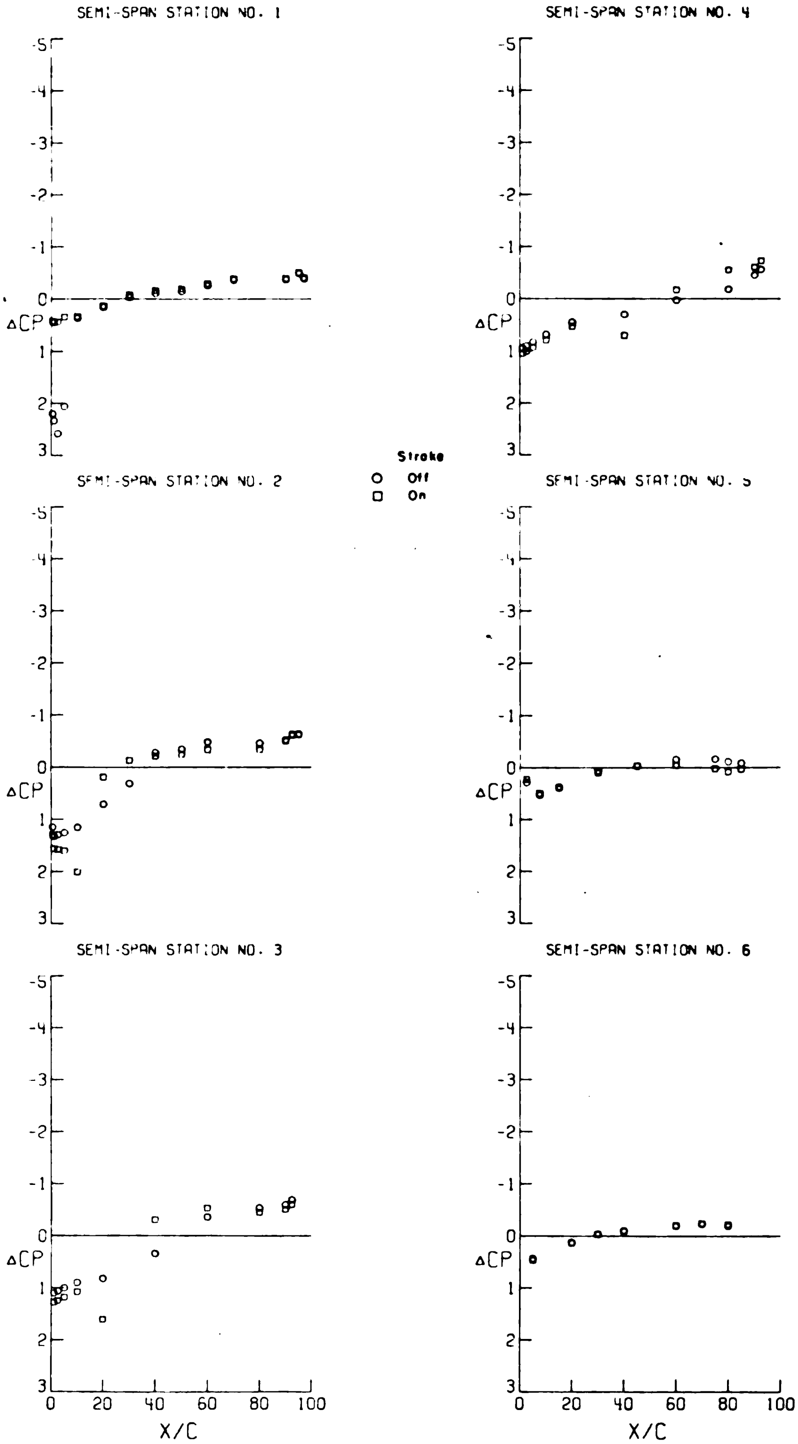

(a) $\alpha = -3.93^{\circ}$.

Figure 8.- Effect of strakes on the incremental pressure coefficients at a Mach number of 0.40. $C_{L,d} = 0.70$.

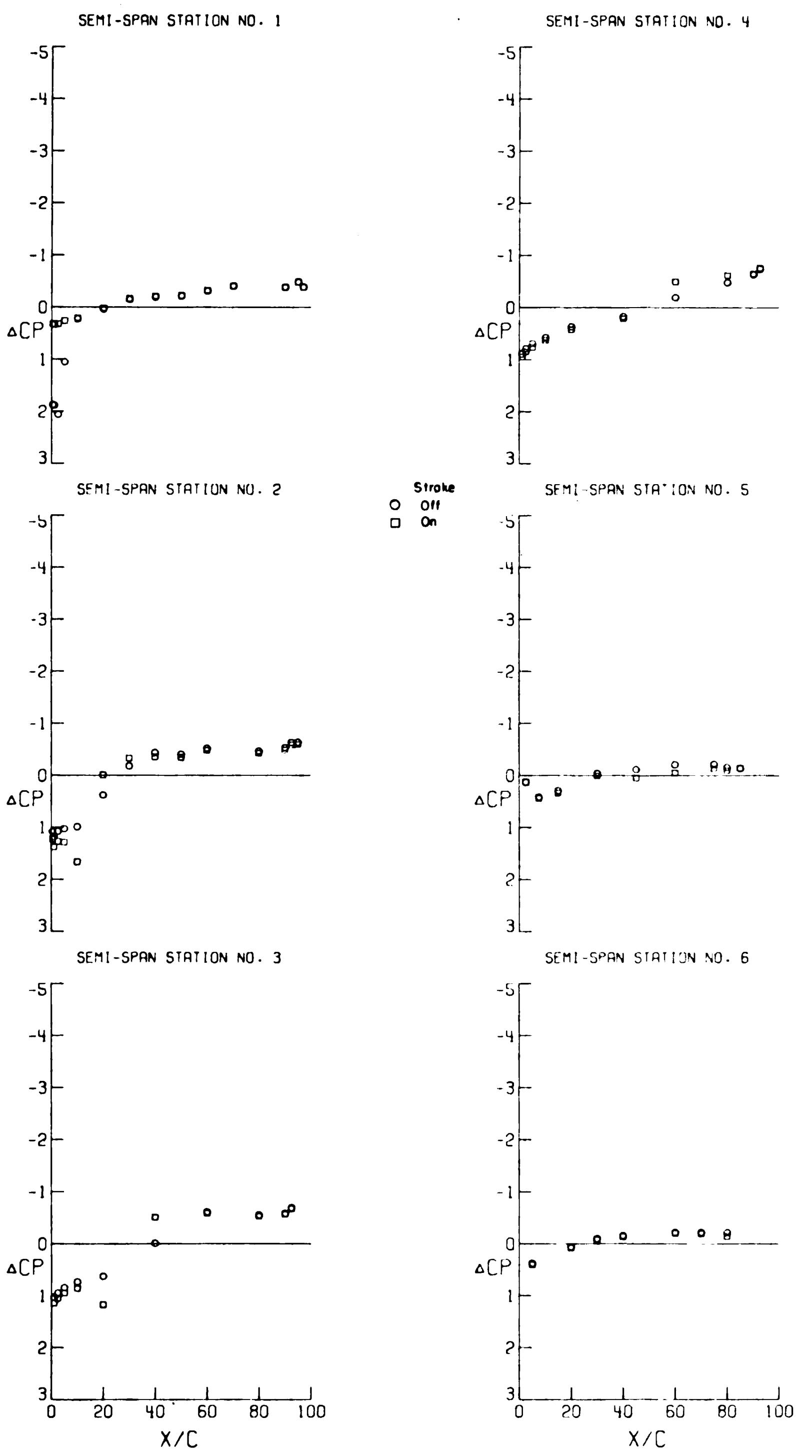

(b) $\alpha = -1.95^o$.

Figure 8.- Continued.

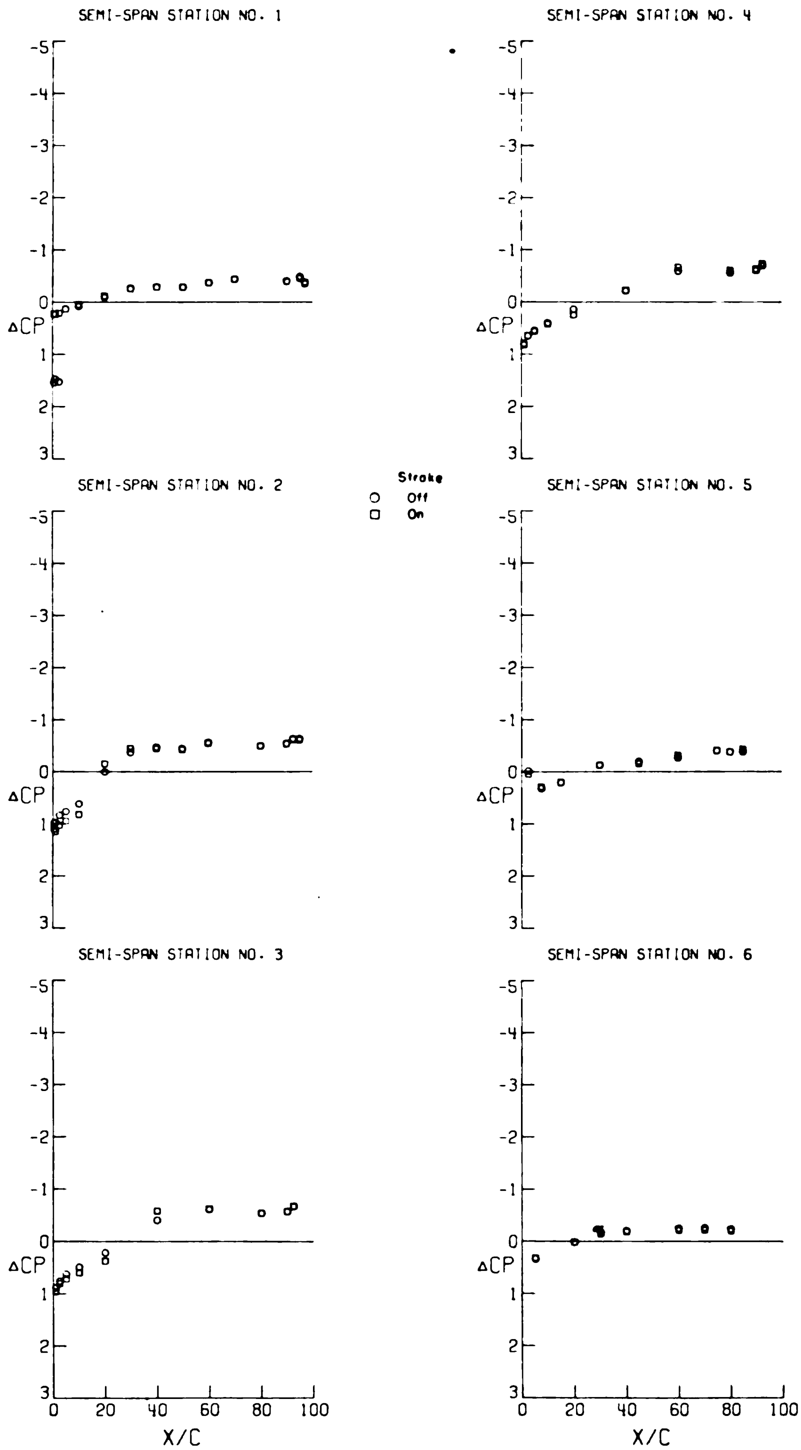

(c) $\alpha = 0.05^{\circ}$.

Figure 8.- Continued.

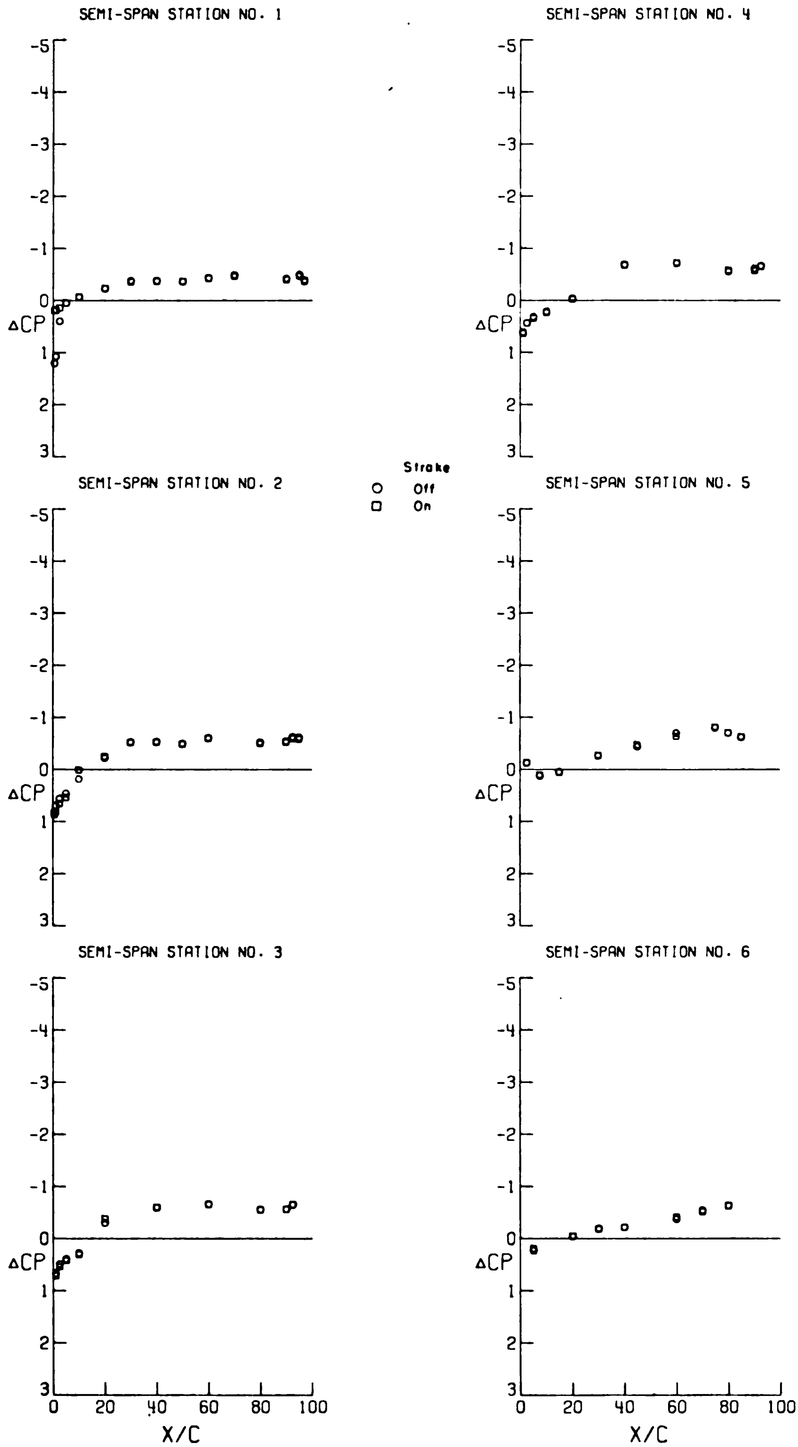

(d) $\alpha = 2.08^{\circ}$.

Figure 8.- Continued.

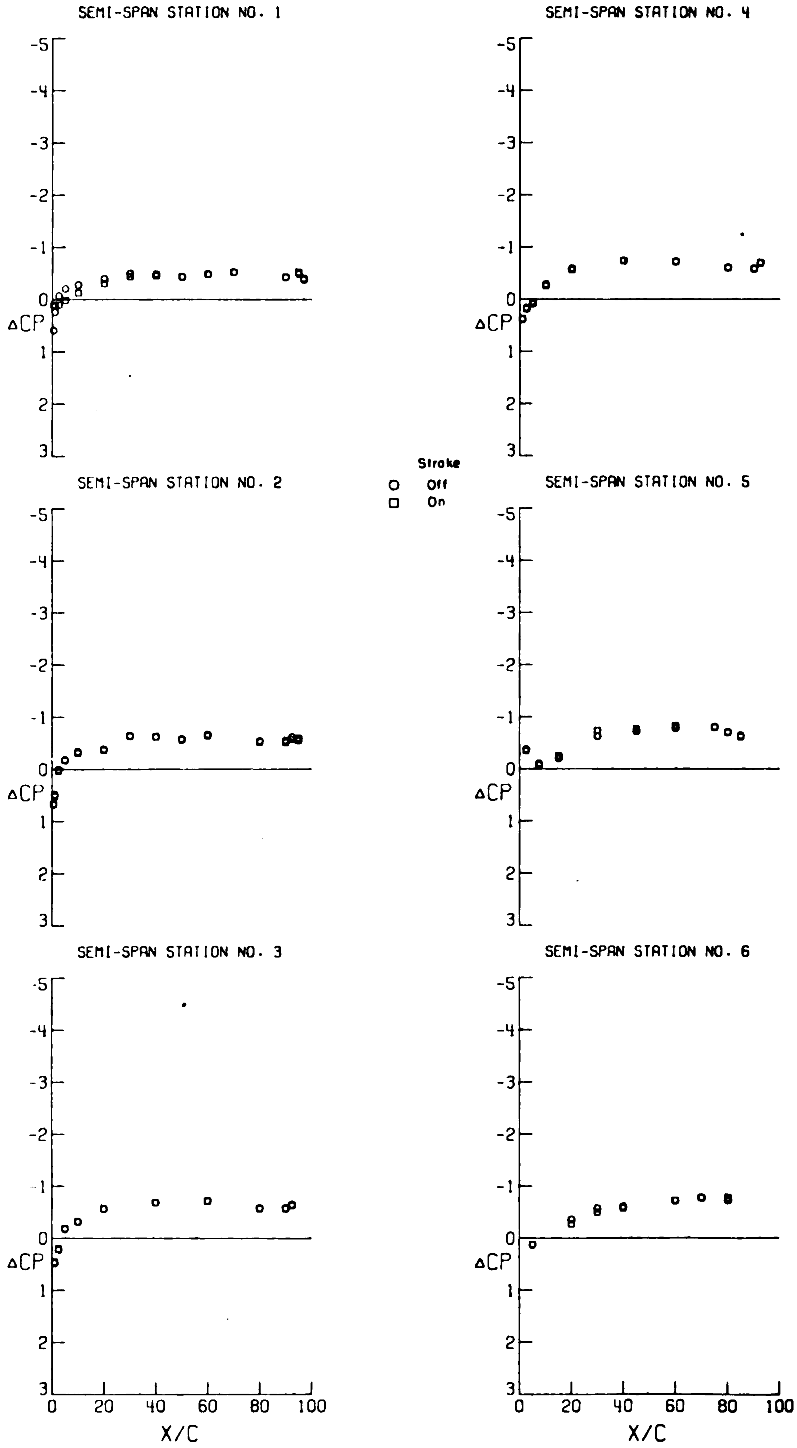

(e) $\alpha = 4.15^{\circ}$.

Figure 8.- Continued.

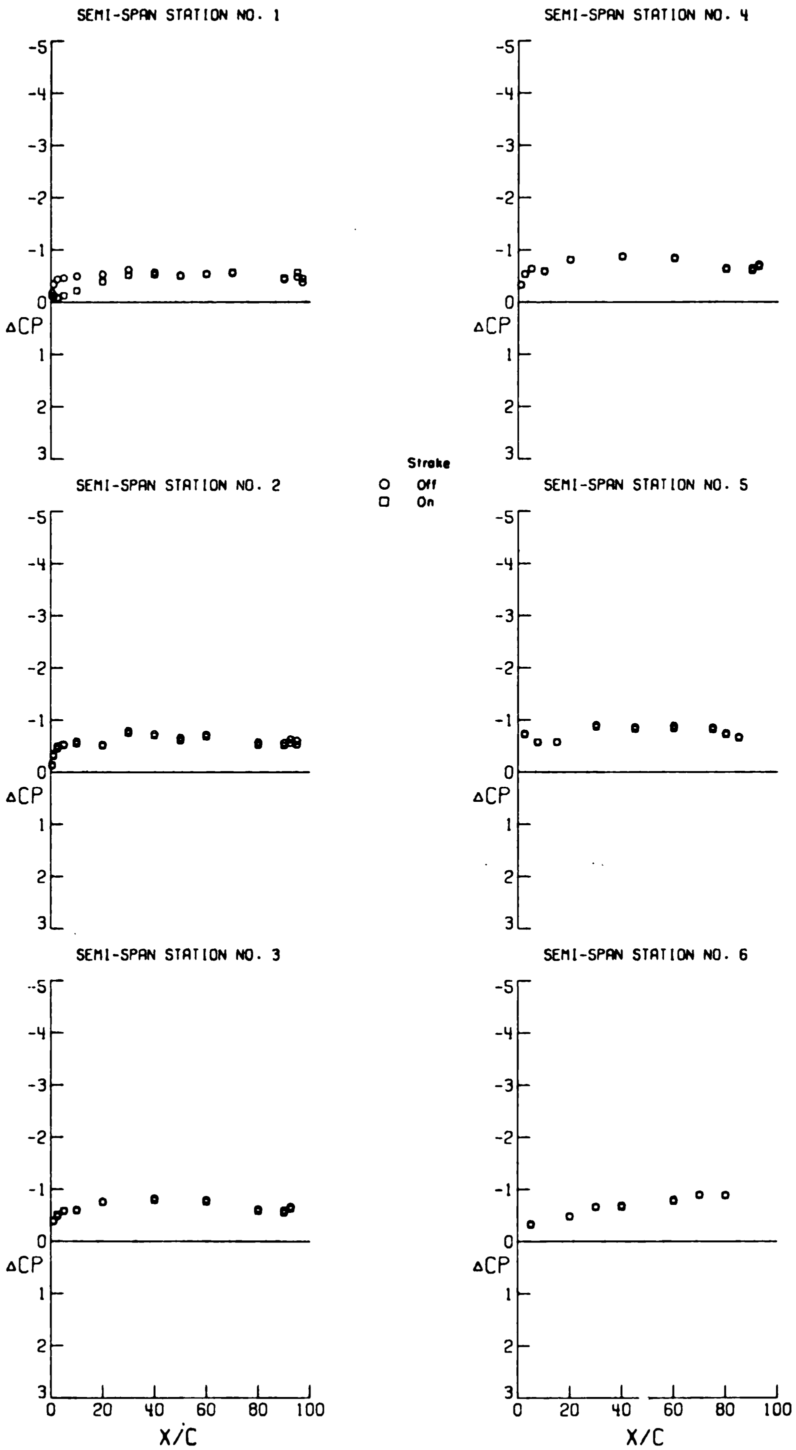

(f) $\alpha = 6.28^{o}$.

Figure 8.- Continued.

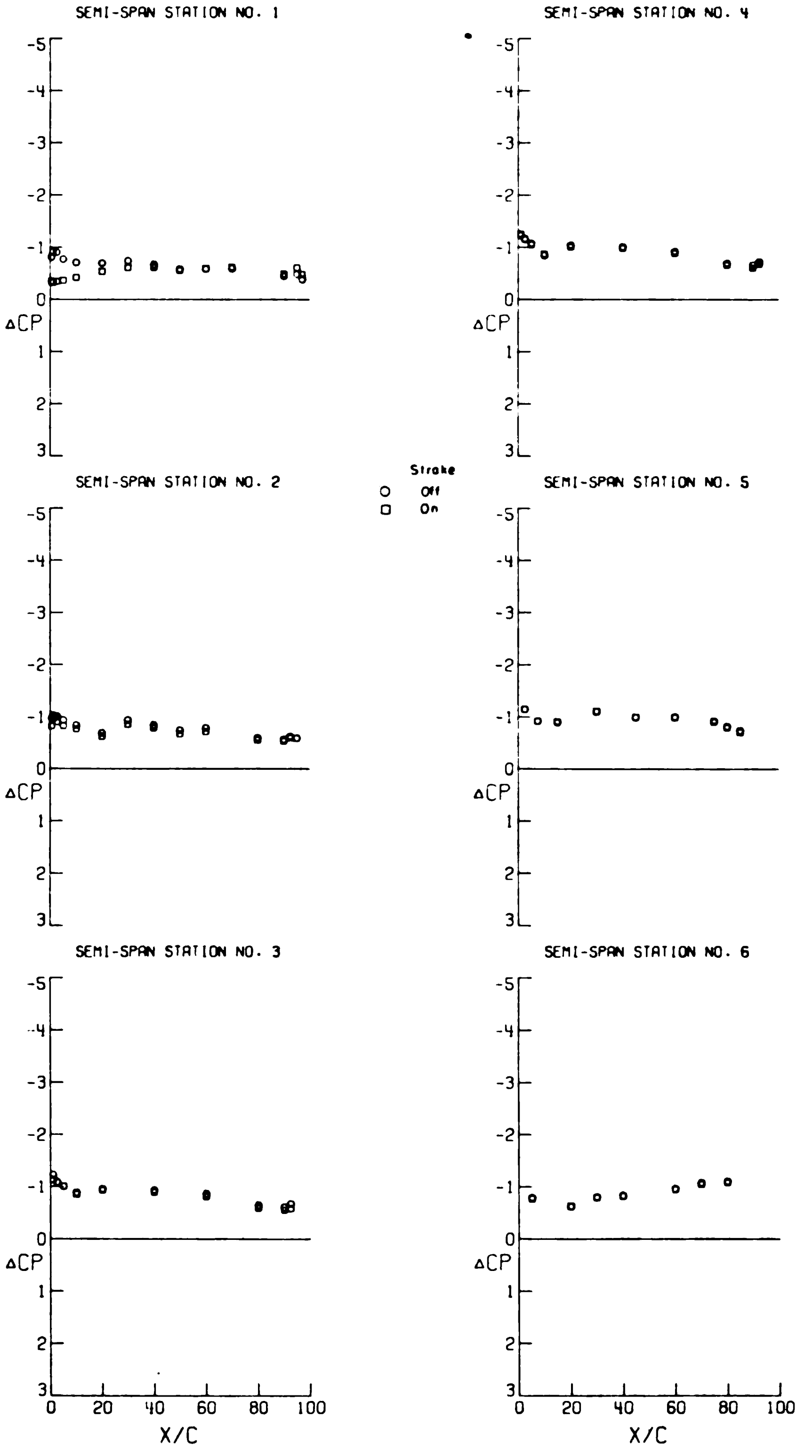

(g) $\alpha = 8.42^{\circ}$.

Figure 8.- Continued.

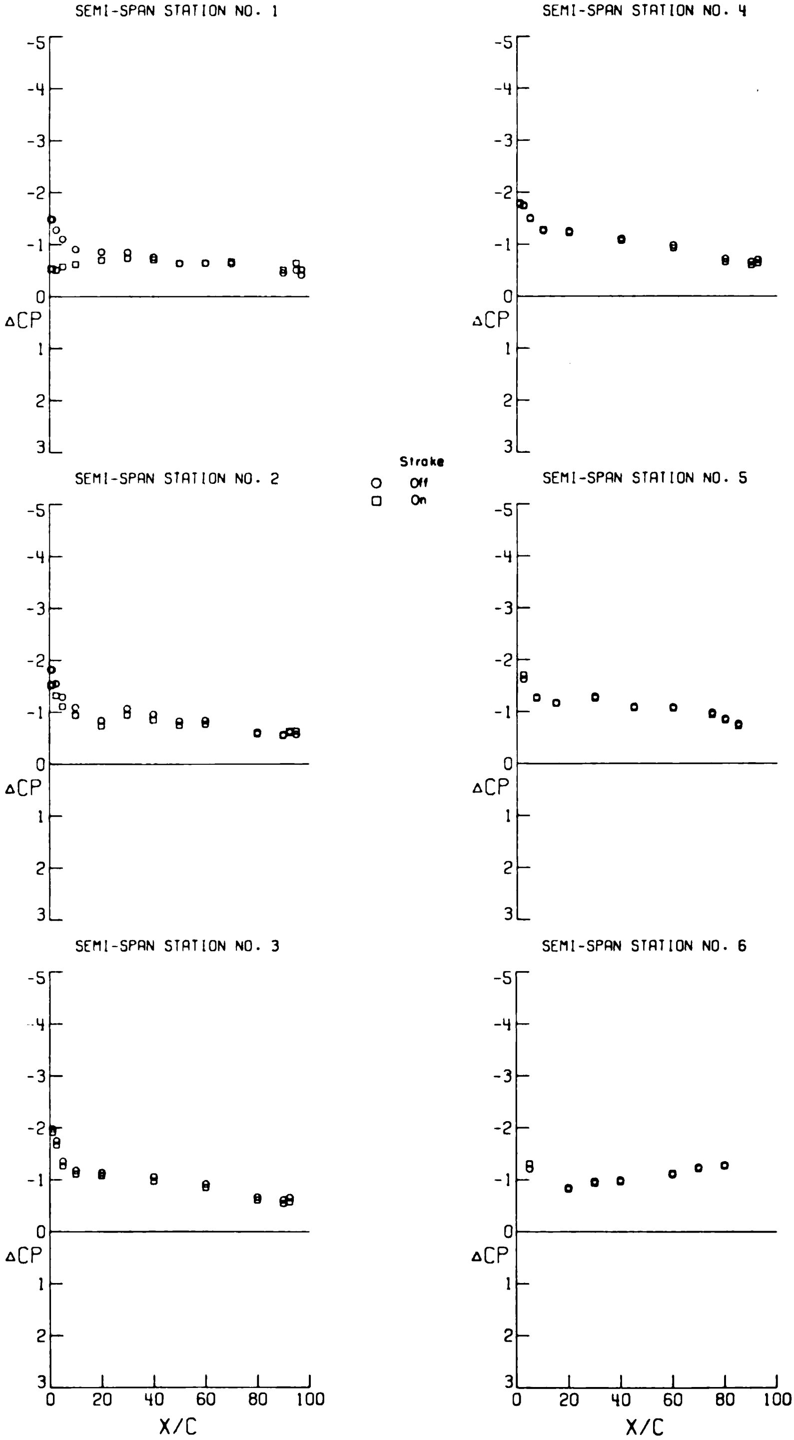

(h) $\alpha = 10.60°$.

Figure 8.- Continued.

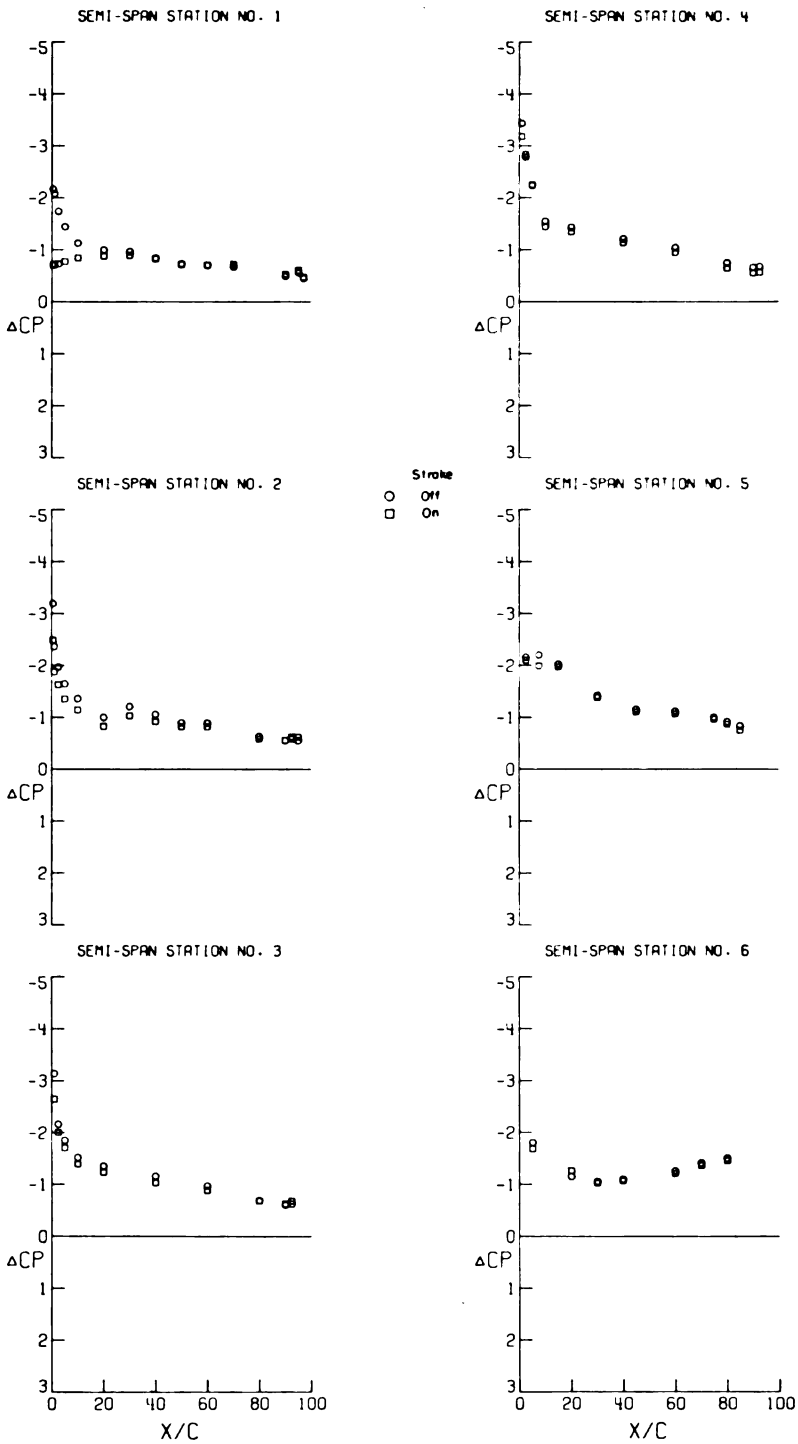

(i) $\alpha = 12.82^{o}$.

Figure 8.- Continued.

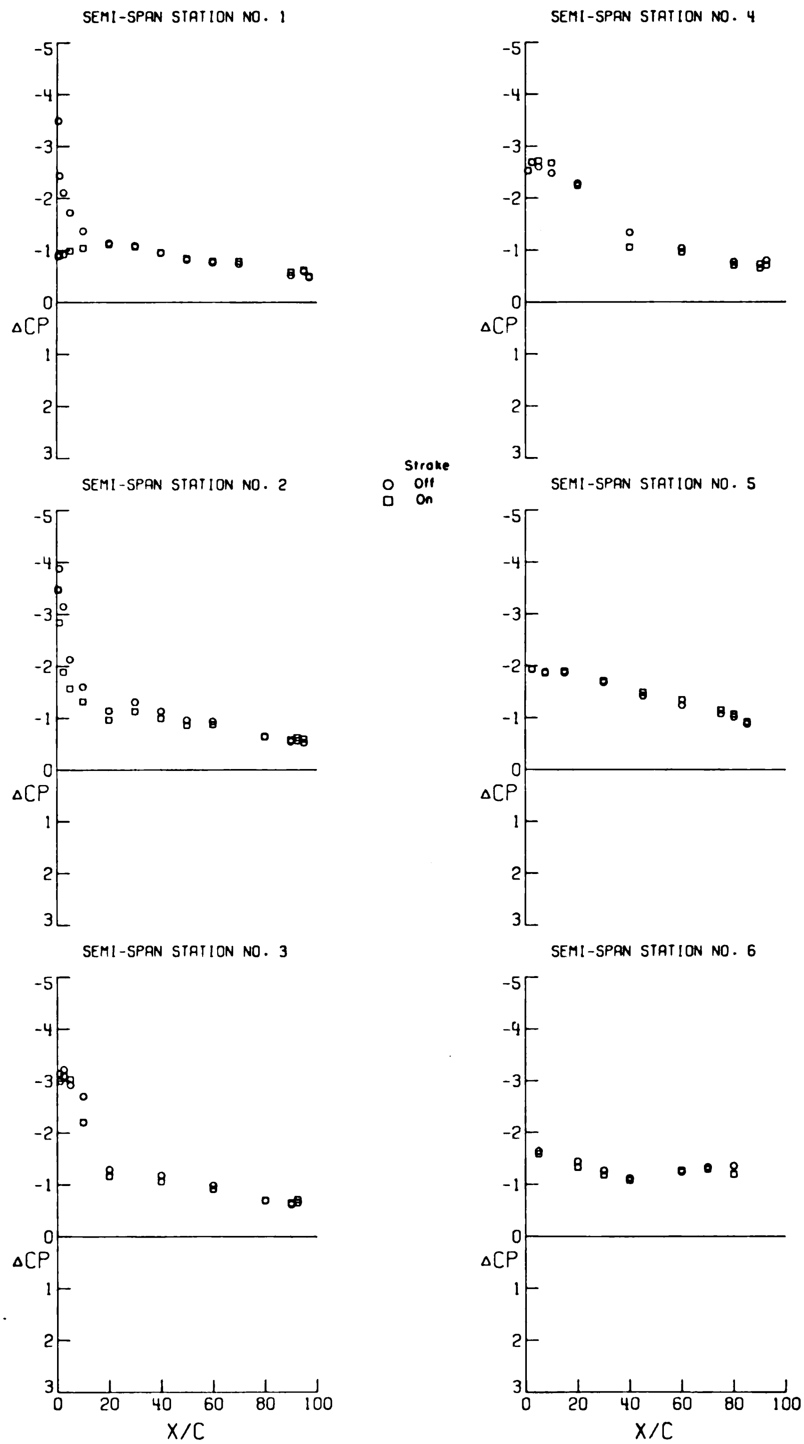

(j) $\alpha = 15.12^{\circ}$.

Figure 8.- Continued.

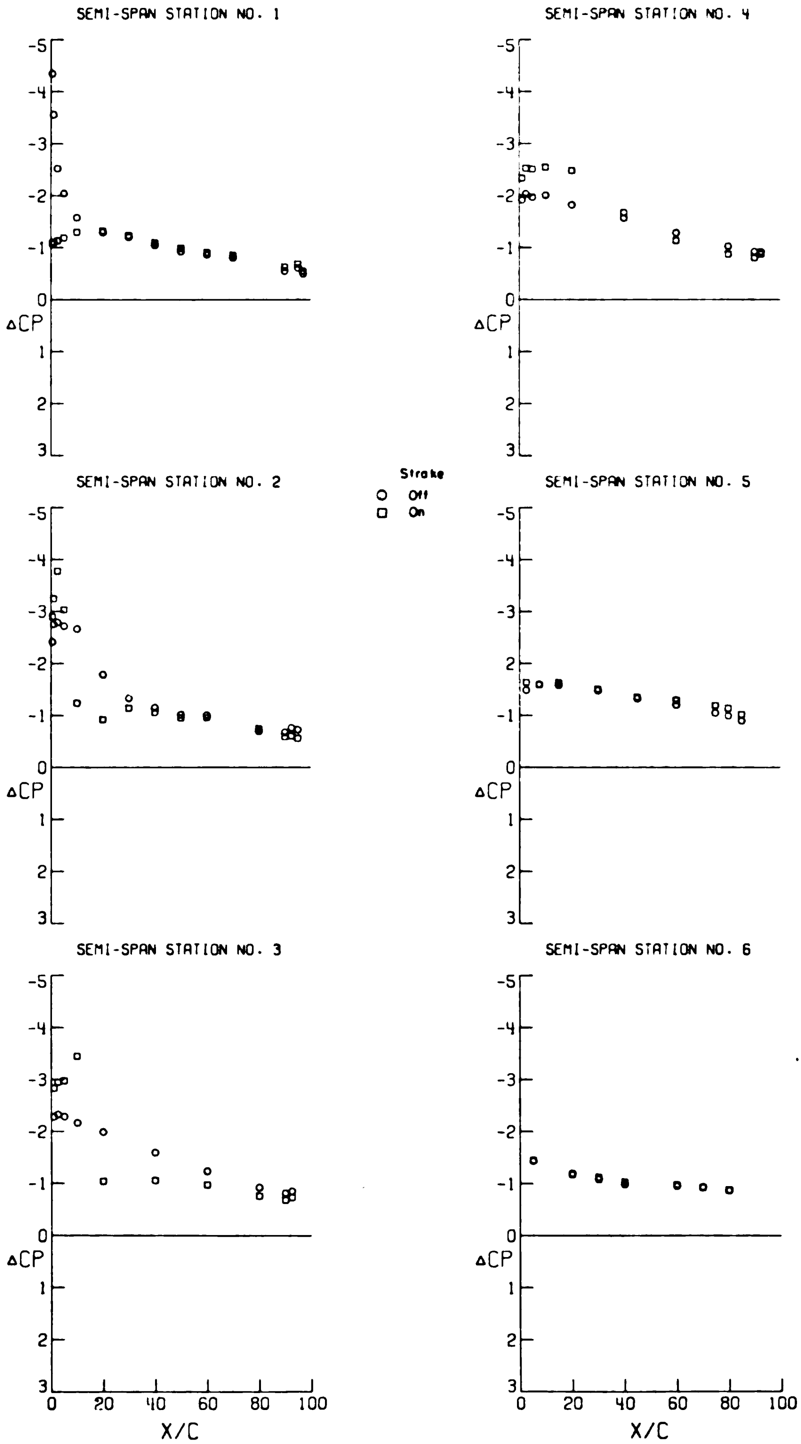

(k) $\alpha = 17.27^{\circ}$.

Figure 8.- Continued.

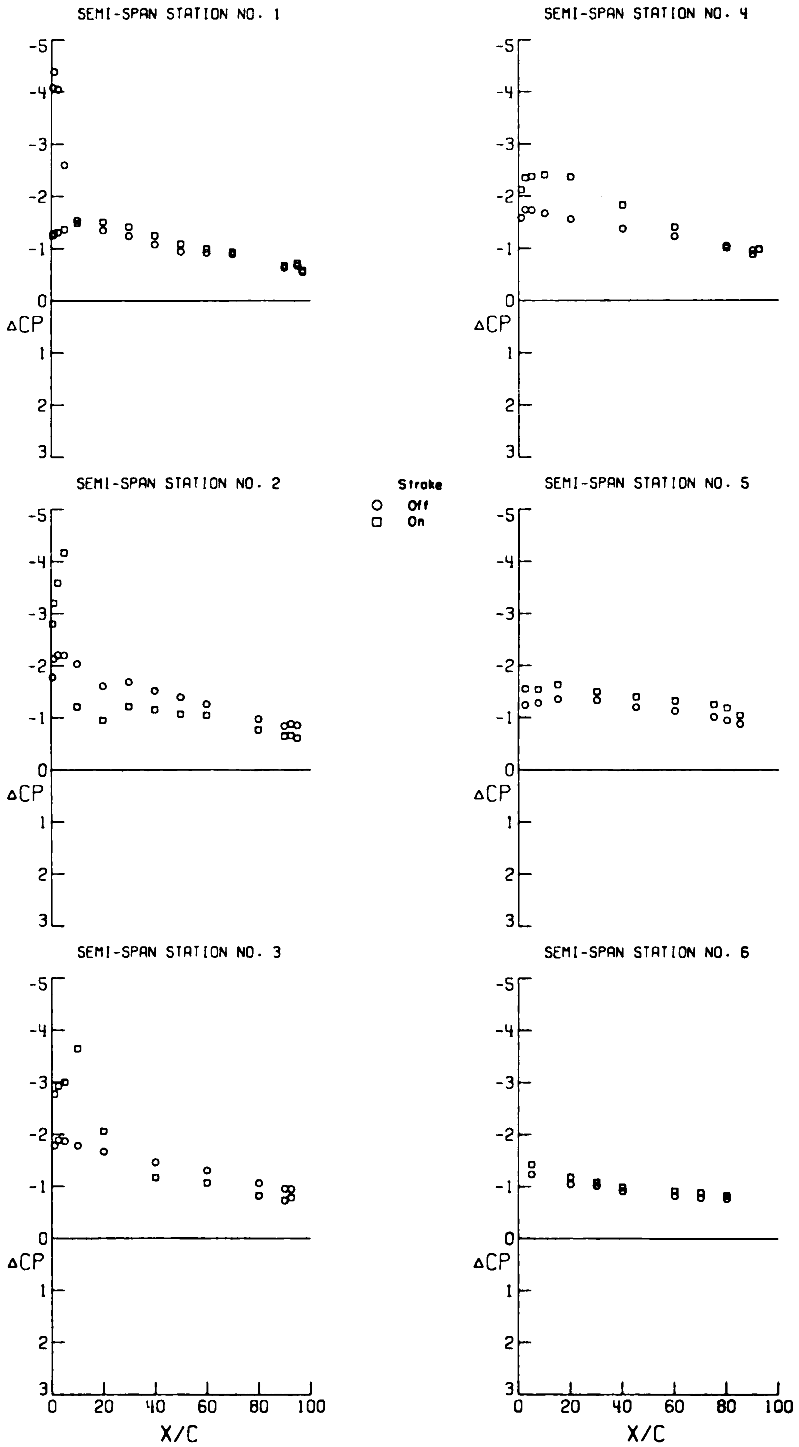

(1) $\alpha = 19.42^o$.

Figure 8.- Continued.

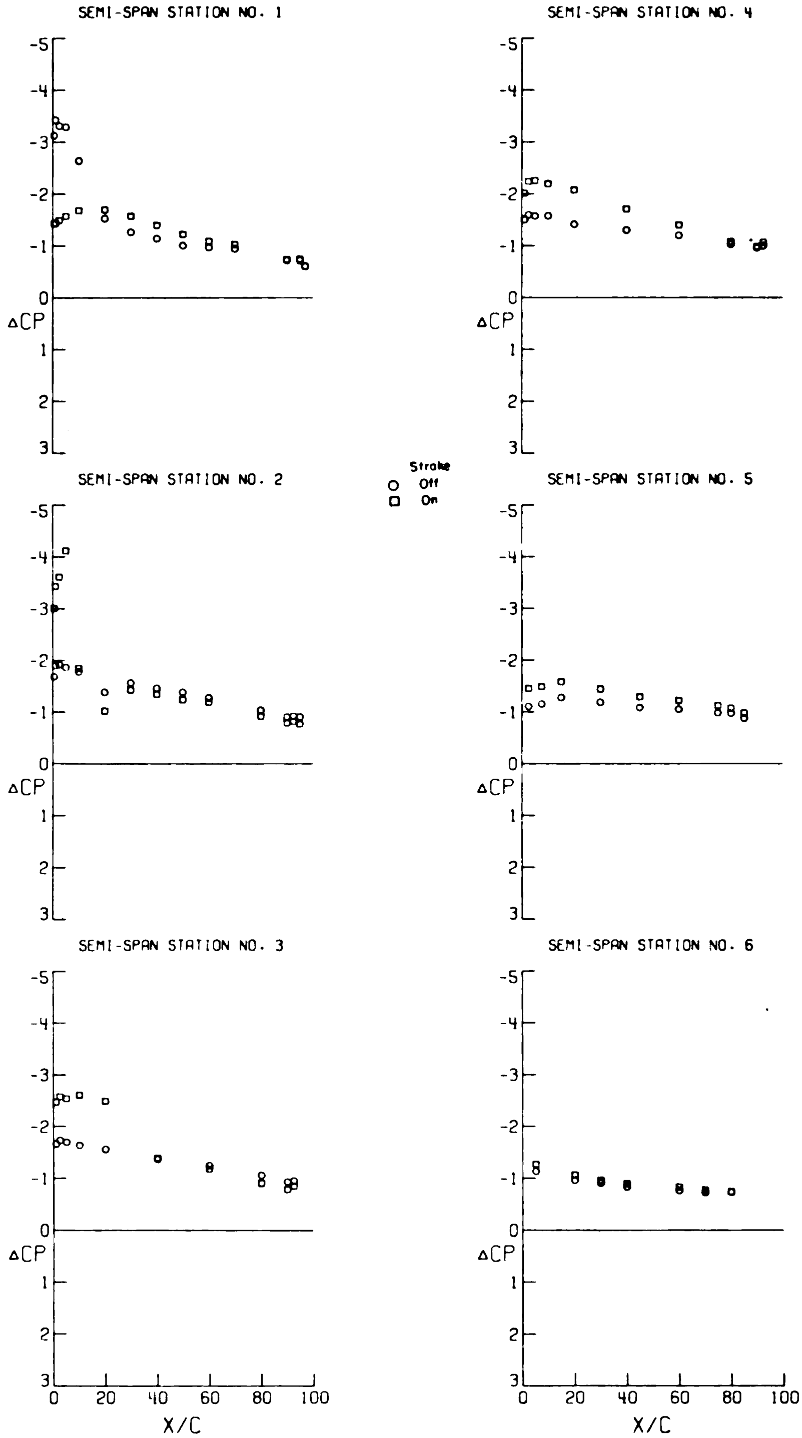

(m) $\alpha = 21.53^{\circ}$.

Figure 8.- Concluded.

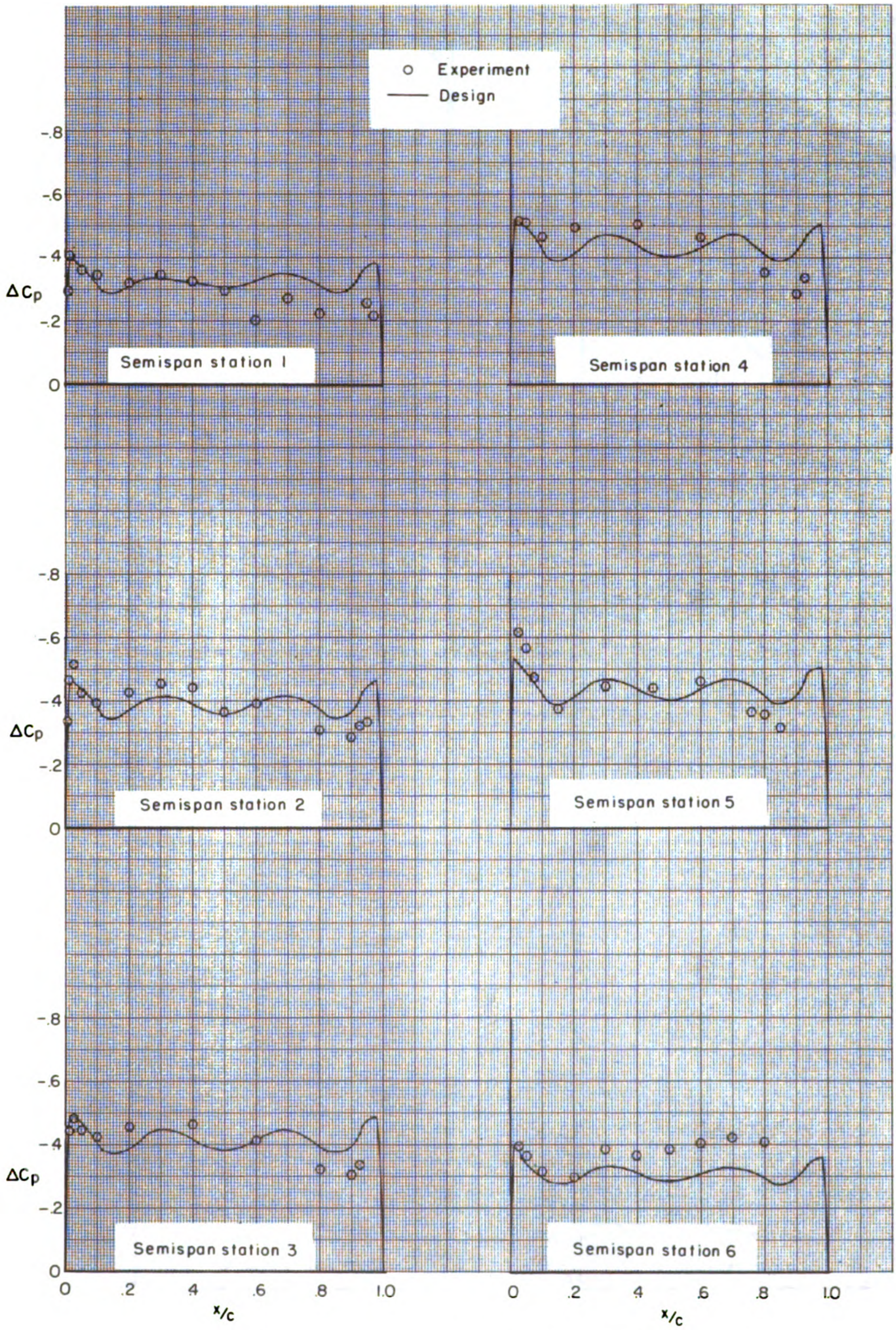

(a) $C_{L,d} = 0.35$ and $\alpha = 4.09^{\circ}$.

Figure 9.- Comparison of experimental and design pressure distribution on the model with strake off.

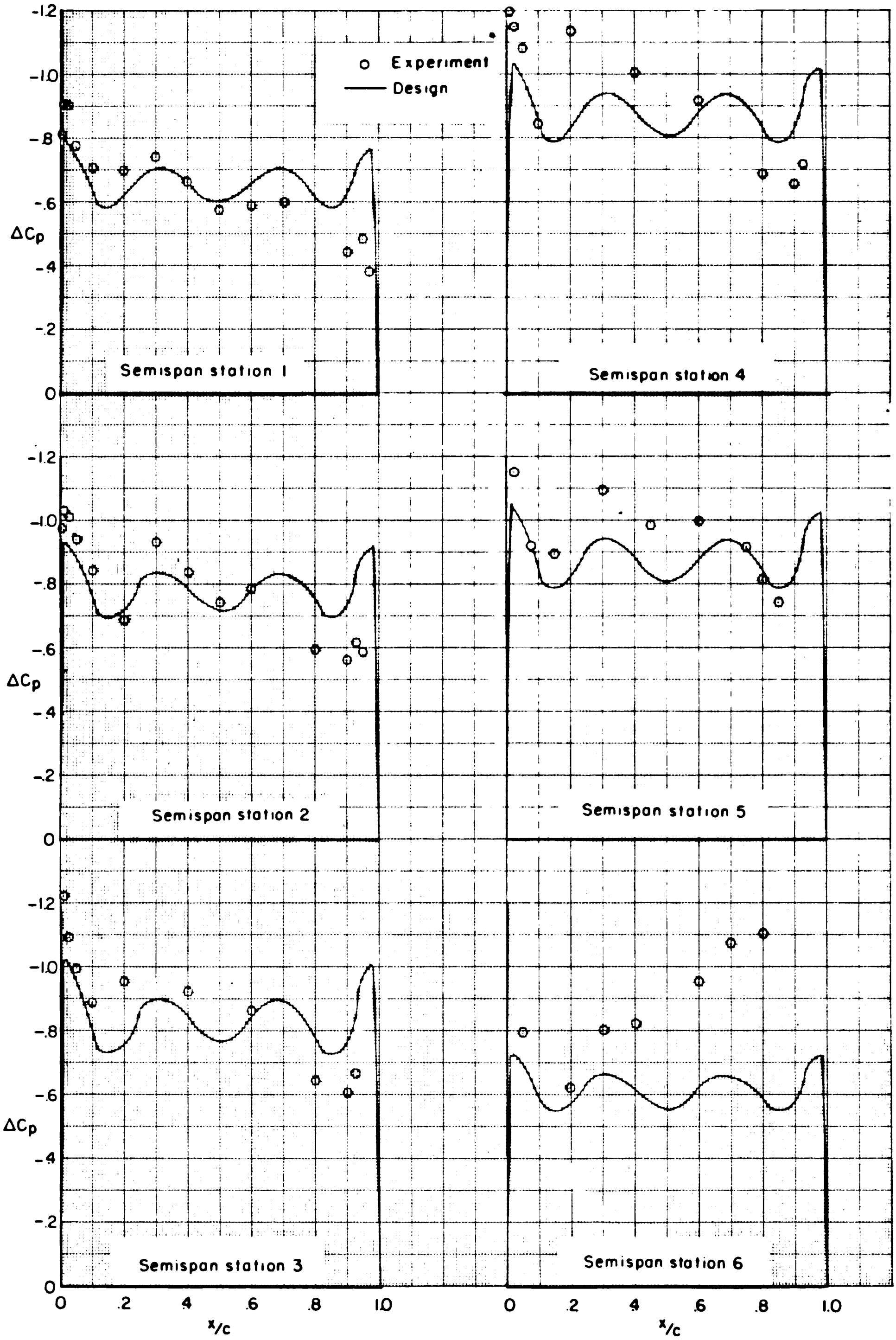

(b) $C_{L,d} = 0.70$ and $\alpha = 8.37^{\circ}$.

Figure 9.- Concluded.

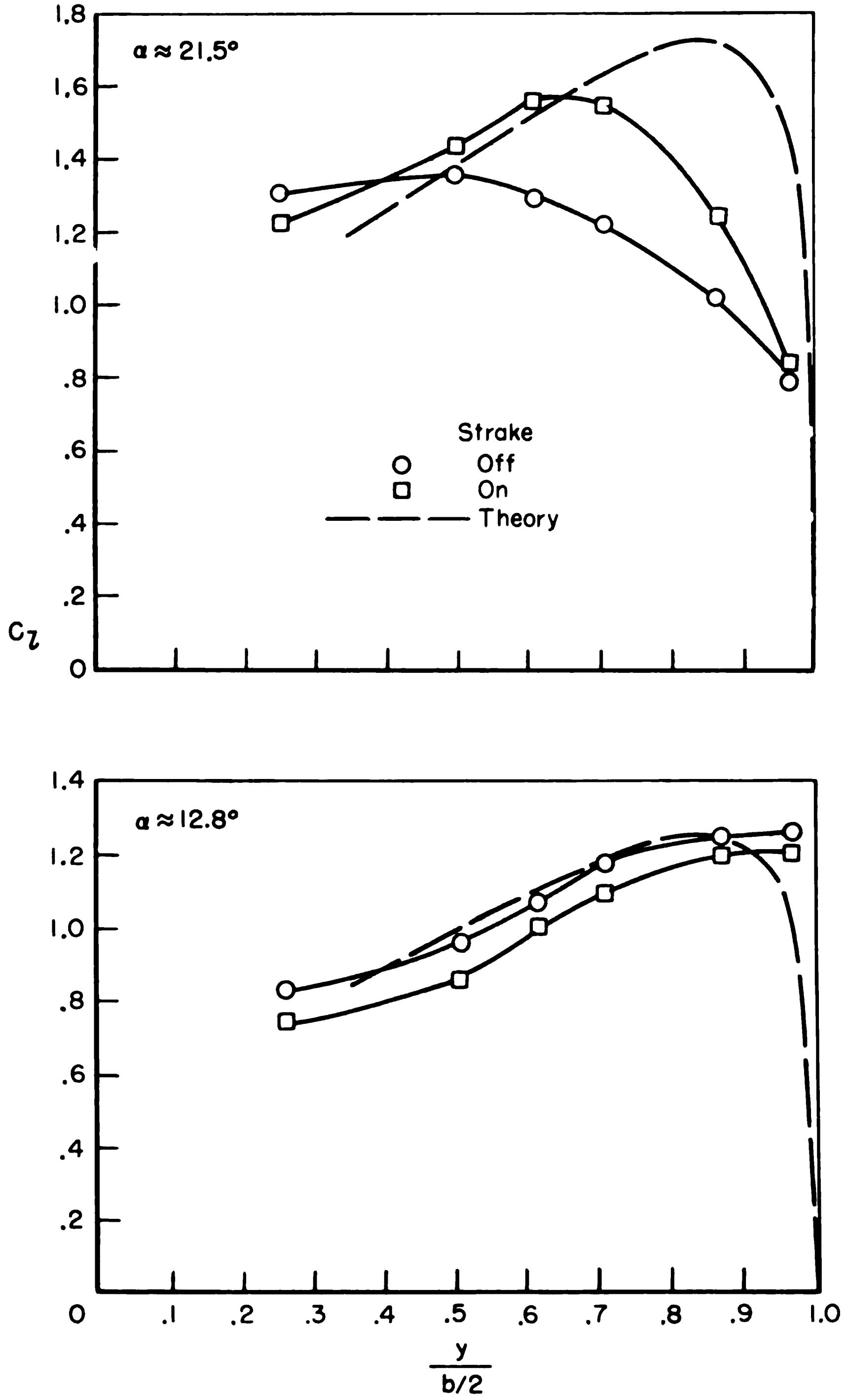

Figure 10.- Comparison of experimental and estimated spanwise lift distribution at two angles of attack for the strake on and off. $C_{L,d}$ = 0.70.

NATIONAL AERONAUTICS AND SPACE ADMINISTRATION
WASHINGTON, D.C. 20546

OFFICIAL BUSINESS
PENALTY FOR PRIVATE USE $300

SPECIAL FOURTH-CLASS RATE
BOOK

POSTAGE AND FEES PAID
NATIONAL AERONAUTICS AND
SPACE ADMINISTRATION
451

U.S.MAIL

734 001 C1 U AL 750711 S00606HU
UNIV OF MICHIGAN
ENGINEERING LIBRARY
ATTN: MR ROBERT T FREESE
ANN ARBOR MI 48104

POSTMASTER : If Undeliverable (Section 15[?]
Postal Manual) Do Not Return

"The aeronautical and space activities of the United States shall be conducted so as to contribute . . . to the expansion of human knowledge of phenomena in the atmosphere and space. The Administration shall provide for the widest practicable and appropriate dissemination of information concerning its activities and the results thereof."

—NATIONAL AERONAUTICS AND SPACE ACT OF 1958

NASA SCIENTIFIC AND TECHNICAL PUBLICATIONS

TECHNICAL REPORTS: Scientific and technical information considered important, complete, and a lasting contribution to existing knowledge.

TECHNICAL NOTES: Information less broad in scope but nevertheless of importance as a contribution to existing knowledge.

TECHNICAL MEMORANDUMS: Information receiving limited distribution because of preliminary data, security classification, or other reasons. Also includes conference proceedings with either limited or unlimited distribution.

CONTRACTOR REPORTS: Scientific and technical information generated under a NASA contract or grant and considered an important contribution to existing knowledge.

TECHNICAL TRANSLATIONS: Information published in a foreign language considered to merit NASA distribution in English.

SPECIAL PUBLICATIONS: Information derived from or of value to NASA activities. Publications include final reports of major projects, monographs, data compilations, handbooks, sourcebooks, and special bibliographies.

TECHNOLOGY UTILIZATION PUBLICATIONS: Information on technology used by NASA that may be of particular interest in commercial and other non-aerospace applications. Publications include Tech Briefs, Technology Utilization Reports and Technology Surveys.

Details on the availability of these publications may be obtained from:

SCIENTIFIC AND TECHNICAL INFORMATION OFFICE

NATIONAL AERONAUTICS AND SPACE ADMINISTRATION

Washington, D.C. 20546

NASA TECHNICAL NOTE

NASA TN D-7947

NASA TN D-7947

EFFECT OF VERTICAL-TAIL LOCATION ON THE AERODYNAMIC CHARACTERISTICS AT SUBSONIC SPEEDS OF A CLOSE-COUPLED CANARD CONFIGURATION

Jarrett K. Huffman

Langley Research Center
Hampton, Va. 23665

NATIONAL AERONAUTICS AND SPACE ADMINISTRATION • WASHINGTON, D. C. • AUGUST 1975

1. Report No.
NASA TN D-7947

2. Government Accession No.

3. Recipient's Catalog No.

4. Title and Subtitle

EFFECT OF VERTICAL-TAIL LOCATION ON THE AERODYNAMIC CHARACTERISTICS AT SUBSONIC SPEEDS OF A CLOSE-COUPLED CANARD CONFIGURATION

5. Report Date
August 1975

6. Performing Organization Code

7. Author(s)
Jarrett K. Huffman

8. Performing Organization Report No.
L-9961

10. Work Unit No.
743-35-12-03

9. Performing Organization Name and Address
NASA Langley Research Center
Hampton, Va. 23665

11. Contract or Grant No.

13. Type of Report and Period Covered
Technical Note

12. Sponsoring Agency Name and Address
National Aeronautics and Space Administration
Washington, D.C. 20546

14. Sponsoring Agency Code

15. Supplementary Notes

16. Abstract

A study was conducted to determine the effects of various vertical-tail configurations on the longitudinal and lateral directional-stability characteristics of a general research fighter model utilizing wing-body-canard. The study indicates that the addition of the high canard resulted in an increase in total lift at angles of attack above 4° with a maximum lift coefficient about twice as large as that for the wing-body configuration. For the wing-body (canard off) configuration, the center-line vertical tail indicates positive vertical-tail effectiveness throughout the test angle-of-attack range; however, for this configuration none of the wing-mounted vertical-tail locations tested resulted in a positive directional-stability increment at the higher angles of attack.

For the wing-body-canard configuration several outboard locations of the wing-mounted vertical tails were found. These outboard locations encountered favorable interference from the canard such that their directional-stability contribution increased in the high angle-of-attack range. However, all locations of the wing-mounted vertical tails caused a loss in total lift coefficient with the inboard, forward location indicating the smallest effect. The results also show that the upper segment of these vertical tails provides the largest contribution to directional stability, particularly at the high angles of attack.

The results of the study indicate that by careful selection of tail location a favorable canard interference is encountered. Therefore it would appear that for a configuration with a more representative fuselage a directional stability should be obtained with reasonably sized surfaces.

17. Key Words (Suggested by Author(s))
Aerodynamics
Stability
Lateral-directional stability

18. Distribution Statement
Unclassified – Unlimited

New Subject Category 02

19. Security Classif. (of this report)
Unclassified

20. Security Classif. (of this page)
Unclassified

21. No. of Pages
49

22. Price*
$3.75

*For sale by the National Technical Information Service, Springfield, Virginia 22161

EFFECT OF VERTICAL-TAIL LOCATION ON THE AERODYNAMIC CHARACTERISTICS AT SUBSONIC SPEEDS OF A CLOSE-COUPLED CANARD CONFIGURATION

Jarrett K. Huffman
Langley Research Center

SUMMARY

A study was conducted to determine the effects of various vertical-tail configurations on the longitudinal and lateral directional-stability characteristics of a general research fighter model utilizing wing-body-canard. The study indicates that the addition of the high canard resulted in an increase in total lift at angles of attack above 4° with a maximum lift coefficient about twice as large as that for the wing-body configuration. For the wing-body (canard off) configuration, the center-line vertical tail indicates positive vertical-tail effectiveness throughout the test angle-of-attack range; however, for this configuration none of the wing-mounted vertical-tail locations tested resulted in a positive directional-stability increment at the higher angles of attack.

For the wing-body-canard configuration several outboard locations of the wing-mounted vertical tails were found. These outboard locations encountered favorable interference from the canard such that their directional-stability contribution increased in the high angle-of-attack range. However, all locations of the wing-mounted vertical tails caused a loss in total lift coefficient with the inboard, forward location indicating the smallest effect. The results also show that the upper segment of these vertical tails provides the largest contribution to directional stability, particularly at the high angles of attack.

The results of the study indicate that by careful selection of tail location a favorable canard interference is encountered. Therefore it would appear that for a configuration with a more representative fuselage a directional stability should be obtained with reasonably sized surfaces.

INTRODUCTION

In the studies presented in references 1 to 8, it was shown that the addition of canard surfaces may provide performance improvements to maneuvering aircraft configurations.

These studies have concentrated almost entirely on the longitudinal aerodynamic characteristics of the configurations over a wide angle-of-attack range. In order to take advantage of the increased maneuvering performance that a canard or any other maneuvering concept may offer, the configuration must exhibit good handling qualities over a wide range of maneuvering conditions. Because of the interest in the longitudinal aerodynamic characteristics, a knowledge of the interference effects of the canard and canard flow fields on the lateral-directional characteristics of a representative configuration at high angle of attack is of increased importance. Therefore, the present paper presents the results of a research program which studied the effects of vertical-tail locations on the aerodynamic characteristics of a close-coupled canard configuration. This study was conducted in the Langley high-speed 7- by 10-foot tunnel at a Mach number of 0.30. The angle-of-attack range of the study varied from -4° to 40° at sideslip angles of 0° and $\pm5^{\circ}$.

SYMBOLS

The International System of Units, with the U.S. Customary Units presented in parentheses, is used for the physical quantities in this paper. Measurements and calculations were made in the U.S. Customary Units. All data presented in this report are referred to the stability-axis system as indicated in figure 1.

A aspect ratio, b^2/S (2.50)

b wing span, 50.8 cm (20 in.)

C_D drag coefficient, $\frac{\text{Drag}}{qS}$

C_L lift coefficient, $\frac{\text{Lift}}{qS}$

C_l rolling-moment coefficient, $\frac{\text{Rolling moment}}{qSb}$

C_{l_β} rolling moment due to sideslip, $\frac{\partial C_l}{\partial \beta}$, per deg

C_m pitching-moment coefficient, $\frac{\text{Pitching moment}}{qS\bar{c}}$

C_n yawing-moment coefficient, $\frac{\text{Yawing moment}}{qSb}$

C_{n_β} yawing moment due to sideslip, $\frac{\partial C_n}{\partial \beta}$, per deg

C_Y side-force coefficient, $\frac{\text{Side force}}{qS}$

C_{Y_β} side force due to sideslip, $\frac{\partial C_Y}{\partial \beta}$, per deg

c local chord, cm (in.)

$\bar{c}$ wing mean geometric chord, 23.32 cm (9.18 in.)

$\Delta C_{l_{\beta,C}}$ interference effect of the canard on the effective dihedral parameter $\left(C_{l_{\beta,WBCVT}} - C_{l_{\beta,WBVT}}\right)$

$\Delta C_{n_{\beta,C}}$ interference effect of the canard on the directional stability $\left(C_{n_{\beta,WBCVT}} - C_{n_{\beta,WBVT}}\right)$

$\Delta C_{l_{\beta,VT}}$ effect of vertical tail on the effective dihedral parameter $\left(C_{l_{\beta,WBCVT}} - C_{l_{\beta,WBC}}\right)$

$\Delta C_{n_{\beta,VT}}$ vertical tail effectiveness $\left(C_{n_{\beta,WBCVT}} - C_{n_{\beta,WBC}}\right)$

M.S. model station, cm (in.)

q free-stream dynamic pressure

S reference area of wing with leading and trailing edges extended to plane of symmetry, 0.1032 m^2 (1.1109 ft^2)

S_C exposed canard area, 0.30S

α angle of attack, deg

β angle of sideslip, deg

Subscripts:

B body

C canard

fb forward balance

VT vertical tail

W wing

DESCRIPTION OF MODEL

A drawing of the general research model is shown in figure 2. Figure 3 presents a photograph of the model without the vertical tail mounted in the Langley high-speed 7- by 10-foot tunnel. The basic model as illustrated in figure 2(a) consisted of a mid-wing, high-canard combination with the uncambered and untwisted wing having an aspect ratio of 2.5, a taper ratio of 0.20, a wing leading-edge sweep of 44°, and a circular-arc airfoil section with a thickness of 6 percent at the body juncture and 4 percent at the wing tip.

The canard had a leading-edge sweep of 51.7° and an exposed area $\left(S_c\right)$ of 30 percent of the reference wing area. It was untwisted and uncambered with a circular-arc airfoil section that varied in thickness ratio from 6 percent at the body juncture to 4 percent at the tip. (See fig. 2(a).) The canard was tested at a location above the wing chord plane as shown in figure 2(a).

A single vertical tail mounted along the fuselage center line (see figs. 2(b) and 4) as well as wing-mounted vertical tails (see figs. 2(c) and 4) were investigated. The center-line tail had a leading-edge sweep of 51.7° and an exposed area of 16 percent of the reference wing area (see fig. 2(b)) with a circular-arc airfoil section that varied from 6 percent at the body juncture to 4 percent at the tip. The wing-mounted vertical tails were located on the upper and lower surfaces of the wing with their total exposed area equal to the area of the single center-line vertical tail. The wing-mounted vertical tails were of constant thickness with beveled trailing edges and rounded leading edges as shown in figure 2(c). Their location was varied longitudinally and spanwise as shown in figure 4.

The moment reference point was taken to be at fuselage station 59.16 cm (23.29 in.) as shown in figure 2(a).

APPARATUS, TESTS, AND CORRECTIONS

This investigation was made in the Langley 7- by 10-foot high-speed (atmospheric) wind tunnel. Forces and moments were measured by two internally mounted, six-component strain-gage balances. The forward balance was rigidly mounted to the aft section of the model and measured the loads on the forward segment of the fuselage (shaded area of fig. 2(a)); this balance is referred to as the forward balance. There was a small unsealed gap of 0.229 cm (0.090 in.) between the segments of the fuselage in order to prevent fouling of the forward balance. (See fig. 2.) The second balance, which was located in the aft segment of the model, measured the total load on the model; this balance is referred to as the main balance.

The test was made at a Mach number of about 0.3 which corresponded to a Reynolds number of 1.53×10^6 based on the mean geometric chord. The angle-of-attack range was -4° to 40° at sideslip angles of 0° and $\pm 5^{\circ}$. The angles of attack and angle of sideslip have been corrected for the effects of balance and sting bending under aerodynamic loads. The drag measurements of the main balance were adjusted to a condition of free-stream static pressure acting on the base of the model. Transition strips 0.08 cm (0.031 in.) in width and No. 90 carborandum grains were placed 1.14 cm (0.45 in.) streamwise from the leading edge of the wing, vertical tails, and canard as well as 3.28 cm (1.29 in.) behind the nose of the fuselage as in reference 9.

PRESENTATION OF RESULTS

The longitudinal characteristics are presented in figures 5 to 9 and the lateral-directional characteristics in figures 10 to 14. The following list of figures is presented as an aid in locating the results of a particular configuration:

DISCUSSION

Longitudinal Characteristics

Figures 5 to 9 present the basic longitudinal aerodynamic characteristics for the wing-body and wing-body-canard configurations. The addition of the high canard to the wing-body configuration (data presented in figs. 5 and 6 and compared in fig. 15) resulted in an increase in total lift at angles of attack above about 4° with a total maximum lift nearly twice as large as that produced by the wing-body configuration. However, the wing lift (see fig. 15(c)) shows a loss at low and moderate angles of attack caused by the canard downwash, with an increase in maximum wing lift of about 28 percent. These results can be attributed to mutual beneficial interference effects of the canard on the wing and of the wing on the canard and are discussed in more detail in references 8 and 10.

The variation in the pitching-moment coefficient with the lift coefficient (see fig. 15(a)) was linear up to the stall, above which the canard configurations initiated a pitchup while the wing-body configuration showed a stable break. The center-of-gravity location was chosen to obtain a stable wing-body configuration; therefore, the wing-body-canard configuration is unstable because the lift generated by the canard surface is acting ahead of the center of gravity. As discussed in reference 10 and shown in the data herein, the wing-body-canard configuration exhibited a significantly lower drag due to lift than did the wing-body configuration. (See fig. 15(b).)

When the single vertical tail is added at the body center line (see fig. 2), the longitudinal characteristics of either the wing-body or the wing-body-canard configurations, as would be expected, are generally unaffected. (See figs. 5 and 6.)

Placing the twin vertical tails on the wings of the wing-body-canard configuration in positions 1, 2, or 3, as shown in figure 4, caused a significant loss in lift at the higher angles of attack, an increase in drag due to lift, and a pitchup tendency which occurred at a lower lift coefficient than with tails off. (See fig. 5.) The loss in lift is probably caused by an interaction of the wing-canard flow field with the wing-mounted vertical tails resulting in both a wing flow separation and a loss in vortex lift on the wing panel. This result is evidenced by the absence of large effects of the vertical tails on the wing-body characteristics. (See fig. 6.) As the vertical tails are moved inboard (see fig. 4 and the data of fig. 5) from the wing tips (position 1) the lift decreased and the drag increased significantly, especially in the moderate angle-of-attack range (16° to 24°). It should be noted that the loss in maximum lift coefficient caused by the addition of the wing-mounted vertical tails is not just associated with the wing, but the disturbances are felt forward on the canard such that about 25 percent of the lift loss is on the canard surface. (See fig. 5(b).)

Moving the vertical tails forward on the wing to positions 4 and 5 (see figs. 7 and 8) recovered some of the lift loss previously shown for the rear positions of the vertical tails (positions 1, 2, and 3). For the vertical tails in position 4, nearly all of the lift loss is recovered. The vertical tails in this position appear to have minimum interference with the beneficial effects attributed to the leading-edge vortex.

Figure 9 shows the effect of removing the lower surface vertical tails for the vertical tails located at position 3 on the wing-body-canard configuration. The data indicate that removal of the lower surface vertical tails has no effect on the longitudinal aerodynamic characteristics up to a lift coefficient of about 1.3. Above 1.3 a slight increase in maximum lift is noted when compared to the complete configuration with the upper and lower wing-mounted vertical tails. It would appear that the upper surface vertical tails were the major contributor to the lift loss.

Lateral-Directional Stability Characteristics

The effects of the various vertical-tail configurations on the lateral-directional derivatives are presented in figures 10 to 14 as a function of the angle of attack. The following discussion is based on incremental effects, since the fuselage of the model tested does not represent the fuselage that would be utilized on an actual aircraft. The total effects of the canard on the directional stability and the effective dihedral parameter $\left(\Delta C_{n_{\beta,C}}\right.$ and $\left.\Delta C_{l_{\beta,C}}\text{, respectively}\right)$ as a function of angle of attack are presented in figure 16. The addition of the canard caused a large negative directional-stability increment at angles of attack above 20°. This negative increment associated with the addition of the canard is present regardless of the vertical-tail configuration and appears to be primarily the result of a change in sidewash on the aft fuselage. The addition of the center-line vertical tail resulted in an even greater adverse effect on the directional-stability increment associated with the canard as well as a more negative effective dihedral parameter at moderate and high angles of attack. This further indicates that the sidewash is adverse in the region of the vertical tail. A slight destabilizing incremental contribution is noted from the forward fuselage section of the model upon the addition of the canard. (See figs. 10(b) and 12(b).)

The results for the wing-mounted vertical tails at locations 1, 2, and 3 are also presented in figure 16. The large unfavorable effect of adding the canard to the configuration with the vertical tails off is significantly reduced for the configuration with the twin vertical tails. This reduction would indicate that the twin tails may be located in a region of favorable sidewash at the higher angle of attack. The data also show that as the vertical tails are moved inboard along the same longitudinal line (same tail length) little or no effect is noticed up to an 18° angle of attack, above which angle inboard movement from positions 1 to 2 resulted in a decrease in the unfavorable canard directional-stability increment and a more negative effective dihedral-parameter increment. However, inboard movement from positions 2 to 3 resulted in only a slight change in the directional-stability increment with essentially no change in the effective dihedral-parameter increment.

When the vertical tails are located at position 4, the results show a slight, favorable stability increment up to about a 19° angle of attack and large unfavorable stability effects at the higher angles of attack. In the range of angles of attack between 20° and 26°, the unfavorable effect appears larger than for the tail-off configuration, indicating an unfavorable sidewash on the twin vertical tails. At position 5 the data indicate that the twin tails are in an unfavorable sidewash field up to angles of attack of about 30°. (Note the larger unfavorable increment for the twin tails than for the tail job.) Thus, for the wing-mounted vertical-tail locations investigated, a location inboard of the wing tip and outboard of the canard tip encounters favorable canard interference, thereby reducing the overall adverse canard effect.

The vertical-tail effectiveness parameter and the effect of the vertical-tail configuration on the effective dihedral parameter, respectively, as a function of angle of attack are presented in figures 17 and 18. For the canard-off configuration (right side of figure) the center-line vertical tail shows positive effectiveness over the entire test angle-of-attack range. The data for the wing-body configuration with the vertical tails off presented in figure 12(a) indicate a favorable interference effect at high angles of attack resulting in the configuration exhibiting positive stability at angles above 23°. This effect is the result of a favorable sidewash on the aft fuselage of the configuration. This favorable sidewash was undoubtedly carried over to the configuration with the center-line vertical tail as evidenced by the positive increment in stability above a 24° angle of attack. When the vertical tails are wing mounted (canard off), the vertical-tail effectiveness is at best neutral at angles of attack above 23°, indicating that the wing-mounted vertical tails are located in an unfavorable sidewash field.

The addition of the canard to the configuration with the center-line vertical tail resulted in a loss in tail effectiveness such that, at an angle of attack above 24°, the contribution of the vertical tail to stability was destabilizing. This effect is probably caused by the canard flow field altering the induced sidewash in the area of the vertical tail. For the wing-mounted vertical tails 1, 2, and 3 (canard on), the effectiveness is positive and essentially constant up to 18° angle of attack; above this angle the effectiveness increases with increasing angles of attack. At positions 2 and 3, because of a favorable canard interference, a positive effectiveness over the entire angle-of-attack range results. The data for the configuration utilizing wing-body-canard with wing-mounted vertical tails at positions 4 and 5 indicate that at position 4 the vertical tails show positive effectiveness with an increasing angle of attack; at position 5 the effectiveness is positive up to about 23°. The data of figure 18 indicate little or no effect of the vertical-tail configurations on the effective dihedral parameter. However, the addition of the canard in general caused a slightly more positive effective dihedral parameter for all vertical-tail configurations at high angles of attack.

The vertical-tail effectiveness for the wing-mounted vertical tails at position 3 for upper and lower surface-mounted and for upper surface only is shown in figure 19. The data indicate that at low to moderate angles of attack the upper surface vertical tails provide about half of the directional-stability increment, while at angles of attack above 23° they provide about two-thirds of this total increment.

CONCLUSIONS

A study to determine the effects of various vertical-tail configurations on the longitudinal and lateral stability characteristics of a general research fighter model utilizing wing-body-canard indicated the following results:

1. The addition of the high canard to the wing body resulted in an increase in total lift at angles of attack above about 4° with a maximum lift coefficient about twice as large as that produced by the wing-body configuration.

2. For the wing body (canard off), the center-line vertical tail indicated positive vertical-tail effectiveness throughout the test angle-of-attack range.

3. For the wing-body configuration none of the wing-mounted vertical-tail locations tested resulted in a positive directional-stability increment at the higher angles of attack.

4. The addition of the canard to the wing-body center-line vertical-tail configuration produced a large negative increment in directional stability at the higher angles of attack.

5. For the wing-body-canard configuration several outboard locations of the wing-mounted vertical tails were found to have favorable interference from the canard such that their directional-stability configurations increased in the higher angle-of-attack range.

However, all locations of the wing-mounted vertical tail caused a loss in total lift coefficient. The inboard, forward location indicated the smallest effect.

6. The results showed that the upper segment of the vertical tail provided the largest contribution to directional stability, particularly at the higher angles of attack.

7. The results of the study indicated that by careful selection of tail location a favorable canard interference was encountered. Therefore, it would appear that for a configuration with a more representative fuselage, a directional stability should be obtained with reasonably sized surfaces.

Langley Research Center,
National Aeronautics and Space Administration,
Hampton, Va., May 20, 1975.

REFERENCES

1. Behrbohm, Hermann: Basic Low Speed Aerodynamics of the Short-Coupled Canard Configuration of Small Aspect Ratio. SAAB TN 60, Saab Aircraft Co. (Linköping, Sweden), July 1965.
2. Lacey, David W.; and Chorney, Stephen J.: Subsonic Aerodynamic Characteristics of Close-Coupled Canards With Varying Area and Position Relative to a 50° Swept Wing. Tech. Note AL-199, Naval Ship Res. & Develop. Center, Mar. 1971. (Available from DDC as AD 882 702L.)
3. McKinney, Linwood W.; and Dollyhigh, Samel M.: Some Trim Drag Considerations for Maneuvering Aircraft. J. Aircraft, vol. 8, no. 8, Aug. 1971, pp. 623-629.
4. Dollyhigh, Samuel M.: Static Longitudinal Aerodynamic Characteristics of Close-Coupled Wing-Canard Configurations at Mach Numbers From 1.60 to 2.86. NASA TN D-6597, 1971.
5. Krouse, John R.: Effects of Canard Planform on the Subsonic Aerodynamic Characteristics of a 25° and a 50° Swept-Wing Research Aircraft Model. Evaluation Rep. AL-91, Naval Ship Res. & Develop. Center, May 1972.
6. Lacey, David W.: Transonic Characteristics of Close-Coupled Canard and Horizontal Tail Installed on a 50 Degree Sweep Research Aircraft Model. Evaluation Rep. AL-81, Naval Ship Res. & Develop. Center, Aug. 1972.
7. Ottensoser, Jonah: Wind Tunnel Data on the Transonic Aerodynamic Characteristics of Close-Coupled Canards With Varying Planform, Position and Deflection Relative to a 50° Swept Wing. Test Rep. AL-88, Naval Ship Res. & Develop. Center, May 1972.
8. Gloss, Blair B.; and McKinney, Linwood W.: Canard-Wing Lift Interference Related to Maneuvering Aircraft at Subsonic Speeds. NASA TM X-2897, 1973.
9. Braslow, Albert L.; Hicks, Raymond M.; and Harris, Roy V., Jr.: Use of Grit-Type Boundary-Layer-Transition Trips on Wind-Tunnel Models. NASA TN D-3579, 1966.
10. Gloss, Blair B.: Effect of Canard Location and Size on Canard-Wing Interference and Aerodynamic-Center Shift Related to Maneuvering Aircraft at Transonic Speeds. NASA TN D-7505, 1974.

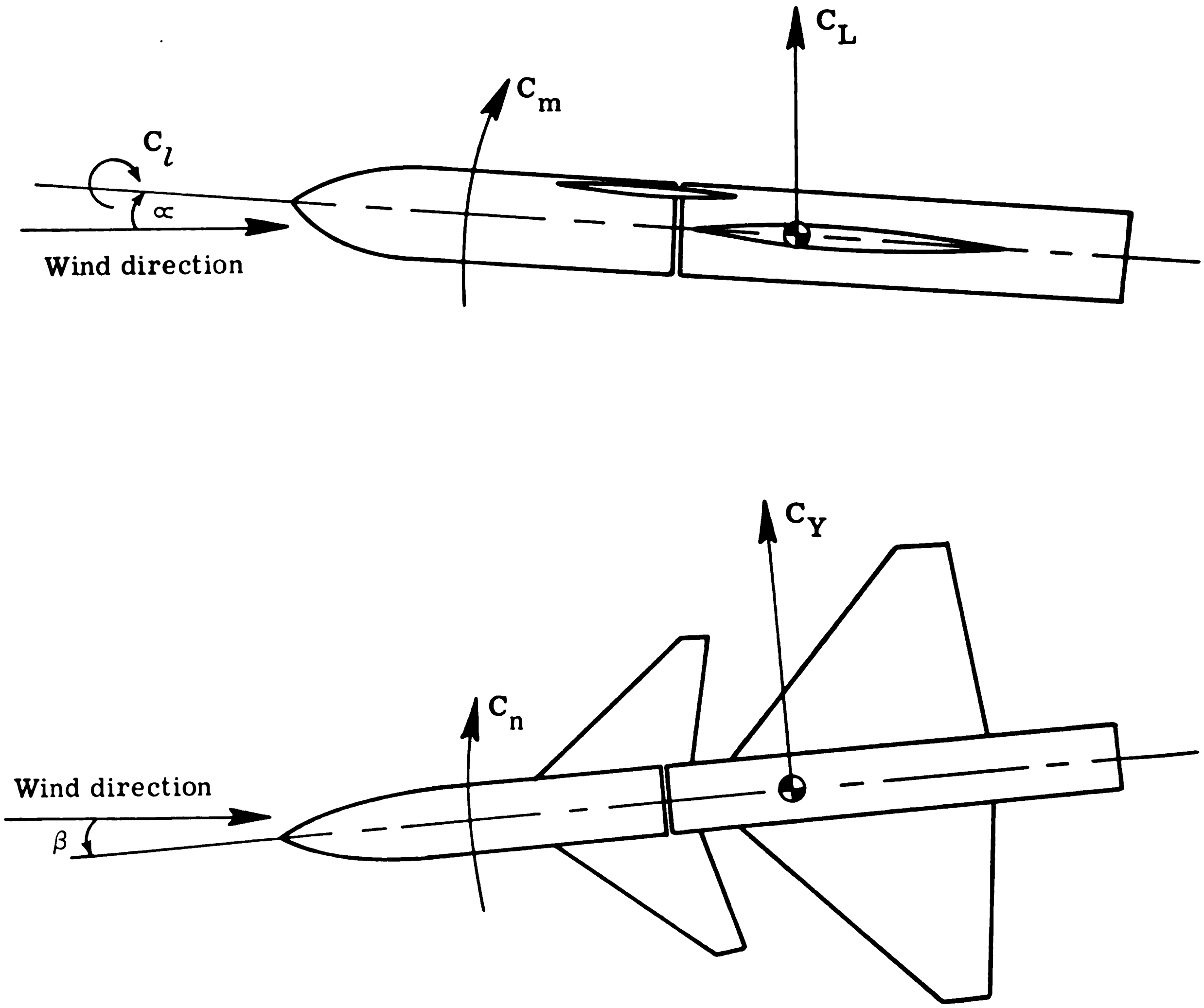

Figure 1.- System of axes used showing positive directions of forces, moments, angles, and velocities.

Wing:

A	2.5
b, cm (in.)	50.8 (20.00)
c, cm (in.)	23.31 (9.18)
Airfoil section	Circular arc
Root chord (exposed, percent c)	6.0
Tip chord (percent c)	4.0
S (area extended to plane of symmetry), sq cm (sq ft)	1032.2 (1.11)

Canard:

A	4.13
b, cm (in.)	34.50 (13.58)
S_c (exposed), sq cm (sq ft)	288.83 (0.31)
Airfoil section	Circular arc
Root chord (percent c)	6.0
Tip chord (percent c)	4.0

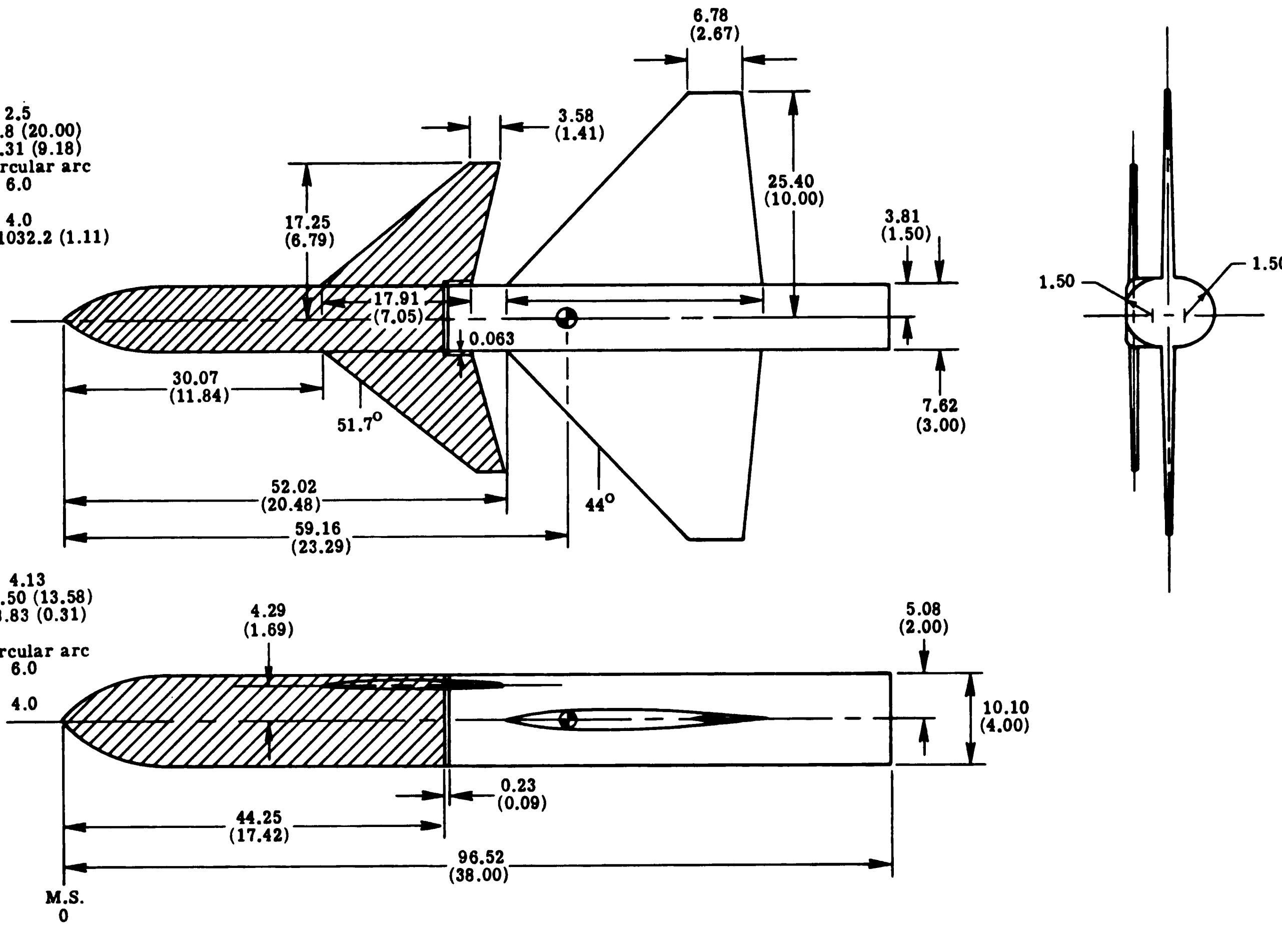

(a) Three-view drawing of test model.

Figure 2.- Model drawings. (All dimensions in cm (in.).)

A	1.25
b, cm (in.)	14.38 (5.66)
S_{VT} (exposed), sq cm (sq in.)	165.30 (25.61)
Airfoil section	Circular arc
Root chord (percent c)	6.0
Tip chord (percent c)	4.0

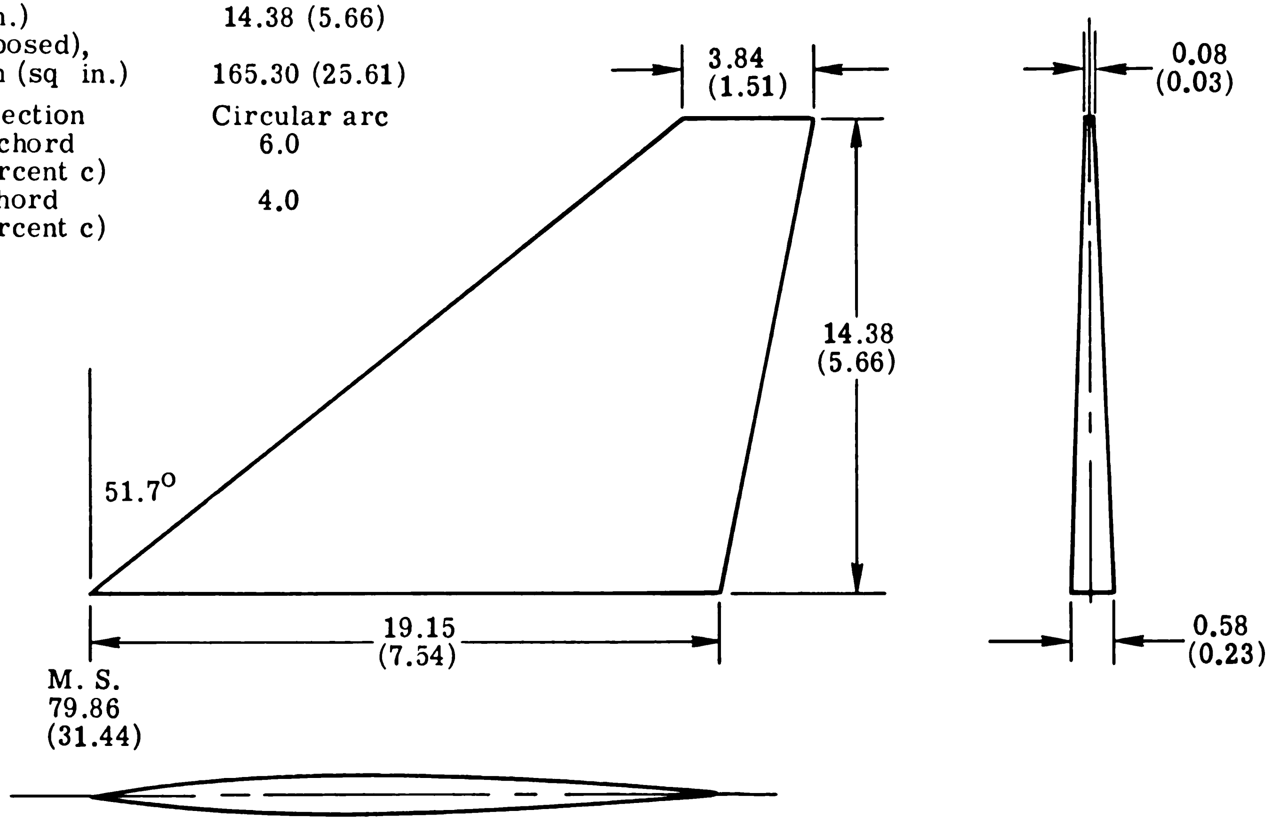

(b) Center-line vertical tail.

Figure 2.- Continued.

Geometry (each element)

A	1.25
Tail span (exposed) cm (in.)	7.19 (2.83)
Area (exposed) cm^2 (in^2)	41.38 (6.41)

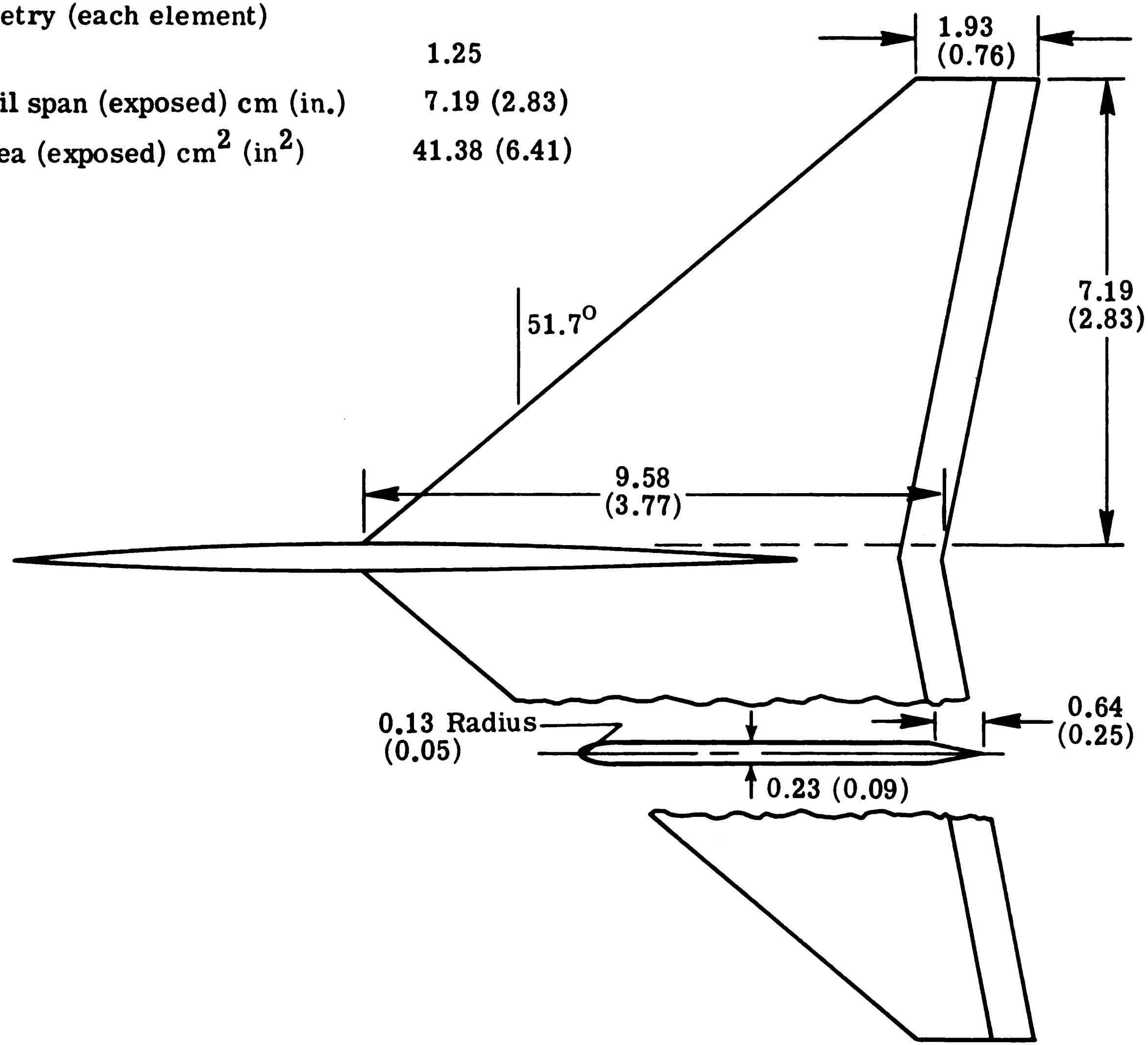

(c) Upper and lower surface wing-mounted vertical tails.

Figure 2.- Concluded.

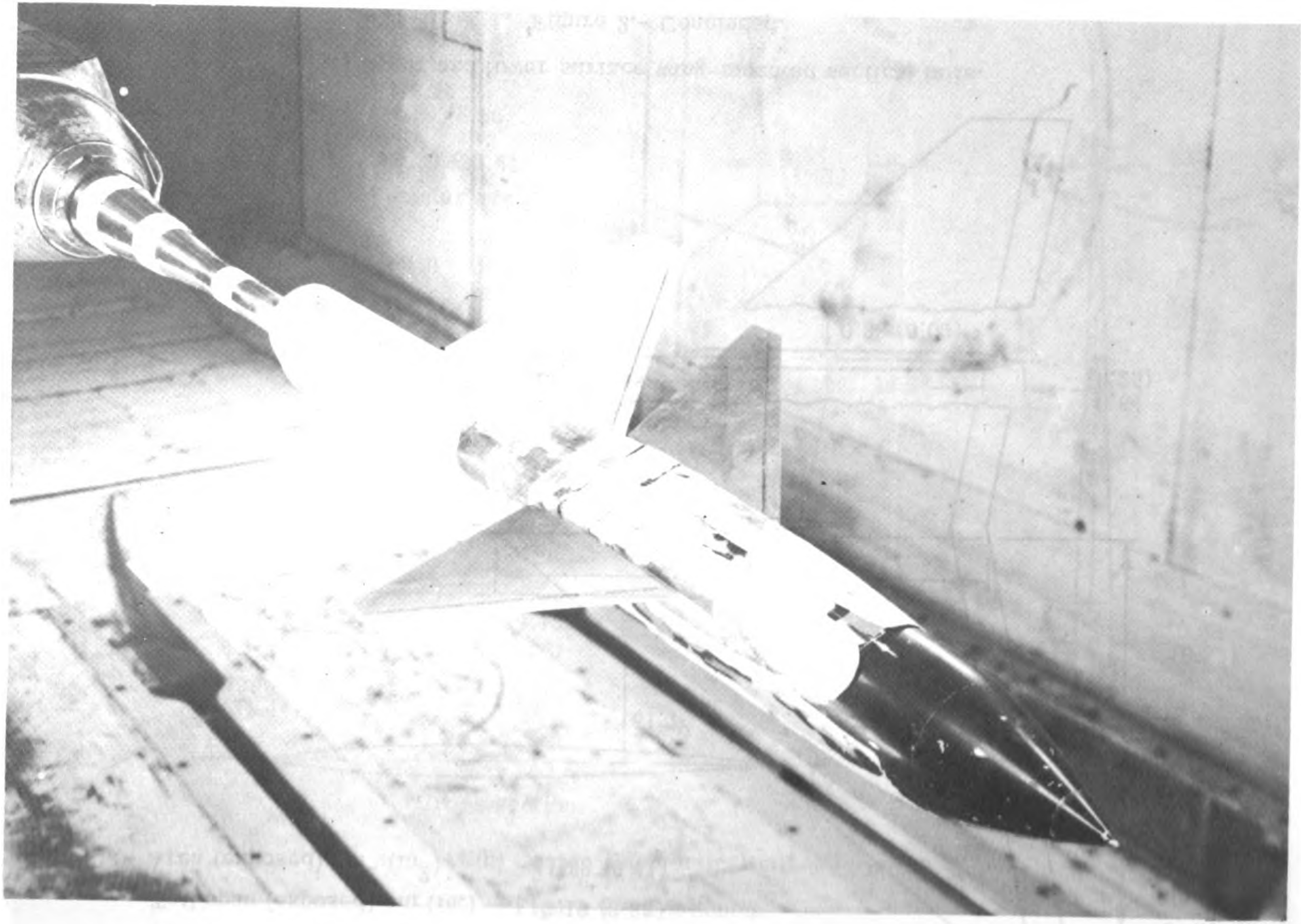

L-73-8751

Figure 3.- Model mounted in tunnel for testing.

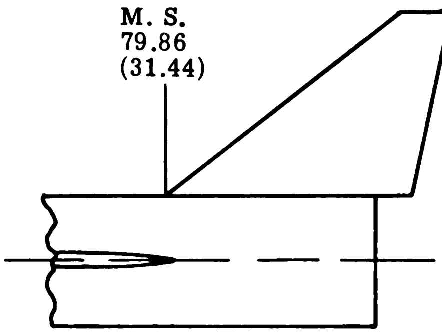

Center-line vertical tail

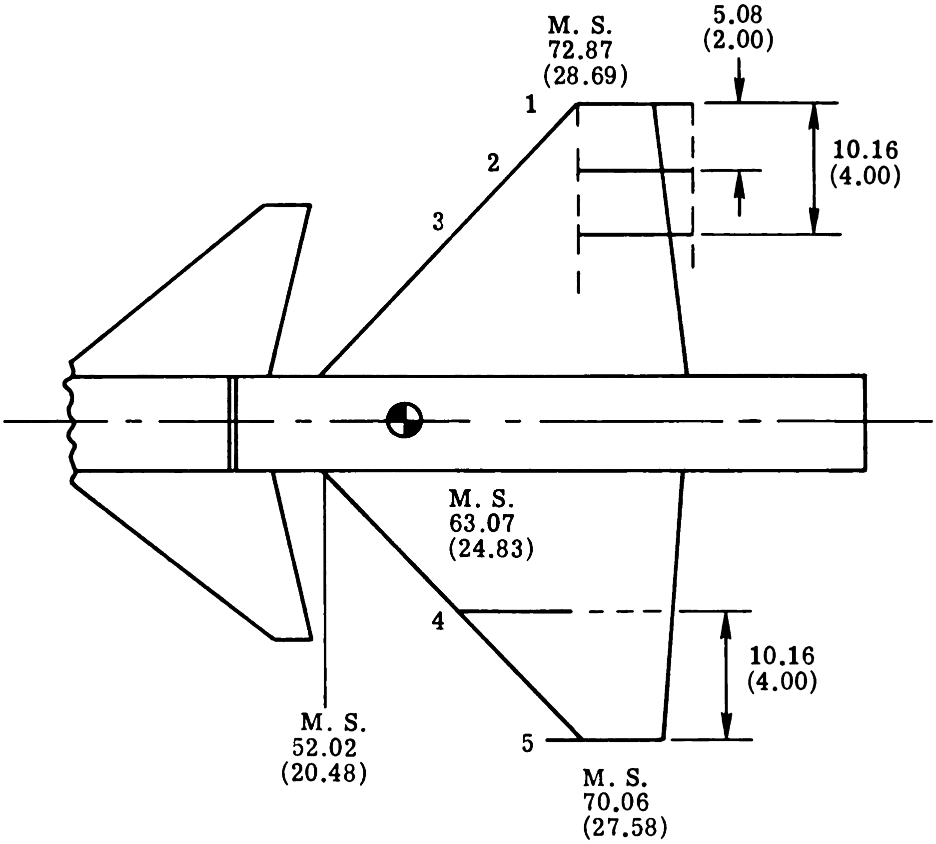

Wing-mounted vertical tails

Figure 4.- Location of the various vertical-tail configurations. (All dimensions in cm (in.).)

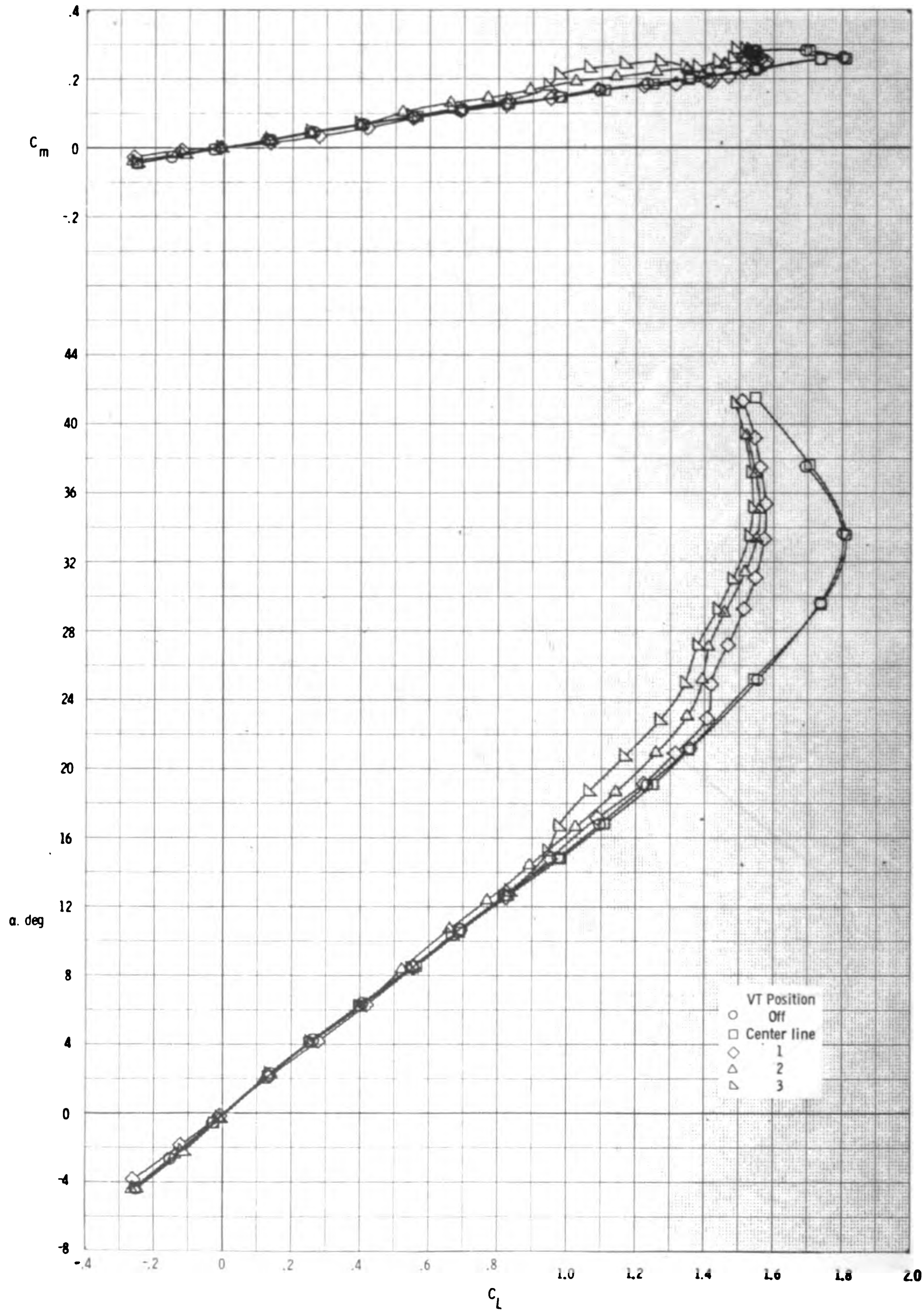

(a) Total longitudinal characteristics.

Figure 5.- Longitudinal aerodynamic characteristics of wing-body-canard configuration with center-line vertical tail or wing-mounted vertical tail at locations 1, 2, and 3.

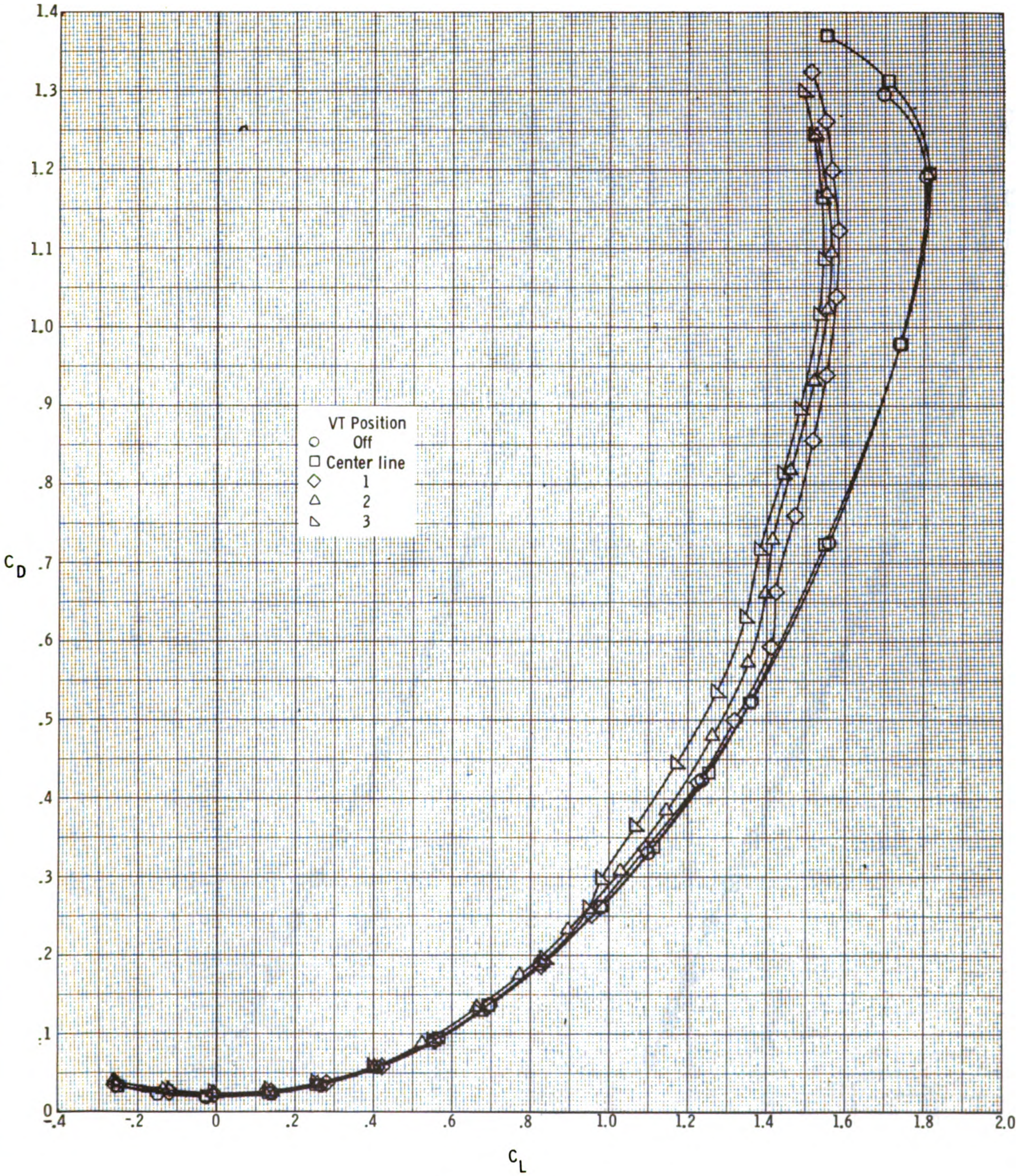

(a) Concluded.

Figure 5.- Continued.

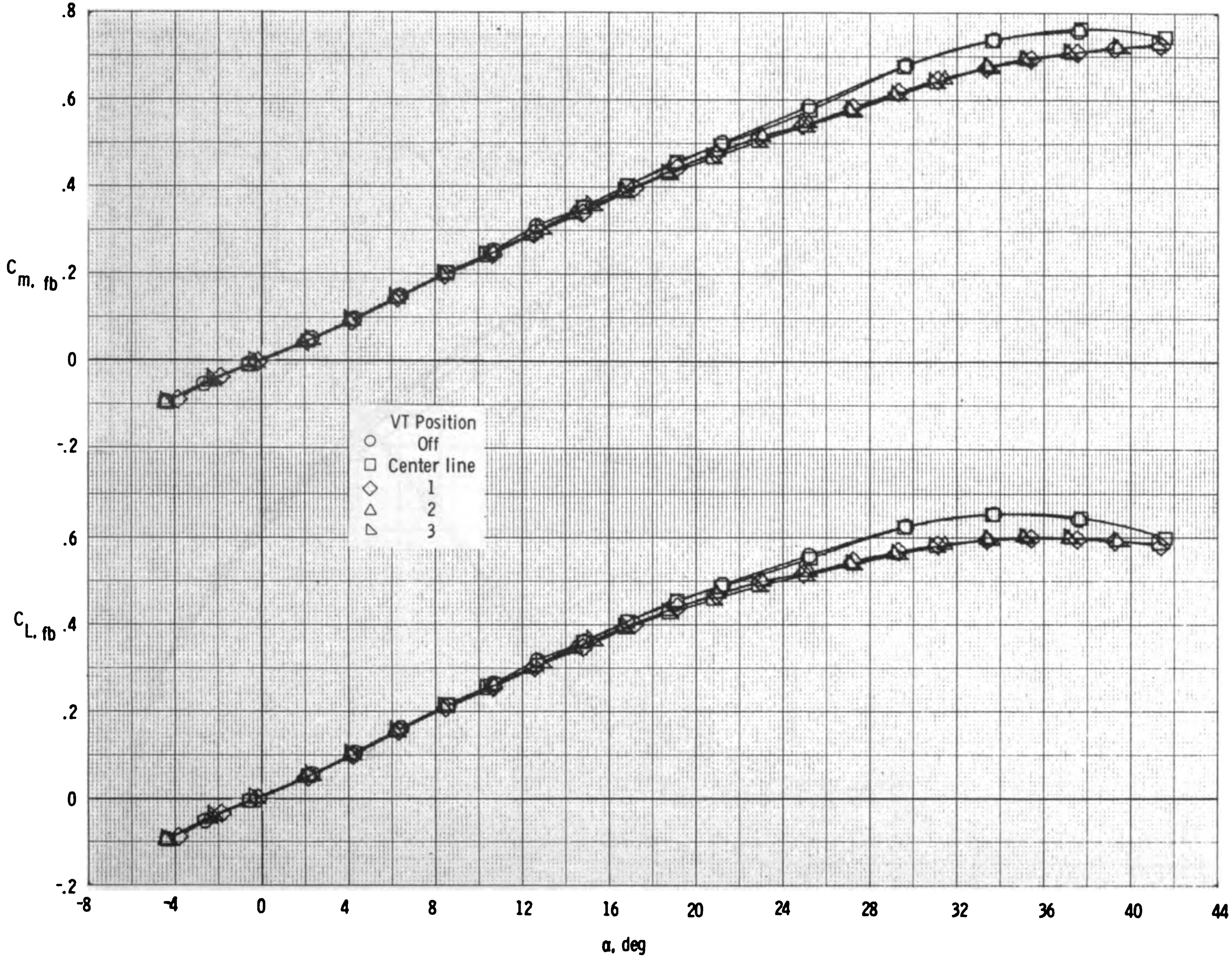

(b) **Forward fuselage longitudinal characteristics.**

Figure 5.- Concluded.

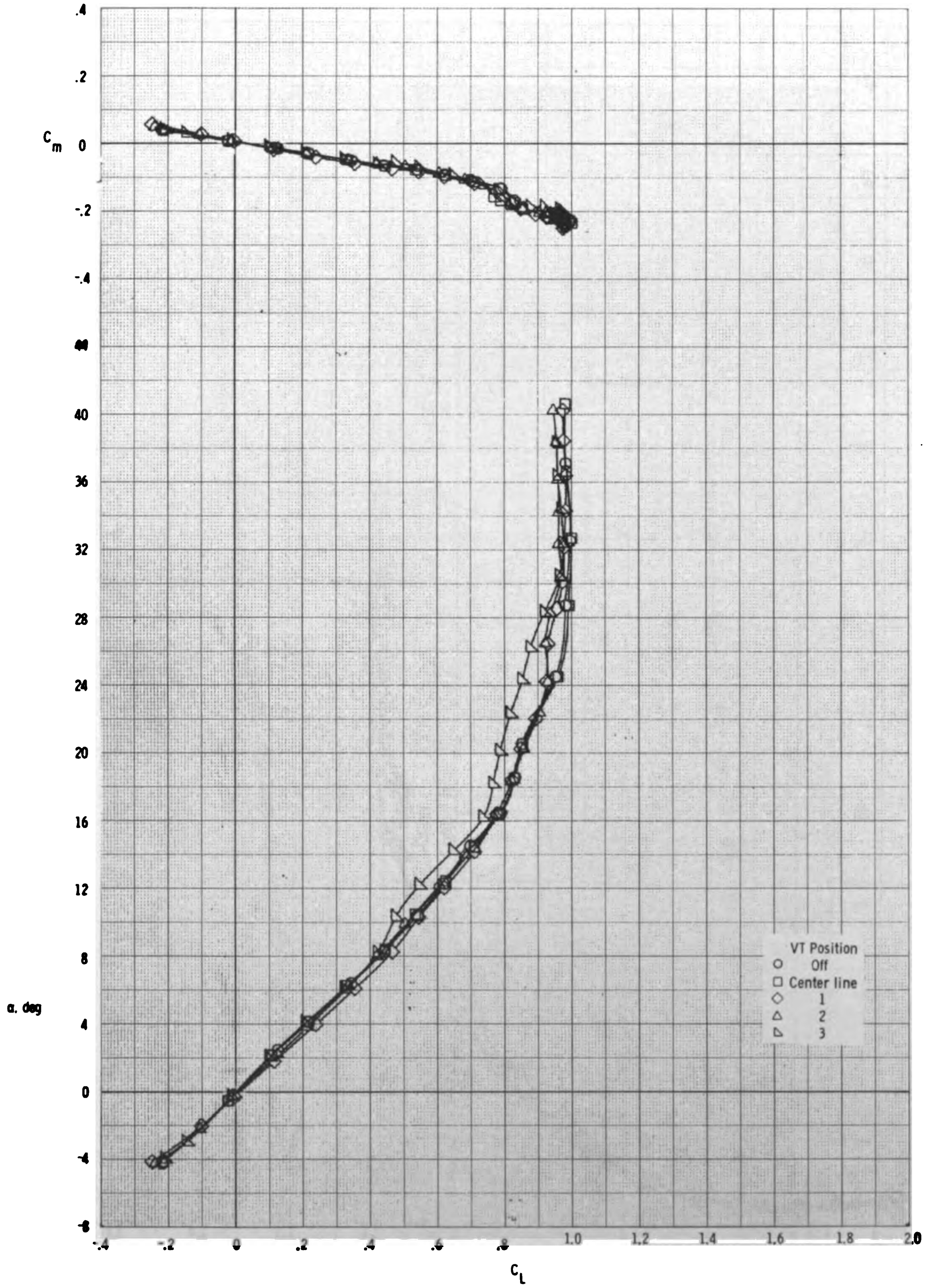

(a) Total longitudinal aerodynamic characteristics.

Figure 6.- Longitudinal aerodynamic characteristics of the wing-body configuration with center-line vertical tail or wing-mounted vertical tails at locations 1, 2, and 3.

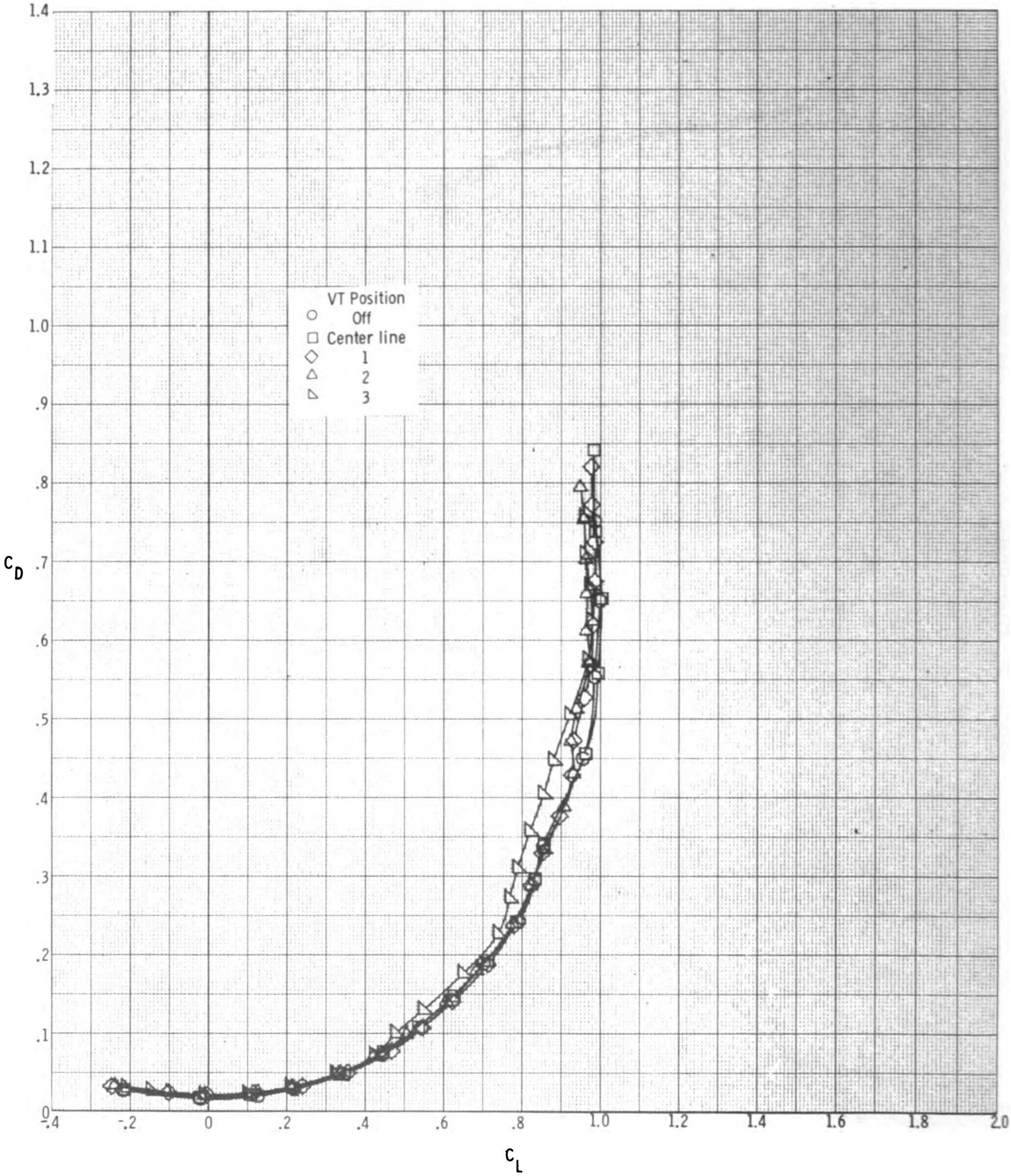

(a) Concluded.

Figure 6.- Continued.

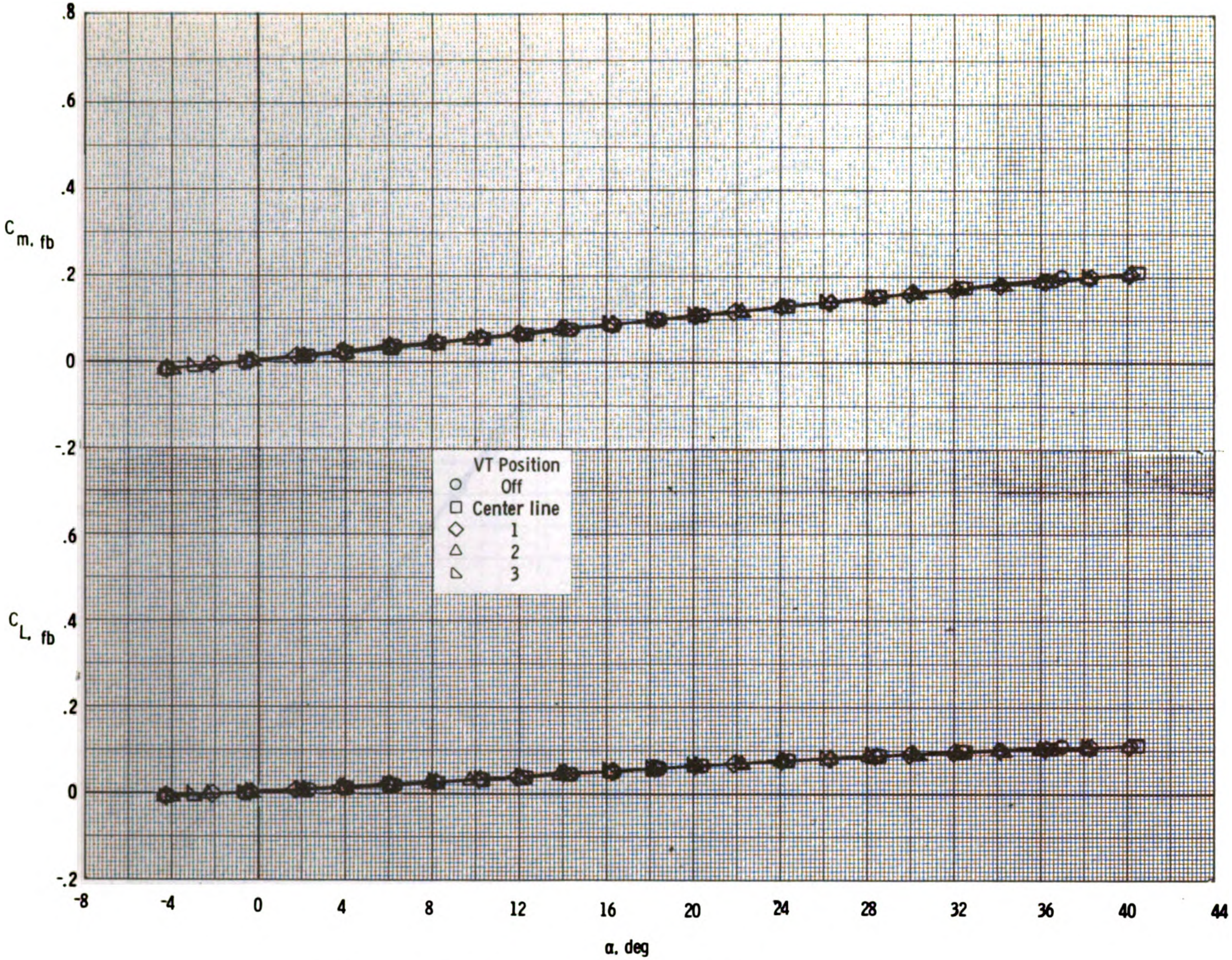

(b) Forward fuselage aerodynamic characteristics.

Figure 6.- Concluded.

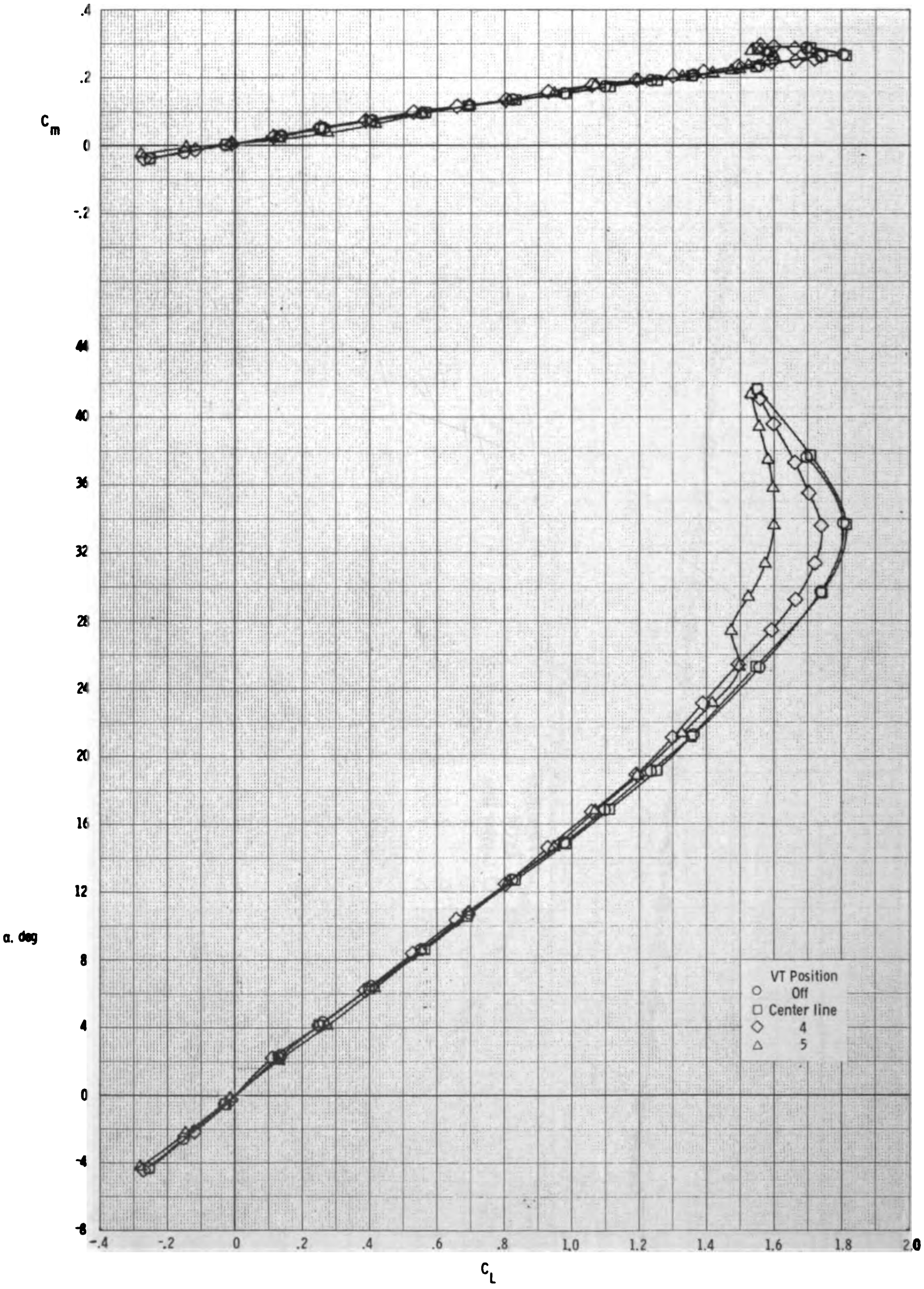

(a) Total longitudinal characteristics.

Figure 7.- Longitudinal aerodynamic characteristics of wing-body-canard configuration with center-line vertical tail or wing-mounted vertical tails at positions 4 and 5.

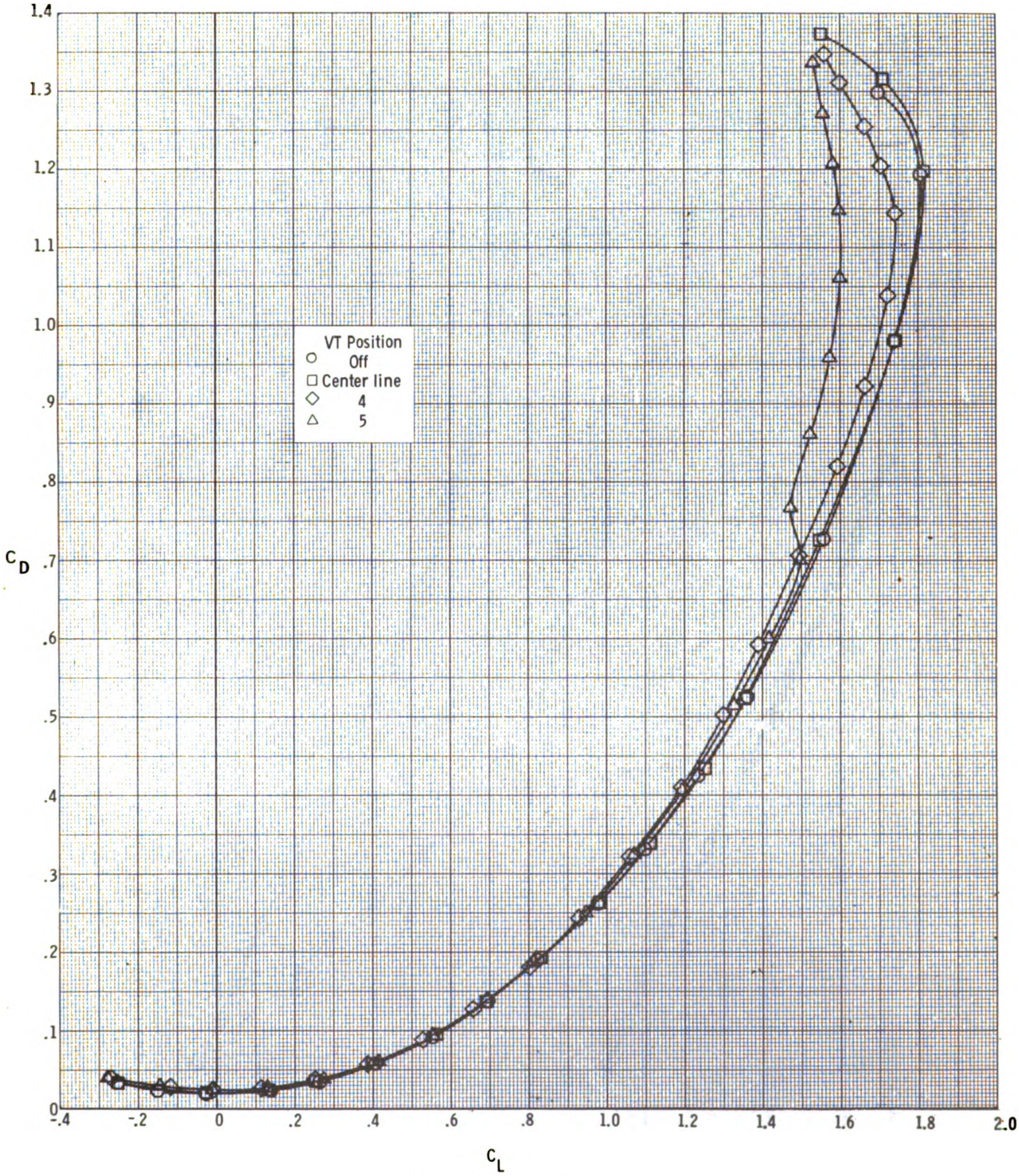

(a) Concluded.

Figure 7.- Continued.

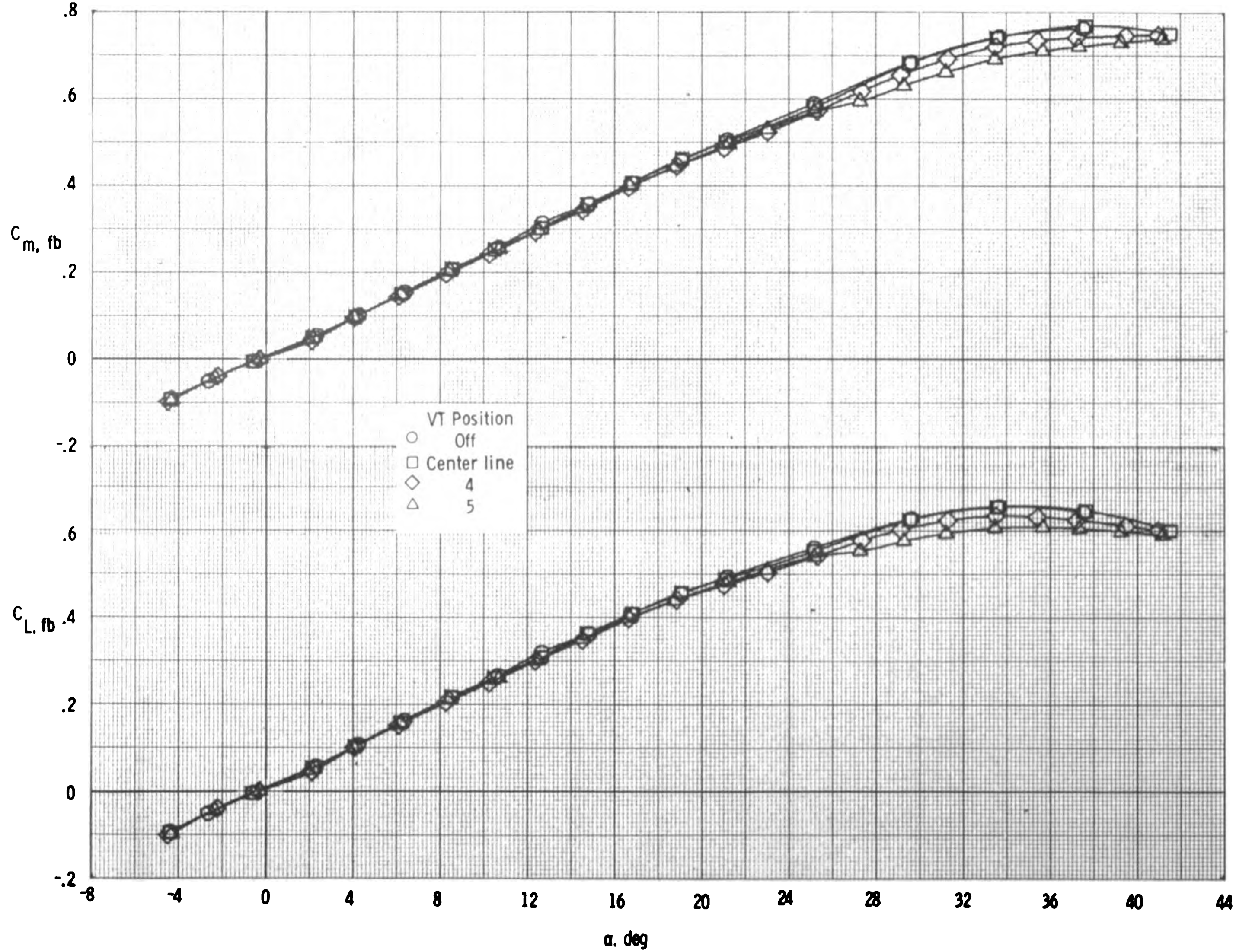

(b) Forward fuselage longitudinal characteristics.

Figure 7.- Concluded

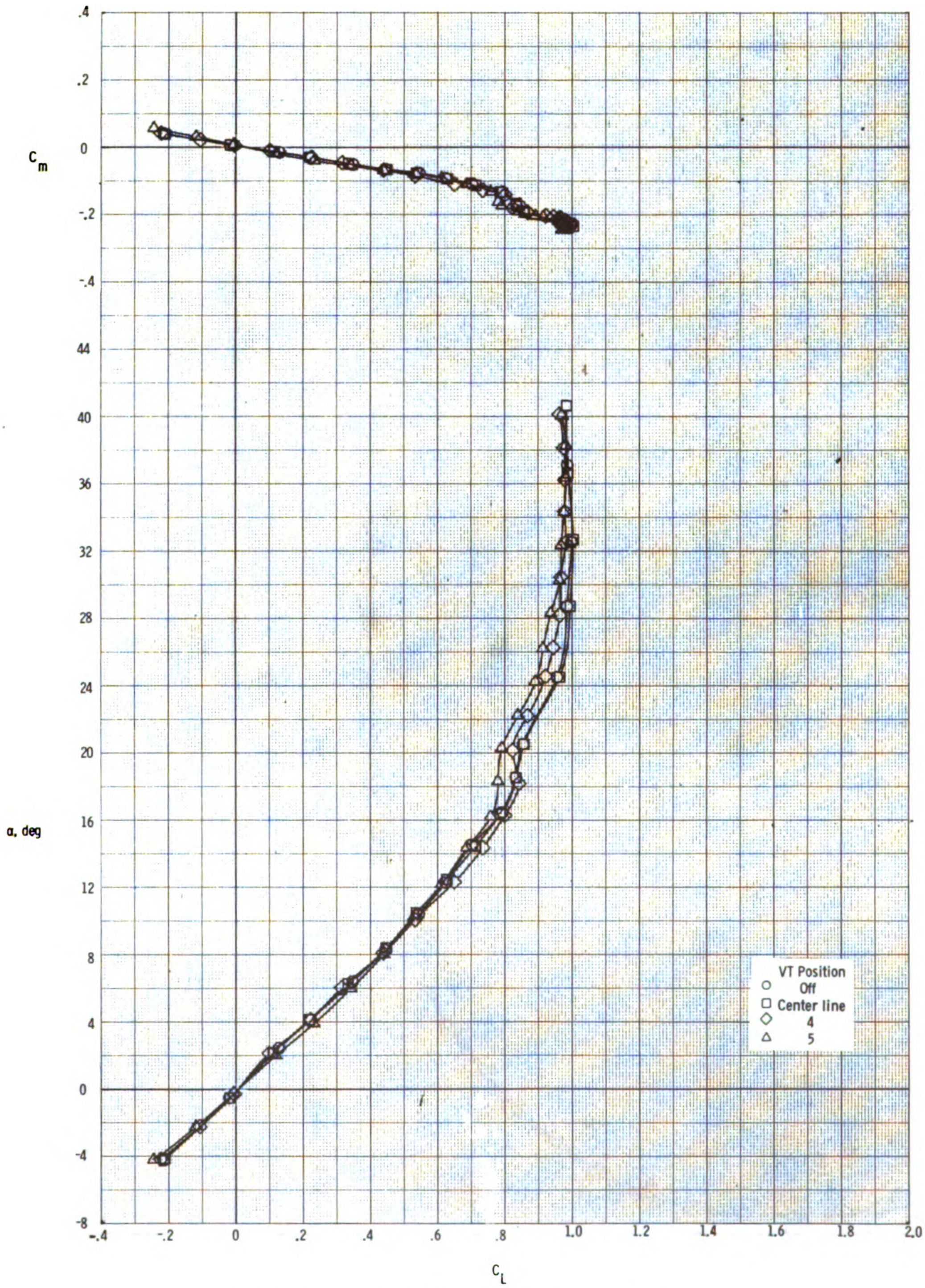

(a) Total longitudinal characteristics.

Figure 8.- Longitudinal aerodynamic characteristics of the wing-body configuration with center-line vertical tail or wing-mounted vertical tails at locations 4 and 5.

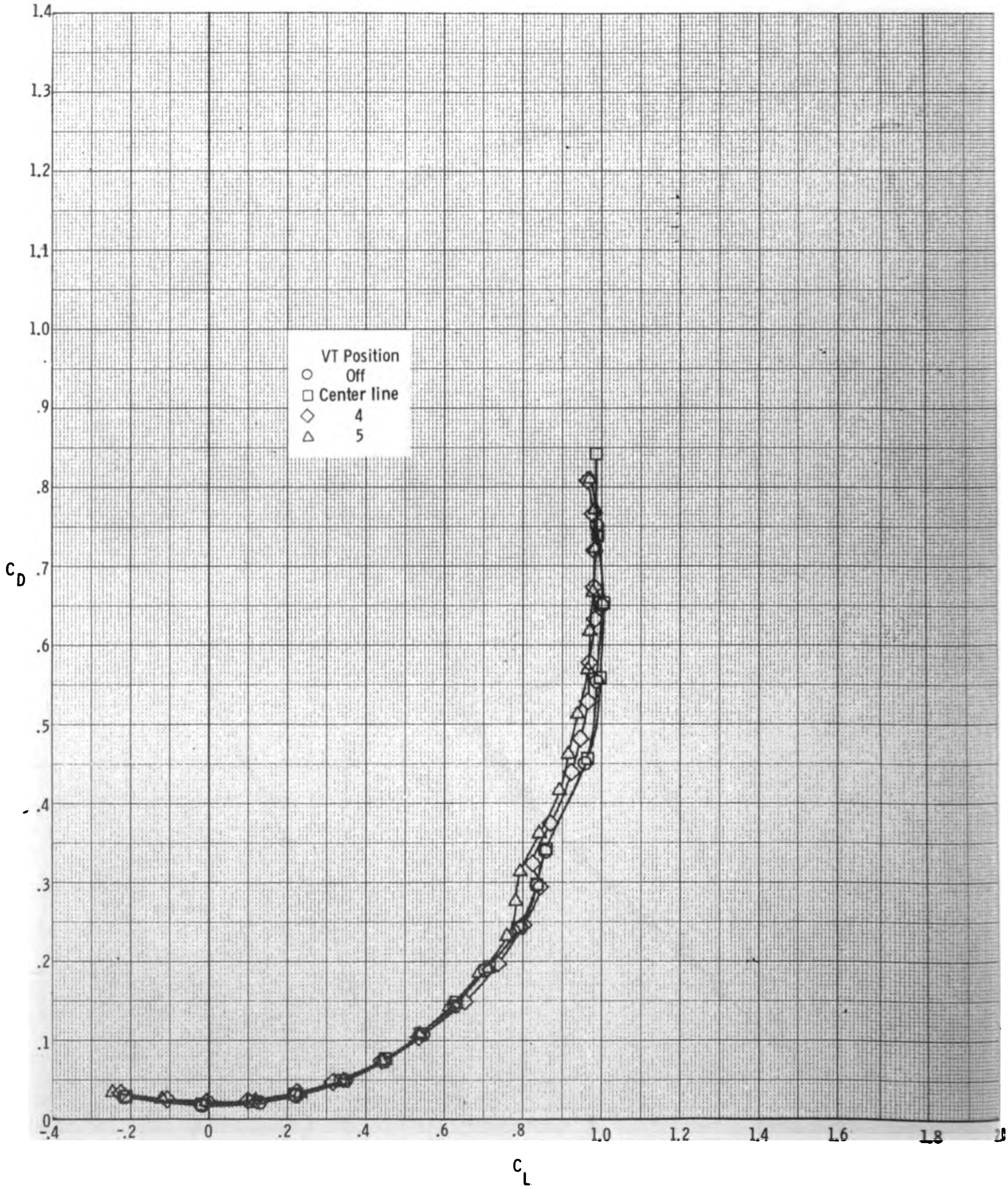

(a) Concluded.

Figure 8.- Continued.

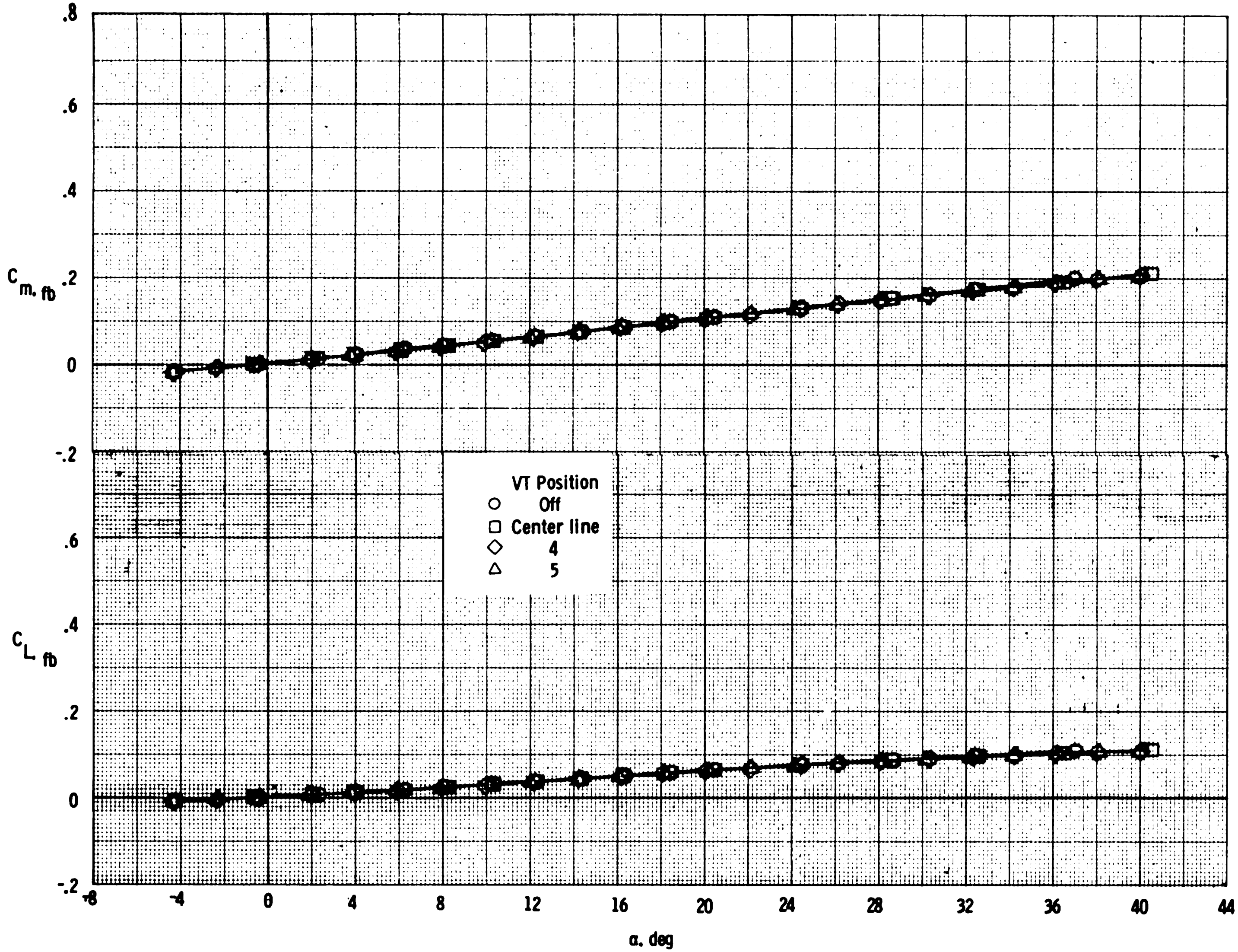

(b) Forward fuselage longitudinal characteristics.

Figure 8.- Concluded.

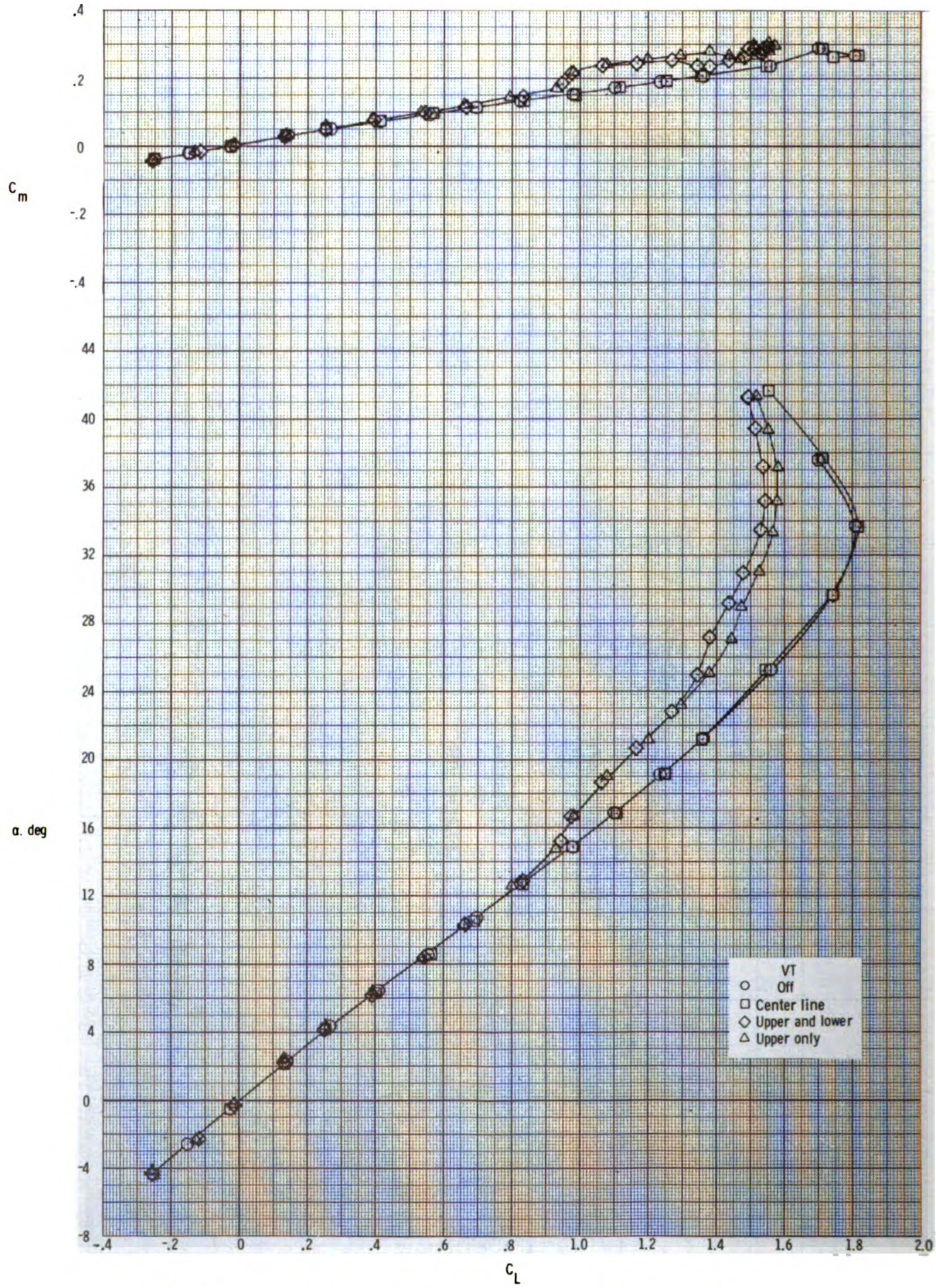

(a) Total longitudinal aerodynamic characteristics.

Figure 9.- Comparison of longitudinal aerodynamic characteristics of wing-body-canard configuration with center-line vertical tail or wing-mounted vertical tails with lower surface vertical tail on and off at location 3.

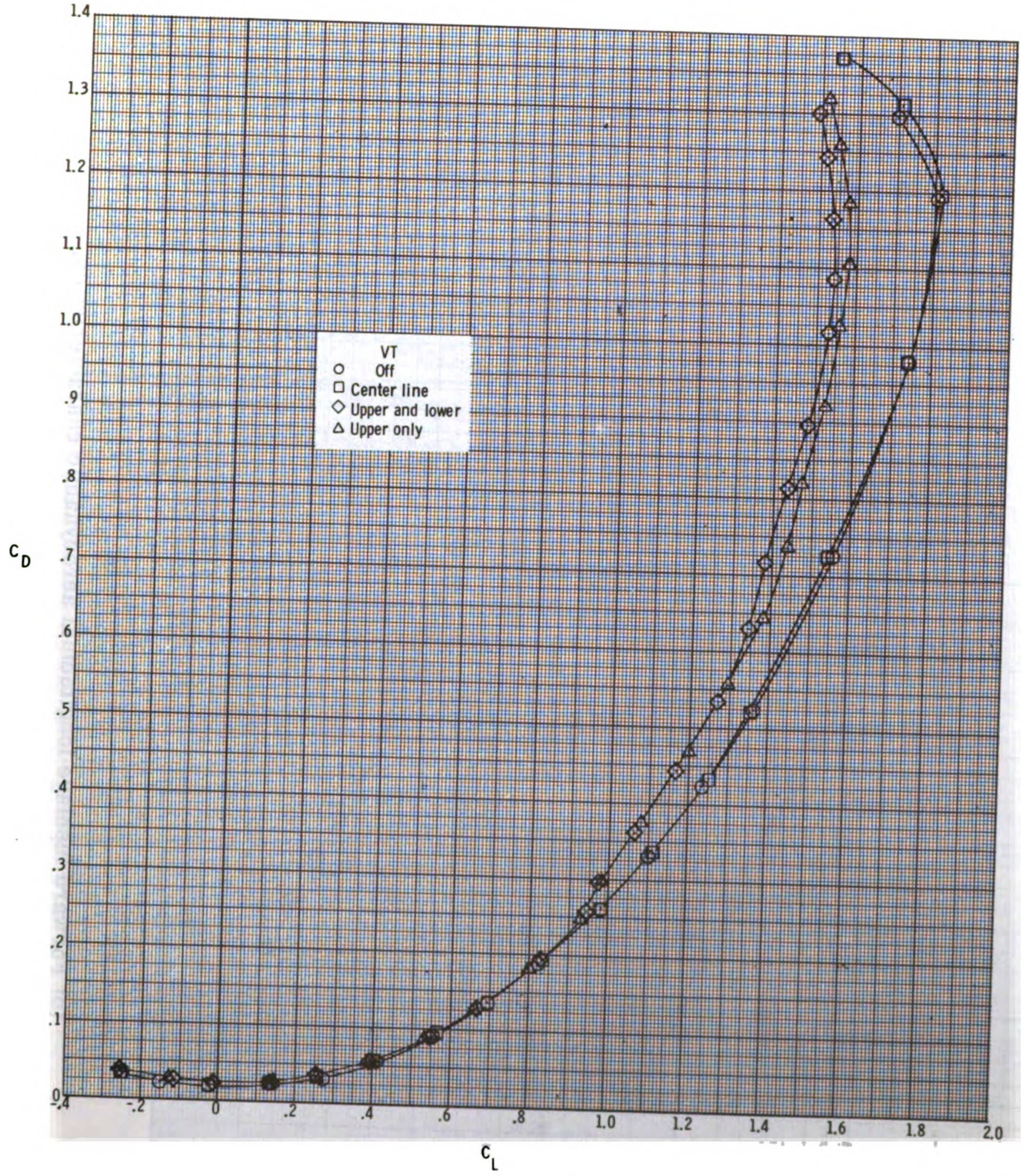

(a) Concluded.

Figure 9.- Continued.

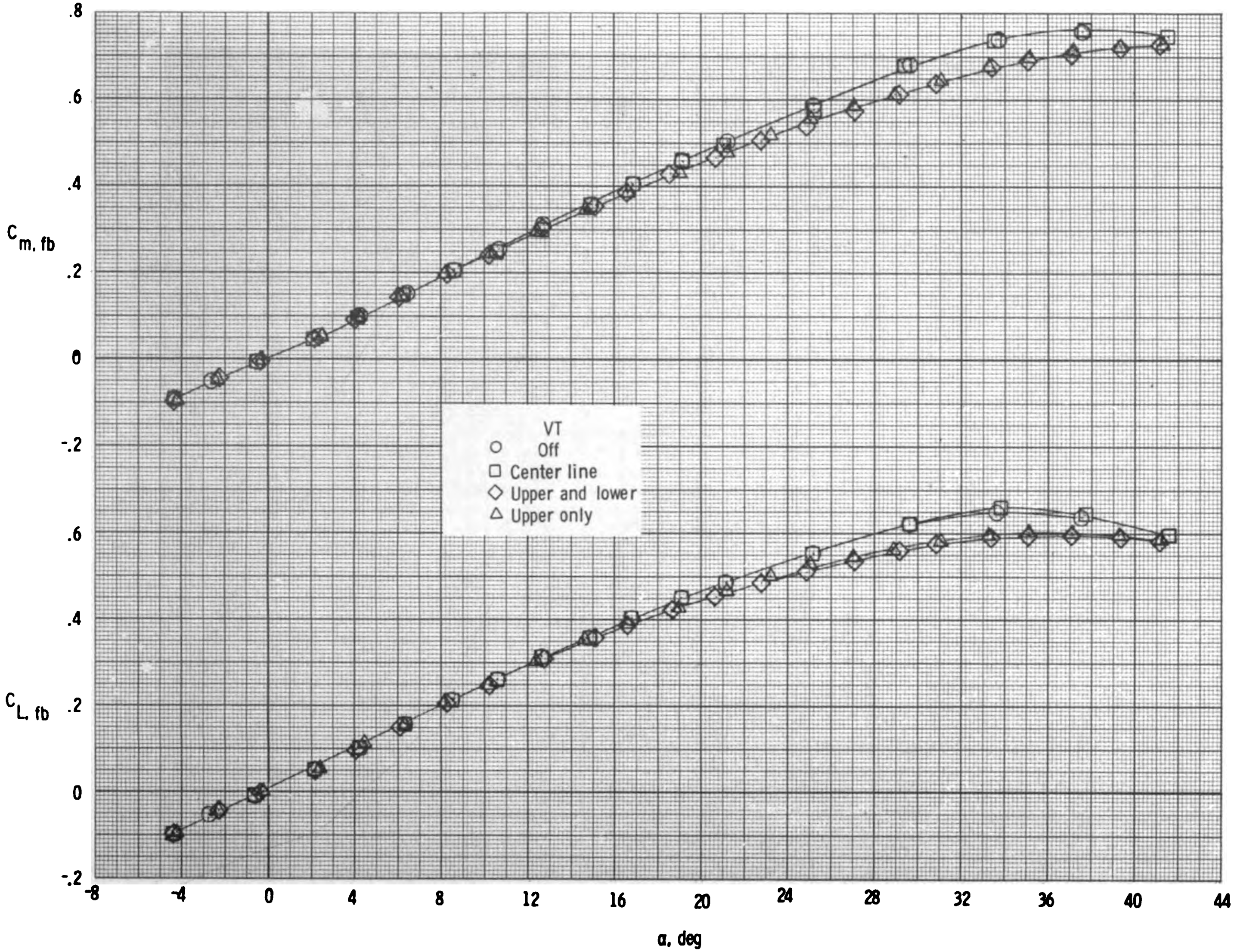

(b) Forward fuselage longitudinal aerodynamic characteristics.

Figure 9.- Concluded.

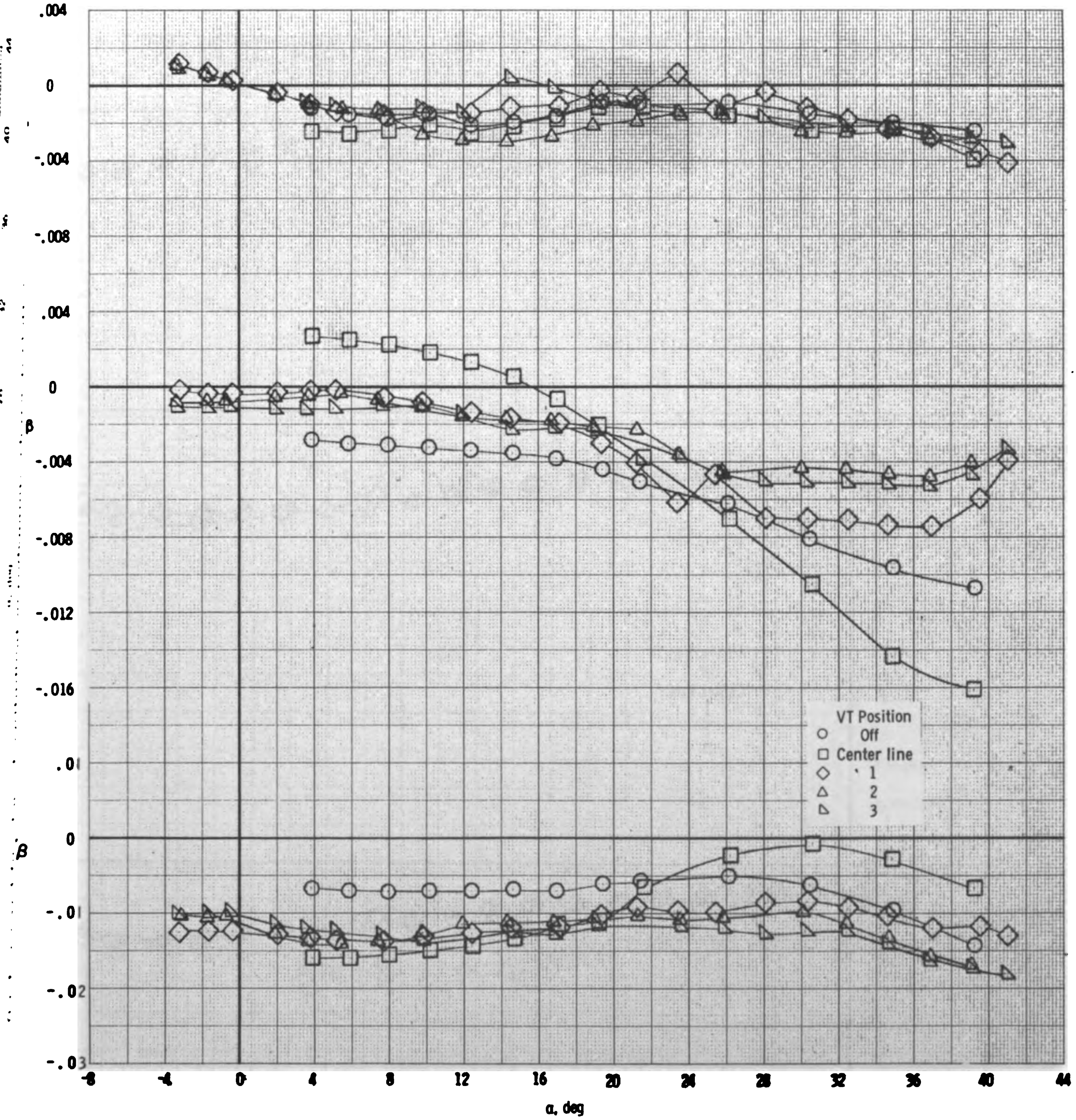

(a) Total derivatives.

Figure 10.- Lateral-directional derivatives for wing-body-canard configuration with center-line vertical tail or wing-mounted vertical tails at locations 1, 2, and 3.

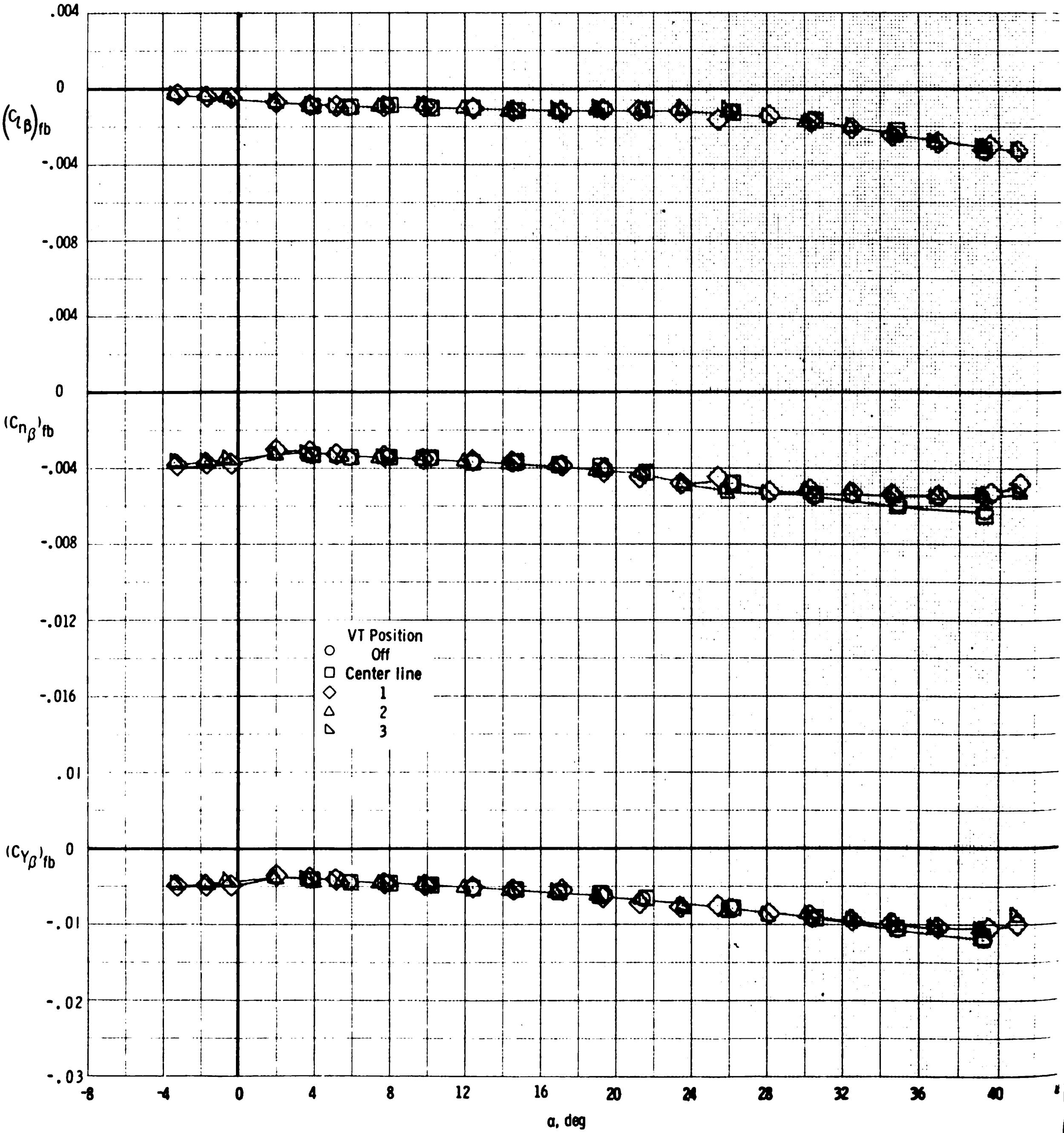

(b) Forward fuselage derivatives.

Figure 10.- Concluded.

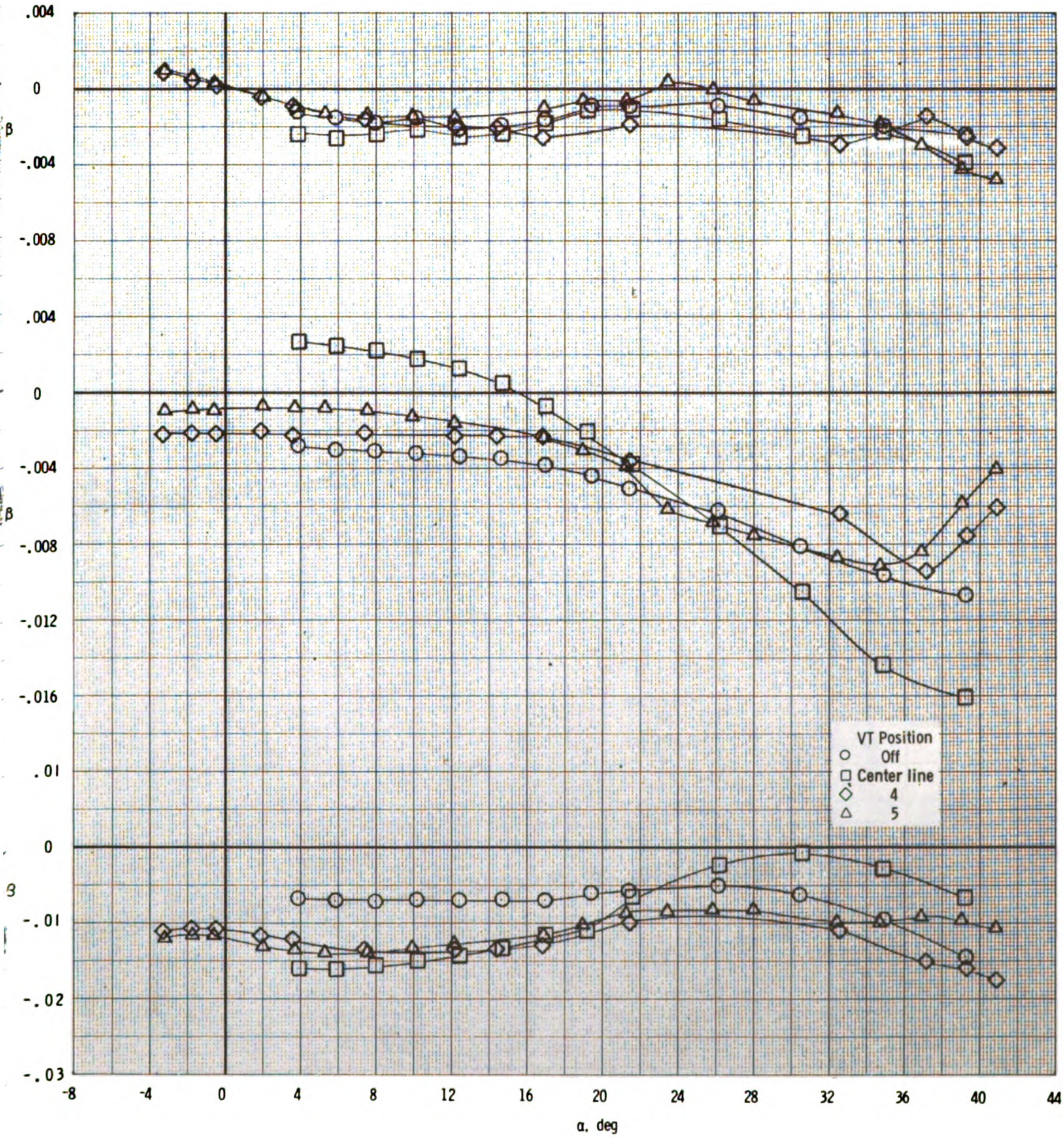

(a) Total derivatives.

igure 11.- Lateral-directional derivatives for wing-body-canard configuration with center-line vertical tail or wing-mounted vertical tails at locations 4 and 5.

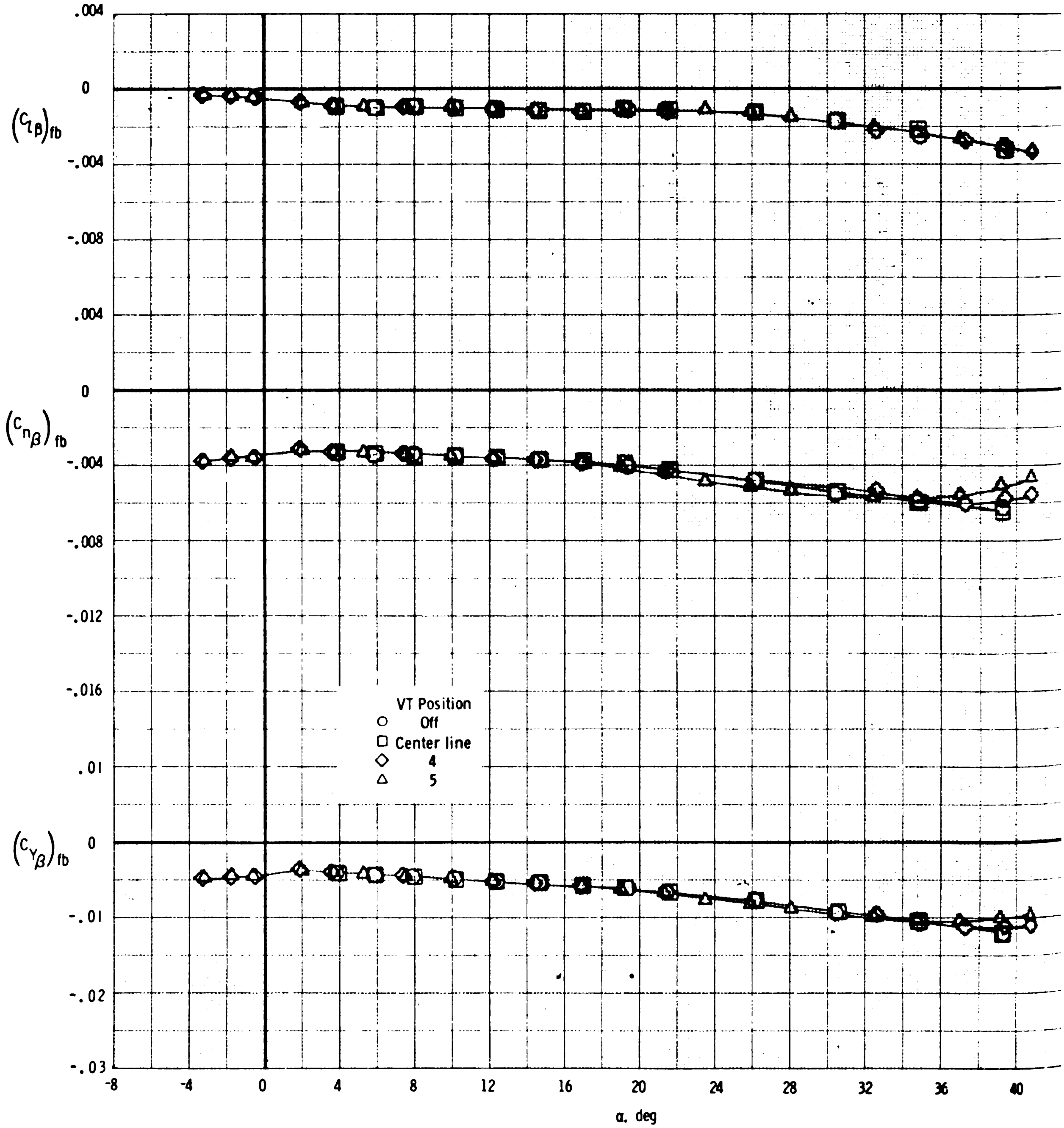

(b) Forward fuselage derivatives.

Figure 11.- Concluded.

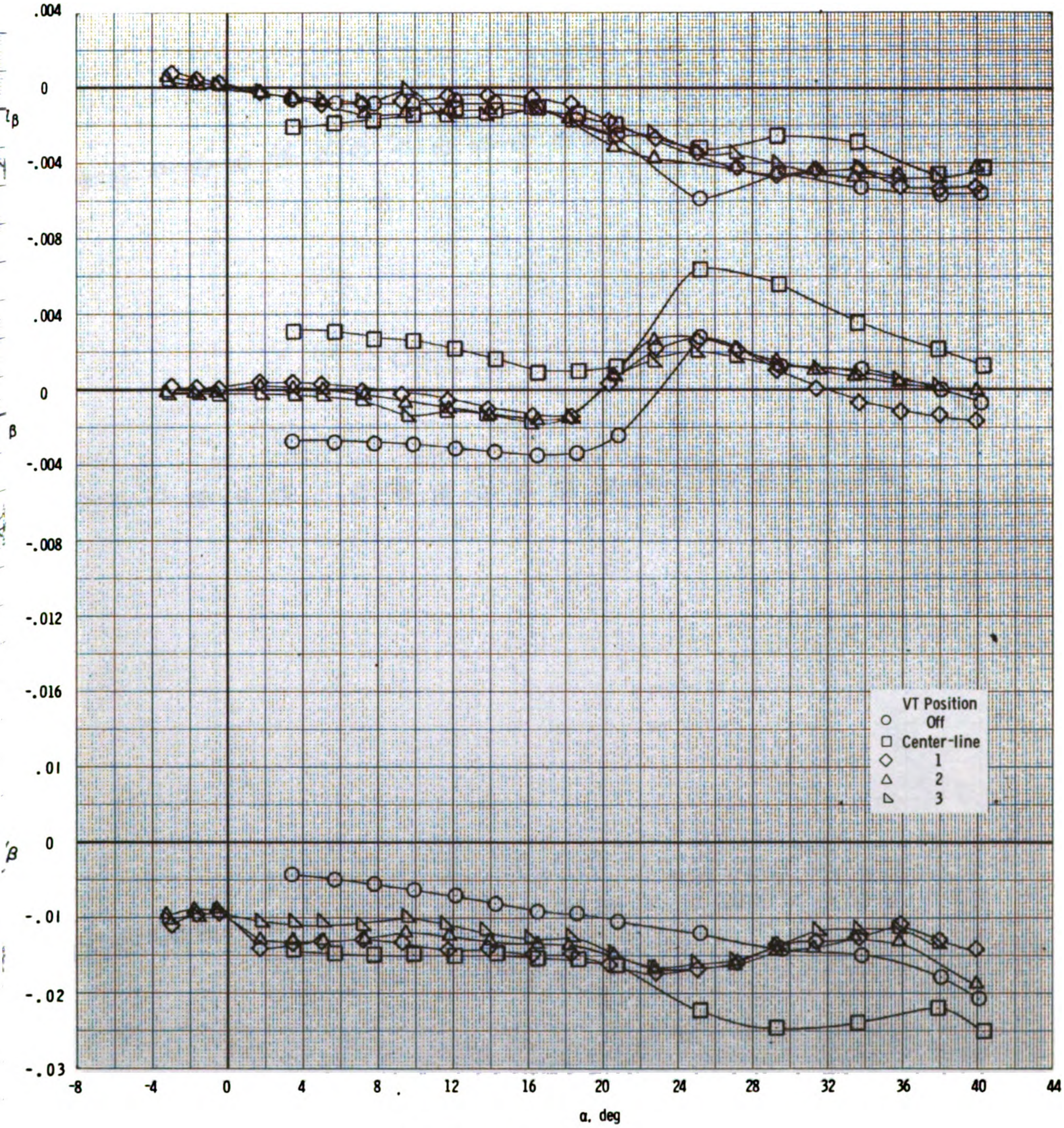

(a) Total derivatives.

Figure 12.- Lateral-directional derivatives for wing-body configuration with center-line vertical tail or wing-mounted vertical tails at locations 1, 2, and 3.

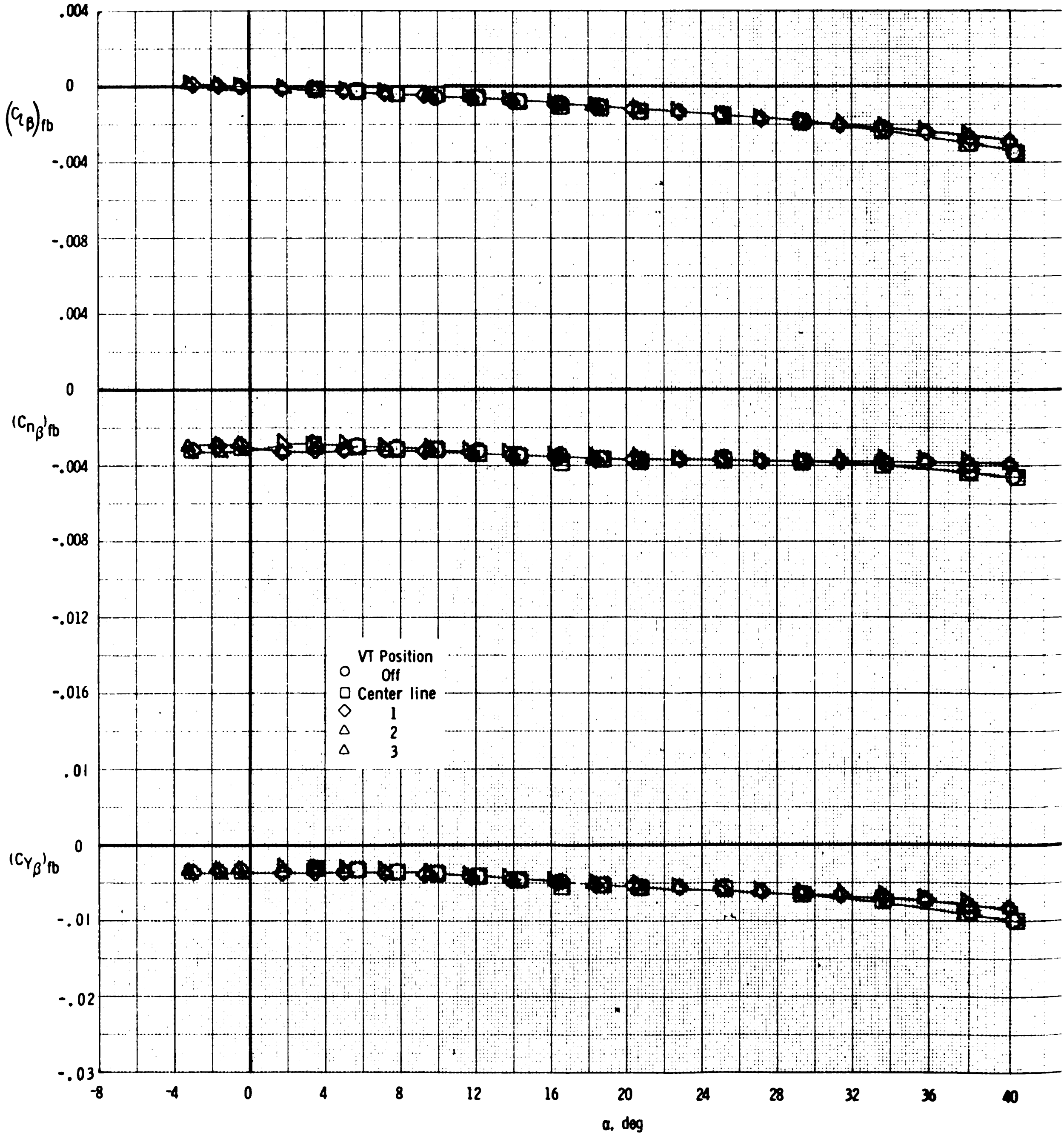

(b) Forward fuselage derivatives.

Figure 12.- Concluded.

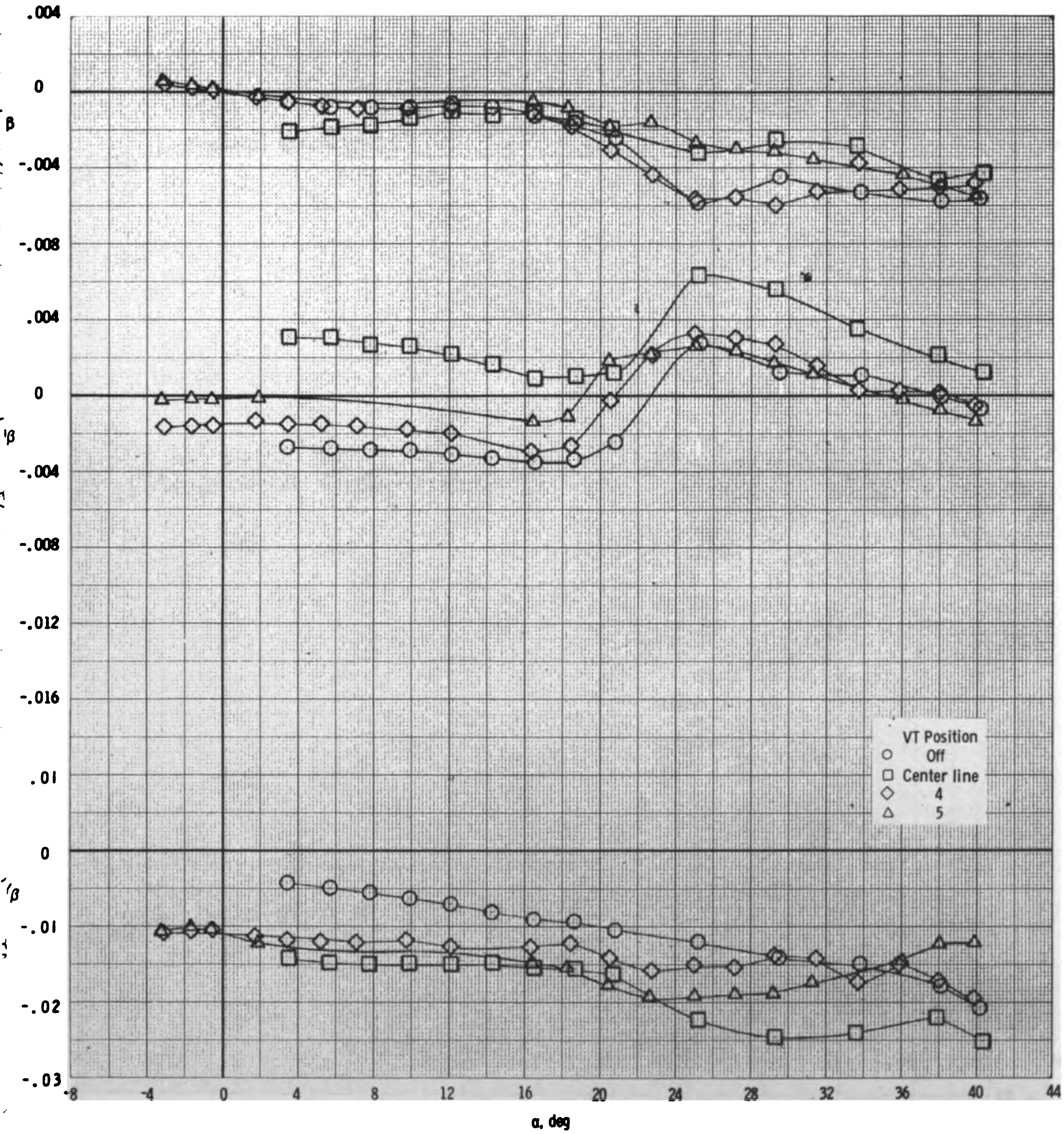

(a) Total derivatives.

Figure 13.- Lateral-directional derivatives for wing-body configuration with center-line vertical tail or wing-mounted vertical tails at locations 4 and 5.

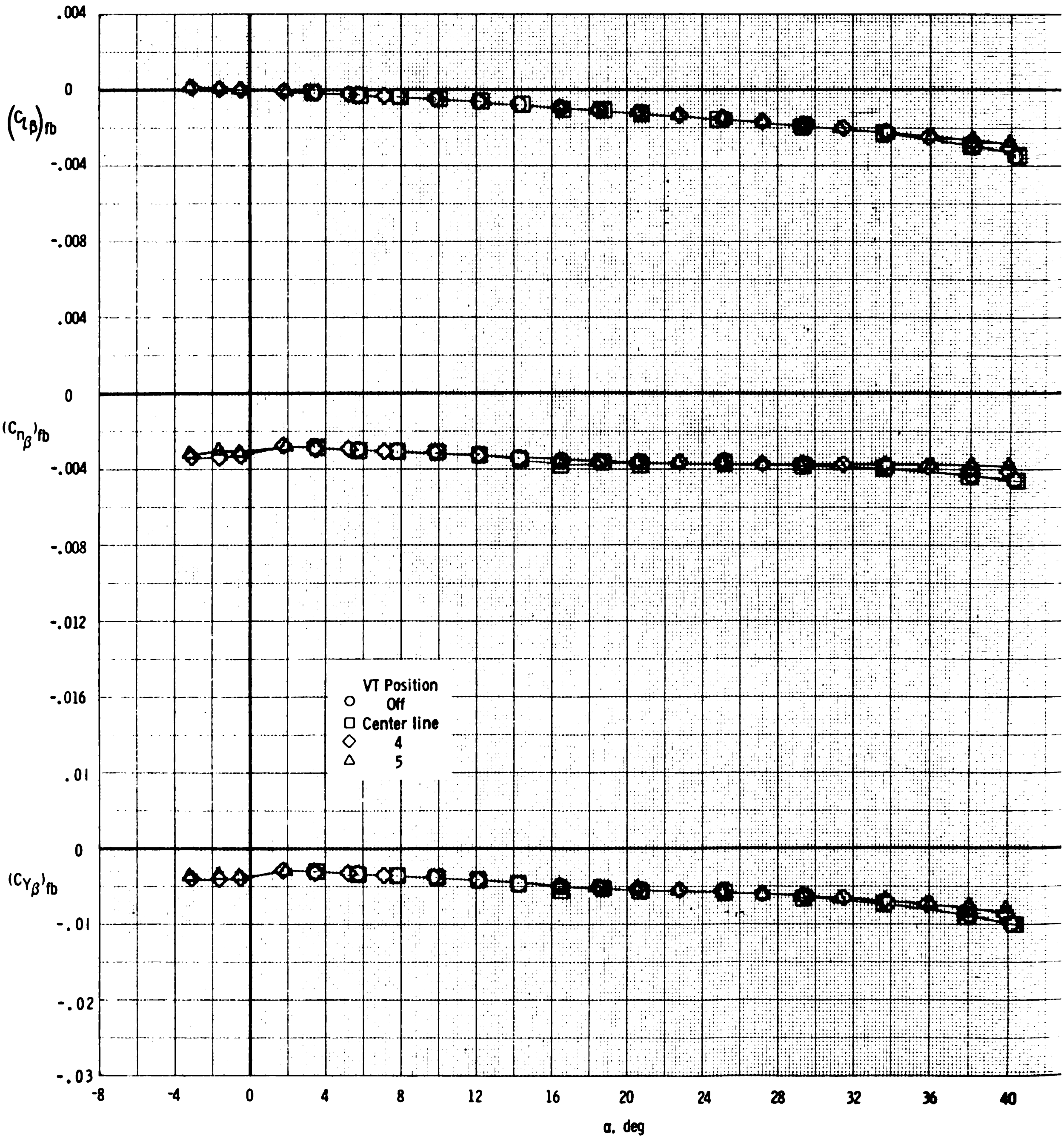

(b) Forward fuselage derivatives.

Figure 13.- Concluded.

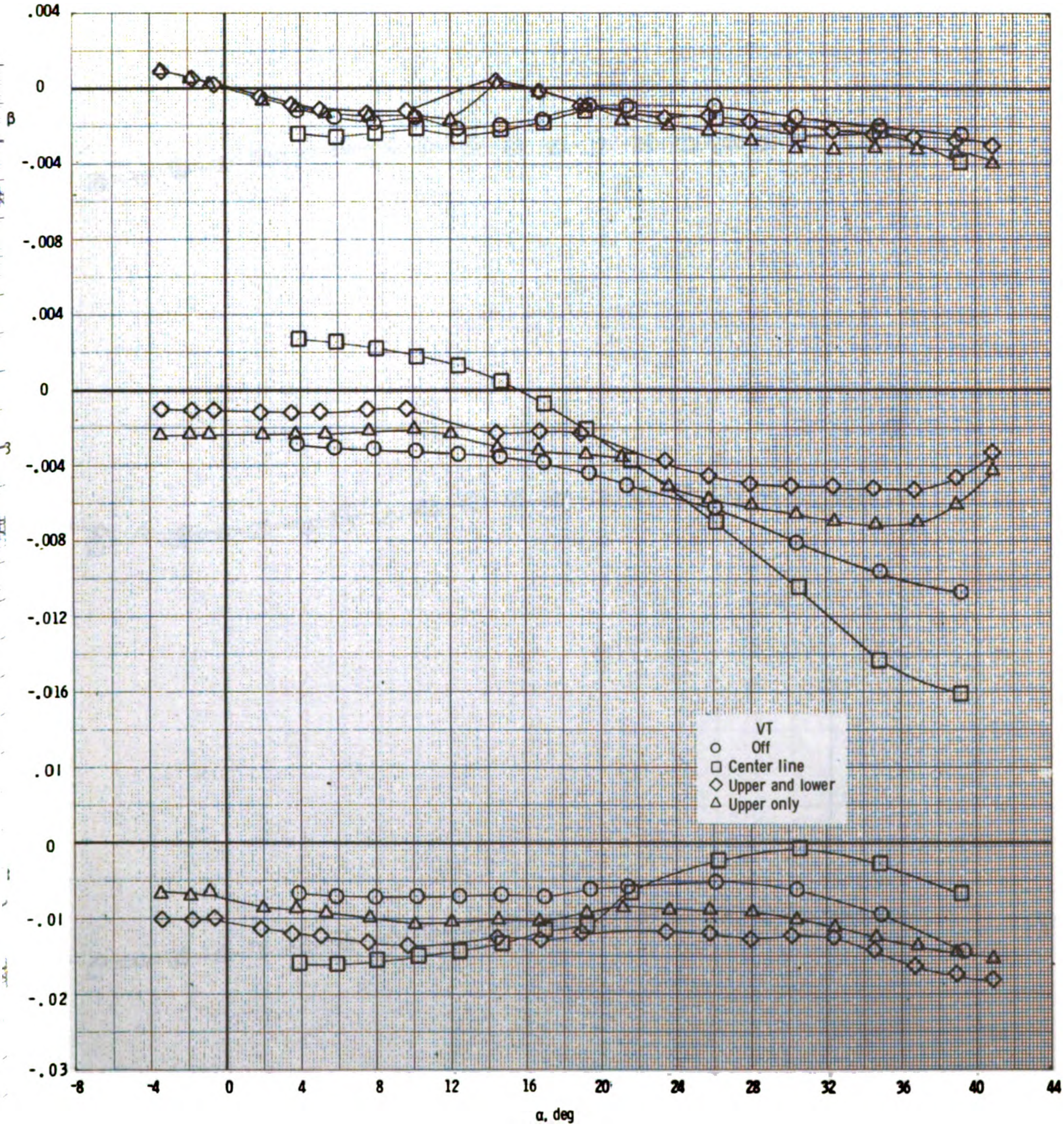

(a) Total derivatives.

igure 14.- Comparison of lateral-directional derivatives of wing-body-canard configuration with center-line vertical tail or wing-mounted vertical tails with the lower surface vertical tail on and off at location 3.

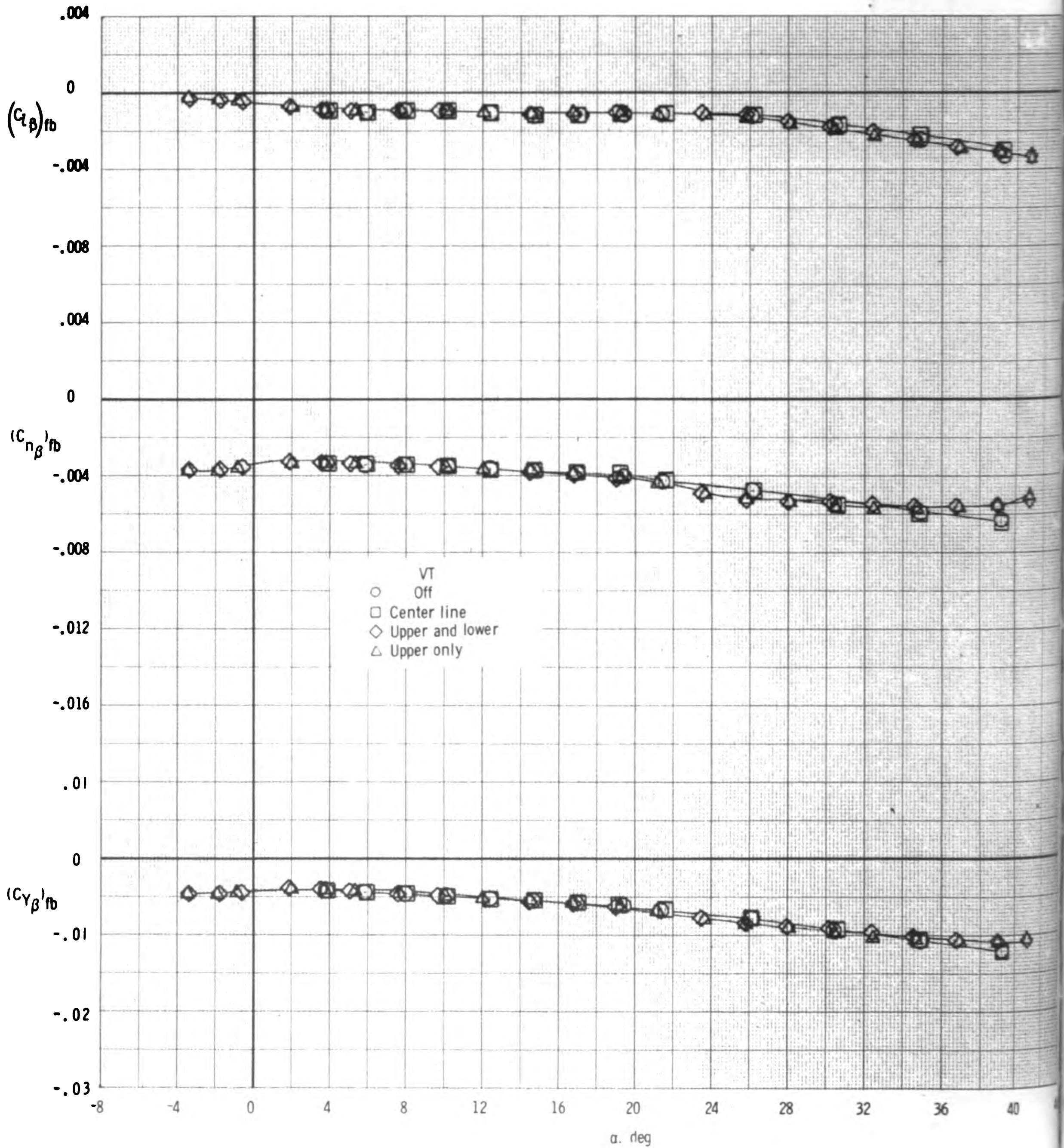

(b) Forward fuselage derivatives.

Figure 14.- Concluded.

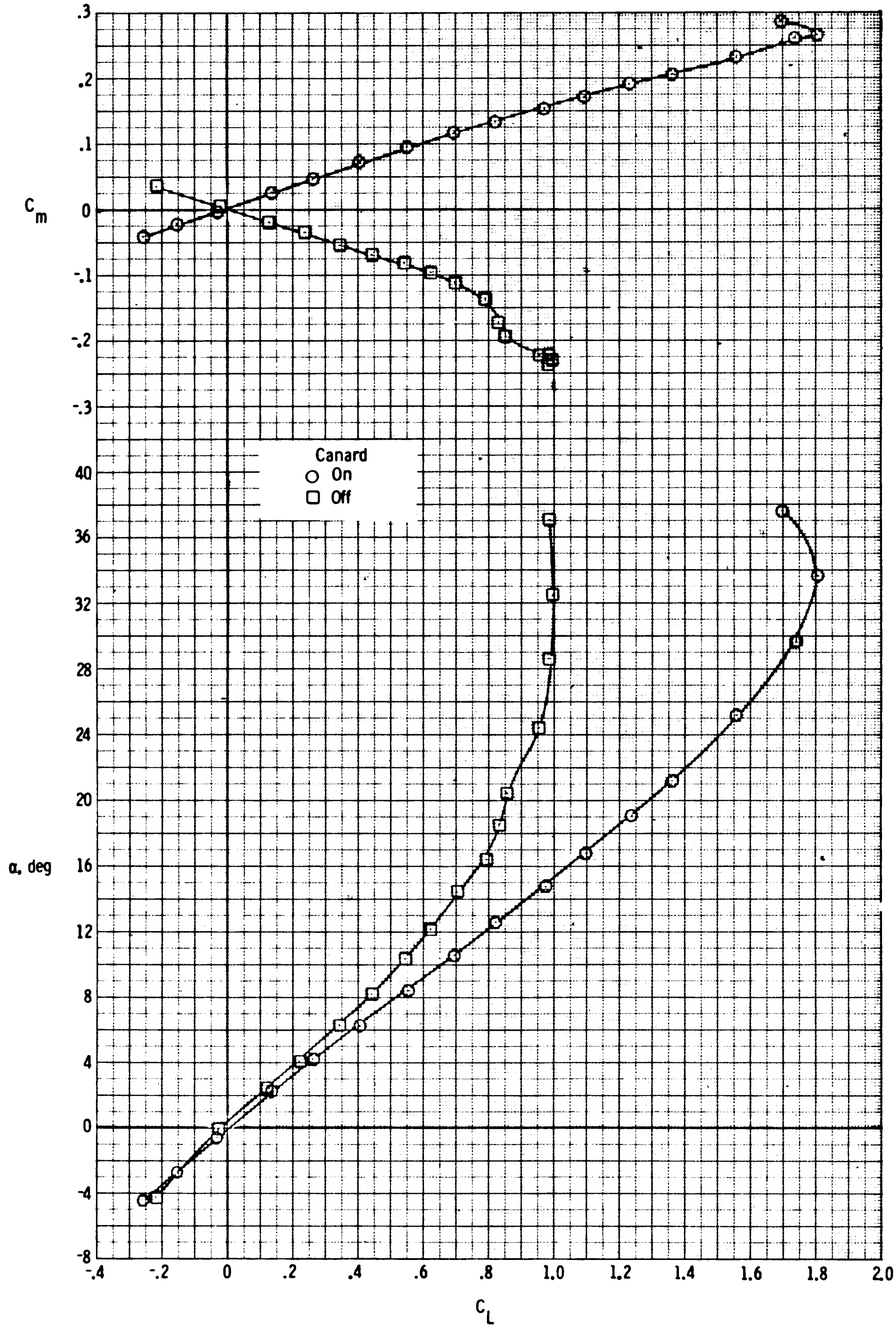

(a) C_m and α plotted against C_L.

igure 15.- Effect of canard on the longitudinal aerodynamic characteristics of the basic model with vertical tail off.

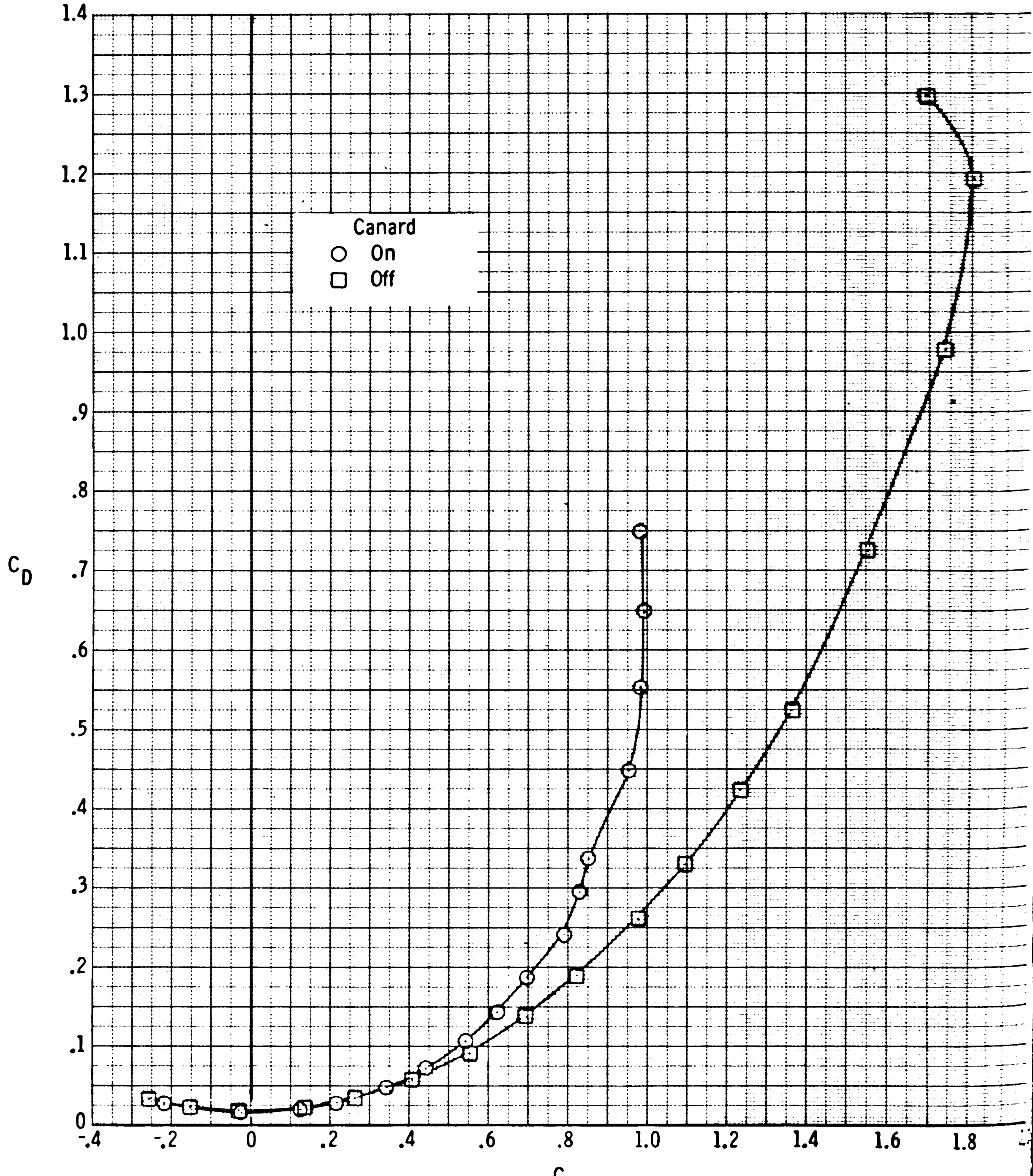

(b) C_D plotted against C_L.

Figure 15.- Continued.

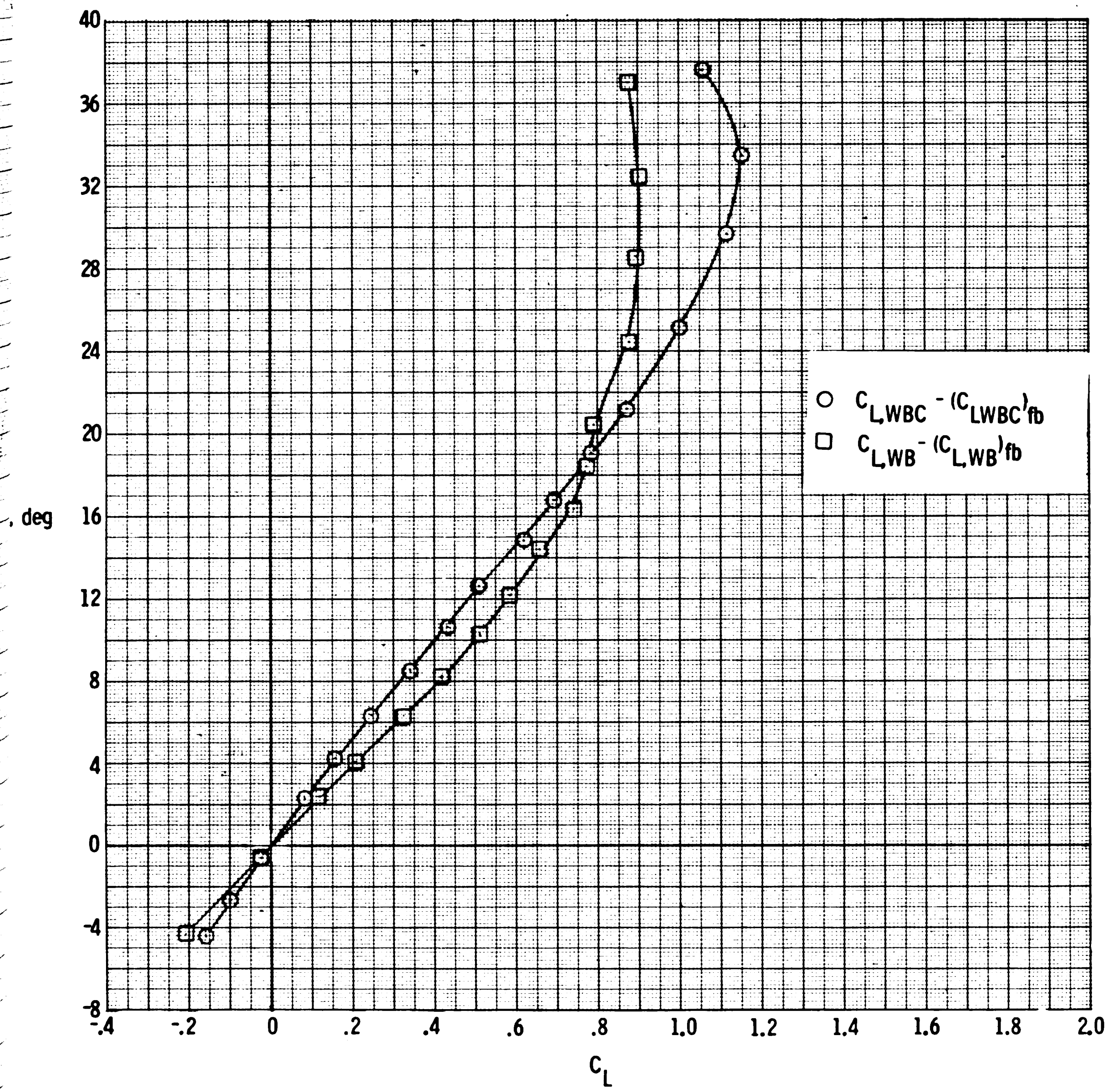

(c) Interference effects of the canard on wing lift.

Figure 15.- Concluded.

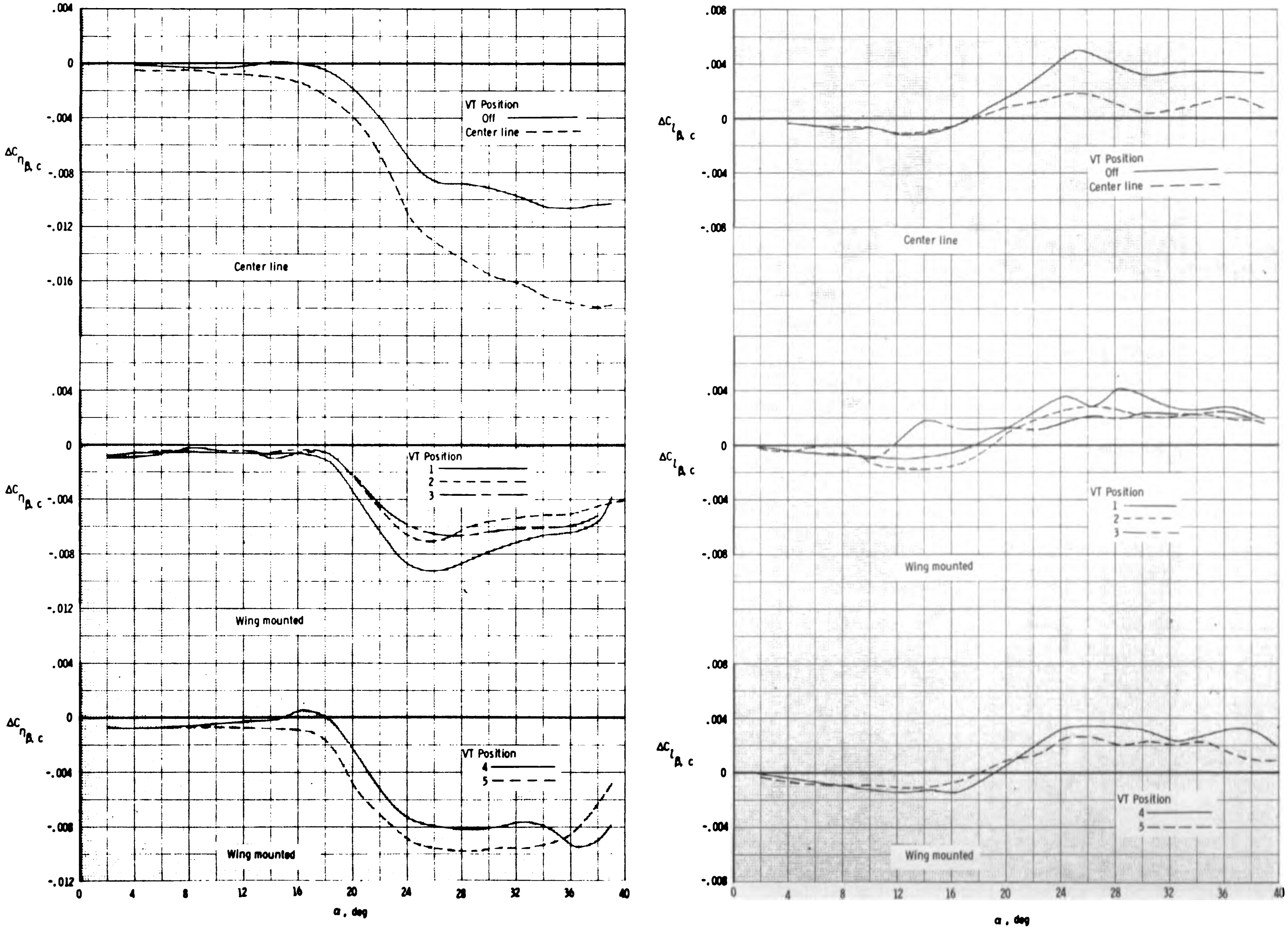

Figure 16.- Interference effects of the canard on lateral-directional derivatives of test models with various vertical-tail configurations.

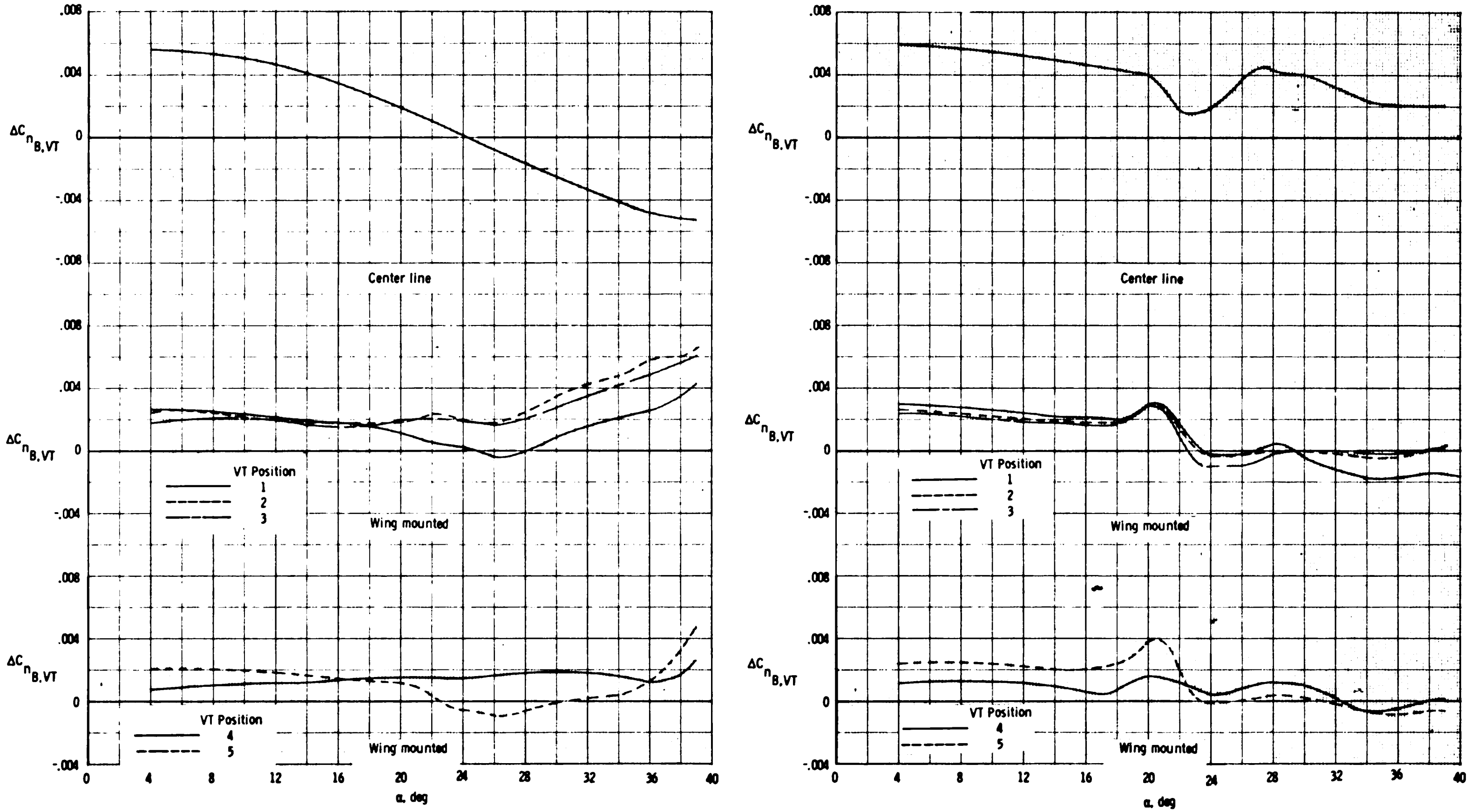

(a) Canard on.

(b) Canard off.

Figure 17.- Vertical-tail effectiveness for the various vertical-tail configurations.

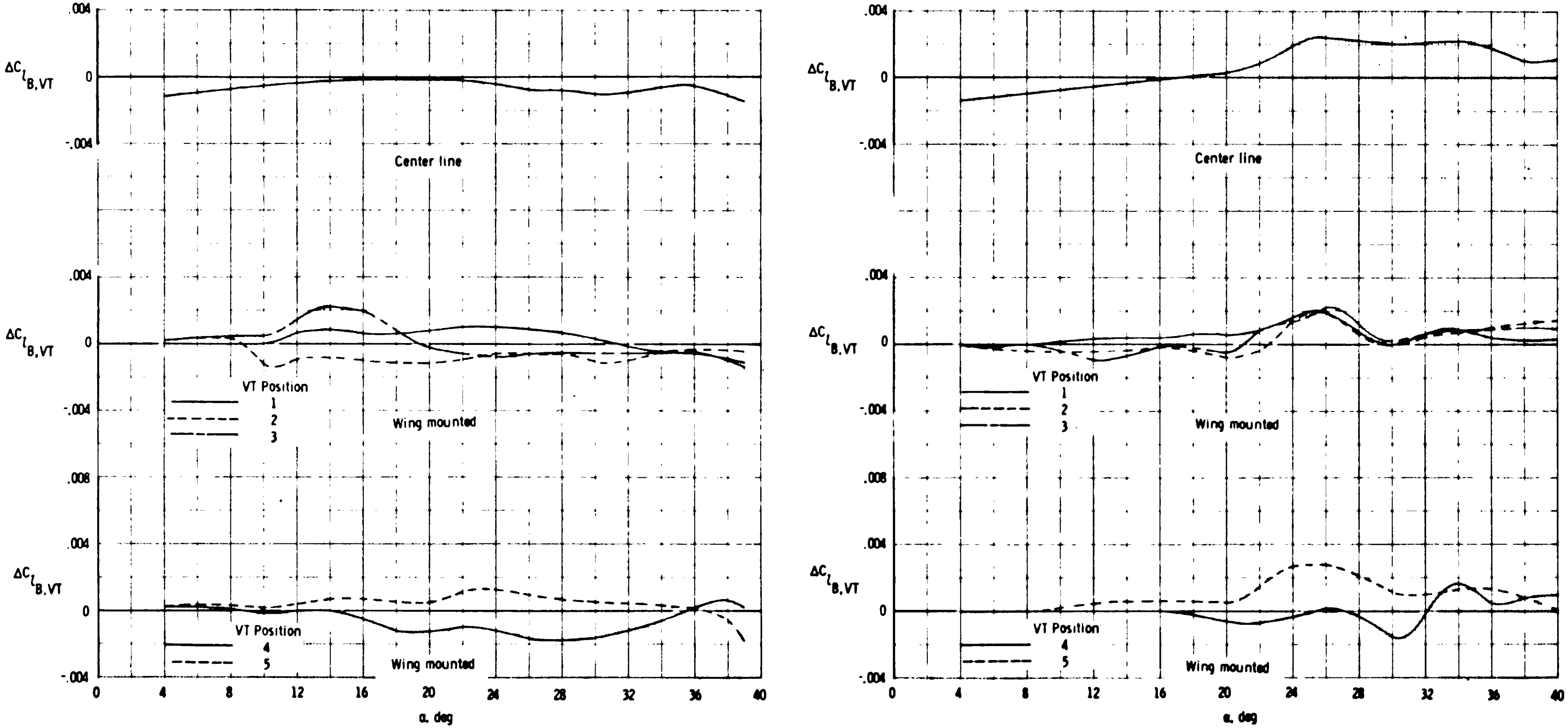

(a) Canard on.

(b) Canard off.

Figure 18.- Effect of the various vertical-tail configurations on the effective dihedral parameter.

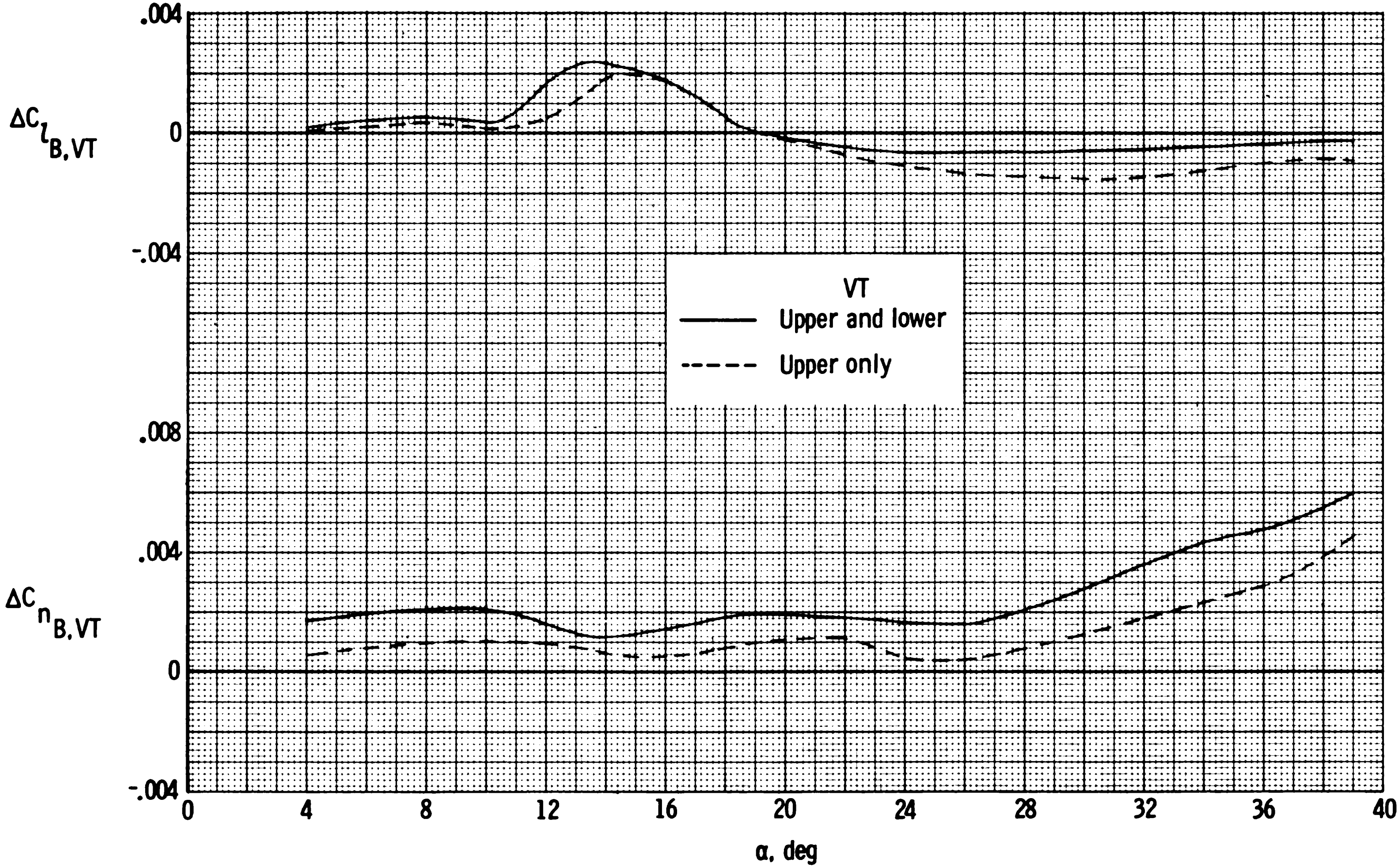

Figure 19.- Vertical-tail effectiveness for the wing-mounted vertical tails at position 3 for the wing-body-canard configuration.

NATIONAL AERONAUTICS AND SPACE ADMINISTRATION
WASHINGTON, D.C. 20546

OFFICIAL BUSINESS
PENALTY FOR PRIVATE USE $300

SPECIAL FOURTH-CLASS RATE
BOOK

POSTAGE AND FEES PAID
NATIONAL AERONAUTICS AND
SPACE ADMINISTRATION
451

U.S.MAIL

756 001 C1 U AL 750718 S00606HU
UNIV OF MICHIGAN
ENGINEERING LIBRARY
ATTN: MR ROBERT T FREESE
ANN ARBOR MI 48104

POSTMASTER: If Undeliverable (Section 1[illegible]
Postal Manual) Do Not R[illegible]

"The aeronautical and space activities of the United States shall be conducted so as to contribute . . . to the expansion of human knowledge of phenomena in the atmosphere and space. The Administration shall provide for the widest practicable and appropriate dissemination of information concerning its activities and the results thereof."

—NATIONAL AERONAUTICS AND SPACE ACT OF 1958

NASA SCIENTIFIC AND TECHNICAL PUBLICATIONS

TECHNICAL REPORTS: Scientific and technical information considered important, complete, and a lasting contribution to existing knowledge.

TECHNICAL NOTES: Information less broad in scope but nevertheless of importance as a contribution to existing knowledge.

TECHNICAL MEMORANDUMS: Information receiving limited distribution because of preliminary data, security classification, or other reasons. Also includes conference proceedings with either limited or unlimited distribution.

CONTRACTOR REPORTS: Scientific and technical information generated under a NASA contract or grant and considered an important contribution to existing knowledge.

TECHNICAL TRANSLATIONS: Information published in a foreign language considered to merit NASA distribution in English.

SPECIAL PUBLICATIONS: Information derived from or of value to NASA activities. Publications include final reports of major projects, monographs, data compilations, handbooks, sourcebooks, and special bibliographies.

TECHNOLOGY UTILIZATION PUBLICATIONS: Information on technology used by NASA that may be of particular interest in commercial and other non-aerospace applications. Publications include Tech Briefs, Technology Utilization Reports and Technology Surveys.

Details on the availability of these publications may be obtained from:

SCIENTIFIC AND TECHNICAL INFORMATION OFFICE

NATIONAL AERONAUTICS AND SPACE ADMINISTRATION

Washington, D.C. 20546

-7948

NASA TECHNICAL NOTE

NASA TN D-7948

NASA TN D-7948

SPACECRAFT HIGH-VOLTAGE POWER SUPPLY CONSTRUCTION

John F. Sutton and Jesse E. Stern

Goddard Space Flight Center
Greenbelt, Md. 20771

NATIONAL AERONAUTICS AND SPACE ADMINISTRATION • WASHINGTON, D. C. • APRIL 1975

1. Report No.	2. Government Accession No.	3. Recipient's Catalog No.
NASA TN D-7948		

4. Title and Subtitle	5. Report Date April 1975
Spacecraft High-Voltage Power Supply Construction	6. Performing Organization Code 325
7. Author(s) John F. Sutton and Jesse E. Stern	8. Performing Organization Report No. G-7448
9. Performing Organization Name and Address Goddard Space Flight Center Greenbelt, Maryland 20771	10. Work Unit No. 320-039-23-01-01 11. Contract or Grant No.
12. Sponsoring Agency Name and Address National Aeronautics and Space Administration Washington, D.C. 20546	13. Type of Report and Period Covered Technical Note 14. Sponsoring Agency Code

15. Supplementary Notes

16. Abstract

The design techniques, circuit components, fabrication techniques, and past experience which have been used in successful high-voltage power supplies for spacecraft flight systems are described. A discussion of the basic physics of electrical discharges in gases is included and a design rationale for the prevention of electrical discharges is provided. Also included are typical examples of proven spacecraft high-voltage power supplies with typical specifications for design, fabrication, and testing.

17. Key Words (Selected by Author(s))	18. Distribution Statement
High-voltage breakdown, Electrical discharge, Corona, High-voltage power supply, Gas discharge	Unclassified–Unlimited Cat 33

19. Security Classif. (of this report)	20. Security Classif. (of this page)	21. No. of Pages	22. Price*
Unclassified	Unlimited	161	$6.25

*For sale by the National Technical Information Service, Springfield, Virginia 22151.

The requirement for the use of the International System of Units (SI) has been waived for this document under the authority of NPD 2220.4, paragraph 5.d.

PREFACE

Studies have shown that voltage breakdown is a recurring problem in high-voltage spacecraft systems and that about 75 percent of the breakdown problems are attributable to faulty design of the high-voltage power systems. The major reason for the recurrence of high-voltage power breakdown problems is the lack of documentation describing those special design and fabrication techniques which have yielded successful flight high-voltage power supply hardware.

The information contained in this document has been gathered from many sources in the aerospace industry and in the Government. It includes the fundamentals of voltage breakdown, specific information on materials, components, parts selection, processing, encapsulation and conformal coating, stresses on parts, outgassing, venting, and mechanical arrangement. Typical examples of successful high-voltage power supplies are included.

J. F. Sutton
J. E. Stern

CONTENTS

SPACECRAFT HIGH-VOLTAGE POWER SUPPLY CONSTRUCTION

John F. Sutton and Jesse E. Stern
Goddard Space Flight Center

INTRODUCTION

Breakdowns associated with spacecraft high-voltage power supplies are a recurrent problem. Because three out of four breakdowns can be attributed to faulty design (Reference 1), a collection of design data parameters for high-voltage power supplies should prove useful to experimenters. This document includes design aids and listings of some material properties. Although this collection of data is not comprehensive, it is representative of the types of problems that are frequently encountered.

A brief description of breakdown fundamentals is presented to serve as a basis for the parameters and problems explored. Also presented are details of design experience associated with encapsulation techniques (a promising new encapsulation technique is briefly discussed) the depressurization and outgassing of unpotted power supplies; and problems experienced with individual electronic components.

In order for designers to benefit from past experience in equipment designed for use in the severe space environment, current design practices and several successful high-voltage power supplies are described. These incorporate several techniques for solving the breakdown problem and may aid in new designs.

The appendixes include three documents which provide examples of careful attention to detail given during the design, fabrication, and testing of power supplies. They are JPL Des. Req. DM505139 A, GSFC Specification 31187B "Helios A & B Missions Detector Bias Supplies and Low Voltage Power Supplies for Experiment," and "Specifications for Photomultiplier Tube Power Converter PS-13A," a GSFC internal specification (Trainor). Successful high-voltage power supplies have been produced and flown in NASA spacecraft using these design requirements and specifications.

It is hoped that the data and suggestions included here will prove helpful to new spacecraft experiment design groups. Suggestions, comments, and new data will be welcomed by the authors.

BREAKDOWN FUNDAMENTALS OF GASES

Changes in gas insulation properties resulting from electric field variations, pressurization and surface effect of electrodes, and solid dielectric failures are fundamental contributors to high-voltage breakdown. This section provides some basic theory and experimental results applicable to spacecraft high voltage systems.

GASES-THEORY

A gas progresses from an almost perfect insulator to a semiconductor and finally to a conductor, when a uniform electric field of increasing intensity is applied. This progression is illustrated in Figure 1. (For a detailed study of electrical breakdown in gases see Reference 2.)

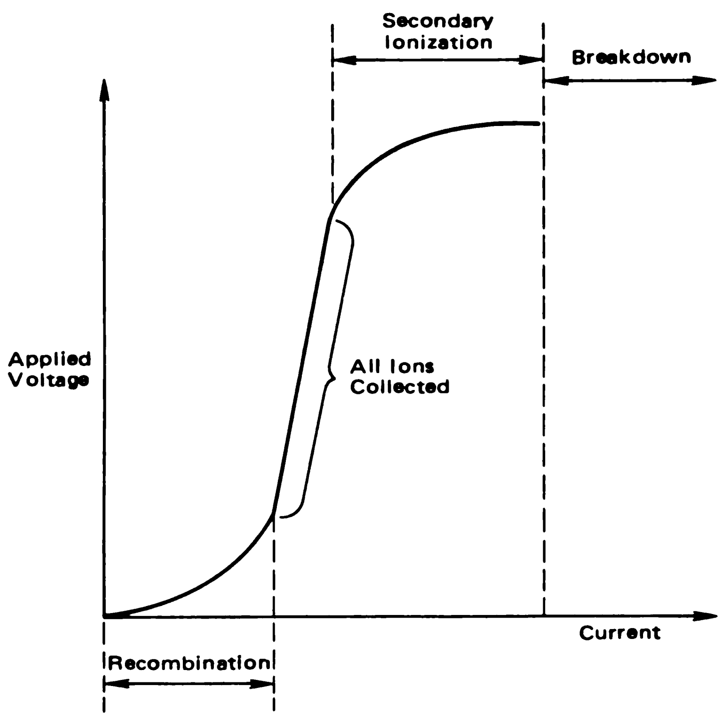

Figure 1. Voltage-Current Characteristic for a Gas in a Uniform Electric Field.

The first region of interest in Figure 1 is labeled Recombination. In this region, electrons released from a cathode by background radiation, for example, cosmic rays, tend to return to the cathode by back diffusion and because of the space charge field. At a higher applied field intensity, these effects are largely overcome so that essentially all of the ions and electrons are collected by the electrodes. In the Secondary Ionization region, N_0 initiating electrons each cause α ionizations per unit distance traveled in the field direction resulting in a rate of release of new electrons of

$$dN = N_0 \alpha dx$$

from which is derived the number of electrons that reach the anode at a distance d. That is,

$$N = N_0 e^{\alpha d}$$

The next region, Breakdown, exhibits a rapidly increasing current due to the production of additional electrons at the cathode. These electrons are generated principally by positive ion bombardment. The effect of this secondary emission due to positive ion bombardment may be understood by following the sequence of events illustrated in Figure 2. (This discussion follows that given in Reference 3.)

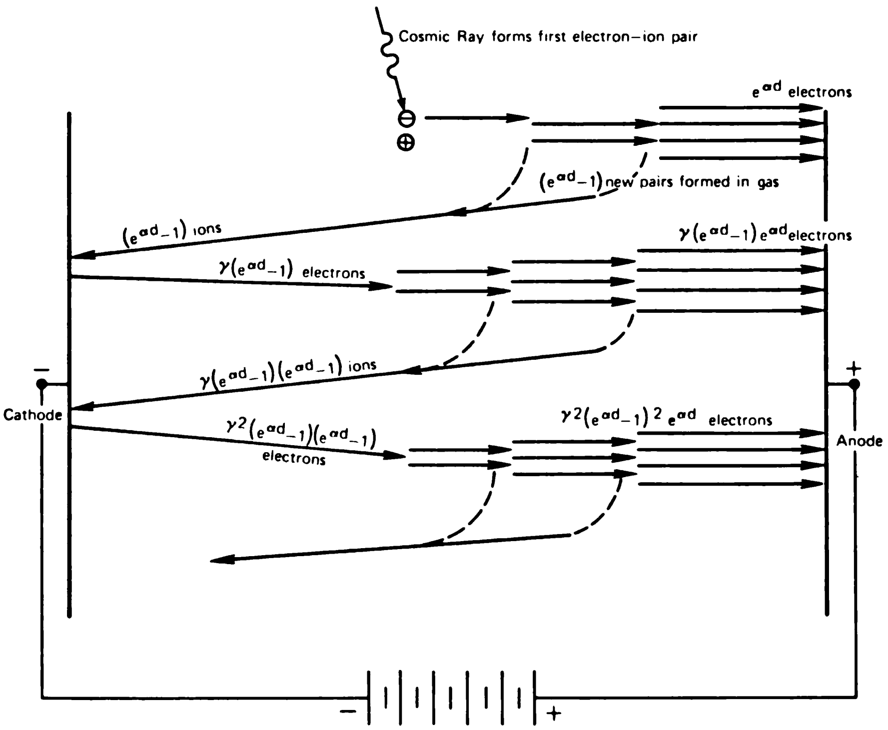

Figure 2. Derivation of Townsend's Breakdown Criterion.

A cosmic ray releases an electron which causes an avalanche resulting in $e^{\alpha d}$ electrons being collected by the anode; that is, $(e^{\alpha d}-1)$ new ions are formed in the gas and are collected at the cathode. A fractional number, γ, of electrons is released at the cathode by each of these ions and results in anode secondary emission of $\gamma (e^{\alpha d}-1)$ electrons. Each of these electrons causes an avalanche, so $\gamma (e^{\alpha d}-1) e^{\alpha d}$ new electrons travel to the anode. This process repeats so that N_0 initial cosmic-ray-produced ion-electron pairs cause a total number, N, of electrons to flow to the anode, where

$$N = N_0 [e^{\alpha d} + \gamma (e^{\alpha d} - 1) e^{\alpha d} + \gamma^2 (e^{\alpha d} - 1)^2 e^{\alpha d} + \ldots]$$

$$= N_0 e^{\alpha d} [1 + \gamma(e^{\alpha d} - 1) + \gamma^2 (e^{\alpha d} - 1)^2 + \ldots]$$

$$\equiv N_0 e^{\alpha d} \frac{1}{[1 - \gamma (e^{\alpha d} - 1)]}$$

N becomes infinite (Townsend sparking criterion) when the denominator is zero. If the number of ion pairs $(e^{\alpha d}-1)$ produced by one original ion is much greater than one, then $(e^{\alpha d}-1) \approx e^{\alpha d}$, and the breakdown condition becomes $\gamma e^{\alpha d}=1$. This criterion is subject to certain limiting factors as noted by von Engel (Reference 4).

GASES-EXPERIMENTAL RESULTS

The above theoretical treatment can be used as a basis for understanding electrical breakdown in gases. Experimentally, Paschen's Law for uniform fields is a useful design tool for avoiding breakdown. Basically, the average amount of kinetic energy an electron gains between collisions depends on the mean free path length, λ, (Figure 3) which is determined by the collision cross section and gas density. The kinetic energy gained between collisions in turn determines the cross section for ionization of a gas molecule. Thus, it is expected that the breakdown potential should be some complex function of density and electrode system geometry. This is indeed the case as illustrated by the Paschen curves of Figure 4 (Reference 5). At high pressures (that is, density), λ is small; therefore, electrons gain too little energy per path to produce ionization. At low pressures there are too few atoms to produce substantial numbers of ions. At pd values of ~1 torr-cm, a gas composition-dependent minimum of ~350 volts occurs. Assuming a 1-cm electrode separation as typical, one can readily see by referring to Figure 5 that sounding rocket or spacecraft instruments which must operate while passing through altitudes of 30 to 65 km are particularly prone to corona problems.

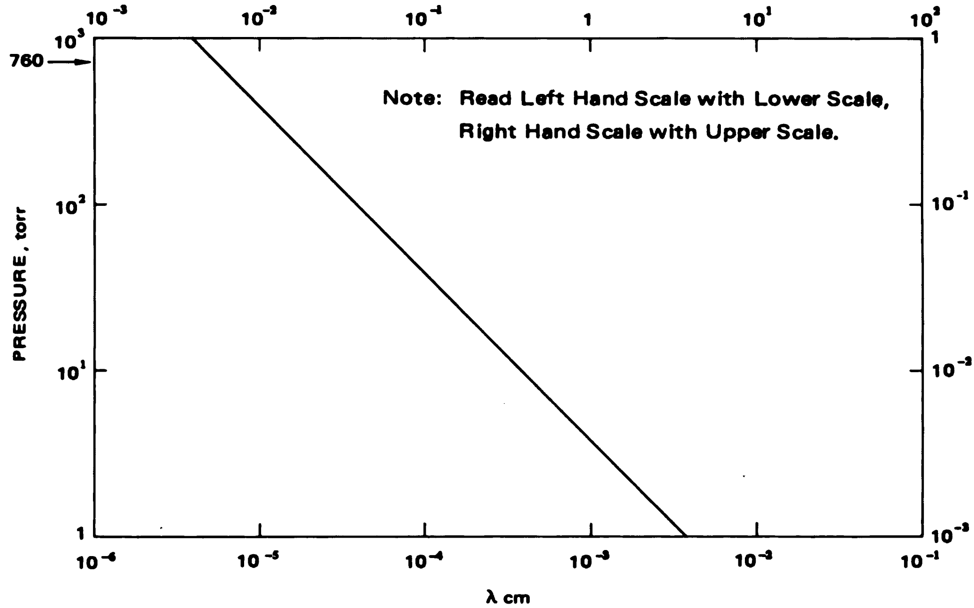

Figure 3. Electron Mean Free Path in Air vs. Pressure.

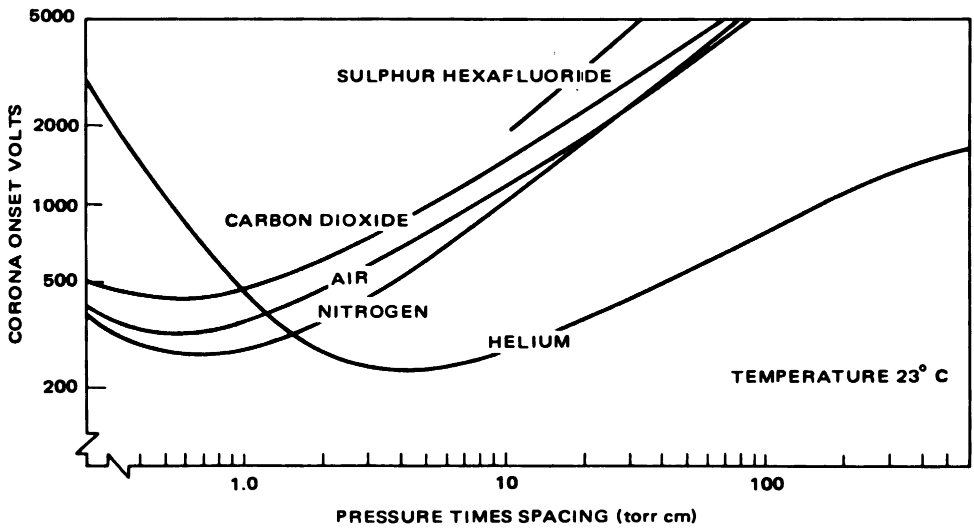

Figure 4. Direct Current Breakdown Voltage Between Parallel Plates for Several Gases.

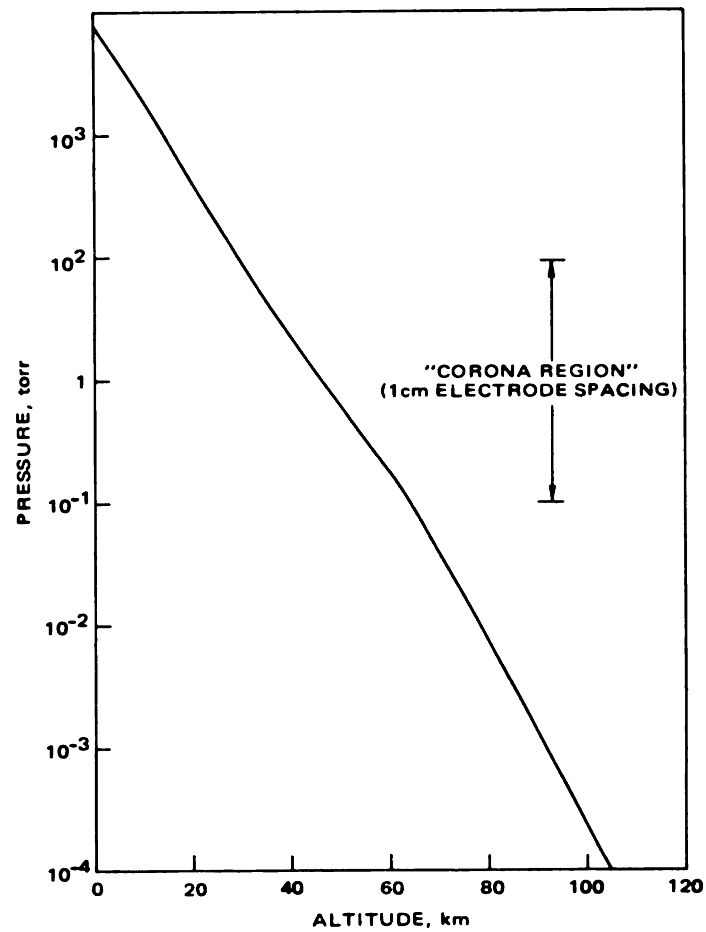

Figure 5. U.S. Standard Atmosphere, 1962, NASA, USAF, and USWB, 1962. (Reference 6)

In practice, one rarely deals with uniform fields. Nevertheless, Paschen-type curves such as those in Figures 6, 7, and 8 can be used to qualitatively predict the results of design perturbations.

Table 1 is a useful compilation of data that can be applied to estimate the maximum field which would be developed for any common electrode arrangement or to choose the better of two alternatives. Note, for example, that the hemisphere-in-a-plane configuration results in a lower maximum field than that of the sphere-and-plane configuration when $a \gg r$. Also, the maximum field produced between parallel wires is the same as that between wires crossing at right angles.

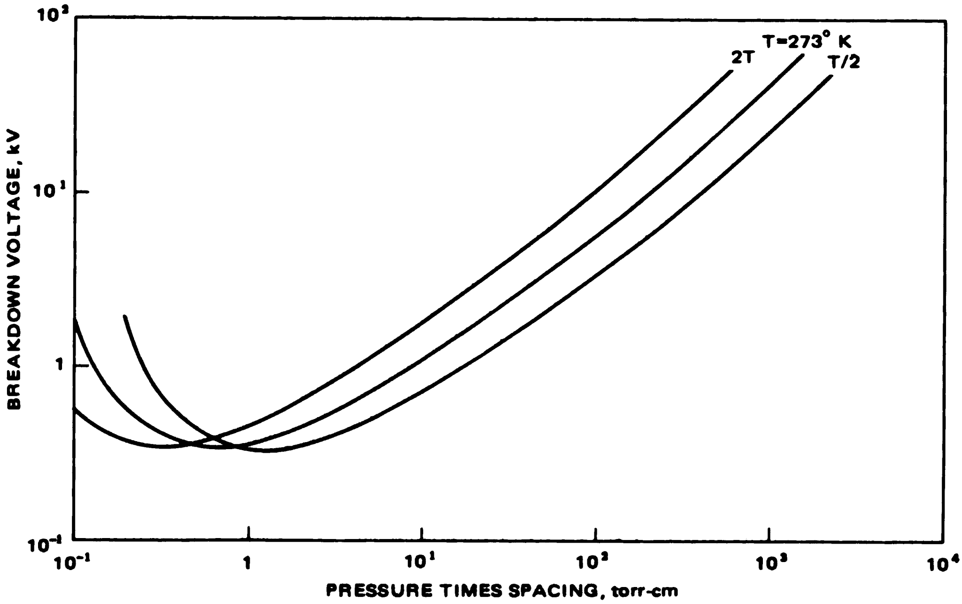

Figure 6. Effect of Temperature on Paschen Curve.

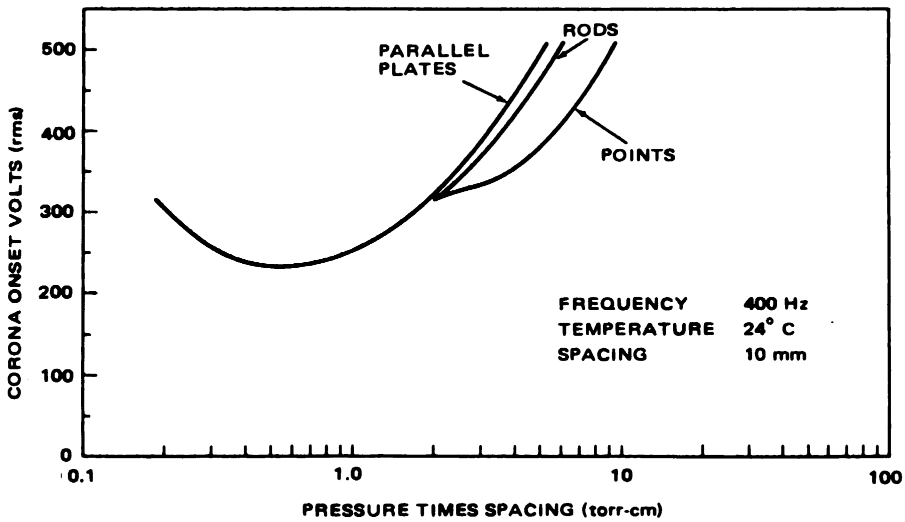

Figure 7. Effect of Electrode Geometry on Breakdown Characteristic in Air. (Reference 5)

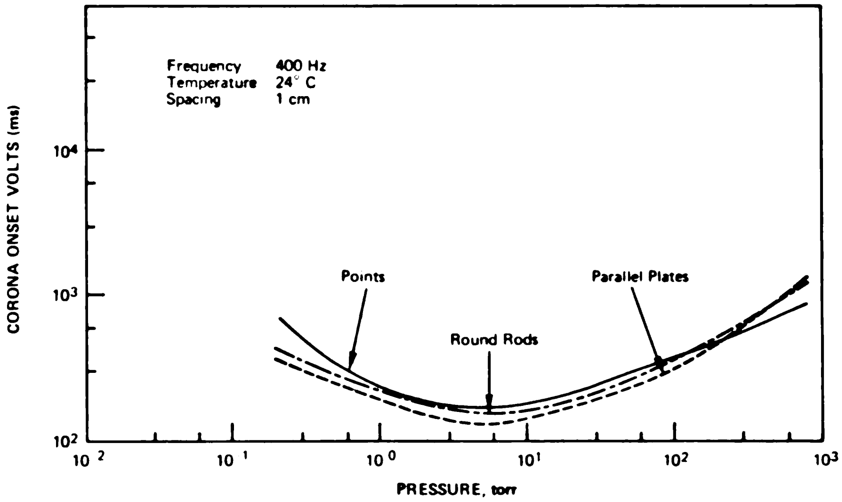

Figure 8. Effect of Electrode Geometry on Breakdown Characteristic in Helium. (Reference 5)

It is the gas density, not pressure, which is important when considering gas breakdown. The temperature variation, Figure 6, is found from the perfect gas law; that is,

$$\frac{p_1 V_1}{p_2 V_2} = \frac{n_1 R T_1}{n_2 R T_2}$$

If $p_1 = p_2$ and $V_1 = V_2$ then

$$\frac{n_1}{n_2} = \frac{T_2}{T_1}$$

Thus, in order to see the effect on a Paschen curve of doubling the temperature, the curve should be replotted with pressure values halved.

Further complications relate to the type and condition of the electrode surfaces. The type of material can significantly affect the breakdown potential (Table 2). This should be expected under high field conditions on the basis of variations in Townsend's second coefficient. Surface irregularities forming high field concentrations on sharp points can lead to field emission. The charging of insulating particles on electrode surfaces leading to high fields (Malter effect) and the transfer of particles from one electrode to the other (clumping), with resulting thermally-assisted electron emission, are other mechanisms that cause departure from ideal behavior. The curve of Figure 9, having a plateau at low pd values, is one example of such behavior under nonideal conditions.

Table 1
Maximum Field Strength E with a Potential Difference U Between the Electrodes, for Several Electrode Configurations (Reference 7)

Configuration		Formula for E	Example
Two parallel plane plates	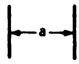	$\frac{U}{a}$	U = 100 kV, a = 2 cm, E = 50 kV/cm.
Two concentric spheres		$\frac{U}{a} \cdot \frac{r+a}{r}$	U = 150 kV, r = 3 cm, a = 2 cm, E = 125 kV/cm.
Sphere and plane plate		$0.9 \frac{U}{a} \cdot \frac{r+a}{r}$	U = 200 kV, r = 5 cm, a = 8 cm, E = 58.5 kV/cm.
Two spheres at a distance a from each other	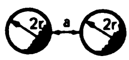	$0.9 \frac{U}{a} \cdot \frac{r + a/2}{r}$	U = 200 kV, r = 5 cm, a = 12 cm, E = 33 kV/cm.
Two coaxial cylinders	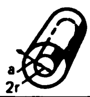	$\frac{U}{2.3\, r\, \lg \frac{r+a}{r}}$	U = 100 kV, r = 5 cm, a = 7 cm, E = 22.9 kV/cm.
Cylinder parallel to plane plate	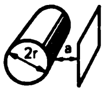	$0.9 \frac{U}{2.3\, r\, \lg \frac{r+a}{r}}$	U = 200 kV, r = 5 cm, a = 10 cm, E = 32.8 kV/cm.
Two parallel cylinders	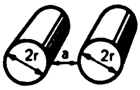	$0.9 \frac{U/2}{2.3\, r\, \lg \frac{r+a/2}{r}}$	U = 150 kV, r = 6 cm, a = 20 cm, E = 11.5 kV/cm,
Two perpendicular cylinders	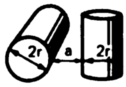	$0.9 \frac{U/2}{2.3\, r\, \lg \frac{r+a/2}{r}}$	U = 200 kV, r = 10 cm, a = 10 cm, E = 22.2 kV/cm.
Hemisphere on one of two paralel plane plates	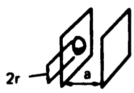	$\frac{3U}{a}$; $(a \gg r)$	U = 100 kV, a = 10 cm, E = 30 kV/cm.
Semicylinder on one of two parallel plane plates	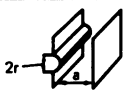	$\frac{2U}{a}$; $(a \gg r)$	U = 200 kV, a = 12 cm, E = 33.3 kV/cm.
Two dielectrics between plane plates ($a_1 > a_2$)	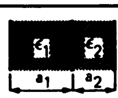	$\frac{U\epsilon_1}{a_1\epsilon_2 + a_2\epsilon_1}$	U=200kV, ϵ_1=2, ϵ_2=4, a_1=6 cm, a_2=5cm, E = 11.8 kV/cm.
Point and Plane $\frac{L}{a} = 160$	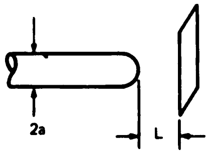	$\frac{0.605\ U}{a}$	U = 1kV, L=160 cm, a=1cm E = 606 volts/cm. Compare parallel plate capacitor with E = 6.25 volts/cm
Ellipsoidal Boss on one of two Parallel Planes II	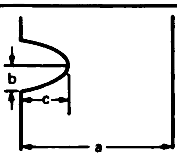	$\frac{U}{a} \times \beta$ $\beta = [n(\coth^{-1} n - 1/n)(n^2 - 1)]^{-1}$ where $n = c\,(c^2 - b^2)^{1/2}$	$\frac{c}{b} = 10, \beta \approx 50$

Table 2
Breakdown Voltages for Several Electrode Materials
(Reference 9)

(1-mm gap after conditioning with glow discharge)

Material	Breakdown Voltage (kV)
Steel	122
Stainless Steel	120
Nickel	96
Monel Metal	60
Aluminum	41
Copper	37

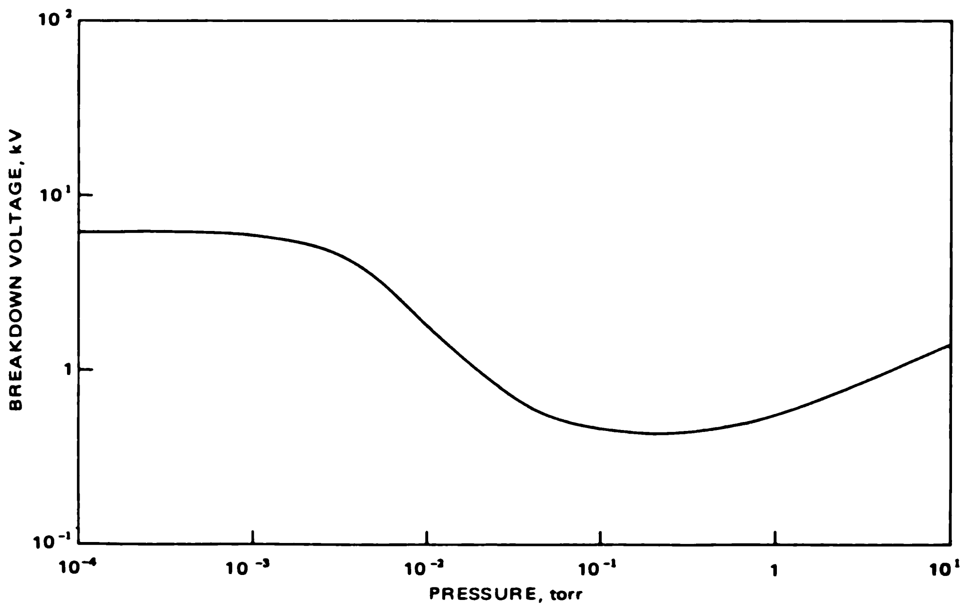

Figure 9. Breakdown Under Nonideal Conditions Showing Plateau at Low Pressures (after G. Biddison, private communication, 1968).

The importance of minute surface irregularities should not be overlooked. The microscopic field enhancement factor, β_1, due to an ellipsoidal boss on one plate of an ideal parallel plate capacitor is plotted in Figure 10. Total field enhancement is the product of β_1 times an electrode geometry factor, β_2, which can range from 1 to 10 (Reference 8). Such enormous field enhancement factors ($\beta_1 \beta_2$ products of $\sim 10^2$ - $\sim 10^5$) can easily lead to field emission with subsequent voltage breakdown. They account for some of the wide variations in breakdown voltages reported in the literature.

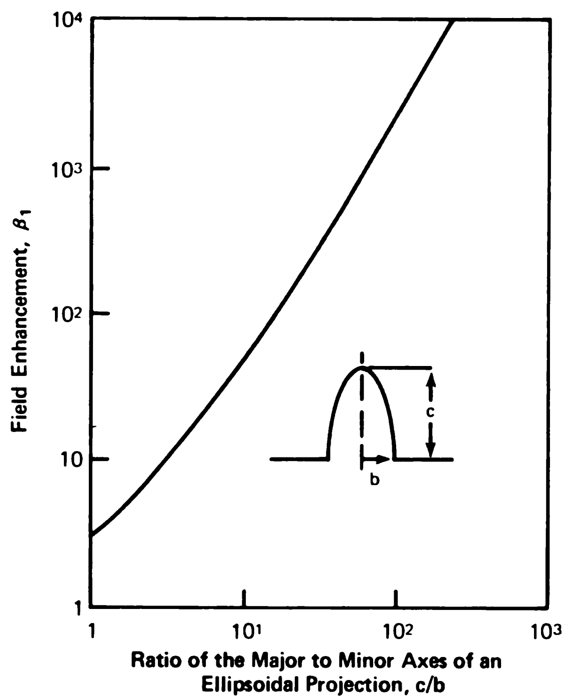

Figure 10. Microscopic Field Enhancement Factor β_1 as a Function of Geometry for an Ellipsoidal Boss on an Otherwise Flat Infinite Plane.

At very low pressures (vacuum insulation) and voltages below ~20 kV, breakdown is initiated by electron emission from the cathode. Above ~20 kV, processes that depend on the total voltage become more important than field emission (Reference 9). These processes include electron and ion bombardment of the electrode surfaces accompanied by emission of positive ions, electrons, and photons. The effect of such charged particles and photon interchange between the electrodes is to make required electrode spacings increase rapidly with applied voltage (Figure 11). It must also be remembered that surface materials are often not the same as the base materials and can radically affect breakdown voltage. Aluminum oxide, for example, exhibits a much higher secondary electron yield than that of aluminum.

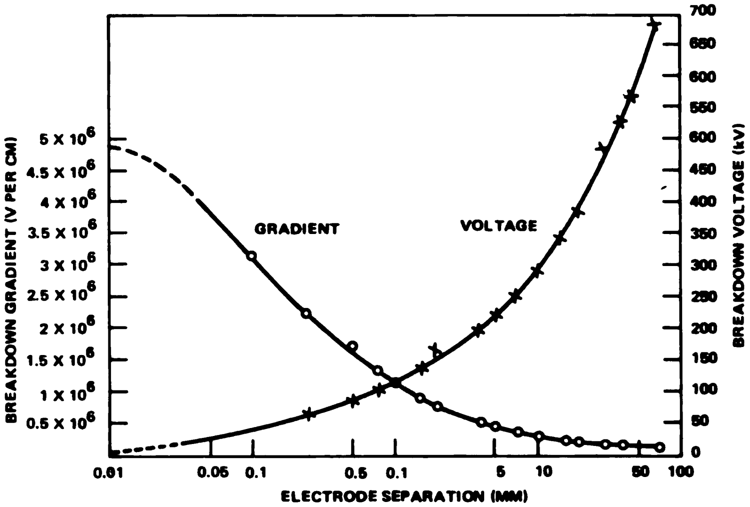

Figure 11. Breakdown Voltage and Breakdown Voltage Gradient Between a Steel Sphere, of 1-in. Diameter, and a Steel Disc, of 2-in. Diameter, in Vacuum. (Reference 10)

Surface Effects

As shown in Figure 12, the addition of dielectric surfaces between two electrodes can reduce breakdown voltage by a factor of 2 or more at high pressures, whereas there is very little effect at low pressures (Reference 11). Such behavior is probably due to adsorbed water vapor as suggested by the study by Sprengling and Ponemone (Reference 12). They found that volume resistivity of epoxy glass circuit laminates along the warp and woof directions was reduced several decades by exposure to high humidity. Sprengling (Reference 13) has found a long term irreversible susceptibility to reduction in surface resistivity due most likely to oxidation caused by the adsorbed water. Silicones and fluorocarbons were found to be the most resistant to this type of degradation.

A major problem with surface breakdown is the development of conductive paths or tracks which can lead to permanent short circuiting of the high voltage. Table 3 is a listing of the arc resistances and other characteristics of some materials commonly used in fabrication of electronic devices.

PRESSURIZATION AND ELECTRONEGATIVE GAGES

Normally, high-voltage power supplies employed on spacecraft take advantage of the high values of breakdown voltage available at low pressures. It is also possible to take advantage of the high V_b values at the other end of the Paschen curve by pressurization. For example, as shown in Figure 13, it is possible to double V_b by pressurization to ~350 kN/m^2 (~50 psig) with air or CO_2 or N_2. A better approach is the use of an electronegative gas,

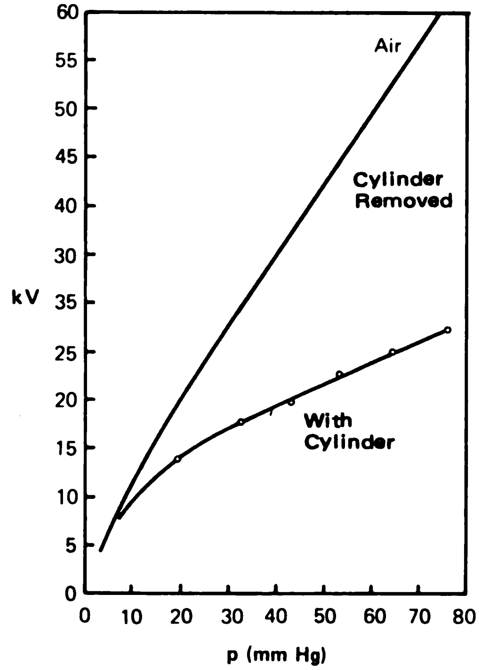

Figure 12. Breakdown Voltage for Sparkover Across Surface of a 2-cm-long Glass Cylinder in Air. Curve Labelled "Air" Gives Breakdown Voltage of the Gap with the Glass Cylinder Absent. (Reference 11)

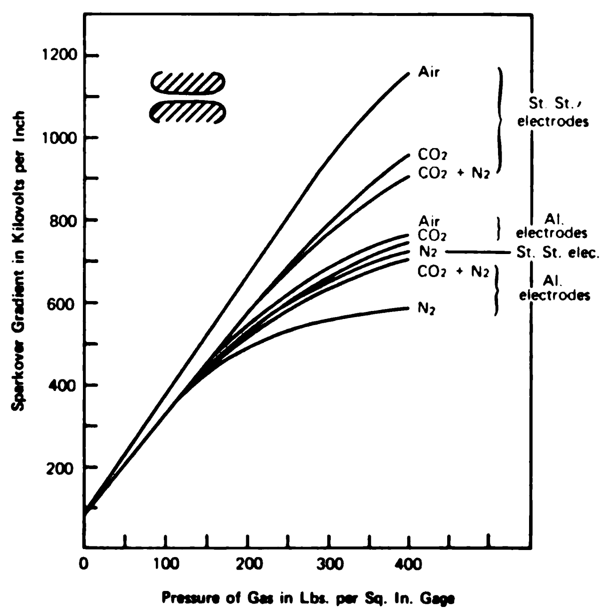

Figure 13. Comparative Insulating Strength of Several Gases at High Pressures for Uniform Fields Between S.S. and Aluminum Electrodes. (Reference 10)

Table 3
Dielectric Strength and Arc Resistance for Selected Insulation Materials Suitable for Molding, Extrusion or Casting*

Material	Arc Resistance (seconds)	Dielectric Strength (volts per mil)	Volume Resistivity Ω-cm	Dielectric Constant
Acetal resin copolymer	240	500–2100	10^{14}	
Acetal resin homepolymer	129–240 (burns)	500–1210	$1-6\times10^{14}$	
Acrylic resins	no tracks	400–500	2×10^{16}	
Acylonitrile Butadiene–Styrene	71–82	310–460	10^{16}	
Alkyd molding compound	180+	375	10^{14}	5.8–6.2
Cellulose acetate	50–310	230–365	$10^{10}-10^{14}$	3.5–4.0
Cellulose acetate butyrate	unknown	250–400	$10^{10}-10^{16}$	3.6–6.4
Chlorinated Polyether	unknown	400	10^{15}	
Ethyl cellulose	60–80	800	$10^{12}-10^{15}$	
Delrin	125–190	400	$10^{15}-10^{16}$	2.7–3.7
Deallyl phthalates	105–140	350–400	$3.9\times10^{12}-1.8\times10^{16}$	6.2
Expoxies	45–300	300–550	$10^{12}-10^{17}$	3.3–5.5
Ethylene	unknown	525–550	$10^{8}-10^{9}$	
Fluorinated ethylene and propylene (copolymer)	>300	500–600	$>2\times10^{18}$	
Kel–F	>360	~500–1000	$2.5-4\times10^{16}$	
Melamine with glass Fibers	180	170	10^{11}	
Mica–glass bonded	240–300 +	360–400	$10^{12}-10^{17}$	
Neoprene	unknown	150–600	10^{11}	
Nylons	130–140	342–470	$1.5\times10^{11}-4\times10^{14}$	3.9–7.6
Nylons with glass fibers	92–148	400–580	$3.0-5.5\times10^{14}$	
Phenolic molding compound	tracks	300–40C	$10^{11}-10^{12}$	
Phenolic molding compound with glass fibers	0.4 to 150	100–450		
Oxide resins	unknown	500–550	10^{17}	
Phenylene oxide resins with glass fibers	70–120	1020	10^{17}	
Polycarbonate	120	400	$2-1\times10^{16}$	3.1
Polychlor otrifluoroethylene	>360	530	1.2×10^{18}	
Polyethylene, irradiated	unknown	2500	$>10^{15}$	2.25–3.2
Polyimides	230	560	$10^{16}-10^{17}$	
H film (5 mil)	183 tracks	3600	10^{18}	
Polypropylene	unknown	750–800	$>10^{16}$	
Polypropylene with glass fibers	73–77	317–475	1.7×10^{16}	
Polystyrene (heat resistant)	60–135	400–600	$10^{16}-10^{17}$	
Polysulfones	122	425	10^{16}	
Polytetrfluoroethylene	>300	480	$>10^{18}$	
Polyvinyl chloride (Flexible)	unknown	250–800	$10^{11}-10^{14}$	12.0
Polyvinyl chloride (Rigid)	60 – 80	425–1300	$>10^{16}$	2.4
Polyvinylidene fluoride	>50	260–1280	2×10^{14}	
Silicone, Mineral filled	230	390	5×10^{13}	4.8
Styrenes with glass fibers	28 – 41	354–424	$3.2-3.7\times10^{16}$	
Urethanes	unknown	6.7-7.5 (60 Hz.)	2×10^{11}	
Viton, fluoroelastomer	unknown	500	2×10^{13}	
Vespel	230	400	$10^{16}-1^{17}$	3.0–3.5

*These values are obtained under standard test conditions and may not be obtained in engineering applications.

especially SF_6. Molecules of SF_6 readily capture electrons and form heavy negative ions with much lower mobility than the electrons. In addition, SF_6 is stable below 423°K (150°C), is nontoxic, and does not burn. Figures 14 and 15 illustrate the significant improvement in V_b obtainable through the use of SF_6 (Reference 14). A 100-kV power supply, described later in this report, has been successfully designed using pressurization with SF_6.

SOLID DIELECTRIC FAILURES

Solid dielectric failures are generally of two types: mechanical and chemical. Mechanical breakdown is failure due to mechanical overstress of the material by electrically produced physical forces. This failure mode occurs relatively infrequently.

Chemical breakdowns, which occur frequently, result from chemical changes and erosion of the dielectric material due to corona in voids or at external surfaces. Another factor which aids in the degradation of the electrical properties of dielectrics is heat produced by flow of leakage currents.

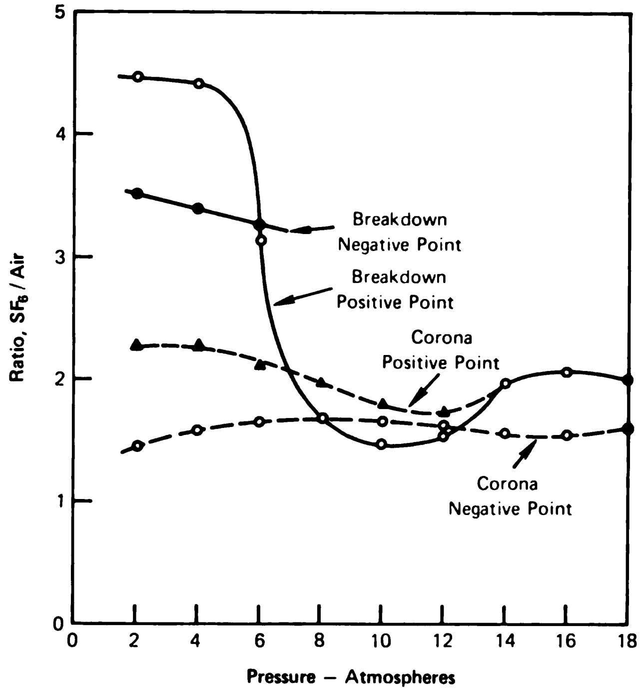

Figure 14. Ratio of Corona and Breakdown Voltage for Air and SF_6 as a Function of Testing Conditions in Nonuniform Fields. (Reference 14)

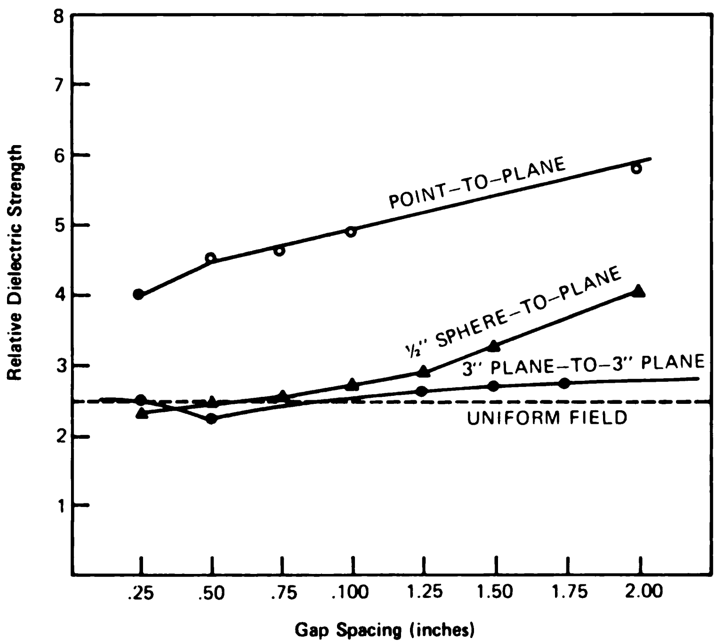

Figure 15. 60-Hz Relative Strength of SF_6 to Dry Air as a Function of Configuration and Spacing of Electrodes. Gases at 25°C and Atmospheric Pressure. (Reference 14)

Inhomogeneity of leakage resistance within the body of the dielectric coupled with poor heat conductivity can produce high temperatures with attendant chemical changes. These changes can cause a decrease of resistivity by several decades (Figure 16) of a portion of the material. The thickness of the dielectric is therefore effectively reduced and can lead to complete failure. This is the probable cause of the thickness effect—the variation of material dielectric strength with thickness in which the corona threshold voltage increases with dielectric thickness as expected (Figure 17), but the dielectric strength drops markedly (Figure 18).

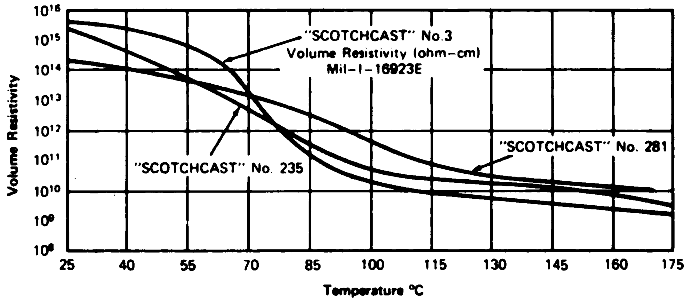

Figure 16. Volume Resistivity vs. Temperature for Three Encapsulant Materials.

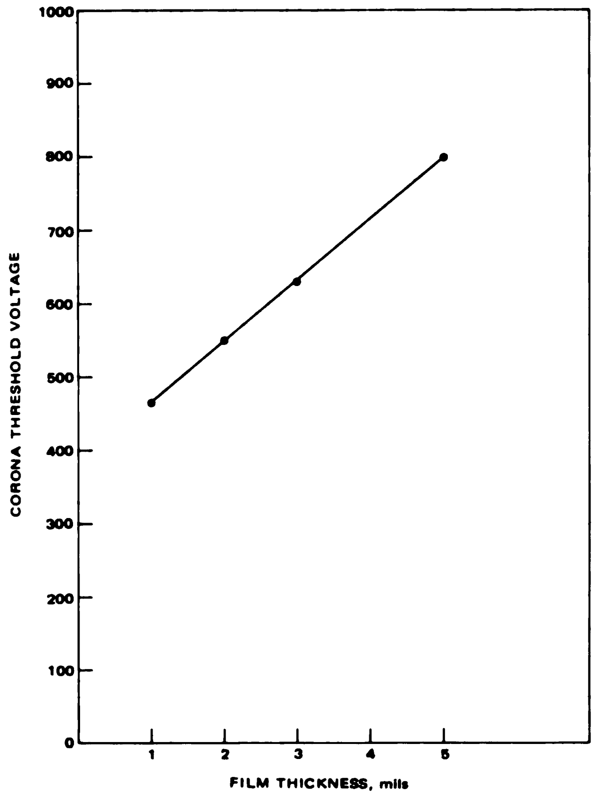

Figure 17. Dupont Kapton H-Film Corona Threshold Voltage vs. Film Thickness.

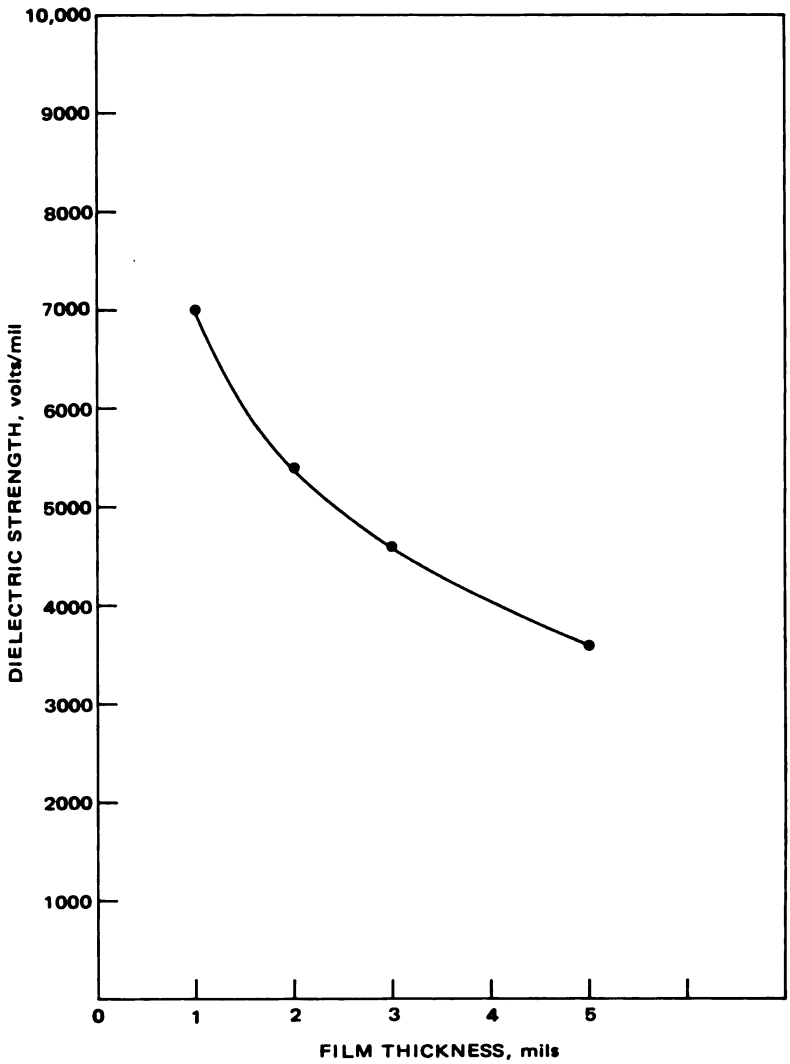

Figure 18. Dupont Kapton H-Film Dielectric Strength vs. Film Thickness.

DESIGN EXPERIENCE

Based on past experience, this section presents basic design information regarding individual components and processes. These include encapsulation techniques, selection of material and salient characteristics, voltage breakdown with regard to circuit boards, depressurization and outgassing of unpotted power supplies, and design information regarding problems with individual electronic components.

ENCAPSULATION

One method of preventing a gas discharge-voltage breakdown is to exclude gases from the high-voltage areas. This can be accomplished by encapsulating the high-voltage circuitry. Encapsulation provides the system with mechanical protection from external damage, structural support for the components against shock and vibration, and protects the high-voltage system from gas discharge damage.

Encapsulation of a high-voltage system is predetermined by the environmental conditions under which the system is expected to function successfully. The decision to encapsulate should be made during the initial design concept phase and incorporated in the subsequent hardware design. In this manner, a total system approach to the design can be taken, yielding a power supply with minimum problems that can arise from encapsulation or potting. This will permit the optimum choice of components, parts, materials, mechanical arrangements, manufacturing techniques, and the methods of functional and environmental testing.

Selection of Encapsulant

There are three general classes of encapsulants, potting materials or conformal coating materials, which are generally acceptable for spacecraft use: (1) epoxies, (2) silicones, and (3) polyurethanes. The main characteristic of selected members of these three polymer types is their low outgassing behavior, which reduces the problems of spacecraft contamination and internal spacecraft pressures conducive to electrical discharge. A list of specific polymers acceptable for flight use is given in GSFC Report, TM X-65679 and NASA TN D-7362. Other polymer characteristics that should be considered are dielectric strength, dielectric constant, resistivity, arc resistance or tracking, viscosity during the pouring period, pot life, shelf life, ease of handling during preparation and pouring, chemical activity with the parts to be encapsulated, need for primers on parts to be encapsulated, adhesion to parts, temperatures generated during the polymerization of the encapsulant, thermal coefficient of expansion of the polymer, and shrinkage during polymer cure. The use of flight-acceptable encapsulants is not without some hazards. A knowledge of what they are and how to avoid these hazards will greatly improve the probability of a successful and functional high-voltage system.

A major problem in encapsulation is the occurrence of voids in the encapsulant. This is particularly serious if voids occur in the neighborhood of large voltage gradients because an electrical breakdown in the void can be expected. This problem can be minimized by using care in the selection of an encapsulant and the encapsulation processing techniques. Dissolved gases should be removed from the encapsulant materials (resin and catylist), and gases should be prevented from becoming entrained in the encapsulant during the mixing and pouring stages. The technique for achieving these conditions is vacuum degassing of the encapsulant materials before mixing, then mixing and pouring in vacuum. To further ease the void problem, use an encapsulant which has a low viscosity in which entrained gas bubbles can easily rise and can be quickly removed from the fluid. It will also permit easy penetration of all the spaces between the circuit parts being encapsulated and help prevent void formation within the embedment. The mechanical arrangement and spacing of components also should be designed to prevent void formation and gas traps: for example, provide increased spacing between components when a more viscous encapsulant is to be used, and provide holes in circuit boards or other large surfaces to improve the distribution of the encapsulant around the surfaces and throughout the embedment assembly.

Another encapsulation problem is the mechanical stresses developed between the encapsulant and the embedded parts due to elevated temperatures, temperature differences, and encapsulant shrinkage. These stresses can be sufficiently severe to cause mechanical failure of the embedded circuit elements (breakage of leads, welded and soldered joints and electronic components under tension, compression or shear arising from a high shrinkage rate of the encapsulant or from a difference in thermal coefficient of expansion between the electronic part and the encapsulant).

This problem can be satisfactorily solved by choosing an encapsulating material whose physical, mechanical, and thermal characteristics are compatible with the components to be embedded. These properties can be modified by the addition of fillers to the encapsulant. In general, the fillers will decrease these values of thermal conductivity, coefficient of expansion (see Figure 19), mold shrinkage, exotherm temperature rise and mechanical strength, and increase the values of viscosity (see Figure 20) and dielectric constant. The curing rate of an exothermic polymerization reaction can be controlled during encapsulation to prevent the development of excessive temperatures and the accompanying thermal stresses. The encapsulated package should be designed such that heat dissipates as quickly as possible. A conformal coating of an elastomer also can help reduce the shear and

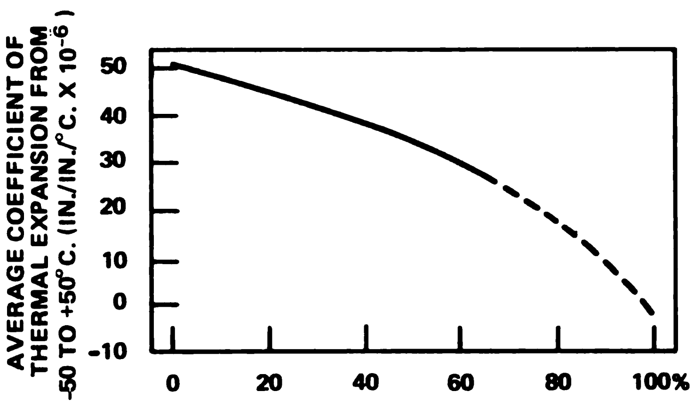

Figure 19. Coefficient of Thermal Expansion of Shell EPON 828 Castings with Silica Filler.

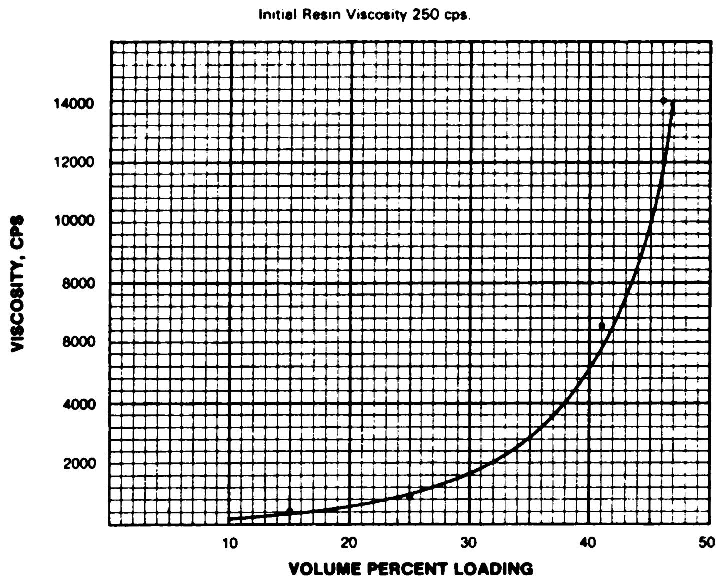

Figure 20. Effect on a Polyester Resin Viscosity Due to Filling with Glass Bubbles (3M Co.).

tensile stresses when a rigid encapsulation is desired. Some typical low outgassing conformal coatings are:

- Dow Corning 93-500, Polydimethyl Siloxane,
- Thiokol Solithane 113-300, Polyester type polyurethane,
- Hughson Chemical Chem Glaze Z 004, and
- Shell Epon 828/General Mills Versamide in a 50:50 to 70:30 ratio mix.

Assurance of a good bond between encapsulant and circuit parts is a requirement for a successful high-voltage encapsulation. This is dependent upon the chemical nature of the surfaces to be coated and the potting compound. Foreknowledge of the coating materials and the processing fluids to which the part has been exposed during manufacture and test will be very helpful in selecting the methods and materials for a successful encapsulation. It will determine the need for such surface preparations as chemical etching; mechanical abrasion (sand blasting or other surface scoring techniques); priming, when and as recommended by the encapsulant manufacturer; conformal coating; and cleaning. Cleanliness of surfaces to be coated is mandatory—no fingerprints, oils, or moisture should remain on the surfaces. Materials which are difficult to bond should be avoided. Teflon, in particular, should not be used in any potted system even though it can be surface treated. A typical cleaning fluid is a 1:1 solution of toluene and acetone of Certified Grade purity or better.

Epoxies

In addition to the low outgassing, low vapor pressure characteristics of epoxies, there are other properties which make them suitable as potting materials for spacecraft use. These include excellent electrical properties (dielectric constant = 3.0 to 5.0; dielectric strength = 400 to 600 volts/mil; volume resistivity = 10^{12} to 10^{16} ohm-cm; arc resistance = 50 to 180 s); good structural properties; low water absorption (0.17 - 0.50%); good adhesion to metals; and low mold shrinkage (0.007-0.009 in./in.). These properties are affected by the treatment and processing techniques. Volume resistivity, temperature coefficient of resistivity, dissipation factor, dielectric constant, heat conductivity, temperature coefficient of expansion, and viscosity are changed by the quantity and chemical nature of the hardening agents, fillers, plasticizers, and curing temperatures. Thermal conductivity of unfilled epoxies range from 4 to 5×10^{-4} cal/cm^2/s/cm/°C. Thermal coefficients of expansion for epoxies range from 40 to 100×10^{-6}/°C. The addition of suitable mineral fillers can reduce these coefficients to values more closely matching the temperature coefficients of the encapsulated parts thereby minimizing thermally induced stresses on these parts. Fillers also increase heat conductivity, decrease exotherm temperature rise, increase resin viscosity in amounts greater than 20% by weight, and reduce mold shrinkage.

The epoxies may be divided into two general classes: (1) those which are hardened at high temperatures by anhydride hardeners and (2) those which are hardened at about room temperatures by amine or amide hardeners. A comparison of the two classes shows that the anhydride hardened epoxies generally have better electrical properties (lower dissipation factors, higher volume resistivity (see Figure 21), electrical stability at elevated temperatures), higher heat distortion temperature, longer pot life and lower viscosity

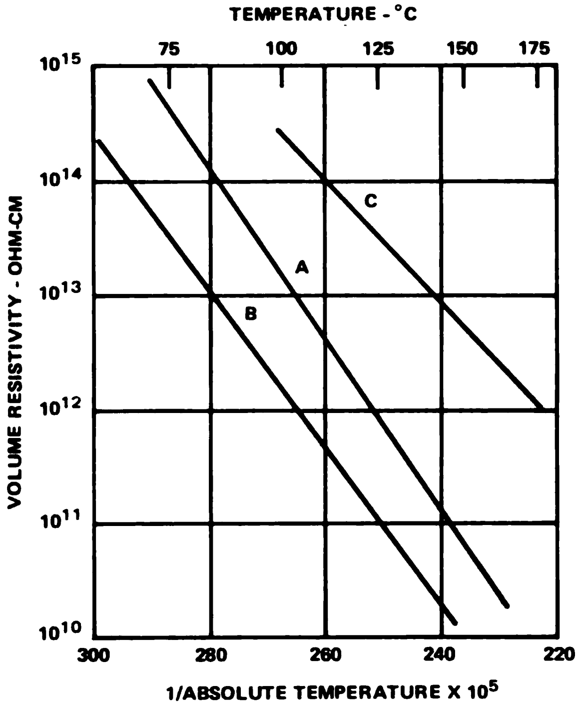

Figure 21. The Temperature-Resistivity Relation in Epoxy Resin as Affected by the Use of Different Hardening Agents. (Reference 15)

(easier to degas). The anhydride cured epoxy, however, does require an elevated cure temperature (100°C to 200°C) which will be injurious to circuit parts with temperature ratings less than the cure temperature. The amine-amide cured epoxies are curable at lower temperatures (room temperature–100°C) but have a higher viscosity and a high exotherm temperature. The higher viscosities make it more difficult to degas and prevent bubbles and voids from occurring in the cured encapsulant. The exotherm temperature rises can be as high as 250°C and will damage low temperature rated circuit parts. Note that epoxy resistivity varies markedly during the curing process as in Figure 22; therefore, it is essential to be certain of a complete cure. Some typical anhydride formulations are:

Epon 828–10 parts by weight	48-hr cure at
Linorid 8–9 parts by weight	70°C + 1 hr at
DMP 30–0.1 part by weight	100°C
Stycast 1269/A–10 parts by weight	16-hr cure at 100°C
Stycast 1269/B–10 parts by weight	+ 16 hr at 150°C

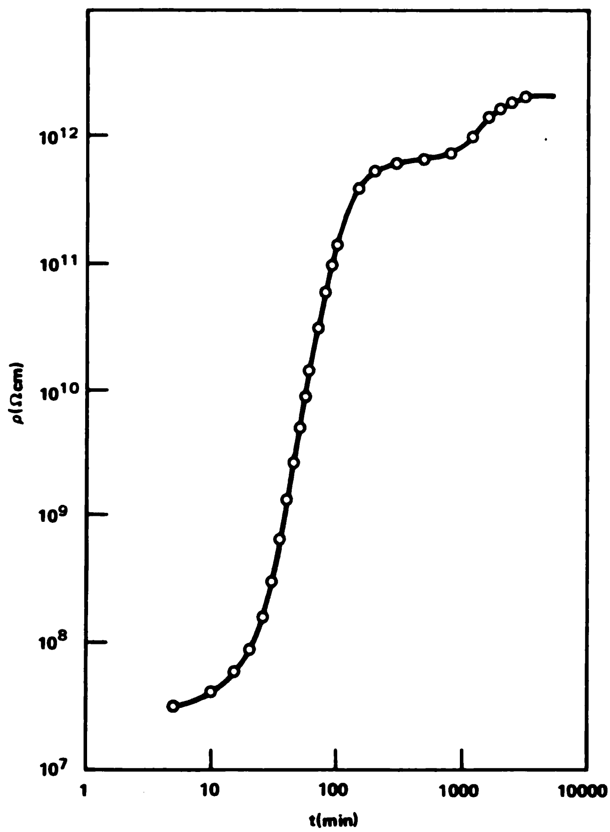

Figure 22. A Resistivity vs. Time Plot Showing Two Reactions Occurring at 80°C Using an Epoxide/Polyamide Ratio of 2g:1.5g. (Reference 16)

Some typical amine and amide formulations are:

Epon 828—10 parts by weight
(Teta) Triethylene Tetramine—1 part by weight

Epon 828—10 parts by weight
(DTA) Diethylene Triamine—1 part by weight

Epon 828—6 parts by weight
Versamide 140—4 parts by weight

Also ratios 7:3 and 1:1 can be used

Silicones

Silicone polymers also have additional characteristics which make them desirable encapsulants. These include superior electrical properties (dielectric constant = 3.0 to 5.0; dielectric strength = 300 to 600 volts/mil; volume resistivity = 10^{11} to 10^{14} ohm-cm; arc resistance = 300 to 450 s); excellent thermal properties (low degradation under continual exposure to temperatures greater than 200°C); a heat distortion temperature about

300°C; flexibility at low temperatures; no exotherm during the curing period; low mold shrinkage during cure (less than 0.005 in./in.); low viscosity and temperature coefficient of viscosity; low water absorption; long shelf and generally long pot life; and easy repairability.

Some silicone properties which can create design problems if neglected are a high temperature coefficient of expansion (200 to 400 $\times$ 10^{-6}/°C); a low thermal conductivity (3 to 5 $\times$ 10^{-4} cal/cm^2/s/cm/°C). Silicones are attacked by aliphatic and aromatic solvents and some mineral oils. Some of the volatile constituents of the silicones can be pyrolytically decomposed into silicon dioxide at elevated temperatures. This can be detrimental to bearings, gears, and so forth, in the neighborhood of the silicone resin. Other volatile constituents can also deposit out on optical surfaces and degrade optical and thermal behavior. The silicone encapsulants, which give off acetic acid during their cure, should not be used because the acid is corrosive to the circuitry.

Suitable silicone encapsulants for high-voltage spacecraft applications are DC 93-500, a 2-part unfilled silicone, and GE RTV 566, a filled phenylated polydimethyl siloxane.

Polyurethanes

Additional characteristics of the polyurethanes that make them desirable as potting and encapsulating polymers for high-voltage flight systems include good electrical properties (dielectric constant = 3 to 6, dielectric strength = 400 to 650 volts/mil, volume resistivity = 10^{12} to 10^{15} ohm-cm, arc resistance = 130 to 180 s); a good adhesion to most materials, although a primer coating on metals will insure a better bond; low water absorption; good heat resistance to about 125°C; low exotherm temperature rise (less than 55°C; low mold shrinkage (0.005 to 020 in./in.); long shelf life; long pot life; and easy repairability.

The linear thermal coefficient of expansion lies in the range 150 to 200 $\times$ 10^{-6}/°C greater than the epoxies but smaller than the silicones. The thermal conductivity falls in the range 2 to 6 $\times$ 10^{-4} cal/cm^2/s/cm/°C similar to those of the silicones and epoxies. These thermal properties should be considered when potting fragile components. Thermally induced stresses can cause component failure.

The preparation and handling of the polyurethanes should be performed with care since the prepolymers and curing agents can be health hazards. Chlorinated aniline curing agents (MOCA) should be avoided because they have been found to be carcinogenic. The prepolymers are isocyanates whose vapors can cause respiratory irritations. The repair of cured polyurethane potted systems, in which high temperatures are present (hot soldering iron), can generate cyanate and cyanide vapors which are highly toxic.

Operations with the polyurethanes should be performed in well ventilated, hooded areas. A polyurethane which has been highly successful as a high voltage encapsulant is Thiokol Corp. Solithane 113. It is a polyether based resin, which is more resistant to high humidity and cures at a lower temperature than polyester base urethanes.

Foams*

There are times when it becomes necessary to reduce the weight of spacecraft systems to keep within the allowable weight limits prescribed for a successful flight. One way this can be accomplished is to use foamed polymers as encapsulants thereby reducing the weight of the potted system. Where high-voltage systems are to be potted, it is not recommended that encapsulants be used that have been foamed by blowing gas methods. The void or bubble sizes in these foams are large and variable. This type of foam is conducive to a gas discharge, particularly where the voids are in large electric fields that exist in the neighborhood of small gaps between conductors, sharp points, or other geometric discontinuities of high-voltage conductors. A syntactic foam, one made by combining a resin with a hollow-sphere filler, is recommended when a foam is required. The hollow-sphere fillers, commonly known as microballoons or glass balloons, are very small and have a known size distribution (20 to 130, 30 to 125, 10 to 250 μm, and so forth). The probability of a breakdown occurring in these spheres is small, even in a comparatively high electric field, because the pressure in the small spheres is about 760 torr and the maximum gap is about 0.250 mm. This would require a voltage across the sphere of about 300 volts for a breakdown or an electric field of about 1200 volts/mil.

The balloons can be obtained in glass or ceramics, coated or uncoated. In selecting the suitable balloon, the coating should be checked to determine the effect on the electrical properties affecting high-voltage breakdowns (resistivity and dielectric constant). The addition of balloons greatly increases the viscosity of the polymers. This problem can be partly overcome by increased polymer temperatures during potting.

Resistivity and Voids

Although dielectric constant ratios determine the voltage distribution among layers of dielectrics in a capacitor with an applied a.c. potential, it is the resistivities that are important when considering d.c. potentials. As an example, consider the following simplified study of a parallel plate capacitor with three dielectrics in series (Figure 23). The middle dielectric will later be considered to be air at low pressure so that the model is that of a void in an encapsulant.

*Foams also are used to reduce mechanical stresses due to temperature changes.

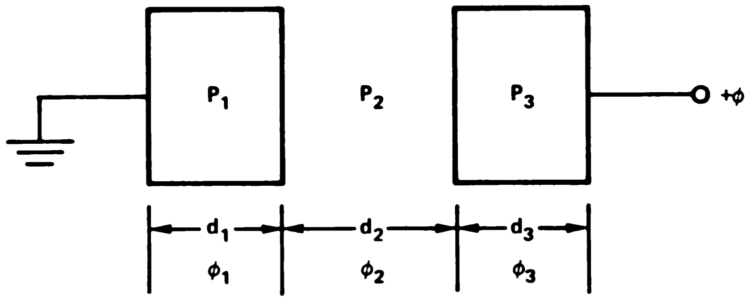

Figure 23. Simple Model of a Void.

The sum of the potential drops must be equal to the applied potential:

$$\phi = \sum_{i=1}^{3} \phi_i \ .$$

From symmetry and Ohm's Law it follows that the potential drop across each dielectric will be proportional to its thickness d_i and its resistivity P_i:

$$\phi_i = \frac{\phi \, P_i \, d_i}{\sum_i P_i \, d_i} \ .$$

The field is the negative gradient of potential, so

$$|\vec{E}_i| = \frac{\phi \, P_i}{\sum_i P_i \, d_i} \ .$$

Therefore, $|E| = \alpha \, P_i$ as would be expected.

If

$$P_1 = P_3 \ll P_2$$

then

$$|\vec{E}_2| \approx \frac{\phi}{d_2} \ .$$

That is, due to the conductivity of the dielectric, the capacitor plates effectively move in to the boundaries of the void thereby greatly increasing the intensity of the electric field in the void.

When the potential drop across the void reaches the corona onset voltage, a discharge occurs, followed again by gradual voltage buildup. The process repeats indefinitely leading to corona-induced degradation of the dielectric material. The repetition rate of this relaxation oscillator system can be estimated by use of the following equation adapted from Reference 17 for the special case of spherical voids.

$$f \approx 1.13 \times 10^{11} \left(\frac{\sigma}{\epsilon - 1}\right) \frac{E'}{E_i},$$

where σ is the volume conductivity of the encapsulant in mhos/m
ϵ is the dielectric constant of the encapsulant
E' is the applied electric field
E_i is the field across the void required to produce breakdown.

Putting typical values into the equation, that is,

$\epsilon = 2.3$

$E'/E_i = 1$

$\sigma = 5 \times 10^{-15}$ mho/meter

the result is

$$f \approx 4.35 \times 10^{-4} \text{ Hz} \approx 2 \text{ pulses/hr void.}$$

In this approximation it was assumed that the surface conductivity of the void is zero. This yields a maximum pulse rate for purposes of convenient calculations. The example illustrates the importance of making encapsulations void free. Pulse rates of this order have been observed on the outputs of spacecraft high-voltage power supplies. Laminar shaped voids in encapsulated systems can develop pulse repetition rates as high as double those of spherical voids. Note also that any sealed high-voltage connector necessarily contains voids and can therefore become degraded with time if under sufficient voltage stress, depending on the pressure in the void.

Bubbles Rising in Uncured Encapsulants

To illustrate the problems that can arise, even from initially small bubbles in encapsulants, consider Figure 24. This figure shows the diameter of a bubble in a typical encapsulant as a function of depth (Reference 18). The size of the bubble varies as it rises due to hydrostatic pressure. Note that,

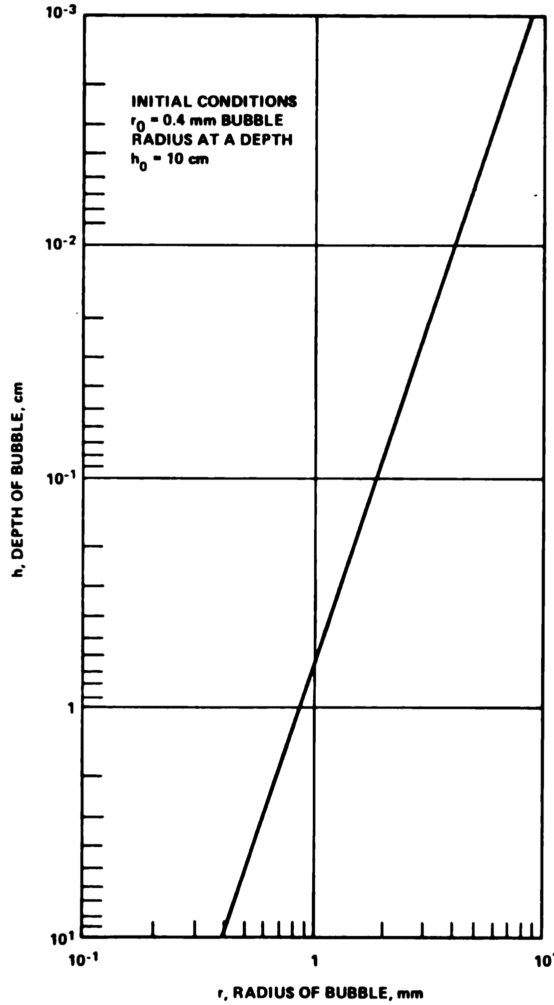

Figure 24. The Effect of Hydrostatic Pressure on the Size of a Bubble Rising in an Uncured Resin. From the relation $r = r_0 (h_0/h)^{1/3}$. (Reference 18)

if a bubble rises far enough through the encapsulant such that the diameter doubles, the volume is multiplied by a factor of 8 causing the pressure inside the bubble to be reduced by a factor of 8. This implies that the pd product for the bubble becomes reduced by a factor of 4. Due to the doubling of the diameter the voltage drop across the bubble is doubled. These combined effects correspond, for example, to movement along the straight line in Figure 25. The criterion for prevention of breakdown in the bubble, therefore, is operation below the straight line, not merely below the Paschen curve. As an example, a bubble having an initial pd product of 1.0, as at A, will not breakdown because it is below the Paschen curve. However, the bubble can rise and expand such that its parameters trace the straight line path to B where intersection of the Paschen curve takes place

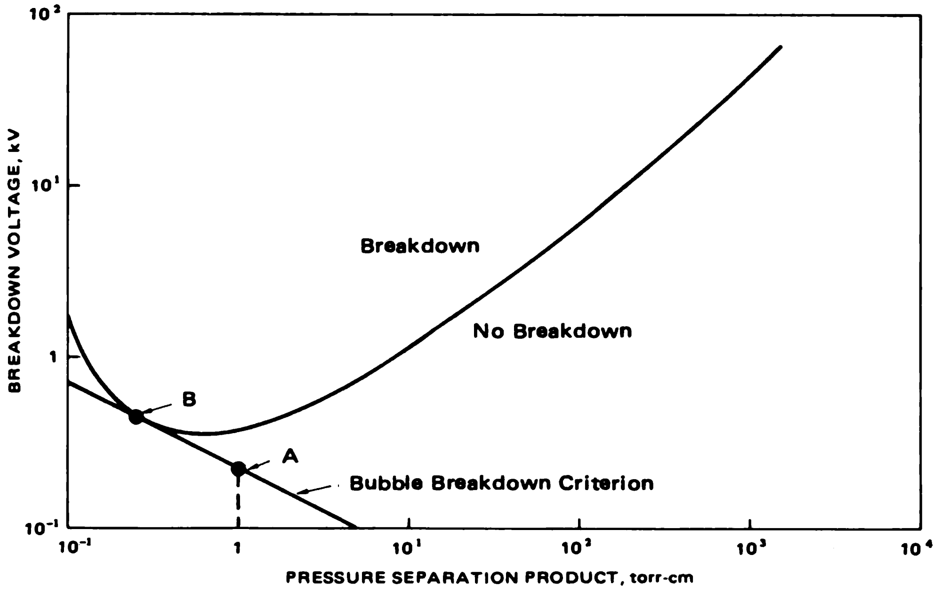

Figure 25. Typical Paschen Curve with Breakdown Criterion for Bubble Rising in Uncured Encapsulant.

and breakdown can occur. Bubbles initially smaller will trace paths parallel to the path shown, but will not intersect the Paschen curve and will not break down.

Poly Sandpile

One potting technique which helps to reduce the probability of trapping voids during encapsulation has recently been tested (J. E. Carey, Shell Development Company, private communication, 1973). It involves the use of μm-size glass spheres as a filler. Unlike the usual technique, the module to be potted is first filled with the dry filling material during mechanical agitation to ensure that the fine particles fill all recesses. A low viscosity encapsulation compound is then poured into the module under vacuum. The liquid flows through the filler by capillary action like water through a sponge. In addition to eliminating voids, the glass spheres almost entirely eliminate component breakage due to differential thermal expansion.

It is to be noted that high quality electrical grade glass spheres are preferable to alkali glass spheres. The presence of alkali ions on the latter can aid in causing voltage breakdown.

General Comments

The success of encapsulated high-voltage flight systems is dependent upon early planning, good engineering, careful system and hardware design, and meticulous care in fabrication. Close quality control should be exerted during the production stages. Because there are several manufacturers whose formulations are somewhat different for similar encapsulants, it is wise to read and adhere to the manufacturers instructions and recommendations regarding his materials and processes. The physical, electrical, and mechanical properties of some commonly used encapsulants are listed in Tables 4 and 5.

Table 4
Physical and Electrical Properties of Some Commonly Used Encapsulants

Material	Manufacturer	Coefficient of Thermal Exp. cm/cm °C $\times 10^{-4}$	Thermal Conductivity, cal/cm sec °C $\times 10^{-4}$	Chemical Composition	Specific Gravity	Water Absorption Wgt %	Shore Hardness Number	Transparency and Color	Service Temperature Range (°C) from	to	Shelf Life Months
XR-5192	3M			Two part filled epoxy	1.53	0.36 (240 hours at 96% RH)	D72	Gray		+130	12
Scotchcast 235	3M	1.6	4.0	Unfilled epoxy	1.10	1.3 (1000 hour immersion)	D55	Brown		+130	12
Scotchcast 281	3M	1.5	12.0	Two part filled epoxy	1.43	0.4 (1000 hour immersion)	D65	Brown		+155	12
Scotchcast 3	3M	2.0	4.0	Unfilled epoxy	1.10	0.8 (1000 hour immersion)	D80	Clear		+130	12
RTV-11	GE	2.5	7.0	Silicone	1.18		A45	White	-59	+204	6
RTV-60	GE	2.1	7.4	Silicone	1.47		A60	Red	-59	+204	6
RTV-602	GE	2.9	4.1	Silicone	0.99		A15	Clear	-59	+204	6
RTV-615	GE	2.8	4.5	Silicone	1.02		A35	Clear	-59	+204	6
RTV-616	GE	2.7	6.6	Silicone	1.22		A45	Black	-59	+204	6
1090-SI	Emerson & Cuming	0.54	4.1	Epoxy resin syntactic foam	0.78	0.4 (24 hour immersion)	D78		-73	+107	6
3050	Emerson & Cuming	0.40	9.5	Epoxy resin	1.55	0.2 (24 hour immersion)	D88			+125	
EP-3	Emerson & Cuming			Two part epoxy resin			D80	Clear	-55	+120	6
IC-2	Emerson & Cuming			Two component urethane			A80	Clear	-55	+120	6
93-500	DOW	3.0	3.5	Silicone	1.08	< 0.10 (7 day immersion	A46	Clear	-65	+200	12
XR-63-489	DOW	3.0	3.5	Two part silicone	1.05	< 1.5 (7 day immersion)	A35	Clear	-55	+150	12
Sylgard-182	DOW	3.0	3.5	Two part silicone	1.05	0.1 (7 day immersion)	A40	Clear	-65	+200	12
Sylgard-184	DOW	3.0	3.5	Two part silicone	1.05	0.1 (7 day immersion)	A35	Clear	-65	+200	6
Sylgard-186	DOW			Two part silicone	1.12	0.1 (7 day immersion)	A32	Translucent	-65	+250	6
RTV-3140	DOW		2.9	One part silicone	1.06	0.4 (7 day immersion)	A21	Clear	-65	+250	6
RTV-3145	DOW		4.0	One part silicone	1.12	0.4 (7 day immersion)	A33	Gray	-65	+250	6
K230	CONAP		5.0	Two part epoxy	~1.4	0.37 (24 hour immersion)	D65-70	Clear			12
CE-1155	CONAP			Two part solvent-based polyurethane			Sward 70	Clear	-130		12
Epon 828-Versamid 140 50% - 50%	Shell Gen Mills			Two part epoxy			Rockwell M 80				
Solithane 113	Thiokol			Urethane prepolymer	1.07	~0.2 (24 hour immersion)	A-35 to D-60	Clear		+121	
Humiseal 1B12	CTC			One part, 20% solids acrylic	1.05	0.18 (24 hour immersion			-59	+138	12
2# Custom Foam 6-1104	Rogers Foam		0.83	Polyester-Polyurethane				Black			
Uralane 8267	Furane			One component urethane				Clear			6
B-6-640-1	Westinghouse							Red			<12

*For dielectric constant of 3.00, the test frequency is 100 kHz.

Table 4 (continued)
Physical and Electrical Properties of Some Commonly Used Encapsulants

Material	Dielectric Constant	Dissipation Factor	Test Frequency	Dielectric Strength, Volts/mil	Arc Resistance Seconds	Surface Resistivity ohm-cm	Volume Resistivity ohm-cm
XR-5192	4.62	3.1	100 Hz	276	168		1.5×10^{13}
Scotchcast 235	5.2	0.05	100 Hz	325			1×10^{15}
Scotchcast 281	4.9	0.05	100 Hz	375			$>1 \times 10^{14}$
Scotchcast 3	3.3	0.005	100 Hz	300			$>1 \times 10^{15}$
RTV-11	3.6	0.019	60 Hz	500	≥ 100	$\sim 10^{15}$	6.0×10^{14}
RTV-60	3.7	0.020	60 Hz	500	≥ 100	$\sim 10^{15}$	1.3×10^{14}
RTV-602	3.0	0.001	60 Hz	500	≥ 100	$\sim 10^{15}$	1.0×10^{14}
RTV-615	3.0	0.001	60 Hz	500	≥ 100	$\sim 10^{15}$	1.0×10^{15}
RTV-616	3.0	0.001	60 Hz	500	≥ 100	$\sim 10^{15}$	1.0×10^{15}
1090-SI	3.7 3.1 2.9	0.02 0.01 0.01	60 Hz 1 kHz 1 MHz	375			1×10^{13}
3050	4.4 4.2 3.9	0.01 0.02 0.04	60 Hz 1 kHz 1 MHz	400			1×10^{14}
EP-3	4.4	0.006	1 kHz	400			10^{13} Ω/square
IC-2	5.0 5.0	0.04 0.04	60 Hz 100 MHz	>400			$>1 \times 10^{12}$
93-500	2.75 2.73	0.0011 0.0013	100 Hz 100 kHz	570			6.9×10^{13}
XR-63-489	2.88 2.88	0.002 0.002	100 Hz 10 kHz	500	115	3.6×10^{14}	1×10^{14}
Sylgard-182	2.70 2.70	0.001 0.001	100 Hz 1 MHz	550	115		2.0×10^{14}
Sylgard-184	2.75 2.75	0.001 0.001	100 Hz 1 MHz	550	115		1.0×10^{14}
Sylgard-186	3.01 3.00	0.0009 0.001	100 Hz 1 MHz*	575		$>7 \times 10^{16}$	2×10^{15}
RTV-3140	2.64 2.63	0.0016 0.0006	100 Hz 1 MHz	500	50		5×10^{14}
RTV-3145	2.81 2.78	0.0015 0.0028	100 Hz 1 MHz	600	50		5.0×10^{14}
K230	3.35	0.03	1 MHz	2000 (5 mil film)		1.25×10^{14}	1×10^{14}
CE-1155	3.50 3.43	0.0142 0.0138	100 Hz 1 kHz	3000 (2 mil film) 1045 (22 mil film)		5.66×10^{14}	1.18×10^{16}
Epon 828-Versamid 140 50% - 50%	3.23 3.19 2.99	0.0036 0.0070 0.019	60 Hz 1 kHz 1 MHz			5.5×10^{15}	1.22×10^{16}
Solithane 113	2.8-5.0	0.014-0.162	1 kHz @ 80°F	340-512		1.5×10^{15}	7×10^{12} to
	4.5-5.1	0.006-0.079	1 kHz @ 185°F				3.6×10^{14}
Humiseal 1B12 2# Custom Foam	2.8 97% voids intercon-necting cells	0.01	1 MHz	6000V. (MIL-I-46058B)			2.5×10^{14}
Uralane 8267	4.4 3.6	0.049 0.053	1 kHz 1 MHz	2500 (3 mil film)	149		3.0×10^{12}
B-6-640-1				1200 (5 mil film)	126	2×10^{13}	

Table 5
Mechanical Properties of Some Commonly Used Encapsulants

Material	Tensile Strength (kpsi.)	Tensile Elongation, %	Pot Life, hours	Viscosity, Poises	Principal Characteristics
XR-5192	0.995	75			High arc and track resistance
Scotchcast 235	1.3	75	0.25	15	Low viscosity, permanent flexibility
Scotchcast 281	2.1	45	0.3	480	Permanent flexibility, high temp. stability
Scotchcast 3	4.4	1.8	0.3	16	Lowest viscosity, excellent electrical properties
RTV-11	0.35	180	1-6	120	Flexible
RTV-60	0.80	130	1-5	500	Flexible, high temperature
RTV-602	0.10	200	0.5-8	12	Transparent
RTV-615	0.925	150	~4	40	Transparent, high temperature
RTV-616	0.925	125	~4	90	High temperature
1090-SI				18	Low density
3050				5	Low viscosity
EP-3			6	2.4	Surface coating, good mechanical and water resistance
IC-2		400		4.0	Surface coating, good mechanical and water resistance, high temperature
93-500	0.790	110	1	80	Low weight loss in hard vacuum
XR-63-489	0.90	100	8	50	Transparent, flexible, for laminating glass
Sylgard-182	0.90	100	8	30	Low viscosity, low cure shrinkage, wide temperature range
Sylgard-184	0.90	100	2	30	Low viscosity, low cure shrinkage, wide temperature range
Sylgard-186	0.70	420	2	450	High strength, wide temperature range
RTV-3140	0.30	350		350	Clear conformal coating, no acetic acid evolved during cure
RTV-3145	0.70	675			Clear, high strength, noncorrosive, wide temperature range
K230	2.0		1-1.5		Clear epoxy, kit form
CE-1155			6	.72	Coating with good moisture and abrasion resistance
Epon 828-Versamid 140 50% - 50%	8.3	3.9 (?)		~160	
Solithane 113	0.16-3.2	60-120	0.3-8	200	Versatile, soft to extremely rigid depending on catalyst used
Humiseal 1B12				0.3 stokes	Low viscosity coating
2# Custom Foam 6-1104					Excellent vibration and shock protection
Uralane 8267				1.5-3.0	Repairable, solder-through, transparent coating
B-6-640-1			12		Tough, resilent nontracking surface coating

CIRCUIT BOARDS

The construction of most small, high-voltage power supplies used in space applications involves the use of circuit boards. The most popular board materials are epoxy impregnated fiberglass, types G-10 and G-11. The latter is apparently slightly superior.

Data for voltage breakdowns between adjacent conductors on circuit boards seem to be unavailable,* so a simple breakdown test was performed at GSFC. A test circuit board was constructed using the same techniques employed for space-rated boards. The etched circuit pattern consisted of several 4-inch straight, parallel conductors spaced 0.5 mm, 1.0 mm, and 2.5 mm apart. Voltages were applied to the electrodes inside a vacuum bell jar via insulated wires and a vacuum feedthrough from an external high-voltage power supply. A cathode ray oscilloscope (CRO) in series with the ground return lead was employed for monitoring breakdown, leakage, and corona currents. Sensitivity was such that a current as low as 10^{-9} A could be readily measured. Pressure was $\sim 2 \times 10^{-7}$ torr.

Test results indicate that an uncoated board fabricated of G-11 material is corona free with applied voltages and circuit element spacings such that the ratio: volts applied/spacing = 10 kV/mm.* This does not imply that 100 kV could be successfully applied to electrodes separated 10 mm apart, however, due to high field emission at the sharp edges of the conductors. A value of ~20 kV appears to be the practical limit for uncoated boards with reasonable (~1 cm) conductor spacing. Results of tests conducted with the same board after coating with Solithane 113 indicate that ~15 kV/mm is an upper limit for coated boards. Above this value, random current spikes of up to 5×10^{-7} A were observed, although no catastrophic breakdowns occurred. At 40 kV/mm (20 kV, 0.5 mm), a gradually increasing direct current of $\sim 2 \times 10^{-8}$ A was noted. This was undoubtedly caused by nonuniform leakage currents causing localized heating of the Solithane 113 coating.

Figure 26 is a plot of corona onset voltage versus pressure for the same (uncoated) circuit board described above. These curves can shift to much lower voltages when fingerprint contamination is present. This is readily understandable on the basis of the resistance versus humidity curves of Figure 27. Note that surface resistivities can shift by over two orders of magnitude, illustrating the importance of cleanliness during handling procedures. These curves also suggest that drying of circuit boards in a hard

---

*Measurements made by R. S. Bever, Private Communication, GSFC, August 1973, indicate a flashover value of about 2 kV/mm at 1 atmosphere of ordinary air. The boards tested were not thoroughly outgassed; however, this discrepancy emphasizes the importance of adsorbed water vapor in determining surface flashover voltages.

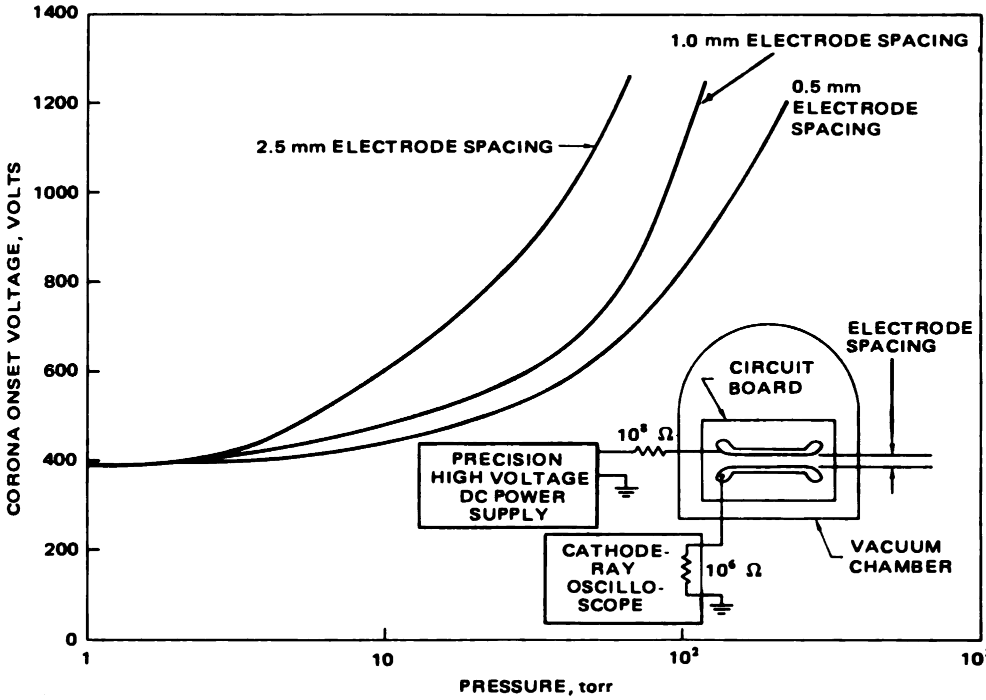

Figure 26. Corona Onset Voltage for Parallel Conductors on G-11 Circuit Board.

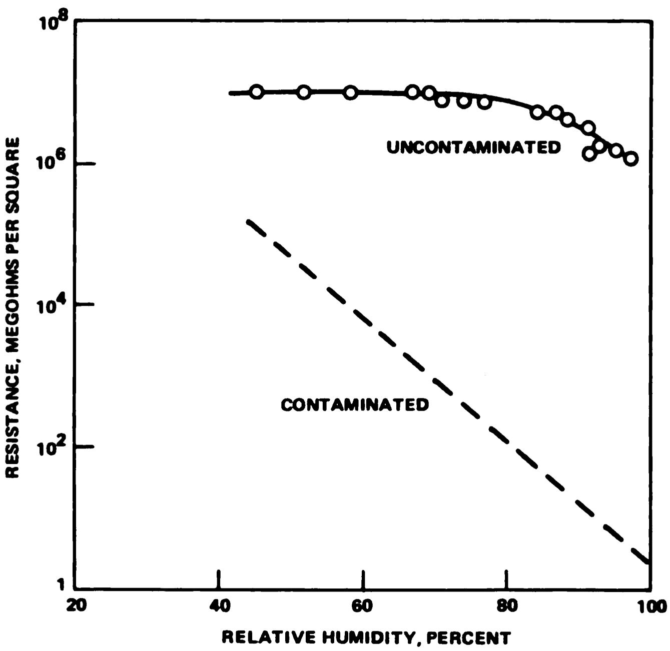

Figure 27. Surface Resistance of Epoxy Resin Fiberglass Laminated Board as Affected by Fingerprint Contamination When Exposed to Air at High Humidity.

vacuum just prior to conformal coating is a desirable procedure. Various mechanical, physical, and electrical properties for circuit board materials are included in Table 6. Table 7 is a listing of properties of some common coating materials (Reference 19).

DEPRESSURIZATION AND OUTGASSING

Unpotted power supplies are generally built with the electronic components mounted inside a metal box. (See Reference 20 for discussion of Outgassing and Pressure.) A question of practical importance involves the amount of perforation of the box required for reasonably fast depressurization to assure that low enough pressures will exist prior to supply turn-on. From simple effusion theory it can be shown that the pressure inside the box, with zero outside pressure, is

$$p(t) = p(o)\, e^{-\left(\frac{\bar{v} A t}{4V}\right)}$$

where $p(o)$ is the initial pressure in the box at $t = o$,
A is the total area of the perforations,
t is the time,
V is the volume of the box,
$\bar{v}$ is the mean molecular speed; that is,

$$\bar{v} = \sqrt{\frac{8\,kT}{\pi m}}$$

in which

k is the Boltzmann constant,
T is the absolute temperature, and
m is the mass of a gas molecule.

For nitrogen at room temperature,

$$\bar{v} \approx 4.6 \times 10^4 \text{ cm/s}.$$

A useful guide is derived by noticing that the time constant in the above exponential becomes

$$\tau \approx 0.1\ V/A$$

when V is measured in liters,
A is measured in cm^2,
T is room temperature ($T = 20°C$), and
the gas is air or N_2.

This rule, coupled with use of Figure 28, can simplify depressurization time calculations. As an example, a 10-cm-radius sphere with a 1-cm^2 opening has a time constant of ~0.4 s. Using Figure 28, one finds immediately

Table 6
Properties of Laminated and Reinforced Plastics

NEMA Grade	Min. Flexural Str., 1/16", psi LW (X10³)	CW (X10³)	Min. Izod Impact Str., ft-lb/in notch, edge LW	CW	Min. Bond Str., lbs.	Water Abs., Max., 1/16" %	Min. Diel. Str., § kv.	Max Diel. Const., 1 MHz 1/32" or more	Thermal Coeff. of Exp. cm/cm °C X10⁻⁴	Max Diss. Factor, 1 MHz 1/32" or more	Min. Arc Resist., secs.	Tensile Str., psi LW (X10³)	CW (X10³)
X	25	22	0.55	0.50	700	6.00						20	16
XP	13	11				3.60	40					12	9
XPC	10	8				5.50						10.5	8.5
XX	15	14	0.40	0.35	80	2.00	40	5.5		0.045		16	13
XXP	14	12			0	1.80	60	5.0		0.040		11	8.5
XXX	13.5	11.8	0.40	0.35	950	1.40	50	5.3		0.038		15	12
XXXP	12	10.5				1.00	60	4.6		0.035		12.4	9.5
XXXPC	12	10.5				0.75	60	4.6		0.035			
ES-1	13.5	13.5	0.25	0.22		2.50							
ES-2			0.25	0.22									
ES-3	13.5	13.5	0.25	0.22		2.50							
C	17	16	2.10	1.90	1800	4.40	15					10	8
CE	17	14	1.60	1.40	1800	2.20	35					9	7
L	15	14	1.35	1.10	1600	2.50	15					13	9
LE	15	13.5	1.25	1.00	1600	1.95	40	5.8		0.055		12	8.5
A	13	11	0.60	0.60	700	1.50	5					10	8
AA	16	14	3.60	3.00	1800	3.00						12	10
G-3	20	18	6.5	5.5	850	2.70						23	20
G-5	50	40	7.0 (to 1/2")	5.5	1570	2.70	23	7.8		0.020	180	37	30
G-7	20	18	6.5	5.5	650	0.55	32	4.2		0.003	180	23	18.5
G-9	60	40	13.0	8.0	1700	0.80	60	7.5		0.018	180	40	25
G-10	60	50	7.0	5.5	2000	0.25	45	5.2		0.025	128	35	30
G-11	60	50	7.0	5.5	1600	0.25	45	5.2		0.025	115	35	30
N-1	10	9.5	3.0	2.0	1000	0.60	60	3.9		0.038		8.5	8
FR-2	12	10.5				0.75	60	4.6		0.035		12.4	9.5
FR-3	20	16				0.65	60	4.6		0.035		12	9
FR-4	60	50	7.0	5.5	2000	0.25	45	5.2	1.5	0.025	128	35	30
FR-5	60	50	7.0	5.5	1600	0.25	45	5.2	1.5	0.025	128	35	30
GPO-1	18	18	8.0	8.0	850	1.00	40	4.3		0.03	100	12	10
GPO-2	18	18	8.0	8.0	850	0.9	40				100	10	9
Dialyte ‖	40						35	4.0	0.13	0.008	>60		
	50						35	4.8	0.1	0.020	180		
Polyimide ‖													
Fluorglas ‖	15	11				0.05		2.54	0.1	0.0008	180	19	15
Rexolite ‖	11.5	11.5	0.3			0.05		2.53	0.7	0.00012		7	7
AL300 ‖	71	55	19	18	2000	<0.25		4.0	0.1	0.02	180	40	40

All tests conducted in accordance with applicable NEMA and/or ASTM standards.

* See NEMA Pub. No. LI 1-1971, Standards Publication for Industrial Laminated Thermosetting Products, regarding test methods, conditions, etc.

† Usually made with these resins. These grades are engraving stock.

‡ These are only typical values obtained from a number of sources and should not be used in establishing specifications or standards–consult manufacturers.

§ Parallel to lamination, Step-by-Step, 1/16" thick.

‖ Atlantic Laminates Co. data

Table 6 (continued)
Properties of Laminated and Reinforced Plastics

NEMA Grade	Compr. Str., psi Flat (X10³)	Compr. Str., psi Edge (X10³)	Rockwell Hardness M Scale	Sp. Gr.	Diel. Str., Perp. to Lam., vpm Short time	Diel. Str., Perp. to Lam., vpm Step by Step	Thick. Range Inch min.	Thick. Range Inch max.	Base Material	Volume Resistivity ohm-cm	Resin	Surface Resistance, Megohms (BS1137, Appendix H)
X	36	19	110	1.36	700	500	.010	2	Paper		Phen.	
XP	25		95	1.33	650	450	.010	1/4	Paper		Phen.	
XPC	22		75		600	425	1/32	1/4	Paper		Phen.	
XX	34	23	105	1.34	700	500	.010	2	Paper		Phen.	
XXP	25		100	1.32	700	500	.015	1/4	Paper		Phen.	
XXX	32	25.5	110	1.32	650	450	.015	2	Paper		Phen.	
XXXP	25		105	1.30	650	450	.015	1/4	Paper		Phen.	
XXXPC	25		105	1.31	650	450	1/32	3/16	Paper		Phen.	
ES-1				1.58			3/64	1/4			Mel.†	
ES-2				1.46			.085	1/4			Phen.†	
ES-3				1.48			3/64	1/4			Mel.†	
C	37	23.5	103	1.36	150		1/32	10	Cotton		Phen.	
CE	39	24.5	105	1.33	500	300	1/32	2	Cotton		Phen.	
L	35	23.5	105	1.35	150		.010	2	Cotton		Phen.	
LE	37	25	105	1.33	500	300	.015	2	Cotton		Phen.	
A	40	17	111	1.72	225	135	.025	2	Asb. Paper		Phen.	
AA	38	21	103	1.70			1/16	2	Asb. Fabric		Phen.	
G-3	50	17.5	100	1.65	700	500	.010	2	Cont. Gl.		Phen.	
G-5	70	25	120	1.90	350	220	.010	3 1/2	Cont. Gl.		Mel.	
G-7	45	14	100	1.68	400	350	.010	2	Cont. Gl.		Sil.	
G-9	65			1.90	400	350			Cont. Gl.		Mel.	
G-10	70	30	110	1.75	700	500	.010	1	Cont. Gl.	>10¹²	Epoxy	>10⁴
G-11	70	30	110	1.75	700	500	.010	1	Cont. Gl.	>10¹²	Epoxy	>10⁴
N-1	28		105	1.15	600	450	.010	1	Nylon		Phen.	
FR-2	25		105	1.30	650	450	.030	1/4	Paper		Phen.	
FR-3	28			1.45	600	500	1/32	1/4	Paper		Epoxy	
FR-4	70	30	110	1.75	700	500	.010	1	Cont. Gl.	>10¹²	Epoxy	>10⁴
FR-5	70	30	110	1.75	700	500	.010	1	Cont. Gl.	>10¹²	Epoxy	>10⁴
GPO-1	30	20	100	1.5-1.9	400		1/16	2	Gl. Mat		Polyes.	
GPO-2	30	20	100	1.5-1.9			1/16	2	Gl. Mat		Polyes.	
Dialyte‖					750				Gl.	>5X10¹⁴	Polyes.	>9X10⁸
					750				Gl.	>6X10¹⁰	Polyimide	>6X10⁴
Polyimide‖												
Fluorglas‖					45kv/1/16"					>10¹²	PTFE	>10⁴
Rexolite‖				1.05	30kv/1/16"					>10¹⁶	Styrene Copolymer	>10⁸
AL300‖	77	35	115		1000				Glass	>10¹⁴	Polyimide	12X10⁵

All tests conducted in accordance with applicable NEMA and/or ASTM standards.

* See NEMA Pub. No. LI 1-1971, Standards Publication for Industrial Laminated Thermosetting Products, regarding test methods, conditions, etc.

† Usually made with these resins. These grades are engraving stock.

‡ These are only typical values obtained from a number of sources and should not be used in establishing specifications or standards - consult manufacturers.

§ Parallel to lamination, Step-by-Step, 1/16" thick.

‖ Atlantic Laminates Co. data

Table 7
Typical Properties of Common Coating Materials

Base polymer	Surface resistivity	Relative permittivity (60 Hz-1 MHz)	Dissipation factor (60 Hz-1 MHz)	Solderability	Resistance to humidity	Resistance to chemicals
	Ω					
alkyd	10^{12}	3-9	0-505	fair	excellent	good
Acrilan	10^{13}	4-0	0-015	good	good	fair
epoxide (room-temp. cure)	10^{13}	3-6	0-020	fair	good	good
epoxide (elevated temp. cure)	10^{14}	4-0	0-010	poor	excellent	excellent
polyurethane	10^{11}	4-5	0-025	fair	good	good

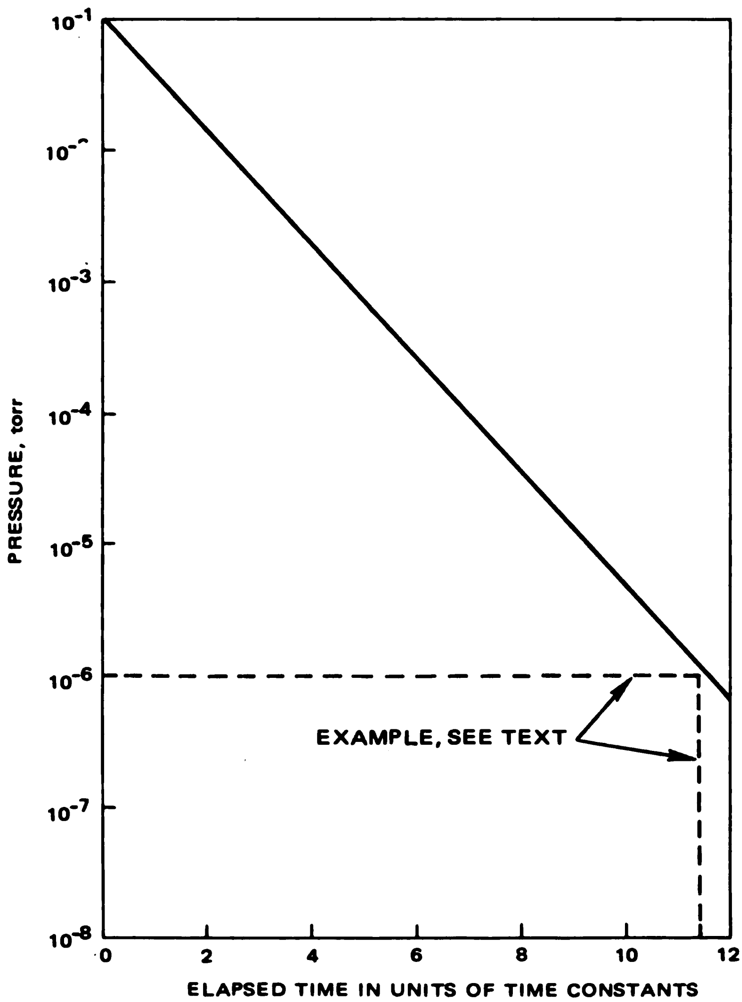

Figure 28. Pressure vs. Time (Simple Effusion Theory, see text).

that the pressure will drop from 10^{-1} to 10^{-6} torr in about 11 time constants, or about 4.5 s. Of course, material- and temperature-dependent outgassing of the surfaces inside the container can considerably lengthen the depressurization time as illustrated in Figures 29, 30, and 31 (Reference 21).

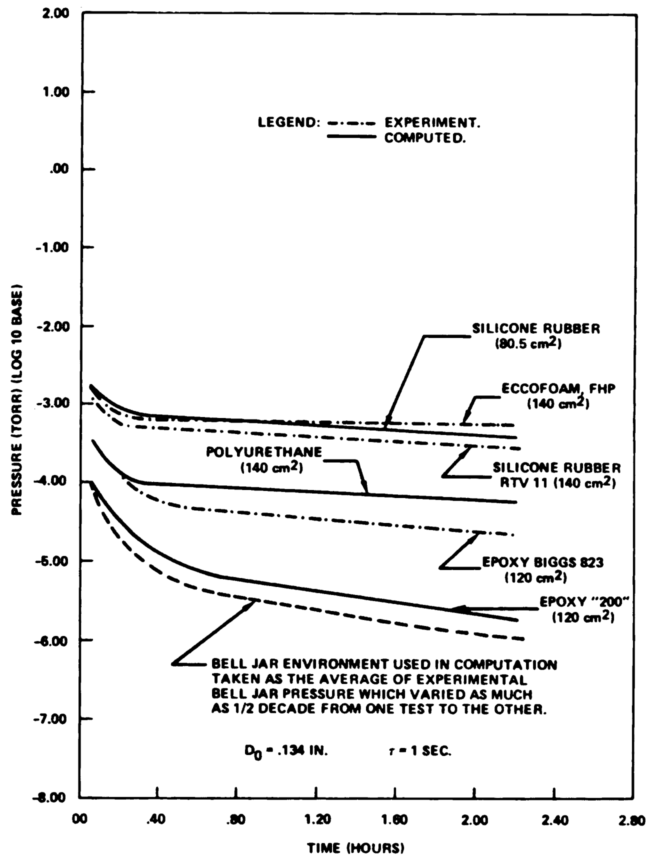

Figure 29. Comparison of Experimental and Computed Results for a 1-liter Compartment with Orifice Diameter 0.134 in., τ = 1.0 s, Ambient Temperature. (Reference 21)

A handy design figure is to provide a V/A = 10,000 cm to achieve approximately a one second time constant. Here the value of V must be in cubic centimeters and the value of A must be in square centimeters. This V/A value should be increased by a factor of 2 or 3 if the outgassing passages are labyrinthine.

As described in Reference 21 and illustrated in Figures 29, 30, and 31, after the initial depressurization period of about one hour, the pressure decreases much more slowly with a combination of an exponential time dependence (first order surface desorption), a $t^{-1/2}$ dependence (diffusive processes in outgassing of elastomers or outgassing of glass), and a t^{-1} dependence due to outgassing of metals. The net results for a 1-liter glass cylinder containing a sample of RTV-11 was an approximately exponential decay with a 3-day outgassing time constant. Note

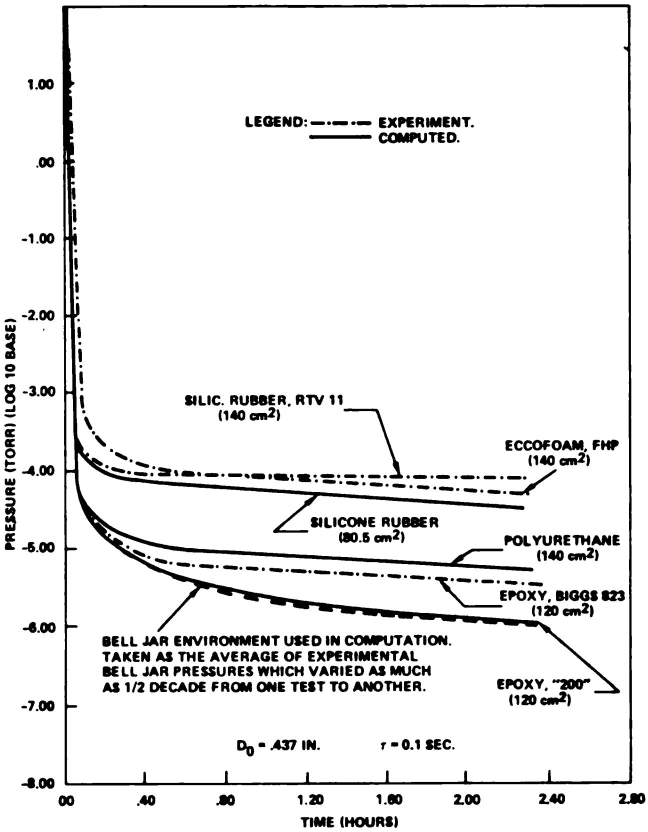

Figure 30. Comparison of Experimental and Computed Results for a 1-liter Compartment with Orifice Diameter 0.437 in., τ = 0.1 s, Ambient Temperature. (Reference 21)

that the pressure remained near the corona region for several hours (Figure 31) when the chamber time constant was adjusted to 10 s.

COMPONENT CONSIDERATIONS

Documents, specifications, and lists of component types that have been screened and approved for space flight use are available. Use of these guides does not, however, eliminate all the difficulties which can occur in the final application of these components. The following descriptions illustrate some of these problems.

Resistors

High-voltage resistors used successfully in spacecraft power supplies include Victoreen MOX1125, Caddock MG680, RPC type BBMW, and Caddock MG721.

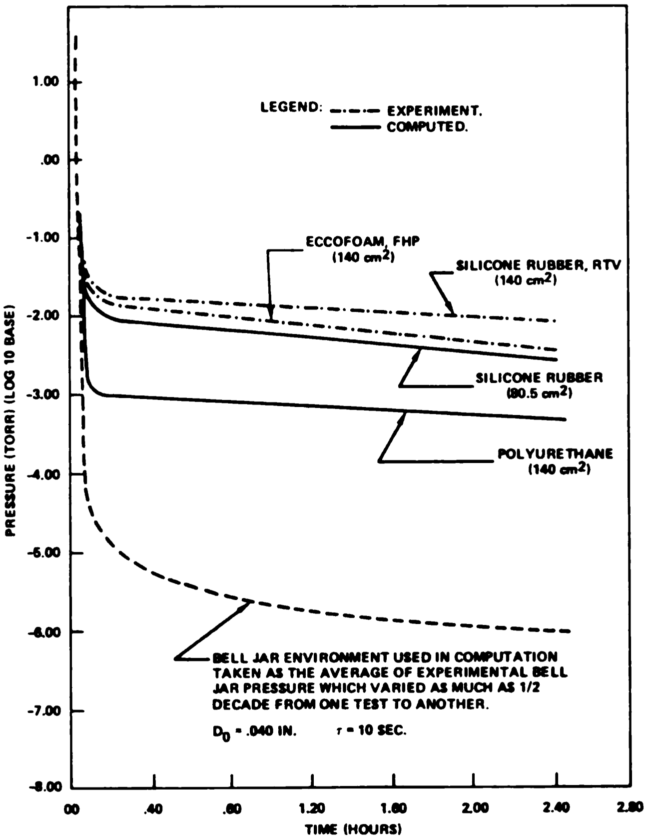

Figure 31. Comparison of Experimental and Computed Results for a 1-liter Compartment with Orifice Diameter 0.040 in., τ = 10 s, Ambient Temperature. (Reference 21)

One well known difficulty experienced with high-voltage film resistors involves corona developed in gases trapped in hollow ceramic cores. Another less known (suspected) problem involves the inductance caused by the helical form of the resistance element. Current surges through such elements due to sparking elsewhere in the circuit may cause resistor failure due to the resonance action of the inductance with circuit capacitance. Where such a failure mechanism is suspected, the serpentine form (noninductive) film resistors manufactured by Caddock (Figure 32) may provide a solution.

An unusual problem encountered during cleaning operations involved MOX1125 resistors. It was found that the cleaning solvent employed, trichlorethylene, dissolved the blue coating material on the resistor bodies.

Diodes

Diodes favored by the designers interviewed include 1N649's, 1N4586's, Semtech SFM-70 7KV, SFM-25 2.5 kV, Semtech 1N5184, and Microsemiconductor MC002.

One problem noted with plastic molded diodes is the slow diffusion of moisture onto the diode junction over a period of years.

The designer should be wary also of gas leakage from glass-cased diodes. This can lead to corona inside potted modules. Two problems have developed with the microminiature epoxy bead diodes. One is a quality control problem having to do with the proper alignment of the ribbon leads during insertion into the bead. The other problem involves breakage of junction leads due to thermal expansion at temperature extremes.

Capacitors

Capacitors used successfully by the designers interviewed include high voltage ceramic discs manufactured to several EIA specified dielectric formulations including X5P; X5R; W5R; and Z5U. Manufacturers include Centralab, Erie, and Sprague.

Difficulties have been experienced with porous epoxy coated disc ceramic capacitors. Standard varieties are supplied by the manufacturer with a wax impregnated durez coating which prevents adhesion of encapsulants. The wax coating is difficult to remove, but if uncoated units were employed it was found that corona problems developed. In one case, capacitors used for filtering proved self-defeating because they were themselves sources of noise due to corona. Coatings such as the Erie "Jet Seal" hard epoxy coating and the Centralab blue Hysol XDK-R13 epoxy coating do not exhibit this undesirable behavior.

An unusual problem involves high current degradation in Mylar capacitors. Apparently, high surge currents can evaporate some of the metal coating on the Mylar film, resulting in reduced capacitance. If used, this type of capacitor should not be allowed to become short-circuited or otherwise subjected to large currents.

Another problem which designers have encountered is the very large variation of capacitance with applied voltage and with temperature exhibited by the X5U; W5R; and Z5U dielectric formulations for ceramic discs. Some typical capacitance curves which illustrate these effects are given in Figures 33 and 34.

The combined effects of high voltage and extreme temperatures can render a Cockroft-Walton multiplier inoperative because of the severe reduction in the capacitance. The obvious solution is to overdesign both in the direction of higher voltage and in the direction of higher capacitance once a dielectric material has been chosen.

Connectors

The problem of connecting high-voltage power supplies to the spacecraft instruments being powered is far from trivial. Standard or specially fabri-

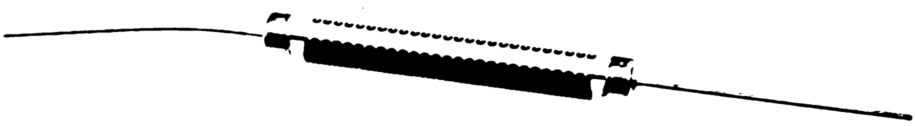

Figure 32. Caddock Serpentine Film Resistor.

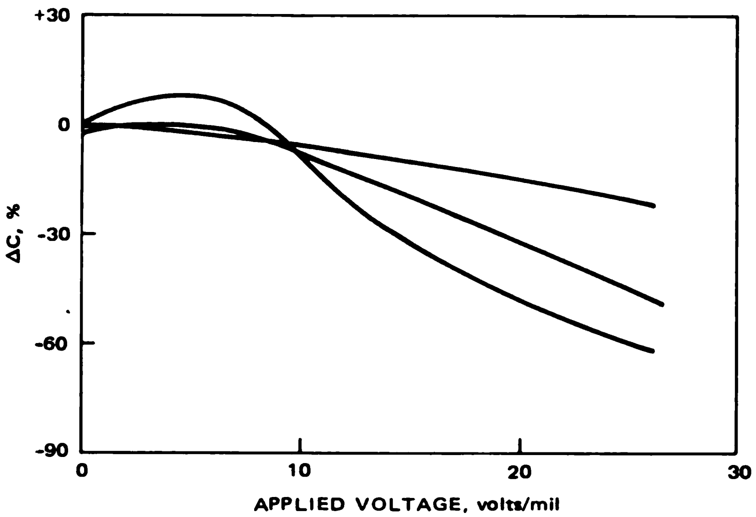

Figure 33. Capacitance Variation with Voltage (ceramic dielectric).

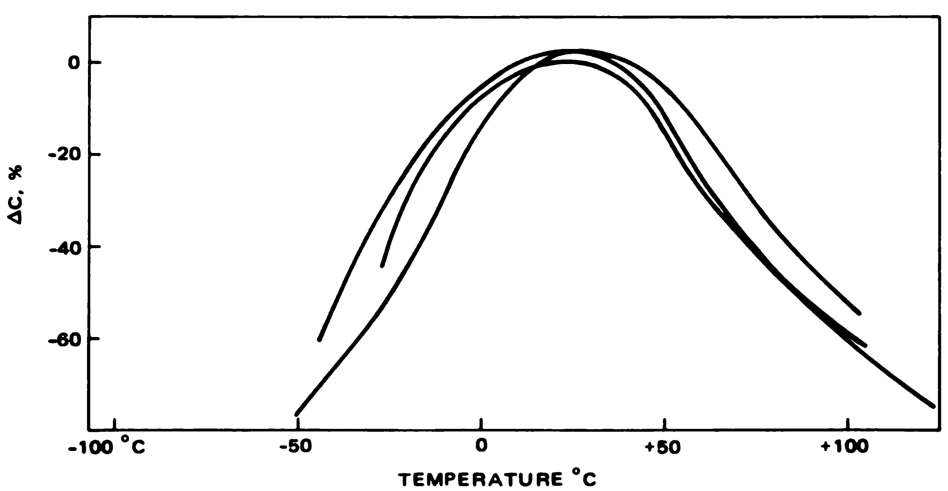

Figure 34. Capacitance Variation with Temperature (ceramic dielectric) EIA-Z5U formulation.

cated high-voltage connectors have been used with some success when modified for the space environment; that is, by drilling holes to allow for adequate venting. Usually, however, connectors have been specially designed or designed out of the system entirely in order to avoid corona problems. This leads to difficult and inconvenient assembly and testing.

A new type subminiature (0.25-in. O.D.) connector, Reynolds Industries Series 600, is available for voltages up to 10 kV and any pressure from atmospheric to hard vacuum. The male connector features a diallyl phthalate liner the whole length of the cylindrical wall (Figures 35 and 36). In addition, an O-ring around the base of the pin seals against the center insulator of the female connector. This construction results in long leakage paths and almost total immunity to corona. A sample pair of connectors was tested for one week at GSFC at 10 kV, both polarities, at several pressures from atmospheric to 5×10^{-7} torr. No corona or voltage breakdowns were observed. Designers are urged to consider this type of connector for use in future spacecraft.

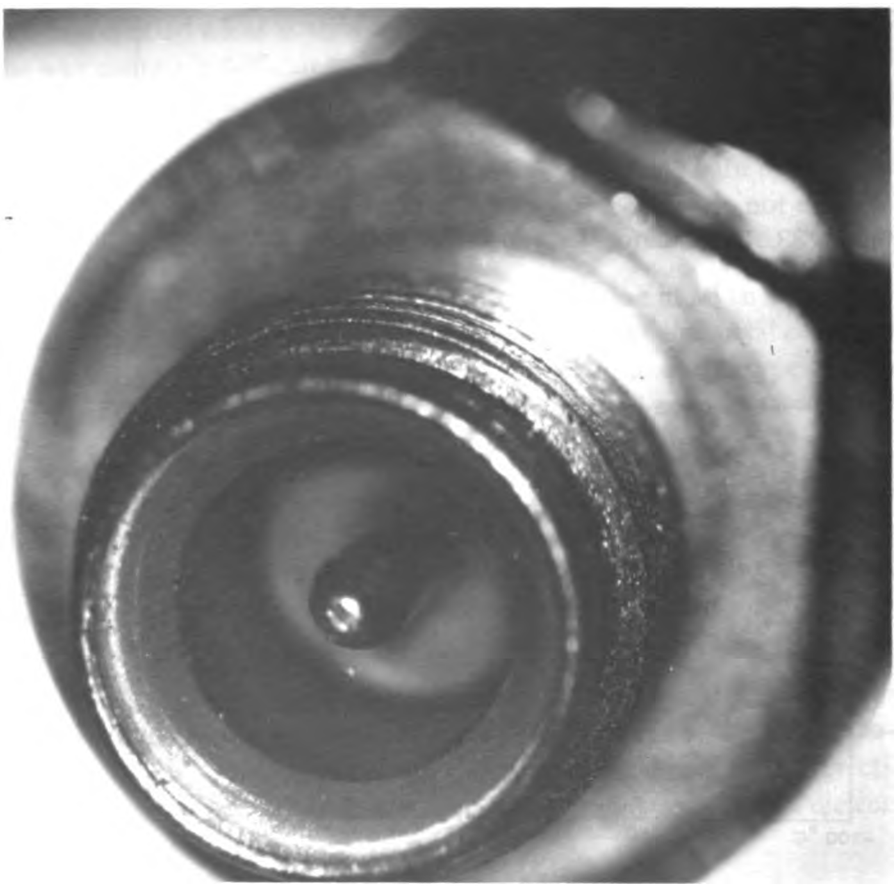

Figure 35. Reynolds High-Voltage Connector.

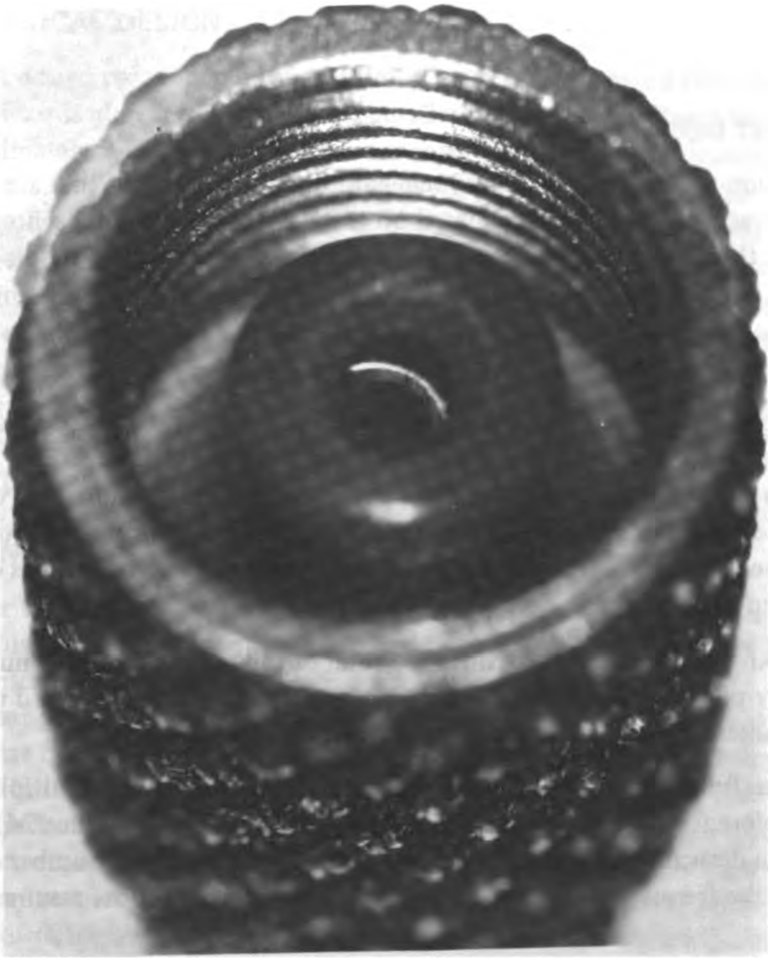

Figure 36. Reynolds High-Voltage Connector.

CURRENT DESIGN PRACTICE

This section presents electrical and mechanical design practices that are currently accepted and that are based on the theories and data presented earlier in this document. Examples of successful power supplies are discussed.

ELECTRICAL DESIGN

Small high-voltage power supplies designed to supply current to spacecraft-borne photomultiplier tubes and particle analyzers have employed the oscillator-Tesla coil (resonant transformer) Cockroft-Walton multiplier combination almost exclusively. The reasons given for not choosing other techniques include considerations of efficiency and the high-voltage ratings of components.

The Cockroft-Walton circuit divides the total output potential into a number of smaller potential increments. Each diode and capacitor is subjected to one of these increments instead of to the total output potential.

Several useful articles relevant to the design of Cockroft-Walton multipliers exist (References 22, 23, and 24). The article by Weiner (Reference 24) includes a derivation of the output voltage as a function of the number of stages n, the frequency f, and the capacitance C. (All capacitors assumed equal):

$$V = n V_{in} \left(1 - \frac{4n^2 + 3n^{-1}}{6fC}\right).$$

The author notes that, for maximum efficiency, the capacitance values should be tapered, the first capacitor in the chain having n times the capacitance of the n*th*. This could mean an important weight and space saving for spacecraft applications where some of the capacitors near the top of the chain would be physically smaller than the ones at the bottom. The article by Rumble (Reference 24) gives a useful summary of all possible voltage multiplier arrangements.

It is well known that when a charged capacitor is connected to an equal but uncharged capacitor, half of the charge transfers to the second capacitor. Also, half of the energy is radiated away from the system and lost. The paper by Mostov et al. (Reference 25) includes design curves and describes techniques for reducing these losses which can be appreciable in the case of the energy transfer to an arc jet or other high power device.

MECHANICAL DESIGN

Current design practice involves the use of epoxy impregnated fiberglass circuit boards almost exclusively for supplies with output voltages below approximately 3 kV. Circuit boards are being used, with modifications, up to about 15 kV. These modifications include potting and conformal coating of high-voltage sections of the circuit boards (front and back), milling slots through boards to lengthen surface breakdown paths, and mounting the components that are subject to high-voltage stress on stand-offs to eliminate surface breakdown problems. Type G-11 board material has been found to be preferable to type G-10 because of increased leakage resistance. Some designers prefer potted cordwood construction for the Cockroft-Walton multiplier section because of space limitations and to reduce problems of surface leakage and tracking.

DESIGN EXAMPLES

In order to illustrate typical successful high-voltage power supply designs as graphically as possible, photographs of actual flight models were obtained. Brief descriptions of the most important, or unusual, features of each power supply accompany the photographs presented. It must be kept in mind that in each case a host of factors besides the electrical requirements entered into the evolution of the final form of the finished unit. These factors include the obvious constraints and requirements such as: specific launch environment (vibration, shock, thermal, pressure), size, weight and efficiency restrictions, time of turn-on, flight duration, required reliability, effects of outgassing and noise on the supply, noise and outgassing cleanliness requirements of other spacecraft experiments, location of supply on the spacecraft, rotation and orbit parameters of the spacecraft, and orbital radiation and charged particle environments. A number of less obvious considerations involving individual component reliability and the extremely difficult multiparameter problem of encapsulation also affected the final results.

An exhaustive discussion of the design examples including all of these factors is beyond the scope of this presentation. More detailed information on the construction, layout of components, choices of components, or encapsulation techniques may be obtained directly from the designers listed in specific examples. Several monographs (see Appendixes and References) that describe general design considerations, construction techniques, and quality control procedures are available.

Design Example 1—~1.5 kV, $-10^\circ < T < +50^\circ C$*

A well filtered (1-mV noise level) Cockroft-Walton multiplier power supply employs circuit board construction (Figures 37 and 38) and encapsulation with an Emerson and Cuming 1090-SI potting compound (shown prior to encapsulation). This material is filled with glass microballoons and has about the same thermal expansion coefficient as aluminum. It has been found to be very effective in eliminating component breakage due to differential expansion at temperature extremes.

Components employed include Erie Corona-Free Jet Seal high-voltage disc ceramic capacitors, teflon-covered wire used in transformer windings, and 1N649 and 1N4586 high-voltage diodes.

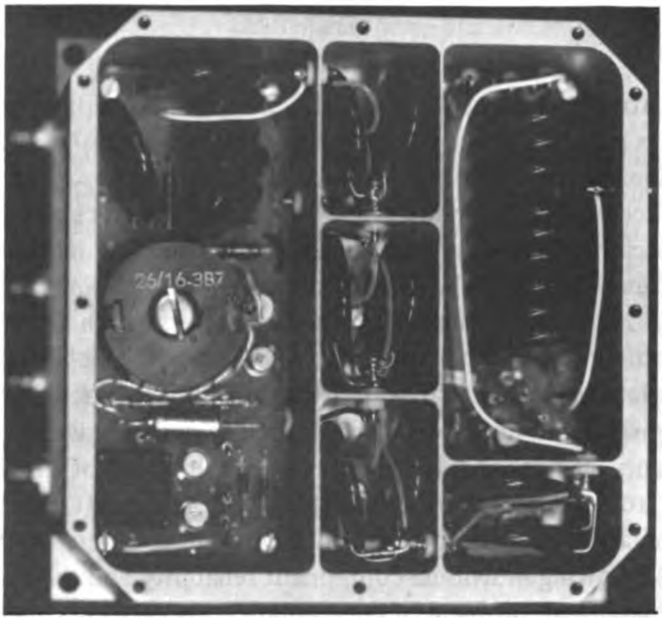

Figure 37. Design Example 1, ~1.5 kV.

A unique feature of the pot core transformer design is the use of partitioned nylon winding bobbins, Figure 39. The integral partitions allow placement of primary and secondary coils side-by-side rather than one on top of the other, eliminating the problem of lead dress. It becomes a simple matter to bring the leads of the primary and secondary, respectively, out opposite sides of the transformer with a partition of nylon completely separating the windings. After completion, the transformers were injection filled with Dow Corning RTV 3140.

---

*F. C. Hallberg, GSFC, private communication.

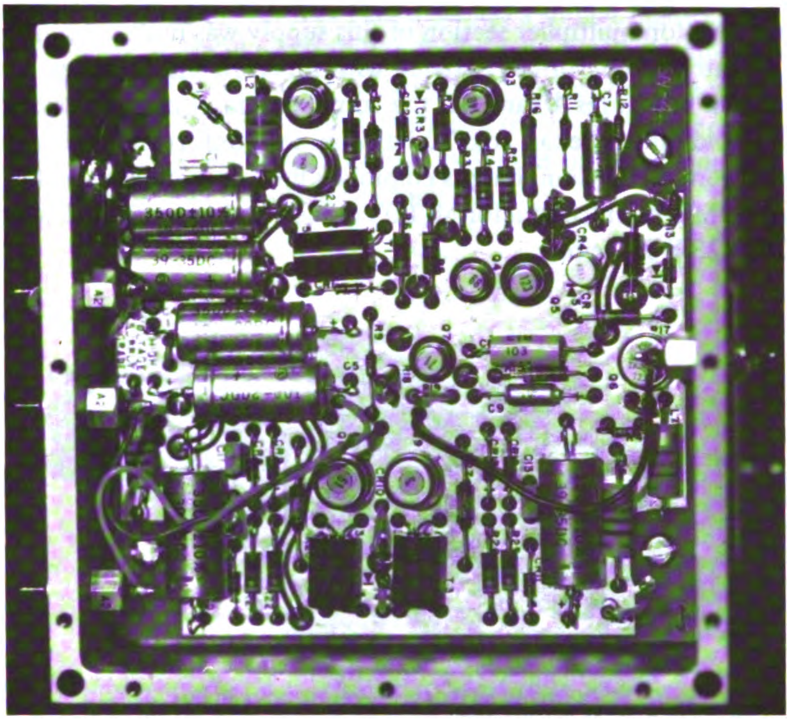

Figure 38. Design Example 1, ~1.5 kV.

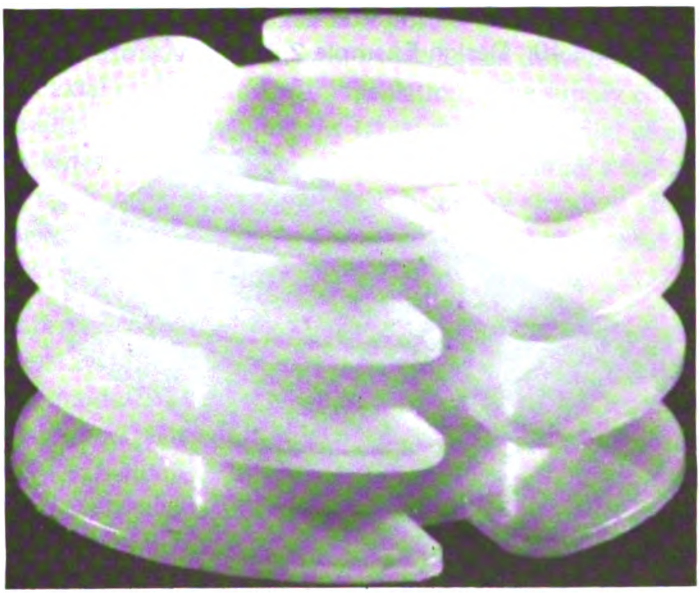

Figure 39. Partitioned Winding Bobbin.

Design Example 2—~1.8 kV*

The Cockroft-Walton multiplier section of this supply was built up on a ceramic substrate and conformally coated with Emerson and Cumings EP-3. As shown in Figures 40 and 41, the completed multiplier was assembled inside a gold plated Lexan box. Other than the conformal coating, no encapsulants were used. Components employed include Victoreen MOX-1125 resistors, Microsemiconductor MC002 diodes, and Monolithic Dielectric type 200R23W capacitors.

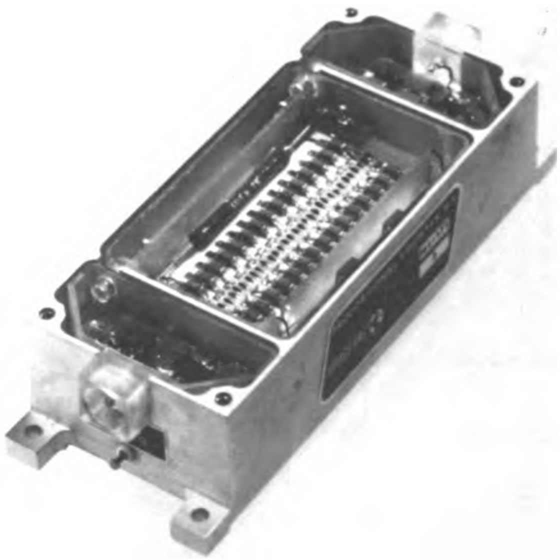

Figure 40. Design Example 2, ~1.8 kV.

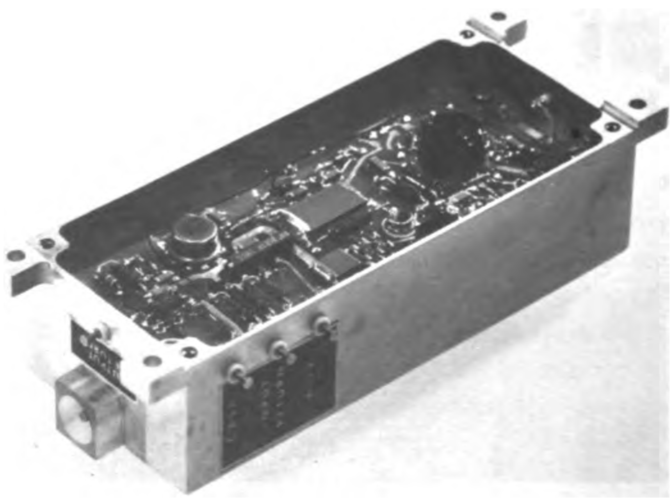

Figure 41. Design Example 2, ~1.8 kV.

*J. H. Trainor, GSFC, private communication.

The 500-volt supply shown in Figure 42 has a similar high-voltage section and illustrates a useful construction technique. Small circuit boards soldered to the mother board are supported against the effects of shock, acceleration, and vibration by an open-cell foam. This material, made by Rogers Foam Corporation, is made of polyester polyurethane and has been used successfully in the space environment.

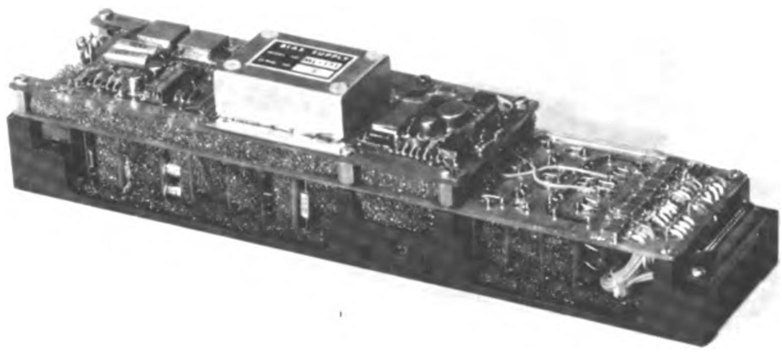

Figure 42. Design Example 2, Use of Open Cell Foam.

Design Example 3—~3.7 kV*

This triangular-shaped supply, Figure 43, developed for the AE spacecraft, generates three voltages selectable by telemetry commands +3700, +3950, and +4200 volts. It features a high-voltage Cockroft-Walton multiplier section built into a gold plated Lexan box potted with DC 93-500. High-voltage leads pass through the box walls inside Lexan dowels. Output leads are Tensolite coaxial cables with H-film insulation. The supply consists of four potted modules: one containing the transformer-multiplier chain, one containing the series current limiter resistors, one containing a voltage reference resistor network, and one containing servo control circuitry. Interbox connections are made with coaxial cable with the shield removed. The multiplier capacitor chain was self supporting prior to potting.

Components employed include Victoreen MOX high voltage resistors, Centralab epoxy coated disk ceramic capacitors, and Semtech type F 25 diodes. The modules are supported by G10 circuit board material etched such that a ground plane is provided beneath the multiplier module. Potting of the modules, including the pot core transformer, was done by pouring at atmospheric pressure and then evacuating to forepump pressures. The transformer was epoxied in place to eliminate bolts and the possibility of attendant trapped gasses.

*J. A. Gillis, GSFC, private communication.

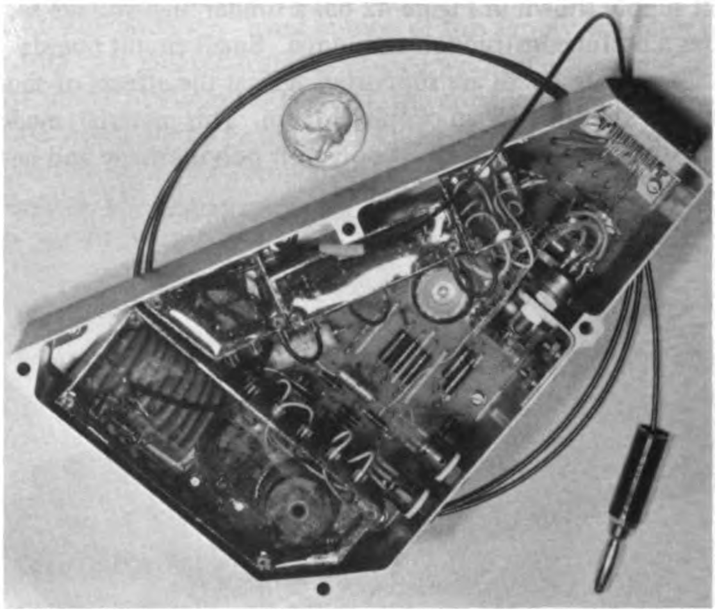

Figure 43. Design Example 3, ~3.7 kV.

Design Example 4—4 kV, 20 μA*

As shown in Figures 44 and 45, this 5-stage Cockroft-Walton supply design incorporated straight-forward circuit board techniques. Components were soldered to an etched G-10 epoxy fiberglass board which was mounted inside a metal box. The components were additionally supported by a conformal coating of Solithane 113. The box was gold plated for thermal control and perforated to allow depressurization to the pressures of orbital altitudes. Teflon tape was applied between layers of windings of the toroidal oscillator transformer, and teflon-covered wire with a 1 kV rating was used for low-voltage circuitry.

Components employed included Centralab blue epoxy coated 6 kV capacitors, Semtech SFM-70 7 kV diodes, and Victoreen solid core, high-voltage resistors. A Reynolds subminiature (0.25 in. O.D.) type 167-2896 10 kV coaxial cable and connector assembly was used to connect the high-voltage supply to the experiment to which it supplied power.

Design Example 5—4 kV†

Figure 46 is a photograph of a unique high-voltage (4-kV) distribution device used to connect several connectors to one power supply. Design requirements were RFI shielding, fast depressurization, absence of outgassing materials, accessibility of the circuit terminations without disruption of experiment integrity, and corona-free operation at pressures as high as

*S. Highley, USNRL, private communication.

†J. T. McChesney, GSFC, private communication.

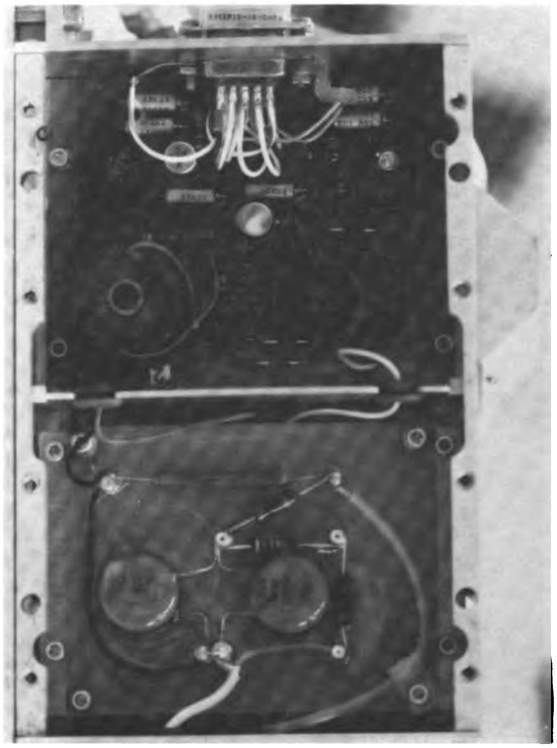

Figure 44. Design Example 4, 4 kV.

6.5×10^{-4} torr. A wire from each detector is soldered into a blind hole in a thick, gold plated, beryllium-copper washer. The washer terminations from several detectors are then clamped in a nut and bolt assembly with hemispherical ends. The assembly is supported inside a metal compartment by corrugated Kel-F stand offs. Kel-F is a fluorocarbon material with excellent electrical properties and good machinability.

Design Example 6—4.5 kV*

The 4500-volt, 10-stage Cockroft-Walton power supply illustrated in Figures 47 and 48 features an unusual construction technique. The high-voltage section is entirely unencapsulated. Instead, spaces for the multiplier components are machined out of blocks of Vespel-1, a tracking resistant polyimide material. Corona paths are confined to seams between the cavities, and surface leakage paths are relatively long. In addition, a resistor-diode current limiting circuit and a current limiting voltage regulator reduce the energy of the discharge should corona develop.

*D. P. Peletier, Johns Hopkins University.-APL, private communication.

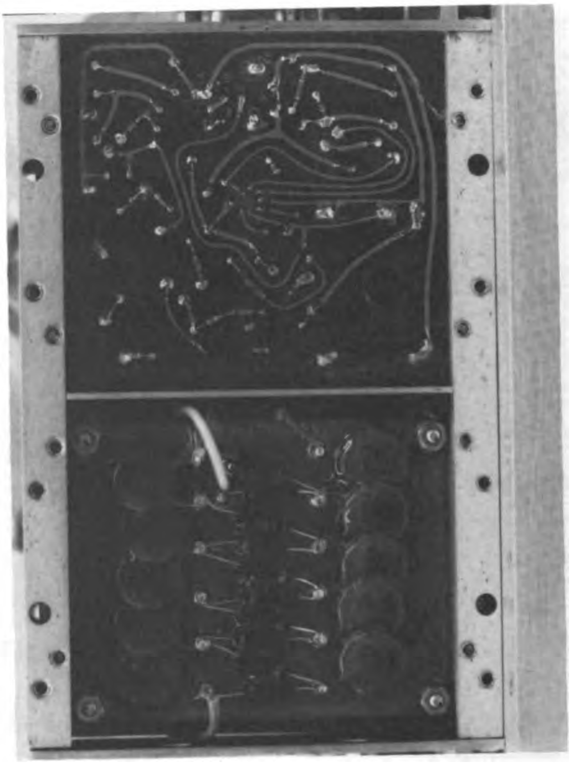

Figure 45. Design Example 4, 4 kV.

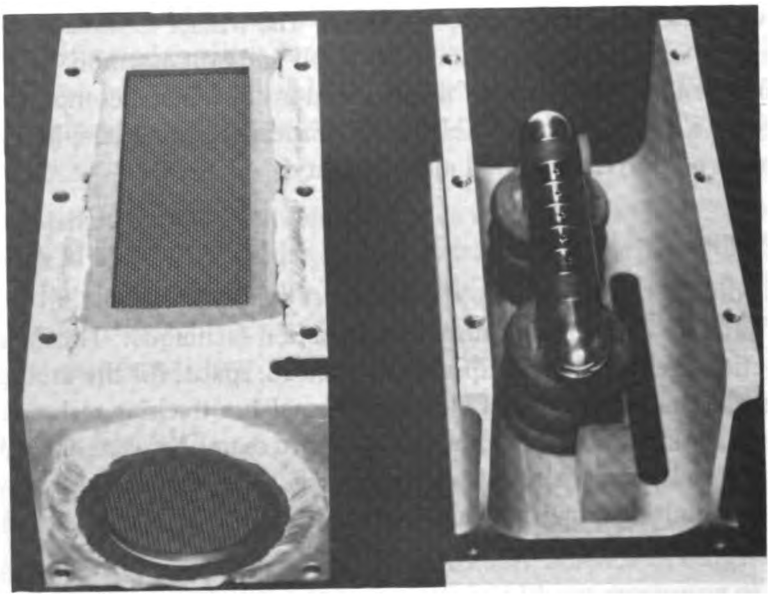

Figure 46. Design Example 5, 4 kV.

Figure 47. Design Example 6, 4.5 kV.

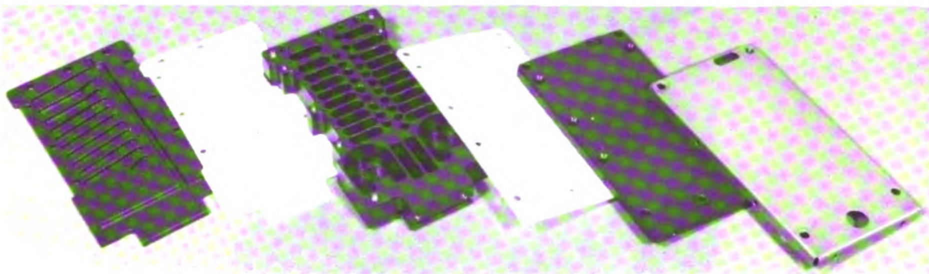

Figure 48. Design Example 6, 4.5 kV.

Components employed include microsemiconductor MH402 diodes, Erie type 808-000-X5RO and 848-026-X5RO capacitors, and Victoreen MOX-400 high-voltage resistors.

Design Example 7—~10 kV*

This power supply shown in Figures 49 and 50, incorporated circuit board construction combined with potting of the Cockroft-Walton diode array and potting of the high-voltage portion of the conductor side of the board as well. The potting compounds employed were GE RTV-615, a two-part clear cuttable compound, and RTV-616 (black) with GE 4153 blue primer, RTV-11 and DC 93-500.

Components employed include Spacetac pot core transformers, G-10 board material, Victoreen MOX1125 high-voltage resistors, Monolithic Dielectric 2-kV ceramic capacitors, and Semicon Corporation #5040J 4-kV diodes.

During construction of several versions of this basic design, breakdowns were observed in voids under the conformally coated high-voltage capacitors. Shimming of these components up 30 mils from the circuit board surface allowed sufficient space to permit flow of the coating material underneath,

*J. Caine, University of Maryland, private communication.

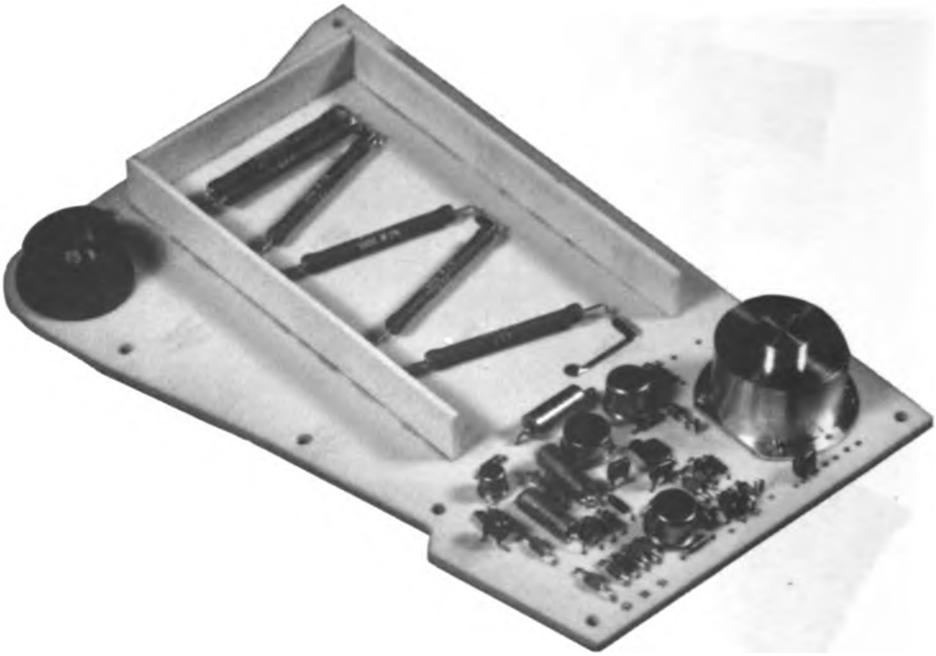

Figure 49. Design Example 7, ~10 kV.

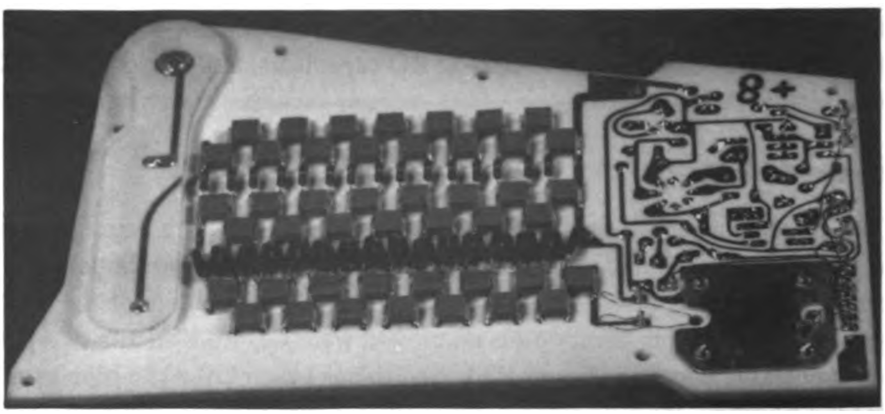

Figure 50. Design Example 7, ~10 kV.

thus eliminating the problem. Another problem, typical of potted modules, was the occurrence of internal discharges of tiny voids with a repetition rate of the order of one per hour per void.

The aluminum cylinder at one end of the supply encases and supports the pot core transformer. The round object at the other end is a special high-voltage connector fabricated of Dupont Vespel. The box over the high-voltage resistors (shown with cover removed) is for physical protection.

Features of this design include small size, light weight, and high efficiency.

Design Example 8—15 kV*

This 10-stage Cockroft-Walton type power supply, Figures 51 and 52, was designed to be located immediately adjacent to the device to which it supplied power, thus eliminating the need for high-voltage cables and connectors. As shown prior to potting in Figure 53, the high-voltage output lead is connected to a terminal located at the center of the circuit board. Lead length was adjusted so that the wire would form a helix through the encapsulant (RTV-615). This construction increases the electrical leakage path along the surface of the wire insulating jacket. The lead connected physically with a corona control electrode through a Kel-F insulated barrier directly above the circuit board.

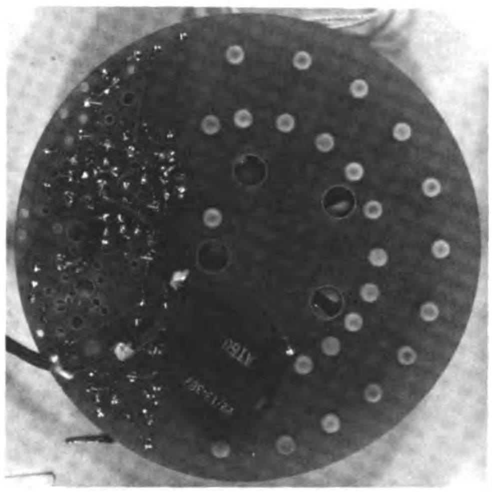

Figure 51. Design Example 8, 15 kV.

After cleaning and inspection, the ceramic capacitors were coated with a 50-50 mixture of Epon 828 and Versamid 140 and overcoated with 93-500. The latter material adhered well to the RTV-615 encapsulant.

All of the high-voltage components were mounted on etched Teflon standoffs in order to keep high potentials well separated from the chassis which is located 0.25 in. from the bottom of the board. Etching was necessary to ensure adhesion to the RTV-615 encapsulant.

The pot core transformer was constructed with the high-voltage winding wound on top of the low-voltage winding. Layers of H-film tape were placed over every third layer of windings. High-voltage lead breakout was made at the extreme perimeter on the opposite side of the core from the primary leads.

*J. L. Westrom, GSFC, private communication.

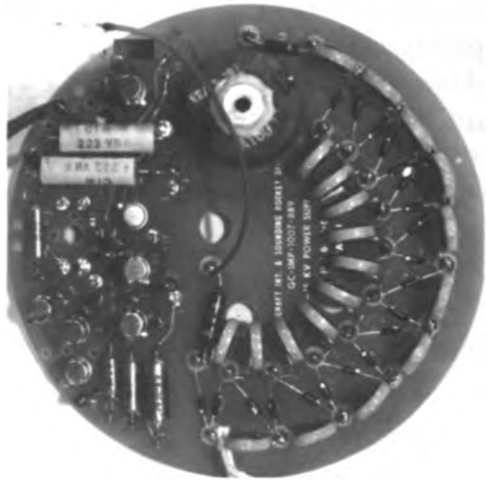

Figure 52. Design Example 8, 15 kV.

Figure 53. Design Example 9, 25 kV.

Design Example 9—25 kV, -55°C to +100°C*

As shown in Figures 53 and 54, this 25-kV supply was potted as a solid block in a metal box. The multiplier array was self supporting prior to potting with a combination of Sylgard 186 and Sylgard 184. This unusual compound is flexible and performs satisfactorily as an insulator over the required temperature range. The design features field stress reduction at junctures in the array through the use of metal balls welded to the component leads.

*R. G. Reynolds, USNRL, private communication.

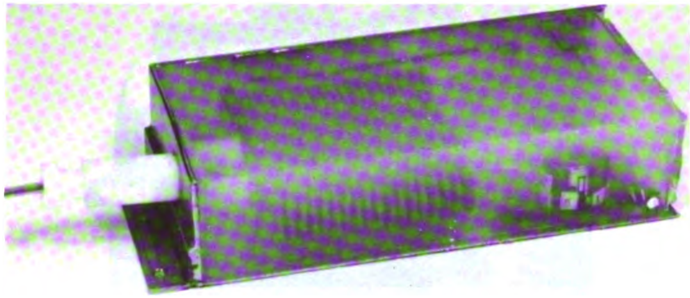

Figure 54. Design Example 9, 25 kV.

Component types employed include Erie 3889-810-X5R0 capacitors with Jet-Seal coating, Vitramon CKR06BX capacitors, Semtech SFM-70 7-kV diodes, Caddock MG721 series high-voltage resistors, and Daburn etched Teflon shielded cable.

Design Example 10—~100 kV, Sounding Rocket Experiment*

The 100-kV, 5-μA supply shown in Figures 55 through 58 was designed as a Cockroft-Walton device contained within a vessel pressurized to 15 psig with SF_6. The concept of employing only ceramics, metals, and SF_6 in the construction wherever possible follows the design practice developed over many years for construction of Van de Graaf generators. No encapsulants were employed.

The stack of fins visible in Figures 56 and 57 separate sandwich pairs of uncoated capacitor wafers, Sprague type 41C-0Z5-C23C. Metallic lead wafer separators were employed to relieve local stress concentrations in the ceramic capacitor dielectrics.

A 150-megohm series limiting resistance consisting of ten 15-megohm Caddock MG 689 film resistors was employed. Other components employed in this high-voltage supply were a Feroxcube type 4229 PLOO/3BZ pot core transformer, 40 Semtech type 1N5184 diodes, and a 10^{11} Ω voltage sampling resistance consisting of twenty 5×10^9 Ω RPC type BBMW resistors.

A unique feature of this supply design was the shape of the high-voltage electrodes. The structure is that of two flat plates forming a parallel plate capacitor separated by the Cockroft-Walton diode array. That is, the whole upper end of the cylindrical container is a conductor at high potential. As can be seen by referring to Table 1, this results in lower electric field stresses than would occur, for example, between a small electrode (connector) and the base plate.

---

*F. Scherb, University of Iowa, private communication.

Figure 55. Design Example 10, ~100 kV.

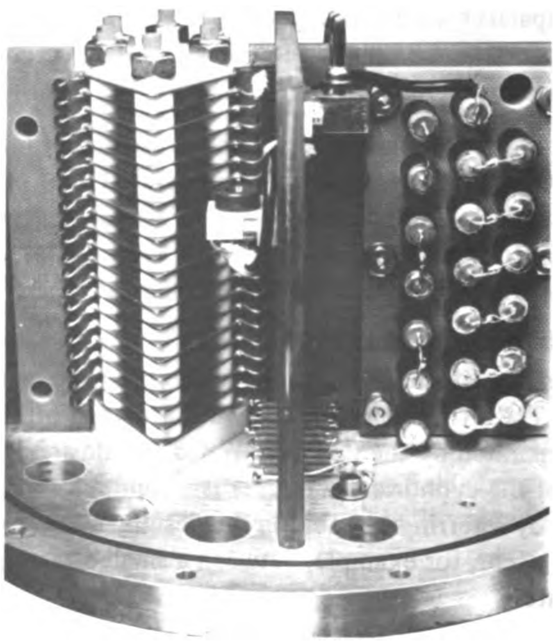

Figure 56. Design Example 10, ~100 kV.

Figure 57. Design Example 10, ~100 kV.

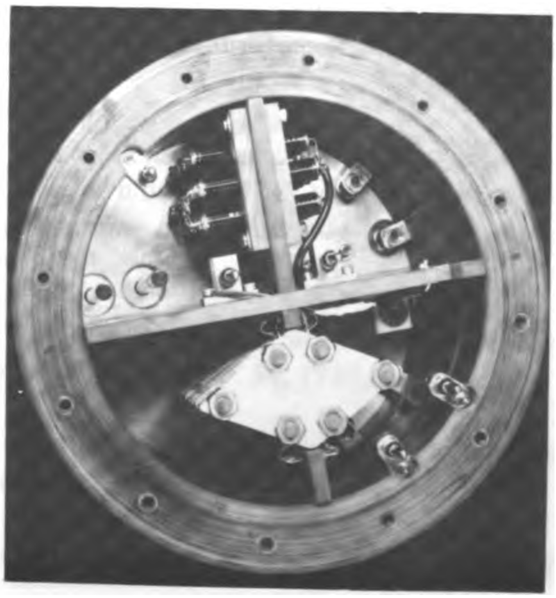

Figure 58. Design Example 10, ~100 kV.

ACKNOWLEDGMENTS

We would like to thank all the contributors who have provided us with detailed information on their successful methods for avoiding electrical breakdown in spacecraft high-voltage systems. These methods include specific techniques, materials, and components which have been used and developed at various test facilities.

Special thanks are given to John Westrom and Dr. Ben Seidenberg of Goddard Space Flight Center. Mr. Westrom contributed much information on the techniques and details of electronic and electrical circuit design. Dr. Seidenberg assisted us greatly with the preparation of the section on encapsulants.

Goddard Space Flight Center
National Aeronautics and Space Administration
Greenbelt, Maryland

December 1974
039-23-01-01-51

REFERENCES

1. Stern, J.E., and K.E. Mercy, "A Study of Voltage Breakdown in Spacecraft Systems from Test and Flight Experience," Proceedings of the Second Workshop in Electronic Equipment at Low Air Pressure, Tech. Memorandum 33-447, Jet Propulsion Laboratory, March 1969.

2. Meek, J. M., and J. D. Craggs, *Electrical Breakdown of Gases*, Oxford, 1953.

3. Krebs, W. H., and A. C. Reed, "Low Pressure Electrical Discharge Studies," STL/TR-59-0000-09931, Air Force Contract 04 (647)-309, December 1959.

4. Von Engel, A., *Ionized Gases*, Oxford, 1965.

5. Dunbar, W. E., "Corona Onset Voltages of Insulated and Bare Electrodes in Rarefied Air and Other Gases," AF APL-TR-65-122, The Boeing Co., June 1966.

6. *U.S. Standard Atmosphere 1962*, NASA, USAF, and USWB, 1962.

7. Bowers, A., and P. G. Cath, "The Maximum Electrical Field Strength for Several Simple Electrode Configurations," *Philips Tech Review*, 6, 1941, p. 270.

8. Alpert, D., D. A. Lee, E. M. Lyman, and E. E. Tomaschke, "Initiation of Electrical Breakdown in Ultra High Vacuum," *Proceedings of the International Symposium on Insulation of High Voltages in Vacuum*, M.I.T., October 1964.

9. Anderson, H. W., "Effect of Total Voltage on Breakdown in a Vacuum," *Electrical Engineering*, 54, 1935, p. 1315.

10. Trump, J. G., and R. J. Van de Graaf, "The Insulation of High Voltages in Vacuum," *J. Appl. Phys.*, 18, 1947, p. 327.

11. Inge, L., and A. Walther, *Arch. Elektrotech.*, 26, 1932, p. 409.

12. Sprengling, G. R., and S. J. Ponemone, "Volume Resistance Behavior of Laminated Circuit Boards under High Humidity Conditions," *10th Proceedings of the Electrical Insulation Conference*, 1971, p. 161.

13. Sprengling, G. R., "Effects of Humidity on Polymer Surfaces," *Annual Report of the Conference on Electrical Insulation and Dielectric Phenomena 1971*, 1971, p. 83.

14. Milek, J. T., "EPIC (Electronic Properties Information Center)" AFML-RTD-AFSE, AF 33 (615) - 1235, Sulfur Hexafluoride Data Sheets DS-140, October 1964.

15. Clark, F. M., "Insulating Materials for Design and Engineering Practice," John Wiley, 1962, p. 699.

16. Sacher, E., "Resistivities of Curing Epoxy Systems II. Bisphenal-A Diglycidyl Ether/Polymide," *Annual Report of the Conference on Electrical Insulation and Dielectric Phenomena 1971*, 1971, p. 249.

17. Rogers, E. C., and D. J. Skipper, "Gaseous Discharge Phenomena in High Voltage D.C. Cable Dielectrics," *Proc. of the Institution of Electrical Engineers*, **107**, Part A, No. 33, June 1960, p. 241.

18. Dosser, D. M., "Electrical Shorts," 3M Company.

19. Lee, E. A. R., "Laminated Materials for Printed Circuit Boards," *Electronics and Power*, November 1972, p. 392.

20. Scialdone, J. J., "The Outgassing and Pressure in a Spacecraft," *Proc. of Institute of Environ. Sciences*, Mt. Prospect, Ill., 1974.

21. Scialdone, J. J., "Internal Pressures of a Spacecraft or Other Systems of Compartments Connected in Various Ways and Including Outgassing Materials in a Time Varying Pressure Environment," NASA TM X-63869, August 1969.

22. Everhart, E., and P. Lorrain, "The Cockroft-Walton Voltage Multiplier Circuit," *Rev. Scientific Instrum.*, *24*, 1953, p. 221.

23. Rumble, G. P., "A Universal Voltage-Multiplier Circuit," *QST*, March 1973, p. 48.

24. Weiner, M. W., "The Cockroft-Walton Voltage Multipliers with an Arbitrary Number of Stages," *Rev. of Scientific Instrum.*, **40**, February 1969, p. 330.

25. Mostov, P. M., L. J. Neuringer, and D. S. Riguiy, "Optimum Capacitor Charging Efficiency for Space Systems," *Proc. of the IRE*, May 1961, p. 941.

APPENDIX 1

HIGH VOLTAGE ELECTRONIC PACKAGING FLIGHT EQUIPMENT

DESIGN REQUIREMENTS

CODE IDENT NO. 23835

DES. REQ. DM505139 REV. A

ISSUE DATE 24 November 1971

SUPERSEDING

DATED

HIGH VOLTAGE ELECTRONIC PACKAGING FLIGHT EQUIPMENT

ENGINEER: E. R. Bunker, Jr., Cognizant Engineer — DATE 11/23/71

PREPARED AND RELEASED BY SECTION 356: G. Inouye, Design Section Group Supervisor — DATE 11/24/71

APPROVED BY SECTION 357: E. J. Dieckman, Group Supervisor — DATE 11/23/71

APPROVED BY SECTION 357: for N. G. Comuntzis, Section Manager — DATE 11/23/71

JET PROPULSION LABORATORY

CALIFORNIA INSTITUTE OF TECHNOLOGY

PASADENA, CALIFORNIA

CHANGE INCORPORATION LOG

CHG LTR	WRITER		AUTHORITY	PAGES AFFECTED	DATE	ENG APPROVAL	
	INITIAL	SECTION				INITIAL	SECTION
A .	GI	356	FLIGHT		11/24/71	ERB	357

1. SCOPE

1.1 Scope. This document covers the design requirements for the protection of high voltage flight equipment from damage due to arcing or corona breakdown.

1.2 Applicability. The high voltage protection requirements described herein are to be applied to packaging design and testing of electronic equipment operating above the voltage minimum as specified in 3.2.1.

1.3 Objectives. The main objective of high voltage electronic packaging requirements described herein is to assure that the electronic equipment employing high voltages will survive and operate without damage due to an intentional or inadvertent turn-on while in the critical pressure area during testing, or a high Earth altitudes, other planetary atmospheres, or the vacuum of space. Demonstration by actual testing is required to demonstrate that the high voltage electronic equipment will survive operation in this environment. Another objective is to qualify details of design such as:

a. Design concept.
b. Adequacy of interconnections.
c. Effectiveness of protective devices.
d. Effect on other subsystems.
e. Quality of workmanship.

Voltage breakdown considerations not included in this document are break downs at frequencies above 1.0 GHz in cavities or wave guides in vacuum due to secondary emission (multi-pacting) or other effects not requiring ionization of a gas for initiation.

1.4 Classes of electronic equipment. Electronic equipment will be classified as Class 1 or Class 2 in accordance with 1.4.1 and 1.4.2.

1.4.1 Class 1 equipment. Class 1 equipment will be designed to operate to specification requirements throughout its operational lifetime without voltage breakdown (arcing or corona) present at any pressure, unless such arcing or corona is a proper functional requirement (e.g., spark gaps).

1.4.2 Class 2 equipment. Class 2 equipment will be designed so that any voltage breakdown which may appear during operation at any pressure will not cause damage to its internal components or to other external equipment, or degrade the mission to an unacceptable limit. During the time that voltage breakdown is occurring, operation to specification requirements is not required. In applications where insulation to prevent corona or arcing cannot be used because of interference with the proper functioning of the unit (e.g., plasma detector screens), protective devices such as horn or ring gaps will be used to reduce the possibility of arcing or corona occurring in the unit. Power supply output may be self limiting to prevent damage due to arcing or corona.

2. APPLICABLE DOCUMENTS

2.1 The following documents, of the issue specified in the contractual instrument, form a part of this document to the extent specified herein.

SPECIFICATIONS

Jet Propulsion Laboratory

FS500443	Process Specification, Transformer and and Inductors, Electronic Packaging, General Specification for
FS505284	Process Specification, Printed Wiring Boards and Assemblies, Double Sided, Solder Plated, Detail Specification for
FS505789	Process Specification, Fabrication of Multilayer Printed Circuit System with Plated-Through Holes, Detail Specification for
FS506079	Process Specification, Printed Wiring Boards and Assembly, Detail Specification for

Military

MIL-T-27C	Transformers and Inductors (Audio, Power, and High Power), General Specification for

STANDARD

Military

MIL-STD-202C	Military Standard, Test Methods for Electronic and Electrical Component Parts

DRAWINGS

Jet Propulsion Laboratory

ST10591	Terminal, Electrical, Slotted, Swage Mount
ST11308	Terminal, Electrical, Slotted, Swage Mount

(Copies of specifications, standards, procedures, drawings, and publications required by suppliers in connection with specific procurement functions should be obtained from the procuring activity or as directed by such activity.)

3. REQUIREMENTS

3.1 Conflicting requirements. In case of conflict between the requirements of this document and the requirements of any document referenced herein, this document shall have precedence.

3.2 General. All flight electronic equipment to be exposed to the critical pressure region (refer to 6.1.3) and employing voltages above the minimum specified in 3.2.1 (a function of frequency) shall comply with the requirements of this document. This requirement is in addition to the basic electronic packaging requirements of the applicable design requirement and functional requirement documents.

3.2.1 High voltage limits. The requirements of this document shall be mandatory for flight electronic equipment with circuit conductors having instantaneous voltages (with respect to other circuit conductors, to the common ground, or to the subchassis) in excess of 250 volts peak. This limit is applicable to frequencies from d.c. to 60 Hz, and shall be reduced in accordance with Figure 1 for frequencies above 60 Hz.

At voltages lower than that specified in 3.2.1, compliance may be desirable for one or more of the following reasons:

a. The conductive plasmas generated by a corona or arc, or other mechanisms such as passage of the vehicle through low pressure gaseous environments, can drift across bare conductors carrying much lower voltages (e.g. 24 volts), initiating arcing in these circuits also.

b. The theoretical breakdown voltage minimum of 270 volts peak is for air; other gases, especially the noble ones, even in trace quantities, can cause breakdown to occur at much lower voltages.

c. Other conditions being the same, reduction of large voltage gradients, by suitable gradient control techniques, will markedly improve the long term reliability of high voltage circuits.

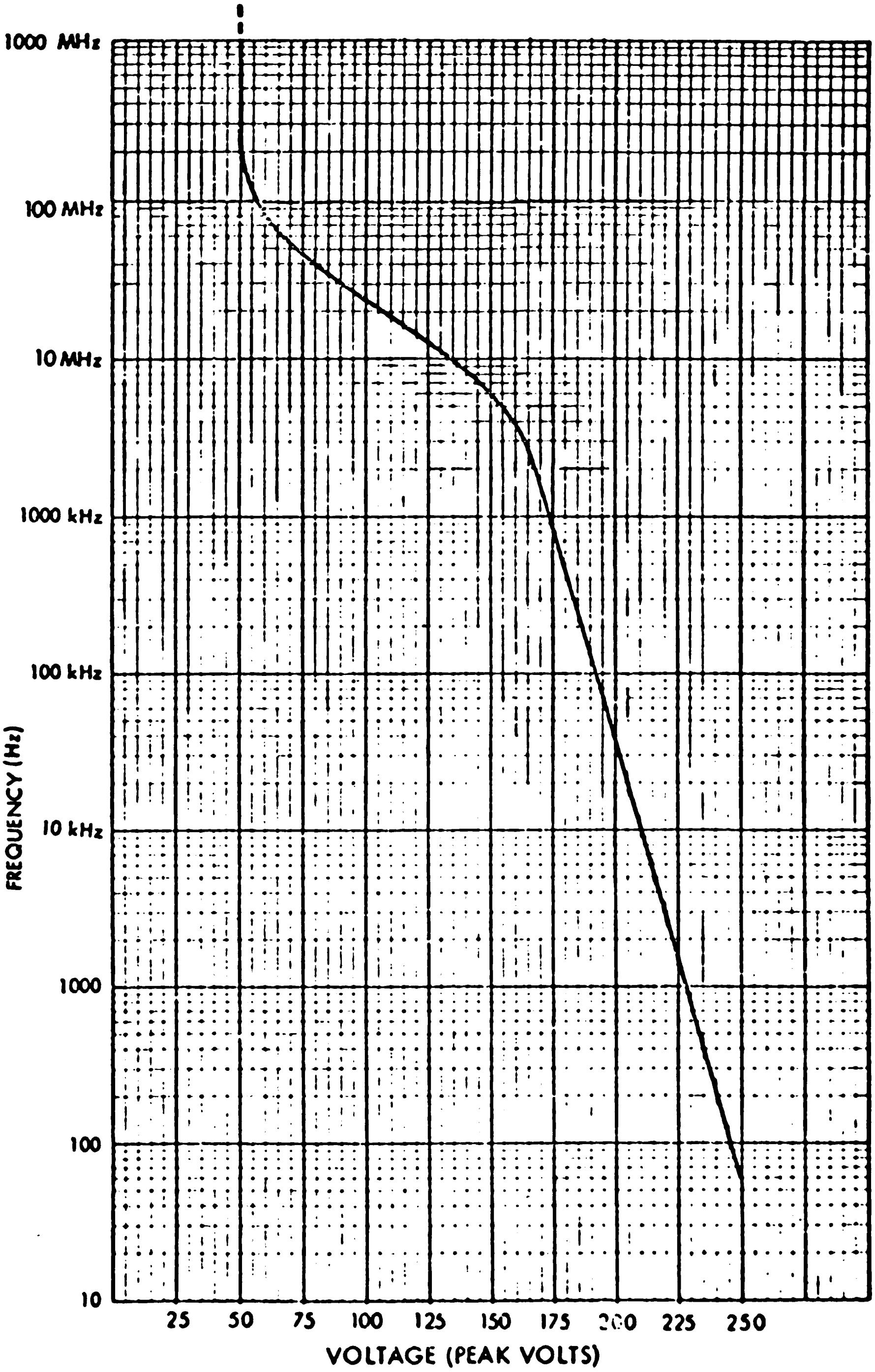

Figure 1. Lower Voltage Breakdown Limit versus Frequency for Earth Atmosphere

3.2.2 Frequency range. The range of frequencies governed by this document shall be from d.c. to 10 GHz for sinusoidal waveforms, or from d.c. to 1.0 GHz for all other waveforms.

3.3 Circuit geometry of printed wiring and terminal boards. Printed wiring (etched circuit) conductors shall not be used in circuits with voltages between conductors in excess of 1000 volts peak unless special precautions are taken to reduce the voltage gradients along the conductor edges. Printed wiring boards and assemblies shall be in conformance to the requirements of JPL Specification FS505284, FS505789, or FS506079.

Terminal boards, using swaged terminals per JPL Specification FS505284 or FS506079, using discrete components and solid bus wire for interconnection, or similar packaging techniques where voltage gradient control can be demonstrated or calculated, shall be used for high voltage circuits operating at voltages above 1000 volts peak.

Terminal pads shall not be used under swaged terminals in circuits with voltages above 1000 v peak. Printed wiring and terminal boards used in high voltage circuits shall meet the requirements of 3.3.1 through 3.3.12.

3.3.1 Separation of high voltage circuits. Circuits employing high voltage shall be physically separated from low voltage circuits with a minimum common boundary when located on the same printed wiring or terminal board, as shown on Figure 2. The minimum distance between high and low voltage conductors shall be as given in 3.3.3 and 3.3.4.

3.3.2 Low voltage circuit protection. A ground bus shall be located between high and low voltage circuitry to prevent possible creepage currents or arcs causing interference or damage with the low voltage circuits as shown on Figure 2. Where the high voltage circuit is physically separate from the low voltage circuit board, a ground bus around the perimeter of the high voltage board shall be used to prevent a possible arcing to the low voltage circuits. Where high voltage exists on both sides of the printed wiring or terminal board, the ground bus shall be on both sides, preferably superimposed one above the other as shown on Figure 3. This ground bus should be wider than regular conductors to provide a lower impedance return path for an arc. A ground bus shall be used in each layer of a multilayer circuit to isolate the high voltage circuits from the low voltage circuits. In selected areas, the ground buses may be staggered instead of superimposed to allow conductors to pass between the high and low voltage areas by transferring from one layer to an adjacent one; or the ground bus on a given layer may be interrupted to allow passage of such conductors. The connection to the ground point for this bus shall be so that the currents from a possible arc will not be coupled into the ground returns of any other circuits.

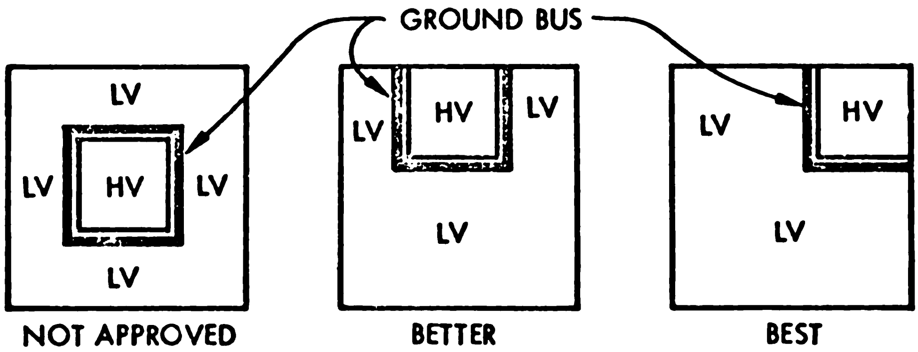

Figure 2. Common Boundary, HV & LV Circuits

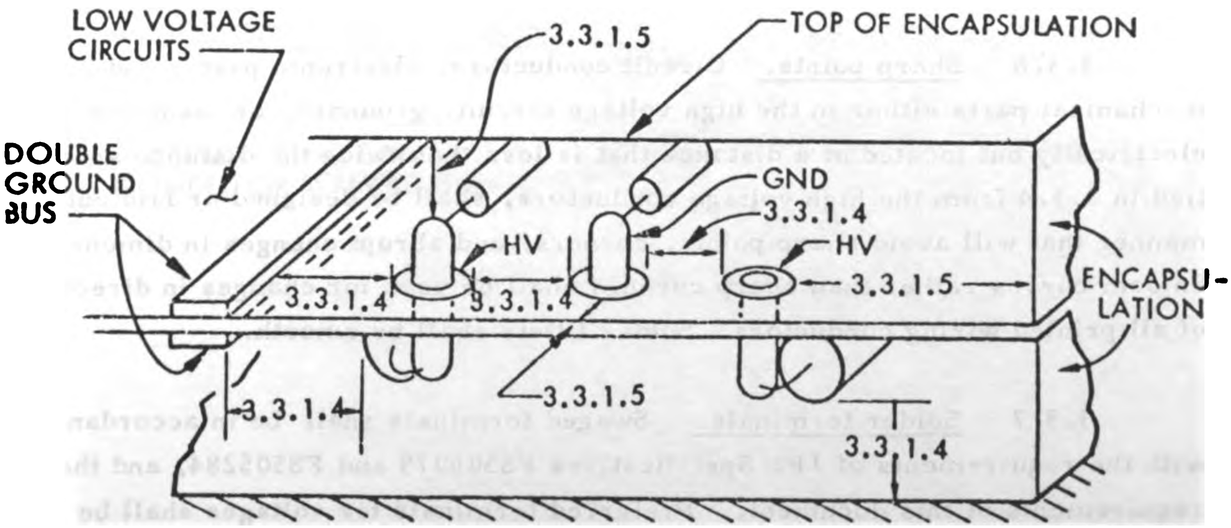

Figure 3. Required Separation of High Voltage Parts

3.3.3 Measurement of conductor separation. The distance between conductors, terminals, or other metallic surfaces with high voltages between them shall be measured in a straight line from the points of closest approach, including worst tolerance buildup, and disregarding any intervening insulation materials. The linear voltage gradient is computed in accordance with 3.3.10.

3.3.4 Conductor spacing. The minimum separation of conductors carrying voltages in accordance with 3.2.1 on the same side of the printed wiring or terminal board shall be as given by the empirical equation:

$$d = 0.250 \sqrt{V}$$

(where d is in inches and V is the maximum peak voltage difference between the conductors in kilovolts.)
The minimum separation shall be 0.125 inch. Distances shall be measured along the surface between the conductors and shall be the minimum distance possible. Layout of the high voltage circuitry should consider gradient reduction by placing conductors in order of decreasing voltages, if such locations do not cause adverse effects on the performance of the circuit.

3.3.5 Spacing from edge. The minimum distance of the conductors from the edge of the printed wiring or terminal board shall be 1.5 times the value obtained from the equation in 3.3.4, as shown on Figure 3.

3.3.6 Sharp points. Circuit conductors, electronic parts, and mechanical parts either in the high voltage circuit, grounded, or insulated electrically but located at a distance that is less than twice the distance specified in 3.3.4 from the high voltage conductors, shall be designed or laid out in a manner that will avoid sharp points, corners, and abrupt changes in dimensions. Smooth curves rather than sharp corners shall be used for changes in direction of all printed wiring conductors. Solder fillets shall be smooth.

3.3.7 Solder terminals. Swaged terminals shall be in accordance with the requirements of JPL Specifications FS506079 and FS505284, and the requirements of this document. Preferred terminals for voltages shall be per JPL Drawing ST10591 or ST11308. For applications which require larger terminals, the bifurcated terminals specified in JPL Specification FS505824 shall be permitted, subject to the following additional requirements of this paragraph and Figure 4. Ends of part leads shall be flush with the edge of the terminal to 0.030 shorter. After part leads are installed, the terminals at voltages above 1.0 kv shall have any excess length of the bifurcation trimmed off as shown on Figure 4. A smooth solder joint shall be made to enclose all cut ends of leads and trimmed bifurcations to reduce the voltage gradient. A smooth solder ball or other conductive material shown on Figure 4 is allowable for high voltage terminals. For circuits above 1.0 kv, the terminals shall have a hemispherical conducting cap to reduce the voltage gradient at the edge of the swage as shown on Figure 4. Use of solder terminals should be kept to a minimum in high voltage circuits.

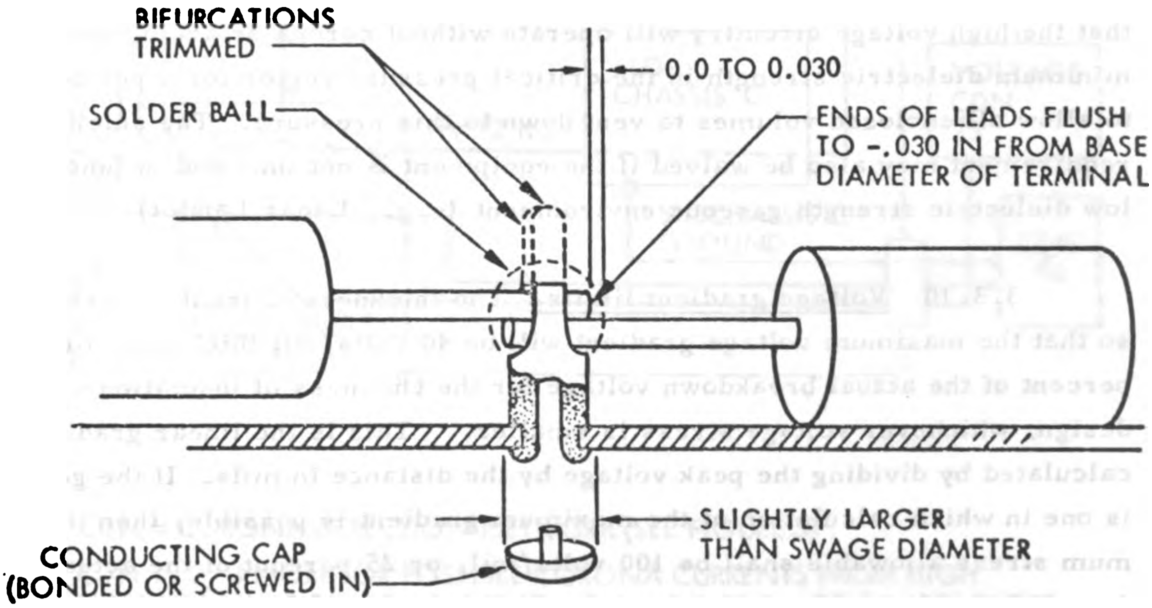

Figure 4. Solder Terminals

3.3.8 Grounding. Chassis ground leads shall be separate from signal and power return leads to prevent corona or arc currents from adversely affecting or damaging other circuits. Provisions shall be made so that corona detection networks may be inserted in series with chassis grounding leads during subsystem tests as shown on Figure 5. Ground lead continuity is through the corona detection networks, which have a very low impedance at low frequencies. Ground leads shall be such that ground loops are not permitted.

3.3.9 Grounded shield for ac circuits. High voltage ac circuits, which are encapsulated per 3.4, shall be enclosed by a conducting ground shield to prevent the occurrence of corona at the surface of the encapsulant when operating in the critical pressure region. Special precautions shall be taken to prevent the inclusion of any bubbles or voids between the shield and the high voltage conductors. This shielding requirement may be waived if it can be demonstrated that the high voltage circuitry will operate without corona or arcing while at the minimum dielectric strength in the critical pressure region for a period of time to allow all enclosed volumes to vent down to this pressure. The shielding requirement may also be waived if the equipment is not intended to function in a low dielectric strength gaseous environment (e.g., Lunar Lander).

3.3.10 Voltage gradient limits. The thickness of insulation shall be so that the maximum voltage gradient will be 40 volts/mil thickness, or ten percent of the actual breakdown voltage for the thickness of insulation used in the design, whichever voltage stress is smaller. This is the linear gradient, calculated by dividing the peak voltage by the distance in mils. If the geometry is one in which calculation of the maximum gradient is possible, then the maximum stress allowable shall be 100 volts/mil, or 25 percent of the actual breakdown voltage for the same thickness, whichever is smaller.

3.3.11 High voltage pulse circuits. Minimum separation as specified in 3.3.4 of conductors carrying pulses may be reduced by multiplying factor $\frac{t}{t + 0.8}$ (where t is the pulse width in microseconds). The pulse duty cycle shall be less than five percent for this reduction to apply.

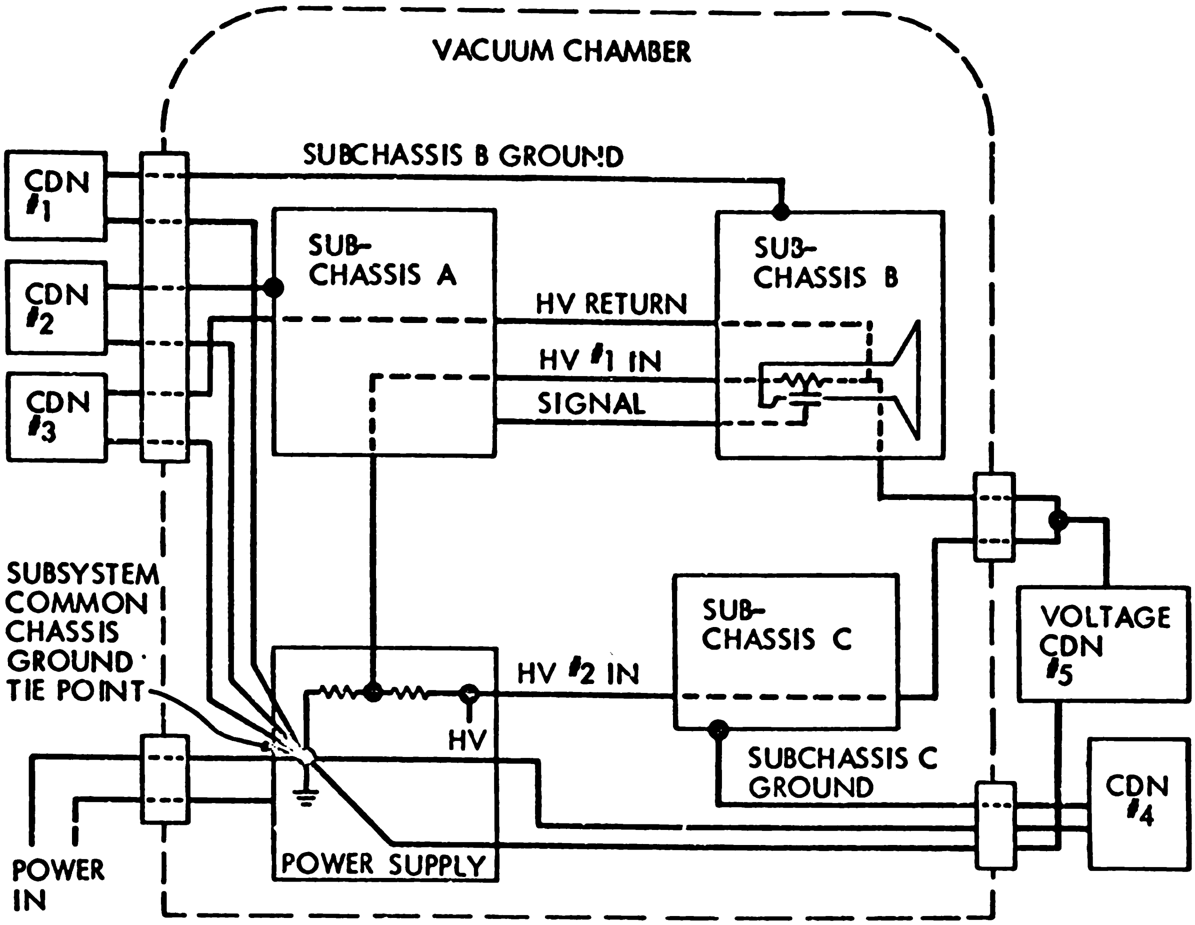

NOTES.

1. CDN = CORONA DETECTION NETWORK (SEE FIGURE 3).
2. CDN 1, 2, 4 MONITOR POSSIBLE CORONA CURRENTS FROM HIGH VOLTAGE LINES TO CORRESPONDING SUBCHASSIS. CDN 3 MONITORS POSSIBLE CORONA CURRENTS BETWEEN HV #1 CONDUCTOR AND RETURN.
3. IN CASES WHERE IMPEDANCE IN RETURN OR CDN ADVERSELY AFFECTS SUBSYSTEM OPERATION, VOLTAGE TYPE (CDN #5) MAY BE CONNECTED TO HV LEAD (#2) AS SHOWN.
4. ONE CDN WITH GROUNDING SWITCH COULD BE USED IN PLACE OF CDN 1, 2, 3, 4.

Figure 5. Insertion of Corona Detection Networks in Subsystem Ground Returns

3.3.12 Enclosures. Enclosures which are not hermetically sealed shall be vented directly to the ambient vacuum of space. The total area of vent opening shall allow the pressure in the enclosed volume to bleed down to 3×10^{-3} torr in 60 seconds or less, when the pressure is reduced from ambient sea level to 10^{-5} torr in six seconds or less. The pressure referred to includes both residual air and outgassing in the enclosure. Experience has shown that venting of enclosures may not be adequate to reduce the pressure below the critical region. Consequently, high voltage circuits contained in the enclosure shall be assumed to be exposed to the lower end of the critical pressure region, e.g. 10^{-3} to 5×10^{-4} torr, unless otherwise demonstrated by suitable tests.

Hermetically sealed enclosures shall be acceptable if the product of the measured leak rate and the mission time is one in which the resultant pressure in the enclosure is above the critical pressure region.

3.4 High voltage insulation materials. High voltage insulation materials shall have the following requirements.

3.4.1 Dielectric strength. Insulating materials having the higher dielectric strengths shall be used in high voltage applications when other properties or characteristics pertinent to the application are similar. Materials with dielectric strengths of less than 400 volts/mil measured between parallel plates at the thickness required should be avoided.

3.4.2 Dielectric constant. Insulating materials with low dielectric constants shall be selected for insulation of ac voltages. Where two different insulating materials are in contact, they should be selected so that the difference in their dielectric constants is minimal. Materials with dielectric greater than five shall be avoided.

3.4.3 Air dielectric strength. For purposes of equipment design in accordance with this document, air shall be assumed to have a zero dielectric strength in the critical pressure region.

3.4.4 High frequency applications. Insulation materials selected for use in the high frequency (nominally above 1.0 MHz) applications shall have the dielectric constants and dielectric losses small enough so that blistering, delamination, or other internal damage cause by internal heating will not occur during normal operation.

3.4.5 Foams. Expanded or syntactic foam materials, or materials that are porous, shall not be used for high voltage insulation applications.

3.4.6 Low arc resistant materials. Organic insulating materials, which have a tendency to sustain arcing under any pressure condition or which deteriorate or outgas under arcing conditions, shall not be used in contact with bare conductors emerging from the insulating material and exposed to the ambient pressure. Inorganic insulating materials, which do not sustain arcing, shall be used to provide the interface of an emerging bare conductor from the embedment or conformal coating as shown on Figure 6.

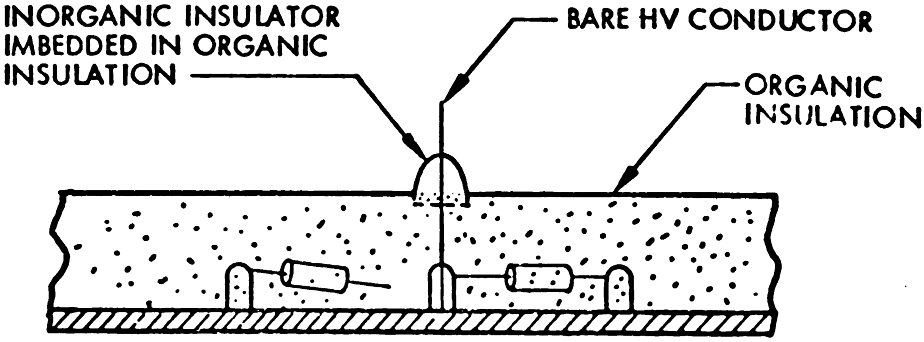

Figure 6. Inorganic Insulation Material

3.4.7 Filled materials. Insulation, which employs fillers or discrete materials mixed throughout its volume, shall have a dielectric strength design limit within the requirements of 3.3.10 computed for that material of the mixture with the lowest dielectric strength.

3.4.8 Insulation coating. All exposed conductors carrying high voltages shall be conformally coated or embedded in a plastic material in conformance with this document. Conductors, which must be exposed to the ambient pressure for proper functioning (e.g., spark gaps), shall be exempt from this requirement.

3.4.9 Adhesion of polymeric materials. Selection of polymeric insulation materials and preparation of solid surfaces in contact with such materials shall assure proper adhesion of the polymeric materials to eliminate creepage paths between conductors.

3.4.10 Removal of absorbed gas. Insulation materials in liquid form prior to polymerization shall be exposed to a vacuum sufficient to remove entrapped gas. Suitable precautions shall be taken to prevent re-entry and trapping of air into the insulation material prior to use and during application. Pouring of insulation material into mold while both items are under vacuum will prevent air entrapment.

3.5 Electronic parts for high voltage applications. In addition to requirements imposed by project parts documents, the electronic parts used in high voltage circuits shall meet the following requirements.

3.5.1 High voltage transformers and inductors. Transformers and inductors shall meet the requirements of JPL Specification FS500443, and 3.5.1.1 through 3.5.1.5 herein.

3.5.1.1 Maximum voltage between turns. The thickness of the enameled magnet wire insulation coat and winding technique shall be so that the maximum possible voltage between any two adjacent wires in a winding shall be accordance with 3.3.10, and in no case larger than 40 volts peak. Voltages at terminations of windings and between wires in excess of this value shall employ additional insulation in accordance with 3.3.10. In high voltage pulse transformers with pulse widths of 10 μsec or less, the allowable voltage limit between wires may be 200 volts peak.

3.5.1.2 Core connection. Electrically conductive cores electrically insulated from the mounting base of the transformer or inductor shall have an auxiliary lead brought out to facilitate hypot tests between the core and the windings to test core insulation integrity (if there is no internal connection between a winding and the core). Cores fabricated from high permeability magnetic materials and encased in plastic matter by the manufacturer shall be exempt from this requirement, provided that the plastic material is in accordance with 3.4 and is sufficiently transparent to allow measurement of the minimum thickness of insulation separating the core from the winding. Cores encased with metallic covers and covered with insulation material also shall be exempt provided that the insulating material is in accordance with 3.4, and the low voltage winding (primary) is between the high voltage windings and the core.

3.5.1.3 Interwinding insulation. Insulation between windings shall be in accordance with 3.4 and shall be capable of withstanding, without damage, the tests described.

3.5.1.4 Winding embedment. Windings shall be impregnated and then encapsulated or shall be embedded with suitable materials and techniques in accordance with 3.4, so that all wires are securely anchored and no pockets or voids occur.

3.5.1.5 Winding terminations. Windings terminated into insulated lead wires shall be embedded in accordance with 3.5.1.4 and the requirements of this paragraph. Terminals employed for termination of transformer or inductor windings shall meet the requirements of 3.3.7, prior to conformal coating or encapsulating in accordance with 3.4. The conformal or encapsulant material shall be compatible with the lead wire insulation and achieve a thorough bond so that creepage paths from the conductor to the outside of the module will not occur. The length of the path from the conductor to the outside shall be 0.25 inch, or in accordance with 3.3.4, whichever is greater to assure a sufficient length of bond to prevent breakdown. Provisions shall be made to anchor the wire as it emerges from the encapsulant; or other precautions shall be taken so that subsequent handling does not mechanically stress the bond between the encapsulant and the wire insulation.

3.5.2 Connectors. Connectors shall not be used as high voltage interfaces in Class 1 (1.4.1) equipment unless compliance of such connectors with the requirements of this document is demonstrated by suitable tests called out herein.

3.5.2.1 Venting. The void enclosed between the interface of the mated connector and the other volumes sealed off by cable clamps, etc., shall be vented in accordance with 3.3.12.

3.5.2.2 Insulation. The connector insulation material shall be selected in accordance with 3.4.

3.6 Performance testing. The performance of high voltage parts, components and subsystems shall be substantiated by testing as specified in Section 4 herein.

3.7 Environmental testing. Requirements for type approval (TA) and flight acceptance (FA) tests are stated in 3.7.1 and 3.7.2 respectively.

3.7.1 TA testing. TA testing shall comprise of testing of electronic parts and components (3.7.1.1) and subsystems (3.7.1.2) testing.

3.7.1.1 Electronic parts and components testing. Electronic parts selected for high voltage applications shall be exposed to test conditions sufficiently severe in the critical pressure region to establish margins and to test the design, construction and types of insulation materials used in accordance with 4.3.2. Such parts shall have previously met the requirements of applicable project parts documents. If the parts are encapsulated in the flight subsystem, the parts undergoing part type qualification may be encapsulated in identical material with the approximate thickness and geometrical configuration as the flight model.

3.7.1.2 Subsystem testing. Subsystems, employing high voltages, shall be exposed to operation in the critical pressure region during TA tests, if possible; otherwise a separate test shall be made. The length of time and test conditions shall be as specified in 4.2.2.1.

3.7.2 FA testing. FA testing shall comprise of testing of electronic parts and components (3.7.2.1) and subsystems (3.7.2.2) testing.

3.7.2.1 Electronic parts and components testing. Electronic parts, after meeting the requirements of applicable project parts documents shall undergo FA tests per 4.3.3 for high voltage applications. Flight acceptance test parameters shall be of magnitudes that adequately screen the parts for the intended application without causing degradation or deterioration.

3.7.2.2 Subsystem testing. Subsystems, employing high voltages which are required to operate in a critical pressure region during some portion of the flight mission, shall be operated in the critical pressure region to demonstrate compliance with this document in accordance with 4.2.2.2. Subsystems, employing high voltages which are not required to function in the critical pressure region at any time during the mission and have a record of successful tests per 3.7.1.2, may be specifically waived from this requirement.

3.8 Workmanship. All parts and components intended for high voltage usage shall be manufactured to a high standard of workmanship. Uniformity of shapes, dimensions, and construction shall permit interchangeability of replaceable parts and assemblies. The use of smooth fillets, rounded edges and corners to eliminate points shall be emphasized. There shall be no cracks, breaks, chips, bends, burrs, loose attachments, illegible markings, or other evidence of workmanship defects which could adversely affect the performance of the life of parts and components.

4. QUALITY ASSURANCE PROVISIONS

4.1 General. Inspections and tests as specified herein shall be performed on all subsystems, parts and components used in high voltage applications to substantiate the requirements of Section 3.

4.2 Subsystem testing. Subsystems, employing high voltages, shall be operated in the critical pressure region for both TA and FA tests with instruments of suitable sensitivity to detect any possible corona or arcing occurring in the subsystem (as required by 4.2.2.1, TA; and 4.2.2.2, FA). In addition, suitable corona detection instruments shall be employed during spacecraft system TA and FA tests to monitor for any unexpected breakdowns during such environmental testing.

4.2.1 Test objectives. The principal objective of operating a subsystem employing high voltage in the critical pressure region, as a part of TA testing, shall be to demonstrate the capability of the subsystem to survive operation in this environment. An additional objective shall be to qualify details of design such as:

a. Design concept
b. Adequacy of interconnections
c. Effectiveness of protective devices
d. Effect on other subsystems, and
e. Quality of workmanship.

The objective of operating a subsystem in the critical pressure region for FA tests shall be to verify the quality of workmanship and to detect errors so that intentional or unanticipated exposure of the high voltage electronic equipment to the critical pressure region during flight will not degrade the mission.

4.2.2 Environmental testing. Environmental testing of TA and FA equipment shall include both Classes 1 and 2 equipment.

4.2.2.1 TA testing. The TA tests required in this document are in addition to those test required by the applicable project documents.

4.2.2.1.1 Class 1 equipment. Testing of subsystems, employing Class 1 equipment per 1.4.1 for TA, may be run concurrent with thermal vacuum test if:

a. Corona detection equipment is properly connected into the high voltage equipment and monitored continuously throughout the thermal vacuum test for evidence of corona or arcing breakdown. If the subsystem has inherent corona detection capability which is demonstratable to the satisfaction of JPL, the requirement for external corona detection equipment may be waived.

b. Pressure is held through the 0.1 to 1 torr region for a period of time compatible with the mission profile or 3 days, whichever is longer with the subsystem functioning to specification through all modes of operation. Subsystems, which are not normally exposed to operation in the critical pressure regions (e.g., lunar landers) may be tested by operation at ambient room pressure with the subsystem in the mode most likely to experience breakdown. Then while operating, pump down to 0.1 torr with 30 minutes or less; hold at this pressure for 3 days; then switch through all modes of operation 6 times minimum while monitoring for voltage breakdown. If the number of mode changes is limited so that 6 times is an appreciable fraction of the total allowable, then this number may be revised downward upon specific approval of JPL.

Subsystems, which are required to operate in the critical pressure region at the end of the flight (e.g., Mars Lander) may fulfil the mission profile requirement by being exposed to 10^{-4} torr or higher vacuum for 3 days. Then while functioning in the mode most likely to experience breakdown, the subsystem shall return to 1 torr and shall operate in this region for a minimum of 3 days.

Any indication of corona or arcing on any corona detection network, or from the operation of the subsystem (if the subsystem has inherent corona detection capability) shall be cause for rejection.

4.2.2.1.2 Class 2 equipment. (Refer to 1.4.2.) Tests of subsystems employing Class 2 equipment may be run concurrent with thermal vacuum tests, or a separate test may be performed. Monitoring for voltage breakdown is required by one of the following methods:

a. Suitable corona detection equipment

b. Inherent capability of the subsystems to detect corona, or

c. By visual means.

Prior to turn on, the subsystem shall be exposed to 0.1 to 1.0 torr region for 24 hours. The subsystem shall then be operated in all possible modes while at 0.1 to 1.0 torr region at the high temperature range, where functioning is required in the thermal vacuum test. The length of time of operation in each mode shall be the time at which the approximate temperature equilibrium is established. Upon completion of the tests, the high voltage subsystem shall be disassembled for visual inspection. Degradation of components or damage to the subsystem shall be cause for rejection.

4.2.2.2 FA testing. The FA tests required in this document are in addition to those tests required by applicable project documents.

4.2.2.2.1 Class 1 equipment. Tests of subsystems with Class 1 equipment, which is required to operate in the critical pressure area, may be run concurrently with FA tests, if operation in vacuum is required. If operation in vacuum is not required, then a separate test in a vacuum chamber shall be necessary. Suitable corona detection equipment shall be required to monitor for possible voltage breakdown, unless the functioning subsystem has an inherent capability for corona detection, which has been previously demonstrated. The subsystem shall be exposed to the 0.1 to 1.0 torr region for 6 hours, and then turned on. Operation in each mode shall be of sufficient duration, typically several minutes, to allow a thorough detection opportunity for any corona or arcing which may occur. The presence of corona or arcing shall be cause for rejection.

Subsystems with high voltage equipment, which are normally not required to operate in the critical pressure region, may be exempt from this test if corona-free operation of an identical subsystem was demonstrated during the TA tests of 4.2.2.1, and a special waiver is given by JPL.

4.2.2.2.2 Class 2 equipment. FA testing of subsystems with Class 2 equipment may be waived if adequacy of the protective devices or designs has been demonstrated in the TA tests of 4.2.2.1. Any test required by this section shall be run at 1.0 torr for the minimum time necessary to verify the workmanship and to detect flaws in materials or fabrication. Inspection of the protective devices shall be made after a test. Pitting or burning of the protective devices shall be cause for rejection, unless the defects can be removed by suitable and careful polishing techniques acceptable to JPL prior to flight.

4.3 Electronic parts and components testing. In the following paragraphs, the term "electronic parts" shall be interpreted to include components as defined in 6.1.5.

4.3.1 Test objectives. The main objective of imposing qualification tests on the parts, in addition to those required by applicable parts documents, shall be to determine the suitability of the part for high voltage applications with regards to such factors as:

a. Adequacy of design
b. Quality of workmanship
c. Spacing of leads
d. Stresses caused by high voltage gradients
e. Dielectric materials employed
f. Presence of voids, and
g. Heat dissipation.

The objectives of performing acceptance tests on high voltage parts, in addition to those previously required by applicable parts documents, shall be to verify workmanship, including detection of errors.

To accomplish these objectives, all electronic parts used in high voltage circuits shall be tested for designated period of time in accordance with the type of test and the test setup specified. These test conditions shall be applicable to all electronic parts except those specially named under appropriate paragraphs of this document. Applicable paragraphs of MIL-STD-202 C, Method 301, which are not in conflict with this document, may be used as a guide for electronic part tests.

4.3.2 General electronic part design qualification. Electronic parts used at high voltages shall be tested for corona or arcing in the critical pressure region to determine the adequacy of construction of the electronic part from the high voltage considerations. Following suitable precaustions to minimize external corona or arcing, the voltages shall be applied while the electronic part is in the critical pressure region. It is expected that applied voltages in design qualification tests will be high enough to cause some failures, in order to establish a margin of confidence. Voltages applied to electronic parts shall be greater than normal operating voltages in order to accelerate failure of marginal or defective components. For convenience in testing, a functional group of electronic parts which form a component of the subsystem may be tested in accordance with this document (rather than for each electronic part separately).

4.3.2.1 Test procedure. Test voltages as given in the respective paragraphs shall be applied to the electronic parts undergoing test in a vacuum chamber at room pressure. Corona detection networks as shown on Figure 7 shall be used in appropriate leads to monitor for corona or arcing. With the voltage continuously applied, the air pressure shall be reduced to the lower limit (see 6.1.3), and this pressure shall be varied between the upper and lower limits several times for the time interval specified in 4.3.2.7. If several voltage tests are to be made on the same electronic part or on several parts in the same chamber, the test voltages may be applied in sequence by switching (provided that the chamber pressure is varied between the limits of 6.1.3 for each test). At the conclusion of the test, the voltage shall be removed, and the electronic parts shall be brought back to ambient room pressure. During the test, any evidence of corona or arcing shall be cause for rejection. Voltage lines and feed-throughs to the component in the test chamber shall be a construction that will preclude the formation of corona.

4.3.2.2 Electronic parts mounting. Electronic parts undergoing test shall be mounted in a similar to that in the subsystem, especially with

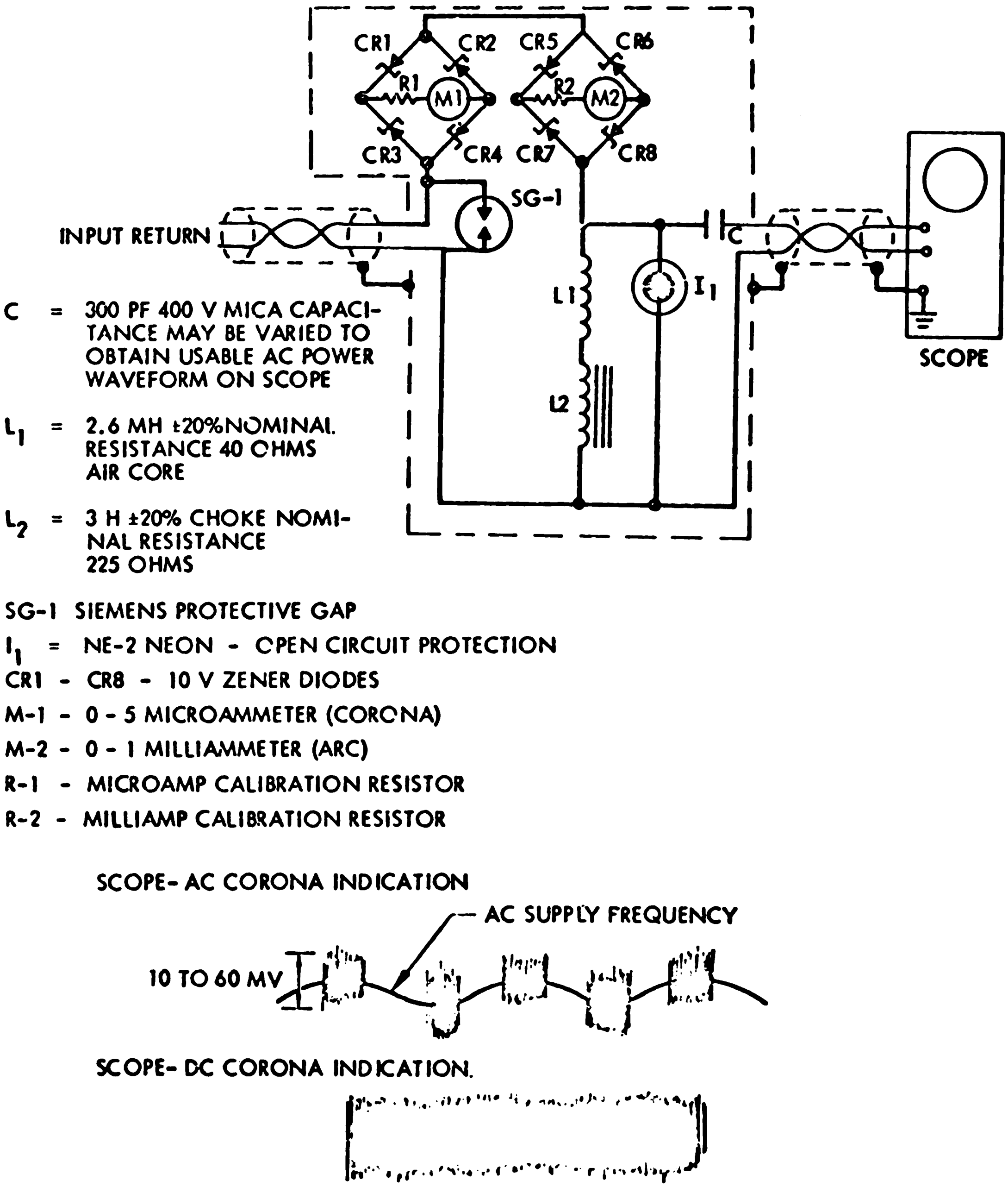

NOTES:

1. IF ELECTRODE CONFIGURATION IS UNSYMMETRICAL, CORONA BURTS ON ONE POLARITY OF SUPPLY FREQUENCY WAVEFORM MAY BE ABSENT.
2. ABRUPT BREAKS IN SCOPE TRACE OR BURST AMPLITUDES > 0.5 VOLT PEAK-TO-PEAK INDICATE ARCING, RATHER THAN CORONA.
3. SCOPE SENSITIVITY 10 MV/CM.

Figure 7. Corona Detection Network Schematic

regard to adjacent metallic surfaces, terminals, etc. Potting, coating or encapsulation shall be similar to that applied to the electronic part in the complete subsystem.

4.3.2.3 Test voltage amplitude. The test voltage shall be twice the maximum operating voltage. If both ac and dc voltages are applied simultaneously to an electronic part during normal operation, the test voltage shall be an ac sine wave with a peak amplitude equal to twice the sum of the dc and ac operating voltages. If it can be shown that application of the test voltage specified herein will exceed the manufacturer's rating. the test voltages may be reduced to 130 percent of maximum operating voltage upon written approval by JPL (if the objectives of 4.3.1 can still be met).

4.3.2.4 Test voltage frequency. The frequency of the test voltage shall be within ±10 percent of that experienced by the electronic part during normal operation. DC voltages shall not be applied to electronic parts normally operating at ac potentials. Electronics parts, which normally operate on dc voltages, shall be tested by the application of a dc voltage in accordance with 4.3.2.3. Electronic parts which normally operate on ac shall be tested by sine wave voltages of a peak amplitude as specified in 4.3.2.3. If more convenient, a 60 Hz sine wave instead of the normal operating frequency may be used, subject to the restriction that the 60 Hz test frequency shall not be nearer than ±20 percent of the resonant frequency of the part, such a test frequency shall not cause damage to the part, and the normal operating frequency is under 6 kHz. Electronic parts normally operating at frequencies above 6 kHz shall be tested at their nominal operating frequency.

4.3.2.5 Test voltage application. Voltages shall be applied between terminals of the electronic part. If the terminals are insulated from the metallic case or mounting hardware, the test voltage shall also be applied between the terminal and the case or the mounting hardware.

4.3.2.6 Rate of voltage application. The test voltage shall be raised uniformly from nominally zero to the final value at a nominal rate of 500 volts per second, dc or rms, unless otherwise specified.

4.3.2.7 Test duration. The test voltages shall be applied in accordance with applicable paragraphs of this document for the minimum length of time of 1.0 hour in the critical pressure region.

4.3.3 General electronic part acceptance tests. Acceptance tests at sea level conditions of electronic parts for flight subsystems shall be performed on all electronic parts rather than a sampling basis to screen out electronic parts with defective workmanship or concealed damage.

4.3.3.1 Operating test voltage. The voltage applied between the terminals of an electronic part shall be 130 percent of the operating voltage for the test time specified in 4.3.3.5.

4.3.3.2 Insulation test voltages. Transformers with graded insulation shall be exempt from the requirements of this paragraph. In transformers without graded insulation, voltages applied between all the terminals tied together and mounting hardware shall be of sufficient magnitude to stress the dielectric at the narrowest section to 80 percent of the rated dielectric strength of the insulation material for the period of test time specified in 4.3.3.5. Components with no conducting mounts or enclosures shall be buried in metallic shot or have a conducting foil wrapped on the surface of the insulation to serve as the voltage return. Corona detection networks shall be used to monitor possible corona or arcing.

4.3.3.3 Frequency. The frequency of the applied voltage shall be the same as that under normal operating conditions. If this is not practical, then 4.3.2.4 shall apply.

4.3.3.4 Rate of application. The rate of application of test voltages may be instantaneous. The minimum rate shall be as required in 4.3.2.6.

4.3.3.5 Test duration. The minimum time for the full voltage to be applied to the electronic part shall be 5.0 ±1.0 seconds.

4.3.4 Transformer/inductor tests. Qualification tests of transformers and inductors shall be in accordance with 4.3.2. The tests specified in 4.3.4.1

through 4.3.4.5 shall be a requirement for acceptance prior to installation in a subsystem. Part acceptance tests as well as design qualification tests on transformers and inductors shall be performed in the critical pressure region.

4.3.4.1 Test configuration. The configuration for testing transformers and inductors shall be as shown on Figures 8 and 9. Electrical connectors and wire leads shall be corona proof when the pressure is in the critical pressure region.

4.3.4.2 Interwinding insulation. The insulation integrity between windings, between a winding and the core, and between a winding and the case if one is used, or between windings and mounting inserts, if used, shall be tested by applying a voltage between the various windings, cores, etc., in accordance with Figure 8 and Table I for the length of time specified in 4.3.3.5.

Table I. Interwinding Insulation Test Voltages

Working Voltage (dc plus peak ac)	Test Voltage (rms)
250 to 700 volts	2.8 x working v.
Above 700 volts	1.4 x working v. plus 1000

4.3.4.3 Intrawinding insulation. Transformers shall be subjected to a voltage sufficient to cause twice the rated voltage to appear across all windings at the critical pressure region. The test voltage may be applied to any winding as shown on Figure 9. Care shall be taken to terminate all transformer terminals so that external corona or arcing is prevented. Mountings and windings shall be grounded as they would be in service. The test frequency shall be far enough from any resonant frequency, so that voltages more than twice rated voltage will not occur in any winding. Twice the rated voltage shall be applied across an inductor winding at approximately twice the normal frequency or in a manner that will not exceed twice rated current.

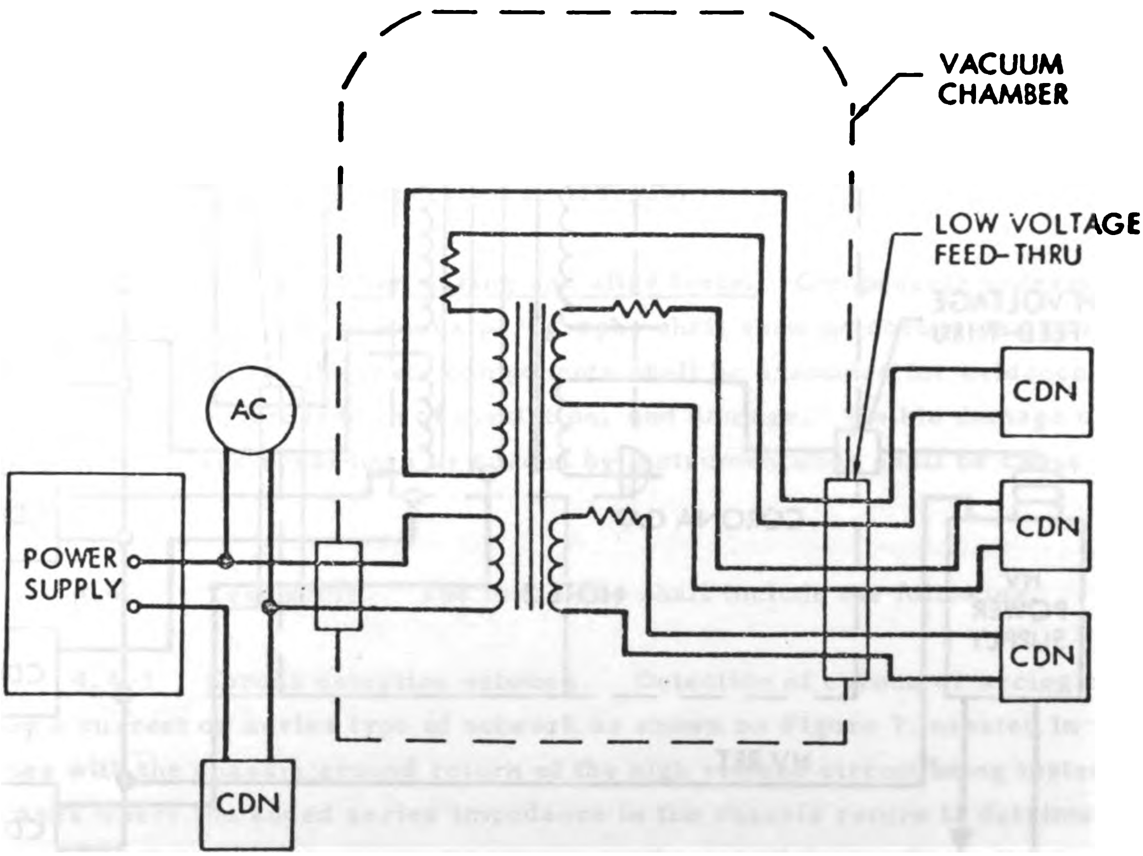

NOTES:
1. RESISTORS ARE LOADING R'S FOR SECONDARY WINDINGS. (MAY BE LOCATED OUTSIDE OF CHAMBER)
2. NEON INDICATOR I_1 SHALL BE BYPASSED FOR THIS TEST.
3. POWER SUPPLY VOLTAGE SHALL BE TWICE RATED VOLTAGE FOR THE WINDING ENERGIZED WITH THE FREQUENCY RAISED SO THAT AC CURRENT FLOW IS EQUAL TO OR LESS THAN RATED CURRENT.
4. GROUNDING TYPE SELECTOR SWITCH MAY BE USED WITH ONE CORONA DETECTION NETWORK.
5. CDN = CORONA DETECTION NETWORK (SEE FIGURE 2).

Figure 8. Transformer Intrawinding Breakdown Test

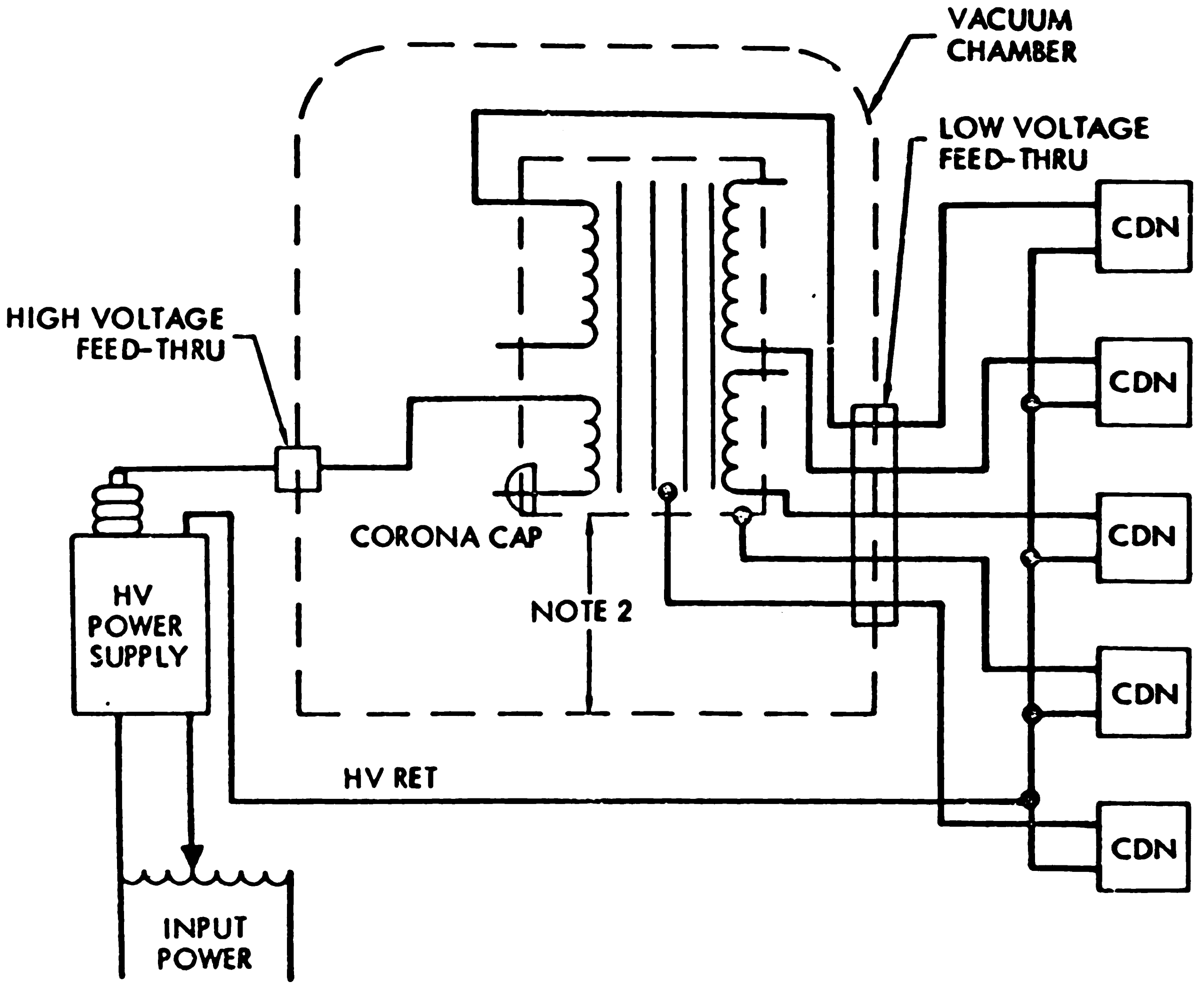

NOTES: 1. GROUNDING TYPE SELECTOR SWITCH MAY BE USED WITH ONE CORONA DETECTION NETWORK.

2. TRANSFORMER MUST BE ELECTRICALLY INSULATED (LOW VOLTAGE) FROM VACUUM CHAMBER GROUND.

3. CDN = CORONA DETECTION NETWORK (SEE FIGURE 2).

Figure 9. Transformer Interwinding Breakdown Test

4.3.4.4 Test duration. Test duration requirements shall be as follows:

a. Design qualification: Test duration for component design qualification tests shall be as specified in 4.3.2.7.

b. Component acceptance: Test duration for component acceptance shall be as specified in 4.3.3.5.

4.3.4.5 Examination during and after tests. Components undergoing tests as described in the previous paragraphs shall show no corona or arcing during the test. After the test, components shall be examined for evidence of arcing, flashover, breakdown of insulation, and damage. Visible damage or detection of voltage breakdown or corona by instrumentation shall be cause for rejection.

4.4 Test setup. The test setup shall include the following.

4.4.1 Corona detection network. Detection of corona or arcing shall be by a current or series type of network as shown on Figure 7 inserted in series with the chassis ground return of the high voltage circuit being tested. In cases where the added series impedance in the chassis return is detrimental to the operation of the component or system, the parallel or voltage type described in MIL-T-27C shall be used. Selection of the type detection network used shall be based on the following criteria.

a. The current or series type shown on Figure 7 is composed of low voltage rating elements in the chassis ground or low voltage return side of the circuit, and enables isolation of the of the returns so that the location of the corona may be determined.

b. The high voltage or shunt type specified by MIL-T-27C consists of a high voltage capacitor and inductor in series with the capacitor connected directly to the high voltage terminal and the inductor grounded. The common node provides the input to an oscilloscope. The capacitor shall be corona-free, otherwise, corona occurring in it will be indistinguishable from that occurring in the equipment undergoing tests.

The current or series type of corona detection net work is the only setup that can be used with equipment in which the high voltage connections are located inside the vacuum chamber and are not accessible. An additional advantage of this network shall be that it will be possible to distinguish between corona externally at a component terminal and internally through the case insulation. Corona occurring at a terminal in a vacuum chamber, which is not a defect of the component, will not abort the test by preventing the detection of corona occurring in the component. The parallel type described in MIL-T-27C does not have this capability.

4.4.1.1 Series corona detection network. The current type corona detection network is inserted in series with return or chassis ground lines to monitor the corona or arc current flowing in the circuit. The input to the corona detection network consists of two zener diode rectifier bridges and two inductors, all in series as shown on Figure 7. Meter M1 in the first bridge measures corona currents in the 0 to 5 microampere (μa) range. The second bridge covers the 0 to 1.0 milliampere (ma) range. Currents in excess of 5.0 μa cause a voltage drop of 10 volts across R1; the zener diodes then conduct thus protecting the microammeter from excessive currents. With the microammeter protected, the currents in the 0 to 1.0 ma range due to arcing will be indicated on M2. Arc currents, whether pulses or continuous, in excess of 1.0 ma cause a corresponding 10 volt drop across R2, zener diodes CR-5 to CR-8 conduct, protecting the milliammeter. Inductances L1 and L2 in series provide a significant ac impedance from audio frequencies to nearly 0.5 mHz, the frequency range of corona voltage. The function of the capacitor C is to attenuate the ac supply frequency to a sufficient degree, but to pass the corona burst pulses so that the maximum sensitivity of the oscilloscope may be utilized. The power supply waveform appearing on the oscilloscope serves as a reference for corona bursts, as shown by the waveform sketch on Figure 7. Corona bursts can thus be distinguished from extraneous noise in the circuit. This circuit will operate with either ac or dc corona currents, or combination of both, without switching.

4.4.1.1.1 Network ac operation. The positive and negative sections of the ac current waveform are rectified by alternate branches of the bridge, with the resulting dc passing unidirectionally through the meter circuit. Since the meters cannot distinguish between corona current and any capacitive current, the main reliance for corona indication is the oscilloscope. A typical ac waveform with corona burst is shown on Figure 7.

4.4.1.1.2 Network dc operation. In dc operation, capacitor C1 will attentuate power supply ripple or low frequency noise. The high frequency corona burst may or may not appear on the oscilloscope depending on the geometry, voltage, polarity, and other factors. DC corona indication may also be a burst rather than a continuous smear as shown. In this event, the microammeter will indicate the presence of corona.

4.4.2 Vacuum chamber. The vacuum equipment should have sufficient capacity to pump down to the critical pressure region within 20 minutes with the chamber air and outgassing loads present.

4.4.2.1 Vacuum chamber penetration. Where possible, to eliminate any terminals in a vacuum, all high voltage connections required through the interface may consist of insulated wires embedded in the component and long enough to pass through the vacuum port without splicing. Vacuum sealing can be achieved by "O" ring seals under compression around the wire insulation. A continuous pumping system can tolerate the leakage of these seals, with the moderate vacuum requirements of the critical pressure region. After acceptance, the component leads can be cut to installation length.

4.4.3 Electrical connections. Connections to high voltage, especially ac, terminals of equipment inside the vacuum chamber or splices in high voltage cables should be kept to a minimum. Where such connections are unavoidable, they can be encapsulated in a resilient, easily removable resin using applicable paragraphs of 3.4 as a guide only, because of the temporary nature of the connections. To minimize air bubble formation, the requirements of 3.4.10 should be followed. After polymerization for a high voltage dc connection, a conducting shell of foil shall be wound on the resin and connected to a corona detection network to monitor the connection for corona or arcing. Any voltage breakdown occurring through the encapsulated connection may give a false indication of a voltage breakdown in the component or subsystem. For a dc connection, the insulation integrity shall be monitored by enclosing the encapsulation with a conductive material (e.g., foil) which is connected through the vacuum interface to a corona detection network. An ac connection shall require similar enclosure of the encapsulation with a conductive material, but with the added requirements of 3.3.9. Monitoring of the insulation integrity shall be with the corona detection network which will be more difficult due to the capacitive current possibly masking a low level corona.

4.4.3.1 Switching. Switching of component or subsystem high voltage leads shall be accomplished external to the vacuum system.

4.4.4 Oscilloscope. The frequency response of the vertical amplifiers of the oscilloscope shall be flat from low audio frequencies of 1.0 MHz or higher. Deflection sensitivity of the trace shall be 10 millivolts/cm or higher. The zero trace of the oscilloscope shall be blanked out visually by opaque tape so that the intensity can be turned up sufficiently to see the corona bursts.

4.5 Rejection and resubmittal. High voltage parts and components that fail to meet all the requirements of this document shall be rejected and returned to the contractor. Prior to resubmittal, if applicable, the contractor shall furnish the JPL procurement division representative and the JPL cognizant engineer full particulars in writing regarding the cause of failure and the action taken to correct the deficiencies.

5. PREPARATION FOR DELIVERY

Not applicable.

6. NOTES

6.1 Definitions. Definitions applicable to this document are as follows:

6.1.1 Voltage breakdown. Voltage breakdown as used in this document refers to either arcing or corona.

6.1.1.1 Corona. An incomplete or partial voltage breakdown of the air or gas adjacent to one or both electrodes or conductors, resulting in a current flow of the order of 10^{-7} to 10^{-6} amp rms.

6.1.1.2 Arcing. A complete voltage breakdown of dielectric between two conductors, with currents of the order of milliamperes or higher, limited only by power supply impedance.

6.1.2 Damage. Damage within the requirements of this document is hereby defined as any degradation, deterioration, or gross change in a circuit component or subsystem that would significantly shorten its operating life or cause permanent out-of-tolerance change in performance.

6.1.3 Critical pressure region. The range of pressure through which the dielectric strength of the air reduces to 20 percent or less of the dielectric strength of 20°C and sea level pressure, shall be the critical pressure region for the purpose of this document. Nominal limits of the critical pressure region in air are 50 torr (60,000 feet altitude) to 5×10^{-4} torr (310,000 feet altitude).

6.1.4 Electronic parts. In this document electronic parts refer to common items such as resistors, capacitors, transistors, and diodes.

6.1.5 Components. A component consists of several electronic parts assembled, interconnected, to perform a function not possible with single part; e.g., diode bridge, filter network, regulator and cable harness.

6.1.6 Equipment. Equipment refers to a collection of components and parts to perform a function such as power supply and modulator.

6.1.7 TA. Designates Type Approval or qualification tests.

6.1.8 FA. Designates Flight Acceptance level of tests for flight parts, components, or equipment.

APPENDIX 2

HELIOS—A AND —B
EXPERIMENT 7 POWER SUPPLIES

May 14, 1971

GSFC Specification 31187B

Helios A & B Missions

Detector Bias Supplies and Low Voltage

Power Supplies for Experiment 7

1.0 INTRODUCTION

This specification describes power supplies which will be utilized in a cosmic radiation experiment for the Helios A & B missions, a German-U.S. cooperative project. These supplies provide the biases required for the solid state detectors and the x-ray proportional counters; the voltage required for the PHA and coincidence system described in Specification 31187A; and other voltages as described in Sec. 3.1.3.1. Mission lifetime is at least two years. Reliability and quality assurance of these systems is of the utmost importance, and considerable effort in these areas will be required. In addition, weight and power requirements are extremely stringent and must be rigidly adhered to in the conception and design of these systems.

2.0 APPLICABLE DOCUMENTS

The documents listed below form a part of this specification to the extent specified herein. In the event of conflict between this specification and those of any of the following documents, the requirements of this specification shall prevail.

S-702-P-1A, Specification for Reliability and Quality Assurance Provisions for Helios Project Instruments, Goddard Space Flight Center, August 7, 1970.

3.0 ELECTRICAL CHARACTERISTICS

3.1 General

The power converter is supplied 28 volts ± 2% at its input terminals from a solar-cell/chemical-battery power system. The low voltage outputs power both low-level analog circuitry and fast digital circuitry. Thus, isolation of these two classes of output from each other as well as from the detector biases is required in order to keep ground looping and system noise to a minimum.

3.1.1 Converter Input Characteristics

3.1.1.1 Voltage - The regulated output voltage from the main spacecraft inverter is 28.0 volts. Connector, relay and wire resistances are in series with the 28 volts. You are to assume that the regulation is ± 2% at the converter input. The experiment power bus is energized through a spacecraft relay by command.

3.1.1.2 Ripple and Noise Tolerance - Except for transient excursions described in 3.1.1.3 below, the power supply shall be capable of operating within specifications when the input power includes electrical noise of 1.5 volts peak to peak in the frequency range 4 Hz to 5MHz.

3.1.1.3 Transient Voltage Excursions - Temporary loss of power may occur at any time as the S/C power distribution system automatically dumps loads to protect itself from an overloaded condition. Experiments would then be turned on one at a time by command. Additionally, transients can occur when the spacecraft switches between redundant regulators, etc. Thus, the S/C has imposed the following survival tests for spikes on the power lines. In the frequency range 2 Hz to 20 KHz, the amplitude of the spikes (pos. and neg.) is to be 7 volts. For a single pulse, the amplitude shall be 28 volts, positive and negative. All pulses are referenced to 28 volts dc and the pulses will rise to peak values in 1 microsecond and decay to zero in approximately 10 microseconds. Additionally, the power supply shall be designed to survive application of 35 volts dc indefinitely and 56 volts dc for at least 100 milliseconds.

3.1.1.4 Source Impedance - The model of the spacecraft power output is a voltage source of 0.1 ohms inherent resistance shunted by 500 μF. To this must be serially added the 0.3 ohms of the harness, connectors, etc.

3.1.1.5 Power Switching - The spacecraft delivers a power synch signal for synchronization of the experiment power converters. It is specified as follows:

a. frequency: 39,947 KHz

b. frequency accuracy: 10^{-4}

c. duty cycle: 1:2

d. Accuracy of duty cycle: $\pm$ 10%

e. Rise/Fall time: $\leq$ 1 μsec

f. Input "0": 0 to 0.7 volts

g. Input "1": + 2.0 to + 5.5 volts

h. Reference: + 28 volt return line

i. Source Resistance: $1\ K\Omega < R_s < 1.2\ K\Omega$

It is intended that the power converter divide the incoming synch frequency by 2 and thus that the converter operate at 19,973 Hz. All primary side circuitry must operate from + 28 volts to the + 28 volt return line.

3.1.1.6 Input Grounding - Note that the mechanical chassis of this power supply will be attached directly to S/C chassis ground. The input voltage and input return are delivered on a twisted pair, and the maximum capacitance allowed from either line to chassis ground is 1000 pf.

3.1.1.7 Turn-on Current Limitation - The turn-on current in excess of the nominal current must average to less than or equal to 0.5 milliampere-seconds during the 1 millisecond period following turn-on.

3.1.1.8 Reflected Ripple - When operating from the power source described in Sec. 3.1.1.4 and fully loaded, the converter shall not feed back on the S/C power bus electrical current noise in excess of that shown in Fig. 3.11 and 3.12. The limits for radiated emission are given in Figs. 3.13 and 3.14.

3.1.2 Operating Characteristics

3.1.2.1 Frequency - The converter may operate at 19,973 Hz as described in Sec. 3.1.1.5 or at any frequency in excess of 200 KHz, or separate sections may operate at different frequencies (e.g. the low voltage at 19,973 KHz and the high voltage at 350 KHz, for instance). The choice of operating frequency should be made on the basis of converter efficiency, weight and RFI considerations.

3.1.2.2 Starting Time - The low voltages shall be within limits at full load within 20 seconds after being off at least two hours at any operating temperature. The detector bias outputs shall exhibit a delayed turn-on/off characteristic described later in this specification.

3.1.2.3 Efficiency - The available power for this mission is seriously limited, thus as high an efficiency as possible is required. Design goal shall be 80%. Converter designs which provide less than 75% efficiency at any temperature or input voltage within the nominal requirements of this specification, when the outputs are nominally loaded as listed below, are not acceptable.

3.1.3 Low Voltage Output Characteristics

3.1.3.1 Low Voltage Outputs - The low voltage outputs required, and the nominal load on each are as follows:

Voltage or System	Current	Power
+ 12 volts	8 ma	96 mw
+ 7.5 volts	128 ma	997 mw
+ 4.7 volts	60 ma	282 mw
- 2.0 volts	80 ma	160 mw
- 10 volts	1 ma	10 mw
PHA & Coin System, Spec 31187A		930 mw
Detector Bias Supplies		150 mw
	Secondary total	2.625 watts

In computing the above total we have assumed that the PHA and coincidence system described in Specification 31187A required 930 mw. This estimate is extrapolated from our past experience. Note that the - 10 volt bias may be any stable voltage from - 10 to - 15 volts. For this calculation we have assumed that the bias supplies require 150 mw, operating from regulated secondary voltages. However they may operate from the primary 28 volt source if the proposer wishes.

At 80% efficiency with a 28.0 volts bus at 23^{o}C, this load of 2.625 watts will draw 3.28 watts from the bus, and at 75% efficiency will draw 3.50 watts.

3.1.3.2 Regulation - The + 4.6, and - 2.0 outputs are used for digital applications. They shall be constant within ± 4% for all temperatures and input conditions specified, and for all load conditions from 0.7X to 1.3X nominal as listed above.

All remaining low voltage outputs shall be constant within ± 1.5% for all temperature and input conditions specified, and for all load conditions from 0.7X to 1.3X nominal as listed above.

3.1.3.1 Ripple Content - The maximum ripple and noise content on any low voltage output under any combination of environmental, input, and output loading conditions specified, shall not exceed 10 mV, peak to peak. Ripple shall be measured at the output terminals with the converter fully loaded and with an oscilloscope of DC to 50 MHz bandwidth.

3.1.1.4 Grounding - Output circuit common for the digital outputs shall be separate from the output common for all remaining output voltages, and of course both shall be isolated from input common as specified above. The common for the detector biases shall be separate from both the digital and analog voltages. Note that the experiment will tie the secondary grounds together.

3.1.3.5 Short Circuit Protection - The converter must be designed so that a short circuit condition on one or more outputs will not cause permanent damage. This includes short circuit or any of the detector bias outputs as well.

3.1.4 Detector Bias Output Characteristics

3.1.4.1 Solid State Detector Biases - The converter shall supply bias voltages for use on the solid state detectors as listed below. The maximum load shown occurs only at the high temperature extreme, while the minimum load occurs at the low temperature extreme. The nominal load should be used for purposes of satisfying Sec. 3.1.3.1.

Voltage	Current		
	Minimum	Nominal	Maximum
500 V	1 μa	30 μa	150 μa
55 V	0.1 μa	1 μa	10 μa
25 V	0.1 μa	1 μa	8 μa

3.1.4.2 Regulation - The solid state detector bias outputs shall be within ± 3% of nominal for all conditions of temperature, input voltage and output load from zero to maximum current as shown in 3.1.4.1.

3.1.4.3 Ripple and Noise Content - The bias supply outputs must contain an absolute minimum of ripple and noise. Under no conditions shall the solid state detector biases contain more than 10 mv peak to peak in any frequency region. Ripple and noise shall be measured at the converter output terminals with an oscilloscope of DC to 50 MHz bandwidth. The measurement shall be made for minimum, nominal and maximum load. Input and output commons must be isolated.

3.1.5.5 Proportional Counter Bias - The proportional counter requires a nominal bias of 1600 volts. The design of the supply should allow for adjustment in this output bias in approximate 25 volt steps to ± 100 volts of the 1600 volts. The load current is usually near zero, but design for a 0.5 μa nominal load and a 2 μa maximum load. The selected proportional counter bias shall be within 0.2% of nominal for all conditions of temperature, input voltage and output load from zero to maximum current. The noise and ripple specification 3.1.4.3 applies.

3.1.4.5 Grounding - Bias output common shall be isolated from the digital and analog supply commons. The experiment will make the connections between commons in the final wireup. Bias common will always be isolated from the + 28 volt return as previously specified.

3.1.4.6 Turn-on Characteristics - Any transients on the bias outputs are coupled to the input of the low-level charge-sensitive preamplifiers. The turn-on and turn-off characteristics of the bias outputs shall be slow to avoid damage to the preamps. This requirement includes a slow decay or rise due to input voltage drop-out. Specifically, the turn-on/off characteristic shall be similar to a ramp or exponential shape, with at least 3 seconds between the 10 and 90% points, and preferably 5 to 10 seconds.

3.1.4.7 Special Considerations - The high voltage outputs shall be such that with no power applied to the input, 25 volts may be applied to the 25 and 55 volt outputs. The DC impedance of the un-powered outputs shall be such that not more than 20 nA will flow into the converter outputs from the external source. 100 volts may be applied to the 500 volt output with a converter design such that less than 50 nA will flow into the converter outputs from the external source.

3.1.5 Alternate Load Specification

For those proposers who wish to bid on the power/bias supplies exclusive of the PHA and coincidence system per Specification 31187A, we have assembled a voltage/current specification for bidding purposes. The exact voltages other than those explicitly given in Sec. 3.1.3.1 will not be known until the PHA and Coincidence system contractor is selected. At that time, negotiations will proceed with those proposers who are in the competitive range.

Voltage	Current	Power
+ 12	8 ma	96 mw
+ 7.75	128 ma	997 mw
+ 6.0	60+ma	361 mw
+ 4.7	60 ma	282 mw
+ 3.0	69 ma	207 mw

Voltage	Current	Power
- 2.0	80 ma	160 mw
- 6.0	60⁺ma	361 mw
- 12.0	1 ma	12 mw
Detector biases		150 mw
	Secondary Total	2.626 watts

All other specifications apply exactly.

4.0 MECHANICAL CHARACTERISTICS

4.1 Packaging

Outline drawings of the low voltage converter and the detector bias supplies are shown in NASA/GSFC drawings GD-1324980 and GC-1324981 respectively. The locations of the mounting holes are called out, but a proposer can propose alternate locations on the same faces. Similarly, the location areas for the interconnection terminals are specified. Since weight and efficiency are of primary concern, all dimensions should be taken as maxima.

The detector bias supplies may be broken into two assemblies if desired, one for the solid state detector biases and one for the proportional counter supply (1600 volts). In this case, the solid state detectors bias supply should package well within the specifications of drawing GC-1324981. It is our thought in writing this paragraph that it may be to our advantage to mount the proportional counter power supply directly to the top flat surface of the proportional counter itself, thus minimizing the cable runs, interconnection problems, etc. There is a wide range of acceptable packaging arrangements for the proportional counter power supply, but the precise details will have to be worked out after the precise mechanical details of the proportional counter are firm.

4.2 Weight

The complete converters with digital, analog and detector bias outputs are assigned 390 grams or 0.86 pounds. This weight includes the weight of all shielding necessary to meet the rfi requirements.

4.3 Heat Sink

The large flat mounting surface of the low voltage power supply will be in direct contact with the experiment baseplate which is a good thermal sink and which will never exceed + 30° C in flight. Note that the chases of these power supplies will be attached directly to S/C chassis ground, and that galvanic isolation between chassis ground and the + 28 volt return line and the power supply grounds (experiment signal ground) must be maintained. The maximum capacitance allowed between (1) the 28 volt power line and chassis ground and (2) the power supply grounds (summed) and chassis ground is 1000 pf for each of the two cases.

4.4 Thermal Range

The qualification limits for this experiment are - 40°C and + 40°C. All electrical performance specifications hold over this range, and the contractor must test the system over this range, document the tests to verify the performance and furnish such documentation with each delivered unit.

4.5 Vibration Tests

The launch vehicle presently assigned to these missions is a Titan-Centaur. The following tables summarize the qualification levels for vibration and shock.

4.5.1 Sinusoidal Vibration Test Schedule

Axis	Frequency Range	Acceleration
	Hz	g's (0-peak)
Thrust	5-10	0.45 inches(d.a.)
	10-50	15
	50-150	23
	150-200	10
	200-2000	4
Lateral	4-9	0.45 inches(d.a.)
	9-30	12
	30-100	25
	100-200	10
	200-2000	4

The rate of change of frequency shall be 2 octaves per minute.

4.5.2 Random Motion Vibration Test Schedule

Axis	Test Duration (min)	Freq. Range (Hz)	PSD (g^2/Hz)
All three axes	4.0 per axis	20-200	6 db/octave to 0.1125 g^2/Hz at 200 Hz
		200-2000	0.1125 g^2/Hz

Overall level 14.4 g rms duration 4 minutes each axis.

4.5.3 Acoustic Vibration

Each instrument will be tested for susceptibility to acoustic shock by subjecting it to programmed noise per method 515, MIL-S-810 to the following levels for a total duration of 2.0 minutes.

Octave Band Center Frequency	Sound Pressure Level Ref: 0.0002 microbar
16 Hz	123 db
31.5	128
63	135
125	141
250	144
500	142
1000	137
2000	133
4000	132
8000	132
Overall	148

4.6 Interconnection

For reliability and weight considerations, all input and output connections will be by solder terminals except for the low voltage power supply (ref. drawing GD-1324980). If connectors can be included within the weight constraints, only Cannon Royal D, single density connectors will be considered. All connectors will be furnished in a non-magnetic version by NASA/GSFC. In the case of solder terminals, use of a pigtail cable with connector is encouraged to facilitate connections for testing and, if used, should remain attached when delivered. The pigtail would be used for all testing and integration at GSFC up to final assembly. This would eliminate unnecessary soldering and un-soldering of wires on the terminations.

Wherever practicable, connections between these terminals and internal printed circuits shall be accomplished by means of insulated wire at least one-half inch long. This is to prevent overheating pads or crystallizing solder when connections are made to the terminals.

4.7 Construction and Materials

Circuitry may be designed using printed circuits, integrated circuits, thick film, thin film, welded-wire modules, point-to-point wiring, soldering or any combination thereof. The converters shall be conformally coated. Polyurethane coatings are preferred and should be selected with the concurrance of NASA/GSFC to ensure compatibility with the silicon nuclear particle detectors within the experiment.

Particular care shall be taken in surface preparation to insure complete adhesion of potting material to all components and surfaces.

Construction and assembly techniques shall be such that reliable repairs are possible should any part fail.

Non-magnetic materials shall be used wherever possible. Nickel wire is not acceptable in the welded construction. Magnetic shielding material may not be used without the concurrence of the technical representative. See Sec. 6.0.

5.0 PARTS SELECTION

Parts shall be selected on the basis of proven qualification in a space flight application. All parts on the current NASA/GSFC Preferred Parts List are candidates. An additional list of parts is included within this specification (Sec. 5.1).

All parts should be purchased to the appropriate MIL specification as listed in the parts lists. All semiconductors should have a precap visual inspection to MIL-STD-883, Method 2010.1, Condition A or to the manufacturer's standard in-house viaual inspection which is comparable to the MIL-STD-883 test method and conditions indicated above (NASA/GSFC approval is required for this latter step). All parts should be screened as outlined in the GSFC Preferred Parts List, Appendix C, Screening of Electronic Parts for Flight Equipment. This Appendix is attached to this specification. Parts should be serialized, with the exception of carbon resistors and ceramic capacitors, prior to electrical screening.

All parts must receive formal, written approval by NASA/GSFC before a contractor can finally commit his design to them. A complete list of all parts and their purchase specifications must be furnished to NASA/GSFC. Approval or disapproval of parts from the current NASA/GSFC Preferred Parts List will occur within 5 working days of GSFC receipt of the list. Approval or disapproval of parts not on the current NASA/GSFC Preferred Parts List will occur within 15 working days of GSFC receipt of the list.

Component packages other than standard can be considered--e.g., a transistor normally supplied in a metal TO-5 package can be specified in a ceramic flat package which is hermetic and of low magnetic signature; however, the part will be subject to approval/disapproval as a part not on the GSFC Preferred Parts List. Any part carrying a special or house number designation shall be described by means of the procurement specification including electrical parameters before the part can be considered for approval/disapproval.

5.1 Additional Acceptable Parts

Type	Manufacturer, Code
Capacitor, low TC	Vitramon VY10, VY15
Resistor, variable	Bourns, 3082 Cermet
Zener Diodes	Fairchild, FCT 1121-1125
Tunnel Diode	Gen. Electric, STD-860
Hot Carrier Diode	Hewlett Packard, HP2800
Op. Amp.	National, NH0001F/883
Const. Current Diodes	Motorola, 1N5291-1N5297
Transistor	Solitron, 2N3751

The above parts have been listed by the manufacturer's common designation. However, they should be procured to the highest existing MIL specification available at the time of procurement; viaual inspection to the conditions of MIL-STD-883 should be specified for semiconductors; and they should undergo the screening called out in Appendix C of the GSFC Preferred Parts List.

6.0 MAGNETIC REQUIREMENTS

The Helios spacecraft is a magnetically clean spacecraft. The design of the systems specified here must meet the following specifications. The maximum tolerable field in the three orthogonal directions should each be less than that listed as maximum for the radial field measurements.

Test Condition	Maximum Radial Field at 18 Inches
1. Post 30 gauss deperm	1.0 gamma
2. Post 15 gauss exposure	16 gamma
3. DC Stray field	0.1 gamma
4. Perm field after power ON/OFF	1.0 gamma

7.0 QUALITY ASSURANCE AND RELIABILITY

High reliability of the system shall be assured by choice of good design, inspection and testing. The supplier shall maintain an effective and timely reliability and quality assurance program which satisfies at a minimum the requirements of GSFC Specification S-702-P-1A, "Reliability and Quality Assurance Provisions for Helios Project Instruments. Monitoring of the supplier's inspection system will be accomplished through the combined efforts of NASA/GSFC personnel and the designated government inspection agency. The authority and responsibilities of the government inspection acency will be defined subsequent to contract award by GSFC through a letter of delegation to the inspection agency.

Inspection standards shall be established at the part, component, module or board, and systems levels to detect fabrication errors, contamination, poor workmanship, etc. Inspection shall be on a 100% basis.

7.1 In-Process Inspection

The physical in-process inspection of the equipment produced for flight use only shall be performed in a sequence specified by a production flow chart to be submitted. All inspections shall be documented or approval indicated by QC stamps on the assembly print or QA traveller on each module and made available to NASA upon request.

7.2 Receiving Inspection

100 per cent of electrical and electronic parts for the flight units shall be inspected for visual damage prior to assembly. Particular emphasis shall be placed on those characteristics for which deficiencies may not be detected during subsequent inspections and tests.

7.3 Changes

The contractor shall notify GSFC of any proposed changes in design, fabrication method, inspection procedure, or process previously approved by GSFC, including changes which may affect the quality of the end-item, and obtain written approval of the change from the GSFC Technical Representative.

7.4 Parts Records

During fabrication and test of all units, installation of all serialized parts (with the exception of carbon resistors and ceramic low voltage capacitors) and contractor serialized modules will be recorded on assembly prints and test records to scrupulously maintain traceability of piece parts within each system. All GFE parts will be screened and serialized before shipment to the contractor for assembly. Contractor manufactured electronic parts, such as thick film wafers, will be serialized by the contractor.

7.5 Parts Control

All electronic parts and materials to be used in this system shall be controlled and segregated to avoid intermixing of Helios parts with those of any other program. Helios parts and materials shall be stored in a restricted area or locker clearly identified and which may be secured against unauthorized entry. They shall be subjected to a minimum amount of handling, and if necessary, handling shall be done by a limited number of authorized personnel.

7.6 Age Control and Life Limited Products

Parts and materials which degrade with age or use shall be marked to indicate when useful life was initiated, and the time or cycle of expiration at which useful life will be expended.

7.7 Identification Requirements

At the time of manufacture of each module, the installation of a serialized part shall be recorded by serial number on an assembly print designating the serial number of the wafer, module or assembly. Each part, component, module or assembly destined for a Helios flight unit shall be uniquely identified and suitably marked.

8.0 OPERATIONAL TESTING AND DOCUMENTATION

8.1 Operational Testing

Operational testing of each power supply system shall include at least the following throughout the range of temperature - 40°C to + 40°C:

1. Measurement of each output voltage when all outputs are simultaneously loaded at 0.7X, 1X, and 1.3X nominal at both high and low input limit (i.e. 28 V $\pm$ 0.5 V).
2. Photographs of ripple waveform and content under the conditions specified above and with input ripple and noise added per 3.1.1.2 and 3.1.1.3. This need be done at room ambient only. Output waveforms shall be observed during temperature tests, and deviations from the photographed pattern noted in the test record. Peak to peak value of ripple and spiking shall always be recorded in the test log.
3. Input current under each of the conditions specified in (1) above.

4. Calculation of efficiency under each of the conditions specified above.

5. Frequency(ies) of operation as a function of load and temperature.

6. Verification of proper starting and proper interface characteristics with the 28 V input source.

Performance parameters as listed above shall be recorded in a system log book or other suitable form, and will be delivered with each system.

Final temperature testing prior to shipment is subject to witness by the NASA technical representative, or his designee.

Environmental qualification testing will be conducted by GSFC to the levels indicated in this specification.

8.2 Module Testing

Module operational testing data, if any, taken on completed flight modules shall be recorded on data sheets or in a log for each module. Each data sheet or page shall contain the module type, part number and serial number. In addition, the data sheets shall contain part numbers and serial numbers of all transistors and/or diodes utilized in each module or alternately reference an assembly print where this information may be found. Individual and/or spare modules shipped to GSFC shall be accompanied by a copy of the respective operational test data sheets and/or assembly prints with part serialization included.

8.3 System Testing Documentation

A chronological log record shall be completed for each flight system which shall include the following information:

a. System name

b. Serial number

c. Serialized components list which contains all modules installed in the system by matrix module positions, type number and serial number. This is to provide ultimate traceability of each part into a system through a serialized module.

d. Module Operations Test Data Sheets as applicable.

e. Test and Inspection Summary which includes a description of all failures or unusual performance, operating and physical discrepancies observed and all repairs or adjustments made.

f. Certification of compliance with the requirements of the specification.

A copy of this log record shall accompany each flight system assembly shipped to NASA/GSFC.

8.4 Acceptance Testing for Delivery

The flight systems will be officially accepted by GSFC only after a full exercise of each system over the range of electrical and thermal requirements of this specification at the contractor's facilities and following vibration and shock tests at GSFC. GSFC is responsible for carrying out the vibration and shock testing within seven working days of actual delivery. Final testing at the contractor's facilities is subject to witness by technical representative or his designee.

8.5 Documentation

In addition to the orderly compilation of test data required by this specification, the contractor shall provide a complete set of circuit schematics; a parts list identifying manufacturer and type for all parts; a circuit performance description; and full assembly print for all modules and mother boards, showing PC interconnect patterns and location of parts referenced to schematic designations; and a complete set of mechanical drawings.

8.6 Marking

Each module, circuit board and package shall be unambiguously marked. Individual modules must be individually marked in a consistent manner to be determined by the contractor, so that no two modules can be confused.

8.7 Data Package

The data package which is referred to in the statement of work is made up of the documents required by Sec. 8.1, 8.2, 8.3 and 8.5.

8.8 Monthly Reports

The contractor shall submit a brief letter-type report covering the activities, progress and problems of a given month. The report shall be submitted by the 10th of the following month. The first monthly report will include an informative milestones schedule and subsequent reports will assess progress relative to this original schedule.

9.0 DISPOSITION OF NON-CONFORMING PARTS AND ASSEMBLIES

During the electrical screening process, rejection of more than 10% of a parts lot is cause for a telephone report to the technical representative within one working day. Subsequent to screening, when any part is rejected for any reason, or fails or malfunctions at any time, the technical representative shall be notified within 24 hours by telephone. The part or parts shall be removed carefully, and segregated from / conforming items and held for GSFC review. In general, all items will be returned to GSFC for failure analysis.

All instrument malfunctions which occur after initial assembly shall be reported to the technical representative by telephone, within 24 hours. Systems exhibiting minor deviations in performance from specifications may be submitted for acceptance upon concurrence of the technical representative.

10.0 EXCEPTIONS TO REQUIREMENTS OF THESE SPECIFICATIONS

If a proposing contractor takes exception or proposes an alternate to any specification or requirement stated within these specifications, he must describe the exception and his reasoning in detail in his proposal. Specifically, if minor relaxation of of certain specifications would significantly increase efficiency or decrease weight, or improve schedule considerations, such items should be discussed in the technical proposal.

11.0 SCHEDULE

Ultimately it is anticipated that four units will be procured as a result of this specification. Three units will be the subject of the original contract with the fourth unit to be an option to be exercised by NASA/GSFC by August 1, 1972.

	Delivery to GSFC
Unit #1	24 weeks after award
Unit #2	35 weeks after award
Unit #3	46 weeks after award
Unit #4	November 1, 1972

The limits for radiated emission are given in Figs. 3.13 and 3.14.

List of Figures, etc.

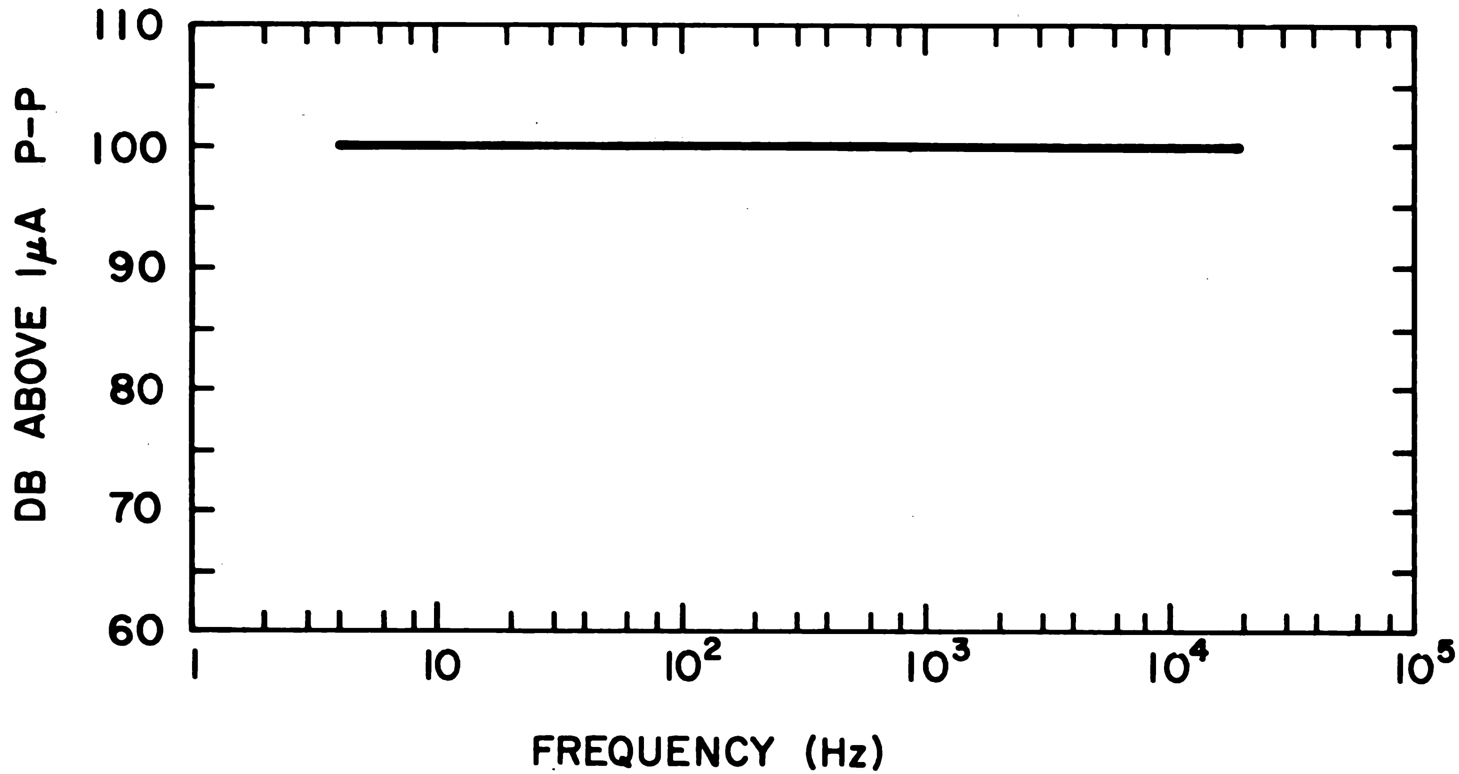

Fig. 3.11

LIMITS FOR CONDUCTED EMISSION, 4Hz-100KHz

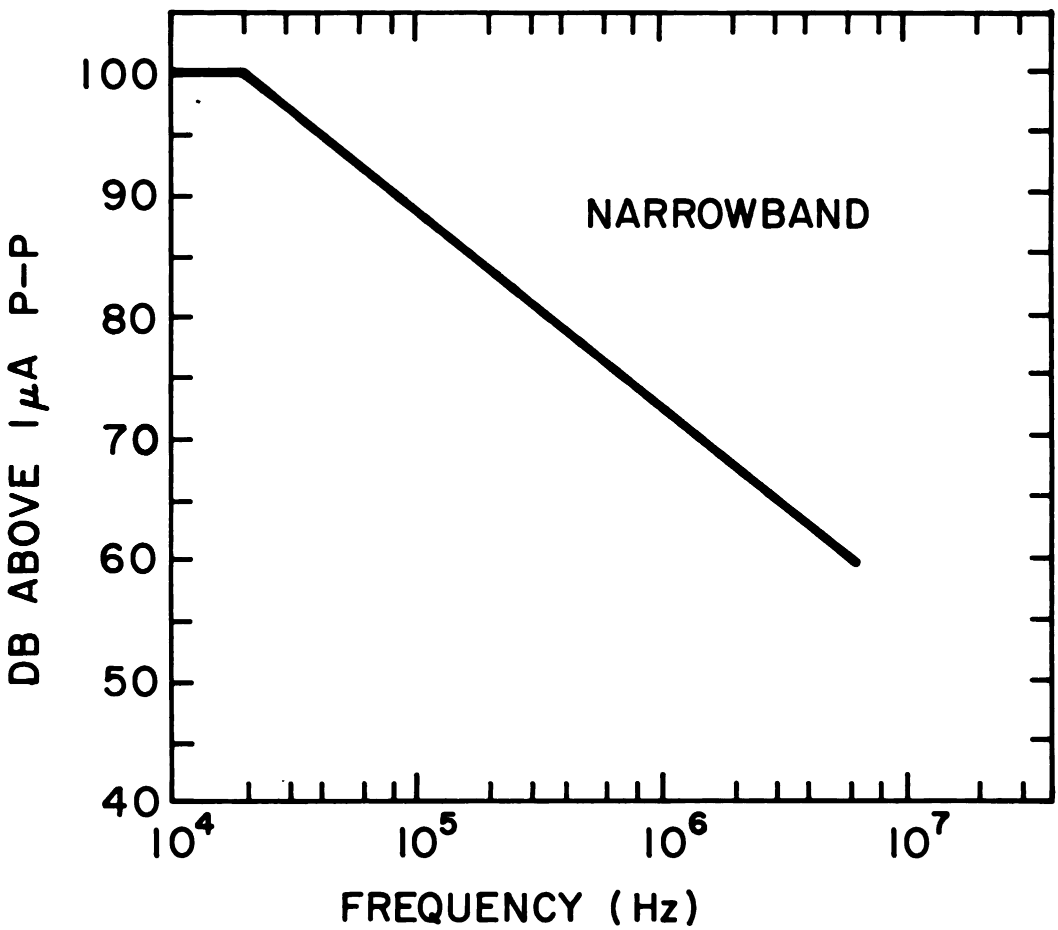

Fig. 3.12
LIMITS FOR CONDUCTED EMISSION,
100 KHz-6 MHz

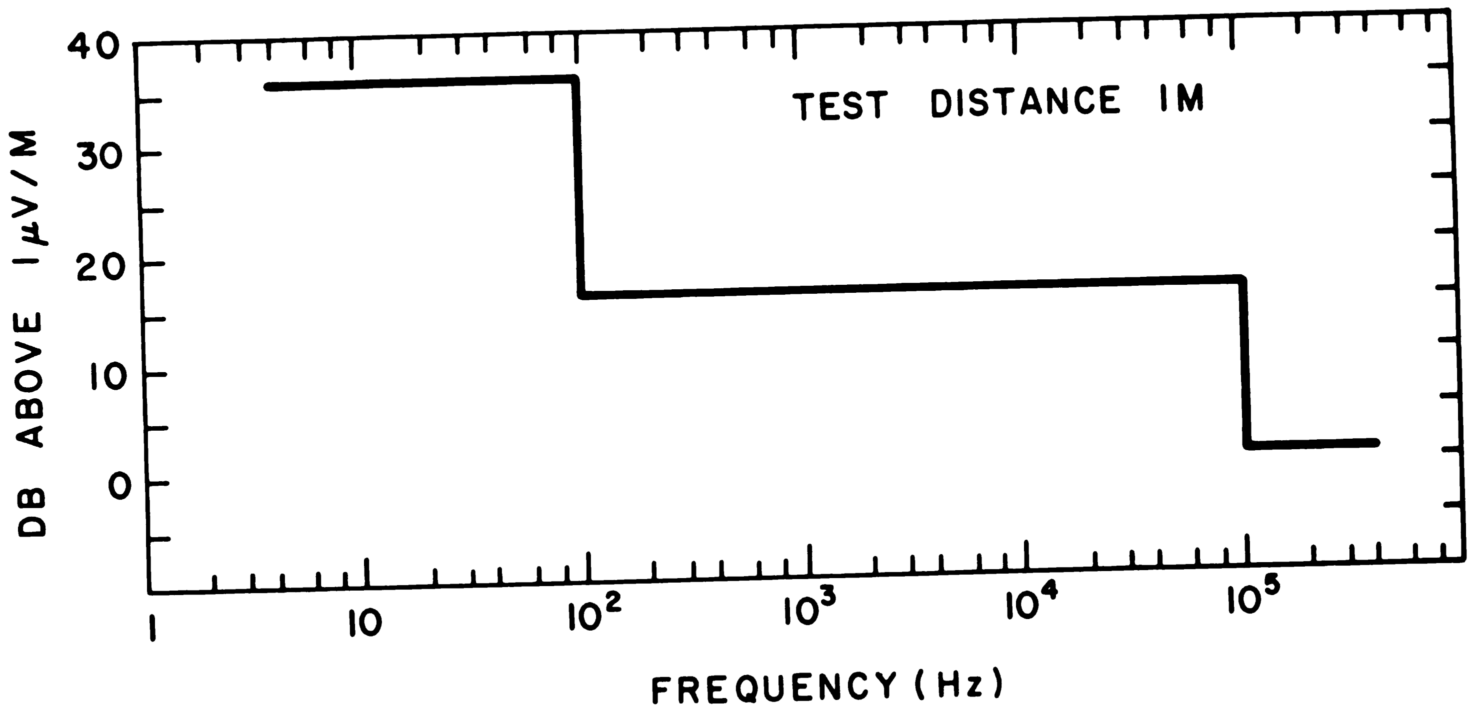

Fig 3.13

LIMITS FOR RADIATED EMISSION
ELECTRIC FIELD

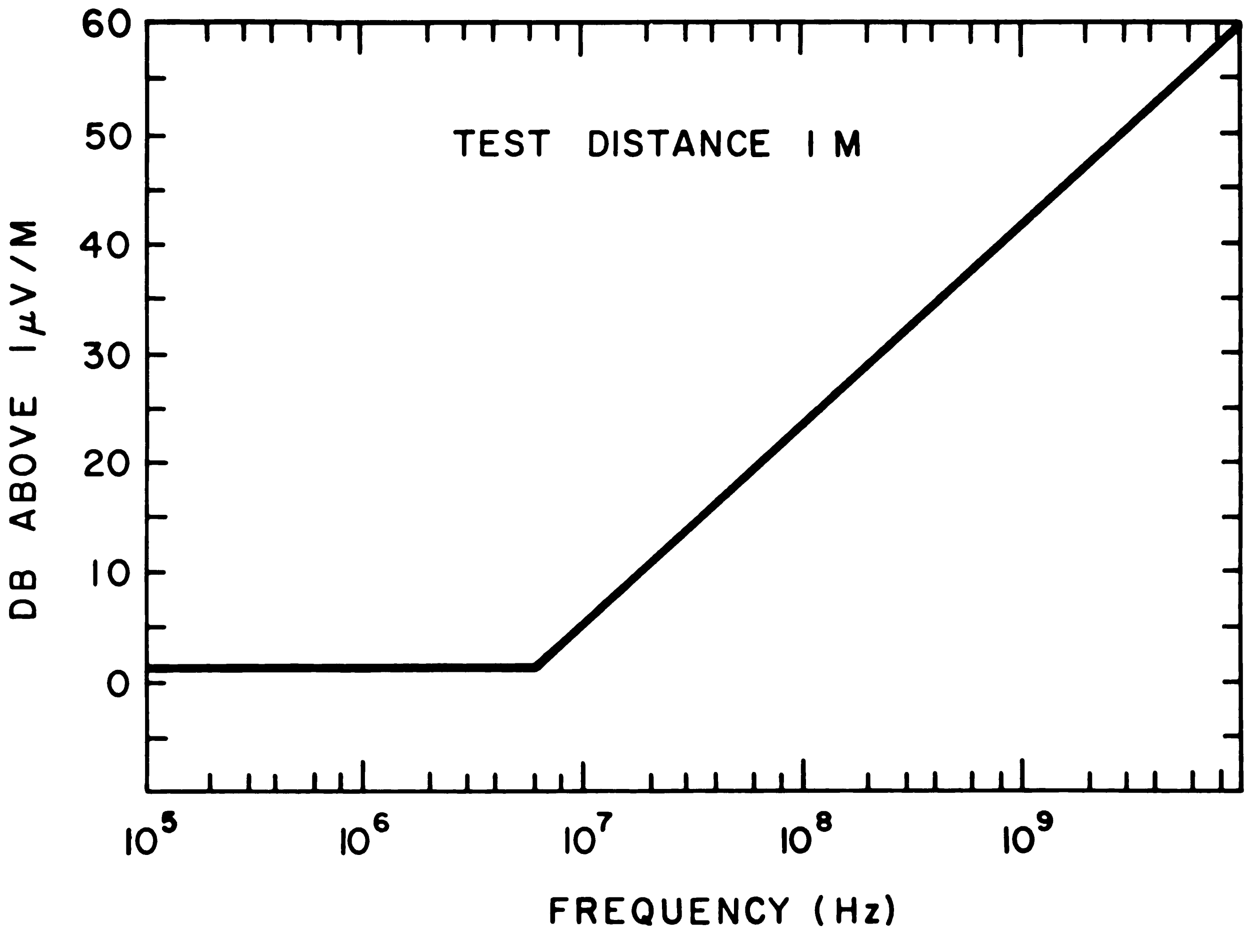

Fig 3.14

LIMITS FOR RADIATED EMISSION
ELECTRIC FIELD

APPENDIX C

Screening of Electronic Parts for Flight Equipment

This appendix to the PPL is intended to provide nominal levels of screening which may be used to upgrade conventional MIL parts for flight applications when Established Reliability (ER), TX, or other high reliability parts are not available. The GSFC specifications referenced in the PPL include screening. Reference is made to the Preface for a brief explanation of ER and TX parts specifications.

It is important to emphasize that the screening tests suggested here are nominal in the sense that many have been drawn from existing MIL and NASA part specifications. They are considered a baseline level on which more protective, and selective screens can be built depending on the program needs, capability, reliability objectives and mission requirements.

The screening tests are tabulated in a general outline format to permit project personnel to estimate screening costs and scheduling. Detail test procedures and criteria may be derived from referenced documents or by contacting the Applications Section. There are many other screening techniques in use which may be suitable, such as those contained in GSFC Specifications S-450-P-3A and S-450-P-4A developed for the NIMBUS Program.

Table 01.—Screening Outline for Capacitors[1]/

Category \ Test Sequence	1 Initial Measurements 2/	2 Temperature Cycling	3 Seal Leak Tests	4 Voltage Conditioning	5 Final Measurements and Tests	Reference Documents
a) Ceramic, Gen. Purpose	D.W.V.; I.R.; Cap; D.F.	-55 to 85°C per MIL-STD-202 Method 102, Cond. D	----	2 x rated voltage at rated elevated Temp. (but ≤ 125°C) for 100 hours	Repeat initial measurements	MIL-C-39014; GSFC S-450-P-4A
b) Ceramic, T.C.: Porcelain	D.W.V.; I.R.; Cap; D.F. or Q	-55° to 85 C per MIL-STD-202, Method 102, Cond. D	----	1.5 x rated voltage at rated elevated Temp. (but 125 C) for 100 hours	Repeat initial measurements	GSFC S-450-P-4A; MIL-C-20; MIL-C-11272
c) Glass	D.W.V.; I.R.; Cap; D.F. or Q	----	----	3 x rated voltage at 25 C for 50 hours	Repeat initial measurements	GSFC S-450-P-4A; MIL-C-23269
d) Tantalum (Wet Slug)	D. C. leakage; Cap; D.F. or P.F.	-55° to 85 C per MIL-STD-202, Method 102, Cond. D. Measure dc leakage immediately after final cycle.	1) Hermetic-sealed: Fine and gross leak tests 2) Elastomer-sealed: Acid indicator test	Rated voltage at 85°C for 168 hours	Repeat initial measurements on all units. Perform acid indicator test on elastomer-sealed units, only.	MIL-C-39006; GSFC S-450-P-4A
Tantalum 3/ (solid)	D.C. leakage; Cap; D.R. or P.F.	-55 to 85 per MIL-STD-202, Method 102, Cond. D	----	Rated voltage at 85 C for 168 hours	Repeat initial measurements	MIL-C-39003
e) Film (paper or plastic)	D.W.V.; I.R.; Cap; D.F.	-55 to 85 C per MIL-STD-202 Method 102, Cond.D	"CP" and "CH" styles, only: Gross leak test	1.4 x rated voltage at 85 C for 100 hours	Repeat initial measurements	GSFC S-450-P-4A; MIL-C-25; MIL-C-27287 MIL-C-18312
f) Mica	D.W.V.; I.R.; Cap D.F. or Q	----	----	1) Wire lead units: 2 x rated voltage at 125 C for 48 hours 2) Button: 1.5 x rated voltage at 25°C for 100 hours	Repeat initial measurements	GSFC-S-450-P-4A; MIL-C-5 MIL-C-10950
g) Variable, Glass	D.W.V.; I.R.; Cap; Q, Torque	3 cycles: -55° to 125°C	----	----	Repeat initial measurements. Perform visual inspection	GSFC S-450-P-4A; MIL-C-14409

Notes: 1/ Test procedures and requirements are in accordance with those in the applicable Military or NASA procurement document. For additional information, and to establish rejection criteria, see the reference documents or consult the Applications Section.

2/ Legend: D.W.V. = Dielectric Withstanding Voltage; I.R. = Insulation Resistance; D.F. = Dissipation Factor; P.F. = Power Factor.

3/ Recommended screening for non-standard, "non-E.R." solid tantalum capacitors.

TABLE 04. SCREENING OUTLINE FOR SUBMINIATURE FUSES

Test Sequence / Category	1	2	3	4	Reference Documents
	Initial Measurements	Temperature Cycle	Burn-in	Final Measurements	
Fuses, Subminiature	Visual and Mechanical Inspection, Resistance Voltage Drop @ 75% rated current	MIL-STD-202, Method 102, Cond. C	75% of rated current for 168 hours.	Visual, Voltage Drop @ 75% rated current.	

TABLE 05. SCREENING OUTLINE FOR INDUCTORS 1/

Test Sequence / Category	1	2	3	4	5	Reference Documents
	Initial Measurements 2/	Thermal Shock	Temperature Cycle	Seal Leak Test	Final Measurements and Tests	
a) Coils, fixed molded, RF	D.C. Resistance, IR, DWV, Inductance, Q, Self Resonant Freq.	----	MIL-STD-202 Method 102A, Cond. D	----	Repeat initial measurements and visual	MIL-C-39010 GSFC-S-450-P-4A
b) Transformers, Miniature Audio	DWV, Induced Voltage, IR, DC Resistance of PRI and SEC, Resistance Unbalance (where applicable), Inductance, Inductance Unbalance (where applicable), Polarity.	MIL-STD-202 Method 107B Cond. A.	----	MIL-T-27 Para. 3.7 (Gross leak test)	Repeat initial measurements and visual	MIL-T-39013 GSFC-S-450-P-4A

1/ Test procedures and requirements are in accordance with those in the applicable Military or NASA Procurement Document. For additional information, and to establish rejection criteria, see the referenced documents or consult the Applications Section.

2/ Legend: DWV —Dielectric Withstanding Voltage; IR—Insulation resistance.

TABLE 06. GENERAL SCREENING OUTLINE FOR RELAYS [1]

Test Sequence / Category	1	2	3	4	5	6	7	8	Reference Document [2]
	Seal Leak Test	Initial Meas-ments	Vibration	High Temp Soak	Low Temp Miss Test	Room Temp Miss Test	Seal Leak Test	Final Meas-ments	
Relays-Latching and Non-Latching	Para. 4.5.1 Fine leak radio active tracer or mass Spec-trometer Para. 4.5.2 Gross leak test	Para. 4.6 Coil Resis-tance Pull in and Drop out Voltage Contact Re-sistance Contact transfer Charac-teristics Insulation Resistance Dielectric Strength	Para. 4.7 100-2000 Hz 30g peak	Para. 4.9 16 hrs at 125°C	Para. 4.11 1000 opera-tion miss test at -65 C	Para. 4.12 5000 opera-tion miss test at 25°C	Para. 4.5.1 and 4.5.2 Repeat test sequence no. 1	Para. 4.6 Repeat test sequence no. 2	GSFC-S-311-P2

1/ For additional information, and to establish rejection criteria, see the referenced documents or consult the Applications Section.
2/ Other screening tests in this specification are provided for special applications.

TABLE 07. SCREENING OUTLINE FOR RESISTORS 1/

Test Sequence / Category	1 Initial Measurements	2 Bake	3 Temperature Cycle	4 Seal Leak Test	5 Burn-in	6 Final Measurements and Tests	Reference Document
a) Resistors, Fixed Carbon Comp.	--	48 hrs at 100°C	MIL-STD-202 Method 102A Cond. D	--	--	Resistance and Visual	GSFC-S-450-P-4A
	The necessity for screening and the type of screening for a carbon composition resistor is governed by the type of construction, manufacturer, application stability requirement and the storage history.						
b) Resistors, Fixed Film, General Purpose	Resistance	—	MIL-STD-202 Method 102A Cond. D	--	1.5 x rated pwr for 24 hrs. at Room Temp.	Resistance and Visual	MIL-R-39017 Group A Insp. Subgroup 1
c) Resistors, Fixed Film, High Stability	Resistance	--	MIL-STD-202 Method 102A Cond. C	Immerse 2/ in Dye Liq, Vacuum 30 min.; Pressure 30 min.	5 x rated pwr (1/20, 1/10, and 1/8 w) 4 x rated pwr (1/4 w) 2-1/4 rated pwr (1/2 and 3/4 w) for 1 hr. at Room Temp.	Resistance and Visual	MIL-R-55182 Group A Insp. Subgroup 1A
d) Resistors, Fixed Wirewound, Accurate	Resistance	--	MIL-STD-202 Method 102A Cond. C	--	1.0 x rated pwr for 100 hrs. at 125°C	Resistance and Visual	MIL-R-39005 Group A Insp. Subgroup 1
e) Resistors, Fixed Wirewound, Power Chassis Mount Resistors, Fixed Wirewound, Accurate Power	Resistance	--	MIL-STD-202 Method 102A Cond. C	--	1.0 x rated pwr for 100 hrs. at 25°C	Resistance and Visual	MIL-R-39007/ MIL-R-39009 Group A Insp. -- Subgroup 1
f) Resistors, Variable, Low Power Trimmers	Resistance	24 hrs at 150°C	MIL-STD-202 Method 102A Cond. C	--	1.0 x rated pwr for 1-1/2 hr on 1/2 hr off for 96 hrs. at 25°C	Resistance, Peak Noise, and Visual	MIL-R-39015 Group A Insp. Subgroup 1
g) Resistors, Variable, Wirewound, Power	Resistance	24 hrs at 150°C	MIL-STD-202 Method 102A Cond. C	--	1.0 x rated pwr for 1-1/2 hrs on 1/2 hr off for 96 hrs at 25°C	Resistance, Peak Noise, and Visual	

1/ Test procedures and requirements are in accordance with those in the applicable Military or NASA procurement document. For additional information, and to establish rejection criteria, see the referenced documents or consult the Applications Section.

2/ This test is only for hermetically sealed parts.

TABLE 08. SCREENING OUTLINE FOR DIODES [1]

Test Sequence / Category	1 High [2] Temperature Storage	2 Thermal Shock	3 Seal Leak Test	4 Pre Burn-in Test	5 Burn-in Test	6 Post Burn-in Test	Reference Document
a) Diodes, General Purpose	200°C for 48 hours	MIL-STD-750 Method 1051 Test Condition C except 10 cycles total, 15 min. rest at each temperature extreme	Fine Leak: MIL-STD-202 Method 112 Test Condition C and Gross Leak	Measure I_R and V_F at 25°C	168 hours at 100°C at specific values of V_R and I_O	Repeat pre burn-in Test No. 4	See. MIL-S-19500/118C MIL-S-19500/240B
b) Diodes, Rectifier, Silicon	200°C for 48 hours	Same	Same	Same	168 hours at 100°C at specific values of V_R and I_O	Same	MIL-S-19500/15[illegible]
c) Diodes, Reference, Silicon, 5% Tolerance	175°C for 48 hours	Same except high temperature is 175°C	Same	Measure BV, I_R and Z at 25°C	168 hours at 100°C at specified I_Z	Same	MIL-S-19500/115 MIL-S-19500/117 MIL-S-19500/124
d) Diodes, Switching	200°C for 48 hours	Same as Diodes, General Purpose a)2	Same	Measure I_R and V_F at 25°C	168 hours at 100°C at specific values of V_R and I_O	Same	MIL-S-19500/116 MIL-S-19500/144 MIL-S-19500/169D MIL-S-19500/231B
e) Diodes, Variable Capacitance	150°C for 48 hours	Same as a)2	Same	Measure I_R @ max WV I_F @ specified V_F C @ specified V_R	168 hours at 100°C at specified max continuous working voltage (V_R)	Same	MIL-S-19500/329

1/ Test procedures and requirements are in accordance with those in the applicable Military or NASA procurement document. For additional information, and to establish rejection criteria, see the referenced documents or consult the Applications Section.

2/ All high temperature testing must be performed in an inert atmosphere to avoid tarnishing of leads. The user should assure himself that high temperatures will not tarnish leads.

TABLE 09. SCREENING OUTLINE FOR TRANSISTORS 1/

Category \ Test Sequence	1 High 2/ Temperature Storage	2 Thermal Shock	3 Reverse Bias Burn-in	4 Acceleration	5 Seal Leak Test	6 Pre Burn-in Test	7 Burn-in Test	8 Post 3/ Burn-in Test	Reference Document
a) Transistors; Germanium	Not recomenaed for Flight Use (See Appendix A)								
b) Transistors, NPN, Silicon, Low Power and Switching	200°C for 24 hours	MIL-STD-750 Method 1051, Test Cond. C. except 10 cycles total. 15 min. rest at each temp. extreme	None	MIL-STD-750 method 2006, except 20,000 g's Y, orientation, one time only	MIL-STD-202 Method 112, Test Cond. C, and gross leak	Measure I_{CBO} or I_{CES} and h_{FE} at specified values of V_{CB}, V_{CE} and I_C	168 hours at 25 C at specified V_{CB} and P_T	Repeat the Pre-Burn-in Test No. 6 $\Delta h_{FE} = \pm 15\%$ $\Delta I_{CBO} = 100\%$ or 5 nA*	MIL-S-19500/181C, 225 C 251E, 312B
c) Transistors, PNP, Silicon, Low Power and Switching	Same	Same	12 hours at 175°C with V_{CB} and I_E specified	Same	Same	Measure I_{CBO} and and h_{FE} at specified V_{CB}, V_{CE} and I_C	Same	Same	MIL-S-19500 29?B 291B 323
d) Transistors, NPN, Silicon, High Power	Same	Same	None	None	Same	Measure I_{CE}, h_{FE} and I_{EBO} at specified V_{CE}, V_{EB} and I_C	168 hours at 100 C at specified V_{CE} and P_C	Same Except, $\Delta I_{EBO} = 100\%$ or 100 A*	MIL-S-19500 262E
e) Transistors, Dual Matched Pair NPN or PNP Silicon Transistors	Test same as NPN or PNP silicon low power and switching transistors, each transistor of matched pair is tested separately, but simultaneously in time.								MIL-S-19500 270B MIL-S-19500/355
f) Transistor, Unijunction	200°C for 24 hours	Same	None	Same	Same	Measure , I_{EB_2O} and R_{BB} at specified V_{B_2E}, I_{B_1}, $V_{B_2B_1}$ & I_E	168 hours at 125 C at specified V_{BB} and I_E	Repeat No. 6 $R_{BBO} = \pm 20\%$ $= \pm 5\%$ $I_{EB_2O} = 100\%$ or 50 nA*	MIL-S-19500/75B
g) Transistor, Field Effect	200°C for 24 hours	Same	None	Same	Same	Measure I_{GSS}, I_{DSS} and $\lvert y_{fs}\rvert$ at specified V_{GS} and V_{DS}	168 hours at 125°C at specified V_{GS} and V_{DS}	Repeat No.6 $\Delta I_{DSS} = \pm 10\%$ $\Delta \lvert y_{fs}\rvert = \pm 20\%$ $\Delta I_{GSS} = 100\%$ or 5nA*	MIL-S-19500/378

1/ Test procedures and requirements are in accordance with those in the applicable military or NASA procurement document. For additional information, and to establish rejection criteria, see the referenced documents or consult the Applications Section.

2/ All high temperature testing must be performed in an inert atmosphere to avoid tarnishing of leads if tinned leads are used. The user should assure himself that high temperatures will not tarnish leads.

3/ The listed maximum acceptable delta (Δ) changes in the electrical parameters are guideline values only. The proper delta (Δ) change criteria for device rejection must be determined individually by the user.

* Whichever is greater.

TABLE 10. SCREENING OUTLINE FOR MICROCIRCUITS

Test Sequence / Category	1	2	3	4	5	6	7	
	High Temperature Storage	Thermal Shock	Mechanical Shock	Acceleration	Radiographic	Seal Leak Test	Burn-in	Reference Document
Microcircuits	Screen in accordance with MIL-STD-883, Method 5004, Class A. Pre-cap inspections shall be performed by the manufacturer. Lot qualification (Para. 3.1.14 of 5004) may be waived, depending upon the particular procurement and application.							

TABLE 14. SCREENING OUTLINE FOR THERMISTORS 1/

Test Sequence / Category	1	2	3	4	5	6	
	Initial Measurements	Bake	Temperature Cycle	Seal Leak Test	Burn-in	Final Measurements and Tests	Reference Document
a) Thermistors, (Thermally Sensitive Resistor) (Negative Temp. Coef.)	Zero-Power Resistance at 25°C and IR	24 hrs at 125 C	MIL-STD-202 Method 102A Cond. C	--	--	Zero-Power Resistance at 25 C and Visual	GSFC-S-450-P-4A
b) Thermistors, Fixed Silicon (Positive Temp. Coef.)	Zero-Power Resistance at 25°C	--	MIL-STD-202 Method 102A Cond. C	--	1.5 x rated pwr. for 96 hrs at 25 C	Zero-Power Resistance at 25 C and Visual	GSFC-S-450-P-4A

1/ Test procedures and requirements are in accordance with those in the applicable Military or NASA procurement document. For additional information, and to establish rejection criteria, see the referenced documents or consult the Applications Section.

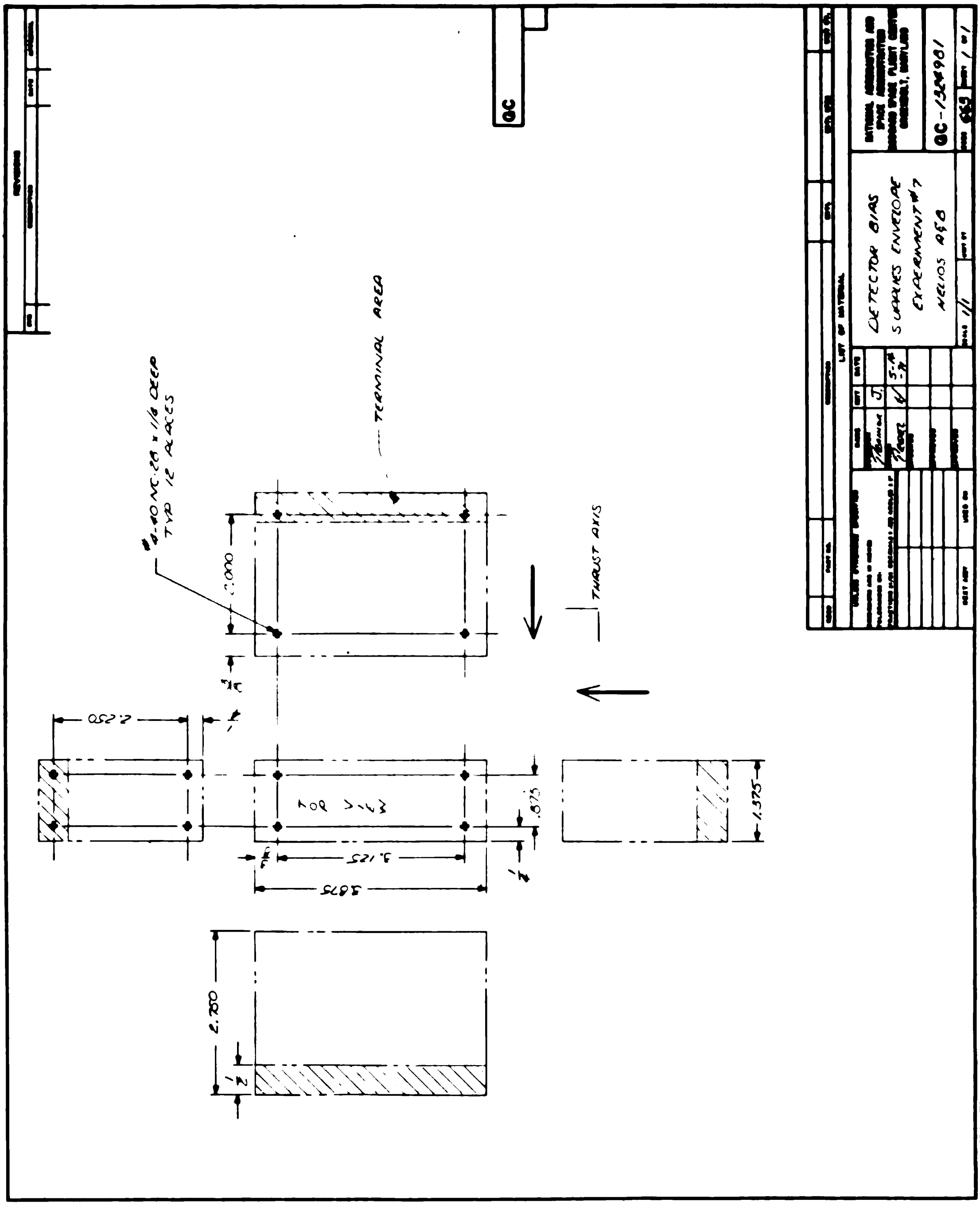
TERMINAL AREA
THRUST AXIS
TOP VIEW
DETECTOR BIAS
HELIOS A&B
GC

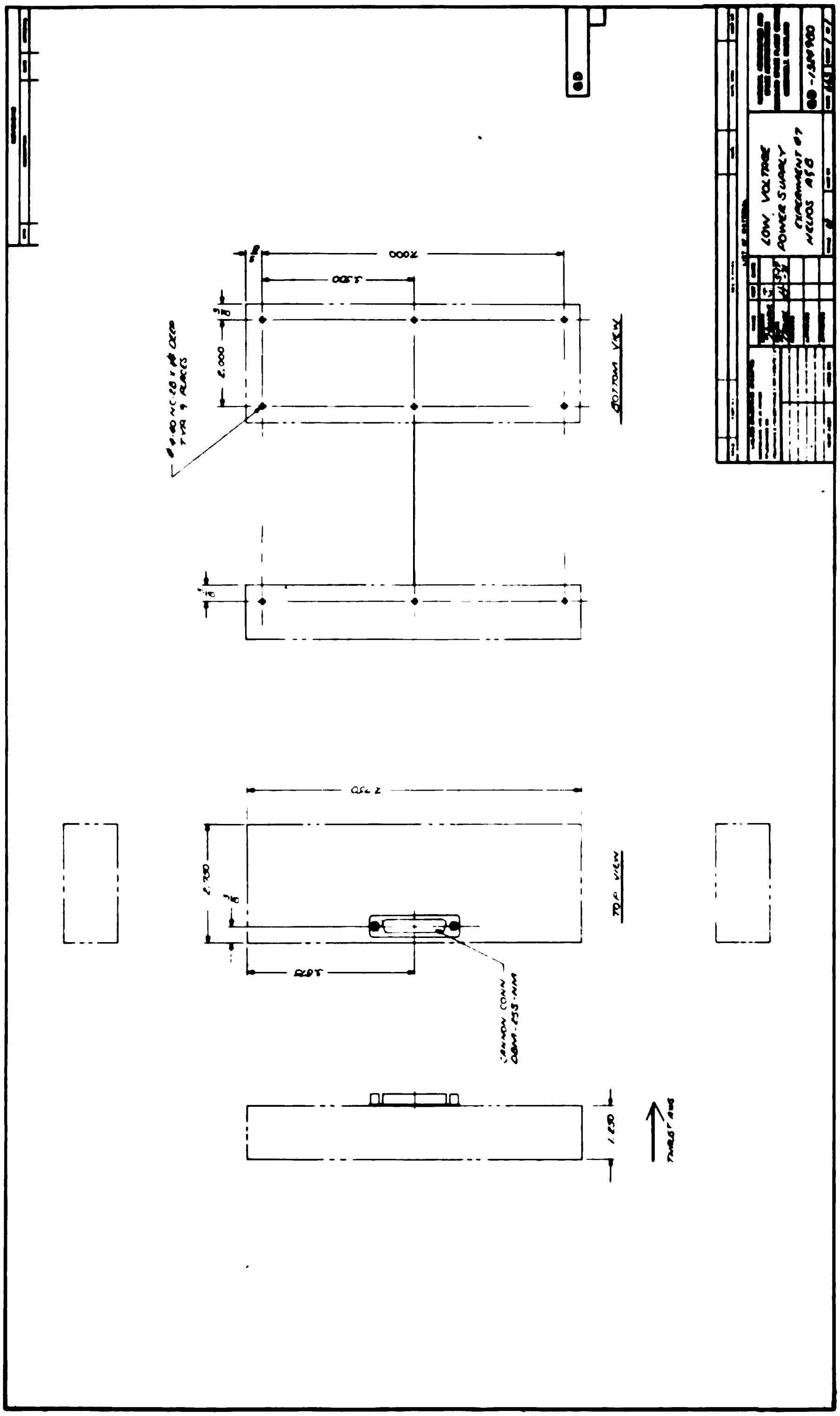
LOW, VOLTAGE
POWER SUPPLY
EXPERIMENT 7
HELIOS A&B
BOTTOM VIEW
TOP VIEW
CANNON CONN
DBM-25S-NM
THRUST AXIS
7.000
3.500
2.000

APPENDIX 3

SPECIFICATIONS FOR PHOTOMULTIPLIER TUBE

SPECIFICATIONS FOR
PHOTOMULTIPLIER TUBE
POWER CONVERTER PS-20

March 6, 1969

1.0 General

These specifications are intended to cover a general purpose high-voltage, high frequency DC to DC converter for use with photomultipliers in scintillation detectors for spacecraft pulse height analysis applications. A complete system will consist of from one to four multiplier stacks for single photomultiplier tubes and a main converter with a capability of driving as many as four multipliers. The number of multipliers shall be selectable after delivery.

1.1 Applicable Documents

1.1.1 GSFC X-325-67-70, "Magnetic Field Restraints for S/C Systems and Subsystems."

1.1.2 GSFC S-320-S-1 "General Environmental Test Specifications for Spacecraft and Components using Launch Environments Dictated by Scout FW-4 and Scout X-258 Launch Vehicles," May 20, 1966.

1.1.3 NPC 200-3: NASA Inspection System Provisions for Suppliers of Space Materials, Parts, Components and Services.

1.1.4 NGB 5300.4 (3A): NASA Quality Requirements for Hand Soldering of Electrical Connections.

1.1.5 MSFC-STD-271: NASA, Marshall Space Flight Center, Standards for Fabrication of Welded Electronic Modules.

1.1.6 Where differences exist between the requirements of this specification and the documents listed above, the requirements of this specification shall apply.

2.0 Operating Characteristics

2.1 Input

2.1.1 Voltage: The source operating limit is 10.7 Vdc +10% -15%.

2.1.2 Grounding: The negative power input line will be at circuit common potential but isolated from the output circuit common by more than 100K resistive impedance and less than 100 picofarads capacitance.

2.1.3 Input Power: The input power at no load and any operating input voltage shall not exceed 100 milliwatts and may increase to no more than 150 milliwatts at full load.

2.1.4 Source Impedance: The dc internal impedance of the source power will be less than 1.5 ohms and will increase to no more than 4.5 ohms up to one mHz.

2.1.5 Ripple Tolerance: The power supply shall be capable of operating within specifications when the power source contains electrical noise between power bus lines and common mode noise with respect to output circuit common. This electrical noise can have a maximum amplitude of 300 millivolts peak-to-peak and a bandwidth from 10 to 10^6 Hz.

2.1.6 Input Current Limiter: A current limiter shall be located on the input line to limit total input current to twice the normal full load value. The limiting action shall have no effect when operating at less than this value.

2.1.7 Noise Feedback: The ac component of input current feeding back to the power source shall be less than 0.5 milliamperes peak-to-peak. Paragraph 2.1.4 is applicable when measuring this current.

2.1.8 Overvoltage Protection: The converter shall not be damaged and the functional performance shall not be permanently impaired or degraded if the applied voltage polarity is reversed or if there are input transients of any peak amplitude up to 16 volts for a duration of ten milliseconds or less. The converter shall not be damaged and its functional characteristics not impaired by application of any supply voltage from 0 to 12.3 volts dc indefinitely, nor shall the output voltages exceed 20% of the nominal value. Components must be rated for this extreme. Current limiting per paragraph 2.1.6 is also applicable.

2.1.9 Temperature Limits: Normal temperature operating limits will be between -20°C and +40°C.

2.2 Operation

2.2.1 Starting Time: The converter shall start at full load in less than five seconds after being off for a period of at least two hours and at any operating temperature or input voltage. The output voltage shall stabilize to ± 0.25% of that value within one minute after turn-on.

2.3 Output

2.3.1 A twelve stage multiplier shall provide tapped outputs to operate an RCA C7151Q photomultiplier tube. The voltage distribution is as follows: Equal voltage between all dynodes and last dynode and anode and twice that value between photocathode and first dynode.

2.3.2 A fourteen stage multiplier shall provide tapped output to operate an EMI 9712 photomultiplier tube. The voltage distribution is as follows: Equal voltage between all dynodes and last dynode and anode and three times that value between photocathode and first dynode.

2.3.3 The converter shall be designed so the dynode voltage increment can be set independently for each multiplier at any value from 110 to 150 volts in increments of five volts, measured from any dynode to an adjacent dynode. In addition, the converter output shall be adjustable by resistor or zener diode selection over a range of ±10%. The converter shall not be damaged if the voltage adjust network is left open or shorted.

2.3.4 Grounding: The secondary circuit common point must be selectable from any one of the dynode, anode or photocathode leads on individual multipliers driven from a common converter.

2.3.5 Load Regulation: All output voltages shall be regulated within ±0.25% for single anode currents up to six microamperes each between 9.6 and 12.3 input volts and for all operating temperatures.

2.3.6 Overload Protection: The anode supply shall current limit with the threshold occurring between 6.0 and 8.0 microamperes on each tube. The individual dynodes shall current limit at 0.5 ± 0.25 of the limiting value of the preceding stage at least down to the eighth dynode, and no less than 0.1 microampere at any dynode below the eighth. The unit must be so designed that a direct short on any output lead from the central converter or any multiplier output shall not result in permanent damage.

2.3.7 Ripple: Under all photomultiplier tube load and input conditions up to the current prescribed in paragraph 2.3.4, all dynode and anode output lines shall have a ripple or noise amplitude less than one millivolt peak-to-peak measured from any dynode output or anode output to circuit common.

3.0 Mechanical

3.1 General: The converter and multipliers may be designed using printed circuits, welded wire, welded modules, point to point, solder or any combination of techniques. However, mechanically moving parts or potentiometers may not be employed.

3.2 Solder Terminals: All connections between external terminals and internal printed circuits shall be accomplished by means of insulated wire at least one-half inch long. This is intended to prevent overheating the printed circuit pad when external connections are made to the terminals. The output terminals may be arranged in any convenient order. See Figure 2.

3.3 Connectors: Connector types are called out in Figures 1 & 2. In no case must the center conductor be at more than $\pm$ 160 volts peak from output circuit common. The shield shall be at output circuit common potential. Connectors may not be mounted on the top or bottom surface of the converter.

3.4 Cables: Interconnecting cables shall be a coaxial type with suitable right angle connector compatible with paragraph 3.3. The contractor will recommend a cable type which will meet the radiation requirements of MIL-I-26600. The output characteristics of the supply shall be independent of the cable length for lengths eighteen inches and less. Multipliers will be supplied with two cables each: connector-to-connector, 18" long, and connector-to-blank, 18" long.

3.5 Size: Refer to Figures 1 & 2.

3.6 Weight Schedule:

Converter	120 grams maximum
Multiplier (each type)	70 grams maximum (each)

3.7 Encapsulation: The main converter and multipliers shall be conformally coated in polyester base epoxy or polyurethane as approved by the technical representative.

4.0 Environmental Perturbation:

4.1 Materials: Non-magnetic materials should be used wherever possible and construction should be in accordance with magnetic field restraints as specified in references 1.1.1 and 1.1.2, and summarized as follows:

4.1.1 After a 15 gauss exposure each assembly (one converter and four multipliers) must have a residual magnetism of less than 32 gamma at eighteen inches.

4.1.2 After a 50 gauss deperm each assembly must have a residual magnetism of less than two gamma at eighteen inches.

4.1.3 Each assembly must have a stray magnetism of less than two gamma at eighteen inches.

4.2 RF Radiation: The converter and multipliers shall be enclosed in shielded containers electrically connected to the output circuit common such that the external electric field is less than one microvolt per meter at a distance of ten inches from any multiplier or the converter when measured with an rms reading field strength meter. The stray ac magnetic field measured at one meter shall be less than 10^{-4} gammas.

4.3 Harmonic Content: The voltage multiplier driving voltage must contain not more than 10% harmonic distortion from a true sine wave to minimize harmonic radiation.

4.4 GSFC will provide for testing of requirements set forth in paragraphs 4.1 and 4.2.

5.0 Environmental Testing: The converter shall be capable of passing the SAS-B environmental specifications in accordance with the documents listed in paragraph 1.1. The levels for the environmental design qualification test applicable to this converter are as follows:

5.1 Storage temperature: (non-operative)

-50°C	6 hours
+75°C	6 hours

5.2 Humidity: 95% relative humidity at 40°C for 50 hours.

5.3 Acceleration: (operative) 28 g for three minutes in three mutually perpendicular directions.

5.4 Vibration: (operative) Each vibration is done once in each of three mutually perpendicular directions.

5.4.1 Sinusoidal:

Frequency (Hz)	Level
10-24	0.4 inches (double ampl.)
24-30	±12.0 g
30-80	±20.0 g
80-110	±37.0 g
110-2000	±12.0 g

5.4.2 Random Vibration (4 min/axis):

Frequency Band (Hz)	APSD level (g^2/Hz)
20-43	0.07
43-56	0.20
56-70	0.40
70-100	1.50
100-150	.60
150-200	.20
200-2000	.07

OA: 14.9 g rms

5.5 Shock: (operative) 40 g, 1/2 sine wave, 6 milliseconds, each of three mutually perpendicular directions.

5.6 Thermal Vacuum: (operative) Pressure equal to 10^{-5} mm Hg or less. Temperature of case 50°C for 24 hours and -10°C for 24 hours.

5.7 Corona Discharge

The contractor shall perform the corona discharge test as follows: Pressure in the range 10^{-3} to one mm Hg, all high voltage points encapsulated with RTV-60. Connect 0.01 uf capacitor between one anode and oscilloscope. The pressure shall be held between 100 and 200 microns Hg for at least two hours. No transients having amplitudes greater than 2 millivolts shall occur at the anode connection during this entire test.

6.0 Quality Assurance and Reliability:

High reliability of the system shall be assured by choice of good design, inspection and testing. A suitable reliability and quality assurance program shall be in effect. Demonstrated compliance with the provisions of NASA Quality Assurance Specifications NPC-200-3 and NHB5300.4(3A) is required. As a design goal the power supply shall have a 95% probability of operating in a space environment without failure for 10,000 hours, with the calculation based on individual component and connection reliability.

6.1 Design: The system design shall be as simple as possible to assure high reliability. Provisions shall be made to allow for component or element value drift. The components or elements shall be derated to reduce the chance of parts failure due to overvoltage or excessive power dissipation. The use of germanium semiconductors must be cleared with the technical representative.

6.2 Inspection: Inspection standards shall be established at the component, module or board, and systems levels to detect fabrication errors, contamination, poor workmanship, etc. Inspection shall be on a 100% basis.

6.3 Electrical Testing: An adequate testing program shall be established to ensure compliance with the provisions of this specification. All critical components, including all semiconductors and tantalum capacitors, are to be given accelerated aging tests. The pertinent component parameters are to be measured and recorded before and after the accelerated aging test and comparisions made to determine whether the parameter values drift abnormally. The aging is to consist of powered storage for at least five days. Powered storage is defined as follows:

Tantalum Capacitors: Stored at 85°C with manufacturer's voltage rating impressed.

6.3.1 Semiconductor Screening: Only hi-rel parts will be used in the SAS spacecraft. The GSFC Preferred Parts List specifies certain requirements for parts procurement and screening. In addition to those, the SAS Project has specific requirements for semiconductor screening that apply to all diodes, transistors, and integrated circuits. Specifically, 100% of all semiconductor devices used in prototype or flight hardware must undergo the following test sequence:

a) Visual inspection before sealing with a minimum magnification of 40.

b) Temperature cycling from -65°C. to maximum rated storage temperature.

c) Centrifuge

d) Electrical Test

STATEMENT OF WORK

The proposal resulting from this RFP and the contract shall be based on:

a. Design of a power supply system meeting the requirements of the attached specifications, Photomultiplier Tube Power Converter PS-20

b. Development of plans for inspection and testing to meet all specification requirements.

c. Delivery shall be made on each of the following items:

1 each engr. model system consisting of

1 each PS 20C converter
4 each PS 20M12 multipliers
2 each PS-20M14 multipliers

3 each flight system consisting of

6 each PS 20C converters
12 each PS 20M12 multipliers
4 each PS 20M14 multipliers

d. Delivery of the engr. model shall be made 90 days after receipt of contract.

e. Acceptance of the engr. model by the purchaser shall precede start of construction of the flight units.

f. Delivery of the flight units shall follow 90 days after acceptance of the prototype by the purchaser. A minimum of ten days will be required for the prototype acceptance testing.

g. Preliminary drawings shall be delivered with the prototype assembly and reproducibles as stipulated in the specifications shall be delivered with the flight systems.

e) 336 hours ± 36 hour burn-in at 100°C. at 80% of part rated power.

f) Electrical Test

g) Fine and gross leak tests

h) Final inspection including X-ray, if possible.

6.4 Testing of Power Supply: Each system shall be tested under all conditions of input voltage from 9.6 to 12.3 volts, output load from zero current to short circuit at anode, and temperature from -40°C to 50°C at atmospheric pressure. Performance curves shall be plotted as follows: Anode and all dynode voltages shall be plotted as a function of load. Separate graphs shall be plotted for input voltages of 9.6, 10.7 and 12.3 and temperatures of -40°C, -10°C, 25°C and 50°C. The load shall consist of an RCA type 6199, or EMI 9530 photomultiplier tube as appropriate, with a variable (non-pulsing, light source. The light intensity shall be varied to produce the desired anode current. These graphs, and all the data from the testing of the individual components and the assembly shall be delivered to GSFC at the same time as delivery of each converter.

7.0 Documentation:

In addition to the test data specified above, the contractor shall provide a complete set of specifications, complete reproducible circuit schematics including assembly prints showing artwork, a parts list identifying manufacturer and type for all parts, and a circuit description at the time of delivery of the first system.

8.0 Marking:

Each module shall be unambiguously marked: The marking shall be as follows:

Converter: PS 20 C - (Serial Number)

Multiplier: PS 20 M12 - (Serial Number)

PS 20 M14 - (Serial Number)

Serial numbers shall begin with one for each type module (converter and multiplier) and run consecutively.

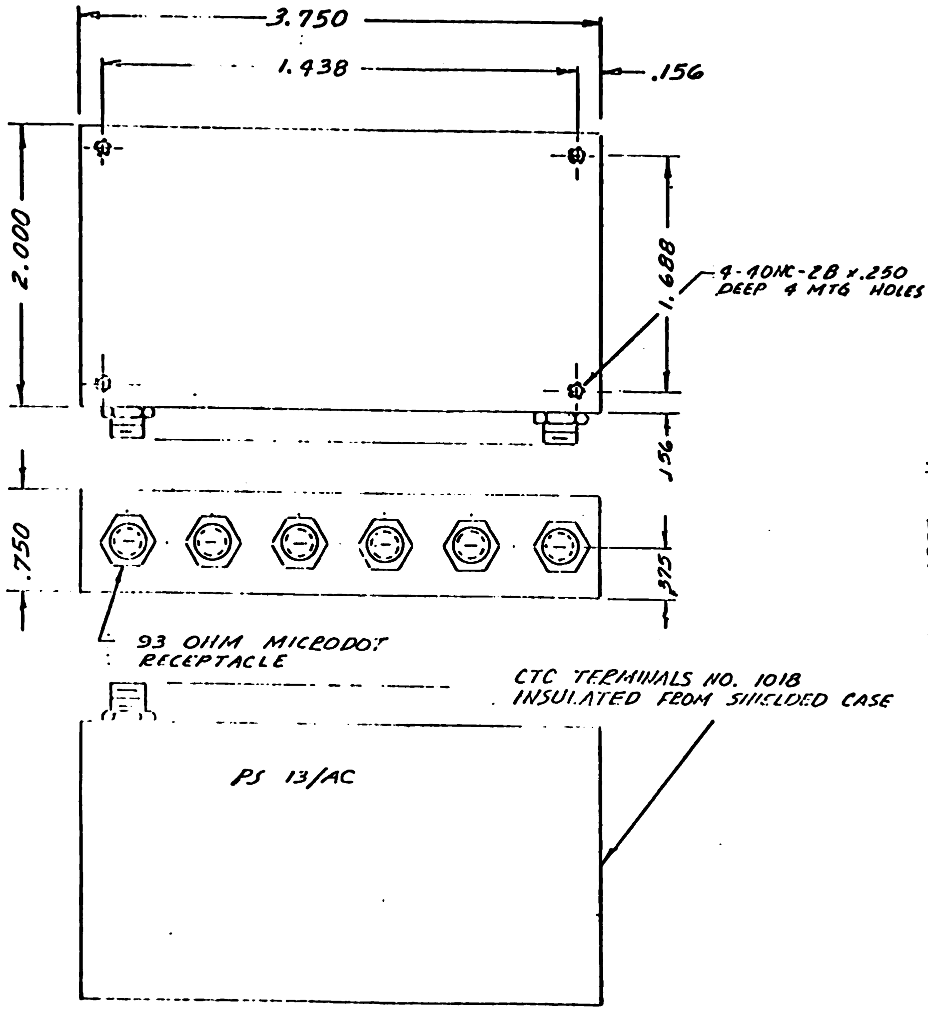

FIGURE 1

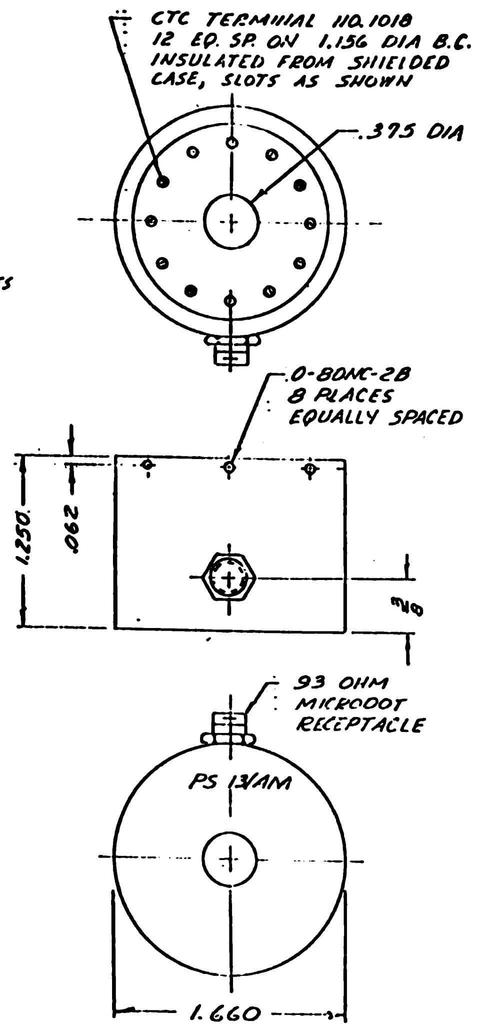

FIGURE 2

TIONAL AERONAUTICS AND SPACE ADMINISTRATION
WASHINGTON, D.C. 20546

OFFICIAL BUSINESS
PENALTY FOR PRIVATE USE $300

SPECIAL FOURTH-CLASS RATE
BOOK

POSTAGE AND FEES PAID
NATIONAL AERONAUTICS AND
SPACE ADMINISTRATION
451

U.S.MAIL

488 001 C1 U AL 750411 S00606HU
UNIV OF MICHIGAN
ENGINEERING LIBRARY
ATTN: MR ROBERT T FREESE
ANN ARBOR MI 48104

POSTMASTER: If Undeliverable (Section 15 Postal Manual) Do Not Return

"The aeronautical and space activities of the United States shall be conducted so as to contribute . . . to the expansion of human knowledge of phenomena in the atmosphere and space. The Administration shall provide for the widest practicable and appropriate dissemination of information concerning its activities and the results thereof."

—NATIONAL AERONAUTICS AND SPACE ACT OF 1958

NASA SCIENTIFIC AND TECHNICAL PUBLICATIONS

TECHNICAL REPORTS: Scientific and technical information considered important, complete, and a lasting contribution to existing knowledge.

TECHNICAL NOTES: Information less broad in scope but nevertheless of importance as a contribution to existing knowledge.

TECHNICAL MEMORANDUMS: Information receiving limited distribution because of preliminary data, security classification, or other reasons. Also includes conference proceedings with either limited or unlimited distribution.

CONTRACTOR REPORTS: Scientific and technical information generated under a NASA contract or grant and considered an important contribution to existing knowledge.

TECHNICAL TRANSLATIONS: Information published in a foreign language considered to merit NASA distribution in English.

SPECIAL PUBLICATIONS: Information derived from or of value to NASA activities. Publications include final reports of major projects, monographs, data compilations, handbooks, sourcebooks, and special bibliographies.

TECHNOLOGY UTILIZATION PUBLICATIONS: Information on technology used by NASA that may be of particular interest in commercial and other non-aerospace applications. Publications include Tech Briefs, Technology Utilization Reports and Technology Surveys.

Details on the availability of these publications may be obtained from:

SCIENTIFIC AND TECHNICAL INFORMATION OFFICE

NATIONAL AERONAUTICS AND SPACE ADMINISTRATION

Washington, D.C. 20546

NASA TECHNICAL NOTE

NASA TN D-7949

APOLLO EXPERIENCE REPORT - GUIDANCE AND CONTROL SYSTEMS: LUNAR MODULE MISSION PROGRAMER

Jesse A. Vernon

Lyndon B. Johnson Space Center
Houston, Texas 77058

NATIONAL AERONAUTICS AND SPACE ADMINISTRATION • WASHINGTON, D. C. • APRIL 1975

1. Report No. NASA TN D-7949	2. Government Accession No.	3. Recipient's Catalog No.
4. Title and Subtitle APOLLO EXPERIENCE REPORT GUIDANCE AND CONTROL SYSTEMS: LUNAR MODULE MISSION PROGRAMER		5. Report Date April 1975
		6. Performing Organization Code
7. Author(s) Jesse A. Vernon		8. Performing Organization Report No. JSC S-414
		10. Work Unit No. 914-50-00-00-72
9. Performing Organization Name and Address Lyndon B. Johnson Space Center Houston, Texas 77058		11. Contract or Grant No.
		13. Type of Report and Period Covered Technical Note
12. Sponsoring Agency Name and Address National Aeronautics and Space Administration Washington, D.C. 20546		14. Sponsoring Agency Code
15. Supplementary Notes		

16. Abstract

A review of the concept, operational requirements, design, and development of the lunar module mission programer is presented, followed by a review of component and subsystem performance during design-feasibility, design-verification, and qualification tests performed in the laboratory. The system was further proved on the unmanned Apollo 5 mission. Several anomalies were detected, and satisfactory solutions were found. These problems are defined and examined, and the corrective action taken is discussed. Suggestions are given for procedural changes to be used if future guidance and control systems of this type are to be developed.

17. Key Words (Suggested by Author(s))	18. Distribution Statement
• Automation • Checkout • Remote Controls	STAR Subject Category: 12

19. Security Classif. (of this report)	20. Security Classif. (of this page)	21. No. of Pages	22. Price
Unclassified	Unclassified	12	$3.25

APOLLO EXPERIENCE REPORT

GUIDANCE AND CONTROL SYSTEMS:

LUNAR MODULE MISSION PROGRAMER

By Jesse A. Vernon
Lyndon B. Johnson Space Center

SUMMARY

The lunar module mission programer was designed to enable the lunar module to meet the requirements for unmanned near-Earth orbiting missions and to be adaptable to restricted unmanned lunar landing missions within the capability of the ultra-high-frequency/very-high-frequency communication links if adequate command and service module transmission capability were provided. An onboard lunar module mission programer would not preclude a manned mission involving two crewmembers.

The mission programer was used for sequencing functions in an unmanned spacecraft to prove proper functioning of the system and to ensure spacecraft readiness for manned flights. The lunar module mission programer was composed of the following functional components: (1) a program reader assembly, (2) a digital command assembly, (3) a program coupler assembly, and (4) a power distribution assembly.

The functional components of the mission programer were subjected to design-feasibility, design-verification, and qualification tests. The units successfully completed all tests with only minor problems. However, from the beginning of the program, the program coupler assembly was plagued with relay problems, many of which were a direct result of contamination inside the sealed relay can. Others were unexplained — no contamination or other causes of failures were ever found.

The lunar module mission programer performed all the required functions throughout the Apollo 5 mission. From lift-off until 6 minutes 10 seconds into the flight, the programer was operated in the primary mode with the guidance computer in control; then the backup mode was activated, and the programer controlled all sequencing throughout the mission. The lunar module mission programer was flown on only one mission. A modified mission programer, the ascent-engine arming assembly, was flown on the Apollo 9 and 10 missions. This assembly permitted the ascent engine to be armed after crew departure and to be fired to fuel depletion after the ascent stage was separated from the command and service module.

INTRODUCTION

Electrical and electronic equipment has been used in many areas to perform functions previously performed by man. Technologists have continued to develop automated techniques and have extended the scope to include the sequencing of functions in an unmanned spacecraft to prove proper functioning of the system and to ensure spacecraft readiness for manned flights. The lunar module mission programer (LMP) is one such device. The LMP concept, design, development, and flight performance are described in this report. The LMP was flown on only one mission (Apollo 5/lunar module 1 (LM-1)) and performed all required functions when it was activated 6 minutes 10 seconds after lift-off.

As an aid to the reader, where necessary the original units of measure have been converted to the equivalent value in the Système International d'Unités (SI). The SI units are written first, and the original units are written parenthetically thereafter.

CONCEPT

The LMP was designed to enable the LM to meet the requirements for unmanned near-Earth orbiting missions and to be adaptable to restricted unmanned lunar landing missions within the capability of the ultra-high-frequency (uhf)/very-high-frequency (vhf) communications links if adequate command and service module (CSM) transmission capability were provided. An onboard LMP would not preclude a manned mission involving two crewmembers.

OPERATIONAL REQUIREMENTS

The operational requirements of the LMP were as follows:

1. Noncontingency mission performance without ground-command control of unmanned flights

2. Nonsimultaneous manned and LMP system operation on the same flight (manned operation possible before LMP activation and after LMP deactivation)

3. Control of LM subsystems as required to control functions in an optimum manner to meet flight test objectives

4. Ground-command selection of alternate test sequences in the backup mode or in the primary mode (within the capacity of the LM guidance computer (LGC))

5. Priority of ground command over onboard command

6. One LMP configuration compatible with all unmanned mission operations

EQUIPMENT DESCRIPTION

The LMP consisted of the following functional components: (1) a program reader assembly (PRA), (2) a digital command assembly (DCA), (3) a program coupler assembly (PCA), and (4) a power distribution assembly (PDA). The PRA contained a contingency program to be used if the primary mode failed or if special subsystem contingency operations became necessary. The DCA provided an uplink capability so that ground commands could be routed to the LGC, the PRA, or the PCA. The PCA provided coupling of the LGC, PRA, and certain DCA commands to control the basic LM subsystems. The PDA provided the dc power distribution and current protection for the LM components.

Program Reader Assembly

The PRA was programed to contain commands to provide open-loop backup sequencing if a failure was detected by the primary guidance, navigation, and control system (PGNCS). The PRA provided only those commands necessary to operate the LM subsystems for LM testing after a primary-mode failure. It did not provide vehicle guidance or attitude information. The PRA consisted of three subassemblies: (1) a power supply subassembly, (2) a tape reader subassembly, and (3) a program control subassembly.

The power supply subassembly provided the internal voltages required for PRA operation and supplied isolation of signal and power grounds within the PRA. It also protected the PRA from damage resulting from abnormal vehicle conditions.

The tape reader subassembly was a bidirectional reader using programed tape. The tape was capable of storing a maximum of 64 000 bits of information. The stored information was sensed by a read head. A tape "hole" was a binary one; a tape "no hole" was a binary zero. Capability to sense the beginning and end of the tape was incorporated in the PRA.

The program control subassembly was used to select, control, and issue — as a function of time — the information stored in the PRA. External control commands were provided to the PRA by means of uplink commands through the DCA. The program control subassembly placed the PRA in the standby mode or the normal (either search or readout) mode. To inform the ground station that the PRA was sequencing, the program control subassembly provided a "compare" pulse and, in the readout mode, transmitted a 1-pulse/sec clock pulse to the ground.

Digital Command Assembly

The DCA received, decoded, and processed commands received from the ground by uhf transmission. These commands were sent to the LGC to accomplish limited program control, to the PRA to enable selection and initiation of a segment of the PRA program, or to the ground relay matrix of the PCA to accomplish real-time control of certain functions of the LM subsystems. The DCA also had a self-test and verification capability controlled by the Manned Space Flight Network. The DCA consisted of a uhf receiver, two decoders (redundant), a phase-shift-keying (PSK) demodulator, and a power supply.

The uhf receiver was a miniaturized solid-state, double-conversion, superheterodyne device that received and demodulated frequency-modulation/PSK signals in the uhf band. The decoder decoded digital messages from the PSK demodulator and allowed partial messages from the residue of rejected messages to be received without transferring them to associated assemblies. The PSK demodulator converted the PSK signal from the receiver into a series of digital bits for the decoder and also provided a set of reference clock pulses for the decoder. The power supply provided the regulated power and signal ground isolation required for DCA operation.

Program Coupler Assembly

The PCA received commands from the LGC, the PRA, or the DCA and coupled these commands to the LM subsystems by means of magnetic latching relays. Each relay contained two directional diodes and was half-crystal can size. The PCA consisted of a decoder subassembly, a power supply subassembly, and a switching subassembly. The decoder subassembly selected and decoded command words from the LGC or the PRA. The LGC command word contained 12 bits (4 address bits and 8 data bits). The PRA command word contained only 8 data bits. The power supply subassembly provided the regulated power required for PCA operation and for isolation of power and signal grounds within the PCA. The switching subassembly contained two matrices of latching relays. The prime matrix was controlled by the LGC or PRA output commands by means of the decoder subassembly. These relays were controlled on a real-time basis. The real-time command relays were used to correct or compensate for failures of the programed relays and to correct or compensate for certain LM subsystem failures. The switching subassembly also contained the uplink-activated interlocking relays to allow ground-control priority if a PCA prime relay failed. These relays, when activated, disabled specific control circuits in the LMP prime-relay matrix.

Power Distribution Assembly

The PDA provided dc power distribution and current protection for the DCA, the PCA, and the PRA and provided the dc power required for LMP control of the ac inverters. The PDA contained manually operable circuit breakers that enabled and disabled the LMP. Additional relays performed high-power switching functions required for proper LM operation. These relays were controlled by relays in the PCA.

DESIGN

The LMP was designed and constructed to satisfy the individual specification requirements of structural and electrical design and of performance.

The calculated reliability goal for a DCA was met through the use of redundancy in the digital decoder section only. A self-checking and fail-safe feature was included to prevent an invalid message from performing a function. Integrated circuits were used wherever possible in designing the DCA because of their high reliability, low power consumption, small size, and light weight. Discrete components were used in those areas in which the circuit constraints precluded the use of integrated circuits.

The PCA design goal was to achieve high reliability. To accomplish this goal, numerous broad-based design objectives — such as minimum weight, optimum thermal design, high packaging density, and adaptability to design changes — were met early in the PCA design.

The minimization of weight was a prime consideration. The following design concepts were used to fulfill the rigorous environmental and operational requirements effectively while maintaining the concept of minimum weight.

Integrated circuits were used instead of discrete components where practical. A single flatpack performed the task of approximately 34 discrete components with obvious weight-saving results. Welded-wire cordwood assemblies were used, where practical, rather than conventional solder. This procedure added reliability to the electrical junction and provided substantial weight savings. All parts used represented the state-of-the-art high-reliability versions of products being manufactured at the time.

To provide the best possible thermal path from heat-dissipating parts to the mounting flange, all parts and components were bonded directly to the module web with an adhesive having high thermal conductivity. All cordwood assemblies were completely encapsulated. The encapsulant then paralleled the path of the part lead, which resulted in a further reduction in thermal resistance.

Every effort was made to design a package that incorporated high-density design concepts. In many cases, the electrical requirements and the available parts limited the miniaturization effort (i.e., transformers, chokes, capacitors, relays, etc.).

Because of the nature and functions of the PCA, the conceptual design within the PCA and the several interfacing electronic assemblies changed. Therefore, designing the PCA to accept these changes was difficult. The use of flexible harness and the inclusion of spare terminals on each module to provide the simplest means for executing changes are examples of the adaptability to design changes. If a hardwired multilayer or printed circuit board (mother board) had been used, a complete redesign would have been necessary to incorporate a change in module interwiring.

The PRA had an integrated planar photodiode array, which was used to read digital data stored on 35-millimeter photographic film. The tape (photographic film) was advanced by a simple step servosystem that required a minimum number of moving parts and gears. The tape-transport system, drive sprockets, and supply and takeup spools were identical in concept to the components and system used in space-flight-proven programers. The programed film was, for all practical purposes, indestructible. This was not true for magnetic-tape and magnetic-core systems in which the data can be inadvertently erased. The decision to use a photoelectric readout was based primarily on a program to develop an integrated planar photodiode array that was significantly more reliable than any existent reader. The program tape had an end-of-tape word that, when sensed, stopped either the forward or reverse search mode. The end-of-tape word was repeated three times; hence, a forward or reverse search command issued in the same direction after the word was first sensed could cause the program tape to unwind off the tape spool. The corrective action to minimize program impact was to repeat the end-of-tape word many times, which would make unwinding the tape from the tape spool almost impossible.

DEVELOPMENT

Developmental tests were performed to provide data that were used to support the design of a specific component or subassembly. Developmental tests were also used to determine operating characteristics under off-design conditions. In conjunction with the general thermal design, developmental tests were performed on the equipment in a simulated thermal environment to ensure that the thermal requirements had been satisfied. Developmental tests were categorized as design-feasibility tests and design-verification tests.

The design-feasibility tests included all tests performed for the following purposes:

1. Selection of components and parts

2. Investigation of the performance of breadboard models, components, and subassemblies under various environmental conditions

3. Selection of materials

4. Substantiation of safety margins or of other analytical assumptions

The design-verification tests were performed on two production models in simulated ground and flight environments and under off-design conditions to determine whether the design would meet mission requirements. The equipment was subjected to numerous environmental conditions. No replacement of parts, adjustments, or maintenance was permitted during design-verification testing. Successful completion of these tests, excluding overstress, was a prerequisite to the start of qualification tests.

QUALIFICATION

Qualification tests were performed on two production units to demonstrate attainment of design objectives, including margins of safety. The qualification test was performed in two separate phases: (1) the design-limit test (equipment subjected to test-sequential, singly applied environments at design-limit conditions), and (2) the endurance test (equipment subjected to one operational cycle and one subsequent mission cycle at nominal mission conditions).

Program Reader Assembly

The PRA, part number LSC-300-72, had the following physical parameters: weight, 6.24 kilograms (13.75 pounds); length, 24.64 centimeters (9.7 inches); width, 13 centimeters (5.12 inches); and height, 17.8 centimeters (7.0 inches). The PRA was subjected to the qualification test in accordance with the test plan (Certification Test Requirement (CTR) LCQ-300-005). Each of the qualification-test programs (design limit and endurance) was successfully implemented in accordance with the applicable specified requirements and was approved with no deviation or waiver requested or issued. Data generated during the performance of the qualification-test programs indicated that each PRA successfully completed all the requirements specified for operation and performance during acceptance testing with no waivers or deviations.

Power Distribution Assembly

The PDA, part number LDW-390-28153-1, had the following physical parameters: weight, 4.08 kilograms (9 pounds); length, 64.77 centimeters (25.5 inches); width, 17.15 centimeters (6.75 inches); and height, 19.68 centimeters (7.75 inches). The PDA was subjected to the qualification test in accordance with test plan LTP-390-15 (CTR LCQ-390-015).

The test article was initially configured with a polyurethane collar between the circuit breaker panel and the main assembly of the PDA. The purpose of the collar was to provide vibration isolation to the MS-type circuit breakers. After the successful completion of these tests, data from the lunar test article 3 (LTA-3) vibration test indicated that significantly lower vibration levels should have been used. Testing at the lower vibration levels indicated that the vibration isolation provided by the polyurethane collar was not required. In consideration of the potential fire hazard of polyurethane and of the reduced vibration levels, the polyurethane collar was eliminated, the circuit breakers were hard mounted, and the PDA was successfully tested in a supplemental qualification test.

Program Coupler Assembly

The PCA, part number LSC-300-710-5, had the following physical parameters: weight, 23.59 kilograms (52 pounds); length, 70.49 centimeters (27.75 inches); width, 13.018 centimeters (5.125 inches); and height, 19.05 centimeters (7.5 inches). The PCA was subjected to the qualification test in accordance with test plan LTP-303-20 (CTR LCQ-300-004).

A number of relay failures occurred on the qualification endurance assembly. These were of two types: shorts to case caused by contaminants (tipoff pin) inside the relay case and shorts to case caused by the diode leads.

The changes incorporated into the high-reliability-type relay to prevent these kinds of failures were as follows:

1. A new tipoff pin was used that had a head large enough to prevent it from dropping into the relay case.

2. Two layers of insulating Mylar were put on the coil-diode assembly to prevent possible shorts of diodes to the case.

3. Different assembly techniques were applied to the coil-diode unit, and more rigid inspections were used to eliminate any possibility of an internal diode in the relay shorting to a coil.

It was recommended that the PCA be requalified because of the relay failures that occurred during the qualification test. The requalification testing was consistent with the requirement not to jeopardize the status of the particular PCA unit as a flight spare. The requalification or delta-qualification test was aborted on the first start because of two relay failures, one of which could not be explained. The second attempt at the delta-qualification test was completed with one failure (attributed to contamination). The delta-qualification test was abbreviated to preserve the flight integrity of the particular PCA unit. It should be noted that there was never a functional failure of this particular PCA unit; that is, there was never a failure of a redundant relay and a primary relay that caused the loss of a function. Therefore, the decision was made that this particular unit was flight qualified.

Digital Command Assembly

The DCA, part number 380-0050, had the following physical parameters: weight, 6.24 kilograms (13.75 pounds); length, 29.85 centimeters (11.75 inches); width, 17.15 centimeters (6.75 inches); and height, 17.78 centimeters (7.0 inches). The DCA was subjected to the qualification test in accordance with test plan LTP-4614-11 (CTR LCQ-380-005).

Each of the qualification-test programs (design limit and endurance) was completed; however, three failures occurred during these tests. These failures were related in nature and were traced to a workmanship problem that involved (1) an open weld connection (discovered during vibration testing) and (2) a loose cordwood (a potted module) that caused breakage of interconnecting leads (also discovered during vibration testing). The vibration spectrum exceeded the specification levels except for a small portion in the high-frequency region. However, the test levels always remained above the actual LTA-3 vibration levels, which were used to check validity of requirements. After the two qualification models were modified, no further deviations were necessary, and the tests were successfully completed.

RELIABILITY AND QUALITY CONTROL

A reliability and quality-control program was established for the LMP in accordance with NASA publications NPC-200-2 and NPC-200-3. The implementation of this program included inspections and testing to determine conformance of the system to contractual and specification requirements before submission of the article to NASA for acceptance. Identification and traceability were controlled in accordance with the approved quality-control program. Quality-control procedures were also implemented to ensure interchangeability, as required. A reliability program was also implemented in accordance with NASA reliability publication NPC-250-1 and the LM-contractor-approved reliability program plan (LPL-550-1).

MISSION PERFORMANCE

The LMP performed all required functions throughout the Apollo 5 mission (the only mission on which a complete LMP, as previously described, was flown). From lift-off until 06:10:00 ground-elapsed time (GET), the LM was operated in the primary mode with the LGC in control. At 06:10:00 GET, the backup mode was activated. In this mode, the LMP controlled all sequencing. Sequences III and V were used. Periodically throughout the mission, the ground-command capability was used; and, except for periods of abnormal signal strength, performance was nominal. Abrupt changes of approximately 34 decibels in spacecraft-received uhf-signal strength were detected throughout the mission. These abrupt changes in received power frequently caused the command signal to be below the message-acceptance threshold. Corresponding changes did not occur in the ground-received signal strength from the vhf data transmitters that shared the same antennas through a diplexer. Consequently, command transmission had to be delayed or repeated. The variations in received signal power were consistent with an intermittent condition in the DCA radiofrequency stage, in the coaxial-cable assembly connecting the diplexer and DCA, or in the internal diplexer connections.

On subsequent missions (Apollo 9 and 10), a modified LMP was used. The Apollo 9 LMP consisted of the DCA and the ascent-engine arming assembly (AEAA). The AEAA permitted the ascent engine to be armed and to be fired to fuel depletion after ascent-stage separation from the CSM. The Apollo 10 LMP consisted of the digital uplink assembly, which replaced the DCA, and an AEAA of a different configuration. This AEAA performed the same function on the Apollo 10 mission that the AEAA did on the Apollo 9 mission. In addition, it contained a provision for switching the guidance from the PGNCS to the abort guidance system after the ascent engine was started for the burn-to-depletion maneuver.

CONCLUDING REMARKS

Data from the design-verification test, the qualification test, and the subsequent vehicle tests as well as data from the mission show that the lunar module mission programer fulfilled all design requirements.

After qualification testing, the program reader assembly had one anomaly that might warrant one minor design change if the unit were to be redesigned. The program tape had an end-of-tape word that, when sensed, stopped either the forward or reverse search mode. The end-of-tape word was repeated three times; hence, a forward or reverse search command issued in the same direction after the word was first sensed could cause the program tape to unwind from the tape spool. The corrective action to minimize program impact was to repeat the end-of-tape word many times so that it was almost impossible to unwind the tape from the spool. If the unit is redesigned, a more positive end-of-tape sensor should be incorporated.

The program coupling assembly was plagued with relay problems from the beginning of the program. Many of the problems were a direct result of contamination inside the sealed relay can; others were unexplained problems in that no contamination or other causes of failures were ever found.

Each relay contained two directional diodes and was half-crystal can size. Therefore, the relay complexity was greatly increased. Two recommendations for redesigning the relays are that (1) the switching matrix should be a solid-state device and (2) the directional diodes should remain outside the relay can if the relay is to be used in the switching matrix.

Lyndon B. Johnson Space Center
National Aeronautics and Space Administration
Houston, Texas, September 9, 1974
914-50-00-00-72

NASA-Langley, 1975 S-414

"The aeronautical and space activities of the United States shall be conducted so as to contribute . . . to the expansion of human knowledge of phenomena in the atmosphere and space. The Administration shall provide for the widest practicable and appropriate dissemination of information concerning its activities and the results thereof."

—NATIONAL AERONAUTICS AND SPACE ACT OF 1958

NASA SCIENTIFIC AND TECHNICAL PUBLICATIONS

TECHNICAL REPORTS: Scientific and technical information considered important, complete, and a lasting contribution to existing knowledge.

TECHNICAL NOTES: Information less broad in scope but nevertheless of importance as a contribution to existing knowledge.

TECHNICAL MEMORANDUMS: Information receiving limited distribution because of preliminary data, security classification, or other reasons. Also includes conference proceedings with either limited or unlimited distribution.

CONTRACTOR REPORTS: Scientific and technical information generated under a NASA contract or grant and considered an important contribution to existing knowledge.

TECHNICAL TRANSLATIONS: Information published in a foreign language considered to merit NASA distribution in English.

SPECIAL PUBLICATIONS: Information derived from or of value to NASA activities. Publications include final reports of major projects, monographs, data compilations, handbooks, sourcebooks, and special bibliographies.

TECHNOLOGY UTILIZATION PUBLICATIONS: Information on technology used by NASA that may be of particular interest in commercial and other non-aerospace applications. Publications include Tech Briefs, Technology Utilization Reports and Technology Surveys.

Details on the availability of these publications may be obtained from:

SCIENTIFIC AND TECHNICAL INFORMATION OFFICE

NATIONAL AERONAUTICS AND SPACE ADMINISTRATION

Washington, D.C. 20546

-7950

NASA TECHNICAL NOTE

NASA TN D-7950

NASA TN D-7950

APOLLO EXPERIENCE REPORT - SAFETY ACTIVITIES

Charles N. Rice

Lyndon B. Johnson Space Center
Houston, Texas 77058

NATIONAL AERONAUTICS AND SPACE ADMINISTRATION • WASHINGTON, D. C. • APRIL 1975

1. Report No.	2. Government Accession No.	3. Recipient's Catalog No.
NASA TN D-7950		

4. Title and Subtitle	5. Report Date
APOLLO EXPERIENCE REPORT SAFETY ACTIVITIES	April 1975
	6. Performing Organization Code JSC-05864
7. Author(s) Charles N. Rice	8. Performing Organization Report No. JSC S-422
9. Performing Organization Name and Address Lyndon B. Johnson Space Center Houston, Texas 77058	10. Work Unit No. 039-00-00-00-72
	11. Contract or Grant No.
12. Sponsoring Agency Name and Address National Aeronautics and Space Administration Washington, D.C. 20546	13. Type of Report and Period Covered Technical Note
	14. Sponsoring Agency Code

15. Supplementary Notes

16. Abstract

This paper describes the flight safety experiences gained during the Apollo Program and discusses safety from the viewpoint of program management, engineering, mission planning, and ground test operations. Emphasis is placed on the methods used to identify the risks involved in flight and in certain ground test operations; in addition, there are discussions on the management and engineering activities used to eliminate or reduce these risks.

17. Key Words (Suggested by Author(s))	18. Distribution Statement
• Flight Safety • Safety Management • Hazards • Trade-Off Studies • Mission Risk Assessment • Manned Flight Awareness Program • EVA Safety Assessment	STAR Subject Category: 12 (Astronautics, General)

19. Security Classif. (of this report)	20. Security Classif. (of this page)	21. No. of Pages	22. Price*
Unclassified	Unclassified	18	$3.25

*For sale by the National Technical Information Service, Springfield, Virginia 22151

CONTENTS

APOLLO EXPERIENCE REPORT

SAFETY ACTIVITIES

By Charles N. Rice
Lyndon B. Johnson Space Center

SUMMARY

The success of the United States manned space-flight program has been, to a great extent, a direct result of the emphasis placed on safety by NASA management. The reorganization of the NASA Lyndon B. Johnson Space Center (formerly the Manned Spacecraft Center) safety efforts after the Apollo spacecraft 204 fire was necessary for a concerted safety effort. All the relevant safety activities were coordinated through a single office and resulted in a strong, centralized approach to crew and mission safety. The establishment of a formal documented hazard analysis for each mission was effective in identifying significant hazards and assuring satisfactory resolution of hazards at an appropriate high level in the Lyndon B. Johnson Space Center organization.

A safety program requires an adequate complement of qualified engineers, a free hand to conduct independent assessments, and the full support of top management. With these ingredients, an effective safety program is assured.

The Manned Flight Awareness Program introduced early in the Apollo Program was a motivational program to achieve a high level of safety, reliability, and quality consciousness of all program participants. Its success was greatly enhanced by astronaut participation.

INTRODUCTION

The success of the United States manned space-flight program has been, to a great extent, a direct result of the emphasis placed on safety by NASA management. The basic safety objective has been to identify hazards and to ensure that these hazards are either eliminated or reduced to an acceptable level. With the exceptions of the Apollo spacecraft (SC) 204 fire and perhaps the Apollo 13 mission, the hazards had been adequately identified and properly resolved. Throughout the series of manned space-flight programs (Mercury, Gemini, and Apollo), the safety of the crew was given primary consideration during hardware design, manufacturing, testing, mission planning, and flight operations.

The purpose of this paper is to summarize the safety-oriented activities of personnel at the NASA Lyndon B. Johnson Space Center (JSC) (formerly the Manned Spacecraft Center (MSC)) and at major contractor plant sites. Although everyone is expected to be safety conscious, some things that are inherently unsafe under certain conditions are not easily recognized. The identification of hazards requires a dedicated and conscious effort by appropriately trained safety personnel who possess the experience and capability to properly assess the risks throughout all phases of the manned program and to take appropriate action to eliminate or reduce the risks to an acceptable level.

During Project Mercury, the Gemini Program, and the early stages of the Apollo Program, a Flight Safety Office at MSC reported to the Center Director. The function of this office was to coordinate the overall safety effort at NASA and the major contractors. It had a small staff and acted in an advisory capacity to each program office. Throughout Project Mercury and the Gemini Program, crew safety and mission safety activities were carried out by the Flight Safety Office, the responsible program offices, and the engineering and other support groups at both NASA centers and major contractors. This method worked well because the groups were small enough for the individuals to maintain good communications, were personally known to each other, and had a broad view of the requirements so that the safety efforts were well integrated.

As the Apollo Program progressed from design definition to hardware fabrication, substantial numbers of new personnel were added to the program, numerous reassignments of personnel were made, and functional reorganizations were implemented over a period of months. Coupled with these changes, the hardware testing phases brought added activity, and the resolution of test hardware failures absorbed more and more time. During this period, the size and technical makeup of the Flight Safety Office did not grow sufficiently to maintain visibility into the rapidly expanding Apollo Spacecraft Program hardware and procedures activities. All the above resulted in some loss of communication and visibility between the Flight Safety Office and the engineering and test operational elements.

After the Apollo SC-204 fire, one of the organizational changes made at MSC grouped most of the Center safety organizations into the Flight Safety Office reporting directly to the Center Director. Another change was the creation of a staff position in the Apollo Spacecraft Program Office (ASPO) as the MSC point of contact with the Apollo Systems Safety Office at NASA Headquarters. This staff position, called the ASPO Assistant Program Manager for Flight Safety, was a position designed to expedite implementation of the MSC Flight Safety Office policies and procedures. This provided a good opportunity to integrate the efforts of the MSC Flight Safety Office and the ASPO flight safety activities. The arrangement worked very well by opening up the communications channels between the various groups working different aspects of flightcrew and mission safety. At the same time, several reliability and quality assurance elements at MSC were also combined into a single office reporting directly to the Center Director. Although these changes in the reliability and quality assurance (R&QA) organizations did not directly affect the Flight Safety Office, they had the indirect effect of making available, on a day-to-day basis, data and information that were essential to Flight Safety Office personnel in performing their tasks. This interchange and coordination was aided by placing both organizations under the direction of one person.

A further enhancement of the MSC Flight Safety Office capabilities occurred in late 1967 when additional support (contract) manpower was made available to the Flight Safety Office; this support consisted of experienced engineers trained in safety techniques and procedures. The local MSC group was part of a larger contract covering engineering and safety at MSC, NASA Headquarters, and the other NASA centers involved in the manned space-flight effort; thus, a large reservoir of experienced engineering talent was available to provide assistance when required. These changes, both organizational and personnel, were sufficient to reestablish a planned, orderly, and coordinated approach to crew and mission safety.

THE MSC SAFETY OFFICE ACTIVITIES

Evolution of Systems Safety Discipline

Under the new organization previously described, the MSC Safety Office activities were defined as follows.

1. To examine all phases of each mission for hazards (i.e., flight plans, crew procedures, mission rules, design changes, contingency plans, training, etc.)

2. To examine all mission-related ground activities that involved the flightcrews and backup crews for hazards (i.e., extravehicular-activity (EVA) procedures, crew training, ground test and checkout, simulated flight tests, vacuum chamber tests, recovery training, etc.)

3. To assure that hazards identified in items (1) and (2) were appropriately resolved for future missions and ground operations (Resolution of hazards was to be accomplished through normal channels used to implement the Apollo Spacecraft Program.)

As a part of the foregoing effort, the safety offices of the major contractors were strengthened to ensure the proper integration of their own and their subcontractors' safety efforts. The MSC did not require that the subcontractors institute a dedicated safety office; it was considered that the responsibility for safety should rest with the major contractors who would eventually receive the hardware/software from the subcontractors. In this manner, the major contractors maintained an overall safety effort with their own safety staffs. The approach proved acceptable.

The Safety Office personnel conducted their duties by active participation in design reviews, test procedure reviews, and the development of crew procedures. As safety issues were identified, they were resolved immediately or were presented to the ASPO for resolution at scheduled meetings and milestone reviews. Typical reviews that safety personnel participated in are as follows:

1. Configuration Control Board
2. Configuration Control Panel
3. Preliminary Design Review
4. Critical Design Review
5. Design Certification Review
6. Customer Acceptance Readiness Review
7. Flight Readiness Review
8. Crew Procedures Change Board
9. Mission Rules Review
10. Launch Readiness Review

The ASPO and the MSC directorates involved in the Apollo Spacecraft Program provided adequate forums for formal discussion by the MSC Safety Office of any hazards that required attention. This management visibility in depth, operating in an atmosphere that encouraged personnel with problems to come forth and be heard, was a major contributing factor in enhancing the safety of the Apollo missions. In addition to these meetings and milestone reviews, the MSC Safety Office presented formal analyses and assessments of systems safety and mission risks to the ASPO and to the Center Director at each mission Flight Readiness Review. At that time, the Mission Hazard Analysis (refer to the appendix), which identified safety concerns as well as the rationale for acceptance of the risks, was documented for the Flight Readiness Review Board.

Hazardous and Critical Tests

The MSC flight safety engineers participated with teams composed of specialists from varying disciplines in reviewing the development and installation of facilities, test procedures, and special safety procedures to support hazardous test activities at MSC. Chief among these were the thermal-vacuum tests conducted in the Space Environment Simulation Laboratory in which manned spacecraft modules were subjected to simulated space environments in vacuum chambers. Safety personnel were concerned with the safety of test personnel and test subjects. They assessed and evaluated the safety of the chambers including the associated plumbing, wiring, evacuation systems, environmental control systems, and pressure vessels. Detailed and thorough operational readiness inspections and test readiness reviews were conducted before commencement of manned tests. Safety personnel had key roles in these tasks and in the development of safety parameters and their limits for use in manned testing. Certified test safety officers participated in the manned tests to ensure adherence to these established parameters and limits.

System Safety Assessments

System safety assessments consisting of hazard analyses and special safety studies of Apollo contractor-furnished equipment, Government-furnished equipment, ground support equipment, and experiments were performed. These assessments were accomplished by (1) analyses of ground support equipment to determine interfaces with flight hardware that could adversely affect crew safety; (2) performance of detailed evaluations in those design and operational areas shown to exhibit risk potential; (3) performance of or participation in hazard trade-off studies of designs, operational procedures, and mission concepts; and (4) detailed analyses of those proposed changes to subsystems, operational procedures, plans, rules, and activities considered to have safety impact.

To aid in the safety analysis of extremely complex systems, "fault-tree" analyses were conducted. These were logic diagrams that represented the mechanical, electrical, and/or chemical interfacing points between subsystems. The analyses were a valuable tool in identifying potential hazards.

In the Apollo Program, hazard analyses were performed for man/machine interface to isolate crew safety concerns. Trade-off studies and engineering assessments for compliance with system safety criteria were performed relating to crew safety, operational personnel safety, and system safety. Trade-off studies were also performed for specific hardware and operational areas, so that the relative crew risks for any of several alternative solutions might be compared.

Operational safety assessments were performed on crew procedure changes, flight plans, mission rules, crew checklists, and crew training to ensure adequacy and compatibility of crew procedures and flight operations for each Apollo mission. Hazardous procedures were identified and recommendations were made to reduce the risk by modification of the existing procedures. The review of operational tasks resulted in procedure change requests, special studies of potential operational concerns, safety evaluation of mission operations, and documentation of crew and mission operational hazards.

Safety evaluations of flight hardware consisted of (1) assessment of the configuration differences between vehicles to determine whether system or subsystem changes had introduced any new hazards into the vehicle; (2) review of waivers or deviations of specifications in manufacturing, test, or checkout procedures; and (3) sneak circuit analyses (SCA) of wiring systems to detect potential hazards from wiring or electrical system incompatibilities. A sneak circuit is a latent electrical path that can cause an unwanted function to occur or inhibit a desired function without regard to component failures. The SCA was first used on the Apollo 7 spacecraft and was performed for all subsequent spacecraft of the Apollo Program, both the LM and the CSM.

Mission Risk Assessment

Concurrent with the effort to provide system safety assessments, each individual mission was analyzed as an integral unit in an effort to isolate and assess risks to mission operations and crew safety. Once a hazard was identified and evaluated, it was brought to the attention of program management. It was then tracked throughout the mission preparation period until corrected by an engineering or procedural change (usually a decision of the Configuration Change Board or Panel) or approved by the Safety Office and the ASPO as an acceptable risk.

Periodic meetings were held with the safety personnel of the major contractors to discuss and evaluate hardware and operational problems that might have potential crew safety impact. The reports emanating from these meetings provided an up-to-date status of safety concerns under evaluation and of safety issues to be resolved. A safety concern was a specific hazard requiring positive action to correct; a safety issue was a potential hazard, the implications of which had not been completely resolved. The status report was forwarded to the ASPO and to the R&QA organizations which, in periodic meetings with safety personnel, considered each safety concern for proper resolution.

A mission risk assessment was performed for each Apollo mission to provide a final and definitive evaluation of residual hazards and risks affecting the crew. The mission risk assessment supported the Flight Readiness Review at MSC. This report highlighted the more significant crew safety risks assessed during the mission buildup period, the results of analyses of these risks, and supporting rationale for acceptance of residual hazards, where appropriate. A portion of the Apollo 16 Mission Risk Assessment is included in the appendix.

Mission Monitoring and Postflight Evaluation

The work described in previous paragraphs dealt with preflight safety activities. However, the responsibility of the MSC Safety Office did not end with the launch of an Apollo mission. Mission monitoring support was provided to enable real-time safety engineering support in the assessment and evaluation of mission discrepancies and identification of hazardous trends that might have a potential impact on crew safety or mission success. Continuous monitoring of flight hardware and the flightcrew made possible the identification of real or potential safety hazards. Recommendations for the resolution or elimination of these hazards were routed through the Spacecraft Analysis Network (SPAN) for verification by the appropriate subsystem monitor, and to the Mission Control Center for final approval and implementation by the Flight Director.

The Safety Office further participated in the postflight review of failures and anomalies associated with system performance or crew procedures that had safety implications on succeeding missions. Any such failure or anomaly was examined at the appropriate contractor's plant to make a determination of the actual cause. When such a determination was made, the suspect part or procedure for each succeeding mission was reevaluated, redesigned, retested, rewritten, or eliminated.

Audits

To ensure that the safety requirements were being met and that continued emphasis was being placed on system safety by all participants, periodic audits were performed by the MSC Safety Office at major contractor production, assembly, checkout, and test facilities. The contractors were required to develop system safety checklists that detailed those steps introduced in their facilities to ensure adherence to the safety requirements. The checklists were used by MSC Safety Office personnel at the contractor facilities to provide on-the-spot assurance that the requirements were actively implemented.

Motivational Programs

To achieve a high level of safety, reliability, and quality consciousness in all program participants, it became evident that a singular motivational program was required. People tend to think of safety, reliability, and quality as abstract terms; the problem was to make that abstraction real, tangible, and relatable and then to keep the awareness of these important functions as an active effort constantly before them.

The Manned Flight Awareness Program was introduced early in the Apollo Program to fill this need. The cooperation of a popular cartoonist was solicited to make his comic beagle "Snoopy" (from the cartoon strip "Peanuts") the principal spokesman for the program. Motivational posters featuring Snoopy in space togs were soon in evidence wherever people were at work on the Apollo Program. The Snoopy messages constantly emphasized the need for care and attention to detail.

The astronauts contributed to the success of the program. They attended functions at each of the space-flight centers, honoring contributors to the program by presenting Snoopy pin awards. Apollo crewmen toured the facilities of the major contractors to meet the workers who were building and testing the Apollo mission hardware.

Special Studies and Assessments

As the Apollo Program matured and progressed, missions became longer and more complex. The NASA began to take optimum advantage of lunar surface exploration through the use of more sophisticated experiments packages and of the command and service module (CSM) lunar orbits by incorporation of experiment hardware in a bay of the service module. Each element of growth contained potential crew hazards, and each was the subject of a special safety assessment by the MSC Safety Office. The principal special assessments are discussed in the following paragraphs.

Extravehicular activities. - The Apollo Program included a wide variety of EVA's beginning with Apollo 9 when the lunar module (LM) pilot first stepped out of the LM while in Earth orbit. The first Apollo EVA safety assessment (conducted before the mission) resulted in a listing of 10 criticality 1 hazards, each of which had to be analyzed to determine its probability of occurrence. Each potential hazard was finally deemed improbable after a lengthy rationale was prepared, which reinforced confidence in the hardware design and testing. None of the following 10 potentially hazardous events occurred.

1. Ventricular fibrillation in the LM pilot could occur.

2. Collision with the spacecraft might rupture the pressure garment assembly (PGA).

3. The EVA astronaut might lose contact with and attachment to the spacecraft.

4. The EVA astronaut might have a failed portable life-support system/oxygen purge system (PLSS/OPS).

5. Undetected carbon monoxide might be present in the EVA astronaut PGA.

6. The open failure of the oxygen purge system (OPS) might cause a rupture in the PGA.

7. The EVA astronaut rescue capability might not be immediately available.

8. The OPS redundancy might be lost.

9. Degradation of the OPS would leave only marginal contingency EVA capability.

10. Loss of the LM attitude control might render the LM unstable and would make recovery difficult.

In a similar manner, the first lunar surface EVA on Apollo 11 was analyzed before the mission, and this analysis isolated the following 11 potentially hazardous areas of concern. The Safety Office prepared recommendations for the elimination or reduction of these potential hazards and forwarded them to the appropriate organizations for consideration. Most of the recommendations were accepted.

1. Pyrophoric reaction of lunar material with the LM oxygen atmosphere might occur.

2. A rupture of the lunar contingency sample container might occur in the cabin.

3. Damage to the extravehicular mobility unit (EMU) might occur if a crewman were to fall on the lunar surface.

4. Crewmen might be unable to detect the presence of sinkholes, deep dust pits, or subsurface faults.

5. Because of scratching or tearing on spacecraft protuberances, a compromise of the EMU pressure, thermal, or radiation integrity might occur.

6. Inability of the crewmen to obtain adequate footing on the plus-Z footpad could be caused by dust or debris acquired at landing.

7. Inability to determine the temperature of tools, equipment, et cetera, could result in damage to the EMU upon touch.

8. A fallen crewman might be unable to recover and return to the LM before the loss of EMU consumables.

9. Crewmen ingress or egress could be difficult when the plus-Z footpad is not in contact with the lunar surface.

10. Deployed television camera cable and S-band antenna cables could pose a tripping hazard to crewmen.

11. The crewman inside the LM might be unable to observe the egressing crewman.

Apollo lunar surface experiments.- Apollo 11 carried a comparatively simple package of scientific hardware for deployment on the lunar surface. These experiments, however, had some inherent potential hazards that were assessed before the flight. Of major concern was the fuel capsule for the radioisotopic thermoelectric generator used to supply power to the Apollo lunar surface experiments package. The capsule used plutonium-238 as its isotope, and the inadvertent release of this radioactive substance was a matter of great concern. The capsule was subjected to analysis by the Safety Office and representatives of the Atomic Energy Commission who concluded that the device was safe to use when used according to the prescribed procedures. To illustrate the thoroughness of this assessment, consideration was given to the possibility that the fuel capsule might be returned to the Earth atmosphere in the event of a mission abort. The analysis concluded that the capsule, as designed, was adequate to survive reentry and would release no radioactivity. This conclusion proved correct when the Apollo 13 mission aborted and the LM (which had served as a "lifeboat" for the astronauts when the CSM was partly disabled) reentered the Earth atmosphere and broke up over the Pacific Ocean. The fuel capsule was still on board and, as predicted by the preflight analysis, did not contaminate the atmosphere with radioactive material.

Other significant studies.- Other significant studies made between 1969 and 1972 included a system safety engineering hazard analysis of the LM pyrotechnics and the CSM launch vehicle separation pyrotechnics (Feb. 1969), a LM-6 critical switch study (Sept. 1969), a CSM circuit breaker accessibility study (Sept. 1969), a LM circuit breaker review (Sept. 1969), a study of crew distractions during critical mission phases (Feb. 1970), a system safety assessment of the Apollo 12 anomalies and of the failure mechanism during the initial boost phase (Feb. 1970), a study of the active seismic experiment (Aug. 1970), a study of the CSM return enhancement provisions (Dec. 1970), and a study of the lunar seismic profiling experiment (Dec. 1972).

CONCLUDING REMARKS

The success of the United States manned space-flight program has been, to a great extent, a direct result of the emphasis placed on safety by the management of the NASA Lyndon B. Johnson Space Center (formerly the Manned Spacecraft Center). The basic safety objective has been to identify hazards and to ensure that these hazards are either eliminated or reduced to an acceptable level. With the exception of the Apollo spacecraft 204 fire and perhaps the Apollo 13 abort, the hazards have been adequately identified and properly resolved.

The reorganization of the NASA Headquarters and Lyndon B. Johnson Space Center safety efforts after the spacecraft 204 fire was necessary for the complex and expanded efforts of the Apollo Program. A greatly enhanced Safety Office visibility and comprehension of day-to-day safety status resulted in the reestablishment of a satisfactory approach to crew and mission safety. The fundamental change in organization that proved most effective was gathering the safety efforts under a single office that reported to the Center Director.

The establishment of formally documented hazard analyses for each mission was effective in identifying all significant hazards and assuring a satisfactory resolution of hazards at an appropriately high level in the center organization.

A safety program requires an adequate complement of qualified safety engineers, a free hand to make independent assessments, and the full support of management. With these ingredients, an effective safety program is assured.

The Manned Flight Awareness Program, introduced early in the Apollo Program, was a motivational tool used to achieve a high level of safety, reliability, and quality consciousness in all program participants. Its success was greatly enhanced by astronaut participation.

Lyndon B. Johnson Space Center
National Aeronautics and Space Administration
Houston, Texas, November 14, 1974
039-00-00-00-72

APPENDIX

APOLLO 16 MISSION RISK ASSESSMENT

EXCERPTS AND SUMMARIES

The following pages have been extracted as typical examples of the Apollo 16 Mission Assessment Report.

"1.2 PURPOSE

The purpose of this assessment is to define and evaluate the risks associated with the Apollo 16 flight and lunar surface activities, to provide justification for discounting or accepting these risks, and to present an overall picture of the mission relative to crew safety.

"1.3 SCOPE

This document is limited to the presentation of the assessment of the Apollo 16 mission as related to flight crew safety from lift-off through earth landing. The assessment included analysis of each mission phase, including procedures, configurations, and potential impact of previously-observed anomalies on flight crew safety. This document applies to the MSC Flight Readiness commitments. Subsequent anomalies are evaluated on a day-to-day basis up to the launch time and are incorporated into this document as required.

"1.4 CONCLUSIONS

1.4.1 The new risks introduced into the Apollo 16 mission are acceptable and provide no flight constraints.

1.4.2 Assessment of the planned lunar surface activities, including the longer EVA's, longer traverses, and delta lunar surface experiments has uncovered no safety concerns which preclude the lunar activities or any planned lunar surface experiments. Improvement in the active seismic experiment from Apollo 14 has increased the safety margin for Apollo 16.

1.4.3 Assessment of the rendezvous technique changes which are incorporated for Apollo 16 indicate they should minimize controllable errors in the rendezvous calculations, thus improving overall mission success and crew safety.

1.4.4 Boom retraction modification of adding proximity switches has increased safety by enabling determination if booms are sufficiently retracted before an SPS[1] burn. (See note 1 below.)

1.4.5 Planned CM[2] in-flight demonstrations have been assessed for concerns related to crew safety, and no constraining safety concerns were identified. (See note 2 below.)

Note 1. The mass spectrometer and gamma ray spectrometer experiments were extended from the SM[3] Scientific Instrumentation Module by retractable booms. It is critical to have assurance that these booms are properly retracted before attempting an SPS burn; an unretracted boom could conceivably wrap around the SPS nozzle extension. Proximity switches were added on Apollo 16 to provide the crew positive assurance of boom retraction prior to the SPS burn. In addition, a boom jettison capability was added.

Note 2. During transearth coast, Apollo 16 crew conducted the following inflight demonstrations, each requiring experiment hardware and procedures which were subjected to safety analysis:

(1) ALFMED (Apollo Light Flash Moving Emulsion Detector)

(2) MEED (Microbial Ecology Evaluation)

(3) Electrophoresis In-Flight Demonstration

(4) Biostack Experiment (M211)

1.4.6 Safety assessments of anomalies occurring during manned environmental tests, previous flights, and vehicle ground tests have disclosed no significant safety concerns.

"1.5 RECOMMENDATIONS

None.

---

[1]Service propulsion system.

[2]Command module.

[3]Service module.

"1.6 SAFETY STATEMENT APOLLO 16 MISSION

The Safety Office assessment of the planned Apollo 16 mission, spacecraft functions, and hardware failures disclosed no safety concerns which constrain the Apollo 16 flight scheduled for April 16, 1972. The assessment is based on safety analyses performed in coordination with and obtained from the Program Office, E&D, FOD, FCOD, MR&OD, SR&QA,[4] and the hardware contractors."

Section 2.0 provided a discussion of all constraining and nonconstraining safety concerns evaluated during the mission assessment. These concerns were assessed for crew safety during the period leading to the preparation of the report and were published in the MSC Safety Concerns document, released biweekly. The information included the issue, action, and status of each concern. The following list enumerates the concerns contained in the Apollo 16 Mission Assessment Report.

1. Range/range-rate meter glass shattered
2. Command and service module (CSM) criticality 1 switches
3. Gyro-display coupler aline function
4. Scratched Lexan window shade
5. Loose object in the cabin fan
6. Unexplained pressure increase in the CSM tunnel
7. Broken bacteria filter on water gun
8. Main oxygen regulator failure
9. Premature deployment of main parachute
10. Failure of docking ring to sever
11. Extravehicular glove wear
12. Command module (CM) reaction control system (RCS) fuel tank excessive delta pressure
13. Parachute reefing-line cutter

[4]Engineering and Development Directorate; Flight Operations Directorate; Flight Crew Operations Directorate; Medical Research and Operations Directorate; and Safety, Reliability, and Quality Assurance Office.

14. Entry monitor subsystem "thrust on" light

15. Pressure garment assembly qualification test failure

16. Suited or unsuited scientific instrument module door jettison

17. The CM RCS oxidizer tank bladder overpressure

18. Impact test failure of helmet

19. CSM-113 propellant utilization and gaging system anomaly

20. Trapped CM RCS propellant overpressure

21. Circuit breaker mechanical latch problem

22. Earth landing system main parachute failure

The following information is contained in the report covering item 22, which illustrates the depth at which each item (1 to 22) was considered.

"Issue - The crew verified and photographic coverage confirmed that one main parachute collapsed at an altitude of 6,000 feet during the Apollo 15 mission. Four of the six nylon risers had released their suspension-line load. Loss of one main parachute exposed the crew to higher, but acceptable, loads; however, failure of more than one parachute could result in crew loss.

"Action - An NR[5] investigation and analysis revealed the cause of main parachute collapse not to be forward heat shield, the suspension links, or the steel risers being pulled from the flower pot. The most probable cause of the anomaly was the burning raw fuel (monomethylhydrazine) being expelled during later portions of the depletion firing. This resulted in the exceeding of the parachute-riser and suspension-line temperature limits. Corrective action taken has been to change the mode 1A abort timer to 61 seconds, to design and qualify new connection links made of Inconel 718, to load propellants to achieve a slightly oxidizer-rich mixture for a possible depletion-burn purge, and to require certification of the CM to land in the water with pressurized propellants onboard. Oxidizer and parachute tests at the NASA WSTF (White Sands Test Facility) are being conducted to investigate the effects of the CM RCS dump burn depletion and purge on the parachute assemblies. Recovery procedures and training are being updated to avoid possible crew exposure to toxic propellants as a result of the single failure points of the pressurized tanks at shutdown.

---

[5] North American Rockwell Corporation, prime Apollo contractor.

"Status - The concern has been closed on the basis of:

(a) The decision to land on water with pressurized tanks and

(b) The decision to extend the mode 1Z regime. The Safety Office will continue to scrutinize the current WSTF RCS/oxidizer tests for impact."

Section 3.0 of the Mission Assessment Report contained the Flight Operations Safety Analysis. The analysis was divided into approximately nine areas with each addressing a mission phase; for example, launch through orbit insertion, lunar orbit insertion, lunar module powered descent, lunar surface activities, et cetera.

Section 4.0 defined the safety evaluation of flight hardware differences between the mission under assessment and previous missions, the waivers and deviations, and the sneak circuit analyses for the upcoming mission.

Section 5.0 covered the manned environmental ground tests pertinent to the upcoming mission performed at the Space Environment Simulation Laboratory at the MSC.

Section 6.0 subjected anomalies from previous missions to analysis. Included were numerous anomalies from the previous missions that were evaluated for safety impact; breakdown by command and service module, lunar module, and Government-furnished equipment; and the status of each with respect to the upcoming mission.

Section 7.0 was an evaluation of real-time flight problems and was not contained in the first two releases of the Mission Assessment Report; this section was added after splashdown and recovery.

NASA-Langley, 1975 S-422

ONAL AERONAUTICS AND SPACE ADMINISTRATION
WASHINGTON, D.C. 20546

OFFICIAL BUSINESS
PENALTY FOR PRIVATE USE $300

SPECIAL FOURTH-CLASS RATE
BOOK

POSTAGE AND FEES PAID
NATIONAL AERONAUTICS AND
SPACE ADMINISTRATION
451

U.S.MAIL

490 001 C1 U AL 750411 S00606HU
UNIV OF MICHIGAN
ENGINEERING LIBRARY
ATTN: MR ROBERT T FREESE
ANN ARBOR MI 48104

POSTMASTER: If Undeliverable (Section 158 Postal Manual) Do Not Return

"The aeronautical and space activities of the United States shall be conducted so as to contribute . . . to the expansion of human knowledge of phenomena in the atmosphere and space. The Administration shall provide for the widest practicable and appropriate dissemination of information concerning its activities and the results thereof."

—National Aeronautics and Space Act of 1958

NASA SCIENTIFIC AND TECHNICAL PUBLICATIONS

TECHNICAL REPORTS: Scientific and technical information considered important, complete, and a lasting contribution to existing knowledge.

TECHNICAL NOTES: Information less broad in scope but nevertheless of importance as a contribution to existing knowledge.

TECHNICAL MEMORANDUMS: Information receiving limited distribution because of preliminary data, security classification, or other reasons. Also includes conference proceedings with either limited or unlimited distribution.

CONTRACTOR REPORTS: Scientific and technical information generated under a NASA contract or grant and considered an important contribution to existing knowledge.

TECHNICAL TRANSLATIONS: Information published in a foreign language considered to merit NASA distribution in English.

SPECIAL PUBLICATIONS: Information derived from or of value to NASA activities. Publications include final reports of major projects, monographs, data compilations, handbooks, sourcebooks, and special bibliographies.

TECHNOLOGY UTILIZATION PUBLICATIONS: Information on technology used by NASA that may be of particular interest in commercial and other non-aerospace applications. Publications include Tech Briefs, Technology Utilization Reports and Technology Surveys.

Details on the availability of these publications may be obtained from:

SCIENTIFIC AND TECHNICAL INFORMATION OFFICE

NATIONAL AERONAUTICS AND SPACE ADMINISTRATION

Washington, D.C. 20546